PROCEEDINGS
of the VAK-2024 conference

300 years
Russian Academy of Sciences

MODERN ASTRONOMY:
FROM THE EARLY UNIVERSE TO EXOPLANETS AND BLACK HOLES

25-31 August 2024

SAO RAS
Nizhny Arkhyz

Special Astrophysical Observatory
of the Russian Academy of Sciences

MODERN ASTRONOMY:

FROM THE EARLY UNIVERSE TO EXOPLANETS AND BLACK HOLES

Proceedings of the VAK-2024 conference,
Aug 25–31, 2024

Edited by Yu.Yu. Balega, A.M. Cherepashchuk et al.

Moscow
RIOR
2024

UDK 52
BBK 22.6

Modern astronomy: from the Early Universe to exoplanets and black holes. Proceedings of the VAK-2024 conference, Aug 25–31, 2024 — Moscow, RIOR, 2024 (989 pp.)

ISBN 978-5-369-02160-6

Editors-in-Chief
Balega Yu. Yu., Cherepashchuk A. M.

Executive Editors-in-Chief
Kaisina E. I., Sotnikova Yu. V.

Scientific coordinators
Balega Yu. Yu., Bisikalo D. V., Churazov E. M., Korablev O. I., Makarov D. I., Malkov O. Yu., Obridko V. N., Postnov K. A., Rastorguev A. S., Samus N. N., Shematovich V. I., Shevchenko I. I., Silchenko O. K., Vlasyuk V. V., Zasov A. V., Zinchenko I. I.

Technical editors
Cherepkova Yu. V., Komarova V. N., Kudryavtsev D. O., Mikhailov A. G., Moiseeva A. V., Semenova T. A., Sotnikova Yu. V., Yakunin I. A.

Editors of the English translation
Arshinova A., Khairutdinova A. N., Kudryavtsev D. O., Sokolova T. N., Iuzhanina K. V.

Cover designer
Chmyreva E.G.

This volume contains papers based on the talks presented at the Russian Astronomical Conference VAK-2024 and comprises a wide range of astronomical and astrophysical subjects.
We are grateful to all referees for their reports that helped us improve the Proceedings of the VAK-2024 conference.

© SAO RAS, 2024
© Authors, 2024

All-Russian Astronomical Conference (VAK-2024)
"Modern astronomy: from the Early Universe to exoplanets and black holes"

The Special Astrophysical Observatory of the Russian Academy of Sciences (SAO RAS), the Sternberg Astronomical Institute of the Moscow State University (SAI MSU), and the Scientific Council on Astronomy (SCA) of the Department of Physical Sciences of the Russian Academy of Sciences have taken an initiative to hold the All-Russian Astronomical Conference VAK-2024 on all topical areas of astronomical research carried out in the astronomical institutes of the Russian Federation. The aim of the conference is to bring together experienced experts and novice researchers in different fields of astronomy, observers and theorists, to exchange the ideas and methods and to join their efforts in solving scientific challenges.

The conference was held on August 25-31, 2024 at SAO RAS (Nizhny Arkhyz, Karachai-Cherkess Republic).

KEY CONFERENCE TOPICS

- High Energy Astrophysics
- Physics of Galaxies and Cosmology
- Stars and the Interstellar Medium
- Sun, Solar System, and Space Weather
- Exoplanets
- Celestial Mechanics and Astrometry
- Astronomical Instruments and Methods
- Astronomical Databases and Information Technology
- Astronomy Education and Outreach

SCIENTIFIC ORGANIZING COMMITTEE

Balega Yu. Yu. (SAO RAS, Dr. Sci., Full Member of RAS), Co-Chairman
Cherepashchuk A. M. (SAI MSU, Dr. Sci., Full Member of RAS, Chairman of the SCA), Co-Chairman
Valyavin G. G. (SAO RAS, PhD), Deputy Chairman
Bisikalo D. V. (INASAN, Dr. Sci., Full Member of RAS)
Bykov A. M. (Ioffe Institute, Dr. Sci., Corresponding Member of RAS)
Grigoryev V. M. (ISTP SB RAS, Dr. Sci., Corresponding Member of RAS)
Zherebtsov G. A. (ISTP SB RAS, Dr. Sci., Full Member of RAS)
Zeleny L. M. (IKI, Dr. Sci., Full Member of RAS)
Ivanchik A. V. (Ioffe Institute, Dr. Sci., Corresponding Member of RAS)
Ipatov A. V. (IAA RAS, Dr. Sci., Prof.)
Ikhsanov N. R. (GAO RAS, Dr. Sci.)
Korablev O. I. (IKI, Dr. Sci., Corresponding Member of RAS)
Levshakov S. A. (Ioffe Institute, Dr. Sci.)
Marov M. Ya. (Vernadsky Institute, Dr. Sci., Full Member of RAS)
Novikov I. D. (LPI RAS, Dr. Sci., Corresponding Member of RAS)
Obridko V. N. (IZMIRAN, Dr. Sci., Prof.)

Postnov K. A. (SAI MSU, Dr. Sci., Corresponding Member of RAS)
Romanyuk I. I. (SAO RAS, Dr. Sci.)
Rostopchina-Shakhovskaya A. N. (CrAO RAS, PhD)
Samus N. N. (INASAN, Dr. Sci., Prof.)
Sakhibullin N. A. (KFU, Dr. Sci., Prof.)
Silchenko O. K. (SAI MSU, Dr. Sci.)
Stepanov A. V. (GAO RAS, Dr. Sci., Corresponding Member of RAS)
Sunyaev R. A. (IKI, Dr. Sci., Full Member of RAS)
Shevchenko I. I. (St. Petersburg State University, Dr. Sci.)
Shustov B. M. (INASAN, Dr. Sci., Corresponding Member of RAS)

CO-CHAIRMEN OF THE LOCAL ORGANIZING COMMITTEE
Kaisina E. I. (SAO RAS, PhD)
Romanyuk I. I. (SAO RAS, Dr. Sci.)

INVITED SPEAKERS
Balega Y. Y. (SAO RAS) Instrumental basis of domestic astronomy
Cherepashchuk A. M. (SAI MSU) Triumph of black holes
Karachentsev I. D. (SAO RAS) Dark and light matter in the Local Volume of the Universe
Korablev O. I. (IKI) Study of the atmospheres of Mars and Venus from spacecraft
Kovalev Y. Y. (MPIfR) Astrophysical sources of high-energy neutrinos
Larchenkova T. I. (LPI RAS) Millimetron: science and technology
Nakaryakov V. M. (SAO RAS) Magnetohydrodynamic seismology of the solar corona
Shustov B. M. (INASAN) Small Solar System bodies: scientific challenges and practical aspects
Silchenko O. K. (SAI MSU) External accretion as the basic driver of galaxy evolution
Sunyaev R. A. (IKI; Max-Planck-Institut für Astrophysik) Review of the results of the eRosita X-ray telescope on the SRG Orbital Observatory
Valyavin G. G. (SAO RAS) Extrasolar worlds: a review of the current state of exoplanet studies in Russia and the world

The conference was held in combined offline and online format.

In total, 347 reports have been presented offline and 142 online. More than 350 astronomers from various scientific institutes of Russia and some foreign countries have participated in the conference.

These proceedings contain 188 articles, the total volume of the book is almost 1000 pages. Single-blind peer review of the papers was carried out by scientific coordinators of the key conference sections along with a fairly wide pool of Russian scientists at the suggestion of the coordinators. The technical and English editing of the proceedings was carried out by the SAO RAS staff.

The organizers thank the Scientific Organizing Committee for the high scientific level of the conference, and the Local Organizing Committee and SAO RAS staff for creating the necessary conditions for its successful work.

RESOLUTION OF VAK-2024

The All-Russian Astronomical Conference 2024 "Modern Astronomy: from the Early Universe to Exoplanets and Black Holes" (with international participation) has been held on August 25–31 at SAO RAS, Nizhny Arkhyz. More than 500 researchers from 65 astronomical institutes of Russia have participated in the conference. Foreign scientists from 15 countries have also joined the event. Over 470 talks have been presented, including 347 offline and 127 online. The conference has been held at a high level of scientific and organizing activity.

The participants thank SAO RAS for the good organization and the large work that has been done.

The Conference has adopted the following resolution.

1) We note the successful implementation of the Spektr-RG space experiment as well as the work of Russian observatories on the optical follow-up of the X-ray observations. Outstanding results have been obtained.

2) We note the fundamental contribution of Soviet and Russian scientists to the discovery of black holes in the Universe:

a) creation of the theory of matter accretion onto black holes;

b) successful implementation of the domestic X-ray experiments Mir/Kvant and Granat as well as the international experiments Integral and Spektr-RG;

c) first optical identifications of X-ray binary systems and study of their optical manifestations;

d) domestic idea of a laser gravitational-wave antenna and experimental development at the Physics Department of Moscow State University and at the Institute of Applied Physics of the Russian Academy of Sciences, which formed the basis for the creation of the Laser Interferometer Gravitational-Wave Observatory (LIGO);

f) idea of intercontinental radio interferometry with ultrahigh angular resolution, proposed in the USSR in the mid-1960s.

3) We support the development of the research on high-energy neutrinos of cosmic origin carried out by the Institute of Nuclear Physics of the Russian Academy of Sciences (INR RAS) in cooperation with other organizations at the Baikal Deep Underwater Neutrino Telescope and Baksan Underground Scintillation Telescope.

4) We emphasize the importance of the introduction into observations the new instruments of the National Heliogeophysical Complex of the Institute of Solar-Terrestrial Physics of the Siberian Branch of the Russian Academy of Sciences: the Siberian Radioheliograph and the Large Solar Telescope, which together with the Gallium-Germanium Neutrino Telescope of the INR RAS will provide new breakthrough knowledge about the physics of the Sun.

5) We support the efforts of the astronomical community to create high-altitude observatories for millimeter-wave research, which will give us an opportunity to participate in interferometry with global baselines. The Conference recommends organizing a consortium of scientific institutions and industrial enterprises to create a new-generation millimeter-range telescope.

6) We note the great scientific significance and prospects of the domestic space astrophysical projects Spektr-UV, Spektr-M, and MSU-270 as well as the projects to explore the Moon and planets of the Solar system. We note the importance of the implementation of the Interhelioprobe and Arka space projects. We support the efforts of the head institutions to develop these instruments.

7) We urge for the start of the work on choosing the location, on the territory of Russia, for the installation of a modern large national optical telescope with a diameter of 4–8 meters. We support the development of domestic telescopes equipped with active and adaptive optical systems.

8) We support the efforts to conduct coordinated systematic observations of exoplanets at domestic observatories.

9) We note the high importance of the astronomical research that have significant practical importance, such as the astronomical support of the national positioning, navigation, and timing system, the creation of an astronomical segment in the planetary defense system, and the development of the national solar service.

10) We have decided to appeal to the Ministry of Science and Higher Education of the Russian Federation with a request to restore the classes of astronomy in Russian schools.

11) We support the efforts of Russian astronomers to create protected zones around the leading domestic observatories.

Co-Chairmen
of the VAK-2024 Scientific Committee,
full members of RAS

Yu.Yu. Balega

A.M. Cherepashchuk

CONTENTS

PLENARY TALKS

Cherepashchuk A.
Triumph of black holes ... 15

Shustov B.
Small bodies of the Solar system—scientific challenges and practical aspects ... 27

Valyavin G., Gadelshin D.
Extrasolar worlds: a review of the current state of exoplanet research in Russia and the world ... 39

HIGH ENERGY ASTROPHYSICS

Barsukov D., Khalyapin A.
The differential flow near by polar cap surface of neutron star in the case of inclined magnetic field ... 51

Barsukov D., Matevosyan A.
The influence of space curvature on pulsar braking indexes ... 55

Barsukov D., Morozov I., Popov A.
The influence of inclination angle on polar cap heating of J0901-4046 radiopulsar ... 59

Beskrovnaya N., Ikhsanov N.
The radius of magnetosphere and the equilibrium radius are not the same! ... 63

Bezrukov I., Gayazov I., Dyakov A., Ivanov D., Ipatov A., Kurdyubov S., Marshalov D., Melnikov A., Mikhaylov A., Olifirov V., Rakhimov I.
Observations of Giant Pulses from B0531+21 at the Institute of Applied Astronomy ... 67

Butuzova M., Gorbachev M., Guseva V., Zhovtan A., Nazarov S., Baida G., Krivenko A.
Correlation and evolution of the blazar S5 1803+784 short-term variability properties during 01.2022 – 01.2023 ... 71

Chmyreva Elizaveta Georgievna, Beskin G.
On the detection of emission near the event horizons of accreting stellar-mass black holes ... 77

Gorbachev M., Butuzova M., Pit N., Krivenko A.
The results of simultaneous TESS and multiband photometric observations of BL Lac during a high activity ... 81

Kovalev Yu. A., Zhekanis G., Kovalev Yu. Yu., Sotnikova Yu., Troitsky S., Popkov A., Plavin A., Erkenov A., Mingaliev M., Nizhelsky N., Tsybulev P., Bursov N.
Search for proton jets in blasars as possible emitters of high-energy neutrinos ... 85

Krylova N., Red'kov V.
Dirac particle in gravitational field of black hole with Newman-Unti-Tamburino parameter ... 89

Mikhailov A., Sotnikova Yu., Khabibullina M., Kudryavtsev D., Vlasyuk V., Volvach A., Mufakharov T., Kovalev Yu. A., Kovalev Yu. Yu., Popkov A., Stolyarov V., Mingaliev M., Semenova T., Kharinov M., Andreeva T., Rakhimov I., Udovitskiy R., Morozova D.
Multiwavelength variability of the blazar Ton 599 ... 93

Popov A., Barsukov D., Ivanchik A., Bobashev S.
Spectrum of positrons produced due to interaction of gamma-ray background photons with soft background photons ... 97

Trushkin S., Shevchenko A., Bursov N., Nizhelskij N., Tsybulev P.
The flaring activity of microquasars is the key to understanding the processes of accretion and generation of jet emission ... 101

Vlasyuk Valery Valentinovich, Sotnikova Yu., Volvach A., Mufakharov T., Kovalev Yu. A., Spiridonova O., Khabibullina M., Kovalev Yu. Yu., Mikhailov A., Stolyarov V., Kudryavtsev D., Mingaliev M., Semenova T., Kudryashova A., Bursov N., Trushkin S., Popkov A., Erkenov A., Rakhimov I., Kharinov M., Gurwell M., Tsybulev P., Moskvitin A., Fatkhullin T., Emelianov E., Arshinova A., Iuzhanina K., Andreeva T., Volvach L.
Multi-band variability of the blazar AO 0235+164 ... 107

Zagorulia D., Lisakov M.
Classification of jets in active galactic nuclei using machine learning ... 113

PHYSICS OF GALAXIES AND COSMOLOGY

Arkhipova N., Fedorov N.
The evolution of fields in the process of preheating in the early Universe ... 117

Chugunov I., Marchuk A.
Decomposition of distant galaxies with spiral arms ... 121

Dolgosheeva P., Makarov D.
Is the orientation of galaxies in the Local Supercluster related to its Plane? ... 127

Goradzhanov V., Chilingarian I., Demianenko M., Katkov I., Grishin K., Toptun V., Rubtsov E., Gasymov D., Kuzmin I.
Optical spectroscopy of host-galaxies of intermediate mass black holes: evolution of central black holes ... 133

Gusev A., Shimanovskaya E.
Regular distribution of star formation regions along the spiral arms and rings of disk galaxies ... 139

Karataeva G., Merkulova O.
Spectral study of peculiar galaxies ... 145

Khoperskov A., Khrapov S., Sirotin D., Zasov A.
Merging of spiral galaxies: observations and modeling ... 149

Khrapov S., Khoperskov A., Khrapov N.
Retrograde fall of intergalactic gas onto the S-galaxy: polar rings and activity of galactic nuclei ... 155

Kopylova F., Kopylov A.
Estimation of the Hubble constant from the scatter of the fundamental plane distances of groups and clusters of galaxies (71.1 ± 2.8 km s^{-1} Mpc^{-1}) ... 161

Kopylova F., Kopylov A.
Fundamental plane of groups and clusters of galaxies: distances and peculiar velocities of superclusters of galaxies on small scales ... 167

Kostiuk V., Marchuk A., Gusev A.
Analysis of corotation radii in spiral galaxies ... 171

Kozyrev K., Makarov D. I., Makarov D. D.
Mass of the Andromeda Galaxy on a scale of up to 300 kpc ... 177

Lovyagin N., Raikov A., Yershov V.
Constraints on the population of Galactic objects in the JWST UNCOVER survey catalogue ... 181

Makarov D. D., Makarov D. I., Makarova L., Kozyrev K.
The mass of the Milky Way based on the kinematics of satellites ... 187

Malinovsky A.
Supermassive binary black holes in the centers of galaxies and prospects for their observation. ... 191

Mitichkin N., Postnov K., Alexandrovich, Chekh I.
Primordial intermediate-mass binary black holes in space laser interferometers ... 195

Moiseev Yu., Sazhina O.
A strategy for wormhole search using observational astronomy ... 201

Nazarova A., Cannon J., Karachentsev I., Makarov D., Chazov M.
First results of HI survey of recently discovered close dwarf galaxies ... 207

Piotrovich M., Krasnikov S., Buliga S., Natsvlishvili T.
Accretion on a Wormhole with Monopole Magnetic Field ... 213

Raikov A., Yershov V., Lovyagin N.
Cosmological interpretation of JWST observations ... 219

Temirova A., Bursov N., Kudryashova A.
Analysis of the update sample of USS objects and search of candidates to GPS sources in the RZF survey ... 225

Vladimirova K., Makarov D., Chazov M., Makarova L.
Peculiar structure of isolated dwarf galaxy ESO 149−003 ... 229

Zasov Anatoly Vladimirovich, Zaitseva N., Saburova A.
Star formation in low brightness galaxies and in the extended gaseous disks of normal galaxies ... 233

Zhelenkova O., Parijskij Yu., Soboleva N., Temirova A.
Current status of the Big Trio search program for distant radio galaxies. New radio data ... 239

Zhelenkova O., Temirova A.
CR~J090511.74+045536.8 — a candidate for the most distant radio galaxies ... 245

STARS AND THE INTERSTELLAR MEDIUM

Abdulmyanov T.
Formation of single stars and their planetary systems, typicality of the Solar system ... 249

Aitov V., Korchagina E., Valyavin G.
Observations of magnetic white dwarfs in the Special Astrophysical Observatory of the Russian Academy of Sciences ... 256

Antoniuk O., Antoniuk K., Pavlenko E., Shugarov S., Dubovsky P.
Photometry of the outburst of the WZ Sge-type dwarf nova IK Leo in 2024 ... 260

Bayazitov R., Mashonkina L.
Modeling of the magnetic chemically peculiar star HD 188101 264
Butorina M., Dyachenko V., Beskakotov A., Mitrofanova A., Maksimov A.
The speckle interferometric multiplicity of T Tauri type stars in the Taurus-Auriga star-forming region 270
Bychkov V., Bychkova L., Madey J.
33 Lib is an analogue of Gamma Equulei? 276
Bychkov V., Bychkova L., Madey J.
About the periodic variation of the stellar magnetic fields 280
Bychkov V., Bychkova L., Madey J., Komissarova G., Metlova N.
Magnetic and photometric variability of the super-slowly rotating Ap star GY And (HD 9996) 286
Dryomova G., Dryomov V., Tutukov A.
Hypervelocity and S-type stars as possible paired components of the parent binary star in the past 290
Eretnova O., Tarasova D., Dryomova G.
The mass function of young spectroscopic binaries and stars with protoplanetary disks 296
Frol D., Khaibrakhmanov S.
Modelling the spectral energy distributions of the accretion disks of young stars with fossil magnetic field 300
Galazutdinov G.
Interstellar medium of Galaxy in the optical range 304
Ganiev J., Mirtadjieva K.
On the instabilities of small-scale oscillation modes on the background of a collapsing model of a Protogalaxy 310
Goranskij V.
Peculiarities of mass exchange between components of binary systems in the dynamic mode: V694 Mon and SS 433 314
Grigoriev S., Dyachenko V.
Frequency analysis of Gamma Doradus variables observed by TESS 320
Ikhsanov N., Beskrovnaya N., Kim V., Korol'kova O.
"Magnetospheric gate" in polars 325
Ikhsanov N., Beskrovnaya N., Kim V.
Stellar wind velocity of the massive component in the high mass X-ray binary OAO 1657−415 329
Ismailov N., Pogodin M., Kholtygin A., Adigozalzade H., Bashirova U., Kozlova O., Ivanova A.
Spectral and photometrical peculiarities of the unusual Herbig Ae star HD 179218 333
Karteyeva V., Nakibov R., Ozhiganov M., Medvedev M., Vasyunin A.
Laboratory study of the IR spectra of methane ices in the polar environment 339
Kholtygin A., Yakunin I., Ryspaeva E., Mokshin D.
A nature of the X-ray and optical emission from gamma Cassiopeia stars 343
Klochkova V., Zhuklevich G., Panchuk V.
On the kinematic state of the atmosphere within IRAS 07430+1115 system 349
Kobozeva V., Khaibrakhmanov S.
Dynamics of dust grains and small bodies in accretion disks of young stars with fossil magnetic field 355
Kondratieva T.
Evolution of non-spherical porous dust grains in galaxies 359
Korotin S., Kiselev K.
Grid of NLTE corrections for sulfur lines in the atmospheres of A–K stars 363
Krayani H., Il'in V.
Interstellar polarisation towards a region around B5 367
Kulesh M., Seleznev A.
Estimation of the dynamic masses of open star clusters 371
Mikhnevich V., Plotnikova A., Seleznev A., Carraro G.
Empirical isochrones for single and binary stars in open clusters 377
Mokshin D.
Investigation of polarized and photometric radiation of a star γ Cassiopeiae 383
Motorina E., Shimansky V., Dudnik A., Borisov N.
Determination of the dwarf novae parameters and their temporal changes 389
Nikiforov I., Sobolev P., Veselova A.
Velocities-distance optimization of the rotation model of a homogeneous flat subsystem of Galactic objects: masers 395
Nuritdinov S., Mirtadjieva K., Omonov A.
Analysis of Data on Lopsided Galaxies and Theories of Their Formation 401

Nuritdinov S., Mirtadjieva K.
Behavior of sectorial instabilities depending on the parameters of the generalized model of a self-gravitating disk 405

Orlov A., Khaibrakhmanov S.
The evolution of the fossil large-scale magnetic field in turbulent accretion disks of young stars 409

Ostashova M., Rastorguev A.
Fractality and kinetics of the stellar medium in the Solar neighborhood based on Gaia DR2 data 413

Ostashova M., Rastorguev A.
Random force distribution for fractal stellar medium in the solar neighborhood based on Gaia DR2 data 417

Panferov A., Kolotkov D., Beskin G., Karpov S., Plokhotnichenko V., Maryeva O.
Quasi-periodic pulsations in flares of UV Ceti-type stars 421

Pazukhin A., Zinchenko I., Trofimova E.
Study of the physical and chemical properties of dense clumps in several high-mass star-forming regions 425

Permyakova T., Carraro G., Kirsanova M., Ladeyschikov D., Seleznev A.
Study of clusters in the star forming region G174+2.5 431

Pirogov L., Zemlyanukha P.
Radial profiles of systematic velocities in massive protostellar cores 437

Podkuichenko D., Blinnikov S.
The impact of non-ideality effects in dense plasma on the evolution of white dwarfs 443

Podzolkova E., Melnik A.
Periodic changes in the orientation of orbits and the age of the Galactic bar 449

Prokhorov M., Zakharov A., Krusanova N., Moshkalev V., Stekolshchikov O., Tuchin M.
What changes in multi-color sky survey will be required by the transition from the ISS to ROS 455

Romanyuk I., Semenko E., Yakunin I., Moiseeva A., Kudryavtsev D., Korchagina E., Aitov V.
Evolution of large-scale magnetic fields of chemically peculiar stars 461

Shaposhnikov I.
Wolf–Rayet stars mass-loss rates determined from spectroscopic measurements of the orbital evolution for close WR + OB binary systems 467

Sharina M., Maricheva M., Acharova I., Shimansky V.
Stellar populations of extragalactic globular clusters 473

Sibgatullin A., Dodon V., Galiullin I.
An X-ray study of the dwarf nova candidate OGLE-BLG-DN-0064 using Chandra data 479

Staritsin E.
Formation of Be stars in binary systems with conservative mass exchange 485

Sultanov I., Khaibrakhmanov S.
MHD-Modeling of the molecular filament evolution with numerical FLASH code 490

Tarasov A.
Spectroscopy of B stars in the very young open star cluster IC 1805 495

Tarasova T.
Activity of symbiotic star CI Cyg between 2008 and 2012 499

Trofimova E., Zinchenko I., Zemlyanukha P., Punanova A., Henkel C.
Study of a compact source with an enhanced NH2D/NH3 abundance ratio in the S187 region 503

Zagorulia D., Beskin G.
A sphere or a disk? Accretion of gas onto isolated stellar-mass black holes 507

Zinchenko Igor, Liu S., Ojha D., Su Y., Zemlyanukha P.
Study of the high-mass star-forming region S255IR at various scales 511

THE SUN AND SOLAR SYSTEM, SPACE WEATHER

Andreeva O.
Comparison of the dynamics of coronal holes identified by two detection methods in solar activity cycles~24-25 517

Bogod V., Lebedev M., Ovchinnikova N., Ripak A., Kurochkin E.
Radio spectroscopy of the solar corona 523

Busarev V.
Asteroid activity: spectral features and probable physical reasons 529

Derteev S., Sapraliev M., Shividov N., Mikhalyaev B.
Formation of quasi-periodic oscillations in the solar corona 535

Feoktistova E., Rodionova Zh., Shevchenko V.
Morphometric parameters of fresh lunar craters ... 541

Fursyak Yu.
Longitudinal magnetic field gradients and vertical electric currents in active regions with different flare productivity levels ... 545

Gopasyuk O.
Magnetic reconnection flux in eruptive and confined solar flares ... 551

Grunskaya L., Isakevich V., Isakevich D.
Susceptibility of electromagnetic fields in the Solar System to gravitational wave effects from relativistic binary star systems ... 557

Haneychuk V.
Magnetic multipoles of the Sun from observations of the mean magnetic field ... 563

Kiselev N., Shcherbina M., Busarev V., Zhuzhulina E., Karpov N., Shein A.
Diversity and similarity of linear polarization among low-albedo NEAs: extremely high polarization of NEA 25330 (1999 KV4) ... 569

Koryagin S., Viktorov M.
Fire-hose instability of the torsional Alfven oscillation as a mechanism of plasma layering in an experimental coronal solar loop-type magnetic arch ... 573

Koynash G., Sharykin I., Zimovets I., Ivanov E., Kiselev V., Nizamov B.
Multi-wavelength observations of the impulsive C2.8 class flare producing photospheric impact at the penumbra region of the leading sunspot in NOAA 13256 ... 579

Motyk I., Kashapova L.
Morphology of average solar flares time profiles in microwave range ... 585

Nagnibeda V., Topchilo N., Kovalenko A., Rakhimov I.
The structure of the chromosphere along the northern limb of the Sun according to eclipse observations with RT-22 PRAO AKTs FIAN at a wavelength of 1.4 cm ... 589

Petrov D., Zhuzhulina E., Kiselev N.
Interpretation of polarimetric observations of hyperbolic comets ... 595

Podgorny A., Podgorny I.
Study of the physical mechanism of a solar flare using MHD modeling over an active region: the onset of an extended surface of magnetic lines passing through a chain of current density maxima ... 599

Shamsutdinova J., Kashapova L.
Recognition of solar flares in the microwave range of observations using machine learning ... 605

Sharykin I., Zimovets I.
Investigation of the dynamics of the magnetic field and vertical electric current during the precursors of the M6.5 class solar flare of June 22, 2015 using vector 135-second HMI magnetograms ... 609

Sharykin I., Zimovets I., Myshyakov I., Anfinogentov S.
Investigation of magnetic free energy dynamics in the M1.2-class complex solar flare of March 15, 2015 using the 135-second HMI vector magnetograms ... 613

Sharykin I., Zimovets I.
Photospheric disturbances and acoustic sources of the helioseismic "circular" X1.5 flare of 10 may 2022 ... 617

Shcherbina M., Busarev V.
Using UBVRI -photometry to detect signs of asteroid activity ... 623

Shcherbina M., Kovaleva D.
Gaia Data Release 3: analysis of reflectance spectra of near-Earth asteroids and Mars-crossers ... 629

Stepanov A., Zaitsev V., Kupriyanova E.
Peculiarities of the Joule dissipation in solar atmosphere ... 635

Tlatova K., Tlatov A.
Differential rotation of sunspots of different magnetic polarity ... 641

Topchilo N., Rakhimov I., Andreeva T., Peterova N., Nagnibeda V.
Prospects for observing the near-limb zone of the Sun using the radio telescopes RT-32 IAA RAS ... 647

Tsap Yu., Stepanov A., Kopylova Yu.
Electric currents in the solar corona and the kink instability of magnetic flux rope ... 653

Zhukova A., Abramenko V.
The features of the north-south asymmetry of the magnetic flux in active regions with different magnetic morphology in solar cycles 23 and 24 ... 659

Zimovets I., Sharykin I.
Statistics of magnetic energies in solar active regions of different Hale and McIntosh classes ... 665

Zimovets I., Sharykin I.
Multipoint multiwavelength observations of a near-the-limb eruptive solar flare with quasi-periodic pulsations ... 669

Zolotarev R., Shustov B.
On the parameters of encounters of NEOs with Earth ... 675

EXOPLANETS

Baluev R., Galazutdinov G., Valyavin G., Aitov V., Gadelshin D., Valeev A., Sendzikas E., Sokov E., Mitiani G., Burlakova T., Yakunin I., Antonyuk K., Vlasyuk V., Romanyuk I., Rzaev A., Yushkin M., Ivanova A., Tavrov A., Korablev O.
Doppler confirmation of TESS planet candidate TOI-1408.01: updated analysis and fitting 681

Baluev R., Sokov E.
Cleaning the TESS observations of WASP-33\,b transits from the host star photometric variability 687

Bekesov E.
Determination of the exoplanet HD 189733b atmospheric structure based on the multicolor photometric transit observations obtained with the HST and at the Caucasian Mountain Observatory 693

Fedotov A., Baluev R.
Investigation of the infrared profiles of exoplanet HD209458b secondary eclipses 698

Garmash A.
ExoClock: Up-to-date ephemerides for the ARIEL mission 704

Golubovsky M., Shaikhislamov I., Rumenskikh M.
Measurement of the metastable helium atomic rates important for astrophysical observations 710

Ibrahimov M.
Exotic red flares on stars as the observational manifestation of the asteroids in exoplanet systems 714

Ipatov S.
Migration of planetesimals and dust particles in the Proxima Centauri exoplanetary system 720

Ipatov S.
Migration of planetesimals in the TRAPPIST-1 exoplanetary system 726

Kuznetsov E., Perminov A.
Investigation of the dynamical evolution of the compact planetary system K2-72 730

Miroshnichenko I., Sharipov S., Rumenskikh M., Shaikhislamov I.
Interpretation of the Balmer-alpha line absorption in the exoplanet WASP-69\,b 736

Sharipov S., Miroshnichenko I., Shaikhislamov I., Rumenskikh M.
Simulation of the Hα absorption for the~hot~Jupiter HAT-P-32\,b 742

Shepelin A., Golubovsky M., Shaikhislamov I.
Transit absorption in the oxygen lines for constraining the atmosphere temperature of~hot~exoplanets 749

CELESTIAL MECHANICS AND ASTROMETRY

Chernetenko Yu., Pavlov S.
Orbital dynamics of the superactive comets 46P/Wirtanen and 103P/Hartley 755

Denisenko S., Petrov S.
Length of day multifractal dynamics 761

Gayazov I., Kurdubov S., Skurikhina E.
On the issues of estimating the accuracy of Earth rotation parameters 765

Ipatov S.
Exchange of meteorites between the terrestrial planets and the Moon 771

Izmailov I., Khovrichev M., Tolstoy A., Pavlov S., Bikulova D.
Detecting low signal-to-noise meteor images in the astronomical camera video stream 777

Kumakshev S., Perepelkin V.
Gravitational influence of the Moon on the Earth's poles movement 781

Kuznetsov V., Chernetenko Yu.
Determination of the mass of asteroid (16) Psyche and masses of other asteroids of the taxonomic class M by the dynamic method 787

Kuznetsov E., Safronova V., Perminov A., Vasileva M.
Formation scenarios of the young Emilkowalski asteroid family 791

Lobanova K., Melnikov A.
The influence of uncertainty in the shape of an asteroid on the estimate of perturbation magnitudes in its rotational dynamics when approaching the Earth 797

Medvedev Yu., Chernetenko Yu., Pavlov S.
On mechanisms of the outbursts activity of comets 29P and 174P 801

Melnikov A., Khovrichev M., Balyaev I., Lobanova K.
Tidal changes in the rotational state of asteroids as evolution factor of the magnitude of the Yarkovsky effect 807

Melnikov A., Lobanova K.
Perturbations in the rotational dynamics of small asteroids when approaching the Earth..... 811

Mikryukov D., Shevchenko I.
The effect of encounters with interstellar objects of planetary and substellar masses on the Solar system dynamics 817

Pavlov S., Medvedev Yu., Galushina T., Baturin A.
Accuracy of orbits of small celestial bodies obtained using different software 823

Sannikova T.
Estimation of short-period disturbances in the motion of NEAs in the presence of an inverse-square perturbing acceleration 829

Smirnov S., Gorshkov V., Scherbakova N., Movsesyan P., Petrov S.
The scientific potential of the Pulkovo velocity of GNSS-stations database: geodynamics of the East European Craton 833

Starikov K., Petrov S.
Integer phase ambiguity resolution method for absolute GLONASS observations..... 839

Vinogradova T.
Identification of a new asteroid family 3854 George in the Hungaria group..... 843

ASTRONOMICAL INSTRUMENTS AND METHODS

Afanasieva I., Murzin V., Ardilanov V., Ivaschenko N., Pritychenko M.
Large-format photodetecting system pCam6060 with a GSENSE6060BSI CMOS detector, developed at SAO RAS and optimized for photometric methods..... 847

Bolbasova L., Lukin V.
Study of astroclimate at Baikal Astrophysical Observatory..... 853

Bujakas V., Glotov M.
Precise two-stage deployment of a petal space antenna..... 857

Dzaparova I., Yanin A., Gorbacheva E., Kurenya A., Petkov V.
Liquid scintillation detector based on an acrylic sphere and silicon photomultiplier matrices..... 861

Ermakov A., Vasilkov V., Voitsik P., Kovalev Yu., Lisakov M., Kovalev Yu.
RadioAstron project: calibration of the space radio telescope during the flight in 2011-2018 in the 1.35, 6.2, 18, 92 cm bands using improved primary calibration scales 865

Fadeev E., Andrianov A., Burgin M., Popov M., Rudnitskiy A., Smirnova T., Soglasnov V.
The impact of technical constraints on the possibility of resolving the pulsar magnetosphere by observing its scintillations 869

Fokin M., Komarov V., Shaldyrvan I., Komarova V.
New panoramic camera for SAO RAS BTA..... 873

Ibrahimov M., Nalivkin M., Shugarov A.
Four-channel wide-field cluster for survey tasks and synchronous multicolor photometry 877

Ibrahimov M., Nalivkin M., Naroenkov S., Shugarov A., Ponce-Rodriguez O., Barcenas-Fonseca Z.
The new 50-cm multipurpose telescope of the Russian-Cuban Observatory..... 881

Ivanov V., Ipatov A., Rakhimov I., Andreeva T.
Measurements of the flux densities and variability of the standard flux scale ``Artificial Moon'' sources on time scales of 1–8.5 years 885

Kaygorodov P.
Tomo-V: a new tool for Doppler tomography 889

Kazantseva E., Bondarenko Yu., Marshalov D., Medvedev Yu.
Obtaining the Chandrayaan-3 lander coordinates on the lunar surface by the Doppler measurements of the transmitted signal with an Earth-based receiving system 893

Khabibullina M., Stolyarov V., Mikhailov Alexander, Kudryavtsev D., Vlasyuk V., Sotnikova Yu., Mufakharov T., Morozova D.
Methods for analyzing the light curves of the non-thermal radiation in active galactic nuclei 897

Khaikin V., Shikhovtsev A., Mironov A., Kopylov E., Khudchenko A., Nazarov G., Zemlyanukha P., Makoev G., Yao Y., Qian X.
A review of astroclimate conditions at possible locations for the Eurasian Submillimeter Telescopes (ESMT) 901

Komarov V., Shaldyrvan I., Komarova V., Fokin M.
Universal viewing camera for SAO RAS BTA 905

Kononov A., Bezrukov I., Melnikov A.
Testing the DiFX VLBI correlator in a cloud service infrastructure..... 909

Panchuk V., Klochkova V., Yushkin M., Zhuklevich G.
Challenges of high-resolution spectroscopy in the Nasmyth focuses of the BTA 913
Sergeev S., Kazakevich Yu.
Fast implementation of coherent dispersion compensation 919
Shaldyrvan I., Komarov V., Komarova V., Fokin M.
Implementation of the ALPHA UMi monitoring system at SAO RAS 923
Shugarov A., Shustov B.
SODA: a system to detect daytime asteroids of the "Milky way" project 927
Tsybulev P., Nizhelskij N., Borisov A., Kratov D., Udovitskiy R..
Continuous spectrum receiving complexes on the RATAN-600 radio telescope 933
Yershov V., Raikov A., Popova E.
Systematic effect in the standard processing of gravitational-wave signals 938

ASTRONOMICAL DATABASES AND INFORMATION TECHNOLOGY

Berezin I., Illarionov E., Tlatov A.
Interactive multi-instrumental database of solar activity observations 944
Rozhkova D., Kashapova L., Gubin A.
A method to reveal and catalog solar flares observed with the Siberian Radioheliograph: first results 949
Sapraliev M., Mikhalyaev O., Kharldaev L., Mikhalyaev B.
Interactive service of geoeffective phenomena 953
Bezrukov I., Salnikov A., Vasiliev V., Plotnikov R., Evseev A., Abramov A.
Improving the Quasar VLBI Network fordata transfer with the National Research Computer Network of Russia 959
Zhelenkova O., Plyaskina T., Shergin V., Mal'kova G., Velichko A., Kyabishev M.
Information system and general archive of SAO~RAS observations 963

ASTRONOMY EDUCATION AND OUTREACH

Arkhipova N., Luzhnov A., Fedorov N.
Teaching the basics of data science on astronomical data and catalogs 969
Grigoriev V.
Comparison of educational results in Astronomy for high school students in St. Petersburg 973
Kuznetsova I., Prokhorov M.
Practical work on asteroid-comet hazard based on open data as a component of astronomical education 979
Starikov K.
Creation and development of domestic scientific and educational space infrastructure and its use as a tool for ground-based and space astronomy 984

Triumph of black holes

A. Cherepashchuk

Lomonosov Moscow State University, Sternberg Astronomical Institute, Moscow, 119234 Russia

Abstract. The properties of black holes are so extreme that it is hard to believe in their existence. Sixty years ago, in 1964, the seminal works of Ya.B. Zeldovich and E.E. Salpeter on the nonspherical accretion of matter onto black holes were published and it was shown that accreting black holes can be observed in the hard range of electromagnetic radiation. The review describes the 60-year history of observational studies of black holes. The results of observations of black holes in the X-ray and optical ranges, in the gravitational wave range, as well as in the short-wave radio range with ultra-high angular resolution (Event Horizon Telescope program) are briefly summarized. It can be concluded that by now black holes have won the "citizenship rights" among the classical objects of the Universe, and the existence of these highly peculiar objects can be considered proven.

Keywords: black holes; gravitational waves; X-ray binaries

DOI: 10.26119/VAK2024.001

1 Introduction

Black holes are a prediction of Einstein's theory of General Relativity (GR). A black hole is understood as a region of space-time whose gravitational field is so strong that no signal, even a light signal, can move away from it to the spatial infinity of the future (Novikov and Frolov 1986). The properties of black holes are so extreme that it is hard to believe in their existence.

For many decades, the idea of a black hole (BH) was purely theoretical. However, in 1964, two outstanding scientists, Ya.B. Zeldovich (1964) and E.E. Salpeter (1964), examined the nonspherical accretion of matter onto a BH and showed that accreting BHs can be observed in the hard range of the electromagnetic spectrum. It can be said that today (2024) is the 60th anniversary of the beginning of observational programs of BH studies.

It is also important that 62 years ago, in 1962, the first X-ray source Sco X-1≡V818 Sco was discovered outside the Solar system (Giacconi et al. 1962). From that time, the era of X-ray astronomy began.

In 1972–73, the theory of disk accretion of matter onto BH in binary systems was developed (Shakura 1973; Shakura and Sunyaev 1973; Pringle and Rees et al. 2021; Novikov and Thorne 1973). About the same years, the theory of evolution of close binary systems (CBS) with mass exchange up to the very late stages of two relativistic objects was developed (Tutukov and Yungelson 1973a,b; van den Heuvel 1976).

According to the modern concepts of stellar evolution taking into account the GR effects, if the mass of the core of the star M_c, where thermonuclear reactions take place, exceeds $3M_\odot$, then at the end of the evolution of the star relativistic collapse of its core occurs and a BH is formed. If the M_c mass is less than $3M_\odot$, a neutron star (NS) or white dwarf (WD) is formed at the end of the star's evolution.

The masses of stars are most reliably determined by the motion and interaction of components in CBS. Therefore, the ability to "weigh" relativistic objects makes close binary systems a powerful tool for the discovery and study of NS and BH. Thus, with the beginning of the era of X-ray astronomy, CBS became very important objects for relativistic astrophysics. The emergence and development of X-ray astronomy brought the problem of CBS studies, previously a purely classical field of astronomy, to the forefront of modern astrophysics.

The launch of the first specialized American X-ray observatory UHURU in 1971 marked the beginning of systematic observations of the sky in X-rays. About 300 X-ray sources were discovered, most of which are X-ray binary systems—CBS, in which a normal optical star—a matter donor—feeds accretion onto a relativistic object (NS or BH). The disk accretion theory (Shakura 1973; Shakura and Sun-

yaev 1973; Pringle and Rees et al. 2021; Novikov and Thorne 1973) allowed us to quickly understand the nature of compact X-ray sources discovered by the UHURU observatory as accreting relativistic objects in X-ray binary systems.

To determine the masses of relativistic objects, identifications of X-ray binary systems with optical stars were required. The first optical identifications of X-ray binary systems were made in Cherepashchuk et al. (1972), Bahcall and Bahcall (1972). In Cherepashchuk et al. (1972) and Lyutyi et al. (1973) the main types of optical manifestations of X-ray binary systems—reflection and ellipticity effects—were discovered and investigated, which were further widely used for optical identifications of X-ray binary systems and for determining the masses of relativistic objects.

In Margon et al. (1979), Crampton et al. (1980), and Cherepashchuk (1981) the object SS 433 was discovered—the first example of a microquasar with manifestations of supercritical accretion on a relativistic object, predicted in Shakura and Sunyaev (1973).

Later on, it was X-ray astronomy and the astronomy of binary star systems that provided the first breakthrough in the search for and studies of massive compact objects—candidates for BH. The discovery of gravitational waves from mergers of BHs in binary systems in 2015 and the imaging of the nearest neighborhoods of a supermassive BH in the core of the galaxy M 87 in 2019 and in the center of our Galaxy in 2022 allowed us to finally prove the reality of BHs in the Universe. As a result, by now, BHs have won "citizenship rights" among classical objects of astronomy: stars, galaxies, galactic clusters, etc. A new field of astrophysics is successfully developing—demography of BH, that studies the birth, growth of BHs and their connection with classical objects of the Universe.

2 Initial observations of BHs

Studies of the optical manifestations of X-ray binary systems have allowed us to develop efficient methods for estimating the masses of X-ray sources in binary systems, including accreting BHs (see, e.g., the review by Cherepashchuk 2022 and references therein).

In Webster and Murdin et al. (1972), the mass function of the optical star, the supergiant B0Ib, in the X-ray binary system Cyg X-1 $f_v(M) \cong 0.2M_\odot$ was measured. In Lyutyi et al. (1973) the effect of ellipticity of the optical star in the Cyg X-1 system was discovered and from the analysis of this effect an estimate of the orbital inclination in this system was made and one of the first estimates of the black hole mass $M_x > 5.6M_\odot$ was obtained. In Paczynski (1974), constraints were placed on the mass of a BH in the Cyg X-1 system, taking into account the known distance to this

system. The fact that one of the first discovered compact X-ray sources turned out to be an accreting BH, gave scientists optimism and hope that in the near future many massive X-ray sources, candidates for BH, would be discovered. But in practice, everything turned out to be much more complicated. For 11 years, the Cyg X-1 object was the only known candidate for a BH. And the vast majority of compact X-ray sources discovered by the UHURU program turned out to be accreting NS. In this regard, many researchers had doubts: maybe there are really no BHs in the Universe? These doubts were reinforced after the publication by Paczynski's group (Bahcall et al. 1974) in which Cyg X-1 model was represented as a triple system consisting of two optical stars with significant mass differences and an accreting NS.

Since the percentage of triple systems among stars is not small, this model had a right to exist. After that the number of optimists in the program of search for BH went down and exactly in these years the supporters of theories of gravitation alternative to GR (for example, the rector of MSU academician A.A. Logunov) were the most active. At scientific seminars at the Physics Department of MSU and on the pages of the journal "Physics-Uspekhi" a sharp discussion between supporters of GR (Ya.B. Zeldovich, L.P. Grishchuk) and opponents of this theory (A.A. Logunov) took place.

Only in 1983 the Canadian scientist Ann Cowley and her coworkers succeeded in discovering a second BH candidate (Cowley et al. 2021) in the X-ray binary system LMC X-3, whose mass was estimated to be $8M_{\odot}$.

In 1986, American scientists McClintok and Remillard discovered the first BH in the low-mass (optical star mass $\sim 1M_{\odot}$) X-ray binary system A0620-00 (McClintock and Remillard 1986). That was a great surprise to scientists, as they had previously searched for BH in massive X-ray binary systems with optical star masses much larger than the solar mass. At the time, it was assumed that binary stars most often formed as pairs of stars with similar masses. Since BHs are formed when the nuclei of massive stars collapse, scientists chose massive X-ray binary systems to search for BH. And they miscalculated. In further studies it, turned out that the distribution of CBS on the ratio of component masses is very wide, and the ratio of masses close to unity is not emphasised in any way. But the main thing is that the time of nuclear evolution of a massive star is thousands of times shorter than the time of evolution of a low-mass star.

Therefore, the accretion and X-ray source stage in a binary system with a massive optical star is thousands of times shorter than the accretion and X-ray source stage in a low-mass X-ray binary system. Therefore, it is much less likely to detect a BH in a massive X-ray binary system than in a low-mass one. This explains the fact that the successes of the discovery of BH in massive X-ray binary systems at first were

very modest. To date, more than 30 candidates for BH in X-ray binaries have been discovered, and more than two-thirds of them are observed in low-mass X-ray binary systems.

Since the mid-1970s, many specialized space X-ray observatories have been launched, including the Soviet and Russian Mir/Kvant (1987–1996) and Granat (1989–1998) observatories. Much work is being done by Russian scientists at the international space gamma-ray observatory Integral, as well as at the space X-ray observatory Spectrum-X-Ray-Gamma-ray. The initiator and scientific leader of all these Russian X-ray experiments is R.A. Syunyaev and his remarkable scientific team at Space Research Institute. These investigations were supported by Ya.B. Zeldovich.

To date, many thousands of X-ray binary systems have been discovered and studied. The masses of many dozens of stellar-mass black holes and about a hundred neutron stars have been measured so far.

A very beautiful result is revealed: NS and BH differ not only on masses, but also on observational manifestations in full agreement with the predictions of GR. In all about 100 cases when the relativistic object shows signs of observable surface (phenomenon of X-ray pulsar, radio pulsar, X-ray burster of the 1st type) its mass does not exceed $3M_\odot$ in full agreement with the prediction of GR about existence of the upper limit of mass of NS in $3M_\odot$. At the same time, none of more than 30 massive ($M > 3M_\odot$) X-ray sources shows signs of an observable surface (is neither an X-ray nor a radio pulsar nor an X-ray burster of the 1st type) in full agreement with the prediction of GR about the existence of an event horizon in the BH.

This remarkable result, obtained for 60-year period of investigation of relativistic objects, is an indirect evidence of presence of an event horizon at BH. Unfortunately, this result cannot serve as a final proof of existence of BHs, since there are also NS, which also do not show signs of an observable surface. For example, if the axis of rotation of an NS coincides with the axis of a magnetic dipole, the X-ray pulsar phenomenon will not be observed, and a heavy NS can be confused with a BH. In addition, it is obvious that one cannot make a final judgment about the nature of an object based on the absence of any features.

3 Observations of supermassive BHs in galactic nuclei

In the early 1990s, the determination of the masses of supermassive BHs (SMBHs) in the nuclei of galaxies began. The first estimates of the masses of SMBHs in the nuclei of very active galaxies—quasars—were made back in 1964 by Ya.B. Zeldovich and I.D. Novikov (1965) under the condition of equality of the quasar luminosity and the critical Eddington luminosity. These masses turned out to be very large—of about

$10^8 M_\odot$. Systematic determinations of the masses of supermassive compact objects (BH) in the nuclei of Seyfert galaxies were carried out in the 1980s by E.A. Dibai (1984). To determine the mass of an object, it is sufficient to know the velocity of a "test body" (star, gas cloud, gas disk) rotating around it under the action of gravitational attraction and the distance of this body to the central object under study.

According to the width of powerful and broad emission lines of hydrogen and other chemical elements in the spectrum of the galactic nucleus, E.A. Dibai determined the characteristic velocity of gas clouds rotating around the central supermassive object, and according to the full intensity of these lines, using the photoionization model of the galactic nucleus, the characteristic volume of radiating gas was found and, as a consequence, the characteristic distance of gas clouds from the central supermassive compact object was estimated on the order of magnitude. The estimates of the masses of supermassive compact objects in the nuclei of Seyfert galaxies obtained in this way were of the order of magnitude $10^8 M_\odot$.

In 1973, A.M. Cherepashchuk and V.M. Lyutyi discovered the effect of delayed variability of emission lines in the spectra of active galactic nuclei relative to the continuum variability (Cherepashchuk and Lyutyi 1973). This allowed us to estimate the characteristic distance of gas clouds from the central SMBH not on the order of magnitude, but much more precisely. By measuring the lag time, it is possible to give a reliable estimate of the distance of gas clouds—"test bodies" radiating in the line from the central BH. At known velocity of gas clouds, determined by the widths of emission lines, it is possible to determine the mass of a supermassive BH in this way.

The lag effect was the basis for the method of determining the masses of SMBH, called the reverberation mapping method. The first ideas of the reverberation mapping method were expressed in 1983 in the work of I.I. Antokhin and N.G. Bochkarev (Antokhin and Bochkarev 1983). The advantage of this method is that here the velocities of "test bodies" and their distances from the central BH are estimated indirectly. Therefore, the reverberation mapping method can be applied to numerous distant galaxies for which the resolving power of the telescope is insufficient to directly "see" the "test bodies". To date, the masses of hundreds of supermassive BHs in active galactic nuclei have been measured by reverberation mapping.

In recent years, the reverberation mapping method has been generalized in the works of Yu.N. Gnedin and V.L. Afanasiev and collaborators to the case of spectropolarimetric observations of the nuclei of active galaxies (Gnedin et al. 2012). The involvement of the polarization of radiation in the lines makes it possible to estimate the geometry of the emitting region near a supermassive BH, which makes

it possible to better calibrate the results obtained by the reverberation mapping method.

In the case of sufficiently close galaxies, using the methods of increasing the angular resolution of the telescope, one can directly "see" "test bodies", near a SMBH and measure their velocities and distances from the BH. In this way, the method of "resolved kinematics", is realized, which allows us to obtain the most reliable and accurate estimates of the masses of SMBHs.

For example, the motion of about three dozen stars, including the star S2 with an orbital period of 15.6 years, around a SMBH in the center of our Galaxy has been studied using observations in the IR range and the mass of the central SMBH has been determined with an accuracy better than 10% using Kepler's third law: $M_{\rm BH} = (4.31 \pm 0.36) \times 10^6 M_\odot$ (Gillessen et al. 2009).

In the case of elliptical galaxy nuclei, where regular galaxy rotation velocities are hardly revealed against the background of large random stellar velocities, the mass of the central SMBH is estimated with the help of the dispersion of stellar velocities using the laws of stellar dynamics.

There are also express, less accurate methods for estimating the masses of supermassive black holes in galactic nuclei based on statistical correlations. As a rule, such methods are calibrated using the results of reverberation mapping and "resolved kinematics" methods.

To date, the masses of thousands of SMBHs have been measured with the help of different methods. These masses lie in the range of $10^6 \div 10^{10} M_\odot$. Estimates of the radii of SMBHs are most often obtained from observations of the rapid variability of galactic nuclei on times up to tens of minutes, which corresponds to values less than 10 gravitational radii.

Thus, by 2000–2015 years the observational data on stellar BHs, as well as on SMBHs in the nuclei of galaxies according to the successful statement of V.L. Ginzburg strengthened our confidence in the real existence of BHs in the Universe.

The definitive evidence for the existence of the BHs came after 2015 from gravitational-wave astronomy (the LIGO[1] experiment and others) and from ultra-high angular resolution astronomy at short radio waves (the Event Horizon Telescope experiment).

4 Gravitational-wave astronomy and black holes

In 2015, bursts of gravitational-wave radiation from mergers of BHs in binary systems were discovered (Abbott et al. 2016). Reliable detection of gravitational waves (GW)

[1] Laser Interferometer Gravitational-Wave Observatory.

was realized at two laser GW antennas of American LIGO laboratories, separated by a distance of approximately 3000 km.

The initiators of LIGO were American scientists K. Thorne, R. Weiss, and R. Driver. The idea to use the Michelson optical laser interferometer for GW registration was suggested by M.E. Gerzenstein and V.I. Pustovoit in 1962 (Gertsenshtein and Pustovoit 1963). The international LIGO Scientific Collaboration included representatives of the Physics Department of Lomonosov Moscow State University, a group of V.B. Braginsky, and a group from the A.V. Gaponov-Grekhov Institute of Applied Physics of the Russian Academy of Sciences led by E.A. Khazanov.

On September 14, 2015 on both LIGO antennas (H1 in Hanford, Washington and L1 in Louisiana, Livingston) gravitational-wave signal with a duration of about half a second was registered, and it was named LIGO GW150914 (if you read the numbers from right to left, we get 140915—the date of registration of the signal). The signal is a quasi-sinusoidal oscillation with increasing frequency and increasing amplitude followed by a sharp decay (the so-called ring-down stage). The observed GW signal is well described in the framework of GR by the model of merger of two BHs.

With the discovery of GW, a new science, Geometrodynamics, which began to develop in the late 1950s and early 1960s in the works of J. Wheeler, K. Thorne, I.D. Novikov, Ya.B. Zeldovich and other scientists, was put on a solid observational basis. Geometrodynamics is a science that studies the nonlinear dynamics of curved space-time. Gravitational-wave astronomy gives us a unique opportunity to study not only various material bodies, such as stars, galaxies, etc., but also empty space-time, which can be considered as one of the types of matter, whose properties, such as curvature and curl parameters, can be actually studied with the help of GW telescopes.

Especially brightly space-time properties are revealed at mergers of BHs in binary systems. Therefore, the discovery of GW signals from the merger of BHs takes the problem of BH research to a qualitatively new level. Earlier, at investigations in the electromagnetic channel, we could only passively observe the X-ray "halo" around the BH, caused by accretion of the satellite matter and determine the mass of the BH by the motion of this satellite. Now we can as if "experiment" with black holes in binary systems, study the process of their merger, the formation of a common event horizon, and study different modes of damped oscillations of this horizon. This gives us a fundamental possibility of the final experimental proof of the existence of the event horizon (Cherepashchuk 2016).

To date, a number of GW observatories (LIGO, Virgo, KAGRA, etc.) have discovered about 90 GW events, mostly associated with mergers of BHs in binary systems

(see Abbott et al. 2021 catalog). In addition, GW from several neutron star mergers in binary systems have been discovered (Abbott et al. 2017). By comparing the arrival times of the GW and the optical signal from these mergers, the scientists were able to show that the speed of GW propagation in space coincides with the speed of light with great precision ($\sim 10^{-15}$). This allowed them to reject a number of theories of gravitation that are alternative to GR.

The fact that the first GW signals were discovered from the merger of BHs, rather than NSs, was not unexpected for scientists. Back in 1997, astrophysicists from the Sternberg State Astronomical Institute V.M. Lipunov, K.A. Postnov, and M.E. Prokhorov (Lipunov et al. 1997) predicted that the LIGO observatory should register signals from mergers of BHs earlier than from NSs. Although the frequency of BH mergers in binary systems ($\sim 10^{-5} \div 10^{-6}$ mergers per year per standard galaxy) is significantly lower than the frequency of NS mergers ($\sim 10^{-4}$), BH mergers release much more energy in the form of GW. This makes it possible to detect GW emission from much greater distances. Since the volume of space is proportional to the cube of the distance, the number of merging pairs of BHs available for observations increases and, consequently, the probability of their detection by GW telescopes increases as well.

Since the problem of determining the parameters of the system of two BHs (masses, angular momenta, etc.) from the observed GW signal is overdetermined (the number of sought parameters is much smaller than the number of equations describing the observed points on the curve of the GW signal), in GW observations of merging binary BHs it is possible not only to determine the masses of BHs, but also to check many times the validity of the GR equations in the dynamics in superpower variable gravitational fields. In all cases, no inconsistencies between GR and observations of the GW are found.

This allow us to conclude that stellar-mass BHs (with masses of about $4 \div 100\ M_\odot$) are finally discovered.

5 Ultra-high angular resolution astronomy and supermassive black holes (Event Horizon Telescope)

In recent years, scientists have been able to construct images of the nearest neighborhood of SMBHs in the core of the galaxy M 87 (Akiyama et al. 2019) and in the core of our Galaxy (Akiyama et al. 2022). The ground-based intercontinental radio interferometer system Event Horizon Telescope (EHT) was used, which is a global network of submillimeter radio telescopes, including radio telescopes of the USA,

Germany, Japan, Chile, Taiwan, and other countries, including the radio telescope located at the South Pole.

It is important that these telescopes operate in the short radio wavelength range ($\lambda\,1.3$ mm). Only in the short-wavelength range it is possible to "break through" to the event horizon of the central SMBH, which is surrounded by a relatively dense magnetized plasma emitting both thermal and non-thermal synchrotron radiation. At long wavelengths, due to scattering of radio emission on plasma inhomogeneities and due to synchrotron self-absorption, the central SMBH is inaccessible for direct observations.

At a wavelength of 1.3 mm, the angular resolution of the EHT is 2.3×10^{-5} arcsec, and at a wavelength of 0.9 mm, the angular resolution will be 1.5×10^{-5} arcsec. For SMBHs in the centers of our Galaxy ($M_{\rm BH}=4.3\times10^6\ M_\odot$) and of the galaxy M 87 ($M_{\rm BH}=6.6\times10^9\ M_\odot$) at such short radio wavelengths we can directly observe the nearest neighborhood of the BH: the inner part of the accretion disk and the dark shadow in its center, caused by the capture of photons by the photon sphere of the BH. We emphasize that only an extremely strong gravitational field of the BH is able to make photons propagate at a speed of 300 000 km/s moving along circular trajectories near the BH. The gravitational field of a NS is not strong enough to make photons' trajectories circular (a NS has no photon sphere). Therefore, the detection of a dark shadow in the center of the accretion disk around the central compact supermassive object is a direct evidence that this object is a BH.

In the case of the Schwarzschild BH, the observed linear diameter of the shadow (gravitationally-lensed image of the photon sphere of the BH) is $\sim$2.6 times larger than the Schwarzschild diameter of the BH ($2R_{\rm Schw}=4GM/c^2$).

For the SMBH in the center of our galaxy ($M_{\rm BH}=4.3\times10^6\ M_\odot$), which is 8.33 pc away from us, the angular diameter of the shadow is 5.3×10^{-5} arcsec, which exceeds the resolving power of the EHT (2.3×10^{-5} arcsec). For the SMBH at the center of the galaxy M 87 ($M=6.6\times10^9M_\odot$), for which the distance is 1.8×10^4 Mpc, the shadow diameter is 3.8×10^{-5} arcsec.

Thus, it is quite realistic to "see" images of dark shadows for the SMBHs in the centers of the M 87 galaxy and our Galaxy with the help of the EHT.

The large and complex work on performing interferometric observations and their mathematical processing has led the EHT science team to a tremendous success (Akiyama et al. 2019, 2022). Shadow images were constructed for the SMBHs in the centers of our Galaxy and the galaxy M 87. The observed sizes of these shadows are in a good agreement with their sizes calculated with the help of the GR formula for those values of BH masses, which are independently determined from the motion of stars near these BHs.

Thus, thanks to the achievements of the EHT scientific team, the existence of SMBHs in the nuclei of galaxies can be considered definitively proven.

6 Conclusion

Many years (more than 60 years) of hard work of scientists from many countries to search for BHs in the Universe to date crowned with convincing evidence that BHs—these highly extreme objects, in the existence of which is hard to believe, really exist in the Universe.

X-ray astronomy provided the first breakthrough in observational studies of accreting BHs. Rich data on many candidates for BHs were accumulated. A new science—relativistic astrophysics was developed. A very beautiful result was obtained. It has appeared that NSs and BHs differ not only on masses, but also on observational manifestations in full agreement with predictions of GR. According to the apt statement of V.L. Ginzburg, it strengthened our confidence in the real existence of BHs in the Universe.

Since 2015, with the advent of gravitational-wave astronomy and ultrahigh angular resolution astronomy, strong evidence has been obtained that both stellar-mass BHs and supermassive BHs really exist in the Universe. By the present time all doubts in the existence of BHs have disappeared, and these objects have won "citizenship rights" among classical objects of the Universe—stars, galaxies, etc. A new science was born—demography of BH, which studies the processes of BH birth and growth, as well as the evolutionary connection between BHs and classical objects of the Universe.

A new aspect of the BH problem has appeared—the study of binary SMBHs. The task of searching for wormholes in the Universe is set. New observational experiments are being planned and developed. Hundreds of thousands of new X-ray binary systems with BH have been discovered by the Spectrum-X-Ray-Gamma-ray Observatory. The planned Russian space experiment Millimetron is supposed to observe SMBHs in the nuclei of galaxies with angular resolution up to 10^{-8} seconds, as well as to search for wormholes. New generations of GW observatories, including space GW observatories, are aimed at detailed studies of stellar-mass and supermassive BHs, including binary SMBHs. The important role of BHs is taken into account in studies of the evolution of the Universe and its structures.

The discovery of BHs means a breakthrough in our understanding of the nature of matter and space-time.

We can conclude that *we are currently experiencing the triumph of BHs.*

Funding

The author thanks the Russian Science Foundation for financial support (grant 23-12-00092).

References

Abbott B., Abbott R., Abbott T.D., et al., 2016, Physical Review Letters, 116, 6, 061102.
Abbott B., Abbott R., Abbott T.D., et al., 2017, Astrophysical Journal Letters, 848, id. L12
Abbott R., Abbott T.D., Acernese F., et al., 2023, Physical Review X, 13, 041039
Akiyama K., Alberdi A., Alef W., et al., 2019, Astrophysical Journal Letters, 875, id. L6
Akiyama K., Alberdi A., Alef W., et al., 2022, Astrophysical Journal Letters, 930, 2, id. L14
Antokhin I.I., Bochkarev N.G., 1983, Soviet Astronomy, 27, p. 261
Bahcall J.N., Bahcall N.A., 1972, Astrophysical Journal, 178, L1
Bahcall J.N., Dyson F.J., Katz J.I., et al., 1974, Astrophysical Journal, 189, p. L17
Cherepashchuk A.M., 1981, Monthly Notices of the Royal Astronomical Society, 194, p. 761
Cherepashchuk A.M., 2016, Physics-Uspekhi, 59, p. 910
Cherepashchuk A.M., 2022, Astronomy Reports, 66, suppl. 1, p. S412
Cherepashchuk A.M., Efremov Yu.N., Kurochkin N.E., et al., 1972, IBVS 9720, 1.
Cherepashchuk A.M., Lyutyi V.M., 1973, Astrophysical Letters, 13, p. 165
Cowley A.P., Crampton D., Hutchings J.B., et al., 1983, Astrophysical Journal, 272, p. 118
Crampton D., Cowley A.P., Hutchings J.B., 1980, Astrophysical Journal, 235, p. L131
Dibai E.A., 1984, Soviet Astronomy, 28, p. 123
Gertsenshtein M.E., Pustovoit V.I., 1963, Soviet Physics JETP, 16, p. 433
Giacconi R., Gursky H., Paolini F.R., et al., 1962, Physical Review Letters, 9, p. 439
Gillessen S., Eisenhauer F., Trippe S., et al., 2009, Astrophysical Journal, 692, p. 1075.
Gnedin Yu., Afanasiev, V.l., Borisov, N.V., et al., 2012, Astronomy Reports, 56, 8, p. 573
Lipunov V.M., Postnov K.A., Prokhorov M.E., 1997, Monthly Notices of the Royal Astronomical Society, 288, p. 245
Lyutyi V.M., Syunyaev R.A, Cherepashchuk A.M., 1973, Soviet Astronomy, 17, p. 1
Margon B., Ford H.C., Katz J.I., et al., 1979, Astrophysical Journal, 230, L41
McClintock J.E, Remillard R.A., 1986, Astrophysical Journal, 308, p. 110
Novikov I.D. and Frolov V.P., Physics of black holes, Moscow, Izdatel'stvo Nauka, 1986, 328 pp.
Novikov I.D., Thorne K.S., 1973, Black holes, Ed C. DeWitt, B. DeWitt, Gordon and Breach, N.Y., p. 343
Paczynski B., 1974, Astronomy & Astrophysics, 34, p. 161
Pringle J.E., Rees M.J., 1972, Astronomy & Astrophysics, 21, p. 1
Salpeter E.E., 1964, Astrophysical Journal, 140, p. 796
Shakura N.I., 1973, Soviet Astronomy, 16, p. 756
Shakura N.I., Sunyaev R.A, 1973, Astronomy & Astrophysics, 24, p. 337
Tutukov A.V., Yungelson L.R., 1973, Nauchnye Informatsii, 27, p. 58
Tutukov A.V, Yungelson L.R., 1973, Nauchnye Informatsii, 27, p. 70
van den Heuvel E.P.J., 1976, Structure and Evolution of Close Binary Systems, Eds P.P. Eggleton, B. Mitton, J. Whelan, Dordrecht, Reidel Publ. Comp., p. 35
Webster N.L., Murdin P., 1972, Nature, 235, p. 37
Zeldovich Ya.B., 1964, Soviet Physics Doklady, 9, p. 195
Zeldovich Ya.B., Novikov I.D., 1965, Soviet Physics Doklady, 9, p. 834

VAK 2024 MODERN ASTRONOMY: FROM THE EARLY UNIVERSE TO EXOPLANETS AND BLACK HOLES 300 years Russian Academy of Sciences

Small bodies of the Solar system—scientific challenges and practical aspects

B. Shustov

Institute of Astronomy of the Russian Academy of Sciences,
Pyatnitskaya 48, Moscow, 119017 Russia

Abstract. The study of small bodies of the Solar system provides the key to understanding the processes of its formation and evolution. Basic science here is closely related to the applied aspects. First of all, this is true in relation to Near-Earth Objects (NEOs). The brief overview focuses on the discussion of such links. In particular, the following two topics connecting fundamental and practical issues are considered: origin, characteritics, and evolution of the NEO population ⟷ the problem of asteroid-comet hazard; meteoroids of both cometary and asteroid origin ⟷ safety of space activities in near-Earth space. The issues of coordination of research on small bodies topic both at the domestic and international levels are briefly d i s cussed t o o . S p e cial attention is paid to the prospects for coordinating research work on small bodies within the framework of the federal project "Mlechny Put" (Milky Way).

Keywords: small bodies of the Solar system, Near-Earth Objects, planetary defense, meteoroids, safety of space activities

DOI: 10.26119/VAK2024.002

1 Introduction

Resolution B5 of the General Assembly of the IAU[1] specifies concept of "small bodies of the Solar system". These are objects that, by their characteristics, cannot be attributed either to dwarf planets or to planets or their moons. It is explained that this group includes most of the asteroids of the Solar system, most of the trans-Neptunian objects, comets and other bodies.

Meteoroids and interplanetary dust also belong to the small bodies of the Solar system. Until recently, there was no clear criterion for separating the concepts of "asteroid"and "meteoroid", "interplanetary dust". In 2017 the IAU F1 Commission adopted recommendations on the use of the terms "meteoroid" and "interplanetary dust",[2] allowing for a unambiguous use of these terms. According to these recommendations:

- meteoroids—solid objects ranging in size from about 30 microns to 1 m, moving in interplanetary space;
- interplanetary dust—solid interplanetary objects up to 30 microns in size.

It follows from these definitions that asteroids (and comet nuclei) are solids larger than 1 m.

The topic of small bodies is a gigantic field of scientific research. As noted in Jacobson et al. (2021), "small bodies are time-capsules of different eras of the Solar system history from the most primitive materials within the Solar system to evolved pieces of larger bodies".

Small bodies carry information about all corners of the Solar system. We get some of this information by studying meteorites, but although our meteorite collections are an important source of knowledge about the history of the Solar system, they provide an incomplete understanding of the properties and fate of solids in space. Growing attention is being paid to the study of small bodies both by methods of ground-based astronomy and using spacecraft.

In addition to basic science, the small bodies of the Solar system are of great practical interest. This is also very true for near-Earth objects (NEOs). This brief overview focuses on discussing such relationships. In particular, the following topics linking fundamental and practical issues are considered:

- The origin and evolution of the NEO population $\longleftrightarrow$ the problem of asteroid-comet hazard (Section 2).
- Meteoroids of both cometary and asteroidal origin $\longleftrightarrow$ safety of space activities in near-Earth space (Section 3).

[1] https://www.iau.org/static/resolutions/Resolution_GA26-5-6.pdf—accessed: 14 July 2024.
[2] https://www.iau.org/static/science/scientific_bodies/commissions/f1/meteordefinitions_approved.pdf—accessed: 14 July 2024.

The issues of coordination of research on small bodies at the domestic and international levels are briefly discussed too. Special attention is paid to the prospects for coordinating the research of small bodies within the framework of the federal project "Milky Way" (Section 4).

2 NEOs and planetary defense

Near-Earth objects (NEOs) are asteroids (NEAs) and comets (NECs) with a perihelion distance $q < 1.3$ AU. The subset of NEOs—Potentially hazardous objects (PHOs)—are bodies whose orbits can approach the Earth's orbit to a minimum orbit intersection distance (MOID) of no more than 0.05 AU. In the literature this (dynamic) definition of PHOs was added by the requirement that the absolute asteroid magnitude of the body H should not exceed 22.0.[3] With some average value of the asteroid albedo $A = 0.15$, the size of a spherical body with $H = 22$ is estimated at approximately 140 m according to the formula $D = 10^{3.1236-0.5 \log A-0.2H}$ (Harris and Harris 1997). Currently, the critical size limit is being revised and reduced from 140 m to at least 50 m (the size of the Tunguska body), and more recently even to ~ 10 m (the practical lower limit confirmed by the Chelyabinsk event).

The concept of NEO is closely related to the concept of asteroid-comet hazard (ACH aka NEO problem). ACH is a hazard of possible collisions of small bodies with the Earth causing major damage to the population of the planet up to the destruction of civilization. Regarding the problem of near-Earth objects, astronomy as a fundamental science is expected to answer the following questions:

- Number of NEOs in the Solar system.
- Characteristics of NEOs important for planetary defense purposes.
- Frequency of collisions of NEOs with the Earth.
- How to construct an efiicient system for detecting and monitoring hazardous space objects.

Very brief answers to some of these questions can be found in the diagram shown in Fig. 1 taken from the NASA's document "National Preparedness Strategy and Action Plan for Near-Earth Object Hazards and Planetary Defense".[4] Of course, this diagram shows only some "average" estimates. First of all, this concerns the distribution of NEOs by size.

[3] https://cneos.jpl.nasa.gov/about/neo_groups.html—accessed: 24 July 2024.

[4] www.whitehouse.gov/wp-content/uploads/2023/04/2023-NSTC-National-Preparedness-Strategy-and-Action-Plan-for-Near-Earth-Object-Hazards-and-Planetary-Defense.pdf—accessed: 24 July 2024.

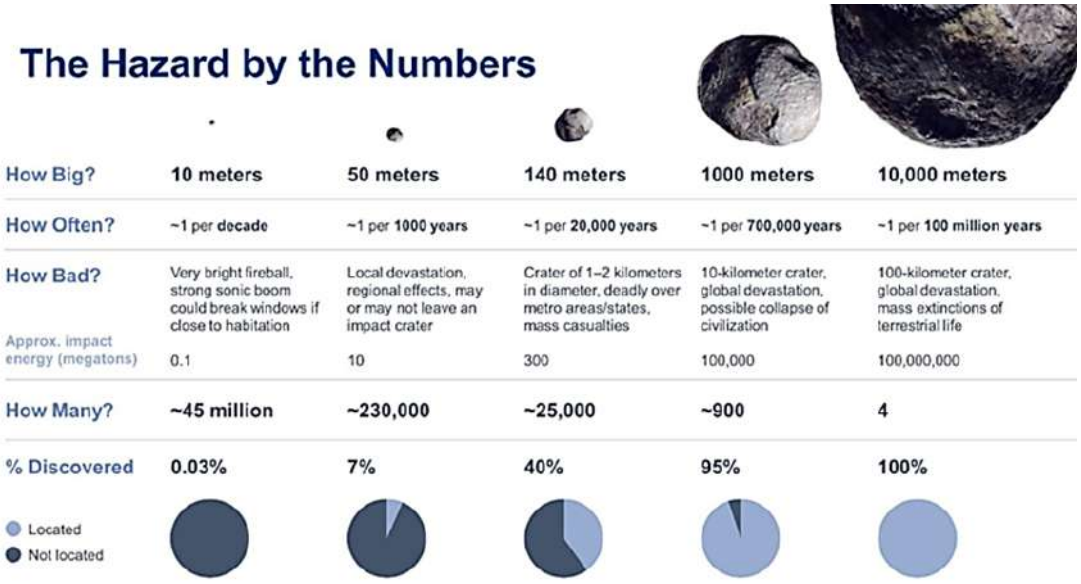

Fig. 1. NEO size, frequency of Earth-impact, and hazard

It is customary to illustrate the number of detected NEOs and detection completeness degree with a well-known and permanently updated diagram[5] (Fig. 2). The inset in Fig. 2 shows the number of potentially hazardous asteroids and comets. Obviously, the share of comets in the total number of NEOs is very small, and the statistics of detected NEOs well represents the complete statistics of NEOs.

The completeness of NEO detection is increasing and it can be assumed that by now the completeness of detection of bodies larger than ~ 1 km (more precisely 0.7 km) has been achieved at a level of $\sim 90-95\%$. However the NEO problem relates to collisions with bodies ranging in size from decameters to half a kilometer. Larger bodies collide with the Earth so rarely that practical interest is not expressed here. For smaller near-Earth objects, observations are not complete enough, so different models are used. The models give a very large spread, the larger the smaller the body.

Figure 3 represents cumulative distribution of known NEOs by H (also by diameter D). The diagram is constructed using the model of Granvik et al. (2018) (marked as "This work") and models presented in the works of other authors. The identification of the mass spectrum of small asteroids remains a serious scientific challenge.

[5] https://cneos.jpl.nasa.gov/stats/totals.html—accessed: 24 July 2024.

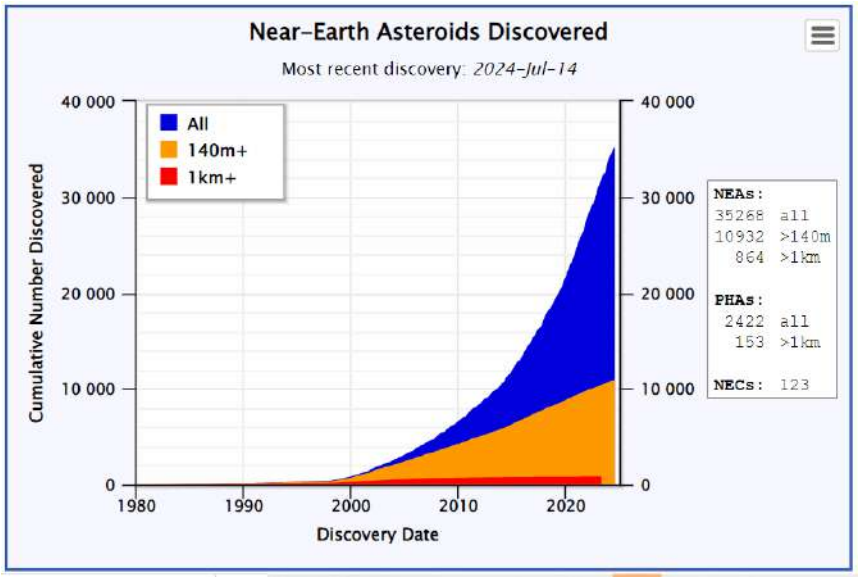

Fig. 2. Near-Earth asteroid detection statistics.

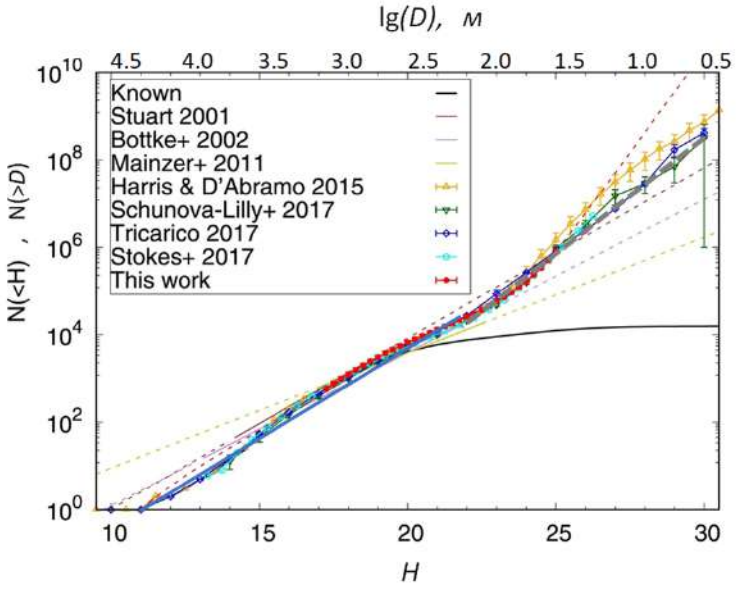

Fig. 3. The observed cumulative distribution of NEOs by H (also by diameter D) according to the model of Granvik et al. (2018) (marked as 'This work'), and models presented by other authors.

Characterisation of NEOs is vitally important for proper planning of planetary defense activities. Barbee et al. (2020) presented a high-level notional priority of NEO characteristics for measurement for planetary defense purposes. These are (in order of decreasing notional priority): precise orbit; mass; binarity; shape (taking into account the mass, the bulk density can be determined); strength; internal structure (including porosity); mineral composition; and detailed surface topology.

The major practical issues of the NEO problem are:

1. Detection (identifying) of all dangerous bodies and revealing their properties.
2. Risk assessment in a case of a specific collision threat.
3. Counteraction and mitigation (damage reduction).

The first problem and a large part of the second problem are the responsibility of astronomers. Obviously, the first problem has the highest priority.

To select the most effective instruments and observation strategies for NEO detection, it is important to determine the input requirements for such instruments. The problem of NEO detection can be solved only with the help of optical and infrared ground-based and/or space-based telescopes. As practice shows, the creation of a universal instument (telescope) for the timely detection of NEOs of all sizes (from 10 m and more) is hardly possible. Neither the large working telescopes (like the famous Pan-STARRS, the "Fly eye" NEOSTEL telescope (Marchiori et al. 2022), nor the future giant ($\omega = 3°$, $\varnothing 8$ m) ground-based telescope LSST (Ivezić et al. 2019), nor the space infrared observatory NEO Surveyor (Mainzer et al. 2023) are a panacea.

Shustov et al. (2013) proposed a two-mode structure for constructing a ground-based NEO detection system:

Long-range detection mode (NEO size $\gtrsim 50$ m)

– Lead time ~ 30 days (i.e., first detection time > 35 days).
– Time for all-sky survey (cadence) $\lesssim 5$ days.
– The main assets are telescopes of the visible ranges. It is necessary to work at the limit of $23^{\rm m}$ V, which requires for wide-angle ($\omega > 1°$) large-aperture ($\varnothing \sim 1$ m) telescopes.

Near-field detection mode (NEO size $\gtrsim 10$ m)

– Lead time ~ 1 day.
– The time for all-sky survey $\lesssim 1$ hour.
– The main element is an expanded network of wide-angle ($\omega > 4°$) low-aperture ($\varnothing \lesssim 0.5$ m) telescopes of the visible range. It is necessary to work at the limit of $17^{\rm m}$ V.

There are networks that can be classified as middle class. For example, ATLAS, the Asteroid Terrestrial-impact Last Alert System of 50-cm telescopes, is a robotic

astronomical survey and early warning system optimized for detecting smaller near-Earth objects a few weeks to days before they impact the Earth (Tonry et al. 2018). However, such networks still do not have sufficient cadence to detect extremely small and close NEOs.

In recent years robotic observation pipelines for small bodies in the Solar system based on open-source software and commercially available telescope hardware are becoming popular (see, e.g., Hoffmann et al. 2022). There is a tendency to create multi-aperture robotic systems for the near-field detection mode. An example is the Mini-MegaTORTORA (MMT-9) instument (Karpov et al. 2016), which is successfully used at SAO RAS. The aperture of the telescopes is too small, but the version with an aperture of 30 cm, which is being prepared for implementation, will already be a sufficiently powerful and at the same time very economical instrument.

In Shustov et al. (2015) it is shown that the creation of a system for the near-field detection of PHOs coming from the daytime sky requires the use of a space-based system. A concept of such a system has been developed in which one or more optical telescopes are placed in the vicinity of the L1 libration point for the Sun-Earth system (Shugarov et al. 2021).

3 Meteoroids and safety of space activity

A variety of small bodies either reside in near-Earth space, or approach the Earth, sometimes coming from the farthest regions of the Solar system. The smallest bodies constantly collide with the Earth, larger ones hit our planet less often, but, as a rule, arouse great interest among people. Figure 4 shows summary statistics of the total number of collisions of natural objects with the Earth (per year).

The original figure (from Drolshagen et al. 2017) is supplemented with gray shading to identify meteoroids, indicators of methods for observing particles of different mass ranges, and a straight line that qualitatively corresponds to the universal law of the mass spectrum of different objects in the Universe. A discussion of this universal mass spectrum can be found in Shustov (2019).

Unlike relatively large bodies (asteroids and comets), meteoroids and dust particles in near space are studied by the manifestations of their interaction with the Earth's atmosphere using meteor astronomy methods or with the help of collision sensors on board spacecraft. The meteoroid risk in near-Earth space is basically caused by 1–10 mm meteoroid bodies (Murtazov 2018). Collisions with larger projectiles can cause more serious damage, but their number is relatively small. According to the model of Cour-Palais (1969), the flux of meteoroids with a mass greater than m can be estimated by the formula $\log N = -14.37 - 1.213 \log m$, where N is measured

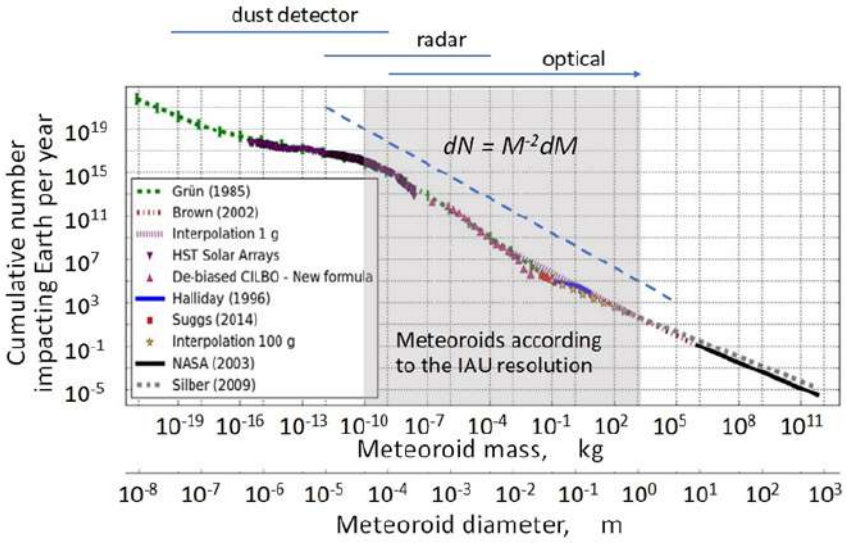

Fig. 4. Frequency of collisions with the Earth.

in $1/(\mathrm{m}^2\,\mathrm{s})$, and m in grams. For $m = 10^{-6}$ g the flux is $\sim 2.5\,\mathrm{m}^{-2}\mathrm{yr}^{-1}$, for $m = 1$ g the flux is almost negigible $\sim 1.4 \times 10^{-7}\,\mathrm{m}^{-2}\mathrm{yr}^{-1}$.

There are three main families of models (software) of the meteoroid environment.

In Russia, since 1987, we have been using the national standard GOST 25645.128-85, which establishes a model for the spatial distribution of meteor bodies with a mass of $10^{-6} - 10^{2}$ g in the ecliptic plane up to distances of $\sim 10^{6}$ km and bodies with a mass of $10^{-9} - 10^{-6}$ g within 200–1000 km from the Earth. In relation to space debris, since 2022, we have been using the national standard GOST R 25645.167-2022 "Space environment (natural and artificial). A model of the spatiotemporal distribution of the density of flows of technogenic matter in near-Earth space".

The ESA MASTER (Meteoroid and Space Debris Terrestrial Environment Reference) model is designed in such a way as to give a realistic description of the natural environment and the environment consisting of solid particles created by man. Meteoroid environment is described by Grün interplanetary flux model (Grün et al. 1985), which assumes an isotropic distribution of meteoroids based on lunar crater data, zodiacal light, and in situ measurements. The latest version, MASTER–8, is described in Braun et al. (2021).

The NASA Orbital Debris Engineering Model (ORDEM) Series is designed to provide reliable estimates of the flux of orbital debris onto spacecraft and into the field of view of a telescope or radar (see, e.g., Flegel et al. 2010). The meteoroid situation

is handled by NASA's Meteoroid Environment Office (MEO).[6] MEO is responsible for support of the Meteoroid Engineering Model (MEM). Some of the revolutionary aspects of MEM are a) identification of the sporadic radiants with real sources of meteoroids, such as comets, b) a physics-based approach that provides accurate fluxes and directionality for interplanetary spacecraft in the range from 0.2 AU to 2 AU, and c) velocity distributions obtained from theory and confirmed by observations. Given a state vector, the model outputs mass-limited or penetrating fluxes and average impact speeds and distributions on the surfaces of a cube-like structure with the ram face oriented along the spacecraft velocity. The current version of MEM, MEM 3 (see Moorhead 2019), generates environment data for spacecraft orbiting the Earth, Moon, Mercury, Venus, or Mars, or traveling through interplanetary space.

The models presented above relate to the situation in near-Earth space. It is clear that meteoroids and dust are our guests. Many researchers believe that comets are the sources of the dust (see, e.g., Yang and Ishiguro 2018). However in Busarev et al. (2016) and other papers by these authors it was shown that a number of asteroids exhibit so-called sublimation-dust activity and asteroids can lose solid matter in significant quantities. Shustov et al. (2022); Zolotarev and Shustov (2023) argued in favor of the fact that the rate of dust emission from asteroids activated by collisions can be comparable to a cometary source. It is important to deal with the issue of particle balance, because particles of asteroidal origin differ significantly in density (and in breakdown properties) from cometary particles. Also, to create a comprehensive dynamic model of the meteoroid environment in near-Earth space, improved models of the origin and dynamics of meteoroid streams are needed.

4 The need for cooperation

Both the NEO Problem and problem of safety of space activities in the near-Earth space are global in nature. This implies the need for international cooperation. On the other hand, effective participation in international cooperation requires a substantial national program.

The documents adopted by the UN note the leading role of three information and analytical centers on the NEO problem (two of them controlled by the United States):

- MPC (Minor Planet Center).[7] It works under the auspices of the IAU, is located in the USA and funded by NASA;

[6] https://www.nasa.gov/meteoroid-environment-office/—accessed: 24 July 2024.
[7] https://minorplanetcenter.net/—accessed: 24 July 2024.

- NASA NEO Program Office at JPL (NASA Program Center on the NEO problem in the Jet Propulsion Laboratory);[8]
- ESA NEO Coordination Centre.[9] The NEOCC is ESA's centre for computing asteroid and comet orbits and their probabilities of Earth impact.

There are no Russian centers in this elite list, but there is hope that after the implementation of the "Milky Way" project a Russian center with a world-famous name will appear here.

Two major project (programs) for international cooperation in the NEO field are supported by the UN. They are IAWN and SMPAG:

IAWN (International Asteroid Warning Network)[10]

The IAWN is a virtual network of institutions performing functions such as detecting, monitoring and physically characterizing the population of potentially hazardous near-Earth objects, as well as maintaining an internationally recognized coordination center for receiving, confirming and processing all near-Earth object observations. The current list of IAWN signatories (currently 52 names) include major space agencies, institutes (five instistutions from Russia among them), observatories and experienced amateurs (e.g., G. Borisov from Russia). INASAN has been involved in the network since 2016. As part of the international cooperation of IAWN, an observational experiment was conducted in 2017 to recover and follow-up the asteroid 2012 TC4. For four months, astronomers from the USA, Canada, Colombia, Germany, Israel, Italy, Japan, the Netherlands, Russia, and South Africa tracked the asteroid using ground-based and space telescopes in the optical and radio ranges in order to study its orbit, shape, rotation features and composition (see Reddy et al. 2019). The rich observational material obtained during the campaign made it possible, in particular, to accurately calculate the orbit of the asteroid 2014 TC4. On the Russian side, observations of the asteroid 2012 TC4 were conducted by the Terskol observatory with the Zeiss-2000 telescope (see Fig. 5).

Space Mission Planning Advisory Group (SMPAG)[11]

This is a group of Member States that have space agencies. The primary objective of SMPAG is to prepare an international response to the NEO threat by sharing information, developing joint research options and mission capabilities, and conducting NEO mitigation planning activities. Roscosmos is a member of SMPAG, but is not yet active.

[8] https://cneos.jpl.nasa.gov/—accessed: 24 July 2024.
[9] https://neo.ssa.esa.int/—accessed: 24 July 2024.
[10] https://iawn.net/about/members.shtml—accessed: 24 July 2024.
[11] https://www.cosmos.esa.int/web/smpag—accessed: 24 July 2024.

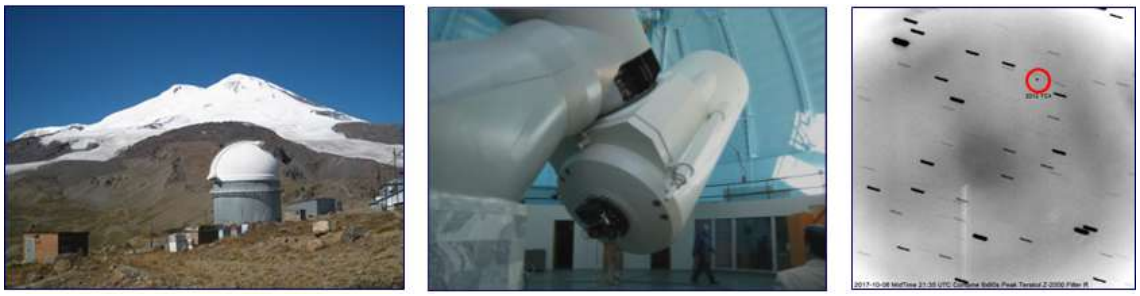

Fig. 5. Terskol observatory, Zeiss-2000 telescope, 2012 TC4 (in a red circle).

The Working Group on Astronomy of the BRICS countries (BAWG) initiated the project "BRICS Intelligent Telescope and Data Network (BITDN)"[12] (former name—"BRICS Optical Transient Network"). It is a dedicated flagship programme of the BRICS countries to develop a network of ground-based optical telescopes to survey the entire sky to detect short-duration optical transients and provide the capability to follow-up multi-wavelength and multi-channel transient objects (see Buckley et al. 2021). In terms of NEO topics, BITDN will meet the goal of successfully detecting and determining the orbit of NEOs down to tens of meters in size across the entire sky every few hours, reaching a limiting magnitude 20^{m}. The survey observation strategy will allow targeted tracking of PHO alerts, allowing the path of an approaching object to be tracked and the most likely impact location to be calculated.

In recent years Roscosmos is developing a new Russian system of telescopes and satellites called the Milky Way which is designed to ensure the safety of space activities in near-Earth space[13]. The Milky Way system will play an important role in monitoring and warning about dangerous situations in outer space near the Earth. It includes up to 65 telescopes, as well as a space segment represented by a group of satellites that will constantly monitor near-Earth space. The first of them is planned to be launched in 2027. The project will deal with several problems: space debris, spaceweather and NEO problem. The introduction of the Russian Milky Way will contribute to the development of scientific potential, more accurate forecasts and responses to potential threats in and from space.

[12] https://www.bricsastronomy.org/brics-intelligent-telescope-and-data-network/—accessed: 28 July 2024.
[13] https://tass.com/science/1792063?ysclid=lz5maokqlw391262954—accessed: 28 July 2024.

Funding

The work is supported by the RSF grant No. 22-12-00115.

References

Barbee B. W., Sarli B., Lyzhoft J., et al., 2020, LPI Contrib., 2242, id. 2009
Braun V., Horstmann A., Lemmens S., et al., 2021, 8th European Conference on Space Debris, id. 18
Buckley D., McBride V., Barres De Almeida U., et al., 2021, Anais da Academia Brasileira de Ciências, 93, id. e20200917
Busarev V.V., Barabanov S. I., and Puzin V. B., 2016, Solar System Research, 50, 4, p. 281
Cour-Palais B. G., 1969, "Meteoroid Environment Model-1969: Near Earth to Lunar Surface", NASA SP-8013 (Washington, DC: NASA)
Drolshagen G., Koschny D., Drolshagen S., et al., 2017, Plavetary and Space Science, 143, p. 21
Flegel S.K., Krisko P., Gelhaus J., et al., 2010, 38th COSPAR Scientific Assembly, 38, p. 12
Granvik M., Morbidelli A., Jedicke R., et al., 2018, Icarus, 312, p. 181
Grün E., Zook H.A., Fechtig H., et al., 1985, Icarus, 62, 2, p. 244
Harris A.W. and Harris A.W. 1997, Icarus, 126, 2, p. 450
Hoffmann T., Gehlen M., Plaggenborg T., et al., 2022, Frontiers in Astronomy and Space Sciences, 9, id. 895732
Ivezić Ž., Kahn S.M., Tyson J.A., et al., 2019, Astrophys. J., 873, 2, id. 111
Jacobson S., Bose M., Bodewits D., et al., 2021, Bulletin of the American Astronomical Society, 53, 4, id. 171
Karpov S., Beskin G., Biryukov A., et al., 2016, Revista Mexicana de Astronomia y Astrofisica Conference Series, 48, p. 91
Mainzer A.K., Masiero J.R., Abell P.A., et al., 2023, Planetary Science Journal, 4, 12, id. 224
Marchiori G., Tordi M., Ghedin L., et al., 2022, Proc. SPIE, 12182, id. 121824K
Moorhead A.V., 2019, LPI Contrib., 2109, id. 6054
Murtazov A.K., 2018, Open Astronomy, 27, p. 144
Reddy V., Kelley M.S., Farnocchia D., et al., 2019, Icarus, 326, p. 133
Shugarov A., Shmagin V., Boqian X., et al., 2021, 7th IAA Planetary Defense Conference, id. 100
Shustov B.M., 2019, INASAN Science Reports, 4, p. 356
Shustov B.M., Naroenkov S.A., Emel'yanenko V.V., et al., 2013, Solar System Research, 47, 4, p. 288
Shustov B.M., Shugarov A.S., Naroenkov, S. A., 2015, Astronomy Reports, 59, 10, p. 983
Shustov B.M., Zolotarev R.V., Busarev V.V., et al., 2022, Astronomy Reports, 66, 11, p. 1098
Tonry J. L., Denneau L., Heinze A.N., et al., 2018, PASP, 130, id. 064505
Yang H. and Ishiguro M., 2018, Astrophys. J., 854, 2, id. 173
Zolotarev R.V. and Shustov B.M., 2023, Astronomy Reports, 67, 10, p. 1019

Extrasolar worlds: a review of the current state of exoplanet research in Russia and the world

G. Valyavin and D. Gadelshin

Special Astrophysical Observatory of the Russian Academy of Sciences,
Nizhny Arkhyz, 369167 Russia

Abstract. The history of the discovery and the main results of the study of extrasolar planets (exoplanets) in the world and in Russia are presented. The main emphasis is on describing the methods and results of the most successful space and ground-based research projects. The most striking examples among the studies of exoplanets discovered around stars of different types egiven. The Russian projects over the past few years for the search and study of exoplanets, their results, and immediate prospects are described.

Keywords: planets and satellites: detection; methods: observational; techniques: photometric, spectroscopic

DOI: 10.26119/VAK2024.003

1 Introduction

The theme of the plurality of worlds in the Universe has occupied the minds of thikers and nations of all times for thousands of years. In attempts to understand the structure of our world and the place of humanity in it, some thinkers of the past, long before the advent of modern observational means, even expressed the opinion that the stars are distant suns, around which planets like Earth and other planets of the Solar system can revolve. In particular, Giordano Bruno, who lived in the 16th century, suggested that life is not only on Earth, that it is distributed in an infinite Universe on planets with diverse conditions, and that the forms it takes are infinitely diverse (Bruno 1584). He also believed that life inevitably gives rise to intelligence. Currently, the truth of many of Bruno's amazing statements is confirmed by modern science. Meanwhile, despite such interest, systematic studies of extrasolar planets began only recently.

In fact, the first confidently confirmed extrasolar planets (hereinafter referred to as "exoplanets", or simply "planets") date back to the nineties of the 20th century (Wright and Gaudi 2013), although such research could have begun much earlier and been successful. Apparently, such a historical delay was associated with pessimistic expectations regarding the detectability of exoplanets. In particular, the existence of hot Jupiters—exoplanets with a mass close to the mass of Jupiter but orbiting in orbits close to the stars with periods of less than 10 days—turned out to be a surprise for astronomers (Bryant et al. 2023). Massive planets orbiting red dwarf stars exhibit very deep transits (Kanodia et al. 2023), which could once be detected even by photoelectric methods. They also demonstrate amplitudes of variability in the radial velocities of stars up to several hundred $\mathrm{m\,s^{-1}}$, which could easily be detected within the framework of classical high-spectral resolution spectrographs of the generation of the 60–70s of the 20th century.

The history of the systematic search and study of exoplanets started in the 80s of the last century. However, most reports of positive detections of planetary mass objects before 1995 turned out to be erroneous. Only two of them have been confirmed and recognized by the world scientific community. In particular, in 1988, Canadian astronomers B. Campbell, G. Walker, and S. Young (Campbell et al. 1988) reported the discovery of a massive planet around the main component of the binary star γ Cephei, which was finally confirmed in 2003 by Hatzes et al. (2003). Also, in 1992, Polish astronomer A. Wolszczan, using the Arecibo radio telescope, discovered two super-Earth-mass planets near the millisecond pulsar PSR B1257+12 (Wolszczan and Frail 1992).

Meanwhile, the first unequivocal discovery of a planetary mass object orbiting a normal main sequence star was announced by Swiss astronomers M. Mayor and

D. Queloz in October 1995 (Mayor and Queloz 1995). Using the ELODIE spectrograph mounted on the 1.93-m telescope at the Haute–Provence Observatory in France, Queloz et al. (1998) detected sinusoidal Doppler oscillations of the Sun-like star 51 Pegasi, located 50 light-years from Earth. The short period (4.2 days) and significant amplitude of oscillations indicated that the planet should have of about 0.5 mass of Jupiter. Thus began a triumphant march of massive discoveries and detailed studies of the physical properties of new extrasolar worlds.

2 The most important results in the history of exoplanet observations

From the mid-nineties of the last century until the present day, a number of dozens of ground and space missions have successfully added to the list of more and more extrasolar worlds. Among the most successful, it is necessary to note the work of the space observatories Kepler (Dupree 2009), CoRoT (Baglin et al. 2007), and TESS (Ricker et al. 2014) as well as the work of ground-based photometric surveys of exoplanets such as the famous SuperWASP (Street et al. 2003) or the lesser-known domestic "Kourovka Exoplanet Survey" (Burdanov et al. 2016). Thanks to all these missions, we now have a list of over ten thousand extrasolar planets and candidates. Based on these studies, the physical properties of a significant part of the confirmed planets became known, which turned out to be much more diverse than the characteristics of the planets of the Solar system. Without being able to present all this amazing diversity within the framework of this work, we will dwell only on the most significant, in our opinion, discoveries in the world of extrasolar worlds of the last few years.

February 2017. Discovery of a very compact system of seven transiting Earth-sized planets orbiting the nearby ultra-cool red dwarf TRAPPIST-1 (Gillon et al. 2017). At least three of the seven planets are in the habitable zone of their parent star.

February 2021. Direct observations with the upgraded VISIR instrument on the VLT of the stars α Centauri A and α Centauri B in the mid-IR range led to the discovery of a candidate exoplanet with a radius of 3–11 $R_\oplus$ orbiting in the habitable zone of star A at a distance of about 1.1 AU (Wagner et al. 2021). This image artifact, however, may be the exozodiacal disk of α Centauri A.

January 2022. A study of transits of the gas giant Kepler-1708 b, orbiting in the habitable zone of a Sun-like star, revealed signs of the presence of a natural satellite in the orbit of the parent planet (Kipping et al. 2022). The exomoon's radius can be 2.6 times greater than Earth's, and its orbital period can be 4.6 days.

July 2022. The beginning of the scientific program of the infrared James Webb Space Telescope (JWST) marked a new stage in the development of astronomy in general, and exoplanetary research in particular (Pontoppidan et al. 2022). The observatory was designed and developed by the National Aeronautics and Space Administration (NASA) in collaboration with the European and Canadian Space Agencies (ESA and CSA), and has a segmented mirror with a total diameter of 6.5 meters. The beginning of a massive study of the atmospheres of exoplanets with a wide variety of sizes, both in direct light (Lustig-Yaeger et al. 2023) and in reflected light.

March–September 2023. Using JWST, several emission and transmission spectra of two inner planets of the TRAPPIST-1 system, b and c, were obtained (Lim et al. 2023). Due to their proximity to the star, both are tidally locked. The high brightness temperature and lack of heat redistribution from the day side to the night side suggest the absence of noticeable atmospheres—both planets probably resemble Mercury with a bare surface.

September 2023. Using JWST, the transmission spectrum of mini-Neptune K2-18 b was obtained at wavelengths of 0.9–5.2 μm (Madhusudhan et al. 2023). The presence of methane and carbon dioxide as well as the absence of ammonia was detected. This may indicate the existence of an ocean of liquid water under a temperate, hydrogen-rich atmosphere. The water probably forms clouds in deeper layers of the atmosphere than was accessible to James Webb.

March–June 2024. Using JWST, transmission spectra of LHS 1140 b, a planet with a radius of 1.73 $R_\oplus$ orbiting in the habitable zone of a red dwarf, were obtained at wavelengths of 0.65–5.18 μm (Cadieux et al. 2024). A hydrogen-rich atmosphere was excluded, but the spectrum showed evidence of Rayleigh scattering in a nitrogen-dominated atmosphere. The water clouds likely form deep enough to remain undetected.

3 Basic methods for detecting and studying exoplanets

Today, there is a significant collection of methods for diagnosing the exoplanetary environment of stars of various types. Among them, probably the only direct one is the method of obtaining images of exoplanets using coronagraphs and adaptive cameras in the case of ground-based observations. Using this method, the presence of entire families of outer planets in the surroundings of several bright stars was discovered (see, e.g., Marois et al. 2010). The advantages of the method are obvious, so they are not discussed here.

The disadvantages include the limited application of the method under ground-based observations. All other methods are indirect in one way or another. Let us consider only those of them that, in our opinion, are the main ones and the combination of which provides unambiguous information about the presence and physical properties of exoplanets in the orbits of their parent stars.

3.1 Photometric transit method

This is one of the most productive methods of searching for the planets the orientation of whose orbits makes it possible to observe the events of their passage against the background of the disks of their parent stars. For ground-based instruments, the method makes it possible to detect exoplanets that are capable of causing a drop in the light flux from the parent star from several percent ("Jupiters" against the background of small stars) to 0.1% ("super-Earths" and even "Earths" against the background of red dwarfs). Figure 1 shows an example of a comprehensive observation of super-Earth transits in the star system HD 219134 (Valyavin et al. 2018). These results, obtained using the 1-m telescope of the Special Astrophysical Observatory of the Russian Academy of Sciences (SAO RAS), clearly illustrate the precision capabilities of ground-based astronomy in the study of exoplanets. In this case, the transit depth obtained in total from five events is determined at the level of $0.13 \pm 0.027\%$ (Valyavin et al. 2018).

Often within the framework of the method, depending on the forms of transits, it is possible to speak with a high degree of probability about a transit event of a planetary nature even without the involvement of additional research. Figures 2 and 3 show different examples of the shapes of transit curves obtained using the robotic 0.5-m telescopes of SAO RAS (Valyavin et al. 2022a,b). The observed data are taken from Yakovlev et al. (2022, 2023).

As you can see, the registered forms of transits can be different. The example in Fig. 2 represents the so-called sliding transit. In this case, as a rule, there is great uncertainty in establishing the size of the eclipsing body relative to the disk of the parent star. Such transits are quite often diagnosed as false. Meanwhile, examples of central transits (Fig. 3) immediately give an idea of the size of the eclipsing body. Such transits, as a rule, require minimal additional diagnostics to confirm their planetary nature.

Among these methods, the main one is the radial velocity method.

3.2 Radial velocity method

Along with the photometric transit method, the radial velocity method based on Doppler spectroscopy is traditionally one of the most popular and effective methods

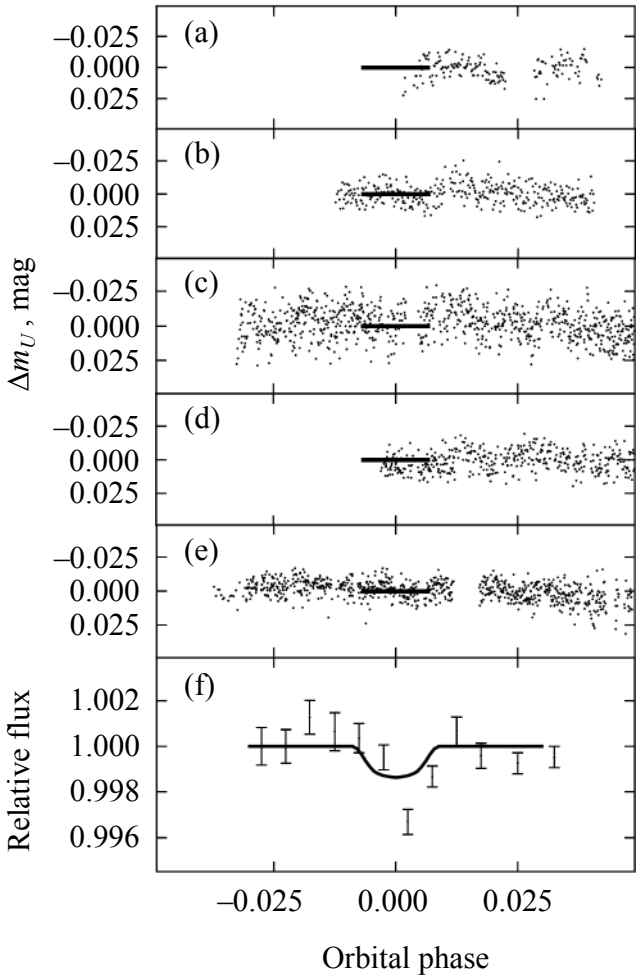

Fig. 1. Phased time series of flux in the Johnson system U band from the star HD 219134 in units of residual magnitudes for different dates (a, b, c, d, e) and their average (f). For details, see Valyavin et al. (2018).

for searching and studying the physical characteristics of exoplanets. Despite this, just like the transit method, Doppler diagnostics is not self-sufficient. There are a number of effects that mimic the Doppler variability of the radial velocities of stars. In particular, the presence of global magnetic fields with secular stability can cause rotationally modulated variability of radial velocities in such stars. For example (see Lee et al. 2018), the star χ Dra A exhibited signs of the presence of a global magnetic field, the variability of which coincided with the rotation of the star. Detected

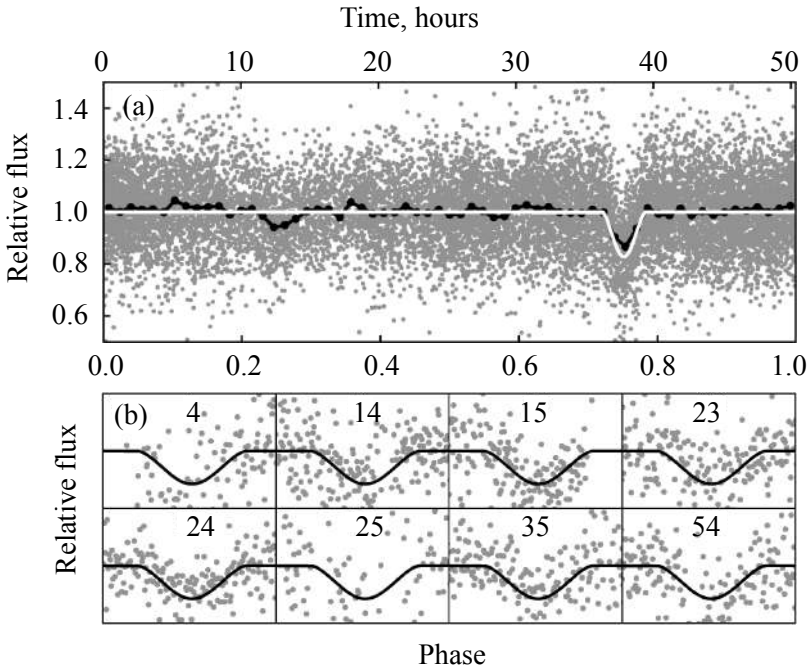

Fig. 2. Light curve of SOI-2 (Yakovlev et al. 2022, 2023). Top: phase convolution with the rotation period (dots), median values (black line), and the model curve (white line). Bottom: fragments of individual transits with the same model curve (black line).

variability of the radial velocities of the star (Lee et al. 2018) folded with the found rotation period is shown in Fig. 4. The arguments presented in Han et al. (2018) indicate that the desired variability in the radial velocity of the star is caused not by an exoplanet but by a rotationally modulated magnetic field.

Of course, the found change in the star's radial velocity may also be associated with a synchronously rotating planet, but uncertainty of this kind in this particular case cannot be resolved unambiguously. Meanwhile, for systems whose planetary orbits are visible "edge-on" to an observer on Earth, the radial velocity method in combination with the transit method in the vast majority of cases provides an accurate diagnosis of the planetary nature of the registered transit event. In this regard, let us dwell on the spectroscopic technique of testing the variability of the radial velocities of stars in a little more detail.

It is known (Valenti et al. 1995) that the observed spectra of stars are presented by the convolution of their true spectra with the instrumental profile (IP) of the spectrograph. In the general case, the IP is a multiparameter function depending on

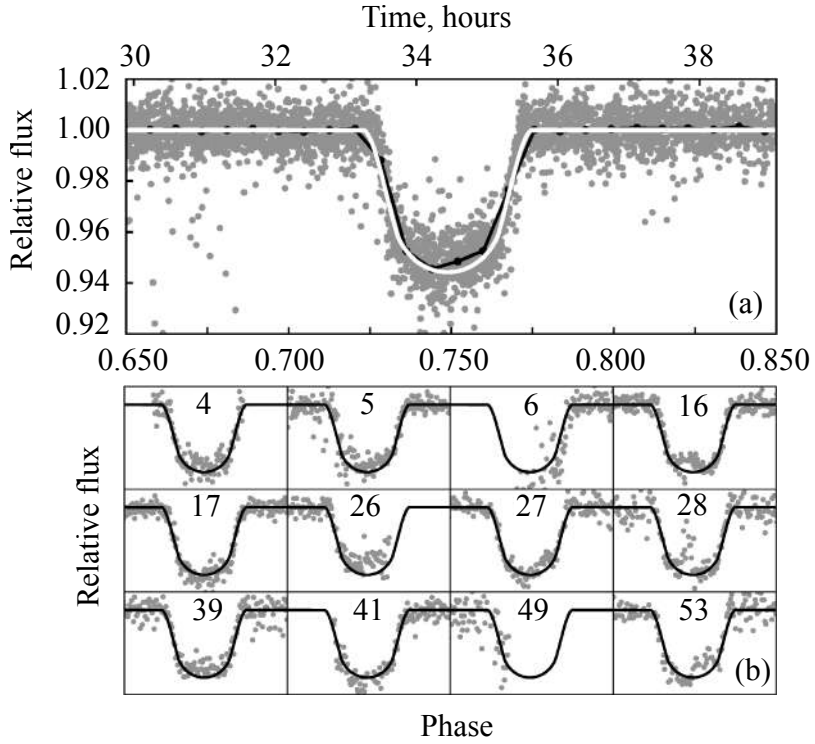

Fig. 3. Light curve of SOI-3 (Yakovlev et al. 2022, 2023), explanations are given in the caption to Fig. 2.

the slit width, the quality of the instrument optics, etc. For classical spectrographs, which do not provide uniform illumination of the slit by the light of the star being studied and/or stabilization of its image on the slit, the IP is also a function of the position of the star (object) on the slit and weather conditions. For this reason (lack of sufficient optical stabilization), also in the absence of thermal and mechanical stabilization of the spectrograph, the IP is a variable function depending on time. The presence of this variability can introduce distortions in the position of spectral lines in the observed spectra of stars up to several $\mathrm{km\,s^{-1}}$. Thus, in the matter of achieving the accuracy of measurements of stellar radial velocities necessary for detecting exoplanets, there are two methods. The first is associated with the technique of wavelength calibration, which allows determining the IP in each observation and taking into account its variability when calculating the Doppler shift in the spectra of stars. To date, the most proven method for determining the IP uses the so-called absorption iodine cell (Valenti et al. 1995). The iodine cell is a transparent, sealed flask

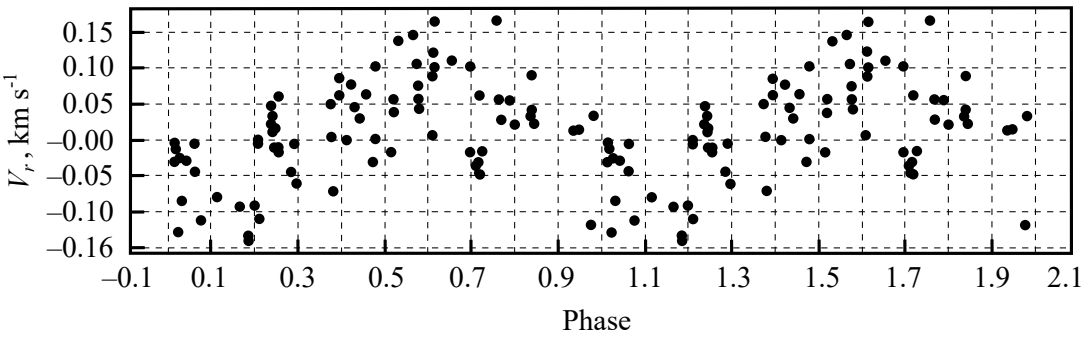

Fig. 4. Residual curve of variation in the radial velocity of χ Dra A convolved with the star rotation period $P = 22\overset{\mathrm{d}}{.}2$.

filled with molecular iodine gas I 2. When light from a star passes through the cell, a system of molecular lines of I 2 is generated in the resulting spectrum between wavelengths of 500 nm and 600 nm in addition to the spectrum of the star. The shapes and residual intensities of these lines are weakly sensitive to changes in pressure and temperature of the environment. And, since they are recorded under conditions absolutely identical to recording the stellar spectrum, precise knowledge of the shapes of their profiles allows one for each wavelength in the range of 500–600 nm to obtain the IP shape directly at the moment of observing the star. In turn, this allows correction almost all distortions related to spectrograph instability. Thus, the use of iodine cells in combination with slit spectrographs, even without expensive optical-mechanical stabilization, is capable of demonstrating the accuracy of measuring the variability of radial velocities of stars sufficient for searching for exoplanets near them. This is the main advantage of the method. The disadvantages include a limited spectral range and significant loss of light due to absorption by iodine in the working range of 500–600 nm.

The second method involves the maximum possible optical-mechanical stabilization of the spectrograph. The use of a fiber-optic input instead of a slit has revolutionized this type of spectrograph. For a long time, the world leader in this concept was the HARPS fiber-optic input spectrograph (Mayor et al. 2003). This instrument took all possible measures for its optical, mechanical and thermal protection. In addition, the entire spectral part of HARPS is placed in a vacuum chamber, which, among other things, eliminates the instability of the resulting spectrograms due to fluctuations in air refraction in the optical path of the spectrograph. With the help of this instrument, over the past two decades, probably the most accurate Doppler studies of exoplanets have been obtained, up to 20 cm s^{-1} and even higher.

As our practice has shown (Burlakova et al. 2020; Gadelshin et al. 2020; Valyavin et al. 2022a,b; Galazutdinov et al. 2023) with the BTA FFOREST fiber-optic spectrograph (Valyavin et al. 2014, 2015, 2020; Galazutdinov et al. 2023), this path has significantly greater prospects compared to the previous method, although it is more financially expensive.

3.3 Transmission spectroscopy

Transmission spectroscopy methods, which can detect changes in the radii of transiting exoplanets with wavelength, provide a unique opportunity to study the physical and chemical properties of their atmospheres. The transmission spectrum is the dependence of the exoplanet radius, obtained by observing a planet transit in a number of bands over the spectral range, on the wavelength. To construct broadband and midband transmission spectra, multicolor photometric and spectrophotometric observations are carried out on telescopes of different apertures. Analysis of such spectra helps draw conclusions about the vertical structure and internal structure of the planet's atmospheric layers and study their evolution. Transmission spectroscopy also allows us to reconstruct absorption and scattering lines in the exoplanet's atmosphere. More details on the method can be found in Valyavin et al. (2018) and references therein.

4 Russian ground-based projects for the study of exoplanets and their future prospects

Unfortunately, in Russia, for various reasons, this area lags far behind the level of world science, especially in terms of observational astronomy. Meanwhile, over the past 10 years, several domestic working groups on the study of exoplanets have been formed from astronomers of the Kourovka and Pulkovo Observatories, SAO RAS, and Kazan Federal University. Through their efforts, together with groups from other countries, almost ten exoplanets have already been discovered. Also, several scientific groups from INASAN, SAI MSU, IKI RAS, and others are known for their strong theoretical studies of exoplanets.

Since the creation of the Russian Science Foundation in 2014, financial support for instrumental scientific projects on a competitive and private basis has created a stable trend in Russia in the direction of experimental research of exoplanets by ground-based observational means. In particular, the efforts of young enthusiastic scientists united around the photometric project MASTER (for the results from the part of it at the Kourovka Observatory, see Burdanov et al. 2016) allowed the first, Kourovka survey of exoplanet candidates to begin and the first exoplanet in Russia

to be discovered based on additional diagnostics of these candidates by different methods at SAO RAS and other observatories.

Another successful working project, which allowed systematic observations of exoplanets by the Doppler method and which at about the same time began to give positive detections (Yılmaz et al. 2017), is the Russian-Turkish project, headed on the Russian side by Kazan University, the owner of a 1.5-m telescope on an equal basis with the Turkish side. This telescope has a high spectral resolution spectrograph, which allowed achieving the accuracy necessary for discovery with an iodine cell.

Young Russian astronomers have also achieved some success in the search for exoplanets using the TTV (Transit Time Variation) method. As part of their research (Sokov et al. 2018), a second exoplanet TrES-5c was discovered in the TrES-5 system.

Finally, the EXPLANATION (EXoPLANet And Transient Events InvestigatiON) project has been running since 2022. The goal of the project is a mass search for non-stationary events in the Universe using photometric, speckle interferometric, spectral, and radiobolometric observing methods as well as the study of exoplanets. The core of the project is all optical telescopes of SAO RAS and a number of other observatories. The philosophy of the project and the first results of its work are presented in Valyavin et al. (2022a,b); Yakovlev et al. (2022, 2023). We associate further prospects for the development of exoplanet research in Russia with this project as well as with the upcoming launch and operation of the Russian space mission WSO-UV (Sachkov et al. 2022).

References

Baglin A., Auvergne M., Barge P., et al., 2007, AIP Conf. Proc., 895, p. 201

Bruno G., 1584, On the Infinite Universe and Worlds (Boston: MA: Birkhäuser)

Bryant E.M., Bayliss D., and Van Eylen V., 2023, MNRAS, 521, 3, p. 3663

Burdanov A.Y., Benni P., Krushinsky V.V., et al., 2016, MNRAS, 461, 4, p. 3854

Burlakova T.E., Valyavin G.G., Aitov V.N., et al., 2020, Astrophysical Bulletin, 75, p. 482

Cadieux C., Doyon R., MacDonald R.J., et al., 2024, Astrophys. J., 970, id. L2

Campbell B., Walker G.A.H., and Yang S., 1988, Astrophys. J., 331, p. 902

Dupree A., 2009, APS New England Section Fall Meeting Abstracts, APS Meeting Abstracts, id. F1.002

Gadelshin D.R., Valyavin G.G., Lee B.-C., et al., 2020, Astrophysical Bulletin, 75, 4, p. 437

Galazutdinov G.A., Baluev R.V., Valyavin G., et al., 2023, MNRAS, 526, 1, L111

Gillon M., Triaud A.H.M.J., Demory, B.-O., et al., 2017, Nature, 542, 7642, p. 456

Han I., Valyavin G., Galazutdinov G., et al., 2018, MNRAS, 479, 2, p. 1427

Hatzes A.P., Cochran W.D., Endl M., et al., 2003, Astrophys. J., 599, 2, p. 1383

Kanodia S., Mahadevan, S., Libby-Roberts J., et al., 2023, Astron. J., 165, 3, p. 120

Kipping D., Bryson S., Burke C., et al., 2022, Nature Astronomy, 6, p. 367

Lee B.-C., Gadelshin D., Han I., et al., 2018, MNRAS, 473, 1, L41

Lim O., Benneke B., Doyon R., et al., 2023, Astrophys. J., 955, 1, id. L22
Lustig-Yaeger J., Fu G., May E.M., et al., 2023, Nature Astronomy, 7, p. 1317
Madhusudhan N., Sarkar S., Constantinou S., et al., 2023, Astrophys. J., 956, 1, id. L13
Marois C., Zuckerman B., Konopacky Q.M., et al. 2010, Nature, 468, 7327, p. 1080
Mayor M., Pepe F., Queloz D., et al., 2003, The Messenger, 114, p. 20
Mayor M. and Queloz D., 1995, Nature, 378, 6555, p. 355
Pontoppidan K.M., Barrientes J., Blome C., et al., 2022, Astrophys. J., 936, 1, id. L14
Queloz D., Mayor M., Sivan J.P., et al., 1998, ASP Conf. Ser., 134, p. 324
Ricker G.R., Winn J.N., Vanderspek R., et al., 2014, Proc. SPIE, 9143, id. 914320
Sachkov M., Gómez de Castro A.I., Shustov B., et al., 2022, Proc. SPIE, 12181, id. 121812S
Sokov E.N., Sokova I.A., Dyachenko V.V., et al., 2018, MNRAS, 480, 1, p. 291
Street R.A., Pollaco D.L., Fitzsimmons A., et al., 2003, ASP Conf. Ser., 294, p. 405
Valenti J.A., Butler R.P., and Marcy G.W., 1995, PASP, 107, p. 966
Valyavin G., Beskin G., Valeev A., et al., 2022a, Astrophysical Bulletin, 77, 4, p. 495
Valyavin G., Beskin G., Valeev A., et al., 2022b, Photonics, 9, 12, id. 950
Valyavin G.G., Bychkov V.D., Yushkin M.V., et al., 2014, Astrophysical Bulletin, 69, 2, p. 224
Valyavin G.G., Bychkov V.D., Yushkin M.V., et al., 2015, ASP Conf. Ser., 494, p. 305
Valyavin G.G., Gadelshin D.R., Valeev A.F., et al., 2018, Astrophysical Bulletin, 73, 2, p. 225
Valyavin G.G., Musaev F.A., Perkov A.V., et al., 2020, Astrophysical Bulletin, 75, 2, p. 191
Wagner K., Boehle A., Pathak P., et al., 2021, Nature Communications, 12, id. 922
Wolszczan A. and Frail D.A. 1992, Nature, 355, 6356, p. 145
Wright J.T. and Gaudi B.S., 2013, Planets, Stars and Stellar Systems. Volume 3: Solar and Stellar Planetary Systems, ed. T.D. Oswalt, L.M. French, P. Kalas, p. 489
Yakovlev O.Ya., Valeev A.F., Valyavin G.G., et al., 2023, Astrophysical Bulletin, 78, 1, p. 79
Yakovlev O.Ya., Valeev A.F., Valyavin G.G., et al., 2022, Frontiers in Astronomy and Space Sciences, 9, id. 903429
Yılmaz M., Sato B., Bikmaev I., et al., 2017, A&A, 608, id. A14

The differential flow near by polar cap surface of neutron star in the case of inclined magnetic field

D. Barsukov[1] and A. Khalyapin[2,3]

[1] Ioffe Institute, Saint-Petersburg, 194021 Russia
[2] Higher School of Economics – National Research University, Saint-Petersburg, 190008 Russia
[3] ITMO University, Saint-Petersburg, 197101 Russia

Abstract. The flow due to the closure of the magnetospheric current in a liquid layer at the neutron star surface is considered. The only case of a homogeneous magnetic field is considered, but the possibility of inclination of the field to the neutron star surface is taken into account. It is shown that the inclination of the magnetic field may lead to the appearance of a vertical liquid flow velocity comparable to the horizontal one.

Keywords: pulsars: general; stars: neutron

DOI: 10.26119/VAK2024.004

1 Introduction

The current braking is one of the main mechanisms of pulsar braking (Beskin 2018). It occurs due to the electric current closure inside the neutron star (Beskin 2018; Sob'yanin 2023). Current distribution in this case has been considered, for example, by Sob'yanin (2024). In the paper, we assume that neutron star crust is covered by a plane liquid layer and consider a liquid flow in the layer caused by current closure.

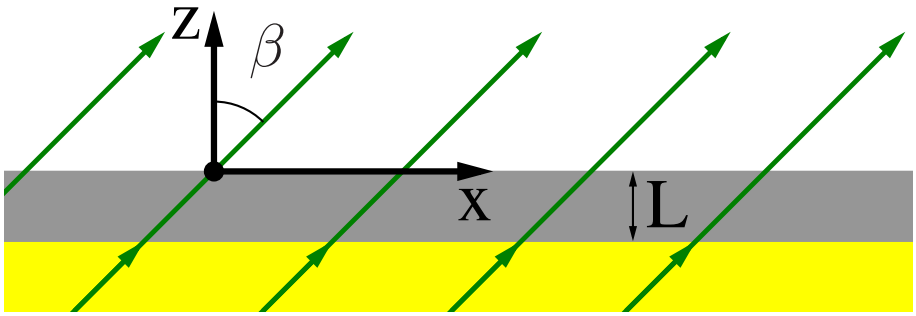

Fig. 1. This sketch shows the liquid layer on the neutron star surface. The liquid layer is shown in gray color, the rigid star crust is shown in yellow color, and the magnetic field direction is shown by green lines.

2 Model

In this paper, we use the same model as Vorontsov & Barsukov 2019; Tsygan et al. 2014. We consider only the simplest case with plane geometry and a homogeneous magnetic field, see Fig. 1, with isotropic conductivity and viscosity. We also use the simplest equation of state $p = p(\rho)$, where p and ρ is liquid pressure and density, respectively, and for the sake of simplicity, we assume that the crust has infinite conductivity. Following Tsygan et al. 2014, we consider only stationary flow. Hence, the magnetic hydrodynamic equations in the frame of references rotating with the neutron star may be written as

$$\rho\,(2\,[\mathbf{\Omega}\times\mathbf{v}]+(\mathbf{v}\cdot\nabla)\mathbf{v}) = -\nabla p+\frac{1}{c}\,[\mathbf{j}\times\mathbf{B}]+\boldsymbol{\mathcal{F}}_{\rm vis}+\rho\,\mathbf{g}, \tag{1}$$

$$-\nabla\,\Phi+\frac{1}{c}\,[\mathbf{v}\times\mathbf{B}] = R\,\mathbf{j}\,,\ \ {\rm div}\mathbf{B}=0\,,\ \ {\rm rot}\mathbf{B}=\frac{4\pi}{c}\,\mathbf{j}\,,\ \ {\rm div}\,(\rho\,\mathbf{v})=0, \tag{2}$$

where $\mathbf{v}$ is liquid velocity, $\mathbf{B}$ is magnetic induction, $\mathbf{j}$ is electric current density, Φ is electrostatic potential, R is liquid resistivity, $\mathbf{\Omega}$ is angular velocity of the neutron

star rotation, $\Omega = 2\pi/P$ where P is radiopulsar period, $\mathcal{F}_{\rm vis}$ is viscous force and $\mathbf{g} = -g\mathbf{e}_z$ is gravitational force and we assume that g is constant. At first, we consider the 0th approximation when magnetosphere electric current is absent and, in this case, we assume that electrical current is the liquid layer and liquid flows are absent, so we have $\mathbf{v}_{(0)} = 0$, $\mathbf{j}_{(0)} = 0$ and also $\nabla p_{(0)} = \rho_{(0)} \cdot g\,\mathbf{e}_z$. We denote the values in 0th approximation by sign $_{(0)}$. In the paper we assume that $\mathbf{B}_{(0)} = B_{(0)}\,(\cos\beta\,\mathbf{e}_z + \sin\beta\,\mathbf{e}_x)$, where $B_{(0)}$ and β are some constants, see Fig. 1. We also assume that $\Phi_{(0)} = 0$ and density $\rho_{(0)}$ depend only on z. Now we consider small perturbations caused by magnetospheric electric current. In the linear approximation of the perturbations we have

$$2\,\rho_{(0)} \cdot [\mathbf{\Omega} \times \mathbf{v}] = \frac{B_{(0)}}{c} \cdot [\mathbf{j} \times \mathbf{e}_B] + \boldsymbol{\mathcal{F}}_{\rm vis} - \nabla\delta p - \delta\rho \cdot g\,\mathbf{e}_z, \tag{3}$$

$$-\nabla\,\Phi + \frac{B_{(0)}}{c} \cdot [\mathbf{v} \times \mathbf{e}_B] = R_{(0)}\,\mathbf{j}\,, \;\; {\rm div}\mathbf{j} = 0 \quad \text{and} \quad {\rm div}\left(\rho_{(0)}\,\mathbf{v}\right) = 0, \tag{4}$$

where $\mathbf{v}$ and $\mathbf{j}$ are considered as perturbations of liquid velocity and electric current correspondingly, $\delta p = p - p_{(0)}$ and $\delta\rho = \rho - \rho_{(0)}$ are perturbations of pressure and density correspondingly, $\mathbf{e}_B = \mathbf{B}_{(0)}/B_{(0)}$ and $c_s^2 = \frac{\partial p}{\partial \rho}(\rho_{(0)})$. Let us consider the boundary conditions $\frac{\partial v_x}{\partial z}\big|_{z=0} = 0$, $\left.\frac{\partial v_y}{\partial z}\right|_{z=0} = 0$, $j_z|_{z=0} = \frac{1}{\cos\beta} \cdot \left.\hat{j}_B^{(m)}\right|_{z=0}$ and $\Phi|_{z=-L} = 0$, $\mathbf{v}|_{z=-L} = 0$, where $\mathbf{j}^{(m)} = j_B^{(m)}\,\mathbf{e}_B$ is electric current flow in magnetosphere. In the case of ${\rm Ha}^2 \gg E^{-1} \gg 1$, where ${\rm Ha} = (B_{(0)}L)/(c\sqrt{\eta_{(0)}R_{(0)}})$ is Hartmann number, $E = \eta_{(0)}/(\Omega L^2\rho_{(0)})$ is Ekman number and $\eta_{(0)}$ is liquid shear viscosity coefficient, we can use "force free" approximation outside the boundary layers. Hence the approximate solution of equations (3) and (4) outside the boundary layers may be written as

$$v_x = -\frac{1}{\cos^2\beta} \cdot \frac{c^2}{B_{(0)}^2} \cdot (K_x - K'_x) \;\text{ and }\; v_y = \frac{1}{\cos^2\beta} \cdot \frac{c^2}{B_{(0)}^2} \cdot \left(K_y + K'_y\right), \tag{5}$$

$$v_z = {\rm tg}\beta \cdot \frac{c}{B_{(0)}} \cdot \frac{1}{\rho_{(0)}(z)} \cdot \frac{\partial\hat{j}_B}{\partial y} \cdot \tilde{K}_z(z), \tag{6}$$

where we define $K_x = R_f\,\frac{\partial\delta\hat{p}_0}{\partial\tilde{x}} + {\rm tg}\beta\,\tilde{R}_f\,\frac{\partial^2\delta\hat{p}_0}{\partial y^2}$, $K'_x = \frac{B_{(0)}}{c} \cdot \frac{\partial\hat{j}_B}{\partial y} \cdot \left(\tilde{R}_{(0)} + \frac{\sin^2\beta}{\rho_{(0)}(z)}\,\tilde{K}_z(z)\right)$ and $K_y = -R_f\,\frac{\partial\delta\hat{p}_0}{\partial y} + {\rm tg}\beta\,\tilde{R}_f\,\frac{\partial^2\delta\hat{p}_0}{\partial\tilde{x}\,\partial y}$, $K'_y = \frac{B_{(0)}}{c} \cdot \left(\sin\beta\cos\beta\,R_{(0)}\,\hat{j}_B - \tilde{R}_{(0)}\,\frac{\partial\hat{j}_B}{\partial\tilde{x}}\right)$ and also we introduce $\tilde{K}_z(z) = \int_{-L}^{z} \rho_{(0)}(z')\,R_{(0)}(z') \cdot (f(z')\,K_0 - 1)\;dz'$, $\tilde{R}_{(0)}(z) = \int_{-L}^{z} R_{(0)}(z')\,dz'$, $R_f(z) = R_{(0)}(z) \cdot f(z)$, $\tilde{R}_f(z) = \int_{-L}^{z} R_f(z')\,dz'$ and the value K_0 is defined as $K_0 = \int_{-L}^{0} \rho_{(0)}(z')\,R_{(0)}(z')\,dz' \,/\, \int_{-L}^{0} \rho_{(0)}(z')\,R_{(0)}(z')\,f(z')\,dz'$. The function $f(z)$ is defined as

$f(z) = \exp\left(\int_z^0 g\,/\,c_s^2(z')\,dz'\right)$. The values $\delta\hat{p}_0$ and $\hat{j}_B$ depend only on $\tilde{x} = x - \mathrm{tg}\beta\, z$ and y. And the function $\delta\hat{p}_0$ may be written as

$$\delta\hat{p}_0(\tilde{x}, y) = \cos\beta \cdot \sin\beta \cdot \frac{B_{(0)}}{c} \cdot \frac{K_0}{2\pi} \cdot \int_{-\infty}^{+\infty} \ln(\tilde{r}) \cdot \frac{\partial \hat{j}_B}{\partial y}(\tilde{x}', y')\, d\tilde{x}'\, dy', \qquad (7)$$

where $\tilde{r} = \sqrt{(\tilde{x} - \tilde{x}')^2 + (y - y')^2}$. The pressure and density perturbations δp and $\delta\rho$ are equal to $\delta p = \delta\hat{p}_0(\tilde{x}, y) \cdot f(z)$ and $\delta\rho = \delta p / c_s^2(z)$ correspondingly. The function $\hat{j}_B(\tilde{x}, y)$ is defined as $\hat{j}_B(\tilde{x}, y) = \hat{j}_B^{(m)}(x = \tilde{x}, y, z = 0)$.

3 Results

The solutions (5) and (6) show that vertical flow velocity may sometimes be comparable with horizontal flow velocities. For, example, in the case of $\rho \sim 10^6\,\mathrm{g\,cm^{-3}}$ (Haensel et al. 2007), $\eta_{(0)} \sim 10^4\,\mathrm{g\,cm^{-1}\,s^{-1}}$ (Chugunov & Yakovlev 2005; Ofengeim & Yakovlev 2015), $R_{(0)} \sim 10^{-19}$ SGS (Potekhin 1999) we have $E \sim 10^{-11}$ and $\mathrm{Ha} \sim 10^{11}$. So in the case of $\beta \sim \frac{\pi}{4}$, $P \sim 1$ s, $B_{(0)} \sim 10^{12}$ G and $j_B^{(m)} \sim \Omega B_{(0)}/(2\pi c)$ we may estimate $v_z \sim v_x \sim 10^{-10} - 10^{-8}\mathrm{cm\,s^{-1}}$. It means that electric current almost does not close in the liquid layer, which is consistent with the result of Sob'yanin (2023) and supports the conclusion of Sob'yanin (2024) that pulsar J0901-4046 brakes due to electric closure in the rigid crust or possibly in deeper layers. It is also possible that such flow may lead to a very slowly growing instability similar to the one that was considered in Kuznetsov & Mikhailov 2024.

Acknowledgements. The authors thank A. I. Tsygan and M. V. Vorontsov for support, discussions and helpful comments, A. I. Chugunov, A. V. Biryukov, I. F. Malov, V. A. Urpin and E. A. Mikhailov for comments and helpful discussions.

References

Beskin V., 2018, Physics-Uspekhi, 61, p. 353
Chugunov A. and Yakovlev D., 2005, Astronomy Reports, 49, p. 724
Haensel P., Potekhin A., and Yakovlev D., 2007, *Neutron stars I. Equation of State and Structure*, Springer, N. Y.
Kuznetsov E. and Mikhailov E., 2024, eprint arXiv:2402.16989
Ofengeim D. and Yakovlev D., 2015, Europhysics Letters, 112, id. 59001
Potekhin A., 1999, Astronomy and Astrophysics, 351, p. 787
Sob'yanin D., 2023, Physical Review D, 107, id. L081301
Sob'yanin D., 2024, Physical Review D, 109, id. L061302
Tsygan A., Shalybkov D., Barsukov D., and Goglichidze O., 2014, St. Petersburg State Polytechnical University Journal: Physics and Mathematics, 2, p. 120
Vorontsov M. and Barsukov D.P, 2019, Journal of Physics: Conference Series, 1400, id. 022022

BAK 2024 MODERN ASTRONOMY: FROM THE EARLY UNIVERSE TO EXOPLANETS AND BLACK HOLES 300 years Russian Academy of Sciences

The influence of space curvature on pulsar braking indexes

D. Barsukov[1] and A. Matevosyan[2]

[1] Ioffe Institute, Saint-Petersburg, 194021 Russia
[2] SPbPU, Saint-Petersburg, 195251 Russia

Abstract. The influence of space curvature on the input of pulsar magnetic field outside star to effective moment of inertia of neutron star and its influence on pulsar braking indexes is considered. It is shown that it leads to the changing of braking indexes estimates only in two or ten times. So a majority of pulsar braking indexes may be explained by a simple model of neutron star precessed due to its anomalous torque as well as without taking into account the space curvature influence nearby neutron star.

Keywords: stars: neutron; stars: magnetic field

DOI: 10.26119/VAK2024.005

1 Introduction

The radiopulsars are rapidly rotating neutron stars with highly strong magnetic field, surrounding neutron star (Beskin 2018). As any other matter, this magnetic field has energy and, consequently, mass. And up to light cylinder this mass rotates together with neutron star. A such mass influences the neutron star rotation (Goglichidze et al. 2015, see also Beskin & Zheltoukhov 2014), leading to star precession. This precession has period $T_{\rm pr} \sim 10^3 - 10^4$ years and may give input to cyclic changing of pulsar parameters and low frequency component of "red noise" (Biryukov et al. 2012). It also may be related to the repeating of FRB burst in some sources (Sob'yanin 2020). In this paper we consider the influence of space curvature on star precession and maximal possible values of pulsar braking indexes due to this precession.

2 Model

In the paper we use results of papers Goglichidze et al. (2015) and Matevosyan & Barsukov (2023). Following these papers let us first consider a case of magnetic field described by one harmonic with numbers l and m defined in coordinate system with axis Oz directed as $\mathbf{e}_{lm}$. In the paper, for the sake of simplicity, we do not consider special case $m = \pm 1$ (Goglichidze et al. 2015). Hence, the rotational momentum $\mathbf{L}^f_{lm}$ of such magnetic field may be written as (Goglichidze et al. 2015):

$$\mathbf{L}^f_{lm} = I^f_{lm}\,\mathbf{\Omega} + \delta I^f_{lm}\,\mathbf{e}_{lm}\,(\mathbf{e}_{lm}\cdot\mathbf{\Omega}), \tag{1}$$

where $\mathbf{\Omega}$ is neutron star angular velocity, $\Omega = 2\pi/P$ and P is pulsar period. Now, let us consider a neutron star with dipolar magnetic field and, in addition, a surface small scale magnetic field. We describe the dipolar magnetic field by one field harmonic $(lm) = (10)$ and, for the sake of simplicity, we also describe a surface small scale magnetic field by one field harmonic with numbers (lm), where $l > 5$. In this case the rotational momentum $\mathbf{L}^f$ of such magnetic field may be written as (Matevosyan & Barsukov 2023):

$$\mathbf{L}^f = (I^f_{10} + I^f_{lm})\,\mathbf{\Omega} + \delta I^f_{10}\,\mathbf{e}_{10}\,(\mathbf{e}_{10}\cdot\mathbf{\Omega}) + \delta I^f_{lm}\,\mathbf{e}_{lm}\,(\mathbf{e}_{lm}\cdot\mathbf{\Omega}). \tag{2}$$

We also introduce the value $\nu = \sqrt{< B^2_{lm} > / < B^2_{10} >}$, where $< B^2_{lm} >$ is square of magnetic induction averaged over neutron star surface (Matevosyan & Barsukov 2023). The value ν may be considered as a ratio of harmonics on star surface. Now let us consider an axisymmetric case $\mathbf{e}_{lm} = \mathbf{e}_{10}$. Hence, the rotational momentum $\mathbf{L}^f$ may be written as

$$\mathbf{L}^f = I^f\,\mathbf{\Omega} + \delta I^f\,\mathbf{e}_{10}\,(\mathbf{e}_{10}\cdot\mathbf{\Omega}), \tag{3}$$

where $\delta I^f = \delta I^f_{10} + \delta I^f_{lm}$ and $I^f = I^f_{10} + I^f_{lm}$. This additional "star" rotational momentum leads to star precession with period $T_{\rm pr} \sim 10^3 - 10^4$ years. During precession the electric currents flowing through inner gaps may be modulated (Barsukov & Tsygan 2010) and, hence, we have the increasing of observed pulsar braking index $n = \ddot{P}\,P/(\dot{P})^2$ (Biryukov et al. 2012). The maximal input $n_{\rm max}$ to pulsar braking index due to such precession may be estimated as (Matevosyan & Barsukov 2023, see also Barsukov & Tsygan 2010; Biryukov et al. 2012):

$$n_{\rm max} = \frac{K_{\rm est}}{4\pi^2} \cdot \frac{\delta I^f}{m^2_{10}} \cdot c^3\, P, \tag{4}$$

where $K_{\rm est} \sim 1$ is a number of the order of unity, which highly depends on exact magnetic field structure in inner gaps, pulsar inclination angle χ and the phase of precession (Barsukov & Tsygan 2010), m_{10} is pulsar dipolar magnetic momentum, which corresponds to harmonic $(lm) = (10)$, χ is angle between vectors $\mathbf{\Omega}$ and $\mathbf{e}_{10}$.

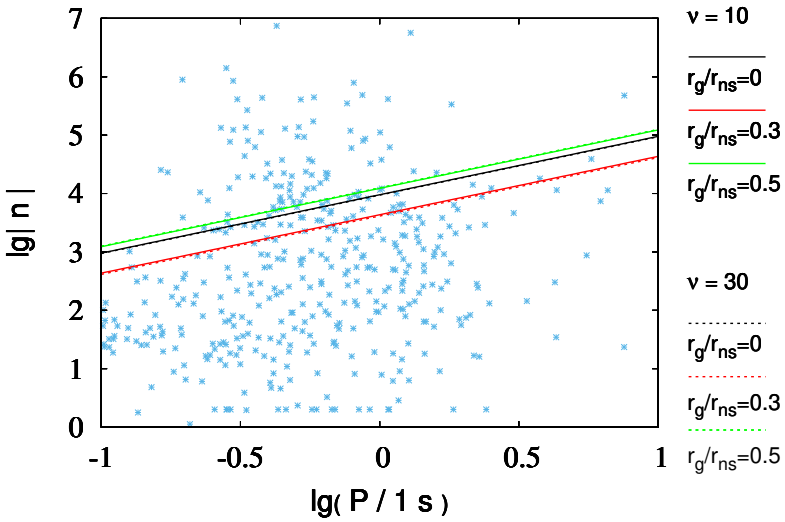

Fig. 1. The estimated maximal braking index values $n_{\rm max}$ in case of $l = 20$ and $m = 20$ are shown by lines. The observed braking index values n taken from Manchester et al. (2005) are shown by stars.

3 Results

The comparison of estimation $n_{\max}$ of maximal possible value of braking index with observed values of braking indexes[1] (Manchester et al. 2005) is shown in Fig. 1. As can be seen from Fig. 1 the majority of pulsar braking indexes may be explained by this simple model. Although, some of pulsars have very large braking indexes. This could mean that its neutron star crust is highly deformed, in order to its star has a short precession period $T_{\rm pr}$ (Jones et al. 2017) or that we see magnetic field decay (Biryukov et al. 2017). Also, it may be related to peculiarity of braking index observation (Biryukov & Beskin 2023).

References

Barsukov D. and Tsygan A., 2010, Monthly Notices of the Royal Astronomical Society, 409, p. 1077

Beskin V., 2018, Physics-Uspekhi, 61, p. 353

Beskin V. and Zheltoukhov A., 2014, Physics Uspekhi, 57, p. 799

Biryukov A., Astashenok A., Karpov S., et al., 2017, Journal of Physics: Conference Series, 932, id. 012044

Biryukov A. and Beskin G., 2023, Monthly Notices of the Royal Astronomical Society, 522, p. 6258

Biryukov A., Beskin G., and Karpov S., 2012, Monthly Notices of the Royal Astronomical Society, 420, p. 103

Goglichidze O., Barsukov D., and Tsygan A., 2015, Monthly Notices of the Royal Astronomical Society, 451, p. 2564

Jones D., Ashton G., and Prix R., 2017, Physical Review Letters, 118, id. 261101

Manchester R., Hobbs G., Teoh A., et al., 2005, The Astronomical Journal, 129, p. 1993

Matevosyan A. and Barsukov D., 2023, Astronomy Letters, 49, p. 560

Sob'yanin D., 2020, Monthly Notices of the Royal Astronomical Society, 497, p. 1001

[1] https://www.atnf.csiro.au/research/pulsar/psrcat/

MODERN ASTRONOMY: FROM THE EARLY UNIVERSE TO EXOPLANETS AND BLACK HOLES

The influence of inclination angle on polar cap heating of J0901-4046 radiopulsar

D. Barsukov, I. Morozov, and A. Popov

Ioffe Institute, Saint-Petersburg, 194021 Russia

Abstract. The influence of inclination angle to electron-positron pairs production in inner gap and polar cap heating by reverse positron current in case of J0901-4046 radiopulsar is considered. It is shown that J0901-4046 pulsar "work" may be explained by the presence of a highly curved small scale surface magnetic field without the substantial increasing of its dipolar magnetic field at inclination angle values $\chi \lesssim 30°$.

Keywords: pulsars: general, individual (J0901-4046)

DOI: 10.26119/VAK2024.006

1 Introduction

The pulsar J0901-4046 is the slowest known pulsar among normal rotating-powered radiopulsar (Caleb et al. 2022). Its rotation period is $P = 75.89$ s, $\dot{P} = 2.25 \cdot 10^{-13}$. According to the "standard" magnetic field estimation (Manchester et al. 2005), it corresponds to the induction $B_{\rm dip} = 2.6 \cdot 10^{14}$ G of the magnetic dipolar field on star surface at the magnetic pole (Caleb et al. 2022). Its spin-down age is $\tau = P/(2\,\dot{P}) \approx 5.3 \cdot 10^6$ years, its spin-down luminosity is $\dot{E} \approx 2.0 \cdot 10^{28}$ erg s^{-1} (Caleb et al. 2022). The distance to the pulsar may be estimated by using dispersion measure DM as $D \approx 328$ pc or as $D \approx 467$ pc (Caleb et al. 2022). This pulsar has been considered in many papers, see, for example, Sob'yanin 2023; Beskin & Istomin 2022. Although, the value of its inclination angle χ, which is the angle between the dipolar magnetic momentum $\mathbf{m}$ of radiopulsar and the angular rotation velocity $\mathbf{\Omega}$ of neutron star, is not very well known at present. The detailed analysis of its radio radiation properties has been made in Sob'yanin (2023) and gives the value $\chi \approx 10^\circ$ so this pulsar is close to being aligned. Also, the pulsar was assumed to be close to aligned in Barsukov et al. (2023). However, in the paper Beskin & Istomin (2022) it is assumed that this pulsar is close to orthogonal $\chi \approx 90^\circ$. The attempt to estimate inclination angle χ by its radio pulse width $W_{50} \approx 296 - 299$ ms (Caleb et al. 2022) gives us the values $\chi \approx 11^\circ$ if we use minimal pulse width estimation $W_{\rm min} \approx 2.45^\circ \cdot (P/1{\rm s})^{-1/2}$ taken from Rankin (1990), $\chi \approx 50^\circ$ or $\chi \approx 90^\circ$ when using estimations $W_{\rm min}$ taken from Malov & Nikitina (2011). It is worth to note that its impact parameter $\beta \lesssim 0.2^\circ$ (Caleb et al. 2022), where β is an angle between magnetic momentum $\mathbf{m}$ and the line of sight. Hence, the estimation of inclination angle χ by pulse width seems to be very close to its real value. Due to these uncertainties of inclination angle value, in this paper, we consider the influence of inclination angle on electron-positron pairs production and polar cap heating by the reverse positron current in the framework of the J0901-4046 pulsar model considered in Barsukov et al. (2023) (see also Kantor & Tsygan 2003).

2 Results

In this paper, we use the same model as Barsukov et al. (2023). Following Barsukov et al. (2023) we assume the presence of the small scale magnetic field component on the surface of the star with induction $\mathbf{B}_{\rm sc}$ and space scale $\ell \approx r_{\rm ns}/20$, where $r_{\rm ns}$ is neutron star radius. The geometry of field near by inner gap is shown in Fig. 1 (see Kantor & Tsygan 2003 for details). The calculations of electron-positron production and reverse positron current are made in the same way as in Barsukov et al. (2023). In order to roughly estimate the influence of a possible positronium annihilation, we

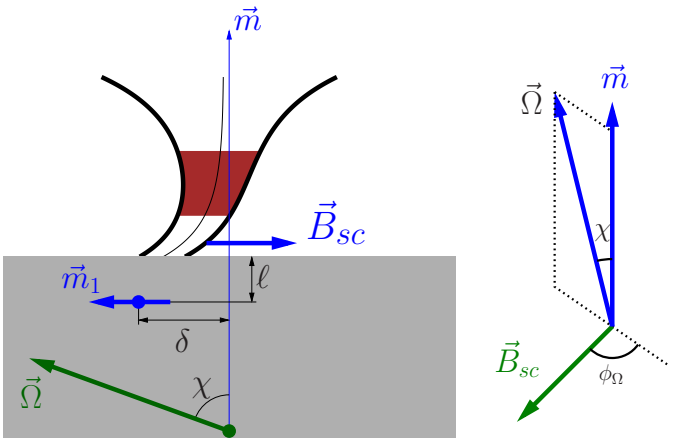

Fig. 1. The sketch of used geometry of magnetic field near by the inner gap, which is shown by the red area. Neutron star crust is shown by the gray area.

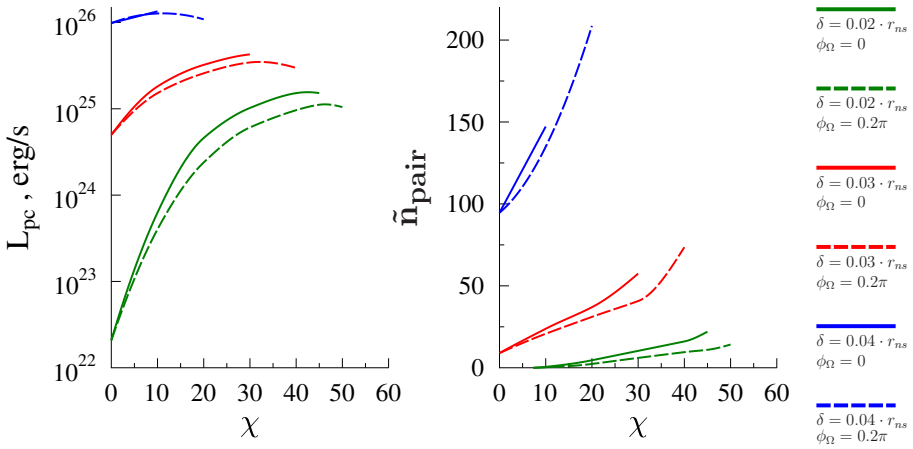

Fig. 2. The dependence of polar cap heating $L_{\rm pc}$ on inclination angle χ for some small scale field configuration is shown in the left graph. The same, but in case of the number density of produced unbounded positrons $\tilde{n}_{\rm pair}$ in units $(\Omega\, B)/(2\pi ce)$ is shown in the right graph. In both cases angle χ is in degrees.

assume that $(1-f)$ part of positronium immediately decays after its production and f part of positronium does not decay at all. Temperature of neutron star surface is assumed to be equal to $T_{\rm surf} = 3 \cdot 10^5$ K (Barsukov et al. 2023). The dependence of polar cap luminosity $L_{\rm pc}$ due to the reverse positron heating and unbound pairs multiplicity $\tilde{n}_{\rm pair}$ in case of $B_{\rm sc} = 0.7 \cdot B_{\rm dip}$ and $f = 0.3$ (Barsukov et al. 2023) is shown in Fig. 2. You can see from Fig. 2 that the J0901-4046 pulsar "work" may be explained in the framework of model Barsukov et al. (2023) at inclination angles $\chi \lesssim 30^\circ$. So if the pulsar has larger inclination angle value $\chi \sim 60-90^\circ$ it is necessary to give preference to other models, for example, to the model considered in Beskin & Istomin (2022) in the case of nearby orthogonal pulsar $\chi \approx 90^\circ$.

Acknowledgements. The authors thank D. N. Sob'yanin, I. F. Malov, E. B. Nikitina, A. Yu. Istomin and V. M. Kontorovich for useful discussion and helpful comments, A. I. Chugunov, A. V. Biryukov, Yu. A. Shibanov and V. A. Urpin for support and useful comments.

References

Barsukov D., Morozov I., and Popov A., 2023, Astronomy Letters, 49, p. 806
Beskin V. and Istomin A., 2022, Monthly Notices of the Royal Astronomical Society, 516, p. 5084
Caleb M., Heywood I., Rajwade K., et al., 2022, Nature Astronomy, 6, p. 828
Kantor E. and Tsygan A., 2003, Astronomy Reports, 47, p. 613
Malov I. and Nikitina E., 2011, Astronomy Reports, 55, p. 878
Manchester R., Hobbs G., Teoh A., et al., 2005, The Astronomical Journal, 129, p. 1993
Rankin J., 1990, Astrophysical Journal, 352, p. 247
Sob'yanin D., 2023, Physical Review D, 107, id. L081301.

VAK 2024 MODERN ASTRONOMY: FROM THE EARLY UNIVERSE TO EXOPLANETS AND BLACK HOLES 300 years Russian Academy of Sciences

The radius of magnetosphere and the equilibrium radius are not the same!

N. Beskrovnaya[1] and N. Ikhsanov[1,2]

[1] Pulkovo Observatory, 65 Pulkovskoye shosse, Saint-Petersburg, 196140 Russia
[2] Institute of Applied Astronomy of the Russian Academy of Sciences, 10 Kutuzov Emb., Saint-Petersburg, 191187 Russia

Abstract. The process of accretion onto a neutron star with strong magnetic field is discussed. The equilibrium radius, which is defined by equating the pressure of the accreting material with the magnetic pressure due to the dipole magnetic field of the neutron star, is estimated for the cases of a spherical accretion flow and a Keplerian accretion disk. It is emphasized that the magnetospheric radius of an accreting star is defined by equating the mass accretion rate observed in the system with the rate of plasma diffusion into the magnetic field of the neutron star at the magnetospheric boundary. Following this definition we obtained a system of equations, which are the continuity equation and the pressure balance equation. We show that the radius of magnetosphere evaluated in this way significantly differs from the equilibrium radius. In particular, the Alfv´en radius (which is just the equilibrium radius in a peculiar case of a spherically symmetric accretion flow) under the same conditions exceeds the magnetospheric radius of an accreting neutron star by more than an order of magnitude.

Keywords: accretion, accretion disks; pulsars: general; magnetic fields

DOI: 10.26119/VAK2024.007

1 Introduction

We consider a Neutron Star (NS) with the mass $M_{\rm ns}$, the radius $R_{\rm ns}$, the surface magnetic field $B_{\rm ns}$ and the dipole magnetic moment $\mu = (1/2)B_{\rm ns}R_{\rm ns}^3$, which accretes matter at a rate $\dot{\mathfrak{M}}$. The questions are (i) at which distance (from the center of the NS) the balance between the pressure of the accretion flow and the pressure of the NS magnetic field can be reached (the equilibrium radius), and (ii) at which distance the rate of penetration of the accretion flow into the magnetic field of the NS reaches the rate of mass accretion $\dot{\mathfrak{M}}$, which is considered constant (a stationary accretion picture). We examine these questions for both the spherical and disk accretion scenarios within the corotation approximation, which implies that the angular velocity of matter at the inner radius of the accretion flow is equal to the angular velocity of the NS.

2 The equilibrium radius

The equilibrium radius, $r_{\rm eq}$, is defined by equating the magnetic pressure due to the dipole magnetic field of a NS, $p_{\rm m}(r) = \mu^2/2\pi r^6$, with the external pressure of the accretion flow, $p_{\rm acc}$.

The pressure of a spherical accretion flow is dominated by the dynamic (ram) pressure, which leads us to the equilibrium radius,

$$r_{\rm eq}^{\rm (sph)} = \left(\frac{\mu^2}{\dot{\mathfrak{M}}\sqrt{2GM_{\rm ns}}}\right)^{2/7} \simeq 1.2\times10^9\,{\rm cm}\,\mu_{30}^{4/7}\,\dot{\mathfrak{M}}_{15}^{2/7}\,m^{1/7}, \tag{1}$$

which is known as the Alfvén radius. Here $\mu_{30} = \mu/10^{30}\,{\rm G\,cm^3}$, $\dot{\mathfrak{M}}_{15} = \dot{\mathfrak{M}}/10^{15}\,{\rm g\,s^{-1}}$, and $m = M_{\rm ns}/1.4\,{\rm M}_\odot$.

The pressure of an accretion disk in the corotation approximation is contributed mainly by the thermal gas pressure. The equilibrium radius in this case (Beskrovnaya & Ikhsanov 2024),

$$r_{\rm eq}^{\rm (d)} \simeq \frac{34\,\alpha^{8/27}\,\mu^{8/27}}{\dot{\mathfrak{M}}^{7/27}\,(GM_*)^{7/27}} \simeq 3.6\times10^8\,{\rm cm}\,\alpha^{8/27}\,\mu_{30}^{16/27}\,\dot{\mathfrak{M}}_{15}^{-7/27}\,m^{-7/27}, \tag{2}$$

is smaller than the Alfvén radius under the same conditions. Here $\alpha = v_{\rm t}\ell_{\rm t}/c_{\rm s}h_0 \leq 1$ is the efficiency parameter which is used to normalize the velocity, $v_{\rm t}$ and scale, $\ell_{\rm t}$, of turbulent motions to the sound speed, $c_{\rm s}$, and half-thickness of the disk, h_0.

3 The magnetospheric radius

The magnetospheric radius of an accreting star is defined by equating the rate of plasma penetration into the magnetic field of the NS, $\dot{\mathfrak{M}}_{\rm in}$, to the mass accretion rate beyond the magnetospheric radius, $\dot{\mathfrak{M}}$. The penetration rate in the general case is limited as $\dot{\mathfrak{M}}_{\rm in} \geq \dot{\mathfrak{M}}_{\rm diff}$, where

$$\dot{\mathfrak{M}}_{\rm diff}(r) = S(r)\, v_{\perp}(r)\, \rho(r), \tag{3}$$

is the rate of plasma diffusion into the magnetic field of a NS at a given radius r. Here $S \simeq 4\pi r h_0$ is the area of interaction between the accretion disk and the NS magnetic field; $v_{\perp} \simeq \delta_{\rm m}/t_{\rm ff}$ is the velocity of plasma diffusion across the magnetic field lines, where $\delta_{\rm m} \simeq (D_{\rm eff} t_{\rm ff})^{1/2}$ is the thickness of the diffusion layer for the diffusion coefficient $D_{\rm eff}$ and $t_{\rm ff}$ is the free-fall time, which in the considered case represents the time of diffusion process; $\rho \simeq \mu^2/2\pi r^6 c_{\rm s}^2$ is the density of the accretion flow at the inner radius of the disk, which can be evaluated from the equation of pressure balance between the disk and the magnetosphere at its boundary.

Evaluating $\dot{\mathfrak{M}}_{\rm diff}(r)$ for the case of Bohm diffusion and solving equation $\dot{\mathfrak{M}}_{\rm diff}(r) = \dot{\mathfrak{M}}$ for r one finds $r = r_{\rm N}$, where (Beskrovnaya & Ikhsanov 2024)

$$r_{\rm N} \simeq \frac{0.16\, \lambda_0\, \mu^{6/11}}{\dot{\mathfrak{M}}^{4/11}\, (GM_{\rm ns})^{1/11}} \simeq 5.6 \times 10^7\, {\rm cm}\, \times\, \lambda_0\, \mu_{30}^{6/11}\, \dot{\mathfrak{M}}_{15}^{-4/11}\, m^{-1/11}, \tag{4}$$

and λ_0 is a dimensionless parameter of the order of unity. The radius $r_{\rm N}$ represents the minimum possible value of the magnetospheric radius of an accreting star. The inflowing matter cannot approach the NS at a closer distance since the rate of its diffusion into the stellar magnetic field at this radius reaches the rate of mass transfer in the disk. Furthermore, the radial velocity of plasma across the magnetic field lines at this radius is equal to the radial velocity of plasma in the disk.

4 Discussion

It is important to note that the physical problem of describing magnetospheric accretion essentially differs from the situation with the Earth magnetosphere. The solar wind in the latter case overflows the magnetic field of the Earth and only a tiny fraction of it penetrates into the magnetosphere. This occurs because of a high velocity of the solar wind which by a factor of 30–50 exceeds the parabolic velocity at the Earth's surface (so the Bondi radius proves to be much smaller than the radius of the Earth). The minimum size of the magnetosphere (a distance of the closest approach between the solar wind and the Earth) in this case can be roughly evaluated by

equating the pressure of the dipole magnetic field of the Earth and the ram pressure of solar wind.

The situation with an accreting star is essentially different. The accretion flow is gravitationally bound with the accreting star (the Bondi radius is much larger than the magnetospheric radius). Almost all of the inflowing matter in this case is accreted onto the stellar surface. A stationary accretion picture under these circumstances can be constructed only if the rate of plasma penetration into the magnetosphere at its boundary is equal to the total mass accretion rate. Hence, the primary condition is the continuity equation and the pressure balance is a complementary (although a very important) condition which helps to reduce a number of free parameters of the model.

Historically, the magnetospheric radius of an accreting NS was calculated for the spherical accretion flow using the pressure balance equation with the Alfvén radius as a solution. But the rate of plasma diffusion into the magnetosphere in this case is too low to explain the observed luminosity of X-ray pulsars. To solve this problem an assumption about instabilities of the magnetospheric boundary had been invoked (for discussion see, e.g., Ikhsanov & Pustil'nik 1996, and references therein).

The equilibrium magnetospheric boundary of a NS accreting from a spherical flow under the condition $T(r_{\rm A}) = T_{\rm ff}(r_{\rm A})$ is interchange stable (Arons & Lea 1976). Here $T(r_{\rm A})$ and $T_{\rm ff}(r_{\rm A})$ are the gas and the free-fall temperature at the magnetospheric boundary. The boundary could be unstable under the condition $T(r_{\rm A}) \ll T_{\rm ff}(r_{\rm A})$. But the equilibrium shape of the magnetosphere for this case has been never investigated. Instead, the stability analysis was performed extrapolating the solution for the case of $T(r_{\rm A}) = T_{\rm ff}(r_{\rm A})$ to the case of $T(r_{\rm A}) \ll T_{\rm ff}(r_{\rm A})$. A validity of this extrapolation is rather questionable. Furthermore, the matter in this situation tends to overflow the magnetospheric boundary towards the magnetic pole regions and to accumulate in the magnetic cusps, which are interchange stable (Michel 1977). It therefore appears that the continuity equation for the case of spherical accretion has not been solved so far. The diffusion-driven accretion scenario is currently available for the case of disk accretion in which, as shown above, the magnetospheric radius significantly differs from the traditionally invoked Alfvén radius, which is just the equilibrium radius in the case of a NS undergoing spherical accretion.

References

Arons J. and Lea S., 1976, Astrophysical Journal, 207, p. 914
Beskrovnaya N. and Ikhsanov N., 2024, Astrophysical Bulletin, 79, p. 104
Ikhsanov N. and Pustil'nik L., 1996, Astronomy & Astrophysics, 312, p. 338
Michel F., 1977, Astrophysical Journal, 216, p. 838

VAK 2024 MODERN ASTRONOMY: FROM THE EARLY UNIVERSE TO EXOPLANETS AND BLACK HOLES 300 years Russian Academy of Sciences

Observations of giant pulses from B0531+21 at the Institute of Applied Astronomy

I. Bezrukov, I. Gayazov, A. Dyakov, D. Ivanov, A. Ipatov, S. Kurdyubov, D. Marshalov, A. Melnikov, A. Mikhaylov, V. Olifirov, and I. Rakhimov

Institute of Applied Astronomy of the Russian Academy of Sciences, Kutuzov emb. 10, Saint Petersburg, 191187 Russia

Abstract. This paper presents the results of observations of giant pulses from the pulsar B0531+21 (the Crab Nebula pulsar) conducted at the Institute of Applied Astronomy of the Russian Academy of Sciences (RAS). The primary aim of the study was to establish a domestic monitoring service and compute the ephemerides for this pulsar. Observations commenced in mid-2023 using the RT-13 telescopes of the Quasar-KVO network, operating in the S, X, and Ka bands. To achieve the research goals, we utilized the VLBI (Very-Long-Baseline Interferometry) registration system along with specially developed software and algorithms for data processing. A monitoring service for giant pulses was created, providing weekly ephemerides of the pulsar for over one and a half years. The period and its derivative were determined separately by timing the main pulses and interpulses. The obtained results demonstrate a high accuracy of period determination, consistent with the data from the Jodrell Bank Observatory, with a root mean square deviation of 7 picoseconds.

Keywords: pulsars: general, individual (B0531+21); radio astronomy; observational techniques

DOI: 10.26119/VAK2024.008

1 Introduction

The study of giant pulses from pulsars provides valuable insights into the emission mechanisms and the extreme physical conditions in pulsar magnetospheres. The Crab Pulsar (B0531+21) is a well-known (Hankins & Rickett 1975) source of giant pulses, making it an ideal target for such studies. This paper describes the observation setup, data processing techniques, and results of recent observational sessions at the Institute of Applied Astronomy of the Russian Academy of Sciences (IAA RAS).

2 First experiment

In our first experimental session (Kurdubov & Marshalov 2022), we conducted a 20-minute observation of the Crab pulsar to test the capabilities of our equipment. The observations were performed using the RT-32 and RT-13 radio telescopes at the Svetloe, Badary, and Zelenchukskaya observatories. The setups included L-band (Svetloe and Badary 32m) with a bandwidth of 128 MHz and frequency range from 1589.5 to 1717.5 MHz, and S and X-bands (Svetloe, Badary, Zelenchukskaya 13m) with a bandwidth of 512 MHz and frequency ranges from 2163.8 to 2675.8 MHz (S-band) and from 8591.6 to 9103.6 MHz (X-band). Data were recorded in the VDIF (VLBI Data Interchange Format) format with coherent de-dispersion for enhanced time resolution.

Key system performance metrics included an SEFD (System Effective Flux Density) of 280 Jy (RT-32, L-band), 1000 Jy (RT-13, S-band), and 800 Jy (RT-13, X-band), with 1-sigma sensitivities of 44 Jy at 8 μs (RT-32, L-band), 63 Jy at 1.6 μs (RT-13, S-band), and 60 Jy at 1.6 μs (RT-13, X-band).

Overall, 712 pulses were detected at Badary and 657 at Svetloe in the L-band, while 262 pulses were detected at Badary, 182 at Svetloe, and 51 at Zelenchuk in the S-band. Detection rates were 36 pulses per minute (L-band) and 12 pulses per minute (S-band). These detection rates are comparable to previous observations at Goldstone and Arecibo observatories (see, for example, Majid et al. 2011).

3 Regular observations

After success of experimental session, regular observations of B0531+21 were conducted 5–6 times per day over a period of 1.5 years. These observations were integrated into the standard observation programs R and RX. Each session consisted of one-minute scans in the X and S bands using the RT-13 radio telescopes at Svetloe, Badary, and Zelenchuk observatories. The observations covered a frequency range from 2163.8 to 2675.8 MHz (S-band) and from 8591.6 to 9103.6 MHz (X-band) with

a bandwidth of 512 MHz. Only the right polarization was recorded using 2-bit quantization. For all detected pulses, fragments of the original data were saved for further analysis.

The regular observation data were analyzed using a thresholding algorithm to identify pulses with a signal-to-noise ratio (SNR) greater than 7. Maximum SNR for single pulse in S-band were 72, 78, 75 for 13m telescopes in Badary, Zelenchukskaya and Svetloe.

The dispersion measure (DM) for individual pulses was estimated, and the timing analysis was performed using the `tempo2` software. The pulsar ephemeris was constructed for the entire observation period, with determined parameters F0, F1, and F2. Pulses were divided into main pulses and interpulses, and weekly ephemerides were generated based on the arrival times of the main pulses. Monthly ephemerides were also generated based on the interpulse arrival times.

The timing residuals for the entire observation period were calculated and compared with the ephemerides from Jodrell Bank (Lyne et al. 1993). The results showed good agreement, with the added benefit of higher operational frequency and timeliness from the IAA RAS observations.

Our weekly ephemeris by main pulse, monthly ephemeris by interpulse and Jodrell ephemeris for comparison shown at Fig. 1. The common polynomial was calculated by our MP time series and substracted from all time series of pulsar period. The coefficients of polynomial are on the plot. Also, the RMS differences of period time series were calculated by interpolating it on the same epochs. The RMS differences of our values of epoch periods and Jodrell Bank ones were 7 ps.

4 Discussion

Our observational setup and data analysis techniques have proven effective in detecting giant pulses from the Crab Pulsar. The rates of detected pulses align well with those from other major observatories, demonstrating the capability of our instruments. Future work will focus on improving the sensitivity and timing accuracy, as well as expanding observations to other pulsar sources.

5 Conclusion

The successful detection of giant pulses from the Crab Pulsar using the IAA RAS facilities highlights the effectiveness of our observational and data processing methods. Continuous monitoring and improvements in our techniques will further enhance our understanding of pulsar emission mechanisms.

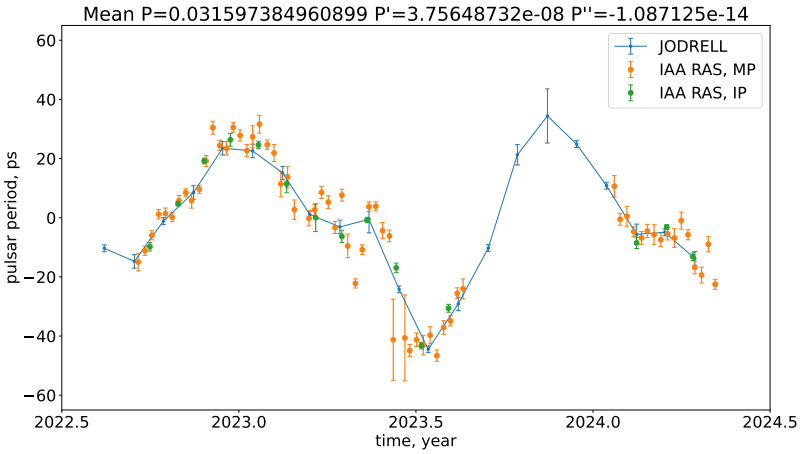

Fig. 1. Our results of the determination of Crab pulsar period by interpulses and main pulses, Jodrell monthly ephemeris. Mean polynomial was calculated using our MP results and excluded from all three period time series, parameters are presented in title.

The establishment of a monitoring service for the Crab Pulsar's pulses has enabled the IAA RAS to provide up-to-date ephemerides that align well with those from Jodrell Bank. The ability to detect and analyze giant pulses on a regular basis enhances the understanding of the pulsar's emission mechanisms and contributes valuable data for ongoing research. The results from these observations are available for immediate dissemination and can be published in real-time on the IAA RAS website.

Acknowledgements. The observations were carried out at the Badary, Svetloe, Zelenchukskaya radio observatories.

References

Hankins T. and Rickett B., 1975, Methods in Computational Physics: Advances in Research and Applications, 14, p. 55

Kurdubov S. and Marshalov D., 2022, Journal of Astronomical Instrumentation, 11, p. 2250015

Lyne A., Pritchard R., and Graham Smith F., 1993, Monthly Notices of the Royal Astronomical Society, 265, p. 1003

Majid W., Naudet C., Lowe S., and Kuiper T., 2011, The Astrophysical Journal, 741, p. 53

MODERN ASTRONOMY: FROM THE EARLY UNIVERSE TO EXOPLANETS AND BLACK HOLES

Correlation and evolution of the blazar S5 1803+784 short-term variability properties during 01.2022–01.2023

M. Butuzova, M. Gorbachev, V. Guseva, A. Zhovtan, S. Nazarov, G. Baida, and A. Krivenko

Crimean Astrophysical Observatory of the Russian Academy of Sciences, Nauchny, 298409 Russia

Abstract. The blazar S5 1803+784 has a unique high temporal resolution data series for about a year provided by the TESS satellite. By performing our aperture photometry of summarized on 10–30 the full-frame image cuts to reduce Poisson noise, we obtained the blazar light curve from 01.2022 to 01.2023.
Using a new method for de-termining the shortest characteristic variability time and supplementing the study with data from long-term multiband ZTF and AZT-8 observations, we trace the evolution of the micro-variability parameters and their correlation to the long-term variability char-acteristics. We draw a conclusion regarding the mechanism, forming the S5 1803+784 micro-variability.

Keywords: radiation mechanisms: non-thermal; relativistic processes; techniques: photometric; BL Lacertae objects: individual (S5 1803+784); galaxies: jets

DOI: 10.26119/VAK2024.009

1 Introduction

The predominant part of the observed blazar radiation is formed in their ultra-relativistic jets and is characterized by strong variability in the entire observable electromagnetic spectrum. The study of optical radiation is of interest because it comes from a region located in extreme proximity to the place of collimation and acceleration of matter in the jet. In the optical range, studies of intra-day variability are important for determining the variability mechanisms, and, as a consequence, the structure of jet flow (see, for example, Marscher 2014; Butuzova 2021).

At the same time, the duration of the data series is limited due to the Earth's daily rotation and weather conditions. The situation has been changed by space observatories specialized in searching for exoplanets. Namely, the Kepler satellite obtained the 181-day light curve of BL Lac object W2R 1926+42 (Edelson et al. 2013). For blazars S5 0716+714 (Raiteri et al. 2021a) and S4 0954+65(Raiteri et al. 2021b), characteristic variability times exceeding one day were identified based on TESS data for one or more sectors. The study of the temporal variability characteristics on time scales of several days requires a statistically significant data set and, consequently, the duration of a (quasi)uniform series of observations over at least several sets of TESS. Such a data series can be obtained for blazars located near the ecliptic poles, which TESS monitors during 13 sets interchangeably.

2 Light curve and spectral index of S5 1803+784

The TESS observations of blazar S5 1803+784 cover sectors 47–55 and 56–60 (entire period is 01.01.2021–18.01.2023). The light curves obtained by the standard algorithms for extracting SAP and PDCSAP fluxes are not applicable in our case because they are highly susceptible to Poisson noise due to the low brightness of the object and the small number of pixels containing the image of the object (Butuzova et al. 2024). We obtained the S5 1803+784 light curve by aperture photometry summed up by ten TESS full-frame image cuts for the object and comparison stars (Fig. 1). Depending on the object brightness and the TESS frame exposure, the time resolution of the data studied ranged from 67 to 300 minutes. Figure 2 shows the obtained light curves of the blazar S5 1803+784 and the control star, supplemented by photometric observations of ZTF (band r) and AZT-8 (band R of the Johnson system). There is a good correspondence between the light curves, except for the period of low brightness of the object. We believe that the difference in the variability amplitude in sectors 47, 51, 58–60 arises because the blazar's brightness has become the same or less than the brightness of the neighboring star and, consequently, the contribution of the latter's radiation to the aperture has increased and become significant.

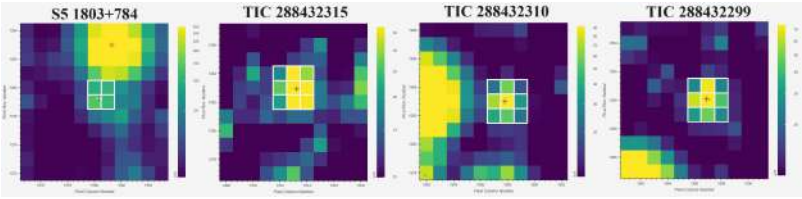

Fig. 1. TESS full-frame image cuts of S5 1803+784 and comparison stars for 53 sectors. The cross denotes the position of the specified objects. The white border marks the pixels of the aperture.

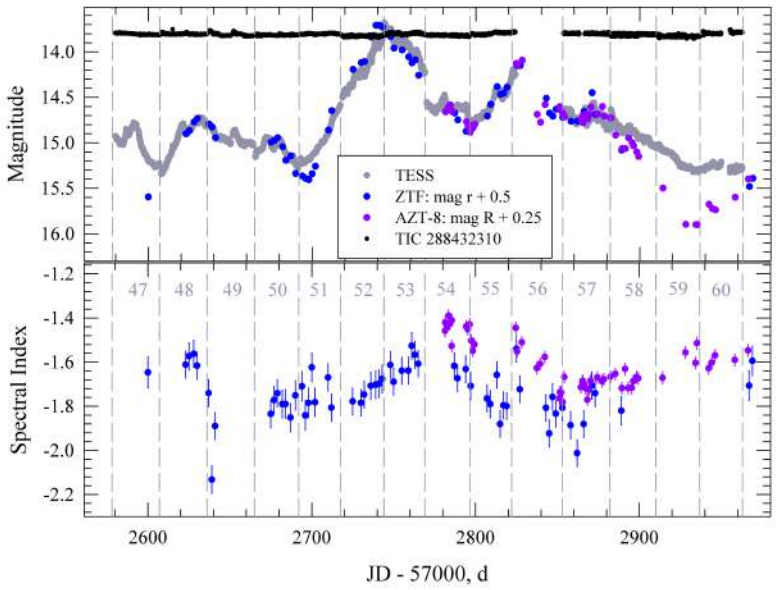

Fig. 2. The light curve of S5 1803+784 (top) and the evolution of the spectral index (bottom) from 01.01.2021 to 18.01.2023 according to TESS, ZTF, and AZT-8 data. Vertical dashed lines mark the boundaries of the TESS sectors, the number of which is shown in gray.

We determined the spectral index α ($F \propto \nu^{\alpha}$) from quasi-simultaneous observations in two or more bands. The errors of the α values were estimated according to the method described by Gorbachev et al. (2024). The spectral index varied from -1.4 to -2.2, not correlating with changes in brightness (Fig. 2, bottom panel).

3 Temporal parameters of variability

The high-time resolution light curve S5 1803+784 (Fig. 2) can be characterized as a superposition of variations occurring on different time scales. Taking into account the measurement accuracy, it is natural to assume that there is some minimum characteristic variability time τ, the value of which can evolve. We assume that in the radiating region, at each moment, there is one dominant process leading to the observed micro-variability, which then changes its parameters or is replaced by another one, having a different τ. Determining the characteristic variability time, for example, by the structure function (SF, Simonetti et al. 1985), when using a light curve containing the results of several such short-term processes, is incorrect. It is because, on a short time scale, processes with different τ neutralize each other's manifestation, and the type of structural function will be influenced by a process operating on a longer time scale.

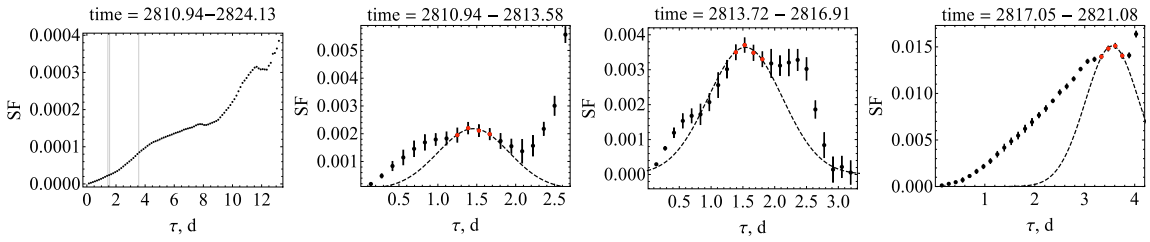

Fig. 3. SF for continuous light curve part of 55th sector (left) and SFs for small time interval within it. Vertical lines mark found τs.

To determine the shortest τ, we divided the TESS light curve of S5 1803+784 into parts within which no more than one point was allowed to be consecutive omitted in a uniform data series and acted according to the algorithm described by Butuzova et al. (2024). Namely, for each of these parts, an initial interval limited to twenty points was taken, and the SF was calculated. This interval was increased until τ, defined as the position of the SF peak, was found. Then we moved on to the next 20-point interval and performed the described algorithm. Figure 3 shows an example of the result of interval separation on the light curve characterized by different τ.

It can be seen that the found τ does not appear on the SF, constructed from all the data, the initially selected part of the light curve. The evolution of the mean magnitude, τ, and the square of the mean variability amplitude $\mathrm{SF_{max}}$ (defined as the value of the SF peak) are shown in Fig. 4.

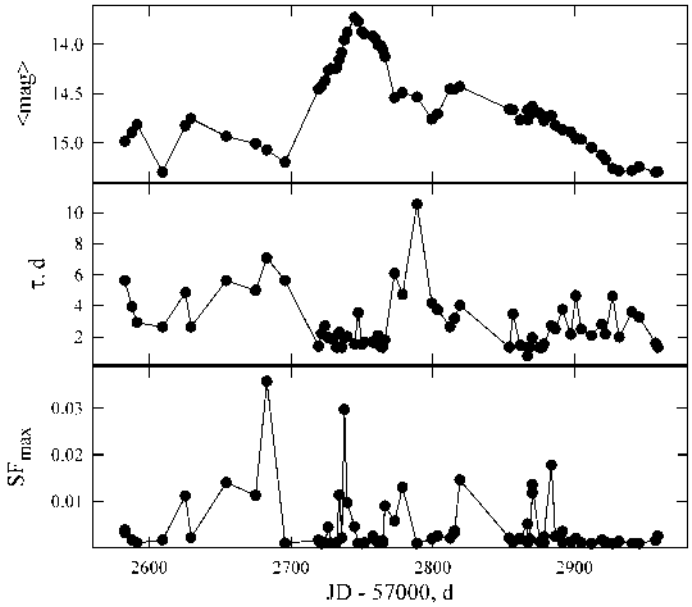

Fig. 4. The evolution of the average magnitude, characteristic variability time, and the square of the average amplitude of the micro-variability (from top to bottom).

4 Results

Due to the absence of the $\mathrm{SF_{max}}(\tau)$ correlation (Fig. 5), it follows that there is the action of either several micro-variability mechanisms or one determined by two or more independent parameters. These parameters do not depend on the characteristics of long-term variability, such as the average brightness <mag> and the maximum brightness change Δmag in the intervals corresponding to the found characteristic variability times.

We believe that the natural explanation for the observed properties of micro-variability is as follows. Regardless of the parameters and mechanisms of long–term

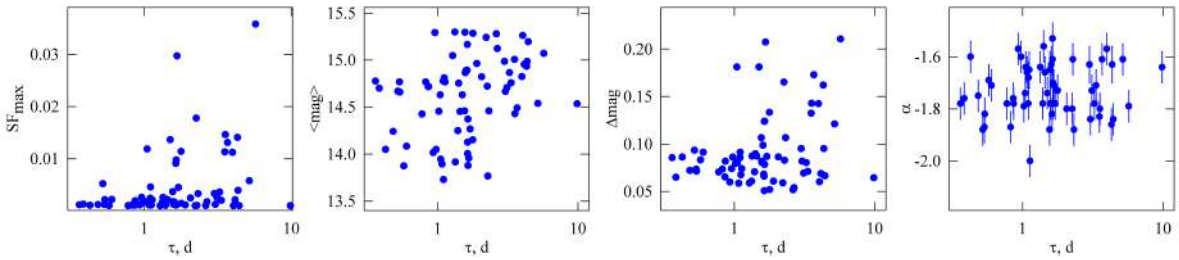

Fig. 5. Dependencies of the micro-variability parameters (SF_{max}, <mag>, Δmag) and the spectral index on τ.

variability, there are sub-components in the jet flow, which are parts of the emitting region, having motion direction differing slightly (within a few degrees) from the main trajectory. It leads to the fact that the sub-components have a Doppler factor that differs from the Doppler factor of the main flow, which results in micro-variability events. In this case, the absence of $SF_{max}(\tau)$ dependence indicates that the sub-components have different volumes. Further detailed modeling of the sub-components with different relations between their volume and the Doppler factor will allow us to draw conclusions about the structure of the jet flow.

Acknowledgements. The observations were performed with the AZT-8 scientific facility. We used TESS data from the MAST data archive at STScI and ZTF data, supported by NSF grant No. AST1440341 and AST2034437.

Fundin

Partly supported by Russian Science Foundation, No. 24-22-00343.

References

Butuzova M., 2021, Astroparticle Physics, 129, id. 102577
Butuzova M., Guseva V., Gorbachev M., Krivenko A., and Nazarov S., 2024, in prep.
Edelson R., Mushotzky R., Vaughan S., et al., 2013, Astrophys. J., 766, p. 16
Gorbachev M., Butuzova M., Nazarov S., and Zhovtan A., 2024, Astroparticle Physics, 160, id. 102965
Marscher A., 2014, Astrophys. J., 780, p. 87
Raiteri C., Villata M., Carosati D., et al., 2021a, Monthly Not. Roy. Astron. Soc., 501, p. 1100
Raiteri C., Villata M., Larionov V., et al., 2021b, Monthly Not. Roy. Astron. Soc., 504, p. 5629
Simonetti J., Cordes J., and Heeschen D., 1985, Astrophys. J., 296, p. 46

BAK 2024 MODERN ASTRONOMY: FROM THE EARLY UNIVERSE TO EXOPLANETS AND BLACK HOLES 300 years Russian Academy of Sciences

On the detection of emission near the event horizons of accreting stellar-mass black holes

L. Chmyreva[1] and G. Beskin[1,2]

[1] Special Astrophysical Observatory of the Russian Academy of Sciences, Nizhny Arkhyz, 369167 Russia
[2] Kazan Federal University, 18 Kremlyovskaya St, Kazan, 420008 Russia

Abstract. We discuss the possibility of detecting signs of the existence of stellar-mass black hole (BH) event horizons in the emission of interstellar gas accreting on them. We consider a sample of invisible compact objects detected as companions of Main Sequence stars in wide binaries. Theoretical luminosities and accretion rates of the interstellar gas were obtained within the framework of the spherical accretion model. BH velocities estimated from binary system dynamics, as well as the density of the surrounding ISM, were used in the calculations. Based on the sensitivity data of existing and projected ground-based and space-based telescopes (JWST, GMT, TMT, ELT, MILLIMETRON), we estimated the possibility of direct detection of both stationary and variable halo emission around the BHs.

Keywords: black hole physics; accretion; stars: black holes; methods: observational

DOI: 10.26119/VAK2024.010

1 Introduction

According to current evolutionary predictions, the number of isolated stellar-mass black holes (BHs) in our Galaxy reaches 10^8 (Wiktorowicz et al. 2019). Detecting manifestations of their event horizons, and therefore proving their existence, is very important: horizons are a generic feature of all BHs (Beskin et al. 2008). Direct high temporal resolution observations of their interaction with the surrounding medium (flares generated by beams of electrons in the direct vicinity of a BH) would allow us to obtain information on the structure of space-time near a BH. Such data can be obtained only for an isolated BH: in this case the accretion rate is low and the horizon is not obscured by the accreting matter.

However, detecting isolated black holes is very difficult compared to those that are members of X-ray binaries and whose masses can be estimated. At the same time, in the case of detached binaries, when the separation between the companions is sufficient and there is no interaction between them, a BH would accrete matter as a single object, unaffected by the primary star. For our purpose, such BHs can be considered as isolated, and accretion onto an isolated BH, regardless of its metrics, is usually spherical. Luminosity for this type of accretion remains nearly constant over a wide range of frequencies (10^{14}–10^{20} Hz). A BH would exhibit a featureless spectrum and variable emission with an amplitude ranging from fractions of a percent to ten percent; the duration of individual flares would be 10^{-6} to 10^{-3} s (Shvartsman 1971; Bisnovatyi-Kogan & Ruzmaikin 1974; Meszaros 1975; Ipser & Price 1982).

In this work we consider a sample of wide binaries with no Roche lobe overflow, hosting invisible compact companions, and estimate their theoretical luminosities under the assumption of spherical accretion and discuss the possibility of their direct detection by existing and future instruments.

2 Sample binaries and calculations

Recently, several non-interacting binaries comprising a compact object and a main sequence star have been reported by various authors (El-Badry et al. 2023; Chakrabarti et al. 2023; Andrews et al. 2022; Shahaf et al. 2023; Tanikawa et al. 2023; Gaia Collaboration et al. 2024; Jayasinghe et al. 2021) based on Gaia DR3[1] data. For our analysis, we selected 17 wide non-interacting pairs with compact objects which masses allow us to assume that they might be BHs. Some lower-mass compact objects that may be neutron stars were also considered, if their mass uncertainties allow the possibility that these objects could be more massive. The primary objects in the sample binaries

[1] https://www.cosmos.esa.int/web/gaia/dr3

are mostly bright ($m_V \sim 12-17$) stars of roughly solar mass, with several OB stars. We excluded candidates with suspected accretion disks and interaction between the components, leaving a sample of 10 systems.

The accretion rate $\dot{m}$ onto a BH and luminosity L of the halo around it are determined by its mass, ISM density, and velocity relative to the surrounding gas (Bondi & Hoyle 1944; Shvartsman 1971; Beskin & Karpov 2005):

$$L \propto M_{10}^3 n^2 (V^2 + c_s^2)_{16}^{-3} \ \text{erg s}^{-1}, \tag{1}$$

where M_{10} is the BH mass in units of $10M_\odot$, n is the ISM density in cm^{-3}, and V and c_s are the total BH velocity and sound speed normalized to 16 km s^{-1}. Using the data available on the orbital parameters of the sample systems, we estimated the total space velocities of the BHs from their Keplerian orbital motions and the system center-of-mass velocity. The local ISM densities were estimated from the G-Tomo[2] Galactic extinction maps taking into account stellar winds, calculated assuming spherically-symmetric wind from a star of the corresponding spectral type. The contribution from the winds turned out to be negligibly small in most cases. We did not consider the general galactic gas velocities, as they are below the uncertainty level of our BH velocity estimates. The densities were then used to determine the temperatures and speeds of sound in the surrounding gas. The resulting luminosities, accretion rates, and expected visual magnitudes are presented in Table 1.

Table 1. Parameters of the compact companions: luminosities, accretion rates, visual magnitudes, masses, distances, and velocities.

Source ID	L	$\dot{m}$	m_V	M	D	V
Gaia DR3	erg s^{-1}	$\dot{M}/\dot{M}_{Edd}$	Mag	$M_\odot$	pc	km s^{-1}
4373465352415301632	$(6.6 \pm 4.4) \times 10^{25}$	$(2.5 \pm 0.9) \times 10^{-9}$	$32.3^{+1.6}_{-0.2}$	9.3 ± 0.2	480 ± 4	77 ± 12
4314242838679237120	$(7.5 \pm 7.4) \times 10^{30}$	$(1.7 \pm 1.6) \times 10^{-7}$	$23.6^{+3.9}_{-5.1}$	2.8 ± 1.4	358 ± 18	20 ± 15
5593444799901901696	$(5.2 \pm 4.7) \times 10^{26}$	$(4.2 \pm 2.9) \times 10^{-8}$	$31.1^{+1.9}_{-1.6}$	2.6 ± 0.8	1506 ± 120	15 ± 10
6328149636482597888	$(7.7 \pm 7.3) \times 10^{23}$	$(3.6 \pm 2.7) \times 10^{-10}$	$40.0^{+1.5}_{-1.8}$	3.3 ± 0.9	816 ± 10	384 ± 13
3263804373319076480	$(7.5 \pm 7.4) \times 10^{29}$	$(4.1 \pm 4.0) \times 10^{-7}$	$28.3^{+3.8}_{-7.8}$	2.8 ± 0.5	291 ± 13	32 ± 30
6601396177408279040	$(4.1 \pm 0.7) \times 10^{22}$	$(1.3 \pm 0.2) \times 10^{-10}$	$41.2^{+0.4}_{-0.3}$	2.6 ± 0.5	652 ± 50	162 ± 49
6588211521163024640	$(8.5 \pm 8.4) \times 10^{28}$	$(1.5 \pm 1.4) \times 10^{-7}$	$33.4^{+5.7}_{-8.4}$	2.4 ± 0.4	779 ± 70	63 ± 60
5870569352746779008	$(7.1 \pm 4.0) \times 10^{27}$	$(2.6 \pm 0.9) \times 10^{-8}$	$27.4^{+0.8}_{-0.9}$	8.9 ± 0.3	1164 ± 25	65 ± 9
3104145904761393408	$(4.8 \pm 4.7) \times 10^{25}$	$(3.0 \pm 2.6) \times 10^{-9}$	$34.5^{+3.5}_{-2.2}$	3.0 ± 0.1	515 ± 15	39 ± 30
4318465066420528000	$(9.4 \pm 3.7) \times 10^{24}$	$(5.2 \pm 1.0) \times 10^{-10}$	$35.3^{+0.5}_{-0.4}$	32.7 ± 0.8	591 ± 6	566 ± 3

[2] https://explore-platform.eu/sda/g-tomo

3 Results and discussion

The velocities derived for the compact companions are the parameters that contribute the most to the high uncertainty in luminosity and accretion rate. Calculations have shown that most of the sources, if they are indeed BHs, are predictably faint - so far, none of the considered objects have been directly detected in observations. However, several of them may be within the sensitivity range of already operating and planned instruments. (e.g., JWST, GMT, MILLIMETRON, TMT, ELT). In particular Gaia DR3 4314242838679237120, 3263804373319076480, and 5870569352746779008 show promise in that regard.

We emphasize that the critical test for registering manifestations of an event horizon is the detection of fast variations in the emission of plasma accreting onto a BH. The flare amplitude for a given accretion rate can reach a level of 5.5 % of the luminosity in the X-ray range, making it possible to detect such events. Note that when magnetic field lines in the current sheets reconnect, their maximal Lorentz factor may reach 10^4–10^5; therefore, the flares may be detected by instruments with nanosecond and microsecond temporal resolution. Thus, there are possibilities of registering the emission of BHs in different wavelength ranges and with different temporal characteristics, and therefore, it may be possible to detect observational manifestations of their horizons.

References

Andrews J., Taggart K., and Foley R., 2022, arXiv e-prints, arXiv:2207.00680
Beskin G., Biryukov A., Karpov S., et al., 2008, Advances in Space Research, 42, 523
Beskin G. and Karpov S., 2005, A&A, 440, 223
Bisnovatyi-Kogan G. and Ruzmaikin A., 1974, Ap&SS, 28, 45
Bondi H. and Hoyle F., 1944, MNRAS, 104, 273
Chakrabarti S., Simon J., Craig P., et al., 2023, AJ, 166, 6
El-Badry K., Rix H., Quataert E., et al., 2023, MNRAS, 518, 1057
Gaia Collaboration, Panuzzo P., Mazeh T., et al., 2024, A&A, 686, L2
Ipser J. and Price R., 1982, ApJ, 255, 654
Jayasinghe T., Stanek K., Thompson T., et al., 2021, MNRAS, 504, 2577
Meszaros P., 1975, A&A, 44, 59
Shahaf S., Bashi D., Mazeh T., et al., 2023, MNRAS, 518, 2991
Shvartsman V., 1971, Soviet Astronomy, 15, 377
Tanikawa A., Hattori K., Kawanaka N., et al., 2023, ApJ, 946, 79
Wiktorowicz G., Wyrzykowski L., Chruslinska M., et al., 2019, ApJ, 885, 1

The results of simultaneous TESS and multiband photometric observations of BL Lac during a high activity

M. Gorbachev, M. Butuzova, N. Pit, and A. Krivenko

Crimean Astrophysical Observatory of the Russian Academy of Sciences, Nauchny, 298409 Russia

Abstract. For the blazar BL Lac, we analyze data from TESS and multiband observations that were obtained using the MTM-500 telescope of the Crimean Astrophysical Observatory from 1.09.2022 to 30.09.2022.
During this period, BL Lac showed strong variability, both accompanied and unaccompanied by changes in spectral index.
The shortest characteristic variability times are mainly in the range from 0.2 to 1 day and do not depend on the object brightness, the spectral index, and the average amplitude of the variability within the corresponding intervals of the light curve.
It indicates that the mechanisms of short-term variability are characterized by two or more independent parameters.

Keywords: radiation mechanisms: non-thermal; relativistic processes; techniques: photometric; BL Lacertae objects: individual (BL Lac); galaxies: jets

DOI: 10.26119/VAK2024.011

1 Introduction

The blazar BL Lac was in a highly active state like never before during 05.2021–12.2023. It was very bright and showed a large amplitude of brightness fluctuations (Bachev et al. 2023). To compile a complete picture of the processes that led to such violent variability, the observations in different spectral ranges and on different time scales are necessary. Earth's daily rotation complicates observations of micro-variability. However, during 01.09.2022–30.09.2022 BL Lac was in the field of view of the TESS space mission (Ricker et al. 2015), conducting almost continuous optical monitoring of a section of the sky for 27 days with high temporal resolution. Supplementing these data with the results of simultaneous multiband photometric observations performed on the MTM-500 telescope of the CrAO RAS, we got the opportunity to investigate the correlation between the temporal and spectral properties of the BL Lac variability on time scales from several hours to several days.

2 Observations and data analysis

Intraday B-, V,-R-, I-observations of BL Lac were performed by the telescope MTM-500 (Rublevski & Kiselev 2019)

As a result of the nested ANOVA test, intraday variability was detected on 15 out of 23 nights according to MTM-500 data. Figure 1 shows the light curves for the entire observation period and the night MJD=59840. Converting magnitudes to the radiation flux (Mead et al. 1990), we determined the spectral index α under the assumption of a power-law spectrum $F \propto \nu^{\alpha}$ (Fig. 2). We calculated the uncertainty of the α value arising from errors in flux measures according to the method described by Gorbachev et al. (2024).

Due to the dense stellar environment near BL Lac, its relatively weak brightness, and the large pixel size (21″), TESS does not provide automatic processing results for this source. It leads us to the need to perform our photometric processing of TESS full-frame image cuts summed up by 10. There is an acceptable agreement with the MTM-500 data (Fig. 1). However, there are some differences, in particular, the difference in the amplitude of the variability ($\Delta m_{\text{MTM-500}} = 1.225$ and $\Delta m_{\text{TESS}} = 1.102$). We attribute this fact to the change in the spectral index with variability, as well as the wide bandwidth of the TESS filter (600–1000 nm).

If one process is responsible for variability on small time scales, its parameters may change over time. Or this process can be replaced by another one. Then, we can expect a change in the shortest characteristic variability time τ. Assuming that a single process dominates the variability at some time interval, we define τ using the structure function (SF) for consecutive intervals on the light curve using TESS

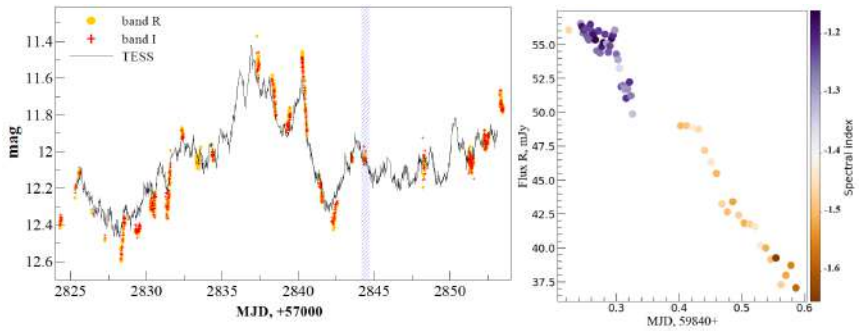

Fig. 1. The left panel shows combined BL Lac light curve according to MTM-500 and TESS data. For better clarity of the light curves, the values in the R and I bands were reduced by 1.1 and 0.36 magnitude, respectively. The shaded area marks the night, the light curve of which is shown on the right panel.

telescope data (for more details, see Butuzova 2021). Figure 3 shows the absence of explicit dependencies of τ on the square of the average variability amplitude (SF_{max}), defined as the value of the SF maximum, the maximum brightness change, and the average brightness at the corresponding intervals.

The evolution of the spectral index and τ demonstrates different behavior: curves show both correlation and anticorrelation intervals as well as significant changes in τ with α constant (Fig. 2).

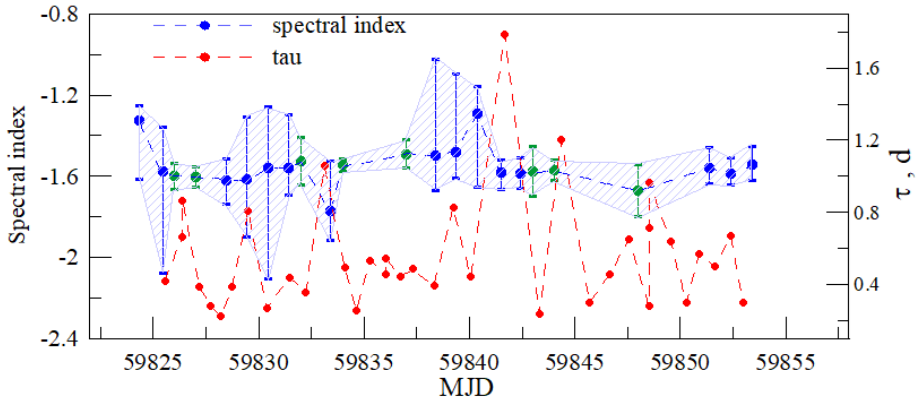

Fig. 2. Evolution of the BL Lac spectral index and the shortest characteristic variability time τ. The blue and green symbols mark the median values of α for nights with and without detected intra-day variability, respectively. The error bars show the maximum change in α during the night. The shortest characteristic variability time τ is highlighted in red.

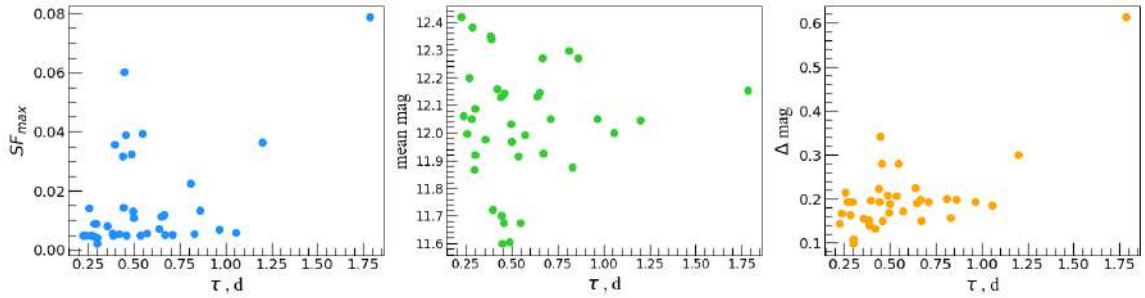

Fig. 3. The dependence of micro-variability parameters (SF_{max}, <mag> and Δmag) on τ.

3 Summary

Intra-day variability of BL Lac was detected on 15 of the 23 nights, with 7 nights showing changes in spectral index. For the first time, we prove that the difference in the variability amplitude in TESS and ground-based telescope data is caused by a change in α at a wide TESS bandwidth. The shortest characteristic variability times are mainly in the range from 0.2 to 1 day. No correlation was found between the temporal and spectral variability characteristics. It indicates that the mechanisms of short-term variability are characterized by two or more independent parameters.

Acknowledgements. The observations were performed with the MTM-500 scientific facility. We used TESS data from the MAST data archive at STScI.

Funding

This work is partly supported by the Russian Science Foundation, No. 24-22-00343.

References

Bachev R., Tripathi T., Gupta A., et al., 2023, Monthly Not. Roy. Astron. Soc., 522, p. 3018
Butuzova M., 2021, Astroparticle Physics, 129, id. 102577
Gorbachev M., Butuzova M., Nazarov S., and Zhovtan A., 2024, Astroparticle Physics, 160, id. 102965
Mead A., Ballard K., Brand P., et al., 1990, Astron. Astrophys. Suppl. Ser., 83, p. 183
Ricker G., Winn J., Vanderspek R., et al., 2015, JATIS, 1, id. 014003
Rublevski A. and Kiselev N., 2019, Izvestiya Krymskoj Astrofizicheskoj Observatorii, 115, 63

BAK 2024 MODERN ASTRONOMY: FROM THE EARLY UNIVERSE TO EXOPLANETS AND BLACK HOLES 300 years Russian Academy of Sciences

Search for proton jets in blasars as possible emitters of high-energy neutrinos

Yu. A. Kovalev[1,2], G. Zhekanis[3], Yu. Yu. Kovalev[4], Yu. Sotnikova[3], S. Troitsky[2], A. Popkov[1,5], A. Plavin[6], A. Erkenov[3], M. Mingaliev[3], N. Nizhelsky[3], P. Tsybulev[3], and N. Bursov[3]

[1] Lebedev Physical Institute of the Russian Academy of Sciences, Moscow, 117997 Russia
[2] Institute for Nuclear Research of the Russian Academy of Sciences, Moscow, 117312 Russia
[3] Special Astrophysical Observatory of the Russian Academy of Sciences, Nizhny Arkhyz, 369167 Russia
[4] Max Planck Institute for Radio Astronomy, Bonn, 53121 Germany
[5] Moscow Institute of Physics and Technology, Dolgoprudny, 141700 Russia
[6] Black Hole Initiative at Harvard University, Cambridge, MA 02138 USA

Abstract. We continue the RATAN-600 observations of instantaneous 1-22 GHz spectra of active galactic nuclei at 5-7 frequencies in 1997-2024. The main task is the analysis of the results including the CATS database for data beyond 1-22 GHz and the Hedgehog model proposed by N. S. Kardashev in 1969. The new goal is to study the physical parameters of jets in VLBI-blazars and search for compact bright strong variable proton jets as possible sources of high-energy neutrinos in proton-proton and proton-photon processes. Main results of estimating values for magnetic fields, brightness temperatures and angular sizes of both proton and electron jets in 9 blasars are presented. This allows to explain the RadioAstron extra-high brightness temperatures and magnetic fields as well as extremely compact cores in radio jets and to link proton sources of high-energy neutrinos with some radio jets.

Keywords: galaxies: active, jets; neutrinos; magnetic fields

DOI: 10.26119/VAK2024.012

1 Introduction

Analysis of extragalactic possible "radio-neutrino" sources leads to the preliminary hypothesis that their main properties may be the following (Troitsky 2021; Kovalev et al. 2022): 1) long-term wide-range variability of radio emission with strong (including repeated) flow bursts up to 10–20 times in amplitude and quasiperiods up to tens of years in the cm and mm ranges; 2) maximum brightnesses, close to the RadioAstron extremely high, and minimum angular size, close to extremely small; 3) two parts of the proton energy distribution – with high energies $E_p > 500$ TeV (in order to participate in the birth of neutrinos with energies $E_\nu > 25$ TeV) and with E_p up to 1 TeV (in order to generate the jet radio emission). It was previously shown that the radio emission from variable extragalactic objects can be described by synchrotron radiation of electrons or protons in a strong quasi-radial magnetic field of a relativistic jet in the Hedgehog model proposed by N. S. Kardashev in 1969 and developed later by a number of authors (Kovalev et al. 2000).

2 Observation, analysis and results

The report summarizes previous results and continues the model analysis of the main physical parameters for quasars and galaxies – from their subsample with the strongest long-term variability of radiation as measured by RATAN-600. For B0235+16, a repetition of spectrum changes was discovered for the first time during a strong burst in the range 1–22 GHz – after 22 years. The results of RATAN-600 measurements of instantaneous radio spectra at 1–22 GHz in 1997–2024 (Kovalev et al. 2022), and the data outside this range from the CATS database (Verkhodanov et al. 2005) were used. Using these data and the Hedgehog jet model, estimates of the physical parameters for electron and proton jets were obtained – magnetic field, brightness temperature, angular size (similar to Sotnikova et al. 2022). The results of fits and estimations are shown in Fig. 1 and in Table 1 and do not contradict VLBI/RadioAstron measurements (see Kovalev et al. 2020). For the sake of simplicity, the red shift is still neglected and it is assumed that for all the objects under consideration, the parameter $\gamma_E = E/(M \cdot c^2) \sim 300$ at the frequency ν_m of the jet spectrum maximum, where E is the energy and M is the mass of emitted electrons or protons (see also Sotnikova et al. 2022). Protons for the radio emission and for the production of neutrinos may be accreted from the disk and accelerated to the required energy distribution (including the Faraday induction mechanism) in a region with a strong magnetic field in the vicinity of the SMBH or, in addition, could be accelerated during bursts due to precessing binary black holes that occasionally cross the accretion disk similar to Ivanov & Zhuravlev (2024).

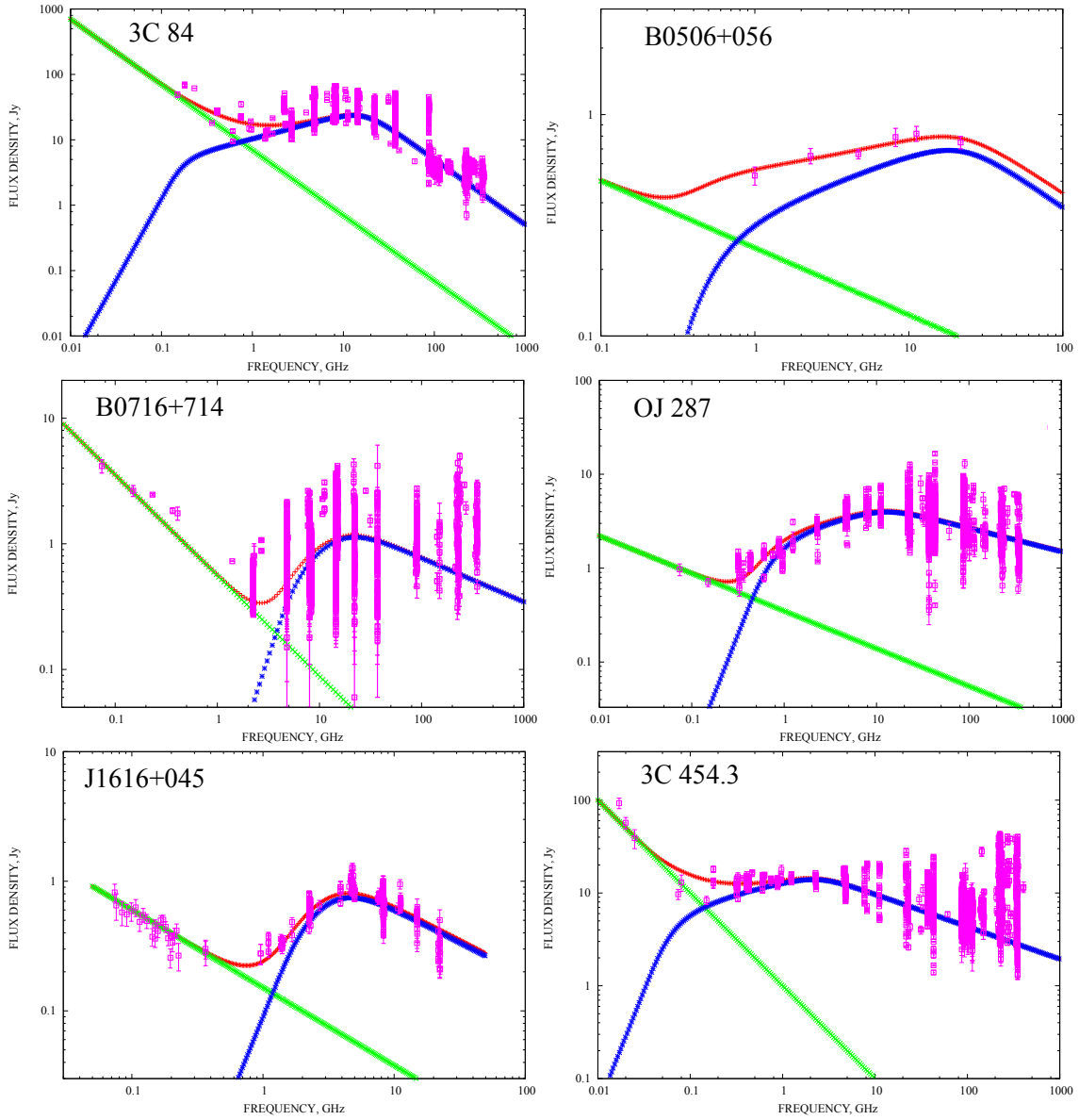

Fig. 1. Results of fitting the Hedgehog model (Kovalev et al. 2000) to the mean 0.01–500 GHz spectra of observed flux density in Jy for 6 examples of 9 AGNs in Table 1. The sum of two spectral model components have been fitted. The High Frequency Component (HFC, a curve spectrum of the jet) is variable, it is emitted by the relativistic jet in the strong quasi-radial magnetic field. The Low Frequency Component (LFC – a line spectrum) is practically non-variable and is emitted by the other parts of the source. The 1–22 GHz data are the RATAN-600 data, in general. The data at other frequencies and partly at 1–22 GHz were taken from the CATS data base (Verkhodanov et al. 2005). Fitting for B0506+056 is shown for the instantaneous spectrum on the RATAN-600 data only; more data for it see in the paper by Baikal-GVD collaboration et al. (2024).

Table 1. Results of the model fitting the magnetic field B, brightness temperature T_b and angular size Θ of the jets near the maximum of the spectra. The equracy is of the order of the values.

Object	Particles	B	T_b	Θ	References
		Gauss	K	mas	
+3C 84	electrons	9	$5 \cdot 10^{10}$	1	
	protons	$2 \cdot 10^4$	$9 \cdot 10^{13}$	0.03	
+B0506+056	electrons	6	$5 \cdot 10^{10}$	0.1	
	protons	$1 \cdot 10^4$	$9 \cdot 10^{13}$	0.003	
S5 0716+71	electrons	0.5	$5 \cdot 10^{10}$	1.5	
	protons	900	$9 \cdot 10^{13}$	0.03	
+OJ287	electrons	5	$5 \cdot 10^{10}$	0.3	
	protons	$8 \cdot 10^3$	$9 \cdot 10^{13}$	0.007	
+3C279	electrons	15	$5 \cdot 10^{10}$	3	
	protons	$3 \cdot 10^4$	$9 \cdot 10^{13}$	0.07	
+B1502+10	electrons	7	$5 \cdot 10^{10}$	0.6	Sotnikova et al. (2022)
	protons	$1 \cdot 10^4$	$9 \cdot 10^{13}$	0.014	
+J1616+04	electrons	0.15	$5 \cdot 10^{10}$	0.1	
	protons	300	$9 \cdot 10^{13}$	0.002	
+3C 454.3	electrons	2	$5 \cdot 10^{10}$	4	
	protons	$4 \cdot 10^3$	$9 \cdot 10^{13}$	0.08	
+0954+658	electrons	20	$5 \cdot 10^{10}$	0.08	Vlasyuk et al. (2023)
	protons	$4 \cdot 10^4$	$9 \cdot 10^{13}$	0.002	

Acknowledgements. The observations were carried out with the RATAN-600 scientific facility. The work is supported in the framework of the State project "Science" by the Ministry of Science and Higher Education of the Russian Federation under the contract 075-15-2024-541.

References

Baikal-GVD collaboration et al., 2024, MNRAS, 527, p. 8784
Ivanov P. and Zhuravlev V., 2024, MNRAS, 528, p. 337
Kovalev Yu. Yu., Kardashev N., Sokolovsky K., et al., 2020, Adv.Sp.Rec., 65, p. 705
Kovalev Yu. A., Kovalev Yu. Yu., and Nizhelsky N., 2000, PASJ, 52, p. 1027
Kovalev Yu. A., Nizhelsky N., Kovalev Yu. Yu., et al., 2022, Proceedings of Science, 425, id. 27
Sotnikova Yu., Kovalev Yu. A., Kovalev Yu. Yu., et al., 2022, Proceedings of Science, 399, id. 9
Troitsky S., 2021, Physics-Uspekhi, 64, p. 1261
Verkhodanov O., Trushkin S., Andernach H., and Chernenkov V., 2005, Bull.SAO, 58, p. 118
Vlasyuk V., Sotnikova Yu., Volvach A., et al., 2023, Astrophys. Bulletin, 78, p. 464

MODERN ASTRONOMY: FROM THE EARLY UNIVERSE TO EXOPLANETS AND BLACK HOLES

Dirac particle in gravitational field of black hole with Newman-Unti-Tamburino parameter

N. Krylova[1,2] and V. Red'kov[1]

[1] B. I. Stepanov Institute of Physics of the National Academy of Sciences of Belarus, 68-2 Nezavisimosti Ave., Minsk, 220072 Belarus

[2] Belarusian State Agrarian Technical University, 99 Nezavisimosti Ave., Minsk, 220023 Belarus

Abstract. We study the quantum-mechanical problem of a spin 1/2 particle in gravitational field of the black hole with Newman–Unti–Tamburino (NUT) parameter. Separation of the variables has been performed in the Dirac equation. The system of angular equations has been solved analytically in terms of hypergeometric functions. The quantization condition for the angular parameter is derived. In the massless case, the radial system is reduced to separate systems of two first-order equations which are solved in terms of the confluent Heun functions. Generalized tortoise-like coordinate is introduced, and expressions for the effective complex-valued potentials are found. We may expect that the present analysis can permit us to elucidate the physical interpretation for the Newman–Unti–Tamburino metric. The question arises about possible existence of the Hawking-like radiation in this model.

Keywords: black hole physics: Newman–Unti–Tamburino black hole; equations: individual (Dirac, Heun); spin 1/2 particle

DOI: 10.26119/VAK2024.013

1 Introduction

Recently, the metrics with Newman–Unti–Tamburino (NUT) parameter have attracted the interest of scientific community. NUT parameter is usually interpreted as a gravitomagnetic charge (monopole) or as a linear source of a pure angular momentum (the twisting of the surrounding spacetime), see, e. g., Galtsov & Kobialko 2017; Chakraborty & Mukhopadhyay 2023. So, the black holes with NUT parameter are considered as physically meaningful systems with some special characteristics. Being axially-symmetric, the NUT black holes can exhibit new effects, such as asymmetry of black hole shadow or as the Lense–Thirring effect demonstrated by the rotating black holes (Ghasemi-Nodehi et al. 2021; Chakraborty & Mukhopadhyay 2023). The presence of the NUT-parameter in anti-de-Sitter metric leads to the appearance of a region with negative Gibbs free energy in thermodynamics of black holes that is associated to the phase transition (Awad & Elkhateeb 2023). The purpose of this work is to study the quantum-mechanical behavior of fermions in the background of the gravitational field of the NUT black hole.

2 Dirac equation in NUT space-time

To study a spin 1/2 particle in gravitational field of the black hole with NUT parameter, we search the solutions of the general covariant Dirac equation

$$\left[i\gamma^a\left(e^{\alpha}_{(a)}\frac{\partial}{\partial x^{\alpha}}+\frac{1}{2}\sigma^{mn}\gamma_{mna}\right)-M\right]\Psi=0. \tag{1}$$

Gravitational field of NUT black hole is took into account as the NUT spacetime background with metric

$$ds^2=\Phi\left(dt+4a\sin^2(\frac{\theta}{2})d\phi\right)^2-\frac{dr^2}{\Phi}-\left(a^2+r^2\right)\left(d\theta^2+\sin^2(\theta)d\phi^2\right),$$

where $\Phi=1-\frac{r_g r+2a^2}{r^2+a^2}$, a is a NUT parameter. We assume the Weyl basis and the bispinors are written in terms of two-component spinors as $\Psi=\begin{vmatrix}\xi\\ \chi\end{vmatrix}$, then the Dirac equation (1) takes the explicit form (let $\rho^2=r^2+a^2$, $\Delta=r^2-r_g r-a^2$, $\Phi=\frac{\Delta}{\rho^2}$)

$$\sigma_1\Big(\frac{1}{\rho}\chi_{,2}+\frac{1}{2\rho\tan\theta}\chi\Big)+\sigma_2\Big(\frac{1}{\rho\sin\theta}\chi_{,3}-\frac{2a}{\rho}\tan\frac{\theta}{2}\,\chi_{,0}\Big)$$

$$+\sigma_3\Big[\frac{\sqrt{\Delta}}{\rho}\chi_{,1}+\Big(\frac{\Delta'}{4\rho\sqrt{\Delta}}+\frac{\sqrt{\Delta}}{2\rho^3}\rho_-\Big)\chi\Big]+\frac{\rho}{\sqrt{\Delta}}\chi_{,0}+iM\xi=0,$$

$$\sigma_1\Big(\frac{1}{\rho}\xi_{,2}+\frac{1}{2\rho\tan\theta}\xi\Big)+\sigma_2\Big(\frac{1}{\rho\sin\theta}\xi_{,3}-\frac{2a}{\rho}\tan\frac{\theta}{2}\,\xi_{,0}\Big)$$

$$+\sigma_3\Big[\frac{\sqrt{\Delta}}{\rho}\xi_{,1}+\Big(\frac{\Delta'}{4\sqrt{\Delta}\rho}+\frac{\sqrt{\Delta}}{2\rho^3}\rho_+\Big)\xi\Big]-\frac{\rho}{\sqrt{\Delta}}\xi_{,0}-iM\chi=0;$$

where we apply the notations $\partial_\alpha =_{,\alpha}$, $\rho_+ = r+ia$, $\rho_- = r-ia$. To separate the variables we take into account the time independence and symmetry of the NUT spacetime and search spinors in the form $\xi=\Delta^{-1/4}\rho_+^{-1/2}e^{-i\epsilon t}e^{im\phi}X(r,\theta)$, $\chi=\Delta^{-1/4}\rho_-^{-1/2}e^{-i\epsilon t}e^{im\phi}Y(r,\theta)$, with the substitutions $X_1=R_1(r)T_1(\theta)$, $X_2=R_2(r)T_2(\theta)$, $Y_1=R_3(r)T_1(\theta)$, $Y_2=R_4(r)T_2(\theta)$. This procedure leads to angular equations

$$\frac{dT_1}{d\theta}+\Big(\frac{1}{2\tan\theta}-\frac{m}{\sin\theta}-2a\epsilon\tan\frac{\theta}{2}\Big)T_1-\Lambda T_2=0,$$

$$\frac{dT_2}{d\theta}+\Big(\frac{1}{2\tan\theta}+\frac{m}{\sin\theta}+2a\epsilon\tan\frac{\theta}{2}\Big)T_2-\Lambda T_1=0;$$

and the radial equations

$$\Big(\sqrt{\Delta}\frac{d}{dr}-\frac{ia\sqrt{\Delta}}{\rho^2}-\frac{i\epsilon\rho^2}{\sqrt{\Delta}}\Big)R_3+iM\rho_-R_1=\Lambda R_4,\ \Big(\sqrt{\Delta}\frac{d}{dr}-\frac{ia\sqrt{\Delta}}{\rho^2}+\frac{i\epsilon\rho^2}{\sqrt{\Delta}}\Big)R_4-iM\rho_-R_2=\Lambda R_3,$$
$$\Big(\sqrt{\Delta}\frac{d}{dr}+\frac{ia\sqrt{\Delta}}{\rho^2}+\frac{i\epsilon\rho^2}{\sqrt{\Delta}}\Big)R_1-iM\rho_+R_3=\Lambda R_2,\ \Big(\sqrt{\Delta}\frac{d}{dr}+\frac{ia\sqrt{\Delta}}{\rho^2}-\frac{i\epsilon\rho^2}{\sqrt{\Delta}}\Big)R_2+iM\rho_+R_4=\Lambda R_1.$$

The system of angular equations has been solved analytically in terms of hypergeometric functions G (let $z=\sin^2\frac{\theta}{2}$); there arises the quantization rule for the separation parameter Λ:

$$\Lambda^2=-(m+n_1+1/2)(m+n_1+1/2+4a\epsilon),\ m>0.$$

In the massless case, the radial system is reduced to separate systems of two first-order equations which are solved in terms of the confluent Heun functions $H(v)$; for instance the general solution for R_1 is

$$R_1=\frac{\epsilon^{1+i\epsilon r_g}e^{i\epsilon(r-r_1)}\,(r-r_1)^{\frac{1}{2}+i\epsilon r_1}\,(r-r_2)^{\frac{1}{2}+i\epsilon r_2}\sqrt{r+ia}}{\sqrt{r-ia}}H(v),\ \ v=\frac{r-r_2}{r_1-r_2}. \qquad (2)$$

Analysis of the radial solution allows to conclude that the asymptotic behavior at infinity is not influenced by NUT parameter a, while near the exterior horizon the a-dependent phase shift arises.

Let find the effective potential (in massless case). In order to compare the present study with the results in Schwarzschild case, we introduce variables $f(x) = R_1 + R_2, g(x) = i(R_1 - R_2); x = \epsilon r$, and the generalized tortoise-like coordinate w

$$\frac{d^2w}{dx^2} + \Big[\frac{\Delta'}{\Delta} - \frac{2}{x+ia}\Big]\frac{dw}{dx} = 0, w = x + \frac{(a-ix_1)^2\ln(x-x_1) - (a-ix_2)^2\ln(x-x_2)}{x_2-x_1},$$

which in the limiting case of $a = 0$ reduces to ordinary tortoise-like coordinate $w = x + \ln(x-1)$ (Chichurin et al. 2024). The second-order radial equations take the structure

$$\Big[\frac{d^2}{dw^2} + P(w)\Big]f = 0, \qquad \Big[\frac{d^2}{dw^2} + Q(w)\Big]g = 0.$$

Here $P(w)$ and $Q(w)$ are effective potentials. For instance, P is

$$P = \frac{(x-x_1)^2(x-x_2)^2}{(a-ix)^4}\Big(\frac{\left(a^2+x^2\right)^2}{\Delta^2} + \frac{ia\Delta'}{\Delta\left(a^2+x^2\right)} + \frac{2\Lambda x}{\sqrt{\Delta}\left(a^2+x^2\right)} - \frac{a(a+4ix)}{\left(a^2+x^2\right)^2} - \frac{\Lambda\Delta'}{2\Delta^{3/2}} - \frac{\Lambda^2}{\Delta}\Big).$$

The dependence of the absolute value of the effective potential $P(x)$ is a decreasing monotonic curve similarly to the case of Schwarzschild metric, that evidence the absence of bounded states for such systems. However, $P(x)$ is a complex-valued function, which at the exterior horizon $x \to x_2$, $P = (x_2 - ia)^2/(x_2 + ia)^2$; at the infinity $x \to \infty$, $P = 1$. It indicates the twisting character of the surrounding spacetime due to NUT-charge.

3 Summary

We may expect that the present analysis can permit us to elucidate the physical interpretation for the Newman–Unti–Tamburino metric. The question arises about possible existence of the Hawking-like radiation in this model.

Funding

This work was supported in the framework of the national project N.10.12/2021-41-13 by the National Academy of Science of the Republic of Belarus.

References

Awad A. and Elkhateeb E., 2023, Phys. Rev. D, 108, id. 064022
Chakraborty C. and Mukhopadhyay B., 2023, Eur. Phys. J. C, 83, p. 937
Chichurin A., Ovsiyuk E., and Redkov V., 2024, Romanian Reports in Physics, 76, p. 110
Galtsov D. and Kobialko K., 2017, Memoirs of the Faculty of Physics Lomonosov Moscow State University, p. 1740901
Ghasemi-Nodehi M., Chakraborty C., Yu Q., and Lu Y., 2021, Eur. Phys. J. C, 81, p. 939

MODERN ASTRONOMY: FROM THE EARLY UNIVERSE TO EXOPLANETS AND BLACK HOLES

Multiwavelength variability of the blazar Ton 599

A. Mikhailov[1], Yu. Sotnikova[1,2], M. Khabibullina[1], D. Kudryavtsev[1], V. Vlasyuk[1], A. Volvach[3], T. Mufakharov[1,2], Yu. A. Kovalev[4], Yu. Yu. Kovalev[5], A. Popkov[4,6], V. Stolyarov[1,7], M. Mingaliev[1,2,8], T. Semenova[1], M. Kharinov[8], T. Andreeva[8], I. Rakhimov[8], R. Udovitskiy[1], and D. Morozova[9]

[1] SAO RAS, Nizhny Arkhyz, 369167 Russia
[2] Kazan Federal University, Kremlyovskaya 18, Kazan, 420008 Russia
[3] CrAO RAS, Nauchny, 298409 Russia
[4] ASC, LPI RAS, Profsoyuznaya 84/32, Moscow, 117997 Russia
[5] Max Planck Institute for Radio Astronomy, Auf dem Hügel 69, Bonn, 53121 Germany
[6] MIPT, Institutsky per. 9, Dolgoprudny, 141700 Russia
[7] Astrophysics Group, Cavendish Laboratory, University of Cambridge, JJ Thomson Av., Cambridge, CB3 0HE UK
[8] IAA RAS, Kutuzov emb. 10, St. Petersburg, 191187 Russia
[9] Saint Petersburg State University, Universitetskaya emb. 7/9, St. Petersburg, 199034 Russia

Abstract. We present a study of the multiwavelength variability of the blazar Ton 599 based on the radio-to--ray data covering the period of 1997-2024. The data are represented by the 1-22 GHz measurements from the SAO RAS RATAN-600 radio telescope, the 5 and 8 GHz data from the IAA RAS RT-32 telescopes, and the 37 GHz data from the RT-22 telescope of CrAO RAS. The optical measurements in the R-band were collected with the SAO RAS 1-m Zeiss-1000 and 0.5-m AS-500/2, SPbSU 0.4-m LX-200, and CrAO RAS 0.7-m AZT-8 telescopes. We also used the archive data at 230 GHz from the Submillimeter Array (SMA) and the -ray data in the 0.1-100 GeV band from the Fermi-LAT point source catalogue 4FGL-DR2. The blazar exhibits extreme variability properties with a variability index varying from 0.47 to 0.98. A characteristic feature of the light curves is the presence of double and triple flares with different spectral properties. A significant correlation ($\geq 2\sigma$) between the radio, optical, and -ray bands is found with time delays from 0 to 365 days. The L-S periodograms show the significant peaks ($> 3\sigma$) related to periods of 2.4–3.9 years, which coincides with global oscillations obtained earlier on the time scale of 1987–2010.

Keywords: galaxies: active; quasars: individual (Ton 599); radiation mechanisms: non-thermal; methods: data analysis, statistical

DOI: 10.26119/VAK2024.014

1 Introduction

The bright blazar Ton 599 at redshift $z = 0.725$ (Hewett & Wild 2010) is classified as a flat-spectrum radio quasar (FSRQ). The blazar belongs to the family of TeV sources detected with ground-based Cherenkov telescopes (Mukherjee & VERITAS Collaboration 2017). Ton 599 demonstrates a flaring activity with complex structure of flares in the γ-ray, optical, and high-frequency radio bands. This source had the strongest flares in 2017 and 2021–2023 (e.g., Prince 2019; Patel & Chitnis 2020; Manzoor et al. 2024). Quasi-periodical behaviour of the Ton 599 radio light curves in the centimeter range was reported earlier by Wang et al. (2014); Liu & Liu (2014). The investigation of the long-term light curves provides an opportunity to obtain constraints on the structure and physical conditions of the AGN central engine; the flare characteristics allow us to track dynamical processes in the central parts of AGNs. To this end, we constructed and investigated a set of multi-wavelength (MW) long-term light curves of Ton 599 from γ-ray to radio bands covering a period of several decades.

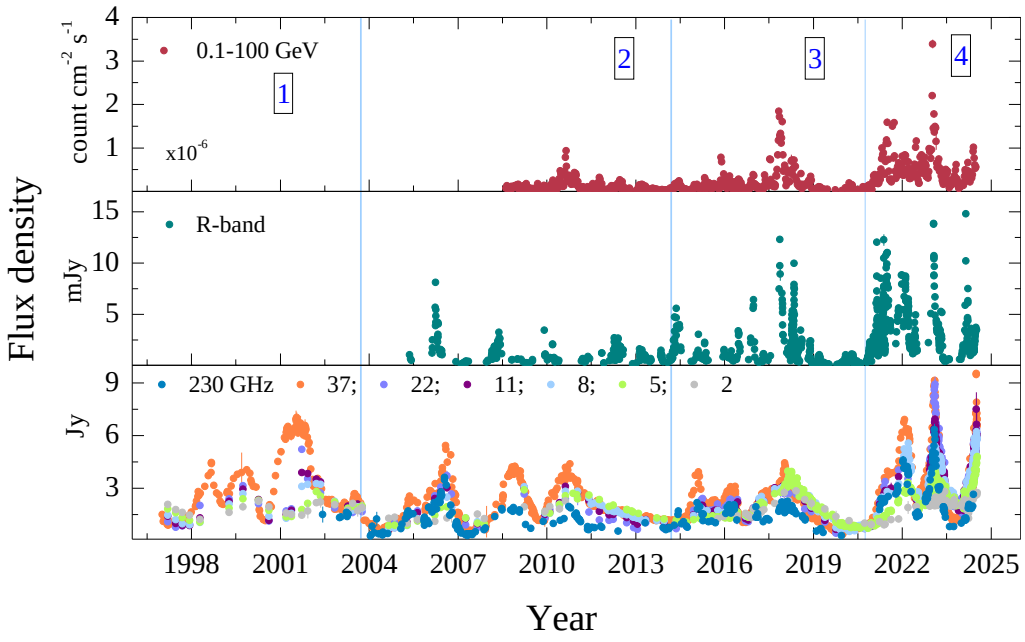

Fig. 1. Multiband light curves of Ton 599 in 1997–2024. The four epochs chosen for analysis are depicted by straight vertical lines.

2 Data

The MW light curves (Fig. 1) are constructed using the γ-ray data from Fermi-LAT in 2008–2024 (Abdollahi et al. 2023), the optical R-band measurements in 2005–2024 from the Zeiss-1000 and AS 500/2 (SAO RAS), LX-200 (SPbSU), and AZT-8 (CrAO RAS) telescopes, and the mm-band 230 GHz SMA measurements in 2002–2024[1] (SMA; Gurwell et al. 2007). The radio light curves are based on the monitoring in 1997–2024: at 37 GHz with the radio telescope RT-22 (CrAO RAS), at 1–22 GHz with RATAN-600 (SAO RAS), and at 5 and 8 GHz with the RT-32 (IAA RAS). To analyze certain flaring events, we divided the entire light curve into 4 epochs, as it is shown in Fig. 1.

3 The properties of MW variability

The blazar exhibits extreme emission variability in a wide wavelength range with a variability index V_S (Aller et al. 1992) varying from 0.47 to 0.98 on a time scale of 27 years. For example, the flux density changes from 0.4 to $\sim$9.5 Jy at 37 GHz. An interesting feature of the Ton 599 light curves is the presence of double and triple flares with different spectral properties (Fig. 1) as well as the presence of a possible periodicity of flux density at high radio frequencies of 22–230 GHz. Moreover, at 37 GHz a triple structure of active states is clearly visible over four epochs: 1997–2004, 2004–2013, 2013–2020, and 2020–2024+. The periods of the triple flares lasted 7–9 years at 37 GHz.

The variability properties were analysed using the standard methods: (i) the structure function to estimate the variation time scale, (ii) the discrete correlation function to search for correlation and time lags between the flares at different wavelengths, (iii) the Lomb–Scargle (L–S) periodogram to search for periodicities. The structure function analysis reveals variability time scales $t_{\rm var}$ = 100–1000 days within the four activity epochs. Based on these values, the upper limit of the size of emitting regions R are 1.2–12.3 pc, assuming $R \leq c \cdot t_{\rm var} \cdot \delta/(1+z)$, where c is the speed of light and $\delta = 25$ (Kang et al. 2021) is the Doppler factor.

A cross-correlation analysis between MW light curves reveals that flares at lower frequencies follow flares at higher frequencies, with different time delays during individual epochs. The time lag decreases with frequency in the range from 0 to 120 days for epoch 2, from 0 to 145 days for epoch 3, and from 0 to 60 days for epoch 4. For epoch 1 the time lags vary from 0 to 365 days for the pair of frequencies 2–37 GHz. Based on the time lags $t_{\rm lag}$, we have estimated the distance D between the

[1] http://sma1.sma.hawaii.edu/callist/callist.html

emitting regions from the expression $D = \beta \cdot c \cdot t_{\rm lag}/[(1+z) \cdot \sin\theta]$, where $\beta \approx 7.4$ is the apparent jet speed and $\theta = 4.2^\circ$ is the viewing angle (Ramakrishnan et al. 2014). We have obtained $D \leq 5$ pc for epoch 2, $D \leq 6$ pc for epoch 3, and D up to 2.5 pc for epoch 4.

To find the long-term periodicity, we used the L–S periodograms (Lomb 1976; Scargle 1982), which are widely used in astronomy for unevenly sampled time series. The L–S periodograms show significant peaks (above 3σ) related to periods of 2.4–3.9 years for all the wavelength bands, this coincides with the second and third harmonic modes (2.4 and 3.4 yrs) obtained by Wang et al. (2014) at 4.8, 8, and 14.5 GHz on the time scale of 1987–2010. These periods can be attributed to the mean distance between individual peaks in the triple flares that are seen in our radio light curves, especially at frequencies of 37 and 22 GHz. If we apply the L–S method to search for periodicities in a wider range, the resulting periods appear in the range between 5.6 and 8.3 years, which reflects the distance between these triple flares.

Funding

This study was funded by the Ministry of Science and Higher Education of the Russian Federation under contract 075-15-2022-1227.

References

Abdollahi S., Ajello M., Baldini L., et al., 2023, ApJ Supplement Series, 265, 2, id.31
Aller M., Aller H., and Hughes P., 1992, ApJ, 399, p. 16
Gurwell M., Peck A., Hostler S., et al., 2007, ASP Conf. Ser., 375, p. 234
Hewett P. and Wild V., 2010, MNRAS, 405, p. 2302
Kang S., Lee S., Hodgson J., et al., 2021, A&A, 651, id. A74
Liu B. and Liu X., 2014, Ap&SS, 352, p. 215
Lomb N., 1976, Ap&SS, 39, p. 447
Manzoor A., Shah Z., Sahayanathan S., et al., 2024, MNRAS, 529, p. 1356
Mukherjee R. and VERITAS Collaboration, 2017, The Astronomer's Telegram, 11075
Patel S. and Chitnis V., 2020, MNRAS, 492, p. 72
Prince R. 2019, ApJ, 871, id. 101
Ramakrishnan V., Leon-Tavares J., Rastorgueva-Foi E., et al., 2014, MNRAS, 445, p. 1636
Scargle J., 1982, ApJ, 263, p. 835
Wang J., An T., Baan W., and Lu X., 2014, MNRAS, 443, p. 58

MODERN ASTRONOMY:
FROM THE EARLY UNIVERSE TO EXOPLANETS AND BLACK HOLES

Spectrum of positrons produced due to interaction of gamma-ray background photons with soft background photons

A. Popov, D. Barsukov, A. Ivanchik, and S. Bobashev

Ioffe Institute, Saint-Petersburg, 194021 Russia

Abstract. The interaction of the cosmological gamma-ray background photons with soft cosmological background with producing electron-positron pairs is considered. It is shown that the majority of positrons are produced with energies of 10 Gev – 1 TeV. However, the interaction of "X-ray" cosmological background photons may produce the positrons with energies of 10–100 keV.

Keywords: cosmology: cosmic background radiation; positrons

DOI: 10.26119/VAK2024.015

1 Introduction

The cosmological background radiation (CBR) is near isotropic homogeneous radiation which fills the Universe (Hill et al. 2018). The various components of background radiation have various origin. The main component of CBR is the microwave background radiation (CMB) which is a relic of the epoch of recombination which occurs in the early Universe at redshift $z \sim 10^3$ (Hill et al. 2018). The second important component of CBR is optical and infrared extragalactic background light (EBL) which mainly consists of radiation of stars (Franceschini et al. 2008; Cooray 2016). The cosmological ultraviolet background radiation (CUB) mainly consists of the light radiated by hot young stars and nebulas (Hill et al. 2018). The cosmological X-ray background radiation (CXB) is mainly produced by accretion in galactic nuclei (Ajello et al. 2008). The cosmological gamma-ray background radiation (CGB) had been mainly radiated by AGN and supernovas (Ackermann et al. 2015). The main source of perturbation of CBR photons spectrum is the scattering on intracluster gas (Grebenev & Sunyaev 2020). In addition to the scattering on intracluster gas, CRB photons may also interact with each other producing electron-positron pairs (Gould & Schreder 1967) which also may give a small input into its spectra perturbation. Moreover, it is possible that the produced positrons may give some input into annihilation line (Nizamov & Pshirkov 2023).

2 Model

In this paper we consider the interaction of two photons with electron-positron pair production. The positron production spectra is calculated in the same way as in Popov et al. (2023). We consider only the interaction of CGB photons with EBL, CUB and CXB photons. Also, we consider the interaction of CXB photons with each other. We use the simplified model and assume that spectra profiles do not depend on redshift z and coincide with profile of corresponding spectra observed at $z = 0$. The CGB spectrum is taken from Ackermann et al. (2015), CXB and EBL spectra are taken from Ajello et al. (2008) and from Franceschini et al. (2008) correspondingly. In case of CUB spectrum we use the upper limit of CUB photon density taken from Hill et al. (2018). We assume that photon density depends on z and is proportional to star formation rate (SFR) at this redshift. To calculate the SFR we use its approximation, taken from Behroozi et al. (2013):

$$S(z) = \frac{C}{10^{A\,(z-z_0)} + 10^{B\,(z-z_0)}}, \tag{1}$$

where $S(z)$ is SFR at redshift z, $z_0 = 1.243$, $A = -0.997$, $B = 0.248$ and $C = 0.180\,M_\odot\,\mathrm{year}^{-1}\,\mathrm{Mpc}^{-3}$ in comoving frame (Behroozi et al. 2013). The used spectra

at $z = 0$ are shown in Fig. 1. The power law extrapolation of CXB spectrum upto CUB and CGB spectra is shown by dashed lines.

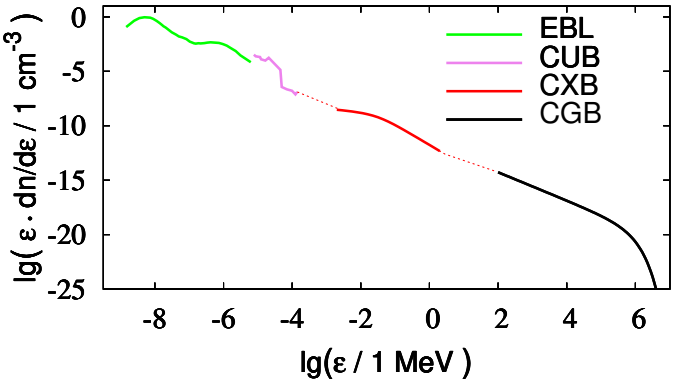

Fig. 1. The used spectra of background radiation are shown. The ε is photon energy in MeV and $\frac{dn}{d\varepsilon}$ is photons number per 1 cm^3 in 1 MeV energy interval.

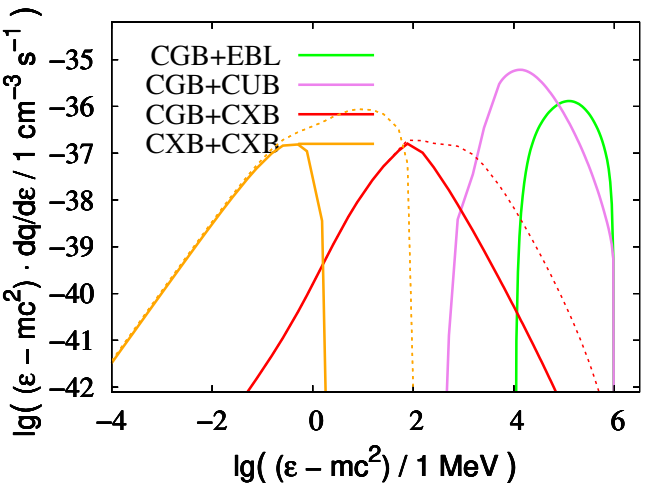

Fig. 2. The calculated positrons spectrum at $z = 1.5$ is shown. The ε is positron energy in MeV, mc^2 is positron rest energy in MeV and the $\frac{dq}{d\varepsilon}$ is positron production rate in units $1\mathrm{cm}^{-3}\,1\mathrm{s}^{-1}\,1\mathrm{MeV}^{-1}$.

3 Results

The calculated positron spectrum at $z = 1.5$ is shown in Fig. 2. Dashed lines correspond to extrapolated CXB spectra. Majority of positrons are produced with energies of 10 Gev – 1 TeV. Such positrons almost do not annihilate due to the interaction with intracluster gas and slowly accumulate in space between galaxies (Nizamov & Pshirkov 2024). However, the interaction CXB photons with itself may produce the positrons with small energies of $10 - 100$ keV. Life time of such positrons may be estimated as $(1 - 3) \cdot 10^9$ years, so it may give input into annihilation line (Nizamov & Pshirkov 2023).

References

Ackermann M., Ajello M., Albert A., et al., 2015, Astrophysical Journal, 799, id. 86
Ajello M., Greiner J., Sato G., et al., 2008, Astrophysical Journal, 689, p. 666
Behroozi P., Wechsler R., and Conroy C., 2013, Astrophysical Journal, 770, id. 57
Cooray A., 2016, Royal Society Open Science, 3, p. 150555
Franceschini A., Rodighiero G., and Vaccari M., 2008, Astronomy and Astrophysics, 487, p. 837
Gould R. and Schreder G., 1967, Physical Review, 155, p. 1408
Grebenev S. and Sunyaev R., 2020, Astronomy Letters, 45, p. 791
Hill R., Masui K., and Scott D., 2018, Applied Spectroscopy, 72, p. 663
Nizamov B. and Pshirkov M., 2023, Astronomy Letters, 49, p. 9
Nizamov B. and Pshirkov M., 2024, Astronomy Letters, 50, p. 186
Popov A., Barsukov D., Ivanchik A., and Bobashev S., 2023, Technical Physics, 68, p. 1619

BAK 2024 MODERN ASTRONOMY: FROM THE EARLY UNIVERSE TO EXOPLANETS AND BLACK HOLES 300 years Russian Academy of Sciences

The flaring activity of microquasars is the key to understanding the processes of accretion and generation of jet emission

S. Trushkin[1,2], A. Shevchenko[1], N. Bursov[1], N. Nizhelskij[1], and P. Tsybulev[1]

[1] Special Astrophysical Observatory of the Russian Academy of Sciences, Nizhny Arkhyz, 369167 Russia
[2] Kazan Federal University, 18 Kremlyovskaya St, Kazan, 420008 Russia

Abstract. We present a study of the flaring radio variability of four microquasars during last ten years with RATAN-600. The main aim of researches is a study of the daily light curves at seven frequencies of 1.2–30 GHz and in multi-azimuthal (MA) mode, when for 5h the fluxes are measured every 5–10 minutes at 4.7 and 8.2 GHz. In SS 433 dozens of bright flares were detected over last ten years. The brightest flare (5.5 Jy at 2.3 GHz) in the total history of GRS 1915+105 research occured in August 2023. In 2024 we have detected five giant radio flares in Cyg X-3 during hypersoft-to-hard X-ray states transits. These flares reached fluxes of 13–18 Jy and have similar properties: optically thick phase in the spectra in the beginning of a flare and the exponential fading for 5–30 days. We relate these events with an efficient formation of relativistic jets during the accretion of matter from a normal star. In the Gamma-ray binary LSI+61d303 with regular flares every 26.5 days, we have detected second period of 26.93 days that can be precession period of jets. We find a clear similarity of bright flares in microquasars.

Keywords: X-rays: binaries; radio continuum: stars; radiation mechanisms: non-thermal, synchronton radiation

DOI: 10.26119/VAK2024.016

1 Introduction

Microquasars – X-ray binary stars with relativistic motions are a rare type of Galactic radio sources. According to the traditional scenario, variable syntrotron radiation is generated gradually as ejected blobs move along the jet, losing energy of electrons in matter from the vicinity of black holes or neutron stars under certain conditions that are not known in detail, but which are obviously related to the accretion process of matter coming from a donor star. This has been confirmed by a lot of examples of the so-called "disk-jet coupling", which manifests itself in the "hysteresis" dependence of the evolution of X-ray radiation in the HID (hardness-intensity-diagram). The radio jets are located on a line in the "soft and bright location" in HID. However, the process of jet ejection formation remains unclear, despite the fact that R. Blandford and colleagues proposed models for the transfer of matter with momentum and energy from the disk to the jet. In any case, radio flares are critical indicator of jet formation processes.

2 Observations

Observations of the sample were conducted with the RATAN-600 radio telescope during 2011–2024 at frequencies of 1.24, 2.3, 4.7, 8.2, 11.2, 21.7 and 30 GHz simultaneously. These receivers are equipped with the modern HEMT amplifiers and can measure fluxes of cosmic sources at the level of 5–30 mJy in the conditions without interference. The flux densities were measured with a typical error of about 3–5 % at 4.7–11.2 GHz and 5–10 % at 1.2, 2.3, 21.7, 30 GHz. Observations of the standard calibrators: 3C 48, 3C 138, 3C 161, 3C 286, NGC 7027, DR 21, from the commonly accepted radio scales (Baars+ 1977 and Ott+ 1994) are included in all astronomical programs. Observations are carried out with the Northern sector and with the Southern sector paired with the Flat mirror of telescope in the mode of transit of sources through fixed antenna beams. Thus we obtain the daily points of measured fluxes at different frequencies. Also we use multi-azimuthal mode, when during ±2.5 hours from culmination time of sources we can take up to 63 measurements of the fluxes at frequencies 4.7 and 8.2 GHz (each 5–10 minuts), receivers of which are established on the special secondary mirror cabin, capable of change of focus and azimuth of the three-mirror antenna "Southern sector + Flat mirror".

3 Long-term light curves of microquasars

3.1 SS 433

SS 433 is the well-known bright X-ray, optical binary having the precessing jets, visible in X-rays, and on the VLA and VLBI maps. In the Fig. 1 (left) we plotted the total light curves at three frequencies during 13 years. In the Fig. 1 (right) the example of the recent bright flare is shown with exponential fading of the flare. The flares are usually optically thin in the range of 1–21 GHz.

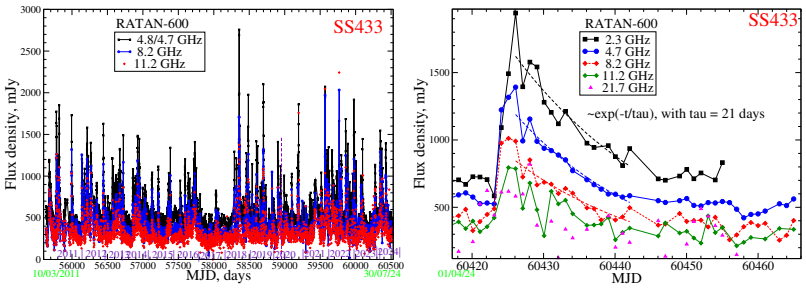

Fig. 1. *Left:* The light curves of the SS 433 at different frequencies in 2011–2024. *Right:* The light curves of the SS 433 at different frequencies in 2024.

3.2 Cyg X-3

Cyg X-3 is the famous flaring source, the X-ray and Gamma-ray binary, consisting of the Wolf–Rayet star and low mass black hole. It contains the relativistic jets that

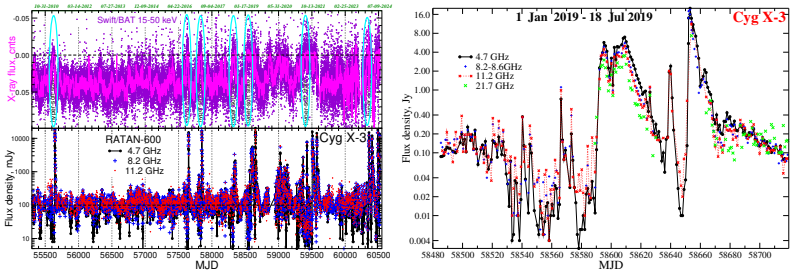

Fig. 2. *Left:* The light curves of the Cyg X-3 measured with RATAN-600 at 4.7, 8.2 and 11.2 GHz and X-ray ones with Swift/BAT at 15–50 keV in 2010–2024. *Right:* The RATAN radio light curves of the Cyg X-3 at 4.7–21.7 GHz in 2019.

were detected with VLBI mapping. These jets are as a rule one-side during the flares, but in a quiet state images could be double-side. Thus radio images are exposed to boosting according to the Doppler effect along the line of sight. In the Fig. 2 (Left) the light curves of the Cyg X-3 are shown for radio range (RATAN) and for X-ray band of the Swift/BAT at 15–50 keV. Obviously the hypersoft-to-hard X-ray states transit, marked by the blue ellipses, coincided with the giant radio flaring events. In the Fig. 2 (right) we show the characteristic light curves of some flaring events together with X-ray (Swift) and gamma-ray (Fermi) light curves. In the Fig. 3 we show the radio flaring light curves and the gamma-ray curves (Fermi 0.1–300 GeV) in 2024. Obviously high energy Gamma-ray emission correlated with radio flares.

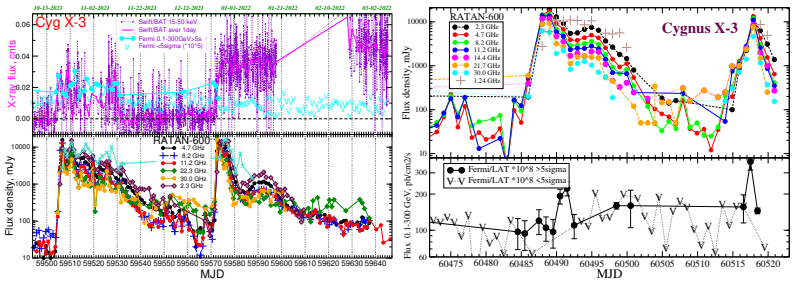

Fig. 3. *Left*: The radio light curves of the Cyg X-3 measured with RATAN-600 at 4.7–21.7 GHz in 2021. *Right*: The same in 2024 together with Fermi data.

3.3 GRS 1915+105

In the giant flare of GRS 1915+105, the peak flux reached 5.5 Jy at 2.3 GHz, which is 3–4 times higher than ever before. We followed up this flare between August 1–9, 2023 at 4.7 GHz and 8.2 GHz in the daily MA-mode observations (Fig. 4), when fluxes were measured every 8.6 minutes within interval of ± 2.5 hours from the local culmination time. In the synchrotron optically thin radio spectrum, the spectral index changed smoothly from +0.15 to −0.95 from August 1 to August 9, and within the interval of MA observations, the spectra (4.7–8.2 GHz) also changed noticeably. In the MA observations fluxes were changed with periods ranging from 30 to 300 minutes. Moreover, in eight MA measurements, QPOs less than 10 % of the average flux were detected on time scales of about 30 minutes at both frequencies. We related the flare activity of GRS 1915+105 with a more efficient formation of relativistic jet emissions during the accretion of matter from a normal star. We find a clear similarity of the flare events in GRS 1915+105 with five giant flares in Cyg X-3 microquasars in 2024.

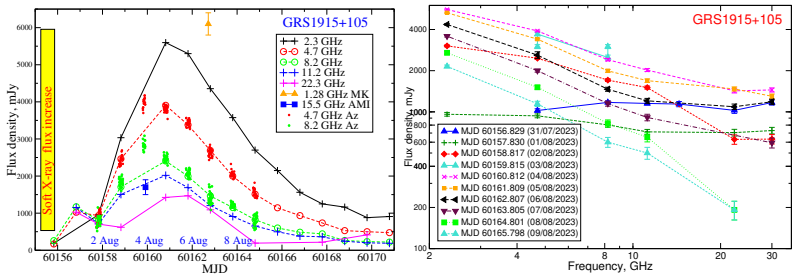

Fig. 4. *Left*:The radio light curves of the giant flare of GRS 1915+105 in 2023. *Right*: Evolution of spectra during this flare.

The brightness of the flares increased linearly with time, and their decay went exponentially ($e^{-t/\tau}$), where the parameter τ slowly changed from 4.3 to 2.7 days with the increase of frequency from 2.3 to 30 GHz. The optically thin spectrum index changed in the range from -0.7 to -0.4. In the second outburst, the exponential law was generally maintained, but the τ at the beginning of the fading was noticeably higher than later.

3.4 LSI+61d303

The X-ray binary LSI+61d303 with detected radio pulsar as a relativistic component lies apart from the main sample of microquasars, although it is the single Galactic radio source showing the clear flaring (orbital) periodicity. The nature of these flares remains the subject of intense debate, and it cannot yet be firmly established that renewable jets are in action. Based on the data we have obtained, we confirm that there are two characteristic periods of 26.49 days (orbital) and 26.93 days in the light curves, which speaks rather in favor of jets. Last one could be the precession period of the expected jets. Thus, the detected super-orbital (SO) period of 1660 days could be explained by usual beating of the close frequencies. Indeed, we can clearly see the modulation of the flares by SO-period in Fig. 5 (Left). The repeated flares in 2022 of LSI+61d303 are well visible in Fig. 5 (Right), where the orbit phase 0.6 are marked by triangles.

4 Discussion

We have studied the variability of the four microquasars during long-term period and found a lot of special properties of the radio emission together with optical and X-ray bands (see for details, Trushkin et al. 2021–2024; Cherepashchuk et al. 2022; Medvedev et al. 2022; Broderick et al. 2021; Egron et al. 2021; Trushkin et al.

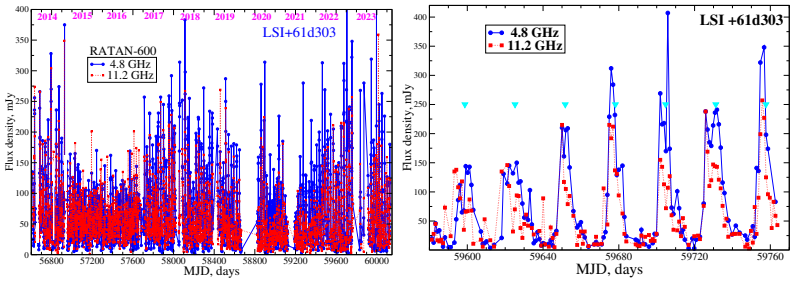

Fig. 5. *Left*: The radio light curves of the LSI+61d303 measured with RATAN-600 at 4.7 and 11.2 GHz during 2013–2023. *Right*: The radio light curves of the LSI+61d303 measured with RATAN-600 at 4.7 and 11.2 GHz during 2022.

2023; Veledina et al. 2023, 2024). Numerous examples of the detected flares from the microquasars give us a list of the main properties of radio emission: the synchrotron spectrum, often having one index from 2 GHz to 200 GHz, optically thick firstly, and optically thin after the maximum, while spectra become steeper; the increase of flux is linear in time; flares fade follows an exponential law; the flares in BH binaries are random in nature, but are definitely related to the X-ray states of them, started after hyper-soft X-ray state. Any model should take into account these properties of flares. Soon, we will discuss the finite jet segment model in application of Cyg X-3 (Marti et al. 1992) and the hollow conical jet emission model for SS 433 (Hjellming & Johnston 1988).

Funding

This work was supported in the framework of the national project “Science” by the Ministry of Science and Higher Education of the Russian Federation under the contract 075-15-2022-1227.

References

Broderick J., Russell T., Fender R., et al., 2021, MNRAS, 504, p. 1482
Cherepashchuk A., Dodin A., Postnov K., et al., 2022, Astronomy Reports, 66, p. 451
Egron E., Pellizzoni A., Righini S., et al., 2021, Astrophysical Journal, 906, id. 10
Hjellming R. and Johnston K., 1988, Astrophysical Journal, 328, p. 600
Marti J., Paredes J., and Estalella R., 1992, Astronomy and Astrophysics, 258, p. 309
Medvedev P., Khabibullin I., Semena A., et al., 2022, Astronomy Letters, 48, p. 389
Trushkin S., Bursov N., Shevchenko A., et al., 2021–2024, The Astronomer’s Telegram, #14821, #15142, #15671, #15709, #15964, #15974, #16168, #16289, #16581
Trushkin S., Shevchenko A., Bursov N., et al., 2023, Astrophysical Bulletin, 78, p. 225
Veledina A., Muleri F., Dovčiak M., et al., 2023, Astrophysical Journal, 958, p. L16
Veledina A., Muleri F., Poutanen J., et al., 2024, Nature Astronomy, 8, p. 1031

MODERN ASTRONOMY: FROM THE EARLY UNIVERSE TO EXOPLANETS AND BLACK HOLES

Multi-band variability of the blazar AO 0235+164

V. Vlasyuk[1], Yu. Sotnikova[1,2], A. Volvach[3], T. Mufakharov[1,2], Yu. A. Kovalev[4,5], O. Spiridonova[1], M. Khabibullina[1], Yu. Yu. Kovalev[6], A. Mikhailov[1], V. Stolyarov[1,7], D. Kudryavtsev[1], M. Mingaliev[1,2,8], T. Semenova[1], A. Kudryashova[1], N. Bursov[1], S. Trushkin[1], A. Popkov[9,4], A. Erkenov[1], I. Rakhimov[8], M. Kharinov[8], M. Gurwell[10], P. Tsybulev[1], A. Moskvitin[1], T. Fatkhullin[1], E. Emelianov[1], A. Arshinova[11], K. Iuzhanina[1,2], T. Andreeva[8], and L. Volvach[3]

[1] SAO RAS, Nizhny Arkhyz, 369167 Russia
[2] Kazan Federal University, 18 Kremlyovskaya St, Kazan, 420008 Russia
[3] Crimean Astrophysical Observatory of the RAS, Nauchny, 298409 Russia
[4] Astro Space Center, Lebedev Physical Institute of RAS, Moscow, 117997 Russia
[5] Institute for Nuclear Research of RAS, 60th October Anniv.Prosp. 7a, Moscow, 117312 Russia
[6] Max Planck Institute for Radio Astronomy, Auf dem Hugel 69, Bonn, 53121 Germany
[7] Astrophysics Group, University of Cambridge, Cambridge, CB3 0HE UK
[8] Institute of Applied Astronomy of RAS, Kutuzova Emb. 10, St. Petersburg, 191187 Russia
[9] Moscow Institute of Physics and Technology, Institutsky per. 9, Dolgoprudny, 141700 Russia
[10] Center for Astrophysics, Harvard & Smithsonian, 60 Garden Str., Cambridge, MA 02138 USA
[11] St. Petersburg State University, 7/9 Universitetskaya Emb., St Petersburg, 199034 Russia

Abstract. We present a study of the multiwavelength (MW) variability of the blazar AO 0235+164 based on the radio-to-γ-ray data covering a period from 1997 to 2023. The radio data are represented by the measurements from the SAO RAS, IAA RAS, and CrAO RAS telescopes. The optical measurements were collected with the SAO RAS 1-m and 0.5-m reflectors. The archive data at 230 GHz from the Submillimeter Array and the γ-ray data from the Fermi-LAT mission were used too. A significant correlation between different spectral bands is found with time delays up to 1.7 years. The relation between time delay and frequency is well described by a linear law. The revealed features of MW variability for the quiet period and for flaring states suggest that the mechanisms dominating the radio–γ-ray variations are not substantially different. AO 0235+164 shows a total variability period of ∼6 years for all wavelength bands, and 1.4–2.3 years during the low state, which may reflect its general properties.

Keywords: galaxies: active; BL Lacertae objects: individual (AO 0235+164)

DOI: 10.26119/VAK2024.017

1 Introduction

Blazars are a specific type of active galactic nuclei (AGN) known for their relativistic jets aligned with the observer's line of sight, which causes the radiation to be highly Doppler boosted (Urry & Padovani 1995). Blazars include two types of AGN: BL Lacertae objects (BL Lacs) and Flat Spectrum Radio Quasars (FSRQs). BL Lacs display a continuous, featureless emission or weak narrow emission lines in their optical/UV spectra, while FSRQs exhibit prominent broad emission lines. The fluxes over various ranges, polarization, and spectra of blazars are strongly variable from radio to γ-rays on different time-scales, ranging from minutes to several decades (e.g., Miller et al. 1989; Gupta et al. 2004 and references therein). The jet, presumably originating from accretion onto a supermassive rotating black hole (SMBH) surrounded by an accretion disk, contains relativistic electrons, which produce soft photons from radio up to UV (or even soft X-rays) through synchrotron emission and high-energy photons up to GeV and TeV energies.

One of the effective ways to understand relativistic jet emission is studying the changes in the blazar physical properties that cause the observed multiwavelength (MW) light-curve variations (e.g., Krishna Mohana et al. 2024).

The BL Lac blazar AO 0235+164 at $z = 0.94$ (Cohen et al. 1987) is a good candidate for a MW study of variability processes in AGNs, exhibiting extreme variability of non-thermal radiation across all EM spectrum at time-scales from less than tens of minutes to several years (Volvach et al. 2015; Fan et al. 2017 and references therein). The Very Long Based Interferometric observations indicate on extreme compactness of blazar nuclei on submilliarcsecond scales with superluminal apparent speeds and on a broad projected jet opening angle (Jorstad et al. 2017; Kutkin et al. 2018).

For AO 0235+164 the quasi-periodic oscillations (QPO) at 3–6 year time-scale on base of data taken between 1975–2000 in the radio and optical light curves were found by Raiteri et al. (2001). Roy et al. (2022) present a comprehensive analysis of a long-term optical light curve from 1982 to 2019, revealing a periodicity of $\sim$8 years. The five major flares were followed by minor flares roughly after ~ 2 years. This double-peaked periodicity is consistent with the hypothesis of a binary supermassive black hole system, proposed by Volvach et al. (2015).

One of the main goals of this study is checking of QPO presence in MW emission of AO 0235+164—from γ-rays to centimeter radio range on maximal time interval.

2 Observations of AO 0235+164

We have collected MW datasets from three Russian radio telescopes: RATAN-600 (SAO RAS), RT-32 (IAA RAS), RT-22 (CrAO RAS) and 1-meter Zeiss-1000 and

0.5-m AS-500/2 optical reflectors of SAO RAS. Part of the data are from public archives, and most recent results are published for the first time.

At 230 GHz (1.3 mm) we utilized measurements from the Submillimeter Array[1], obtained in the period from October 2002 to December 2023. We have made use of the γ-ray light curves available in the Fermi Large Area Telescope (Fermi-LAT) public Light Curve Repository (LCR)[2]. We adopted the 7-day binned light curves for γ-rays with energies between 100 MeV and 100 GeV to have more evenly-sampled time series with higher time cadence in the period from August 2008 to end of 2023.

2.1 Radio data

Flux densities for AO 0235+164 at 1–22 GHz were obtained with the RATAN-600 radio telescope in 1997–2023. Broad-band radio spectra at six frequencies from 1 to 22 GHz were measured within 3–5 minutes. The flux densities were measured with a standard error of about 10–30%. The descriptions of the RATAN-600 antenna, its radiometers, and data reduction are given by Sotnikova (2020).

Flux densities of blazar radio emission at frequencies of 4.8 and 8.6 GHz were measured at several observing epochs using three RT-32 radio telescopes of IAA RAS: Svetloe, Zelenchukskaya and Badary (Shuygina et al. 2019). All the antennas and receivers have similar parameters: bandwidth = 900 MHz for both ranges; beam width at half-power level $7'$ and $3.'9$, respectively; flux density limit — about 20 mJy per scan with a time constant of 1 s for both frequencies. Observations were performed in the elevation or azimuth drift scan mode.

The data on the flux densities at the 36.8 GHz frequency for AO 0235+164 were obtained with the 22-metre RT-22 radio telescope (CrAO RAS). The beam-modulated receivers were used to acquire the data. Observations of the blazar consisted of 5–20 measurements to achieve a required signal-to-noise ratio. Details of the observations and data reduction are presented in Volvach et al. (2023). The period of observations with the RT-22 spans the time interval since February 2002 till October 2023.

2.2 Optical measurements

The optical study (mainly in the R-band) was carried out with the 1-metre Zeiss-1000 (August 2002—December 2023) and 0.5-metre AS-500/2 (January 2021—December 2023) optical reflectors of SAO RAS.

[1] http://sma1.sma.hawaii.edu/callist/callist.html
[2] https://fermi.gsfc.nasa.gov/ssc/data/access/lat/LightCurveRepository/about.html

The main observations with the optical telescope Zeiss-1000 were conducted with CCD photometer in the Cassegrain focus, equipped with a 2048 × 2048 px back-illuminated E2V chip CCD 42-40. Details of the instrumental setup are described in our paper Vlasyuk et al. (2023). The main characteristics of the instrumental complex of an AS-500/2 reflector are presented in Valyavin et al. (2022). In order to improve the system parameters we installed in July 2023 a smaller but more sensitive detector: the back-illuminated electron-multiplying CCD camera Andor IXon^{EM}+897.

The typical integration time for observations of the blazar was 300 s for Zeiss-1000 and 120 s for AS-500/2 (or 30 s for the period of high intensity of the object for better time cadence). The optical data are collected from 568 observing nights spanning between August 2002 and December 2023.

3 MW light curves

Figure 1 shows the MW light curves of AO 0235+164 collected from March 1997 to December 2023.

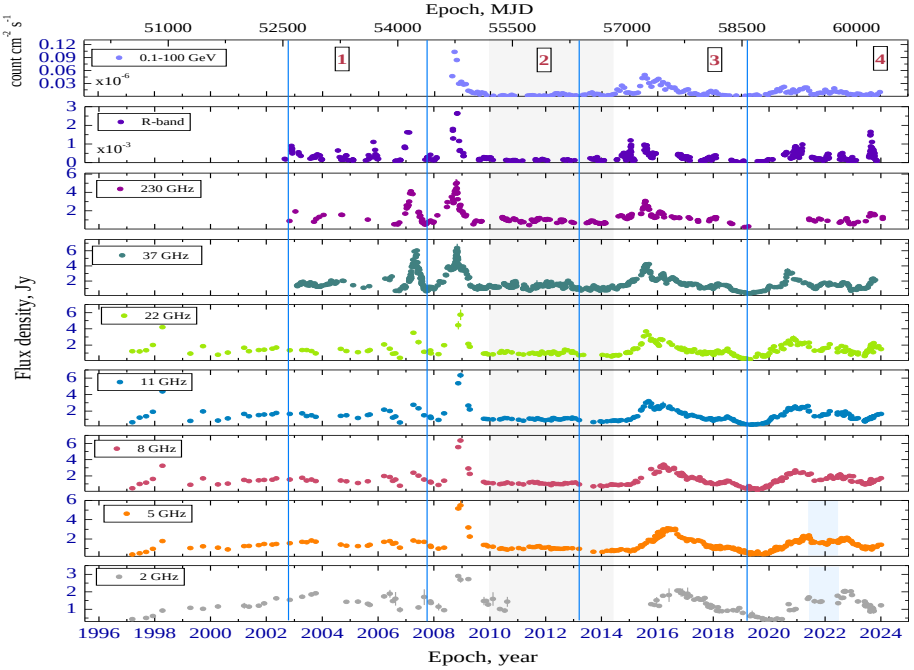

Fig. 1. Multiband light curves of AO 0235+164 in 1997–2023: radio data at 230, 37, 22, 11, 8, 5, 2 GHz, optical data (R-band) and γ-rays (from bottom to top).

The most complete light curves covering this period are those at radio frequencies of 5–22 GHz. The data for 37 GHz, 230 GHz, and the R-band span a shorter interval: between 2002 and 2023. The low-frequency radio curve at 2 GHz contains extended gaps due to strong radio interference.

The light curves show continuous flux density variations with four prominent flares at the epochs near 2006, 2008, 2015 and 2020, respectively. Most of them are well modeled by exponential laws with common maximum. During the years 2009–2014, AO 0235+164 has been showing quiescent broadband behaviour with a remarkable feature: very low activity lasting over 4.5 years.

4 Studies of AO 0235+164 MW properties

To analyze properties of multi-wavelength variability we apply some statistical instruments, which are well adapted for search specific features. There are: calculation of a fractional variability, structure functions method, pairwise cross-correlation method, the Lomb–Scargle method of periodicity searches. Application of these method both to total time interval and to individual epochs allow us to make the following conclusions about variability features of AO 0235+164:

1. The pairwise cross-correlation analysis of light curves has shown that time lag decreases with frequency in the range from 0 to 450 days. The relation between lag and frequency is described by a linear fit with a negative slope of -10 day GHz^{-1} for the pairs of most radio frequencies versus high-energy emission.
2. A smooth decrease of variability time-scale from radio waves to γ-rays is observed for all the epochs, as it follows from structure function analysis. During the low state, the variability time-scale practically does not vary with frequency, suggesting a similar size of the non-thermal emission region for all the bands.
3. For four years of low activity in 2009–2014, we have measured clear variability throughout the electromagnetic spectrum. The highest flux density variations occurred in the R-band and γ-rays. This variability might be caused by interaction between the remnants of the shocks followed from major outbursts.
4. The Lomb–Scargle periodogram method reveals significant peaks with close values, near 6 years, for all the wavelengths (see, for example, periodogram for optical light curve Fig. 2, left). For the low state in 2009–2014, a shorter period of ~ 2 years was revealed (see periodogram at Fig. 2, right).

The quasi-period of 6 years reflects the time between the most prominent outbursts in the light curves. These flares have probably a stochastic nature, and the detected quasi-periodicity does not have tight connection with the characteristics of the active nucleus and relativistic jet. On the other side, we suppose that the periodicity found for the low state reflects general AGN properties.

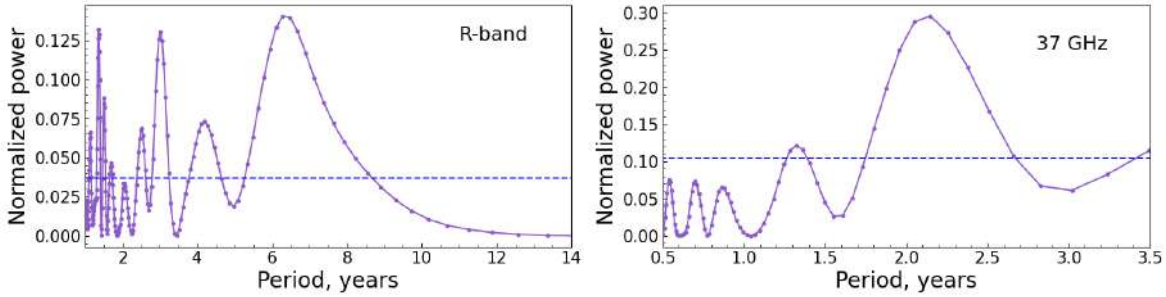

Fig. 2. The L–S periodograms for the total flux variations in the optical R-band (left) and for total flux variations at 37 GHz during the low activity state in 2009–2014. The most significant peaks correspond to components with periods of 6.4±0.1 and 2.1±0.1 years, respectively. The dashed lines show the FAP = 1 per cent (false alarm probability) level accordind to Baluev (2008).

Funding

Observations with the SAO RAS telescopes are supported by the Ministry of Science and Higher Education of the Russian Federation.

References

Baluev R., 2008, Mon.Not.RAS, 385, p. 1279
Cohen R., Smith H., Junkkarinen V., et al., 1987, Astrophysical Journal, 318, p. 577
Fan J., Kurtanidze O., Liu Y., et al., 2017, Astrophysical Journal, 837, p. 45
Gupta A., Banerjee D., Ashok, N., et al., 2004, Astron.&Astrophys., 422, p. 505
Jorstad S., Marscher A., Morozova D., et al., 2017, Astrophysical Journal, 846, p. 98
Krishna Mohana A., Gupta A., Marscher A., et al., 2024, Mon.Not.RAS, 527, p. 6970
Kutkin A., Pashchenko I., Lisakov M., et al., 2018, Mon.Not.RAS, 475, p. 4994
Miller H., Carini M., Goodrich B., 1989, Nature, 337, p. 627
Raiteri C., Villata M., Aller H., et al., 2001, Astron.&Astrophys., 377, p. 396
Roy A., Chitnis V., Gupta A., et al., 2022, Mon.Not.RAS, 513, p. 5238
Shuygina N., Ivanov D., Ipatov A., et al., 2019, Geodesy and Geodynamics, 10, p. 150
Sotnikova Yu., 2020, Ground-Based Astronomy in Russia. 21st Century, Proc. All-Russian Conf., ed. I. Romanyuk, I. Yakunin, A. Valeev, D. Kudryavtsev, p. 32
Urry C. and Padovani P., 1995, PASP, 107, p. 803
Valyavin G., Beskin G., Valeev A. et al., 2022, Photonics, 9, p. 950
Vlasyuk V., Sotnikova Yu., Volvach A., et al., 2023, Astrophys.Bull., 78, p. 464
Volvach A., Larionov M., Volvach L., et al., 2015, Astron.Reports, 59, p. 145
Volvach A., Volvach L., Larionov M., 2023, Galaxies, 11, p. 96

BAK 2024 MODERN ASTRONOMY: FROM THE EARLY UNIVERSE TO EXOPLANETS AND BLACK HOLES 300 years Russian Academy of Sciences

Classification of jets in active galactic nuclei using machine learning

D. Zagorulia[1] and M. Lisakov[2,3]

[1] Moscow Institute of Physics and Technology, Dolgoprudny, 141701 Russia
[2] Institute of Physics, Pontifical Catholic University of Valparaíso, Casilla, Valparaíso, 4059 Chile
[3] Astro Space Center of P. N. Lebedev Physical Institute of the Russian Academy of Sciences, Moscow, 117997 Russia

Abstract. This work explores the application of machine learning techniques to classifying jetted active galactic nuclei (AGN) based on Very-Long-Baseline Interferometry (VLBI) observations at frequencies 1–90 GHz. Building upon previous work by Fanaroff and Riley, who classified relativistic jets in radio galaxies on kiloparsec scales, we extend this classification to parsec scales, closer to the central supermassive black hole. This approach enables detailed study of jet spatial structures and can help enhancing accuracy in global positioning systems. We define four morphological classes: single Gaussian source, double Gaussian source, and sources with single or double-sided jets. Synthetic models of AGN jets were generated to create a training dataset for a convolutional neural network (CNN). The CNN was trained on these synthetic data and subsequently applied to classify 130 thousand AGN jet images from the Astrogeo database. The distribution of images into designated classes, predicted by CNN, qualitatively matches the expected outcome.

Keywords: galaxies: active; quasars: general; techniques: high angular resolution; methods: machine learning

DOI: 10.26119/VAK2024.018

1 Introduction

About 10 % of all normal galaxies host an active nucleus, a bright central part that emits more radiation than the stars within it due to the accretion of matter onto a supermassive black hole. The total estimated power of an active galactic nucleus (AGN) can reach 10^{48} erg/s. About 10 % of these active nuclei eject narrowly focused ultrarelativistic streams of plasma (jets). All the energy powering these jets is generated in an incredibly compact region less than one parsec in size. The relativistic plasma ejections themselves can propagate far beyond the host galaxy, reaching up to hundreds of kiloparsecs (Blandford et al. 2019).

The kiloparsec structure of radio-loud galaxies was studied earlier by Fanaroff and Riley (Fanaroff & Riley 1974), who distinguished two classes of jetted radio sources, whose luminosity decreases with increasing distance along the jet from the central galaxy (FR-I) and whose luminosity, on the contrary, increases toward the edges of the jet (FR-II). It turned out that this difference in morphology correlates with the total luminosity of these objects.

But with the advent of Very-Long-Baseline Interferometry (VLBI), images on parsec scales appeared (Lister et al. 2018), and what is the most interesting is that the direction of jets on small and large scales do not always coincide. Parsec and kiloparsec scales are separated in both space and time. Thus the changes in the jet morphology could serve as an indication of the evolution of the intrinsic direction of the jet and possibly the accretion regime.

2 Data preparation

In the Astrogeo database[1] (Astrogeo VLBI FITS image database), more than 130 thousand interferometric measurements and images of 20 thousand AGNs have been collected, which were mainly observed for astrometry and geodesy purposes. However, image processing was performed automatically and we discovered that some images were defective. To exclude these images from the further processing, the criterion of a defective image was formulated, which consisted of two parts:

1. Mismatch between the coordinates of the map centre and the coordinates of the maximum intensity of the image;
2. Signal-to-noise ratio less than 10.

Such properties are typical in the presence of amplitude and phase calibration errors of individual telescopes, incorrect pointing or poor automatic processing. [2]

[1] http://astrogeo.org/vlbi_images

[2] This simple criterion immediately filtered out 2.3 % of images.

3 Morphological classification

3.1 Synthetic images

For image classification, convolutional neural networks (CNNs) (LeCun et al. 1989) have proven their efficiency. Due to the fact that one of the desired results is to determine the probability of the morphological classes for each image of AGN, a synthetic image dataset was developed to supervise learning of the CNN. Real images are a spatial convolution of the brightness distribution in the sky with the corresponding point spread function (PSF).

Therefore, from the filtered sample of AGN images, only those with known PSF parameters (major and minor axes, position angle) were selected. Next, clustering was performed in this parameter space using the K-MEANS (Forgy 1965; Lloyd 1982) algorithm to identify 10 characteristic values. Two of which were eventually discarded due to the fact that the major axis of the PSF was 2–3 times larger than the other clusters. The centroids of remaining clusters were used as Gaussian filters to convolve with 4 model sources. The model sources (Fig. 1, top row) included: a Gaussian source, double Gaussian source, a single- and double-sided jet sources (Gaussian with a line segment).

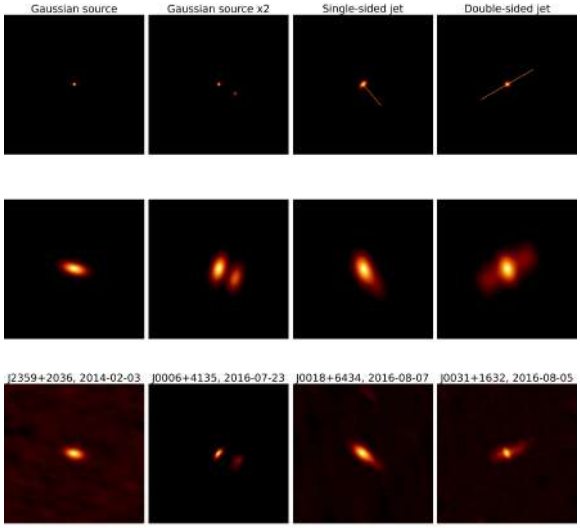

Fig. 1. Top row – model sources, middle row – model sources after convolution with PSF, bottom row – examples of real objects.

These morphological classes were chosen for their utility in both astrometry and astrophysics. In astrometric applications, Gaussian sources can improve the accuracy of global positioning systems. They also allow for the precise localization of a source behind the core, rather than being affected by the local brightening of the jet in double Gaussian objects. For astrophysical research, sources with single and double-sided jets are especially valuable. They help in studying core shifts at different frequencies and investigating the correlation between source morphology and total luminosity.

3.2 Image predictions

After training developed CNN[3], we used it for classification of 130 thousand images from Astrogeo[4]. We got the following distribution: 58.6 % – Gaussian sources, 11.5 % – double Gaussian sources, 27.5 % and 2.4 % for single- and double-sided jet sources respectively. For comparison we have manually classified a little over 500 random images and obtained the following result: 41.2 % – Gaussian sources, 11.8 % – double Gaussian sources, 42.6 % and 4.4 % for single- and double-sided jet sources.

4 Summary

We have developed a CNN model for distinguishing images of AGNs by their spatial structures and obtained predictions for Astrogeo database. Currently, we are working on improving obtained predictions.

In the near future, we plan to investigate correlation of luminosity and AGN morphology on parsec scales and morphological dependencies between VLBI images (Petrov 2016, 2021) and VLA (Very Large Array) images. For the latter, we will use data from the first two rounds of VLASS observations (Lacy et al. 2020), which are already available for public use. Developed software will be used to analyse the morphology at kiloparsec scales.

References

Blandford R., Meier D., and Readhead A., 2019, Annu. Rev. Astron. Astrophys, 57, p. 467
Fanaroff B. and Riley J., 1974, MNRAS, 167, p. 31P
Forgy E., 1965, Biometrics, 21, p. 768
Lacy M., Baum S., Chandler C., et al., 2020, PASP, 132, id. 035001
LeCun Y., Boser B., Denker J., et al., 1989, Neural Comput., 1, p. 541
Lister M., Aller M., Aller H., et al., 2018, ApJ Supp. Serires, 234, p. 12
Lloyd S., 1982, IEEE Trans. Inf. Theory, 28, p. 129
Petrov L., 2016, The 13th EVN Symposium and Users Meeting Proceedings, arXiv:1610.04951
Petrov L. 2021, AJ, 161, p. 14

[3] https://github.com/dimicorn/astrogeo_image_classifier
[4] We classified images of AGNs and different images of the same AGN could be classified differently.

VAK 2024 MODERN ASTRONOMY: FROM THE EARLY UNIVERSE TO EXOPLANETS AND BLACK HOLES 300 years Russian Academy of Sciences

The evolution of fields in the process of preheating in the early Universe

N. Arkhipova[1] and N. Fedorov[2]

[1] National Research University "Higher School of Economics", 20 Myasnitskaya str., Moscow, 101000 Russia

[2] St.Petersburg State Maritime Technical University, 3 Lotsmanskaya str., St. Petersburg, 190121 Russia

Abstract. The long-term evolution of fields on the stage of primary heating of the Universe after inflation is investigated. Preheating is the stage of evolution of the Universe at which the inflaton, after the stage of slow rolling down on inflation, begins to oscillate near the minimum of its potential energy and act as a compelling external force in the equations of motion of other fields that were in a quantum state with a relatively small amplitude on inflation. Numerical calculations of the system's dynamics for long times shows that during the early phase of preheating, the energy of the material field is due to parametric resonance it grows to the energy of the inflaton. However, after a considerable duration, when the energies of the fields become aligned and there is a multiple transfer of energy from one field to another, the energy of the material field decreases faster than the energy of the inflaton. This could suggest that parametric resonance may not be sufficient for the disintegration of the inflaton and pumping its energy into the energy of material fields.

Keywords: cosmology: dark energy, early universe, inflation

DOI: 10.26119/VAK2024.019

1 Introduction

At the moment, there are several ways to explain the presence of dark energy in cosmological models:

1. the cosmological constant Λ (Linde 2005);
2. vacuum energy is the vacuum condensate remaining after a series of phase transitions in the universe, but this value, calculated according to the laws of microphysics, turns out to be 120 orders of magnitude greater than the value following from astrophysical observations (Arkhipova & Pilipenko 2016);
3. an unknown evolving scalar field — quintessence — a scalar field different from the inflaton, the density of which was very small, but over time, due to evolution, it began to dominate (Arkhipova & Pilipenko 2016; Avsadzhanishvili et al. 2014);
4. gravity modified over long distances (Rubakov & Tinyakov 2008);
5. the relic of inflation is an undeveloped part of the inflaton field.

   In this paper, we will focus on the last point.

The theory of cosmological inflation, which leads to the exponential evolution of the scale factor, thanks to a certain scalar inflaton field, has solved many problems existing in cosmology (Linde 2005). These includes the flatness problem, the isotropy and uniformity of space and time, independence from the initial conditions, the sufficient growth of primary inhomogeneities, and the isotropy of cosmic background radiation anisotropy.

According to modern concepts, inflation occurred in the time interval from 10^{-42} s to 10^{-36} s. The condition of inflation is the condition of slow rolling, i.e. the excess of the potential energy of the field over the kinetic one, during this process the potential energy of the field decreases. At the end of inflation, the inflaton begins to oscillate near the minimum of its potential energy. And this moment, the history of the hot universe begins, as inflaton energy is pumped into material fields that are inflated in a quantum state. Particles are formed, thermalize, and the concept of temperature appears, which is quite high at this moment.

A "parametric resonance" is proposed as a possible explanation of the mechanism of this stage. There are various methods to establish the type of inflaton potential and material fields, along with the nature of their interactions, leading to a diverse range of models. The specific type of potential and interaction, as well as the method of setting initial values, is determined by the selected theory.

2 Inflation and preheating model

In this paper, we solve the problem of the numerical modeling of postinflationary heating using Lagrangian fields in the early Universe of the form $L = L_\phi + L_\chi$,

consisting of a part belonging to the inflaton ϕ and some scalar field χ, which was at the stage of inflation in a quantum state with a very small amplitude, where

$$L_\phi = \frac{1}{2}\phi_{;i}\phi^{;i} - V(\phi), \tag{1}$$

$$L_\chi = \frac{1}{2}\chi_{;i}\chi^{;i} - g^2\phi^2\chi^2, \tag{2}$$

and $g^2(\phi)^2\chi^2$ is responsible for the interaction of fields.

In this article, the potential of the ϕ field is considered as follows eq. (3):

$$V(\phi) = \frac{1}{2}m^2\phi^2. \tag{3}$$

By varying the Lagrangians eq. (1)–(2) over the fields, we derive a system of equations that describes all stages of the system's evolution:

$$\ddot{\phi} + 3H\dot{\phi} + V_{,\phi} = 0, \tag{4}$$

$$\ddot{\chi} + 3H\dot{\chi} + V_{,\chi} = 0, \tag{5}$$

$$H^2 = \frac{\ddot{a}}{a} = \frac{8\pi G}{3}(\frac{\ddot{\phi}^2}{2} + \frac{\ddot{\chi}^2}{2} + V(\phi) + V(\chi)), \tag{6}$$

where H — is the Hubble parameter.

The numerical solution of this system (3)–(6) for the evolution of field energy is shown in Fig.1.

3 Results and conclusions

Numerical calculations of the system's dynamics for a long time shows that immediately after inflation, during initial phase of preheating, the energy of the material field increases due to parametric resonance to the energy of the inflaton, and its energy is pumped into the energy of the material fields. And after quite a considerable time, the energies of the fields become aligned, and energy is pumped from one field to another and back. Then the energy of the material field decreases faster than the energy of the inflaton.

In this model, with a given fixed constant of interaction between the inflaton and the material field, the mechanism of parametric resonance does not result in the complete disintegration of the inflaton and pumping of its energy into the energy of

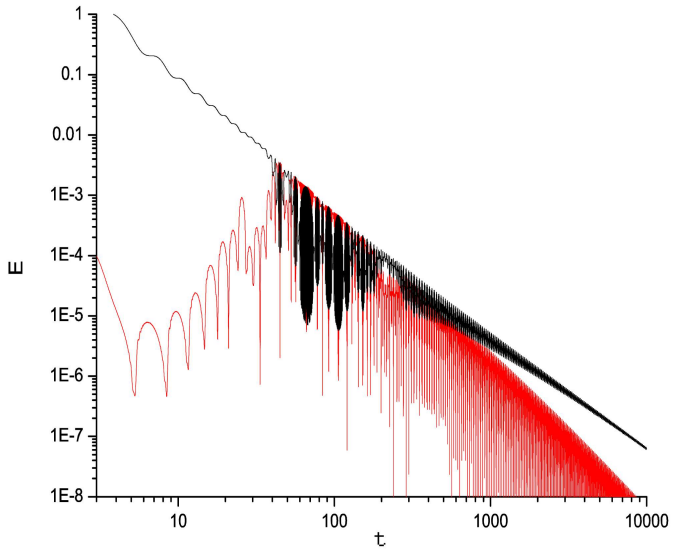

Fig. 1. The evolution of field energy in the model, $g = 100$. The black curve shows the evolution of the inflaton, and the red one shows the evolution of the energy of the material field. Time is measured in conventional units.

the material field. Moreover, the remaining energy of the inflaton tends to dominate over time, which can be interpreted as a manifestation of dark energy contributing to the repeated accelerated expansion of the Universe (Riess et al. 1998; Perlmutter et al. 1999).

In the future, there are plans to explore the impact of the interaction constant value and various types of inflaton potentials on the process of preheating.

References

Arkhipova N.A. and Pilipenko S.V., 2016, Journal of Modern Physics D, 25 (14), id. 1650109
Avsadzhanishvili O., Arkhipova N.A., Samushiya L., et al., 2014, European Physical Journal C, 74, 11, id. 3127
Linde A., 2005, Contemp.Concepts Phys., 5, 2, p. 1
Perlmutter S., Aldering G., Goldhaber G., et al., 1999, Astron. J., 517, p. 565
Riess A.G., Filippenko A.V., Challis P., et al., 1998, Astron. J., 116, p. 1009
Rubakov V.A. and Tinyakov P.G., 2008, Phys. Usp., 51, 2, p. 759

Decomposition of distant galaxies with spiral arms

I. Chugunov[1] and A. Marchuk[1,2]

[1] Pulkovo Astronomical Observatory, Russian Academy of Sciences, St. Petersburg, 196140 Russia
[2] St. Petersburg State University, St. Petersburg, 198504 Russia

Abstract. We perform the photometric decomposition, including spiral arms, of 159 galaxies at $0.1 \leq z \leq 3.3$ imaged by HST and JWST in optical and near-infrared in rest-frame. We measure various properties of spiral structure and, in particular, we confirm that pitch angles increase and azimuthal length decrease with increasing z, implying that spiral structure becomes more wound with time. We also measure band-shifting effects, or the spiral-to-total ratio and width relative to the disc exponential scale, and find that band-shifting effects can be as significant, or even stronger than, evolutionary effects. Furthermore, the spiral structure becomes more asymmetric at higher redshifts.

Keywords: galaxies: high-redshift, spiral, evolution

DOI: 10.26119/VAK2024.020

1 Introduction

The majority of luminous galaxies in the local Universe have spiral structures. Questions about the origin and evolution of spiral arms in galaxies are still unresolved, and observational evidence is needed to test various theories that aim to answer these questions. There are a significant number of studies devoted to the spiral structure in local galaxies (see discussion and references in Sellwood & Masters 2022). Spiral galaxies are still abundant at high redshifts, and the fraction of spiral galaxies is expected to remain significant at least up to $z \approx 4$, but systematic works concerned specifically with the spiral structure of distant galaxies are scarce and usually concern only a limited set of parameters.

Photometric decomposition is a powerful tool for examining the properties of galaxy components, including potentially spiral arms. The key idea of decomposition is to model the distribution of light in a galaxy as the sum of several components, each described by an analytical model. Nowadays, most decompositions ignore the spiral arms, mostly because of complex structure of these features. However, some papers do model the spiral arms. For example, the `GALFIT` photometric decomposition package (Peng et al. 2010) allows one to model various non-axisymmetric features, including spirals, with Fourier and bending modes, and this approach has been used in different works. In our previous works (Chugunov et al. 2024; Marchuk et al. 2024) we have developed our own model of spiral arms and utilized it to perform the decomposition of local galaxies, showing the viability of this method.

2 Data and methods

2.1 Images

To study spiral structure in distant galaxies, we utilize data from the COSMOS survey of HST (Koekemoer et al. 2007) and from two surveys of JWST, namely CEERS (Bagley et al. 2023) and JADES (Rieke et al. 2023). The depth and high resolution of these images allow one to observe the structure of distant galaxies, including their spiral arms, and for our further analysis we select images of galaxies with recognizable spiral structure. Our final sample consists of 159 spiral galaxies at redshifts $0.1 \leq z \leq 3.3$ in 329 individual images. Of this sample, 126 galaxies are taken from the HST COSMOS survey at $0.10 \leq z \leq 1.02$, while the JWST CEERS and JADES surveys are the source for the remaining 33 objects at $1.05 \leq z \leq 3.30$. For these 33 objects, multiwavelength data are available in several filters, and we have analyzed 203 images of them in different wavelengths. Taking into account the redshift, the rest-frame wavelengths are located from the blue to the near-infrared

parts of the spectrum. For the COSMOS sample, we used only a single near-infrared filter.

2.2 Spiral arms model

To model the 2D light distribution in spiral arms, we use a function with 21 parameters for each arm, taken from our previous work, with small, mostly technical changes (see Section 3 in Chugunov et al. 2024). The most complete description of the model and the changes from the version used in the previous work can be found at https://github.com/IVChugunov/IMFIT_spirals.

We briefly remind that our model is capable to produce each single spiral arm with different pitch angle, which can vary as 3rd degree polynomial of azimuthal angle. The distribution of light along the arm is mostly exponential with radius, since spiral arms are part of a disk, but with a truncation near the beginning and end. The distribution of light along the arm can be asymmetric, is described by the Sérsic function, and the width can be variable.

2.3 Decomposition

To perform the photometric decomposition of the images, we use the `IMFIT` package (Erwin 2015), which we have modified to implement our spiral function (available at https://github.com/IVChugunov/IMFIT_spirals). For each galaxy, we use a model with a few appropriate components, which usually including a disk and bulge, and a bar if necessary, as well as an appropriate number of spiral arms. Fig. 1 shows an example of our decomposition model.

3 Results

We have measured a large number of parameters using photometric decomposition. Tables with these results are available at https://github.com/IVChugunov/Distant_spirals_decomposition.

3.1 Dependence on lookback time

First, we will focus on the parameters of the spiral arms that depend on the redshift z or, equivalently, on the lookback time t_L. The pitch angle μ and the azimuthal length l_ψ (i.e., the angle between the beginning and end of the spiral arm with respect to the center) are the most notable of these. (Since different arms have different parameters, we consider the weighted average by luminosity over all spiral arms in a galaxy). The average value of μ over the sample is 16.0 deg, and for l_ψ it is 244 deg. The dependence

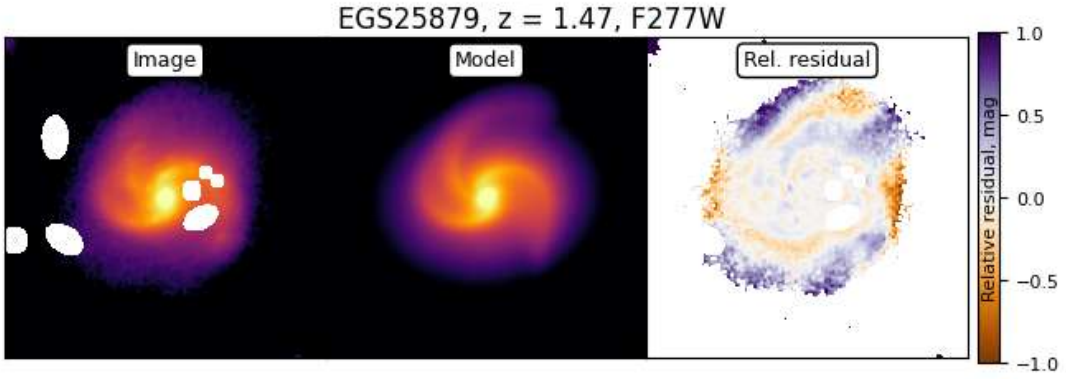

Fig. 1. Decomposition example of one of the galaxies in the sample. From left to right: image, model with spiral arms, relative residual (with a corresponding color bar on the right: pixels where the image flux is underestimated by the model are in purple, and where it is overestimated are in orange).

of these two parameters on t_L is shown in Fig. 2. The pitch angle clearly increases with t_L at a rate of 0.5 deg/Gyr, implying a decrease as we get closer to the modern epoch. Length decreases with larger t_L by 7 deg/Gyr. Taking together, these trends imply that the spiral arms have become more wound with time.

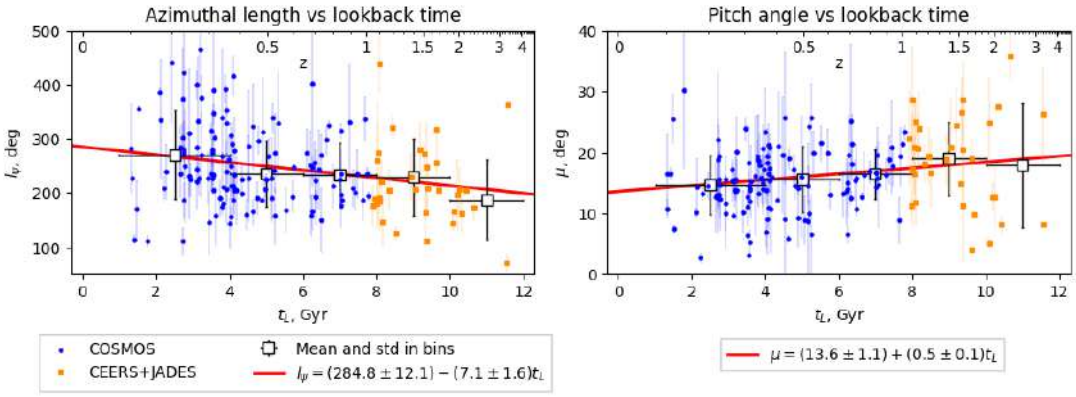

Fig. 2. Dependence of azimuthal length l_ψ (left) and pitch angle μ on lookback time t_L. The linear approximation is shown for the full sample, as well as for some subsamples.

3.2 Dependence on rest-frame wavelength

Since a fraction of the galaxies in our sample have multiwavelength data available, we can examine the dependence of different parameters of the spiral pattern on wavelength. Redshift means that images in a single filter of galaxies at different z capture the different rest-frame wavelength, and one needs to distinguish evolutionary effects from band-shifting effects. To do this, we perform a bilinear fit of several parameters as a function of the lookback time t_L and rest-frame wavelength $\lambda_{\rm rf}$, and show the results in Fig. 3. Most importantly, we observe that the relative width of the spiral arms w/h (which is the spiral arm width w normalized to the disk exponential scale h) strongly depends on $\lambda_{\rm rf}$, with w/h increasing by 0.37 per 1 μm of wavelength in the optical and near-infrared. This dependence affects the observed width even more than any evolutionary effects, and is probably related to the different

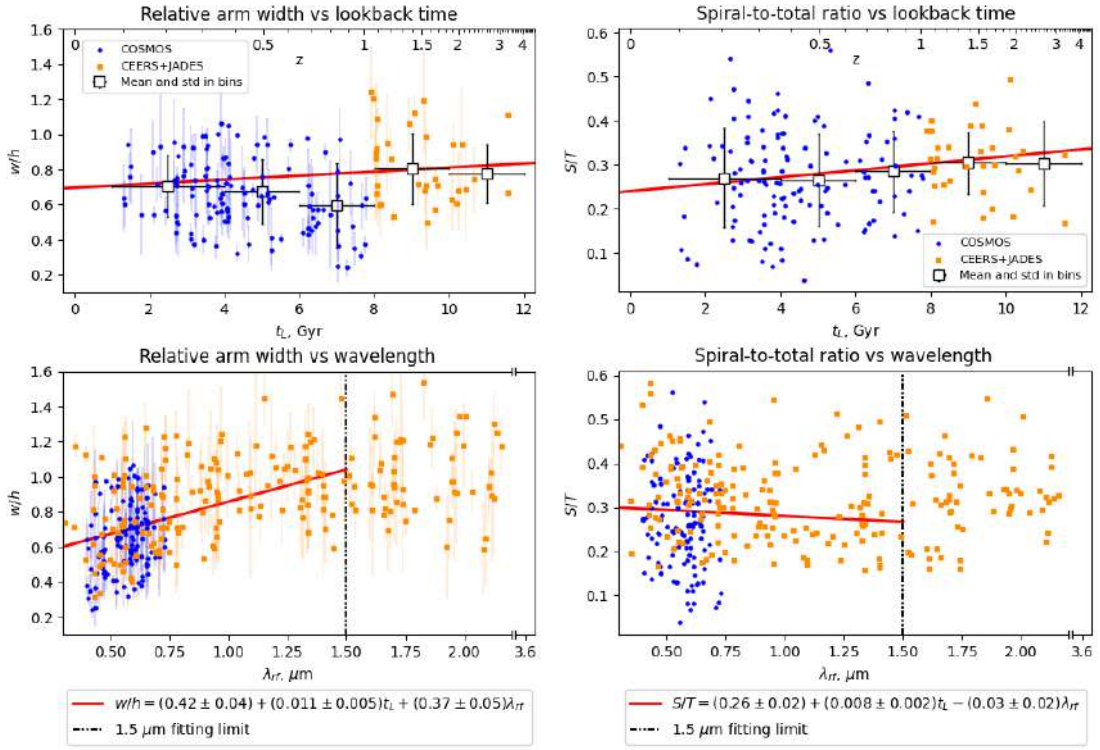

Fig. 3. Dependence of relative width w/h (left) and spiral-to-total ratio S/T (right) on lookback time t_L (top row) and rest-frame wavelength $\lambda_{\rm rf}$ (bottom row). For both parameters a bilinear fit to t_L and $\lambda_{\rm rf}$ was performed. In the bottom row, each point represents a single image, i. e. each galaxy from CEERS and JADES is marked by a few points, corresponding to different wavelengths.

distribution of stellar populations of different ages and colors in a spiral arm. For the spiral-to-total ratio S/T, band-shifting effects also take place, but they are weaker than for w/h, with S/T decreasing by 0.03 per 1 μm.

4 Summary

1. We have performed the spiral arm decomposition for the sample of 159 distant galaxies, up to $z = 3.3$.
2. We have found that the pitch angle has decreased and the azimuthal length has increased since the early times of the Universe, at rates of -0.5 deg/Gyr and 7 deg/Gyr, respectively. In other words, the spiral arms have become more wound over time.
3. We have measured the band-shifting effects for spiral arms. We observe that in some cases, namely for the spiral arm width, these effects are stronger than the evolutionary effects. For the spiral-to-total ratio, they are at least comparable to evolutionary changes.

Acknowledgements. This research is based on observations made with the NASA/ESA Hubble Space Telescope obtained from the Space Telescope Science Institute, which is operated by the Association of Universities for Research in Astronomy, Inc., under NASA contract NAS 5–26555. This work is based in part on observations made with the NASA/ESA/CSA James Webb Space Telescope. The data were obtained from the Mikulski Archive for Space Telescopes at the Space Telescope Science Institute, which is operated by the Association of Universities for Research in Astronomy, Inc., under NASA contract NAS 5–03127 for JWST.

References

Bagley M.B., Finkelstein S.L., Koekemoer A.M., et al., 2023, The Astrophysical Journal, 946, id. L12

Chugunov I.V., Marchuk A.A., Mosenkov A.V., et al., 2024, Monthly Notices of the Royal Astronomical Society, 527, p. 9605

Erwin P., 2015, The Astrophysical Journal, 799, id. 226

Koekemoer A.M., Aussel H., Calzetti D., et al., 2007, The Astrophysical Journal Supplement Series, 172, p. 196

Marchuk A.A., Chugunov I.V., Gontcharov G.A., et al., 2024, Monthly Notices of the Royal Astronomical Society, 528, p. 1276

Peng C.Y., Ho L.C., Impey C.D., et al., 2010, The Astronomical Journal, 139, p. 2097

Rieke M.J., Robertson B., Tacchella S., et al., 2023, The Astrophysical Journal Supplement Series, 269, id. 16

Sellwood J.A. and Masters K.L., 2022, Annual Review of Astronomy and Astrophysics, 60, id. 36

VAK 2024 MODERN ASTRONOMY: FROM THE EARLY UNIVERSE TO EXOPLANETS AND BLACK HOLES 300 years Russian Academy of Sciences

Is the orientation of the galaxies in the Local Supercluster related to its Plane?

P. Dolgosheeva[1] and D. Makarov[2]

[1] St. Petersburg State University, 7/9 Universitetskaya nab., St. Petersburg, 199034 Russia
[2] Special Astrophysical Observatory of the Russian Academy of Sciences, Nizhny Arkhyz, 369167 Russia

Abstract. Modern cosmological models predict a close correlation between the angular momentum orientation of galaxies relative to the large-scale structure of the Universe. In the landmark 2004 paper, based on a sample of 30 galaxies, it was shown that the direction of the rotation axes of edge-on galaxies is predominantly in the plane of the Local Supercluster, supporting the theory of galaxy angular momentum formation by tidal forces. In the last two decades, the sample of known Local Supercluster galaxies has increased 7–8 times, giving us hope to estimate the correlation more accurately. We test the orientation of edge-on galaxies with respect to the Local Supercluster plane as a function of their redshift, position, luminosity, and color. We did not find a statistically significant correlation in any of the subsamples we examined. Most likely, the correlation found in the pioneering paper is due to the extremely small statistics.

Keywords: galaxies: evolution; cosmology: large-scale structure of universe

DOI: 10.26119/VAK2024.021

1 Introduction

The tidal-torque theory, developed in the works of Peebles (1969), Doroshkevich (1970), White (1984), describes the acquisition of angular momentum (spin) by proto-galaxies in the early Universe under the influence of tidal torques. Proto-galaxies form within the gravitational potential wells of dark matter halos in the cosmic web of filaments, sheets, and voids. As these proto-galaxies collapse, they experience gravitational torques from nearby mass concentrations, such as neighboring proto-galaxies and large-scale structures. The torque exerted by the tidal field causes the proto-galaxy to spin. The direction of this angular momentum is influenced by the surrounding large-scale structures. The main prediction of tidal-torque theory is that galaxy spins should be nearly perpendicular to the minor axis of the shear tensor associated with the distribution of the surrounding matter. In other words, the spin of a galaxy must be perpendicular to the axis of greatest compression of the element of the large-scale structure to which it belongs.

In this contex, the Local Supercluster is an ideal laboratory to test this hypothesis. This nearby supercluster is one of the most studied structures in the Universe. Due to the location of our Galaxy within the Local Sheet, the Local Supercluster clearly stands out in the distribution of nearby galaxies on the sky as a narrow band with a noticeable concentration of galaxies around the center in the Virgo cluster. This fact makes easy to identify the plane of the Local Supercluster, which is determined by the great circle of the Supergalactic coordinate system. Edge-on disk galaxies allow us to reliably determine the spin direction. For arbitrarily oriented galaxies, the determination of the inclination angle is burdened with large errors and ambiguities. The use of the edge-on galaxies further simplifies the problem, reducing it to the measurement of the position angle (PA) of the galaxy's major axis in the Supergalactic coordinates. Using this approach, Navarro et al. (2004) found that the planes of nearby edge-on disk galaxies are predominantly oriented perpendicular to the plane of the Local Supercluster, which is consistent with numerical models of galaxy angular momentum formation within the Fig. 1, taken from the paper Navarro et al. (2004), shows the well-defined excess of objects with PA $< 20^\circ$ for nearby galaxies with velocities $cz < 1200$ km/s.

Thanks to massive deep photometric and redshift surveys, the sample of known Local Supercluster galaxies has increased by at least an order since work by Navarro et al. (2004), allowing us to significantly improve the statistics and study correlations more precisely. In addition, new catalogs of edge-on galaxies have recently been published. All this allows us to use the approach proposed by Navarro et al. (2004) and to test the alignment of galaxy spins with respect to the plane of the Local Supercluster at a new level.

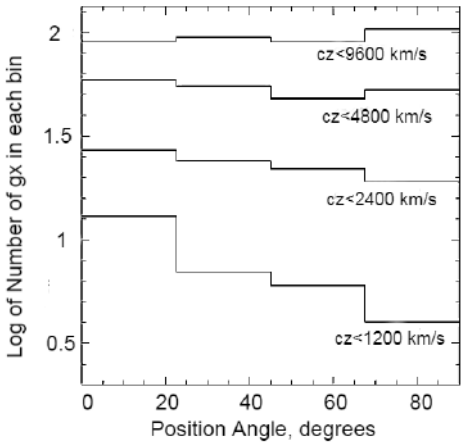

Fig. 1. Results from the article (Navarro et al. 2004).

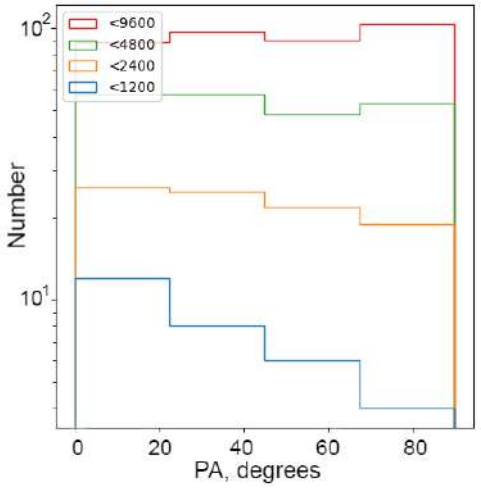

Fig. 2. Our reproduction of the results of (Navarro et al. 2004).

2 Sample

Our work is based on the catalog of 16551 Edge-on Galaxies In Pan-STARRS1 (EGIPS, Makarov et al. 2022), which is the largest list of edge-on galaxies to date. The Pan-STARRS1 survey (Pan-STARRS1, Chambers et al. 2019) covers three quarters of the sky above $\delta = -30°$. Due to the structure of the survey and the neural network used to search for galaxies, the EGIPS catalog may undercount the largest galaxies, as well as low surface brightness galaxies. To fill these gaps, we use the catalog of 5749 Edge-on Galaxies In SDSS (EGIS, Bizyaev et al. 2014). To update our sample, we manually checked all highly inclined $i > 85°$ near $cz_{\rm LG} < 4000$ km/s objects from the HyperLeda database (Makarov et al. 2014) to exclude false cases. Finally, our sample consists of 1986 edge-on galaxies, 230 of which are within $cz < 1200$ km/s, which is about 7.5 times larger than the 30 galaxies from the paper Navarro et al. (2004).

3 Analysis

We analyze the distribution of PA of the edge-on galaxies in the Supergalactic coordinates. We use the standard equations of spherical trigonometry to convert PA from the J2000.0 equatorial system to the Supergalactic one. We reduce PA to the

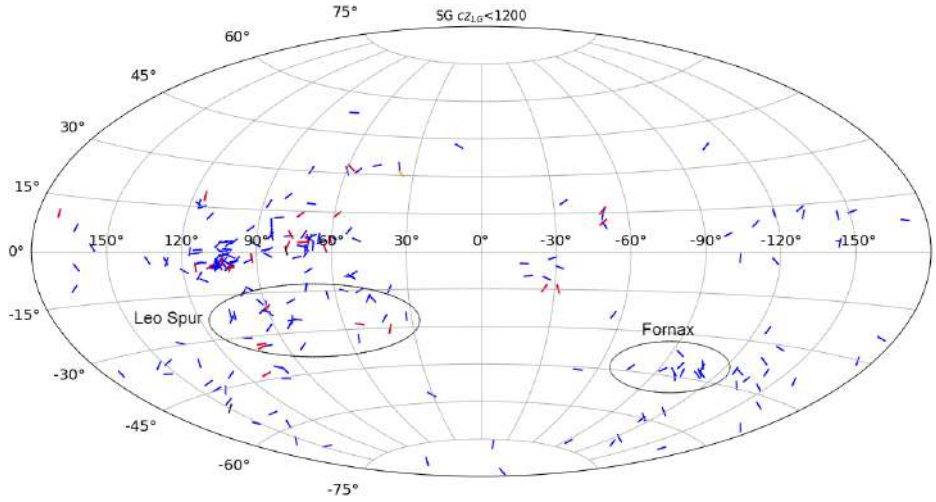

Fig. 3. Distribution of the close edge-on galaxies, $cz_{\rm LG} < 1200$ km/s in the Aitoff projection in the Supergalactic coordinates. The galaxy disk planes are indicated by dashes. The red, orange, and black dashes correspond to edge-on galaxies from the sample of Navarro et al. (2004). There are 27 reds in our sample, 1 orange falls in the range of $1200 < cz_{\rm LG} < 2500$ km/s, and 2 black are not in our samples.

range $[0°, 90°]$, since we are interested in the orientation with respect to the Local Supercluser plane, and in this sense the angles $\alpha > 90°$ and $(180° - \alpha)$ are equivalent.

First, to test our methodology, we replicated the sample from Navarro et al. (2004) as closely as possible, using the 1989 version of the Principal Galaxy Catalog (Paturel et al. 1989) and the prescription to identify spiral galaxies with an axis ratio $b/a < 0.175$ as edge-on oriented. As can be seen in Fig. 2, we can reproduce the original correlation well. The nearest galaxies, $cz < 1200$ km/s, show a well-defined tendency to be oriented perpendicular to the plane of the Local Supercluster.

The all sky distribution of the subsample of the closest, $cz_{\rm LG} < 1200$, edge-on galaxies indicating their orientations is plotted in Fig. 3. Most of the galaxies are concentrated within a 30° layer along the Local Supercluster plane. The concentration of edge-on galaxies in the Leo Spur and a near periphery of the Fornax Supercluster is also well defined. To our surprise, edge-on galaxies do not exhibit the expected prominent perpendicular orientation to the Local Supercluster plane.

The PA distribution for different subsamples of the edge-on galaxies is shown in Fig. 4. There is a clear peak at 90° in the EGIPS+EGIS subsample, but it disappears when HyperLeda galaxies are added. The main impression is that the distribution of galaxies across the PA is fairly uniform and show no statistically significant dominance in orientations.

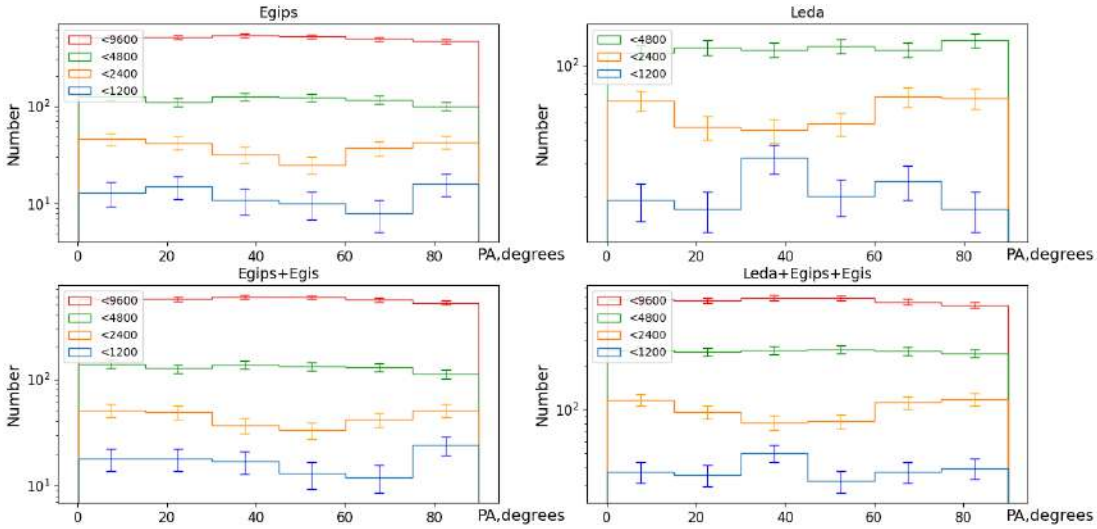

Fig. 4. PA distribution of edge-on galaxies in different subsamples at different scales.

Galaxies in the virial zone of a cluster should be randomized in their velocities, positions, and orientations. So we excluded the Virgo cluster galaxies within 6° of M 87 with velocities $cz_{\rm LG} < 3500$ km/s to cleanse the statistics from their influence. As in the previous case, the edge-on galaxies outside the virial zone show no obvious correlations or significant excess over the random distribution over PA.

We also tested different subsamples of edge-on galaxies for position, morphology, and luminosity. To identify galaxies taht belong exclusively to the Local Supercluster sheet, we considered four subsamples within $cz_{\rm LG} < 2500$ and $cz_{\rm LG} < 1200$ km/s, which lie within the ±2 and ±5 Mpc layers from the Local Supercluster plane. The virial zone of the Vigro cluster was excluded from consideration.

To account for galaxy morphology, we divide the sample into two equal parts of blue and red galaxies, and into faint and bright galaxies using the stellar mass. The $(g-i)_0$ color and the stellar mass, $\log M_*$, were taken from the 50 Mpc Galaxy Catalog (Ohlson et al. 2024).

We perform the one-sample Kolmogorov–Smirnov test under the null hypothesis that the PA are uniformly distributed. The test shows that the PA distributions of edge-on galaxies in all but one sample are not different from random at the $\alpha = 0.05$ significance level. The only exception is the case of small galaxies in the ±2 Mpc layer of $cz_{\rm LG} < 2500$ km/s, where $p-$value $= 0.036$ is a slightly smaller limit. However, this is very weak evidence given the extremely small subsample size of 45 galaxies, where the one-sample Kolmogorov–Smirnov test should be treated

with caution, and because the lack of the effect in the ±5 Mpc layer and for closer galaxies $cz_{\rm LG} < 1200$ km/s.

We checked if the small increase of perpendicular ($PA = 0°$) and parallel ($PA = 90°$) oriented galaxies in the case of the sample with $cz_{\rm LG} < 2400$ km/s (see Fig. 4) is related to galaxy morphology. However, blue and red galaxies have similar PA distributions and do not show the morphological separation.

4 Summary

We analyzed the distribution of the galaxy orientations relative to the Local Supercluster plane, following the idea proposed by Navarro et al. (2004). Our sample consists of 1986 edge-on galaxies within $cz_{\rm LG} < 4000$ km/s. The correlations were studied in different subsamples selected by redshift, the Local Supercluster sheet membership, morphological type, and stellar mass. In contrast to the work of Navarro et al. (2004), we did not find any statistically significant correlations. Testing the dependence of stellar populations on mass and color also revealed no correlations. The discovery of the correlation in the early work by Navarro et al. (2004) may be due to the extremely small sample size, only 30 galaxies. Our work represents a more complete compilation of current modern catalogs and gives the possibility to make more accurate estimates. The lack of the spin alignment predicted by theory may be due to the fact that galaxies located in the plane of the Local Supercluster are part of different filaments and are subject to complex tidal influences from the surrounding large-scale structure. Thus, although tidal force fields should lead to spin alignment, the intersections of filaments (knots) and the presence of sheets create complex time-varying gravitational fields that can lead to random orientation of spins. The interactions at these junctions can disrupt any initial alignment.

Acknowledgements. This work was supported by the Russian Science Foundation grant № 24–12–00277, https://rscf.ru/project/24-12-00277.

References

Bizyaev D.V., Kautsch S.J., Mosenkov A.V., et al., 2014, ApJ, 787, id. 24
Chambers K.C., Magnier E.A., Metcalfe N., et al., 2019, The Pan-STARRS1 Surveys
Doroshkevich A.G., 1970, Astrofizika, 6, p. 581
Makarov D., Prugniel P., Terekhova N., et al., 2014, A&A, 570, id. A13
Makarov D., Savchenko S., Mosenkov A., et al., 2022, MNRAS, 511, p. 3063
Navarro J.F., Abadi M.G., Steinmetz M., 2004, ApJ, 613, id. L41
Ohlson D., Seth A.C., Gallo E., et al., 2024, AJ, 167, id. 31
Paturel G., Fouque P., Bottinelli L., et al., 1989, A&AS, 80, p. 299
Peebles P.J.E., 1969, ApJ, 155, p. 393
White S.D.M., 1984, ApJ, 286, p. 38

MODERN ASTRONOMY: FROM THE EARLY UNIVERSE TO EXOPLANETS AND BLACK HOLES

Optical spectroscopy of host-galaxies of intermediate mass black holes: evolution of central black holes

V. Goradzhanov[1,3], I. Chilingarian[2], M. Demianenko[4], I. Katkov[5,6], K. Grishin[1,7], V. Toptun[8], E. Rubtsov[1], D. Gasymov[1], and I. Kuzmin[1,3]

[1] Sternberg Astronomical Institute, M.V.Lomonosov Moscow State University, Moscow, 119992 Russia
[2] Center for Astrophysics — Harvard and Smithsonian, Cambridge, MA 02138 United States
[3] Department of Physics, M.V. Lomonosov Moscow State University, Moscow, 119234 Russia
[4] Max-Planck-Institut für Astronomie, Heidelberg, 69117 Germany
[5] New York University Abu Dhabi, Abu Dhabi, United Arab Emirates
[6] Center for Astro, Particle, and Planetary Physics, NYU AD, Abu Dhabi, United Arab Emirates
[7] Université Paris Cité, CNRS(IN2P3), Astroparticule et Cosmologie, Paris, 75013 France
[8] European Southern Observatory, Garching bei München, 85748 Germany

Abstract. Intermediate-mass black holes (IMBHs) with masses below ($2 \times 10^5 M_\odot$) are key to understanding the origin and growth mechanisms of supermassive black holes (SMBHs) in galactic nuclei. This study focuses on the search for and detailed analysis of central lightweight black holes in various galaxies. An extended sample of IMBH candidates was selected from the RCSED optical spectral catalog, followed by refined spectral observations using large telescopes, including the Magellan, SALT, Keck, and CMO telescopes. Analysis of more than 70 spectra has obtained accurate virial masses, stellar population parameters, and kinematics. One significant result includes the detection of a binary black hole system with masses of ($1.7{\times}10^5 M_\odot$) and ($1.4{\times}10^6 M_\odot$). Our results indicate that IMBHs and their low-mass SMBH counterparts do not necessarily co-evolve with their host galaxies, suggesting that super-Eddington accretion is the dominant growth mechanism. This research improves the precision of virial mass estimates and provides new insights into the $M_{\rm BH} - \sigma_{\rm bulge}$ relation, with potential implications for future high-redshift SMBH observations using next-generation facilities.

Keywords: cosmology: observations; early universe; galaxies: active, nuclei, Seyfert; quasars: supermassive black holes

DOI: 10.26119/VAK2024.022

1 Introduction

About a hundred so-called intermediate-mass black holes (IMBH, $M_{\rm BH} < 2*10^5 M_\odot$) have already been discovered. In the coming decades, even more IMBHs will be discovered by the Laser Interferometer Space Antenna (LISA) (Amaro-Seoane et al. 2023) and the Multi-AO Imaging Camera for Deep Observations (MICADO) (Davies et al. 2016; Demianenko et al. 2024b) at the Extremely Large Telescope (ELT). Currently, the origin and evolutionary mechanisms of these objects are not well understood. Understanding the origin and evolution of IMBHs is extremely important in modern astrophysics, as it will provide a key to understanding an even more global problem — the mystery of the origin and growth mechanisms of supermassive black holes (SMBHs) in the nuclei of galaxies. This work is dedicated to the search and study of central light-weight black holes in galaxies of different types.

The discovery of quasars in the early Universe (z > 6.3, only 750–900 Myr after the beginning of the expansion of the Universe) containing SMBHs with masses of the order of $10^{10} M_\odot$ (Mortlock et al. 2011) cannot be explained only by accretion of gas onto stellar-mass black holes alone. Even if black holes were formed shortly after the beginning of the expansion of the Universe, by the collapse of the nuclei of population III stars, it would take more than 1 billion years for the SMBH to grow, unless the accretion rate significantly exceeds the Eddington limit for a long time.

At the same time, IMBHs are too massive to be formed by the gravitational collapse of a single star, but too light to be considered supermassive. However, there are currently hypotheses about the formation of IMBHs as a result of the collapse of supermassive stars of population III (Schneider et al. 2002).

SMBHs are thought to co-evolve with the spheroids of their host galaxies (hereafter host galaxies) (Kormendy & Ho 2013). Thus, there is a so-called "scaling relation" between the black hole mass and the velocity dispersion of the host galaxy.

In recent years we have expanded the known sample of IMBH candidates and confirmed several times more IMBHs (Chilingarian et al. 2018, 2023; Goradzhanov et al. 2022; Toptun et al. 2022); by optical variability Demianenko et al. (2022, 2024a)). The basis of our galaxy sample is the RCSED optical spectral catalog of galaxies (Chilingarian et al. 2017), in which in turn we have analyzed the SDSS spectra (Abazajian et al. 2009). The resolution of the SDSS spectra (R 2000) is not suitable for obtaining accurate virial masses, but allows us to make an initial selection of galaxies with low-mass black holes at the center. After selecting IMBH candidates and so-called 'light-weight' SMBHs (LWSMBH, $< 10^6 M_\odot$), we followed them up with spectral observations in the optical range on large telescopes (6.5-m Magellan Telescope, 10-m Southern African Large Telescope, 10-m Keck Telescope, 2.5-m Caucasus Mountain Observatory Telescope).

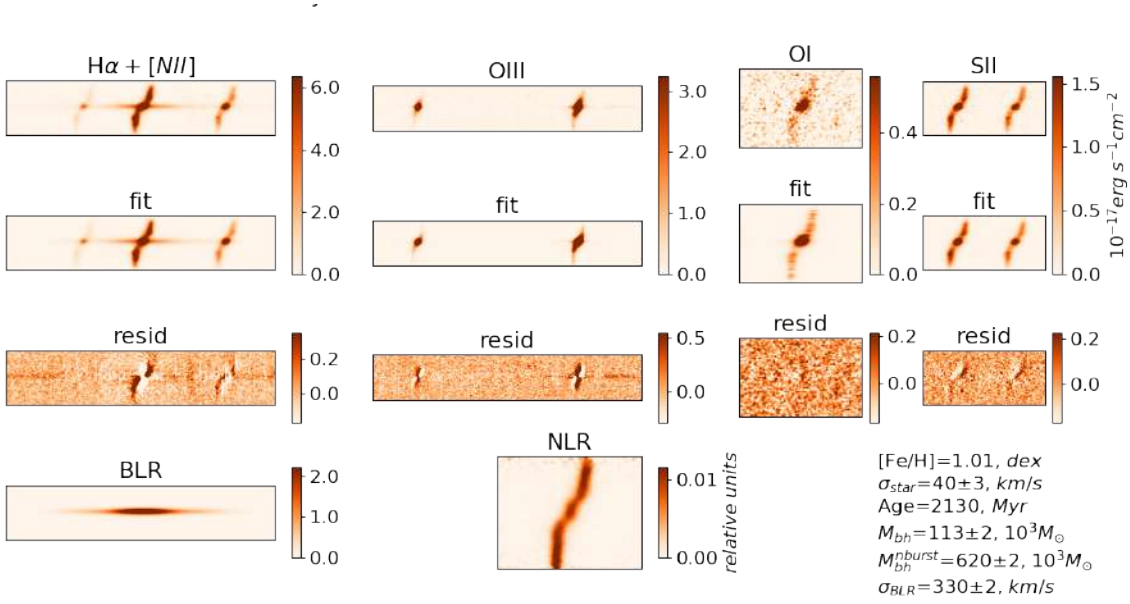

Fig. 1. The result of the 2d nonparametric reconstruction of the NLR-component profile. The top line is the emission spectrum of one of the sample galaxies in the selected spectral regions, the second line is the line fit, and the third line is the fit residuals. The fourth line shows the profiles of the parametric BLR component and the nonparametric NLR-component. Also shown in the bottom right are the parameters of the BLR component, the parameters of the stellar population model — metallicity and age of the stars, black hole mass from the NBURSTs decomposition, and from the nonparametric analysis are displayed.

2 Follow-up observations and their analysis

Spectra of more than 70 galaxies have now been obtained from the MagE (Magellan, echelle), ESI (Keck, echelle), RSS (SALT, long-slit), and TDS (CMO, long-slit) instruments. First, a standardized reduction of our observations was performed by the pipeline we wrote. Flux calibration of the spectra was carried out to obtain accurate virial masses of the black holes. The primary analysis of the spectra consisted in finding the parameters of the stellar population (metallicity, age, kinematics) with our NBURSTs method (Chilingarian et al. 2007).

Then the stellar continuum is subtracted from the original spectra and only the emission spectrum is analyzed. A nonparametric decomposition of the H_α line profile into BLR and NLR components is performed. The NLR profile reconstruction method approximates all strong emission lines simultaneously: H_β, [OIII], [OI], H_α, [NII], [SII] by a linear combination of a narrow line component with a nonparametric shape and

a broad Gaussian component in the Balmer lines. The BLR parameters: the velocity dispersion ($\sigma_{\rm BLR}$), the radial velocity of the center of the BLR component, and the parameters h3 and h4 are fit in a nonlinear minimization loop. The parameters psf and the BLR center on the slit are also fit in this loop, since we are dealing with the two-dimensional case, Fig.1. The broad Hα flux and width are then used to estimate the virial $M_{\rm BH}$ using the calibration from Reines et al. (2013): $M_{\rm BH} = 3.72 \cdot 10^6 ({\rm FWHM}_{\rm H\alpha}/10^3 {\rm km/s})^{2.06} \cdot (L_{\rm H\alpha}/10^{42} {\rm erg/s})^{0.47}$. The calculated masses have been corrected for the slit light losses.

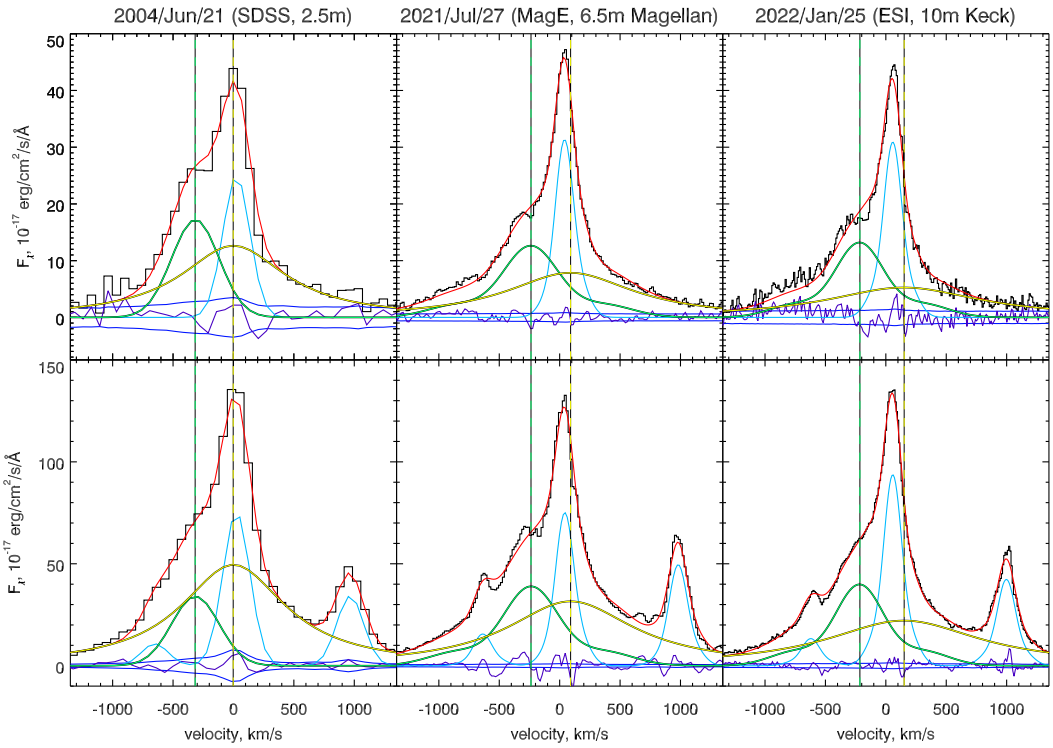

Fig. 2. The picture shows spectra of the host galaxy of a binary black hole at different instruments with subtracted stellar continuum. Top panel — spectra (from right to left SDSS, MagE, ESI) of the binary black hole near the H_β line, bottom panel — near the H_α.

3 Evolution of central black holes

As a result of the analysis of one of the spectra obtained at MagE, a binary black hole has been detected in one of the galaxies, based on the presence of a double broad

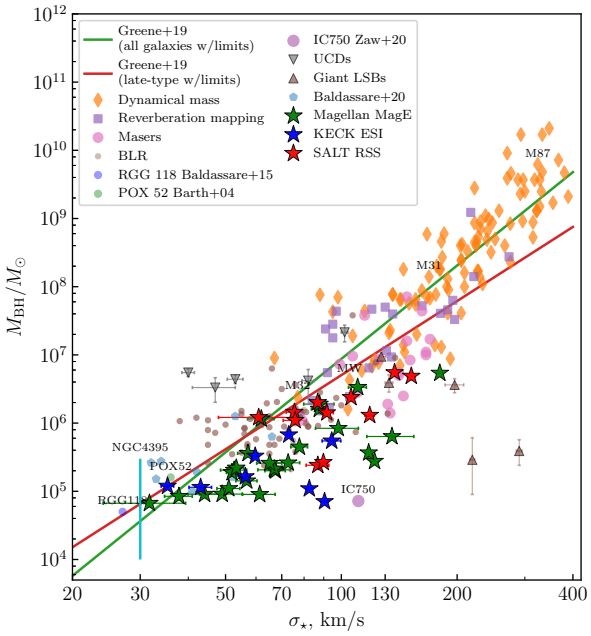

Fig. 3. The $M_{\rm BH} - \sigma_*$ relation featuring IMBHs and light-weight SMBHs. Only one IMBH has a mass estimate based on masers (Zaw et al. 2020); the rest of the data points are virial estimates from Hα. New data from MagE, ESI, and SALT are shown by green, blue, and stars, respectively.

component in the Balmer line series, Fig.2. The black hole masses are $1.7 \cdot 10^5 M_\odot$ and $1.4 \cdot 10^6 M_\odot$ respectively. The two BLR components are separated by 150 km/s. After the discovery of this object on MagE, we made observations of this galaxy on other telescopes: Keck and CMO. This object is currently under multi-wavelength study.

As a result of our analysis, the masses of more than 70 IMBH candidates have been refined. The optical spectra (with good spectral resolution) of the currently largest sample of IMBH and LWSMBH have been analyzed: the parameters of the stellar populations, the kinematics of stars and gas have been obtained, and the virial masses of the central black holes have been measured. The values of the virial masses of the black holes are more accurate than those obtained from the SDSS. The higher spectral resolution has allowed the AGN outflow to be separated from the BLR component of the Balmer lines.

The dependence $M_{\rm BH} - \sigma_{\rm bulge}$ is constructed from the obtained dispersions of the bulge velocities and the virial masses of the black holes, Fig.3. From the results obtained for low-mass black holes based on the $M_{\rm BH} - \sigma_{\rm bulge}$ relation, we can conclude

that IMBHs in the nearby Universe do not appear to evolve with their host galaxies: they grow by accretion, while their hosts grow secularly (although gas sources may be associated). The scaling relations are preserved, but the dependence of the black hole mass on the velocity dispersion is different. If the same happens at high redshifts, then (super) Eddington accretion is the dominant mechanism for the growth of supermassive black holes at low masses, and we expect to see supermassive black holes with large z in X-rays with the next-generation facilities Athena or Lynx. However, there may be another explanation for the position of IMBHs on the $M_{\rm BH} - \sigma_{\rm bulge}$ relation: the Reines et al. (2013) scaling relation for black hole mass estimation is not valid for small black hole masses. To test the reliability of the $M_{\rm BH} - {\rm FWHM}_{{\rm H}\alpha}$ relation, we started a BLR reverberation campaign with narrow Hα filters (Demianenko et al. in prep.) at the CMO of the Sternberg Astronomical Institute of Moscow State University (SAI MSU).

Acknowledgements. This project is supported by the Basis Foundation Grant 23-2-2-50-1.

References

Abazajian K.N., Adelman-McCarthy J.K., Agüeros M.A., et al., 2009, ApJS, 182, p. 543
Amaro-Seoane P., Andrews J., Arca Sedda M., et al., 2023, Living Reviews in Relativity, 26, id. 2
Chilingarian I., Bauer F., Grishin K., et al., 2023, American Astronomical Society Meeting Abstracts, 242, id. 309.03
Chilingarian I., Prugniel P., Sil'chenko O., et al., 2007, Proceedings of IAU Symposium, 241, p. 175
Chilingarian I.V., Katkov I.Y., Zolotukhin I.Y., et al., 2018, ApJ, 863, id. 1
Chilingarian I.V., Zolotukhin I.Y., Katkov I.Y., et al., 2017, ApJS, 228, id. 14
Davies R., Schubert J., Hartl M., et al., 2016, Society of Photo-Optical Instrumentation Engineers (SPIE) Conference Series, 9908, id. 99081Z
Demianenko M., Grishin K., Toptun V., et al., 2022, Astronomy at the Epoch of Multimessenger Studies, p. 359
Demianenko M., Grishin K., Toptun V., et al., 2024a, Astronomical Society of the Pacific Conference Series, 535, p. 283
Demianenko M., Pott J.-U., Polsterer K., 2024b, arXiv e-prints, arXiv:2404.06558
Goradzhanov V., Chilingarian I., Katkov I., et al., 2022, Astronomy at the Epoch of Multimessenger Studies, p. 367
Kormendy J. and Ho L.C., 2013, ARA&A, 51, p. 511
Mortlock D.J., Warren S.J., Venemans B.P., et al., 2011, Nature, 474, p. 616
Reines A.E., Greene J.E., Geha M., 2013, ApJ, 775, id. 116
Schneider R., Ferrara A., Natarajan P., et al., 2002, ApJ, 571, p. 30
Toptun V., Chilingarian I., Grishin K., et al., 2022, Astronomy at the Epoch of Multimessenger Studies, p. 304
Zaw I., Rosenthal M.J., Katkov I.Y., et al., 2020, The Astrophysical Journal, 897, p. 111

VAK 2024 MODERN ASTRONOMY: FROM THE EARLY UNIVERSE TO EXOPLANETS AND BLACK HOLES 300 years Russian Academy of Sciences

Regular distribution of star formation regions along the spiral arms and rings of disk galaxies

A. Gusev and E. Shimanovskaya

Sternberg Astronomical Institute, Lomonosov Moscow State University, 13 Universitetsky Pr., Moscow, 119234 Russia

Abstract. Recent studies have indicated that the spatial regularity in the distribution of young stellar population along the spiral arms and rings of galaxies, which was previously thought to be uncommon, is actually a fairly common occurrence. Spatial regularity has been found in the spiral arms and rings of galaxies with different morphologies, from lenticular to extremely late-type spiral. The characteristic regularity scale is equal to 350–500 pc or a multiple of that in all the galaxies studied. Theoretical models suggest a scale of instability for the stellar-gas disk around a few kpc, which is larger than what has been observed. Recent magneto-hydrodynamic simulations, however, indicate the formation of regular chains of star formation regions in spiral arms on a scale of 500–700 pc for galaxies similar to the Milky Way. Modern high-quality surveys, like PHANGS–MUSE, provide the necessary observational data (surface densities and velocity dispersions of gas and stellar population) to directly calculate the regularity scales in galaxies, with high spatial resolution and a wide field of view, which is a promising direction for research in this field.

Keywords: HII regions; galaxies: star clusters: general; galaxies: ISM, spiral, star formation

DOI: 10.26119/VAK2024.023

1 Introduction

Elmegreen & Elmegreen (1983) first brought attention to the fact that neighboring HII regions in the spiral arms of some galaxies are located at equal distances from each other. They noted the rarity of this phenomenon: the only $\approx 10\%$ of the galaxies studied had visually detectable regular chains of HII regions with the characteristic distances λ between neighbouring HII regions of 1–4 kpc in different galaxies. Later, Efremov (2009) found a similar regularity in the distribution of HI superclouds in the Carina and Cygnus spiral arms of the Milky Way with $\lambda = 1.5$ and 1.3 kpc, respectively. He also identified a regular chain of stellar complexes within the northwestern arm of M31 with a characteristic distance of 1.1 kpc (Efremov 2010).

The rarity of spatial regularities in the distribution of gas and stellar condensates in spiral arms of galaxies seems quite understandable. Theoretical studies of the gravitational instability of stellar-gas disks (Safronov 1960; Rafikov 2001; Romeo & Falstad et al. 2013) show that the wavelength of the instability depends on a comprehensive set of parameters, including gas and stellar surface densities and their velocity dispersions. The regularity in the distribution of gas clouds and their descendants, star formation regions, requires the constancy of these physical parameters in the stellar-gas disk over a wide range of galactocentric distances. However, such constancy should be a rare phenomenon in classical galactic disks.

Note that considering typical values of the parameters of the stellar and interstellar medium, all theoretical models predict the instability wavelength to be on the order of several kiloparsecs (Marchuk 2018; Inoue et al. 2021a), which is in agreement with the observational results of Elmegreen & Elmegreen (1983) and Efremov (2009, 2010).

In the last decade, however, studies of the regularity of the distribution of the young stellar populations and gas clouds along the spiral arms and rings of galaxies have reshaped our understanding of the prevalence of this phenomenon and its characteristic spatial scales. The aim of this paper is to survey the latest observational and numerical modelling results on the patterns of spatial distribution patterns of the young stellar population and gas clouds along the spiral arms and rings of galaxies of different types. These results have been obtained both by our own research team and by other scientific groups.

2 Review of results

Since 2013, the regular chains of HII regions, HI clouds, and star formation regions have been identified in the spiral arms of NGC 628 (Gusev & Efremov 2013), NGC 4321 (Elmegreen et al. 2018), NGC 895, NGC 5474, NGC 6946 (Gusev et al.

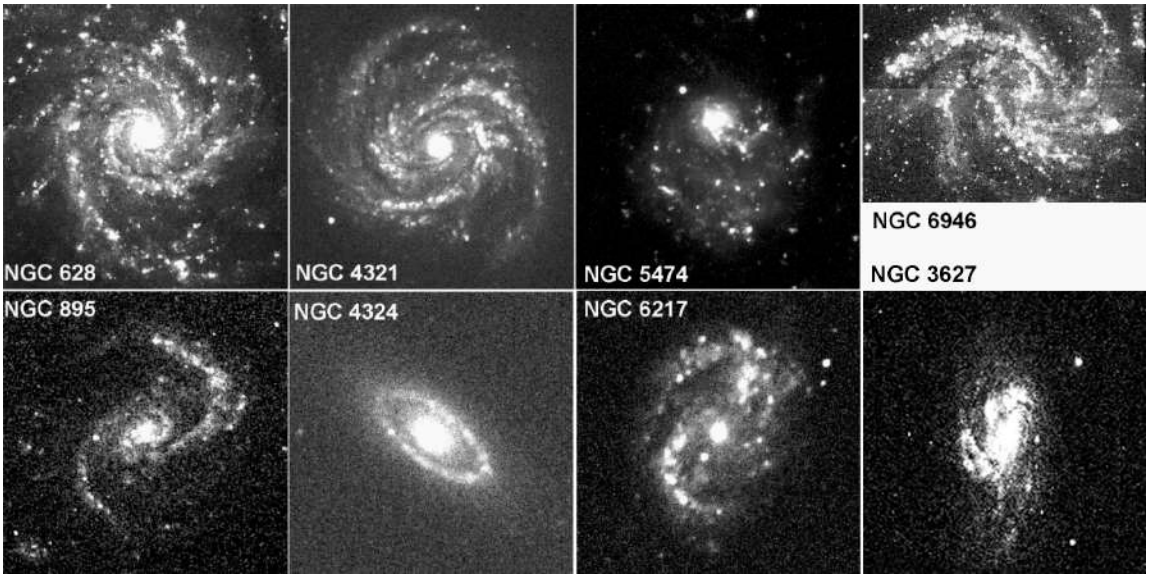

Fig. 1. Images of galaxies with regular chains of star formation regions found in their spiral arms or rings. Images of NGC 3627 and NGC 4324 are from the SDSS u band; other galaxies are shown in the U band. North is top, east is to the left.

2022), and NGC 3627 (not yet published), as well as in the Carina Arm of the Milky Way (Park et al. 2023) and in the rings of NGC 6217 (Gusev & Shimanovskaya 2020) and NGC 4324 (Proshina et al. 2022). The maps of these galaxies are shown in Fig. 1. The image of NGC 4321 is from the figure obtained in Marcum et al. (2001) and was taken from the NED database.[1] Images of NGC 3627 and NGC 4324 are from the SDSS survey database.[2] Images of other galaxies are based on observations made using the authors' programmes (see Gusev & Efremov 2013; Gusev & Shimanovskaya 2020; Gusev et al. 2022).

The results are derived from the analysis of images of galaxies in the ultraviolet (*GALEX* FUV and NUV bands), optical (UB bands and Hα line), infrared (*Spitzer* 8μm) and radio (21 cm). We present the summary data on the characteristic distances between neighbouring star formation regions (gas clouds, HII regions) in the spiral arms and rings of these galaxies in Fig. 2.

A detailed description of the technique and analysis of the results has been given in the relevant papers and summarized in the survey by Gusev (2023). The only exception is NGC 3627, which has not been previously described. To study the regularities in this galaxy, we used its FUV image obtained by *GALEX* (Gil de Paz

[1] http://ned.ipac.caltech.edu/
[2] http://www.sdss.org/dr13/

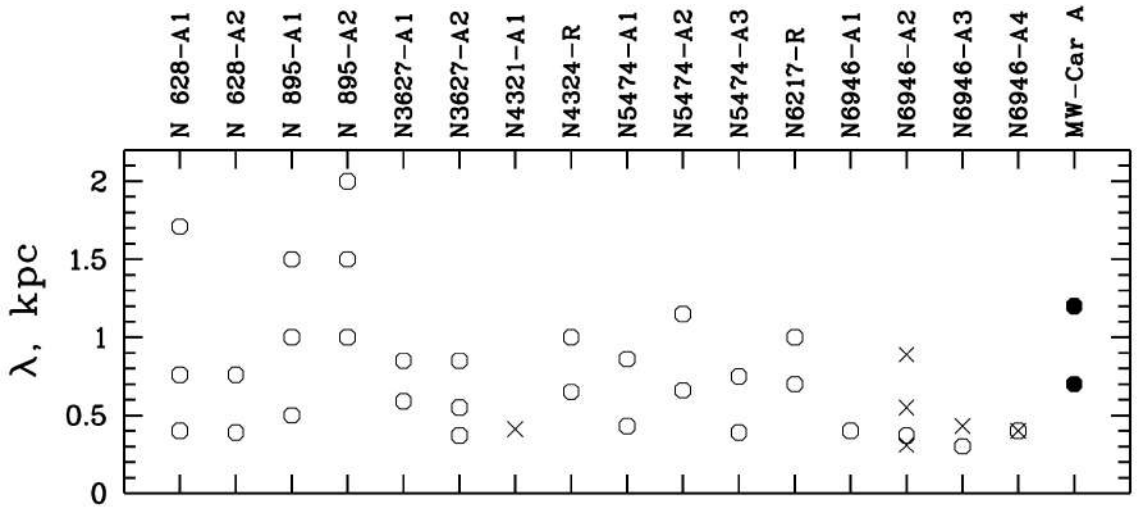

Fig. 2. Characteristic distances λ between neighbouring local brightness maxima in spiral arms and rings of different galaxies, obtained from ultraviolet and optical (open circles), infrared (crosses) and radio data (filled circles).

et al. 2007), the SDSS u image (Brown et al. 2014), and the Hα image from the *SIRTF Nearby Galaxies Survey (SINGS)*[3] (Kennicutt et al. 2003). All images were downloaded from the NED database.

Using photometric profiles along the arms, we found 18 local brightness maxima (condensations of the young stellar population) in each of the spiral arms of NGC 3627. The results of the analysis of the distances between neighbouring young stellar condensations are shown in Fig. 3. In both arms the histogram shows a main peak at 590 ± 30 pc in the western arm (Arm 1) and 550 ± 40 pc in the eastern spiral arm (Arm 2). Half of the star formation regions in each spiral arm have a neighbour at a distance of $\sim$ 550–600 pc. Secondary peaks (at least three separations) are observed at 850 ± 30 pc in Arm 1 and 375 ± 25 and 850 ± 25 pc in Arm 2 (Fig. 3). The main peaks in the arms are also confirmed by the Fourier analysis data, which gives a value of 670 ± 20 pc in Arm 1 and 525 ± 20 pc in Arm 2 (Fig. 3).

Summarizing the observational data, we can conclude that (i) regularity in the spatial distribution of young stellar populations and gas clouds along the spiral arms and rings of galaxies of different morphology and structure is observed more frequently than expected (see Fig. 1); (ii) the characteristic distance between neighbouring zones of concentration of the young stellar population is equal to or a multiple of 350–500 pc; (iii) brighter and larger stellar clusters (gas clouds) are located at greater (multiples) distances from each other than smaller and less massive (Gusev

[3] http://irsa.ipac.caltech.edu

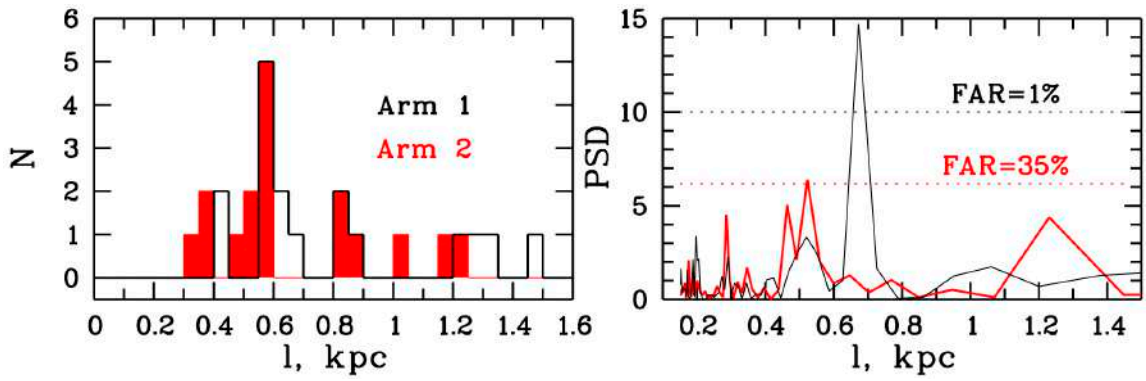

Fig. 3. The number distribution histograms of local brightness maxima by separation between adjacent young stellar condensations along the spiral arms of NGC 3627 (left) and the normalized power spectral density of the function $p(s)$ for the spiral arms in NGC 3627 (right). The function $p(s)$ is a collection of Gaussians on the points of local brightness maxima on the profiles, with a dispersion equal to the peak positioning error; dotted lines are the false-alarm probability (FAP) levels of 1% for Arm 1 and 35% for Arm 2 (see Gusev et al. 2022, for details).

& Efremov 2013; Park et al. 2023); (iv) the presence or absence of shock waves does not affect the formation of regular chains of star formation regions along galactic spirals and rings (Gusev & Efremov 2013; Gusev & Shimanovskaya 2020).

Although theoretical models predicted a scale of the stellar-gas disk instability on the order of a few kpc,Arora et al. (2024) recently used magneto-hydrodynamic simulations in a galaxy like the Milky Way to predict the formation of regular chains of star formation regions in spiral arms on scales of $\sim$ 500 pc in the hydro case (without magnetic field) and $\sim$ 650 pc in the magnetic case.

3 Discussion and conclusions

Despite the simulation of Arora et al. (2024), the question of agreement between the observational data, which show a scale of $\sim$ 350–500 pc, and theoretical models (scale $>$ 1 kpc) remains open. We believe that a promising direction for research in this field is the use of modern high-quality surveys such as PHANGS–MUSE, which provide the necessary observational data (parameters of the gas and stellar populations and kinematics of the disk) for the direct calculation of regularity scales in galaxies with high spatial resolution and wide field of view.

At the same time, the question arises: how accurately do existing theoretical models predict the scale of gas cloud fragmentation? Simulations by Arora et al. (2024) and Inoue et al. (2021b) showed that the separations obtained from numerical simulations turned out to be 1.5–2 times less than the wavelength of the disk instability. A possible explanation for this discrepancy could be the difference between the local

physical parameters of the gas disk at the moment of fragmentation and the observed ones. Park et al. (2023) showed that if the observed HI clouds in the Carina Arm were formed by gravitational instabilities in a previously more uniform spiral arm gas, then the velocity dispersion σ in this gas should to be less than or equal to $\sim$ 4 km/s whereas the observed σ = 8–8.5 km/s. An alternative possibility is the higher surface density of the gas at the moment of fragmentation, caused by shock waves.

Acknowledgements. This research has made use of the NASA/IPAC Extragalactic Database (NED; http://ned.ipac.caltech.edu), SIRTF Nearby Galaxies Survey (SINGS; http://irsa.ipac.caltech.edu), the Sloan Digital Sky Survey 0.25cm(SDSS; http://www.sdss.org), and the Galaxy Evolution Explorer (GALEX; http://galex.stsci.edu) data.

References

Arora R., Federrath C., Banerjee R., et al., 2024, Astronomy & Astrophysics, 687, id. A276
Brown M.J.I., Moustakas J., Smith J.D.T., et al., 2014, The Astrophysical Journal Supplement Series, 212, id. 18
Efremov Y.N., 2009, Astronomy Letters, 35, p. 507
Efremov Y.N., 2010, Monthly Notices of the Royal Astronomical Society, 405, p. 1531
Elmegreen B.G. and Elmegreen D.M., 1983, Monthly Notices of the Royal Astronomical Society, 203, p. 31
Elmegreen B.G., Elmegreen D.M., Efremov Y.N., 2018, The Astrophysical Journal, 863, id. 59
Gil de Paz A., Boissier S., Madore B.F., et al., 2007, The Astrophysical Journal Supplement Series, 173, p. 185
Gusev A.S. and Efremov Y.N., 2013, Monthly Notices of the Royal Astronomical Society, 434, p. 313
Gusev A.S. and Shimanovskaya E.V., 2020, Astronomy & Astrophysics, 640, id. L7
Gusev A.S., Shimanovskaya E.V., Zaitseva N.A., 2022, Monthly Notices of the Royal Astronomical Society, 514, p. 3953
Gusev A.S., 2023, Astronomy Reports, 67, p. 458
Inoue S., Takagi T., Miyazaki A., et al., 2021a, Monthly Notices of the Royal Astronomical Society, 506, p. 84
Inoue S., Yoshida N., Hernquist L., 2021b, Monthly Notices of the Royal Astronomical Society, 507, p. 6140
Kennicutt R.C., Armus L., Bendo G., et al., 2003, The Publications of the Astronomical Society of the Pacific, 115, p. 928
Marchuk A.A., 2018, Monthly Notices of the Royal Astronomical Society, 476, p. 3591
Marcum P.M., O'Connell R.W., Fanelli M.N., et al., 2001, The Astrophysical Journal Supplement Series, 132, p. 129
Park G., Koo B.-C., Kim K.-T., et al., 2023, The Astrophysical Journal, 955, id. 59
Proshina I.S., Moiseev A.V., Sil'chenko O.K., 2022, Astronomy Letters, 48, p. 139
Rafikov R.R., 2001, Monthly Notices of the Royal Astronomical Society, 323, p. 445
Romeo A.B. and Falstad N., 2013, Monthly Notices of the Royal Astronomical Society, 433, p. 1389
Safronov V.S. 1960, Annales d'Astrophysique, 23, p. 979

VAK 2024 MODERN ASTRONOMY: FROM THE EARLY UNIVERSE TO EXOPLANETS AND BLACK HOLES 300 years Russian Academy of Sciences

Spectral study of peculiar galaxies

G. Karataeva and O. Merkulova

St. Petersburg University, 13B Universitetskaya Emb., St Petersburg, 199034 Russia

Abstract. A study of five peculiar galaxies (SPRC-69, SPRC-100, SPRC-260, SPRC-269, and SPRC-136) from the new catalog of polar ring galaxies (Sloan-based Polar Ring Catalog, SPRC). Panoramic (3D) spectral data were obtained with the 6-m telescope of the Special Astrophysical Observatory of the Russian Academy of Sciences with the using the Fabry–Perot interferometer. The large-scale velocity fields, velocity dispersion fields, and monochromatic images of objects in the Hα emission line were analyzed in detail. All galaxies showed the complex structure and kinematics of their gaseous components. The "tilted-ring" method was used to analyze the velocity fields. It was concluded that all the objects studied belong to are classical polar ring galaxies, with the exception of SPRC-100.

Keywords: galaxies: peculiar, structure, kinematics and dynamics, individual (SPRC-69, SPRC-100, SPRC-260, SPRC-269, SPRC-136)

DOI: 10.26119/VAK2024.024

1 Introduction

One of the most unique and beautiful types of peculiar objects is a polar ring galaxy (PRG), which is a system consisting of a disk of the main galaxy and an outer ring of gas, dust, and stars rotating approximately in the perpendicular plane. This paper is devoted to the results of the spectral study of five peculiar galaxies (SPRC-69, SPRC-100, SPRC-260, SPRC-269, and SPRC-136) that are candidates for PRGs, selected from the Sloan-Based Polar Ring Catalog (SPRC, Moiseev et al. 2011).

The observations of the objects under study were performed at the primary focus of the 6-m telescope of the Special Astrophysical Observatory of the Russian Academy of Sciences using the Fabry–Perot interferometer (FPI) (Afanasiev et al. 2005; Moiseev 2015). The large-scale velocity fields, velocity dispersion fields and monochromatic images of the ionized gas were constructed by gaussian fitting of the Hα emission line profiles. The "tilted-ring" method (Begeman 1989) was used to analyze the velocity fields.

2 Results and discussion

2.1 SPRC-69

Optical images from SPRC-69 (II Zw 092) show that an outer, highly inclined ring surrounds the central body.

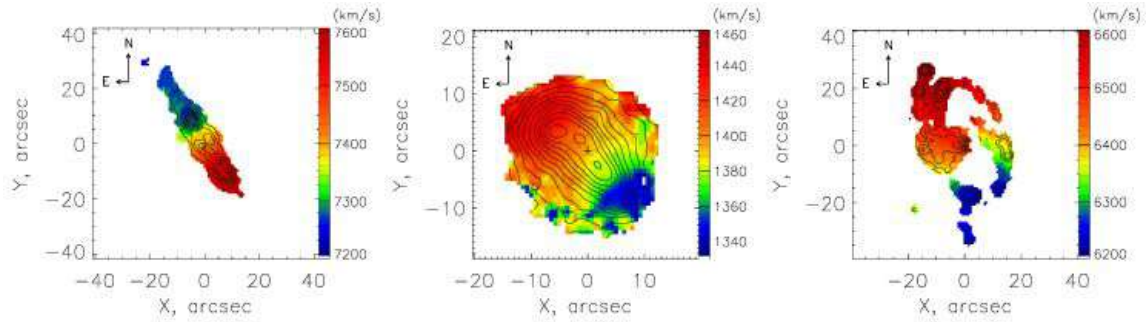

Fig. 1. Line-of-sight velocity fields in the Hα line with contours of the Hα image of the galaxies: SPRC-69 (left), SPRC-100 (centre), SPRC-260 (right).

The velocity field in the Hα emission line (Fig. 1, left) is typical of disk structures: lines of equal radial velocity (isovels) indicate rotation around the major axis of the galaxy. The stellar velocity field (obtained from the MaNGA[1] survey) has also been

[1] https://www.sdss4.org/surveys/manga/

analyzed using the "tilted-ring" method. An angle between the planes of the ionized gas of the ring and the stellar disk of the main body was estimated: $\Delta i \approx 83°$. Our study of SPRC-69 using 3D spectral data confirmed the conclusion that SPRC-69 belongs to the PRG, which was made in Moiseev et al. (2011) using long-slit data. The maximum rotational velocity ($V_{\max} = 104$ km/s), the stellar velocity dispersion (≈ 100 km/s), the mass of the stellar disk ($\geq 5.2 \cdot 10^9 M_\odot$), and the gas of the main body is concentrated in its central part allowed us to suggest that the main body of SPRC-69 is a lenticular galaxy (S0).

2.2 SPRC-100

The optical images of SPRC-100 (CGCG 124-041) show a slightly curved, central galaxy surrounded by an elliptical, roughly perpendicularly elongated envelope. The velocity field in the Hα emission line (Fig. 1, centre) is typical for disk galaxies: isovels indicate rotation of the ionized gas around the minor axis of the galaxy. Analysis of the 3D spectral data for SPRC-100 has shown that no kinematically decoupled subsystems are observed in it, and therefore, SPRC-100 most likely does not belong to the PRGs. The value of $V_{\max} \approx 77$ km/s and the mass estimate ($\geq 1.7 \cdot 10^9 M_\odot$) are in agreement with the results of Ciesla et al. (2014), where it is assumed that this object is a BCD (Blue Compact Dwarf) galaxy.

2.3 SPRC-260

The optical images of SPRC-260 (CGCG 068-056) show a disk-shaped central body with an extended ring around it. The velocity field in the Hα line (Fig. 1, right) shows the rotation of the ring structure: the southern side is approaching the observer, while the northern side is moving away. The analysis of photometric and spectral data for SPRC-260 has shown that at least two systems are observed in it. One of them is associated with a central stellar system elongated in the E-W direction. The second is associated with a gaseous ring rotating at an angle of 62° or 112° to the stellar system. So SPRC-260 can probably be classified as a PRG. The disky shape of the central body and the small amount of gas allowed us to suggest that the main body of SPRC-260 is an S0 type galaxy.

2.4 SPRC-269 and SPRC-136

SPRC-269 and SPRC-136 (Fig. 2, left) form a pair of interacting galaxies, VV328. Both objects are candidates for the PRG. The velocity field of the gaseous component of SPRC-269 (Fig. 2, centre) shows the general direction of rotation of the ring: the southern side is moving away from us, and the northern side is approaching

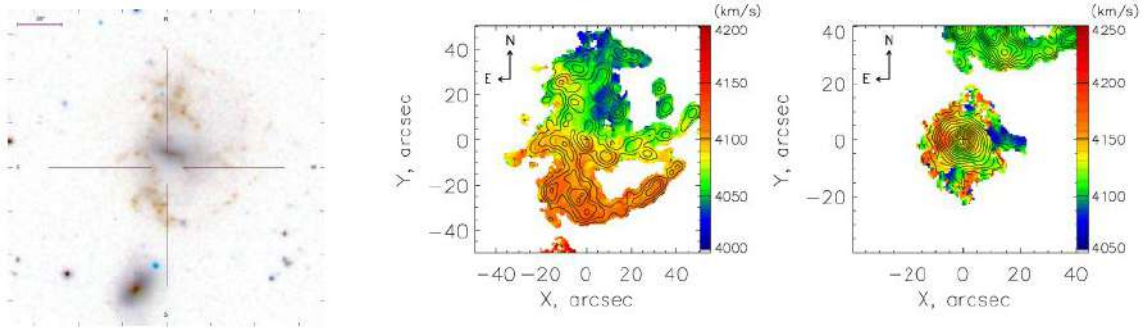

Fig. 2. Left: the *gri* composite image of SPRC-269 and SPRC-136 from the SDSS (http://www.sdss.org/). Middle: the line-of-sight velocity field of SPRC-269 in the Hα line with contours from the Hα image. Right: the line-of-sight velocity field of SPRC-136 in the Hα line with contours from the Hα image.

us. Analysis of the photometric and spectral data for SPRC-269 has shown that it contains at least three systems are observed in it: 1) a central stellar disk with $\mathrm{PA_{kin}} = 75°$, 2) a central gaseous disk, inclined relative to the stellar disk with $\mathrm{PA_{kin}} = 215°$, 3) an outer warped gaseous ring with $\mathrm{PA_{kin}}$, varying from 155° to 175°; and the angle between the stellar disk and the gas ring is 55° or 102°. Therefore, SPRC-269 can probably be classified as a PRG. Almost the entire velocity field of SPRC-136 (Fig. 2, right) was described with two models. The kinematic parameters ($\mathrm{PA_{disk}} = 328°$, $i_{\mathrm{disk}} = 40°$ and $\mathrm{PA_{ring}} = 55°$, $i_{\mathrm{ring}} = 55°$) indicate for the presence of a polar ring rotating around the major axis of the main body.

Acknowledgements. The authors thank A.V. Moiseev for data reduction and useful comments.

References

Afanasiev V.L., Gazhur E.B., Zhelenkov S.R., et al., 2005, Bulletin of the Special Astrophysical Observatory, 58, p. 90

Begeman K.G., 1989, Astronomy and Astrophysics, 223, p. 47

Ciesla L., Boquien M., Boselli A., et al., 2014, Astronomy and Astrophysics, 565, id. A128

Moiseev A.V., 2015, Astrophysical Bulletin, 70, p. 524

Moiseev A.V., Smirnova K.I., Smirnova A.A., et al., 2011, Monthly Notices of the Royal Astronomical Society, 418, p. 244

MODERN ASTRONOMY: FROM THE EARLY UNIVERSE TO EXOPLANETS AND BLACK HOLES

Merging of spiral galaxies: observations and modeling

A. Khoperskov[1], S. Khrapov[1], D. Sirotin[1], and A. Zasov[2,3]

[1] Volgograd State University, 100 Prospect Universitetsky, Volgograd, 400062 Russia
[2] Sternberg Astronomical Institute, Moscow M.V. Lomonosov State University, 13 Universitetskij pr., Moscow, 119234 Russia
[3] Faculty of Physics, Moscow M.V. Lomonosov State University, 1 Leninskie gory, Moscow, 119991 Russia

Abstract. We present a study of the dynamics of multi-component models of spiral galaxies at different stages of grand mergers. The numerical models include a self-consistent account of the dynamics of collisionless stellar subsystems and N-body dark matter, as well as gaseous components. The calculation of gas heating and cooling processes allows us to consider a wide temperature range from 80 to 100 thousand degrees. The use of the method of Smoothed-particle hydrodynamics to solve the hydrodynamic equations makes it possible to follow the evolution of the gas of each galaxy, calculating the content of gaseous components of each object in the process of complex exchange of matter. The gravitational interaction is determined in a direct way by summing the contributions according to Newton's law, which minimizes the modeling error. This requires significant computational resources using graphics accelerators on a hybrid computing platform CPU + multi-GPUs. The study aims to reconcile theoretical models with the morphology and kinematics of a number of observed systems. In particular, Taffy-type objects are considered, where two galaxies are connected by a gas bridge with a characteristic small-scale gas structure after the disks have passed through each other in an approximately flat orientation. Examples of such systems are the observed galaxy pairs UGC 12914/UGC 12915, NGC 4490/NGC 4485, UGC813/UGC816 etc.

Keywords: galaxies: interactions, evolution, structure

DOI: 10.26119/VAK2024.025

1 Introduction

Galactic interactions are the most important factor in the evolution of a significant fraction of these stellar systems. The most large-scale events are associated with major mergers, leading to the formation of complex tidal structures, a significant restructuring of star formation history, determining the morphology and kinematics in the process of merging of galaxies (Condon et al. 1993; Lisenfeld et al. 2019; He et al. 2024).

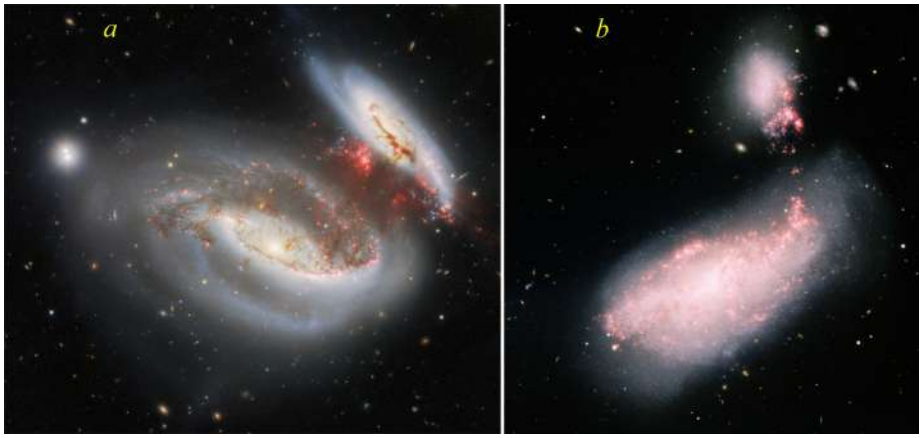

Fig. 1. Images of Taffy galaxies: *a* — UGC 12914 (bottom) and UGC 12915 (top); *b* — NGC4490 and NGC4485 (Gemini North, https://noirlab.edu).

A very curious and rare class of interacting objects are the systems of recently collided disky galaxies, the study of which began with the pair UGC 12914/12915, called Taffy (Condon et al. 1993). A near head-on collision occurred about 25 million years ago, and a gas bridge with a peculiar morphology and physical state of matter is clearly visible between the disks of the galaxies (Fig. 1).

The goal of this paper is to construct numerical dynamical models of a nearly face-on collision of two S-galaxies that reproduce the main properties of the observed of Taffy-like objects. The model of each galaxy includes stellar and gas disks immersed in a living dark halo. We study the influence of various parameters of the galactic pair on the properties of the gas bridge observed in the in the Taffy and Taffy-like systems.

2 Features of Taffy pairs and their modeling

The pair UGC 12914/12915 is a classic example of Taffy galaxies, which was highlighted in the work of Condon et al. (1993). The presence of thin filamentary gas structures between two S-galaxies is a distinctive feature of Taffy. This observed feature is formed as a result of the recent passage of the disks through each other.

Some characteristics of UGC 12914/12915 are as follows (Condon et al. 1993; Lisenfeld et al. 2019; He et al. 2024; Joshi et al. 2019). 1) An almost head-on collision of two counter-rotating disks occurred several tens of millions of years ago. 2) There is a massive multiphase gas bridge containing filamentary structures. 3) The gas bridge containes warm molecular hydrogen. 4) Star formation in the bridge is low, if any, and apparently suppressed by the strong gas turbulence. 5) The soft X-ray emission from the bridge is associated with hot gas with a mass in the range of $(0.8–1.3) \times 10^8 M_\odot$, which is about 1% of the total mass of the gas between the disks (Appleton et al. 2015).

The pair NGC 4490 and NGC 4485 is also Taffy-type (Fig. 1), although the impact geometry was apparently different from the UGC 12914/12915 system. Note that warm molecular hydrogen has been detected in gas outflows in M82. Such superwinds are a fairly common phenomenon, and their structure is also filamentary.

3 Numerical simulation of Taffy galaxies

We present preliminary results from simulations of two colliding galaxies, each containing a stellar disk, a gas disk, and a dark halo. The basic model consists of identical galaxies with star masses $M_d = 3.72 \times 10^{10} M_\odot$, gas $M_g = 3.72 \times 10^9 M_\odot$, dark matter $M_h = 6.02 \times 10^{10} M_\odot$ (within the optical radius $R_{\rm opt} = 9$ kpk). The total mass of the simulated dark halo is $24.92 \times 10^{10} M_\odot$ in each galaxy.

Two galaxies with stellar disks of masses $M_d^{(1)}$ and $M_d^{(2)}$ and dark halos of masses $M_h^{(1)}$ and $M_h^{(2)}$ are simulated by collisionless N-body particles. The gas dynamics are computed by the smoothed-particle hydrodynamics (SPH) method. The gravitational interaction is calculated by summing of the contributions of all particles (N-body + SPH-particles) (Khoperskov et al. 2024, 2021; Titov & Khoperskov 2022).

Figure 2 shows the distribution of gas density along the line of sight during a head-on collision of two identical galaxies. The time $t = 183$ Myr corresponds to the first contact of the gas disks. The following frames show the formation of a gas bridge between the galaxies. Filamentary structures are a characteristic feature of the dynamics of the gas ejected by the impact. The bridge region contains no stars. The flat-type impact considered distorts the stellar disk much less than the gas disk, which undergoes the dramatic changes.

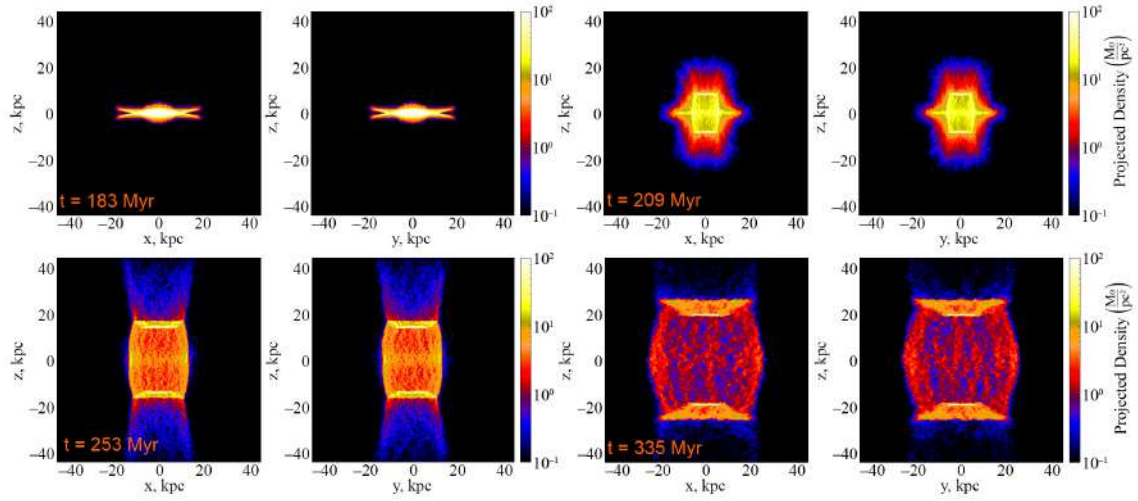

Fig. 2. An example of a head-on collision simulation of a Taffy-type pair with retrograde rotation of the disks.

The following regions of the Taffy system can be conditionally distinguished (see Fig. 2): I — gas inside stellar disks; II — gas bridge between galactic disks, defined by the conditions $z_1^{(\mathrm{disk})} < z < z_2^{(\mathrm{disk})}$, $r < R_{\mathrm{gas}}^{(\mathrm{disk})}$; III — outer zone relative to the bridge between the galaxies, $z_1^{(\mathrm{disk})} < z < z_2^{(\mathrm{disk})}$, $r > R_{\mathrm{gas}}^{(\mathrm{disk})}$, IV and V — remaining zones outside the galactic disks, $z > z_1^{(\mathrm{disk})}$ (IV), $z < z_2^{(\mathrm{disk})}$ (V). Figure 3 shows the evolution of the gas abundance with time for these four regions.

Figure 4 shows the distribution of gas between the disks as function of gas temperature for a symmetrical head-on impact. Hot gas at a temperature of 3000–10000 K is fairly uniformly distributed. There are only remnants of increased concentration near the plane of symmetry ($z = 0$), which is associated with the position of the initial impact. Relatively cool gas (100–500 K) forms inhomogeneous filamentary structures.

The cold gas forms a shell structure in contrast to the hotter component, which occupies the entire volume of the bridge. This feature is due to the complete symmetry of the system when two identical galaxies collide. Simulating the impact of dissimilar galaxies, or the lack of geometric symmetry of the initial interaction, critically alters the properties of the gas bridge.

The overall result is that the gas bridge can contain up to 90% of the total gas mass immediately after the collision. This mass decreases to 30% as the disks move away from each other. The bridge loses gas due to gas deposition on the disks of the galaxies and gas expansion in the bridge region. We calculate the gas fractions in each

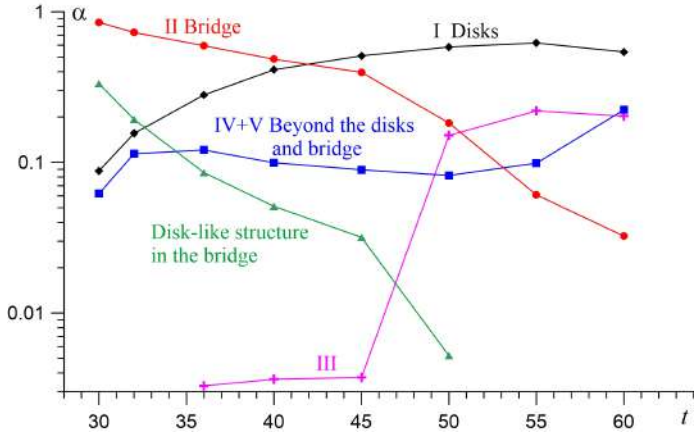

Fig. 3. Dependence of the gas mass in the different regions of the interacting system during the evolution process, $t = 1 \to 63.2\,\mathrm{Myr}$.

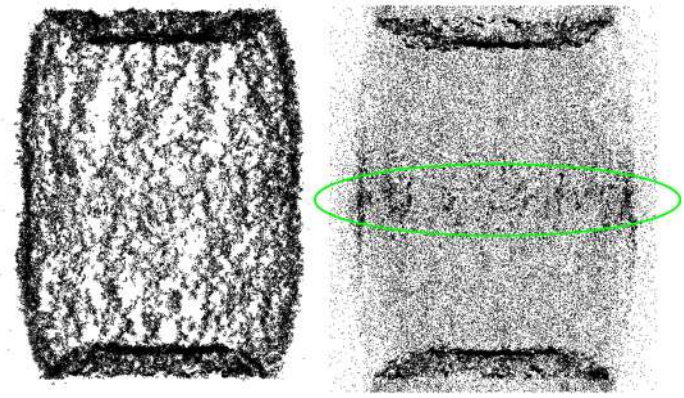

Fig. 4. Structure of warm gas (left) and neutral hydrogen (right) between galaxies 70 million years after the initial impact. The disk-like structure in the bridge area is highlighted by the green line.

region of each galaxy separately. For example, $\alpha_1^{(\mathrm{I})}$ is the fraction of the gas mass in region I from the first galaxy. If the initial galaxies are not identical or the collision geometry is not symmetric, then $\alpha_1^{(\mathrm{II,III})} \neq 1/2$. Computational experiments show a rather strong dependence of the α parameter on the collision conditions. We also calculate the enrichment of the first galaxy in the gas of the second one and vice versa. These properties $\alpha_{12}^{(\mathrm{I})}$ and $\alpha_{21}^{(\mathrm{I})}$ are quite sensitive to the initial collision conditions. The green line in Fig. 3 shows the presence of a massive disk-like structure in the bridge region (more than 30% of the total gas) immediately after the collision in the $z = 0$ plane for identical galaxies (see Fig. 4). However, this gas quickly dissipates.

Figure 4 (right) shows the remaining remnants of this gas 70 million years after the initial impact.

4 Summary

The results allow us to account for the presence and a structure of inhomogeneous multi-component media observed in Taffy-type galaxies. We have performed more than 30 computational experiments to study the structures formed when disk galaxies collide almost face-on. The main focus of the study is to determine the properties of the gas in the bridge region between the disks of the galaxies. Our results show that the spatial structure of the gas and its thermodynamic properties are very sensitive to the impact geometry and parameters of the parent galaxies. Our numerical models allow us to distinguish gas components that form the spatially distinct subsystems with different temperatures in the range of $50 \div 2 \cdot 10^5$ K.

Funding

This work was supported by the Russian Science Foundation (grant no. 23-71-00016, https://rscf.ru/project/23-71-00016/). The research also relied on the shared research facilities of the HPC computing resources at the Lomonosov Moscow State University.

References

Appleton P.N., Lanz L., Bitsakis T., et al., 2015, Astrophysical Journal, 812, 2, id. 118
Condon J.J., Helou G., Sanders D.B., et al., 1993, Astronomical Journal, 105, 5, p. 1730
He C., Xu C., Lisenfeld U., et al., 2024, Research in Astronomy and Astrophysics, 24, 5, id. 055005
Joshi B.A., Appleton P.N., Blanc G.A., et al., 2019, Astrophysical Journal, 878, 2, id. 161
Khoperskov A.V., Khrapov S.S., Sirotin D.S., 2024, Galaxies, 12, 1, id. 1
Khoperskov S., Zinchenko I., Avramov B., et al., 2021, Monthly Notices of the Royal Astronomical Society, 500, 3, p. 3870
Lisenfeld U., Xu C.K., Gao Y., et al., 2019, Astronomy & Astrophysics, 627, id. A107
Titov A.V. and Khoperskov A.V., 2022, Vestnik St. Petersburg University, Mathematics, 55, 1, p. 124

BAK 2024 MODERN ASTRONOMY: FROM THE EARLY UNIVERSE TO EXOPLANETS AND BLACK HOLES 300 years Russian Academy of Sciences

Retrograde fall of intergalactic gas onto the S-galaxy: polar rings and activity of galactic nuclei

S. Khrapov, A. Khoperskov, and N. Khrapov

Volgograd State University, 100 Prospect Universitetsky, Volgograd, 400062 Russia

Abstract. The dynamics of intergalactic gas accretion in a gas-rich spiral galaxy has been studied. We use numerical simulations to determine the conditions that lead to the formation of counter-rotating stellar and gas components within the galaxy and promote the influx of gas into the central part of the galaxy with a radius of less than one kiloparsec. The focus is on the dynamic interaction between the intergalactic flow and the gas-rich disc galaxy. The study of the mechanism by which gas is supplied to the central region to fuel the activity of galactic nuclei is a critical part of our work. The retrograde fall of the gas forms a massive, concentrated gas halo at the center of the galaxy, which may provide fuel for the activity of galactic nuclei. An angle of incidence of the gas flow of about 20 degrees to the galactic plane is the most effective and provides maximum gas concentration. Deviations from this angle lead to a decrease in the velocity of the gas flow into the galactic center. The prograde infall of intergalactic gas is incapable of cardinal disruption of the disc and does not result in an effective inflow of gas within 1 kpc radius. This accretion mode provides 100 times less gas mass within the 1 kpc radius compared to retrograde infall. An important additional result of retrograde accretion is the appearance of rotating gas rings at the periphery of the galaxy, which are mainly formed by falling intergalactic gas. The inclination of these rings with respect to the galactic plane varies widely, from 10 to 90 degrees, and depends on the angle of incidence of the intergalactic gas. The numerical simulations of counter-rotating stellar-gas discs cover all stages of the interaction with the falling intergalactic flow over a period of about 7 billion years.

Keywords: physics and evolution of galaxies: gas accretion; active galactic nuclei; polar rings

DOI: 10.26119/VAK2024.026

1 Introduction

Outer polar rings are a common galactic phenomenon, perhaps accounting for 1–3 % of S-galaxies (Moiseev et al. 2011; Mosenkov et al. 2024). There is strong observational evidence that the presence of polar rings correlates with central nuclear activity (La Marca et al. 2024). Mergers can enhance the influx of gas into the galactic center towards the supermassive black hole by several physical mechanisms (Blumenthal & Barnes 2018). Dust-obscured active galactic nuclei (AGN) are likely to be in the stage of rapid growth of the central supermassive black hole, so that powerful AGNs are fed by the resulting galaxy mergers (La Marca et al. 2024).

Analysis of some cosmological simulations does not show a clear connection between mergers and AGN activity (Sharma et al. 2024), creating additional intrigue in understanding the physical influence of strong interactions on AGN (Smirnov & Reshetnikov 2020). We have studied the efficiency of gas delivery to the central kiloparsec as a result of retrograde and prograde accretion of intergalactic gas under different conditions of matter infall into the galaxy.

The formation of polar rings is associated with galactic mergers. A special case is the interaction of a gas-rich spiral galaxy with an intergalactic gas flow (Khrapov & Khoperskov 2024). Our efforts are aimed at studying the conditions for the formation of tilted rings, as a more general class of polar rings (Moiseev et al. 2011; Mosenkov et al. 2024). We also note that the geometry and kinematics of the gas in the outer tilted ring can be an important tool for analyzing the properties of the dark halo (Combes et al. 2013).

2 Simulation results

The study uses numerical simulations of the dynamics of a collisionless N-body system (stars + dark matter) together with computational fluid dynamics using the method of Smoothed-particle hydrodynamics on a hybrid computing platform CPU + multi-GPUs (Khoperskov et al. 2021; Khrapov & Khoperskov 2024). We consider the accretion of intergalactic gas onto an S-galaxy with a sufficiently massive gas disk ($M_{\rm gas} \sim 0.2 M_{\rm stars}$). The accreting intergalactic matter is modeled by eight closely flying spheroidal gas clouds (discrete jet) with a velocity of ~ 100 km/s. The angle of incidence of the gas onto the galaxy, Θ_g, varies in different computational experiments. Both prograde and retrograde accretion types are considered. The most interesting results occur during retrograde infall, which leads to both the formation of tilted (polar) rings and hundredfold increase in the feeding of the supermassive black hole at the center of the galaxy.

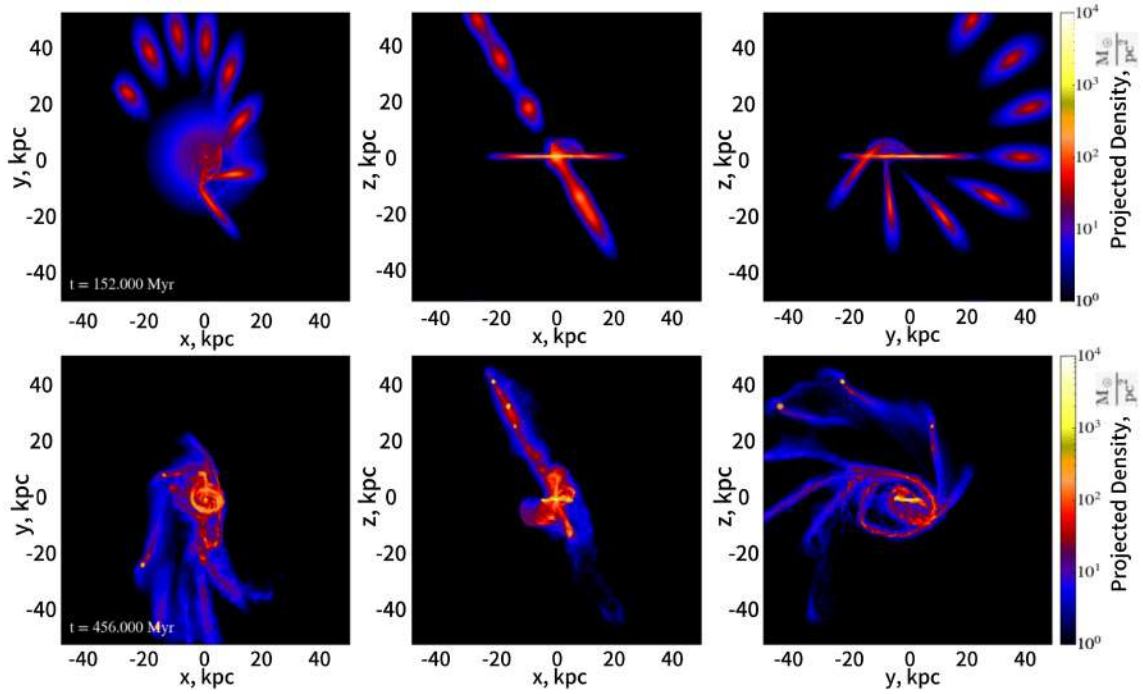

Fig. 1. Accretion of intergalactic gas onto a spiral galaxy in our numerical model. The moment of collision is shown in the top panel and the initial stage of polar ring formation is shown in the bottom panel (at ~ 300 Myr after the collision). Each frame has a size of 100×100 kpc along each projection (XY, XZ, YZ). The range of variation of the surface gas density along the line of sight is 1–10^4 $M_\odot/pc^2$.

Figure 1 shows the moment of the first impact of the intergalactic retrograde jet with $\Theta_g = 60^\circ$ into the gas disk of the model galaxy and the initial stage of the polar ring formation. The gas clouds of the intergalactic flow are strongly deformed by the tidal forces as they move towards the galaxy. The first impact and subsequent ones lead to the galactic and accreting gas to be ejected into intergalactic space. The remaining gas in galactic region forms an extended polar ring $\sim$ 40–50 kpc in size after approximately 300 Myr. In addition, a compact gas disk with high central density is formed in the central part of the galaxy. The dynamics of the polar gas ring, gas and stellar disks are shown in Fig. 2. A stable structure of the polar ring is formed by the time ~ 3 Gyr. Then there is a slow precession of its plane of rotation around the axis Z. A slow precession of the plane of the gas and stellar disks around the axes Y and X is observed.

The main results of the simulation are summarized in Fig. 3. Panel *a* shows the efficiency of gas delivery into the central parsec of the galaxy as a function of the

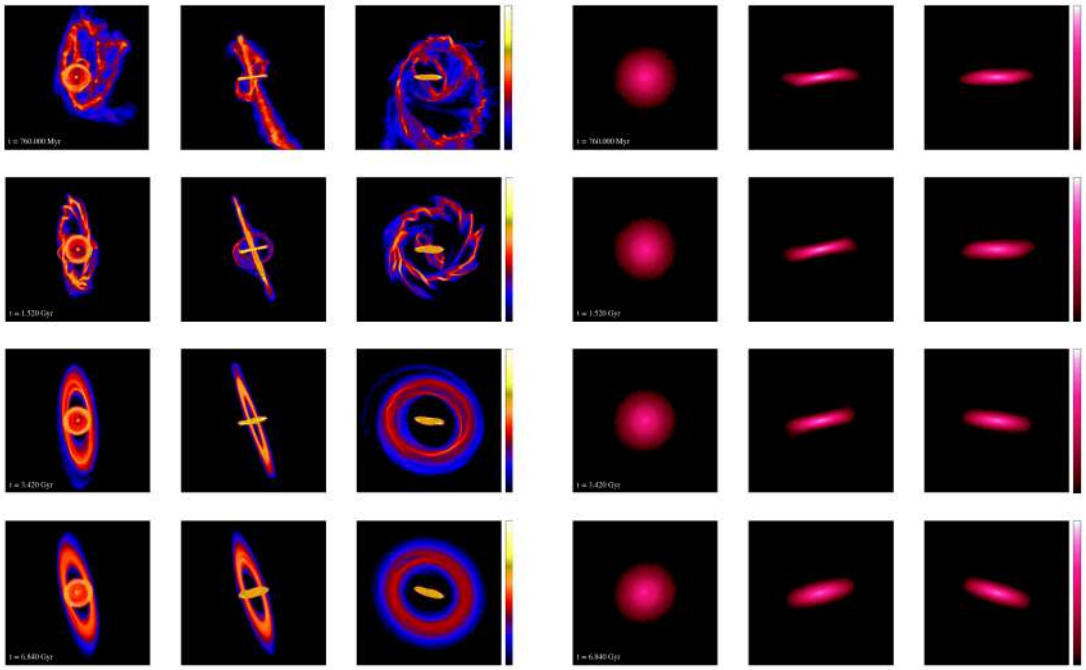

Fig. 2. Evolution of the polar gas ring in the galaxy over the time interval from 760 Myr to 6.84 Gyr. The gas subsystem of the galaxy (left) and the stellar disk (right) are shown. The frame has a size of 50×50 kpc along each of the projections (XY, XZ, YZ). The range of variation of the surface density along the line of sight is within 1–10^4 $M_\odot/pc^2$ for the gas and — 10–10^4 $M_\odot/pc^2$ for the stars.

angle of attack of the extragalactic flow Θ_g. Comparing prograde and retrograde infall, the mass flow $M_{\rm core}$ into the central parsec ($R_{\rm core} = 1\,$kpc) is a factor of 100 larger in the second case than in the first. Only the counter-rotating flow is able to be an efficient fuel source for the central galactic activity. The efficiency of the co-rotating accreting flow is small.

The angle of incidence of the gas on the galaxy Θ_g is one of the key factors determining the influx of gas mass into the core region $M_{\rm core}$. Very small angles produce glancing blows that facilitate the efficient removal of the angular momentum of the gas component. Large angles of incidence ($\Theta_g \gtrsim 40°$) change the interaction pattern and enhance the ejection of gas from the stellar disk region. Therefore, the influx of gas into the central kiloparsec is significantly reduced and relationship $M_{\rm core}(\Theta_g = 20°)/M_{\rm core}(\Theta_g = 45°) \simeq 100$. The best conditions for gas supply to the galactic center are obtained at an angle of $\Theta_g \simeq 20°$.

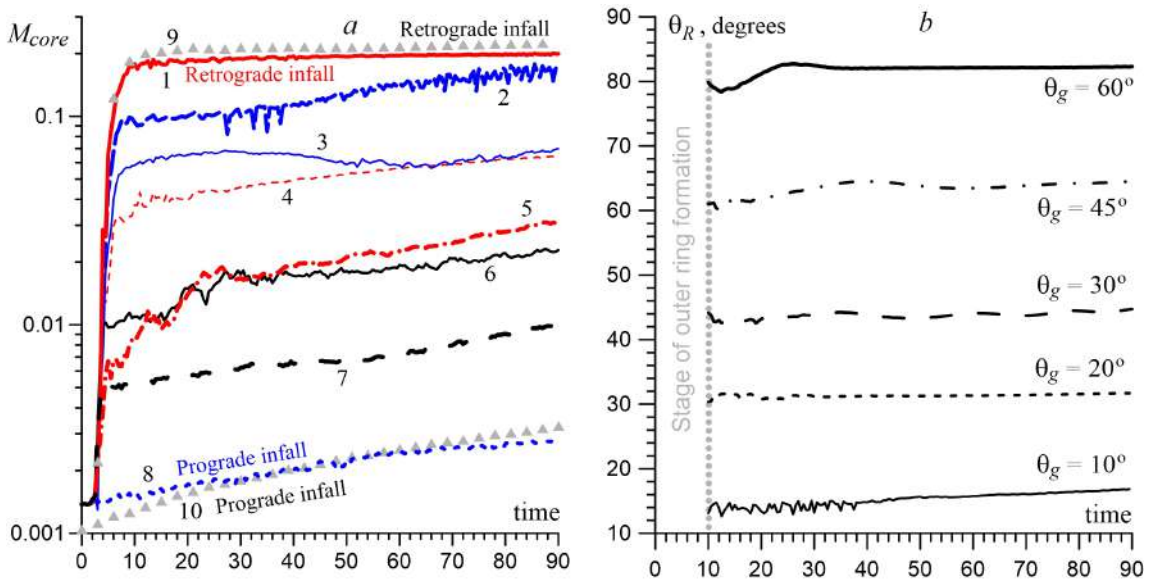

Fig. 3. *a* — Dependence of the gas mass inside 1 kpc for different angles of attack of the accreting intergalactic gas flow. Models of the bulgeless galaxy with retrograde infall (Khrapov & Khoperskov 2024): $\Theta_g = 20°$ (curve 1), $\Theta_g = 10°$ (2), $\Theta_g = 5°$ (3), $\Theta_g = 30°$ (4), $\Theta_g = 40°$ (5), $\Theta_g = 45°$ (6), $\Theta_g = 60°$ (7); prograde infall model at $\Theta_g = 20°$ (8); models with the bulge at $\Theta_g = 20°$ (curves 9 and 10). *b* — Outer gas ring tilt angles Θ_R vs. time (t) for different Θ_g.

The outer ring formation stage lasts for approximately 600–800 Myr (see vertical dotted line in Fig. 3b, $t = 10 \rightarrow 760$ Myr). Then the tilt angle of the gas ring Θ_R changes very little over 6 billion years in the absence of other external influences. The tilt angle of the outer ring with respect to the plane of the main galaxy is always greater than the angle of incidence of the initial gas flow, $\Theta_R > \Theta_g$. The ratio of the angles $\alpha_{Rg} = \Theta_R/\Theta_g$ is between 1.3–1.7 and depends on the angle Θ_g. We focus on the fact that the gas flow at the angle $\Theta_g > 60°$ forms a polar ring at angle $\Theta_g > 80°$. Thus, we have predominantly perpendicular external structures in the form of typical polar rings.

3 Summary

We studied the dynamics of the fall of an intergalactic gas flow onto a gas-rich spiral galaxy. This accretion regime can lead to two observed phenomena simultaneously. The result is both an additional influx of gas into the region of the central supermassive black hole and the formation of outer gas rings similar to polar-ring systems.

The angle of incidence of the intergalactic gas flow onto the spiral galaxy (Θ_g) is a key parameter in our study. The efficiency of the gas inflow into the AGN region is very sensitive to the angle Θ_g and is maximal at $\Theta_g \simeq 20°$. The presence of a stellar bulge in the main galaxy has little effect on the gas inflow into the central kiloparsec. The additional mass in the center of the galaxy is approximately 100 times greater for the retrograde infall of intergalactic gas than for the prograde case. This is due to more favorable conditions for the removal of angular momentum in the gas disk.

The outer inclined gas rings are a typical result of the considered accretion of intergalactic matter at angles of incidence $\Theta_g = (10–90)°$ in all numerical experiments with retrograde rotation. The angle between the outer ring and the main disk Θ_R depends on the value of Θ_g, but the condition $\Theta_R \geq 1.3 \cdot \Theta_g$ is always satisfied. Falling gas onto the galaxy with $\Theta_g = (55–90)°$ ensures the formation of a polar ring with $\Theta_R \simeq 90°$.

Funding

This work was supported by the Russian Science Foundation (grant no. 23-71-00016, https://rscf.ru/project/23-71-00016/). The research also relied on the shared research facilities of the HPC computing resources at the Lomonosov Moscow State University.

References

Blumenthal K.A. and Barnes J.E., 2018, Monthly Notices of the Royal Astronomical Society, 479, p. 3952

Combes F., Moiseev A., Reshetnikov V., Astronomy & Astrophysics, 2013, 554, id. A11

Khoperskov S., Zinchenko I., Avramov B., et al., 2021, Monthly Notices of the Royal Astronomical Society, 500, 3, p. 3870

Khrapov S.S. and Khoperskov A.V., 2024, Open Astronomy, 33, 1, id. 20220231

La Marca A., Margalef-Bentabol B., Wang L., et al., 2024, arXiv:2407.18238 [astro-ph.GA]

Moiseev A.V., Smirnova K.I., Smirnova A.A., et al., 2011, Monthly Notices of the Royal Astronomical Society, 418, 1, p. 244

Mosenkov A.V., Bahr S.K.H., Reshetnikov V.P., et al., 2024, Astronomy & Astrophysics, 681, id. L15

Sharma R.S., Choi E., Somerville R.S., et al., 2024, Monthly Notices of the Royal Astronomical Society, 527, 3, p. 9461

Smirnov. D.V. and Reshetnikov V.P., 2020, Astronomy Letters, 46, 8, p. 501

MODERN ASTRONOMY: FROM THE EARLY UNIVERSE TO EXOPLANETS AND BLACK HOLES

Estimation of the Hubble constant from the scatter of the fundamental plane distances of groups and clusters of galaxies (71.1 ± 2.8 km s^{-1} Mpc^{-1})

F. Kopylova and A. Kopylov

Special Astrophysical Observatory of the Russian Academy of Sciences, Nizhny Arkhyz, 369167 Russia

Abstract. To determine the peculiar velocities of galaxy clusters relative to the Hubble Flow, we need to measure the distances of galaxy systems using some method that is sensitive to their distances. The fundamental plane (FP) of early-type galaxies is one such method and is widely used for such problems. Using the FP, we determined the angular distances of 140 groups and galaxy clusters in the local Universe ($z < 0.15$) and constructed a Hubble diagram between distances and radial velocities in the CMB reference frame in the framework of the flat Λ CDM model ($\Omega_{\rm m}$=0.3, $H_0 = 70$ km s^{-1} Mpc^{-1}). We obtained the average deviation of the relative distances γ from the Hubble dependence for this model $< \Delta\gamma >= -0.0066 \pm 0.0023$ ($N = 140$). The minimum deviation we found corresponds to the value of the Hubble constant 71.1 km s^{-1} Mpc^{-1}. We found that the logarithmic standard scatter of the relative distances of groups and clusters of galaxies on the Hubble diagram (subtracting peculiar velocities) is ± 0.0173 ($N = 140$), which corresponds to the deviation of the Hubble constant 71.1 ± 2.8 km s^{-1} Mpc^{-1}. For a sample of galaxy clusters ($N = 63$) with X-ray luminosity in the range (0.15–4)$\times 10^{44}$ erg/s, we obtained 71.1 ± 2.1 km s^{-1} Mpc^{-1}.

Keywords: galaxies: clusters, elliptical and lenticular, fundamental parameters, distances and redshifts; cosmology: large-scale structure of universe

DOI: 10.26119/VAK2024.027

1 Introduction

The gravitational attraction of the elements of a large-scale structure is the main cause of the peculiar velocity of galaxies, clusters of galaxies. The peculiar velocity of galaxies at small z can be estimated as $V_p \approx cz_{\rm obs} - cz_{\rm H} \approx cz_{\rm obs} - H_o D$, where D is the comoving distance of the galaxy, H_o is the Hubble constant. To determine the peculiar velocities of galaxy clusters relative to the Hubble Flow, it is necessary to measure the relative distances of galaxy systems using some distance sensitive method. The fundamental plane of early-type galaxies (Dressler et al. 1987; Djorgovski & Davis 1987) is widely used to study the properties of galaxies and to determine the relative distances and peculiar velocities of galaxy clusters (for example, Hudson et al. 1999; Batiste & Batuski 2013).

Previously, using the FP for a large sample of galaxy systems ($z < 0.1$), we determined the relative distances and peculiar velocities of galaxy clusters in the Leo, Hercules, Bootes, Coropa Borealis, and Ursa Major superclusters based on SDSS (DR4, 8 data) (Kopylova & Kopylov 2007, 2014, 2017). In addition to superclusters of galaxies, our sample included groups and clusters of galaxies (the most distant galaxy systems in our sample) located in the region of the large void in the distribution of rich Abell clusters (Giant Void, $\alpha \approx 13^h, \delta \approx 40^\circ, < z > \approx 0.107$, the maximum diameter is equal to 214 Mpc) (Kopylov & Kopylova 2002).

It is known that in the expanding Universe the surface brightness changes as $SB \propto (1+z)^{-4}$ (z is the redshift of the galaxy, SB is the surface brightness of the the galaxy): a cosmological dimming of the surface brightness occurs. The factor $(1+z_{\rm H})^{-2}$ is due to the cosmological expansion of the Universe, the factor $(1+z_{\rm obs})^{-2}$ is due to relativistic effects. This gives the correction for the cosmological dimming of the surface brightness of galaxies in an expanding Universe, for example Mohr & Wegner (1997) — $C = 5\log(1+z_{\rm obs}) + 5\log(1+z_{\rm H})$. In this paper we show that if we take into account only the first part of the correction $5\log(1+z_{\rm obs})$, caused by the motion of galaxies, then the evolution of the average surface brightness with z is $Q_r = 3.76$ mag/arcsec^2.

We will also look at a sample of identical measurements of the relative distances of 140 groups and clusters of galaxies as a whole. The work was carried out by us using data from the SDSS[1] (Sloan Digital Sky Survey Data Realease 7, 8) and NED[2] (NASA Extragalactic Database).

[1] http://www.sdss.org
[2] http://nedwww.ipac.caltech.edu

2 The fundamental plane distances of groups and clusters of galaxies

Our sample contains 140 groups and clusters with the number of early-type galaxies grater than 3 within our chosen radius R_{200}. The measurement of the dynamical parameters of galaxy clusters is described in detail, for example, in Kopylova & Kopylov (2017). The selection of early-type galaxies within the radius R_{200} was done in the same way for all clusters of galaxies. We applied the following criteria to the parameters of the galaxies (as in Kopylova & Kopylov 2017). Using the above criteria, we selected 2654 early-type galaxies in galaxy systems and constructed a common fundamental plane for them in the comoving coordinate system using the least squares method. The FP equation is: $\log R_e(\mathrm{kpc}) = (0.991 \pm 0.124)\log\sigma + (0.318 \pm 0.020) < \mu_e > +\gamma$, where R_e is the effective radius of the galaxy in kiloparsecs, $< \mu_e >$ is the mean effective surface brightness within this radius, σ is the central dispersion of the radial velocities of the stars, and γ is the zero-point of the FP, which varies with distance when $\log R_e$ is measured in arcseconds. The zero-point of our sample was obtained for the accepted standard model ΛCDM and is equal to $\gamma = -8.066 \pm 0.003$. The standard deviation of the FP zero-point is 0.071, which corresponds to a $\sim 16\%$ error in determining the distance of one galaxy. The formal error in determining the cluster distance depends on the number of galaxies used and varies from 2% to 12%.

Galaxy cluster angular distances γ ($\log R_e$ in arcsec) are converted to redshifts z_{FP} using the Peebles approximation (Peebles 1993): $D = (cz/H_o\,(1-0.225z)/(1+z)$. Part of the surface brightness dimming of the galaxies ($5\log(1+z_{\mathrm{H}})$) is taken into account in the zero-point of the FP. Figure 1 shows the Hubble diagram (upper panel) between the relative distances — γ zero-points and redshifts (CMB). Clusters around the Giant Void (the most distant galaxy systems in our sample) are shown as empty blue circles. It can be noted that in Fig. 1 the Hubble relation correctly describes the FP distances of groups and clusters of galaxies, starting from the Coma cluster ($z = 0.024$) to the Giant Void ($z < 0.15$). The lower panel shows the residuals of the Hubble law.

The given Hubble diagram makes it possible to determine the corresponding redshift of the z_{FP} cluster from the observed individual distance in arcseconds, $\log R_e$. The peculiar velocities in the comoving coordinate system are equal to the difference between the spectroscopic and photometric redshifts, that is, $V_{\mathrm{pec}} = c\,(z_{\mathrm{CMB}} - z_{\mathrm{FP}})/(1 + z_{\mathrm{FP}})$, where c is the speed of light, and z_{CMB} is the redshift of the cluster relative to the CMB, z_{FP} is the redshift of the cluster corre-

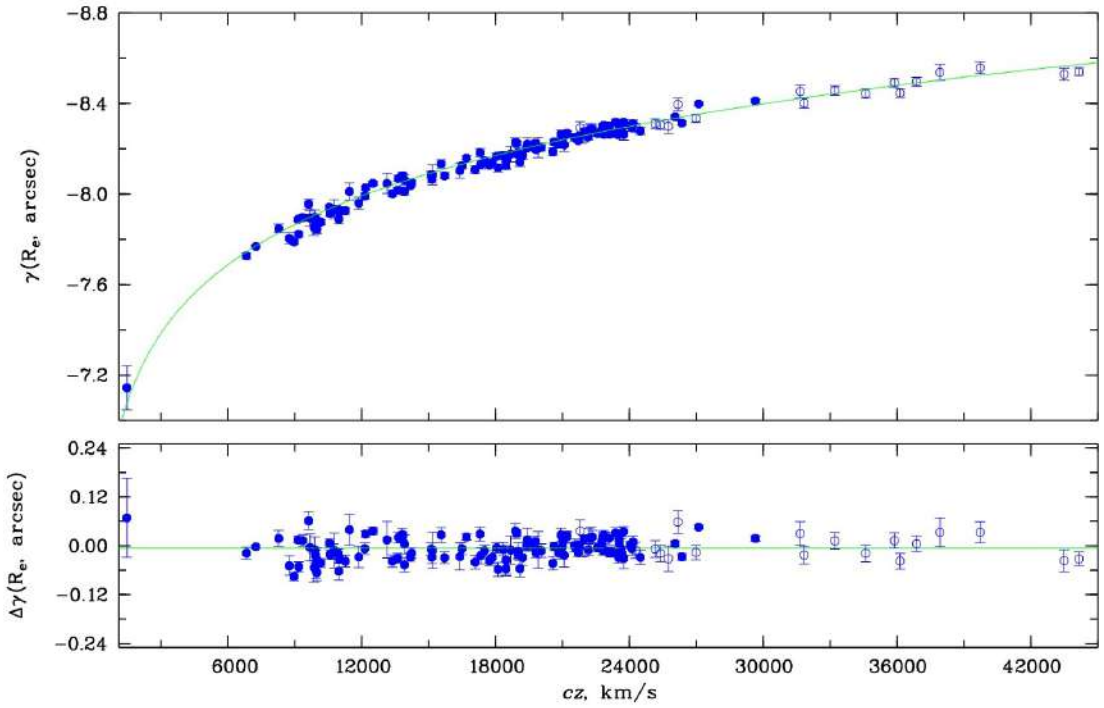

Fig. 1. FP distances of 140 groups and clusters of galaxies, zero-points of the fundamental plane γ, as a function of radial velocity (CMB) (Hubble diagram). Empty circles show the systems of galaxies ($N = 19$) around the Giant Void. The thick line shows the expected Hubble dependence in the ΛCDM cosmological model with $\Omega_m = 0.30$. The lower curve shows the deviations from the Hubble dependence.

sponding to the distance determined from the FP. Peculiar velocities of systems of galaxies are determined in Kopylova & Kopylov (2024).

The sample of groups and clusters of galaxies with more than 7 members has a peculiar velocity relative to the CMB frame $V_{\rm pec} = +170 \pm 90$ km/s. For a sample of clusters in the interval $L_{\rm X} = (0.151–4) \times 10^{44}$ erg/s we have obtained $V_{\rm pec} = -80 \pm 100$ km/s. ($N = 63$). The standard deviations of the radial peculiar velocities with quadratic allowance for the errors are $< V^2_{\rm pec} >^{1/2} = 714 \pm 7$ km/s and $< V^2_{\rm pec} >^{1/2} = 600 \pm 7$ km/s. The outflow rates of clusters of galaxies from the void are about $\sim 250 \pm 410$ km/s. The average peculiar velocity of 5 superclusters of galaxies is $+240 \pm 250$ km/s.

3 Hubble diagram and deviations from it

There is a contradiction in the definition of the constant H_o, one of the fundamental cosmological parameters. The constant H_o estimated on the local distance ladder (Cepheid-supernova distance ladder) does not agree with the value extrapolated from the CMB data, assuming the standard cosmological model, 74.0 ± 1.4 km s^{-1} Mpc^{-1} (Riess et al. 2019) and 67.4 ± 0.5 km s^{-1} Mpc^{-1} (Planck Collaboration 2020) respectively.

In Fig. 1 the thick green line shows the Hubble relation between the radial velocity in the CMB reference frame and the angular FP distance of groups and clusters of galaxies. The line corresponds to the flat ΛCDM model $\Omega_\Lambda = 0.7$, $\Omega_\mathrm{m} = 0.3$ and to the Hubble constant $H_0 = 70$ km s^{-1} Mpc^{-1}. The bottom figure shows the deviations from the Hubble law. We have obtained the average deviation from the Hubble law of the sample ($N = 140$) $< \Delta\gamma > = -0.0066 \pm 0.0023$. The corresponding logarithmic standard scatter is 0.0275. For a sample in the interval $L_\mathrm{X} = (0.151 - -4) \times 10^{44}$ erg/s, we obtained the average deviation from the Hubble law
$< \Delta\gamma > = 0.0017 \pm 0.0028$ ($N = 63$) with a standard scatter 0.0224, corresponding to a deviation of 5.11% ($\pm$3.6 km s^{-1} Mpc^{-1}). If we subtract the peculiar velocities of groups and clusters of galaxies in the Fig 1, then the distance measurement errors actually determine the scatter in the Hubble diagram. In this case, the logarithmic standard scatter is 0.0173 for the whole sample ($N = 140$) and is equal to the Hubble constant deviation of $\pm$2.8 km s^{-1} Mpc^{-1}). For a sample in the interval $L_\mathrm{X} = (0.151–4) \times 10^{44}$ erg/s, we found that the logarithmic standard scatter is 0.0130 for ($N = 63$) and corresponds to the Hubble constant deviation of $\pm$2.1 km s^{-1} Mpc^{-1}. The minimum standard scatter corresponds to the value of the Hubble constant 71.1 km s^{-1} Mpc^{-1}.

4 Conclusions

In the course of this work we found that the peculiar velocities of most galaxy systems are small, but show a dependence on their X-ray luminosity. We have found that the average peculiar velocity of five galaxy superclusters of galaxies is +240 $\pm$ 250 km/s, and the outflow rate of groups and clusters of galaxies from the Giant Void, measured from 19 galaxy systems, is $\sim 250 \pm 410$ km/s. We have measured the average deviation from the Hubble relation between distance and radial velocity (within the flat ΛCDM model) of groups and clusters of galaxies (without peculiar velocities). The logarithmic standard scatter is $\pm$0.0173, which corresponds to the deviation of the Hubble constant $H_0 = 71.1 \pm 2.8$ km s^{-1} Mpc^{-1}. For a sample with

$L_X = (0.151–4) \times 10^{44}$ erg/s we obtained a deviation with a standard scatter corresponding to the deviation of the Hubble constant $H_0 = 71.1 \pm 2.1$ km s^{-1} Mpc^{-1}.

References

Batiste M. and Batuski D.J., 2013, Monthly Notices of the Royal Astronomical Society, 436, 4, p. 3331

Djorgovski S. and Davis M., 1987, Astrophysical Journal, 313, p. 59

Dressler A., Lynden-Bell D., Burstein D., et al., 1987, Monthly Notices of the Royal Astronomical Society, 313, p. 42

Hudson M.J., Smith R.J., Lucey J.R., et al., 1999, Astrophysical Journal, 512, 2, p. L79

Kopylov A.I. and Kopylova F.G., 2002, Astronomy and Astrophysics, 382, p. 389

Kopylova F.G. and Kopylov A.I., 2007, Astronomy Letters, 33, 4, p. 211

Kopylova F.G. and Kopylov A.I., 2014, Astronomy Letters, 40, p. 595

Kopylova F.G. and Kopylov A.I., 2017, Astrophysical Bulletin, 72, 4, p. 363

Kopylova F.G. and Kopylov A.I., 2024, Astronomy Reports, 68, 8, p. 761

Mohr J.J. and Wegner G., 1997, Astronomical Journal, 114, p. 25

Peebles P.J.E, 1993, Principles of Physical Cosmology, Princeton University Press

Planck Collaboration, 2020, Astronomy and Astrophysics, 641, id. A6

Riess A.G., Casertano S., Yuan W., et al., 2019, Astrophysical Journal, 876, 1, p. 85

VAK 2024 MODERN ASTRONOMY: FROM THE EARLY UNIVERSE TO EXOPLANETS AND BLACK HOLES 300 years Russian Academy of Sciences

Fundamental plane of groups and clusters of galaxies: distances and peculiar velocities of superclusters of galaxies on small scales

F. Kopylova and A. Kopylov

Special Astrophysical Observatory of the Russian Academy of Sciences, Nizhny Arkhyz, 369167 Russia

Abstract. We have studied the relationships between the basic properties of 172 groups and clusters of galaxies based on archival data from the SDSS, 2MASX, and NED catalogs. The measured parameters ($\log R_e$, $<\log I_e>$ and $\log \sigma$ of the clusters of galaxies determine the fundamental plane (FP) in the near infrared:
$\log R_e = 0.98(\pm0.06)\ \log \sigma - 0.56(\pm0.04)\ <\log <I_e>> + 3.57(\pm0.07)$, which can be used to determine the distances of the galaxy systems. The root-mean-square devia-tion of the FP zero-point is 0.07, which corresponds to an error of 16% in determining the distance of the group or cluster of galaxies. For the first time we have measured the peculiar velocities of the superclusters of galaxies. The mean peculiar velocity of the 5 superclusters of galaxies relative to the CMB is $+75 \pm 360$ km/s.

Keywords: galaxies: groups and clusters: distances and redshifts; cosmology: large-scale structure of universe

DOI: 10.26119/VAK2024.028

1 Introduction

The gravitationally bound systems — globular clusters of stars, galaxies, clusters of galaxies — obey the virial theorem in the form $M \propto R\sigma^2$, have similar relationships between parameters, for example, the fundamental plane. The FP is the empirical relationship between three observable properties of early-type galaxies: physical size (R), radial velocity dispersion along the line of sight (σ), and surface brightness. For the first time, the FP of galaxy clusters themselves has been constructed using photometric observational properties for a sample of 16 rich galaxy clusters ($z < 0.2$) (Schaeffer et al. 1993).

The aim of this work is to construct a FP between the parameters of 172 groups and clusters of galaxies that have redshifts in the range $0.012 < z < 0.10$ and the radial velocity dispersions 200 km/s $< \sigma <$ 1100 km/s. The properties we determine, L_K ($< \log I_e >$), σ, R_e (found from $N_{\rm tot}/2$) and the relations between them (the fundamental plane), give us the opportunity to measure the relative distances of galaxy clusters in superclusters, the galaxy superclusters themselves, and to find the standard logarithmic scatter of groups and clusters of galaxies on the Hubble diagram. The work was carried out by us using data from the catalogs SDSS, 2MASS XSC, NED.

2 Method

In the paper Kopylova & Kopylov (2016) we showed that in galaxy clusters it is possible to find an effective radius that contains half of the galaxy halos, in order to construct a common FP for both poor groups and rich galaxy clusters. To do this, for groups/clusters of galaxies, we determine the splashback radius $R_{\rm sp}$, following the methodology outlined in Kopylova & Kopylov (2016), and find the number of galaxies within it, corrected for the background (determined by the slope of the straight line). The determination of the total luminosity of a galaxy cluster using the luminosity function (LF) within a selected radius consists of two steps, described in detail in Kopylova & Kopylov (2024): first the LF is normalised to the observed number of galaxies, then it is extrapolated into the region of faint magnitudes to a selected limit.

Figure 1 shows the received FP of our entire sample of 172 groups and clusters of galaxies, and individual members of each galaxy supercluster are highlighted with large circles. Red circles correspond to groups of galaxies, blue ones to clusters of galaxies. The line shows the regression relation obtained from galaxy clusters with $\sigma > 400$ km/s. It looks like: $\log R_e = 0.98(\pm0.06)\log\sigma - 0.56(\pm0.04)\langle\log I_e\rangle + 3.57(\pm0.07)$.

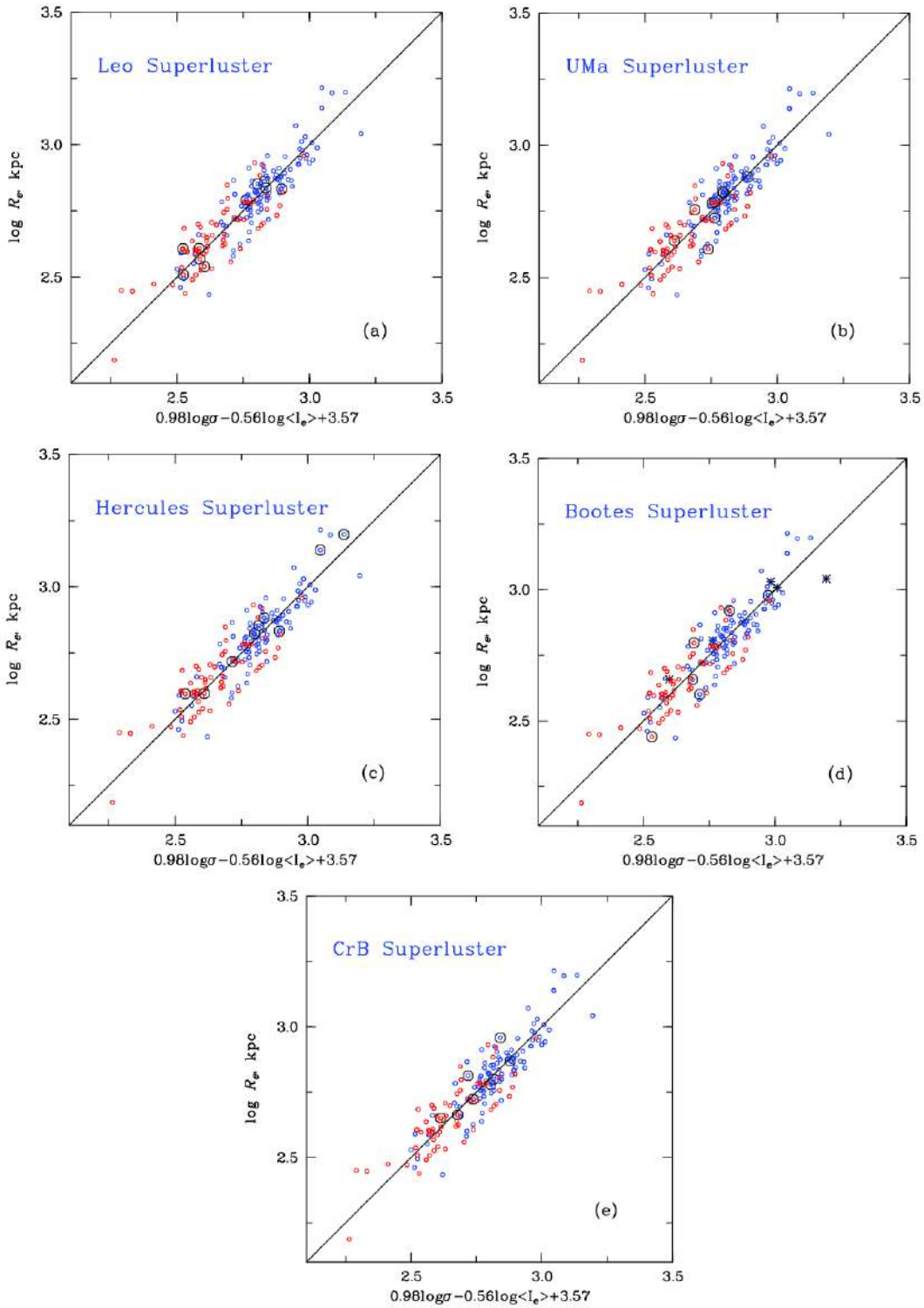

Fig. 1. Fundamental plane of 172 groups and clusters of galaxies in the IR region along the long axis, $\log R_e$. Members of the superclusters of galaxies Leo, Ursa Major, Hercules, Bootes, Corona Borealis are circled.

This ratio has a small scatter and is suitable for measuring the relative distances of galaxy systems when $\log R_e$ is measured in arcseconds. Thit means that the zero point of the FP changes depending on the distance to the galaxy systems.

In practice, the difference between the cluster zero point $\gamma_{\rm cl}$ and the overall mean zero point γ is used to calculate photometric redshifts: $z_{\rm FP} = z_{\rm CMB} \times 10^{(\langle\gamma\rangle - \gamma_{\rm cl})}$. Then the peculiar velocities of the galaxy clusters in the comoving system are equal to the difference between the spectroscopic and photometric redshifts: $V_{\rm pec} = c\,(z_{\rm CMB} - z_{\rm FP})/(1 + z_{\rm FP})$. We have found that the average peculiar velocity of galaxy superclusters relative to the CMB is $V_{\rm pec} = +75 \pm 360$ km/s.

3 Results

In this work we constructed the fundamental plane of 172 clusters and groups of galaxies and show that the FP is consistent with the results of other authors using other methods (Schaeffer et al. 1993). The main results of this study are given below: the general FP of 172 groups and clusters of galaxies in the K-band has the form: $L_K = R_e^{0.64\pm0.08}\sigma^{1.45\pm0.06}$ with $rms = 0.13$.
For the first time, the FPs of members of 5 superclusters of galaxies (Leo, Hercules, Ursa Major, Bootes, Corona Borealis) have been constructed, and the relative distances and peculiar velocities of the groups/clusters of galaxies have been determined.

References

Kopylova F.G. and Kopylov A.I., 2016, Astrophysical Bulletin, 71, 3, p. 257
Kopylova F.G. and Kopylov A.I., 2024, Astrophysical Bulletin, 79, 1, p. 1
Schaeffer R., Maurogordato S., Cappi A., et al., 1993, Monthly Notices of the Royal Astronomical Society, 263, p. L21

MODERN ASTRONOMY: FROM THE EARLY UNIVERSE TO EXOPLANETS AND BLACK HOLES

Analysis of corotation radii in spiral galaxies

V. Kostiuk[1], A. Marchuk[2,3], and A. Gusev[1]

[1] Sternberg Astronomical Institute, Lomonosov Moscow State University, 13 Universitetsky pr., Moscow, 119234 Russia

[2] Central (Pulkovo) Astronomical Observatory, Russian Academy of Sciences, 65/1 Pulkovskoye chaussee, St. Petersburg, 196140 Russia

[3] Saint Petersburg State University, 28 Universitetsky pr., St. Petersburg, 198504 Russia

Abstract. The corotation radius is one of the key parameters of a galaxy, since it not only influences the course of the dynamical processes, but also allows to determine the nature of the spiral structure. A clearly defined corotation radius indicates the presence of a spiral density wave, while an uneven distribution of positions suggests a transient nature to the spiral structure. In this study, we collected measurements of the corotation radius from the literature for 547 galaxies, obtained using 12 different methods. After analyzing the collected data, we found that only a quarter of the galaxies had consistent measurements of the resonance positions within the error limits when at least two different methods were used. As an indicator of the consistency of the collected measurements, we considered two values for each galaxy: the fraction of total error coverage and a dimensionless parameter related to the separation of average values. These quantities were found to be independent of the number of measurements taken, the methods used, and the values of the rotation radius with large uncertainties. In addition, no relationship was found between our results and the distance to the galaxy or its morphological type. Furthermore, we have shown that the consistency measure between the corotation radii does not depend on the type of spiral structure or the presence of a bar. Therefore, the obtained results can be explained by the different nature of the spiral arms in galaxies from the collected sample, where a dominant number of objects have a transient structure. As an example, we have examined in detail three galaxies to which several methods for estimating the corotation radius were applied. After a detailed analysis, we found that all three galaxies may have different nature of spiral arms. NGC 3686 shows a density wave, while NGC 4321 has dynamic (transient) spirals. The spiral structure of NGC 2403, on the other hand, most likely consists of several different spiral modes.

Keywords: galaxies: spiral, kinematics and dynamics

DOI: 10.26119/VAK2024.029

1 Introduction

More than 70% of the galaxies observed in the Local Universe have a spiral structure, which has long captured the attention of astrophysicists. Despite extensive research on these structures, a comprehensive understanding of their nature is still lacking. Currently, two opposing theories offer possible explanations for the nature of spiral structures. One of these, known as the quasi-stationary density wave theory (Lin & Shu 1964), has received significant attention. This theory proposes that spiral arms are manifestations of density waves propagating through the galactic disk. The key assumption of this theory is that the angular velocity of the spiral density wave remains constant relative to the distance from the galactic center. The specific point where the angular velocities of the disk and the spiral pattern coincide is called the corotation radius (R_c). In contrast, the transient spiral theory considers the spiral structure to be dynamic in nature (Sellwood & Carlberg 1984). According to this theory, the angular velocity of the spiral pattern changes in a manner similar to the angular velocity of the disk rotation. Consequently, the positions of the corotation radii can be found at multiple locations throughout the disk of the galaxy, rather than being limited to a single fixed position.

The aim of this study is to collect corotation radius measurements from the literature, obtained by different methods, and to analyze the consistency of the gathered R_c positions for each galaxy. This approach allows not only to find "reliable" positions of corotation resonances, but also to determine which mechanism of spiral formation is most common among disk galaxies. In addition, we have used several methods to estimate corotation for selected galaxies in this study. The measurements we obtained confirmed some positions and allowed us to draw conclusions about the nature of the spiral arms in these galaxies.

2 Data and methods

In this study, we gathered a dataset of 1711 corotation positions for 547 galaxies, estimated using 12 methods.[1] For 300 of these objects more than one corotation position was found. Note that a reliable determination of corotation requires at least two different methods to be used on the same object. This requirement was met for 161 of the galaxies in our sample.

The methods used to estimate corotation radii were divided into conditional groups, based on their main assumptions and techniques. Thus, according to the *P-D (Puerari–Dottori)* and *offset* methods (shown in dark gray and red in Fig. 1,

[1] This dataset is publicly available on GitHub https://github.com/ValerieKostiuk/CRs_dataset

right), there is an angular offset between stellar populations of different ages, and the corotation radius is located at the point where this value changes sign. The *width* method analyzes the azimuthal distribution of matter along the spirals. The *T-W (Tremaine–Weinberg)* (dark blue) method allows us to obtain the pattern speed directly, while the *model* (purple) method adjust this value until the simulated galaxy has the same morphological features as the real one. The *potential-density* (cyan) and metallicity (green) methods use the radial profiles of the phase shift and the abundances. R_c of gathered sample have also been estimated by analyzing residual velocities (*F-B (Font–Beckman)*: gray) and morphological features (*morph (morphological)*: yellow). Detailed descriptions of the listed methods are presented in Kostiuk et al. (2024).

3 Consistency analysis

We examined the distributions of corotation radii for galaxies with at least two measurements obtained by different methods (examples of such distributions are shown in the right panel of Fig. 1). About 25% of these galaxies have a visually consistent R_c, while the remaining galaxies show no consistency in their distributions. This can be explained by the recurrence of spiral structure in some galaxies. To investigate the other factors causing these results, we calculated the total coverage error Σ_{err} in determining the R_c position and the measure of consistency. The first quantity is defined as the sum of measurement uncertainties when R_c positions intersect within the error limits, otherwise as the addition of the error covers. To compare objects of different sizes, we normalized Σ_{err} to the optical radius (r_{25}). The second one is calculated as the ratio of the average difference between the measurements to the square root of the average variance. The larger this value, the greater the discrepancy in the corotation radius positions for a given galaxy. Note that the magnitude of this this dimensionless parameter can reach high values in some cases due to small error values.

Figure 1 (left) shows the distributions of the total coverage error and the measure of consistency for each object in our dataset. This figure visually separates the sample into different groups. Galaxies with a well-defined corotation radius are located in the bottom left corner of this plot. Distributions with an intermediate value of Σ_{err}/r_{25} may have multiple corotation radii (see the distribution for NGC 1042 on the right panel). Other points represent objects for which the estimated corotation radii from different methods do not agree. The top and bottom panels in Fig. 1 illustrate how measurements can be inconsistent with large and small coverage errors, respectively. Before drawing any serious conclusions about the dominant mechanism

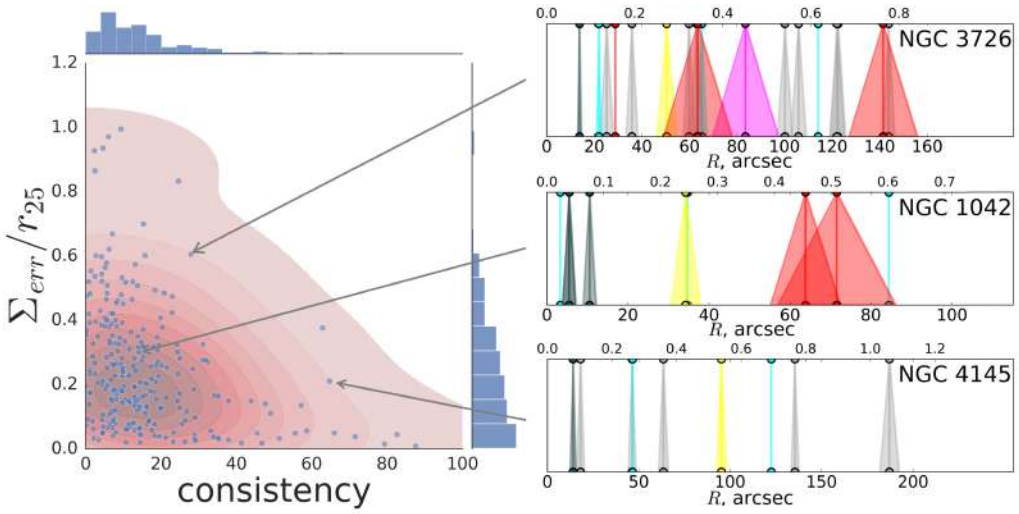

Fig. 1. The left panel shows the relationship between the error coverage fraction and the consistency measure. Each point represents a galaxy with at least two measurements. The histograms of the corresponding values are shown on the right and top. On the right panel are examples of R_c distributions for the objects indicated by the arrows. The shaded areas show the error of each value (base of the cone). Their color indicates the method used (see text for details). The lower scale indicates their positions in arcseconds, and the upper scale indicates their positions in units of the optical radius.

of spiral formation, we tested other reasons that might affect the obtained discrepancy. We found that the number of measurements did not affect the magnitude of the consistency. In addition, we examined the validity of the measurements and the correctness of the methods used, and found that the discrepancy did not disappear after excluding either measurements with high uncertainties or R_c values obtained by one method or another. Furthermore, we found no dependence on the Hubble type or the presence of a bar. Our analysis also showed that inconsistencies in the measurements were not related to the type of spiral structure, which challenges the idea that the type of spiral structure can determine its origin.

4 Investigation of individual galaxies

Although the results obtained can be better explained by transient spirals in a significant fraction of galaxies, it is still possible that a different combination of the above reasons could be realized for each object. Therefore, it would be more appropriate to study galaxies individually. For this reason, we selected three objects from our sample, NGC 3686, NGC 4321, and NGC 2403, which have completely different pat-

terns of corotation radii distributions. We have not only verified each measurement to ensure its validity, but also implemented and applied the *offset*, *metallicity* and *F-B* methods to the observational data of the selected galaxies.

According to Fig. 2, the top panel shows that the combination of measurements of NGC 3686 obtained in this study and from the literature clearly shows consistent corotation positions estimated by 5 different methods. The estimate of the R_c position was made by fitting the distribution of the measurements with an asymmetric Gaussian function (see the blue line at the top). This is strong evidence for the existence of a spiral density wave. In contrast, the corotation positions for NGC 4321, shown in the bottom panel of Fig. 2, have an absolute discrepancy in distribution. In addition, we have not observed an angular offset between the young and old stellar populations as predicted by density wave theory. Taken together, this may indicate the dynamic nature of the spirals in this galaxy (Egusa et al. 2009).

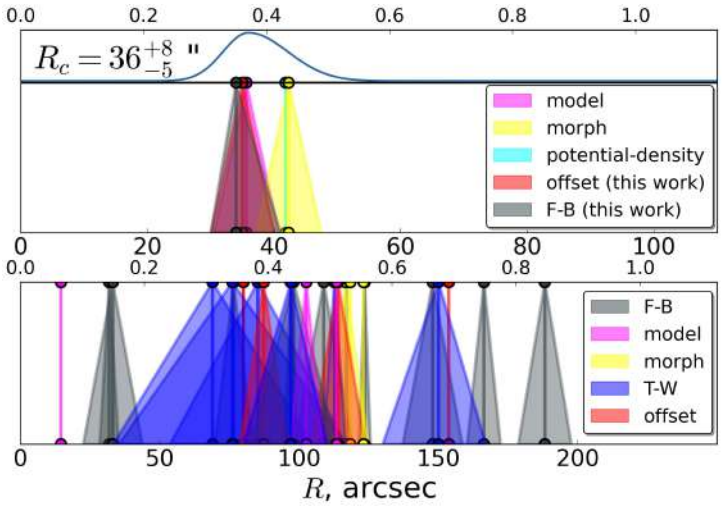

Fig. 2. The distributions of the corotations for NGC 3686 (top) and NGC 4321 (bottom) taken from the literature and obtained in this work (the same as in Fig. 1 right). The blue line at the top shows the fitted asymmetric Gaussian function.

The third analyzed galaxy, NGC 2403, is predicted to have multiple spiral modes rotating at different pattern speeds. In this study, we have confirmed the locations of several corotation resonances using measurements obtained by implemented methods. The top panel of Fig. 3 shows two reliable corotation positions at 140″ and 300″, confirmed by two and four independent measurements, respectively. In addition, according to the bottom panel of Fig. 3, we found the intersection of the corotation and

outer Lindblad resonances for the second and first modes, respectively. This feature is expected for a galactic disk with multiple spiral modes. Furthermore, in this figure we see that the ultraharmonic resonance of the second mode is coupled within errors to the corotation of the third mode, proving the location of R_c at 390″.

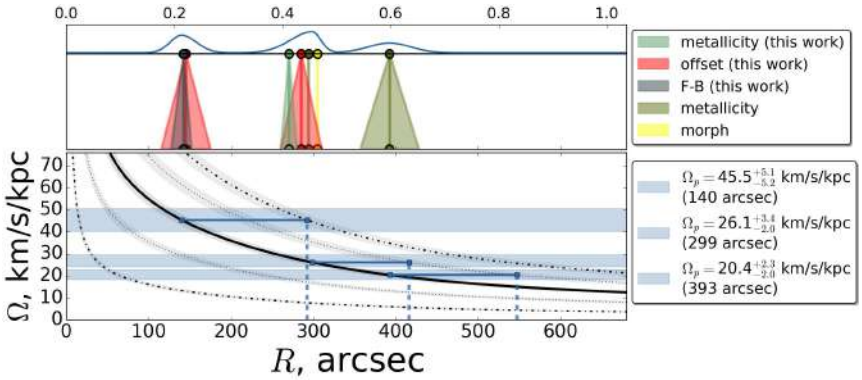

Fig. 3. *The top panel:* the same as in Fig. 2. *The bottom panel:* the black solid line shows the angular velocity profile of NGC 2403. To the left and right of it, dashed lines define the areas of inner and outer Lindblad resonances. Ultraharmonic resonances are represented by dotted lines. The blue horizontal lines connect the positions of the corotation radius and the OLR (or ultraharmonic resonance) for the angular pattern speed, whose value is given in the legend.

In summary, we have shown that the estimation of corotation radii is still a challenging problem in astrophysics due to discrepancies in their measurements. Using three examples, we have shown that the distribution of corotation measurements can be linked to the nature of the spiral structure. Furthermore, we have illustrated the coexistence of galaxies whose spirals may have different origins.

Funding

V.K. acknowledges the support of "BASIS" Foundation for the Development of Theoretical Physics and Mathematics (grant No. 23-2-2-6-1).

References

Egusa F., Kohno K., Sofue Y., et al., 2009, Astrophysical Journal, 697, p. 1870
Kostiuk V., Marchuk A., Gusev A., 2024, Research in Astronomy and Astrophysics, 24, 7, id. 075007
Lin C. and Shu F., 1964, The Astrophysical Journal, Astrophysical Journal, 140, p. 646
Sellwood J. and Carlberg A., 1984, Astrophysical Journal, 282, p. 61

Mass of the Andromeda Galaxy on a scale of up to 300 kpc

K. Kozyrev[1], D.I. Makarov[2], and D.D. Makarov[2]

[1] Kazan Federal University, 18 Kremlyovskaya St, Kazan 420008, Russia
[2] Special Astrophysical Observatory of the Russian Academy of Sciences, Nizhny Arkhyz, 369167 Russia

Abstract. By analysing the kinematics of the satellites of giant galaxies, it is possible to estimate the total mass of systems within 300 kpc. The Andromeda Galaxy (M 31) is the closest giant galaxy with a well known three-dimensional satellite system. Estimating its total mass is extremely important for understanding the halo distribution of dark matter, as well as for studying the kinematics and dynamics of the Local Group of galaxies. In this work we use the improvement of the projected mass method to take into account the three-dimensional distribution of the satellites, which allows us to obtain more reliable and accurate estimates of the total mass of the system. Using a sample of 29 satellites with precise distance measurements and radial velocities, we estimate the total mass of M 31 to be $M = (1.7 \pm 0.4) \times 10^{12}\ M_{\odot}$ on a scale of 300 kpc. This result is in good agreement with the work of other studies.

Keywords: galaxies: kinematics and dynamics, Local Group, dwarf

DOI: 10.26119/VAK2024.030

1 Introduction

The determination of the virial masses of the Milky Way and the Andromeda Galaxy, or M 31, is one of the most important issues in the study of the Local Group. Knowledge of the mass distribution in the system is a significant contribution to the resolution of kinematic and dynamical processes. M 31 is the nearest giant galaxy and was one of the first galaxies for which mass determination was attempted. Over almost a century of research, a variety of approaches have been used, including the disk rotation curves, consideration of the kinematics of globular clusters and/or dwarf satellite galaxies, as well as the kinematics of the Local Group as a whole, construction of mass models, and, more recently, cosmological simulations. The results have varied over the decades, but as the accuracy of the measurements improves and more new galaxies are discovered in the Local Group, the task becomes increasingly feasible. We have collected recent distance and velocity measurements from the literature for 55 galaxies within 525 kpc of M 31. Their distribution shows the famous satellite plane and the well known skew towards our Galaxy (see Fig. 1).

In this work we use an improved method of the predicted mass that takes into account the three-dimensional distribution of satellites in space.

2 Projected mass

The classical way to estimate the mass of a galaxy group is to use the virial theorem. Bahcall & Tremaine (1981) noted that the virial theorem has a number of unrecoverable drawbacks due to projection effects and proposed an alternative approach, the so-called projected mass estimator. In the case of a central mass surrounded by test particles, which can be considered a good approximation for the system of satellites around the Andromeda Galaxy, Bahcall & Tremaine (1981) use $GM = \alpha V_{\rm los}^2 R_\perp$ as a proxy for mass estimation, where $V_{\rm los}$ is the line-of-sight velocity relative to the central body and $R_\perp$ is the projected distance from the central galaxy. The coefficient α is derived by averaging over all possible satellite orbits. Knowledge of the three-dimensional distribution of the satellites can reduce the uncertainty and improve the accuracy of the mass estimate in this relation. For the case where a group of galaxies is observed from the outside, and assuming an isotropic distribution of orbits, $\langle e^2 \rangle = 1/2$, we obtain the following relation: $GM = 4\langle V_{\rm los}^2 R_{\rm 3D} \rangle$, where $R_{\rm 3D}$ is the distance from the central galaxy.

From the total list of 55 satellites around M 31, we excluded all objects with unknown, questionable or imprecise distance measurements, as they could be a source of large systematic errors. These include 8 objects from the Pan-Andromeda Archaeological Survey (PAndAS) without distance measurements. We have also excluded

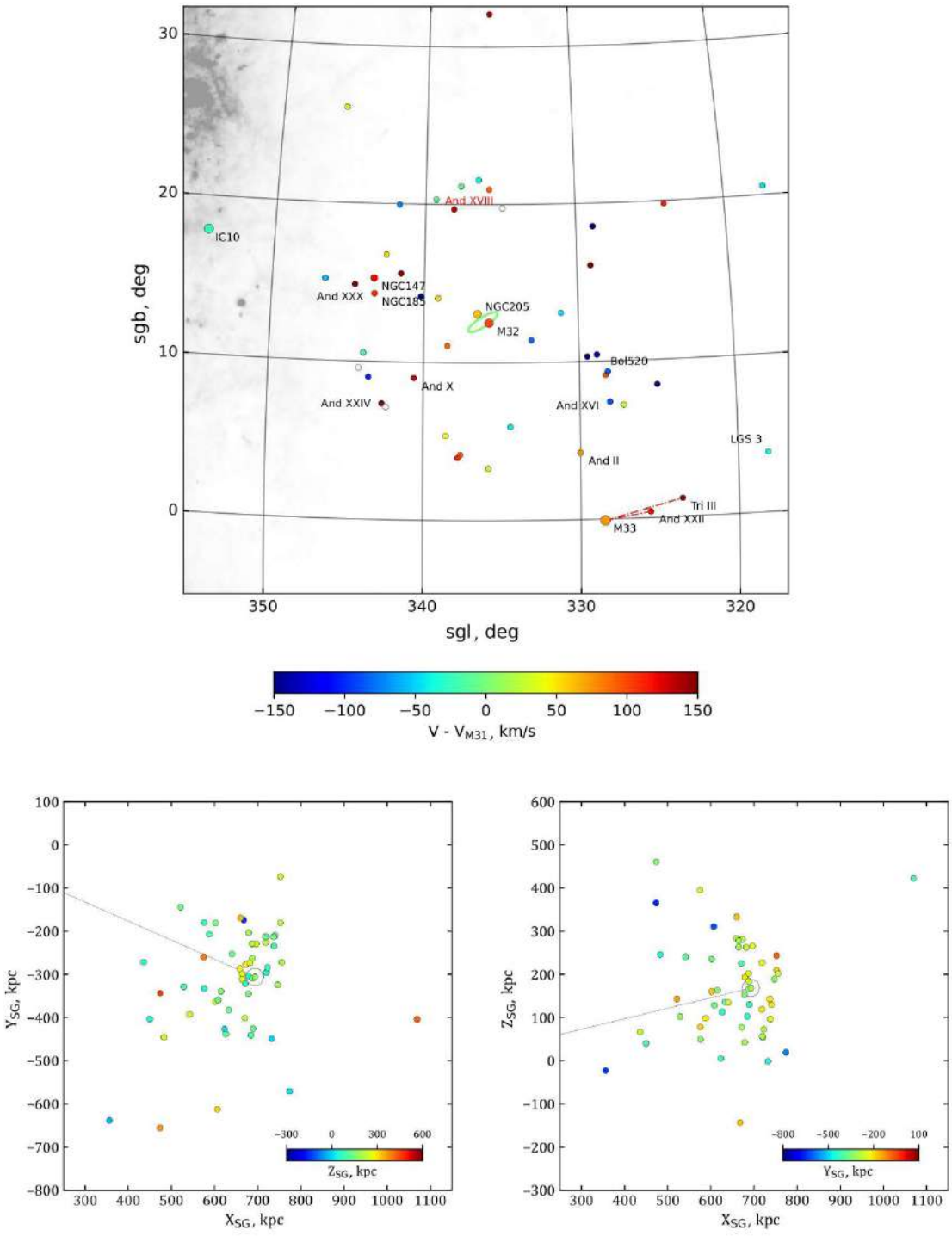

Fig. 1. *Top panel*: distribution of the M 31 satellites in the Aitoff projection on the celestial sphere. M 31 itself is indicated by a central ellipse. The color reflects the velocity difference relative to the central galaxy. The open dots mark galaxies with unknown line-of-sight velocities. The IRAS interstellar extinction map is given by gray clouds. *Bottom panel*: Distribution of objects within a sphere of radius 520 kpc from M 31 in Cartesian Supergalactic coordinates. The dotted line indicates the direction towards the Milky Way.

all objects with a relative distance measurement error greater than 5 %. Among them is Tri III ($e/D = 23.2\%$) probably belongs to the first infall group associated with M 33; the globular cluster Bol 520 (9.6%); IC 10 (5.7%) and And XXVII (5.7%) are in the high extinction region of the Milky Way. After careful analysis, we have also excluded M 33 with its suite of And XXII and Tri III, which completed its first flyby of M 31, and And XXX as a galaxy undergoing a primary infall into the M 31 group. Thus, based on a sample of 30 satellites within 300 kpc of M 31, we estimate the total mass of the Andromeda Galaxy equal to $M = (1.70 \pm 0.37) \times 10^{12}\ M_{\odot}$ with a maximum variation between $M = 1.3 \times 10^{12}\ M_{\odot}$ for purely circular orbits, $\langle e^2 \rangle = 0$, and $M = 2.6 \times 10^{12}\ M_{\odot}$ for purely radial orbits, $\langle e^2 \rangle = 1$.

The classical approach of Bahcall & Tremaine (1981), based on using only projected distances and radial velocities, using the same galaxies, gives a very close mass estimate of $M = (1.74 \pm 0.50) \times 10^{12}\ M_{\odot}$, but with worse accuracy. However, it also allows us to include objects in the analysis without precise distance measurements in the analysis and improve the accuracy through statistics. Using all 41 confirmed satellites and candidates within 300 kpc of the Andromeda Galaxy, we obtain a mass estimate of $M = (1.74 \pm 0.44) \times 10^{12}\ M_{\odot}$. Note that the accuracy is still lower than in our approach. This indicates the importance of knowing the distribution of satellites in space for a more accurate estimate of galaxy mass.

3 Summary

We estimate the total mass within 300 kpc of the Andromeda Galaxy equal to $M = (1.70 \pm 0.37) \times 10^{12}\ M_{\odot}$. This result is in good agreement with the estimates of other authors over the last 10—15 years. The last time a similar method was used for satellites by Watkins et al. (2010). On the same scale, they obtained an estimate of $M = (1.4 \pm 0.3) \times 10^{12}\ M_{\odot}$, which is within the measurement errors of our estimate. By applying the tracer mass estimator to globular clusters, Veljanoski et al. (2013) obtained a mass of $M = (1.35 \pm 0.35) \times 10^{12}\ M_{\odot}$. The difference in estimates may also be due to a more complete sample in our work, supplemented by the discovery of new satellites and refinement of parameters over the last decade.

Acknowledgements. This work was supported by the Russian Science Foundation grant № 24–12–00277, https://rscf.ru/project/24-12-00277.

References

Bahcall J. and Tremaine S., 1981, The Astrophysical Journal, 244, p. 805

Veljanoski J., Ferguson A., Mackey A., et al., 2013, The Astrophysical Journal Letters, 768, id. L33

Watkins L., Evans N., An J.H., 2010, Monthly Notices of the Royal Astronomical Society, 406, p. 264

MODERN ASTRONOMY: FROM THE EARLY UNIVERSE TO EXOPLANETS AND BLACK HOLES

Constraints on the population of Galactic objects in the JWST UNCOVER survey catalogue

N. Lovyagin[1], A. Raikov[2], and V. Yershov[3]

[1] Department of Computer Science, St. Petersburg State University, St. Petersburg, 199034 Russia
[2] St. Petersburg Branch of the Special Astrophysical Observatory of the Russian Academy of Sciences, St. Petersburg, 196140 Russia
[3] St. Petersburg State University of Aerospace Instrumentation, St. Petersburg, 190000 Russia

Abstract. The paper assesses the potential galactic nature of small distant objects (also known as "little red dots") in the SUPER galaxy catalogue of the James Webb Space Telescope (JWST) UNCOVER survey. The estimate is based on the assumption that these objects could be brown dwarfs or similar objects with temperatures of a few hundred degrees — if the radiation from the low-temperature bodies was interpreted as the photometric redshift of a typical galaxy. The hypothetical number density of these objects in our galaxy is calculated, such as to match the observed number of "little red dots" in the survey. The physical possibility of having this number density in our Galaxy is discarded as contradictory to the dynamical constraints based on the halo mass of our Galaxy estimated elsewhere.

Keywords: cosmology: observations; galaxies: distances and redshifts

DOI: 10.26119/VAK2024.031

1 Introduction

The first published catalogue of objects discovered in the deep-field images from the James Webb Space Telescope (JWST) contains more than 65,000 objects with photometric redshifts up to $z \approx 20$ and about 400 objects with reliably determined spectral redshifts up to $z = 7$ (Bezanson et al. 2022; Weaver et al. 2024). Most of these objects are identified in the catalogue as galaxies, with their angular radii θ. This allows us to perform a cosmological test by plotting a diagram which relates galaxy angular sizes with redshifts (the θ–z test).

The left panel of Fig. 1 presents a θ–z diagram for all 65,000 objects from the catalogue. In this plot, there are noticeable moments, particularly the presence of a large family of objects with small angular radii. These are seen as a uniform stripe of very small objects at the bottom of the diagram. Sometimes they are called "little red dots", as many of them are highly redshifted. Since they cover the entire redshift range, it raises the question about the nature of these objects: could some of them be part of our Galaxy? For example, they could be brown-dwarf stars with their low surface temperatures. Without a clear certainty about their nature, performing the θ–z test will be improper.

The authors of the catalogue (Weaver et al. 2024) note that objects fainter than $m = 25^m$ require additional scrutiny, so we are examining the question above. When extracting a sample of relatively bright objects with $m < 25^m$, the resulting catalogue is significantly smaller, consisting of approximately 5500 objects with photometric- and around 300 objects with spectroscopic redshifts. The θ–z diagram for this small sample is shown in the right panel of Fig. 1. The nature of the remaining $60,000$ small faint objects with their photometric redshifts $0 \lesssim z_{\rm phot} \lesssim 20$ remains a matter of debate. We can approach this issue as follows.

If the spectral energy distribution of such an object has a maximum at, say, $\lambda = 0.5\,\mu$m, then it might be a low-temperature nearby object — a brown dwarf with $1.25\,\mathrm{R}_{\jmath}$ (in Jupiter-radius units). Then its temperature will be equivalent to a certain photometric "pseudo-redshift" – $z_{\rm pseudo}$. The temperatures corresponding to pseudo-redshifts $0 < z_{\rm pseudo} < 20$ vary from ~ 200K to ~ 2000K, and the luminosity varies from $\sim 10^{-6} L_\odot$ to $\sim 10^{-2} L_\odot$ (assuming the blackbody spectral-energy distribution of the object).

Given the sensitivity limit of the JWST, it is possible to determine the maximum distance at which a brown dwarf could be detected. Thus, the number of objects from the UNCOVER catalogue provides an estimate of their hypothetical number density within the Milky Way and its halo.

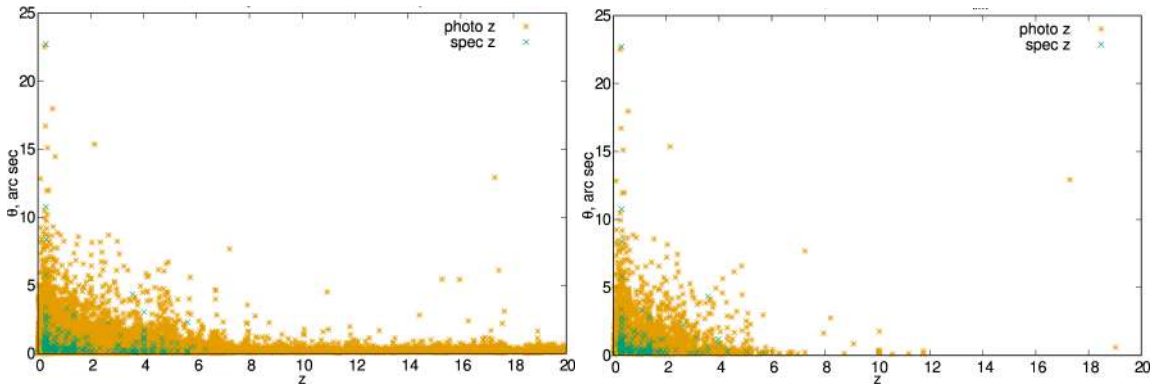

Fig. 1. Left panel: θ–z chart, for all JWST UNCOVER catalogue objects identified in this catalogue as galaxies. Right panel: the same chart, but for the objects brighter than 25^m. Yellow colour indicates the objects with photometric redshifts, and the green dots correspond to the objects with spectroscopic redshifts.

2 Assessment of a number density of possible brown dwarfs by their z_{pseudo} values

Only objects with photometric redshifts were selected from the UNCOVER catalogue for this assessment. The entire range of $0 \lesssim z_{\mathrm{phot}} \lesssim 20$ was broken down into 50 equal redshift bins. In each redshift bin, the number ΔN of the catalogue objects was counted. For the center of each bin, the blackbody temperature T and the brown-dwarf luminosity corresponding to this temperature were calculated. These luminosities are converted into absolute magnitudes (taking $M_\odot = 4.7^m$ and $L_\odot = 3.827 \cdot 10^{26}$ W). Next, the limiting distance D_{lim} at which this object can be seen was calculated using the JWST aperture. The calculation was performed for two options: (1) using all objects from the catalogue, assuming the object's apparent magnitude limit $m_{\mathrm{lim}} = 30^m$, and (2) using only objects brighter than $m_{\mathrm{lim}} = 25^m$.

Based on the obtained value of D_{lim}, the number density of objects corresponding to the selected redshift bin was calculated. In each redshift bin, the number of objects is equal to ΔN. The calculation refers to the limiting distance D_{lim} (the radius of a sphere), while the catalogue's deep field size of 49 square arcminutes (Weaver et al. 2024) was extrapolated to the entire sphere. Graphs of the number of the observed objects and the number densities of brown dwarfs matching the given number ΔN for each bin are shown in Fig. 2. It should be noted that with the approach used, the observational selection effect is excluded, since the selection of objects with the same temperature (a slice of the bin on z_{pseudo} gives a complete volume sample — i.e. a sample of objects with a given luminosity, whose number density is calculated

in a sphere in which all of the objects are visible, while outside of this sphere they are not visible.

Summing up the number density values for all bins, we obtain the total number density of brown dwarfs that would be required to obtain the same observed number of objects that are included in the catalogue. In the case (1) of using all objects from the catalogue, the total number density is equal to $5.42 \cdot 10^{23}$ pc^{-3}. In the case (2), when sampling only objects up to 25^m, the total number density obtained is equal to $8.14 \cdot 10^{23}$ pc^{-3}. If we take a value of 1% $M_\odot$ as the lower estimate of the brown dwarf mass, then, with the 16 kpk-radius of our Galaxy, we can extrapolate the resulting number density to the whole Milky Way and obtain a value equal to $\sim 5 \cdot 10^3$ pc^{-3}. Thus, this number density leads to an estimate of the contribution of the brown dwarfs to the mass of all objects in the Galaxy, equal to $\sim 10^{15}\, M_\odot$. This is about 10^3 times larger than the observational estimates based on the Milky Way's halo-mass dynamics (Watkins et al. 2019; Ou et al. 2024).

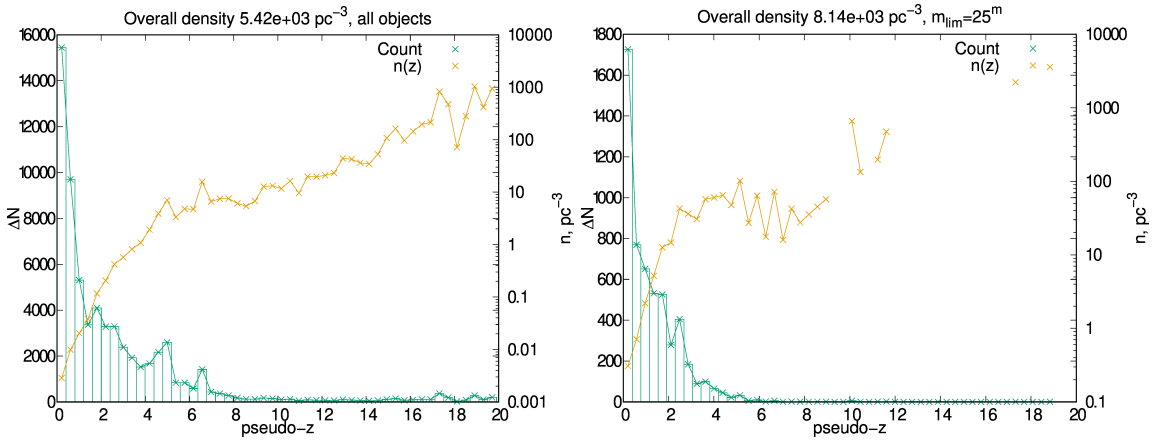

Fig. 2. An estimate of the brown dwarfs number densities from the JWST UNCOVER catalogue in redshift bins of $z_{\rm pseudo}$ corresponding to effective temperatures) of all catalogue objects (left panel) and of a sample limited to $m > 25^m$ (right panel).

In accordance with this estimate, it can be concluded that the proportion of brown dwarfs among the faint objects of the JWST UNCOVER catalogue cannot be larger than 0.1%. Otherwise, it will be in conflict with the dynamical properties of the Milky Way deduced from observational data. Therefore, it is most likely that 99.9% of the faint objects with small angular sizes in the UNCOVER catalogue are extragalactic and that the photometric estimates of their redshifts are not pseudo-redshifts but approximately correspond to the real redshifts of these objects.

Indirect evidence favouring the extragalactic nature of the disputed objects consists in the fact that the obtained estimates of number densities for the total number of objects and for the objects with $m < 25^m$ turned out to be of the same order. In this context, the "little red dot" objects are viewed as part of the group of objects accurately classified as galaxies in the UNCOVER catalogue. However, at the moment, it is premature to assert with 100% certainty that all of these objects are of extragalactic nature.

In principle, it is possible to carry out similar estimates for objects of other types (for example, diffuse nebulae), which have the same low temperatures as brown dwarfs, but which are larger. It is understandable that, as the radius R of an object increases, while the temperature is maintained, the brightness increases as R^2, and, therefore, the maximal distance from which the object is seen also increases as R^2. That is, the number density will fall as R^{-6}. For example, dust clouds with radii of $\sim 10\,\mathrm{R}_{\not\odot}$ can be used to achieve "reasonable" number densities. Due to their lower density, these objects, unlike brown dwarfs, will not make a "catastrophic" contribution to the total mass of the Galaxy. Note, however, that the number density of hypothetical "brown dwarfs" (Fig. 2) exhibits growth at large z_{pseudo}, which should not be the case if these objects indeed were brown dwarfs: there should be a number density peak for the temperatures $\sim$ 300–500K ($z_{\mathrm{pseudo}} \sim$ 6–10). On the other hand, this growth does not contradict to the possible dusty nature of the objects, if their number density increases with a decrease in temperature, including a decrease below the available JWST wavelength sensitivity limit ($z_{\mathrm{pseudo}} = 20$, $T \sim 100K$). We think that further assessment of these issue is required.

3 Angular-size vs. redshift test

Considering the concerns about the nature of the "little red dots," we conducted the angular-size — redshift test for them. In each redshift bin, the average angular size and its dispersion were calculated. The results are shown in Fig. 3, his figure presents the theoretical predictions of the ΛCDM model and of the toy model based on Zwicky's tired light (TL) hypothesis — the latter being taken as an example of a cosmological model based on a static spacetime metric.

The results of this test show a strong disagreement with the ΛCDM predictions and some agreement with the TL model, which may indicate that either the discussed objects are not galaxies, or that the increase in the linear size of galaxies due to evolution precisely compensates for the geometrical changes with time of the coordinate reference frame predicted by the expanding-universe model. These test results align with the findings of other works, including our previous review (Lovyagin et al. 2022).

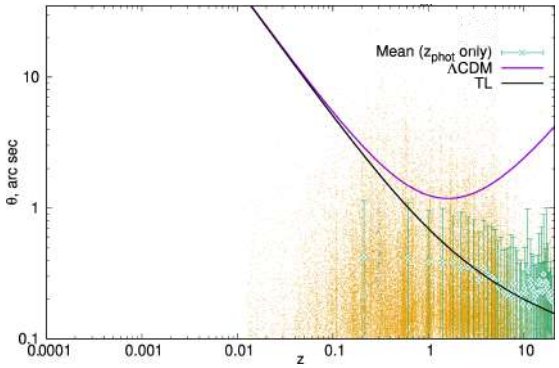

Fig. 3. The angular size — redshift relation (θ–z) for all of the objects with photometric redshifts from the JWST UNCOVER catalogue.

The combination of the recently identified issues regarding the age of the Universe and the challenges in explaining the formation of high-redshift galaxies within the standard cosmological model may suggest a potential need for a reassessment of the model.

4 Conclusions

A study of faint objects with small angular dimensions ("little red dots") from the JWST UNCOVER catalogue showed that only a negligible fraction of these objects (0.1%) can belong to the population of brown-dwarfs in the Milky Way and/or its halo. It is most likely that the majority of these objects are real distant galaxies.

References

Bezanson R., Labbe I., Whitaker K. E., et al., 2022, arXiv:2212.04026
Lovyagin N., Raikov A., Yershov V., et al., 2022, Galaxies, 10, id. 108
Ou X., Eilers A.-C., Necib L., et al., 2024, MNRAS, 528, p. 693
Watkins L.L., van der Marel R.P., Sohn S.T., et al., 2019, ApJ, 873, id. 118
Weaver J.R., Cutler S.E., Pan R., et al., 2024, ApJ Suppl. Ser., 270, id. 7

BAK 2024 MODERN ASTRONOMY: FROM THE EARLY UNIVERSE TO EXOPLANETS AND BLACK HOLES 300 years Russian Academy of Sciences

The mass of the Milky Way based on the kinematics of satellites

D. D. Makarov[1], D. I. Makarov[1], L. Makarova[1], and K. Kozyrev[2,1]

[1] Special Astrophysical Observatory of the Russian Academy of Sciences, Nizhny Arkhyz, 369167 Russia
[2] Kazan Federal University, 18 Kremlyovskaya St, Kazan, 420008 Russia

Abstract. The Milky Way satellite system is the most studied group of galaxies. Currently, 64 satellites within 260 kpc are known. We have measured high-precision distances, radial and tangential velocities for most of them. We have estimated the total mass of our galaxy to be $M = (7.9 \pm 2.1) \times 10^{11}\ M_\odot$ using a modification of the projected mass method that takes into account the three-dimensional distribution of galaxies in the group, assuming an isotropic distribution of satellite orbits. The infall of galaxies located outside the virial zone at a distance of 400 kpc allows us to estimate the mass of the system to be of the order of $9 \times 10^{11}\ M_\odot$, which is in excellent agreement with the mass inside the virial zone of our Galaxy.

Keywords: The Galaxy; Galaxy: kinematics and dynamics

DOI: 10.26119/VAK2024.032

1 Introduction

Recently, thanks to deep optical surveys, our knowledge of the satellite system around our Galaxy has expanded dramatically. Currently, there are 64 known satellites of our Galaxy within the 260 kpc region. Thanks to the Gaia (Gaia Collaboration et al. 2018) mission, the proper motions of most of our Galaxy's satellites have been measured, allowing us to unambiguously determine all 6 components of satellite position in phase space. This information is being actively used to refine the structure of our Galaxy and to estimate its total mass. However, even a simple analysis of the radial velocity distribution can reveal unexpected and interesting effects. Recently, it was discovered that the dipole component of the radial velocity field of nearby satellites at distances less than 100 kpc has an unexpectedly large amplitude of bulk motion of about 200 km/s (Makarov et al. 2023). The analysis showed that this anomaly is caused by only 8 galaxies (crossed out with red crosses in the left panel of Fig. 1), including the Large Magellanic Cloud (LMC) and three galaxies from its escort. Numerical simulations show that the velocity pattern is consistent with the assumption of the first flyby of the massive LMC around our Galaxy and the perturbation it causes in the motion of the Galaxy's satellites. This example shows the importance of a careful selection of "the test particles" for the kinematic analysis. Such objects have not had time to virialize and should be excluded from consideration when estimating the total mass of the system.

2 Mass inside the virial zone

The radial velocity-distance distribution of the satellites around our Galaxy is shown in Fig. 1. There is a clear separation between well randomized companions below 260 kpc, indicating the extent of the virial zone, and three galaxies with systematic negative velocity at a distance of 400 kpc. The galaxies Eridanus II, Phoenix, and Leo T are probably in the stage of approaching the Milky Way halo. To estimate the mass of our Galaxy, we exclude 8 objects that most strongly distort the behavior of the solar apex (Makarov et al. 2023). We use a modification of the projected mass method (Bahcall & Tremaine 1981) that takes into account the three-dimensional distribution of galaxies in the group. Assuming an isotropic distribution of the satellite orbits, we estimate the total mass of the Milky Way to be $M_{\rm MW} = (7.9 \pm 2.1) \times 10^{11}\ M_\odot$ (left panel of Fig 2).The known presence of satellite planes does not affect this estimate, since it depends only on the shape of the orbits, but not on their distribution in space. As can be seen from Fig. 3, our estimate is in good agreement with numerous estimates by other authors (see reviews Wang et al. 2020; Bobylev & Bajkova 2023).

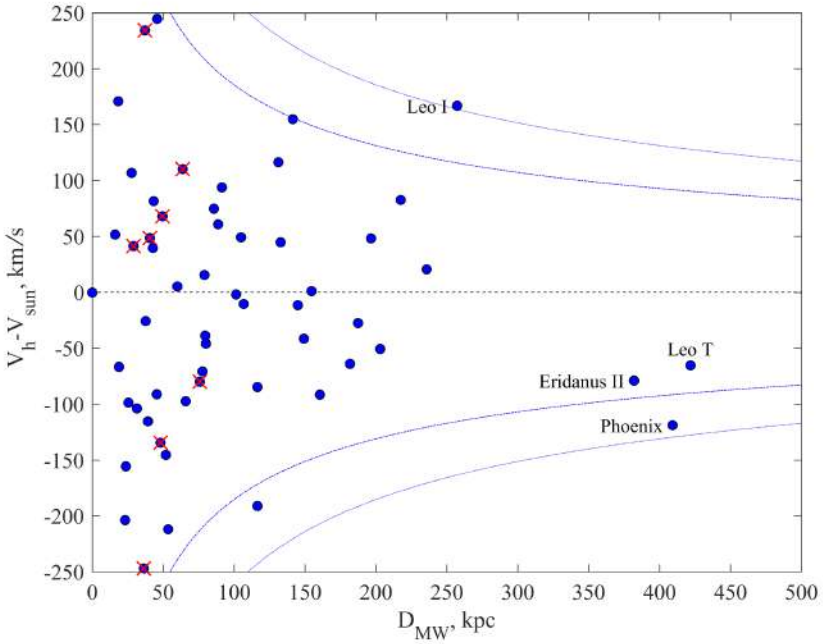

Fig. 1. Velocity-distance distribution of the nearest galaxies. The line-of-sight velocity is given relative to the center of the Galaxy. The dot-dashed and dotted lines correspond to circular and escape velocities for a point mass of 8×10^{11} $M_\odot$, respectively.

3 Mass from the infall region

We can try to use the Eridanus II, Phoenix, and Leo T galaxies outside the virial zone of the Milky Way to estimate the total mass within 400 kpc. Note that these galaxies are deep inside the Local Group stop radius of about 1 Mpc and to describe their infall the linear approximation is not applicable and more complex models must be used. Baushev (2020) found an exact analytical solution to the Hubble flow for a spherically symmetric distribution of matter, which we can use to estimate the mass of our Galaxy. Using the distances and radial velocities of Eridanus II and Leo T, we estimate the mass of the Milky Way from the flow model to be $M_{\rm MW} = 9.1 \times 10^{11}$ and 8.6×10^{11} $M_\odot$, respectively. These values are slightly larger, but still in excellent agreement with our previous mass estimate of $M_{\rm MW} = (7.9 \pm 2.1) \times 10^{11}$ $M_\odot$ within the virial zone (see Section 2). This shows the validity of the spherically symmetric Hubble flow model for estimating mass even deep inside the stop radius of galaxy groups, and provides a tool for measuring mass outside the virial zones of groups.

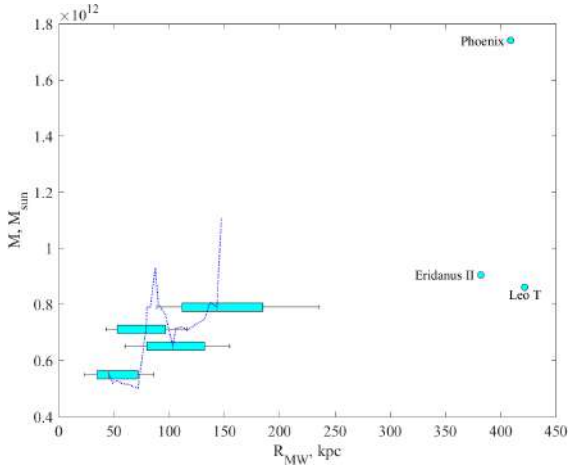

Fig. 2. Estimation of the Milky Way mass versus the distance within the virial zone (cyan boxes) and from the Hubble flow model (cyan dots).

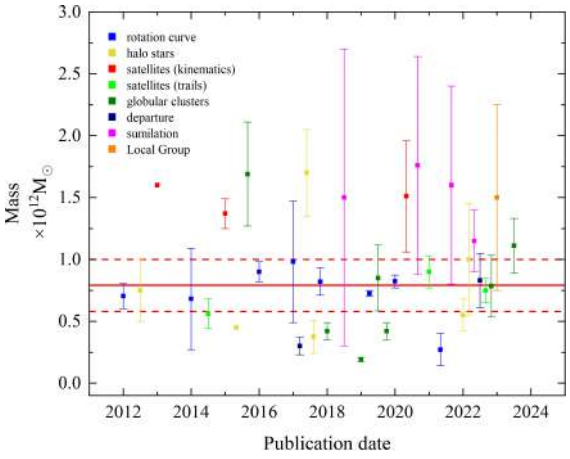

Fig. 3. Comparison of our estimate of the mass of the Milky Way with recent measurements obtained by other authors.

However, using the Phoenix galaxy we obtain a mass value of $17 \times 10^{11}\ M_{\odot}$, which does not fit into this picture. Observations show that the HI gas in the Phoenix galaxy is significantly offset from the stellar body (St-Germain et al. 1999) and it is likely that Phoenix has experienced a recent impact and cannot be considered as a free-falling test particle.

Funding

This work was supported by the Russian Science Foundation grant № 24–12–00277, https://rscf.ru/project/24-12-00277.

References

Bahcall J.N. and Tremaine S., 1981, ApJ, 244, p. 805
Baushev A.N., 2020, Phys. Rev. D, 102, id. 083529
Bobylev V.V. and Bajkova A.T., 2023, arXiv e-prints, arXiv:2305.18408
Gaia Collaboration, Brown A.G.A., Vallenari A., et al., 2018, A&A, 616, id. A1
Makarov D., Khoperskov S., Makarov D., et al., 2023, MNRAS, 521, p. 3540
St-Germain J., Carignan C., Côte S., et al., 1999, AJ, 118, p. 1235
Wang W., Han J., Cautun M., et al., 2020, Science China Physics, Mechanics and Astronomy, 63, id. 109801

MODERN ASTRONOMY:
FROM THE EARLY UNIVERSE TO EXOPLANETS AND BLACK HOLES

Supermassive binary black holes in the centers of galaxies and prospects for their observation

A. Malinovsky

Astro Space Center of the P.N. Lebedev Physical Institute of the Russian Academy of Sciences, Moscow, 119991 Russia

Abstract. A list of candidates for supermassive binary black holes has been compiled based on an analysis of available data regarding variability in the optical range and the shape of the emission spectrum. An artificial neural network has been constructed to estimate the radiation flux at a frequency of 240 GHz. For the candidates of supermassive binary black holes where the network construction process was feasible, the criterion for the possibility of observing the source at the Millimetron Space Observatory has been tested. The study presents its results in a table that lists 17 candidates for supermassive binary black holes.

Keywords: quasars: supermassive black holes; techniques: interferometric

DOI: 10.26119/VAK2024.033

1 Introduction

It is believed that a supermassive black hole (SMBH) exists in the central region of virtually every massive galaxy. In turn, according to current understanding, the gravitationally bound halo of dark matter, which is the dynamically dominant component of any galaxy, experiences multiple mergers with smaller-mass halos during its evolution. Numerical simulations can also highlight a major merger event, during which the halo interacts with another halo of similar mass. This suggests that for some period, multiple SMBHs should be present within galaxies, leading to the existence of supermassive binary black holes (SMBBHs).

2 Search for SMBBHs

One of the main directions in the search for SMBBHs is the analysis of the optical variability of active galactic nuclei, primarily quasars. For instance, in Graham et al. (2015), the Catalina Real-time Transient Survey (CRTS) catalog, comprising 243,500 spectroscopically confirmed quasars, was analyzed. As a result of the search, 111 objects exhibiting signs of variability, with periods on the order of one year, were selected as candidates for SMBBHs.

A search for SMBBH candidates was also conducted in Charisi et al. (2016) through an analysis of the Palomar Transient Factory (PTF) catalog, which includes 35,383 spectroscopically confirmed quasars. The analysis of this catalog identified 50 quasars with statistically significant periodicity. Additionally, combining data with the CRTS catalog contributed 33 new sources to the list of SMBBH candidates. Together with OJ 287, the famous candidate for SMBBH, this totals 145 candidates for SMBBHs.

3 Simulation of the Spectra of the SMBBH candidates

For the purposes of the study, among the 145 known candidates for SMBBHs, those were selected for which data on fluxes at frequencies higher and lower than 240 GHz were available. This resulted in a total of 17 objects. Additionally, 7 more DSMBH candidates found in other publications were added to this list.

To model the radiation flux at a frequency of 240 GHz, an artificial neural network was developed. The input data for this network consisted of the observed frequencies, and the output included the radiation flux densities at those frequencies. Initially, the model was trained on the available public data (see NASA/IPAC Extragalactic Database (NED)). Then, the trained network determined the radiation flux density

at the frequencies of interest. The programming language used was Python, and the machine learning library was TensorFlow.

An example of the modeling for one of the 24 sources is shown in Fig. 1.

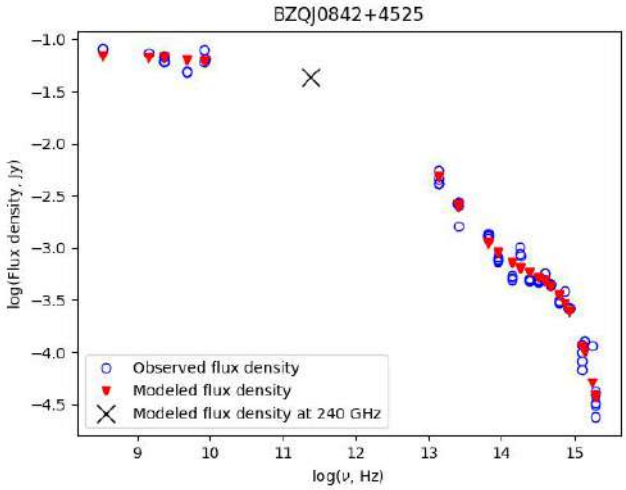

Fig. 1. Modeled spectra of BZQ J0842+4525.

4 SMBBHs and space-VLBI

The small angular sizes of supermassive black holes (SMBHs) make space-ground VLBI observations in the millimeter and submillimeter range particularly important, as noted by Ivanov et al. (2019). In the same work, a criterion for selecting sources for observations at the Millimetron Space Observatory (MSO) was formulated. This criterion was modified by the authors for the purposes of this study, utilizing a frequency of 240 GHz as the primary frequency.

Table 1 summarizes the results of the analysis conducted. It presents the sources for which there is a range of baseline projections where the amplitude of the visibility function is above a threshold value, which is 6.45 mJy for 240 GHz for MSO. Table 1 provides the source name, its right ascension α and declination δ for epoch J2000, the flux F_{ANN} obtained from modeling, expressed in Jansky (Jy), the angular size of the shadow of the more massive component of the SMBBH system θ (defined as in Mikheeva et al. 2019), expressed in arc microseconds, and the angular separation between the components of the binary system d, also expressed in arc microseconds.

Table 1. Candidates for supermassive binary black holes that meet the selection criteria.

Source	α, h m s	δ, ^{o} $'$ $''$	$F_{\rm ANN}$, Jy	θ, μs	d, μs
CSO 0402+379	04 05 09.3	+38 03 32.2	0.043	0.068	6580
FBQS J081740.1+232731	08 17 40.2	+23 27 32.0	0.027	0.220	1.375
BZQ J0842+4525	08 42 15.3	+45 25 45.0	0.050	0.173	1.385
OJ 287	08 54 48.9	+20 06 30.6	2.72	1.935	11.96
MCG +11-11-032	08 55 12.5	+64 23 45.6	0.23	0.067	4.82
SBS 0924+606B	09 28 37.98	+60 25 21.0	0.019	0.087	9.69
SDSS J102349.38+522151.2	10 23 49.5	+52 21 51.8	0.027	0.237	1.717
SDSS J124044.49+231045.8	12 40 44.5	+23 10 46.1	0.014	0.058	1.072
BZQ J1305-1033	13 05 33.0	−10 33 19.1	0.37	0.035	1.794
SDSS J132103.41+123748.2	13 21 03.4	+12 37 48.1	0.016	0.055	1.0935
SDSS J133654.44+171040.3	13 36 54.4	+17 10 40.8	0.032	0.101	0.935
3C 298.0	14 19 08.2	+06 28 35.1	0.022	0.213	1.498
TEX 1428+370	14 30 40.6	+36 49 03.9	0.14	0.025	0.319
SDSS J150243.09+111557.3	15 02 43.1	+11 15 57.3	0.014	0.01	25500
FBQS J150911.2+215508	15 09 11.2	+21 55 08.8	0.0094	0.029	0.411
PG 1553+113	15 55 43.0	+11 11 24.4	0.06	0.01	0.73
PKS 2203-215	22 06 41.4	−21 19 40.5	0.17	0.059	0.602

5 Conclusion

The results of the conducted study are presented in Table 1. The list includes 17 candidates for SMBBHs, whose duality may be confirmed through observations with a space-based interferometer that has an orbit and sensitivity at a frequency of 240 GHz, similar to the planned Millimetron Space Observatory.

The table with SMBBH candidates may be extended after additional observations or studies, as the main reason why the list is much shorter than the initial number of SMBBH candidates is the lack of observational data around a frequency of 240 GHz (at which the modeling was carried out), mainly at lower frequencies.

References

Charisi M., Bartos I., Haiman Z., et al., 2016, MNRAS, 463, p. 2145
Graham M., Djorgovski S., Stern D., et al., 2015, MNRAS, 453, p. 1562
Ivanov P., Mikheeva E., Lukash V., et al., 2019, Phys. Usp., 62, p. 423
Mikheeva E., Lukash V., Repin S., et al., 2019, Astronomy Reports, 63, p. 343

MODERN ASTRONOMY: FROM THE EARLY UNIVERSE TO EXOPLANETS AND BLACK HOLES

Primordial intermediate-mass binary black holes in space laser interferometers

N. Mitichkin[1,2], K. Postnov[1,2], and I. Chekh[1,2]

[1] Sternberg Astronomical Institute, Moscow State University, 13 Universitetsky pr., Moscow, 119234 Russia

[2] Faculty of Physics, M.V. Lomonosov Moscow State University, 1 Leninskie Gory, Moscow, 119991 Russia

Abstract. Primordial black holes (PBHs) with log-normal mass distributions reaching obtained $\sim 10^4$–10^5 solar masses may form following the quantum chromodynamic (QCD) phase transition in the early Universe, potentially due to modified Affleck–Dine baryogenesis. The expected frequency of detection of binary PBHs with intermediate masses using the TianQin space laser interferometer has been calculated based on the model of binary PBH formation and the assumed parameters of the log-normal distribution of primordial black holes. The obtained results are consistent with the LIGO-Virgo-KAGRA (LVK) data.

Keywords: black hole physics, relativistic processes, gravitational waves; cosmology: dark matter, early universe, primordial nucleosynthesis, observations; instrumentation: detectors

DOI: 10.26119/VAK2024.034

1 Introduction

Currently, there are two primary types of black holes are observed, which differ in mass: stellar-mass black holes (Raidal et al. 2019) and supermassive black holes (SMBHs) (Kormendy & Ho 2013). At the same time, intermediate-mass black holes (IMBHs) with masses around 100–10^5 solar masses remain poorly studied. IMBHs may form from the collapse of very massive Population III stars (Schneider et al. 2002), arise from dynamical evolution in dense star clusters (Fujii et al. 2024; Gonzalez Prieto et al. 2024), or have a primordial origin (Blinnikov et al. 2016). IMBHs located at the centers of galaxies can play a key role in tidal disruption events (Eftekhari et al. 2024), act as templates for the formation of SMBHs (Kovacs et al. 2024; Mezcua 2017), and be an important source of signals for space-based laser gravitational-wave interferometers (Fragione & Loeb 2023).

This paper analyzes the potential for detecting primordial binary IMBH mergers using the TianQin laser space interferometer (Luo et al. 2016; Mei et al. 2021). One of the features of these events could be their origin at high redshifts ($z > 20$), prior to the onset of active star formation, when traditional astrophysical mechanisms typically do not predict the existence of binary IMBHs.

2 Primordial binary black holes

PBHs may form in the early Universe due to primordial density perturbations with their mass equal to the mass inside the cosmological horizon at the moment of PBH formation (Carr 1975; Zeldovich & Novikov 1967) at the stage of radiation dominance. In this work, we use a model of PBHs formation with a log-normal mass spectrum (Dolgov & Silk 1993; Dolgov et al. 2009):

$$\frac{dn}{dM} = \mu^2 \exp\left[-\gamma \ln^2\left(\frac{M}{M_0}\right)\right], \tag{1}$$

where γ is a dimensionless constant, and the parameters μ and M_0 have the dimension of mass. In this model, PBHs are formed due to isocurvature perturbations with a high baryon charge, which are created before the end of the inflationary stage. These perturbations turned into large density perturbations during the QCD phase transition ($T_{\rm QCD} \sim$ 100–150 MeV), at which point massless quarks gain mass from the primordial quark-gluon plasma. The QCD phase transition temperature is still undetermined and depends on the chemical potential (density of the substance), possible magnetic fields, etc (Arefeva et al. 2023). Thus, reducing the $T_{\rm QCD}$ with a non-zero chemical potential helps create PBH with a higher central mass.

For a log-normal mass distribution eq. (1), the overall mass function is $\psi(M) = (M/\rho_{\rm pbh})(dn/d\ln M)$ ($\int \psi(M) d\ln M = 1$), where $\rho_{\rm pbh} = f_{\rm pbh}\Omega_{\rm dm}\rho_{\rm cr}$ is the energy density of PBH and $f_{\rm pbh} \leq 1$ represents the fraction of PBH in dark matter and reads:

$$\psi(M) = \sqrt{\frac{\pi}{\gamma}} e^{-1/\gamma} \left(\frac{M}{M_0}\right)^2 e^{-\gamma \ln^2 (M/M_0)}. \quad (2)$$

In what follows, masses will be used in units of the central mass M_0 ($m \equiv M/M_0$). Guided by the results of LVK (Andres-Carcasona et al. 2024; Dolgov et al. 2020; Liu et al. 2023), for the numerical estimates below we will use $M_0 = 10, 17, 25\ M_\odot$ and $\gamma = 1$. We will also use the standard flat cosmological model ΛCDM with $H_0 = 70$ km/s/Mpc, $\Omega_{\rm m} = 0.3$ and $\Omega_\Lambda = 0.7$ where necessary. Also, here we use $\hbar = c = k_{\rm B} = 1$ values. The exponentially small tail of this distribution could suggest that the IMBH fraction may not be present. However, integration over volumes of space up to large redshifts detectable by space interferometers, along with the inverse relationship of the merger rate of primordial IMBH binaries to cosmic time $t(z)$, contributes for this and lead to a reasonable probability of detecting such TianQin mergers over several years of observation (Fragione & Loeb 2023).

In this work we use the model of binary black hole formation developed in Raidal et al. (2019):

$$\frac{d\mathcal{R}(z)}{d\ln m_1 d\ln m_2} = \frac{3.2\times10^6}{\rm Gpc^3\times yr} S(m_1, m_2, z) f_{\rm pbh}^{53/57} \left(\frac{t(z)}{t_0}\right)^{-34/37} \times \psi(m_1)\psi(m_2) M^{-32/37}\eta^{-34/37}. \quad (3)$$

Here $S \leq 1$ is the suppression factor which we will set to 1 (Hutsi et al. 2021; Raidal et al. 2019), t_0 is the age of the Universe, $M = (m_1+m_2)/M_\odot$, $\eta = m_1m_2/(m_1+m_2)^2$. Here we change m_1, m_2 to $\mathcal{M}, q$, where $\mathcal{M} = (m_1m_2)^{3/5}/(m_1+m_2)^{1/5}$ is the chirp-mass of binary system in units M_0 and $q = m_2/m_1 \leq 1$ is the binary mass ratio. Substituting $m_1 = \mathcal{M}(1+q)^{1/5}/q^{3/5}, m_2 = \mathcal{M}q(1+q)^{1/5}/q^{3/5}$ and the Jacobian $J(\mathcal{M}, q) = \mathcal{M}(1+q)^{2/5}/q^{6/5}$.

After substituting eq. (2) into eq. (3) and performing integration over q in eq. (3) we obtain the specific rate

$$\frac{d\mathcal{R}(z)}{d\mathcal{M}} = A \times \mathcal{M}^{42/37}\mathcal{M} e^{-2\gamma\ln^2\mathcal{M}} \times \int_0^1 \Phi(q, \mathcal{M}) dq. \quad (4)$$

Here $f_q = (1+q)^{1/5}/q^{3/5}$, also

$$A = \frac{3.2\times10^6}{\rm Gpc^3\times yr} f_{\rm pbh}^{53/57} \left(\frac{t(z)}{t_0}\right)^{-34/37} \frac{\pi}{\gamma} e^{-2/\gamma} \left(\frac{M_\odot}{M_0}\right)^{-32/37}, \quad (5)$$

and

$$\Phi(q,\mathcal{M}) = q^{-3/5}(1+q)^{6/5} e^{-\gamma(\ln^2 f_q + \ln^2 f_q q)} \left(f_q^2 q\right)^{-2\gamma \ln \mathcal{M}} \frac{(1+q)^{2/5}}{q^{6/5}}. \tag{6}$$

The merging rate of binary PBHs $d\mathcal{R}/d\mathcal{M}$ at redshift $z = 0$ for various model parameters is presented in Fig. 1a. Integrating $d\mathcal{R}/d\mathcal{M}$ over $\mathcal{M}$ gives the overall merging rate of binary PBHs as a function of z (Fig. 1b). In contrast to the astrophysical binary black hole, in the adopted model the merging rate of binary PBHs increases monotonically with increasing redshift according to the law $\mathcal{R}(z) \sim 1/t(z)$ for all z.

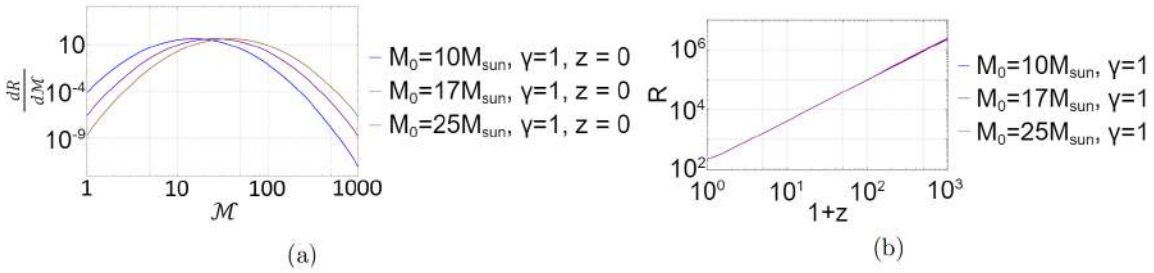

Fig. 1. (a) Expected distribution of the primordial binary IMBH rate over chirp-mass (in solar masses) $d\mathcal{R}/d\mathcal{M}$ [Gpc^{-3}yr^{-1}] at $z = 0$ for $f_{\rm pbh} = 10^{-3}$, $\gamma = 1$ and different $M_0 = 10, 17, 25 M_\odot$. (b) The comoving merging rate of primordial binary PBHs (3) as a function of redshift $\mathcal{R}(z) \sim t(z)^{-34/37}$.

3 Predictions for the detection of merging binary primordial IMBHs at the TianQin detector

The noise sensitivity curve of the detector determines the maximum distance from which a binary system with chirp-mass and mass ratio can be detected at a given signal-to-noise ratio (SNR). We take the sensitivity of TianQin and perform the SNR calculation according to Feng et al. (2019). The limiting redshift $z_{\rm lim}(\mathcal{M})$ with chirp-mass $\mathcal{M}$ for different SNR values is shown in Fig. 2a.

The expected merging rate of binary PBH with taking into account the detector sensitivity is obtained by integrating the rate $d\mathcal{R}/d\mathcal{M}$ in eq. (4) (with eq. (5) and eq. (6)) over redshift up to $z_{\rm lim}(\mathcal{M})$:

$$\frac{dN}{dt d\mathcal{M}} = \int_0^{z_{\rm lim}(\mathcal{M})} \frac{d\mathcal{R}(z)}{d\mathcal{M}} \frac{1}{1+z} \frac{dV(z)}{dz} dz, \tag{7}$$

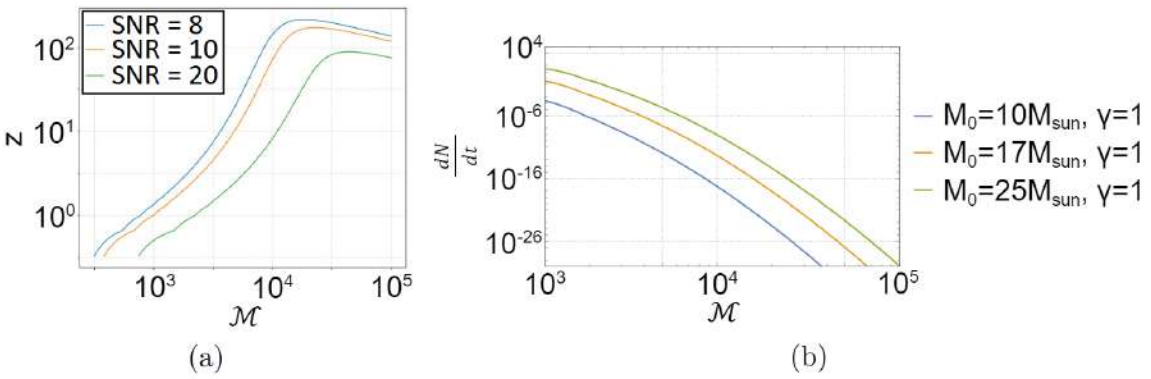

Fig. 2. (a) Limiting redshift $z_{\rm lim}(\mathcal{M})$ (in the source's frame) for detecting of coalescing binary black holes (BHs) with chirp-mass $\mathcal{M}$ (in solar masses) at TianQin threshold $SNR = 8, 10, 20$. (b) The expected cumulative detection rate $\frac{dN}{dt}(> \mathcal{M})$ of the primordial binary IMBH with chirp-mass $\mathcal{M}$ (in solar masses) by the TianQin interferometer for $SNR = 8, f_{\rm pbh} = 10^{-3}, \gamma = 1$.

where

$$\frac{dV(z)}{dz} = \frac{1}{H_0} \frac{4\pi D_m^2}{\sqrt{\Omega_{\rm m}(1+z)^3 + \Omega_\Lambda}}. \tag{8}$$

Here, D_m is the metrical distance from the source to the detector. And finally, in eq. (7) according eq. (8) we can obtain a cumulative detection rate:

$$\frac{dN}{dt}(> \mathcal{M}) = \int_{\mathcal{M}}^{\infty} \frac{dN}{dt d\mathcal{M}} d\mathcal{M}. \tag{9}$$

The obtained cumulative detection rate $\frac{dN}{dt}(> \mathcal{M})$ in eq. (9) is shown in Fig. 2b. It can be seen that a few primordial binary IMBH mergings can be detected. A feature of such mergers may be zero effective spins and a large redshift $z > 20$, at which nothing but primordial black holes are believed to exist.

4 Conclusions

Using a specific model for the formation of binary PBHs, we calculated the expected rate of detection of such binary BHs using the TianQin interferometer (Fig. 2b). It has been shown that for PBH formation parameters corresponding to the registration rate and distribution of mergers of binary BHs by LVK interferometers ($M_0 \sim 10$–$20\ M_\odot$, $\gamma \sim 1$) and a moderate fraction of PBHs in the dark matter density $f_{\rm pbh} = 10^{-3}$, the expected number of detections of merging IMBHs with a mass

$M \sim 10^3$–$10^4\ M_\odot$ can range from several to hundreds of events over several years of observations, depending on the parameters. Thus, we can conclude that space-based laser gravitational-wave interferometers such as TinQin have the potential to provide evidence for the existence of primordial IMBHs.

Acknowledgements. The authors thanks A. Dolgov for discussions.

Funding

The work of N. Mitichkin was supported by the Russian Science Foundation grant 22-12-00103 and the BASIS Foundation grant 22-2-10-2-1. The works of K. Postnov and I. Chekh were supported by the Russian Science Foundation grant 23-42-00055.

References

Andres-Carcasona M., Iovino A., Vaskonen V., et al., 2024., arXiv e-prints, arXiv:2405.05732
Arefeva I., Ermakov A., Rannu K., et al., 2023, European Physical Journal, 83, 1, id. 79
Blinnikov S., Dolgov A., Porayko N., et al., 2016, JCAP, 2016, 11, id. 036
Carr B., 1975, Astrophysical Journal, 201, p. 1
Dolgov A. and Silk J., 1993, Phys. Rev. D, 47, 10, p. 4244
Dolgov A., Kawasaki M., Kevlishvili N., 2009, Nuclear Physics B, 807, 1-2, p. 229
Dolgov A., Kuranov A., Mitichkin N., et al., 2020, JCAP, 2020, 12, id. 017
Eftekhari T., Tchekhovskoy A., Alexander K., et al., 2024, arXiv e-prints, arXiv:2404.10036
Feng W., Wang H., Hu X., et al., 2019, Phys. Rev. D, 99, 12, id. 123002
Fragione G. and Loeb A., 2023, Astrophysical Journal, 944, 1, id. 81
Fujii M., Wang L., Tanikawa A., et al., 2024, Science, 384, 6703, p. 1488
Gonzalez Prieto E., Weatherford N., Fragione G., et al., 2024, arXiv e-prints, arXiv:2404.11646
Hutsi G., Raidal M., Vaskonen V., et al., 2021, JCAP, 2021, 3, id. 068
Kormendy J. and Ho L., 2013, Annual Review of Astronomy and Astrophysics, 51, 1, p. 511
Kovacs O., Bogdan A., Natarajan P., et al., 2024, Astrophysical Journal Letters, 965, 2, id. L21
Liu L., You Z., Wu Y., et al., 2023, Phys. Rev. D, 107, 6, id. 063035
Luo J., Chen L., Duan H., et al., 2016, Classical and Quantum Gravity, 33, 3, id. 035010
Mei J., Bai Y., Bao J., et al., 2021, Progress of Theoretical and Experimental Physics, 5, id. 05A107
Mezcua M., 2017, International Journal of Modern Physics D, 26, 11, id. 1730021
Raidal M., Spethmann C., Vaskonen V., et al., 2019, JCAP, 2019, 2, id. 018
Schneider R., Ferrara A., Natarajan P., et al., 2002, Astrophysical Journal, 571, 1, p. 30
Zeldovich Y. and Novikov I., 1967, Soviet Astronomy, 10, p. 602

VAK 2024 MODERN ASTRONOMY: FROM THE EARLY UNIVERSE TO EXOPLANETS AND BLACK HOLES 300 years Russian Academy of Sciences

A strategy for wormhole search using observational astronomy

Yu. Moiseev[1] and O. Sazhina[1,2]

[1] Department of Celestial Mechanics, Astrometry and Gravimetry, Faculty of Physics, Moscow State University, 1 Leninskie Gory, stroenie 2, Moscow, 119991 Russia
[2] Sternberg Astronomical Institute, Moscow State University, 13 Universitetsky pr., Moscow, 119991 Russia

Abstract. We present a promising strategy for wormhole (WH) search using astronomical observations. By identifying a net effect of anomalous gravitational acceleration may allow for assumptions regarding the hidden WH nature of a black hole (BH). We provide an upper estimate of this effect for several stars in known BH systems such as S2 and S62 orbiting around Sgr A*; along with modeling a synthetic system consisting of a traversable WH, a star on our side and a perturbing object on the other side of a WH. We also consider recently discovered objects from GAIA catalogue data — GAIA BH1, BH2 and BH3. We show that in the traversable WH model a perturbing object (star) located on the other side of the WH throat is capable of causing a significant anomalous acceleration of an object (star) on the observer's side. This effect is observed to be more significant than other competing factors, including disturbances from nearby stars and the influence of the dark matter halo. The estimated magnitude of the anomalous acceleration varies from 10^{-4} to 10^{-2} cm/sec^2, which corresponds to the current accuracy of acceleration measurements. In the future, this may allow for a more precise estimation of the desired effect.

Keywords: gravitation, black hole physics; astrometry; binaries: general

DOI: 10.26119/VAK2024.035

1 Introduction

A wormhole (WH) is a peculiar hypothetical object with non-trivial topology that connects distant regions of spacetime through a tunnel-like structure called a WH throat. WH-like objects are valid solutions of the Einstein field equations, hence they are consistent with General Theory of Relativity (GTR), though predicted by other theories of gravity as well. The study of WHs has its origins in the Einstein and Rosen paper (Einstein & Rosen 1935). This research has since progressed with significant theoretical advancements that present models explaining the mechanisms of the formation of WHs in the early Universe and their stability, including the development of a stable traversable throat.

So-called traversable WHs are of particular interest for investigating their observational properties on our side (hereinafter referred to as "side 1"), as these objects can exhibit electromagnetic or gravitational effects from perturbing objects on the other side (hereinafter referred to as "side 2") of their throat.

Thus, a non-stationary gravitational source on side 2 (for example, a massive star with known orbital parameters around the WH) is capable of causing a certain perturbation in the movement of an object on side 1. This effect may be detectable during an observational program.

2 Anomalous acceleration

In order to estimate the anomalous acceleration caused by a perturbation, we will use a model based on a simple Schwarzschild WH in a short-throat and thin-shell approximation. Based on the methodology proposed by Dai & Stojkovic (2019), assuming a perturbing object on an elliptic orbit on side 2, the acceleration variation of an object on side 1 can be calculated using the formula:

$$\Delta a = \mu\Big(\frac{R}{r_{\mathrm{p}}} - \frac{R}{r_{\mathrm{a}}}\Big) \cdot \frac{1}{r_1^2}, \tag{1}$$

where μ — effective mass of the object (star) on side 2, $r_{\mathrm{p}}, r_{\mathrm{a}}$ — it's periapsis and apoapsis, r_1 — radial coordinate on side 1, R — radius of a WH throat.

2.1 Estimated effect

Since BH and WH cannot be distinguished with the current astrophysical data, this work will assume that what are currently interpreted as BH may actually be WH. We will refer to these objects as "WH candidates."

As both WH and BH are associated with extreme states of matter, it is reasonable to search for the perturbing acceleration of massive objects (stars) near known BHs in order to test their nature. To obtain the estimated magnitude of the effect, we chose several stars orbiting WH-candidates in our Galaxy:
– S2 and S62 orbiting around Sgr A*
and recently discovered wide binary systems of BH and stellar companion from Gaia data:
– Gaia BH1 (El-Badry et al. 2023);
– Gaia BH2 (El-Badry et al. 2023);
– Gaia BH3 (Gaia Collaboration 2024).

By varying the parameters of the perturbing object (mass, semimajor axis) we estimated (using (1)) an average magnitude of acceleration variation $\Delta a \approx 10^{-4}$cm/sec^2, which grows up to $\Delta a_{\max} \approx 10^{-2}$ cm/sec^2 for S62 star in an extreme case with the best parameters of a perturbed possible (with mass of $\approx 50 M_\odot$ and semimajor axis of ≈ 0.01AU).

The relationship between the anomalous acceleration (in cm/sec^2) for objects on side 1 (Sgr A* (S2, S62), Gaia BH1, Gaia BH2, Gaia BH3) and the mass (in units of solar mass) of the perturbing object located on side 2 is illustrated in Fig. 1.

The synthetic scenario involves a binary system: the first component of the pair is a WH with a mass of $5M_\odot$ and the second component is a neutron star with a mass of $1.4M_\odot$. The binary system has an orbital period of 1.5 hours. The parameters of the perturbing object on side 2 are: orbital eccentricity $e = 0.4$ and an orbital period of 1 day. In this case, the magnitude of the anomalous acceleration can reach 1.148 cm/sec^2. If the mass of the perturbing object is fixed at $50M_\odot$, then with an eccentricity of $e = 0.4$, the magnitude of the desired effect can reach 1.683 cm/sec^2.

2.2 GAIA BH systems

Table 1. Gaia BH parameters and estimated acceleration accuracy.

	M	m	e	P	σ_a
Gaia BH1	$9.62 \pm 0.18 M_\odot$	$0.93 \pm 0.05 M_\odot$	0.451 ± 0.005	$185.59 \pm 0.05 d$	$1.9 \cdot 10^{-1}$cm/sec^2
Gaia BH2	$8.94 \pm 0.34 M_\odot$	$1.07 \pm 0.19 M_\odot$	0.5176 ± 0.0009	$1276.7 \pm 0.6 d$	$1.8 \cdot 10^{-2}$cm/sec^2
Gaia BH3	$32.7 \pm 0.82 M_\odot$	$0.76 \pm 0.05 M_\odot$	0.7291 ± 0.0048	$4253.1 \pm 98.5 d$	$4.5 \cdot 10^{-2}$cm/sec^2

Strong limitations on the ability to extract the net effect described above are associated with the low accuracy of the accelerations known, stemming from uncertainties in the orbital solutions for the systems under investigation. The highest

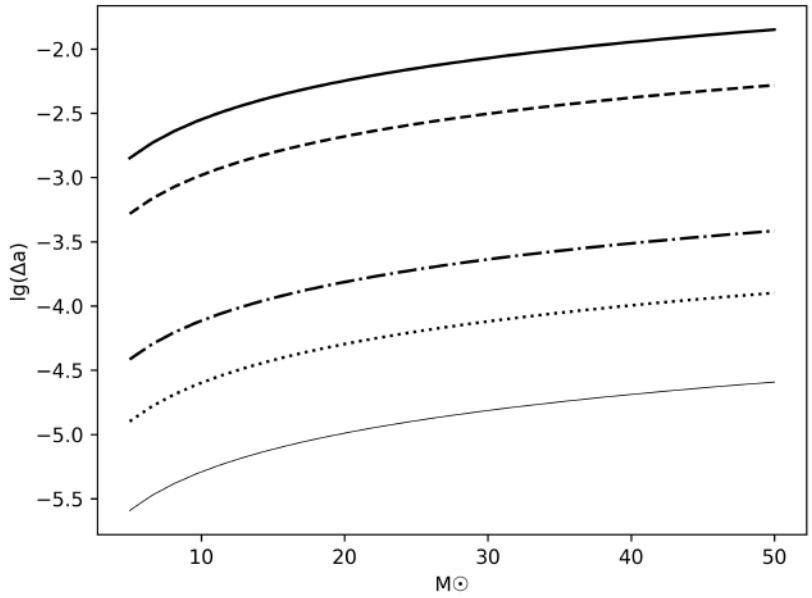

Fig. 1. Dependence of the anomalous acceleration on mass of perturbing object (in logarithmic scale). From top to bottom: solid line — S62, dashed line — Gaia BH2, dash-dot line — Gaia BH1, dotted line — Gaia BH3, thin solid line — S2.

achieved precision is associated with the S2 star, attributed to the extensive observational data collected. However, the detection of the possible effect remains at the limits of our capabilities.

Gaia astrometry has identified several Galactic wide-binary systems containing dormant BHs, which may be suitable for further examination due to the precision of Gaia data. We evaluate the accuracy of indirect acceleration measurements from Gaia orbital solutions and present this data in Table 1.

3 Competing effects

The dark halo density distribution in the center of our Galaxy is estimated to be around $10^{-2} M_{\odot}$ per pc^3. The region under consideration (for S2 and S62) does not exceed 0.05 pc in radial distance and contains dozens of stars; hence, we neglect the dark halo's gravitational influence.

The stellar density in the center of our Galaxy appears to have a flat distribution for late-type stars (i.e., the number of stars per unit of observable area remains

constant within the cluster). The effective boundary of the central cluster, according to various estimates, ranges from 0.02 to 0.05 pc. For early-type stars, there is a decline that follows a power law $r^{-\Gamma}$.

To estimate the contribution of the stellar medium, we will analyse the star S2 at the pericenter of its orbit around Sgr A* inside both homogeneous and non-homogeneous spheres with corresponding density profiles: flat with characteristic density of 2.5 stars per arcsec^2 and declining $\rho(r) \approx r^{-\Gamma}$, where Γ varies from 0.8 to 0.9 according to various estimates.

The equations of motion in this case should be as follows:

$$\begin{array}{l} \frac{\partial^2 x}{\partial t^2} = -\frac{\mathrm{GM}\cdot x}{r^3} - \frac{4}{3}\pi G\rho x, \\ \frac{\partial^2 y}{\partial t^2} = -\frac{\mathrm{GM}\cdot x}{r^3} - \frac{4}{3}\pi G\rho y, \end{array} \tag{2}$$

for a homogeneous sphere and:

$$\begin{array}{l} \frac{\partial^2 x}{\partial t^2} = -\frac{\mathrm{GM}\cdot x}{r^3} - \frac{4\pi G\cdot \mathrm{const}}{r^2} \cdot \frac{x}{r} \int\limits_0^r dr r^{2-\Gamma}, \\ \frac{\partial^2 y}{\partial t^2} = -\frac{\mathrm{GM}\cdot y}{r^3} - \frac{4\pi G\cdot \mathrm{const}}{r^2} \cdot \frac{y}{r} \int\limits_0^r dr r^{2-\Gamma}, \end{array} \tag{3}$$

for a non-homogeneous sphere, where const $= \frac{(3-\Gamma)M}{4\pi R^{3-\Gamma}}$ is a scaling constant, based on the estimate of enclosed mass M.

Integrating the motion of the star, using (2) and (3), and then numerically differentiating the result twice leads to the determination of the star's acceleration within a perturbing stellar medium. We can then calculate the acceleration variation as the average difference between the acceleration in the frame of Keplerian motion and the perturbed one.

The computed values for the homogeneous and non-homogeneous stellar medium are $8.6\cdot\ 10^{-9}$ cm / sec^2 and $1.0\cdot 10^{-6}$cm/sec^2, respectively. This indicates that neither can provide a sufficient impact to fully account for the contribution from the desired effect.

4 Summary

In this study, we introduce a sensitive test to determine whether a BH may be a potential WH-candidate, assuming the presence of a perturbing object on side 2 to estimate the detectable features on side 1. For this purpose, we analyze the supermassive BH Sgr A* located at the center of our Galaxy with two stars: S2 and S62 on its orbit, as well as three recently identified stellar-mass dormant BHs based on Gaia data.

All the candidates indicate potential results for a possible anomalous acceleration effect, demonstrating the ability to extract its manifestation despite the presence of other disturbing factors. We demonstrate that the influence of nearby stellar sources or dark matter halo can not provide enough force to obscure the desired perturbation. This makes examining the stellar motion around BHs a robust test for non-BH nature in future observations.

References

Dai D. and Stojkovic D., 2019, Phys. Rev. D 100, id. 083513
Einstein A. and Rosen N., 1935, Phys. Rev., 48, 1, p. 73
El-Badry K., Rix H.W., Cendes Y., et al., 2023, Monthly Notices of the Royal Astronomical Society, 521, 3, p. 4323
El-Badry K., Rix H.W., Quataert E., et al., 2023, Monthly Notices of the Royal Astronomical Society, 518, 1, p. 1057
Gaia Collaboration, 2024, Astronomy & Astrophysics, 686, id. L2

VAK 2024 MODERN ASTRONOMY: FROM THE EARLY UNIVERSE TO EXOPLANETS AND BLACK HOLES 300 years Russian Academy of Sciences

First results of HI survey of recently discovered close dwarf galaxies

A. Nazarova[1], J. Cannon[2], I. Karachentsev[1], D. Makarov[1], and M. Chazov[1]

[1] Special Astrophysical Observatory of the Russian Academy of Sciences, Nizhny Arkhyz, 369167 Russia
[2] Department Physics and Astronomy, Macalester College, 1600 Grand Avenue, Saint Paul, MN 55105 USA

Abstract. We describe the results of observations with the 100m Robert C. Byrd Green Bank Telescope (GBT) in the HI line of 54 nearby dwarf galaxies found mainly in the DESI Legacy Imaging Surveys. Of these, we detected 35 galaxies with the following median parameters: the HI-flux of 0.53 Jy km/s, heliocentric velocity of 1123 km/s, and W_{50} line width of 33 km/s. Most of them are isolated irregular objects, and some have turned out to be new probable satellites of nearby disc galaxies: NGC 2787, NGC 3556, NGC 4490, and NGC 5055. The detected galaxies are predominantly gas-rich systems with a median gaseous-mass-to-stellar-mass ratio of 2.41.

Keywords: galaxies: dwarf; galaxies

DOI: 10.26119/VAK2024.036

1 Introduction

Most existing galaxy catalogues are samples limited by an apparent magnitude or flux of objects in a fixed spectral range. However, the results of modeling the large-scale structure of the Universe within the framework of the standard cosmological model ΛCDM need to be compared with an ensemble of galaxies limited to a fixed volume. The most suitable sample of this type is the Updated Nearby Galaxy Catalog (UNGC, Karachentsev et al. 2013), whose regularly updated database (https://www.sao.ru/lv/lvgdb/) contains about 1400 galaxies with distances $D < 11$ Mpc. It is obvious that the population of this Local Volume (LV) can either increase with the advent of deeper sky surveys, or decrease somewhat as the distances of the galaxies are refined. A great advantage of the UNGC catalog is the predominance of low-luminosity dwarf galaxies, which are usually inaccessible to observations at large distances.

The search for new LV objects (Karachentsev & Kaisina 2022; Karachentseva et al. 2023; Karachentsev et al. 2024) using the DESI Legacy Imaging Surveys (Dey et al. 2019) led to the discovery of more than a hundred high declination dwarf galaxies. About half of them turned out to be spheroidal systems (dSph) with a low neutral hydrogen content. After excluding dSphs, we selected 54 dwarf galaxies with evidence of active star formation to measure their radial velocities with the Green Bank Telescope (GBT).

2 GBT observations of the nearby dwarfs

We observed 54 dwarf galaxies with the National Radio Astronomy Observatory 100m Robert C. Byrd Green Bank Telescope (GBT). The total effective frequency coverage was from 1406 MHz to 1426 MHz. This covers the approximate velocity range of -1000 to $+3000$ km/s, which is sufficient to probe the LV within 10 Mpc. Data were acquired during 14 observing sessions in August and October 2023 ($\sim$ 50 hours in total).

The HI signal was detected in 35 galaxies out of 54 targets. Examples of images from the DESI Legacy Imaging Surveys along with their spectra near the HI line are shown in Fig. 1.

All data reduction was carried out in the IDL environment[1] using the GBTIDL package developed at NRAO. For most galaxies, the velocity and width measurements and their errors were obtained by fitting a single Gaussian component to the line profile after continuum fitting and subtraction. The HI-line total flux was calculated as the area under the real spectrum in a selected region.

[1] Exelis Visual Information Solutions, Boulder, CO.

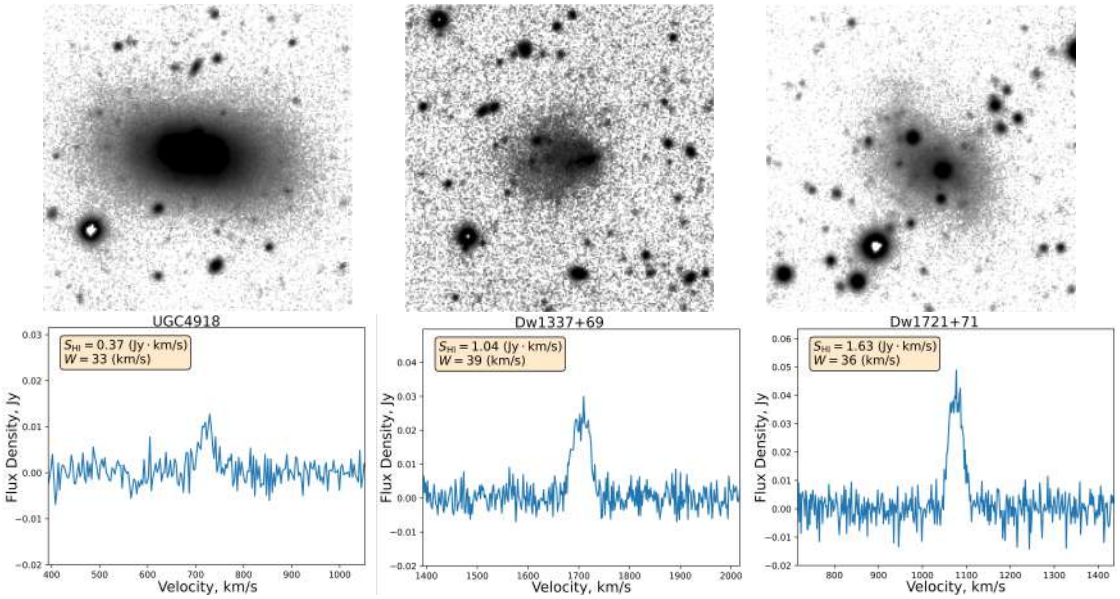

Fig. 1. *Top row.* Images of nearby late-type dwarf galaxies taken from the DESI Legacy Imaging Surveys. Each image side is 2′, North at the top and East at the left. *Bottom row.* HI spectra of these dwarf galaxies detected with the GBT. The total HI-flux $S_{\rm HI}$ and the line width W_{50} are given in each panel.

3 Photometry

Deep multicolour photometry was performed for 52 of the 54 galaxies, using images from the DESI Legacy Imaging Surveys (DR10). The total g, r magnitudes were measured for all 52 objects, z values only for the brightest objects, and i values only when the corresponding images were available. Two targets (Dw1351+50 and Dw1354+44) turned out to be false, non-existent objects.

We measured photometric growth curves using standard ellipse-fitting and aperture photometry techniques in the Astropy *photutils*[2]) package. This was preceded by background subtraction. Foreground and bright background objects were also masked, and the corresponding pixels were then replaced by the mean flux in the elliptical annulus contained in the mask. The resulting growth curve was fitted using a slightly modified exponential law. Some photometric steps are shown in Fig. 2.

4 Discussion

The combination of GBT-observations and optical photometry has been used to estimate the masses of hydrogen $M_{\rm HI}$, neutral gas $M_{\rm gas}$, and the stellar population

[2] https://photutils.readthedocs.io/en/stable/

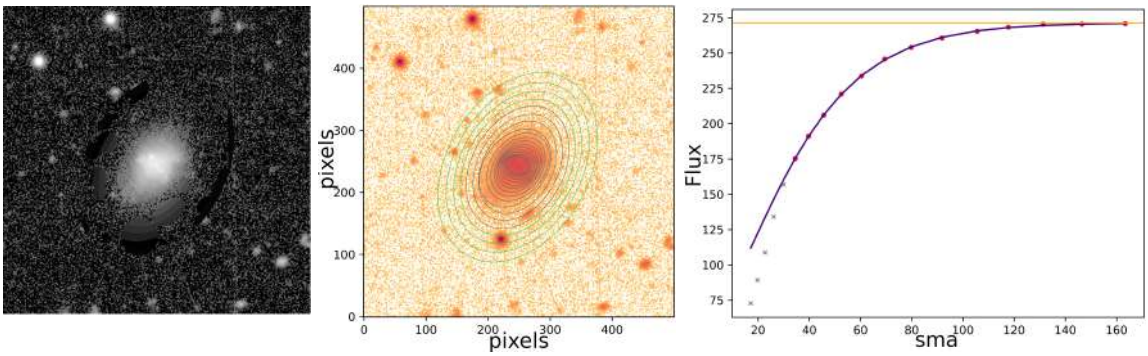

Fig. 2. *Left.* Image of the Dw1558+67 with masked pixels replaced by the mean flux in the aperture rings. *Middle.* Elliptical isophotes fitted to the galaxy image. *Right.* Corresponding growth curve fitted with a modified exponential low.

M_*. It turns out that the mass equality of gas and stars $M_{\rm gas} = M_*$ occurs when $m_{21} = B + 1.00 \pm 0.11$ mag, where $m_{21} = 17.4 - 2.5\log(S_{\rm HI})$, $S_{\rm HI}$ — HI-flux. Consequently, in the late-type dwarf galaxies with $m_{21} - B < 1^m.00$, the gas component predominates.

The distribution of galaxies in our sample according to m_{21} and B magnitudes is shown in the left panel of Fig. 3. Galaxies not detected in the HI line are indicated by open dots with $m_{21} = 20.0$. The diagonal lines correspond to the values of the parameter $\mu = M_{\rm gas}/M_*$ equal to 0.1, 1.0 and 10. The majority of the detected galaxies are gas-dominated systems with a median ratio of $\mu = 2.41$.

The m_{21} versus B distribution of 266 late-type T = 9, 10 dwarf galaxies with accurate TRGB distance estimates from the UNGC catalog by magnitudes m_{21} and B is shown in the right panel of Fig. 3. As can be seen from these plots, 97% of late-type dwarf galaxies reside in the interval μ = [0.1–10], with a median near $\mu = 1.5$.

Being significantly gas-dominated systems, the late-type dwarf galaxies show the expected correlation between their hydrogen mass and the HI line width W_{50}, which is a baryon analogue of the Tully & Fisher (1977) relation between the integral absolute magnitude of the galaxy, $M_{\rm B}$, and W_{50}. The left panel of Fig. 4 shows the relation between M_{21} and W_{50} for 34 galaxies detected by us. The horizontal bars indicate the standard errors of W_{50}. The dashed line in the panel indicates the relation $M_{\rm B} = -7.27(\log W_{50} - 2.5) - 19.99$ according to Tully et al. (2008) that has been obtained for disc-dominated galaxies. As can be seen from these data, dwarf galaxies satisfactorily follow the classical Tully–Fisher relation when M_{21} magnitudes are used instead of $M_{\rm B}$.

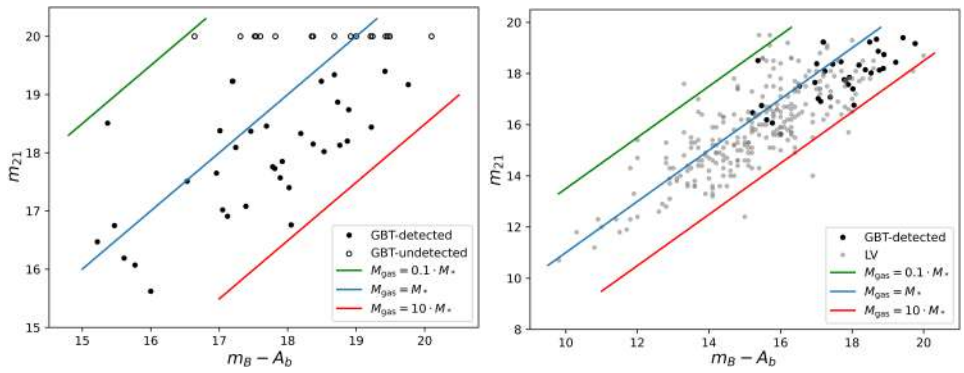

Fig. 3. Distribution of dwarf galaxies by m_{21}-magnitude and B-magnitude corrected for Galactic extinction A_b. Three diagonal lines correspond to μ equal to 0.1, 1 and 10. *Left.* Dwarf galaxies observed with GBT. For undetected galaxies are assigned $m_{21} = 20.^m0$. *Right.* Dwarf galaxies detected with GBT are combined with 266 late-type (T= 9, 10) in the Local Volume with TRGB distance estimates.

The scatter of late-type galaxies in Fig. 4 is not so much caused by measurement errors of W_{50} and S_HI, but by the irregular shape of the dwarfs caused by turbulent motions in them. One would hope that taking the inclination angle of the galaxy into account would reduces the dispersion in the M_{21} vs. W_{50} diagram. The right panel of Fig. 4 exhibits the distribution of irregular dwarfs through M_{21} and corrected for their inclination angle line width W_{50}^c. As one can be seen, taking the tilt into account does not reduce the dispersion of galaxies in the diagram, but actually increases it slightly. The likely reason for the scatter is the real difference in the shape of irregular dwarfs from the ellipsoid of rotation, especially in relation to the shape of their gas component (Roychowdhury et al. 2010).

5 Concluding remarks

The search for new nearby dwarf galaxies using data from the DESI Legacy Imaging Surveys data led to the discovery of more than 50 late-type dwarfs that became targets for observations in the HI line with the GBT. HI fluxes, radial velocities and W_{50} line widths have been measured for 2/3 of the objects. Their median values are 0.53 Jy km/s, 1123 km/s and 33 km/s respectively. According to their D_NAM[3] values, a median distance of 17.3 Mpc and about 40% of the detected galaxies turn out to be new members of the Local Volume with $D < 11$ Mpc. The hydrogen masses are in the range $\log(M_\mathrm{HI}/M_\odot) = [5.68–9.06]$ with a median of 7.68.

[3] D_NAM — kinematic distance of the galaxy in Mpc, calculated via its radial velocity taking into account local streams according to the Numerical Action Method model (Shaya et al. 2017; Kourkchi et al. 2020)

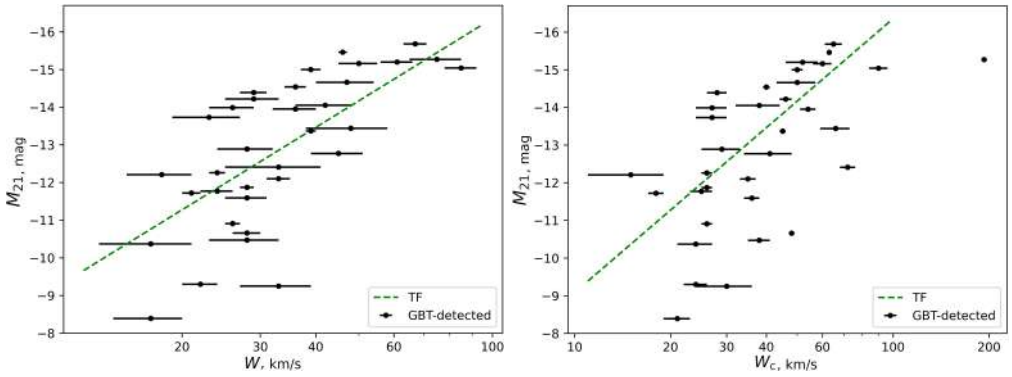

Fig. 4. *Left.* M_{21}-magnitude vs. line width relation for dwarf galaxies detected with the GBT. The horizontal bars show the standard errors of W_{50}. The dashed line displays the Tully–Fisher relation. *Right.* M_{21}-magnitude vs. line width relation for the same galaxies, but with a correction for galaxy inclination.

Our radial velocity measurements led to the discovery of 4 new probable satellites around the LV disc galaxies: NGC 2787, NGC 3556, NGC 4490 and NGC 5055. Also 3 dwarf galaxies: UGC 6451, Dw1235−02 and KDG 162 are close to the bright LV spiral galaxies: M 81, M 104 (Sombrero) and NGC 4605 respectively.

Funding

AN, IK, DM, and MC are supported by the Russian Science Foundation grant № 24–12–00277.

References

Dey A., Schlegel D.J., Lang D., et al., 2019, The Astronomical Journal, 157, p. 168
Karachentsev I.D. and Kaisina E.I., 2022, Astrophysical Bulletin, 77, p. 372
Karachentsev I.D., Karachentseva V.E., Kaisin S.S., et al., 2024, Astrophysics, 66, p. 441
Karachentseva V.E., Karachentsev I.D., Kaisina E.I., et al., 2023, Astronomy & Astrophysics, 678, id. A16
Karachentsev I.D., Makarov D.I., Kaisina E.I., 2013, The Astronomical Journal, 145, p. 101
Kourkchi E., Courtois H.M., Graziani R., et al., 2020, The Astronomical Journal, 159, id. 67
Roychowdhury S., Chengalur J.N., Begum A., et al., 2010, MNRAS, 404, id. L60
Shaya E.J., Tully R.B., Hoffman Y., et al., 2017, The Astrophysical Journal, 850, p. 207
Tully R.B. and Fisher J.R., 1977, Astronomy & Astrophysics, 54, p. 661
Tully R.B., Shaya E.J., Karachentsev I.D., et al., 2008, The Astrophysical Journal, 676, p. 184

MODERN ASTRONOMY: FROM THE EARLY UNIVERSE TO EXOPLANETS AND BLACK HOLES

Accretion on a wormhole with monopole magnetic field

M. Piotrovich, S. Krasnikov*, S. Buliga, and T. Natsvlishvili

Central astronomical observatory at Pulkovo RAS, Saint-Petersburg, 196140 Russia
* Deceased 19.03.2024

Abstract. The presence of even simple magnetized wormholes may have observable consequences. If the wormhole and its surrounding magnetic fields a re s tatic, symmetrical, and spherical, and gas in the vicinity falls radially into the wormhole, the resulting spectrum would feature bright cyclotron or synchrotron lines caused by interactions between charged plasma particles and the magnetic field. This radiation would be non-polarized due to the symmetry of the system. The emission of this exotic, non-thermal yet non-polarized type of radiation could serve as a signature for wormholes. Additionally, in this scenario, the formation of an accretion disk is still possible at some distance from the wormhole; however, a monopole magnetic field may complicate this process and lead to the emergence of asymmetrical and one-sided relativistic jets.

Keywords: accretion, accretion disks, magnetic fields, gravitation

DOI: 10.26119/VAK2024.037

1 Introduction

The study of wormholes is of serious interest, as their properties and potential existence may influence our understanding of cosmology in the Universe. Kardashev et al. (2007) proposed the hypothesis that some galactic nuclei are in fact wormhole mouths.

Many authors have explored the distinct observational features of wormholes, specifically identifying characteristics that differentiate them from black holes. However, almost all of them have concluded that those features, even when present, are often challenging to observe with current astronomical equipment, and in some instances, it may not be possible at all. In our work, we utilize objects and physical mechanisms that are established in astrophysics, which enables us to achieve significant observational results.

Wormholes have unique properties that present a theoretical opportunity for generating a monopole magnetic field. And there are many works linking wormholes with a monopole field (Misner & Wheeler 1957; Bronnikov 1973; Ellis 1973).

Polarization, which is responsive to the anisotropy of matter distribution, is important in the examination of optically unresolved central regions of AGNs, including the accretion disk.

Previously (Piotrovich et al. 2020a,b) we have considered the possible accretion of matter into a wormhole. We examined the scenario where accretion into a traversable wormhole takes place from both sides, each positioned at the center of the active galactic nucleus. As a result, high-energy accretion flows collide inside the wormhole, which can lead to plasma heating to extremely high temperatures up to 10^{14}K. And plasma with such parameters will have a very specific spectrum, different from the spectrum of ordinary active galactic nuclei.

Now we will consider the accretion in the presence of a magnetic field, considering that the wormhole has a monopole magnetic field, which greatly distinguishes it from the much better studied Kerr black hole. In this work, we propose that the existence of even simplest magnetized wormholes may result in observable consequences that have not been previously discussed in the literature, to the best of our knowledge.

2 Our model and some calculations

The simplest compact radially magnetized object could be a wormhole based on the framework of Reissner–Nordström spacetime (actually, as long as the magnetic field outside the object is monopole, the structure of the former is irrelevant).

Select three positive parameters: $Q,\ m$, where $m > Q$, and r_0, of which the former two will describe, correspondingly, the magnetic charge and "mass" of the wormhole;

while r_0 will obey the inequality $r_0 > r_{\text{Horizon}}, r_{\text{Horizon}} \equiv m + \sqrt{m^2 - Q^2}$ and characterize "the size" of the wormhole. The auxiliary "half-wormhole", W_1, is defined as $W_1 : \mathrm{d}s^2 = -\nu(r)\,\mathrm{d}t^2 + \nu(r)^{-1}\mathrm{d}r^2 + r^2(\mathrm{d}\theta^2 + \cos^2\theta\,\mathrm{d}\phi)$, where $r > r_0, t \in \mathbb{R}$, $\nu \equiv 1 - \frac{2m}{r} + \frac{Q^2}{r^2}$.

W_1 is *almost* the sought-for spacetime: it is static, spherically symmetric and resolves the Maxwell–Einstein equations when a radial magnetic field $\boldsymbol{B} = \left(Q/r^2\right)\boldsymbol{e}_{\hat{r}}$ is applied. A characteristic of W_1 is that it has a single asymptotically flat end, which means W_1 is an extendable structure referred to as one of its extensions U_1, and it functions as a funnel rather than a wormhole. To address this aspect, we will define the wormhole, W, as a pair of equal funnels, U_1 and U_2, with their stems identified (the existence of a suitable isometry relating regions U_1 and U_2 is a non-trivial condition), see Fig. 1 from Morris et al. (1988).

This work focuses on spherical accretion; however, it but one can reasonably assume that a monopole field will impede the movement of plasma along Keplerian orbits near the wormhole and, in particular, will complicate the formation of an accretion disk. The formation of an accretion disk remains a possibility at a certain distance from the wormhole, where the low magnetic field and temperature (resulting in a low degree of ionization) of the accreting matter may limit the influence of the monopole field on the matter. It should be noted that accretion disks near wormholes without their own magnetic fields have been discussed in the literature (Harko et al. 2009; Lobo 2017; Piotrovich et al. 2020b).

A phenomenological study can be conducted on the formation of relativistic jets by the accretion disk at a wormhole with a monopole magnetic field. The disk wind may be influenced by the monopole field, indicating that jet formation is primarily facilitated through the Blandford–Znajek mechanism (Blandford & Znajek 1977). In this process, the surrounding interstellar matter, which does not originate from the disk, is collimated through the interaction between the disk's poloidal magnetic field and the rotating black hole or wormhole. Thus, if the wormhole rotates, then jets can, in principle, form. Moreover, if the monopole field of the wormhole is much stronger than the dipole field of the accretion disk, then the cyclotron radiation from them may be significantly stronger and at different frequencies compared to the case of a black hole. It is also possible that the jets themselves will be more powerful/faster, but this is not certain. If the wormhole monopole field strength is similar to the disk dipole field, there may be a decrease in field strength at one of the dipole field's poles due to the superposition of fields. This could lead to a reduction in cyclotron radiation from that side of the jet and possibly result in a jet that is less powerful, less collimated, or potentially not formed at all. However, the mechanism of jet formation is complex and not completely understood, so these

outcomes are not definitive. Note that asymmetrical and one-sided jets have been observed near some active galactic nuclei (Cawthorne 1991), and explaining this phenomenon poses challenges for classical theories, while our wormhole model offers a simple explanation.

Let's analyse the movement of single charged particle near a gravitating object with a monopole magnetic field in a simplified fictional space $\mathbb{R}^3$ (which is the Newtonian approximation of our metric W) in which we use the Newton gravity approximation (here the "mass" and the charge of the wormhole are described by the parameters m and Q, and it is a point-like object at the origin). In this case, the trajectory of a particle moving far enough from a gravitating object (so that relativistic effects can be neglected as a first approximation) can be obtained relatively easily (in our model we use non-relativistic Maxwell equations). Let's take for example a proton near a point-like object with the mass of the Sun $M_\odot$. In order to define the magnetic field strength we set the value of the field B_{10} at the radius $R = 10$ km. To simplify the analysis, we disregard the loss of proton energy from cyclotron radiation, as the trajectory is considered over a time interval of only 0.01 seconds.

We have numerically calculated the proton trajectories for various values of parameters such as the magnetic field strength B_{10}, starting position $R_{\rm st}$ and velocity $V_{\rm st}$ of a proton using a rather simple method. The total force acting on the proton can be expressed as the sum of the Lorentz force and the gravitational force: $\mathbf{F} = \mathbf{F_L} + \mathbf{F_g} = q_p/c[\mathbf{V} \times \mathbf{B}] - GM_\odot m_p \mathbf{r}/r^3$, where q_p is the proton charge, c is the speed of light, $\mathbf{V}$ is the proton speed, G is the gravitational constant, m_p is the proton mass, $\mathbf{r}$ is the radius vector, $\mathbf{B} = \mu\mathbf{r}/r^3$ is the magnetic monopole field strength, μ is the magnetic permeability, which in our case is $\mu = B_{10}R^2$.

Thus, 10^9 iterations were made for the proton flight time of 0.01 seconds. If the proton flew closer to the central object than 10 km, then we considered that it will inevitably fall on the object and the calculation stopped. To minimize errors, we ensured that the total (kinetic plus potential) energy of the proton divided by the proton mass $E_p/m_p = (\dot{x}^2 + \dot{y}^2 + \dot{z}^2)/2.0 - GM_\odot/\sqrt{(x^2 + y^2 + z^2)}$ did not vary by more than 0.001.

Figure 1 shows some of these trajectories. We see that even a relatively weak ($B_g \sim 1$G) monopole magnetic field prevents, as we conjectured earlier, the emergence of classical Keplerian orbits around the object. Instead, the proton begins to form spiral trajectories around radial magnetic field lines. The form of this spiral and the direction of the proton movement strongly depend on the parameters. In particular, at ~ 67000 km/s the proton's trajectory becomes closed (see the bottom picture in Fig.1). This is a kind of the "first escape velocity" for this particular situation. (However, it's important to note that the presence of energy loss from cyclotron ra-

diation prevents these circular orbits will from lasting long, causing them to become spiral orbits.) Consequently, at speeds below $\sim$ 67000 km/s, the proton is drawn towards the central object, whereas at speeds exceeding $\sim$ 67000 km/s, it moves away from the central object. As the magnetic field strength increases, the radius of the helix quickly decreases, resulting in motion of the proton that approaches a more radial path.

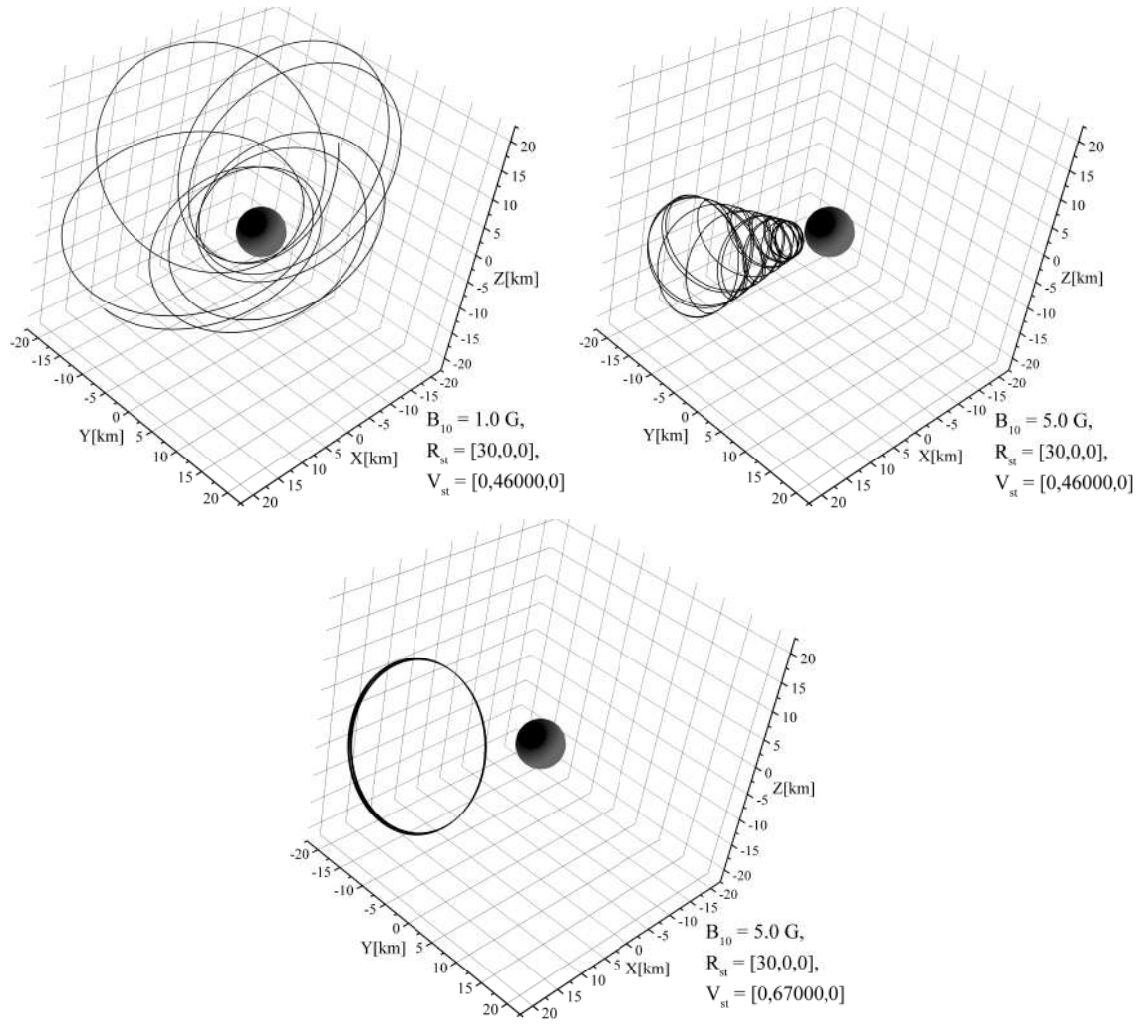

Fig. 1. Trajectories of a proton near a point-like gravitating object in the fictional space with the mass of the Sun and a monopole magnetic field for different starting parameter values. B_{10} is the magnetic field strength at $R = 10$km, $R_{\rm st}$ and $V_{\rm st}$ are starting position and speed of a particle in km and km/s respectively.

3 Conclusions

Current work has demonstrated that a wormhole with a monopole magnetic field can generate non-polarized cyclotron radiation, which is not commonly observed in known astrophysical objects. Possible candidates for such objects include both supermassive relativistic objects located in the centres of galaxies, as well as primordial wormholes of medium and small "mass" that may have formed in the early Universe. In particular, the latter may appear as star-like objects with an unusual non-polarized non-thermal spectrum consisting of cyclotron or synchrotron emission. Calculations based on a toy model suggest that even a relatively weak ($\sim$ 1G) monopole magnetic field may inhibit the formation of classical Keplerian orbits around the object. This result supports the idea that accretion is primarily radial at a close distance from the wormhole. However, the formation of an accretion disk is still quite possible at some distance from the wormhole. Also, if we consider the case of an accretion disk, a monopole magnetic field may impact its formation near the wormhole and result in the emergence of asymmetrical and one-sided relativistic jets.

References

Blandford R. and Znajek R., 1977, Monthly Notices of the Royal Astronomical Society, 179, p. 433
Bronnikov K., 1973, Acta Physica Polonica B, 4, 3, p. 251
Cawthorne T., 1991, Beams and Jets in Astrophysics, 19, p.187
Ellis H., 1973, Journal of Mathematical Physics, 14, p. 104
Harko T., Kovács Z., Lobo F., 2009, Physical Review D, 79, id. 064001
Kardashev N., Novikov I., Shatskiy A., 2007, International Journal of Modern Physics D, 16, p. 909
Lobo F., 2017, Fundamental Theories of Physics, 189
Misner C. and Wheeler J., 1957, Annals of Physics, 2, p. 525
Morris M., Thorne K., Yurtsever U., 1988, Physical Review Letters, 61, p. 1446
Piotrovich M., Krasnikov S., Buliga S., et al., 2020, Monthly Notices of the Royal Astronomical Society, 498, p. 3684
Piotrovich M., Krasnikov S., Buliga S., et al., 2020, Universe, 6, id. 120

MODERN ASTRONOMY: FROM THE EARLY UNIVERSE TO EXOPLANETS AND BLACK HOLES

Cosmological interpretation of JWST observations

A. Raikov[1], V. Yershov[2], and N. Lovyagin[3]

[1] St. Petersburg Branch of the Special Astrophysical Observatory of the Russian Academy of Sciences, 65 Pulkovskoye Shosse, St. Petersburg, 196140 Russia
[2] Saint Petersburg State University of Aerospace Instrumentation, 67 Bol'shaya Morskaya, Saint Petersburg, 190000 Russia
[3] Department of Computer Science, Saint Petersburg State University, 7/9 Universitetskaya Naberezhnaya, Saint Petersburg, 199034 Russia

Abstract. Observational data from the James Webb Space Telescope (JWST) indicate a significant n umber o f g alaxies w ith r edshifts $z > 1\,0$. G alaxies w ith record-breaking redshifts exhibit luminosities comparable to those of galaxies in the local universe, and they are small in size, measuring hundreds of parsecs, as determined within the standard cosmological model, ΛCDM. Within this framework, a satisfactory explanation for their formation and evolution has not yet been found. So, most current research focuses on revising theories of galaxy formation and evolution to align with JWST observational data. In this talk, we discuss cosmological tests based on JWST observations, which could provide an alternative explanation. High-redshift galaxies detected by the JWST exhibit brightness and large masses, yet their sizes are over 10 times smaller than those of low-redshift galaxies with comparable masses. This leads to an increase in the gravitational potential ϕ and, consequently, an increase in the velocity dispersion, which in turn results in the broadening of galaxy spectral lines, including Ly_α. Thus, their spectral lines measured by the JWST must be widened. Checking galaxy spectral line widths constitutes a new physical cosmological test, which can be conduct using the current JWST data. The high rate of star formation in those galaxies implies a high number density of ionizing photons. This leads to a significant tension with the optical depth of reionization based on the cosmic microwave background (CMB). The previously known tensions of the ΛCDM model (H_0, σ_8), along with this new inconsistency, indicate that the method of using CMB to determine cosmological parameters and the concept of *Planck* precision cosmology may require further evaluation.

Keywords: cosmology: observations, dark ages, reionization, first stars, early universe

DOI: 10.26119/VAK2024.038

1 Introduction

Observations by the James Webb Space Telescope (JWST) indicate that at distances associated with high redshifts, there is a significant number of massive galaxies (with masses $> 10^{10}\,M_\odot$) that formed within 500 million years of the beginning of the universe. The observed number density of massive galaxies with $z > 10$ (Finkelstein et al. 2023) does not align with the predictions made by the theory of galaxy formation. The recently published UNCOVER catalogue of JWST galaxies (Weaver et al. 2024) includes a notable number of galaxies with $z \approx 20$. This is consistent with the predictions of the ΛCDM model regarding the redshift at which the first stars and galaxies are expected to form. Therefore, at this redshift there should be much fewer galaxies, which are expected to be shapeless and small in size. The JWST observations indicate that galaxies with $z > 10$ exhibit morphological characteristics, containing significant amounts of dust and metals. They appear similar to late-universe galaxies, except their physical sizes.

Currently, most of the theories focus mainly on the search of a galaxy-formation model that would allow explaining the existence of fully developed galaxies at redshifts that correspond to the young age of the universe, as standard cosmology does not allow enough time for their formation. In our opinion, it is reasonable to explore cosmological model testing again, especially since the JWST provides great opportunities for it. The observational data available for $z > 10$ may be helpful for distinguishing between cosmological models, even considering potential noise and significant statistical uncertainties.

There are two kinds of cosmological tests that can be performed: cosmographic and physical tests (Orlov & Raikov 2016). In the next section, we focus on the cosmographic tests, and in the last Section, we discuss the physical tests.

2 Cosmographic Tests

Angular Size vs Redshift Test. For large redshifts, different cosmological models predict different galaxy angular sizes θ. Figure 1 shows a comparison of observational data and predictions from the ΛCDM and static cosmological models. The red dots indicate observational data obtained from the JWST public data, the black dots correspond to some pre-JWST observations. The references to the catalogues used for this graph are provided in our separate publication (Lovyagin et al. 2022).

The figure reveals that the ΛCDM prediction is inconsistent with observational data, unless we interpret the observed diminished galaxy sizes as the signature of galaxy evolution: the standard model assumes that galaxy sizes grow as galaxies merge with each other over the course of the universe's evolution.

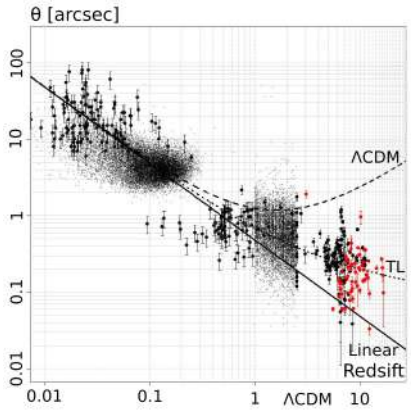

Fig. 1. Angular sizes θ of galaxies as a function of their redshifts z. The red dots indicate observational data obtained by the JWST during its first year of operation in orbit. The black dots correspond to some pre-JWST observations. The theoretical curves are calculated for a medium-sized galaxy (10 kpc) using ΛCDM model (the dashed curve, $\Omega_\Lambda = 0.7$, $\Omega_m = 0.3$, $k = 0$), Zwicky's tired light (TL) model (the dotted curve) and linear Hubble's law (the solid line, $H_0 = 70$ km/s/Mpc).

It should also be noted that, within the ΛCDM model, there is an increase in the linear sizes of galaxies, as well as growth in the sizes of galaxy clusters. Several researchers have noted the presence of small protoclusters up to $z \sim 10$ in JWST surveys, e.g. Castellano et al. (2023). The preliminary assessment indicates that, according to the standard cosmological model, there may be insufficient time for such clusters to form. Additionally, the evolution of their sizes appears to align with the rate of space expansion, which is not typically expected for gravitationally bound objects. This requires additional research. The Zwicky tired-light (TL) prediction is consistent with the JWST observations, while the ΛCDM evolutionary explanation is refuted by the fact that the observed high-redshift galaxies are similar to the late-universe galaxies by their morphology, chemical composition, and dust content.

Surface Brightness Test. Most of the published works dealing with JWST imaging data determine galaxy parameters (luminosity functions, sizes, masses) by measuring Sérsic profiles. These photometric measurements may act as a proxy for Tolman's surface brightness test (Hubble & Tolman 1935; Geller & Peebles 1972). This test is based on the fact that a galaxy with a redshift z changes its surface brightness in proportional to $(1+z)^{-n}$, where $n = 4$ in the context of the ΛCDM model and $n = 1$ in a static case.

The $\propto (1+z)^{-4}$ decline in surface brightness implies that a distant ($z \gtrsim 10$) Milky Way-like galaxies cannot be observed using JWST. Observations of many galaxies at redshift $z \gtrsim 10$ indicate that, within the framework of the ΛCDM model, their physical brightness must increase rapidly with z (i.e., rapidly decrease due to

evolution). This implies that the stellar population in such galaxies is many times denser than in ordinary galaxies. For this reason, the dynamical properties of these small, luminous, and massive galaxies may differ from those of ordinary galaxies in the late universe.

Galaxy Concentration Test. In the ΛCDM model, the proper volume of spherical shells with constant Δz decreases as $(1+z)^{-1}$, while it increases as $(1+z)^2$ in the static model. The observation of a large number of galaxies at $10 \lesssim z \lesssim 20$ (Weaver et al. 2024) implies an extremely high concentration of galaxies in the early universe within the framework of the ΛCDM model which may result in potential physical inconsistencies. This requires further investigation.

3 Physical Tests

Galaxy gravitational potential test. From the perspective of cosmographic tests such as angular size versus redshift and the Tolman test, the critical issue is the evolution of galaxy masses and linear sizes. Note that the gravitational potential of a galaxy, $\phi \propto M/r \propto v^2$, where M is the mass of the galaxy, r is its radius, and v is the linear rotation speed. The rotation speed, in turn, affects the width of the galaxy's spectral lines. Thus, we propose a new physical cosmological test — an independent determination of the evolution of ϕ in galaxies as function of increasing z though the observation of the equivalent width of spectral lines. If the ΛCDM model is correct, a dependence of the spectral line width on z should be observed, reflecting galaxy evolution, whereas in a static universe, such dependence would be absent or relatively weak (assuming slow evolution case). Preliminary analysis by Nakane et al. (2024) shows no evidence of the evolution of the gravitational potential. The complete implementation of this test is a task for future work.

Tension in cosmological parameters. Before the JWST observations, two problems with precision cosmology were already known: the H_0 and σ_8 tensions. According to the calculations (Muñoz et al. 2024), reionization is suggested to have started earlier than the standard model indicates and may have been completed by the time the galaxies observed by the JWST telescope formed. Galaxies observed by the JWST produced an excess of ionizing photons in the early universe. Consequently, the reionization process observed by JWST is currently showing a factor of 2 tension with the findings from *Planck* precision cosmology (Melia 2024). By contrast, in the slowly-evolving or static model such a problem does not occur.

At this moment, it can be observed that the determination of cosmological parameters based on the CMB (including *Planck* parameters) may warrant further veri-

fication. The H_0 – tension is resolved supportive of the value of $H_0 = 73.5\,\mathrm{km/s/Mpc}$. In this case, the corresponding age of the universe is estimated to be 12.6 Gyr (as opposed to the commonly accepted value of 13.8 Gyr from the CMB *Planck* cosmology). The galaxies with $z \approx 20$ observed by the JWST have an age of $\sim$ 160 million years, which raises questions about the feasibility of developing a physically meaningful galaxy-formation model that can account for a well-developed galaxy in such a short timeframe. This observation also prompts considerations regarding the accuracy of the universe's age as described by the ΛCDM model. The natural alternative to resolve this problem is to revise the standard cosmological model.

Infra-red galaxies. In the JWST deep fields, several new objects have also been discovered, referred to as HST-dark Infra-red Galaxies at $3 < z < 8$, including those reported by Williams et al. (2024). While the observation of such objects may have several explanations, the following has not yet been proposed in the literature. The authors propose that these galaxies could be sufficiently old that only the longest-living stars, i.e., red dwarfs, are present in them. In this case, the age of these galaxies must be much older than the age of the universe according to the standard cosmological model. This requires further investigation into the physical properties of these objects, particularly using spectroscopic methods.

4 Conclusions

The ΛCDM model with galaxy formation starting from baryonic acoustic oscillations became recognized as the standard model of "precision cosmology". The discussion of alternative cosmological models was given limited attention, although certain studies (e.g., Geller & Peebles 1972; Sandage & Perelmuter 1990) concentrated on cosmological tests. Precision cosmology relies on observations of the microwave background, which typically feature low angular resolution. In contrast, initial observations from JWST, known for its high resolving power, have revealed discrepancies with existing theoretical predictions. As a result, current discussions are focused on updating the theory of galaxy formation, which may include the role of primordial black holes, despite possible inconsistencies with CMB observations.

In the article, we highlighted the most significant contradictions between JWST observations and the standard cosmological model: cosmographic tests of angular size versus redshift, the galaxy concentration problem, Tolman's test and its physical consequences; *Planck*'s H_0, σ_8, and reionization tensions; and age inconsistencies of objects (insufficient time for the formation of observed objects in the ΛCDM-early universe and potentially overly old objects in the local universe). Although the TL

model can resolve some of these contradictions, but it also known unresolved problems and discrepancies with observations. In the authors' opinion, there is currently insufficient observational data to conclusively determine the nature of cosmological redshift. However, JWST observations clearly indicate the need to revise the age of the universe significantly upwards, and suggest that a static cosmological model provides a more natural explanation for the observed results of cosmographic and physical tests. These contradictions indicate the importance to revive discussions about cosmological models and further research in this direction, including the new Galaxy gravitational potential test proposed in the article.

References

Castellano M., Fontana. A., Treu T., et al., 2023, The Astrophysical Journal Letters, 948, 2, id. L14
Finkelstein S.L., Leung G.C.K., Bagley M.B., et al., 2023, arXiv:2311.04279
Geller M.J. and Peebles J.E., 1972, ApJ, 174, p. 1
Hubble E.P. and Tolman R.C., 1935, ApJ, 82, p. 302
Lovyagin N., Raikov A., Yershov V., et al., 2022, Galaxies, 10, p. 108
Melia F., 2024, arXiv:2407.01581
Muñoz J.B., Mirocha J., Chisholm J., et al., 2024, arXiv: 2404.7250
Nakane M., Ouchi M., Nakajima K., et al., 2024, ApJ, V. 967, p. 28,
Orlov V.V. and Raikov A.A., 2016, Astr. Rep., 60, p. 477
Sandage A. and Perelmuter J. M., 1990, ApJ, 350, p. 481
Weaver J.R., Cutler S.E., Pan R., et al., 2024, ApJ Suppl. Ser., 270, p. 7
Williams C.C., Alberts S., Ji Z., et al., 2024, ApJ, 968, 1., id. 34

BAK 2024 MODERN ASTRONOMY: FROM THE EARLY UNIVERSE TO EXOPLANETS AND BLACK HOLES 300 years Russian Academy of Sciences

Analysis of the update sample of USS objects and search of candidates to GPS sources in the RZF survey

A. Temirova[1], N. Bursov[2], and A. Kudryashova[2]

[1] St. Petersburg Branch of the Special Astrophysical Observatory of the Russian Academy of Sciences, St. Petersburg, 196140 Russia
[2] Special Astrophysical Observatory of the Russian Academy of Sciences, Nizhny Arkhyz, 369167 Russia

Abstract. A deep RATAN-600 Zenith Field (RZF) survey at wavelength $\lambda = 7.6$ cm on the declination of the 3C 84 radio source. In the center of the survey region, 448 objects were detected, and 73 of them have ultra-steep spectra (USS), which are the main indicator for finding possible candidates for distant galaxies. Optical identifications for 31 of the USS objects were made using the SDSS surveys have been used. It turns out that 23 objects are galaxies and 8 are star-forming objects. Photometric redshifts ($z_{\rm ph}$) and radio luminosities at 3.9 and 1.4 GHz ($L_{3.9}$ and $L_{1.4}$) are determined for 31 objects with spectral indices $\alpha < -1.1$, $S_\nu \sim \nu^\alpha$ for objects with published photometric data. In the sample of USS objects, 15 galaxies have $z_{\rm ph} < 0.5$, and 8 of them have relatively high $L_{1.4} > 10^{26}$ W/Hz of type FR II. Seven galaxies at $z_{\rm ph} > 0.5$ are also of type FR II. Five sources are of intermediate type FR I-FR II. Only three radio galaxies at $z_{\rm ph} < 0.5$ turned out to be a rare nearby galaxy with relatively low $L_{1.4} < 10^{25}$ W/Hz (FR I). These radio sources are either located in the dense intergalactic medium of rich clusters or are confined within their host galaxies. Almost all of these sources can be observed with the SAO 6-m telescope. Galaxies with $L_{1.4} > 10^{26}$ W/Hz (FR II) have magnitudes $18 < m_{\rm r} < 23$. The search for Gigahertz Peaked-spectrum (GPS) candidates in the RZF survey was performed, and 29 objects were classified as GPS candidates. The most sensitive radio and optical catalogs, a new blazar candidate catalog, Blazar Radio and Optical Survey (BROS) were used. We propose 7 new candidates for GPS sources and 5 new Megahertz Peaked-spectrum (MPS) sources based on their spectral shape and variability characteristics.

Keywords: surveys; radio continuum: general; radio continuum: galaxies; galaxies: active

DOI: 10.26119/VAK2024.039

1 Introduction

Objects with ultra-steep spectra (USS) are of particular interest because they are an important selection factor in the search for distant radio galaxies (HzRGs). Such galaxies are usually powerful FR II type galaxies. They are often found in protocluster environments (Tielens et al. 1979). These objects may be associated with the first generation of super massive black holes. Powerful radio galaxies formed in the first 10% of the lifetime of the Universe have been found in very deep surveys at centimeter wavelengths with the RATAN-600 radio telescope (Goss et al. 1992). The spectral index-redshift relation is a key tool in the search for HzRG. Detailed studies were then published in Röettgering et al. (1994). These ones are the basis for important selection factors in distinguishing HzRG. However, the relationship between spectral curvature and redshift remains incompletely resolved. A new method to search for distant AGN with megahertz peaked-spectrum (MPS) sources has been proposed by Bursov et al. (2007). A near-zenith deep survey with RATAN-600 at $\lambda = 7.6$ cm (RZF) in the region $0^h \leq$ R.A. $\leq 24^h$, $40°30'42'' \leq$ Dec $\leq 42°30'42''$ revealed a number of USS radio galaxies (Pariiskii et al. 2019). They could be the candidates for very distant objects. We analyze the updated data of radio sources with USS ($\alpha \leq$ -1.1, $S_\nu \sim \nu^\alpha$), in the central strip of the RZF survey (Dec = $41°30'42'' \pm 2'$).

2 Investigation of the sample of USS sources

We analyzed 73 USS-objects from the sample of 448 sources in the central strip of the RZF catalog. Spectra of 18 objects were power-law shaped. Spectra of 6 sources were approximated with only two points at 1.4 GHz and 3.94 GHz. HzRGs had power-law shaped spectra and did not become steeper at high frequencies (Klamer et al. 2006). However, they can turn over at low frequencies due to synchrotron self-absorption (SSA) and free–free absorption (FFA) (Ker et al. 2012). 25 sources were MPS, suggesting that they could be represented as HzRGs (Coppejans et al. 2015). This sample of USS sources had relatively weak flux densities ($\overline{S}_{3.94} = 6.8$ mJy and $\overline{S}_{1.4} = 34.5$ mJy) at centimetre wavelengths. The flux-density ratio $S_{1.4}/S_{3.94}$ ranged from 1.5 to 10.5. Optical identifications of 31 USS objects were made with the SDSS (DR7, DR12). It turned out that 23 objects are galaxies and 8 are star-forming objects. The radio luminosity (L_ν) of the USS sources allows us to classify their possible nature: a radio galaxy, a radio-quiet AGN, or a star-forming galaxy. The photometric redshifts ($z_{\rm ph}$) for the 31 SDSS objects with color properties havee been determined using the PEGAS model. L_ν were calculated using the formula from Pariiskii et al. (2000).

The radio luminosities at 1.4 GHz ($L_{1.4}$) are in the range $1.51 \times 10^{24} \leq L_{1.4} \leq 17 \times 10^{27}$ W/Hz ($\overline{L}_{1.4} \sim 4.25 \times 10^{26}$ W/Hz). The galaxies with $L_{1.4} \geq 10^{26}$ W/Hz are FR II sources. The galaxies with intermediate $L_{1.4}$ $10^{25} \leq L_{1.4} \leq 10^{26}$ W/Hz can be classified as FR I – FR II objects or mixed FR I / FR.

Five sources with $z_{\rm ph} > 0.5$ and $L_{1.4} > 10^{26}$ W/Hz can be classified as radio-loud AGNs (Verkhodanov et al. 2009). Fifteen galaxies are FR II-type sources, with six of which are nearby objects $z_{\rm ph} < 0.5$). Four sources out of six with intermediate $L_{1.4}$ are nearby galaxies. Three of them with $L_{1.4} \leq 10^{25}$ W/Hz are of the FR I type. Such sources are very rare and are mostly found in regions of high baryonic density. A possible explanation is that nearby USS radio sources are almost exclusively located in rich clusters of galaxies.

3 The search of candidates to GPS objects in RZF survey

The gigahertz peaked-spectrum (GPS) and Compact-Steep spectrum (CSS) sources are compact, powerful radio sources with well-defined peaks ($\nu_{\rm int}$) in their radio spectra. The peaked-spectrum (PS) sources could be very young radio galaxies that will evolve into CSS sources on their way to becoming large radio galaxies. The PS and CSS sources could be compact because they are confined (and enhanced in radio power) by interaction with dense gas in their environments. Alternatively, PS sources may be transient or intermittent. There are 3 classes of objects adjacent to GPS, which differ in their spectral maxima: CSS with $\nu_{\rm int} < 0.5$ GHz, High Frequency Peaker (HFP) with $\nu_{\rm int} > 5$ GHz, MPS with ($\nu_{\rm int} < 1$ GHz). The peaks in the spectra are probably due to SSA, although FFA through an inhomogeneous screen may also play a role. GPS galaxies and quasars were researched with RATAN-600 (Sotnikova et al. 2019).

The most sensitive radio and optical catalogs, a new blazar candidate catalog, the Blazar Radio and Optical Survey (BROS), were used.

The search for candidates to GPS objects was carried out at RZF survey (N=745) and small sample of 21 of them turned out to be candidates to ones. Optical candidates for 21 RZF objects were found using the SDSS and GAIA surveys. Among the selected sources, 8 GPS objects are galaxies. 6 of the sources in the sample are QSOs, 2 of them turn out to be GPS objects. One source according to the BROS catalog is a candidate to GPS object - QSO. One is defined as AGN. 5 objects with $\nu_{\rm int} < 500$ MHz are CSS class, one with $\nu_{\rm int} > 5$ GHz is HFP, the rest are defined as MPS with $\nu_{\rm int} < 1$ GHz. Our sample is relatively weak with $\overline{S}_{3.9} = 52$ mJy. Spectral indices were found for 9 sources and photometric distances, L_ν, were calculated. The L_ν of the considered sources vary from 6×10^{42} erg/sec up to 2×10^{44} erg/sec.

4 Conclusion

Using the updated RZF catalog at 3.94 GHz, we detected 73 sources with steep spectra at Dec = 41°30′42″ ±2′. Cross-identification with the optical surveys (SDSS DR7, DR12) was performed. Photometric redshifts were obtained for 31 objects. It was found that 23 sources are galaxies and 8 are star-forming objects, mainly nearby galaxies. These radio sources are either located in a dense intergalactic medium of rich galaxy clusters or are confined within their host galaxies. Fifteen galaxies with $L_{1.4} \geq 10^{26}$ W/Hz are FR II-type sources, objects with intermediate luminosities 10^{25} $< L_{1.4} < 10^{26}$ W/Hz are of mixed FR I − FR II types. The remaining three galaxies with $10^{24} < L_{1.4} \leq 10^{25}$ W/Hz are rare USS FR I sources and are almost exclusively located in rich clusters of galaxies.

8 GPS objects turn out to be galaxies. 6 of the sources in the sample are QSO, 2 of them are GPS objects. 5 objects with $\nu_{\rm int} < 500$ MHz are CSS, 1 with $\nu_{\rm int} > 5$ GHz is HFP, the rest are MPS with $\nu_{\rm int} < 1$ GHz. Our sample is relatively weak with $S_{3.9} = 52$ mJy.

Acknowledgements. The work was performed under the SAO RAS government contract approved by the Ministry of Science and Higher Education of the Russian Federation.

References

Bursov N.N., Pariiskii Y.N., Maiorova E.K., et al., 2007, Astronomy Reports, 51, p. 197

Coppejans R., Cseh D., Williams W. L., et al., 2015, Monthly Notices of the Roy. Astron. Society, 450, p. 1477

Goss W.M., Parijskij Y.N., Soboleva N.S., et al., 1992, Astronomicekij Zhurnal, 69, p. 673

Ker L.M., Best P.N., Rigby E.E., et al., 2012, Monthly Notices of the Roy. Astron. Society, 420, p. 2644

Klamer I.J., Ekers R.D., Bryant J.J., et al., 2006, Monthly Notices of the Roy. Astron. Society, 371, p. 852

Pariiskii Y.N., Semenova T.A., Temirova A.V., et al., 2019, Astronomy Reports, 63, p. 212

Parijskij Y.N., Goss W.M., Kopylov A.I., et al., 2000, Astronomical and Astrophysical Transactions, 19, p. 297

Röettgering H.J.A., Lacy M., Miley G.K., et al., 1994, Astronomy and Astrophys. Supplement Series, 108, p. 79

Sotnikova Y.V., Mufakharov T.V., Majorova E.K., et al., 2019, Astrophysical Bulletin, 74, p. 348

Tielens A.G.G.M., Miley G.K., Willis A.G., 1979, Astronomy and Astrophys. Supplement Series, 35, p. 153

Verkhodanov O.V., Trushkin S.A., Andernach H., et al., 2009, Data Science Journal, 8, p. 34

MODERN ASTRONOMY: FROM THE EARLY UNIVERSE TO EXOPLANETS AND BLACK HOLES

Peculiar structure of isolated dwarf galaxy ESO 149–003

K. Vladimirova[1,2], D. Makarov[2], M. Chazov[2], and L. Makarova[2]

[1] Peter the Great Saint Petersburg Polytechnic University, Saint Petersburg, 195251 Russia
[2] Special Astrophysical Observatory of the Russian Academy of Sciences, Nizhny Arkhyz, 369167 Russia

Abstract. The modern deep sky DESI Legacy Surveys allow us to study of extremely low surface brightness structures. Visual inspection of Local Volume galaxies reveals that the dwarf galaxy ESO 149–003 contains shell-like structures that are characteristic of giant elliptical galaxies. This isolated dwarf galaxy, located at a distance of 7 Mpc in the direction of Antivirgo, appears to have absorbed its neighbour. In this paper we analyse the stellar population and star formation history of this galaxy. We estimate the frequency of similar systems by visual inspection of the Local Volume galaxies using images from the Legacy Survey.

Keywords: galaxies: individual (ESO 149–003), star formation, stellar content, structure

DOI: 10.26119/VAK2024.040

1 Introduction

The Local Volume, because of its proximity, provides a unique opportunity to study a population of dwarf galaxies that is lost at larger distances. ESO 149–003 caught our attention because of its unusual structure, characteristic of shells around giant elliptical galaxies due to head-on collisions with neighbours and tidal interactions. Its images from the Legacy Survey and the Hubble Space Telescope (HST) are shown in Fig. 1. ESO 149–003 is a highly isolated galaxy at a distance of 7 Mpc in the direction of Antivirgo. The nearest giant galaxy, NGC 253, is 3.7 Mpc away. Radio observations revealed perturbations in the kinematics of the gas, but the authors did not find any peculiar structures in optical images of the galaxy (Józsa et al. 2021). ESO 149–003 has been observed with the Hubble Space Telescope (HST), allowing us to analyze its stellar population in detail.

2 Analysis

The image of the galaxy ESO 149–003 was obtained as part of the HST 12546 program (PI: R. B. Tully). The galaxy was observed in the $F606W$ and $F814W$ filters for 15 minutes each. Stellar photometry was performed using the DOLPHOT package (Dolphin 2000, 2016). The photometric limit is about $F814W \approx 27$ mag. For further analysis, we divided the color-magnitude diagram (CMD) into 4 regions according to different stellar populations (see the left panel of Fig. 2). Blue dots correspond to the main sequence branch, purple dots to the red supergiant branch, red dots to the red giant branch, and green dots to the asymptotic branch. This

Fig. 1. The galaxy in frames from the Legacy Survey, an image from the Hubble telescope, and a map of the distribution of stars around the galaxy.

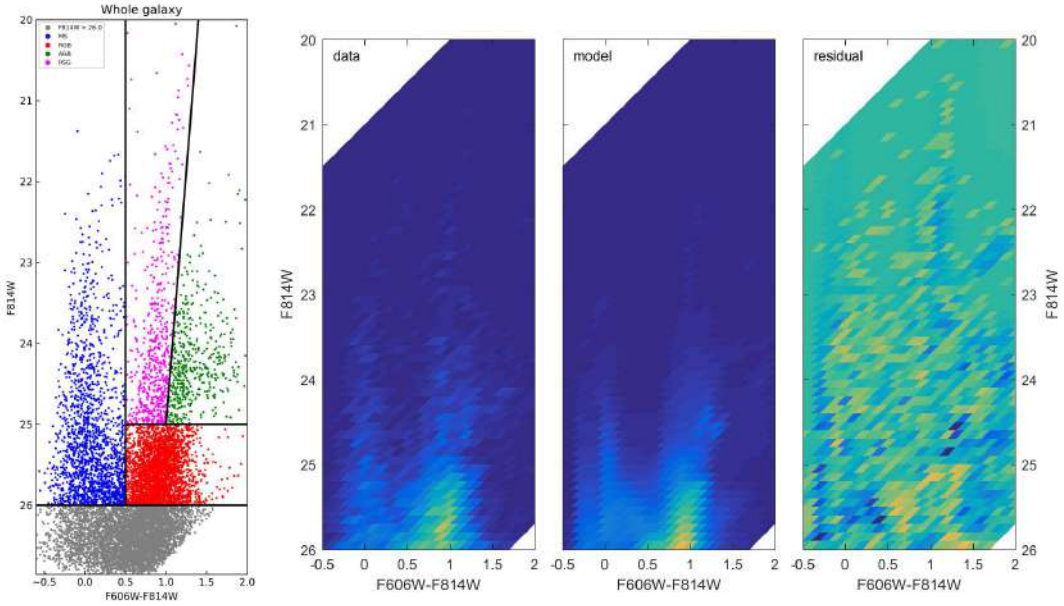

Fig. 2. CMD diagram of stars in the whole galaxy and star formation history diagram.

highlights stellar populations of different ages, from the youngest main sequence stars (age $\lesssim$ 300 Myr) to the oldest stars red giant stars (age $\gtrsim$ 1–2 Gyr). The distribution map of stars in the galaxy is shown in the right panel of Fig. 1. It allows us to check the variation of the stellar populations in different regions of the galaxy. There is a statistically significant difference in stellar populations between the main body and the "skirt"-like structures. The main sequence to red giant ratio in the main body is MS/RGB = 1.08 ± 0.04, while in the skirts the ratio is only MS/RGB = 0.14–0.16 ± 0.02. This suggests that young stars are practically not involved in the formation of these skirt structures.

We reconstructed the star formation history using the StarProbe (Makarov & Makarova 2004) program. It fits the observed CMD by a linear combination of model Hess-diagrams based on the Padova2000 theoretical stellar evolution isochrones (Girardi et al. 2000). We have not constrained the metallicity of the stellar populations. We find that the total stellar mass of ESO 149–003 is $\sim 8.2 \times 10^7\ M_\odot$. During the initial burst of star formation, about 45% of the stellar mass was formed. The stellar mass increased by another 36% during the period from $\sim$ 13 to 1.7 Gyr. The most recent burst of star formation began about 230 Myr ago and formed 12% of all stars.

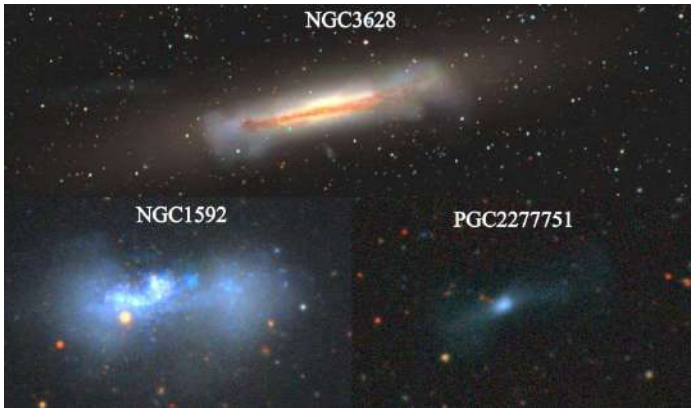

Fig. 3. Examples of galaxies with shells.

The modern star formation rate is $\sim 0.03\ M_\odot\,\mathrm{yr}^{-1}$. The observed Hess diagram, the reconstructed model, and the residuals are shown in Fig. 2.

3 Search for shells

To estimate the frequency of such shells among dwarf galaxies, we performed a visual inspection of all 992 Local Volume galaxies falling within the footprint of the DESI Legacy Surveys (Dey et al. 2019). As a result, we selected 201 out of 992 galaxies that show evidence for the presence of various peculiarities. Of these, 26 dwarf galaxies show the tidal structures similar to ESO 149–003 (see examples in Fig. 3).

Acknowledgements. This work was supported by the Russian Science Foundation grant № 24–12–00277, `https://rscf.ru/project/24-12-00277`.

References

Dey A., Schlegel D.J., Lang D., et al., 2019, AJ, 157, id. 168
Dolphin A., 2016, Astrophysics Source Code Library, record ascl:1608.013
Dolphin A.E., 2000, PASP, 112, 776, p. 1383
Girardi L., Bressan A., Bertelli G., et al., 2000, A \& AS, 141, p. 371
Józsa G.I.G., Thorat K., Kamphuis P., et al., 2021, MNRAS, 501, p. 2704
Makarov D.I. and Makarova L.N., 2004, Astrophysics, 47, 2, p. 229

MODERN ASTRONOMY: FROM THE EARLY UNIVERSE TO EXOPLANETS AND BLACK HOLES

Star formation in low brightness galaxies and in the extended gaseous disks of normal galaxies

A. Zasov, N. Zaitseva, and A. Saburova

Sternberg Astronomical Institute, Moscow State University, 13 Universitetsky pr., Moscow, 119234 Russia

Abstract. We analyze the available observational data on the radial distribution of gas and young stellar populations in the disks of low surface brightness (LSB) galaxies and in the outer regions or the extended disks of normal brightness (HSB) galaxies. These cases involve star formation under special conditions of low volume and surface gas density. There is no well-defined boundary between these subgroups of galaxies that we consider, but in non-dwarf LSB galaxies the rate of current star formation within the wide range of radial distances appears to be higher compared to the outer disks of most of HSB galaxies at similar values of the surface gas density. The factors that could stimulate the compression of the rarefied gas at the periphery of galaxies are briefly discussed. Attention is drawn to the idea that the densities of LSB disks estimated from their brightness may be underestimated.

Keywords: galaxies: stellar content, structure, star formation

DOI: 10.26119/VAK2024.041

1 Introduction

There are two types of non-dwarf galaxies in which weak star formation can be traced to distances from the center where the surface gas density ($\Sigma_{\rm HI}$) is very low and there are no obvious signs of ongoing interaction between the galaxy and its close surroundings that could provoke gas compression. First, there is a certain fraction of disky (usually spiral) galaxies with normal brightness (HSB-galaxies) (hereafter called normal galaxies) that have a continuation of gas disks beyond the optical radius R_{25}, and their faint UV emission suggests the presence of young stars (XUV disks, see Thilker et al. 2007). Second, they are low surface brightness galaxies (LSBs) with the extended disks of giant size, in which signs of star formation can be seen even at distances of tens of kpc from the center, despite the very shallow gravitational potential profile associated with the weak disk gravity. The formation of LSB galaxies and the extended disks of normal galaxies can involve several scenarios and is the subject of active discussion (see e.g. Saburova et al. 2019; Saburova et al. 2021 and references in these papers). In this paper we compare the low density regions of HSB and LSB galaxies in terms of their stellar and gas densities and star formation rates.

2 SFR vs stellar and gaseous densities of disks

Star formation in the disks of LSB galaxies, as well as in the outer disks of some normal spirals, occurs under the specific conditions of a low density of the gas layer, which widens at the disk periphery, and a low angular velocity of disk rotation (the first factor hinders star formation, the second favors it). As in the disks of HSB galaxies, the star formation rate (SFR) in the disks of LSB galaxies correlates with the azimuthally averaged surface gas density $\Sigma_{\rm HI}$, but for LSB galaxies this dependence is more blurred. Due to the low density of the disks, star formation there is not associated with the large-scale disk instability, but with the local sites of gas compression near the disk plane caused by other factors that perturb a gas layer.

It is convenient to characterize the ability of the gas to give birth to stars by the value of the star formation efficiency $\mathrm{SFE} = \mathrm{SFR}/\Sigma_{\rm HI}$, which represents a star formation rate per unit mass of HI per unit area of a disk. In general, the SFE decreases monotonically with radial distance R, so that its inverse, the gas exhaustion timescale, is very high, reaching tens of billions of years or more at the distant periphery even for HSB-galaxies. In Abramova & Zasov (2012) it was shown that the SFE at a given radius R in galaxies of different types is closely correlated not with the gas density, but with the surface and volume densities of a stellar disk in a disk plane where the normal and LSB galaxies form a single sequence (see Fig.1). The volume density calculations were performed for galaxies with known radial distributions of SFR, $\Sigma_{\rm gas}$, and a rotation curve, assuming a fixed value of

the gas velocity dispersion. They were reduced to a joint solution of the Poisson equation and the differential equations of hydrostatic equilibrium of a gas layer in the gravitational field created by disk components and a dark halo. At very low stellar disk densities ($\sigma_{\rm stars} < 3M_*/pc^2$), the relation of SFR or SFE to the density of the stellar-gaseous disk becomes loose. The decrease of the SFE along the radius reflects the increasing thickness of a gas layer and consequently a decrease of the gas volume density, which is in good agreement with the model of Ostriker et al. (2010) of self-regulated star formation in an equilibrium layer of diffuse gas in the disk plane. However, the applicability of this model to extremely low-density disks is not obvious. There, star formation tends to be sporadic and weakly dependent on the disk properties.

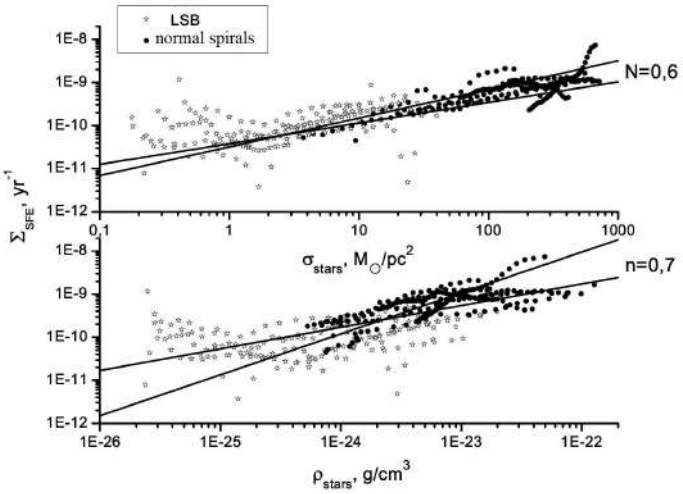

Fig. 1. Correlation between $\Sigma_{\rm SFE}$ and $\sigma_{\rm stars}$ or $\rho_{\rm stars}$ for two different sub-samples: LSB-galaxies (marked as grey pentargams) and normal spiral (marked as black dots). Straight lines correspond to the regressions x(y) and y(x) applied to the set of all points by the method of least squares.

It is worth comparing LSB-galaxies with the low density regions of normal brightness galaxies beyond the conventional optical radius R_{25}. The examples of relatively close galaxies with the weak extension of star forming disks are NGC 289, M83, NGC 628, NGC 2841, NGC 3521, NGC 5055, and some others. To the type of HSB-galaxies with high gas content and observed star formation in the extended disk one can also add the galaxies of the "Bluedisk" sample (Wang et al. 2013), and the "HIX galaxy sample" of gas-rich HSB-galaxies (Lutz et al. 2018). In fact, there is no sharp boundary between LSB galaxies and the outer low brightness disks of HSB galaxies. The example of a normal galaxy with a giant low-luminosity disk that allows us to

refer it also to the LSB-type galaxies is UGC 1378, a massive SBa-type galaxy whose low brightness outer disk can be traced over 50 kpc, making it similar to giant LSB galaxies such as Malin-1, 2 (Saburova et al. 2019).

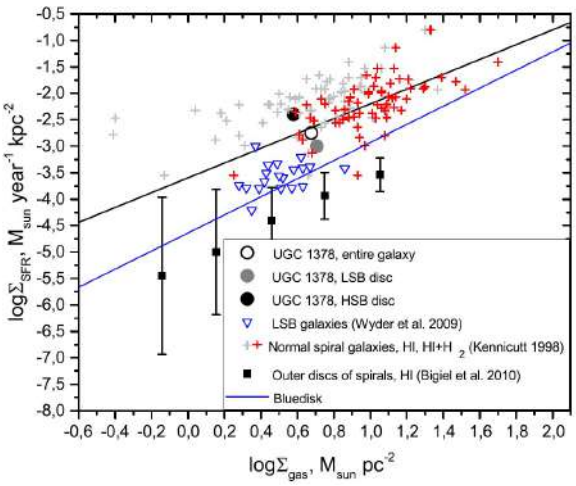

Fig. 2. The SFR surface density versus gas surface density diagram. The sample of normal spirals is plotted as bright and faint crosses corresponding to total and HI gas densities, respectively. The black line corresponds to the Kennicutt-Schmidt law. The blue line is the fit for the Bluedisk galaxies. The circles mark UGC 1378. The empty triangles show the position of the LSB galaxies. The outer parts of normal HSB galaxies (black squares) have a lower SFR for a given gas surface density.

The mechanisms that drive the formation of star-forming regions in such rarefied disks are poorly understood. The rate of star formation there is determined there not only by the mean gas density, but also by how inhomogeneous the gas distribution is on the kiloparsec scale. In the most massive LSB-galaxies we observe a line of stellar spiral arms, but in other cases star formation takes place in randomly distributed areas of a disk which, if they are sufficiently large, can stretch into arcs due to differential rotation. If tidal interactions with nearby galaxies are excluded, strong local density inhomogeneities can be created by the accretion of gaseous flows or dwarf satellites, as well as by the passage of small sub-halos through a disk plane. The efficiency of star formation in these cases depends not only on the gas density, but mostly on the disk environment, which can be very different even for galaxies of the same type.

The observed SFR of the LSB disks turns out to be rather high for their gas density. This is illustrated by Fig.2 (Saburova et al. 2019), which compares the averaged ($\Sigma_{\rm SFR}$) and gas densities of normal (crosses) and LSB (empty triangles) galaxies, as

well as the outer regions of normal spirals (black squares). As can be seen from the diagram, $\Sigma_{\rm SFR}$ is lower in LSB galaxies than in HSB-galaxies, but tends to be higher for a given gas density compared to the outer disks of normal galaxies, most likely due to the lower disk thickness which makes $\rho_{\rm gas}$ higher.

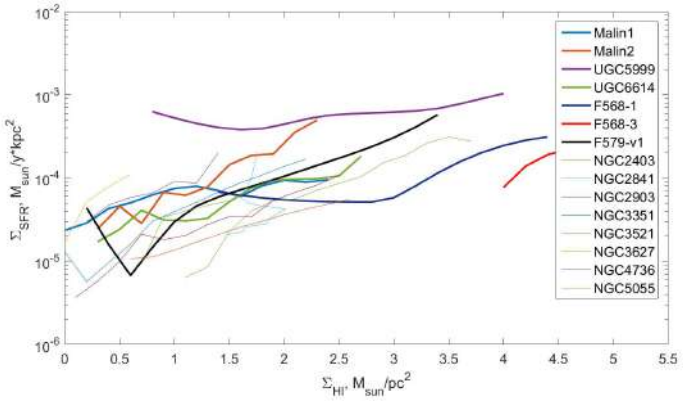

Fig. 3. A comparison of $\Sigma_{\rm SFR}$ and $\Sigma_{\rm HI}$. Thick solid lines represent the sub-sample of LSB-galaxies, while thin solid lines represent the outer regions of normal spiral galaxies. The $\Sigma_{\rm SFR}$ were taken from Leroy et al. (2008) for the THINGS sub-sample and calculated from the GALEX FUV profiles presented in Wyder et al. (2009), following Eq. 4 from that paper.

For a more detailed comparison of LSB disks and low-density extended disks in HSB galaxies, their azimuthally averaged radial distributions of $\Sigma_{\rm SFR}$ and $\Sigma_{\rm HI}$ are compared in Fig. 3 (HSB disks are marked by thin lines there). The diagram confirms that there is no sharp distinction between LSB and the low density disks of HSB galaxies. At the same time, some LSB galaxies (UGC 5999, Malin-1, Malin-2, F579-v1) have systematically higher star formation rates over a wide range of $\Sigma_{\rm HI}$ than the outer regions of HSB galaxies with similar surface gas densities. Their higher rate of star is not related to either the enhanced optical surface brightness or the lower value of the stability parameter $Q_{\rm T}$: the disks of LSB galaxies, like the outer regions of HSB galaxies, have $Q_{\rm T} \sim$ 3–5 in a wide range of radial distance. However, it may reflect the higher (by a factor of several) density of the disks of such LSB-galaxies than would be expected from their low surface brightness, so that a gravitational field of a disk compresses the gas layer more strongly, favoring star formation.

The idea of underestimating the density of LSB disks from surface brightness measurements was first proposed by Fuchs (2003), see also the discussion in Saburova (2012); Saburova & Zasov (2013). The most significant evidence that the low-brightness disks may be denser than suggested by conventional models of their stellar

population is the presence of structural details such as bars and spiral arms in some LSB galaxies, where disk self-gravity should be essential, as well as the similarity of the stability parameter $Q_{\rm T}$ over a wide range of R for the disks of LSB and HSB galaxies, despite the large difference in their surface brightness.

The underestimation of the mass of LSB-disks may be due to the bottom-heavy initial mass function of the stars that make up the bulk of the present-day disks, leading to a higher M_*/L ratio, or it may be caused by the presence of a significant amount of high angular-momentum dark matter in the outer regions of the disks, coming from cosmological filaments, in addition to the conventional baryonic disk components.

3 Summary

In the diagram "Star formation efficiency — volume (or surface) disk density", LSB galaxies continue the sequence constructed for HSB galaxies. However, for the regions of the lowest disk densities the relationships are characterized by a large scatter, i.e. the SFE there is loosely dependent on the disk parameters there. In some LSB galaxies, the observed star formation is more intense than in the extended outer regions of normal spiral galaxies with similar surface HI densities, which may indicate that the disk density of LSB galaxies is higher than it is expected from their low surface brightness.

Funding

This project was supported by the RScF grant 23-12-00146.

References

Abramova O.V. and Zasov A.V., 2012, Astronomy Letters, 38, p. 755
Fuchs B., 2003, Astrophys. Space Sci., 284, p. 719
Leroy A.K., Walter F., Brinks E., et al., 2008, Astron. J., 136, p. 2782
Lutz K.A., Kilborn V.A., Koribalski B.S., et al., 2018, Mon. Not. R. Astron. Soc., 476, p. 3744
Ostriker E.C., McKee C.F., Leroy A.K., 2010, Astrophys. J., 721, p. 975
Saburova A.S., 2012, Astronomical and Astrophysical Transactions, 27, p. 251
Saburova A.S., Chilingarian I.V., Kasparova A.V., et al., 2019, Mon. Not. R. Astron. Soc., 489, p. 4669
Saburova A.S., Chilingarian I.V., Kasparova A.V., et al., 2021, Mon. Not. R. Astron. Soc., 503, p. 830
Saburova A.S. and Zasov A.V., 2013, Astronomische Nachrichten, 334, p. 785
Thilker D.A., Bianchi L., Meurer G., et al., 2007, Astrophys. J., Suppl. Ser., 173, p. 538
Wang J., Kauffmann G., Józsa G.I.G., et al., 2013, Mon. Not. R. Astron. Soc., 433, p. 270
Wyder T.K., Martin D.C., Barlow T.A., et al., 2009, Astrophys. J., 696, p. 1834

MODERN ASTRONOMY: FROM THE EARLY UNIVERSE TO EXOPLANETS AND BLACK HOLES

Current status of the Big Trio search program for distant radio galaxies. New radio data

O. Zhelenkova[1], Yu. Parijskij[2], N. Soboleva[2], and A. Temirova[2]

[1] Special Astrophysical Observatory of the Russian Academy of Sciences, Nizhny Arkhyz, 369167 Russia

[2] St. Petersburg Branch of the Special Astrophysical Observatory of the Russian Academy of Sciences, St. Petersburg, 196140 Russia

Abstract. The Big Trio programme was aimed to search for distant radio galaxies for the purpose of cosmological research. A selection of sources with steep and ultra-steep spectra was made from the radio sources discovered in a series of surveys by the Cold Experiment, which was carried out on the RATAN-600 radio telescope. The results of the studies of 113 sources in this sample were the optical identification of almost the entire sample, spectral studies of the majority of the objects (70%), spectral redshift determinations for half of them, and the discovery of three unique radio galaxies with redshifts $z > 3$ and extremely high radio luminosities. New radio sky surveys with high sensitivity and angular resolution have now become available, allowing additional studies of the radio sources in the sample. These have helped to refine the continuous spectra of the sources and their radiomorphology, as well as the evolutionary state and environment of the radio galaxies. The spectral indices determined from the new radio survey data turned out to be flatter than those from the old data. Based on the spectral curvature parameter and the morphological structure of the sources in the steep spectrum (SS) sample, 10–15% are likely to be young, 40–50% are in an active state, 10% are in the fading phase, and most likely 20–25% are in the restart phase.

Keywords: galaxies: active, high-redshift

DOI: 10.26119/VAK2024.042

1 Introduction

In the early 1990s, SAO RAS began work on the Big Trio programme (Goss et al. 1992; Parijskij et al. 2000), which aimed to search for distant radio galaxies and to study them further for cosmological purposes (Miley & De Breuck 2008). Three large telescopes were used for the observations: the RATAN-600 and VLA radio telescopes (NRAO, USA) and the 6-m BTA telescope. High angular resolution radio observations were made to refine the coordinates and determine the morphological structure of the sample of steep spectrum (SS) radio sources at the VLA. Photometric and spectral studies of the sample were performed on the 6-m BTA telescope. 94% of the radio sources were identified with their host objects, and spectra were obtained for 70% of the SS sample. Three unique radio galaxies with redshifts $z > 3$ and extremely high radio luminosities were discovered (Kopylov et al. 2006; Parijskij et al. 2010, 2014).

Thanks to the modern radio sky surveys TGSS (Intema et al. 2017), GLEAM (Hurley-Walker et al. 2017), RACS (McConnell et al. 2020), VCSS (Peters et al. 2021) and VLASS (Gordon et al. 2021) it was possible to once again refine the continuum spectra of the SS sample once again.

Access and analysis of the survey, catalog and tabular data was performed using the TOPCAT (Taylor 2005) and ALADIN (Bonnarel et al. 2000) software tools. The spg programme from the RATAN-600 (Verkhodanov et al. 1993) data processing system was used to construct the continuum spectra. The spectral index was determined from the spectra constructed by linear and parabolic approximations using weighting coefficients and discarding outliers. The spectral index of a radio source α is defined as $S_\nu \propto \nu^\alpha$.

2 Comparison of old and new continuum spectra

Initially, the selection of sources in the SS sample was made using a two-frequency spectral index $\alpha_{3940}^{365} \leq -0.9$ at 365 and 3940 MHz based on the integrated flux densities from the UTRAO and RC catalogs. In addition, double sources of small angular size were selected. In one of the early papers (Soboleva et al. 1994) 96% of the SS sample sources have a spectral index of ≤ -0.9. The spectra and spectral indices of the SS sample have been determined several times from measurements made with the RATAN-600 radio telescope and from data in publications mentioning the sources under study.

Here we compare the spectral indices of the SS sample sources obtained by fitting the spectra to three sets of integrated flux densities. One set is taken from Bursov et al. (1996). It covers the range 365–4850 MHz, and in some cases for bright sources

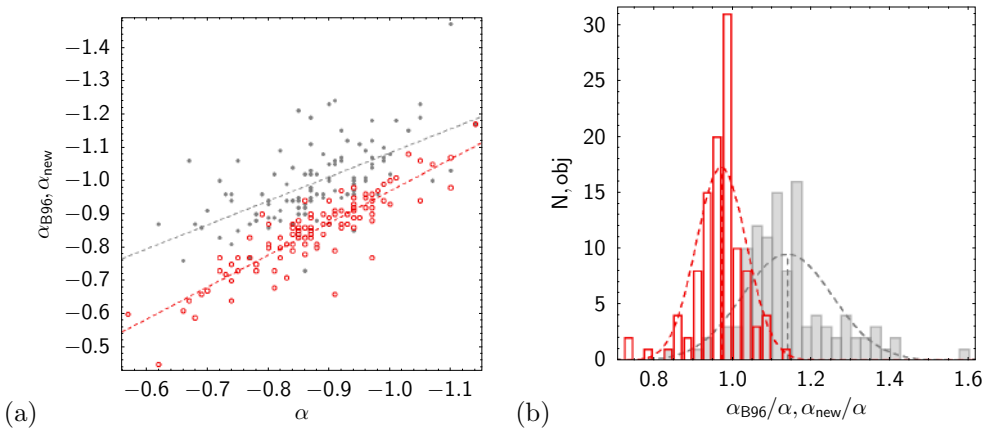

Fig. 1. The figure shows a scatterplot of the spectral indices (a). The spectral indices $\alpha_{\rm B96}$ (grey dots) and $\alpha_{\rm new}$ are plotted on the y-axis, and α on the x-axis. The dotted lines show the linear regression. The histogram (b) shows the distribution of the ratio of $\alpha_{\rm B96}$ to α (grey) and the ratio of $\alpha_{\rm new}$ to α (red). The dotted line shows the approximation of the distribution by the Gaussian function.

from 13 MHz to 11 GHz. The index $\alpha_{\rm B96}$ is determined from this data. The second set contains data from the modern sky surveys VLSSr (Lane et al. 2014), TGSS, GLEAM, VCSS, RACS and VLASS. Flux densities for the sample sources are determined for up to 30 frequencies, mainly from 74 MHz to 3 GHz. The index $\alpha_{\rm new}$ is calculated from these data. And the third data set, the most complete, contains the flux densities of the first two sets, i.e. all the information about the sources that is currently available. The index α is computed using this data set.

With the advent of the low-frequency TGSS and GLEAM surveys, we have been able to refine the spectral characteristics of some sources. For example, 19% of the objects have a curved spectrum of the type C^-. For 9% of the sources the spectrum type can be classified as C^+, which has been refined by adding new high-frequency data. Thus, 28% of the sources have a curved spectrum (C^- and C^+) or a spectrum with a single peak. Such types of spectra are better approximated by a parabola. The statistics of the spectral indices calculated from three sets of flux densities are given in Table 1. Since the linear approximation of curved spectra is at least reflects the spectral shape, the spectral indices will be erroneous. When comparing the spectra constructed by the linear approximation, we used a subsample of sources (72%) with straight spectra (S-type). The table also shows the median of the ratios of the first two spectral indices to the third spectral index, which we consider to be the most reliable. The table also shows the standard deviations for these ratios. This allows us to estimate the accuracy of the spectral indices.

Table 1. SS sample source statistics for three sets of flux densities: *Set* — the set of flux densities corresponding to the spectral index; $\alpha \leq -0.9$ — the percentage of sources in the SS sample that satisfy this condition; $\alpha_{\rm med}$ — the median value of the spectral index for the subsample of sources with $\alpha \leq -0.9$; $\alpha^{\rm SS}_{\rm med}$ – the median of the spectral index for the whole SS sample; *Ratio* – the ratio of the spectral index to α.

Set	$\alpha \leq -0.9$	$\alpha_{\rm median}$	$\alpha^{\rm SS}_{\rm median}$	*Ratio*
Linear fitting (S-type spectra)				
α_{B96}	89%	−1.01	−1.00	1.128±0.094
α_{new}	33%	−0.94	−0.86	0.973±0.040
α	46%	−0.96	−0.88	

Both Table 1 and Fig. 1 show some discrepancy between the spectral indices determined from the old and new data. It can be seen that the old spectral indices are steeper than the new ones.

3 Spectral cuvature and evolutionary state, morphology and environment

During their lifetime in the radio phase, AGNs go through the following stages: the birth of a radio source, its active phase, the fading of the radio source, when the AGN stops feeding jets, and a possible restart. To separate these phases, the spectral curvature parameter (SCP) is often used as the difference between the spectral indices of the high- and low-frequency regions of the spectrum (Murgia et al. 2011). The maximum curvature expected in the active phase is limited by SPC$\leq$0.5. On the other hand, the integral spectra of dying sources are characterised by an exponential cut-off at high frequencies, so that extreme spectral curvatures are possible for them (SCP$>$0.5). Finally, for restarting sources, the injection of new electrons flattens the high-frequency spectrum, resulting in SCP$<$0. This classification should be regarded as having statistical significance. For the SPC to be meaningful, it must be calculated over a frequency range of at least two orders of magnitude.

We calculated SCPs for the SS sample based on the spectra that were constructed using a parabolic fit to all currently available data. The spectral indices were calculated as $\alpha_{\rm low}$ and $\alpha_{\rm high}$ for 500 and 3940 MHz respectively. We also calculated the SCP in a different way. The $\alpha_{\rm low}$ were obtained from the GLEAM data by linear fitting of the spectra and the $\alpha_{\rm high}$ were obtained from the RACS, VCSS, and VLASS data. We found that the fading sources in the SS sample account for 8–10%, and the restarting sources account for 15–17%. Sources of small angular size with a peak in the spectrum (GPS and HFP) are thought to be young objects that later evolve into

FR-I and FR-II radio galaxies (Callingham et al. 2017). We have classified 10–15% of the sources as young.

The morphological structure of the source also carries information about evolutionary phases. The sources showing a double-double or triple structure (Brocksopp et al. 2011; Gopal-Krishna et al. 2012), are classified as AGN with radio phase restart. And we attributed 20–25% of the objects to this type of source. Comparing the NVSS and VLASS cutouts, we found that some sources have radio lobes at 1.4 GHz, but they are absent or weakly expressed in the 3 GHz maps. We classified such sources as fading (10%). And 40–50% of the radio sources in the sample are in the active phase.

The deformation of the lobes of the radio source is an indicator of its environment and/or the processes taking place in the immediate vicinity of the AGN. Tailed sources (Wide-Angle Tailed, Narrow-Angle Tailed, Head-Tailed) indicate that they may be located in clusters or groups of galaxies (Owen & Rudnick 1976; Missaglia et al. 2019). And there are 30% of such sources in the sample. The X-, Z-, S-shaped morphology of the radio lobes is explained by a rapid change in the orientation of the jets, either due to the merger of a small galaxy with a massive elliptical host galaxy, or due to instabilities in the accretion disk (Liu 2004; Joshi et al. 2019). In the sample, 14% of the radio sources have such a morphology.

4 Summary

By comparing the spectral indices obtained by linearly fitting the data from three sets of flux densities, we estimated the accuracy of the spectral indices for a subset of sources with C-type spectra. The error in the determination of the indices was 4–9%. The Figure 1 shows the discrepancy between the spectral indices determined from old and new data. It can be seen that the old spectral indices are steeper than the new ones. The number of sources satisfying the selection condition — spectral index less than or equal to -0.9 according to the new data has almost doubled. This may be due to the appearance of low-frequency data, in particular from the GLEAM survey, which allow continuum spectra to be more accurately determined.

Based on the shape of the deformed radio lobes, 30% of the sample sources are likely to be in a group or cluster of galaxies, and 14% show jet reorientation.

After calculating SCPs for the SS sample using spectral indices at 500 and 3940 MHz, we found that the sample contains 8–10% fading sources, 15–17% in the restart phase, and 10–15% young sources. The analysis of the morphological structure of the radio sources showed that 10% of the sources are fading and 20–25% are restarting. Thus, the SS sample contains radio sources with different evolutionary phases.

Acknowledgements. This research has made use of the VizieR catalogue access tool (Ochsenbein et al. 2000) and the SIMBAD database (Wenger et al. 2000), CDS, Strasbourg, France. The NASA/IPAC Extragalactic Database (NED), operated by the Jet Propulsion Laboratory, California Institute of Technology, on behalf of the National Aeronautics and Space Administration, was used in this search; the CATS database (Verkhodanov et al. 2005), available on the website of the Special Astrophysical Observatory.

References

Bonnarel F., Fernique P., Bienaymé O., et al., 2000, Astron. Astrophys., Suppl. Ser., 143, p. 33
Brocksopp C., Kaiser C. R., Schoenmakers, et al., 2011, Mon. Not. R. Astron. Soc., 410, p. 484
Bursov N.N., Lipovka N.M., Soboleva N.S., et al., 1996, Bulletin of the Special Astrophysics Observatory, 42, p. 5
Callingham J.R., Ekers R.D., Gaensler B.M., et al., 2017, Astrophys. J., 836, p. 174
Gopal-Krishna, Biermann P.L., Gergely L.´A., et al., 2012, Research in Astronomy and Astrophysics, 12, p. 127
Gordon Y.A., Boyce M.M., O'Dea C.P., et al., 2021, Astrophys. J., Suppl. Ser., 255, id. 30
Goss W.M., Pariiskii Y.N., Soboleva N.S., et al., 1992, Sov. Astron., 36, p. 343
Hurley-Walker N., Callingham J.R., Hancock P.J., et al., 2017, Mon. Not. R. Astron. Soc., 464, p. 1146
Intema H.T., Jagannathan P., Mooley K.P., et al., 2017, Astron. Astrophys., 598, id. A78
Joshi R., Krishna G., Yang X., et al., 2019, Astrophys. J., 887, p. 266
Kopylov A.I., Goss W.M., Parijskij Y.N., et al., 2006, Astronomy Letters, 32, p. 433
Lane W.M., Cotton W.D., van Velzen S., et al., 2014, Mon. Not. R. Astron. Soc., 440, p. 327
Liu F. K., 2004, Mon. Not. R. Astron. Soc., 347, p. 1357
McConnell D., Hale C.L., Lenc E., et al., 2020, Publ. Astron. Soc. Aust., 37, id. e048
Miley G. and De Breuck C., 2008, Astron. Astrophys., 15, p. 67
Missaglia V., Massaro F., Capetti A., et al., 2019, Astron. Astrophys., 626, id. A8
Murgia M., Parma P., Mack K. H., et al., 2011, Astron. Astrophys., 526, id. A148
Ochsenbein F., Bauer P., Marcout J., 2000, Astron. Astrophys., Suppl. Ser., 143, p. 23
Owen F.N. and Rudnick L., 1976, Astrophys. J., 205, id. L1
Parijskij Y.N., Goss W.M., Kopylov A.I., et al., 2000, Astronomical and Astrophysical Transactions, 19, p. 297
Parijskij Y.N., Kopylov A.I., Temirova A.V., et al., 2010, Astronomy Reports, 54, p. 675
Parijskij Y.N., Thomasson P., Kopylov A.I., et al., 2014, Mon. Not. R. Astron. Soc., 439, p. 2314
Peters W., Polisensky E., Brisken W., et al., 2021, American Astronomical Society Meeting Abstracts, 237, id. 211.06
Soboleva N.S., Pariiskii Y.N., Naugolnaya M.N., 1994, Astron. Zh., 71, p. 684
Taylor M.B., 2005, Astronomical Society of the Pacific Conference Series, 347, p. 29
Verkhodanov O.V., Erukhimov B.L., Monosov M.L., et al. 1993, Bulletin of the Special Astrophysics Observatory, 36, p. 132
Verkhodanov O.V., Trushkin S.A., Andernach H., et al., 2005, Bulletin of the Special Astrophysics Observatory, 58, p. 118
Wenger M., Ochsenbein F., Egret D., et al., 2000, Astron. Astrophys., Suppl. Ser., 143, p. 9

MODERN ASTRONOMY: FROM THE EARLY UNIVERSE TO EXOPLANETS AND BLACK HOLES

RCR J090511.74+045536.8 — a candidate for the most distant radio galaxies

O. Zhelenkova[1] and A. Temirova[2]

[1] Special Astrophysical Observatory of the Russian Academy of Sciences, Nizhny Arkhyz, 369167 Russia

[2] St. Petersburg Branch of the Special Astrophysical Observatory of the Russian Academy of Sciences, St. Petersburg, 196140 Russia

Abstract. Using modern radio, infrared and optical sky surveys, hosts have been found for the vast majority of radio sources detected by the Cold experiment and included in the RATAN Cold Refined (RCR) catalog. In this paper, we present details of the optical identification of one of the objects in the RCR catalog — a double radio source RCR J090511.74+045536.8. Initially, we matched it with the to SDSS J090511.94+045537.6, which we assumed to be a supernova that exploded in the host galaxy of the radio source. This hypothesis had to be abandoned, however, as to its properties the SDSS database indicated that it was an asteroid. Searching for the host galaxy of the radio source in deeper optical surveys allowed us to detect an object fainter than $r \approx 26^m$ at the expected location of the host relative to the radio source lobes. We cannot use the selection criteria for Lyman-Break Galaxies (LBG) due to the faintness of the host, but we can assume that the object can be classified as one of them, since it is detected in the r-filter and brighter in the i-filter, but is absent in other filters. Then its estimated host redshift may be greater than $z \gtrsim 4$–5, making it a candidate for the most distant radio galaxies.

Keywords: galaxies: active, high redshift

DOI: 10.26119/VAK2024.043

1 Introduction

Radio sources detected in the surveys of the Cold experiment surveys (Parijskij & Korol'kov 1987) and included in the RC (RATAN Cold) catalog (Pariiski et al. 1991; Parijskij et al. 1993), have been studied in the optical regime since 1984 using observations at the 6-m BTA optical telescope and sky surveys. This was done first for the RC sources (Vitkovskij et al. 1987; Parijskij et al. 1996; Zhelenkova & Kopylov 2008, 2009) and then for the RCR catalog (Soboleva et al. 2010; Zhelenkova et al. 2017). Note that massive optical identifications of radio sources became possible with the advent of deep optical surveys and high-angular resolution radio surveys. Thus, the radio sources of the RCR catalog have been almost completely identified (96%) (Zhelenkova et al. 2013).

The double radio source RCR J090511.74+045536.8 has a steep spectral index of -1.05. According to the FIRST (Helfand et al. 2015), RACS (Hale et al. 2021) and VLASS (Gordon et al. 2021) surveys, the northern of the source is twice as bright as the southern. Therefore the host galaxy should be located twice as close to the northern component. Based on the relations $\ll$LAS–$z\gg$ for radio galaxies (Fig. 3, Kapahi (1987)) and $\ll z$–$r\gg$ for 3C radio galaxies (Snellen et al. 1996) and the angular size of the source LAS $= 25.3''$, we obtained a rough estimate of the redshift and apparent magnitude for this source of $z \approx 0.5$ and $r \approx 19.6^m$ respectively.

2 Find a counterpart for RCR J090511.74+045536.8

In the SDSS survey DR7 (Abazajian et al. 2009) there are two suitable candidates J090511.94+045537.6 and J090512.44+045536.4 for a host of the RCR source. In the Gaia DR3 catalog Gaia Collaboration et al. (2023), J090512.44+045536.4 has significant proper motion ($\mu = 8.139$ mas/year). In addition, the object is located closer to the faint component of the radio source. Therefore we do not consider it to be a host. We identified the double radio source RCR J090511.74+045536.8 with the SDSS J090511.94+045537.6. We also note that there are no objects in this position in the sections of the PanSTARRS survey (Chambers et al. 2016) in all filters. And the PanSTARRS observations in this region of the sky were made earlier than the SDSS observations (Table 1, Id1). We therefore hypothesized that the object could be a transient event, most likely a supernova that has erupted in the host galaxy. The object J090511.94+045537.6 has several SDSS flags (see https://www.astro.princeton.edu/~rhl/flags.html). The MOVED flag indicates that the object is a candidate for moving object exclusion. Despite its name, this does not mean that the object is actually moving. However, the DEBLENDED_AS_MOVING flag indicates that an object with the MOVED flag is considered to be moving by the

Table 1. Optical objects in different surveys as host candidates: number of rows Id, surveys and filters with catalog objects $Survey$, coordinates for epoch 2000.0 RAJ and $DecJ$, magnitude Mag, date of observation or realisation $Date$.

Id	$Survey$	RAJ	$DecJ$	Mag	$Date$
1	PanSTARRS-r				2002-03-04
2	SDSS-g J090511.94+045537.6	09:05:11.85	+04:55:38.5	21.52	2002-05-03
3	SDSS-r J090511.94+045537.6	09:05:11.95	+04:55:37.6	20.88	2002-05-03
4	DESI-r J090511.63+045538.3	09:05:11.63	+04:55:38.3	23.57	2017-06-09
5	HSC-i candidate	09:05:12.02	+04:55:37.0	>26.3	2020-08-03

deblender. The creators of the SDSS survey have no doubt that Kuiper belt objects can be detected in the SDSS data. If it is an asteroid, then there is a shift of several arcseconds in the object between exposures in the r and g filters of the SDSS camera. For SDSS J090511.94+045537.6, using the coordinates measured from the brightest pixel in the r and g sections (Table 1, Id2–Id3), we obtained an offset of $\sim 2''$. This offset and the flags assigned to the object make it more likely to be considered an asteroid rather than a supernova.

The deeper DECaLS survey (Dey et al. 2019) was conducted later than the SDSS. Here, a faint galaxy (Table 1, Id4) with a photometric redshift $z = 0.69 \pm 0.48$ (Duncan 2022) appeared in the survey area. It is located closer to the northern component. Judging from the VLASS cutouts, the radio structure of the source cannot be classified as deformed. In the FIRST and RACS-mid cutouts, the source can be considered as S-shaped. The optical candidate is located far enough away from the expected host position. Therefore, it is unlikely to be considered as a parent galaxy.

Finally, in the survey of the Hyper Suprime-Cam Subaru DR3 (Aihara et al. 2022) (HSC) strategic programme, which is almost 3 magnitudes deeper than the SDSS, we found that at the location of the SDSS object there is nothing brighter than magnitude $r \approx 26^m$. In the vicinity of the host location suggested by the morphology of the radio source, five objects about $i \approx 26^m$ were detected. One of them (Table 1, Id5), in position relative to the lobes, is most likely an optical analogue of the source. In the r-filter cutout this object looks like a point object, but in the i-filter it is an elongated diffuse object as a pair of connected objects. Bright pixels at this location can be seen in the HSC z-filter and the J and H LAS UKIDSS (Lawrence et al. 2007) filters. This object is not in the PDR3 object catalog, where detection is carried out at the $S/N = 5\sigma$ level. We cannot use the selection criteria for LBGs due to the weakness of the candidate, but we can assume that the object can be classified as this type, since it is reliably detected in the r and i-filter, but is absent in other bands.

Then the estimate of its redshift can be higher than 4–5. Galactic extinction is not responsible for the weakness of the most likely host, and its apparent magnitude $r > 26^m$ indicates a higher redshift. Currently, the most distant known radio galaxy has a redshift of 5.72 (Saxena et al. 2018).

Acknowledgements. This paper is based on data collected at the Subaru Telescope and retrieved from the HSC data archive system, which is operated by the Subaru Telescope and Astronomy Data Center (ADC) at NAOJ. This work has made extensive use of topcat (Taylor 2005) and Aladin interactive sky atlas (Bonnarel et al. 2000).

References

Abazajian K.N., Adelman-McCarthy J.K., Agüeros M.A., et al., 2009, Astrophys. J., Suppl. Ser., 182, p. 543
Aihara H., AlSayyad Y., Ando M., et al., 2022, Publ. Astron. Soc. Jpn., 74, p. 247
Bonnarel F., Fernique P., Bienaymé O., et al., 2000, Astron. Astrophys., Suppl. Ser., 143, p. 33
Chambers K.C., Magnier E.A., Metcalfe N., et al., 2016, arXiv e-prints, arXiv:1612.05560
Dey A., Schlegel D.J., Lang D., et al., 2019, Astron. J., 157, id. 168
Duncan K.J., 2022, Mon. Not. R. Astron. Soc., 512, p. 3662
Gaia Collaboration, Vallenari A., Brown A.G.A., et al., 2023, Astron. Astrophys., 674, id. A1
Gordon Y.A., Boyce M.M., O'Dea C.P., et al., 2021, Astrophys. J., Suppl. Ser., 255, id. 30
Hale C.L., McConnell D., Thomson A.J.M., et al., 2021, Publ. Astron. Soc. Aust., 38, is. e058
Helfand D.J., White R.L., Becker R.H., 2015, Astrophys. J., 801, id. 26
Kapahi V.K., 1987, Observational Cosmology, 124, p. 251
Lawrence A., Warren S.J., Almaini O., et al., 2007, Mon. Not. R. Astron. Soc., 379, p. 1599
Pariiski I.N., Bursov N.N., Lipovka N.M., et al., 1991, Astron. Astrophys., Suppl. Ser., 87, p. 1
Parijskij Y.M., Bursov N.M., Lipovka N.M., et al., 1993, Astron. Astrophys., Suppl. Ser., 98, p. 391
Parijskij Y.N., Goss W.M., Kopylov A.I., et al., 1996, Bulletin of the Special Astrophysics Observatory, 40, p. 5
Parijskij Y.N. and Korol'kov D.V., 1987, Astrophysics and Space Physics Review, 5, p. 39
Saxena A., Marinello M., Overzier R. A., et al., 2018, Mon. Not. R. Astron. Soc., 480, p. 2733
Snellen I.A.G., Bremer M.N., Schilizzi R.T., et al., 1996, Mon. Not. R. Astron. Soc., 279, p. 1294
Soboleva N.S., Majorova E.K., Zhelenkova O.P., et al., 2010, Astrophysical Bulletin, 65, p. 42
Taylor M.B., 2005, Astronomical Society of the Pacific Conference Series, 347, p. 29
Vitkovskij V.V., Zhelenkova O.P., Karachentsev I.D., et al., 1987, Soobshcheniya Spetsial'noj Astrofizicheskoj Observatorii, 53, p. 86
Zhelenkova O.P. and Kopylov A.I., 2008, Astrophysical Bulletin, 63, p. 346
Zhelenkova O.P. and Kopylov A.I., 2009, Astrophysical Bulletin, 64, p. 109
Zhelenkova O.P., Soboleva N.S., Majorova E.K., et al., 2013, Astrophysical Bulletin, 68, p. 26
Zhelenkova O.P., Soboleva N.S., Temirova A.V., et al., 2017, Astrophysical Bulletin, 72, p. 150

Formation of single stars and their planetary systems, typicality of the Solar system

T. Abdulmyanov

Kazan State Power Engineering University, Krasnoselskaya st. 51, Kazan, 420066 Russia

Abstract. In this paper, we determine the dynamic viscosity for the case of pulsating disturbances in the density of gas-dust disks. The characteristic velocities of the disk dust particles are divided into separate classes of orbits with Keplerian and near-Keplerian motions. For these classes, we obtain formulas for the dynamic viscosity. We analyze the distributions of exoplanets by their masses, major semi-axes, and eccentricities of their orbits. We conclude that hot giant planets can be located on complex, unstable orbits of accretion onto the central star.

Keywords: protoplanetary cloud; gas-dust disk; dynamic viscosity

DOI: 10.26119/VAK2024.044

1 Introduction

In 1980, as a result of the efforts of many researchers, a standard model of the origin of the Solar System was built. The main problems that are not solved in the standard model were discussed in 2010 at a workshop at the SAI MSU (Vityazev & Pechernikova 2010). Two of the most important problems were identified: 1) to date, the correspondence between the stages of evolution of a protoplanetary cloud and the stages of evolution of the Sun at the protostar stage has not been determined; 2) the growth mechanisms of planetesimals, ranging from the size of dust grains (10^{-5} cm) to ten-kilometer sizes, have not yet been clarified. More recent results of research into the problem of the formation and evolution of planetary systems are discussed in monographs of Safronov 1969 and Armitage 2010. The monograph lists the main problems, the solution of which can help explain the features of the large-scale structure of the Solar System: 1) How were the Terrestrial planets and giant planets formed? 2) What mechanisms determined the final structure of the Solar system? 3) What are the reasons for the deficiency of angular momentum of the Sun? 4) If we draw an analogy with the scale of electromagnetic waves, then what is the modern scale of gravitational waves? According to Hawking and Werner, the frequency of gravitational waves can vary from extremely low to high frequencies. The gas and dust disks of the stars MWC 758, HD 100453, HD 135344B have a spiral structure. Large-scale structures of such disks can become the basis for constructing a model of the formation of planetary systems and for testing the adequacy of the model. The dynamic viscosity of motion in gas-dust disks is obtained from the general laws of motion (Navier–Stokes equation) by analytical methods of calculations under certain restrictions on the velocity field.

2 Dynamic viscosity of K_w and K_r disks

We will consider two main mechanisms for the accumulation of dust particles in gas-dust disks. One of them is the inelastic collision and adhesion of dust (the problem of three bodies with two "zero" masses, Abdulmyanov 2011). According to this model, motion in orbits with rotating apsidal lines can lead to rapid accumulation of particles and the formation of small bodies. At small eccentricities of orbits, rapid clearing of the annular zone of the protoplanetary disk will occur. At critically large eccentricities, the orbits will become orbits of accretion of bodies onto the protostar core. Let us denote such a ring-shaped zone by K_w and determine the dynamic viscosity in such a ring. As a result of inelastic collisions, the Keplerian orbits of dust particles are transformed into elliptical orbits with rotating apsidal lines. The speed of orbital

motion in K_w disks is determined using the following formulas (Abdulmyanov 2022):

$$v_r = \frac{dr}{dt} = \frac{ekh\sin(k\phi)}{p}, v_\phi = r\frac{d\phi}{dt} = \frac{kh}{r}, r = \frac{p}{1+e\cos(k\phi)}, \quad (1)$$

where k is a constant characterizing the rotation of the line of apses of the elliptical orbit. Substituting the expressions v_r, v_ϕ into the viscosity formula, we obtain the dynamic viscosity in K_w disks:

$$\eta(r,t) = \left[\left(\frac{k^2h^2}{r^2} + \frac{gM}{r} - \frac{ek^2h^2\cos(\phi)}{pr} - \frac{k^2}{3}\left(\frac{he\sin(\phi)}{p}\right)^2\right)\rho - r^{1/4}\frac{\partial\rho}{\partial r}\right]\frac{3p}{4ekh\sin(\phi)}. \quad (2)$$

At $k = 1$ there will be no rotation of the apsidal line. In this case, the viscosities in the K and K_w disks will be the same. The second mechanism is the mechanism of dust accumulation near the equilibrium orbits of the circular limited three-body problem. In this case, the movement of dust particles will occur along librational orbits of the limited three-body problem (Garfinkel 1976, 1977; Abdulmyanov 2001). The value of the resonance parameter α, at which a small body leaves a given resonance, determines the outer boundary of the ring. The ring, which is determined by the zone of action of the orbital resonance of the form $(s+q)/s$, will be denoted by K_r. Let us determine the dynamic viscosity of motion in the ring K_r. The components of the velocity vector $V = (v_r, v_\phi)$ in this case will be determined using the following velosity formulas (Abdulmyanov 2022):

$$v_r \approx 2mG^3 f_0'(\lambda^*) + eG^4\sin(\phi)\left[\frac{1}{(G+\Gamma)^3} - \frac{s+q}{s}n_1\right], v_\phi \approx G^2\left[\frac{1}{(G+\Gamma)^3} - \frac{s+q}{s}n_1\right]. \quad (3)$$

Substituting the expressions v_r, v_ϕ into the viscosity formula (Abdulmyanov 2022), we obtain:

$$\eta(r,t) = \frac{3}{4}\left[\frac{gM\rho}{r} - r^{1/4}\frac{\partial\rho}{\partial r}\right] / \left[2mG^3 f_0'(\lambda^*) + eG^2\sin(\phi)\left[\frac{1}{(G+\Gamma)^3}\right], (4)\right.$$

where g is the gravitational constant, M is the mass of the Sun (protostar), m is the mass of Jupiter (ring), ϕ, e is the true anomaly and eccentricity of the Keplerian orbit of the asteroid (dust particles). The function $f_0(\lambda^*)$ characterizes the libration motion of asteroids (Abdulmyanov 2001), the angle $\lambda^* = \lambda – n_1(s+q)/s$ is determined as a function of time in the form of a series of Jacobi functions (Abdulmyanov 2022), λ, ϕ, n_1 – average longitude, true anomaly of dust particles and the average motion of Jupiter, s, q – integers that determine the commensurability of the average motions of

Jupiter and the dust particle. According to formula 2, for circular orbits the viscosity will be infinitely large. It is possible that such viscosity in equilibrium circular orbits was the reason for the formation of co-orbital asteroids of Jupiter. An increase in orbital eccentricity occurs in critical cases: in the case of a small body leaving the orbital resonance or in the mode of accretion onto the core of a protostar. To model the exit of a small body from orbital resonance, it is necessary to take into account the influence of the rate of accretion of interstellar matter on the protostar core or the rate of dust sedimentation on the equatorial plane of rotation of the protostar. For this, the resonance parameter in the viscosity formula 4 must evolve and be a function of time. The cases of accretion onto the "embryo" of a planet and accretion onto the core of a protostar should also be distinguished. Data from observations of gas and dust disks of young stars (Garufi et al. 2017; Garufi 2017; Facchini 2017; Ruge et al. 2013) show the existence of both ring-shaped and spiral fragmentation. In order to study the process of formation of small bodies in ring-shaped fragments, it is necessary to use modern computer tools for numerical integration of gas dynamics equations. In this case, all parameters in formulas 2 and 4 will be variable and will be determined by the magnitude and direction of the velocity vector at the current time. The spiral orbits of planets are the result of gravitational disturbances. The deviation of the orbits of planets from elliptical is associated with mutual perturbations of the planets, and is also the result of the action of the accretion mechanism at an early stage of planet formation. The total result of the influence of these mechanisms can be quantitatively expressed in wavelengths GW (Table 1). If we compare the

Table 1. The value of the constant (h^2) of the area integral for K_w orbits and the length of gravitational waves (GW) of the Solar system.

Planets	a (AU)	e	$\Delta\pi$(sec)	$h^2 10^3$	T	L_{GW}, m
Mercury	0.3871	0.2056	+0.93	10.4741	0.2408	3.56×10^{11}
Venus	0.7233	0.0068	+0.84	14.6302	0.6151	6.8×10^{11}
Earth	1.0000	0.0167	+1.03	17.2005	1.0000	9.4×10^{11}
Mars	1.5237	0.0934	+1.1	21.1432	1.8801	1.43×10^{12}
Jupiter	5.2028	0.0485	+0.97	39.2309	11.8622	4.89×10^{12}
Saturn	9.5388	0.0556	+1.18	53.1394	29.4577	8.97×10^{12}
Uranus	19.1818	0.0473	+0.96	75.5387	84.0152	1.81×10^{13}
Neptune	30.0580	0.0086	+0.48	94.6551	164.788	2.84×10^{13}
Pluto	39.5200	0.2530	+0.84	105.6321	247.696	3.62×10^{13}

GW wavelengths with those currently observed from 10^6 m to 10^{-14} m, it is easy to see that the GW waves (from 3.62×10^{13} m to 3.56×10^{11} m) are on the left flank of the interval wavelengths [10^6 m; 10^{-14}] m. In this regard, the planetary system

of the Solar System is the best object for studying gravitational waves: the system itself is an adequate and natural instrument for recording gravitational waves. The wavelength, expressed in kilometers, will be equal to:

$$L_{\mathrm{GW}} = 29.785 \left(\frac{1 + m_1}{a} \right)^{1/2} \left[(1 - e^2)^{1/2} + T \frac{\Delta\pi}{60} \frac{1}{360} \frac{1}{1 + e^2/2} \right] l T^*, \qquad (5)$$

where T^* is the same period of movement along the elliptical orbit T, only expressed in seconds, l is the smallest number of revolutions along the elliptical orbit, after which particle m_1 returns to the starting point, an orbit with a rotating periapsis. The number l is equal to the denominator of the fraction of the best approximation of real numbers by rational numbers.

3 Comparison of modeling results and data from the NASA Exoplanet Archive catalog

According to Fesenkov's hypothesis, the formation of stars and planetary systems occurs almost simultaneously. In this case, the star formation mechanism will influence the process of formation of celestial bodies. The influence of the star formation mechanism on the dynamics in gas-dust disks can be considered using the general gas dynamics equations. Namely, the dynamic viscosity $\eta(r, t)$, which was obtained using these equations, can be used to solve the problem of angular momentum deficiency in the Sun and determine the reason for the appearance of hot giant planets near stars of other planetary systems. According to Fig. 1 the masses of many exoplanets are an order of magnitude greater than the mass of Jupiter. However, many of them have semimajor axes similar to the orbits of the Earth group planets. For example, exoplanets (63) 51 Peg b, (188–191) CoRoT–1 b, (202) CoRoT–12 b, (207) CoRoT–13 b and many others have large masses and small eccentricities ($e < 0.3$). Exoplanets (132) 70 Vir b, (198) CoRoT–11 b, (211) CoRoT–16 b, (232) CoRoT–20 b and others have large masses and large eccentricities ($e > 0.3$). In parentheses before the names of exoplanets are their serial numbers in the NASA Exoplanet Archive (2022) catalog of exoplanets Exoplanet Catalog (http://exoplanetarchive.ipac.caltech.edu). According to the NASA Exoplanet Archive catalog most exoplanets in the catalog have orbits with small eccentricities ($e < 0.3$). The close location of exoplanets with large masses to the main star according to the accretion model considered in this work is a consequence of the loss of their angular momentum as a result of the influence of dynamic viscosity. This process of transfer of angular momentum is associated with the process of formation of celestial bodies and, therefore, is irreversible. That

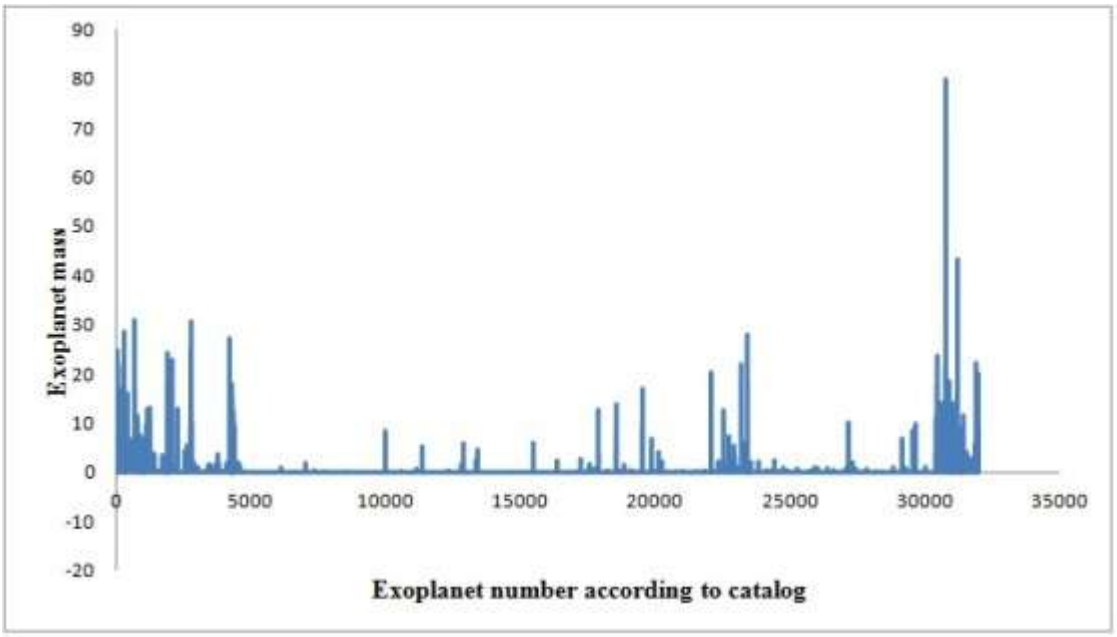

Fig. 1. Distributions of exoplanets by their masses according to the NASA Exoplanet Archive catalog, expressed in Jupiter masses.

is, the reverse migration of large celestial bodies from the central star to the periphery is unlikely or impossible. Consequently, the orbits of gas condensations and "hot Jupiters" located near stars are unstable, rapidly evolving orbits of accretion of interstellar gas onto the central star. According to the results of modeling (Abdulmyanov 2020), for solar mass stars, gravitational compression is from 50 AU up to 5 AU occurs near the boundary of the zone of gas-dynamic instability, and the modeling problem becomes an ill-conditioned problem. In this case, close distances between the planets Pluto–Neptune–Uranus–Saturn (d= 9.5; 10.8; 9.7 AU) cannot also be characteristic of other planetary systems, even if the central star has a mass equal to the mass of the Sun. For such distances to form, it is necessary that accretion rates be exactly the same as for the early Solar System. However, such a coincidence can only be accidental and unlikely. That is, the typicality of the solar planetary system, in comparison with other planetary systems, is not confirmed by both modeling results and observations. The results of observations of exoplanets with masses on the order of the mass of Jupiter near central stars are currently being actively analyzed in publications. A complete review of publications, results and methods of observing exoplanets can be found in the monograph by Sakhibullin 2020.

4 Conclusion

During gravitational compression of a protostellar cloud, the pulsational part of its density disturbances will determine the formation of a large-scale structure of gas and dust disks (Abdulmyanov 2020). In this case, the corresponding dynamic viscosity will participate in the process of disk evolution as a mechanism that transmits and distributes angular momentum. Taking this into account, in this work: 1) the dynamic viscosity of Keplerian and almost Keplerian dust disks of protostars has been determined. It has been shown (Abdulmyanov 2022) that dynamic viscosity determines changes in the accretion rate and the characteristic time of accretion. 2) The results of the analysis of exoplanet catalog data show that exoplanets, whose masses are comparable to the masses of Jupiter, could approach the central star along accretion orbits onto the star. Such migration of exoplanets may be the result of dynamic viscosity and their loss of angular momentum. 3) Gravitational waves in the range from 3.62×10^{13} m to 3.56×10^{11} m are on the left flank of the wavelength scale [10^{6} m; 10^{-14} m].

References

Abdulmyanov T., 2001, Solar System Research., 35, p. 408

Abdulmyanov T., 2011, Vestnik KSPEU, 2 (9), p. 64

Abdulmyanov T., 2020, Astrophysical Bulletin, 75, p. 117

Abdulmyanov T., 2022, Modeling the process of formation of vortex movements in gas and dust disks using computer computing systems, Kazan: KSPU, 391 pp.

Armitage P., 2010, Astrophysics of Planet Formation, Cambridge University Press

Facchini S., 2017, Abstracts PFE-2017, Jena 25–27 Sep., Germany

Garfinkel B., 1976, Celest. mech. 13, p. 229

Garfinkel B., 1977, Astron. J. 82, p. 368

Garufi A., Meeus G., Benisty M., et al., 2017, Astron. Astrophys., 603, id. A21

Garufi A., 2017, Abstracts PFE-2017, Jena 25–27 Sep., Germany

Ruge J., Wolf S., Uribe A., and Klahr H., 2013, Astron. Astrophys., 549, id. A97

Safronov V., 1969, Evolution of the preplanetary cloud and the formation of the Earth and planets, Moscow, Nauka Press, 244 pp.

Sakhibullin N., 2020, Exoplanets, Kazan: Kazan Univ. Publishing House, 2020, 420 pp.

Vityazev A. and Pechernikova G., 2010, Art. from the Workshop, SAI MSU. St. Petersburg, 161

VAK 2024 MODERN ASTRONOMY: FROM THE EARLY UNIVERSE TO EXOPLANETS AND BLACK HOLES 300 years Russian Academy of Sciences

Observations of magnetic white dwarfs in the Special Astrophysical Observatory of the Russian Academy of Sciences

V. Aitov, E. Korchagina, and G. Valyavin

Special Astrophysical Observatory of the Russian Academy of Sciences, Nizhny Arkhyz, 369167 Russia

Abstract. Studies of magnetic white dwarfs in the Special Astrophysical Observatory of the Russian Academy of Sciences (SAO RAS) have been carried out since 1990 with the 6-m telescope using various spectrographs and with the 1-m Zeiss-1000 telescope using the Multi-Mode Photometer-Polarimeter (MMPP). As a result, we have derived direct estimates of the longitudinal magnetic field obtained with spectropolarimetric observations and circular polarization values in the photometric mode. We observed both well-known magnetic white dwarfs and objects with no data about magnetic field. Among well-known magnetic objects, there were white dwarfs with an extremely strong magnetic field of up to hundreds megagauss and weak magnetic white dwarfs with a field of several tens kilogauss. The use of these data and the data obtained by other authors allowed time series of the observations of these objects to be several decades. Analyzing these time series, we estimated the lower limits of the evolution times of the magnetic fields of white dwarfs.

Keywords: stars: white dwarfs, magnetic field, evolution

DOI: 10.26119/VAK2024.045

1 Introduction

SAO RAS astronomers have been conducting a program to search for global (regular) magnetic field of white dwarfs (WDs) since 1990. The main goal of this program is to search for magnetic white dwarfs (MWDs) with a field smaller than a megagauss and to study their distribution by magnetic fields. Analysis of this distribution can provide an answer to the question about the physical nature of these objects, in particular, whether MWDs make a specific subtype of white dwarfs with unique evolutionary features or if MWDs are objects with the strongest magnetic fields in the distribution of magnetic fields of all WDs. In this paper, we again analyze these studies combined with new results of other authors.

Observations for these programs were carried out on the 6-m and 1-m telescopes of the SAO RAS, on the ESO telescopes and on the 3.6-m telescope of the Franco-Hawaiian Observatory (Fabrika et al. 1997; Valyavin et al. 2005, 2006, 2008, 2014; Landstreet et al. 2012, 2016, 2017; Aitov et al. 2022).

2 Estimates of the magnetosphere stability time of white dwarfs

The time series of observations of magnetic objects ranged from several to almost 50 years within the above programs and using the data by other authors. Comparing the results of magnetometric and polarization observations at these time intervals, we obtained lower estimates of the stability time of the MWD magnetospheres. For the stars with known rotation periods, we obtained the amplitudes from sinusoid approximation for different sections of the time series (spaced by years). Then we obtained estimates of the characteristic evolution times using the linear model of the magnetic field secular evolution and the derived amplitudes. For the objects without any data on their rotation, all points were approximated linearly.

Table 1 presents the results. The magnetospheres of these stars remain stable for periods from several decades (for WD 2359−434) to hundreds or more (for GRW +708247 and WD 1312+098) years. First, this confirms the hypothesis of the fossil origin and slow dissipation of magnetic field (Wendell et al. 1987). Second, these MWDs can be used as the circular polarization standards, because their magnetic fields remain stable for periods of decades or more years. So far, there has been no list of such standards.

Table 1. Estimates of evolution time.

Star	Estimates of evolution time, years
WD 0009+501	80
WD 1953−011	100
WD 2047+372	140
WD 2359−434	40
GRW +708247	$\gg 100$
WD 1312+098	$\gg 100$

3 Distribution of white dwarfs' magnetic field

The objects discussed above have magnetic field strengths of several tens of kilogauss and greater. However, most white dwarfs do not show any magnetic properties. The solution to this problem should be sought in the distribution of white dwarfs by their magnetic field strengths.

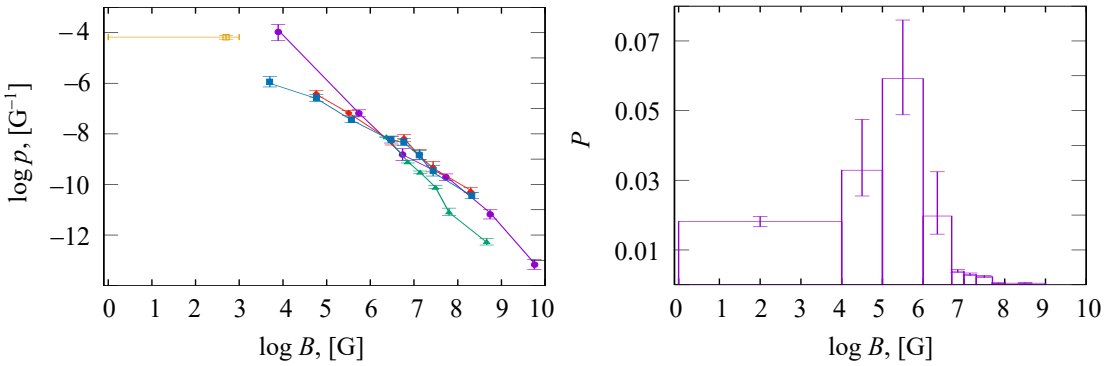

Fig. 1. Left panel: The function of the magnetic field of white dwarfs (MFF, the dependence of the probability density p of detecting the MWD with the set magnetic field strength) according to different authors. The purple circles signs represent the function given in Fabrika & Valyavin (1999), the green triangles represent the function according to Kepler et al. (2013), the red diamonds represent the function according to Bagnulo & Landstreet (2021), the blue solid squares represent the function according to Holberg et al. (2016) with additions from Bagnulo & Landstreet (2021) and Valyavin et al. (2006). The orange open square represents the lower limit of the MFF according to Bagnulo & Landstreet (2021) for the objects in which no magnetic field was detected and the 3σ criterion for which the field was smaller than 1 kG (in the paper, the accuracy of 1σ is indicated). Right panel: Probability P of detecting the MWD with the strength. The figure is drawn according to Kepler et al. (2013) for the objects with strong magnetic fields and according to Bagnulo & Landstreet (2021) for the objects with weak magnetic fields.

For the first time, this distribution (Magnetic Field Function, MFF) was constructed by (Fabrika & Valyavin 1999). We have built new MFFs based on modern reviews; they are shown in Fig. 1 in the left panel. All functions show power dependence. However, the dependence is broken in the area below 100 kilogauss and demonstrates a "fall" that illustrated in the right panel of Fig. 1. Our explanation of this phenomenon is that the symmetry of the magnetic field is caused by dynamic processes in the surface layers of white dwarfs. Therefore, the search for magnetic fields in this region by polarimetric methods becomes ineffective.

4 Conclusion

Estimates of the stability time of the magnetospheres of six MWDs are obtained. They range from several decades to hundreds or more years. This fact makes it possible to use these objects as circular polarization standards.

The MWD distribution by magnetic fields is constructed. A selection "fall" is found in the distribution of the magnetic field strengths below 100 kG. The reason for this phenomenon is the destruction of the global symmetry of the magnetic field by the processes in the surface layers of the MWD.

References

Aitov V.N., Valyavin G.G., Valeev A.F., et al., 2022, Astrophysical Bulletin, 77, 3, p. 301

Bagnulo S. and Landstreet J.D., 2021, Monthly Notices of the Royal Astronomical Society, 507, 4, p. 5902

Fabrika S.N., Shtol' V.G., Valyavin G.G., 1997, Astronomy Letters, 23, 1, p. 43

Fabrika S. and Valyavin G., 1999, ASP Conf. Ser., 169, p. 214

Holberg J.B., Oswalt T.D., Sion E.M., et al., 2016, Monthly Notices of the Royal Astronomical Society, 462, 3, p. 2295

Kepler S.O., Pelisoli I., Jordan S., et al., 2013, Monthly Notices of the Royal Astronomical Society, 429, 4, p. 2934

Landstreet J.D., Bagnulo S., Valyavin G.G., et al., 2012, Astronomy & Astrophysics, 545, id. A30

Landstreet J.D., Bagnulo S., Martin A., et al., 2016, Astronomy & Astrophysics, 591, id. A80

Landstreet J.D., Bagnulo S., Valyavin G.G., et al., 2017, Astronomy & Astrophysics, 607, id. A92

Valyavin G., Bagnulo S., Monin D., et al., 2005, Astronomy & Astrophysics, 439, 3, p. 1099

Valyavin G., Bagnulo S., Fabrika S., et al., 2006, Astrophysical Journal, 648, 1, p. 559

Valyavin G., Wade G.A., Bagnulo S., et al., 2008, Astrophysical Journal, 683, 1, p. 466

Valyavin G., Shulyak D., Wade G.A., et al., 2014, Nature, 515, 7525, p. 88

Wendell C.E., van Horn H.M., Sargent D., 1987, Astrophysical Journal, 313, p. 284

MODERN ASTRONOMY: FROM THE EARLY UNIVERSE TO EXOPLANETS AND BLACK HOLES

Photometry of the outburst of the WZ Sge-type dwarf nova IK Leo in 2024

O. Antoniuk[1], K. Antoniuk[1], E. Pavlenko[1], S. Shugarov[2], and P. Dubovsky[3]

[1] Crimean Astrophysical Observatory of the Russian Academy of Sciences, Nauchny, 298409 Russia
[2] Sternberg Astronomical Institute of the Moscow State University, 13 Universitetskij Pr., Moscow, 119991 Russia
[3] Vihorlatská hvezdáreň Observatory, 4 Mierová, Humenné, 06 601 Slovakia

Abstract. The multicolour photometric observations of the dwarf nova IK Leo in 2024, carried out at the Crimean Astrophysical Observatory, are presented. We obtained a corrected value of the superhump period during the outburst, which is 0.055953 days, and studied the evolution of its changes from the plateau stage to the slow decay of the outburst. Changes in the behaviour of colour indices during the outburst are considered.

Keywords: stars: dwarf novae, cataclysmic variables; individual: WZ Sge, IK Leo

DOI: 10.26119/VAK2024.046

1 Introduction

Dwarf novae are the subclass of cataclysmic variables—close binary systems consisting of a Roche-lobe-filling star that accretes matter onto a white dwarf (Warner 1995). The light curve of WZ Sge-type dwarf novae is characterized by rare (up to decades) and long-lasting bright outbursts (up to 8^{m}). These systems are also characterized by rebrightenings, which are observed during the fading of the main outburst (Kato 2015). Among other dwarf novae, WZ Sge systems have the shortest orbital periods (about 85 min).

The outburst of the dwarf nova IK Leo was reported in February 2024. The previous known similar outburst occurred in 2006 (Uemura et al. 2008). The current observations of this binary were carried out at the Crimean Astrophysical Observatory on the AZT-11 telescope in the $BVRI$ bands. For a more complete analysis of the light curve of the outburst, data from the open sources AAVSO (V-band) and provided by the observers from Slovakia (V and R-bands) were used.

2 Observations

This outburst had an amplitude of over 5^{m}. On the light curve (Fig. 1b) we can distinguish a plateau of the outburst lasting 18 days, after which a "dip", a sharp weakening by 1^{m}, was observed for 3 days. Then there was a rebrightening lasting 7 days and a rapid fading of the outburst within 2–3 days. A pre-outburst brightness was not reached, there was a long phase of slow outburst weakening.

During the outburst, the light curve showed superhumps—periodic light variations typical for many dwarf novae. The average period of superhumps in the stage of the outburst plateau was 0.055953(16) days and it increased at the rate of 0.27×10^{-5} (Fig. 1a). The periodogram and phase curve for this period are shown on (Fig. 2). During the rebrightening, we also observed light variations with a close period, 0.055955(22) days, and during the slow fading phase, superhumps with a smaller period (0.055925 days) were observed too.

The overall light curve of the outburst in the $BVRI$ bands is shown (Fig. 3). It can be seen that the system becomes redder during the outburst weakening. This behaviour is consistent with the classic picture of the accretion disk in dwarf nova outbursts, in which a superhump source lies at the outermost part of the disk. A sharp jump in the B–I indices occurs on the descending branch of the rebrightening, but as the outburst slowly fades, a slight turn to the blue side can be observed.

3 Summary

Comparing the results obtained for the outburst in 2024 with the previously known outburst in 2006, the following conclusions can be made. The interval between neigh-

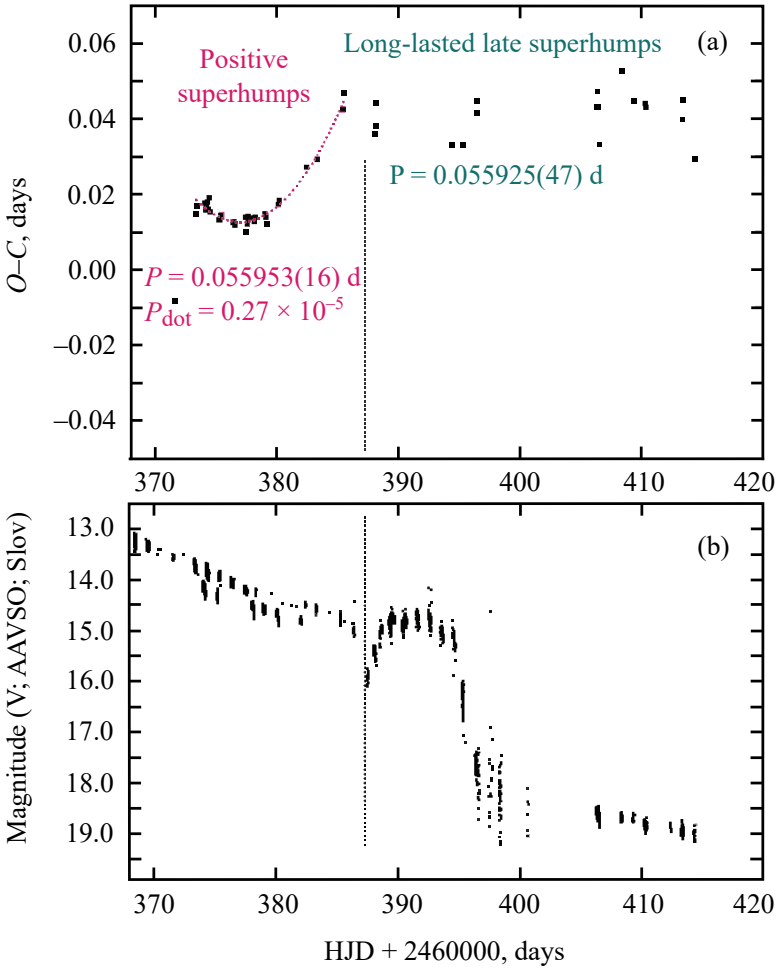

Fig. 1. Panel (a): $O-C$ for superhumps maxima. Panel (b): the overall light curve of the IK Leo outburst in V-band from CrAO, Slovakia, and AAVSO data.

bouring outbursts for this binary can be up to 18 years. The amplitude of the outburst is more than $5^{\rm m}$, and the duration of the outburst with the following rebrightening is about 28 days. During this interval, both outbursts exhibited a characteristic sharp short-term brightening ("dip"). The average superhump period during the outburst was 0.055953 days which is less than the value obtained for 2006. Comparing the superhump period at the plateau stage and during the rebrightening and following slow decay, we can assume the registration of late superhumps after the dip. The changes in the colour indices are consistent with the standard representation for dwarf novae outbursts.

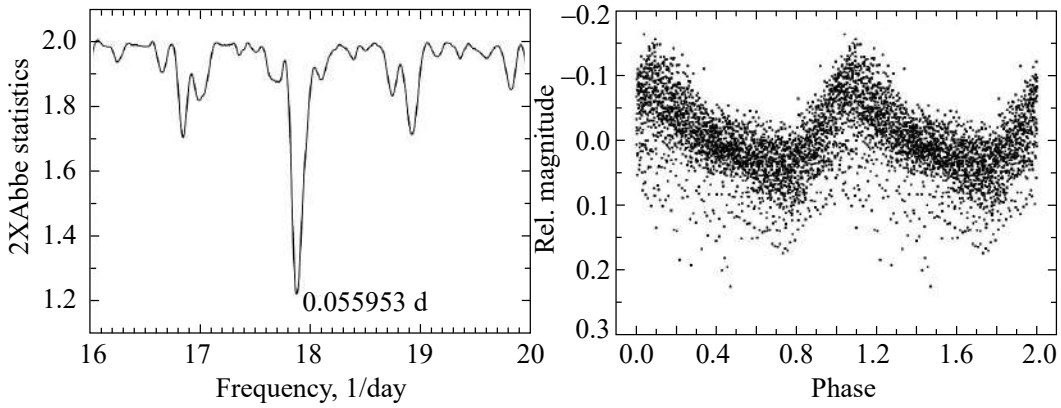

Fig. 2. Periodogram for superhumps at the outburst plateau stage and phase curve for the obtained period.

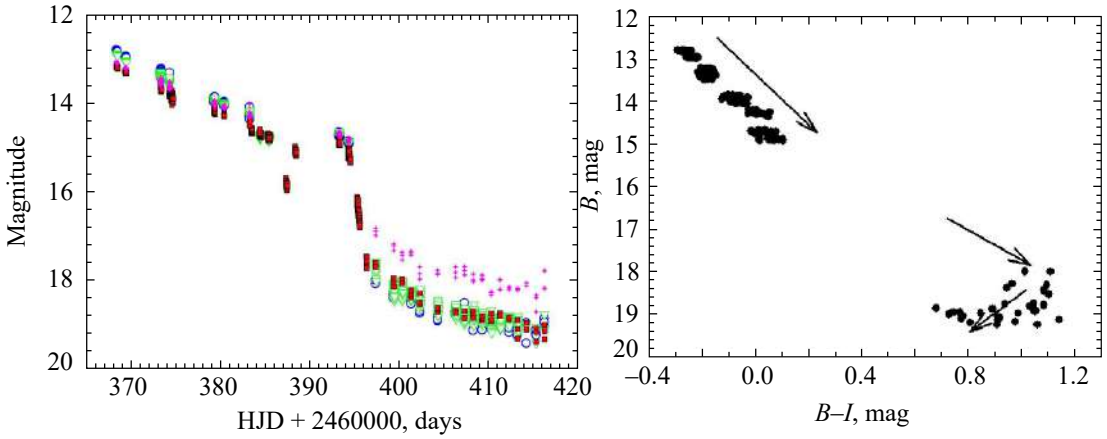

Fig. 3. The light curve of IK Leo in the $BVRI$ bands (blue circles, green triangles, red squares and pink crosses are B, V, R and I bands, respectively) and the changes in the B–I colour indices along the outburst (shown by the arrows).

References

Kato T., Hambsch F.-J., Dubovsky P., et al., 2015, Publications of the Astronomical Society of Japan, 67, 6, id. 105

Warner B., 1995, Cambridge Astrophysics Series, 28

Uemura M., Arai A., Krajci T., et al., 2008, Publications of the Astronomical Society of Japan, 60, 2, p. 227

Modeling of the magnetic chemically peculiar star HD 188101

R. Bayazitov[1] and L. Mashonkina[2]

[1] Kazan Federal University, 18 Kremlyovskaya, Kazan, 420008 Russia
[2] Institute of Astronomy of the Russian Academy of Sciences, 48 Pyatnitskaya, Moscow, 119017 Russia

Abstract. We present the study of the He-weak star HD 188101. Using spectral observations obtained with the Main stellar spectrograph (MSS) and the Nasmyth echelle spectrograph (NES) mounted on the BTA SAO RAS and the data from the literature, we determined the fundamental parameters: $T_{\rm eff} = 15\,600 \pm 4\,00$ K , $\log g_{\rm spec} = 3.87 \pm 0.13$, $R = 2.1$–$3.1\,R_\odot$, $M = 3.8$–$4.8\,M_\odot$. Chemical abundances were determined by the synthetic spectrum method: under the LTE assumption for He, N, Ti, Fe and without LTE for C, O, Mg, Si. For Si and Fe, overabundance of about 0.6 dex relative to the solar abundance was found. The non-LTE calculations with the stellar Si abundance lead to consistent abundances from lines of Si II and Si III, while the difference between LTE abundances amounts to 0.8 dex.

Keywords: stars: chemically peculiar, abundances, atmospheres, magnetic fields

DOI: 10.26119/VAK2024.047

1 Introduction

Chemically peculiar stars make up about 10–20% of B–A type stars of the main sequence. They show deficiency or excess in abundance of some elements relative to the solar abundance. Since atmospheres of B–A type stars are non-convective, the selective diffusion of chemical elements is possible (Michaud 1970) in case of the slow rotation as observed for CP stars. Large-scale magnetic field detected in many CP stars additionally stabilizes the atmosphere and leads to periodic variations in the star's brightness and in the profiles of some spectral lines. These variations are explained by chemical spots on the stellar surface associated with the magnetic field.

From analysis of the Kepler's light curves Hümmerich et al. (2018) selected new candidate CP stars. These stars became targets of a spectropolarimetric monitoring on the 6-m telescope BTA. The results for 10 objects are presented by Yakunin et al. (2023). The hottest star of this sample, HD 188101, was selected for the present study. The star has the sinusoidal light curve and a poorly approximated dependence of the longitudinal magnetic field on the phase. Effective temperature of HD 188101 was estimated as $T_{\rm eff} = 14\,700$ K and the surface gravity as $\log g = 3.8$. It was noted that at the local thermodynamic equilibrium (LTE) assumption effective temperatures of 15 200 K and 17 200 K are needed to reproduce the Si II and Si III lines respectively. The He I λ4471 line profile cannot be reproduced.

In this work we determine the fundamental parameters of HD 188101, abundances of He, C, N, O, Mg, Si, Ti, Fe at the LTE assumption, a type of chemical peculiarity of the star and investigate the non-LTE (NLTE) effects for the C II, O I, Mg II, Si II and Si III lines.

2 Observations

We use spectra obtained in 2019 and 2020 with the Main stellar spectrograph (MSS) of the BTA. Spectral resolving power is $R = \lambda/\Delta\lambda \approx 15\,000$, the signal-to-noise ratio is $S/N = 150$–200, the spectral range covers 4450–5000 Å. We also use the spectrum from the Nasmyth echelle spectrograph (NES) of the BTA obtained in 2019 with $R = 50\,000$, $S/N = 50$, spectral range of 3950–6880 Å. The phases were obtained from the periodogram: JD $= 2455681.4953 + 3.98726E$. We use the parallax obtained by the HIPPARCOS mission and updated later (HIP2007, van Leeuwen 2007) $\pi = 2.82 \pm 0.50$ mas, and the Gaia measurements (Gaia DR3, Gaia Collaboration et al. 2021) $\pi = 2.34 \pm 0.10$ mas.

Photometric data were extracted from the VizieR portal[1] for comparison with a theoretic spectral energy distribution (SED).

[1] https://vizier.cds.unistra.fr/viz-bin/VizieR

3 Fundamental parameters of HD 188101

Interpolation along $T_{\rm eff}$ is carried out in the grid of fluxes calculated by Castelli & Kurucz (2003) to describe the observed fluxes. An angular diameter of the star θ is derived from the infrared flux method (IFRM) using effective wavelengths from 1 μm to 13 μm. The color excess $E(B–V) = 0.08$ is taken from Gontcharov (2017). The best agreement with observations (Fig. 1) was obtained with $T_{\rm eff} = 15500 \pm 500$ K, $\log g = 4.0$, [M/H] = 0.0, $\theta = 0.066$ mas. The uncertainty in $T_{\rm eff}$ was estimated from the TD1 data spread.

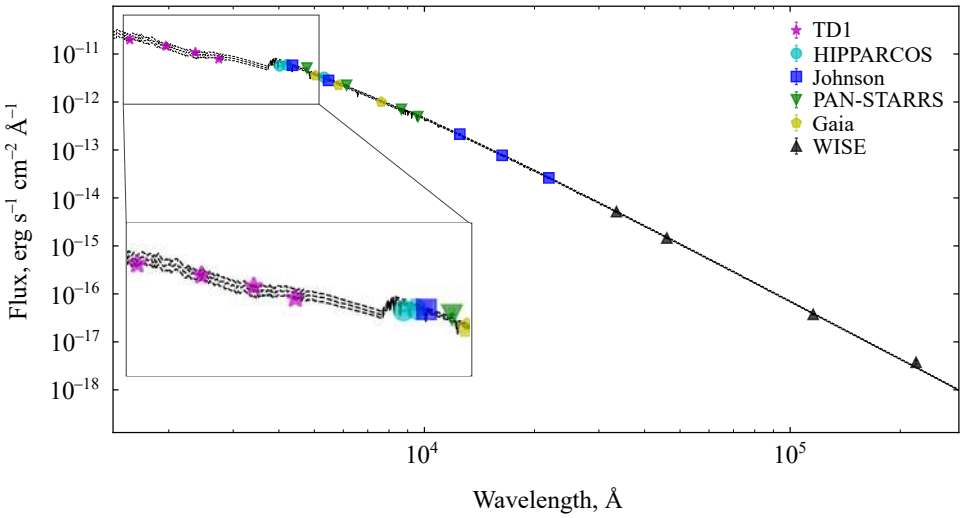

Fig. 1. The observational data of HD 188101 are shown by different type symbols. Synthetic spectra for the models with $T_{\rm eff} = 15\,500 \pm 500$ K, $\log g = 4.0$, [M/H] = 0.0, $\theta = 0.066$ mas are shown by the lines.

Based on the stellar parallax, evolutionary tracks (Dotter 2016), obtained $T_{\rm eff}$ and θ, we conclude that HD 188101 is located near the zero age main sequence, has the mass M and $\log g_{\rm phot}$ indicated in Table 1.

Using the non-LTE synthetic spectra (Lanz & Hubeny 2007), we constrain $\log g_{\rm spec}$ and $T_{\rm eff}$ from fitting the Hβ line profile in the MSS spectrum: $\log g_{\rm spec}$ varies from 3.75 to 4.0 and $T_{\rm eff}$ from 15 000 K to 16 000 K. Similar atmospheric parameters of $T_{\rm eff} = 15610 \pm 440$ K, $\log g = 3.96 \pm 0.06$ were obtained using the `SME` software package (LTE assumption Valenti & Piskunov 1996; Piskunov & Valenti 2017), grid of the `LLmodels` model atmospheres (Shulyak et al. 2004) and VALD3[2] atomic data

[2] http://vald.inasan.ru

base (Ryabchikova et al. 2015). Our analysis is made with the 15 600/4.0/0.0 model atmosphere.

Table 1. The fundamental parameters of HD 188101.

Parameter	Quantity	Method
θ, mas	0.066	IFRM
R, $R_\odot$ (HIP2007)	2.52 ± 0.45	IFRM
R, $R_\odot$ (Gaia EDR3)	3.03 ± 0.12	IFRM
$\log g_{\rm phot}$ (HIP2007)	4.1–4.4	Evolutionary tracks
$\log g_{\rm phot}$ (Gaia EDR3)	4.05–4.20	Evolutionary tracks
M, $M_\odot$	3.8–4.8	Evolutionary tracks
$\log g_{\rm spec}$	3.75–4.00	Hβ
$T_{\rm eff}$, K	$15\,600 \pm 400$	Photometry + Hβ

4 Chemical abundances

Strong lines of Si II, Si III, Fe III, Ti II and weak lines of He I are observed in the MSS spectrum. All the lines of Si II, Si III, Ti II and the strongest magnesium line, Mg II λ4481, show profile variations. Variations in the He I λ4713 profile amount to 20%. We note that the strongest line of Al II λ4663 cannot be detected in the NES spectrum.

NLTE calculations for C I–II, O I, Mg I–II, Si I–II–III were made with the `DETAIL` code (Giddings 1981; Butler 1984; Przybilla et al. 2011) using model atoms described by Sitnova et al. (2004); Alexeeva et al. (2021, 2018) and Mashonkina (2020). Departure coefficients for the atomic levels calculated in the `DETAIL` are implemented into the `SYNTHV_NLTE` code (Tsymbal et al. 2019). Using the `Binmag6` code (Kochukhov 2018), `SYNTHV_NLTE` allows us to fit observations. Atomic data for spectral lines were obtained from the VALD data base. Model atmospheres were calculated with the `LLmodels` code.

NLTE corrections for the Mg II lines range from -0.19 to 0.08 dex, those of the C II lines do not exceed 0.01 dex. For the Si II lines with an excitation energy of the lower level from 8.12 eV to 12 eV, the NLTE corrections reach 1.0 dex. The NLTE corrections for another Si II lines do not exceed 0.7 dex. The NLTE calculations with [Si/H] = 0.6 and [Si/H] = 0.0 lead to different NLTE effects for Si II. We note that the Si II λ6239 line profile is reproduced and the Si II/Si III ionization equilibrium is achieved when [Si/H] = 0.6 dex is used in the NLTE calculations. For the Si III lines, the NLTE corrections range from -0.10 dex to -0.25 dex.

The obtained average abundances $[N_{\rm el}/N_{\rm tot}]$ are presented in Fig. 2. Solar abundances were taken from Asplund et al. (2021). The root mean square error is calculated as a standard deviation $\sigma = \sqrt{\sum (x - \bar{x})^2 / (N_l - 1)}$, where N_l is the number of lines. The abundance of oxygen is determined with large uncertainty due to defects in the spectrum near the O I λ6155, λ6158 lines. The solar abundance was obtained from the Mg II λ4427, λ4433 lines. But the Mg II λ4481 line gives a lower abundance, by 0.5 dex. This discrepancy requires further research.

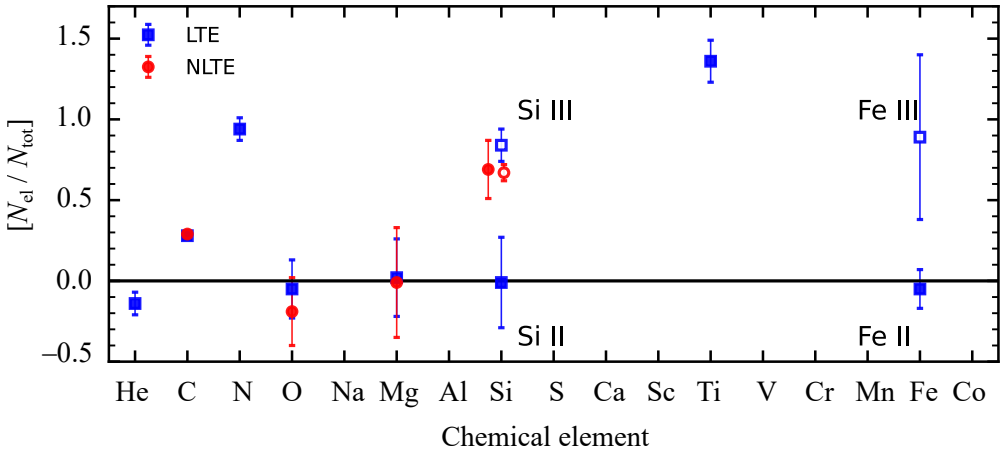

Fig. 2. Stellar chemical abundances relative to the solar ones are obtained from the NES and the MSS (2019.11.17) spectra. Abundances determined from the Fe III and Si III lines are shown by the open symbols. Here $[N_{\rm el}/N_{\rm tot}] = \log(N_{\rm el}/N_{\rm tot})_{\rm star} - \log(N_{\rm el}/N_{\rm tot})_{\rm Sun}$.

5 Summary

Based on the analysis of spectroscopic and photometric data, the following results were obtained for the CP star HD 188101.

1. We determined the fundamental parameters: $T_{\rm eff} = 15\,600 \pm 400$ K and $\log g_{\rm spec} = 3.87 \pm 0.13$. Surface gravity $\log g_{\rm spec}$ based on fitting the Hβ line profile is less by 0.2 dex than $\log g_{\rm phot}$ determined from the evolutionary tracks.
2. Abundances of He, C, N, O, Mg, Si, Ti, Fe were determined with the LTE assumption and without LTE for C, O, Mg, Si. Our analysis finds enhanced abundances of N, Si, Ti, Fe relative to the solar abundances, by about 0.6 dex, and depleted abundance of He. The other elements reveal solar abundances, within 0.2 dex.

HD 188101 is a CP star of a CP4 He-weak, Si type according to the classification proposed by Preston (1974).

3. A difference of 0.85 dex in the LTE abundances between the Si II and Si III lines is removed in the NLTE calculations with [Si/H] = 0.6 characteristic of HD 188101. No signatures of Si stratification in the atmosphere of HD 188101 is found. With the LTE assumption, an abundance difference was also found between lines of Fe II and Fe III. NLTE calculations for Fe II–Fe III are needed to study the sources of such a difference.

References

Alexeeva S., Ryabchikova T., Mashonkina L., et al., 2018, Astrophysical Journal, 866, 2, id. 153

Alexeeva S., Ryabchikova T., Mashonkina L., 2021, Monthly Notices of the Royal Astronomical Society, 462, 1, p. 1123

Asplund M., Amarsi A., Grevesse N., 2021, Astronomy & Astrophysics, 653, id. A141

Butler K., 1984, Ph.D. Thesis, University of London

Castelli F. and Kurucz R.L., 2003, IAU by the Astronomical Society of the Pacific, 210, p. A20

Dotter A., 2016, Astrophysical Journal Supplement Series, 222, 1, id. 8

Gaia Collaboration, Brown A.G.A., Vallenari A., et al., 2021, Astronomy & Astrophysics, 649, id. A1

Giddings J.R., 1981, Ph.D. Thesis, University of London

Gontcharov G.A., 2017, Astronomy Letters, 43, 7, p. 472

Hümmerich S., Mikulášek Z., Paunzen E., et al., 2018, Astronomy & Astrophysics, 619, id. A98

Kochukhov O., 2018, Astrophysics Source Code Library, record ascl:1805.015

Lanz T. and Hubeny I., 2007, Astrophysical Journal Supplement Series, 169, 1, p. 83

van Leeuwen F., 2007, Astronomy & Astrophysics, 474, 2, p. 653

Mashonkina L., 2020, Monthly Notices of the Royal Astronomical Society, 493, 4, p. 6095

Michaud G., 1970, Astrophysical Journal, 160, p. 641

Piskunov N. and Valenti J.A., 2017, Astronomy & Astrophysics, 597, id. A16

Preston G.W., 1974, Annual Review of Astronomy and Astrophysics, 12, p. 257

Przybilla N., Nieva M.-F, Butler K., 2011, Journal of Physics Conference Series, 328, 1, id. 012015

Ryabchikova T., Piskunov N., Kurucz R.L., et al., 2015, Physica Scripta, 90, 5, id. 054005

Shulyak D., Tsymbal V., Ryabchikova T., et al., 2004, Astronomy & Astrophysics, 428, p. 993

Sitnova T.M., Mashonkina L.I., Ryabchikova T.A., 2004, Astronomy Letters, 39, 2, p. 126

Tsymbal V., Ryabchikova T., Sitnova T., 2019, ASP Conference Series, 518, p. 247

Valenti J. and Piskunov N., 1996, Astronomy and Astrophysics Supplement, 118, p. 595

Yakunin I., Semenko E., Romanyuk I., et al., 2023, Astrophysical Bulletin, 78, 2, p. 141

The speckle interferometric multiplicity of T Tauri type stars in the Taurus-Auriga star-forming region

M. Butorina[1], V. Dyachenko[2], A. Beskakotov[2], A. Mitrofanova[2], and A. Maksimov[2]

[1] Kazan Federal University, 18 Kremlyovskaya St, Kazan, 420008 Russia
[2] Special Astrophysical Observatory of the Russian Academy of Sciences, Nizhny Arkhyz, 369167 Russia

Abstract. We present the results of a multiplicity study of T Tau-type stars in the Taurus-Auriga association. The observational data were obtained by speckle interferometry at the 6-meter telescope of the SAO RAS in 2020 and 2024. For the resolved stars, the positional parameters of the components, as well as the magnitude differences, were determined using the reference-independent power spectrum modeling method. Among the sample containing 58 bright stars ($m_V \leq 10$ mag), 12 binary, 5 triple and one quadruple speckle-interferometric systems were detected.

Keywords: stars: pre-main sequence; techniques: high angular resolution

DOI: 10.26119/VAK2024.048

1 Introduction

The Taurus-Auriga association is the closest star-forming region to the Sun (about 140 parsecs, Kenyon et al. 1994). Extending widely across the northern sky (total area about 100 degrees), Taurus-Auriga contains many T Tauri type stars (TTs). These are low-mass objects ($0.5M_{\odot}$ – $2M_{\odot}$) characterized by regular and irregular variations in luminosity, as well as a strong emission in the UV and X-ray due to accretion. As a rule, the spectral classes of these stars are between G and K (Petrov 2003).

Tau-Aur is known to be a low stellar density region with a large number of double stars, especially wide pairs, compared to field stars and star-forming regions with higher stellar densities (Joncour et al. 2017).

In the paper of Leinert et al. (1993), a sample of 104 TTs was studied using various methods, including IR speckle interferometry, among which 57.7 % were unresolved stars, 37.5 % were binary, 2.9 % were triple, and 1.9 % were quadruple. No difference was statistically detected between the multiplicity of classic TTs and weak-lined TTs. The Köhler & Leinert (1998) survey, despite the smaller sample size, confirmed the Leinert et al. (1993) values obtained.

Such surveys make it possible not just to learn the multiplicity statistics in a given star-formation region. Information on positional parameters at different observational epochs allows us to calculate orbital solutions (e.g., the works of Woitas et al. 2001; Schaefer et al. 2014, etc.), which can then be used to directly and independently estimate the masses of the systems. This is very important for young stars because theoretical evolutionary models, while differing among themselves, introduce methodological uncertainties in the mass determinations.

This paper also presents a survey of the brightest TTs, using the speckle interferometry method. We present the calculated positional parameters for the double systems, as well as an estimate of the speckle interferometric multiplicity of the sample we used.

2 Observations

We compiled a sample of 58 T Tauri-type stars towards the Taurus-Auriga star formation region, selected by the brightness criterion ($m_V \leq 10$ mag). Observational data were obtained at the BTA speckle interferometer of SAO RAS based on the Andor iXon Ultra 897 EMCCD detector (Maksimov et al. 2009) in October–November 2020 and January 2024. Repeated observations were necessary to confirm the separation of the components, as well as to obtain new positional parameters.

The standard observational data series contained 2000 speckle interferograms of 512x512 pixels, recorded with an exposure time of 20 milliseconds, using the following interference filters (central wavelength/bandpass): 550/20, 550/50, 700/50, 800/100, 900/80 nm.

The brightness criterion, relying on the speckle interferometer characteristics, provides the possibility of a confident observation of speckles of bright TTs with a high signal-to-noise ratio, as well as the detection of faint components of TTs with a large magnitude differences (up to 6 mag).

The observational data series were used to compute average power spectra and autocorrelation functions (ACFs) (Labeyrie 1970). An example of the autocorrelation function is shown in Fig. 1.

After the initial calibration (taking into account the average flat- and dark-frames), the most accurate model description was selected for each power spectrum using the least squares method. This way, the positional parameters of the components (separation ρ, positional angle θ) for a given epoch were determined (Pluzhnik 2005). The method of splitting the power spectrum into narrow rings was used in the modeling process. Within a ring, the transfer function was considered constant. The boundaries of the rings were set individually for each spectrum. Modeling was carried out in the specified frequency range, excluding low frequencies containing the atmospheric profile, as well as noisy high frequencies.

Table 1 presents the positional parameters for the resolved binary systems. The positional angle θ is given with an accuracy of 180 degrees because of the uncertainty of the component positions on the ACF. The errors for the calculated magnitude differences correspond to the error of the model fitting, so they may be underestimated.

Table 1. The positional parameters for the resolved binary systems. The positional angle θ is given with an accuracy of 180 degrees because of the uncertainty of the component positions on the ACF.

Name	Epoch	Filter	ρ, mas	σ_ρ, mas	$\theta \pm 180$, $\circ$	σ_θ, $\circ$	ΔM, mag	$\sigma_{\Delta M}$, mag
v969 Tau	2020.76429	550	70	1	91.9	0.1	0.44	0.01
	2020.76428	700	69	1	93.1	0.1	0.57	0.01
	2024.08185	550	68	1	0.7	0.1	0.59	0.01
	2024.08186	700	68	1	0.9	0.1	0.53	0.01
HD 25444	2020.76433	550	1635	1	52.0	0.1	2.55	0.02
	2024.08156	550	1703	1	50.8	0.1	2.32	0.01
	2024.08157	700	1701	1	50.8	0.1	1.89	0.01
V1299 Tau	2020.76436	550	298	1	70.4	0.1	0.64	0.01
	2024.08182	550	278	1	69.2	0.1	0.44	0.01
	2024.08188	700	278	1	69.3	0.1	0.40	0.01
AG+18 338	2020.90334	700	285	1	23.0	0.1	4.56	0.04
AG+18 339	2020.90333	700	69	1	14.1	0.3	2.42	0.03
	2024.08169	550	62	1	354.6	0.1	2.43	0.01
HD 283798	2020.90662	800	1609	1	121.1	0.1	5.17	0.03
HD 245059	2020.90937	550	737	1	159.7	0.1	3.23	0.02
	2020.90938	800	737	1	159.7	0.1	1.95	0.01
	2024.08214	550	716	1	161.1	0.1	3.27	0.01
	2024.08215	700	716	1	161.2	0.1	2.54	0.01
HD 245567	2020.90940	550	357	1	137.1	0.2	4.16	0.07
	2020.90940	800	357	1	136.8	0.1	3.17	0.04
	2024.08216	550	358	1	134.1	0.1	4.51	0.02
	2024.08218	700	358	1	134.5	0.1	3.79	0.03
HD 245924	2020.90941	550	899	1	178.5	0.1	3.10	0.02
	2020.90942	800	898	1	178.4	0.1	2.23	0.01
	2024.08219	550	885	1	179.8	0.1	3.12	0.01
	2024.08220	700	884	1	179.9	0.1	2.63	0.01
HD 294207	2020.90918	550	2165	1	36.7	0.1	2.39	0.02
	2020.90918	800	2167	1	36.8	0.1	1.55	0.01
RW Aur	2020.90877	550	1478	1	74.4	0.1	1.92	0.02
	2020.90878	800	1474	1	74.4	0.1	0.81	0.01
HD 31281	2020.90667	800	19	1	4.2	0.2	1.00	0.04
	2020.90666	550	16	1	177.5	0.1	1.42	0.07
HD 284065	2020.90876	800	16	1	0.0	0.2	2.38	0.02
	2024.07952	700	21	1	60.7	0.1	1.44	0.02
HD 280583	2020.90882	550	96	1	72.3	0.1	2.59	0.02
	2020.90883	800	98	1	71.8	0.1	2.70	0.03
	2024.07953	550	112	1	64.9	0.1	2.77	0.01
	2024.07954	700	108	1	65.5	0.1	2.79	0.03

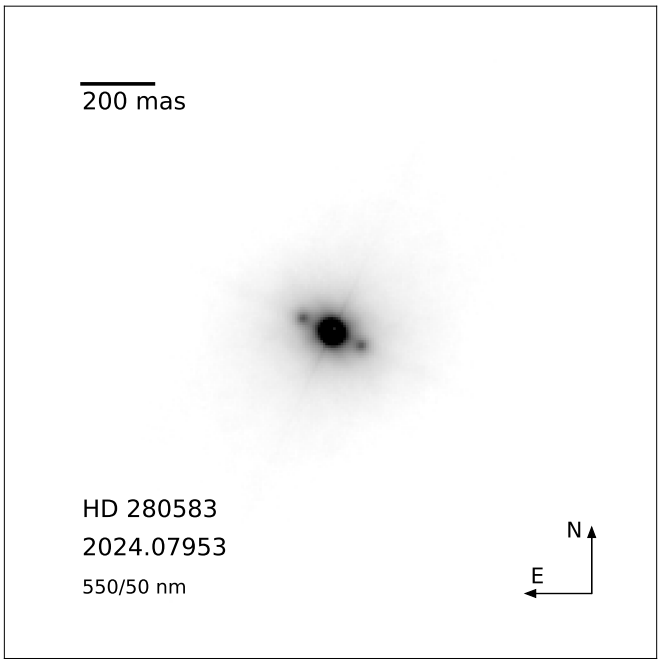

Fig. 1. The central part of the autocorrelation function for the system HD 280583.

3 Conclusion

From a sample of 58 T Tauri type stars selected by the brightness criterion ($m_V \leq 10$ mag), 19 stars were resolved into individual components. Among them, there are 12 binary, 5 triple and one quadruple speckle interferometric system. For each resolved binary system, the positional parameters of their components, as well as the magnitude differences, were obtained by the power spectra modeling (Labeyrie 1970).

The star AG+18 339 is a companion of the star AG+18 338. Each of these stars is resolved as a speckle-interferometric binary. Thus, this system is defined as a quadruple system.

Based on the above results of the processing of the observations, the estimate of the sampling speckle interferometric multiplicity is as follows: of the 58 stars, 68 % are unresolved, 21 % are binary, 9 % are triple and 2 % are quadruple.

Comparing the results with previously mentioned multiplicity surveys (e.g., Leinert et al. 1993), there are differences in the multiplicity percentages due to the different observational methods used. Nevertheless, despite the smaller sample size in this

paper, it can be seen that a relatively high percentage of higher-order multiplicity systems are observed for the included stars.

References

Joncour I., Duchêne G., and Moraux E., 2017, Astronomy and Astrophysics, 599, id. A14
Kenyon S., Dobrzycka D., and Hartmann L., 1994, The Astronomical Journal, 108, p. 1872
Köhler R. and Leinert C., 1998, Astronomy and Astrophysics, 331, p. 977
Labeyrie A., 1970, Astronomy and Astrophysics, 6, p. 85
Leinert C., Zinnecker H., Weitzel N., et al., 1993, Astronomy and Astrophysics, 278, p. 129
Maksimov A., Balega Yu., Dyachenko V., et al., 2009, Astrophysical Bulletin, 64, p. 296
Petrov P., 2003, Astrophysics, 46, p. 506
Pluzhnik E., 2005, Astronomy and Astrophysics, 431, p. 587
Schaefer G., Prato L., Simon M., and Patience J., 2014, The Astronomical Journal, 147, p. 157
Woitas J., Kohler R., and Leinert C., 2001, Astronomy and Astrophysics, 369, p. 249

MODERN ASTRONOMY: FROM THE EARLY UNIVERSE TO EXOPLANETS AND BLACK HOLES

33 Lib is an analogue of Gamma Equulei?

V. Bychkov[1], L. Bychkova[1], and J. Madey[2]

[1] Special Astrophysical Observatory of the Russian Academy of Sciences, Nizhny Arkhyz, 369167 Russia
[2] Astronomical Observatory University of Warsaw, 4 Al. Ujazdowskie, Warszawa, 00–478 Poland

Abstract. In this paper we investigate the periodic variability of the magnetic field of the magnetic Ap star 33 Lib. The period of 83.5 years found by us earlier from the magnetic field estimates and 79.2 years determined later are close to the period of variability of the magnetic field of the known Ap star γ Equ of 97 years. Such a slow rotation is also confirmed by a very small value of the projection of the equatorial velocity onto the line of sight $v_e \sin i = 0.6$ km/s.

Keywords: stars: magnetic field; individual: 33 Lib

DOI: 10.26119/VAK2024.049

1 Introduction

The magnetic field of the Ap star 33 Lib (HD 137949) was first discovered by Babcock (1958). The variability of the magnetic field of 33 Lib was first studied by van den Heuvel (1971). In this work, based on a small number of the magnetic field (MF) estimates, the variability period was supposedly $18\overset{\mathrm{d}}{.}4$. Further, Wolff (1975a) also based on MF, the periods of $23\overset{\mathrm{d}}{.}26$ and $7\overset{\mathrm{d}}{.}194$ were found. The most recent estimate of the period by Romanyuk et al. (2014) is $7\overset{\mathrm{d}}{.}0187$. Attempts to detect the variability of brightness and color of this star were made by Wolff (1975b); Deul & van Genderen (1983) and a number of others were unsuccessful. The researchers recorded the absence of variability of brightness with the accuracy of about $0\overset{\mathrm{m}}{.}01$. For the first time, weak photometric variability with a period of $4\overset{\mathrm{d}}{.}8511$ was recorded by Wraigh et al. (2012) using the data obtained on the STEREO satellite (NASA) observations (Eyles et al. 2009).

Kurtz (1982) discovered rapid photometric variability of this star with the period of 8.2721 minutes. This discovery greatly strengthened the analogy with another very well-known magnetic Ap star γ Equ—the presence of a strong global magnetic field, rapid photometric variability and unusually long rotation periods. Ap stars provide a unique opportunity to unambiguously estimate the rotation periods of stars, as well as the angles of inclination of the rotation axes to the line of sight, etc. Thanks to this, amazing objects were discovered—"standing" stars, the rotation periods of which are decades and can even reach hundreds and even thousands of years, as indicated by Mathys (2017). This is confirmed in the works of Metlova et al. (2014); Bychkov et al. (2016); Hubrig et al. (2018); Giarrusso et al. (2022) and others. The study of long-period variability is always associated with a number of obvious difficulties: it is difficult to obtain a homogeneous series of measurements over tens of years.

2 Analysis of observational data

The probable magnetic period of this star was previously estimated at 83.5 years (30478^{d}) (Bychkov et. al. 2015) based on 21 B_l estimates obtained over about 21 years. This estimate is close to the estimate obtained later by Giarrusso et al. (2022) based on a larger volume of observational material based on 77 B_s estimates obtained over 29 and 79.2 years (28902^{d}). Using this period estimate, we will construct the average magnetic phase curves (MPC) based on the estimates of B_l and B_s, and also obtain the parameters of this variability. These MPCs are presented in Fig. 1a, b respectively.

Another indirect proof of such a slow rotation is the determination of the projection of the equatorial rotation velocity on the line of sight $v_e \sin i$. Such precise

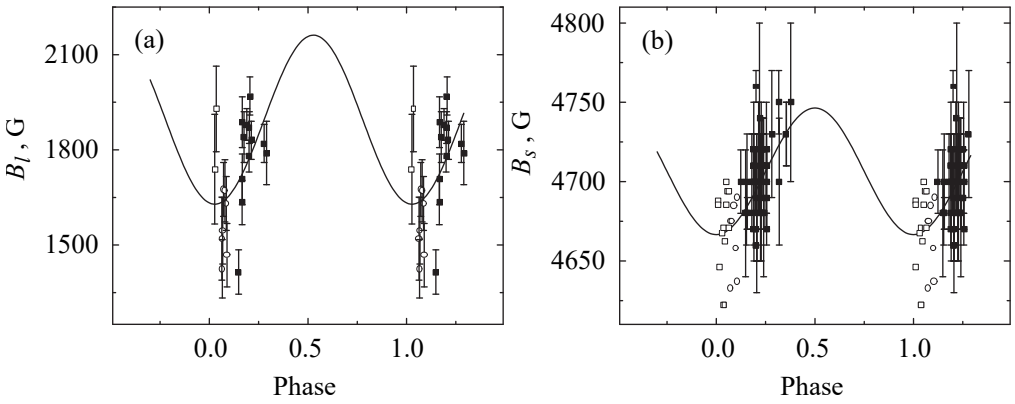

Fig. 1. Average magnetic phase curve obtained from B_l (a) and B_s (b) estimates.

determinations for magnetic stars can be made only by the lines not subject to magnetic broadening. Such lines are the iron lines Fe I λ5434.524, λ5576.089. The spectral regions near these lines were obtained with a resolution of $R = 80\,000$ on the UVES spectrometer (VLT UT2 ESO Paranal telescope). Fitting both lines yields $v_e \sin i = 0.6$ km/s, i.e. the rotation is very slow, almost like that of γ Equ. Fig. 2 shows, as an example, a spectrum region in the region of Fe I λ5434.524. The value of the obtained estimate is limited from above by the spectral resolution of the spectral material used.

3 The discussion of the results and conclusion

At present we have the following observational facts:

1. The projection of the equatorial rotation velocity $v_e \sin i = 0.6$ km/s, i.e. is actually close to zero. This fact can be explained either by extremely slow rotation ($P = 79.2$ years), or the angle i being close to zero, i.e. the axis of rotation of the star is directed towards us.
2. It is unlikely, but possible, that the rotation axis precesses with such a long period. Critical observations for testing both possible scenarios will be polarimetric monitoring of these objects. This will allow us, as in the case of γ Equ (HD 201601) (Leroy et al. 1994; Bychkov et al. 2016) to say unequivocally whether such a long period is the rotation period of the star or it can be explained in some other way.

Unfortunately, at the moment we have a series of estimates covering only a small part of the expected period, no more than 37%. We hope to increase the duration of the observation series in the near future, which will allow us to obtain a more accurate estimate of the period and the parameters of magnetic field variability.

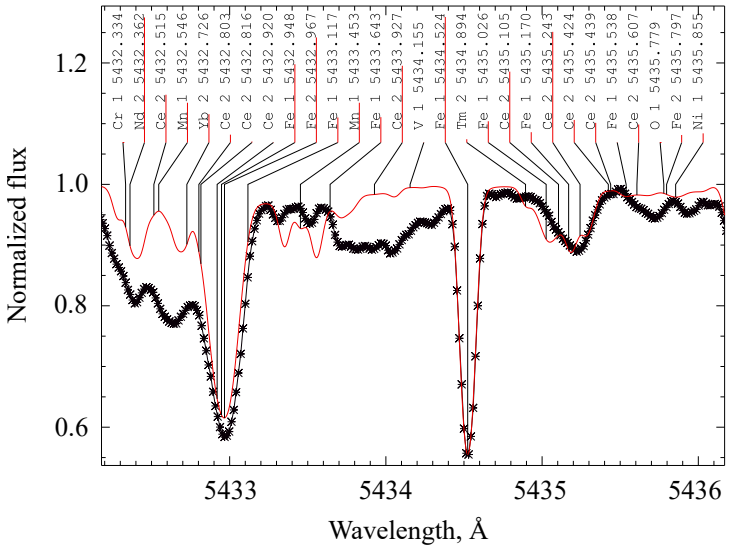

Fig. 2. The spectrum section near the Fe I λ5434.524 line. The line shows the observed spectrum, the asterisks are the results of the synthetic spectrum calculation.

References

Babcock H.W., 1958, Astrophysical Journal Supplement, 3, p. 141

Bychkov V.D., Bychkova L.V., Madej J., 2016, Monthly Notices of the Royal Astronomical Society, 455, 3, p. 2567

Bychkov V.D., Bychkova L.V., Madej J., et al., 2015, arXiv:1506.06234

Deul E.R. and van Genderen A.M., 1983, Astronomy & Astrophysics, 118, p. 289

Eyles C.J., Harrison R.A., Davis C.J., et al., 2009, Solar Physics, 254, 2, p. 387

Giarrusso M., Cecconi M., Cosentino R., et al., 2022, Monthly Notices of the Royal Astronomical Society, 514, 3, p. 3485

van den Heuvel E.P.J., 1971, Astronomy & Astrophysics, 11, p. 461

Hubrig S., Järvinen S.P., Madej J., et al., 2018, Monthly Notices of the Royal Astronomical Society, 477, 3, p. 3791

Kurtz D.W., 1982, Monthly Notices of the Royal Astronomical Society, 200, p. 807

Leroy J.L., Bagnulo S., Landolfi M., et al., 1994, Astronomy & Astrophysics, 284, p. 174

Mathys G., 2017, Astronomy & Astrophysics, 601, id. A14

Metlova N., Bychkov V.D., Bychkova L.V. , et al., 2014, Astrophysical Bulletin, 69, 3, p. 315

Romanyuk I.I., Semenko E.A., Kudryavtsev D.O., 2014, Astrophysical Bulletin, 69, 4, p. 427

Wolff S.C., 1975a, Astrophysical Journal, 202,p. 127

Wolff S.C., 1975b, Astrophysical Journal, 202, p. 121

Wraigh K.T., Fossati L., Netopil M., et al., 2012, Monthly Notices of the Royal Astronomical Society, 420, 1, p. 757

VAK 2024 MODERN ASTRONOMY: FROM THE EARLY UNIVERSE TO EXOPLANETS AND BLACK HOLES 300 years Russian Academy of Sciences

About the periodic variation of the stellar magnetic fields

V. Bychkov[1], L. Bychkova[1], and J. Madey[2]

[1] Special Astrophysical Observatory of the Russian Academy of Sciences, Nizhny Arkhyz, 369167 Russia
[2] Astronomical Observatory University of Warsaw, 4 Al. Ujazdowskie, Warszawa, 00-478 Poland

Abstract. In this work, a general description of the observed variability of magnetic fields in stars of various spectral types is presented. Average magnetic phase curves (MPC) and their parameters are presented in three catalogs. As a result, there are currently medium magnetic phase curves for 415 stars, 258 of which are Ap/Bp stars. Such a large number of Ap/Bp stars allows you to judge not only the parameters variability, the structure of the global magnetic field, but also opens up the possibility of finding the reason explaining the super slow rotation of some of them.

Keywords: stars: magnetic fields, variability

DOI: 10.26119/VAK2024.050

1 Introduction

Magnetic fields play an important role in the physics and evolution of stars. For stars with a sufficient number of B_e measurements and for which the magnetic variability period $P_{\rm mag}$ is known, we obtained average magnetic phase curves (MPC). About 10% OBA stars have fairly strong magnetic fields (Grunhut et al. 2017; Sikora et al. 2019) reaching several thousand gauss in intensity. According to Bychkov et al. (2021a) 75% stars have magnetic harmonic phase curves, and 25% stars have two-wave phase curves. The magnetic fields of hot stars are generally stable throughout the entire period of studies (about 75 years). Only some of them are suspected of slight variability of the MCP parameters (magnetic phase curves) (Bychkov et al. 2021a). Examples of single-wave and double-wave MCP are shown in Fig. 1a, b. All MCPs and their parameters are presented by Bychkov et al. (2005, 2021a).

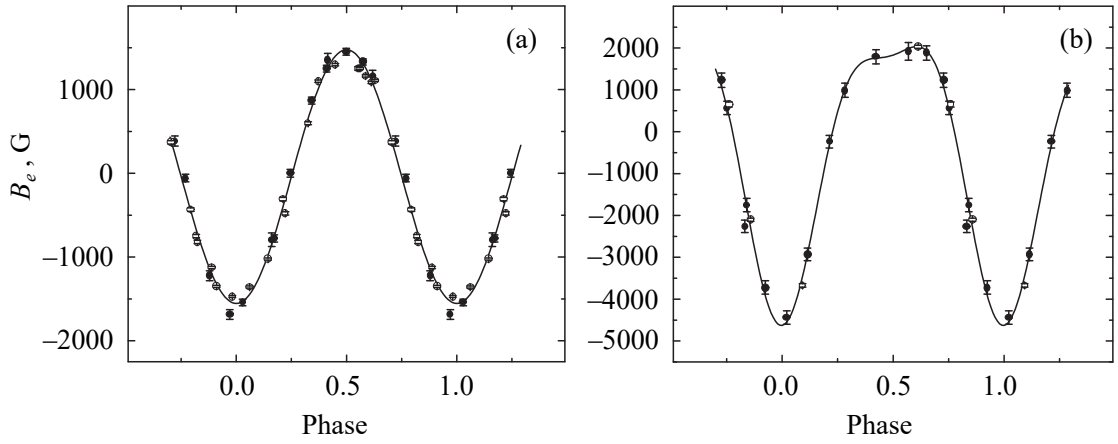

Fig. 1. Examples of single-wave MPC for the star HD 62140 F0pSrEu type (Bychkov et al. 2021a) (a) and double sine wave MPC for the star HD 133880 B8IVpSi (Bychkov et al. 2021a) (b).

2 Types of stars for which MPCs were obtained

Table 1 shows the number of stars by spectral type with famous MPCs.

3 MPC hot stars

Ap/Bp stars have photometric variability due to the presence of relatively cold spots on their surface. Photometric variability provides an excellent opportunity to esti-

Table 1. Number of stars in various classes with known magnetic phase curves.

Type	Number	Type	Number
Ap/Bp	258	Stars hosting planets	8
Var. β Cep	18	Normal chem. comp. stars	6
Slowly Pulsating B stars	9	Be stars	6
High Proper Motion stars	14	Var. δ Sct	3
Var. δ Cep	2	Semi-regular var. pulsating	3
Multiple stars	19	Flare stars	17
Pulsating stars	6	Ae/Be Herbig stars	10
Var. BY Dra	12	T Tau stars	6
Var. Ori type	5	Pre-main sequence	3
Rotationally var. stars	20	EB, Algol + BY Dr	1
Var. RS CVn	2	Blue supergiant star	2
Wolf-Rayet star	2		

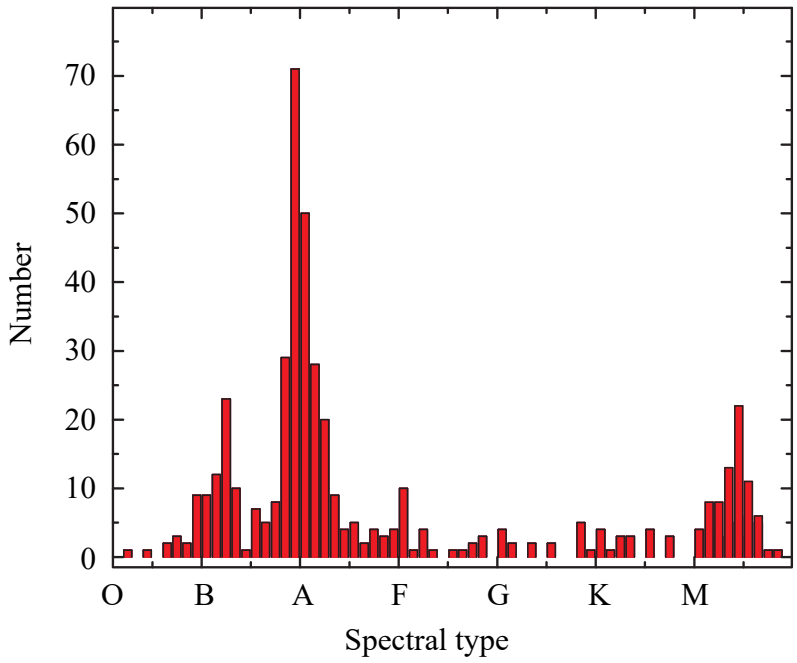

Fig. 2. Number of stars with known MPCs depending on spectral type. 43 objects are included (red dwarfs from M0 to M6), whose magnetic behavior was investigated by Donati et al. (2023).

mate the rotation period of these stars with high accuracy (Saar et al. 1986; Metlova et al. 2014; Renson & Catalano 2001), and many others. This has become especially important with the advent of high-precision photometry from the Kepler, TESS, Gaia and other space missions (Balona et al. 2019; David-Uraz et al. 2019; Sikora et al. 2019). Thanks to Labadie-Bartz et al. (2023) and a number of other researchers it was possible to determine the periods of mCP stars with high accuracy. The possibilities of high-precision space photometry have appeared recently. This limits the search and precise determination of periods longer than 50 days (Mathys et al. 2024). One of the most interesting features of magnetic Ap stars is their slow rotation. On average, Ap stars rotate 4–5 times slower than the same normal stars (Abt & Morrell 1995; Glagolevskij 2021). It is believed that they acquired slow rotation before entering the main sequence. Currently, 24 Ap/Bp stars with rotation periods of more than 100 days are known to have MPC. The possibility of the existence of rotation periods of hundreds and even thousands of years was indicated by Mathys (2017). This is confirmed by Metlova et al. (2014); Bychkov et al. (2016); Hubrig et al. (2018); Giarrusso et al. (2022) and a number of others. The main difficulty in obtaining the MCP for such stars is long-term magnetic monitoring which sometimes lasts for decades.

4 Global magnetic fields of late stars

Stars of late spectral classes have strong surface magnetic fields reaching 3.8 kG. This was first shown for the dwarf M3 AD Leo (Saar & Linsky 1985; Saar et al. 1986). How strongly the MPC parameters vary on such stars was shown by Donati et al. (2008); Bychkov et al. (2021a). A huge contribution to the study of the magnetic behavior of such objects was made by the SPIRou near-infrared magnetic measurement program, carried out at the CHFT (Canada-France-Hawaii Telescope) (Donati et al. 2023). During this survey, 6700 magnetic field estimates were obtained for 43 red dwarfs in the spectral range from M0 to M5.5 in the time interval 2019–2022 with an average accuracy of about 4 G (the error range was from 1 G to 15 G depending on the object). The number of estimates obtained for one object ranged from 50 to 247 and on average was about 150.

It has been convincingly shown that the magnetic phase curves of these stars vary greatly with time. In a first approximation, they can be represented as a superposition of two harmonic dependencies with close periods. It seems that there are two (or more) dipoles, whose axes (respectively, magnetic poles) are spaced apart in latitude. Due to the differential rotation of the star's atmosphere, these dipoles rotate with close but different periods. It is possible that the intensity itself of these magnetic "spots" varies. This will further complicate the observed variability. The observed

MF intensities vary from units to tens of gauss. The rotation periods of these objects vary from several to hundreds of days (Donati et al. 2023). As an example, the MCP for GJ 1289 (spectral class M4Ve) with the main period of 73.66 days is given in Fig. 3, which clearly shows how the phase dependence of the magnetic field varies from period to period.

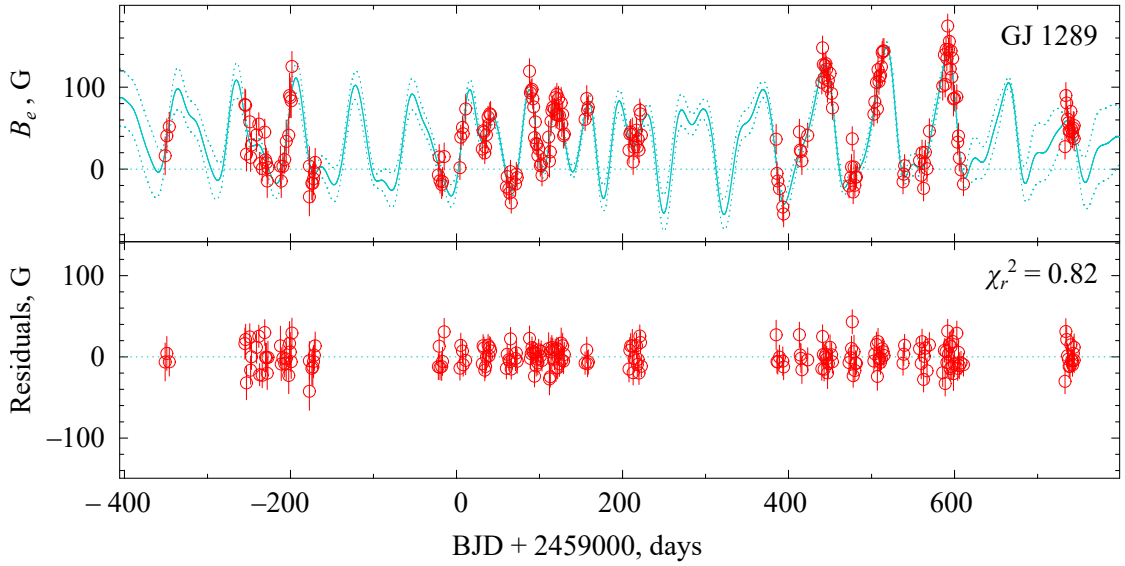

Fig. 3. As an example, magnetic monitoring of the red dwarf GJ 1289 (spectral class M4Ve) is shown, obtained by Donati et al. (2023) with the period of 73.66 days. Red dots indicate magnetic field estimates depending on the time of acquisition. A total of 204 estimates were obtained a little over 3 years. This is more than 15 periods. The solid curve plotted in blue in the figure is an approximation curve describing the magnetic behavior of GJ 1289. The two curves marked with dots indicate the accuracy of the approximation.

5 Summary

The created catalogs serve to present and summarize the observational material of the variability of stellar magnetic fields of different types. This allows us to reasonably judge the origin and evolution of stellar magnetic fields, test hypotheses and conduct statistical analysis, study the mechanism of "magnetic braking" of stellar rotation and much more.

References

Abt H.A. and Morrell N.I., 1995, Astrophysical Journal Supplement, 99, p. 135

Balona L.A., Handler G., Chowdhury S., et al., 2019, Monthly Notices of the Royal Astronomical Society, 485, 3, p. 3457

Bychkov V.D., Bychkova L.V., Madej J., 2005, Astronomy & Astrophysics, 430, p. 1143

Bychkov V.D., Bychkova L.V., Madej J., 2016, Monthly Notices of the Royal Astronomical Society, 455, 3, p. 2567

Bychkov V.D., Bychkova L.V., Madej J., 2021a, Astronomy & Astrophysics, 652, id. A31

Bychkov V.D., Bychkova L.V., Madej J., 2021b, Astronomical & Astrophysical Transactions, 32, 2, p. 143

David-Uraz A., Neiner C., Sikora J., et al., 2019, Monthly Notices of the Royal Astronomical Society, 487, 1, p. 304

Deutsch A.J., 1970, Astrophysical Journal, 159, p. 985

Donati J.-F., Morin J., Petit P., et al., 2008, Monthly Notices of the Royal Astronomical Society, 390, 2, p. 545

Donati J.-F., Lehmann L.T., Cristofari P.I., et al., 2023, Monthly Notices of the Royal Astronomical Society, 525, 2, p. 2015

Giarrusso M., Cecconi M., Cosentino R., et al., 2022, Monthly Notices of the Royal Astronomical Society, 514, 3, p. 3485

Glagolevskij Yu.V., 2021, Astrophysical Bulletin, 76, 1, p. 91

Grunhut J.H., Wade G.A., Neiner C., et al., 2017, Monthly Notices of the Royal Astronomical Society, 465, 2, p. 2432

Hubrig S., Järvinen S.P., Madej J., et al., 2018, Monthly Notices of the Royal Astronomical Society, 477, 3, p. 3791

Labadie-Bartz J., Hümmerich S., Bernhard K., et al., 2023, Astronomy & Astrophysics, 676, id. A55

Mathys G., Holdsworth D.L., Kurtz D.W., 2024, Astronomy & Astrophysics, 683, id. A227

Mathys G., 2017, Astronomy & Astrophysics, 601, id. A14

Metlova N.V., Bychkov V.D., Bychkova L.V., et al., 2014, Astrophysical Bulletin, 69, 3, p. 315

Renson P. and Catalano F.A., 2001, Astronomy & Astrophysics, 378, p. 113

Saar S.H. and Linsky J.L., 1985, Astrophysical Journal, 299, p. L47

Saar S.H., Linsky J.L., Beckers J.M., 1986, Astrophysical Journal, 302, p. 777

Sikora J., Wade G.A., Power J., et al., 2019, Monthly Notices of the Royal Astronomical Society, 483, 2, p. 2300

Sikora J., David-Uraz A., Chowdhury S., et al., 2019, Monthly Notices of the Royal Astronomical Society, 487, 4, p. 4695

MODERN ASTRONOMY: FROM THE EARLY UNIVERSE TO EXOPLANETS AND BLACK HOLES

Magnetic and photometric variability of the super-slowly rotating Ap star GY And (HD 9996)

V. Bychkov[1], L. Bychkova[1], J. Madey[2], G. Komissarova[3], and N. Metlova[3]

[1] Special Astrophysical Observatory of the Russian Academy of Sciences, Nizhny Arkhyz, 369167 Russia
[2] Warsaw University Observatory, 4 Al. Ujazdowskie, Warszawa, 00–478 Poland
[3] Sternberg Astronomical Institute of the Moscow State University, 13 Universitetsky pr., Moscow, 119234 Russia

Abstract. The star GY And (HD 9996) belongs to a very rare and poorly studied class of super-slowly rotating Ap (ssrAp) stars. The main difficulty in conducting studies of such stars is their unusually long periods, often amounting to tens or even hundreds of years. Based on long-term magnetic monitoring conducted at the 1-m telescope of the SAO RAS and photometric monitoring carried out at the 60-cm telescope of the Southern Station of the SAI, the period (which is just over 23 years) and the parameters of magnetic and photometric variability of GY And (HD 9996) have been clarified.

Keywords: stars: magnetic field, rotation

DOI: 10.26119/VAK2024.051

1 Introduction

Super-slowly rotating Ap star (ssrAp) are of great interest to us from the point of view of stellar evolution. At present, there is no complete understanding of how the star lost its angular momentum. On average, Ap stars rotate 4–5 times more slowly than the same normal ones (Abt & Morrell 1995; Glagolevskij 2021). As suggested by Mathys (2017), Ap stars can have rotation periods lasting up to a thousand years, and this is already confirmed by the observations by Bychkov et al. (2016); Hubrig et al. (2018). A mechanism of "magnetic" braking, considered by various authors, is quite possible. But such a mechanism is only possible in the case of a purely dipole structure of the global magnetic field. In the case of a more complex structure (which is exactly what is observed in GY And), the magnetosphere of the star is significantly spherified, which sharply reduces the efficiency of the "propeller" braking mechanism. Another intriguing observed phenomenon is the huge change in the color index B–V during the period, which corresponds to a change in the effective temperature from 8350 K to 14 440 K (Metlova et al. 2014). Such a large change in temperature can only be explained by the presence of very large cold and hot spots (or groups of spots).

2 Observational data

The duration of photometric monitoring conducted at the Southern Station of the SAI (Crimea) has increased by 7.7 years. In addition, during this time, photometric observations obtained by Pyper & Adelman (2017) in the Stremgren system on the Four College Automated Photometric Telescope (FCAPT) at the Fairborn Observatory were published. We used their measurements in the Y filter (close in parameters to the Johnson V filter) after some reduction accordingly. This made it possible to refine the period. According to our estimates, it is $P = 7718 \pm 55$ days. The average photometric curve in the Johnson V filter is shown in Fig. 1a. Magnetic monitoring was continued at the 1-m SAO RAS telescope with the CEGS coude spectrometer and the circular polarization analyzer (CPA) (Bychkov 2008). As a result, the total duration of magnetic monitoring was almost 30 years. The coverage was 1.36 periods. Fig. 1b shows the average magnetic phase curve (MPC), obtained from estimates only at the 1-m SAO RAS telescope. As can be seen from Fig. 1b, the MPC is not strictly harmonic, which indicates a complex structure of the global magnetic field. Fig. 2 shows the MPC obtained from the surface magnetic field estimates, from the work by Giarrusso et al. (2022). This MPC, based on B_s estimates, also indicates a complex structure of the magnetic field of this star.

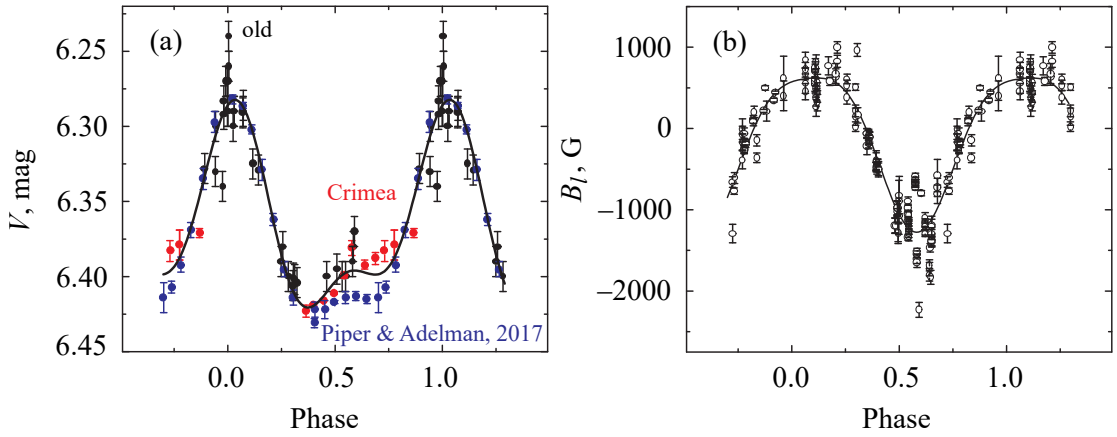

Fig. 1. Average photometric phase curve in Johnson V filter. Average magnetic phase curve obtained from B_l estimates, based on observations with the 1-m telescope of the SAO RAS.

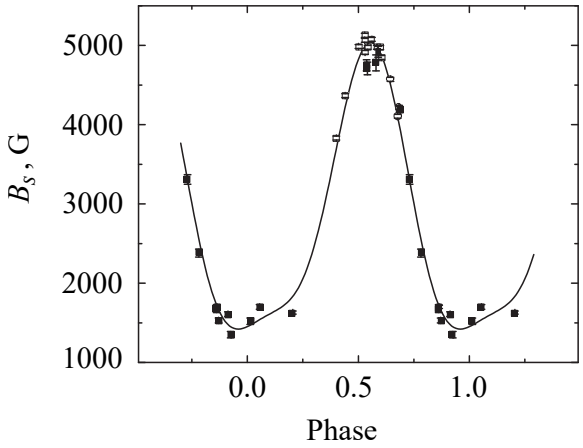

Fig. 2. Average magnetic phase curve obtained from the B_s estimates from paper by Giarrusso et al. (2022).

3 Discussion

A very interesting and still unsolved problem is very long periods observed in some mCP stars. At present, 23 magnetic stars are known, whose rotation period is more than 100 days. The mechanism of "magnetic" braking, considered by various authors for such stars, is quite probable. But the action of such a mechanism is possible only in the case of a purely dipole structure of the global magnetic field. As can be seen from observations, GY And has a complex magnetic field structure. But in this case, the magnetosphere of the star is significantly spherified. This sharply reduces the efficiency of the "propeller" mechanism. The efficiency of braking is sharply reduced due to the interaction with the interstellar medium. The large scatter of measured B_l values relative to the MCP can be explained by the presence of a shorter period of $P = 6.346258 \pm 0.000003$ days, detected by the photometry of the TESS space mission (Giarrusso et al. 2022). But this period should be confirmed undoubtedly by additional measurements. In addition, GY And is part of a wide binary system with a period of $P_{\rm orb} = 272.833 \pm 0.006$ days with a large eccentricity $e = 0.504 \pm 0.004$ (Griffin 2012). This can also affect the properties of the main component.

4 Summary

GY And is a unique ssrAp star that deserves more thorough photometric, magnetic and spectral monitoring. It stands out even against the background of other Ap stars due to its unique properties. The B–V color index change alone reaches a value of 0.3 over the period. This is approximately two orders of magnitude greater than that of other Ap stars. Such features make it necessary to study this object in more detail.

References

Abt H.A. and Morrell N.I., 1995, Astrophysical Journal Supplement, 99, p. 135

Bychkov V.D., Bychkova L.V., Madej J., 2016, Monthly Notices of the Royal Astronomical Society, 455, 3, p. 2567

Bychkov V.D., 2008, Astrophysical Bulletin, 63, 1, p. 83

Giarrusso M., Cecconi M., Cosentino R., et al., 2022, Monthly Notices of the Royal Astronomical Society, 514, 3, p. 3485

Glagolevskij Yu.V., 2021, Astrophysical Bulletin, 76, 1, p. 91

Griffin R.F., 2012, The Observatory, 132, 5, p. 309

Hubrig S., Järvinen S.P., Madej J., et al., 2018, Monthly Notices of the Royal Astronomical Society, 477, 3, p. 3791

Mathys G., 2017, Astronomy & Astrophysics, 601, id. A14

Metlova N.V., Bychkov V.D., Bychkova L.V., et al., 2014, Astrophysical Bulletin, 69, 3, p. 315

Pyper D.M. and Adelman S.J., 2017, Publications of the Astronomical Society of the Pacific, 129, p. 104203

MODERN ASTRONOMY: FROM THE EARLY UNIVERSE TO EXOPLANETS AND BLACK HOLES

Hypervelocity and S-type stars as possible paired components of the parent binary star in the past

G. Dryomova[1], V. Dryomov[1], and A. Tutukov[2]

[1] Russian Federal Nuclear Centre, Vasiliev street 13, Snezhinsk, Chelyabinsk region, 466770 Russia, *G.N.Dryomova@mail.ru*, *V.V.Dryomov@vniitf.ru*
[2] Institute of Astronomy of Russian Academy of Sciences, Pyatnitskaya street 48, Moscow, 119017 Russia, *atutukov@inasan.ru*

Abstract. It is proposed to consider the problem of the evolutionary connectivity of central near-nuclear S-stars and Hypervelocity Stars (HVS) which might have belonged to a common parent binary star in the past, torn apart by the tidal field of a Super Massive Black Hole (SMBH). Observational data from two independent catalogs made by Gillessen et al., 2017 and by Brown et al., 2018 are used for quantitative estimates. The justification of duality of the stars in the past is based on the analysis of reconstructed trajectories of ejection of HVSs with the use of time-inverse integration method in the Galactic potential and checking the distance from the SMBH at the moment of ejection to argue the scenario by Hills. The dynamic stability of S-stars is also investigated due to the possibility of identifying the pairing of HVS and S-stars in the past. The chaotization timescale of stars in the S-cloud is evaluated to understand the limits of applicability of the criterion of the coplanarity of S-star and HVS orbits.

Keywords: hypervelocity stars; central S-stars; super massive black hole

DOI: 10.26119/VAK2024.052

1 Introduction

The components of binaries and multiple stars may experience breaks of gravitational bonds during their evolution. Among the various scenarios leading up to the break, the scenario by Hills (1988), considering the tidal destruction of a binary in the SMBH gravitational field, deserves attention. Its gravitational potential, millions of times greater than the stellar one, imprints "traces" in the kinematics of both components: abnormally high spatial velocities. One of the components gets released and becomes a HVS, and the other one, captured in an orbit around the SMBH, meets rapid orbital rotation, typical for S-stars. High velocities are quite acceptable as a result of the redistribution of angular momentum in the classical problem of three bodies.

In 1988, Hills was looking for indirect evidence in favor of the existence of SMBH, for example, the phenomenon of hypervelocity stars accidentally discovered in the early XXI century by Brown et al. (2005). This fascinating SMBH search story culminated in the 2020 when Andrea Ghez and Reinhard Genzel won the Nobel Prize for a long-term monitoring of S-stars (Eckart & Genzel, 1996; Schödel et al. 2003) and non-trivial analysis of their motion, indicating the presence of a SMBH.

Today S-stars and HVS are no longer hypothetical objects. They are systematized in the catalogs by Gillessen et al. (2017) and Brown et al. (2018), respectively. But the argumentation of their possible duality in the past has yet to be found.

In Dryomova et al. (2023) the cross-analysis of observational data from Gillessen et al. (2017); Brown et al. (2018) was used for reconstruction of populations of S-stars and HVS within the framework of the classical scenario by Hills (1988). From the balance of kinetic energy of an ejected component and gravitational binding energy of its companion remaining in SMBH field, the ejection velocity of a potential companion of a really observable S-star (Gillessen et al. 2017) was estimated. On the other hand, the large semi-axis of the orbit of the hypothetically captured companion of the actually observed HVS (Brown et al. 2018) was evaluated. Their model-reconstructed distributions obtained in Dryomova et al. (2023) are in good agreement with the observed ones and somehow confirm the plausibility of their origin from a once common binary star. This was encouraging and prompted us to research further.

2 Reconstruction of the ejection trajectory of the HVS

One of the indirect evidence of the origin of HVS and S-stars from a common parent binary could be the fact of the HVS "central ejection" This can be determined by the value of the pericenter from calculation of HVS trajectory "returned" to the SMBH. So we need to integrate backwards in time the HVS ejection based on its

current position and spatial velocity, as well as the Galaxy potential, the precise determination of which is a great challenge itself.

In the HVS catalog by Brown et al. (2018) for each star, the galactocentric distance $r_{\rm rf}$ and its right ascension α and declination δ are known. At first, (α, δ) were converted to spherical galactic (b, l) ones centered at the Sun's position:

$$\begin{aligned} b &= \arcsin(\sin\delta \cdot \sin\delta_{\rm NP} + \cos\delta \cdot \cos\delta_{\rm NP} \cdot \cos(\alpha - \alpha_{\rm NP})); \\ l &= l_{\rm Neq} - \Delta l; \\ \sin\Delta l &= \cos\delta \cdot \sin(\alpha - \alpha_{\rm NP})/\cos b; \\ \cos\Delta l &= (\cos\delta_{\rm NP} \cdot \sin\delta - \sin\delta_{\rm NP} \cdot \cos\delta \cdot \cos(\alpha - \alpha_{\rm NP}))/\cos b, \end{aligned} \tag{1}$$

and then converted to Cartesian galactocentric coordinates. The equatorial coordinates of the galactic pole (NP) for the epoch J2000, $\alpha_{\rm NP} = 192^\circ.767$ and $\delta_{\rm NP} = 27^\circ.13$, as well as the longitude of the northern equatorial pole $l_{\rm Neq} = 122^\circ.933$, are used here. R denotes the heliocentric distance of HVS in kpc, and R_0— distance from the galactic center to the Sun ∼8.32 kpc according to Gillessen et al. (2017).

Similarly, decomposition of the vector of the total spatial velocity of HVS into Cartesian components in the galactocentric coordinate system was performed, taking into account the movement of the Sun according to Schönrich et al. (2010). The components of the Sun's velocity ($U = +11.1$ km/s; $V = +245$ km/s; $W = +7.25$ km/s) correspond to the following orientation of the axes: **X** is directed from SMBH in the direction opposite to the direction of the Sun, **Y** increases along the way of the rotation of the disk of the Galaxy, **Z** is directed to the NP of the Galaxy. To calculate the total spatial velocity of HVS one needs information about the radial velocity $V_{\rm r}$ and proper motion components, μ_α and μ_δ, from Brown et al. (2018).

Integration was carried out using four-component Galactic potential from Kenyon et al. (2008), including the central field of point mass SMBH, a spherically symmetric bulge in the model by Hernquist (1990), an axisymmetric disk by Miyamoto & Nagai (1975), and dark matter halo in the model by Navarro et al. (1997):

$$\Phi_{\rm Galaxy}(r) = -\frac{G \cdot M_{\rm SMBH}}{r} - \frac{G \cdot M_{\rm bulge}}{r + a} - \frac{G \cdot M_{\rm disk}}{r_{\rm d} - \frac{G \cdot M_{\rm galo}}{r} \cdot \ln\left(1 + \frac{r}{r_{\rm s}}\right)} \tag{2}$$

Here a— bulge radius, $r_{\rm d=\sqrt{R_{xy}^2+(b+\sqrt{c^2+z^2})^2}}$, R and z — radius and thickness of the disk, b and c — the characteristic scales of the disc length and thickness, respectively, $r_{\rm s}$ — normalizing multiplier of the order of the characteristic scale of the halo. A set of parameters from Fragione et al. (2017) was used in the calculations: $a = 0.1$ kpc, $b = 2.75$ kpc, $c = 0.3$ kpc, $M_{\rm SMBH} = 4.28 \cdot 10^6\ M_\odot$, $M_{\rm bulge} = 3.76 \cdot 10^9\ M_\odot$,

$M_{\rm disk} = 5.36 \cdot 10^{10}\ M_\odot$, $r_{\rm s=}$ 20 kpc, $M_{\rm halo} = 10^{12}\ M_\odot$. For integration we used the velocity formulation of the numerical algorithm by Verlet & Weis (1972), which is an explicit numerical scheme of the second order of accuracy with the conservation of all motion integrals (Tutukov et al. 2007). The integration step is calculated as a millionth of the ratio of the spatial velocity HVS to the instant acceleration in the Galactic potential.

Analysis of the "returned" trajectories reconstructed for 21 Galaxy-unbound HVSs from the catalog by Brown et al. (2018) showed that the ejected HVS-tracks are rather far away from the SMBH, as can be seen from their pericentric distances $r_{\rm app}$ in Fig. 1. Several stars appear to be in relative proximity to the SMBH: the Koposov's star HVS-S5 ($r_{\rm app} = 1.66$ kpc), HVS15 ($r_{\rm app} = 1.4$ kpc); HVS54 ($r_{\rm app} = 5.7$ kpc), HVS6 ($r_{\rm app} = 5.5$ kpc), and HVS3 ($r_{\rm app} = 8.9$ kpc). It should be mentioned that there

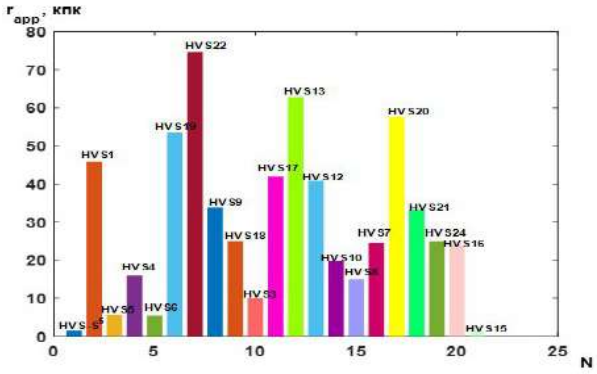

Fig. 1. Pericentric distances $r_{\rm app}$ of reconstructed tracks for HVSs from Brown et al. (2018).

is a problem of large uncertainties Δ_{μ_α} and Δ_{μ_δ} in the measurement of proper motion, often comparable to or even greater than the obtained values. For this reason four additional calculations of the returned trajectories were performed for each of the 21 HVSs $(\mu_\alpha^+, \mu_\delta)$; $(\mu_\alpha^-, \mu_\delta)$; $(\mu_\alpha, \mu_\delta^+)$; $(\mu_\alpha, \mu_\delta^-)$, where $\mu_\alpha^+ = \mu_\alpha + \Delta_{\mu_\alpha}$, $\mu_\alpha^- = \mu_\alpha - \Delta_{\mu_\alpha}$, $\mu_\delta^+ = \mu_\delta + \Delta_{\mu_\delta}$, $\mu_\delta^- = \mu_\delta - \Delta_{\mu_\delta}$. This allowed us to estimate the "error ellipses" with semi-major axes $\mu_\alpha^+ - \mu_\alpha^-$ and $\mu_\delta^+ - \mu_\delta^-$. As it can be seen from Fig. 2 the central trajectories of the ejection are possible for 8 HVS.

3 Dynamic stability of the S-cloud

Another indirect evidence of gravitational binding of the S-HVS pair in the past could be the coplanarity of theirs orbits. A star ejected at 1000 km/s, without collisions

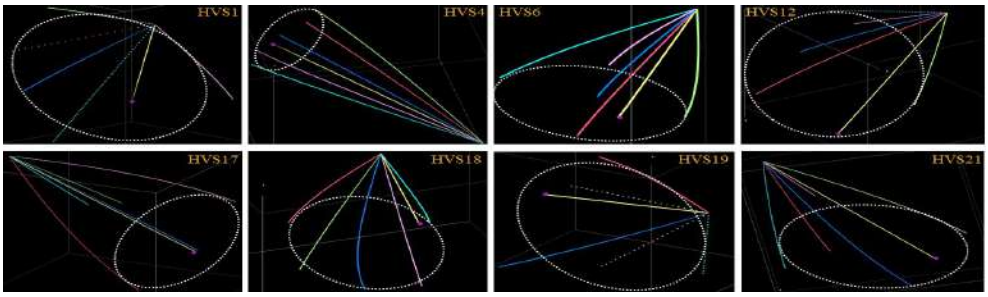

Fig. 2. "Error ellipses" for 8 HVSs from Brown et al. (2018). The purple dot is SMBH. Blue shows the ejection trajectory according to μ_α, μ_δ. Yellow is a possible central ejection trajectory.

or tidal approaches, reaches the neighborhood of the halo in $\sim 10^8$ yrs. During this time, does the original orbital configuration of the captured star in the vicinity of the SMBH, surrounded by a cloud of other previously captured stars, remain the same? The motion of each star in the S-cloud, which is controlled by the SMBH, is perturbed at least by all stars in the cloud. So, what is the time scale this perturbation swings the orbits of the stars?

To estimate the time of chaotization, a model S-cloud of 25 S-stars was "prepared" by Gillessen et al. (2017), which are no farther away from the SMBH than $1''$. In the course of a direct numerical integration in the formulation of the N-body problem (N=26), we tracked the orbital evolution of the S-cloud in the Newtonian potential of SMBH with orbital monitoring of S2 as the most well-studied star due to its short orbital period (∼16 years). As can be seen from the Fig. 3, conservation of the initial spatial configuration of the orbit of S2 is possible on the interval of ∼1,000 revolutions ($\sim 10^4$ years). After that, the change in the spatial configuration of the orbit S2 becomes noticeable. These results are consistent with the conclusion from Beckers et al. (2024), who obtained an estimate of the Lyapunov time of the order of 420 years. Obviously, the condition of coplanarity of S and HVS orbits cannot serve as a reliable criterion for establishing their possible evolutionary relationship in the past.

4 Conclusion

According to the results of numerical simulations, the central ejection can be considered as a reliable criterion for the potential evolutionary relationship between S-stars and HVS in the past. Within the uncertainties of the orbital parameters of HVSs (Brown et al. 2018), it was shown that 9 out of 20 unbound with Galaxy HVSs could be the binary components of S-stars in the past. "Error ellipse" of these stars admits

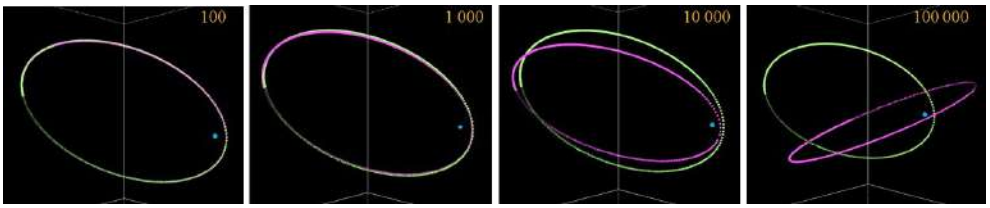

Fig. 3. The positions of the orbit of S2 at the initial moment of time (green color) and at moments after 100, 1,000, 10,000 and 100,000 (from left to right) orbital periods (purple color).

central ejection trajectories. From the bound energy balance, there is quantitative agreement between the velocities of the considered HVSs from Brown et al. (2018) and the gravitation energies of the observed S-stars (Gillessen et al. 2017) in the SMBH field. The perturbing potential of the S-cloud effectively chaoticizes the orbits of stars with a timescale of 10^4 years, changing their spatial configurations. Does this mean that, in principle, it is impossible to establish an evolutionary relationship of the S-HVS pair? In order to determine the further search and identification strategy of S-HVS pairs, we need the knowledge of their chemical composition, metallicity, luminosity, and temperature, on the basis of which we could estimate the age as a criterion of the evolutionary synchronism. The reconstructed chronology of the population of S-stars in the vicinity of the SMBH could provide a constraint on the distance limit of paired to them HVSs.

References

Beckers S., Poppelaars C., Ulibarrena V., et al., 2024, Astron. Astrophys., 685, p. 12
Brown W., Geller M., Kenyon S., et al., 2005, Astrophys. J., 622, p. L33
Brown W., Lattanzi M., Kenyon S., and Geller M., 2018, Astrophys. J., 866, p. 39
Dryomova G., Dryomov V., and Tutukov A., 2023, Astron. Rep., 67, p. 894
Eckart A. and Genzel R., 1996, Nature, 383, p. 415
Fragione G., Capuzzo-Dolcetta R., and Kroupa P., 2017, MNRAS, 467, p. 451
Gillessen S., Plewa P., Eisenhauer F., et al., 2017, Astrophys. J., 837, p. 30
Hernquist L., 1990, Astrophys. J., 356, p. 359
Hills J., 1988, Nature, 331, p. 687
Kenyon S., Bromley B., Geller M., et al., 2008, Astrophys. J., 680, p. 312
Miyamoto M. and Nagai R., 1975, Publ. Astron. Soc. Japan, 27, p. 533
Navarro J., Frenk C., White S., 1997, Astrophys. J., 490, p. 493
Schödel R., Ott T., Genzel R., et al., 2003, Astrophys. J., 596, p. 1015
Schönrich R., Binney J., and Dehnen W., 2010, MNRAS, 403, p. 1829
Tutukov A., Dryomova G., and Dryomov V., 2007, Astron. Rep., 51, p. 435
Verlet L. and Weis J., 1972, Phys. Rev. A, 5, p. 939

MODERN ASTRONOMY: FROM THE EARLY UNIVERSE TO EXOPLANETS AND BLACK HOLES

The mass function of young spectroscopic binaries and stars with protoplanetary disks

O. Eretnova[1], D. Tarasova[1], and G. Dryomova[2]

[1] Chelyabinsk State University, 129 Br. Kashirinykh, Chelyabinsk, 454001 Russia
eretnova@csu.ru
[2] Russian Federal Nuclear Centre, 13 Vasiliev, Snezhinsk, 466770 Russia
G.N.Dryomova@mail.ru

Abstract. The observational data on 58 pre-main sequence (PMS) double-lined spectroscopic binaries (SB2) and 115 stars with protoplanetary disks are compiled for statistical investigation. These stars are located in different star-forming regions. The constructed distributions of young stars by component masses, taking into account the effects of observational selection (discovery probability and/or occupied volume), are approximated with a power law $dN \sim M^{-\Gamma} d\log M$. The slopes are determined on the interval from the maximum of the distributions to the largest mass value and are equal to $\Gamma = 0.92 \pm 0.23$ for the components of SB2 systems and $\Gamma = 1.51 \pm 0.30$ for the stars with disks, respectively, which are close to the Salpeter's mass function. The most probable values of the mass are $M_p = 0.48 \pm 0.02\, M_\odot$ for stars with protoplanetary disks and $M_p = 0.95 \pm 0.05\, M_\odot$ for SB2 components.

Keywords: stars: pre-main sequence, binaries: spectroscopic, mass function; methods: statistical

DOI: 10.26119/VAK2024.053

1 Introduction

The initial mass function (IMF) for main-sequence stars has been investigated by many authors, starting with the pioneer works of E. Salpeter (Lee et al. 2020). Over the last years, the spatial resolution of astronomical instruments have been improved, which made it possible to discover young binaries and stars with disks in star-forming regions. These objects are at the stage of contraction to the IMS and are an intermediate evolutionary link between molecular cloud cores and IMS-stars. This is why the study of the mass distribution of young stars is of considerable interest.

2 Sample of young stars

We used observations on 58 young SB2 systems and 115 stars with protoplanetary disks. The masses of 36 SB2 are reliably determined from observations and are given by Dudorov & Eretnova (2021); Eretnova (2023). Among them 31 systems are eclipsing variables and five are visual binaries. We have added the eclipsing SB2 TIC 43152097 to them (Frasca et al. 2023). The masses of the remaining components are obtained by interpolation between the evolutionary tracks by Baraffi et al. (2015) for stars with 0.1–1.4 $M_\odot$ and by Dotter et al. (2008) for stars with 1.5–5.0 $M_\odot$. The masses of 34 stars with disks are determined from the Keplerian orbit of gas in the disks (Guilloteau et al. 2014; Simon et al. 2019), while other masses are calculated from the tracks obtained by Ginski et al. (2024); Garufi et al. (2024); Valegård et al. (2024).

3 The discovery probability of SB2 system

The discovery probability of SB2 star ($p_{\rm SB2}$) can be divided into two factors. The first one (geometric probability p) is estimated as time fraction during which the duality of the components can be established by measuring the half-amplitudes of their radial velocities K_1 and K_2, i.e.

$$p = 1 - \frac{2}{\pi \arcsin\left(\Delta/K\right)},$$

where Δ is the separation threshold of spectral lines, $K = K_1 + K_2$ (Popov 1970). The second factor (p_K) is the occurrence frequency of SB2 with measured values of K_1 and K_2 among all possible SB2 variants. The relationship $K = 2\pi \sin i A/P$ allows us to run the translation algorithm of the differential probabilities

$$df_{jklm} = f_{M_1}\, dM_1\ f_q\, dq\ f_A\, dA\ f_i\, di,$$

calculated on the basis of known functions of distributions of close binaries by primary mass (M_1), mass ratio (q), semi-major axis (A), and orbital inclination (i), into a

K-matrix of probabilities. The j, k, l, m-indices "run" values of M_1, q, A, i, which would be convenient to divide into intervals to compute K^{jklm} for each parameter in the center of the interval. These values fill the K-matrix with elements, which will be in strict indexical correspondence with the df_{jklm}. Then the definition area of K is divided into n-intervals, inside which the number of elements K^{jklm} is summed up and at the same time the corresponding elements df_{jklm} are also summed by the same indices. Thus, the K-matrix gives the number of elements in the sum and the indices by which the elements of the differential probabilities df_{jklm} should be summed up. Then we construct the distribution $f(K)$, and thus determine p_K and $p_{\rm SB2} = p \times p_K$.

4 Results and discussion

Figure 1a, b show the histograms of the mass distribution of SB2 components and the stars with disks. Important effects of observational selection (OSE) are the discovery probability of SB2 and the space occupied by the stars. The V_i is calculated as a spherical layer with a thickness of 180 pc for stars at the distances $r < 90$ pc (Istomin 1978). As a result, we can estimate the "true" number of stars in a given interval of $\log M_i$ as $dN_0 = \sum 1/p^i_{\rm SB2}$. Then divided by the space volume, in which stars with the given masses are observed, one can evaluate the spatial density of SB2 stars, $dN_V = dN_0/V_i$ pc^3. We exclude three SB2 with $p_{\rm SB2} < 0.005$ and three stars located in NGC 2264 at $r \approx 700$ pc, since it may lead to noticeable distortions of the distribution. The majority of the stars in our sample are located at $r < 450$ pc. For young stars with disks, only the correction for the spatial is considered.

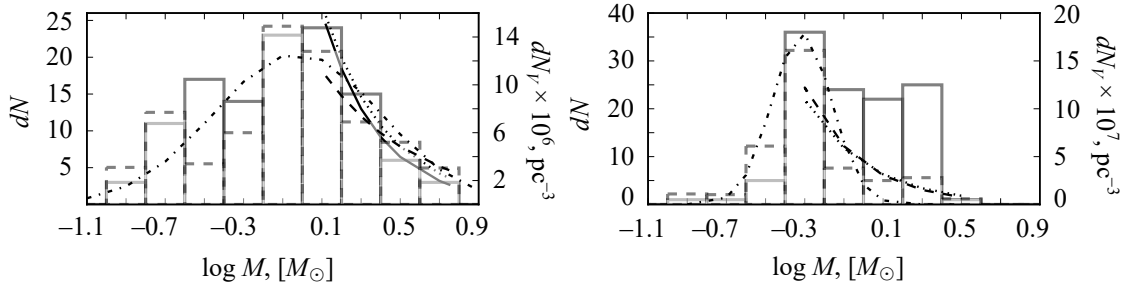

Fig. 1. The mass distributions of the components of young SB2 stars (a) and stars with disks (b). The observed and corrected for OSE histograms and their approximation with a power law are shown by a solid and dashed curves, respectively. A dash-dotted curve shows the approximation of OCE histograms with a lognormal law. A dotted curve shows the Salpeter IMF.

Figure 1 shows that the maximum in OSE-distribution for SB2 stars is slightly shifted towards lower masses compared to the observed distribution. We can identify

a secondary maximum, $\log M/M_\odot \in [-0.8; -0.6]$. For stars with disks, the maxima of both distributions coincide, but in the second case it is more pronounced. These stars are located in the Ophiuchus, Chamaeleon, Taurus, Orion star-forming regions. Orion is the most distant region and the stars in it have masses of $\log M/M_\odot > -0.2$.

The histograms are approximated with a power law $dN \sim M^{-\Gamma} d\log M$. The slopes are $\Gamma = 1.52 \pm 0.42$ for SB2 observed distribution, $\Gamma = 0.92 \pm 0.23$ and $\Gamma = 1.51 \pm 0.3$ for OSE-distributions of SB2 and stars with disks, respectively, constructed on the interval from the distributions maxima to the largest mass. It is close within the error to the Salpeter IMF, $\Gamma = 1.35$. Over the entire mass interval, the corrected for OSE histograms are approximated with a lognormal law:

$$F(\log M_i) = \frac{1}{\sigma\sqrt{2\pi}} \exp\left(-\frac{(\log M_i - \mu)^2}{2\sigma^2}\right).$$

The most probable masses are $M_p = 0.48 \pm 0.02\, M_\odot$ for the stars with disks and $M_p = 0.95 \pm 0.05\, M_\odot$ for SB2 systems. The mass function obtained for molecular cloud cores in Aquila, Cepheus, Perseus give $M_p = 0.4$–$0.6\, M_\odot$. Chabrier obtained $M_p = 0.25\, M_\odot$ from IMF analysis (Lee et al. 2020). PMS stars occupy an intermediate position between pre-stellar cores and IMS stars. The values of M_p are the same for young stars with disks and for molecular cloud cores, while for components of SB2 stars they are significantly larger. This is probably due to the difficulty in SB2 detecting with decreasing stellar mass, that is reflected in the sample incompleteness in the region of $M < 1\, M_\odot$.

Funding

The work of O. Eretnova is supported by the Russian Science Foundation project No. 24-22-20041.

References

Baraffe I., Homeier D., Allard G., et al., 2015, Astronomy & Astrophysics, 577, id. A42
Dotter A., Chaboyer B., Jevremovič D., et al., 2008, Astrophys. Journal Supplement, 178, 1, p. 89
Dudorov A.E. and Eretnova O.V., 2021, Chelyabinskiy Fiziko-Matematicheskiy Zhurnal, 6, p. 347
Eretnova O.V., 2023, Astronomy Reports, 67, 9, p. 902
Frasca A., Alonso-Santiago J., Catanzaro G., et al., 2023, Astronomy & Astrophysics, 677, id. A154
Garufi A., Ginski C., van Holstein R.G., et al., 2024, Astronomy & Astrophysics, 685, id. A53
Ginski C., Garufi A., Benisty M., et al., 2024, Astronomy & Astrophysics, 685, id. A52
Guilloteau S., Simon M., Piétu V., et al., 2014, Astronomy & Astrophysics, 567, id. A117
Istomin L.F., 1978, Zvezdnye skopleniya i dvojnye sistemy, p. 148
Lee Y.-N., Offner S.S.R., Hennebelle P., et al., 2020, Space Science Reviews, 216, 4, id. 70
Popov M.V., 1970, Peremennye zvezdy, 17, p. 209
Simon M., Guilloteau S., Besk T. L., et al., 2019, Astrophysical Journal, 884, 1, id. 42
Valegård P.-G., Ginski C., Derkink A., et al., 2024, Astronomy & Astrophysics, 685, id. A54

BAK 2024 MODERN ASTRONOMY: FROM THE EARLY UNIVERSE TO EXOPLANETS AND BLACK HOLES 300 years Russian Academy of Sciences

Modelling the spectral energy distributions of the accretion disks of young stars with fossil magnetic field

D. Frol[1] and S. Khaibrakhmanov[1,2,3]

[1] Ural Federal University, 19 Mira, Ekaterinburg, 620002 Russia
[2] Saint-Petersburg University, 7-9 Universitetskaya Emb., St. Petersburg, 199034 Russia
[3] Chelyabinsk State University, 129 Br. Kashirinykh, Chelyabinsk, 454001 Russia

Abstract. This work focuses on the study of the thermal structure and observational appearance of the accretion discs of young stars that possess fossil magnetic fields. We analyse the influence of magnetohydrodynamics (MHD) effects on the disc temperature and its spectral energy distribution (SED). The simulations indicate that, with low accretion rates of $\dot{M} < 10^{-8}\,M_{\odot}$/yr, Ohmic heating leads to an increase in the disc temperature by 100 K near the inner boundary. This effect causes an increase in the radiation flux of the disc in the mid-infrared range.

Keywords: ISM: magnetic fields; accretion; accretion disks; magnetohydrodynamics (MHD)

DOI: 10.26119/VAK2024.054

1 Introduction

Accretion discs around young stars are thin rotating structures of gas and dust with sizes of about 100 AU to 1000 AU and mass of $0.001\,M_\odot$ to $0.1\,M_\odot$. The rate of mass accretion onto the star decreases from $10^{-6}\,M_\odot$/yr to $10^{-9}\,M_\odot$/yr during the evolution of these discs. Over time, such accretion discs can turn into protoplanetary discs, where the conditions are favourable for the formation of planets.

Analysis of the observational data allows us to state that accretion discs and protoplanetary discs of young stars have a large-scale magnetic field that may be of a fossil nature (Khaibrakhmanov 2024). Modern models suggest that MHD may impact the structure of accretion and protoplanetary discs of young stars (Khaibrakhmanov & Dudorov 2022).

In the present work, we study the conditions under which Ohmic heating affects the thermal structure of the disc. In order to study the observational appearance of the disks with magnetic field, we calculate the spectral energy distributions (SEDs) of the disks.

2 Model

The MHD model of Khaibrakhmanov & Dudorov (2022) is used to calculate the disc structure. A stationary geometrically thin and optically thick disc in magnetostatic and centrifugal equilibrium is considered. According to the model of Shakura & Sunyaev (1973), the angular momentum is assumed to be transported via turbulence. The magnetic field is calculated taking into account Ohmic and ambipolar diffusion, magnetic buoyancy, and the Hall effect. The influence of Ohmic heating on the thermal structure of the disc is taken into account (Khaibrakhmanov & Dudorov 2019). The main parameters of the model include the turbulence parameter, α, which relates to the efficiency of turbulence in the angular momentum transport, and the accretion rate $\dot{M}$.

The SED calculations use the model developed by Bertout et al. (1988), which assumes that the star and the disc emit radiation as black bodies of specified sizes. In the calculations, the disc was considered to have inner and outer radii of $R_{\rm in} = 0.1$ AU and $R_{\rm out} = 100$ AU, respectively.

The study focused on a typical representative of T Tau type stars of spectral class K7, with the following parameters: $M_\star = 1\,M_\odot$, $R_\star = 2\,R_\odot$, $T_{\rm eff} = 4000$ K, and $L_\star = 2\,L_\odot$. The young stellar object is assumed to be located at a distance of 140 pc from the Earth, with the plane of the disc oriented perpendicular to the line of sight. The algorithm for calculating the SED based on the given disc structure is implemented as a software package in Python.

3 Results

To study the effect of Ohmic heating on the disk thermal structure, two series of numerical simulations were performed:

1) taking into account viscous heating, heating by stellar radiation and cosmic rays,
2) taking into account Ohmic heating additionally. The turbulence parameter α and the accretion rate $\dot{M}$ were varied during the modelling process.

The simulations showed that for standard values of $\alpha = 0.01$ and $\dot{M} = 10^{-8}\,M_{\odot}/\mathrm{yr}$, the MHD effects do not influence the disk structure. The MHD heating rate is significantly lower than the viscous heating rate, meaning that the dissipation of currents does not have a notable impact on the thermal structure of the disc.

In Fig. 1a, b, the radial profiles of the effective temperature of the disk are plotted, as well as corresponding SEDs, for runs with $\alpha = 0.0001$ and $\dot{M} = 10^{-8}\,M_{\odot}/\mathrm{yr}$. Fig. 1a illustrates that the temperature in second run decreases monotonically from 800 K to 20 K as the distance r increases. The comparison of the temperature profiles (Fig. 1a) shows that, for Ohmic heating (line 1), there is a local temperature increase of about 100 K in the inner regions of the disk within the region from 0.2 AU to 0.8 AU.

In Fig. 1b, we plot the SEDs of the star (grey line) and the disc (dashed and dotted lines). The black body SED of the star has a maximum at a wavelength of 10 μm. The SED of the disc for solution (2) shows two maxima at wavelengths of 100 μm and 2 mm, with the first peak representing the inner region of the disc and the second peak corresponding to its periphery. The increase in local temperature within the temperature profile has an effect on the SED, resulting in an increase in the emission flux from the disc associated with Ohmic heating (1). Fig. 1b shows the difference between lines 1 and 2 in the region from 20 μm to 1 mm.

Temperature profiles and SEDs for $\alpha = 0.01$ and $\dot{M} = 10^{-9}\,M_{\odot}/\mathrm{yr}$ are plotted in Fig. 1c, d. For a lower than standard accretion rate, a local temperature increase of 100 K is observed for the solution (3) in the regions from 0.1 AU to 0.2 AU. This temperature increase caused by Ohmic heating leads to an increase in the radiation flux of the disc in the region from about 20 μm to 1 mm.

4 Summary

It has been demonstrated that Ohmic heating affects the disc temperature and its spectral shape, especially with low turbulence parameters (less than $\alpha = 0.01$) and low accretion rates (less than $\dot{M} = 10^{-8}\,M_{\odot}/\mathrm{yr}$). The disks with a small accretion rate are usually at the final stages of their evolution. The study of SED objects with

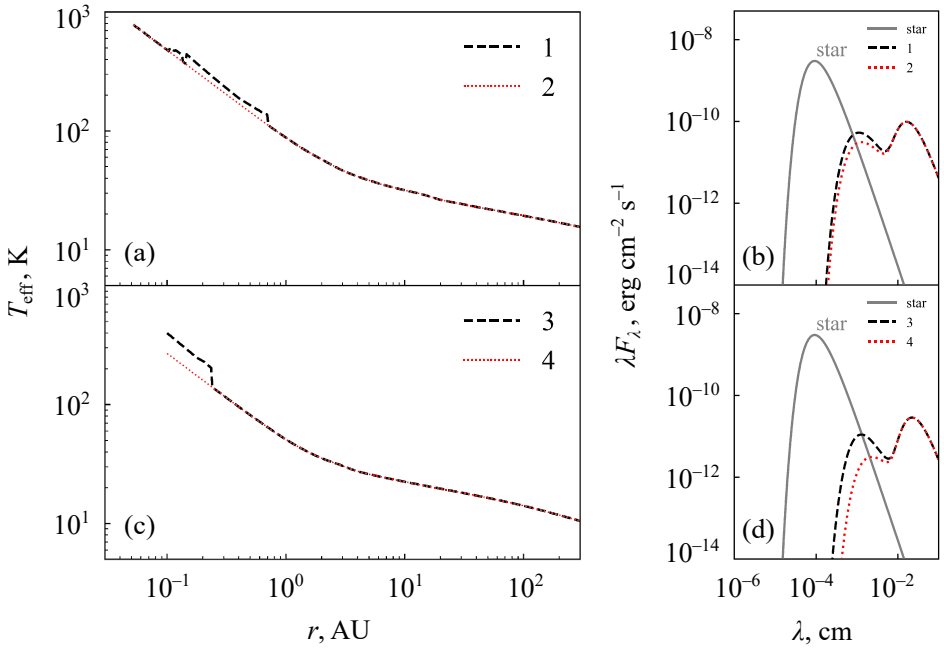

Fig. 1. Left panel: radial profile of the effective temperature of the disc, right panel: spectral energy distributions of the star and protoplanetary disc. The lines corresponding to the solutions considering Ohmic heating are labelled by numbers 1 and 3, without it by numbers 2 and 4. Upper panels: $\alpha = 0.0001$ and $\dot{M} = 10^{-8}\,M_\odot$/yr. Lower panels: $\alpha = 0.01$ and $\dot{M} = 10^{-9}\,M_\odot$/yr.

these characteristics can serve as an important tool to analyse the influence of MHD effects on their structure and evolution.

Funding

This work was financially supported by the Ministry of Education and Science of the Russian Federation (project No. FEUZ-2020-0038).

References

Bertout C., Basri G., Bouvier J., 1988, Astrophysical Journal, 330, p. 350
Khaibrakhmanov S. 2024, Astronomical and Astrophysical Transactions, 34, 2, p. 139
Khaibrakhmanov S. and Dudorov A., 2019, Magnetohydrodynamics, 55, 1/2, p. 65
Khaibrakhmanov S. and Dudorov A., 2022, Astronomy Reports, 66, 10, p. 872
Shakura N. and Sunyaev R. 1973, Astronomy & Astrophysics, 24, p. 337

MODERN ASTRONOMY: FROM THE EARLY UNIVERSE TO EXOPLANETS AND BLACK HOLES

Interstellar medium of Galaxy in the optical range

G. Galazutdinov[1,2]

[1] Crimean Astrophysical Observatory of the Russian Academy of Sciences, Nauchny, 298409 Russia
[2] Special Astrophysical Observatory of the Russian Academy of Sciences, Nizhny Arkhyz, 369167 Russia

Abstract. The paper briefly presents the results of spectral studies of interstellar medium in the wavelength range from near-ultraviolet to near IR. Particular attention is paid to the mysterious diffuse interstellar bands (DIBs), which have remained unidentified since 1922. The connection between different components of the interstellar medium and possible candidates for the carriers of diffuse bands are discussed.

Keywords: ISM: clouds; diffuse interstellar bands

DOI: 10.26119/VAK2024.055

1 Interstellar atoms/ions

More than 150 years have passed since it was proposed that interstellar medium, an absorbing medium of dust and gas (Struve 1847), fills the space between the stars. In the early 20th century Hartmann (1904) demonstrated the first observational evidence for absorption occurring in the interstellar medium, which manifested itself in the form of stationary absorptions (H and K lines of Ca II) observed in the spectra of the binary star δ Orionis.

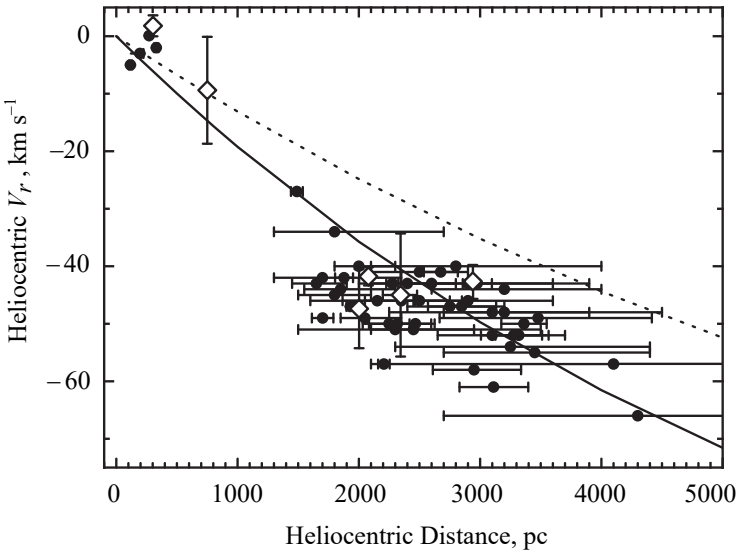

Fig. 1. Radial velocity curve for the direction $l = 135°$. "Flat" rotation (dotted line) and Keplerian (solid line) theoretical curves are shown. Filled circles represent our observed objects (Ca II clouds) and open diamonds represent literature data for open clusters. See Galazutdinov et al. (2015) for details.

Further studies have shown the complex structure of the interstellar medium, for example Beals (1936) discovered double and asymmetric components of the H and K lines visible in the spectra of stars in the constellation Orion. Spectral lines of ionized calcium (H and K) and neutral sodium (D_2 and D_1) are the strongest interstellar lines in the optical range, visible even in the spectra of stars with reddening close to zero. The list of interstellar atomic lines observed in the optical range is relatively short. In addition to the already mentioned strong lines with the wavelengths of 3933.663, 3968.468, 5889.951, 5895.924 Å respectively, one can also see strong lines of the neutral potassium doublet at 7664.994 Å and 7698.965 Å. How-

ever, the 7664.994 Å line is almost always blended with strong telluric lines and cannot be precisely measured. The remaining interstellar atomic lines visible in optical range are very weak even in a case of significant interstellar reddening. Most of them are in the near ultraviolet, but several lines are also observed in the visible range. There are, for example, the lines of Fe I λ3440.607, λ3719.935, λ3859.911; Ti II λ3073, λ3229.19, λ3241.983; in contrast to the D doublet, the ultraviolet sodium doublet 3302 Å is much less affected by the saturation effect; forbidden lines of neutral helium He I* λ3888.63 and λ10 830.3, observed only in the direction of very hot stars; a relatively strong line of neutral calcium 4226.728 Å, usually observed even with moderate interstellar reddening; very weak lines of interstellar lithium 6708 Å; finally, a weak line of interstellar rubidium Rb I λ7800.27. Due to the extremely low density and low temperature typical for H I clouds, interstellar absorptions in the optical spectra are very narrow, i.e. high resolving power is required to study their profiles—at least ($R > 80\,000$) is necessary. With higher spectral resolution and S/N ratio, an increasing number of components are observed in the spectral line profiles. For example, the profiles of interstellar lines of Na I, Ca II, K I, CH, CH+ demonstrate that even ultra-high $R \sim 900\,000$ may be insufficient to separate all individual profile components (Price et al. 2001).

One of most interesting results, based on the analysis of interstellar atomic absorptions, namely, lines of Ca II was obtained by Galazutdinov et al. (2015). Authors demonstrated that the rotation curve of the Galaxy is generally thought to be flat. However, using radial velocities from interstellar molecular clouds, which is common in rotation curve determination, seems to be incorrect and may lead to erroneous conclusion that the rotation curve is flat indeed (Galazutdinov et al. 2015). Tests based on photometric and spectral observations of bright stars may be misleading as well. The rotation tracers (OB stars) are affected by motions around local gravity centers and pulsation effects seen in such early type objects. To get rid of the latter a lot of observing work must be involved. We introduced a method of studying the kinematics of the thin disc of our Galaxy outside the solar orbit in a way that avoids these problems. We proposed a test based on observations of interstellar Ca II H and K lines that determines both radial velocities and distances. We implemented the test using stellar spectra of thin disk stars at galactic longitudes of 135° and 180°. Using this method, we constructed the rotation curve of the thin disk of the Galaxy. The test leads to the obvious conclusion that the rotation curve of the thin gaseous galactic disk, represented by the Ca II lines, is Keplerian outside the solar orbit rather than flat (Fig. 1).

2 Interstellar molecules

The first interstellar molecules (CH, CN, CH+) were discovered in the optical spectra of nearby stars (Dunham 1937; McKellar 1940; Adams 1941; Douglas & Herzberg 1941). Just 30 years later some more complex interstellar molecules were discovered (e.g., NH_3, Cheung et al. 1968). Currently, more than 310 molecules have been discovered in the interstellar and circumstellar medium of the Galaxy. Some 74 molecules have been discovered outside the Galaxy (including three unconfirmed candidates). Molecules are mainly discovered in the radio and submillimeter spectral regions at a rate of several "new" molecules per year. Only about ten simple molecules are observed in the visible part of the electromagnetic spectrum as absorption lines arising in translucent clouds. Among them are homonuclear molecules such as H_2, C_2, C_3, which are inaccessible to radio telescopes. In simple carbon chains (without radicals) there are no pure rotational transitions due to the absence of a permanent dipole moment. Electron-vibrational transitions of such molecules are observed in the wavelength range from the ultraviolet, accessible only for extra-atmospheric observations, to the far infrared range, i.e. they are accessible for observations by optical spectrographs. Determination of the abundance of simple carbon molecules in interstellar clouds is especially important, since they are considered to be the building blocks for many already known interstellar molecules with a carbon base. Douglas (1977) argued that carbon chains may be responsible for the formation of diffuse interstellar bands. Unfortunately, molecular lines observed in the optical range usually are very weak, necessitating high spectral resolution spectra with very high signal-to-noise ratio. Such spectra allows to detect extremely weak features of new molecules or never before observed bands of known molecules as it was done by us in Schmidt et al. (2014), Zhao et al. (2015a,b).

3 Diffuse interstellar bands

According to current knowledge, the composition of the interstellar absorbing matter is very complex: for example, molecules consisting of dozens of atoms have already been detected. Another, perhaps the most striking evidence of complex molecular synthesis/destruction processes occurring in the interstellar medium is the existence of diffuse interstellar bands (DIBs), the oldest unsolved problem in astronomical spectroscopy. DIBs were discovered in 1922 (Heger 1922), but their carriers remain unknown, (with perhaps one exception, see below) despite significant efforts by astronomers and progress in observational astronomy over the past 30 years. The list of discovered DIBs continues to grow, including increasingly weaker lines. The current list of DIBs includes more than 500 items(Galazutdinov et al. 2000, 2017; Fan et al.

2019). For reviews of the properties of DIBs, see, for example, Herbig (1995), Sarre (2006), Krełowski (2018).

The rest wavelengths of DIBs are the parameters of fundamental importance owing to the lack of unambiguous identification for these mysterious features. Recently (Galazutdinov & Babina 2024) we proposed the narrowest known diffuse interstellar band 6196 Å as the best reference for building the "interstellar" wavelength scale. Then, we estimated the magnitude of variation of the gravity center (the effective wavelength) of diffuse bands at 5780, 5797, 6284 Å and 7224 Å measured in 41 lines of sight in the range of interstellar reddening of 0.13–1.06 stellar magnitudes with the lack of evident Doppler-split in profiles of interstellar atomic/molecular lines. DIBs show gradual broadening of their profile widths, accompanied with red-shift of the gravity center, i.e. the red wing of the profiles is most variable part of the profiles. We offered to apply a parameter "effective width" $W_{\rm eff}$, which is a ratio of the equivalent width to the depth of the feature. In contrast to habitual full width at half maximum (FWHM) $W_{\rm eff}$ is not sensitive to the profile shape irregularities and can be measured in noisy spectra with higher precision than it is for FWHM. The gradual increase of $W_{\rm eff}$, accompanied with the red-shift of the gravity center of the profile, may suggest populating of higher transitions of P-branch of the bands of molecules, assuming the latter are DIB carriers. DIBs are broader but shallower in the harsh conditions of σ-clouds, where atomic and molecular lines are weak/absent.

References

Adams W.S., 1941, Astrophysical Journal, 93, p. 11

Beals C.S., 1936, Monthly Notices of the Royal Astronomical Society, 96, p. 661

Cheung A.C., Rank D.M., Townes C.H., et al., 1968, Physical Review Letters, 21, 25, p. 1701

Douglas A.E., Herzberg G., 1941, Astrophysical Journal, 94, p. 381

Douglas A.E., 1977, Nature, 269, 5624, p. 130

Dunham T., 1937, Publications of the Astronomical Society of the Pacific, 49, 287, p. 26

Fan H., Hobbs L.M., Dahlstrom J.A., et al., 2019, Astrophysical Journal, 878, 2, id. 151

Galazutdinov G.A., Musaev F.A., Krełowski J., et al., 2000, Publications of the Astronomical Society of the Pacific, 112, 771, p. 648

Galazutdinov G., Strobel A., Musaev F.A., et al., 2015, Publications of the Astronomical Society of the Pacific, 127, 948, p. 126

Galazutdinov G.A., Lee J.-J., Han I., et al., 2017, Monthly Notices of the Royal Astronomical Society, 467, 3, p. 3099

Galazutdinov G. and Babina E., 2024, Astrophysical Bulletin, 79, 3, p. 428

Hartmann J., 1904, Astrophysical Journal, 19, p. 268

Heger M.L., 1922, Lick Observatory Bulletin, 10, 337, p. 146

Herbig G.H., 1995, Annual Review of Astronomy and Astrophysics, 33, p. 19

Krełowski J., 2018, Publications of the Astronomical Society of the Pacific, 130, 989, p. 071001

McKellar A., 1940, Publications of the Astronomical Society of the Pacific, 52, 307, p. 187

Price R.J., Crawford I.A., Barlow M.J., et al., 2001, Monthly Notices of the Royal Astronomical Society, 328, 2, p. 555
Sarre P.J., 2006, Journal of Molecular Spectroscopy, 238, 1, p. 1
Schmidt M.R., Krełowski J., Galazutdinov G.A., et al., 2014, Monthly Notices of the Royal Astronomical Society, 441, 2, p. 1134
Struve F.G.W., 1847, St. Petersburg: Tip. Acad. Imper., IV, p. 164
Zhao D., Galazutdinov G.A., Linnartz H., et al., 2015a, Astrophysical Journal Letters, 805, 2, id. L12
Zhao D., Galazutdinov G.A., Linnartz H., et al., 2015b, Astronomy & Astrophysics, 579, id. L1

MODERN ASTRONOMY: FROM THE EARLY UNIVERSE TO EXOPLANETS AND BLACK HOLES

On the instabilities of small-scale oscillation modes on the background of a collapsing model of a Protogalaxy

J. Ganiev[1] and K. Mirtadjieva[2]

[1] National University of Uzbekistan, University 4, Tashkent, 100174 Uzbekistan
[2] Ulugh Beg Astronomical Institute of the Uzbek Academy of Sciences, Astronomicheskaya 33, Tashkent, 100052 Uzbekistan

Abstract. This paper examines the instabilities of horizontal small-scale perturbation modes in the context of a collapsing self-gravitating disk model. Instability calculations were performed for three modes of small-scale perturbations: (m=9, N=17); (m=16, N=18); and (m=15, N=21). Critical diagrams were constructed, and instability increments were calculated. Initial conditions for the formation of corresponding small-scale structural formations in the context of a collapsing self-gravitating disk model were found, depending on the value of the initial virial parameter, which characterizes the collapse rate.

Keywords: Galaxy: disk, evolution, kinematics and dynamics, structure; open clusters: general

DOI: 10.26119/VAK2024.056

1 Introduction

It is known that the collapse of a protogalaxy along its rotation axis occurs more strongly than in the perpendicular direction. Due to the gravitational instability of radial motions, gas clouds of protoglobular clusters easily form in a spherical protogalaxy. To study the evolutionary processes of various stellar systems, many authors have used their analog with a gas model for spherical systems with an adiabatic index of 5/3, and for disk-shaped systems with an index of 2. In the works of Antonov (1962); Binney & Tremaine (1987); Fridman & Khoperskov (2013), applications of the results from the gas medium to purely stellar systems were used. In works Nuritdinov et al. (2000); Nuritdinov & Tadjibaev (2014); Tadjibaev et al. (2015), this method was used in a reverse order, i.e., having theoretical results in the field of collisionless spherical stellar systems, they can be applied to gas systems to qualitatively study the corresponding dynamic processes. Thus, during the collapse of a spherical protogalaxy, specific small-scale perturbations can primarily form such structural formations as protoglobular star clusters. It is interesting to find out what might correspond to the instability of small-scale perturbations in a self-gravitating disk. In our opinion, the instability of small-scale perturbations in the disk subsystem can lead to the formation of gas and molecular clouds, and subsequently to the formation of a system of open star clusters (OSC).

2 System of open star clusters (OSC) in our galaxy

It is known that the flat subsystem of our Galaxy primarily contains the OSC system. In work Battinelli & Capuzzo-Dolcetta (1991), the authors investigated the structural characteristics of the OSC system in the vicinity of the Sun using the age distribution of clusters. Carraro & Chiosi (1994) studied the dependence of age on metallicity and also determined the relationship between the metallicity of the cluster and the position of the OSC. The observational properties of the Milky Way's OSC system were also discussed by Moitinho A. (2010) in terms of their influence on the structure of the spiral arms, dynamics, and chemical evolution of star-forming regions. Despite many available data on OSC, the questions regarding the origin of their system remain unresolved. Since the evolution of a collapsing protogalactic cloud occurs under the influence of gravitational instability, it is necessary to construct a radially non-stationary model for its analysis. Against this background, it is now necessary to calculate and analyze small-scale perturbations in collapsing disk-like systems, which has not yet been done by anyone. In this regard, we investigated the gravitational instability of three small-scale perturbations, the results of which can be used to study the problem of the formation of the OSC system in our Galaxy.

3 Calculation results

Previously, Nuritdinov (1993) constructed a non-stationary model of a collapsing disk and found its non-stationary dispersion equation (NDE) with wave numbers N and m. Using the NDE, large-scale modes were initially studied in detail, and a case was noted where the principal perturbation index N approaches infinity, corresponding to wave propagation in the collapsing system (Nuritdinov 1993; Nuritdinov et al. 2008; Mirtadjieva & Nuritdinov 2012). Subsequently, we investigated specific small-scale perturbations (Ganiev & Nuritdinov 2021, 2022).

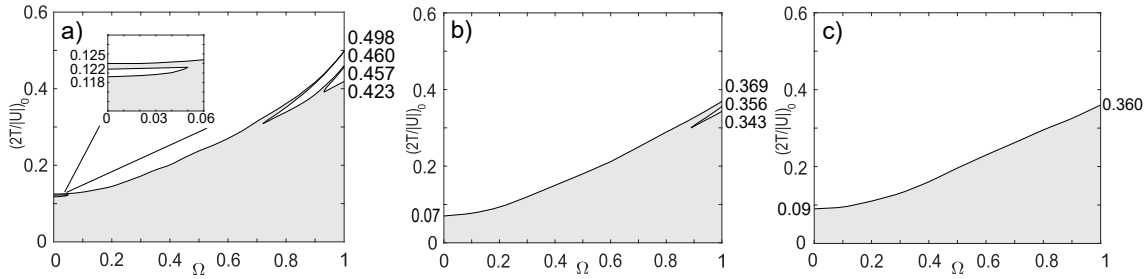

Fig. 1. Critical dependencies of the virial ratio on the rotation parameter for a) (m=9; N=17), b) (m=16; N=18), and c) (m=15; N=21) oscillation modes.

Below, we examine the instabilities of small-scale perturbations for modes (m=9; N=17); (m=16; N=18); and (m=15; N=21). Based on the results, critical dependencies of the initial virial ratio on the rotation parameter were constructed, and instability increments for the considered perturbations were computed. For these modes, corresponding dependencies of instability increments on the virial ratio at the initial collapse moment $(2T/|U|)_0$ were determined. It was found that the relevant instability region begins when $(2T/|U|)_0 \ll 1$. As can be seen, with the increase in the degree of small-scale perturbations, the instability region gradually narrows (Fig. 1). Here, it can be noted that at Ω=0 the critical initial values are $(2T/|U|)_0 \leq 0.118$, $(2T/|U|)_0 \leq 0.070$, $(2T/|U|)_0 \leq 0.090$, for the modes (m=9; N=17), (m=16; N=18) and (m=15; N=21) respectively. The results of calculations conducted in works Ganiev & Nuritdinov (2022, 2021) show that with the increase in the degree of small-scale perturbations, the stability regions in the critical diagrams also grow, while the initial condition values, on the contrary, decrease. However, in our case, regardless of the value of (N), the initial conditions for the mode (16; 18) are smaller than for the mode (15; 21). This may be related to the azimuthal wave

number (m), which significantly affects the results. Comparison of instability increments shows that the strongest mode is $(9; 17)$, and the weakest is $(16; 18)$. We expected that the increment of the mode with the highest main perturbation index (N) $(15; 21)$ would be the smallest for all values of the rotation parameter. However, we found that it is between the other two.

4 Summary

In this work, we considered three small-scale perturbation modes ((m=9; N=17), (m=16; N=18), and (m=15; N=21)) in the context of a collapsing self-gravitating disk model and conducted calculations of their gravitational instabilities. We found the initial conditions for these perturbation modes. Additionally, critical diagrams of the initial virial ratio versus the rotation parameter were constructed, and the increments of the instabilities were calculated. We observe that with the increase in the degree of small-scale perturbations, the stability regions in the critical diagrams also grow. It is noted that the initial conditions for the mode $(16; 18)$ have smaller values than for $(15; 21)$. Possible initial conditions for the formation of OSC systems in our Galaxy were found, depending on the initial virial parameter, which characterizes the collapse rate.

References

Antonov V., 1962, Vestnik Leningradskogo Universiteta

Battinelli P. and Capuzzo-Dolcetta R., 1991, MNRAS, 249, p. 76

Binney J. and Tremaine S., 1987, Galactic dynamics, Princeton University Press

Carraro G. and Chiosi C., 1994, Astronomy and Astrophysics, 287, p. 761

Fridman A. and Khoperskov A., 2013, Physics of Galactic Disks, Cambridge International Science Publishing

Ganiev J. and Nuritdinov S., 2021, Uzbek Physical Journal, 23, p. 1

Ganiev J. and Nuritdinov S., 2022, Open Astronomy, 31, p. 92

Mirtadjieva K. and Nuritdinov S., 2012, Astrophysics, 55, 551

Moitinho A., 2010, Proceedings of the International Astronomical Union., 266, p. 106

Nuritdinov S., 1993, Author's abstract of dissertation for thesis. doctoras degree nat. –mat. sciences., C - Petersburg

Nuritdinov S., Mirtadjieva K., and Sultana M., 2008, Astrophysics, 51, 410

Nuritdinov S., Orazimbetov J., and Tadjibaev I., 2000, Transactions of GAI MSU, p. 197

Nuritdinov S. and Tadjibaev I., 2014, Astrophysics, 57, p. 59

Tadjibaev I., Nuritdinov S., and Ganiev J., 2015, Astrophysics, 58, p. 181

MODERN ASTRONOMY: FROM THE EARLY UNIVERSE TO EXOPLANETS AND BLACK HOLES

Peculiarities of mass exchange between components of binary systems in the dynamic mode: V694 Mon and SS 433

V. Goranskij[1,2]

[1] Sternberg State Astronomical Institute of the Moscow University, 13 Universitetsky Pr., Moscow, Russia 119992

[2] Special Astrophysical Observatory of the Russian Academy of Sciences, Nizhny Arkhyz, 369167 Russia

Abstract. We observe events of dynamic mass transfer in the systems V694 Mon and SS 433. In V694 Mon, accretion occurs from an M5–M6 giant onto a white dwarf, while in SS 433 it occurs from an A4–A7 giant onto a neutron star. Both systems exhibit jets, with SS 433 having relativistic ones. In the symbiotic system V694 Mon, we observed the cessation of the disk accretion over three months in 2018. This was followed by the filling of the white dwarf's Roche lobe over the next three years, leading to the formation of an A4 I star within the Roche lobe by 2024, when hydrodynamic equilibrium was reached. The system is no longer considered symbiotic. In the SS 433 system, the Roche lobe of the neutron star is overfilled, resulting in the formation of a star with a neutron core and a convective envelope, known as a Thorne–Żytkow object. Rare powerful explosions occur accompanied by strong infrared radiation excesses. We interprete these explosions as ejections of the envelope of the neutron star or part of this envelope, these ejections are associated with magnetic activity of the neutron star, specifically a magnetar. Based on the wind speed from the system, we estimate the surface temperature of the newly formed star to be 1.5 million K. The star with the neutron core is the source of the power-law spectrum in optics. This object also causes the ellipsoidal effect in the light curves, and the nutation tidal wave that deflects the relativistic jets.

Keywords: stars: white dwarfs, neutron, binaries: general, mass transfer; individual: V694 Mon, SS 433

DOI: 10.26119/VAK2024.057

1 Introduction

Podsiadlowski (2014)[1] described events of dynamic mass transfer in binary systems. When the radius of the donor star's Roche lobe decreases as the mass is transferred from a more massive star to a less massive one, the donor star overfills its Roche lobe by an increasingly larger amount, leading to runaway mass transfer on a dynamic time scale. The transferred material forms a common envelope of the system. This typically occurs when the donor star is a giant or supergiant with a convective envelope, as such stars tend to expand rather than shrink when they lose mass rapidly, while the Roche-lobe radius shrinks when the mass is transferred from a more massive to a less massive star. These events can occur in binaries when the massive companion expands while evolving towards a red giant.

We have traced such an event in the symbiotic system V694 Mon (MWC 560) between 2018 and 2024. This system comprised an M4–M5 III giant pulsating with the period of 331–339 days and an accreting white dwarf (Gromadzki et al. 2007; Munari et al. 2016). In the spectra of V694 Mon, the absorption components appeared in Balmer lines at radial velocities up to −6500 km/s. This phenomenon was explained by collimated ejections of matter directed along the line of sight. The inclination of the orbital axis of this system is small. Photometric history shows light brightenings with a period of 1875–1930 days (Munari et al. 2016; Doroshenko et al. 1993). The same period was found in variations of the outflow velocities (Iijima 2002), suggesting that this periodicity is related to the precession of the accretion disk. Thus, T. Iijima characterized V694 Mon as an "SS 433 type object with a white dwarf". However, we observed a break in the disk accretion and the filling of the white dwarf's Roche lobe with the accreting matter, leading to the formation of an A4 I star in the white dwarf's lobe (Goranskij et al. 2018, 2021). The phenomena we observe in this event in V694 Mon prompted us to revise the current conception of the relativistic binary SS 433.

2 Observations

Medium-resolution spectroscopic observations of V694 Mon were conducted by us between January 2, 2011 and March 8, 2024, primarily using SAO 1-m Zeiss telescope and UAGS spectrograph. A few spectra were obtained with the 6-m BTA telescope equiped with the SCORPIO-1 and SCORPIO-2 multimode focal reducers (Afanasiev & Moiseev 2005). The spectral resolution ranged from 2.3 Å to 14.8 Å. We also obtained three high-resolution spectra of V694 Mon in 2019, 2022 and 2023 with the BTA and MSS spectrograph, with a resolution of 0.29 Å. In total, we have

[1] https://www-astro.physics.ox.ac.uk/~podsi/binaries.pdf

53 spectra. Additionaly, we collected photometric data, encompassing 4777 epochs including photographic B, photoelectric UBV, Straizys $WBVR$, and CCD Johnson and Cousins $UBVRI$. The earliest plates of V694 Mon, found in the SAI plate collection, were taken at the Moscow Observatory in 1899 and 1900, these plates were suitable for microphotometry and electronic reduction, revealing that the brightness of V694 Mon in the blue band of the spectrum increased by 100 times between 1899 and 2024. We also observed SS 433 using the instruments and devices of the Moscow University and SAO RAS observatories, in addition to collected published photometric data since its discovery in 1978. Moreover, we have results of 21 years of synoptic monitoring of SS 433 using a 25-cm reflector equipped with an electronic image tube with a microchannel plate.

3 V694 Mon = MWC 560

Our photometry and spectroscopy indicate that in 2018 significant changes occured in the star behaviour:

(1) the star ceased its flickering;

(2) the stellar brightness increased 500 days before the end of the 1930-day flare circle, these changes occurred during the conjunction of the star with the Sun;

(3) in the spectra, high-velocity absorption components in Balmer lines disappeared, suggesting the cessation of the accretion into the disk and disappearance of collimated jets.

Our spectroscopy since October 17, 2018 has traced in details the history of filling white dwarf's Roche lobe and formation of an A star photosphere there. From 2018 to 2020, Balmer and metal-line emissions with absorption components evolve with increasing intensities. In November 2021, we registered the absorption spectrum of an A star with unusually strong absorption lines, indicating the presence of an extensive atmosphere. Alongside the deep absorption spectrum, a weak emission-line spectrum appeared. This emission was confirmed by the high-resolution BTA/MSS spectrum taken on February 17, 2022. Notably, these emission lines were absent in the previous high-resolutuon spectrum taken on March 8, 2019.

We identified these emissions with the ions of Y, Zr, Nb, Ba, La, Ce and Nd, with cerium being particulary prevalent. These elements are associated with the s-process (neutron capture), which is believed to occur in AGB stars. Recently, Klochkova & Panchuk (2022) studied strong absorption lines of these elements in the photosphere of the cool post-AGB supergiant GSC 04050−02366. However these lines were not observed in any of the early phases of V694 Mon. This suggests that the donor star was a red giant or an AGB star. We interpret the appearance of such

a spectrum as a manifestation of the lower level of the discarded donor's envelope. We identify the newly formed companion as a A4 I star. With a known distance to V694 Mon $d = 2.36$ kpc ($\pi = 0.424 \pm 0.035$ mas, Gaia) and the recent photometric data $U = 8\overset{\mathrm{m}}{.}54$, $B = 8\overset{\mathrm{m}}{.}59$, $V = 8\overset{\mathrm{m}}{.}34$, $E(B–V) = 0\overset{\mathrm{m}}{.}17$, $A_V = 0\overset{\mathrm{m}}{.}52$, we calculated parameters of the star $M_{\mathrm{bol}} = -4\overset{\mathrm{m}}{.}02 \pm 0\overset{\mathrm{m}}{.}03$, $T_{\mathrm{eff}} = 8600$ K. The A star formed in the Roche lobe is now as luminous, as a post-main sequence A star with a mass of $6.5\,M_\odot$. Previously, the accretor was considered to be a white dwarf.

4 SS 433 = V1343 Aql

SS 433 is an eclipsing system with $P_{\mathrm{orb}} = 13\overset{\mathrm{d}}{.}082$ and moving emission components of H and He I lines due to precession of relativistic jets with the period $P_{\mathrm{prec}} = 162\overset{\mathrm{d}}{.}8$. The inclination of its orbital axis is $78\overset{\circ}{.}83$. The velocity of the ejected matter is $0.26\,c$. The jets also show nutation periodic variations with $P_{\mathrm{nut}} = 6\overset{\mathrm{d}}{.}28$ superimposed on the precession velocity curve. A weak stellar absorption lines in the spectrum of SS 433 were discovered by Hillwig & Gies (2008) and confirmed by subsequent studies. The contribution of this star in the common light in eclipse was 36% if measured in the precession phase T_3. Otherwise, the presence of the A star was called into question by Barnes et al. (2006). They found that the strength of these lines outside an eclipse in the phase "where the accretion disk is close to edge on" is equivalent to the donor contribution of 77%. So the "lines may originate in a clumpy, accretion driven outflow", not in an A star. Note, that the A4 I star we observe now in V694 Mon system is an accretor, while the A4 Iab star in SS 433 is a donor of accretion.

In accurate $UBVRI$ photometry, we deal with a strong Balmer jump, rather than weak absorption lines, confirming the presence of an A4 star in SS 433 system; however, we do not confirm the presence of any accretion disk. The example of V694 Mon suggests, that the strong absorption spectrum may be formed in an extensive envelope of an A star when it has acquired the envelope from the donor but has not yet reached the hydrodynamic equilibrium. Conversely, the A-type donor star with the envelope, overflowing beyond the bounds of its Roche lobe, can have an expanded low-density atmosphere, which was observed by Barnes et al. (2006). Therefore these lines belong to an A star, not to any outflow. The spectroscopic method of measuring the contribution of a star to the total light of a binary, based on the comparison of its spectrum with that of a normal star, may sometimes yield false results.

The predominant content in the SS 433 spectra is a power-low spectrum of a very hot source with a linear distribution of intensity versus wavelength diagram in the logarithmic scale. The maximum of this distribution is in the soft X-rays. $UBVRI$ photometry is useless to measure the temperature of this source. However, the temperature can be roughly estimated using the velocity of the stellar wind

from the source in the hydrogen line with the formula $mv^2/2 = kT$, where m is the mass of a proton, k is a Boltzmann constant. This yelds about 1.5 million K. The power-law spectrum distribution in optical range is close to the spectra of the hottest massive O-type stars. If we attempt to solve the light curve of SS 433 as a binary with an O-type donor in the precession phase -0.20 to $+0.20$, then we will obtain accurate but erroneous solution involving a black hole. Goranskij (2011) extracted the spectral distribution of the A star from common light of SS 433 in the mid-eclipse, and confirmed spectral result by Hillwig & Gies (2008) using Balmer jump of the A star. Its bolometric luminosity is between $-5\overset{\mathrm{m}}{.}9$ and $-5\overset{\mathrm{m}}{.}0$, and the mass ranges from $8.3\,M_\odot$ and $11.0\,M_\odot$. The contribution of its Balmer jump is also evident in the $(U–B)–B$ diagram. With a contribution so small as 36%, the donor cannot be responsible for the observed large ellipsoidal effect in the light curve. This effect is due to the filling or overfilling of the Roche lobe of the compact companion, along with the tidal effect on jets. The accretion disk is excluded because its axisymmetric structure cannot cause the ellipsoidal effect. The supercritical accretion disk is also ruled out.

Using mass ratio $q = 0.1496$ found by Brinkman et al. (1989) based on Ginga X-ray observations of eclipse in May 1987, we obtained the mass of the compact companion as $1.45 \pm 0.20\,M_\odot$. Considering that SS 433 is located at the center of the radio nebula W50, and is believed to be a 10 000 years old supernova remnant, the compact companion should be a neutron star. As noted by Brinkman et al. (1989), the Roshe lobe of the companion is totally eclipsed. The presence of the power spectrum in totality suggests that its Roshe lobe is overfilled. Our photometry shows a strong red and infrared excess over the power-low spectrum, indicating the presence of a massive circumstellar disk resulting from extensive mass exchange between components. Therefore, we observe a star with a neutron core in this system.

The properties of stars with the neutron core are predicted based on theoretical assumptions and model calculations in several investigations, with some predictions that their existence is impossible. Thorne & Żytkow (1977) describe them as M giants with a thin leyer (40 meters) around a compact core, called a halo (Thorne–Żytkow Objects, TŻO). In the halo, gravitational energy is released, and thermonuclear burning occurs in thin layers, with a convection zone extending from the outer edge of the halo up to the photosphere. These objects can originate only in binary systems when the neutron star acquires its envelope from a donor star and later merges with the core of the donor. In SS 433, we can observe and study a real TŻO within the system. In case of SS 433, the convection zone is limited by its Roche lobe, and there are indications of a magnetic field in the neutron star. In SS 433 we have observed three types of photospheric conditions.

1. The most frequent occurance is a wind photosphere above the Roche lobe with weak irregular variability in photometric bands.
2. Rare brightenings last for several orbits with increasing rapid variability of a few tenths of a magnitude, sometimes accompanied by the low-amplitude orbital light variations and even the disappearance of eclipses. We interpret this as a convection zone above the Roche lobe.
3. Large outbursts, characterized by strong IR excesses and the appearance of shoulders in Hα emission lines, are very rare. We attribute these outbursts to the energetic events of a young magnetic neutron star, or magnetar. These events involve the resetting of the envelope or part of it. We assume that the magnetar prevents merger of the neutron star with the donor's core, thereby forming the predicted M giant TŻO, and redirects matter into a circumstellar disk.

5 Summary

This investigation demonstrates that mass transfer in the dynamic mode ultimately results in cessation of accretion through a disk, either by filling or by overfilling the Roche lobe of the accretor, and in subsequent loss of matter into the circumstellar disk, rather than in the formation of a supercritical accretion disc around the accretor. This transfer can occur unexpectedly rapidly and may last only a few years.

Acknowledgements. E. A. Barsukova, A. N. Burenkov, I. M. Volkov, V. V. Komarov, O. A. Maslennikova, N. V. Metlova, S. Yu. Shugarov, O. I. Spiridonova, I. A. Yakunin, and A. V. Zharova participated in observations and data reduction. Author thanks them for support of this investigation.

References

Afanasiev V.L. and Moiseev A.V., 2005, Astronomy Lettes, 31, 3, p. 194
Barnes A.D., Casares J., Charles P.A., et al., 2006, Monthly Notices of the Royal Astronomical Society, 395, 1, p. 296
Brinkman W., Kawai N., Matsuoka M., 1989, Astronomy & Astrophysics, 218, p. L13
Doroshenko V.T., Goranskij V.P., Efimov Yu.S., 1993, Information Bulletin on Variable Stars, 3824
Goranskij V., 2011, Peremennye Zvezdy, 31, 5, p. 1
Goranskij V.P., Zharova A.V., Barsukova E.A., et al., 2018, Astronomer's Telegram, 12227
Goranskij V.P., Zharova A.V., Barsukova E.A., et al., 2021, Astronomer's Telegram, 15061
Gromadzki M., Mikołaewska J., Whitelock P.A., et al., 2007, Astronomy & Astrophysics, 463, 2, p. 703
Hillwig T.C. and Gies D.R., 2008, Astrophysical Journal Letters, 676, 1, p. L37
Iijima T., 2002, Astronomy & Astrophysics, 391, p. 617
Klochkova V.G. and Panchuk V.E., 2022, Astrophysical Bulletin, 77, 3, p. 292
Munari U., Dallaporta S., Castellani F., et al., 2016, New Astronomy, 49, p. 43
Podsiadlowski P., 2014, IAU Symposium, 296, p. 45
Thorne K.S. and Żytkow A.N., 1977, Astrophysical Journal, 212, 1, p. 832

Frequency analysis of Gamma Doradus variables observed by TESS

S. Grigoriev[1] and V. Dyachenko[2]

[1] Kazan Federal University, 18 Kremlyovskaya, Kazan, 420008 Russia
[2] Special Astrophysical Observatory of the Russian Academy of Sciences, Nizhny Arkhyz, 369167 Russia

Abstract. We present a frequency analysis of γ Dor variables based on the TESS photometric data: among 35 objects, period spacing patterns were found in five stars TIC 235680293, TIC 235682463, TIC 416401558, TIC 232620739 and TIC 406927322. We estimate their near-core rotation and make an assumption about the pulsation modes. Also three objects TIC 75784209, TIC 318837103, and TIC 309662501 show pulsations in p-modes and g-modes simultaneously, and we identify them as δ Sct–γ Dor.

Keywords: asteroseismology; stars: oscillations (including pulsations), rotation

DOI: 10.26119/VAK2024.058

1 Introduction

Asteroseismology is the field of astronomy that studies the internal structure of pulsating stars by analyzing their frequency spectrum. Measuring pulsation frequencies requires high-precision photometry, and the data must be continuous in time. The launch of space missions such as Convection Rotation and Planetary Transits (Auvergne et al. 2009), BRIght Target Explorer (Weiss et al. 2014), Kepler (Borucki et al. 2010) and Transiting Exoplanet Survey Satellite (Ricker et al. 2015) made a significant contribution to the development of asteroseismology.

Gamma Doradus variables (γ Dor) are stars that exhibit pulsations in gravitational modes (g-modes) or Rossby modes (r-modes). They are main sequence objects of late A or early F spectral class with the masses of $1.4 < M < 1.9\,M_\odot$ and the pulsation periods from 0.3 days to 4 days (Kaye et al. 1999); g-modes and r-modes are most sensitive to internal stellar structure, so studying γ Dor stars allows us to probe their near-core regions. An asteroseismological instrument such as the period spacing patterns (ΔP–P relation) allows us to identify pulsation modes and measure the near-core rotation rate.

2 Search for period spacing patterns

To search for period spacing patterns, 35 γ Dor stars observed by TESS telescope in more than 20 sectors were selected. This made it possible to achieve high frequency resolution, since the distance between the pulsation periods can reach $0.001\,\mathrm{d}^{-1}$.

The frequencies were determined using the `Period04` (Deeming 1975; Kurtz 1985), which implements two methods: the nonlinear least squares method and the discrete Fourier transform for inhomogeneous time series. As a result, period spacing patterns are observed in five objects: TIC 235680293, TIC 235682463, TIC 416401558, TIC 232620739 and TIC 406927322. All five objects were identified by Skarka et al. (2022) as γ Dor stars. The slope (Σ) of the ΔP–P is directly proportional to the near-core rotation rate. TIC 235680293, TIC 235682463 and TIC 416401558 demonstrate a downward trend (prograde modes; $m > 0$; e.g. Fig. 1) with $\Sigma = -0.048 \pm 0.002$; -0.0264 ± 0.0007 and -0.0368 ± 0.0006 respectively, while TIC 232620739 and TIC 406927322 demonstrate an upward trend (retrograde modes; $m < 0$; e.g., Fig. 2) with $\Sigma = 0.0657 \pm 0.0005$ and 0.067 ± 0.001 respectively. Using the empirical calibration from Li et al. (2019), we were able to estimate the near-core rotation rates and identify the pulsation modes (Table 1).

Also we found three objects TIC 75784209, TIC 318837103, and TIC 309662501, which have frequencies in the p-mode pulsation region ($P < 0.25$ days) as well—therefore we identified them as δ Sct–γ Dor hybrids. Such objects are of great interest

for asteroseismology, as they allow us to study both the inner and outer regions of the star.

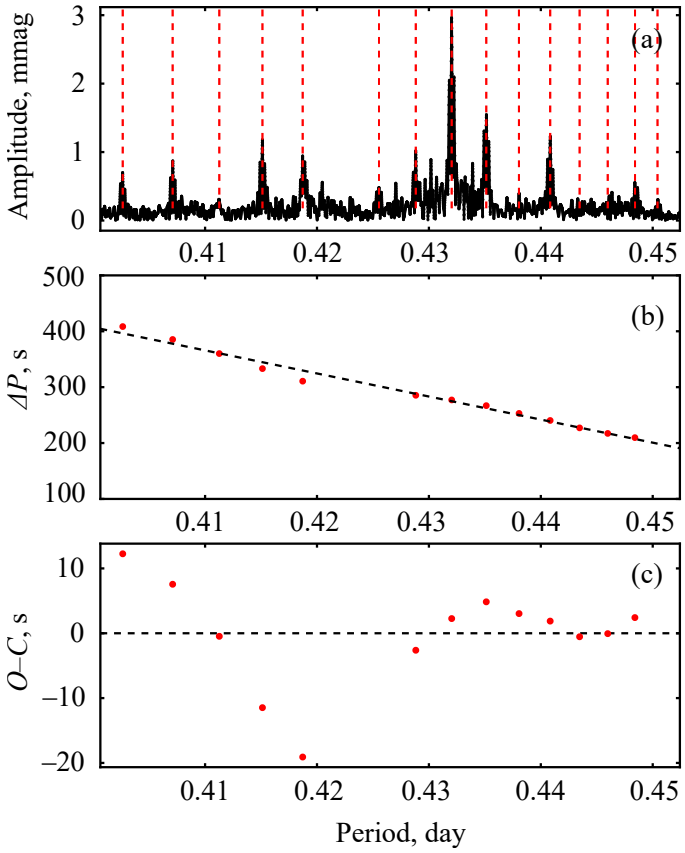

Fig. 1. The period spacing patterns of TIC 235680293. Panel (a): the amplitude spectrum (black line) and peaks with $S/N > 4$ (dashed lines). Panel (b): the period spacing patterns (red dots) and linear approximation with the slope $\Sigma = -0.048 \pm 0.002$ (dashed line). Panel (c): $O-C$ diagram.

3 Summary

Among 35 γ Dor stars with more than 20 TESS observation sectors, we found period spacing patterns in five objects: TIC 232620739, TIC 235680293, TIC 235682463, TIC 406927322, TIC 416401558, the period spacing patterns were found and their slope Σ, $\langle P \rangle$, $\langle \Delta P \rangle$ was determined—the values that allowed us to identify the pulsation modes and the near-core rotation rate (see Table 1), relying on the empirical cal-

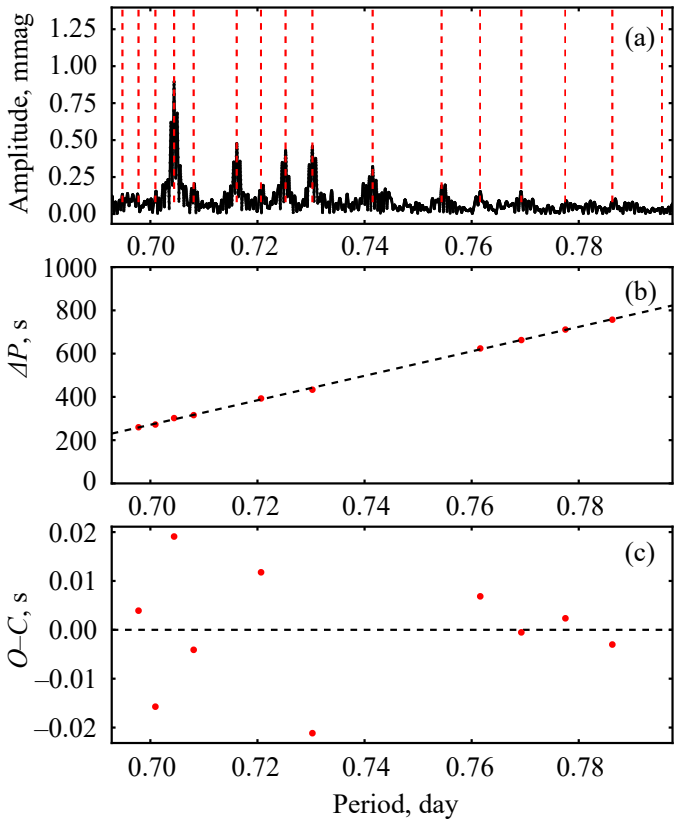

Fig. 2. Same as Fig. 1, but for TIC 232620739. The slope $\Sigma = -0.0657 \pm 0.0005$.

Table 1. The results of the period spacing patterns analysis for five objects. Σ represents the slope of ΔP–P relation; $\langle P \rangle$ is average period; $\langle \Delta P \rangle$ denotes the average period spacing; l is angular degree (only for g-modes); k for r-modes; m is azimuthal order; $f_{\rm rot}$ represents near-core rotation rate.

TIC number	Σ	$\langle P \rangle$ day	$\langle \Delta P \rangle$ s	l	k	m	$f_{\rm rot}$ day^{-1}
232620739	0.0657(5)	0.7	470		−2	−1	1.7
235680293	−0.048(2)	0.4	290	1		1	1.2
235682463	−0.0264(7)	0.8	890	1		1	0.5
406927322	0.067(1)	0.7	370		−2	−1	1.8
416401558	−0.0368(6)	0.5	260	1		1	0.9

ibration calculated by Li et al. (2019). Three objects TIC 75784209, TIC 309662501, TIC 318837103 exhibit pulsations in different modes: p-modes ($P < 0.25$ days) and g-modes. They are identified as δ Sct–γ Dor hybrids.

References

Auvergne M., Bodin P., Boisnard L., et al., 2009, Astronomy & Astrophysics, 506, 1, p. 411

Borucki W.J., Koch D., Basri G., et al., 2010, Science, 327, 5968, p. 977

Deeming T.J., 1975, Astrophysics and Space Science, 36, 1, p. 137

Kaye A.B., Handler G., Krisciunas K., et al., 1999, Publications of the Astronomical Society of the Pacific, 111, 761, p. 840

Kurtz D.W., 1985, Monthly Notices of the Royal Astronomical Society, 213, 4, p. 773

Li G., Van Reeth T., Bedding T.R., et al., 2019, Monthly Notices of the Royal Astronomical Society, 491, 3, p. 3586

Ricker G.R., Winn J.N., Vanderspek R., et al., 2015, Journal of Astronomical Telescopes, Instruments and Systems, 1, id. 014003

Skarka M., Žák J., Fedurco M., et al., 2022, Astronomy & Astrophysics, 2022, 666, id. A142

Weiss W.W., Rucinski S.M., Moffat A.F.J., et al., 2014, Publications of the Astronomical Society of the Pacific, 126, 940, p. 573

VAK 2024 MODERN ASTRONOMY: FROM THE EARLY UNIVERSE TO EXOPLANETS AND BLACK HOLES 300 years Russian Academy of Sciences

"Magnetospheric gate" in polars"

N. Ikhsanov[1,2], N. Beskrovnaya[1], V. Kim[1,3], and O. Korol'kova[1]

[1] Central Astronomical Observatory of the Russian Academy of Sciences at Pulkovo, 65 Pulkovskoye shosse, St. Petersburg, 196140 Russia
[2] Institute of Applied Astronomy of the Russian Academy of Sciences, 10 Kutuzov Emb., St. Petersburg, 191187 Russia
[3] Fesenkov Astrophysical Institute, 23 Observatory, Almaty, 050020 Kazakhstan

Abstract. The mass-exchange process in polars is discussed. We point out that the strong magnetic field of a white dwarf in these systems can under certain conditions prevent the material from flowing through the L1 point operating as a "magnetospheric gate". We show that the condition under which the "magnetospheric gate" is closed is satisfied in the majority of polars known to date. This finding opens the question about a possibility to realize an alternative mechanism of mass exchange in these systems. We briefly discuss application of this mechanism to the best studied polars.

Keywords: stars: cataclysmic variables, polars, magnetic fields; accretion; individual: AM Her, QQ Vul, AR UMa

DOI: 10.26119/VAK2024.059

1 Introduction

Polars are a subclass of magnetic cataclysmic variables. They are close binaries consisting of a magnetic White Dwarf (WD) and a Red Dwarf (RD) which fills its Roche lobe. The rotation of stars in most of these systems is synchronized with the orbital rotation. The radiation of the systems is contributed by a RD, a WD and a source associated with the matter transfer between the system components. The latter manifests itself in X-rays and/or the polarized optical emission and/or the emission lines (Cropper 1990).

The mass transfer in polars is realized according to a so-called channeled accretion scenario. This implies that the matter is streaming from the surface of the RD to the magnetic pole regions of the WD without forming a disk. The factor which prevents disk formation is the magnetic field of the WD. The magnetosphere of a WD under the conditions of interest can be extended up to the surface of a RD making a channel in which the matter flows between the system components (Schneider & Young 2021). Alternatively, if the pressure of the matter at the L1 point is dominating over the magnetic pressure due to the dipole magnetic field of the WD, a stream of matter through the L1 point can be realized (Mukai 1988). This possibility is explored in our paper. We find this condition not to be satisfied in the majority of polars. We suggest that the mass transfer is realized through a magnetic channel made by the process of coupling of the magnetic field of a RD and a WD.

2 Magnetospheric gate at the L1 point

We consider a binary system consisting of a WD and a RD which fills its Roche lobe. The question is under which conditions the matter can flow through the L1 point into the Roche lobe of a WD. A necessary condition reads

$$p_m(r_{\rm L1}) < p_0, \tag{1}$$

where $p_m(r_{\rm L1}) = \mu^2/\left(2\pi r_{\rm L1}^6\right)$ is the magnetic pressure (μ is the dipole magnetic moment of the WD) and p_0 is the pressure of the matter at the L1 point which is contributed mainly by the gas pressure $p_{g0} = \rho_0 c_{s0}^2$ (since the free-fall velocity at the L1 point is equal to zero by definition). Here ρ_0 and c_{s0} are the density and the sound speed in the gas at the L1 point.

The distance from the center of the WD to the L1 point can be estimated as (Plavec & Kratochvil 1964) $r_{\rm L1} \simeq a\big[0.5 - 0.227\log q\big]$, where

$$a \simeq 3.53\times10^{10}\ {\rm cm}\left[M(1)\times(1+q)P_{\rm orb}^2(h)\right]^{1/3}$$

Table 1. Polars: main parameters and the critical period P_0 at which the "magnetospheric gate" at the L1 point is closed (for details see Ikhsanov et al. 2023 and references therein).

Object	Dist	$M_{\rm opt}$	$M_{\rm wd}$	$B_{\rm wd}$	$\dot{M}_{\rm acc}$	$P_{\rm obs}$	P_0
	pc	$M_\odot$	$M_\odot$	MG	$M_\odot$/yr	hr	hr
AM Her	88	0.26	0.78	14	$\leq 10^{-10}$	3.1	4.5
QQ Vul	215	0.35	0.58	20	$\leq 10^{-11}$	3.7	6.5
AR UMa	85	1.4	0.70	235	$\leq 10^{-12}$	1.9	45.5

is the system separation and $q = M(2)/M(1)$ is the mass ratio. Here $M(1)$ and $M(2)$ are the masses of a WD and a RD, respectively, in solar masses, and $P_{\rm orb}(h)$ is the orbital period in hours.

The gas density at the L1 point can be estimated as $\rho_{\rm L1} = \dot{M}/Ac_s$, where $\dot{M}$ is the mass transfer rate, $A = \pi\sigma^2$ and σ is the effective radius of the accretion flow streaming through the L1 point. Combining the above expressions and solving the inequality with respect to $P_{\rm orb}$ one finds $P_{\rm orb} \geq P_0$, where

$$P_0 \simeq 2.2\,{\rm hr} \times \mu_{34}^{1/2}\,\sigma_9^{1/2}\dot{M}_{15}^{-1/4}\,c_6^{-1/4} \times \left[\frac{1}{[0.5 - 0.227\log q][(1+q)M(1)]^{1/3}}\right]^{3/2}. \quad (2)$$

Here $\mu_{34} = \mu \times 10^{-34}\,{\rm G\,cm^3}$, $\sigma_9 = \sigma \times 10^{-9}\,{\rm cm}$, $\dot{M}_{15} = \dot{M} \times 10^{-15}\,{\rm g/s}$ and $c_6 = c_s \times 10^{-6}\,{\rm cm/s}$.

Substituting the values $q = 0.35$, $M(1) = 0.8\,M_\odot$, corresponding to the parameters of the most fully studied polar AM Hercules, into the expression eq. (2), we find

$$P_0(q = 0.35, M(1) = 0.8\,M_\odot) \simeq 4.5\,{\rm hr} \times \mu_{34}^{1/2}\,\sigma_9^{1/2}\dot{M}_{15}^{-1/4}\,c_6^{-1/4}. \quad (3)$$

3 Discussion

The orbital periods of the systems identified with polars are clustered mainly in a range between 1 hour to 5 hours (Norton et al. 2004). In light of this, our result indicates that "magnetospheric gate" at the L1 point is closed in the majority of polars (see Table 1 and Fig. 1).

In the systems where "magnetospheric gate" at the L1 point is closed, mass exchange between the system components can occur through a magnetic channel formed by reconnection between the magnetic fields of a WD and a RD. If the condition of eq. (2) is not met, the magnetic channel will be strong enough to withstand the gas flow from the surface of the RD at a rate observed in the polars characterized by the highest luminosity. At the same time, the characteristic time of stability

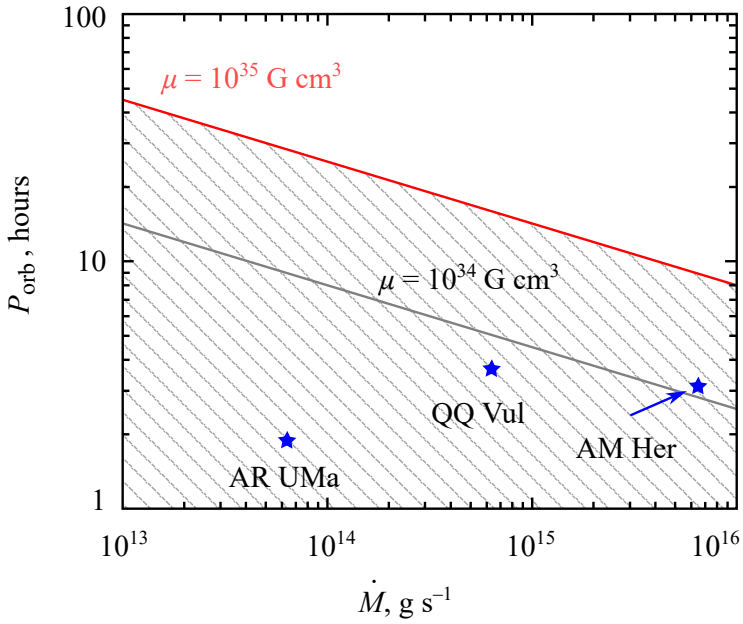

Fig. 1. Critical value of the orbital period, P_0, versus the mass accretion rate, calculated for two values of the WD dipole magnetic moment, $\mu = 10^{34}$ G cm^3 (black) and $\mu = 10^{35}$ G cm^3 (red). The shading shows the range of $P_{\rm orb}$ for which the "magnetospheric gate" at the L1 point is closed.

of such a channel will be determined by the time of reconnection of the field lines, which implies a possibility of a fairly strong variability in the rate of mass exchange between the components. Finally, the mass exchange scenario in which the matter flows along the filed lines, connecting the surfaces of a WD and a RD, allows us to avoid a very complicated question about the mode by which the stream of matter enters the WD magnetosphere (for a discussion see e.g. Ikhsanov & Pustil'nik 1996, and references therein). This question remains open in the scenario of mass-transfer through the L1 point.

References

Cropper M., 1990, Space Science Review, 54, p. 195
Ikhsanov N., Kim V., Korol'kova O., 2023, Publications of the Pulkovo Observatory, 228, p. 118
Ikhsanov N.R. and Pustil'nik L.A., 1996, Astronomy & Astrophysics, 312, p. 338
Mukai K., 1988, Monthly Notices of the Royal Astronomical Society, 232, p. 175
Norton A.J., Wynn G.A., Somerscales R.V., 2004, Astrophysical Journal, 614, 1, p. 349
Plavec M. and Kratochvil P., 1964, Bulletin of the Astronomical Institutes of Czechoslovakia, 15, p. 165
Schneider D.P. and Young P., 1980, Astrophysical Journal, 240, p. 871

MODERN ASTRONOMY: FROM THE EARLY UNIVERSE TO EXOPLANETS AND BLACK HOLES

Stellar wind velocity of the massive component in the high mass X-ray binary OAO 1657−415

N. Ikhsanov[1,2], N. Beskrovnaya[1], and V. Kim[1,3]

[1] Central Astronomical Observatory of the Russian Academy of Sciences at Pulkovo, 65 Pulkovskoye shosse, St. Petersburg, 196140 Russia
[2] Institute of Applied Astronomy of the Russian Academy of Sciences, 10 Kutuzov Emb., St. Petersburg, 191187 Russia
[3] Fesenkov Astrophysical Institute, 23 Observatory, Almaty, 050020 Kazakhstan

Abstract. The parameters of the wind-fed accretion process in the massive X-ray binary OAO 1657−415 are discussed. We show that the X-ray luminosity of an accreting pulsar in this system can be explained only if the velocity of the stellar wind of the massive component in the orbital plane of the binary system is in the range of 200–500 km/s.

Keywords: stars: pulsars: general, winds, outflows; X-rays: binaries; accretion; individual: OAO 1657−415

DOI: 10.26119/VAK2024.060

1 Introduction

Delgado-Martí et al. (2001) showed that the stellar wind velocity of the massive star in the X-ray binary X Persei in the orbital plane does not exceed 150 km/s. Otherwise, the amount of material captured by the neutron star from the wind of its companion is insufficient to explain the observed X-ray luminosity of the system. Their estimate is almost an order of magnitude lower than a typical wind velocity of hot massive stars and is several times smaller than the wind velocity of a star derived from observations of spectral lines in the UV.

In this work, we follow the technique proposed by Delgado-Martí et al. (2001) to estimate the stellar wind velocity of a massive component in the X-ray binary OAO 1657−415.

2 Stellar wind velocity

OAO 1657−415 (hereafter OAO 1657) is a close massive X-ray binary system (see Table 1). It is one of the best studied bright eclipsing quasi-equilibrium accreting X-ray pulsars. The massive component of the system does not fill its Roche lobe and the mass-exchange between the system components operates in accordance with the wind-fed accretion scenario. This implies that the neutron star captures gas from the wind of its massive companion at a rate

$$\dot{\mathfrak{M}}_c = \frac{L_x R_{\rm ns}}{G M_{\rm ns}} = \pi r_G^2 \rho_w v_{\rm rel} = \frac{4\pi (G M_{\rm ns})^2 \rho_w}{v_{\rm rel}^3}, \quad (1)$$

where

$$r_{\rm G} = \frac{2 G M_{\rm ns}}{v_{\rm rel}^2}$$

is the radius of gravitational capture (the so-called Bondi radius) by the neutron star and ρ_w is the density of the stellar wind in the region of its interaction with the neutron star. The velocity of a neutron star relative to the wind in the interaction region is generally estimated by

$$v_{\rm rel} = \left(v_{\rm orb}^2 + v_w^2 + c_{s(w)}^2\right)^{1/2}, \quad (2)$$

where $v_{\rm orb}$ is the orbital velocity of the neutron star, $v_{\rm w}$ is the stellar wind velocity, and $c_{s(w)}$ is the sound speed in the stellar wind.

Under the conditions of interest, the sound speed in the eq. (2) can be neglected (assuming that the temperature of the stellar wind does not exceed several million

Table 1. Observed parameters of the pulsar OAO 1657-415 (for details see Ikhsanov et al. 2024 and references therein).

Sp opt.	$M_{\rm opt}$	$P_{\rm orb}$	a	$P_{\rm s}$	$L_{\rm x}$	d
	$M_\odot$	days	AU	sec	erg/s	kpc
Ofpe [a]	14.3±0.8	10.45	0.24	37.3	(1–20)×10^{36}	6.4±1.5

degrees). The minimum possible value of the relative velocity of a neutron star in this case is determined by the value of its orbital velocity, which, taking into account a small value of the orbit eccentricity and the inequality $M_{\rm ns} \ll M_2$ implemented in the system, can be approximated by the Keplerian velocity, i.e. $v_{\rm rel} \geq v_k^{\rm ns}(a)$, where

$$v_k^{\rm ns}(a) = \left(\frac{GM_2}{a}\right)^{1/2} \simeq 240 \text{ km/s} \left(\frac{M_2}{15\,M_\odot}\right)^{1/2} \left(\frac{a}{0.24\,\text{AU}}\right)^{-1/2}. \quad (3)$$

Here M_2 is the mass of the optical component of the system and a is the orbital separation (close to the radius of the neutron star's orbit). Substituting this velocity into eq. (1) and solving it with respect to ρ_w, we find $\rho_w \geq \rho_0$, where

$$\rho_0 = \frac{L_x R_{\rm ns}}{4\pi\,(GM_{\rm ns})^3} \left(\frac{GM_2}{a}\right)^{3/2} \simeq 10^{-16}\,\text{g cm}^{-3}\,L_{36} R_6 m^{-3} \left(\frac{M_2}{15\,M_\odot}\right)^{3/2} \left(\frac{a}{0.24\text{ AU}}\right)^{-3/2}, \quad (4)$$

where $L_{36} = L_x \times 10^{-36}$ erg/s, $R_6 = R_{\rm ns} \times 10^{-6}$ cm and $m = M_{\rm ns}/1.4\,M_\odot$.

Assuming, on the other hand, that the stellar wind velocity exceeds the orbital velocity of the neutron star within the approximation of a spherically symmetric outflow of stellar wind from a massive component of the system, we estimate, following the method proposed by Delgado-Martí et al. (2001), the X-ray luminosity of the pulsar as $L_x \leq L_0$, where

$$L_0 = \frac{\dot{\mathfrak{M}}_{\rm out}(GM_{\rm ns})^3}{a^2 R_{\rm ns} v_w^4}. \quad (5)$$

Here $\dot{\mathfrak{M}}_{\rm out}$ is the rate of mass loss by the optical component of the system in the form of stellar wind. Solving this equation for v_w, we find $v_w \leq v_{\rm max}$, where

$$v_{\rm max} \simeq 440 \text{ km/s} \times m^{3/4} R_6^{-1/4} L_{36}^{-1/4} \left(\frac{a}{0.24\text{ AU}}\right)^{-1/2} \left(\frac{\dot{\mathfrak{M}}_{\rm out}}{10^{-7}\,M_\odot/\text{ year}}\right)^{1/4}. \quad (6)$$

The X-ray luminosity of the source in this equation is normalized to the value obtained under the assumption that the object we are studying is located at a distance of the order of 6 kpc. Using an estimate of the minimum possible distance to

the source $d \geq 2.5$ kpc, based on Gaia observations (Saavedra et al. 2022), it can be argued that the stellar wind velocity in the orbital plane of the system does not exceed 700 km/s.

3 Conclusions

Our analysis of the wind-fed accretion process in the massive X-ray binary system OAO 1657−415 indicates that the neutron star velocity relative to the stellar wind of its massive companion in this system can be limited as $v_k^{\rm ns}(a) \leq v_{\rm rel} \leq v_{\rm max}$. The lower and upper limits here are determined, respectively, by the eq. (3), (6). The lower limit to the relative velocity is fixed relatively well. The estimate of the upper limit is model dependent. It has been obtained under the assumption about a spherically symmetric outflow of the wind from the massive component of the system with a velocity significantly exceeding the orbital velocity of the neutron star. The estimate of this velocity, in addition, depends on the distance to the object, which is still a subject of debate. At the same time, the value we obtained, represented by the eq. (6), can be further used to analyze the structure of the accretion flow and the accretion pattern as a whole.

References

Delgado-Martí H., Levine A.M., Pfahl E., et al., 2001, Astrophysical Journal, 546, 1, p. 455

Ikhsanov N.R., Kim V.Yu., Beskrovnaya N.G., 2024, Publications of the Pulkovo Observatory, 233, p. 34

Saavedra E.A., Fogantini F.A., Combi J.A., et al., 2022, Astronomy & Astrophysics, 659, id. A48

MODERN ASTRONOMY: FROM THE EARLY UNIVERSE TO EXOPLANETS AND BLACK HOLES

Spectral and photometrical peculiarities of the unusual Herbig Ae star HD 179218

N. Ismailov[1], M. Pogodin[2], A. Kholtygin[3], H. Adigozalzade[1], U. Bashirova[1], O. Kozlova[4], and A. Ivanova[3]

[1] Shamakha Astrophysical Observatory, Shamakha, AZ-5626 Azerbaijan
ismailovnshao@gmail.com,
[2] Central Astronomical Observatory of the Russian Academy of Sciences at Pulkovo, 65 Pulkovskoye Shosse, St. Petersburg, 196140 Russia
[3] Saint-Petersburg University, 7-9 University Emb., St. Petersburg, 199034 Russia
[4] Crimean astrophysical observatory of the Russian Academy of Sciences, Nauchny, 298409 Russia

Abstract. We present the results of the spectroscopic monitoring of the Herbig Ae star HD 179218 carried out at the Shamakha Astronomical Observatory from 2015 to 2021 and the $UBVRI$ photometry at the Crimean Astronomical Observatory, covering the period 2007–2021. This object has a unique orientation of its rotation axis close to "pole-on". The Hβ line profiles are a single emission profile overlapped by blue and red absorption features living about several days. The 17 dates of 77 the Hβ and the He I λ5876 line profiles demonstrated the inverse P Cyg-type profile with the variable velocity of the red edge of the absorption component up to 400 km/s. The period of the variations $P = 1.341 \pm 0.002$ days determined by Lafler–Kinman method is in accordance with the expected rotation period of the star. This observational fact can be a signature of the magnetospheric character of accretion in HD 179218. The inclination angle of the rotation axis is estimated as $i = 23° \pm 3°$. The observed phenomena can be connected with a specificity of stellar magnetism of HD 179218. Additionally, it has been shown that equivalent widths of the Hα and Hβ lines as well as the photometric $UBVRI$ parameters of HD 179218 demonstrate cyclic variability with several periods falling in the range from 19 days to 737 days. A possible interpretation of these phenomena can be a result of presence near HD 179218 of a low-mass binary component or exoplanets. A sudden drop of circumstellar extinction took place in October of 2011, possible interpretations of this phenomenon are considered.

Keywords: stars: variables: Herbig Ae/Be, circumstellar matter; accretion; individual: HD 179218

DOI: 10.26119/VAK2024.061

1 Introduction

Herbig Ae/Be stars are conventionally regarded as pre-main sequence (PMS) objects of intermediate mass (2–10 $M_{\odot}$) (Herbig 1960; Finkenzeller & Mundt 1984; The et al. 1994). They are surrounded by circumstellar (CS) envelopes containing the equatorial accretion disk and a matter outflow (wind) zone at higher latitudes. The Herbig Ae star HD 179218 demonstrates a "pole-on" orientation relative to the line of sight. According to Leinert et al. (2004) its inclination angle i is near 20°. We present here the results of our investigation of this object.

2 Observations

We carried out spectroscopic monitoring of HD 179218 from 2015 to 2021 with echelle-spectrometer installed at the 2-m telescope of the Shamakha Astrophysical Observatory of the Azerbaijan National Academy of Sciences. In total, 86 spectra have been obtained. Additionally, we used in our investigation the results of $UBVRI$ photometry of the object, performed at the Crimean Astrophysical Observatory of the Russian Academy of Sciences between 2007 and 2021 (76 observing dates).

3 Short-term spectral variability

We used temporal behavior of the Hβ profile in spectra of HD 179218 to investigate structural and kinematic properties of its CS gas in the region near the line of sight between the star and the observer. This object demonstrates a wide variety of Hβ profile types observed on different dates: simple single emission profiles, the P Cyg-type and the inverse P Cyg-type profiles, and, at last, multi-component emission profiles with blue as well as red absorption features as it is seen in Fig. 1. Among profiles with the inverse P Cyg-feature, the velocity of the red boundary of the absorption component varied from 235 km/s to 390 km/s on different dates (17 dates). On these dates profiles of another emission line He I λ7876 also demonstrate the inverse P Cyg-type structure with the velocity of the red edge of the absorption component from 50 km/s to 450 km/s. Using the Lafler & Kinman (1965) method we have found the period of the line profile variability for both lines Hβ and He I λ5876. The corresponding periodograms are presented in Fig. 2.

The mean value of the revealed period and its error is $P = 1.341 \pm 0.002$ days with the use of four independent estimations (P and doubled P for both lines seen in periodograms). This value is in correspondence with the expected rotation period of HD 179218. This result can be estimated as a signature of magnetospheric accretion in HD 178218. The values of the rotation period allows us to estimate the inclination

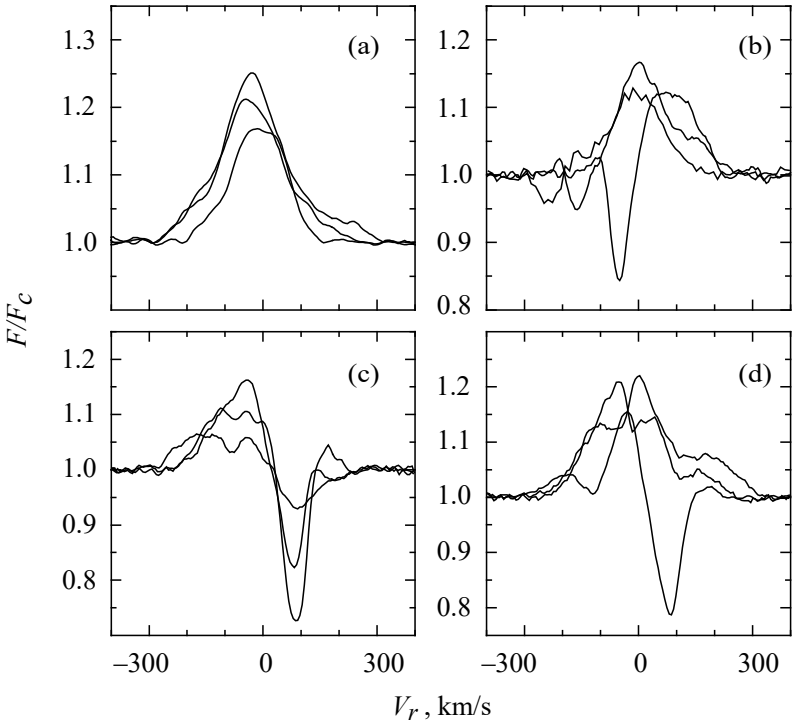

Fig. 1. Normalized to the continuum level Hβ line profiles observed at different dates in the spectrum of HD 179218 after subtracting the stellar atmospheric component: single emission profiles (a); P Cyg-type profiles (b); inverse P Cyg-type profiles (c); multi-component profiles (d).

angle of the rotation axis $i = 23^\circ \pm 3^\circ$, which is in a good accordance with Leinert et al. (2004).

Besides the periodic variations of the Hβ line profile, some other types of variability were registered in the spectra of HD 179218. The most commonly occurring one is an appearance of the local blue or red local absorption features overlapping a single emission profile with the lifetime of several days and stable velocity positions. Examples of such phenomenon are illustrated in Fig. 3. Such temporal behavior excludes rotational modulation of the line profiles as a result of eclipsing of the star by azimuthal CS inhomogeneities, since the rotation period of the star is only 1.34 days. We are forced to accept that at the present time we are unable to propose a single certain interpretation of this phenomenon. We assume that it can be connected with a specificity of stellar magnetism of HD 179218.

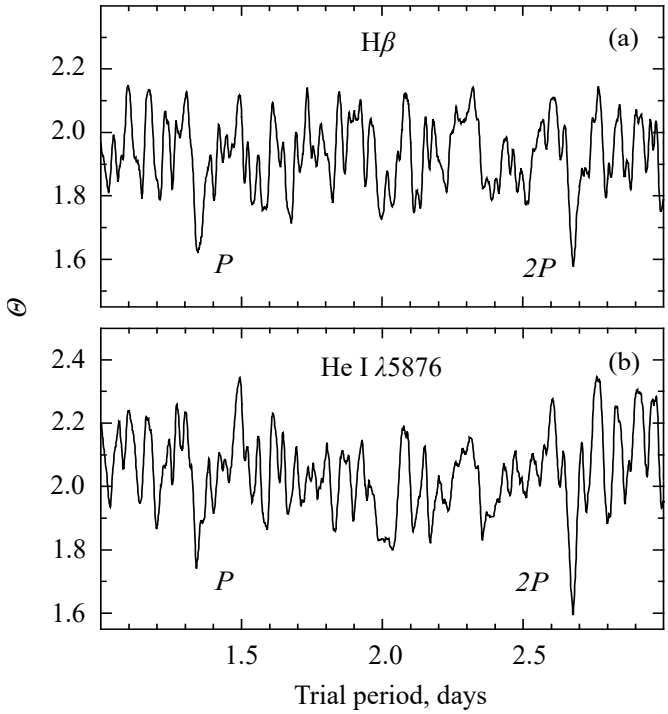

Fig. 2. The the Lafler–Kinman periodogram for $V_{\rm red}$ values for Hβ line (a) and He I λ5876 (b).

4 Long-term photometric variability

To analyze the variability we used photometric data obtained in five bands of the $UBVRI$ system in 2007–2021 at the AZT-11 telescope in Crimean Astrophysical Observatory with the 5-channel Piirola photometer-polarimeter. Besides the cyclic variability, a remarkable abrupt brightness jump was observed in October 2011 in all $UBVRI$ photometric bands. The maximum rise in brightness was in U-band, then its magnitude decreased from U to V. It became almost unnoticeable in the R band, and in the I band the brightness, on the contrary, suddenly decreased. The UVI light curves, illustrating this phenomenon, are shown in Fig. 4a. Dependencies between stellar magnitudes in the UVI bands on V are given in Fig. 4b. We assume that the phenomenon can be connected with a sudden disappearance of dust from the CS region between the star and the observer. This has to lead to a reduction of CS extinction and, consequently, to a rise of brightness in the visual spectral range. But such reduction of amount of CS dust, responsible for the near-IR excess, can result in a fall of the emission in the I band, where this excess starts to be observed.

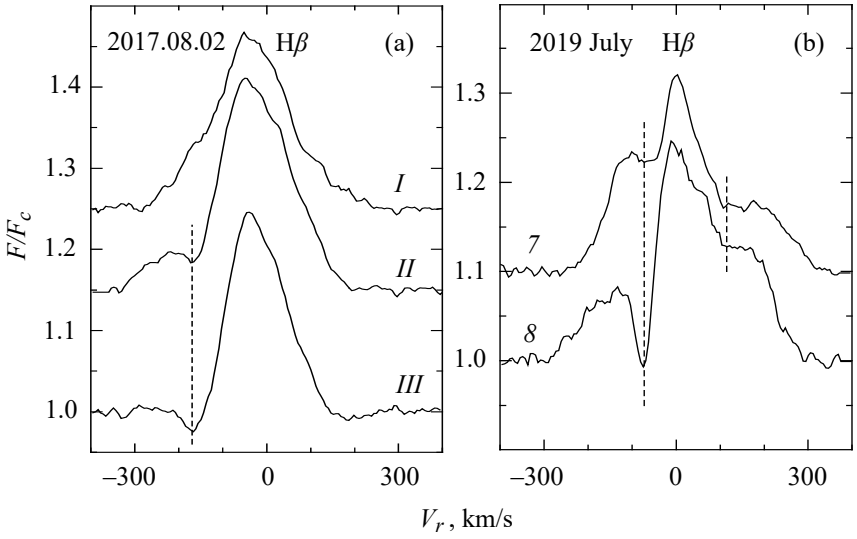

Fig. 3. Profiles of the Hβ line obtained on 29/30.07.2017 with the interval of time of 10 hours (I and II) and 02.08.2017 (III) (a). The vertical dashed line marks are not displaced during three days absorption feature. Profiles of the Hβ line obtained on July 7 and 8, 2019 (b). Two local absorption features at -75 km/s and $+115$ km/s are seen.

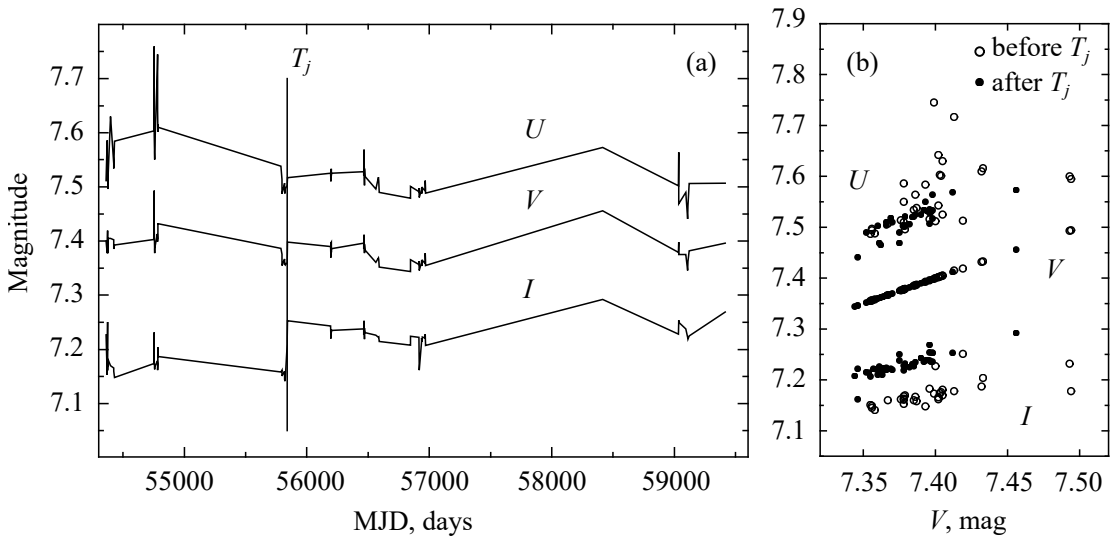

Fig. 4. Time dependencies of the stellar magnitudes of HD 179218 in the U, V, and I bands before and after the jump time T_j (a). Dependence U, V, and I magnitudes on V (b).

Also, we can speculate, that all active phenomena, observed in HD 179218 at the time scales of order of years can be connected with:

a) existence in the CS disk of dense local bodies (protoplanets), rotating at different distances from the star;
b) formation in the disk of azimuthally inhomogeneous (spiral-like) structures (Boccaletti et al. 2020);
c) presence of small-mass components of the main A0e object.

5 Conclusion

In the present paper we continue the study of a very rare subgroup of young Herbig Ae/Be stars: class A stars with an orientation of the rotation axis relative to the observer close to the pole. It is from this angle one can observe the circumpolar regions of the circumstellar envelope, where the gas has the least studied structure and kinematics.

A cyclic variability of the red boundary of the absorption component $V_{\rm red}$ of the Hβ and He I λ5876 line profiles with a period $P = 1.34$ days, corresponding to the expected rotation period of the star, was discovered. The maximum values of the parameter $V_{\rm red}$ reach 350–400 km/s, which is possible only with the magnetospheric nature of accretion. The angle of inclination of the stellar rotation axis to the line of sight is estimated to be $i = 23^\circ \pm 3^\circ$.

The analysis of the Hα and Hβ line profiles in the HD 179218 spectra and photometric data in the $UBVRI$ bands carried out in this work showed the presence of regular spectral and photometric variability with long periods. Such variability may be associated with changes in the accretion rate and precession of the accretion disk. Regular variability over long periods of time may indicate the presence of a distant satellite and, possibly, a distant exoplanet/exoplanets.

Analysis of the dependencies of the stellar brightness in the I band and the V–I color index on the magnitude in the V filter indicates an increase in the absorption of the stellar radiation in the I band in the period from September 20, 2011 to October 3, 2011. This increase in absorption continued through 2021.

References

Boccaletti A., Di Folco E., Pantin E., et al., 2020, Astronomy & Astrophysics, 637, id. L5
Finkenzeller U. and Mundt R., 1984, Astronomy and Astrophysics Supplement Series, 55, p. 109
Herbig G.H., 1960, Astrophysical Journal Supplement, 4, p. 337
Lafler J. and Kinman T.D., 1965, Astrophysical Journal Supplement, 11, p. 216
Leinert C., van Boekel R., Waters L.B.F.M., et al. 2004, Astronomy & Astrophysics, 423, p. 537
The P.S., de Winter D., Perez M.R., 1994, Astronomy and Astrophysics Supplement, 104, p. 315

MODERN ASTRONOMY: FROM THE EARLY UNIVERSE TO EXOPLANETS AND BLACK HOLES

Laboratory study of the IR spectra of methane ices in the polar environment

V. Karteyeva, R. Nakibov, M. Ozhiganov, M. Medvedev, and A. Vasyunin

Ural Federal University, 48 Kuibysheva, Ekaterinburg, 620026 Russia

Abstract. We grew the pure methane ice and mixed binary ices of methane with polar molecules: water, carbon dioxide, methanol and ammonia under ultrahigh vacuum cryogenic conditions similar to those in cold prestellar clouds. The composition of ices was chosen to reflect current astrochemical notions. The following interstellar ice analogues were obtained: $H_2O:CH_4 = 10:1$, $CO_2:CH_4 = 5:1$, $CH_3OH:CH_4 = 2:1$, $NH_3:CH_4 = 1:1$, that are new to the literature and infrared spectra ice analogues databases. We report the significance of deposition temperature for the internal structure of ices, which gets revealed on infrared spectra during the warm up for ices deposited at 6.7 K and 10 K. We link the observed differences to solid methane being in amorphous phase ($T < 9.3$ K) and low-temperature crystalline (9.3 K $< T <$ 20 K) phases. We also note that the direct comparison between laboratory and observational spectra is possible since the deformation mode line shape doesn't depend on the grain size or shape near 7.7 μm, only on the temperature and molecular environment. Solid methane is a fairly abundant molecule in prestellar objects. With the James Webb Space Telescope (JWST) launch the quality of spectra has risen significantly and we hope that this work will be an asset to assigning the methane component in star-forming regions.

Keywords: ISM: molecules, clouds, lines and bands; infrared: ISM; methods: laboratory: solid state; astrochemistry

DOI: 10.26119/VAK2024.062

1 Introduction

Dark cold clouds include matter in gaseous and solid phases. The solid phase includes silicate or carbon dust particles with a frozen component in the form of an ice mantle. The composition of the condensed phase on the surface of dust particles is considered to be partially determined. The main component of ice mantles is water, followed by carbon monoxide, carbon dioxide, methanol, ammonia, methane, etc (Boogert et al. 2015; McClure et al. 2023).

The object of our study is the deformation mode region of methane, which has an absorption band of 1300 cm^{-1} (7.7 μm) in the mid-IR range. For a qualitative description of this region, spectra of mixtures with methane were obtained for the first time at deposition temperatures below 10 K, which corresponds to the phase of amorphous methane. The importance of using the previously little-studied amorphous phase of methane to identify it on observational data is also demonstrated, since only the crystalline phases of methane and band strengths are currently used in the literature. We also found differences in the shape of methane bands in mixtures with water, carbon dioxide, methanol and ammonia.

2 Experiment

Experiments are performed using Ice Spectroscopy Experimental Aggregate (ISEAge). This installation is used to grow analogues of interstellar ice. In the main chamber, the Ge window mounted on a cryogenic holder can be cooled to a temperature as low as 6.7 K and the ultra-high vacuum (up to 2×10^{-10} mbar) is maintained. To check the purity of the studied substances and to control their quantitative content in the main chamber, the ISEAge setup is equipped with a quadrupole mass spectrometer SRS RGA 200. Transmittance IR spectra are acquired using the Thermo Scientific Nicolet iS50 FTIR spectrometer in the range between 4000 cm^{-1} and 630 cm^{-1} (2.5 μm and 15.9 μm) with 1 cm^{-1} resolution.

We obtained the reference laboratory spectra of methane in various polar molecular environments to describe the observational region near 7.7 μm. Methane was codeposited for 120 minutes with polar molecules: water, carbon dioxide, methanol and ammonia.

Methane has three phases: high-temperature (above 20 K), amorphous (below 10 K) and low-temperature (10–20 K) (Gerakines & Hudson 2015). Therefore, the mixtures were obtained at temperatures corresponding to the amorphous and low-temperature phases of methane, 6.7 K and 10 K respectively. The rate of methane deposition was 5.9×10^{12} $cm^{-2}\,s^{-1}$, which corresponds to a column density on the line of sight of 4.25×10^{16} cm^{-2} in all experiments. Methane was supplied from the same

leak valve across all experiments, that valve was opened first, then the valve with the second component, a polar molecule, was opened. As a result, two ice components were deposited together on the substrate. The obtained profiles of the absorption band of methane deformation mode in the case of pure matter and in mixtures are shown in Fig. 1. The obtained spectra are an average of 45 seconds (an average of 32 scans).

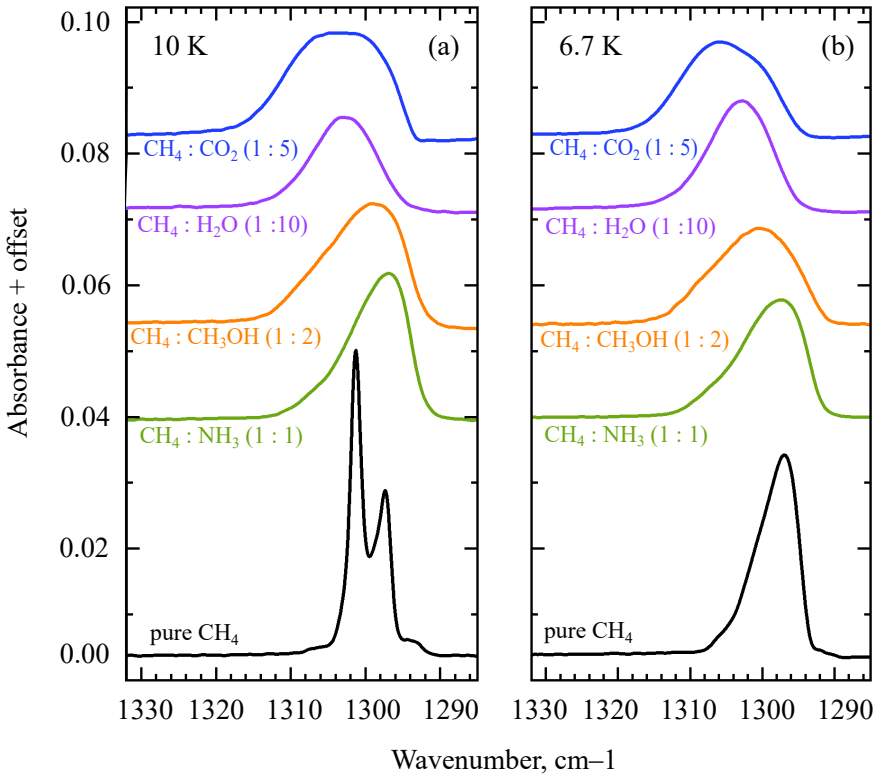

Fig. 1. Laboratory specta of solid pure methane and methane mixed with polar molecules. Panel (a): 10 K and panel (b): 6.7 K.

3 Summary

In this study, we present the reference laboratory spectra in the 7.7 μm region that is commonly assigned to methane deformation mode in different environments. The main results are summarised as follows.

1. For the first time we carried out the experiments in which the IR spectra of methane in mixed ices at temperatures below 10 K were obtained.
2. We report significant differences in line shape and peak position of 1300 cm^{-1} methane band in mixtures with polar molecules.
3. The obtained IR data can be used directly for comparison with the IR data of JWST.

Funding

This research work is funded by the Russian Ministry of Science and Higher Education via the State Assignment Contract No. FEUZ-2020-0038.

References

Boogert A.C.A., Gerakines P.A., Whittet D.C.B., 2015, Annual Review of Astronomy and Astrophysics, 53, p. 541

Gerakines P.A. and Hudson R.L., 2015, The Astrophysical Journal Letters, 805, 2, id. L20

McClure M.K., Rocha W.R.M., Pontoppidan K.M., et al., 2023, Nature Astronomy, 7, p. 431

MODERN ASTRONOMY: FROM THE EARLY UNIVERSE TO EXOPLANETS AND BLACK HOLES

A nature of the X-ray and optical emission from gamma Cassiopeia stars

A. Kholtygin[1], I. Yakunin[1,2], E. Ryspaeva[1,3], and D. Mokshin[1]

[1] Saint-Petersburg University, 7-9 University Emb., St. Petersburg, 199034 Russia
[2] Special Astrophysical Observatory of the Russian Academy of Sciences, Nizhny Arkhyz, 369167 Russia
[3] Crimean Astrophysical Observatory of the Russian Academy of Sciences, Nauchnyi, 298409 Russia

Abstract. To test the origin of the X-ray and optical emission from the γ Cas-type stars, we analyzed their optical spectra obtained on the 6-m telescope BTA, the 1.25-m telescope of the Crimean station of the State Astronomical Institute (SAI, Moscow), the 2.5-m telescope SAI25 of SAI, and the photometric TESS light curves. We compare the optical variability of the γ Cas-type stars with variations of their X-ray luminosity. An overlap between the periods of line profile variations in the spectra of γ Cas stars and the variations in their X-ray brightness allows us to assume that a significant fraction of X-rays emits from the same place where the optical radiation comes from. The γ Cas-type stars HD 45314, HD 45995 and NGC 6649 9 demonstrate the ultrafast X-ray brightness variations with the periods of about 50–90 seconds, which may be the rotation periods of white dwarfs components of binary systems. Thus, we can assume that at least for these stars the X-ray emission goes partly due to accretion onto rapidly rotating white dwarfs. The anomalously hard X-ray emission from the γ Cas stars can be interpreted by assuming that the contribution of non-thermal X-ray emission is generated as a result of a reconnection of the local magnetic field lines of the Be star and its decretion disk.

Keywords: stars: general, emission-line, Be; X-rays: stars

DOI: 10.26119/VAK2024.063

1 Introduction

The most enigmatic group of B stars is the classical Be stars including the rapidly rotating BIII–V stars of III–V luminosity classes with emission lines in their spectrum. Be stars lose gas and angular momentum into a circumstellar decretion disk (Rivinius et al. 2013). Some Be stars spin up at the stage of mass transfer in an interacting binary system (Pols et al. 1991), and the former donor star stands as a stripped, compact remnant (hot subdwarf, neutron star or white dwarf). Close binaries with compact component are known as Be X-ray systems with strong X-rays, while the most of Be stars are low X-ray sources with luminosities close to that of normal B-type stars (Nazé et al. 2022).

The nature of these objects remains mysterious despite more than 150 years of studying them. Emission lines in spectra of Be stars are associated with a decretion disk in the equatorial plane, the formation mechanism of which is unknown up to date. Even more enigmatic objects are γ Cas-type stars (γ Cas analogs) which belong to a small group (about 1%) among Be stars. This type includes Oe/Be stars with anomalously hard X-rays. Their X-ray luminosity is about 10^{31}–10^{33} erg/s. In the present paper we analyse our recent optical observations of selected γ Cas-type stars and compare them with their TESS photometry and X-rays.

The present paper is organized in the following way. In Section 2 the basic knowledge on these stars is given. Section 3 describes our optical observations of selected γ Cas-type stars and their line profile variations (LPVs). X-rays variability of the γ Cas-type stars are analysed in Section 4. A possible nature of γ Cas X-ray and optical luminosity is considered in Section 5.

2 An ensemble of γ Cas-type stars

To date, 26 stars of the γ Cas-type and two candidates of them are known. A list of 24 known γ Cas stars together with a list of candidates is presented by Kholtygin et al. (2022a). The bright star ζ Tau (Nazé et al. 2022) and the star 2XMMJ 180816.6−191939 (Nazé et al. 2020) should be added to this list. The estimated total number of γ Cas-type star in the Milky Way is nearly 5000 objects (Kholtygin et al. 2023a).

According to Nazé et al. (2022), eight of γ Cas-type stars are binaries. The new member of the γ Cas-type group ζ Tau is also a binary star (Ruždjak et al. 2009). Stars HD 44458 (FR CMa), HD 110432 (BZ Cru), HD 119682, HD 161103 (V3892 Sgr) and HD 162718 (V771 Sgr) are considered by Nazé et al. (2022) as presumably binary. This means that more than half (16 out of 26) of γ Cas stars are binary or suspected binary.

The mass of Be components in γ Cas-type binaries is 8–13 $M_\odot$, while the masses of the satellites do not exceed one solar mass excluding the binaries π Aqr (HD 212571). The mass of the secondary in this system is $2.4 \pm 0.5\,M_\odot$ (Nazé et al. 2022).

3 Optical observations

In Russia 17 stars of γ Cas subclass with $\delta > -12^\circ$ can be observed. We obtained spectra of nine of these stars at the 6-m telescope BTA, 1.25-m telescope ZTE in the Crimean station of the Sternberg Astronomical Institute (SAI) of Moscow State University and at 2.5-m telescope SAI25 of the Caucasian Mountain Observatory of SAI. The list of our observations is given in Table 1.

Table 1. Log of γ Cas observations.

Star	Spectral Type	V mag	$N_{\rm sp}$	Exp s	Telescope	Spectrograph	Date yyyy.mm.dd	$N_{\rm sp}^{\rm tot}$
γ Cas	B0.5IVpe	2.39	150	60	BTA	MSS	2020.11.04	4324
			138	60	BTA	MSS	2021.02.01–02	
			1576	2	ZTE	A-Sp	2020.09.13–14	
			2460	1.5	ZTE	A-Sp	2021.09.07–08	
ζ Tau	B1IVe	3.03	51	120	BTA	MSS	2023.01.12	51
HD 45314	O9:npe	6.64	20	600	BTA	MSS	2020.08.05–08	20
HD 45995	B1.5Vne	6.14	17	300	BTA	MSS	2023.01.12	225
			208	30	ZTE	A-Sp	2021.10.10	
SS 397	B0.5Ve	11.9	48	120	BTA	SCORPIO	2024.06.24	48
V558 Lyr	B3Ve	6.34	29	180/300	BTA	MSS	2023.12.01	861
			182	120	SAI25	TDS	2024.04.18	
			650	30	ZTE	A-Sp	2023.06.22–23	
SAO 49725	B0.5III/IVe	9.27	432	5	ZTE	SCORPIO	2021.08.17–18	432
V2156 Cyg	B1.5Ve	8.91	7	20	BTA	SCORPIO	2021.08.18	19
			12	600	BTA	MSS	2023.01.12	
π Aqr	B1III-IVe	4.64	1250	5	BTA	A-Sp	2023.01.12	1250

The total number of γ Cas-type stars spectra is 7230. The BTA spectra were obtained with the Main Stellar Spectrograph (MSS, Panchuk et al. 2014) and the SCORPIO spectrograph (Afanasiev & Moiseev 2005). The spectrograph A-Sp (Ikonnikova et al. 2021) was used to obtain the ZTE spectra, while SAI25 spectra were obtained with the spectrograph TDS (Potanin et al. 2020)[1].

These spectra were analysed by Kholtygin et al. (2021a,b, 2022b,c, 2023a,b). The regular variations of the line profiles in spectra of studied stars with periods

[1] https://obs.sai.msu.ru/cmo/sai25/tds/

4–300 minutes have been detected. Authors supposed that these variations are connected with high modes of the non-radial pulsations.

4 X-ray spectra and X-ray light curves

We analyzed the archival X-ray observations of γ Cas-type stars, obtained by the XMM-Newton and Chandra space observatories. Log of the observations and the procedure of data reduction can be found in the paper by Ryspaeva & Kholtygin (2021).

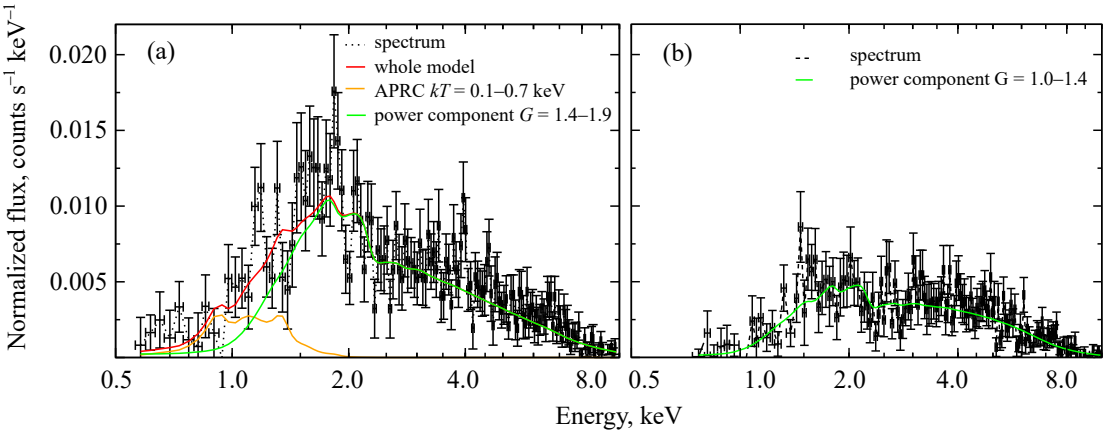

Fig. 1. The best fits of HD 90563 spectrum by APEC+PL (a) and pure PL models (b). The contributions of individual components into the total model X-ray spectrum are marked by colors. Left panel: observations on 2021.01.21. Right panel: joint observations from 2021.06.30 to 2021.08.07.

We approximated the X-rays spectra using `XSPEC 12.10.0` package in 0.2–8 keV energy band. The spectra were approximated by the sums of models `APEC` (Astrophysical Plasma Emission Code by Smith et al. 2001). In order to reach a better fit of the observed spectra we also used an additional power component (Power law, PL) which probably describes the contribution of the non-thermal X-rays.

For all analysed spectra the contribution of the PL component appeared to be significant as it is illustrated in Fig 1a. Moreover, in certain epochs, X-ray spectra can be described by only the PL component (see Fig 1b). It means that the contribution of the non-thermal X-ray emission into the total spectra of γ Cas-type stars seem to be very large as it was pointed out by Ryspaeva & Kholtygin (2021) earlier.

Together with the spectra we extracted X-ray light curves from the XMM EPIC images in the energy ranges of 0.2–8 keV and 2–8 keV for all known γ Cas-type stars.

The periods of optical, TESS photometric, and X-ray variability appeared to be close and correspond to the typical periods of non-radial pulsations (NRPs) of Be stars. It means that the X-ray emission of such stars is formed at least partly in the same place where the optical emission is generated.

5 A nature of optical and X-ray emission of γ Cas stars

There are two main scenarios for the physical cause of the production of hard X-rays of these stars. In the first one, hard X-rays are generated due to the interactions between local magnetic fields on the Be star and those at its decretion disk. In the second one, the matter from the Be star accretes onto a degenerate secondary star WD. Postnov et al. (2017) proposed a scenario in which the binary companion is a rapidly spinning neutron star. Smith et al. (2017) argue that this scenario does not account for the number and observational properties of the γ Cas-type stars.

In support of the first scenario, one can point to the correspondence between the periods of optical and X-ray variability pointed out in Section 4. If such a scenario were to be true, the X-ray emission from γ Cas stars should be flared. The analysis of the X-ray light curves shows that this is precisely the nature of the radiation of stars of this type (e.g., Smith et al. 2012).

The binarity of many of the γ Cas-type stars (Nazé et al. 2022) supports the second scenario. Our analysis shows that γ Cas-type stars HD 45314, HD 45995 and NGC 6649 9 demonstrate the fastest X-ray brightness variations with the periods of about 50–90 seconds, which may be the rotation periods of white dwarfs, components of binaries (Kholtygin et al. 2023b).

The scenario for the formation of Be + WD binary systems is described by Gies et al. (2023). In the case B of mass transfer in the interacting binary the donor filled its Roche surface during the expansion due to the ignition of H-shell burning, and the Be + sdO binaries are probably formed (Pols et al. 1991). After a period of time close to the main-sequence (MS) lifetime of the nearby Be star, the sdO stars will initiate its He-shell burning and again grow in radius and luminosity (e.g., Laplace et al. 2020).

This stage of enlargement leads to a second Roche filling and mass transfer (case BB by Delgado & Thomas 1981). If the remnant after this second mass transfer stage has a core mass lower than $1.4\,M_{\odot}$, then the remnant will rapidly evolve to CO WD or WNe WD (Dewi et al. 2002).

In conclusion, it can be said that the generation of X-ray emission from γ Cas-type stars most likely occurs in a hybrid scenario. The flare part of the total X-ray flux is formed by the interaction of the local stellar magnetic fields and the magnetic

field of the disk, while the hard part is generated due to an accretion onto a rapidly rotating white dwarf.

Funding

Authors thank the Russian Science Foundation project No. 23-22-00090 for the support.

References

Afanasiev V.L. and Moiseev A.V., 2005, Astronomy Letters, 31, 3, p. 194
Delgado A.J. and Thomas H.-C. 1981, Astronomy & Astrophysics, 96, 1-2, p. 142
Dewi J.D.M., Pols O.R., Savonije G.J., et al., 2002, Monthly Notices Royal Astronomical Society, 331, 4, p. 1027
Gies D.R., Wang L., Klement R., 2023, Astrophysical Journal Letters, 942, 1, id. L6
Ikonnikova N.P., Shaposhnikov I.A., Esipov V.F., et al., 2021, Astronomy Letters, 47, 8. p. 560
Kholtygin A.F., Moiseeva A.V., Yakunin I.A., et al., 2021a, Geomagnetism and Aeronomy, 61, p. 923
Kholtygin A.F., Burlak, M.A., Tsiopa, O.A., 2021b, Astronomicheskij Tsirkulyar, 1649, p. 1
Kholtygin A.F., Ryspaeva E.B., Moiseeva A., et al., 2022a, The Multifaceted Universe: Theory and Observations—2022, id. 44
Kholtygin A.F., Moiseeva A.V., Yakunin I.A., et al., 2022b, Geomagnetism and Aeronomy, 62, p. 1136
Kholtygin A., Burlak M., Milanova Y., 2022c, Astronomicheskij Tsirkulyar, 1652, p. 1
Kholtygin A.F., Ryspaeva E.B., Yakunin I.A., et al., 2023a, INASAN Science Reports, 8, 2, p. 86
Kholtygin A.F., Yakunin I.A., Burlak M.A., et al., 2023b, Astrophysical Bulletin, 78, 4, p. 557
Laplace E., Götberg Y., de Mink S.E., et al., 2020, Astronomy & Astrophysics, 637, id. A6
Nazé Y., Motch C., Rauw G., et al., 2020, Monthly Notices Royal Astronomical Society, 493, 2, p. 2511
Nazé Y., Rauw G., Smith M.A., et al., 2022, Monthly Notices Royal Astronomical Society, 516, 3, p. 3366
Panchuk V.E., Chuntonov G.A., Naidenov I.D., 2014, Astrophysical Bulletin, 69, 3, p. 339
Pols O.R., Cote J., Waters L.B.F.M., et al., 1991, Astronomy & Astrophysics, 241, p. 419
Postnov K., Oskinova L., Torrejón J.M., 2017, Monthly Notices Royal Astronomical Society, 465, 1, p. L119
Potanin S.A., Belinski, A.A., Dodin A.V., et al., 2020, Astronomy Letters, 46, 12, p. 836
Rivinius T., Carciofi A.C., Martayan C. 2013, Astronomy and Astrophysics Review, 21, id. 69
Ruždjak,D., Božić H., Harmanec P., et al., 2009, Astronomy & Astrophysics, 506, 3, p. 1319
Ryspaeva E.B. and Kholtygin A.F., 2021, Open Astronomy, 30, 1, p. 132
Smith M.A., Lopes de Oliveira R., Motch C., 2012, Astrophysical Journal, 755, 1, id. 64
Smith M.A., Lopes de Oliveira R., Motch C., 2017, Monthly Notices Royal Astronomical Society, 469, 2, p. 1502
Smith R.K., Brickhouse N.S., Liedahl D.A. et al., 2001, Astrophysical Journal, 556, 2, p. L91

MODERN ASTRONOMY: FROM THE EARLY UNIVERSE TO EXOPLANETS AND BLACK HOLES

On the kinematic state of the atmosphere within IRAS 07430+1115 system

V. Klochkova, G. Zhuklevich, and V. Panchuk

Special Astrophysical Observatory of the Russian Academy of Sciences, Nizhny Arkhyz, 369167 Russia

Abstract. Having obtained high-resolution optical spectra with the NES spectrograph of the 6-m telescope BTA, we investigated the variability of the spectral features and radial velocity for a cold star which passed the asymptotic branch of giants and is associated with the IRAS 07430+1115 source. The optical spectrum of this post-AGB star with altered chemical composition is purely absorbtional, emissions and other peculiarities are absent in the spectrum. From the measurements of the positions of many metal absorbtions (mainly ions of heavy *s*-process metals) a weak variability of the radial velocity was revealed. The velocity varies with the average value $V_r = 37.0$ km/s and the standard deviation $\Delta V_r \approx 0.8$ km/s, which may be a consequence of low-amplitude pulsations in the atmosphere of a far evolved star. The position of the Hα line core varies within 40.5–43.8 km/s. Based on measurements of the positions of the rotational components of the (0;0), (1;0) and (2;0) Swan bands of the molecule C_2 origin in the circumstellar envelope, the average radial velocity V_r(Swan) = 21 km/s and the expansion velocity typical for post-AGB stars envelope $V_{\rm exp} \approx 16$ km/s are determinated. Using the intensity of the infrared triplet of oxygen, we estimated the luminosity of the central star of the IRAS 07430 system $\log L/L_\odot \approx 3.1$ which is within the range of values for post-AGB stars.

Keywords: stars: AGB and post-AGB, oscillations (including pulsations), atmospheres

DOI: 10.26119/VAK2024.064

1 Introduction

Interest in AGB stars and their closest descendants—post-AGB stars is due to their influence on the evolution of the chemical composition of galaxies, since in the depths of these stars, physical conditions arise for the synthesis of heavy metals nuclei, their subsequent dredge-up into the stellar atmosphere and subsequently into the envelope and interstellar medium. As a result of these processes, AGB stars are the main circumstellar suppliers of all elements heavier than iron synthesized through slow neutronization of nuclei (see for details Herwig 2005). The 6-m telescope of the BTA performs detailed spectroscopy of a sample of stars with initial masses in the range of about 2–8 $M_{\odot}$ that passed evolutionary stages with nucleosynthesis, mixing, as well as the episodes with mass loss due to the stellar wind at different rates. Spectral data analysis aims to determine the fundamental parameters and features of the chemical composition of stellar atmospheres of the stars, as well as to search for variability of specific spectral details and patterns of radial velocities. Numerous results obtained by us, during spectroscopy and spectral monitoring, are summarized in the review Klochkova (2019). Our spectroscopy program also includes a pair of related G-supergiants in IR systems IRAS Z02229+6208 (hereinafter named as IRAS Z02229) and IRAS 07430+1115 (IRAS 07430). Reddy et al. (1999) analyzed the data from the echelle high-resolution spectra and published the parameters of this pair of stars and features of the chemical composition of their atmospheres. As a result, the Reddy et al. (1999) came to the conclusion that the metallicity of the stellar atmosphere is reduced: $[\mathrm{Fe/H}]_{\odot} = -0.5$ at large excesses of carbon $[\mathrm{C/Fe}]_{\odot} = +0.8$ and *s*-process heavy metals $[\mathrm{s/Fe}]_{\odot} = +1.4$. Details of the chemical composition indicate that both stars passed the evolutionary stage of AGB and the episode of the third mixing. This study confirmed the related nature of two stars with large IR flux excesses.

Stars with large IR flux excesses are weak in the visible range due to the significant circumstellar extinction. For a long time there was no repeated registration of an optical spectrum of IRAS 07430. Carrying out spectral monitoring is hampered by its weak visible brightness ($V = 12\overset{\mathrm{m}}{.}8$, Hrivnak et al. 2022). In this article, we present the results of the analysis of several optical spectra of IRAS 07430 obtained at the 6-m telescope BTA on arbitrary dates in 2018–2024 to search for possible profile variability of spectral details and temporal behavior of radial velocity patterns in the atmosphere and circumstellar envelope of the star.

2 Observations, results and their discussion

Spectra of IRAS 07430 were obtained with the echelle spectrograph NES (Panchuk et al. 2017), located stationary at the Nasmyth focus of the 6-m telescope. Obser-

Table 1. Results of measurements of heliocentric radial velocity V_r in the IRAS 07430 system, the number of features used are indicated in parenthesis.

Date	V_r, km/s		
	Absorptions	Hα (core)	Swan
19–23.12.1996*	35 ± 1		22 ± 1 (23), 24 ± 1 (12)
06.04.2018	36.6 ± 0.14 (268)	40.5	21.4 ± 0.6 (11)
11.04.2018	36.2 ± 0.12 (380)	41.2	20.2 ± 0.3 (28)
07.12.2019	37.7 ± 0.16 (488)	43.8	20.0 ± 0.2 (28)
27.03.2024	39.2 ± 0.14 (194)	42.3	20.7 ± 0.2 (55)

* — average V_r value for 1996 is based on data from the article Reddy et al. (1999).

vation dates are indicated in Table 1. The recorded spectral range on our spectra is $\Delta\lambda = 470$–778 nm. Identification of details in the spectrum was carried out using the spectral atlas (Klochkova et al. 2007).

The study of variability in the spectra of IRAS 07430 is complicated because of several factors. Firstly, the visible brightness of this star is the limit for high-resolution spectroscopy. But we must reach the signal-to-noise ratio needed, in particular, to identify numerous narrow rotational details of Swan bands (see Fig. 1). Secondly, a high degree of blending caused by the saturation of the spectrum with strong ions absorbtions, the equivalent widths of which are often comparable to or exceed the intensity of Hα. Fragments of the spectrum in Fig. 1 illustrate the fact of the profusion of strong absorbtions. A separate problem is the lack of reliable radiospectroscopy data, which provides the real systemic velocity for stars with envelopes.

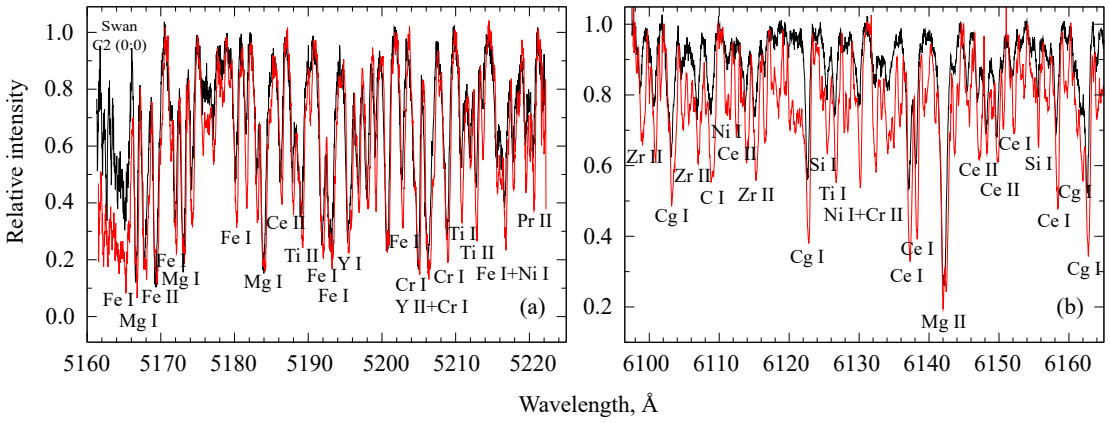

Fig. 1. Fragments of the IRAS 07430 spectrum obtained on 2019.07.12.

The most important milestone in the study of post-AGB stars is the availability of the results from the Gaia mission and the catalog Gaia DR3. Reliable parallaxes of stars provide the determination of distances, luminosity, initial and current masses of stars. The main parameters obtained this way, combined with the detailed chemical composition of atmospheres of evolved stars, provide refinement of the evolution stage and restoration of their history of changes in chemical composition. Modeling based on Gaia DR3 data of parameters for an extensive sample of post-AGB stars was performed by Kamath et al. (2022). In the framework of our work, we are especially interested in the results of this article about the status of the star associated with IR source IRAS 07430, for which extremely low luminosity $L = 20\,L_\odot$ is determined by Kamath et al. (2022). At same time, the luminosity of a related star in the system IRAS Z02229 is many times higher: $L = 12\,959\,L_\odot$ (Kamath et al. 2022). With a large difference in luminosity estimations, both stars have close equivalent widths of the oxygen triplet O I λ7774, which serves as a reliable criterion for the luminosity value M_V for F–G supergiants. In the spectra of IRAS Z02229 and IRAS 07430 W_λ(O I λ7774)= 0.99 Å and 0.91 Å respectively. Using the dependence M_V–W_λ(O I) from the paper Kovtyukh et al. (2012), we obtained for IRAS 07430 the absolute value $M_V \approx -3^{\rm m}$ and luminosity $\log L/L_\odot \approx 3.1$, which is within the range of values for post-AGB stars.

As follows from the data in the third column of Table 1, the position of the Hα core varies within a small interval 40.5–43.8 km/s. Weak asymmetry of its profile is noticeable on some observation nights. The reason may be a weak wind, due to which the blue wing of this line is changed. However, this fact requires new observations with a high S/N ratio.

For the well-studied post-AGB star HD 56126, there is a difference in V_r, measured from absorbtions of different degrees of excitation, formed at different depths in the atmosphere. However, we did not find a similar dependence in the spectrum of IRAS 07430. The independence of V_r(abs) from line depth indicates the absence of velocity stratification in the atmosphere of IRAS 07430.

In each of our spectra, we measured the radial velocities V_r from the positions of photospheric absorbtions, rotational details of Swan molecular bands, circumstellar details of Na I and K I. Average heliocentric velocity of the central star of the source IRAS 07430 for five dates in Table 1 is equal to V_r(abs) = 37.0 km/s with standard deviation of ΔV_r = 0.8 km/s. For the star in the IRAS Z02229 system the velocity of variability is higher: $\Delta V_r \approx 1.4$ km/s (Klochkova & Panchuk 2022). Based on the measurements of the position of the rotational components of the (0;0), (1;0) and (2;0) Swan bands molecules C_2, we obtained the average values of V_r(Swan) for each date, which are given in the fourth column of Table 1 and close to the results of Reddy

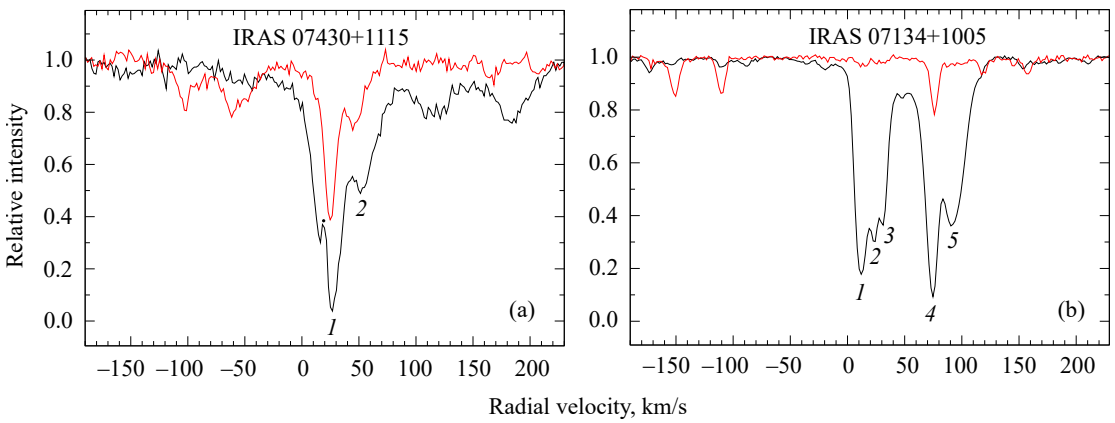

Fig. 2. Profiles of the D-line Na I λ5890 (black line) and K I λ7699 (red line) in the spectrum of IRAS 07430 (a). The dot indicates the position of the telluric emission. On the panel (b) there is the absorbtion profile of Na I λ5890 in the pos-AGB spectrum of the star HD 56126.

et al. (1999). Generally, based on the details formed in the circumstellar envelope, we obtained the average velocity V_r(Swan) = 21 km/s and the envelope expansion velocity $V_{\rm exp} \approx 16$ km/s. This velocity expansion is typical for post-AGB stars. Note, that in the visible wavelength range we did not detect emission components of the Swan bands Reddy et al. (1999) write about. The effect of splitting of strong absorbtions with low excitation potentials (Ba II, La II, Ce II, etc.) was not found for IRAS 07430, detected in the spectrum of IRAS Z02229 by Klochkova & Panchuk (2022).

Let us briefly consider the interstellar features in the spectrum of IRAS 07430. Profile of one of the D-lines of the Na I doublet is presented in the left panel of Fig. 2 together with the line profile K I λ7699. The profiles of both lines contain only two absorbtions: "1"—the envelope component, "2"—the photospheric one. Additional absorbtions, which could be classified as interstellar, are absent. To confirm the conclusion, let us compare the profile of the D2 Na I λ5890 line in the spectra of IRAS 07430 with the profile in the spectrum of a distant (π = 0.3806 mas) star HD 56126 with close galactic coordinates, presented in the right panel of Fig. 2. The position of the component "4" is consistent with the position of the Swan bands, which indicates its formation in the circumstellar envelope. Component "5" is photospheric: its behavior over time corresponds to the behavior of other photospheric absorbtions (Klochkova et al. 2007). Three shortwave absorbtions "1–3" are interstellar lines.

3 Conclusions

From date to date, the photospheric absorbtion velocity varies around the average value $V_r = 37.0$ km/s with the standard deviation of $\Delta V_r \approx 0.8$ km/s, which may be a manifestation of the low amplitude pulsations in the stellar atmosphere. The position of the Hα core varies within 40.5–43.8 km/s. Based on the position of the significant components of the Swan bands (0;0), (1;0) and (2;0) molecule C_2 formed in the circumstellar envelope, the average radial velocity V_r(Swan) of about 21 km/s and the expansion velocity $V_{\rm exp} \approx 16$ km/s, typical for post-AGB stars, were found.

Expected in the spectra of IRAS 07430 features: radiation stratification velocity in the stellar atmosphere, peculiarity of the Hα profile and splitting of strong absorbtions of heavy metals, which was found in the spectra of IRAS Z02229, are absent.

An unexpected and required of the explanation effect was obtained: with a large difference in luminosity, both stars have almost equal equivalent width of the triplet oxygen O I λ7774: $W_\lambda = 0.99$ Å and 0.91 Å in the spectra of IRAS Z02229 and IRAS 07430 respectively. The discrepancy in estimating of the IRAS 07430 luminosity may be caused by possible parallax uncertainty for AGB supergiants with extensive envelopes (see Andriantsaralaza et al. 2022).

Funding

Observations at the 6-m telescope were performed as a part of the SAO RAS government contract approved by the Ministry of Science and Higher Education of the Russian Federation. We acknowledge support by the Russian Scientific Foundation (project No. 22-12-00069).

References

Andriantsaralaza M., Ramstedt S., Vlemmings W.H.T., et al., 2022, Astronomy & Astrophysics, 667, id. A74

Herwig F., 2005, Annual Review of Astronomy & Astrophysics, 43, 1, p. 435

Hrivnak B.J., Lu W., Bakke W.C., et al., 2022, Astrophysical Journal, 939, 1, id. 32

Kamath D., Van Winckel H., Ventura P., et al., 2022, Astrophysical Journal Letters, 927, 1, id. L13

Klochkova V.G., Chentsov E.L., Tavolganskaya N.S., et al., 2007, Astrophysical Bulletin, 62, 2, p. 162

Klochkova V., 2019, Astrophysical Bulletin, 74, 2, p. 140

Klochkova V.G. and Panchuk V.E., 2022, Astrophysical Bulletin, 77, 3, p. 292

Kovtyukh V., Gorlova N., Belik S., 2012, Monthly Notices of the Royal Astronomical Society, 423, 4, p. 3268

Panchuk V.E., Klochkova V.G., Yushkin M.V., 2017, Astronomy Reports, 61, 9, p. 820

Reddy B.E., Bakker E.J., Hrivnak B.J., 1999, Astrophysical Journal, 524, 2, p. 831

VAK 2024 MODERN ASTRONOMY: FROM THE EARLY UNIVERSE TO EXOPLANETS AND BLACK HOLES 300 years Russian Academy of Sciences

Dynamics of dust grains and small bodies in accretion disks of young stars with fossil magnetic field

V. Kobozeva[1] and S. Khaibrakhmanov[1,2]

[1] Saint-Petersburg State University, 13B Universitetskaya Emb., St. Petersburg, 199034 Russia
[2] Chelyabinsk State University, 12 Br. Kashirinykh, Chelyabinsk, 454001 Russia

Abstract. The paper discusses a numerical model that explores the dynamics of dust particles and small bodies within accretion disks that contain fossil magnetic fields. The model equations include gravitational force, centrifugal force, and drag force depending on particle size and speed. The disk structure is simulated using the magnetohydrodynamic model of Dudorov and Khaibrakhmanov, taking into account the effect of magnetic tensions on gas rotation speed. The dynamics of particles ranging in size from 10^{-4} cm to 10^{2} cm in an accretion disk of a typical T Tauri star are modeled. The simulations indicate that the dynamics of particles with a size of 1 m consists in fast sedimentation towards the midplane, followed by a slower radial drift. Sedimentation is accompanied by damped oscillations around the midplane. The slowdown of gas rotation due to magnetic tension leads to an increase in radial drift speed at the disk's periphery. Therefore, the depletion of solid particles in the outer regions of the disks and their accumulation in the "dead" zones with weak magnetic fields may occur more rapidly in disks with magnetic fields.

Keywords: ISM: magnetic fields, dust; accretion disks; magnetohydrodynamics (MHD); protoplanetary disks

DOI: 10.26119/VAK2024.065

1 Introduction

The initial stages of star formation are associated with the formation of gas-dust accretion disks, which may develop into protoplanetary disks. The masses of accretion and protoplanetary disks around young stars are of 0.005–0.1 $M_\odot$, with radii varying from tens to hundreds of AU, and accretion rates between approximately $10^{-6}\,M_\odot$/yr and $10^{-8}\,M_\odot$/yr (Williams & Cieza 2011). Observations indicate that dust grains in the disks grow up to sizes of 1 mm and concentrate near the midplane of the disks.

Observational analysis suggests the existence of a large-scale magnetic field in the disks (Khaibrakhmanov 2024), which may have a notable impact on disk dynamics, particularly by decreasing the gas rotation speed in comparison to the Keplerian speed (Khaibrakhmanov & Dudorov 2022). This effect is expected to influence the radial drift speed of dust grains in disks. In the present work, we study the dynamics of solid particles in accretion disks with strong magnetic fields.

2 Model

Consider the motion of a spherical particle with velocity components $\mathbf{v} = (v_r, v_\varphi, v_z)$ and radius a_d in an accretion disk surrounding a young star with mass of $M = 1\,M_\odot$. The particle is influenced by stellar gravity, centrifugal force, and gas drag. It has the radius vector $\mathbf{r} = (r, \varphi, z)$ and angular momentum $j = rv_\varphi$. The disk is in hydrostatic equilibrium and described with velocity $\mathbf{u} = (u_r, u_\varphi, 0)$. The dynamics of the particle is described by the following systems of equations and initial conditions

$$\begin{cases} \dfrac{dr}{dt} = v_r, \\ \dfrac{dv_r}{dt} = \dfrac{j^2}{r^3} - \dfrac{1}{r^2} - \dfrac{v_r - u_r}{\tau_s}, \\ \dfrac{dj}{dt} = -\dfrac{r}{\tau_s}\left(\dfrac{j}{r} - u_\varphi\right), \\ \dfrac{dz}{dt} = v_z, \\ \dfrac{dv_z}{dt} = -\dfrac{z}{r^3} - \dfrac{v_z}{\tau_s}, \end{cases} \qquad \begin{cases} r(t=0) = r_{\rm init}, \\ v_r(t=0) = 0, \\ j(t=0) = r_{\rm init} v_K(r_{\rm init}), \\ z(t=0) = z_{\rm init}, \\ v_z(t=0) = 0, \end{cases} \tag{1}$$

where τ_s is the dimensionless stopping time, $r_{\rm init}$ and $z_{\rm init}$ are the initial radial and vertical coordinates respectively. Coordinates are expressed in units of $r_0 = 1$ AU, velocity components in units of the Keplerian velocity $v_0 = v_K(r_0) = 2.976 \times 10^6$ cm/s, time is measured in units of $t_0 = r_0/v_0$, and angular momentum is given in units of $j_0 = r_0 v_0$.

The system of eq. (1) is solved numerically using the `LSODA` method, as implemented in the SciPy library for the Python programming language.

The disk structure is calculated using the magnetohydrodynamic model (see Khaibrakhmanov & Dudorov 2022). Three runs for modelling disk structure are considered:

1) an analytical solution of the model equations (Dudorov & Khaibrakhmanov 2014), where the radial profiles of the disk properties are described as power-law functions of r, with a fixed gas velocity deviation from Keplerian $u_\varphi/v_K = 0.9987$;
2) a numerical solution of the model equations that calculates the gas rotation speed considering the contribution of the gas pressure gradient;
3) a numerical solution of the model equations that further incorporates the influence of magnetic tensions on the gas rotation velocity.

In run 2, the value of u_φ/v_K ranges from 0.9960–0.9899 depending on r, while it ranges from 0.9950–0.9798 in run 3. In the simulations of the particle dynamics, the following parameters were used: $a_d = 1$ μm – 1 m, $r_{\rm init} = 1$, 10, 50, 100 AU, and $z_{\rm init} = 3H$, where H is a local scale-height.

3 Results

The simulations indicate that the dynamics of the particle with $a_d = 1$ m involve two stages: a rapid sedimentation towards the equatorial plane, followed by damped oscillations around $z = 0$, and a subsequent slower radial drift towards the star. The sedimentation times are 2.7, 8.1, 89.5, 252 yrs for $r_{\rm init} = 1$, 10, 50, 100 AU respectively, while the drift times are 0.097, 4.459, 84.54, 306 kyr.

In Fig. 1, we plot the radial profiles of the radial drift speed for the particle with $a_d = 1$ m and $r_{\rm init} = 100$ AU. In run 1, the v_r increases as the particle moves from $r_{\rm init}$ towards the star, reaching a maximum value of $2.150 \times 10^{-3} v_0 = 6.397 \times 10^3$ cm/s at $r \approx 0.36$ AU. After that, the speed decreases down to approximately 30 m/s near the inner edge of the disk at $r \approx 0.05$ AU. A small jump in the $v_r(r)$ profile near the maximum corresponds to the transition from the Epstein drag law in the outer disk to the Stokes law in the inner disk. The radial drift time is approximately 85 kyr.

In runs 2 and 3, the drift speed also increases initially and then decreases. However, the drift occurs at a higher speed. In run 2, the velocity is greater by $6.4 \times 10^{-5} v_0 \approx 190$ cm/s in the region from $r_{\rm init}$ to $r \approx 0.3$ AU. In run 3, the drift speed is greater by $2.8 \times 10^{-4} v_0 \approx 833$ cm/s. The higher drift velocities observed in runs 2 and 3 can be attributed to the greater deviations of the gas speed from the Keplerian one.

4 Summary

The simulations show that the dynamics of dust grains and small bodies involve of two stages: sedimentation toward the equatorial plane followed by radial drift

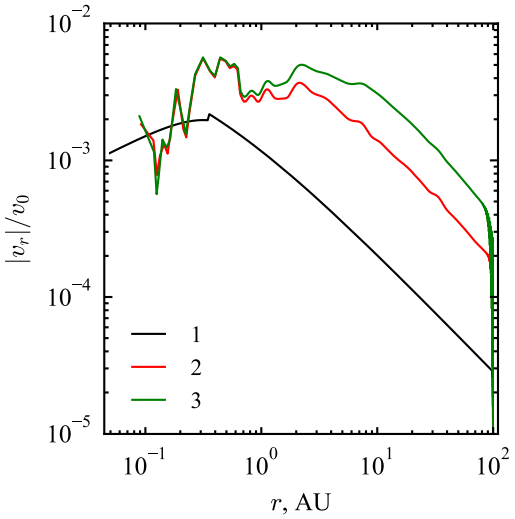

Fig. 1. Radial profiles of the radial drift velocities of particles with a radius $a_d = 1$ m in runs 1–3.

toward the star. Small particles, $a_d \lesssim 1$ cm, move steadily towards the star, while larger bodies accelerate at the disk's periphery and slow down as they near the star. The sedimentation timescales are 1–3 orders of magnitude shorter than the radial drift timescales. After sedimentation, bodies measuring 1 m or more may undergo damped oscillations around the equatorial plane, potentially leading to variations in their size distribution.

The reduction in gas rotation speed relative to the Keplerian one, attributed to magnetic tensions, leads to an increase in radial drift speed at the disk's periphery. This suggests that the depletion of solid particles in the outer regions of the disks and their accumulation in the "dead" zones with weak magnetic fields may occur more quickly in disks with a magnetic field.

Acknowledgements. The work of S. Khaibrakhmanov is supported by the Theoretical Physics and Mathematics Advancement Foundation "BASIS" (project No. 23-1-3-57-1).

References

Dudorov A. and Khaibrakhmanov S., 2014, Astrophysics and Space Science, 352, p. 103
Khaibrakhmanov S., 2024, Astronomical and Astrophysical Transactions, arXiv:2401.14180
Khaibrakhmanov S. and Dudorov A., 2022, Astronomy Reports, 99, 10, p. 832
Williams J. and Cieza L., 2011, Annual Review of Astronomy and Astrophysics, 49, p. 67

BAK 2024 MODERN ASTRONOMY: FROM THE EARLY UNIVERSE TO EXOPLANETS AND BLACK HOLES 300 years Russian Academy of Sciences

Evolution of non-spherical porous dust grains in galaxies

T. Kondratieva

Saint-Petersburg State University of Aerospace Instrumentation, 67 Bolshaya Morskaya, St. Petersburg, 190000 Russia

Abstract. Recent research has examined the evolution of interstellar dust grain size distribution over time scales of up to 10 Gyr, focusing on the primary grain growth and destruction mechanisms present in both the diffuse and dense interstellar medium. The grains were modeled as porous spheres, and for the first time, the porosity was considered to depend on the particle size and time. In this work, it is proposed in the first approximation that non-spherical dust grains have a comparable mass distribution to that of spherical ones. The use of porous spheroids facilitates the calculation of the time evolution of both the interstellar polarization curve and the interstellar extinction curve. As the polarization curve is known to be a critical test for porous dust grain models, the results obtained for spheroids are important for a further understanding of the dust grain evolution in galaxies.

Keywords: ISM: general, dust, extinction, evolution; polarization

DOI: 10.26119/VAK2024.066

1 Introduction

Interstellar (IS) dust consists of small solid particles, usually within the sub-micron size range, and is present in various objects throughout the Universe, including comets and early galaxies. The origin and physical properties of dust grains, including their size and shape distributions, as well as related questions, continue to be areas of active research and discussion.

Information about dust properties can be obtained by modeling the wavelength dependencies of IS extinction and polarization and comparing these models with observations. The recent paper by Hirashita & Il'in (2022) examines variations in the grain size distribution throughout the evolution of galaxies over a period of up to 10 billion years. The particle porosity was assumed to depend on the grain size and change with time. IS extinction curves were constructed for different size and porosity distributions, assuming that the grains are spheres. The curves were compared with observations for our Galaxy.

However, the IS extinction curves do not accurately characterize the porosity of dust grains. The interstellar polarization curves are more sensitive to porosity, as it shifts the IS polarization maximum to the UV wavelengths. Therefore, the aim of this work was to calculate the IS polarization curves by replacing spheres with spheroids that have mass and porosity distributions based on findings of Hirashita & Il'in (2022).

2 Model

We assume that IS dust grains are homogeneous oblate spheroids of a fixed semiaxis ratio a/b ($a \geq b$). An increase in porosity p of the equal mass M particles leads to an increase in their volume, expressed as $V = \dfrac{M}{\rho\,(1-p)} = \dfrac{4\pi a^2 b}{3(1-p)}$. Consequently, the semiaxes maintain a constant ratio, where ρ is the density of the particle material. The grain porosity $p(M,t)$ and mass $n(M,t)$ distributions at various evolution times t are sourced from Hirashita & Il'in (2022). Following that work, we consider amorphous silicate and carbon particles with the standard (same as those of Hirashita & Il'in 2022) refractive indices $m^{\rm sil}(\lambda)$ and $m^{\rm amC}(\lambda)$ respectively.

It is assumed that a fraction $f(M)$ of silicate grains is aligned, whereas the remaining silicate and all carbon grains have a random orientation (Hensley & Draine 2023). The IS extinction $A(\lambda)$ at the wavelength λ is proportional to the mean extinction cross-section $\langle C_{\rm ext}\rangle$ of scatterers, while the IS polarization $P(\lambda)$ relates to the mean polarization cross-section $\langle C_{\rm pol}\rangle$. For spheroids, the cross-sections are influenced by the particle semiaxes a, b, the refractive index m, the incidence angle, α, and the polarization state of radiation, including TE and TM modes which are

oriented perpendicularly. To calculate the cross-sections for spheroids, we apply the code developed by N. V. Voshchinnikov[1].

So, we use the following formulae to find the mean cross-sections:

$$\langle C_{\rm ext}\rangle(\lambda, a/b, \alpha, t) = \int\limits_{M_{\rm min}}^{M_{\rm max}} \left[\bar{C}_{\rm ext}\ (1 - f(M)) + C_{\rm ext}\, f(M)\right]\ n(M,t)\, dM, \qquad (1)$$

$$\langle C_{\rm pol}\rangle(\lambda, a/b, \alpha, t) = \int\limits_{M_{\rm min}}^{M_{\rm max}} C_{\rm pol}\, f(M)\, n(M,t)\, dM, \qquad (2)$$

where $C_{\rm ext} = \left(C_{\rm ext}^{\rm TE} + C_{\rm ext}^{\rm TM}\right)/2$, $C_{\rm pol} = \left(C_{\rm ext}^{\rm TE} - C_{\rm ext}^{\rm TM}\right)$, and $\bar{C}_{\rm ext}$ is the cross-section averaged over all spheroid orientations (Hensley & Draine 2023).

The cross-sections of our porous spheroids have more parameters:

$$C_{\rm ext}^{\rm TE,\,TM}\left[x_V(\lambda, M, t),\ a/b,\ m(m_0(\lambda), M, t),\ \alpha\right]. \qquad (3)$$

Here the diffraction parameter x_V related to the particle volume V is equal to

$$x_V(\lambda, M, t) = \frac{2\pi r_V}{\lambda} = \frac{2\pi}{\lambda}\left(\frac{3\,M}{4\pi\rho\,[1 - p(M,t)]}\right)^{1/3}. \qquad (4)$$

The refractive index reduced by the particle porosity is calculated with the Effective Medium Theory for material with the refractive index $m_0(\lambda)$

$$m(m_0(\lambda), M, t) = g^{\rm EMT}[m_0(\lambda), p(M,t)]. \qquad (5)$$

The fraction of aligned spheroidal particles $f(M)$, is characterized by two parameters: $M_{\rm crit}$ and ΔM, within the interval $[M_{\rm crit} - \Delta M, M_{\rm crit} + \Delta M]$, a transition occurs from the random orientation to the perfect alignment. In the IS dust grain alignment theory, $M_{\rm crit}$ is associated with a mean particle size of approximately 0.1 μm, as noted by Tram & Hoang (2022).

3 Numerical results

We have conducted calculations of the IS extinction and polarization curves based on the model described in Section 2, utilizing the results of galactic evolution of grain size and porosity distributions as outlined by Hirashita & Il'in (2022).

Calculations indicate that commonly used small values of ΔM (a sharp transition from randomly oriented silicate grains to perfectly aligned ones) result in an artifact in the polarization curve $P(\lambda)$ at $\lambda \sim 0.2$ μm.

[1] http://www.astro.spbu.ru/staff/ilin2/SOFTWARE/svm.html

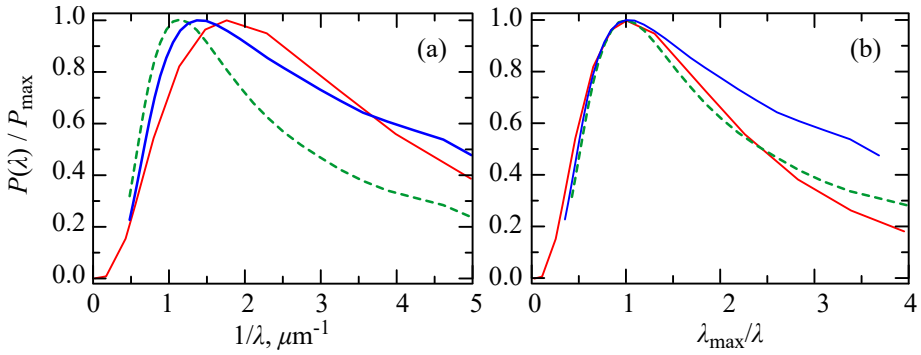

Fig. 1. Interstellar polarization curves: the standard Serkowski law with $\lambda_{max} = 0.55$ μm (red line) and curve obtained by us for the mass distribution from Hirashita & Il'in (2022) at $t = 10$ Gyr for compact (blue line) and porous (green line) oblate spheroidal grains (the aspect ratio $a/b = 2$).

For models with reasonable values of ΔM, we obtain IS polarization curves that are generally in agreement with those observed. Despite Hirashita & Il'in (2022) predict highly porous grains, p reaches 0.7 at the effective size $r_V \approx 0.03$ μm, but being as low as 0.2 at $r_V \sim 0.002$ μm and 0.2 μm. This does not too significantly shift the IS polarization curve maximum as can be seen in Fig. 1a.

The large values of λ_{max} obtained by us are caused by excess (in comparison to MRN) massive grains (size about 0.1–0.4 μm) that are consistently forming in evolved stars, as outlined in the scenario proposed by Hirashita & Il'in (2022). The width of the polarization curve for porous grains is found to well agree with the standard one (see Fig. 1b).

4 Conclusions

In conclusion, a spheroidal grain model has been developed to analyse the changes in the IS extinction and polarization curves during the evolution of ISM of the Galaxy. We applied the model to the findings of Hirashita & Il'in (2022), which assumed that the grain porosity depends on time and particle size. It has been shown that despite the significant porosity identified by Hirashita & Il'in (2022), their results yield IS polarization curves that generally align with the observed data.

References

Hensley B.S. and Draine B.T., 2023, Astrophysical Journal, 948, 1, id. 55
Hirashita H. and Il'in V.B., 2022, Monthly Notices of the Royal Astronomical Society, 509, 4, p. 5771
Tram L.N. and Hoang T., 2022, Frontiers in Astronomy and Space Sciences, 9, id. 923927

BAK 2024 MODERN ASTRONOMY: FROM THE EARLY UNIVERSE TO EXOPLANETS AND BLACK HOLES 300 years Russian Academy of Sciences

Grid of NLTE corrections for sulfur lines in the atmospheres of A-K stars

S. Korotin and K. Kiselev

Crimean Astrophysical Observatory of the Russian Academy of Sciences, Nauchny, 298409 Russia

Abstract. A correction grid is presented to take into account the influence of departures from local thermodynamic equilibrium on sulfur lines in the atmospheres of stars in the range of spectral classes from A to K. The correction grid was obtained using the atomic model of sulfur that takes into account the most modern atomic data on collision rates with electrons and hydrogen. The influence of NLTE effects on lines in both the optical and IR regions, including lines in the H-band, is considered. For some lines of neutral sulfur, which are practically not subject to NLTE effects, the wavelengths and oscillator strengths in the solar spectrum have been refined. The modified atomic model of sulfur, used to determine the sulfur abundance from the spectra of stars of different metallicities, has shown its reliability and adequacy. All sulfur lines are well described by similar element contents, regardless of their sensitivity to the influence of NLTE effects.

Keywords: line: formation, profiles; stars: abundances; Sun: abundances

DOI: 10.26119/VAK2024.067

1 Introduction

The sulfur abundance of stars has been of increasing interest when modeling the chemical evolution of the galaxy. There is still no consensus on the nature of the behavior of the [S/Fe] ratio on metallicity in stars with low metal abundance. A major problem in the accuracy of determining sulfur abundance is the influence of departures from LTE for S I lines. In the optical range, sulfur abundance is usually determined by three groups of lines: 6046–6052 Å (multiplet 10), 6743–6757 Å (multiplet 8) and 8694 Å (multiplet 6). In the near-infrared range, two IR triplets are used: 9212–9237 Å and 10 455–10 459Å. High-resolution IR spectrographs allow the addition of lines in the H-band to the study: 15 400–15 422 Å 15 469–15 478 Å and 22 507–22 707Å. As shown in papers of Takeda et al. (2005) and Korotin (2009), many sulfur lines are, to one degree or another, influenced by departures from LTE in stellar atmospheres. Since new atomic data concerning neutral and ionized sulfur have appeared since these calculations, we have carried out work to modernize the atomic model of sulfur by Korotin (2009) taking into account the most modern atomic data and checking it against the spectra of well-studied stars.

2 Modified atomic model of the sulfur and grid of NLTE corrections for S I lines

The modified `MULTI` software package was used for calculations. The new model of the sulfur atom includes 64 S I levels, 81 S II levels, and the main S III level (Fig. 1). Radiative photoionization rates for all levels considered were calculated using detailed photoionization cross sections from OP TopBASE. For detailed consideration 775 radiative bound-bound and 146 bound-free transitions were selected. Photoionization cross sections and oscillator strengths are taken from OP TopBASE. Unlike the 2009 model, instead of approximation formulas to take into account collision rates with electrons and hydrogen, detailed quantum mechanical calculations from the ADAS database and the work of Belyaev & Voronov (2020) were used. Modernization of the atomic model made it possible to expand the range of effective temperatures of stellar photospheres in the NLTE correction grid to $T_{\rm eff} = 10\,000$ K.

The effects of departures from LTE have different values for various S I lines. The two IR triplets experience the greatest departures. The atomic model was tested to determine the sulfur abundance of 13 stars and showed its adequacy in a wide range of fundamental stellar parameters ($T_{\rm eff}$ from 4850 K to 9600 K, $\log g$ from 2.9 to 4.5, [Fe/H] from −2.0 to +0.25). In the spectra of all test stars, the sulfur lines are described by similar abundances of the element, regardless of the degree of influence of departures from LTE on a specific spectral line.

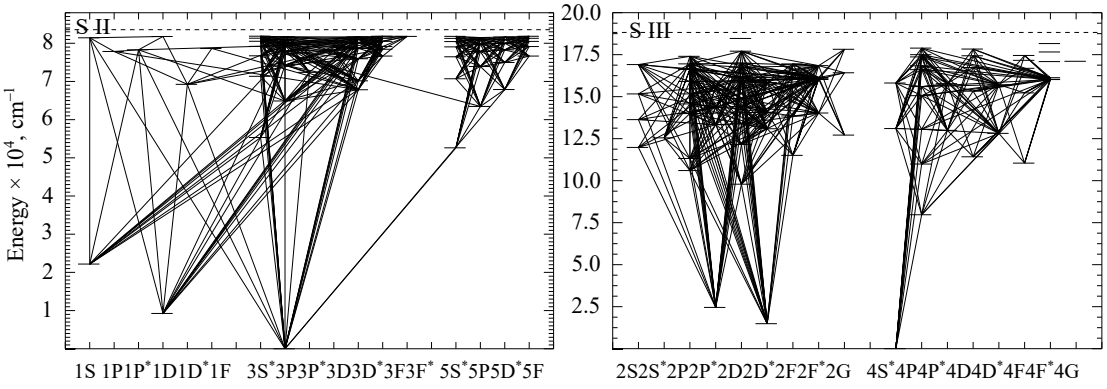

Fig. 1. The Grotrian diagram for atomic model.

The parameters of sulfur lines observed in the optical range have been determined through theoretical calculations and can vary greatly among different authors. When used to calculate a synthetic spectrum with wavelengths and oscillator strengths from the VALD or NIST databases, the lines cannot be described accurately. At the same time, NLTE effects do not influence the lines of the sixth, eighth, and tenth multiplets in the solar atmosphere. Therefore, assuming the sulfur abundance is equal to the meteorite abundance, which is confirmed by the abundance determined from IR triplets, we refined the wavelengths and oscillator strengths of the S I lines in the optical spectrum. The list of recommended sulfur lines for determining abundance is presented in Table 1.

Table 1. Parameters lines of S I.

Wavelength Å	E eV	$\log gf$	$\Gamma_{\rm vw}$	Wavelength Å	E eV	$\log gf$	$\Gamma_{\rm vw}$	Wavelength Å	E eV	$\log gf$	$\Gamma_{\rm vw}$
6052.53	7.87	−1.99	−6.55	8693.16	7.87	−1.29	−6.98	15422.20	8.70	−1.84	−7.00
6052.59	7.87	−1.15	−6.55	8693.95	7.87	−0.45	−6.98	15422.26	8.70	−0.30	−7.00
6052.69	7.87	−0.56	−6.55	8694.64	7.87	0.14	−6.98	15422.28	8.70	0.77	−7.00
6743.47	7.87	−1.24	−6.65	9212.87	6.53	0.39	−7.37	15469.82	8.05	−0.17	−6.90
6743.54	7.87	−0.88	−6.65	9228.09	6.53	0.25	−7.37	15478.48	8.05	0.06	−6.90
6743.65	7.87	−0.94	−6.65	9237.54	6.53	0.02	−7.37	22507.56	7.87	−0.48	−7.44
6748.61	7.87	−1.36	−6.65	10455.45	6.86	0.25	−7.32	22519.07	7.87	−0.25	−7.44
6748.71	7.87	−0.77	−6.65	10456.76	6.86	−0.45	−7.32	22552.57	7.87	−0.04	−7.44
6748.85	7.87	−0.56	−6.65	10459.41	6.86	0.03	−7.32	22563.83	7.87	−0.26	−7.44
6756.86	7.87	−1.71	−6.65	15400.08	8.70	0.43	−7.00	22575.39	7.87	−0.73	−7.44
6757.03	7.87	−0.86	−6.65	15403.72	8.70	−0.30	−7.00	22644.06	7.87	−0.34	−7.44
6757.18	7.87	−0.28	−6.65	15403.79	8.70	0.61	−7.00	22707.74	7.87	0.44	−7.44

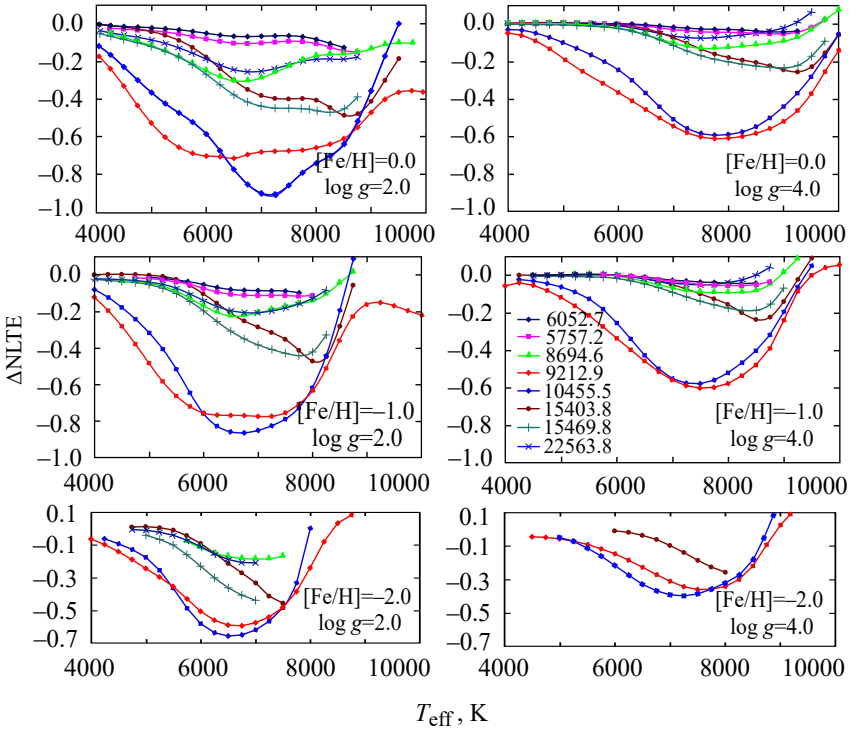

Fig. 2. The grid of non-LTE corrections for S I lines.

The grid of NLTE corrections is calculated for $T_{\rm eff}$ from 4000 K to 10 000 K, $\log g$ from 0 to 5, [Fe/H] from −2.0 to 0.0 and [S/Fe] from 0.0 to +0.8 dex at $V_t = 2$ km/s (Fig. 2). The absolute value of the corrections increases when moving from dwarf stars to giants, since the less dense atmosphere of giants reduces the influence of collisional processes. The lines of the eighth (6743–6757 Å) and tenth (6046–6052 Å) multiplets in dwarf stars have the least corrections and can be used in LTE analysis. The influence of NLTE effects on these lines is significant only for giant stars. The same conclusion can be drawn for all lines from the H-band. The lines of the sixth (8694 Å) multiplet are slightly more sensitive to departures from LTE, and the lines of two IR triplets can only be used if NLTE corrections are taken into account.

References

Belyaev A.K. and Voronov Y.V., 2020, Astrophysical Journal, 893, 1, id. 59
Korotin S.A., 2009, Astronomy Reports, 53, 7, p. 651
Takeda Y., Hashimoto O., Taguchi H., et al., 2005, Publications of the Astronomical Society of Japan, 57, p. 751

MODERN ASTRONOMY: FROM THE EARLY UNIVERSE TO EXOPLANETS AND BLACK HOLES

Interstellar polarisation towards a region around B5

H. Krayani[1,2] and V. Il'in[1,3]

[1] Saint-Petersburg University, 7-9 Universitetskaya Emb., St. Petersburg, 199034 Russia
[2] Peter the Great St. Petersburg Polytechnic University, 29 Politekhnicheskaya, St. Petersburg, 195251 Russia
[3] Central Astronomical Observatory of the Russian Academy of Sciences at Pulkovo, 65 Pulkovskoe sh., St. Petersburg, 196140 Russia

Abstract. Interstellar polarization was known to give information on the direction of galactic magnetic fields. Nowadays, the Gaia parallaxes and various photometric surveys allow the wavelength dependence of this polarization to provide even more information about the magnetic fields and dust grains. We consider the region of the interstellar medium towards the Bok globule Bernard 5 (B5, $l \approx 161°$, $b \approx -17°$). We performed a spectroscopic study of stars in this region at 0.7-m telescope of the Abastumani observatory. We carried out $UBVRI$ polarimetric observations of some of our stars at 1.25-m and 2.6-m CrAO telescopes and determined the parameters of the dependence of polarization on wavelength. Using stellar photometry and parallaxes available from recent sky surveys, we have estimated the visual extinction towards the observed stars. By analyzing the relationship between the parameters of the interstellar polarization and extinction for stars located at different distances and at different angular distances from the B5 globule, the structure and properties of the interstellar medium in the region under consideration are discussed.

Keywords: interstellar dust; polarisation; magnetic fields

DOI: 10.26119/VAK2024.068

1 Introduction

Interstellar polarization is a phenomenon associated with two components of the interstellar medium (ISM)—cosmic dust and galactic magnetic fields—that are widely studied today. Although the phenomenon was independently discovered by Hall, Hiltner and Dombrovsky about 75 years ago, observational data on it is still quite scarce, especially with respect to its wavelength dependence. Nowadays, polarization changes near star-forming regions are of particular interest. Such data become more informative due to stellar photometry and parallax measurements that are now available.

2 Observations

We spectroscopically observed the stars surrounding the B5 globule at the Abastumani Astrophysical Observatory in 1990. Based on this data, we carried out a MK spectral classification of almost 50 bright stars.

A comparison between our results and other data is presented in Fig. 1. We find general agreement in the data, but some details should be noted. The standard work of Cannon and Pickering for HD/HDE stars agrees well with our results, with the exception of the A–F stars. More recent studies, collected in the well-known Skiff catalog, better correspond to our data. Note that our classes of A stars are on average two subclasses earlier than in other works, as shown by the dashed line in Fig. 1.

We also carried out the multi-wavelength polarimetric observations of about 20 of our stars at the Crimean Astrophysical Observatory (at the ZTSh in the $UBVR$ bands and at the AZT-11 in the $UBVRI$ ones) in the 1990s.

Our data on the wavelength dependence of the polarization degree $P(\lambda)$ were approximated by the Serkowski curve. Our fitting was performed using the Levenberg–Marquardt method. For most stars we did not have good enough data to estimate all three parameters of the curve ($P_{\max}$, $\lambda_{\max}$, K) and used the mean relation $K = 1.7\,\lambda_{\max}$ to rule out the curve width parameter K.

3 Photometric spectral classification

Today, one can derive the visual extinction A_V to the stars in different ways. For some reasons, we have selected our own method. We did not fix the parallax and resulting spectral type of our stars, but considered both as free parameters.

To determine the spectral type Sp, distance d and visual extinction A_V, we varird them to find a minimum of the residual between calculated $X_n^{\rm calc}$ and observed $X_n^{\rm obs}$

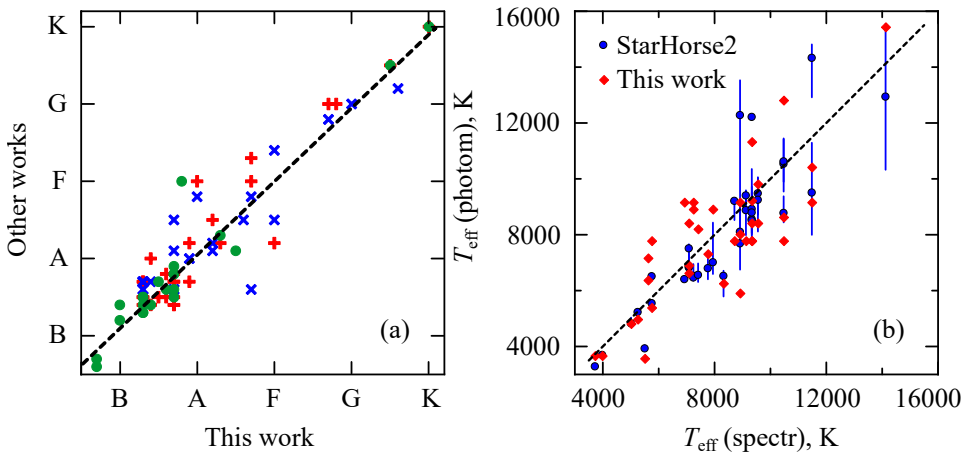

Fig. 1. A comparison of the spectral classification made in this and other works (a): (red) pluses correspond to HD/HDE, (blue) crosses of LAMOST DR7, and (green) circles for some mean classes from the Skiff catalog. A comparison of $T_{\rm eff}$ (b) derived from StarHorse2 (blue circles) and our (red rhombus) photometric classification and from spectral studies.

(with uncertainty σ_{X_n}) stellar magnitudes for $N_{\rm obs}$ bands:

$$\bar{\chi}^2 = \frac{1}{N_{\rm obs}-3}\sum_{n=1}^{N_{\rm obs}}\left(\frac{X_n^{\rm calc}({\rm Sp},A_V,d)-X_n^{\rm obs}}{\sigma_{X_n}}\right)^2. \qquad (1)$$

To calculate the stellar magnitude in an X band, we used the stellar absolute visual magnitudes, the mean intrinsic colours, and the mean galactic extinction curve as follows: $X^{\rm calc}({\rm Sp},A_V,d) = M_V({\rm Sp}) - (V-X)_0({\rm Sp}) + A_X(A_V) + 5\log(d/10)$.

We applied this classification procedure to the photometric and astrometric data available for our stars. The results of our approach were compared to the data from StarHorse2 (Anders et al. 2022). We found that the results were generally consistent, and hence our approach applied to original photometric data (more accurate than in the surveys) can be useful.

We have also compared the values of $T_{\rm eff}$ obtained from spectral and photometric classifications and noticed a larger scatter in the regions of A5–G0 stars and earlier than B9 (see Fig. 1).

4 Discussion

We use our results to consider the relations between the extinction (A_V) and polarisation ($P_{\rm max}$, $\lambda_{\rm max}$, θ) parameters and the distance d to the stars (mostly located at $d = 70$–700 pc).

We deduce that there is no significant contribution of the Perseus molecular cloud complex ($d \sim 300$ pc) assumed in some works. So, we deal mostly with the only dust layer which is related to the Taurus molecular cloud complex (TMC, $d \approx 150$ pc). We find that in this layer $A_V = 0.6$–1.4 mag, $P_{\max} = 0.9 \pm 0.4\%$ changes randomly, while the position angle $\theta = 55^\circ \pm 15^\circ$ remains almost the same with an increase of d. Wavelength of the maximum polarization is also nearly constant $\lambda_{\max} = 0.53 \pm 0.04$ μm. We have compared the results with the estimates of these parameters made in other works that considered close parts of the TMC and found a reasonable agreement.

We have also confronted the obtained relation of the polarizing efficiency $P_{\max}/A_V$ on $\lambda_{\max}$ with theoretical analysis of Voshchinnikov et al. (2016). We find that in the considered part of the TMC the dust is typical of the diffuse interstellar medium, but the magnetic field is tilted more than 45 degrees to the plane of the sky. The low polarization efficiency we achieved cannot be explained by an overestimating of A_V, since this effect can increase $P_{\max}/A_V$ less than by 1.3 times.

5 Summary

We present the results of our spectroscopic and $UBVRI$ polarimetric observations of about 40 stars in a vicinity of the B5 globule. We have also performed photometric spectral classification of the stars to estimate A_V and compared its results with the data of the spectral study and other photometric classifications (like StarHorse2).

We find that for the majority of our stars interstellar extinction and polarization are formed in a dust layer related to the Taurus molecular cloud complex at $d \approx 150$ pc. Our results allow us to evaluate the parameters of this layer: $A_V = 1.0 \pm 0.4$ mag, $P_{\max} = 0.9 \pm 0.4\%$, $\lambda_{\max} = 0.53 \pm 0.04$ μm, $\theta = 55^\circ \pm 15^\circ$. They are in a reasonable agreement with the estimates made by other authors for close fields.

We have compared the derived correlation of the polarizing efficiency $P_{\max}/A_V$ and the maximum polarization wavelength $\lambda_{\max}$ with theoretical dependencies and suggested that the magnetic field in the layer makes an angle less than 45° with l.o.s. In more detail the results will be described by Krayani & Il'in (2024).

References

Anders F., Khalatyan A., Queiroz A.B., et al., 2022, Astronomy & Astrophysics, 658, id. A91

Krayani H. and Il'in V.B., 2024, in preparation

Voshchinnikov N.V., Il'in V.B., Das H.K., 2016, Monthly Notices of the Royal Astronomical Society, 462, 3, p. 2343

MODERN ASTRONOMY: FROM THE EARLY UNIVERSE TO EXOPLANETS AND BLACK HOLES

Estimation of the dynamic masses of open star clusters

M. Kulesh and A. Seleznev

Ural Federal University, 51 Lenin Str., Ekaterinburg, 620000 Russia

Abstract. The determination of star cluster masses is crucial for the study of cluster dynamics, the evaluation of gravitational binding, and the assessment of star formation efficiency. Traditional photometric approaches face challenges such as incompleteness, the problem of evaluating the uncertainty in the mass-luminosity relation, contamination by binaries, and so on. Dynamic (virial) approaches, which provide an estimate of the total cluster mass, have a difficulty in estimating the velocity dispersion. This study proposes a method to calculate the dynamic masses by using proper motions, taking into account for their observational errors. Using modern data for open clusters and samples of their probable members, we estimate dynamic masses of 833 open clusters. The resulting dynamic mass distribution is nearly log-normal with the mode of 2400 $M_{\odot}$.

Keywords: open clusters and associations: general; stars: kinematics and dynamics; methods: statistical

DOI: 10.26119/VAK2024.069

1 Introduction

The determination of star cluster masses is critical for a variety of astrophysical applications, including the study of cluster dynamics, the evaluation of gravitational binding, and the assessment of star formation efficiency in young clusters. Traditional methods for estimating cluster masses include photometric and dynamic (or virial) approaches, each of which has its own challenges.

Photometric mass estimation relies on the cluster member list or luminosity function and a mass-luminosity relation (see for example Seleznev et al. 2017). This method, which uses theoretical isochrones, faces difficulties in evaluating the uncertainty of the mass-luminosity relation. To mitigate this, one can use isochrone tables from different authors or analytical expressions for the mass-luminosity relation (Eker et al. 2015 as an example). However, the photometric mass represents only a lower limit of the real cluster mass due to uncertainties at the lower end of the luminosity function, invisible stellar remnants, and unresolved binaries (Seleznev 2016; Borodina et al. 2021).

Dynamic mass estimation, on the other hand, depends on the velocity dispersion of the cluster stars. While this method takes all cluster stars into account, it requires an accurate determination of the velocity dispersion and the structural properties of the cluster. We use both a simple "virial" formula, and the formula that takes into account the non-stationarity of the cluster and the influence of the Galactic gravitational field (Danilov & Loktin 2015). We determine the necessary structural properties using a numerical model. In addition, when one uses the radial velocities, a contamination by single-line spectroscopic binaries can inflate the velocity dispersion, leading to an overestimation of the dynamic mass. These issues are discussed in more detail in Seleznev et al. (2017) and Kulesh et al. (2024).

Modern catalogs of star clusters include the necessary parameters necessary to estimate the dynamic masses, such as the samples of probable member stars, proper motions and their errors, distance estimates to the clusters, galactic coordinates of their centers, and estimates of the King surface density profile parameters r_t and r_c (King 1962). We use the Hunt & Reffert (2023) catalog based on the Gaia DR3 (Gaia Collaboration et al. 2023) and calculate the virial and dynamic masses from the velocity dispersion of the Gaia DR3 proper motions. In addition, this work proposes a method to account for the observational errors of the proper motions in the final velocity dispersion.

2 Data and processing

We obtained the list of clusters and their parameters from Hunt & Reffert (2023). Then we cut the list to the clusters presented in Dias et al. (2021). As a result, we get a list of 1410 clusters.

For each cluster in the list, a sample of stars with a membership probability greater than 0.5 and a Renormalised Unit Weight Error (RUWE) ≤ 1.4 has been selected. We use the selection by RUWE to exclude probable multiple stars. Then we use the 3-sigma rule for the proper motion distributions μ_α and μ_δ for each cluster sample to remove the outliers.

We then checked the normality of the proper motion distributions using the omnibus test of normality (D'Agostino 1971). After removing the clusters with p-value less than 0.05, 873 clusters remained.

We convert the proper motions μ_α and μ_δ and their errors e_{μ_α} and e_{μ_δ} into tangential velocities v_α and v_δ and their errors e_{v_α} and e_{v_δ}, using the median distance estimate to the cluster (Hunt & Reffert 2023), hereafter referred to as $dist_0$. These errors broaden the velocity distribution. We assume that both the velocity and its error distributions are Gaussian, as in our previous work (see Kulesh et al. 2024 for details). Let the dispersions of these distributions be $\sigma^2_{\mathrm{vis}|\alpha,\delta}$ and $\sigma^2_{\mathrm{err}|\alpha,\delta}$, respectively. Then the corrected dispersion is:

$$\sigma^2_{\mathrm{fix}|\alpha,\delta} = \sigma^2_{\mathrm{vis}|\alpha,\delta} - \sigma^2_{\mathrm{err}|\alpha,\delta}. \quad (1)$$

To estimate the velocity dispersion, we modify the method of Kulesh et al. (2024) and do not use the kernel density estimation for distributions and their analytic approximations, since these procedures introduce additional errors. The dispersion $\sigma^2_{\mathrm{vis}|\alpha,\delta}$ can be estimated simply as the dispersion of the sample, as in the case of the maximum likelihood method. We estimate the dispersion of the errors $\sigma^2_{\mathrm{err}|\alpha,\delta}$ as the square of the median of the error distributions e_{v_α} and e_{v_δ}, respectively. Figure 1 shows the difference between the corrected and uncorrected standard deviations of the total velocity (see below). For 40 clusters, their $\sigma_{\mathrm{err}|\alpha,\delta} > \sigma_{\mathrm{vis}|\alpha,\delta}$. In this case, eq. 1 is obviously incorrect, and we remove these clusters. The final list contains 833 clusters.

Next, we follow to the procedure described in Kulesh et al. (2024) (Section 5). We use the velocity dispersion in the tangential direction to estimate the dynamical mass. We assume that the velocity distribution in the line-of-sight direction is the same as the velocity distribution in both tangential directions, and evaluate the velocity dispersion to be $\sigma^2 = (3/2)(\sigma^2_\alpha + \sigma^2_\delta)$.

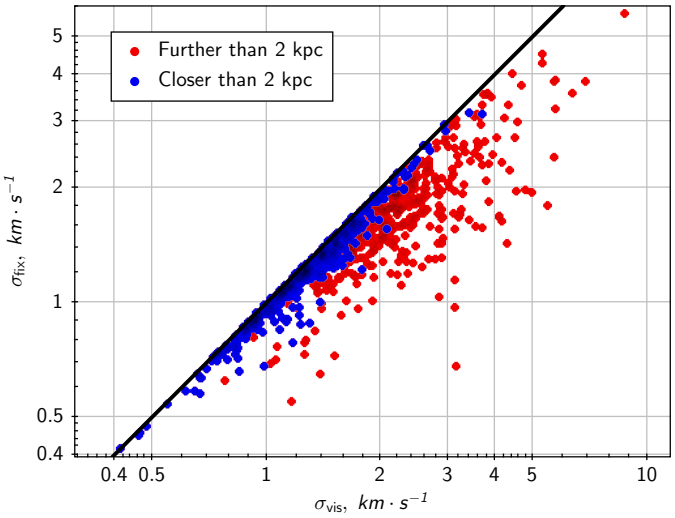

Fig. 1. The difference between the corrected $\sigma_{\rm fix}$ and uncorrected $\sigma_{\rm vis}$ standard deviations of the total velocity. Effect is more dramatic for distant clusters

We estimate the virial cluster mass using the formula:

$$M_{\rm vir} = \frac{2\sigma^2 \bar{R}}{G}, \tag{2}$$

where $\bar{R} = \langle 1/r_{ij} \rangle^{-1}$ is the mean inverse star-to-star distance, G is the gravitational constant. We estimate the cluster's dynamic mass using the formula from Danilov & Loktin (2015). This formula takes into account the gravitational field of the Galaxy and the non-stationarity of the cluster:

$$M_{\rm dyn} = \frac{2R_u\bar{R}}{G\left(\bar{R}+R_u\right)}\left(2\sigma^2 - \frac{\alpha_1+\alpha_3}{3}\left\langle r^2\right\rangle\right), \tag{3}$$

where $R_u = \langle 1/r_i \rangle^{-1}$ is the mean inverse star distance to the cluster centre, $\langle r^2 \rangle$ is the mean square of the star distance to the cluster centre, α_1 and α_3 are the field constants characterising the Galactic potential in the vicinity of the cluster (Chandrasekhar 1942). The values of α_1 and α_3 have been calculated by adopting the Galactic potential model of Kutuzov & Osipkov (1980), using the known galactic coordinates of the cluster l_0 and b_0, together with the known distance to the cluster $dist_0$ and the distance from the Galactic centre to the Sun $R_\odot = 8200$ pc.

The estimates of the King profile parameters r_c and r_t given in Hunt & Reffert (2023) allow us to immediately obtain the analytical form of the probability distribution of stars in the cluster as a function of distance from the cluster centre, following

to the spatial density profile derived in King (1962):

$$\rho(r) \sim \left(\frac{r}{z}\right)^2 \left(\frac{\arccos z}{z} - \sqrt{1-z^2}\right), \quad z = \sqrt{\frac{r_c^2 + r^2}{r_c^2 + r_t^2}}.$$

This allows for simple Monte Carlo modeling via rejection-acceptance sampling and estimation of R_u, $\bar{R}$ and $\langle r^2 \rangle$. The modeling was run 20 times for each sample to estimate the spread of the parameters.

Finally, the resulting virial and dynamic masses were calculated using eq. 2 and eq. 3 with the corrected σ^2_{fix} dispersion of the total velocity.

3 Results

The resulting distribution of M_{dyn} for all clusters in the list is shown in Fig. 2, left. This distribution is almost log-normal with the mode at about 2400 $M_\odot$.

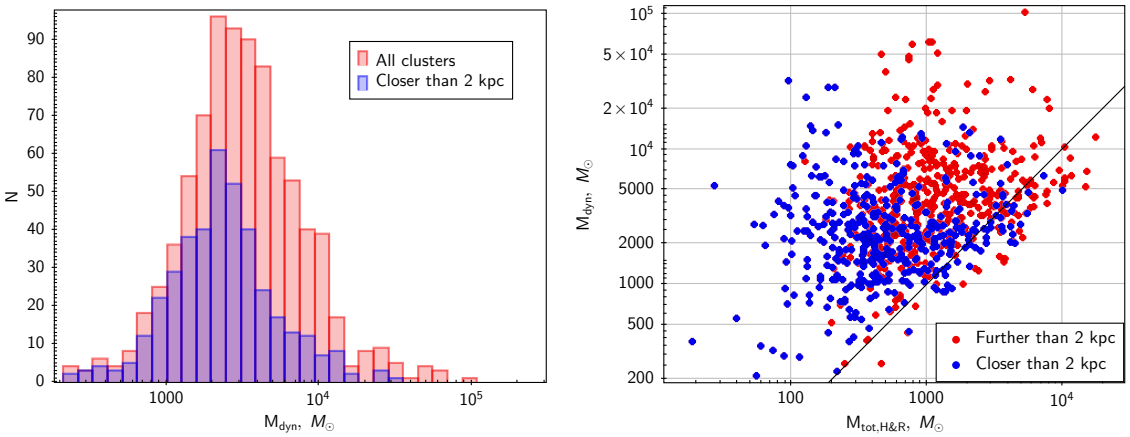

Fig. 2. (Left): Dynamic mass distribution of open clusters is nearly log-normal (with p-value < 0.01 for clusters closer than 2 kpc) with mode at 2400 $M_\odot$ (Right): Relation of M_{dyn} to M_{tot} of the same cluster from Hunt & Reffert (2024); correlation is weak (0.3) and the dynamic masses are systematically greater

We compare our results with the final version of the open cluster catalogue of Hunt & Reffert (2024) (see Fig. 2, right). Their mass distribution is also log-normal too, but with the mode of about 340 $M_\odot$.

M_{tot} from Hunt & Reffert (2024) are systematically less than M_{dyn}. We intend to further analyze this difference in detail.

Acknowledgements. This work has used of data from the European Space Agency (ESA) mission Gaia, processed by the Gaia Data Processing and Analysis Consortium (DPAC). Funding for the DPAC has been provided by national institutions, in particular those participating in the Gaia Multilateral Agreement. This work used of the open source TOPCAT package (Taylor 2005).

Funding

The work of M.V.Kulesh and A.F.Seleznev was supported by the Ministry of Science and Higher Education of the Russian Federation under agreement FEUZ-2023-0019.

References

Borodina O., Carraro G., Seleznev A., and Danilov V., 2021, Astrophysical Journal, 908, p. 60
Chandrasekhar S., 1942, Principles of stellar dynamics, The University of Chicago press
D'Agostino R., 1971, Biometrika, 58, p. 341
Danilov V. and Loktin A., 2015, Astrophysical Bulletin, 70, p. 414
Dias W., Monteiro H., Moitinho A., et al., 2021, Monthly Notices of the Royal Astronomical Society, 504, p. 356
Eker Z., Soydugan F., Soydugan E., et al., 2015, Astronomical Journal, 149, p. 131
Gaia Collaboration, Vallenari A., Brown A., et al., 2023, Astronomy & Astrophysics, 674, id. A1
Hunt E. and Reffert S., 2023, Astronomy & Astrophysics, 673, id. A114
Hunt E. and Reffert S., 2024, Astronomy & Astrophysics, 686, id. A42
King I., 1962, Astronomical Journal, 67, p. 471
Kulesh M., Samirkhanova A., Carraro G., et al., 2024, Astronomical Journal, 167, p. 212
Kutuzov S. and Osipkov L., 1980, Soviet Astronomy, 24, p. 17
Seleznev A., 2016, Monthly Notices of the Royal Astronomical Society, 456, p. 3757
Seleznev A., Carraro G., Capuzzo-Dolcetta, R., et al., 2017, Monthly Notices of the Royal Astronomical Society, 467, p. 2517
Taylor M., 2005, ASP Conf. Ser., 347, p. 29

MODERN ASTRONOMY: FROM THE EARLY UNIVERSE TO EXOPLANETS AND BLACK HOLES

Empirical isochrones for single and binary stars in open clusters

V. Mikhnevich[1], A. Plotnikova[2], A. Seleznev[1], and G. Carraro[2]

[1] Ural Federal University, 51 Lenin Str., Ekaterinburg, 620000 Russia
[2] Dipartimento di Fisica e Astronomia, Universit'a di Padova, Vicolo Osservatorio 3, Padova, I-35122 Italy

Abstract. We compose systems of empirical isochrones for single and binary stars with various components' mass ratio $q = M_2/M_1$ (M_2 – mass of the secondary component, M_1 – mass of the primary component) in order to search for unresolved binaries and multiple stars in open star clusters. We fit an empirical isochrone for single stars across the main sequence (MS) elements assigned using the HDBSCAN algorithm. Isochrones for binaries are obtained by shifting this empirical isochrone to values determined using PARSEC theoretical isochrones. We determine the parameter q for each source that lies within the corresponding intervals between the binary isochrones. We then plot a probability density distribution of the component mass ratio q and estimate the fraction of binaries in the cluster. This work is focuses on the study of close open star clusters with heliocentric distances less than 200 pc. We consider the color-magnitude diagrams (CMDs) in the Gaia photometric system and the two-index diagrams (TIDs) composed of bands in the visible and infrared wavelengths.

Keywords: open clusters and associations: general; binaries (including multiple): close

DOI: 10.26119/VAK2024.070

1 Introduction

Multicolor photometry is currently the most efficient way to detect and classify unresolved binaries in stellar clusters. Malofeeva et al. (2022, 2023) proposed the new method for estimating the fraction of unresolved binaries and higher multiplicity systems, where the two-index photometric diagram was introduced. The advantage of the used (H-W2)-W1 vs W2-(BP-K) color combination is that in this diagram binary stars are more clearly distinguished from single stars even for small values of the components' mass ratio q. This is due to the fact that in the near infrared a binary star has a flux excess compared to a single star of the same mass as the primary component.

The method has got some problems. One is the ability to study the sources only in a relatively narrow range of primary component masses. This is due to the fact that in the high-mass range the theoretical isochrones for single stars, binary stars, and multiple systems nearly coincide in this diagram. In addition, the theoretical isochrones do not follow to the cluster sequence well over its entire length, especially in the region of the low-mass sources. To solve this problem, we propose to obtain the empirical isochrones individually for each cluster.

2 Empirical Isochrones and Unresolved Binary Star Fraction

To consider the problem of the unresolved binary star fraction, one should have the samples of the probable cluster members. We use the catalog of Hunt & Reffert (2023), compiled on the base of the Gaia Data Release 3 (Gaia Collaboration et al. 2023). It contains the latest and most complete data. To implement the approach of Malofeeva et al. (2022, 2023) we also need to match these samples with the 2MASS and WISE catalogs (Skrutskie et al. 2006; Wright et al. 2010).

Each cluster has a concentration of stars along the main sequence (MS) in both CMD and TID, provided that there are enough stars in the cluster. In general, we assume that this concentration along the main sequence contains only single stars, while unresolved binaries are deviated. To assign the single MS stars in the diagram, we use the HDBSCAN algorithm. In the first step we usually observe the peculiarities among the assigned points, even after filtering the points using the membership probability of $> 50\,\%$ in the TID case. Therefore, to reduce the peculiarities, we remove the outliers after the first approximation of the sample of single MS stars by a polynomial, using the distance from the point to the polynomial as a measure of a deviation. Then we conduct the second fit with new cleaned sample, and this last fit we call the empirical isochrone for the single stars of the cluster.

Isochrones for unresolved binary systems of a certain q are computed by shifting the empirical isochrone for single stars by the values specified for each cluster. These values are the average distances between the PARSEC theoretical isochrone (Bressan et al. 2012) for single stars and the theoretical isochrones for binary stars with different q in several parts of the MS (Fig. 1). We plot the theoretical isochrones for binary stars using the theoretical isochrone for single stars and a simple relationship for unresolved binary star magnitude derived from Pogson's formula (see this relationship in Malofeeva et al. 2022). We take the fundamental star cluster parameters for theoretical isochrones from the catalog of Dias et al. (2021).

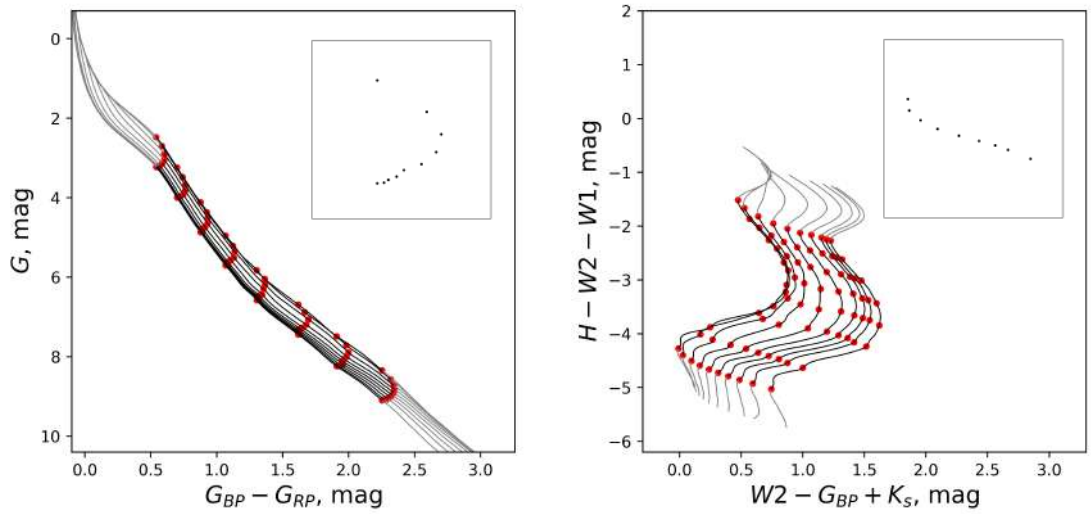

Fig. 1. An illustration of our method for determining the shift values for the empirical isochrones of binary stars. Left: PARSEC theoretical isochrones for single stars and binary stars with different q in CMD. Right: the same for TID. We use the red dots to determine the average shift values for the empirical isochrones of binary stars. These average shift values are shown in small frames with a larger scale.

Diagrams for Melotte 22 (Pleiades) with the empirical isochrones are presented in the top line of Fig. 2. We count the number of sources in the intervals between the isochrones for binary stars and calculate the specific value of the q parameter for each source. Then we use the kernel density estimator (KDE) with the Gaussian kernel to plot the distribution of the component mass ratio q. To estimate the distribution for binaries, we subtract the distribution for sources assigned as single

stars by HDBSCAN from the distribution calculated from all data in a particular mass interval (the bottom line of Fig. 2). To consider the dispersion of stars at both sides of the empirical isochrone for single stars, we should introduce the "negative" q values. All distributions for binary stars have a maximum, as noted in Malofeeva et al. (2023). The mode ranges from 0.71 to 0.80 in the Gaia CMD. In the TID we observe a tendency towards a bimodal distribution with a minimum at $q \approx 0.4$. The fraction of binary stars in the cluster is extracted from the distribution by integrating it with the Simpson method. The results are shown in Table 1.

Table 1. The respective primary component mass intervals and fractions of binary stars for seven star clusters. The first column contains the names of the clusters in Hunt & Reffert (2023). Columns 2 and 3 contain the minimum and maximum primary component masses, implemented in this work. The last two columns contain a binary stars fraction estimated in TID (α_1) and in Gaia CMD (α_2).

cluster	$M_{\min}$	$M_{\max}$	α_1	α_2
IC 2391	0.15	1.55	0.17 ± 0.02	0.19 ± 0.09
IC 2602	0.18	2.27	0.07 ± 0.04	0.1 ± 0.09
Melotte 20	0.22	2.12	0.32 ± 0.04	0.15 ± 0.08
Melotte 22	0.15	1.46	0.22 ± 0.04	0.16 ± 0.07
Melotte 25	0.11	1.76	0.32 ± 0.05	0.23 ± 0.07
NGC 2451A	0.17	1.52	0.11 ± 0.07	0.25 ± 0.08
NGC 2632	0.26	1.78	0.15 ± 0.07	0.15 ± 0.08

3 Summary

In this study we present a new approach to the problem of detecting the unresolved binary stars in the open clusters using multi-color photometry. The introduction of empirical isochrones allows us to achieve a number of advantages:

1. More confident alignment of an isochrone to the main sequence.
2. Exploitation of the Malofeeva et al. (2023) method in a wider range of a primary component mass in the region of low-mass sources.

But this new approach also has the difficulty that the clustering algorithm is not able to distinguish the main sequence condensation (that is, single stars) if the star cluster contains relatively few members or the diagram looks loose.

The results for the binary star fraction show that Malofeeva et al. (2023) tends to overestimate these parameters.

Acknowledgements. This work has been done with data
– from the European Space Agency (ESA) mission *Gaia* (https://www.cosmos.esa.int/gaia), processed by the *Gaia* Data Processing and Analysis Consortium

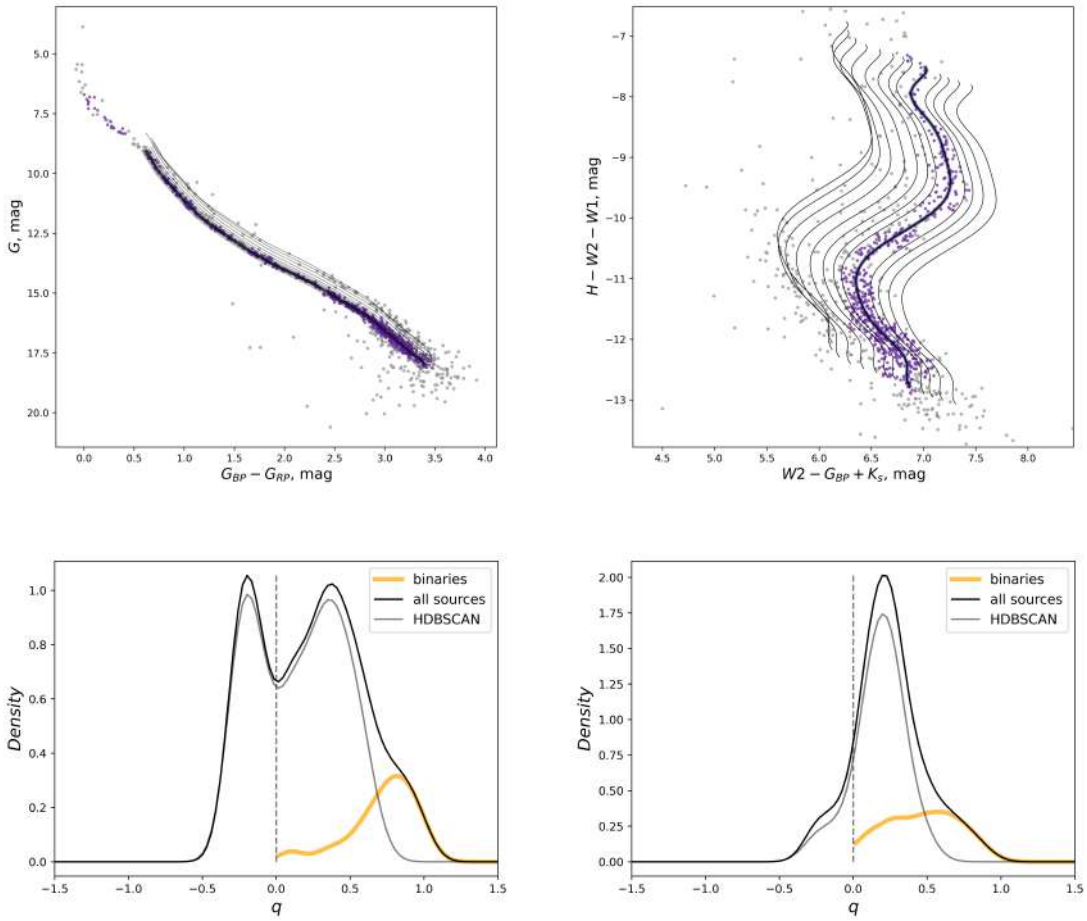

Fig. 2. Top line. Diagrams for Melotte 22. The purple dots indicate HDBSCAN assigned sources (single stars). The thick dark-blue line indicates the empirical isochrone and the thin black lines indicate the empirical isochrones of the binaries. **Bottom line**. The distribution of the component mass ratio q (thick orange line), represented as the subtraction of the distribution for single sources from the distribution for all sources of the cluster in a particular mass interval (see table 1).

(DPAC, https://www.cosmos.esa.int/web/gaia/dpac/consortium). The DPAC is funded by national institutions, in particular those participating in the *Gaia* Multilateral Agreement.

– from the Two Micron All Sky Survey, a joint project of the University of Massachusetts and the Infrared Processing and Analysis Center/California Institute of Technology, funded by the National Aeronautics and Space Administration and the National Science Foundation.
– from the Wide-field Infrared Survey Explorer, a joint project of the University of California, Los Angeles, and the Jet Propulsion Laboratory/California Institute of Technology, and NEOWISE, a project of the Jet Propulsion Laboratory/California Institute of Technology. WISE and NEOWISE are funded by the National Aeronautics and Space Administration.

Funding

This work was supported by the Ministry of Science and Higher Education of the Russian Federation under the agreement FEUZ-2023-0019.

References

Bressan A., Marigo P., Girardi L., et al., 2012, Monthly Notices of the Royal Astronomical Society, 427, p. 127

Dias W., Monteiro H., Moitinho A., et al., 2021, Monthly Notices of the Royal Astronomical Society, 504, p. 356

Gaia Collaboration, Vallenari A., Brown A., et al., 2023, Astronomy and Astrophysics, 674, id. A1

Hunt E. and Reffert S., 2023, Astronomy and Astrophysics, 673, id. A114

Malofeeva A., Mikhnevich V., Carraro G., and Seleznev A., 2023, Astronomical Journal, 165, p. 45

Malofeeva A., Seleznev A., and Carraro G., 2022, Astronomical Journal, 163, p. 113

Skrutskie M., Cutri R., Stiening R., et al., 2006, Astronomical Journal, 131, p. 1163

Wright E., Eisenhardt P., Mainzer A., et al., 2010, Astronomical Journal, 140, p. 1868

MODERN ASTRONOMY: FROM THE EARLY UNIVERSE TO EXOPLANETS AND BLACK HOLES

Investigation of polarized and photometric radiation of a star γ Cassiopeiae

D. Mokshin

Saint-Petersburg University, 28 Universitetsky Pr., St. Petersburg, 198504 Russia

Abstract. The study of Be stars, characterized by emission lines and rotational velocities close to critical, has long been of interest to astrophysicists. These stars are distinguished by the presence of an equatorial disk, the formation mechanism of which remains unknown. To date, no magnetic field has been detected in any of these stars. The nature of the formation of Be star disks and their magnetism is still not well understood, and explaining them is one of the most urgent and complex problems in modern astrophysics. The star γ Cassiopeiae (γ Cas) is a prominent representative of the small group of Be stars, which have increased X-ray luminosity, corresponding to abnormally high plasma temperatures. This study presents the results of a comprehensive study of the magnetic field of γ Cas using archival spectropolarimetric observations obtained with the Main Stellar Spectrograph (MSS) at the 6-m telescope BTA. The results of processing spectropolarimetric observations collected over several years made it possible to estimate the rms field of the star $B_{\rm rms} = 109 \pm 72$ G. The obtained data does not indicate the detection of global magnetic field. We assume that active regions associated with the star's local magnetic fields may be located on the surface of the star. Further research is needed to confirm this result.

Keywords: stars: emission-line, Be, magnetic field; individual: γ Cas

DOI: 10.26119/VAK2024.071

1 Introduction

Among the stars of spectral class B, there are those with emission lines and rotation speeds close to the critical limit. These objects are known as classical Be stars. Another important feature of these stars is the presence of a circumstellar disk. The nature of its formation remains unknown to this day. It is detected by the presence of hydrogen emission lines in the spectra of Be stars, and sometimes lines from other elements as well.

Emission lines are often double-peaked, and their shape depends on the structure of the disk and the physical conditions within it. The optical and X-ray spectra, as well as the luminosity of Be stars, exhibit variability on short timescales. Additionally, the disks are unstable, as evidenced by the rapid variation of emission line profiles in the optical range, including complete disappearance.

Stars of spectral class B have been found to possess strong magnetic fields in about 10% of cases. However, despite extensive spectropolarimetric studies of Be stars, none have been found to exhibit a magnetic field. Notably, Hubrig et al. (2017) results indicate that a magnetic field was measured at the level of 3–4σ for the star λ Eri, but this result requires independent confirmation. The search for magnetic field in Be stars is important, because many disk formation models require the presence of a magnetic field in Be stars (for example, Brown et al. 2008).

2 General information about the star

Among Be stars, a distinct group known as γ Cas analogs can be identified, which exhibit the most pronounced unusual properties of Be stars compared to B stars. Additionally, these stars display X-ray luminosity that is 1 to 2 orders of magnitude higher than that of classical Be stars, and the temperature of the plasma emitting in the X-ray range is anomalously high ($kT \sim 5$–30 keV).

The history of γ Cas-type stars dates back to 1866, when the spectrum of the star γ Cas itself was studied by Secchi (1866). This was the first star in which emission lines were discovered. In 1976, X-ray emission in the 2–11 keV range was detected from the SAS-3 X-ray satellite (Jernigan 1976; Bradt et al. 1977).

Güdel & Nazé (2009) presented the main characteristics of the spectrum of γ Cas. This star is a brighter X-ray source than typical Be stars, yet it is 1.5 orders of magnitude weaker than massive X-ray binaries with Be components. The X-ray spectrum itself exhibits a thermal nature characteristic of hot multicomponent plasma, with temperatures reaching up to 12 keV.

The parameters of the components of the γ Cas system, according to the literature and obtained in the present work, are presented in Table 1.

The luminosity L is estimated from its U, B, and V magnitudes using the relations provided by Nieva (2013). The correction factor A_V for interstellar extinction in the V filter is calculated using the dustmap library (Green 2018). The radius of the star is estimated using the Stefan–Boltzmann formula, employing the determined values of L and $T_{\rm eff}$. The mass and age of the star have been assessed based on evolutionary tracks and isochrones, respectively, constructed using the `PARSEC` code (Bagnulo et al. 2002).

Table 1. Parameters of γ Cas A.

Parameter	Value	Reference
Spectral type	B0.5 IVe	Borre et al. (2020)
m_V, mag	2.39	SIMBAD
$T_{\rm eff}$, kK	28	Smith et al. (2016b)
R, $R_\odot$	5.2	Present work
$\log g$	3.32	Chauville et al. (2001)
$\log L/L_\odot$	4.18	Present work
M, $M_\odot$	13	Smith (2019)
d, pc	117	Megier et al. (2009)
Age τ, Myr	1.6	Present work

From a statistical perspective, only 1% of Be stars exhibit properties similar to those of γ Cas. Currently, a total of 25 γ Cas-type stars and two candidates are known (Smith et al. 2016a; Nazé & Motch 2018; Nazé et al. 2020, 2022).

The criteria for identifying γ Cas-type stars are formulated by Nazé & Motch (2018). This group is characterized by high X-ray luminosity $\log L_X(0.5\text{–}10\,\text{keV}) = 31.6\text{–}33.2$, and their spectra are defined by hardness ratios $HR \gtrsim 1.6$, where HR is the ratio of fluxes in the hard (2–10 keV) and soft (0.5–2 keV) X-ray bands. Such hardness corresponds to anomalously high plasma temperatures.

3 Observations

This study investigates the magnetism of the star γ Cas. The analysis is based on archival spectropolarimetric observations obtained at the Main Stellar Spectrograph (MSS). A total of 144 spectra in the wavelength range of 4400–4900 Å are utilized: 73 spectra were acquired on November 4, 2020, 69 spectra were obtained on January 2–3, 2021, and two spectra were collected on May 30, 2021.

4 Magnetic field measurements of γ Cas

To estimate the stellar magnetic field we used the archival spectropolarimetric observations, and employed three methods: Least Squares Deconvolution (LSD) (Donati

et al. 1997), the modified differential method (MDM) (Kholtygin 2014) and the differential method (DM) (Bagnulo et al. 2002).

In the LSD method, a single mask is employed that includes 20 spectral lines. The mask is constructed based on the atomic database VALD3, with the latest implementation described by Pakhomov et al. (2017). For the modified differential method (MDM), a mask containing 12 lines was used. In this case, unblended lines with symmetric profiles were selected.

Figures 1, 2 present the results of the magnetic field measurements of γ Cas using the LSD method for November 4, 2020, and January 2–3, 2021, as a function of time.

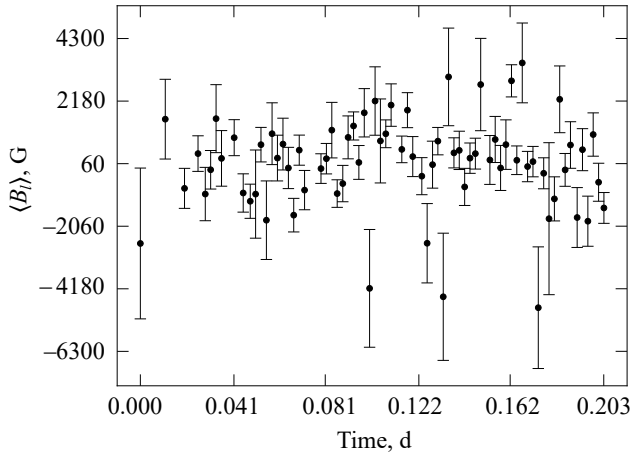

Fig. 1. The measured values of B_l, the longitudinal component of the magnetic field γ Cas, obtained from the analysis of LSD profiles as a function of time (in fractions of a day) from the beginning of observations on different days. The figure displays the measured values for November 4, 2020.

For all measured values of B_l obtained using different methods, the root-mean-square magnetic field $B_{\rm rms}$ is calculated using eq. (1).

$$B_{\rm rms} = \sqrt{\frac{1}{n}\sum_{i=1}^{n}(\langle B_l^i\rangle)^2}. \qquad (1)$$

As a result, the magnetic field $B_{\rm rms}$ values were obtained by three measurement methods. The application of the modified differential (MDM) and differential (DM) methods yields slightly different results from LSD method:

LSD: $B_{\rm rms} = 1384 \pm 809$ G; MDM: $B_{\rm rms} = 900 \pm 425$ G; DM: $B_{\rm rms} = 109 \pm 72$ G.

It is evident that the magnetic field exhibits only minor deviations from the mean value on different dates. However, the measurement of the magnetic field using three

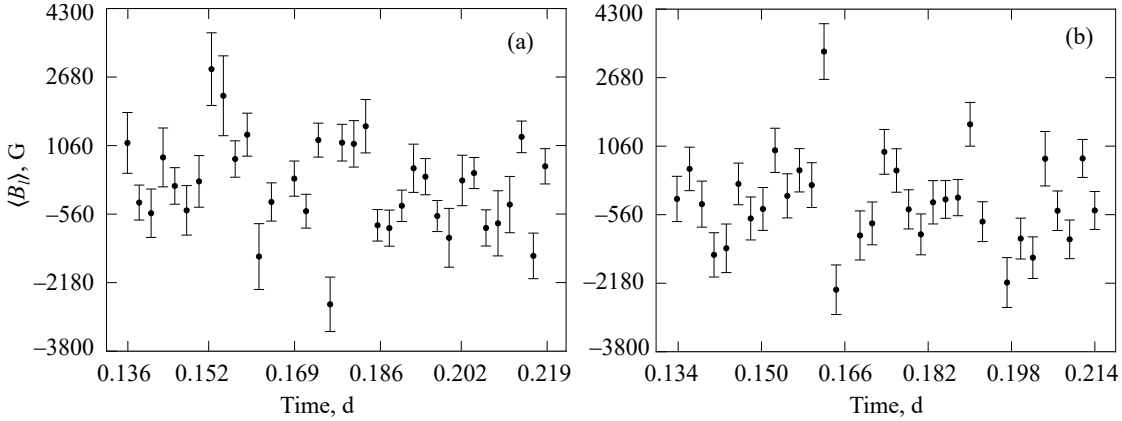

Fig. 2. The measured values of B_l, the longitudinal component of the magnetic field γ Cas, obtained from the analysis of LSD profiles as a function of time (in fractions of a day) from the beginning of observations on different days. Panel (a) for January 2, 2021, and panel (b) for January 3, 2021.

distinct methods yielded varying results. Due to the magnitude of the errors, these field values represent only upper limits for the magnetic field. Furthermore, there is no evidence to suggest that the obtained field values are associated with a global magnetic field of γ Cas.

5 Summary

As a result of the analysis of spectropolarimetric observations of γ Cas, based on 144 archival spectra using three different methods, three distinct estimates of the magnetic field were obtained. The most precise value obtained is $B_{\rm rms} = 109 \pm 72$ G, which can be considered an upper limit for the global magnetic field. Consequently, an upper limit for the magnetic field at the poles of the star can be inferred as $B_p \approx 550$ G.

Funding

Present work was carried out with the support of the Russian Science Foundation project No. 23-22-00090.

References

Bagnulo S., Szeifert T., Mathys G., et al., 2002, ASP Conference Proceedings, 274, p. 610
Borre C.C., Baade D., Pigulski A., et al., 2020, Astronomy & Astrophysics, 635, id. A140

Bradt H.V., Apparao K.M.V., Clark G.W., et al., 1977, Nature, 269, 5623, p. 21
Brown J.C., Cassinelli J.P., Maheswaran M., 2008, Astrophysical Journal, 688, 2, p. 1320
Chauville J., Zorec J., Ballereau D., et al., 2001, Astronomy & Astrophysics, 378, p. 861
Donati J.-F., Semel M., Carter B.D., et al., 1997, Monthly Notices of the Royal Astronomical Society, 291, 4, p. 658
Green G.M., 2018, Journal of Open Source Software, 3, 26, p. 695
Güdel M. and Nazé Y., 2009, Astronomy and Astrophysics Review, 17, 3, p. 309
Hubrig S., Ilyin I., Kholtygin A.F., et al., 2017, Astronomische Nachrichten, 338, 8, p. 926
Jernigan J.G., 1976, International Astronomical Union Circulars, 2900, p. 2
Kholtygin A.F., 2014, Astronomische Nachrichten, 335, 10, p.1049
Megier A., Strobel A., Galazutdinov G.A., et al., 2009, Astronomy & Astrophysics, 507, 2, pp.833
Nazé Y. and Motch C., 2018, Astronomy & Astrophysics, 619, id. A148
Nazé Y., Motch C., Rauw G., et al., 2020, Monthly Notices of the Royal Astronomical Society, 493, 2, p. 2511
Nazé Y., Rauw G., Smith M., et al., 2022, Monthly Notices of the Royal Astronomical Society, 516, 3, p. 3366
Nieva M.-F., 2013, Astronomy & Astrophysics, 550, id. A26
Pakhomov Yu., Piskunov N., Ryabchikova T., 2017, ASP Conf. Ser., 510, p. 518
Secchi A., 1866, Astronomische Nachrichten, 68, p. 63
Smith M.A., Lopes de Oliveira R., Motch C., 2016a, ASP Conf. Ser., 506, p. 299
Smith M.A., Lopes de Oliveira R., Motch C., 2016b, Advances in Space Research, 58, 5, p. 782
Smith M.A., 2019, Publications of the Astronomical Society of the Pacific, 131, 998, p. 044201

MODERN ASTRONOMY: FROM THE EARLY UNIVERSE TO EXOPLANETS AND BLACK HOLES

Determination of the dwarf novae parameters and their temporal changes

E. Motorina[1], V. Shimansky[2], A. Dudnik[1], and N. Borisov[2]

[1] Kazan Federal University, 18 Kremlyovskaya, Kazan, 420008 Russia
[2] Special Astrophysical Observatory of the Russian Academy of Sciences, Nizhny Arkhyz, 369167 Russia

Abstract. We present the development of a method for determining dwarf novae parameters and their temporal changes from the analysis of observations for several times. Using the modeling method of H I lines in the optical spectra of dwarf novae with high-temperature white dwarfs leads to large errors in the measured parameters. Therefore, the idea of using observations for several times was proposed, which will allow to determine the parameters of the system with greater accuracy. The dwarf novae FL Psc, which belongs to the WZ Sge type, was chosen as a test object. Its spectroscopic observations were carried out in 2021 and 2023 years by the 6-m BTA telescope. According to the light curve from the ZTF archive, in 2021 FL Psc was in a quiescent state, and in 2023 observations were made at the final s tage FL P sc of relaxation to the pre-outburst level. The values of white dwarf temperature in both times of observations were obtained using the requirement of the invariability of the gravity value on its surface. However, similar temperature values in both times of observations differ f rom t he l iterature p redictions o n t he t emperature i ncrease o f a white dwarf after a superoutburst.

Keywords: methods: numerical; stars: dwarf novae, fundamental parameters; individual: FL Psc

DOI: 10.26119/VAK2024.072

1 Introduction

Cataclysmic variables are close binary systems consisting of a white dwarf and a low–mass main sequence star that fills its Roche lobe. Dwarf novae belong to cataclysmic variables with a disk form of accretion. SU UMa-type systems are a subclass of dwarf novae that demonstrate ordinary outbursts with the brightness amplitudes of $\Delta m = 2^{\rm m}$–$5^{\rm m}$ and the durations of a few days, as well as superoutbursts with the amplitudes of $\Delta m > 8^{\rm m}$ (Smith 2006). A junior subclass of SU UMa-type dwarf novae are WZ Sge-type dwarf novae, which exhibit only superoutbursts with the amplitudes up to $\Delta m = 9^{\rm m}$ with a long relaxation period to the quiescence (Kato 2015). Determining the parameters of white dwarfs which are a part of cataclysmic variables gets complicated by the predominance of radiation from the accretion disk and flowing matter from the secondary in the optical spectrum. Therefore, it is impossible to apply standard methods for determining the effective temperature and surface gravity of a white dwarf based on modeling of H I profiles. Mitrofanova et al. (2014) analysed the optical spectra of a dwarf novae of WZ Sge-type GSC 02197-00886. In this paper it was shown that the system in quiescence exhibits an optically thin accretion disc and the continuum is dominated by white dwarf radiation. Therefore, the authors made an assumption about the possibility of directly determining the parameters of white dwarfs using the H I absorption line modeling method. The method was implemented in the work of Dudnik et al. (2023), in which a model analysis of the optical spectra of three dwarf novae was performed. The described approach allows us to obtain the most correct assessment of the accuracy of the obtained parameters. According to the results of Dudnik et al. (2023), the method most optimally describes the observed spectra of dwarf novae with the medium-temperature white dwarfs. If the system contained a high-temperature white dwarf, then the error range was large. Therefore, to solve the described problem, the idea of performing the specified model spectrum analysis for several times of observations was put forward. Using this approach will significantly improve the accuracy of determining the obtained parameters of the observed systems.

2 Observations

FL Psc was discovered in the Automatic Sky Survey (ASAS) as a variable object called ASAS 002511+1217.2. Based on the spectrometric and photometric studies, FL Psc was assigned as a dwarf star of the WZ Sge-type, and the orbital period of the system was estimated as $P_{\rm orb} = 81.59 \pm 0.05$ min (Templeton et al. 2006). The brightness increase during the superoutburst was $\Delta m = 7^{\rm m}$, and the maximum interval between the superoutbursts was estimated to be 66 years. The current study

used the observational data that were obtained at the 6-m BTA telescope by the SCORPIO-1 (Afanasiev & Moiseev 2005) on the nights of August 16–17, 2021 and October 21–22, 2023. According to the type of observed spectra FL Psc can be attributed to dwarf novae in a quiescence with a predominance of continuous radiation from a white dwarf and emission lines of an optically thin accretion disk superimposed on its continuum. The normalisation was carried out iteratively by comparing the observed spectrum with the model spectrum of the white dwarf with the parameters obtained from the previous analysis, taking into account the mask, excluding the regions distorted by emissions. Varying the mask boundaries allowed us to establish the optimal parameters of the mask boundaries, which ensured the stability of the determined parameters over the widest possible range of the analyzed spectrum (Fig. 1). The mask parameters were the same for the 2021 and 2023 observations.

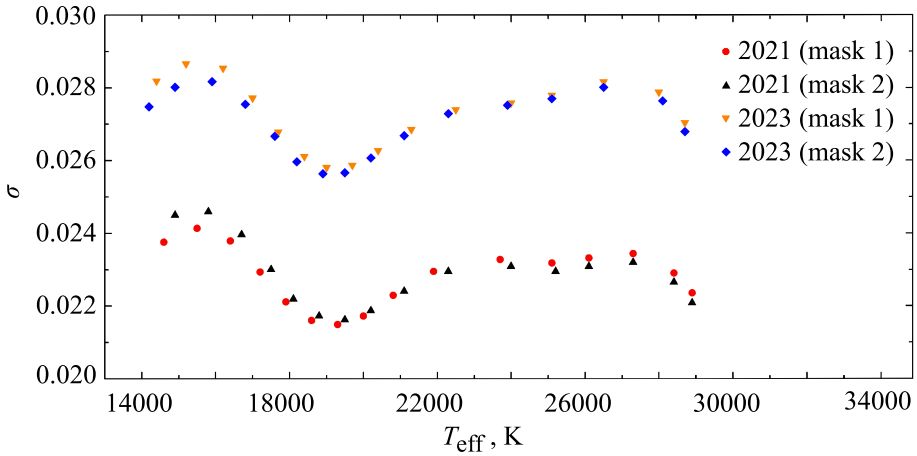

Fig. 1. $\sigma(T_{\rm eff})$ distributions at fixed $\log g$ for FL Psc observations in 2021 and 2023 with different masks.

3 Modeling of optical spectra and determination of white dwarfs atmospheric parameters

Dwarf novae FL Psc turned out to be a good choice for the object: according to the ZTF (Masci et al. 2019) data during the observation period in August 2021, the system was in a quiescence, in May 2023, there was an outburst in the system with the amplitude of $\Delta m \approx 3^{\rm m}$, and at the time of observations in October 2023, the system was at the stage of medium or late relaxation. The method of automatic

analysis and determination of fundamental parameters performed for observations in 2021 and 2023 is completely identical to the method implemented in the work of Dudnik et al. (2023). When analysing the distributions obtained for the 2021 and 2023 observation time, numerical parameters of the atmospheric models of white dwarfs $T_{\rm eff}$ and $\log g$ were obtained, which corresponded to the global minima of the distributions σ (Fig. 1). In the current work, the errors $\log g$ are set as the difference between the obtained optimal values for the observation times of 2021 and 2023. Errors in all other parameters are calculated from the $\log g$ error defined in the specified way. To estimate the mass M_1 and radius R_1 of a white dwarf, a dependence of temperature–mass–radius was used for white dwarfs with a predominance of various chemical elements in the core, taken from the work of Panei et al. (2000). To find the fundamental parameters of the secondary, we simultaneously used the theoretical mass–radius relations for brown (Baraffe et al. 2003) and red (Girardi et al. 2000) dwarfs and the equation from Eggleton (1983). The calculations also used the assumption of Kolbin et al. (2022) about the excess of the radius of the Roche lobe of a cold star over its model radius at the level of 5%, which is due to various factors. The resulting parameters are presented in Table 1. The comparison of the observed spectra with the theoretical ones is shown in Fig. 2.

Table 1. The final values of the parameters. The 2013 data were obtained in the work of Dudnik et al. (2023) and are given for comparison.

Observation	2021	2023	2013
$T_{\rm eff}$, K	19200 ± 1900	19100 ± 2000	22300 ± 1800
$\log g$	8.09 ± 0.25	8.14 ± 0.27	8.14 ± 0.14
M_1, $M_\odot$	0.67 ± 0.16	0.69 ± 0.17	0.70 ± 0.07
R_1, $R_\odot$	0.0122 ± 0.0019	0.0117 ± 0.0021	0.0118 ± 0.0010
M_2, $M_\odot$	0.132 ± 0.010	0.132 ± 0.010	0.114 ± 0.005
R_2, $R_\odot$	0.152 ± 0.011	0.152 ± 0.011	0.132 ± 0.005
A, $R_\odot$	0.575 ± 0.004	0.581 ± 0.005	0.587 ± 0.004
q	0.199 ± 0.014	0.191 ± 0.022	0.158 ± 0.010

4 Discussion

From the obtained results we can conclude that the condition of constancy of the surface gravity $\log g$ is fulfilled. However, comparing the values of the effective temperature $T_{\rm eff}$ requires a separate discussion. The obtained $T_{\rm eff}$ for the observation times of 2021 and 2023 coincide, which causes a discrepancy with the literature data. After a superoutburst, an increase in the temperature of a white dwarf (up to

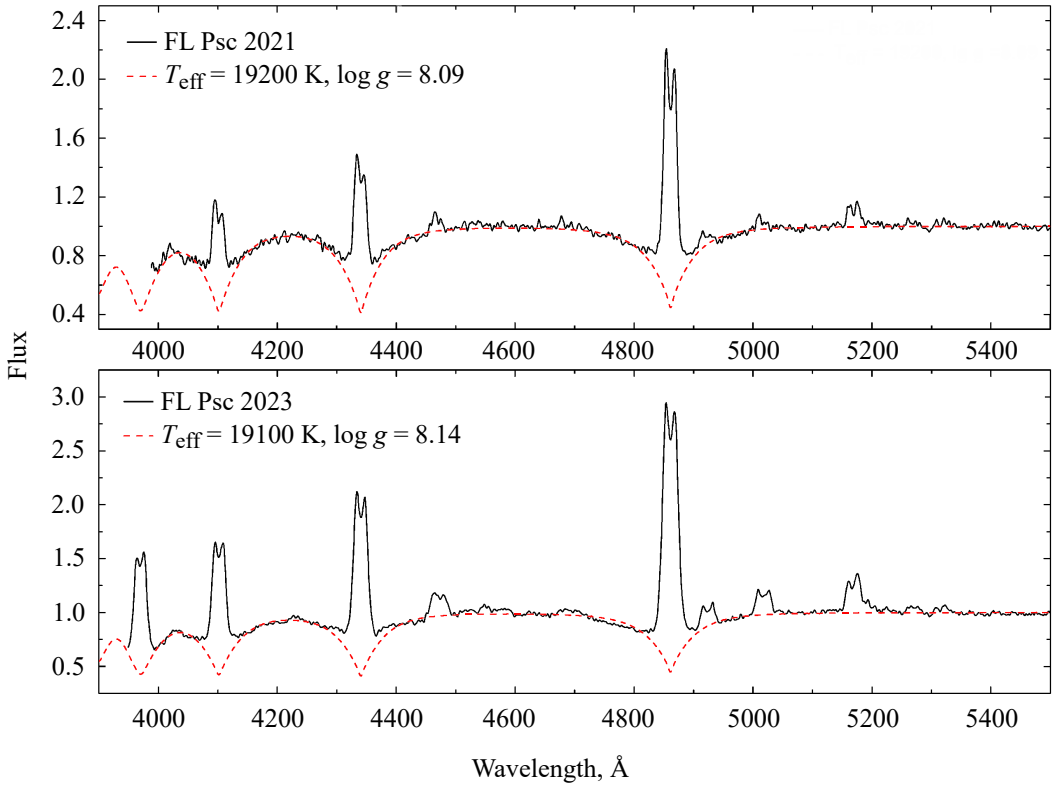

Fig. 2. Observed FL Psc spectra (solid lines) and model spectra (dashed lines) for two observation times.

35 000 K) is always recorded, and the process of its further cooling occurs on a time scale from one year to several years (Long et al. 2004; Godon et al. 2006). According to the light curve obtained from the ZTF data (Masci et al. 2019), it cannot be definitely stated that the dwarf nova FL Psc experienced a superoutburst in May 2023, since its observations at the beginning and maximum of the outburst are absent (amplitude $\Delta m \approx 2\overset{\rm m}{.}5$ in the zr-band). For a typical outburst, the brightness decay time is several days, which also does not correspond to the observed light curve, for which the relaxation time is more than $90^{\rm d}$. It is possible that the excess luminosity can be explained by additional radiation from the accretion disk in the emission lines and optical continuum. Brightness in 2023 is about $0\overset{\rm m}{.}5$ higher than in 2021. Measurements of the integral intensity of the lines in the two spectra showed that radiation in the emission lines can provide no more than 6.1% of the excess luminosity in the V-band, which is at odds with the observations. Therefore, the question

remains open about the contribution of radiation from an optically thin accretion disc to the continuous spectrum in the relaxation-to-quiet phases.

5 Summary

In this paper, we implement a method for determining the parameters of dwarf novae and their temporal changes from the analysis of observations over several times. The idea of this method is to expand the observed series under the study and take into account the requirement of constancy of gravity. The specified requirements were met and the values obtained within the error limits coincided with the measurements made in Dudnik et al. (2023). A comparison of the obtained values of the white dwarf temperatures is presented for discussion: according to the light curve, the system was at the stage of the middle or late relaxation during the observation period of 2023, and the obtained values indicate no temperature change. This contradicts the published data on the increase in the white dwarf temperature after the superoutburst.

Acknowledgements. The study was supported by the grant of the Russian Science Foundation No. 22-72-10064 (https://rscf.ru/project/22-72-10064/). The work on the observational data reduction and modeling the stellar spectra was supported by the grant No. 075-15-2022-262 of the Ministry of Sciences and Higher Education of the Russian Federation (13.MNPMU.21.0003).

References

Afanasiev V.L and Moiseev A.V, 2005, Astronomy Letters, 31, 3, p. 194
Baraffe I., Chabrier G., Barman T., et al., 2003, Astronomy & Astrophysics, 402, p. 701
Dudnik A.A., Shimansky V.V., Borisov N.V., et al., 2023, Astrophysical Bulletin, 78, 1, p. 25
Eggleton P.P., 1983, Astrophysical Journal, 268, p. 368
Girardi L., Bressan A., Bertelli G., et al., 2000, Astronomy and Astrophysics Supplement Series, 141, p. 371
Godon P., Sion E.M., Cheng F., et al., 2006, Astrophysical Journal, 642, 2, p. 1018
Kato T., 2015, Publications of the Astronomical Society of Japan, 67, 6, id. 108
Kolbin A.I., Borisov N.V., Serebriakova N.A., et al., 2022, Monthly Notices of the Royal Astronomical Society, 511, 1, p. 20
Long K.S., Sion E.M., Gänsicke B.T., et al., 2004, Astrophysical Journal, 602, 2, p. 948
Masci F.J., Laher R.,R. Rusholme B., et al., 2019, Publications of the Astronomical Society of the Pacific, 131, 995, p. 018003
Mitrofanova A.A., Borisov N.V., Shimansky V.V., 2014, Astrophysical Bulletin, 69, 1, p. 82
Panei J.A., Althaus L.G., Benvenuto O.G., 2000, Astronomy & Astrophysics, 353, p. 970
Smith R.C., 2006, Contemporary Physics, 47, 6, p. 363
Templeton M.R., Leaman R., Szkody P., et al., 2006, Publications of the Astronomical Society of the Pacific, 118, 840, p. 236

MODERN ASTRONOMY: FROM THE EARLY UNIVERSE TO EXOPLANETS AND BLACK HOLES

Velocities-distance optimization of the rotation model of a homogeneous flat subsystem of Galactic objects: masers

I. Nikiforov, P. Sobolev, and A. Veselova

Saint Petersburg State University, 28 Universitetskij Prospekt, Staryj Peterhof, Saint Petersburg, 198504 Russia; *i.nikiforov@spbu.ru*

Abstract. A statistically correct method for optimizing the parameters of the kinematic model for a homogeneous set of Galactic objects has been developed and implemented, which includes minimizing the squares of relative deviations from the observed radial velocity, proper motions, and distant characteristic. The latter refers to the trigonometric parallax (in the case of absolute distances) or the distance modulus (in the case of relative, i.e., photometric, distances). The solution lies in the technique of the principle of maximum likelihood. The presence of measurement errors and natural (dynamic, astrophysical) velocity dispersion is taken into account; the parameters of the latter (velocity ellipsoid) are estimated. The final iterative algorithm includes optimization of the smoothness of the rotation law and a flexible procedure for eliminating outliers in the data, generalized to a four-dimensional field of residuals. The method, without requiring restrictions on the magnitude of random errors in the distant characteristic, directly takes into account the non-Gaussian distribution of errors in heliocentric distances, thereby correcting the corresponding systematic shifts in the parameters of the model and the average rotation curve of the subsystem under consideration. The inclusion of distance uncertainties in the probabilistic model strongly affects the estimates of natural velocity variances (reduces them), and also generally reduces the variances of model parameters. Applying the method to HMSFR maser sources with trigonometric parallaxes gives the following parameter estimates: distance to the center of the Galaxy $R_0 = 7.88 \pm 0.12$ kpc, angular velocity of rotation of the maser subsystem on the solar circle $\omega_0 = 28.43 \pm 0.22$ km s^{-1} kpc^{-1}, corresponding linear velocity $\theta_0 = 224 \pm 4$ km s^{-1}, the angular velocity of the Sun's rotation around the center of the Galaxy $\omega_\odot = 30.40 \pm 0.20$ km s^{-1} kpc^{-1}.

Keywords: methods: data analysis; Galaxy: fundamental parameters, kinematics and dynamics

DOI: 10.26119/VAK2024.073

1 Introduction

Studies of the kinematics of the Milky Way on a large scale based on data on ensembles of Galactic objects require measurements not only of the components of the velocities of objects, but also of the heliocentric distances to them. However, with appropriate kinematic modeling, the traditional difficulty is taking into account the uncertainty of heliocentric distances. Failure to account for such uncertainty can lead to significant systematic errors in the results. This problem became especially relevant after the appearance of mass joint determinations of proper motions and trigonometric parallaxes – e.g., catalogs of maser sources (Reid et al. 2019; VERA Collaboration et al. 2020), the *Gaia* catalog (Gaia Collaboration et al. 2023) – because objects with large linear and relative errors in distances are guaranteed to be present in such databases.

In early work, Reid et al. (2009) attempted to account for the uncertainty of the parallaxes in the framework of the method of least squares, evaluating model parallax by radial velocity, but then, faced with difficulties, they abandoned this approach and returned to the usual "velocity-only" fitting (Reid et al. 2014, 2019). However, the uncertainty of the distance for many masers turns out to be too large to be ignored. At the same time, the understanding is gradually spreading that the maximum likelihood method (MLM) is a promising tool for such research. Rastorguev et al. (2017) take into account the uncertainty of distances within the framework of the MLM by including partial derivatives of the first order in distance for velocities in the covariance matrix. However, such accounting ignores the non-Gaussian distribution of errors in distances and is suitable only for small uncertainties of the latter.

A better idea is the individual reduction of heliocentric distances by including distributions of distant characteristics of objects in the likelihood function. Pont et al. (1994) applied this approach to photometric distances, using only radial velocities, and while fixing the parameters of the velocity ellipsoid. In the case of involving proper motions and parallaxes, the same approach was implemented within the MLM by Aghajani & Lindegren (2013) and Ding et al. (2013). However, the analytical solution given by these authors for the reduced (corrected) parallaxes is approximate and can only be applied with small parallax errors.

In this paper, we propose a spatial-kinematic modeling method based on the principle of maximum likelihood, which works with a minimum of assumptions, takes into account natural and measurement variances, does not require limits on parallax errors and directly takes into account the non-Gaussian error distribution in heliocentric distances. The method is applied to HMSFR masers.

2 Data

From maser sources, the HMSFR class masers are of the greatest interest for studying the kinematics of the Galaxy as a very "cold" subsystem of a thin disk with absolute distances, moreover, characterized by small parallax uncertainties even for large heliocentric distances (see Nikiforov & Veselova 2018). To obtain a sample of HMSFR measurements, we used the catalogues in Reid et al. (2019); VERA Collaboration et al. (2020), supplementing them with new data from the literature: Xu et al. (2021); Sakai et al. (2021); Bian et al. (2022); Mai et al. (2023); Hyland et al. (2023, 2024). The full sample includes 210 HMSFR masers.

3 Method

A variable, i.e., depending on unknown parameters of the model, part of the logarithmic likelihood function has the following form:

$$\mathcal{L}(\mathbf{a}) = \sum_{j=1}^{N}\left[\ln(\sigma_{V_r})_j + \ln(\sigma_{\mu'_l})_j + \ln(\sigma_{\mu_b})_j\right] + \frac{1}{2}\sum_{j=1}^{N}\min_{\varpi_{0,j}}\left\{\frac{[V_{r,j} - V_{r,\mathrm{mod}}(\varpi_{0,j})]^2}{(\sigma_{V_r})_j^2} + \right.$$
$$\left. + \frac{[\mu'_{l,j} - \mu'_{l,\mathrm{mod}}(\varpi_{0,j})]^2}{(\sigma_{\mu'_l})_j^2} + \frac{[\mu_{b,j} - \mu_{b,\mathrm{mod}}(\varpi_{0,j})]^2}{(\sigma_{\mu_b})_j^2} + \frac{(\varpi_j - \varpi_{0,j})^2}{\sigma_{\varpi,j}^2}\right\}. \quad (1)$$

Here $\mathbf{a}$ is the vector of parameters; $V_{r,j}$, $\mu'_{l,j}$, $\mu_{b,j}$, and ϖ_j are catalog (measured) values of heliocentric radial velocity V_r, longitude ($\mu'_l \equiv \mu_l \cos b$) and latitude ($\mu_b$) proper motions, and parallax ϖ for the jth object; $\varpi_{0,j}$ — the reduced parallax value of the jth object; N is the sample size. The total variances of the velocity characteristics for the jth object are the the sums of two components:

$$(\sigma_{V_r})_j^2 = (\tilde{\sigma}_{V_r})_j^2 + (\sigma^*_{V_r})_j^2, \quad (\sigma_{\mu'_l})_j^2 = (\tilde{\sigma}_{\mu'_l})_j^2 + (\sigma^*_{\mu'_l})_j^2, \quad (\sigma_{\mu_b})_j^2 = (\tilde{\sigma}_{\mu_b})_j^2 + (\sigma^*_{\mu_b})_j^2, \quad (2)$$

where $\tilde{\sigma}_j^2$ are the measuring variance, $\sigma_j^{*2} = \sigma_j^{*2}(l_j, b_j, \varpi_{0,j}; \sigma_R, \sigma_\theta, \sigma_Z, R_0)$ are contributions of natural dispersion, i.e., the velocity ellipsoid $(\sigma_R, \sigma_\theta, \sigma_Z)$. Here l_j and b_j are the longitude and latitude of jth object, correspondingly; R_0 is the distance from the Sun to the center of the Galaxy. The reduced parallax is considered as a random variable distributed according to the normal law $\mathrm{N}(\varpi_j, \sigma^2_{\varpi,j})$, where $\sigma_{\varpi,j}$ is the catalog uncertainty of parallax. The triple of values $(l_j, b_j, \varpi_{0,j})$ determines the point of the (non-orthogonal) projection of the object onto the kinematic model, taking into account all random factors.

The following model was used for velocity characteristics:

$$
\begin{aligned}
V_{r,\mathrm{mod}} &= T_n(\Delta R)\,\frac{R_0}{R}\sin l\cos b - u_\odot\cos l\cos b - v_\odot\sin l\cos b - w_\odot\sin b,\\
k\mu'_{l,\mathrm{mod}} &= T_n(\Delta R)\left(\frac{R_0\cos l}{r} - \cos b\right)R^{-1} - \omega_0\cos b + (u_\odot\sin l - v_\odot\cos l)/r, \qquad (3)\\
k\mu_{b,\mathrm{mod}} &= T_n(\Delta R)\,\frac{R_0}{Rr}\sin l\sin b + (u_\odot\cos l\sin b + v_\odot\sin l\sin b - w_\odot\cos b)/r.
\end{aligned}
$$

Here $T_n(\Delta R) \equiv -2A\Delta R + \sum_{i=2}^{n}\frac{\theta_i}{i!}(\Delta R)^i$ is the contribution of the expansion of the average *linear* rotational velocity $\theta(R)$ of the subsystem in a series of $\Delta R \equiv R - R_0$, $n \geq 1$; A is the Oort parameter; $\theta_i \equiv \left.\frac{d^i\theta}{dR^i}\right|_{R=R_0}$; $R = R(r,l,b)$ is the Galactoaxial distance, $r = 1/\varpi$ is the heliocentric distance; ω_0 is the angular velocity of rotation of the subsystem at R_0; $u_\odot$, $v_\odot$, $w_\odot$ are components of the *residual* velocity of the Sun relative to the rest standard of the subsystem; $k = 4.7406$.

The parameter vector $\mathbf{a}$ is found by minimizing the function $\mathcal{L}(\mathbf{a})$ for the selected value of the model order n. For a fixed sample of objects, a solution was sought for n from 1 to 8. The optimal order of the n_o model was determined based on the behavior of dispersion in the Galactic plane, $\sigma^2_{\mathrm{plane}} \equiv \sigma^2_R + \sigma^2_\theta$, depending on n using a partial F-test (see details in Nikiforov 1999a,b). For optimal order, an outlier exclusion procedure was performed using a one-dimensional algorithm (Nikiforov 2012) and its generalization to a four-dimensional field of residuals based on statistics χ^2_4. The value of the algorithm parameter $L' = 3$ was used to estimate the parameters of the velocity ellipsoid; with $L' = 1$ (a more strong criterion), the remaining parameters were estimated (see details in Nikiforov 2012). After each series of exceptions, solutions were searched anew for different orders of n and the whole procedure was repeated from the beginning until no more exceptions were needed.

4 Results

In all the considered cases, the optimal model was of the order $n_\mathrm{o} = 3$. For this order, the results are presented in Table 1. They show that not taking into account the uncertainty of parallaxes (conventional 3D fitting) leads to a noticeable shift in the estimates of some parameters compared to our proposed method (4D fitting). In particular, the 3D estimate of R_0 is overestimated by $\sim$0.4 kpc; respectively, the estimate of the Oort parameter A is underestimated. The natural dispersions of σ_R and σ_θ with 3D fitting are overestimated by a multiple. At the same time, the non-zero parameters of the velocity ellipsoid, even after excluding outliers within the 4D

fitting, show that the residuals cannot be fully explained only by measurement errors and the natural velocity dispersion is quite measurable for the HMSFR subsystem. It should be emphasized that estimates of R_0 based on these data for 4D fittings are very stable to various calculation options. The final results in Table 1 are highlighted in bold. Figure 1, representing the rotation curve based on HMSFR data and the resulting model, also demonstrates that parallax errors should not be ignored.

Table 1. Results of spatial-kinematic modeling based on HMSFR maser data for a model of optimal order $n_o = 3$

N	DoM	Exclusions	R_0 (kpc)	ω_0 $\left(\frac{\text{km/s}}{\text{kpc}}\right)$	A $\left(\frac{\text{km/s}}{\text{kpc}}\right)$	$u_\odot$ $\left(\frac{\text{km}}{\text{s}}\right)$	$v_\odot$ $\left(\frac{\text{km}}{\text{s}}\right)$	$w_\odot$ $\left(\frac{\text{km}}{\text{s}}\right)$	σ_R $\left(\frac{\text{km}}{\text{s}}\right)$	σ_θ $\left(\frac{\text{km}}{\text{s}}\right)$	σ_z $\left(\frac{\text{km}}{\text{s}}\right)$	θ_2 $\left(\frac{\text{km/s}}{\text{kpc}^2}\right)$	θ_3 $\left(\frac{\text{km/s}}{\text{kpc}^3}\right)$
210	3D	—	8.317	28.43	14.82	3.47	16.41	8.27	20.36	15.79	4.80	−1.83	1.16
			$^{+0.140}_{-0.126}$	±0.39	±0.41	±1.71	$^{+1.92}_{-1.91}$	±0.57	$^{+1.49}_{-1.23}$	$^{+1.49}_{-1.38}$	$^{+0.66}_{-0.64}$	±0.32	±0.20
210	4D	—	7.935	28.3	15.77	6.21	16.0	8.36	11.06	4.8	4.10	−1.29	1.30
			$^{+0.123}_{-0.120}$	±0.2	$^{+0.26}_{-0.25}$	$^{+1.04}_{-1.07}$	±1.0	±0.54	$^{+0.73}_{-0.83}$	±0.9	$^{+0.65}_{-0.64}$	$^{+0.22}_{-0.23}$	$^{+0.18}_{-0.17}$
201	4D	$L' = 3$	7.897	28.46	15.56	6.43	15.67	8.32	**7.13**	**4.64**	**3.45**	−1.30	1.09
			$^{+0.116}_{-0.113}$	±0.22	±0.22	±0.85	$^{+0.93}_{-0.94}$	$^{+0.52}_{-0.53}$	$^{+0.83}_{-0.77}$	$^{+0.84}_{-0.85}$	$^{+0.64}_{-0.65}$	$^{+0.20}_{-0.21}$	$^{+0.14}_{-0.13}$
197	4D	$L' = 1$	**7.881**	**28.43**	**15.46**	**6.09**	**15.55**	**8.22**	(7.13)	(4.64)	(3.45)	**−1.34**	**1.03**
			$^{+0.119}_{-0.115}$	±0.22	±0.23	±0.86	±0.92	±0.52				±0.20	±0.14

The second column "DoM" indicates the dimension of the method: "3D" means that catalog values of parallaxes were used (parallax errors were not taken into account); "4D" means that the reduced parallaxes were found (parallax errors were taken into account).

5 Summary

The proposed method (4D fitting) makes it possible to eliminate systematic errors in the results of kinematic modeling due to the uncertainty of parallaxes. As a result of its application to HMSFR masers, new estimates of fundamental parameters were obtained, in particular, $R_0 = 7.88 \pm 0.12$ kpc, $\omega_0 = 28.43 \pm 0.22$ km s^{-1} kpc^{-1}. The corresponding derived parameters: the linear velocity of rotation of the HMSFRs at $R = R_0$ is $\theta_0 = 224 \pm 4$ km s^{-1}, the angular velocity of the Sun's rotation around the center of the Galaxy is $\omega_\odot = 30.40 \pm 0.20$ km s^{-1} kpc^{-1}, $\theta_\odot \equiv \omega_\odot R_0 = 240 \pm 4$ km s^{-1}.

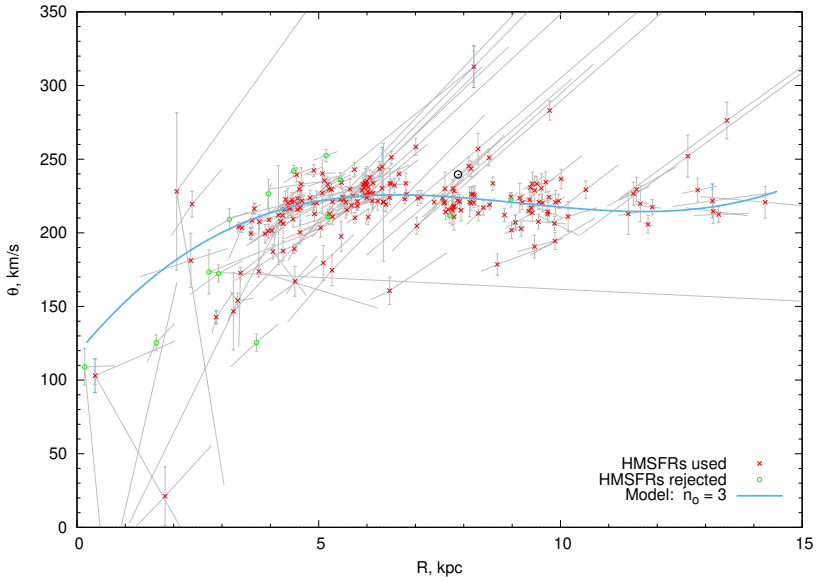

Fig. 1. The rotation curve for the optimal order model ($n_o = 3$) according to the HMSFR maser data. Vertical bars display errors in measuring the velocity characteristics of objects. Inclined ("broken") bars show a change in the position of an object on the rotation curve when the parallax changes by the amount of its uncertainty in both directions. The adjusted uncertainties of proper motions for some objects are shown as additional blue bars. The Sun sign corresponds to the point $(R_0, \theta_\odot)$.

References

Aghajani T. and Lindegren L. 2013, Astron. Astrophys., 551, id. A9
Bian S., Xu Y., and Li J., 2022, Astron. J., 163, id. 54
Ding P., Zhu Z., and Liu J., 2019, Research in Astron. Astrophys., 19, id. 68
Gaia Collaboration, Vallenari A., Brown A., et al., 2023, Astron. Astrophys., 674, id. A1
Hyland L., Reid M., Orosz G., et al., 2023, Astrophys. J., 953, id. 21
Hyland L., Ellingsen S., Reid M., et al., 2024, Proceedings IAU Symposium, 380, p. 106
Mai X., Zhang B., Reid M., et al., 2023, Astrophys. J., 949, id. 10
Nikiforov I., 1999a, Astrophysics, 42, p. 300
Nikiforov I., 1999b, Astron. Rep., 43, p. 345
Nikiforov I., 2012, Astron. Astrophys. Trans., 27, p. 537
Nikiforov I. and Veselova A., 2018, Astron. Lett., 44, p. 699
Pont F., Mayor M., Burki G. 1994, Astron. Astrophys., 285, p. 415
Rastorguev A., Utkin N., Zabolotskikh M., et al., 2017, Astrophys. Bull., 72, p. 122
Reid M., Menten K., Brunthaler A., et al., 2014, Astrophys. J., 783, id. 130
Reid M., Menten K., Brunthaler A., et al., 2019, Astrophys. J., 885, id. 131
Reid M., Menten K., Zheng X., et al., 2009, Astrophys. J., 700, p. 137
Sakai D., Oyama T., Nagayama T., et al., 2021, J. Phys. Conf. Ser., 2145, id. 012011
VERA Collaboration, Hirota T., Nagayama T., Honma M., et al., 2020, Publ. Astron. Soc. Japan, 72, id. 50
Xu Y., Bian S., Reid M., et al., 2021, Astrophys. J. Suppl. Ser., 253, id. 1

MODERN ASTRONOMY: FROM THE EARLY UNIVERSE TO EXOPLANETS AND BLACK HOLES

Analysis of data on lopsided galaxies and theories of their formation

S. Nuritdinov[1], K. Mirtadjieva[1,2], and A. Omonov[1]

[1] National University of Uzbekistan named after Mirzo Ulugbek, Tashkent, 100174 Uzbekistan
[2] Astronomical Institute of the Academy of Sciences of the Republic of Uzbekistan, Tashkent, 100052 Uzbekistan

Abstract. Ground-based and space observations show that the nuclei of many disk-shaped galaxies are significantly offset from their geometric center. This can lead to the excitation of the lopsided mode $m = 1$. To determine the dependence of this effect on the geometry of the system, in this work we have compared a non-stationary disk model with respect to the gravitational instabilities of the lopsided mode $N = 3$; $m = 1$ perturbation. In this work we have also compiled a summary catalog of lopsided disk-shaped galaxies and conducted a statistical analysis of their physical parameters.

Keywords: galaxies: evolution, formation, kinematics and dynamics, structure

DOI: 10.26119/VAK2024.074

1 Introduction

Lopsided structures in galaxies were first noticed in the work (Baldwin et al. 1980) based on the distribution of H I in 20 galaxies. It has been shown that the fraction of lopsided structures in spiral galaxies can reach 30 % or more (Jog & Combes 2009). Obviously, lopsidedness is associated with the nonstationary evolution of the galaxy. The high proportion of galaxies that demonstrate lopsidedness indicates that it is quite stable over a long period of time (Bournaud et al. 2005). Many authors have analysed images of galaxies not only in the optical but also in the near-infrared range and characterised the asymmetry using Fourier analysis. Various physical mechanisms have also been identified that cause the isophotes of the density center to shift from the geometric center in a disk galaxy. For example, the response of the disk to the halo arising from tidal interactions (Jog 1997) or mergers of satellite galaxies (Zaritsky & Rix 1997) or tidal collisions (Mapelli et al. 2008) and asymmetric gas accretion (Bournaud et al. 2005) can lead to the excitation of the lopsided mode $m = 1$.

Until the 2000s, the formation of large-scale galaxy structures was mainly studied within the framework of equilibrium models (Kalnajs 1972), which are unable to explain the observational data regarding the nonlinear nonstationary stage of the evolution of self-gravitating systems. On the other hand, foreign authors have studied the problems of the origin of large-scale structures using numerical experiments (Łokas 2021), setting different degrees of non-equilibrium at the initial moment, which led to in phenomena reproducing the observed structures in real astrophysical systems. However, in numerical experiments, it is impossible to clearly determine the physical mechanism leading to the new observed state and to see possible nonlinear phenomena, resonance processes and the nature of gravitational instabilities that occurred during the experiment. The shortcomings of the above models were first taken into account in the analytical models of the authors (Nuritdinov et al. 2008), where nonlinear nonstationary pulsating models with rotation were built on the base of equilibrium models, describing the initial stages of the formation of self-gravitating systems.

2 Calculation results

We have created a catalog of 2125 lopsided disk galaxies, of which 89 % are spiral galaxies (S) and 11 % are lenticular galaxies (S0). Our main focus was to study the statistical correlation between the physical properties of the catalog. For example, we found that the correlation coefficient between the velocity dispersions of stars in

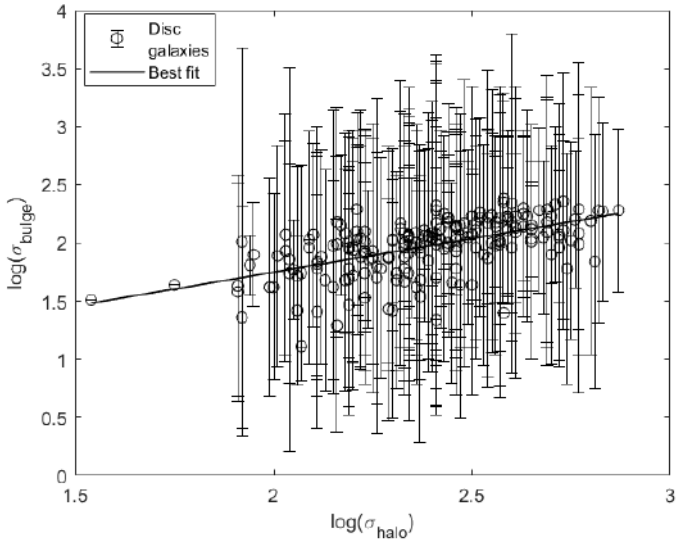

Fig. 1. Dependence of $\sigma_{\rm halo}$ on $\sigma_{\rm bulge}$ for disk galaxies.

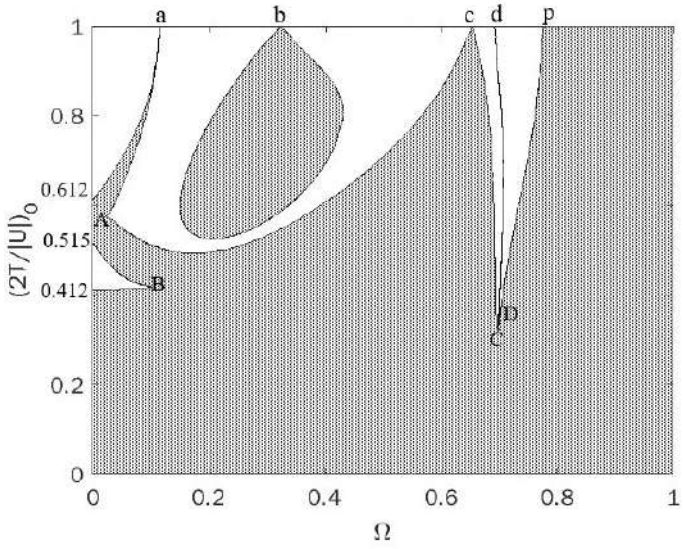

Fig. 2. Dependence of the initial virial ratio on the degree of rotation for different values of the superposition parameter $\nu = 0.75$. Here A $(0.028; 0.576)$, B $(0.101; 0.421)$, C $(0.699; 0.331)$, D $(0.701; 0.348)$, a $= 0.115$, b $= 0.320$, c $= 0.651$, d $= 0.693$, p $= 0.775$.

the bulge and halo is 0.6, and the corresponding relationship is as follows (Fig. 1):

$$\log \sigma_{\text{bulge}} = (0.592 \pm 0.143) + (0.579 \pm 0.060) \cdot \log \sigma_{\text{halo}} \,. \tag{1}$$

Analysis of the results of the numerical calculation of the nonstationary dispersion equation for the superposition parameter $\nu = 0.75$ shows that at $\Omega = 0$ in the range of initial virial ratio values $0 \leq (2\ \mathrm{T}/|\mathrm{U}|)0 \leq 0.412$ the instability of the mode $(3; 1)$ is aperiodic, while in the range $0.515 \leq (2\ \mathrm{T}/|\mathrm{U}|)0 \leq 0.612$ it is oscillatory (Fig. 2). When our nonstationary anisotropic disk model starts to rotate, only oscillatory instability is observed. In the range of rotation parameter values $0 < \Omega < 0.101$ within the instability region, we observe a peninsula of stability. Interestingly, in the stable region within the range $0.15079 \leq \Omega \leq 0.43096$ of the rotation parameter values, a beautiful island of instability was formed. At the rotation parameter values $\Omega = 0.115, 0.320, 0.651, 0.693$ and 0.775, according to our calculations, the oscillation amplitude is $\lambda \approx 0$, which corresponds to the instability of the equilibrium state.

References

Baldwin J., Lynden-Bell D., and Sancisi R., 1980, MNRAS, 193, p. 313
Bournaud F., Combes F., Jog C., and Puerari I., 2005, A&A, 438, p. 507
Jog C., 1997, ApJ, 488, p. 642
Jog C. and Combes F., 2009, Phys. Rep, 471, p. 75
Kalnajs A., 1972, ApJ, 175, p. 63
Łokas E., 2021, A&A, 655, id. A97
Mapelli M., Moore B., and Bland-Hawthorn J.,2008, MNRAS, 388, p. 697
Nuritdinov S., Mirtadjieva K., and Sultana M., 2008, Astrophysics, 51, p. 410
Zaritsky D. and Rix H., 1997, ApJ, 477, p. 118

Behavior of sectorial instabilities depending on the parameters of the generalized model of a self-gravitating disk

S. Nuritdinov[1] and K. Mirtadjieva[1,2]

[1] National University of Uzbekistan named after Mirzo Ulugbek, Tashkent, 100174 Uzbekistan
[2] Astronomical Institute of the Academy of Sciences of Uzbekistan, Tashkent, 100052 Uzbekistan

Abstract. In this work we study the problem of gravitational instability in the generalized model of a nonlinearly radially pulsating disk with an anisotropic velocity diagram relative to sectoral perturbation modes. This model is a nonstationary generalization of the equilibrium self-gravitating disk of Bisnovatyi-Kogan and Zeldovich. Nonstationary analogues of dispersion equations (NADE) are obtained on the background of this generalized model for sectoral modes of perturbations. Based on the results of numerical calculations of NADE, graphs comparing the increments of instability as a function of the initial virial ratio of the system for different values of the parameters α and β, characterizing the difference and the degree of anisotropy of the nonlinearly nonstationary generalized model of the self-gravitating disk, are constructed. In particular, it is found that the development of the bar-like perturbation mode will be the same for all anisotropic models, since the NADE of this mode does not depend on these parameters α and β.

Keywords: galaxies: evolution, formation, kinematics and dynamics, structure

DOI: 10.26119/VAK2024.075

1 Introduction

When studying the early stages of the evolution of disk-shaped self-gravitating systems at the initial collisionless stage of their formation, such as during the collapse of protodisks and the formation of their large-scale structures, it is crucial to identify possible types of instabilities in the considered gravitating systems. Therefore, the construction of analytically solvable nonstationary self-gravitating models and the analysis of the phenomenon of gravitational instabilities against the background of these nonlinear nonequilibrium states is currently the most important and defining link in the study of the early evolution and physics of disk-shaped gravitating systems. This justifies the relevance of this scientific research on a global level. Based on this, in the paper Mirtadjieva 2012 we have constructed a generalized phase model of a radially pulsating disk with an anisotropic velocity diagram, which is based on a nonstationary generalization of the well-known equilibrium isotropic disk model (Bisnovatyi-Kogan & Zeldovich 1970). In the following, on the basis of this generalized model of a radially nonstationary self-gravitating disk, we study the problems of gravitational instabilities of sectoral perturbation modes.

2 NADE of sectoral perturbation modes of the generalized model

In the paper Mirtadjieva 2012 we constructed a nonlinear nonstationary generalized model with an anisotropic velocity diagram of a self-gravitating disk

$$\Psi_a = C_{\alpha\beta}\frac{\sigma_0}{2\pi}\chi(D)\sum_{n=0}^{\beta}\sum_{j=0}^{2\alpha+2n}\frac{(-1)^n\beta!}{n!(\beta-n)!}\binom{2\alpha+2n}{j}(rv_\perp)^j\,(\sqrt{D})^{2\alpha+2n-j}T_{nj}, \qquad (1)$$

where α and β are integers, $T_{nj} = (2\alpha+2n-j-1)!!\cdot g/(2\alpha+2n-j)!!$, with $g = \pi/2$ for even and $g = 0$ for odd j. As is known, in order to find the criteria for instabilities of nonlinear nonstationary models with respect to a specific type of perturbation, it is necessary to derive the corresponding NADE. Note that in this work we consider the case when the perturbations are sectorial ($N = m$), where N is the main perturbation index, and m is the azimuthal wave number. Sectoral modes start with $\mathbf{N = m = 2}$, the so-called "bar modes", which are thought to be important in the formation of bars in SB-type disk galaxies, various ellipticities, and elongated formations. The NADE for this mode of perturbation for the isotropic model was obtained in Nuritdinov et al. 2008:

$$\Lambda\ell_\tau(\psi) = \frac{3\mathrm{c}^{1-\tau}\mathrm{s}^\tau}{2(1+\lambda\cos\psi)^2}\left[\mathrm{G}(\psi)\ell_0(\psi)+\mathrm{Q}(\psi)\ell_1(\psi)\right], \quad \tau = 0;1 \qquad (2)$$

where $\mathrm{G}(\psi) = \mathrm{c} - \mathrm{i}\Omega\mathrm{es}$ and $\mathrm{Q}(\psi) = \mathrm{e}^2 s + \mathrm{i}\Omega\mathrm{ec}$, with $\mathrm{s} = \sin\psi, \quad \mathrm{c} = \cos\psi + \lambda, \quad \mathrm{k} = \sqrt{1-\lambda^2}$. Multiply eq. (2) by the weight function

$$\rho(\Omega) = \mathrm{C}_{\alpha\beta}\Omega^{2\alpha}\left(1-\Omega^2\right)^{\frac{2\beta+1}{2}} \tag{3}$$

and integrate the result over Ω in the interval from -1 to +1. As a result we get the NADE for the bar mode of the generalized model:

$$\Lambda\ell_\tau(\psi) = \frac{3\mathrm{c}^{1-\tau}\mathrm{s}^\tau}{2(1+\lambda\cos\psi)^2}\left[\mathrm{c}\ell_0(\psi) + \mathrm{e}^2\ \mathrm{s}\ell_1(\psi)\right] \tag{4}$$

The sectoral mode $\mathbf{N} = \mathbf{m} = \mathbf{3}$. The manifestations of this "triangular mode" are especially noted in the book Binney & Tremaine 1987. Applying the above averaging method to eq. (31) with $\nu = 0$ from our work we obtain the following NADE for this mode against the background of the generalized model:

$$\Lambda\eta_\tau(\psi) = \frac{15c^{2-\tau}s^\tau}{8(1+\lambda\cos\psi)^4}B(\psi).(\tau = \overline{0,2}). \tag{5}$$

Here $B(\psi) = [(\mathrm{c}^2 + \mathrm{e}^2\ \mathrm{s}^2\mathrm{p})\,\eta_0(\psi) + 4\mathrm{e}^2\,\mathrm{cs}\eta_1(\psi) + (\mathrm{e}^2\ \mathrm{s}^2 - \mathrm{c}^2\mathrm{p})\,\eta_2(\psi)]$, $\mathrm{p} = \frac{2\alpha+1}{2(\alpha+\beta+2)}$. Now consider the case $\underline{\mathbf{N} = \mathbf{m} = 4}$, which corresponds to "boxy" perturbations. Observations show that there are galaxies with isophotes of density in the form of a boxy shape (a typical example is NGC 1600). Therefore this mode is also of certain interest. Averaging formulas (33) at $\nu = 0$ in the work Mirtadjieva 2009 with Ω the weight function (eq. 3), we obtain the following dispersion relation for this perturbation mode for the generalized model:

$$\Lambda\mu_\tau(\psi) = \frac{35c^{3-\tau}\tau}{16(1+\lambda\cos\psi)^6}F(\psi), (\tau = \overline{0,3}), \tag{6}$$

where

$$F(\psi) = \left(c^3 - 3e^2 css^2 p\right)\mu_0(\psi) + \left(e^2c^2s + 2e^2c^2sp - e^4s^3p\right)\mu_1(\psi) + \\ + \left(e^4css^2 + 2e^4c^2p - e^2c^3p\right)\mu_2(\psi) + \left(e^6s^3 - 3e^4c^2sp\right)\mu_3(\psi).$$

3 Conclusions

As can be seen, eq. (4) for the bar mode does not depend on the α and β parameters. This means that the NADE for this mode remains unchanged regardless of whether the model is isotropic or anisotropic in terms of velocity components. It should be noted that the NADE (eq. 5) for the triangular mode does not lend itself to analytical

consideration. It has therefore been studied numerically using the method of stability of periodic solutions (Malkin 2016). For a comparative analysis of the stability of the anisotropic models (eq. 1) with respect to this perturbation mode, using numerical calculations of NADE (eq. 5), we have constructed graphs of the dependence of the instability increments on the initial virial ratio of the models for different values of the parameters α and β (Fig. 1). From Fig. 1 it can be seen that an increase in the

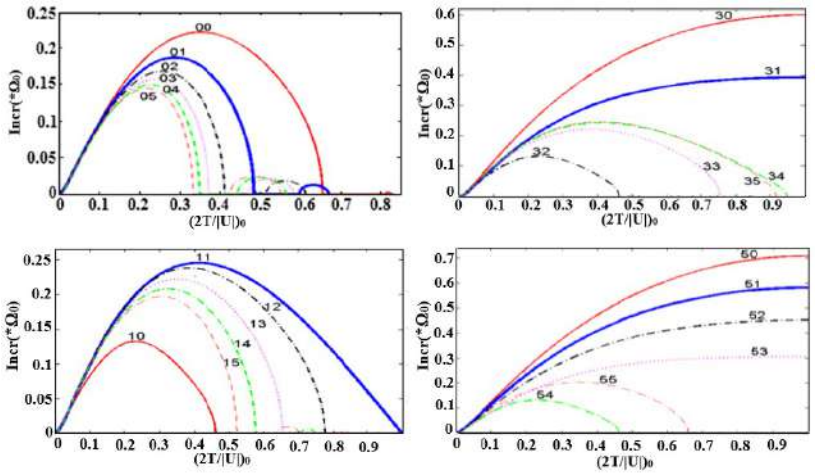

Fig. 1. Comparison of instability increments as a function of the initial virial ratio of models (1) with different values of α and β for the (3;3) mode of sectoral perturbations. The first number in the graphs is α, the second is β.

parameter α has a destabilizing effect during the evolution of this mode against the background of the studied anisotropic models, while the parameter β, on the contrary, plays a "stabilizing" role. However, the observed pattern for β does not fully hold for small values of the parameter α. Moreover, as the value of α increases, the range of the initial virial ratio, where the triangular structure forms against the background of anisotropic models, occupies the entire range of its possible values. Numerical calculations of the NADE (eq. 6) for the boxy mode show that the parameters α and β, which characerize the nonlinear nonstationary anisotropic models of the self-gravitating disk, produce the same effects in the development of this mode as in the triangular mode of sectorial perturbations.

References

Binney J. and Tremaine S., 1987, Galactic dynamics, Princeton Univ. Press
Bisnovatyi-Kogan G. and Zeldovich Ya., 1970, Astrophysics, 6, p. 207
Malkin I., 2016, Theory of Stability of Motion, Moscow, URSS
Mirtadjieva K., 2009, Gravitation and Cosmology, 15, p. 278
Mirtadjieva K. and Nuritdinov S., 2012, Astrophysics, 55, p. 551
Nuritdinov S., Mirtadjieva K., and Sultana M., 2008, Astrophysics, 51, p. 410

BAK 2024 MODERN ASTRONOMY: FROM THE EARLY UNIVERSE TO EXOPLANETS AND BLACK HOLES 300 years Russian Academy of Sciences

The evolution of the fossil large-scale magnetic field in turbulent accretion disks of young stars

A. Orlov[1] and S. Khaibrakhmanov[1,2]

[1] Chelyabinsk State University, 129 Br. Kashirinykh, Chelyabinsk, 454001 Russia
[2] Saint-Petersburg State University, 7-9 Universitetskaya Emb., St. Petersburg, 199034 Russia

Abstract. We study the fossil large-scale magnetic field evolution in a turbulent accretion disk of young T Tauri star. The coefficient of turbulent viscosity is calculated according to the Shakura and Sunyaev model. The modeling is performed taking into account the weakening of the turbulence in the region of low ionization fraction ("dead" zone). The ionization structure is calculated taking into account thermal ionization, cosmic rays and radioactive elements, radiative recombinations and recombinations on dust grains. The magnetic field is calculated taking into account ambipolar diffusion. The simulations show that the magnetic field is frozen in gas and its strength is proportional to the gas surface density in the inner region of the disk, $R < 0.2$ AU. The magnetic field strength increases from 10^2 G to 10^3 G in this region within 5 Myr. The outer boundary of the "dead" zone depends on the dust grain size and ranges from 30 AU for $a_g = 0.1$ μm to 3 AU for $a_g = 10^3$ μm. The size of the "dead" zone decreases with time. The magnetic field strength inside the "dead" zone remains practically constant at around 10^{-3}–10^{-4} G during the disk evolution.

Keywords: stars: protoplanetary disks, magnetic fields, pre-main sequence

DOI: 10.26119/VAK2024.076

1 Introduction

Observations indicate that young stars are surrounded by thin rotating accretion disks of gas and dust (Williams & Ciesza 2011). Various instabilities during the accretion disk evolution can lead to planet formation. The disk at this stage is called a protoplanetary disk.

Accretion disks of young stars have large-scale magnetic field (Khaibrakhmanov 2024). The nature of this field is explained by the fossil magnetic field theory (Dudorov 1995). The large-scale magnetic field is associated with angular momentum transport, efficiency of which depends on the magnetic field distribution. The magnetic field can influence the structure of disks (Khaibrakhmanov & Dudorov 2022). Magnetic field is weakened in the regions of low ionization fraction and effective magnetic diffusion ("dead" zones). Dust grains are effective sources of the recombinations and lead to a decrease in the degree of ionization. In this work, we study the large-scale magnetic field evolution in the accretion disk for various dust grains size.

2 Disk model

We consider a thin gas-dust accretion disk in which angular momentum is transferred by turbulence. The evolution of the disk in this approximation can be described using the following equation (Pringle 1981)

$$\frac{\partial \Sigma}{\partial t} = \frac{3}{R}\frac{\partial}{\partial R}\left(R^{1/2}\frac{\partial}{\partial R}\left[\nu \Sigma R^{1/2}\right]\right), \tag{1}$$

where Σ is the surface density [g/cm^2], ν is the coefficient of turbulent viscosity, R is the radial distance from the star, and t is time. The turbulent viscosity coefficient $\nu = \alpha c_s H$ is calculated according to the model of Shakura & Sunyaev (1973), where c_s is the speed of sound, H is the scale height of the disk, α is a dimensionless parameter, that measures the efficiency of angular momentum transport due to turbulence. In order to take into account the weakening of the turbulence in "dead" zones, we assume that α depends on the ionization fraction (x). Inside the "dead" zone ($x < 10^{-12}$) $\alpha = 10^{-4}$, and outside the "dead" zone ($x \geq 10^{-12}$) $\alpha = 10^{-2}$.

The ionization model includes thermal ionization of alkali metals, cosmic rays and radioactive elements, radiative recombinations and recombinations on dust grains (Dudorov & Khaibrakhmanov 2014).

Magnetic field strength in the frozen-in approximation (magnetic Reynolds number $R_m > 1$) is calculated as

$$B_z = (B_{\rm in}/\Sigma_{\rm in})\Sigma, \tag{2}$$

where $B_{\rm in}$ and $\Sigma_{\rm in}$ are the initial values of magnetic field and surface density at the inner boundary. Magnetic ambipolar diffusion operates inside the "dead" zone ($R_m < 1$) and the magnetic field strength is calculated as:

$$B_z = \sqrt{4\pi x \rho^2 \eta_{\rm in} R |V_r|}, \quad (3)$$

where ρ is the density, $\eta_{\rm in}$ is the coefficient of interaction between ions and neutrals, V_r is the radial velocity.

We use the solution of eq. (1) with fully implicit conservative scheme of first-order accuracy in time and second-order accuracy in coordinate. The equation is solved for the range from 0.01 AU to 1000 AU on a logarithmic grid with $N = 100$ cells. We used analytical stationary solution of Dudorov & Khaibrakhmanov (2014) as an initial condition and adopted typical parameters of solar mass T Tauri stars. The boundary condition at the inner boundary corresponds to the zero viscous stress tensor, and the equality of the densities of the disk and interstellar medium at the outer boundary.

The dust grains in accretion disks can have different sizes. We perform three simulation runs for sizes of 0.1 μm, 1 μm, 10^3 μm.

3 Magnetic field

In Fig. 1a, we plot initial radial profiles of the magnetic field. In the inner region $R < 0.2$ AU, thermal ionization is effective, and the magnetic field is frozen-in, so the the magnetic field strength is proportional to the surface density and does not depend on a_g, $B \approx 100$ G. The distance $R = 0.2$ AU corresponds to the inner boundary of "dead" zone, where the magnetic field strength decreases by 4 orders of magnitude due to magnetic ambipolar diffusion. In the region $R > 0.2$ AU typical value of magnetic field is $B_z = 10^{-3}$ G for $a_g = 0.1$ μm. The outer boundary of the "dead" zone lies at $R = 30$ AU in this case. The magnetic field strength increases with dust grain size. For example, magnetic field strength at $R = 1$ AU is 10^{-1} G for $a_g = 10^3$ μm, and the outer boundary of the "dead" zone is located at $R = 2$ AU. This is explained by the fact that the degree of ionization increases and the size of the "dead" zone decreases in the case of large a_g (Dudorov & Khaibrakhmanov 2014).

The radial profiles of magnetic field at time $t \approx 5$ Myr are plotted in Fig. 1b. Near the the inner boundary, the magnetic field increased to the values of $B_z = 10^3$ G, which is associated with an increase in surface density. Magnetic field strength does not depend on dust grain size and decreases from 10^{-2} G to 10^{-4} G inside the "dead" zone, $r = 0.2$–2 AU. In the outer region of the "dead" zone, a local maximum is

observed, which depends on the radius of the dust grains. The outer boundary of the "dead" zone varies from 30 AU for $a_g = 0.1$ μm to 3 AU for $a_g = 0.1$ μm.

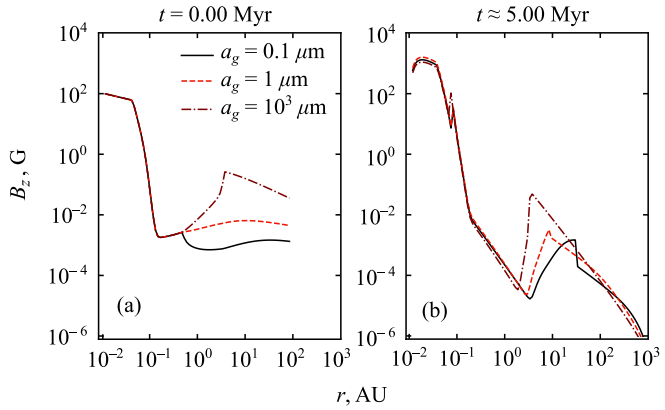

Fig. 1. Radial profiles of the magnetic field for different a_g at the initial moment (a) and at $t = 5$ Myr (b).

4 Summary

The numerical simulations show that the magnetic field changes significantly during the evolution of the disk. In the inner region, the magnetic field increases with increasing density and does not depend on a_g. Inside the "dead" zones, magnetic field remains practically constant with typical values of 10^{-3}–10^{-4} G. Outside the "dead" zone, the magnetic field strength increases with the size of the dust grain. The size of the "dead" zone decreases with time and depends on the size of dust particles. Therefore, it is necessary to take into account the self-consistent evolution of dust grains when studying the evolution of the magnetic flux in disks.

Acknowledgments. S. Khaibrakhmanov is supported by the Theoretical Physics and Mathematics Advancement Foundation "BASIS" (project No. 23-1-3-57-1).

References

Dudorov A., 1995, Astronomy Reports, 39, 6, p. 790
Dudorov A. and Khaibrakhmanov S., 2014, Astrophysics and Space Science, 352, 1, p. 103
Khaibrakhmanov S., 2024, Astronomical and Astrophysical Transactions, 34, 2, p. 139
Khaibrakhmanov S. and Dudorov A., 2022, Astronomy Reports, 66, 10, p. 872
Pringle J., 1981, Annual Review of Astronomy & Astrophysics, 19, p. 137
Shakura N. and Sunyaev R., 1973, Astronomy & Astrophysics, 24, p. 337
Williams J. and Cieza L., 2011, Annual Review of Astronomy and Astrophysics, 49, 1, p. 67

MODERN ASTRONOMY: FROM THE EARLY UNIVERSE TO EXOPLANETS AND BLACK HOLES

Fractality and kinetics of the stellar medium in the solar neighborhood based on Gaia DR2 data

M. Ostashova[1] and A. Rastorguev[1,2]

[1] Sternberg State Astronomical Institute of Moscow State University, 13 Universitetskii pr., Moscow, 119234 Russia

[2] Physical Faculty of Moscow State University, Leninskie Gory, Moscow, 119991 Russia

Abstract. The fractal nature of the stellar medium in the Solar vicinity has been established by studying 200 000 stars of all spectral types at distances of 1 to 100 parsec from the Sun. The fractal dimension is $D \approx 2.41$. Based on the data obtained, we examine the kinetic properties of the fractal stellar medium in the solar vicinity. We show that kinetic parameters such as correlation length, dynamic friction coefficient, effective interstellar distance for fractal stellar medium differ from the corresponding parameters for quasi-homogeneous medium with limited density fluctuations, and depend on the fractal dimension. We find that the fractal structure of the stellar medium leads to a reduction of the relaxation time in our Galaxy.

Keywords: Galaxy: evolution, solar neighborhood, structure; stars: kinematics and dynamics

DOI: 10.26119/VAK2024.077

1 Introduction

The first ideas about the fractal structure of the environment of galaxies are associated with the works of Carpenter (1938) and de Vaucouleurs (1970), who showed that the spatial density in galaxy clusters satisfies the power law $n(r) \sim r^{-1.7}$, where r – the size of a cluster; n - the density of galaxies in a cluster. De Vaucouleurs extended this result not only to clusters of galaxies, but also to the entire galactic medium. He showed that the galactic medium is arranged hierarchically, and therefore any observer, included in the hierarchy, will find that the mean density around them decreases with distance. Mandelbrot (1977) proposed a fractal-hierarchical model to describe the distribution of galaxies:

$$n(r) \sim r^{-\alpha} \,, \tag{1}$$

where r – the characteristic size of the increasing volume around observer included in hierarchy; $n(r)$ – mean star conditional density; α – the exponent. Mandelbrot applied fractal dimension for fractal stellar medium and showed that $D = 3 - \alpha$, where D is the fractal (Hausdorff) dimension, wherein in various gravitating medium $0 \leq D \leq 3$.

Recently, we have studied fractal properties of stellar medium in the solar neighborhood from the observational data of the Gaia (DR2, 2018). Our sample included 200 000 stars of all spectral types at a distance of 1 to 100 parsec from the Sun. Our numerical calculations have shown that the mean conditional stellar density $n(r)$ is approximated by the power laws of the form:

$$n(r) = hr^{-\alpha} \,, \tag{2}$$

where h and α are numerical coefficients: $h = 1.654$, $\alpha = 0.586$, with the Pearson significance level $R^2 \approx 0.992$. It has confirmed the fractal-hierarchical model of de Vaucouleurs-Mandelbrot, and fractal (Hausdorff) dimension: $D = 3 - \alpha \approx 2.41$.

2 Kinetic parameters of the fractal stellar medium

In the present work we study the kinetic parameters of the fractal stellar medium in the solar neighborhood with the fractal (Hausdorff) dimension $D \approx 2.41$. In the paper Chumak & Rastorguev (2016) the important kinetic parameter, the effective interparticle (interstellar) spacing, $r_{\rm m}$ was obtained for the fractal stellar medium from the law of the distribution of the distance to the nearest neighbor:

$$r_{\rm m} = \frac{3}{D} \left(\frac{D}{4\pi h} \right)^{1/D} \Gamma\left(\frac{D+1}{D} \right) , \tag{3}$$

where $\Gamma(x)$ is the gamma function. Substituting our parameters for the space distribution of 200 000 stars in the solar neighborhood $h = 1.654$, $D \approx 2.41$ into the formula (3) yields an average distance between the stars $r_{\rm m} \approx 0.49$ pc for the fractal stellar medium. Traditional estimations for classical model of the homogeneous stellar medium with $D = 3$ and $h \approx n \approx 0.10$ pc^{-3} (we adopt local stellar density from Binney & Tremaine 2008) yield, respectively, $r_{\rm m} \approx 1$ pc, which is almost twice greater than for the fractal case. This result is due to the fact that fractal model takes into account the gravitational clustering ("clumpiness") of the stellar medium.

The second important kinetic parameter is "correlation length" r_0. Davis & Peebles (1983) for the power-law star density distribution introduced a characteristic size r_0, determined from the relation $n(r_0) = 1$. Therefore, in accordance with (2),

$$r_0 = h^{-1/(D-3)} \ . \tag{4}$$

For our fractal model of star distribution we obtain the value of the "correlation length" $r_0 = 2.35$ pc, which is approximately five times the value of the effective interparticle spacing. This value is rather theoretical and is used for different numerical estimates. In classical homogeneous stellar medium such a characteristic is absent.

Kinetic parameter, coefficient of dynamic friction a, is determined by two-point encounters. It was obtained for the fractal stellar medium in the paper Chumak & Rastorguev (2017). It can be approximately estimated using the "correlation length" r_0:

$$a_0 = a(r_0) \approx \frac{8\pi G^2 m^2 h \ln \Lambda}{\nu_0^3} r_0^{D-3} \ , \tag{5}$$

where $ln\Lambda = \ln(p_{\max}/p_{\min})$ is the Coulomb logarithm, G is the gravitational constant, $m = m_f$, the mass of a test star and the field star, $p_{\min} = 2Gm/\nu_i^2$, the impact parameter of the close encounter, in which the test star is deflected by $\pi/2$ angle, $p_{\max}$ is the cutoff parameter for distant interactions (in our case $p_{\max} = 2r_m$), v_0, the velocity of ith star at the time $t = 0$.

From formula (5) for the characteristic deceleration time of a test star as a result of dynamic friction in a fractal medium, we obtain the expression:

$$\tau_{\rm relfr} = \frac{\nu_0^3}{8\pi G^2 m^2 h \ln \Lambda} r^{3-D} \ . \tag{6}$$

For homogeneous stellar medium ($D \to 3, h \to n$) we obtain the well-known formula for the relaxation time:

$$\tau_{\rm rel} = \frac{\nu_0^3}{8\pi G^2 m^2 n \ln \Lambda} \ . \tag{7}$$

From these last two expressions we obtain the relation:

$$\tau_{\rm relfr} = nh^{-1}r^{3-D}\tau_{\rm rel} \ . \tag{8}$$

Substituting the above values for the solar neighborhood into this relationship, and assuming for estimates $r = r_0$, we obtain $\tau_{\rm relfr} = 0.099\,\tau_{\rm rel}$. Thus, the characteristic time of dynamic breaking within the fractal model is approximately ten times less than in homogeneous stellar medium.

3 Summary

Investigation of the fractal properties of the stellar medium in the solar vicinity, using the example of 200 000 stars of all spectral types at a distance of 1 to 100 pc from the Sun, indicates the presence of fractal structures with the fractal dimension $D \approx 2.41$. The study of the kinetic parameters shows that the fractal structure of the stellar medium leads to a reduction in the relaxation time in our Galaxy and that kinetic parameters such as the correlation length, dynamic friction coefficient, and effective interstellar spacing for fractal stellar medium differ significantly from the corresponding parameters for quasi-homogeneous medium.

Acknowledgements. This work has made use of data from the European Space Agency (ESA) mission Gaia (https://www.cosmos.esa.int/gaia), processed by the Gaia Data Processing and Analysis Consortium (DPAC, https://www.cosmos.esa.int/web/gaia/dpac/consortium). Funding for the DPAC has been provided by national institutions, in particular the institutions participating in the Gaia Multilateral Agreement.

References

Binney J. and Tremaine S., 2008, Galactic Dynamics, Princeton Univ. Press

Carpenter E., 1938, Astrophysical Jornal, 88, p. 344

Chumak O. and Rastorguev A., 2016, Astronomy Letters, 42, p. 307

Chumak O. and Rastorguev A., 2017, Monthly Notices of the Royal Astronomical Society, 464, p. 2777

Davis M. and Peebles P., 1983, Astrophysical Journal, 267, p. 465

de Vaucouleurs G., 1970, Science, 167, p. 1203

Mandelbrot, B., 1977, Fractals: Form, Chance and Dimension, W. H. Freedman and Co., San Francisco

MODERN ASTRONOMY: FROM THE EARLY UNIVERSE TO EXOPLANETS AND BLACK HOLES

Random force distribution for fractal stellar medium in the solar neighborhood based on Gaia DR2 data

M. Ostashova[1] and A. Rastorguev[1,2]

[1] Sternberg State Astronomical Institute of Moscow State University, 13 Universitetskii pr., Moscow, 119234 Russia

[2] Physical Faculty of Moscow State University, Leninskie Gory, Moscow, 119991 Russia

Abstract. We examine the law of the distribution of the magnitude of random force in the nearest-neighbor approximation (the generalized Holtsmark distribution) and asymptotics of the Holtsmark distribution for large random forces for the fractal stellar medium in the Solar neighborhood with fractal dimension $D \approx 2.41$. Our investigation is based on the study of 200 000 stars of all spectral types at a distance of 1 to 100 pc from the Sun. We demonstrate that for fractal stellar medium slower decreasing random force distribution takes place. It indicates an important role of strong fields in the kinetics of gravitating medium in comparison with a classical uniform stellar medium.

Keywords: Galaxy: kinematics and dynamics, solar neighborhood, stellar content

DOI: 10.26119/VAK2024.078

1 Introduction

The fractal structure of the environment of galaxies was predicted by Carpenter (1938) and de Vaucouleurs (1970). They found, that the number density n of galaxies in cluster decreases with the growth of their characteristic sizes according to the power law, $n(r) \sim r^{-1.7}$, where r – the size of a cluster, n – density of galaxies in cluster. Mandelbrot (1977) interpreted this law as a special case of stochastic self-similarity of three-dimensional random fractal sets for which the following relation holds:

$$n(r) \sim r^{-\alpha} \, , \tag{1}$$

where r – the characteristic size of the increasing volume, $n(r)$ – mean star conditional density, α – the exponent. Mandelbrot applied fractal dimension for fractal stellar media and showed that the fractal dimension is equal to $D = 3 - \alpha$ and $0 \leq D \leq 3$.

Recently, we have studied the spatial distribution of 200 000 stars of all spectral types in a solar neighborhood at a distance of 1 to 100 parsecs from the Sun from the observational data of the Gaia (DR2, 2018). The analysis of the spatial distribution of stars is carried out by the "mass-radius" method. Our calculations have shown that the mean conditional stellar density $n(r)$ is approximated by power laws of the form:

$$n(r) = h \, r^{-\alpha} \, , \tag{2}$$

where $h = 1.654$ and $\alpha = 0.586$, with the Pearson significance level $R^2 \approx 0,992$. It has confirmed the law of de Vaucouleurs–Mandelbrot for fractal structures in a gravitating media. Thus, the fractal dimension is $D = 3 - \alpha \approx 2.41$.

2 Distribution of the magnitude of random force in the fractal medium

Chumak & Rastorguev (2016) has derived an exact solution for the distribution of the magnitude of the fluctuating random force in the case of homogeneous space distribution of stars. This solution has the form of the Holtsmark distribution:

$$W(|\mathbf{F}|) = H(\beta) a^{2/3} \, , \tag{3}$$

where β is a dimensionless coefficient, and the distribution of relative forces $H(\beta)$ looks like

$$H(\beta) = \frac{2}{\pi\beta} \int\limits_0^\infty \exp\left[-(x/\beta)^{3/2}\right] x \sin x dx \, . \tag{4}$$

In the case of equal-mass stars, $a = (4/15)(2\pi Gm)^{3/2}n$, and $\beta = |\mathbf{F}|/a^{2/3}$.

Chandrasekhar (1943) has shown that the asymptotics of the Holtsmark distribution in the approximation of large random forces exactly coincides with the distribution of the random force acting on a unit-mass test star. We get for the nearest neighbor of mass m located at a distance r: $|\mathbf{F}| = Gm/r^2$.

The asymptotic formula for $W(F)$ can be derived from the distribution of the distance to the nearest neighbor $w(r)$,

$$w(r)dr = 4\pi \exp(-4\pi r^3 n/3) n r^2 dr \ , \tag{5}$$

that results in

$$W(|\mathbf{F}|)d|\mathbf{F}| = 4\pi n (Gm)^{3/2} \exp\left[-(4\pi n/3)(Gm)^{3/2}|\mathbf{F}|^{-3/2}\right] |\mathbf{F}|^{-5/2} d|\mathbf{F}| \ . \tag{6}$$

A generalization of the Holtsmark distribution was obtained for the fractal space star density (Chumak & Rastorguev 2016) assuming that the force acting onto the test star is also determined by its nearest neighbor exclusively and taking into account the fractal structure of the stellar medium. To this end, the distribution of the distance to the nearest neighbor should be derived using eq. (2):

$$w(r)dr = 4\pi h \exp\left[-(4\pi h/D)\, r^D\right] r^{D-1} dr \ . \tag{7}$$

This is an analog of formula (5), i.e., the generalization of the law of the nearest-neighbor distribution for the case of fractal distribution. Further, taking into account (7), it was derived the generalization of formula (6) for the case of power-law density distribution (2):

$$W(|\mathbf{F}|D)d|\mathbf{F}| = 4\pi h (Gm)^{D/2} \exp\left[-(4\pi h/D)(Gm/|\mathbf{F}|)^{D/2}|\right] \mathbf{F}|^{-(D+2)/2} d|\mathbf{F}| \ . \tag{8}$$

Let us define the dimensionless argument of the exponential function in (8), $x = (4\pi h/D)(Gm/F)^{D/2}$. Then eq. (8) can be rewritten as

$$AW(F|D) = (3x)^{(D+2)/2} e^{-x} \ , \tag{9}$$

where $A = (4\pi h)^{2/D}/(Gm)$.

Figure 1 shows the standard Holtsmark distribution (the lower curve) and our derived distribution (the upper curve) which takes into account the fractal nature of the 200 000 local stars with dimension $D \approx 2.41$. It is evident from (9) that the probability distribution $W(F)$ decreases most rapidly for the uniform star distribution, when $D = 3$.

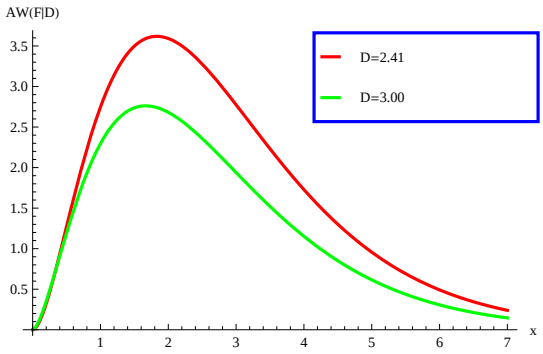

Fig. 1. The distribution $W(F|D)$ ($D \approx 2.41$, the upper curve) and the standard Holtsmark distribution ($D = 3$, the lower curve).

3 Summary

Analysis of space distribution of 200 000 stars of all spectral types at a distance of 1 to 100 pc from the Sun based on Gaia DR2 data indicates the presence of fractal structures with fractal dimension $D \approx 2.41$. The study of probability distribution of magnitude of random force in the nearest-neighbor approximation demonstrate large role of strong fields and therefore paired encounters of stars in collisional kinetics of gravitating medium in comparison with classical uniform stellar medium.

Acknowledgements. This work has made use of data from the European Space Agency (ESA) mission Gaia (https://www.cosmos.esa.int/gaia), processed by the Gaia Data Processing and Analysis Consortium (DPAC, https://www.cosmos.esa.int/web/gaia/dpac/consortium). Funding for the DPAC has been provided by national institutions, in particular the institutions participating in the Gaia Multilateral Agreement.

References

Carpenter E., 1938, Astrophysical Jornal, 88, p. 344
Chandrasekhar S., 1943, Reviews of Modern Physics, 15, p. 1
Chumak O. and Rastorguev A., 2016, Astronomy Letters, 42, p. 307
de Vaucouleurs G., 1970, Science, 167, p. 1203
Mandelbrot B., 1977, Fractals: Form, Chance and Dimension, W. H. Freedman and Co, San Francisco

MODERN ASTRONOMY: FROM THE EARLY UNIVERSE TO EXOPLANETS AND BLACK HOLES

Quasi-periodic pulsations in flares of UV Ceti-type stars

A. Panferov[1,2], D. Kolotkov[3,4] G. Beskin[2,5], S. Karpov[6], V. Plokhotnichenko[2], and O. Maryeva[7]

[1] Togliatti State University, 14 Belorusskaya, Togliatti, 445020 Russia
[2] Special Astrophysical Observatory of the Russian Academy of Sciences, Nizhny Arkhyz, 369167 Russia
[3] University of Warwick, Coventry, CV4 7AL United Kingdom
[4] Ventspils University of Applied Sciences, 101 Inženieru iela, Ventspils, LV-3601 Latvia
[5] Kazan Federal University, 18 Kremlyovskaya, Kazan, 420008 Russia
[6] Institute of Physics of the Czech Academy of Sciences, Prague 8, 18200 Czech Republic
[7] Astronomical Institute of Czech Academy of Sciences, Ondřejov, 25165 Czech Republic

Abstract. Quasi-periodic pulsations (QPPs) were observed in the light curves of solar and stellar flares. The number of stellar QPP events is quite small (213 in 2021), which is why they are interesting. QPPs can be used to investigate the properties of flare regions and they are still a problem for flare models. QPPs were identified in stellar flares across a wide range of wavelengths, from radio to X-rays. In the optical band they are searched mainly in the Kepler and TESS data. The periods of QPPs detected from these sources are longer (tens of minutes) than from the high cadence data. Observations with the 6-m telescope BTA and the MANIA complex, as well as the space observatory GALEX, reveal QPP periods of only tens of seconds. On the other hand, solar flares are typically weaker (energies $\ll 10^{32}$ erg) than stellar flares, that possibly makes them more difficult to detect in white light. Our data on 157 flares of dM-type stars (EV Lac, Wolf 359, Wolf 424, V577 Mon, and UV Ceti), obtained from 70 hours of observations with the BTA telescope in U-band with microsecond time resolution, represents a significant breakthrough in the search for QPPs in stars. In this paper, we present the characteristics of 13 QPPs found in 44 flares. The QPPs have periods ranging from 6 to 107 seconds, and were identified using both Fourier transform and empirical mode decomposition methods. We classify the observed QPPs based on the evolution of their oscillation envelopes and fractional flux amplitudes.

Keywords: stars: flares, oscillations, low-mass

DOI: 10.26119/VAK2024.079

1 Observations and data reduction

We conducted an observation campaign with the MANIA complex (Plokhotnichenko et al. 2021) on the 6-m telescope BTA for the search of M dwarfs flares. A significant number of observed flares show QPPs. To analyze the flare light curves for periodic signals, we used two independent methods: Fourier transform and the EMD. The latter applied to QPPs is extensively used, e.g. Doyle et al. (2018).

2 Results

Figure 1 shows some off-trend light curves from 13 flares, where a pulsating component is visible (we note that QPPs 11 and 12 correspond to the middle and the end of the same flare, respectivelly) and modeled by the EMD oscillation modes as shown by blue line. Their periods $P_{\rm QPP}$ range from 6 to 107 seconds, as seen in Table 1, and they have statistical significance of at least 1σ in Fourier and 2σ in EMD analysis. One can see in Fig. 1 the QPPs evolve in a flare, while the solar QPPs are mainly of narrow band periodicity. There are multiperiodical QPPs, some of which could be multiple.

3 Discussion and conclusions

At a rough guess these QPPs could be differentiated as decaying (QPPs 1, 12 and 14 shown on the left column of Fig. 1), decayless (8, 10, 11 and 13, highlighted on the right column) and transitional among each other (2–7 and 9, highlighted on the central column). By doing so, the first pulse, at flare maximum, is not accounted, because it is as rule distinguished from the others. Its steep amplitude, narrow width or large precedence time are not compliant with an exponentially decaying oscillation. It clearly does not belong to the followed wave train, i.e. has a diffent origin. In some cases it looks like a result of the superposition of several waves different in phase and period as in QPP 1, where the superposition appears also in the wide band saw-like pulses. Such superposition is awaited for stellar flares which are not spatially resolved and the source of QPPs is a bunch of oscillating coronal loops. The oscillations in the decayless parts of some QPPs (e.g., 9, 11 and 13) are amplitude modulated, which also indicates the superposition. In QPP 5 the first half-wave is an artefact of the detrending and three spikes are overlaid on the following wave, which corresponds to the flare maximum. The first wave of QPP 1 is also spiked.

In total, there are three components in all these QPPs: the first one is a possibly spiked pulse detached from the following wave train, the quick decay within 2–3 waves and quasi-decayless oscillation, possibly amplitude-modulated. Such QPP pattern

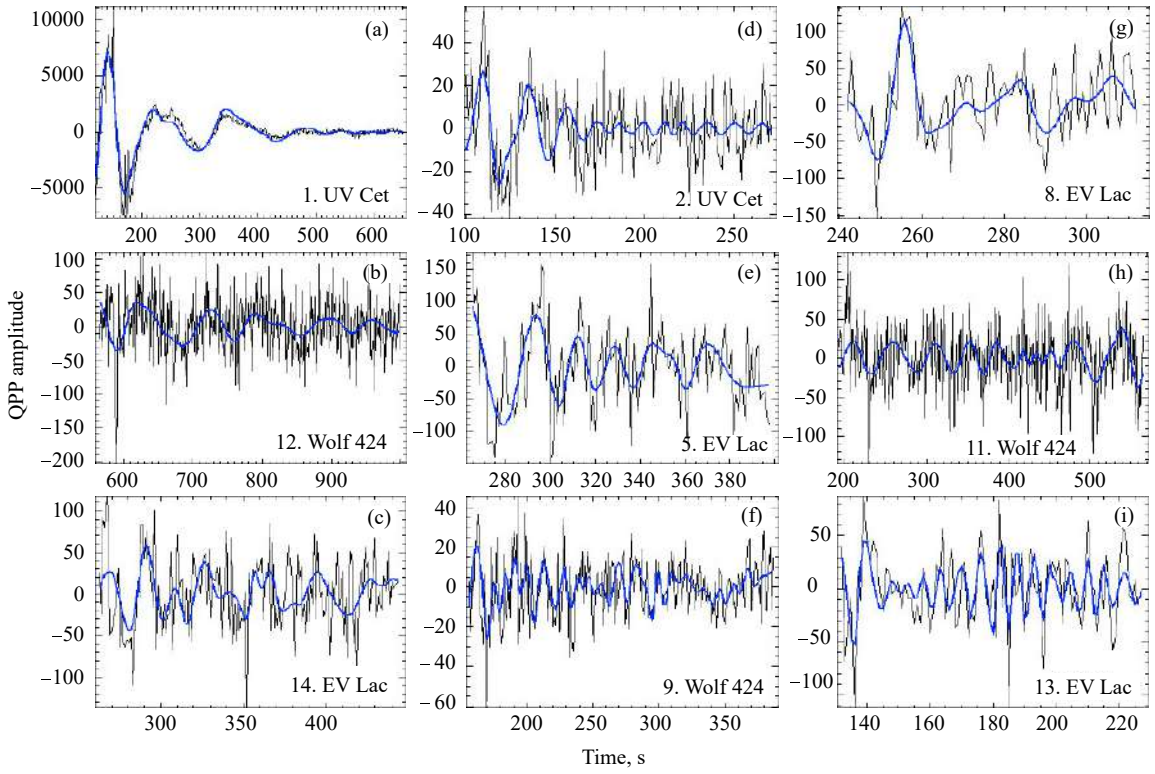

Fig. 1. The oscillating components of flares of M dwarfs EV Lac, Wolf 424 and UV Ceti with superposed model of the EMD oscillation modes by blue line. QPP number in Table 1 precedes the star name on graphs. The transition from decaying to decayless QPPs takes place from the left to the right columns. Time and QPP amplitude along the axes are in arbitrary units.

looks like an imprint of the sequence of MHD events similar to the Sun flare observed by Nisticó et al. (2014), where a quasi-periodic fast (> 1000 km/s) quasi-decayless (≥ 10 wave fronts) wave trains propagate away from a shot of flare region.

The connection between the time characteristics of QPP and energetics of flare is an intriguing question. The fractional flux amplitudes of the QPPs, $A_{\rm QPP} = \Delta F_{\rm QPP}/F_{\rm trend}$ for the second QPP pulse, and flares, $A_{\rm fl} = \Delta F_{\rm flare}/F_{\rm quiescent\,star}$, are in the intervals 0.02–0.13 and 0.2–14.4, the latter corresponding to stellar brightening of $\Delta m_U = 0.2$–3.0 mag. The bolometric energy of a flare is estimated as $E_{\rm fl} = W_{\rm t} L_{\rm bol} \kappa_{\rm s}/\kappa_{\rm f}\eta$, where $W_{\rm t}$ is the equivalent duration of flare (ongoing with the quiescent stellar flux, we should also note its difference from flare duration, $\Delta t_{\rm fl}$), $L_{\rm bol}$ the quiescent star bolometric luminosity, κ the fraction of blackbody flux (determined by the effective temperature of star or flare taken as a typical blackbody tempera-

Table 1. Parameters of flares and QPPs.

QPP	Star	Date yymmdd	$P_{\rm QPP}$ s	$\Delta t_{\rm fl}$ s	$A_{\rm QPP}$	$A_{\rm fl}$	$\Delta m_{\rm U}$ mag	$W_{\rm t}$ s	$E_{\rm fl}$ 10^{33} erg
1	UV Ceti	081228	70 ± 19 107 ± 18	1817:	0.1	14.4	3.0	4210	0.17
2	UV Ceti	090101	24 ± 7	262	0.08	1.46	1.0	92	0.0037
3	Wolf 359	090128	46 ± 20	260	0.1	6.17	2.1	317	0.015
4	EV Lac	090719	19 ± 4	440:	0.07	1.47	1.0	119	0.25
5	EV Lac	090719	26 ± 5	255:	0.03	1.47	1.0	101	0.22
6	EV Lac	090719	26 ± 6	1200:	0.13	7.72	2.4	1326	2.8
7	EV Lac	090721	10 ± 3	300:	0.04	0.391	0.4	24.7	0.053
8	EV Lac	090721	14 ± 2 24 ± 2	135:	0.02	0.391	0.4	22.0	0.047
9	Wolf 424	100610	13 ± 3 57 ± 17	320	0.07	1.75	1.1	120	0.016
10	Wolf 424	100610	15 ± 3	459:	0.07	3.85	1.7	76	0.010
11	EV Lac	100708	49 ± 7	910:	0.03	0.248	0.2	69	0.15
12	EV Lac	100708	87 ± 18						
13	EV Lac	100708	$5.8^{+0.9}_{-1.2}$	340:	0.03	0.426	0.4	30.2	0.064
14	EV Lac	100708	18 ± 7 36 ± 5	550:	0.035	0.561	0.5	66	0.14

Notes. $E_{\rm fl}$ is evaluated using the following stellar effective temperatures and quiescent bolometric luminosities: 2728 ± 60 K and $(1.25 \pm 0.05) \times 10^{-3}\,L_\odot$ for UV Ceti, 2800 ± 50 K and $(1.11 \pm 0.02) \times 10^{-3}\,L_\odot$ for Wolf 359, 3270 ± 80 K and $(1.28 \pm 0.03) \times 10^{-2}\,L_\odot$ for EV Lac and 3013 K (2555/3800 K) and $1.59 \times 10^{-3}\,L_\odot$ for Wolf 424.

ture of 9000 K for a flare continuum) transmitted by the U filter, and $\eta = 0.63$ the fraction of the total flare-radiated energy in the optical continuum. With these we get the flares energies $E_{\rm fl}$ in the interval (0.0037–2.8) $\times 10^{33}$ erg.

Funding

The work was partially carried out within the framework of the state assignment of the SAO RAS, approved by the Ministry of Science and Higher Education of the Russian Federation, and partially supported by the SAL Program of the KFU.

References

Doyle J.G., Shetye J., Antonova A.E., et al., 2018, Monthly Notices of the Royal Astronomical Society, 475, 2, p. 2842

Nisticó G., Pascoe D.J., Nakariakov V.M., 2014, Astronomy & Astrophysics, 569, id. A12

Plokhotnichenko V.L., Beskin G.M., de Boer V.G., et al., 2021, Astrophysical Bulletin, 76, 4, p. 472

BAK 2024 MODERN ASTRONOMY: FROM THE EARLY UNIVERSE TO EXOPLANETS AND BLACK HOLES 300 years Russian Academy of Sciences

Study of the physical and chemical properties of dense clumps in several high-mass star-forming regions

A. Pazukhin[1,2], I. Zinchenko[1], and E. Trofimova[1]

[1] Federal Research A. V. Gaponov-Grekhov Institute of Applied Physics of the Russian Academy of Sciences, 46 Ul'yanov str., Nizhny Novgorod, 603950 Russia
[2] National Research Lobachevsky State University of Nizhny Novgorod, 23 Gagarin Ave, Nizhny Novgorod, 603950 Russia

Abstract. Massive stars play an important role in the Universe. Unlike low-mass stars, the formation of these objects located at great distances is still unclear. It is expected to be governed by some combination of self-gravity, turbulence, and magnetic fields. Our aim is to study the chemical and physical conditions of dense clumps in several high-mass star-forming regions. We performed observations towards 5 high-mass star-forming regions (L1287, S187, S231, DR 21(OH), NGC 7538) with the IRAM 30-m telescope. We covered the 2–3 and 4 mm wavelength bands and analysed the lines of HCN, HNC, HCO^+, HC_3N, HNCO, OCS, CS, SiO, SO_2, and SO. Using the astrodendro algorithm on the 850 μm dust emission data from the SCUBA Legacy catalogue, we identified dense gas clumps and assessed their masses, H_2 column densities, and sizes. Furthermore, the kinetic temperatures, molecular abundances and dynamical state were obtained. The Red Midcourse Space Experiment Source survey (RMS) was utilized to identify the types of clumps. A total of 20 clumps were identified. We found no significant correlation between line width and size, but the linewidth-mass and mass-size relationships are strongly correlated. Virial analysis indicated that the clumps with H II regions and young stellar objects (YSOs) are gravitationally bound. Furthermore, it was suggested that significant magnetic fields provide additional support for clump stability. Molecular abundances show a decreasing trend from YSOs to submm and H II regions.

Keywords: ISM: abundances, molecules; stars: formation, massive; astrochemistry

DOI: 10.26119/VAK2024.080

1 Introduction

High-mass stars (also OB stars, $L > 10^3\,L_\odot$, $M > 8\,M_\odot$) play an important role in the Universe via their feedback. Their formation and evolution are still unclear. According to the review by Zinnecker & Yorke (2007), the evolution phase can be divided into several groups of objects. Objects associated with the initial phase of high-mass star formation are referred to as IR dark clouds (IRDCs). These clouds consist of dense and cold gas, which is believed to represent the initial conditions for high-mass star formation. Hot molecular cores (HMCs) have large masses of warm and dense gas, large abundances of complex organic and maser emission. Finally, ionised radiation from the embedded stellar population influences the parent molecular cloud, leading to the formation of an ultra-compact H II region (UCHII).

2 Observational data

In September 2019, we observed five massive star-forming regions using the IRAM 30-m radio telescope in the framework of the project No. 041-19. The list of sources is given in Table 1. Observations were carried out in the on-the-fly (OTF) mode over a mapping area of $200'' \times 200''$ and covered the 2–3 and 4 mm wavelength bands. A detailed description of the observations and data reduction is available in the published paper on deuterated molecules (Pazukhin et al. 2023). The following lines of molecules were observed: HCN (1–0), HNC (1–0), HCO^+ (1–0) and their ^{13}C isotopologues, HC_3N (8–7), OCS (6–5), $C^{34}S$ (3–2), SiO (2–1), SO (2–1), SO_2 ($6_{0,6}$–$5_{1,5}$), and HNCO ($4_{0,4}$–$3_{0,3}$).

Table 1. List of sources.

Source	RA(J2000) hh:mm:ss	Dec(J2000) °:′:″	$V_{\rm lsr}$ km/s	d kpc	$R_{\rm GC}$ kpc
L1287	00:36:47.5	63:29:02.1	−17.7	0.93	8.64
S187	01:23:15.4	61:49:43.1	−14.0	1.44	9.06
S231	05:39:12.9	35:45:54.0	−16.6	1.56	9.67
DR 21(OH)	20:39:00.6	42:22:48.9	−3.8	1.50	8.04
NGC 7538	23:13:44.7	61:28:09.7	−57.6	2.65	9.48

3 Results

To extract the clumps, we use Python `astrodendro`[1] (Rosolowsky et al. 2008). A dendrogram is employed to represent a hierarchical data structure. The dendrogram consists of two types of structures: branches, which can be divided into branches and

[1] http://www.dendrograms.org

leaves, which represent the final structures. We define the leaves on the dendrogram as clumps. Approximately 20 clumps were identified. The RMS survey (Lumsden et al. 2013) was used to determine the clump types. Three clumps were found to be associated with the H II regions, 10 with YSOs, and 7 with submillimetre emission. Masers were identified from the maser database[2] (Ladeyschikov et al. 2019). Water, hydroxyl, and methanol masers are observed in clumps associated with YSO and H II regions.

Using 850 μm dust emission data from the SCUBA Legacy catalogue (Di Francesco et al. 2008), we analysed the masses, H_2 column density and size of the clumps. To estimate the clump masses, the following equation was used (Kauffmann et al. 2008):

$$M = 0.12\,M_{\odot}\left(e^{14.39(\lambda/\mathrm{mm})^{-1}(T_{\mathrm{dust}}/K)^{-1}}-1\right)\frac{\kappa_{\nu}}{\mathrm{cm^2 g^{-1}}}\times\frac{F_{\nu}}{\mathrm{Jy}}\left(\frac{d}{100\ \mathrm{pc}}\right)^2\left(\frac{\lambda}{\mathrm{mm}}\right)^3, \quad (1)$$

where the gas-to-dust ratio is assumed to be 100, λ is the wavelength, F_{ν} is the integrated flux, T_{dust} is the dust temperature, d is the distance to the object. Dust opacity $\kappa_{\nu} = 1.82$ cm^{2}g^{-1} at 850 μm (Ossenkopf & Henning 1994). The dust temperature was set at T_{dust}. As a result, the H_2 column density and density are derived as

$$N(\mathrm{H_2}) = \frac{M}{\mu_{\mathrm{H_2}} m_{\mathrm{H}} (\pi R_{\mathrm{eff}}^2)}\ ,\ n(\mathrm{H_2}) = \frac{M}{\mu_{\mathrm{H_2}} m_{\mathrm{H}} (4/3\pi R_{\mathrm{eff}}^3)},$$

where m_{H} is the hydrogen mass, a mean molecular weight $\mu_{\mathrm{H_2}} = 2.8$, and R_{eff} as the effective radius derived from the clump area $\sqrt{A/\pi}$.

The virial parameter, which compares the mass of the virial with the gas mass, offers a method to assess cloud stability. The virial parameter is defined as follows (Bertoldi & McKee 1992):

$$\alpha_{\mathrm{vir}} = \frac{5\sigma_{\mathrm{tot}}^2 R_{\mathrm{eff}}}{GM},$$

where G is the gravitational constant. The σ_{tot} is defined by the width of the observed line considering the thermal and non-thermal components.

Kinetic temperature maps were adopted from the integral intensity ratios of the $J = 1$–0 HCN and HNC and their ^{13}C isotopologues as reported by Pazukhin et al. (2023). The column density is estimated under the assumptions of local thermodynamic equilibrium conditions, the optically thin Rayleigh-Jeans approximation, and negligible background.

Larson (1981) defined the relations between linewidth, cloud mass, density, and cloud size. The Larson's laws are as follows:

(1) the velocity dispersion of clouds relative to their size, $\sigma \propto L^{0.38}$;

[2] https://maserdb.net

(2) the velocity dispersion as a function of the cloud mass, $\sigma \propto M^{0.2}$;
(3) the mean density varies with cloud size, with the relationship being $n \propto L^{-1.1}$.

Then, the mass-size relationships can be defined from (1) and (2), $M \propto L^{1.9}$.

In Fig. 1 we show Larson's relations. The results indicate a weak correlation between the $\sigma_{\rm obs}$ and L, with a Spearman's rank correlation coefficient of $r_s = 0.15$ (p-value = 0.533). We estimate the power-law index to be 0.35 ± 0.15. The correlation between $\sigma_{\rm obs}$ and M is strong ($r_s = 0.6$, p-value = 0.008), with a slope of 0.17 ± 0.05. The $n(\mathrm{H_2})$ and L show a strong anti-correlation with $r_s = -0.5$ (p-value = 0.023) and a slope of -0.81 ± 0.38. The mass and size present a strong correlation ($r_s = 0.8$, p-value $= 2.4 \times 10^{-5}$), with a power-law index of 2.2 ± 0.37.

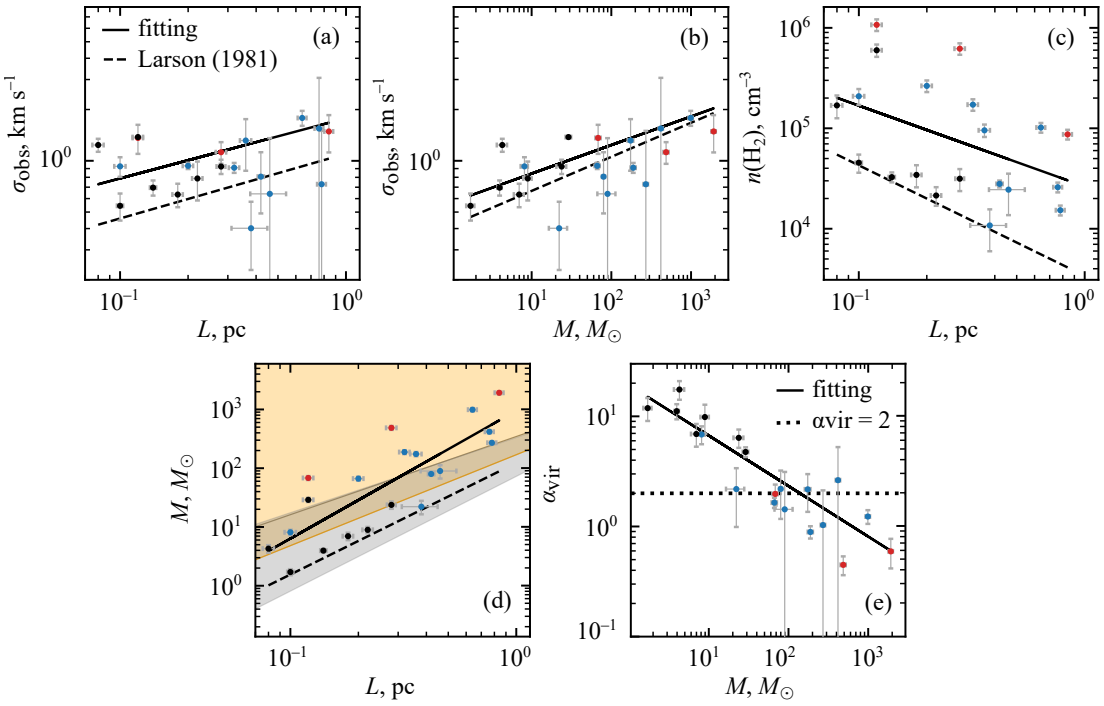

Fig. 1. The relations of $\sigma_{\rm obs}$–L (a), $\sigma_{\rm obs}$–M (b), $n(\mathrm{H_2})$–L (c), M–L (d) and $\alpha_{\rm vir}$–M (e) for clumps associated with submm emissions (black), YSOs (blue), and H II regions (red). In panel (d), the orange shading represents the area where a magnetic field is required for the stability of clumps against gravitational collapse. Region without massive star formation highlighted by gray shading (Kauffmann et al. 2013). In all panels, the black line shows the fitting result. The black dashed line illustrates the original Larson relation (Larson 1981). In panel (e), the horizontal dashed line at $\alpha_{\rm vir} = 2$ gives the critical value expected for non-magnetised clouds.

Figure 1d illustrates the relationships between mass and size, as well as the magnetic fields. The clumps containing YSO and H II regions are found within a magnetic

field region ($B > 0$ μG) and show a low virial parameter ($\alpha_{\rm vir} < 2$). The density and mass of these clouds are such that the thermal pressure and random gas motions do not provide substantial support against self-gravity. This is evidenced by a low virial parameter, which suggests that magnetic fields provide additional support.

Figure 2 illustrates averaged molecular abundances for different clump types. It was observed that molecular abundances decrease from clumps with YSOs to submm and H II regions. The maximum abundance was obtained for HCN (about 10^{-9}), and decreased to approximately 10^{-11} for SiO. Yu & Xu (2016) conducted an investigation of 87 RMS sources. The abundances of N_2H^+, C_2H, HC_3N, and HNC do not show a significant difference between MYSOs and H II regions. Gerner et al. (2014) observed a sample of 59 sources and modelled the chemical evolution. The abundances have increased with the evolutionary phase. Complex and heavy molecules decrease during the UCHII stage. In general, the molecular abundances agree with our results, assuming uncertainties of about 10.

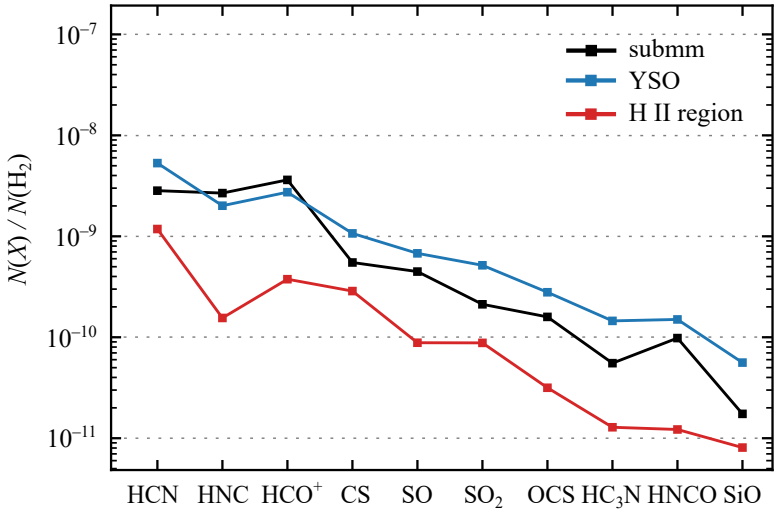

Fig. 2. The mean abundances relative to H_2 for clumps associated with submm emissions (black), YSOs (blue), and H II regions (red).

4 Summary

This work examines the physical and chemical conditions of five high-mass star-forming regions, using observations from the IRAM 30-m radio telescope. The results are as follows:

1. We identified 20 clumps. Three clumps were found to be associated with the H II regions, 10 with YSOs, and 7 with submillimetre emission. The clumps have

typical sizes of around 0.2 pc and masses in range of approximately 100 $M_\odot$ to 1000 $M_\odot$, with kinetic temperatures of about 20 K to 40 K and line widths of roughly 2 km/s.

2. We found no significant correlation between line widths and sizes, but the linewidth-mass and mass-size relationships are strongly correlated. Virial analysis indicated that the clumps with H II regions and YSOs are gravitationally bound. Virial parameter dependence on the mass of $\alpha_{\rm vir} \propto M^{-0.5}$. Furthermore, it was suggested that significant magnetic fields provide additional support for clump stability.
3. The molecular abundances decrease from clumps with YSOs to submm and H II regions. The maximum abundance was obtained for HCN (about 10^{-9}), and decreased to approximately 10^{-11} for SiO.

Acknowledgements. The research is based on observations made by the project No. 041-19 with the 30-m telescope. IRAM is supported by INSU/CNRS (France), MPG (Germany) and IGN (Spain). This paper also made use of information from the RMS survey data base at http://rms.leeds.ac.uk/ which was constructed with support from the Science and Technology Facilities Council of the UK.

Funding

This study was supported by the Russian Science Foundation project No. 24-12-00153.

References

Bertoldi F. and McKee C.F., 1992, Astrophysical Journal, 395, p. 140
Di Francesco J., Johnstone D., Kirk H., et al., 2008, Astrophysical Journal Supplement Series, 175, 1, p. 277
Gerner T., Beuther H., Semenov D., et al., 2014, Astronomy & Astrophysics, 563, id. A97
Kauffmann J., Bertoldi F., Bourke T.L., et al., 2008, Astronomy & Astrophysics, 487, 3, p. 993
Kauffmann J., Pillai T., Goldsmith P.F., 2013, Astrophysical Journal, 779, 2, p. 185
Ladeyschikov D.A., Bayandina O.S., Sobolev A.M., 2019, Astronomical Journal, 158, 6, p. 233
Larson R.B., 1981, Monthly Notices of the Royal Astronomical Society, 194, p. 809
Lumsden S.L., Hoare M.G., Urquhart J.S., et al., 2013, Astrophysical Journal Supplement, 208, 1, id. 11
Ossenkopf V. and Henning T., 1994, Astronomy & Astrophysics, 291, p. 943
Pazukhin A.G., Zinchenko I.I., Trofimova E.A., et al., 2023, Monthly Notices of the Royal Astronomical Society, 526, 3, p. 3673
Rosolowsky E.W., Pineda J.E., Kauffmann J., et al., 2008, Astrophysical Journal, 679, 2, p. 1338
Yu N. and Xu J., 2016, Astrophysical Journal, 833, 2, id. 248
Zinnecker H. and Yorke H.W., 2007, Annual Review of Astronomy & Astrophysics, 45, 1, p. 481

MODERN ASTRONOMY: FROM THE EARLY UNIVERSE TO EXOPLANETS AND BLACK HOLES

Study of clusters in the star forming region G174+2.5

T. Permyakova[1], G. Carraro[2], M. Kirsanova[3], D. Ladeyschikov[1], and A. Seleznev[1]

[1] Ural Federal University, 51 Lenin Str., Ekaterinburg, 620000 Russia
[2] Dipartimento di Fisica e Astronomia, Universitá di Padova, Vicolo Osservatorio 3, Padova, I-35122 Italy
[3] Institute of Astronomy, Russian Academy of Sciences, 48 Pyatnitskaya Str., Moscow, 119017 Russia

Abstract. We study the structure, photometric diagrams and kinematics of four embedded clusters (S235North-West, S235A-B-C, S235Central and S235East1+East2) in the star-forming region associated with the giant molecular cloud G174+2.5. This research uses photometric data from the GPS UKIDSS catalog and astrometric data from the Gaia DR3 catalog. We determine the center positions, radii, and interstellar extinction for clusters in the region. An extinction was determined in two ways — using the NICEST algorithm and the Q-method. The latter method gives a smaller scatter of the color indices on the extinction-corrected photometric diagrams. The membership probability of stars in the clusters, their masses and distances to clusters are also estimated. Additionally, we determine the average proper motions and study the kinematics of the clusters using data from the Gaia DR3 catalog. In all four regions, we estimate the mass of the gas component and the efficiency of star formation. Then, we apply the data obtained to evaluate the total energy of both the stellar and gas systems. It allows us to ascertain whether the clusters are gravitationally bound or not. The boundness of the systems depends on the size of the region where we estimate the mass of gas. If we take the mass of the entire cloud, all four cluster-gas systems appear to be gravitationally bound.

Keywords: open clusters and associations: general; dust, extinction; stars: formation, kinematics and dynamics

DOI: 10.26119/VAK2024.081

1 Introduction

The study of embedded star clusters allows us to improve our understanding of star formation process and of the early evolution of open star clusters after their formation. One of the closest star-forming regions is located in the giant molecular cloud G174+2.5 in the Perseus spiral arm; the distance to it, according to various estimates, ranges from 1.4 to 2.5 kpc. This work includes a study of the structure, photometric diagrams, kinematics and dynamics of four star clusters (S235North-West, S235A-B-C, S235Central and S235East1+East2). For these purposes, we use data from the UKIDSS GPS DR10PLUS (Lucas et al. 2008) and Gaia DR3 (Gaia Collaboration et al. 2023) catalogs and supply them with reddening values determined using the NICEST method (Lombardi 2009).

2 Study of clusters

We study the structure of clusters by the surface density maps and the radial density profiles built with the kernel density estimator method (KDE). Maps were plotted for different limiting magnitudes and kernel half-widths (see Fig. 1 as an example). The cluster centers were determined as the coordinates of local density maxima (2th and 3th columns of Table 1). The cluster radii (4th column of Table 1) were determined from the radial density profiles with the method proposed by Seleznev (2016).

Membership of stars in clusters was determined using the UPMASK package (Krone-Martins & Moitinho 2014) based on stellar magnitudes, color indices, and equatorial coordinates. Below, by clusters we will mean collections of stars with the membership probability greater than or equal to 0.7 (5th column of Table 1).

Table 1. Parameters of the studied clusters.

Name	RA (J2000.0)	Dec (J2000.0)	R	N	D	$M_{\rm ph}$	$M_{\rm Kr}$	SFE
	deg	deg	arcmin	$K \leq 15^m$	kpc	$M_\odot$	$M_\odot$	
1	2	3	4	5	6	7	8	9
S235North-West	85.18981	35.91901	2.4	67	1.7	113	209	0.14
S235A-B-C	85.21402	35.68557	5.5	326	1.9	530	873	0.17
S235Central	85.27761	35.82445	1.3	35	2.2	56	91	0.04
S235East1+East2	85.37212	35.81896	3.2	75	1.7	95	156	0.07

Absorption in clusters was determined in two ways. The first one is the NICEST method. That one blurs greatly the sequences in the photometric diagrams. So, we cannot use such diagrams to determine distances to clusters. The second method is the Q-method. The Q value is a combination of the star's color indices and color

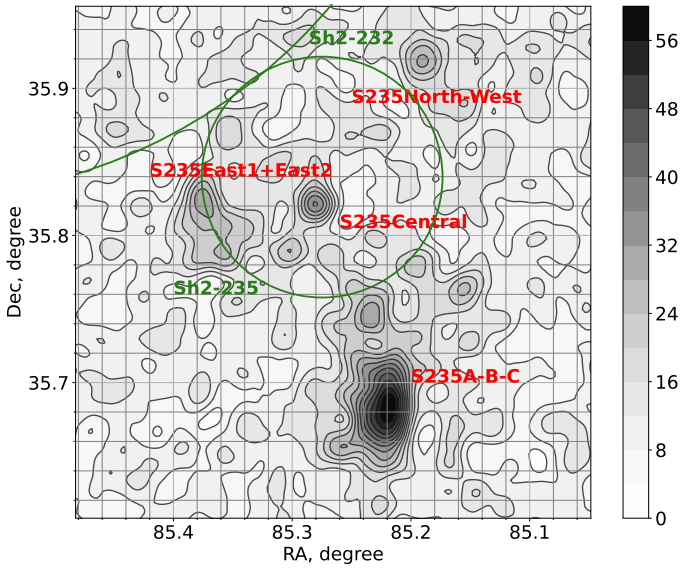

Fig. 1. Stellar density maps of the region based on UKIDSS data. Kernel half-width 1 arcmin, limiting magnitude $K = 15^m$. Clusters are indicated in red. HII regions are indicated in green.

excesses. In this work, we use the equation: $Q = (J - H) - k_R(H - K)$, $k_R = E(J - H)/E(H - K)$. This parameter is considered to be free from the influence of extinction. Thus, using the diagram "color index – Q", we can define the color excess as the difference between the color index value of the star and of the non-reddened sequence.

The main problem of the method is the difficulty to choose which segment of the non-reddened sequence the star belongs to without knowing its spectral class. We solve this problem by comparing the luminosity functions (LFs) of the studied cluster and the non-reddened "reference" cluster (Pleiades, sample of Lodieu et al. 2019). In the LF of the Pleiades, the stars of the left and right segments intersect only in a small range of values. Within this range, we select a certain limit value at which the number of stars in the left segment still significantly exceeds the number of stars in the right segment. We combine the LFs of the "reference" and studied clusters. Next, we assume that all stars with a magnitude less than the limit belong to the left segment, and all stars with a greater magnitude belong to the right one. As a result, Q method gives clearer photometric sequences.

The distances to the clusters were determined by combining extinction-corrected photometric diagrams with isochrones. The obtained estimates of the distances of 1.7–2.2 kpc (6th column of Table 1) are consistent with the data from the literature.

We determined the cluster masses (7th column of Table 1) by the photometric method. We count the number of stars between two adjacent evolutionary tracks plotted in the (H-K; K) plane and multiply this value by the average mass of the stars for which the tracks are built. This method may underestimate the mass, since not all stars are visible and not all visible stars have photometry in three bands.

Further, we plot the mass functions (MFs) of clusters in $\log(M) - \log(dN/d(lg(M)))$ plane. The MFs show a strong decrease in the region of low masses due to the fact that most low-mass stars are not visible because of the incompleteness of the catalog. The slope of the MFs for $\log M \geq -0.2$ for all clusters is close to the initial MF (IMF) of Kroupa (2001).

Suggesting the masses of the cluster stars are distributed with the IMF of Kroupa, we estimated the cluster total masses (8th column of Table 1). The total masses and number of stars are almost 2 and 3 times, respectively, higher than the values derived from visible stars.

To assess the star formation efficiency (SFE) in the region of each cluster, we first estimate the mass of the gas in the regions. To do this, we use observational data on emission in the ^{12}CO(1-0) and ^{13}CO(1-0) lines (Brunt 2004). Integrated radiation temperature maps were converted to the mass-per-pixel maps using the method described in Ladeyschikov et al. (2021). Next, the total mass of pixels in the cluster areas was calculated.

Assuming that most of the parent gas remains in the cluster region or is in the line of sight, we determine the star forming efficiency in the regions under consideration using the equation: $SFE = M_{\rm cl}/(M_{\rm g} + M_{\rm cl})$, where $M_{\rm g}$ is the mass of the gas in the region, $M_{\rm cl}$ is the mass of the star cluster found from the IMF of Kroupa. Our values (9th column of Table 1) range from 0.04 to 0.17, which is consistent with the observed SFE in the Milky Way.

To study the kinematics of clusters, we used data on the proper motions of stars from the Gaia DR3 catalog. With them, we determined the average proper motions of the clusters and plotted the dependencies of the radial and tangential velocity components on the distance from the cluster center and on the position angle relative to the right ascension axis. At the base of these plots we concluded that stars of clusters S235North-West and S235A-B-C have a rather clear translational movement, but the cluster S235East1+East2 may contain some density waves or isolated kinematic groups of stars.

To assess the dynamic state of the clusters, we use the approach of Danilov (2024). If we determine the sign of the total energy, we can deduce whether the cluster-gas system is gravitationally bound or not. The total energy is calculated on

the assumption that the system consists of two components – stars and gas. For the cluster star mass, we use the mass obtained using the MF of Kroupa.

We find the velocity dispersion for the equation of the kinetic energy from the dispersion of the stars' proper motions. Assuming that the radial velocity distribution is the same as the velocity distribution in one tangential direction, the velocity dispersion is: $\sigma^2 = 1.5(\sigma^2_{\rm pmRA} + \sigma^2_{\rm pmDec})$. We take into account the contribution of the proper motion errors, considering the observed velocity distribution, the intrinsic velocity distribution, and the errors distribution to be Gaussian ones. Also, we consider the broadening of the observed velocity distribution by the KDE (a more detailed description of the method is given in Kulesh et al. 2024).

We note that the boundness of the systems depends on the size of the region for which the gas mass is estimated. So, when taking into account the gas located only in the areas of clusters, the total energy of the gas plus stars systems is negative only for the clusters S235Central and S235East1+East2. When the mass of the entire cloud is taken into account, all clusters have a negative total energy and appear to be gravitationally bound.

3 Summary

The work involved a study of four clusters in the star formation region G174+2.5 using data from the UKIDSS and Gaia catalogs.

1. The general parameters of clusters are determined - centers, radii, number of stars, extinction, distance and probabilities of star membership in clusters.
2. The masses of the cluster stars, the masses of gas in the regions under consideration, and the efficiency of star formation are estimated.
3. The average values of the proper motions of stars in clusters are estimated. The kinematics of the clusters have been studied: the clusters S235North-West and S235A-B-C appear to move as a single units, and the cluster S235East1+East2 may contain the isolated kinematic groups of stars.
4. We estimated the total energy of the stars+gas systems in the cluster regions. When the mass of the entire cloud is taken into account, all clusters considered as a stars+gas systems appear to be gravitationally bound.

It should be noted that the star counts and an analysis of the dynamical state of the clusters in our paper are based on the assumption of a spherical symmetry. However, the real structure and formation path differ from one cluster to another. Star formation in the clusters S235 North-West, S235 Central, S235 East1+East2 was rather induced by an expanding HII region Sh2-235 (Kirsanova et al. 2008, 2014). Consequently, these clusters have rather a flattened form. Star formation in

the cluster S235 A-B-C was rather spontaneous. Nevertheless, this cluster has a non-uniform structure and consists of some subclusters. Formation of some clusters in the envelope complicates the determination of the gas mass. A remarkable part of the gas there is ionised and is not visible in the molecular lines. Thus, our investigation can be considered as an attempt to use simple models for the real complex star formation region.

Acknowledgements. Authors are very grateful to Dr. A. M.Sobolev for his constant attention and useful comments. This work has made use of data from the European Space Agency (ESA) mission Gaia (https://www.cosmos.esa.int/gaia), processed by the Gaia Data Processing and Analysis Consortium (DPAC, https://www.cosmos.esa.int/web/gaia/dpac/consortium). Funding for the DPAC has been provided by national institutions, in particular the institutions participating in the Gaia Multilateral Agreement. This work uses data from the UKIDSS GPS catalog (version DR10PLUS) (Lucas et al. 2008).

Funding

These work was supported by the Ministry of science and higher education of the Russian Federation by an agreement FEUZ-2023-0019.

References

Brunt C., 2004, ASP Conf. Ser., 317, p. 79
Danilov V., 2024, Astrophysical Bulletin, 79, p. 71
Gaia Collaboration, Vallenari A., Brown A., et al., 2023, Astronomy and Astrophysics, 674, id. A1
Kirsanova M., Sobolev A., Thomasson M., et al., 2008, Monthly Notices of the Royal Astronomical Society, 388, p. 729
Kirsanova M., Wiebe D., Sobolev A., et al., 2014, Monthly Notices of the Royal Astronomical Society, 437, p. 1593
Krone-Martins A. and Moitinho A., 2014, Astronomy and Astrophysics, 561, id. A57
Kroupa P., 2001, Monthly Notices of the Royal Astronomical Society, 322, p. 231
Kulesh M., Samirkhanova A., Carraro G., et al., 2024, Astronomical Journal, 167, p. 212
Ladeyschikov D., Kirsanova M., Sobolev A., et al., 2021, Monthly Notices of the Royal Astronomical Society, 506, p. 4447
Lodieu N., Pérez-Garrido A., Smart R., et al., 2019, Astronomy and Astrophysics, 628, id. A66
Lombardi M., 2009, Astronomy and Astrophysics, 493, p. 735
Lucas P., Hoare M., Longmore A., et al., 2008, Monthly Notices of the Royal Astronomical Society, 391, p. 136
Seleznev A., 2016, Monthly Notices of the Royal Astronomical Society, 456, p. 3757

BAK 2024 MODERN ASTRONOMY: FROM THE EARLY UNIVERSE TO EXOPLANETS AND BLACK HOLES 300 years Russian Academy of Sciences

Radial profiles of systematic velocities in massive protostellar cores

L. Pirogov and P. Zemlyanukha

Gaponov-Grekhov Institute of Applied Physics of the Russian Academy of Sciences, 46 Ul'yanov str., Nizhny Novgorod, 603950 Russia

Abstract. The knowledge of systematic velocity radial profiles in the star-forming cores is important for theoretical models. We analyzed the HCO^+(1–0) spectral maps of five massive cores from the MALT90 database associated with the regions of high-mass star formation at different stages of evolution. We fitted the maps calculated in the framework of spherically symmetric model into observed ones. An approach based on the principal component analysis and the k-nearest neighbors method was used to find minimum of the error function between model and observed spectral maps. Radial profiles of density, turbulent and systematic velocity are obtained. Densities in the cores decrease with radial distance with power-law indices ranging from 1.5 to 2.5, turbulent velocities decrease with power-law indices ranging from 0.3 to 0.45. Systematic (infall) velocity profiles in the cores are close to $r^{-0.1}$ which differs from what is expected for free fall. Analysis of the ^{13}CO (2–1) SEDIGISM data for three sample objects has revealed the V-shape features on the position-velocity profiles which implies motions from surrounding gas to the cores. Taken together, the results support the scenario of globally contracting cores which interact with their surroundings.

Keywords: stars: formation, dense cores; methods: laboratory: molecular, modelling

DOI: 10.26119/VAK2024.082

1 Introduction

The scenario of massive star formation is still under debate. Theoretical studies of spherically symmetric collapsing cores predict specific solutions depending on their initial state (Whitworth & Summers 1985). Stable cores with little influence of external pressure evolve slowly and quasi-statically towards instability. Singular isothermal sphere (Shu 1977) and turbulent polytropic sphere (McKee & Tan 2003) models are proposed for high-mass star formation. Initially unstable cores evolve rapidly under the influence of external pressure. The model of global hierarchical collapse (Vázquez-Semadeni et al. 2019) considers cores and their parent clouds as nonequilibrium dynamic objects. The cores collapse with constant infall velocity before the protostar formation. After this, both quasi-static and unstable core models have the $r^{-0.5}$ velocity radial profile in the inner free fall region, while the envelope retains its initial velocity structure. The envelope density corresponds to the common r^{-2} profile in both models. To test theoretical scenarios, we need to know systematic velocity profiles in the envelope.

The spatial distribution of systematic velocity within a core can be determined by fitting model spectral maps into observed ones. Among molecular lines, dense gas tracers, the HCO^+ lines are the most sensitive to systematic motions (Yoo et al. 2018). However, the direct fitting of spectral maps is time-consuming and rarely used due to correlations between parameters, dependence on initial conditions and poor convergence. Recently, a method based on a preliminary set of model spectral maps (Pirogov & Zemlyanukha 2021) has been developed using principal component analysis (PCA) and the k-nearest neighbors method (kNN). Using a spherically symmetric model, radial profiles of infall velocity were obtained in the L1287 (Pirogov & Zemlyanukha 2021) and G268.42−0.85 cores (Pirogov et al. 2023). The derived power-law indices are different from free fall, implying that the cores are unstable and globally collapsing. To make general conclusions, it is important to expand the list of analyzed objects.

2 A sample of the MALT90 cores

The MALT90 survey (Jackson et al. 2013) is the largest database of high-mass clumps (over 2000 objects) observed in molecular lines in the 3 mm range and based on the ATLASGAL 870 μm dust continuum Galactic plane survey (Schuller et al. 2009). Among the MALT90 objects with notable HCO^+(1–0) emission (peak $T_a^* \gtrsim 1$ K) we selected 110 ones with asymmetric HCO^+(1–0) lines and/or absorption dips. In 20 cores, the HCO^+(1–0) lines possess dips with "blue" peaks exceeding the "red" one. The peaks of the $H^{13}CO^+$(1–0) and N_2H^+(1–0) lines of lower optical depth are close to the velocity of the HCO^+(1–0) dips, probably implying contraction. In this study

we present the results of analysis of five cores. The list of the sample cores is given in Table 1.

Table 1. The list of the sample cores. Kinematic distances are taken from Urquhart et al. (2022). Evolution statuses (Guzmán et al. 2015; Rathborne et al. 2016) are the following: H II region (H), protostellar core (A) and uncertain (U).

Source	l deg	b deg	RA(J2000) hh:mm:ss	Dec(J2000) $^o:':''$	D kpc	Evolution status	Associations with other sources
G012.418+00.506	12.419	0.507	18:10:51.1	−17:55:49.6	1.8	H	IRAS 18079−1756, EGO
G326.472+00.888	326.472	0.889	15:42:29.6	−53:58:26.7	2.5	U	
G328.567−00.535	328.568	−0.534	15:59:37.4	−53:45:51.7	2.9	H	IRAS 15557−5337, RCW99
G335.586−00.289	335.586	−0.289	16:30:58.7	−48:43:48.0	3.2	A	IRAS 16272−4837, SIRDC, EGO
G343.127−00.063	343.128	−0.063	16:58:17.5	−42:52:04.0	2.8	A	IRAS 16547−4247, EGO

The HCO^+(1–0) integrated intensity maps of the sample cores together with the Spitzer[1] and ATLASGAL maps are shown in Fig. 1. Four sources are associated with bright IRAS sources ($L_{\rm bol}$ are of the order of 10^4–10^5 $L_\odot$), three of them possess maser sources[2]. The masses of cores derived from the dust continuum lie in the range: 280–1200 $M_\odot$ (Csengeri et al. 2017; Lin et al. 2019). Values of dust temperatures vary in the range of 20–35 K (Urquhart et al. 2022). The G326.472 core with no embedded sources is probably at the earliest stage of evolution.

Table 2. Physical parameters of the MALT90 cores obtained from modeling: values of n_0, $V_{\rm turb}$ and $V_{\rm sys}$ in the central layer with the radius of 6.5×10^{-3} pc.

Object	$\log n_0$ [cm^{-3}]	α_n	$V_{\rm turb}$ km/s	$\alpha_{\rm turb}$	$V_{\rm sys}$ km/s	$\alpha_{\rm sys}$	$\log X$ (HCO^+)
G012.418+00.506	$9.0^{+0.1}_{-1.1}$	$2.5^{+0.1}_{-0.2}$	$3.2^{+3.8}_{-0.2}$	$0.38^{+0.02}_{-0.13}$	$-1.6^{+0.6}_{-0.5}$	$0.1^{+0.05}_{-0.05}$	$-9.8^{+0.3}_{-0.7}$
G326.472+00.888	$8.3^{+0.7}_{-0.4}$	$1.5^{+0.3}_{-0.1}$	$8.4^{+3}_{-0.9}$	$0.36^{+0.09}_{-0.06}$	$-1.6^{+0.4}_{-0.3}$	$0.1^{+0.05}_{-0.07}$	$-10.9^{+0.4}_{-0.4}$
G328.567−00.535	$9.1^{+0.1}_{-0.6}$	$2.0^{+0.1}_{-0.5}$	5^{+5}_{-1}	$0.33^{+0.22}_{-0.08}$	$-1.0^{+0.1}_{-1.0}$	$0.06^{+0.14}_{-0.03}$	$-10.3^{+0.3}_{-1.1}$
G335.586−00.289	$9.7^{+0.2}_{-1.0}$	$2.1^{+0.3}_{-0.6}$	$4.8^{+2.8}_{-1.8}$	$0.30^{+0.2}_{-0.05}$	$-1.6^{+0.6}_{-0.5}$	$0.1^{+0.1}_{-0.05}$	$-10.6^{+0.2}_{-0.6}$
G343.127−00.063	$8.7^{+0.8}_{-0.2}$	$2.0^{+0.3}_{-0.2}$	$10^{+0.1}_{-3.4}$	$0.45^{+0.01}_{-0.14}$	$-1.1^{+0.1}_{-0.9}$	$0.06^{+0.09}_{-0.06}$	$-9.9^{+0.3}_{-0.7}$

3 Results and discussion

The performed HCO^+(1–0) spectral maps were modeled using a spherically symmetric multi-layer model, where density n_0, turbulent $V_{\rm turb}$ and systematic $V_{\rm sys}$ velocities depend on radial distance as: $P_0/(1 + (r/R_0)^{\alpha_P})$ (see Appendix to Pirogov &

[1] https://irsa.ipac.caltech.edu/data/SPITZER/GLIMPSE/

[2] The maser sources positions are taken from https://maserdb.net database (Ladeyschikov et al. 2019)

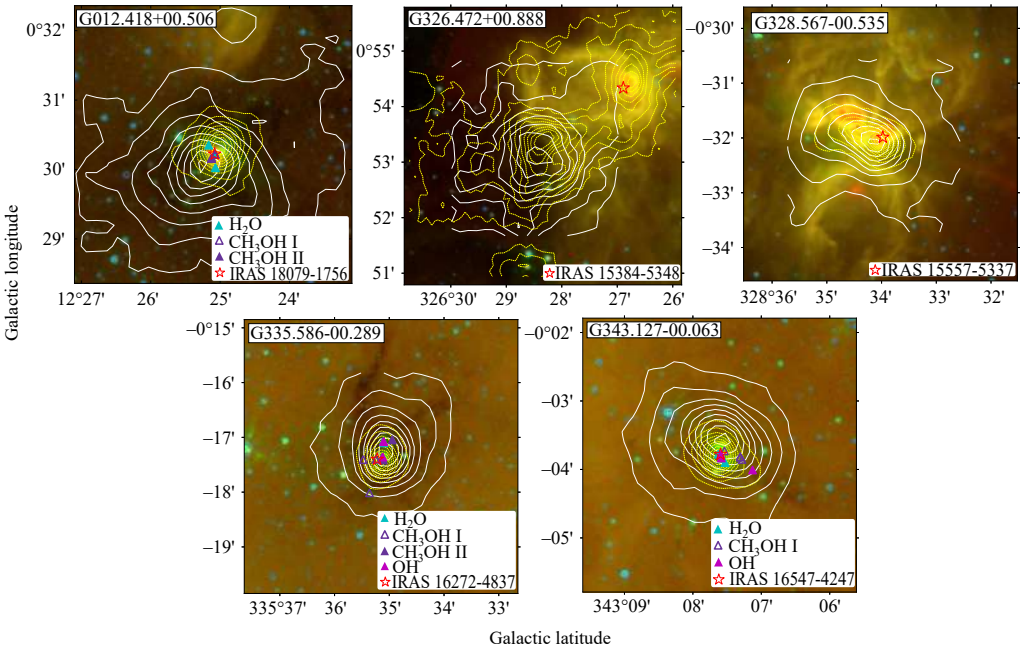

Fig. 1. Maps of the MALT90 sample cores. The colors represent the Spitzer data at 8 μm (red), 5.8 μm (green) and 3.6 μm (blue). The ATLASGAL data are shown by yellow dotted contours. The MALT90 HCO^+(1–0) integrated intensities are shown by white contours. The contours range from 10% to 90% of peak intensities.

Zemlyanukha 2021). The minimum of the error function between model and observed maps was found using the PCA and kNN methods, and the derived parameters are given in Table 2. Uncertainties were obtained from the analysis of the error projections function on the planes of different pairs of parameters (Pirogov & Zemlyanukha 2021; Pirogov et al. 2023).

Density profile power-law indices vary from -1.5 to -2.5. The G012.418 core has the sharpest density profile, the G326.472 core has the most shallow one. All the cores appear to be highly turbulent. Turbulent velocity profile indices vary from -0.3 to -0.45. Systematic velocities are negative corresponding to infall. Their profiles in all the cores are close to $r^{-0.1}$.

In the SEDIGISM survey (Schuller et al. 2021), the regions with the G012.418, G335.586 and G343.127 cores were observed. Analysis of the ^{13}CO(2–1) position-velocity profiles revealed the V-shape features (Fig. 3), which are signatures of accretion motions from surrounding gas to the cores located closer to the observer (e.g., Zhou et al. 2023). The fitting of model radial velocity profiles ($r^{-\alpha}$) with different α values shows that profiles with $\alpha \lesssim 0.5$ are preferable for the cores.

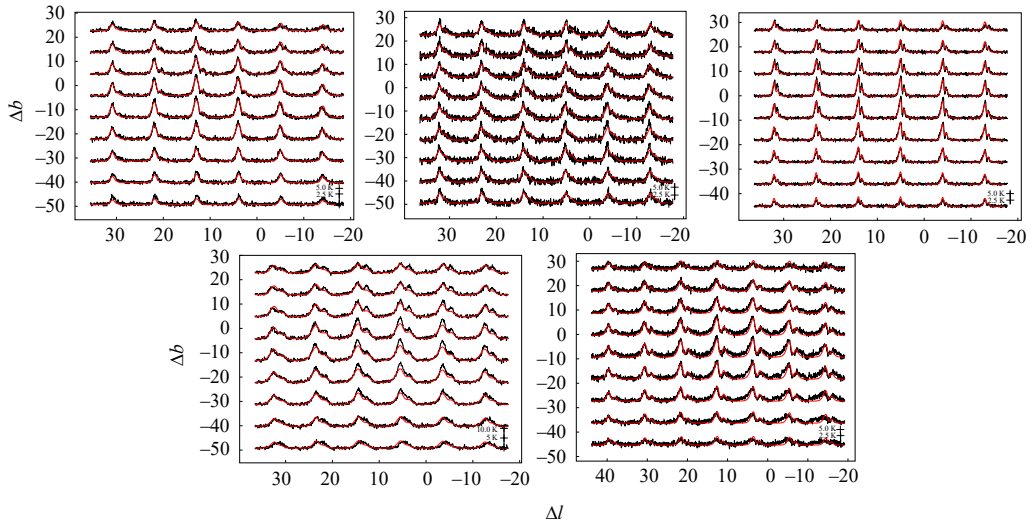

Fig. 2. The observed (black) and model (red) spectral maps of the sample cores in the HCO^+(1–0) line. The axes are the offsets relative to the coordinates from Table 1. Intensity scales are shown in the lower right corners of each panel. Velocity ranges (in km/s) are: [7. . . 26], [−52. . . −29], [−54.5. . . −41] for G012.418, G326.472, G328.567, respectively (upper row) and [−54. . . −39],[−42. . . −20] for G335.586, G343.127, respectively (lower row).

4 Summary

We analyzed the HCO^+(1–0) spectral maps of five massive MALT90 cores associated with the regions of high-mass star formation at different stages of evolution. Using a spherically symmetric model and an algorithm for minimizing the error between model and observed spectral maps, radial profiles of n_0, $V_{\rm turb}$, $V_{\rm sys}$ are obtained. Densities in the cores decrease with radial distance with power-law indices from 1.5 to 2.5, turbulent velocities decrease with power-law indices from 0.3 to 0.45. Systematic (infall) velocity profiles are close to $r^{-0.1}$, which is different from what is expected for free fall. Analysis of position-velocity profiles from the ^{13}CO (2–1) SEDIGISM data revealed the V-shape features in three sample objects implying motions from surrounding gas to the cores. So the results support the scenario of globally contracting cores which interact with their surroundings.

Acknowledgements. This research has made use of the MALT90 Database available in the Australian Telescope Online Archive (http://atoa.atnf.csiro.au), and the SEDIGISM database (https://sedigism.mpifr-bonn.mpg.de) constructed by James Urquhart and hosted by the Max Planck Institute for Radio Astronomy.

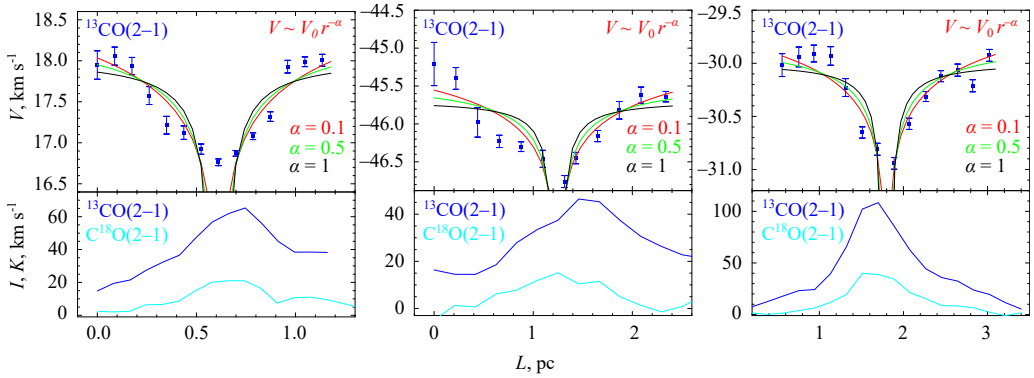

Fig. 3. The position-velocity profiles (upper panels) and the ^{13}CO (2–1) and C^{18}O (2–1) integrated intensity profiles (lower panels) across the G012.418 (left), G335.586 (center) and G343.127 (right) cores. Smooth curves of different colors correspond to the model radial velocity profiles.

Funding

The work is supported by the Russian Science Foundation grant No. 23-22-00139.

References

Csengeri T., Bontemps S., Wyrowski F., et al., 2017, Astronomy & Astrophysics, 601, id. A60
Guzmán A., Sanhueza P., Contreras Y., et al., 2015, Astrophysical Journal, 815, 2, id. 130
Jackson J., Rathborne J., Foster J., et al., 2013, Publ. Astron. Soc. Australia, 30, id. e057
Ladeyschikov D., Bayandina O., Sobolev A., 2019, Astronomical Journal, 158, 6, id. 233
Lin Y., Csengeri T., Wyrowski F., et al., 2019, Astronomy & Astrophysics, 631, id. A72
McKee C. and Tan J., 2003, Astrophysical Journal, 585, 2, p. 850
Pirogov L. and Zemlyanukha P., 2021, Astronomy Reports, 65, 2, p. 82
Pirogov L., Zemlyanukha P., Dombek E., et al., 2023, Astronomy Reports, 67, 12, p. 1355
Rathborne J., Whitaker J., Jackson J., et al., 2016, Publ. Astron. Soc. Australia, 33, id. e030
Schuller F., Menten K., Contreras Y., et al., 2009, Astronomy & Astrophysics, 504, 2, p. 415
Schuller F., Urquhart J., Csengeri T., et al., 2021, Monthly Notices of the Royal Astronomical Society, 500, 3, p. 3064
Shu F., 1977, Astrophysical Journal, 214, p. 488
Urquhart J., Wells M., Pillai T., et al., 2022, Monthly Notices of the Royal Astronomical Society, 510, 3, p. 3389
Vázquez-Semadeni E., Palau A., Ballesteros-Paredes J., et al., 2019, Monthly Notices of the Royal Astronomical Society, 490, 3, p. 3061
Whitworth A. and Summers D., 1985, Monthly Notices of the Royal Astronomical Society, 214, p. 1
Yoo H., Kim K., Cho J., et al., 2018, Astrophysical Journal Supplement, 235, 2, id. 31
Zhou J., Wyrowski F., Neupane S., et al., 2023, Astronomy & Astrophysics, 676, id. A69

MODERN ASTRONOMY: FROM THE EARLY UNIVERSE TO EXOPLANETS AND BLACK HOLES

The impact of non-ideality effects in dense plasma on the evolution of white dwarfs

D. Podkuichenko[1,2] and S. Blinnikov[1,2]

[1] Kurchatov Complex of Theoretical and Experimental Physics of the National Research Center, 25 Bolshaya Cheremushkinskaya, Moscow, 117218 Russia
[2] Sternberg State Astronomical Institute of Moscow State University, 13 Universitetsky Pr., Moscow, 119992 Russia

Abstract. Recently made possible observations of cool and faint white dwarfs using the Gaia and other telescopes provide rich material for refining the modeling of the final stage of their evolution, which in turn can be used to study the behavior of matter under extreme conditions. In this paper, we simulate the thermal evolution of white dwarfs for different atmospheric compositions using equations of state for non-ideal dense plasma. By taking into account the effects of non-ideality in the code for the evolution of white dwarfs, it is possible to reach the stage of crystallization at the center of the star. The subsequent acceleration of cooling is significant for massive white dwarfs ($M \approx 1.3\,M_{\odot}$), for which the cooling time at $T_{\rm eff} \approx 3 \times 10^3\,$K decreases almost 10 times compared to the calculation without non-ideality effects.

Keywords: stars: evolution, white dwarfs; dense matter; equation of state; plasmas

DOI: 10.26119/VAK2024.083

1 Introduction

Gradually cooling down throughout their lives, white dwarfs (WD) reach temperatures of several thousand Kelvin on the surface and ages of the order of the age of the universe. Studying the population of these stars can make it possible to reconstruct the history of Galaxy formation, cosmochronology, and investigate the properties of plasma under conditions unattainable on earth. The coldest objects found so far have temperatures of $T_{\text{eff}} \approx 3050$ K and $T_{\text{eff}} \approx$ 3340 K and the age of about 10 and 9 billion years old, respectively (Elms et al. 2022). In such stars, plasma can pass into the liquid or crystal phase. A large number of observational data requiring explanation on the one hand, as well as the most accurate theories of the plasma state on the other, lead to a demand for the creation of detailed models of the evolution of white dwarfs up to the late stages of cooling, when non-ideality and quantum effects on.

In this paper, the thermal evolution of white dwarfs is modeled using the code created by S. I. Blinnikov and N. V. Dunina-Barkovskaya, which allows to calculate the cooling of white dwarfs on time scales of the order of the age of the universe (Blinnikov & Dunina-Barkovskaya 1993, 1994). Blinnikov's models were originally created for hot white dwarfs. For such objects, plasma can be described by the equation of state of Nadyozhin for an ideal gas, since Coulomb interactions between particles can be neglected (Blinnikov et al. 1996). However, at later stages of evolution, when the temperature decreases it becomes necessary to take them into account, and a different equation of state is needed.

Taking the equation of state for a non-ideal plasma, we have obtained a noticeable decrease in cooling time, which is especially pronounced for massive objects. This is an expected result, since there is a Debye suppression of the heat capacity for a low temperature crystal, which should lead to faster cooling.

Section 2 describes the equations of state and the operation of the program. Section 3 presents obtained evolutionary curves. In Section 4, we discuss the results and consider opportunities for further improvement of the models.

2 The technical part

The construction of models is done in three stages: first, we take the equation of state of matter, then an initial object is created from it, and then its evolution is considered.

We replaced the code block responsible for the equation of state of matter, using Potekhin–Chabrier equations of state (version 2022). These analytical equations for non-ideal plasma allow to calculate the stages of a Coulomb liquid and a crystal consisting of atomic nuclei and a homogeneous electron background, and also take

into account quantum effects that are important for late stages of the evolution of WD (Potekhin & Chabrier 2013). The code for the equation of state is publicly available[1].

For detailed calculations of the evolution, the code uses differential hydrodynamic equations in Lagrangian form for a spherically symmetric star. To start evolution, it is necessary to build initial artificial hydrostatic models, for which cooling is further simulated. These models are built using the Nadyozhin–Razinkova method, the initial radius of the simulated object is much larger than the typical radii of white dwarfs (Nadyozhin & Razinkova 1986).

An important value for describing matter in white dwarfs is the non-ideality parameter Γ, or the Coulomb coupling parameter. This quantity shows the ratio of the forces of interaction between particles to their kinetic energy, showing the degree of applicability of the ideal gas approximation to the description of matter.

For ions, the value of the Coulomb coupling parameter will be as follows:

$$\Gamma_i = \frac{(Ze)^2}{a_i k_B T} = \Gamma_e Z^{5/3}, \tag{1}$$

where a_i is the average distance between ions, $a_i = \left(\frac{4}{3}\pi n_i\right)^{-1/3}$, T and n_i are the temperature and concentration of ions respectively, Γ_e is the Coulomb coupling parameter for electrons.

At $\Gamma << 1$, matter can be described with good accuracy using the ideal gas approximation. Crystallization begins at $\Gamma \approx 180$ (Segretain & Chabrier 1993; Potekhin & Chabrier 2010).

3 Results

The initial models of objects, for which cooling was subsequently calculated, did not differ from each other for the Potekhin and Nadyozhin equations of state, since the effects of non-ideality appear only when the white dwarf has cooled sufficiently so that the interaction between the particles becomes significant.

Figure 1 show the series of obtained cooling curves for luminosity for different values of the mass of a white dwarf and different atmospheric compositions.

For the ages of the white dwarf of the order of a billion years, the differences between models with different equations of state are practically not noticeable, since the white dwarf is still hot enough for Coulomb interactions between particles not

[1] http://www.ioffe.ru/astro/EIP/

to play a role in it. However, later there is a significant increase in the cooling rate for models with the Potekhin equation of state. The crystallized matter cools down faster, as the thermal conductivity decreases according to Debye's law.

The more massive the white dwarf is, the higher the pressure and Coulomb coupling parameter values in it, and the faster it will reach a stage at which Coulomb interactions between particles will be commensurate with kinetic energy. Therefore, the most significant difference between the models is for massive white dwarfs.

Also in Fig. 1, models are shown for two chemical composition options: with a thin ($q_{\rm H} = 10^{-10}\,M_\odot$, $q_{\rm He} = 10^{-2}\,M_\odot$) and a thick layer of hydrogen ($q_{\rm H} = 10^{-4}\,M_\odot$, $q_{\rm He} = 10^{-2}\,M_\odot$). It can be seen that the thick hydrogen-helium shell of the white dwarf slows down cooling due to the high opacity value.

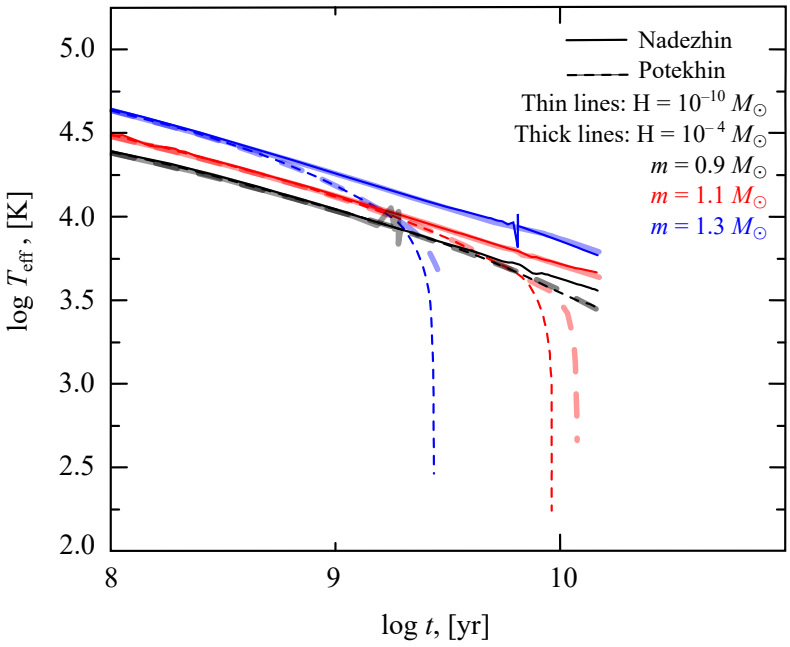

Fig. 1. Dependence of the logarithm of luminosity on the age of white dwarfs. Different colors correspond to models with different values of stellar mass. Dashed curves correspond to models with the Potekhin equation, solid curves correspond to models with the Nadyozhin equation. Thin and opaque curves were plotted for the thin shell model with $q_{\rm H} = 10^{-10}\,M_\odot$, $q_{\rm He} = 10^{-2}\,M_\odot$, thick and translucent corresponds to a model with a thick shell with $q_{\rm H} = 10^{-4}\,M_\odot$,$q_{\rm He} = 10^{-2}\,M_\odot$.

Figure 2 shows a comparison between the evolutionary tracks obtained from three models: with the equation of state of Nadyozhin, Potekhin and the Bergeron model

(all models are constructed for a thin layer of hydrogen in atmospheres) (Fontaine et al. 2001; Bédard et al. 2020). For medium-mass white dwarfs, it can be seen that Bergeron models show faster cooling, since our models do not calculate convection, so the white dwarf reacts slowly to the release of heat in the core, which is of great importance for such objects. For objects with masses 1.0 $M_\odot$ and higher, stars in the model with Potekhin's equation of state cool faster. It is in this range of parameters that the effects of plasma non-ideality are most clearly manifested due to the changes in the heat capacity of the crystal.

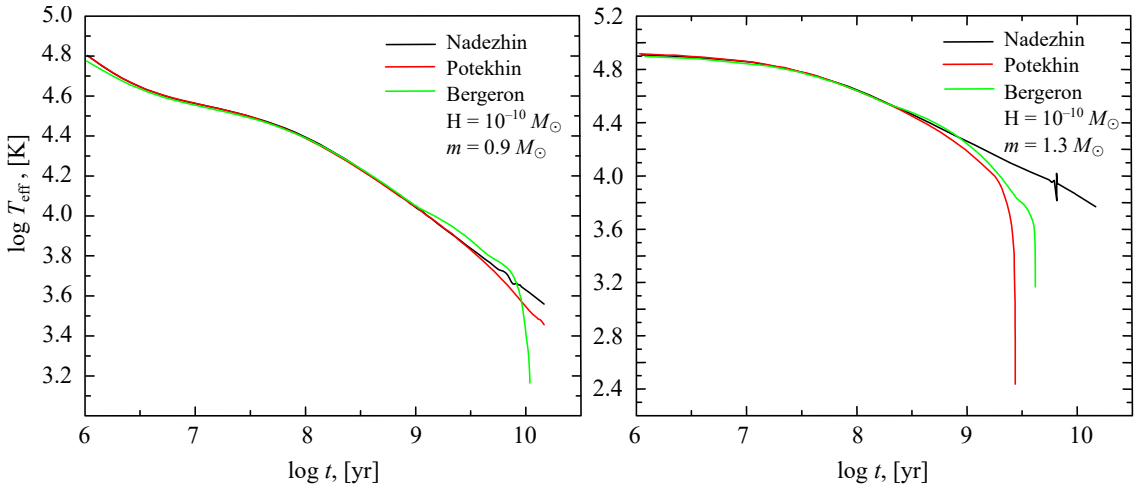

Fig. 2. Dependence of the logarithm of the effective temperature on the age of the white dwarf for three models: the Bergeron model (green line), the model with the Potekhin state equation (red line), the model with the Nadyozhin equation of state (black line) for different masses and thin atmospheres with the masses of hydrogen and helium, respectively $q_{\rm H} = 10^{-10}\,M_\odot$, $q_{\rm He} = 10^{-2}\,M_\odot$.

4 Discussion

We simulated the evolution of white dwarfs using the equation of state for non-ideal dense plasma. This made it possible to reproduce the crystallization and Debye cooling phases.

Our cooling curves do not account for convection, so heat transfer is not as efficient and fails to reproduce the peak in luminosity from the release of latent heat of the phase transition. This also explains the differences from the cooling curves obtained by Bergeron's group for medium-massive white dwarfs. In the region of Debye cooling for massive white dwarfs, our model predicts a faster cooling rate than other studies.

There are ways to further improve the model and account for more subtle effects. Convection must be taken into account to correctly describe the transfer of heat from the interior of a white dwarf to the surface. Also, used equation of state makes it possible to simulate multicomponent plasma (up to 10 elements). Our code uses only mixtures of oxygen and carbon.

Adding neon to the core of a white dwarf and taking diffusion into account makes it possible to run processes such as neon settling and separation of liquid and crystalline phases, which leads to the release of gravitational energy. This factor also affects the cooling rate, so it is taken into account in many works (Bauer 2023), (Camisassa et al. 2022).

References

Bauer E.B., 2023, Astrophysical Journal, 950, 2, id. 115

Bédard A., Bergeron P., Brassard P., et al., 2020, Astrophysical Journal, 901, 2, id. 93

Blinnikov S.I. and Dunina-Barkovskaya N.V., 1994, Monthly Notices of the Royal Astronomical Society, 266, p. 289

Blinnikov S.I. and Dunina-Barkovskaya N.V., 1993, Astronomy Reports, 37, 2, p. 187

Blinnikov S., Dunina-Barkovskaya N., Nadyozhin D., 1996, Astrophysical Journal Supplement, 106, p. 171

Camisassa M.E., Althaus L.G., Koester D., et al., 2022, Monthly Notices of the Royal Astronomical Society, 511, 4, p. 5198

Elms A.K., Tremblay P.-E., Gänsicke B.T., et al., 2022, Monthly Notices of the Royal Astronomical Society, 517, 3, p. 4557

Fontaine G., Brassard P., Bergeron P., 2001, Publications of the Astronomical Society of the Pacific, 113, 782, p. 409

Nadyozhin D.K and Razinkova T.L, 1986, Nauchnye Informatsii, 61, p. 29

Potekhin A.Y. and Chabrier G., 2013, Astronomy & Astrophysics, 550, id. A43

Potekhin A.Y. and Chabrier G., 2010, Contributions to Plasma Physics, 50, 1, p. 82

Segretain L. and Chabrier G., 1993, Astronomy & Astrophysics, 271, p. L13

MODERN ASTRONOMY: FROM THE EARLY UNIVERSE TO EXOPLANETS AND BLACK HOLES

Periodic changes in the orientation of orbits and the age of the Galactic bar

E. Podzolkova[1,2] and A. Melnik[1]

[1] Sternberg Astronomical Institute, Lomonosov Moscow State University, Universitetskij pr. 13, Moscow, 119991 Russia

[2] Faculty of Physics, Lomonosov Moscow State University, Leninskie Gory 1–2, Moscow, 119991 Russia

Abstract. We studied the model of the Galaxy that reproduces the observed median velocity distribution derived from *Gaia* DR3 data along the Galactocentric distance, R. The model profiles of radial velocity, V_R, demonstrate an increase with a period of $P = 2.1 \pm 0.1$ Gyr and form humps at $R = 6$–7 kpc. The average amplitude of variation in the radial velocity is $A = 1.76 \pm 0.20\,\mathrm{km\,s^{-1}}$. The humps are supported by orbits changing orientation relative to the major axis of the bar within the range of $[-45,\ 45]^\circ$. The median period of variation in the angular momentum of hump-supporting orbits is $P = 1.85 \pm 0.17$ Gyr, and 71.6 % of them support ring R_2. The observed profile does not show any humps. In the model profile, humps disappear during the times 2.5 ± 0.3 and 4.5 ± 0.5 Gyr, indicating that the age of the Galactic bar must be close to one of these values. The model disk forms outer resonance rings R_1 and R_2, which demonstrate periodic changes in their morphology with a period of $P = 2.0 \pm 0.1$ Gyr, supported by orbits trapped by the Outer Lindblad Resonance.

Keywords: Galaxy: kinematics and dynamics

DOI: 10.26119/VAK2024.084

1 Introduction

Although there is strong evidence for the existence of a bar in the Galaxy, for example, see Benjamin et al. (2005), its age is still a matter of debate. Different estimates show values ranging from 3 to 8 Gyr. The angular velocity of the bar, Ω_b, usually lies in the range 40–60 $\mathrm{km\,s^{-1}\,kpc^{-1}}$. The rotation of the bar leads to the appearance of resonances:

$$\frac{m}{n} = \frac{\kappa}{\Omega - \Omega_\mathrm{b}}, \tag{1}$$

where m is the number of full epicyclic oscillations that a star makes during n revolutions relative to the bar, and κ is the epicyclic frequency. The conditions $\Omega = \Omega_\mathrm{b}$, $m/n = 2/1$ and $m/n = -2/1$ determine the locations of the Corotation Radius (CR), Inner Lindblad Resonance (ILR) and Outer Lindblad Resonance (OLR), respectively. Weinberg (1994) demonstrated that stars captured by the ILR and OLR frequently exhibit periodic changes in the direction of their orbital elongation relative to the major axis of the bar.

2 Observations and the model

We selected stars with measured line-of-sight velocities from the *Gaia* DR3 catalog (Gaia Collaboration et al. 2023) that lie near the Galactic plane ($|z| < 200$ pc) and within a sector of Galactocentric angles $|\theta| < 15^\circ$. We excluded stars that have parallaxes determined with the relative error of more than 20 % ($\varpi/\epsilon_\varpi < 5$) and with the renormalized error RUWE > 1.4. The final sample includes 9.7×10^6 objects. The solar Galactocentric distance is adopted to be $R_0 = 7.5$ kpc. We calculated the median radial (V_R) and azimuthal (V_T) velocity components in 250-pc wide bins along the distance R. The observed radial velocity profile has specific features: V_R demonstrates a plateau with $V_R \approx 5\,\mathrm{km\,s^{-1}}$ at the distance range of 5—7 kpc and then a smooth fall to the value of $V_R \approx -3\,\mathrm{km\,s^{-1}}$ at the distance $R = 8.5$ kpc (see red dashed line in Fig. 1a, b).

We studied a 2D model of the Galaxy with an analytical Ferrers bar (Athanassoula et al. 1983) that reproduces well the observed velocity profiles. The model has a flat rotation curve at the periphery and includes a bar, a bulge, a disk, and an isothermal halo. Semi-axes of the bar are $a = 3.5$ kpc and $b = 1.35$ kpc, and its mass is $M_{rmb} = 1.2 \times 10^{10}$ $\mathrm{M_\odot}$. The angular velocity of the bar is $\Omega_\mathrm{b} = 55\,\mathrm{km\,s^{-1}\,kpc^{-1}}$, which leads to the positions of the CR and OLR at $R_\mathrm{CR} = 4.04$ kpc and $R_\mathrm{OLR} = 7.00$ kpc, respectively. At the start of the simulation, the model disk is axisymmetric, and the non-axisymmetric component grows over 4 bar rotation periods, which corresponds to $T = 450$ Myr. Model includes 2×10^6 massless particles, and the time of

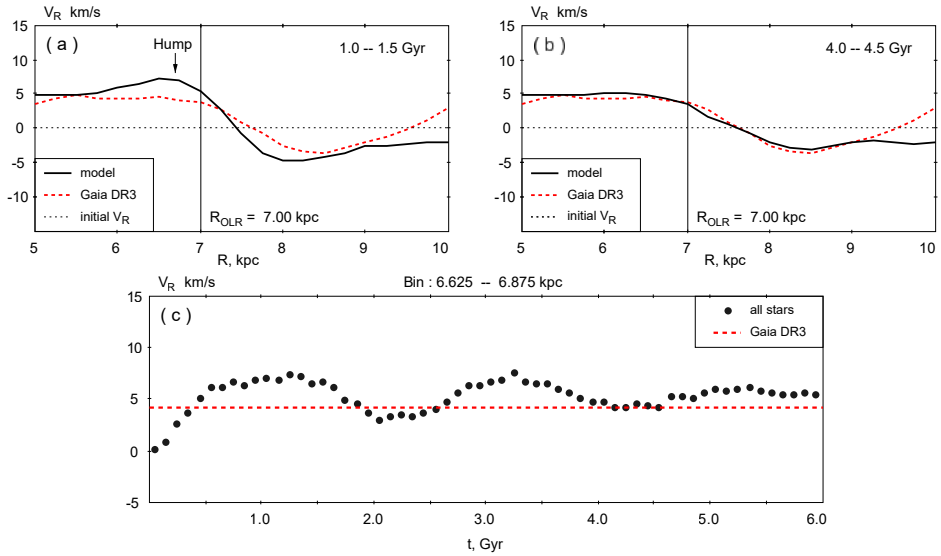

Fig. 1. The appearance of the humps on the radial velocity distribution. (a) Distribution of the median radial velocity, V_R, along the Galactocentric distance in the sector of $|\theta - \theta_\odot| < 15°$, averaged over time interval of $T = 1.0$ – 1.5 Gyr. The model velocity distribution is shown by the black solid line, while the observed one is shown by the red dashed line. The model distribution shows the hump with the maximum height $1.9 \pm 0.12\,\mathrm{km\,s^{-1}}$ at the distance range of $R = 6$–7 kpc. (b) The same distribution calculated for the time interval of $T = 4.0$ – 4.5 Gyr. Note the absence of the hump. (c) Median radial velocity in the bin of the Galactocentric distance of $6.625 < R < 6.875$ kpc over time (black dots). The observed velocity is shown by a red dashed line.

simulation is 6 Gyr. The position angle of the Sun relative to the major axis of the bar is adopted to be $\theta_\odot = -45°$. The order of symmetry of the model is $m = 2$. For more detail, see Melnik et al. (2021).

3 Results and discussion

Figure 1a, b shows model profiles of the radial velocity compared to the observed ones for two time intervals: $T = 1.0$–1.5 Gyr and 4.0–4.5 Gyr from the start of simulation. The model profiles were calculated in the sector of azimuthal angles $|\theta - \theta_\odot| < 15°$ and averaged over the time intervals of 500 Myr. Figure 1a shows an increase in the model velocity in the distance range of 6–7 kpc. Figure 1b shows no hump. Figure 1c shows the variation in the model velocity V_R over time in a sector of maximal height of the hump: $|\theta - \theta_\odot| < 15°$ and $R = 6.625$–6.875 kpc. Amplitude of V_R variations decreases with time. The values of V_R were averaged over intervals of 100 Myr. Parameters of oscillations calculated at the interval 0–6 Gyr are following:

the average amplitude $A = 1.76 \pm 0.20\,\mathrm{km\,s^{-1}}$, the initial phase $\varphi = 257 \pm 5°$, the average velocity is $\overline{V_R} = 5.2 \pm 0.1\,\mathrm{km\,s^{-1}}$, and the period is $P = 2.1 \pm 0.1$ Gyr.

We identified stars that support the humps on the V_R-velocity profiles. These stars appear to lie in the considered sector of the model disk and have negative radial velocities V_R, thereby reducing the median radial velocity within it. We selected a sample of 26308 stars (9 % of all stars which lie both inside and outside the OLR) which change the direction of their orbital elongation relative to the major axis of the bar, θ_0, as $0 < \theta_{01} < 45°$, $-45 < \theta_{02} < 0°$ and $0 < \theta_{03} < 45°$ during time intervals of 0–1, 1–2 and 2–3 Gyr, respectively. The median period of variation in the angular momentum of the sample is $P = 1.85 \pm 0.17$ Gyr, and 71.6 % of orbits are elongated along the major axis of the bar and support the ring R_2.

Figure 2a shows an example of hump-supporting orbit. It is clearly seen that at the time intervals of 0–1 and 2–3 Gyr the orbit is tilted to the right, in the direction opposite to that of the Galactic rotation, while at the interval of 1–2 Gyr it is tilted to the left. Figure 2b shows the orientation of the orbit as a function of time. The periodic character of θ_0 is well seen, as it decreases slowly from 45 to $-45°$, and then grows back quickly.

Figure 2c shows the variation in the beat frequency, w_{bt}. The change in the sign of w_{bt} indicates that the orbit is librating, meaning it reverses the direction of apsidal precession, and its elongation direction oscillates within a certain angle range (see Melnik & Podzolkova 2024, Eq. 9).

After excluding 26308 hump-creating stars, the humps on the V_R profiles disappear. To estimate the influence of these stars, we calculated the ratio of the amplitude A to its uncertainty, ε_A. For all stars in the considered segment, the ratio is $|A/\varepsilon_A| = 8.8$. After excluding hump-creating stars, at the fixed values of the period and phase, we obtained $A = -0.21 \pm 0.19\,\mathrm{km\,s^{-1}}$ ($|A/\varepsilon_A| = 1.1$), so the amplitude becomes close to its uncertainty.

Figure 3 shows the comparison between the model and observed V_R-velocity profiles. The χ^2 function has two minima at 2.5 ± 0.3 and 4.5 ± 0.5 Gyr, corresponding to the times when the model profiles have no humps. This suggests that the age of the Galactic bar must be close to 2.5 ± 0.3 or 4.5 ± 0.5 Gyr (for more details, see Melnik & Podzolkova 2024).

Melnik et al. (2023) studied periodic changes in the morphology of the inner and outer rings. The model disk forms the nuclear ring, the inner combined ring, and the outer resonance rings R_1 and R_2. We found the morphological changes in the outer resonance rings R_1 and R_2 with a period of $P = 2.0 \pm 0.1$ Gyr. These changes are driven by a mechanism similar to that of hump formation. The orbits, similar to the one shown in Fig. 2a, are tilted to the right during time intervals of 0–1

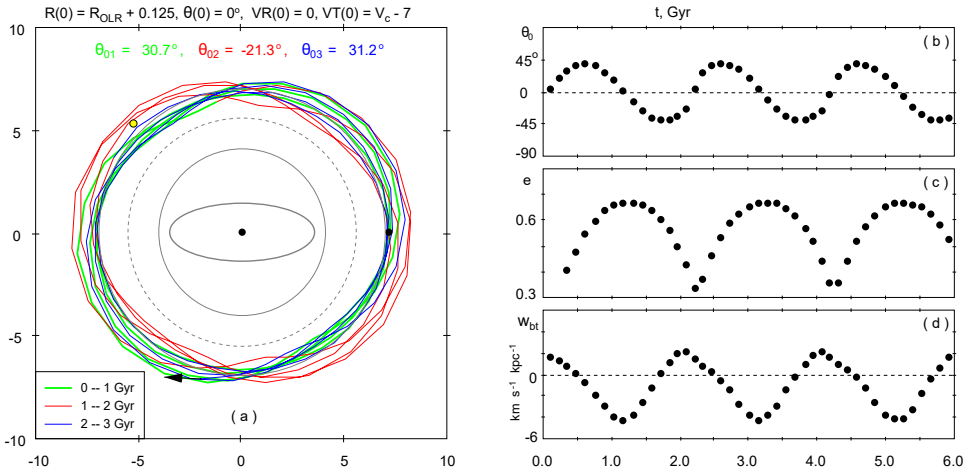

Fig. 2. An example of a hump-supporting orbit. (a) Orbit of the star in the reference frame associated with the rotating bar. The Galaxy rotates counterclockwise, but in the reference frame of the rotating bar the star rotates clockwise. The frame size is 10×10 kpc. The position of the Sun is shown by the yellow circle. At the beginning of the simulation, the star is located in the direction of the bar's major semi-axis at a distance $R(0) = R_{\rm OLR} + 0.125$ kpc (black circle). The initial radial and azimuthal velocities are $V_R(0) = 0$ and $V_T(0) = V_{\rm C} - 7\,{\rm km\,s^{-1}}$, where $V_{\rm C}$ is the velocity of the rotation curve. The angles θ_{01}, θ_{02}, and θ_{03} determine the orientations of the orbit with respect to the major axis of the bar at time intervals of 0–1, 1–2, and 2–3 Gyr, respectively. The bar is shown by the ellipse, the CR and the OLR — by the gray solid lines, and the $-4/1$ resonance — by the dashed line. (b) Variation in the angle θ_0 over time. (c) Changes in the eccentricity of the orbit over time. (d) Changes in the beat frequency $w_{\rm bt}$ over time.

and 2–3 Gyr, supporting the trailing segments of the rings, and to the left during 1–2 Gyr supporting the leading segments. The oscillation period of these orbits, $P \approx 1.91 \pm 0.01$ Gyr, is close to the period of changes in the morphology of the outer rings.

4 Summary

We studied the model of the Galaxy with an analytical Ferrers bar, which demonstrates periodic changes in the median velocities and morphology of the model disk. The radial velocity profiles form the humps with a period of $P = 2.1 \pm 0.1$ Gyr, supported by orbits whose orientations vary within the ranges $0 < \theta_{01} < 45°$, $-45 < \theta_{02} < 0°$ and $0 < \theta_{03} < 45°$ at the time intervals of 0–1, 1–2 and 2–3 Gyr, respectively. When these orbits are excluded from the sample, the humps disappear. Similar orbits with a period of $P \approx 1.91 \pm 0.01$ Gyr support periodic changes in the morphology of

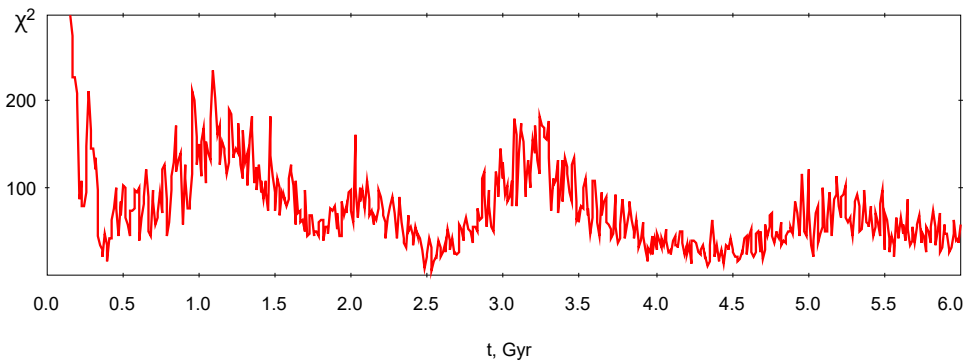

Fig. 3. Variation in the χ^2 function describing the difference between the model and observed (*Gaia* DR3) V_R velocity profiles over time. We see minima at the times 2.5 ± 0.3 and 4.5 ± 0.5 Gyr, which arise due to the disappearance of humps on the model V_R velocity profile at these times.

the outer resonance rings R_1 and R_2. Since the observed radial velocity profile has no hump, and the model profiles have no hump at the times 2.5 ± 0.3 and 4.5 ± 0.5 Gyr, the age of the Galactic bar must be close to 2.5 ± 0.3 or 4.5 ± 0.5 Gyr.

Acknowledgements. This work has made use of data from the European Space Agency (ESA) mission *Gaia* (https://www.cosmos.esa.int/gaia), processed by the *Gaia* Data Processing and Analysis Consortium (DPAC, https://www.cosmos.esa.int/web/gaia/dpac/consortium). Funding for the DPAC has been provided by national institutions, in particular the institutions participating in the *Gaia* Multilateral Agreement. E. N. Podzolkova is a scholarship holder of the Foundation for the Advancement of Theoretical Physics and Mathematics "BASIS" (Grant No. 21-2-2-44-1).

References

Athanassoula E., Bienayme O., Martinet L., et al., 1983, Astronomy and Astrophysics, 127, p. 349
Benjamin R., Churchwell E., Babler B., et al., 2005, Astrophysical Journal, 630, id. L149
Gaia Collaboration, Vallenari A., Brown A., et al., 2023, Astronomy and Astrophysics, 674, id. A1
Melnik A., Dambis A., Podzolkova E., et al., 2021, Monthly Notices of the Royal Astronomical Society, 507, p. 4409
Melnik A. and Podzolkova E., 2024, accepted to Astronomy Letters
Melnik A., Podzolkova E., and Dambis A., 2023, Monthly Notices of the Royal Astronomical Society, 525, p. 3287
Weinberg M., 1994, Astrophysical Journal, 420, p. 597

VAK 2024 MODERN ASTRONOMY: FROM THE EARLY UNIVERSE TO EXOPLANETS AND BLACK HOLES 300 years Russian Academy of Sciences

What changes in multi-color sky survey will be required by the transition from the ISS to ROS

M. Prokhorov, A. Zakharov, N. Krusanova, V. Moshkalev, O. Stekolshchikov, and M. Tuchin

Sternberg Astronomical Institute of M. V. Lomonosov Moscow State University, 13 Universitetkiy Prospekt, Moscow, 119991 Russia

Abstract. The task of conducting a space-based multicolor photometric all-sky survey of high and moderate brightness stars with an emphasis on high accuracy and uniformity of measurements was formulated a long time ago, but remains in demand to this day. It was assumed that such survey would be carried out on board of the ISS (the Lyra-B experiment), but due to the end of the station's operation in 2028–2030 its preparation was stopped. An application has been submitted to conduct a similar survey on board of the Russian Orbital Station (ROS). However, ROS is noticeably different from the ISS; one of the main differences is the sun-synchronous orbit of the station. This article discusses in detail the changes that need to be made to the scientific equipment of the experiment and the methodology of a survey when transferring location of the experiment from the ISS to the ROS. The benefits and disadvantages of the new experimental location are considered.

Keywords: techniques: photometric; catalogs; surveys; space vehicles: instruments

DOI: 10.26119/VAK2024.085

1 Modern large and high-precision photometric catalogues

The need for a highly accurate and uniform multi-color photometric all-sky catalogs of bright and moderate-luminous stars was recognized back in the 1980s. Such catalogs are required both for fundamental research in almost all areas of astronomy, and for applied astronomical work. The following requirements apply to such photometric catalogues:

1. high accuracy of photometric measurements;
2. large catalog size, i.e. large limiting stellar magnitude;
3. many photometric bands;
4. conducting a survey over the entire sky or a significant part of the sky;
5. the ability to detect stellar variability;
6. multiple observations of stars;
7. almost simultaneous measurements of stars in different photometric bands;
8. large dynamic range of star brightness;
9. the ground-based survey must contain the data necessary for the correct removal of photometric measurements beyond the Earth's atmosphere.

Let us explain this list of requirements. The accuracy of stellar photometry (item 1 of the list) can be considered high if the total photometry error does not exceed 0.001^m for bright stars and 0.01^m for stars of moderate brightness. The errors are indicated for non-variable stars; they are obtained by averaging all measurements over the survey duration. The limiting magnitude (item 2 of the list) may be ranked following the space experiment (SE) Gaia: bright ($m < 7$–12), moderate ($m < 15$–17), dim ($m < 20$–21). For moderately bright stars Gaia gives the most accurate coordinates and photometry, while dim stars include all stars in Gaia survey. A large number of photometric bands (item 3 of the list) means that there should be at least 4–5 of them, preferably 10. The requirement for all-sky survey (item 4 of the list) seems almost obvious; we may need information about any star in the sky. However, for statistical studies one can limit oneself to viewing only part of the sky. An example of the latter situation is the SDSS survey (Almeida et al. 2023). The main purpose of its implementation was to study galaxies, therefore the observations did not include areas of low galactic latitudes; the survey covered only 2/3 of the sky.

Detection of stellar variability (item 5 of the list) is possible only with repeated measurements of stars (item 6 of the list). To correctly determine the characteristics of variable stars, measurements in all bands must be carried out within a short time interval (item 7 of the list).

Dynamic range (item 8 of the list) is important for photometric surveys: bright and dim stars must be measured simultaneously. Depending on the limiting magnitude, the typical dynamic range may be 12^m–14^m (flux ratio 60 000–400 000 times)

or 17^m–18^m (flux ratio 6 –16 million times). An example of a solution to this problem can be the star registration system in the SE Gaia (Gaia Collaboration et al. 2016).

Unfortunately not a single present-day photometric catalog satisfies all listed requests. The most precise photometry are in the catalogs of Hipparcos and Gaia DR3 (Hipparcos 1997; Gaia Collaboration et al. 2021, 2023, 0.001^m), WBVR-catalog of SAI is slightly inferior to them (Kornilov et al. 1991; Cherepashchuk et al. 1994, 0.003^m). However, in the Hipparcos catalog there is only one photometric band Hp, in the Hipparcos and WBVR catalogs there are few stars (120 and 15 thousand). The Gaia DR3 catalog contains 1.8 billion stars, has a very high accuracy, but only three photometric bands. The next one in terms of accuracy is Tycho-2 catalog Hog et al. (2000). Its error is acceptable for many problems (0.008^m), but the number of stars is not very large ($2.5 \cdot 10^6$) and there are only two photometric bands $B_{\rm T}$ and $V_{\rm T}$.

Photometry of the 2MASS (Almeida et al. 2023) and SDSS (Cutri et al. 2003) are most often used by astronomers. The 2MASS catalog has three bands JHK, SDSS has five bands $ugriz$. These catalogs contain ∼500 million stars each. The rest of their characteristics as photometric catalogs should be attributed to disadvantages: lower photometric accuracy, almost complete absence of repeated observations, lack of data for removal of measurements beyond the atmosphere.

The USNO A2.0 and USNO B1.0 catalogs contain a lot of stars, but they were obtained from scanning photographic plates of the Palomar POSS-I survey. The photometric accuracy of these catalogs is completely unacceptable.

In the next decades, the final version of the Gaia catalog and the optical survey of the China Space Station Telescope (CSST), can appear.

Stellar photometry in Gaia is obtained by two ultra-low resolution spectrometers, creating spectra with about 30 pixels in blue and red channels (Jordi & Carrasco 2007). Based on them, 14-band photometric system Gaia C1M was introduced, which has now been forgotten. The Gaia DR3 catalog published the brightness of stars in the Bp and Rp bands, which are complete integrals of blue and red microspectra. These quantities have high accuracy (∼0.001^m). It is unknown whether photometry in the C1M system will be presented in the final version of the Gaia catalogue or if it will remain 3-colored (G, Bp, Rp).

Another possible source of high-precision stellar photometry in the near future is a 2-m Chinese Space Station Telescope (CSST). The telescope is expected to be launched into orbit in 2025–2026. Information about the characteristics of CSST is inconsistent. The telescope will be equipped with a 6 or 7-band photometer operating at λ = 255–1000 nm, the limiting magnitude in g band will be 26^m. It is expected

that over 7–10 years, CSST will conduct photometry of stars over an area of 17 500 square degrees. Other characteristics of this possible survey are unclear.

2 Space experiment proposed by SAI MSU

Due to the need need for a high-precision photometric survey of stars, the SAI MSU proposed the SE Lyra-B, which maximally satisfies the above requirements. The Lyra-B project was included in the long-term program of scientific research on ISS. More detailed information about the SE Lyra-B can be found in Zakharov et al. 2013, 2018; Zhmailov & Prokhorov 2020.

The project was implemented with long interruptions. In 2008–2010 preliminary design was developed, in 2018–2019 the design documentation was made. From 2019 SE was suspended. In 2021 it became clear that even with the maximum extension of ISS life, there would not be enough time to complete the Lyra-B SE. At the same time, the scientific task of the research remains relevant (Prokhorov et al. 2022).

In 2023 SAI provided an application to Nebosvod SE onboard Russian Orbital Station (ROS), similar in goals and objectives of Lyra-B SE.

During the development of scientific equipment for Nebosvod SE, many of Lyra-B solutions will be used, however, despite maintaining the basic principles of Lyra-B, transferring its location to ROS will require significant changes in the scientific equipment.

3 Changes in the project due to the transfer to the ROS

There are several reasons to change the design of scientific equipment developed for Lyra-B on ISS due its transfer to the ROS. The main one is the sun-synchronous orbit of ROS, changes in the construction of ROS and the progress of matrix photosensors.

The ROS will revolve around the Earth in a sun-synchronous orbit, such an orbit precesses around the Earth with a period of 1 year. In the coordinate system associated with the station's orbit, the Sun shifts to $\pm 23^\circ\ 26'$ in north–south direction and by several degrees in east–west during the year (in an asynchronous orbit, like the ISS, the Sun may be in almost any position relative to station and telescope). Such movement of the Sun allows the use of a motionless oblique hood at the telescope. In this case, the total length of a lens hood for ROS may be less than an axisymmetric telescope hood for ISS. An issue that requires additional consideration is the use of stationary anti-solar screens at the ROS. This was impossible on the ISS.

On the ISS, the telescope was going to be placed on a high mount and strongly shifted in the horizontal direction. This was because the star trackers of ISS attitude

control were located near the telescope installation place. On ROS there will be no such problem (we hope), which will make the mount much shorter and stronger.

Another important change in ROS design is a planned increase of docking hatches. On the ISS, they were ∅800 mm, which allowed the telescope to have a body of ∅600 mm and the main mirror ∅500 mm. It is assumed that a new hatch will be ∅1000 mm (this is not yet known exactly). With the new hatch the main mirror may be increased to ∅700 mm, which will lead to an increase of the area by 96 % and the limiting magnitude by 0.73^m.

It was assumed that CCD matrices would be used as photodetectors on the ISS (Zakharov et al. 2013). Their development and production was to be entrusted to e2v Ltd., now Teledyne e2v (UK). Unfortunately, today this is no longer possible. There are several possible ways to solve this problem:

- Use of ready-made or custom-made CCD matrices from other manufacturers
  Unfortunately, there are no other manufacturers of CCD ready to carry out the necessary development for Russia. There are also no commercially produced matrices with required characteristics. The latter is related to the overall decline of CCD production, which are replaced everywhere by cheaper and faster CMOS matrices.
- CCD-in-CMOS TDI (Mahato et al. 2021)
  This is a recent development in which, based on CMOS technology, the light-sensitive structure of CCD-matrix is reproduced to operate exclusively in the TDI-mode. The readable part of the chip is a conventional CMOS, the data output is in a digital form. The main disadvantage of CCD-in-CMOS produced today is a high level of electron thermal emission, which either makes it impossible to use them for recording weak astronomical signals, or requires very strong cooling.
- Using a swinging mirror to implement frame mode
  A light flat mirror rotating around an axis perpendicular to the station's orbit is installed in the telescope's optical system. The mirror rotates uniformly for some time at a speed equal to the half of station's orbital angular velocity. At this time, the images of stars in the focal plane are motionless. Then the mirror quickly returns to the initial position, and the frame is read from the matrix. After the cycle of exposure and reading is repeated, the neighboring section of the starry sky is recorded.
  This approach can be used for any type of a matrix. A similar approach was successfully used in 2MASS survey and WISE SE.
- CMOS matrices with fast readout
  The CMOS matrix is located in the focal plane of a telescope so that images of stars move along its rows or columns. The exposure lasts for a time equal

to the movement of star images by one pixel (on a telescope for the ISS this is $\sim$1/300 s). The resulting frames are added with a shift of one pixel. CMOS matrices with the frame frequency of 300 Hz and higher, up to 1000–2000 Hz, are now mass-produced.

4 Conclusion

The creation of a multicolor, high-precision photometric catalog of stars remains an urgent astronomical task. The SE Lyra-B onboard of the ISS has been in preparation for this task during several years at the SAI MSU. Due to the end of ISS operation, it has been proposed to conduct a similar SE Nebosvod on ROS.

The transfer of SE from the ISS to the ROS, while maintaining the tasks and principles of sky survey, requires serious reworking of the scientific equipment. The main reasons for this are the changes in the type of the orbit and the construction of the orbital station, as well as the progress of matrix photodetectors. In the preparation of SE Nebosvod it is necessary to repeat the stages of Preliminary design and Development of design documentation, which have already been carried out for SE Lyra-B. Some issues of the SE Nebosvod require additional research.

The ROS station is proving to be a "more convenient" place for photometric sky survey than the ISS.

References

Almeida A., Anderson S., Argudo-Fernandez M., et al., 2023, Astrophysical Journal Supplement Series, 2023, 267, id. 44

Cherepashchuk A., Khaliullin Kh., Kornilov V., and Mironov A., 1994, Astrophysics and Space Science, 217, p. 83

Cutri R., Skrutskie M., van Dyk S., et al., 2003, The IRSA "2MASS All-Sky Point Source Catalog"

Gaia Collaboration, Brown A., Vallenari A., et al., 2021, Astronomy and Astrophysics, 649, id. A1

Gaia Collaboration, Prusti T., de Bruijne J., et al., 2016, Astronomy and Astrophysics, 595, id. A1

Gaia Collaboration, Vallenari A., Brown A., et al., 2023, Astronomy and Astrophysics, 674, id. A1

Hog E., Fabricius C., Makarov V., et al., 2000, Astronomy and Astrophysics, 355, p. L27

Jordi C. and Carrasco J., 2007, ASP Conference Series, 364, p. 215

Kornilov V., Volkov I., Zakharov A., et al., 1991, Trudy Sternberg Astr. Inst., 63, p. 4

Mahato S., Thijs S., Bentell J., et al., 2021, arXiv:2109.14532

Prokhorov M., Zakharov A., Stekolshchikov O., and Tuchin M., 2022, in Proceedings of VAK–2021 conference "Astronomy at the epoch od multimessenger studies", p. 69

The Hipparcos and Tycho catalogues. Astrometric and photometric star catalogues derived from the ESA Hipparcos Space Astrometry Mission, 1997, ESA SP Series, 1200

Zakharov A., Mironov A., Prokhorov M., et al., 2013, Astronomy Reports, 57, p. 195

Zakharov A., Zhukov A., Mironov A., et al., 2018, in Proceedings of "Modern Star Astronomy. Astronomy–2018", 1, p. 174

Zhmailov S. and Prokhorov M., 2020, Astronomy Reports, 64, p. 34

VAK 2024 MODERN ASTRONOMY: FROM THE EARLY UNIVERSE TO EXOPLANETS AND BLACK HOLES 300 years Russian Academy of Sciences

Evolution of large-scale magnetic fields of chemically peculiar stars

I. Romanyuk[1], E. Semenko[1,2], I. Yakunin[1], A. Moiseeva[1], D. Kudryavtsev[1], E. Korchagina[1], and V. Aitov[1]

[1] Special Astrophysical Observatory of the Russian Academy of Sciences, Nizhny Arkhyz, 369167 Russia
[2] National Astronomical Research Institute of Thailand, Chiangmai, 50180 Thailand

Abstract. We studied the magnetic field of chemically peculiar stars in the young Orion OB1 association and in other five older clusters. We have found new evidence of the validity of the relic origin of the magnetic field. In the Orion OB1 association, the magnetic field values and the occurrence frequency of magnetic stars are systematically higher than in older groups. There is no magnetic field generation during the life of a star on the main sequence. The observations were carried out using the 6-m telescope of the Special Astrophysical Observatory of the Russian Academy of Sciences. We studied the magnetic field of about 80 stars. More than 1 000 spectra were obtained with the circular polarization analyzer on the BTA Main Stellar Spectrograph.

Keywords: stars: magnetic field, chemically peculiar

DOI: 10.26119/VAK2024.086

1 Introduction

Currently, about 600 magnetic chemically peculiar (CP) stars are known. Their physical parameters do not differ from the normal ones of the same spectral classes. The main differences are the presence of a large-scale magnetic field, slower rotation, depressions at the continuum level and anomalies in the chemical abundance of elements.

There are various hypotheses for the large-scale field origin: theories of relict origin, dynamo, "stellar mergers", etc. (Moss 1989; Mestel 2003; Schneider et al. 2019). However, it is still not clear which theory confirms one or another hypothesis of the formation of a magnetic field.

The solution to the problem lies in observing the magnetic field of chemically peculiar stars, constructing and analyzing the dependencies of the field on various parameters, in particular, on age. In most cases, chemically peculiar stars are field objects. Despite the availability of fairly accurate parallaxes from the Gaia and Hipparcos missions, a number of difficulties remain in estimating the physical parameters of these stars. Therefore, by plotting them on the Hertzsprung-Russell diagram, we can only indirectly assess their evolutionary status; the error in age determined in this case will be about 100%. On the other hand, to estimate the age of stars in clusters, one can select the most suitable evolutionary tracks (Bagnulo et al. 2006). Therefore, since 2010, we have been carrying out a comprehensive program of studying the magnetic field of stars—members of open clusters of different ages at the 6-m telescope of the SAO RAS.

2 Magnetic field of stars

2.1 Method of determination

As a result of observations, we obtain only the longitudinal component of the magnetic field averaged over the entire visible surface, which varies with the rotation period of the star. Therefore, the problem arises—what kind of global magnetic field does this star have? Theoretically, this problem can be solved as follows: perform quite a lot of observations in different phases of the rotation period and construct a phase curve of longitudinal field variability, which can then be simulated, and find the magnetic field value at any point on the surface of the star. This approach is quite difficult to implement in practice due to the need to obtain a large number of observations for stars, for which, for the most part, rotation periods are unknown. However, it is worth noting that recently this problem has been actively solved with the help of the Kepler and TESS space missions (Hümmerich et al. 2018). Therefore,

to estimate the magnitude of the star's magnetic field, one can use its root-mean-square value $B_{\rm rms}$. To confirm the magnetic field presence in a star, we use the χ^2/n criterion. The star can reliably be considered magnetic at a value of $\chi^2/n > 5$. The field $B_{\rm rms}$, its error $\sigma_{\rm rms}$ and the criterion χ^2/n are calculated using the following formulas:

$$B_{\rm rms} = \left(\frac{1}{n} \sum_{i=1}^{n} B_e i^2 \right)^{1/2}, \quad \sigma_{\rm rms} = \left(\frac{1}{n} \sum_{i=1}^{n} \sigma_i^2 \right)^{1/2}, \quad \chi^2/n = \frac{1}{n} \sum_{i=1}^{n} \left(\frac{B_e i}{\sigma_i} \right)^2. \quad (1)$$

The accuracy of our measurements at the MSS depends on the stellar physical parameters, in particular, on its rotation speed and the number of lines in the spectrum. For cold stars with slow rotation, field determination errors usually do not exceed 100 G, and for hot stars with a high rotation speed and a small number of lines, errors can exceed 500 G.

2.2 Magnetic stars in the Orion OB1 association

One of the most studied groups in the solar vicinity is the Orion OB1 association. Inside it, Blaauw (1964) identified four regions: subgroups 1a, 1b, 1c and 1d, which differ in age and stellar composition. Brown et al. (1994) carried out the most detailed analysis of the stellar population of the association, and provided the results of the analysis for 814 stars of spectral types O–F.

Romanyuk et al. (2013) identified 85 chemically peculiar stars in the association and showed that all 23 Am stars from this list are foreground objects and do not belong to the association. Taking into account the conditions above, we selected 56 poorly studied chemically peculiar Ap/Bp stars in the association to search for their magnetic field. For this purpose, more than 600 spectra of association stars were obtained with the circular polarization analyzer (Chountonov 2016) at the BTA Main Stellar Spectrograph (MSS) (Panchuk et al. 2014) in the period 2010–2022.

The results of these studies were published in a number of works (Romanyuk et al. 2019, 2021a,b), which are summarized by the publication Semenko et al. (2022).

South of "Orion's belt", the Great Orion Nebula was observed. Of the 27 CP stars from subgroups 1c and 1d of the association, 15 are members of the Nebula. Of these, only three stars have been found to be magnetic, and 12 (80%) are non-magnetic. On the contrary, of the 12 stars located outside the nebula, 10 stars (83%) are magnetic and only two are non-magnetic. We believe that many of the young stars may be Herbig Ae/Be objects.

2.3 Magnetic field of CP stars in other clusters

Having completed our observations in the Orion OB1 association, we began a program of magnetic star's research in older clusters. At the beginning, we conducted a study in the open cluster Pleiades and in the kinematic group of the same name (Romanyuk et al. 2023b). In the Pleiades, we identified four CP stars, in which we did not detect a magnetic field. We further analyzed three clusters: IC 4756, α Per (Melotte 20) and NGC 7092 (Romanyuk et al. 2023a), and none of the 13 stars show field $B_{\rm rms}$ greater than 1 kG. We presented the conclusions of the analysis of these clusters in more detail in Romanyuk et al. (2024).

In this paper, we present the analysis results of two more open clusters: Melotte 111 (Coma Berenices) and the younger Trumpler 37 ($\log t = 7.05$).

In the open cluster Melotte 111 from the WEBDA database we identified eight candidates for mCP stars. However, as a result of our analysis, a magnetic field was detected in only three of them. The average value of the cluster's magnetic field is less than 500 G.

The age of the open cluster Trumpler 37 corresponds to the subgroup 1a in the Orion OB1 association. The WEBDA database indicates that only seven stars are chemically peculiar from this cluster. Having carried out their spectropolarimetric observations, we discovered that the classification for this cluster in the database turns out to be erroneous: among the seven objects there is not a single chemically peculiar one, all of them have strong emission lines and the absence of a magnetic field.

3 Results

We have summarized all the results obtained from the analysis of CP stars in the Orion OB1 association and other clusters in Table 1 and Fig. 1. The columns of the table indicate the names of the studied cluster and subgroups of the Orion OB1 association, arranged in increasing order of their age $\log t$, which was taken from the WEBDA database, the number of chemically peculiar stars $N_{\rm CP}$ and magnetic CP stars $N_{\rm mCP}$, mean magnetic field and its error.

We conclude that chemically peculiar stars are not found in all open clusters. The conditions for star formation in different regions of the Galaxy could be different. This is perfectly illustrated by Fig. 1b, which shows the obtained dependence of the magnetic field on age.

Table 1. Results of the average magnetic field measurements of the studied clusters and subgroups of the Orion OB1 association.

Cluster	$\log t$ [yr]	$N_{\rm CP}$	$N_{\rm mCP}$	$\langle B_{\rm rms}\rangle \pm \sigma$ G
Orion OB1b	6.23	15	11	1831 ± 197
Orion OB1c	6.66	24	13	1060 ± 132
Orion OB1a	7.05	14	7	909 ± 197
α Per	7.81	6	1	440 ± 140
Pleiades	8.06	3	1	121 ± 46
NGC 7092	8.41	5	0	0 ± 140
Melotte 111	8.65	8	3	340 ± 60
IC 4756	8.90	2	1	310 ± 140

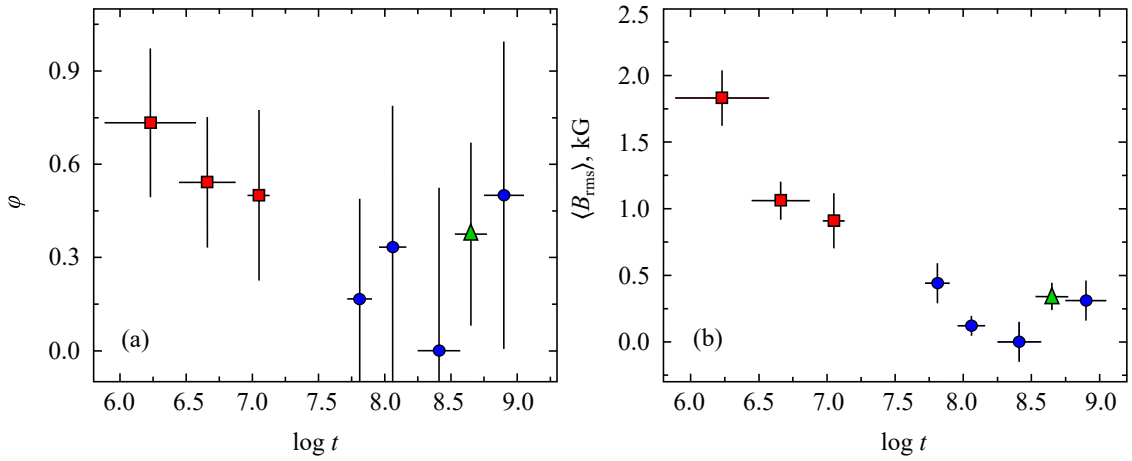

Fig. 1. Dependence of the fraction of magnetic CP stars (a) and the average magnetic field (b) on age. In the figures, red squares show the values of the Orion OB1 subgroups, blue circles show values of characteristics of the clusters α Per, Pleiades, NGC 7092 and IC 4756, green triangle are the values of parameters of the newly studied Melotte 111 cluster.

4 Summary

As a result, we analyzed the magnetic field of 77 chemically peculiar stars that belong to the Orion OB1 association and other older clusters α Per, Pleiades, NGC 7092, Melotte 111 and IC 4756.

For the first time, the magnetic field of 14 stars in the Orion OB1 association was discovered by us. In total, we and our foreign colleagues found 31 magnetic CP stars in the association, which is 55% of all CP stars in it. Noteworthy is the segregation of magnetic CP stars inside and outside the Orion Nebula. To explain this phenomenon,

we proposed a new hypothesis: the magnetic field decrease is not caused by its rapid decay, but is the result of the influence of different conditions during its formation in our Galaxy at different times. However, to confirm our results, we need to supplement our studies with clusters and groupings of different ages.

We have shown that the fraction of magnetic stars and the magnitude of the magnetic field of CP stars in the young Orion OB1 association are significantly greater than in five older groups (Fig. 1a). We see that no magnetic field is generated on the main sequence (Fig. 1b). The large-scale field of Ap/Bp stars was formed at the stages of evolution before the main sequence. Chemically peculiar stars are not found in all open star clusters, as demonstrated by the relatively young open cluster Trumpler 37. The Orion OB1 association is likely unique, where special conditions for the formation of magnetic stars have developed.

Funding

We carried out this work with the support of the Ministry of Science and Higher Education of the Russian Federation No. 075-15-2022-262 (13.MNPMU.21.0003).

References

Bagnulo S., Landstreet J.D., Mason E., et al., 2006, Astronomy & Astrophysics, 450, 2, p. 777
Blaauw A., 1964, Annual Review of Astronomy and Astrophysics, 2, p. 213
Brown A.G.A., de Geus E.J., de Zeeuw P.T., 1994, Astronomy & Astrophysics, 289, p. 101
Chountonov G.A., 2016, Astrophysical Bulletin, 71, 4, p. 489
Hümmerich S., Mikulášek Z., Paunzen E., et al., 2018, Astronomy & Astrophysics, 619, id. A98
Mestel L., 2003, ASP Conf. Ser., 305, p. 3
Moss D., 1989, Monthly Notices of the Royal Astronomical Society, 236, p. 629
Panchuk V.E., Chuntonov G.A., Naidenov I.D., 2014, Astrophysical Bulletin, 69, 3, p. 339
Romanyuk I.I., Semenko E.A., Yakunin I.A., et al., 2013, Astrophysical Bulletin, 68, 3, p. 300
Romanyuk I.I., Semenko E.A., Moiseeva A.V., et al., 2019, Astrophysical Bulletin, 74, 1, p. 55
Romanyuk I.I., Semenko E.A., Moiseeva A.V., et al., 2021a, Astrophysical Bulletin, 76, 1, p. 39
Romanyuk I.I., Semenko E.A., Moiseeva A.V., et al., 2021b, Astrophysical Bulletin, 76, 2, p. 163
Romanyuk I.I., Moiseeva A.V., Yakunin I.A., et al., 2023a, Astrophysical Bulletin, 78, 2, p. 152
Romanyuk I.I., Moiseeva A.V., Yakunin I.A., et al., 2023b, Astrophysical Bulletin, 78, 1, p. 36
Romanyuk I.I., Yakunin I.A., Moiseeva A.V., et al. 2024, Astrophysical Bulletin, 79, 1, p. 95
Schneider F.R.N., Ohlmann S.T., Podsiadlowski P., et al. 2019, Nature, 574, 7777, p. 211
Semenko E., Romanyuk I., Yakunin I., et al., 2022, Monthly Notices of the Royal Astronomical Society, 515, 1, p. 998

MODERN ASTRONOMY: FROM THE EARLY UNIVERSE TO EXOPLANETS AND BLACK HOLES

Wolf–Rayet stars mass-loss rates determined from spectroscopic measurements of the orbital evolution for close WR + OB binary systems

I. Shaposhnikov[1,2]

[1] Lomonosov Moscow State University, Sternberg Astronomical Institute, 13 Universitetsky Pr., Moscow, 119234 Russia

[2] Lomonosov Moscow State University, Faculty of Physics, 1-2 Leninskiye Gory, Moscow, 119991 Russia

Abstract. The most reliable method for estimating the rate of mass-loss by the Wolf–Rayet stars wind is based on the assessment of secular variations in the orbital periods for close binary systems containing such stars, most often WR + OB systems. Previously, almost only photometric observations of well-studied eclipsing close WR + OB binaries were used for these purposes. This report describes the results of the work on the search for mass-loss-induced evolutionary variations in the orbital period for close WR + OB binaries and the mass-loss rates measurements for WR stars in these systems. Orbital period variations were detected in five systems studied: V444 Cyg, CQ Cep, CX Cep, WR 127 (Hen 3-1772), and WR 141 (V2183 Cyg). In addition, phase deviations between the radial velocity curves obtained at different epochs are suspected for the A pair of the GP Cep quadruple system. For eclipsing systems, estimates of the rate of change of the orbital period from the radial velocity curves are in good agreement with the corresponding estimates obtained from the light curves. A secular shortening of the orbital period has been confirmed for the CQ Cep system, which can be explained by the high degree of closeness of this system and the associated mass transfer processes. For the WR 127 and WR 141 systems, dynamic estimates of the change of the orbital period and the rate of mass loss have been obtained for the first time. Estimates of the rate of mass-loss by Wolf–Rayet stars show a power-law dependence on the mass of the star with an exponent of about 2. The effect of the finite size of stars, which turns out to be significant for estimates of the rate of mass loss to the wind in the closest systems, is discussed.

Keywords: stars: Wolf–Rayet, mass-loss, winds, outflows, binaries: spectroscopic

DOI: 10.26119/VAK2024.087

1 Introduction

The significant rate of mass loss by Wolf–Rayet (WR) stars when such a star is part of a close binary system leads to an effective loss of mass and angular momentum, and, as a consequence, to a slow evolution of the orbit. Most often, WR are found in a pair with a massive star of a spectral type O or early B (WR + OB type systems). If a series of photometric (for eclipsing systems) or spectroscopic observations covering a sufficient number of orbital cycles is available, the change in the orbital period can be estimated by superimposing the phase curves corresponding to different epochs (the $O-C$ method). The pioneering work in this direction was performed by Khaliullin et al. (1974) for the V444 Cyg system. Unfortunately, the number of known WR + OB systems with sufficiently pronounced eclipses is limited to a few, so the $O-C$ spectroscopic method based on a comparison of radial velocity curves seems to be more widespread. This opens a way to a model-independent estimate of the mass loss rate of Wolf–Rayet stars and to a study of the empirical relationship between the WR mass loss rates and their masses.

In a recent series of our papers, we studied a number of WR + OB close binary systems: first, we showed that comparisons of radial velocity curves for eclipsing systems yield orbital period variation rates consistent with the results of the $O-C$ photometric method (Shaposhnikov et al. 2023a,b), and then we obtained a result for a system with weak photometric variability (Shaposhnikov et al. 2024). Additionally, we obtained preliminary results for three more systems: WR 141 (V2183 Cyg), WR 145 (AS 422), and the pair A of the GP Cep quadruple system. In this paper we analyze the obtained result. Our estimates of the WR mass-loss rates show a power-law dependence on the mass of the star with an exponent slightly less than 2. We consider the nuances of determining the mass-loss rate from the $\dot{P}$ measurement, such as taking into account the finite sizes of stars and interpreting the $\dot{P} < 0$ cases. We also compare the mass loss rates we determined for systems with observed orbital period increases with the mass loss rates measured by other methods.

2 Observational data

All observations of WR + OB close binaries are carried out using telescopes of the SAI Caucasian Mountain Observatory (CMO). Spectroscopic observations are carried out using a 2.5-m telescope with a low-resolution dual-beam spectrograph TDS (Potanin et al. 2020). In addition, multicolor photometric observations of eclipsing systems were additionally carried out using the 60-cm robotic telescope RC600 (Berdnikov et al. 2020). The constructed light curves and radial velocities for CQ Cep, CX Cep, V444 Cyg and WR 127 are given in the corresponding papers (Shaposhnikov et al. 2023a,b, 2024). The radial velocity curves for WR 141, WR 145 and GP Cep are

shown in Fig. 1. Fig. 2 shows the $O-C$ curves for all systems studied so far. For eclipsing systems, the $O-C$ curves for photometric data are plotted on the same graph as the spectral data.

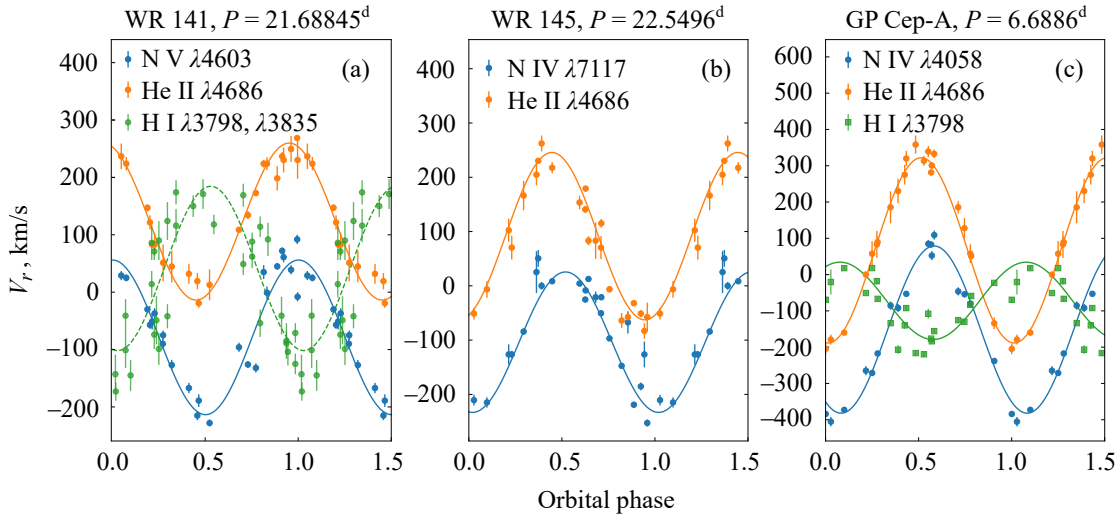

Fig. 1. WR 141 (a), WR 145 (b) and GP Cep-A (c) radial velocity curves from CMO observations.

3 WR + OB obrital evolution interpretation

Table 1 provides a summary of all systems studied to date. Five of the seven systems studied showed an increase in orbital period $\dot{P} > 0$. According to the well-known Jeans mode formula, the rate of mass loss from the system can be expressed as $\dot{M}/M = -1/2 \times \dot{P}/P$. However, this formula may give incorrect results for the closest systems, where it is necessary to take into account the sizes of the stars and possible mass transfer between the stars. The formula linking the orbital evolution of a close binary system of outflowing spherical (with radii $R_{1,2}$) tidally synchronized stars was derived in Shaposhnikov et al. (2023a) and has the form:

$$\frac{\dot{P}}{P} = -\frac{\dot{M}_1}{M_1}\left\{3 + 3\frac{x-\beta}{q} - \frac{\alpha+x}{1+q} - 3\frac{1+q}{q}\left(\alpha\left[\left(\frac{q}{1+q}\right)^2 + \frac{2}{3}\left(\frac{R_1}{a}\right)^2\right] + \right.\right.$$
$$\left.\left. + x\left[\left(\frac{1}{1+q}\right)^2 + \frac{2}{3}\left(\frac{R_2}{a}\right)^2\right]\right)\right\}, \quad (1)$$

where index "1" means a more massive star, $q = M_1/M_2$, and α, β and x describe relationships between wind and transfer parts of mass-loss as $\dot{M}_1 = \dot{M}_{1,w} + \dot{M}_{1,t} = \alpha\dot{M}_1 + \beta\dot{M}_1$ ($\alpha + \beta = 1$), $\dot{M}_2 = \dot{M}_{2,w} - \dot{M}_{1,t} = x\dot{M}_1 - \beta\dot{M}_1$.

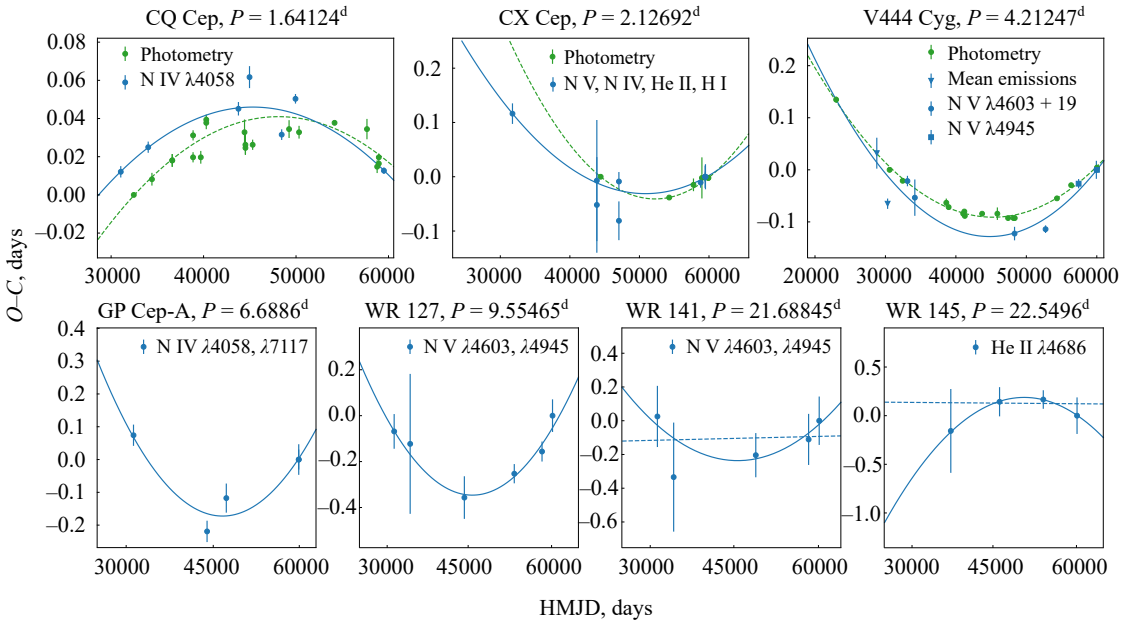

Fig. 2. $O-C$ curves for studied WR + OB systems.

For the CX Cep system, taking into account the sizes of the stars and the presence of a wind from the O-star under realistic assumptions the estimate of $\dot{M}_{\rm WR}$ changes by approximately 30% (Shaposhnikov et al. 2023a), while for the case of V444 Cyg the correction is only about 3% (Shaposhnikov et al. 2023b). Thus, these corrections turn out to be significant for the closest systems.

As the data in Table 1 show, there is a correlation between the WR mass and $\dot{M}_{\rm WR}$. Fig. 3 shows a graph of $\dot{M}_{\rm WR}$ versus $M_{\rm WR}$, with the obtained points for systems with $\dot{P} > 0$ plotted on it. The point corresponding to the GP Cep system is also plotted on the graph, but the $\dot{P}$ observed in this case may be partially due to the motion along a wide orbit in a quadruple system and is not reliable. The lower error limit for CX Cep corresponds to the estimate of $\dot{M}_{\rm WR}$ determined without taking into account the radii. The main coefficient of the straight line in Fig. 3 is drawn through our points (except for GP Cep) is 1.61 ± 0.29.

In addition, we also decided to compare our results with measurements of $\dot{M}_{\rm WR}$ made by other methods. In Fig. 3 the results for polarization (St.-Louis et al. 1988),

Table 1. Close binary systems WR + OB type with measured orbital evolution by spectroscopic $O-C$ method and $\dot{M}_{\rm WR}$ estimations.

WR#	Alias	SpT	P days	$M_{\rm WR}$ $M_\odot$	$\dot{P}$ s/yr	$\dot{M}_{\rm WR}$ $10^{-5}\,M_\odot$/yr
127	Hen 3-1772	WN3+O9.5V	9.55465	21.0±2.5	0.83±0.14	2.6±0.5
139	V444 Cyg	WN5+O6II-V	4.21247	10.7±1.1	0.119±0.003	0.60±0.04
141	V2183 Cyg	WN5-w+O5V-III	21.68845	39±10	1.6±0.9	3.1±1.9
145	AS 422	WN7o/CE+O7V(f)	22.5496	17.7±2.8	<= 0?	?
151	CX Cep	WN4+O5V	2.12692	13.9±0.7	0.062±0.005	$0.91^{+0.10}_{-0.31}$
153	GP Cep	WN6o+O6I (A)	6.6886	6.6±1.5	0.43±0.11	1.1±0.3
155	CQ Cep	WN6o+O9.5V	1.64124	~ 11	-0.0151±0.0013	~ 1

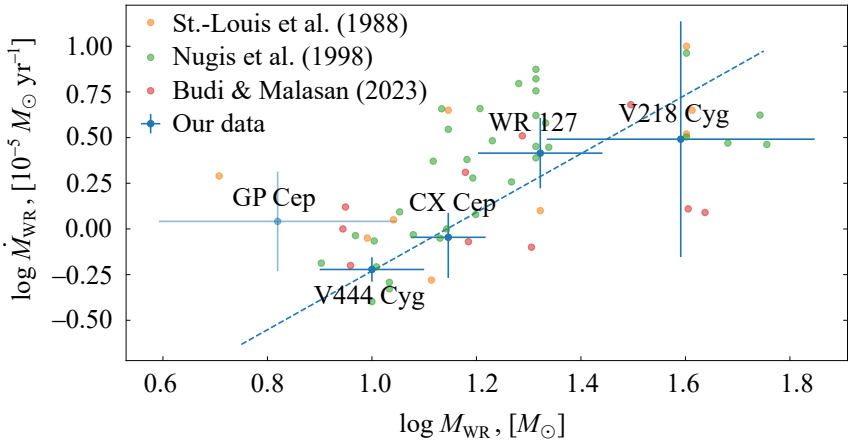

Fig. 3. Relationship between $M_{\rm WR}$ and $\dot{M}_{\rm WR}$. Blue dots with error bars—our estimations. Orange—polarimetric measurements (St.-Louis et al. 1988), green—from IR/radio fluxes (Nugis et al. 1998), red—from spectral lines profiles (Budi & Malasan 2023).

IR/radio fluxes (Nugis et al. 1998) and recent results of spectral line profile measurements (Budi & Malasan 2023) are plotted. In general, the results of measurements by all methods are in good agreement with each other.

As for the two cases out of seven in which $\dot{P} < 0$ were detected, there can be found a physical interpretation for CQ Cep. This system is the closest among all known systems of the type under consideration; the O star is close to filling the Roche lobe and realizes the flow of matter onto the WR star. Since $M_O > M_{\rm WR}$ in the case of CQ Cep, this flow tends to equalize the masses of the stars and shorten the orbit. In turn, the winds from WR and O carry away mass and angular momentum from the system and partially resist the convergence of the stars. Unfortunately, based on the observed $\dot{P}$ value alone, it is impossible to give specific estimates of

$\dot{M}_{\rm WR}$; only order estimates and wide ranges of accessible parameters (Shaposhnikov et al. 2023a) are available. The CQ Cep case is truly nontrivial and requires further study, including in the field of gas-dynamic modeling and the development of orbital evolution models for close binary systems. For the WR 45 = AS 422 system the result does not seem reliable, unlike the WR 141 = V2183 Cyg system with a similar period, but with a huge mass and the strength of the WR stellar wind. Thus, we are forced to conclude that systems with periods $P \geq 20^{\rm d}$ are no longer available for studying the mass loss rate by the dynamic method, except for the cases of the most massive stars.

4 Summary

The change in the orbital period of a close binary system is an observable characteristic of its evolution, and in the case of WR + OB systems it can provide a way to determine one of the key parameters of the evolution of massive stars—the rate of mass loss to the stellar wind. The results obtained from the comparison of radial velocity curves for the studied systems are in good agreement with both the available estimates from the light curves and those obtained by other model-dependent methods. We plan to expand the sample of studied WR + OB systems, covering all systems in the northern sky with orbital periods up to 20–30 days, and, if possible, supplementing it with systems in the southern sky with a sufficient number of archival epochs of spectroscopic observations.

Acknowledgements. The author is grateful to A. M. Cherepashchuk, A. V. Dodin and K. A. Postnov for valuable discussions and mentoring that made this work possible.

Funding

This work is supported by the Russian Science Foundation project No. 23-12-00092.

References

Berdnikov L.N., Belinskii A.A., Shatskii N.I., et al., 2020, Astronomy Reports, 64, 4, p. 310
Budi B.D.S. and Malasan H.L., 2023, Preprint SSRN, 4620956
Khaliullin Kh.F., 1974, Soviet Astronomy, 18, p. 229
Nugis T., Crowther P.A., Willis A.J., 1998, Astronomy & Astrophysics, 333, p. 956
Potanin S.A., Belinski A.A., Dodin A.V., et al., 2020, Astronomy Letters, 46, 12, p. 836
Shaposhnikov I.A., Cherepashchuk A.M., Dodin A.V., et al., 2023a, Monthly Notices of the Royal Astronomical Society, 523, 1, p. 1524
Shaposhnikov I.A., Cherepashchuk A.M., Dodin A.V., et al., 2023b, Monthly Notices of the Royal Astronomical Society, 526, 3, p. 4529
Shaposhnikov I.A., Cherepashchuk A.M., Dodin A.V., et al., 2024, Astronomy & Astrophysics, 683, id. L17
St.-Louis N., Moffat A.F., Drissen L., et al., 1988, Astrophysical Journal, 330, p. 286

MODERN ASTRONOMY: FROM THE EARLY UNIVERSE TO EXOPLANETS AND BLACK HOLES

Stellar populations of extragalactic globular clusters

M. Sharina[1], M. Maricheva[1], I. Acharova[2], and V. Shimansky[1]

[1] Special Astrophysical Observatory of the Russian Academy of Sciences, Nizhny Arkhyz, 369167 Russia
[2] Department of Physics, Southern Federal University, 5 Zorge, Rostov-on-Don, 344090 Russia

Abstract. Globular clusters (GCs) are the oldest (ages up to 13.6 Gyr), but not the most metal-poor ($-2.9 <$ [Fe/H] < 0 dex) objects in the Universe. Studying properties of their stellar populations and comparing them with the properties of structural components of galaxies and stellar streams is necessary to understand the processes of nucleosynthesis and galaxy formation. We analyse integrated-light (IL) spectra of extragalactic GCs in order to determine the properties of their horizontal branch stars, ages and chemical composition. For this purpose, we compare the observed and synthetic spectra of clusters calculated using stellar atmosphere models. In this paper, we address the questions: 1) what signatures of multiple stellar populations can be inferred from the analysis of IL low-resolution spectra of GCs; and 2) what the origin of GCs is and their multiple stellar populations. For the second question, we consider only two sources of multiple stellar populations: asymptotic giant branch and rapidly rotating massive stars, and briefly consider the problems in this scientific area.

Keywords: galaxies: abundances; galaxies: star clusters: general

DOI: 10.26119/VAK2024.088

1 Introduction

Our method of population synthesis of integrated-light (IL) spectra of globular clusters (GCs) has been described in detail by Sharina et al. (2024) (hereafter: S2024; see also references therein). According to this method, synthetic IL spectra of GCs are computed using stellar atmosphere models, selected isochrones of stellar evolution and a stellar mass function. Selection of isochrones with varying helium mass fraction (Y) (e.g. Bertelli et al. 2008) allows us to estimate for GCs not only the chemical composition and age, but also $T_{\rm eff}$ and $\log(g)$ for bluest horizontal branch (HB) stars. The optimum parameters of isochrones used to model IL spectra are determined by comparing the intensities of Balmer and metal lines in the observed and synthetic IL spectra. We have studied the influence of $T_{\rm eff}$ and luminosity of HB stars on the hydrogen lines profiles in IL spectra (S2024). The results of our study serve for more accurate analysis of color-magnitude diagrams of extragalactic GCs and determining distances to them. The comparison of our results for extragalactic and Galactic globular clusters contributes to improving models of stellar evolution and methods of population synthesis.

All methods of population synthesis of IL spectra of GCs are based on the selection of the stellar evolution models capable of characterising the observed data. However, it is known from literature studies of Galactic GCs that most of them contain stars with physical parameters and chemical composition that can not be described by simple stellar populations (e.g. Milone & Marino 2022 and references therein, hereafter: MM2022). In this paper we discuss signatures of multiple stellar populations (MPs) in GCs that can be detected using our method and briefly consider possible sources of MPs and problems with their recognition.

2 Can we detect multiple stellar populations in GCs by analyzing their low-resolution IL spectra?

Many Galactic GCs host two stellar populations that differ in the abundances of light elements (He, C, N, O, Na, Al, and in some cases Mg, Si, and K): the first population with the abundances similar to those of stars in the galactic field at a given metallicity, and the second population with the abundances of elements modified by high-temperature hydrogen burning in the CNO cycle and NeNa and MgAl chains (MM2022). Rare anomalous GCs exhibit variations in the abundance of Fe and s-process elements among cluster stars. They are the most massive GCs in the Galaxy and are thought to be the nuclei of destroyed dwarf galaxies.

The second-parameter problem of the HB morphology is related to the phenomenon of MPs in GCs. The problem is that GCs of the same age and metallicity

have different HB morphologies. The colour distribution (i.e., T_{eff} and luminosity) of HB stars varies with age, metallicity, Y and mass-loss efficiency of red giants (e.g. Lee et al. 2000). First population stars are located at the red end of the HB and have lower Y than the stars of the second population enriched in helium and hotter. The scatter in Y for HB stars in a GC, $\Delta Y_{\rm HB}$, correlates with the mass of the cluster, as well as the scatter in element abundances for the cluster stars (MM2022). The higher $\Delta Y_{\rm HB}$, the higher the abundances of N, Na, and Al and the lower C, O, and Mg are observed in the enriched stellar populations. Carbon abundances obtained from the analysis of IL spectra can not serve as an indication of the presence of MPs due to the change in the chemical composition of stellar atmospheres during their evolution (Kraft 1994). As a result, there is a systematic difference between [C/Fe] values determined using IL spectra of GCs and the corresponding C abundances in the red giants of these GCs obtained from the absorption line analysis in high-resolution spectra (Sharina et al. 2020).

From our analysis of low-resolution IL spectra (S2024), we can judge the presence of MPs in the studied GCs using the obtained Mg, Ca, and Na abundances and T_{eff} of bluest HB stars, according to the parameters of the employed isochrones. Mg is the α-process element mainly produced by explosive C-burning in massive stars and in core-collapse supernovae (CCSNe). Na can be produced by C-burning in the interior of massive stars. Ca is mainly produced in CCSNe and SNe Ia. Low [Mg/Fe] and high [Na/Fe] and [Ca/Fe] obtained from IL spectra are considered as evidence of the predominance of the second stellar population, which is expressed in Mg-Al, Mg-Na and Na-O anti-correlations among cluster stars, as well as the presence of stars with extreme Mg depletion (MM2022, Larsen et al. 2022, S2024).

Six of the eight very metal-poor GCs studied by S2024, have -0.4 $\leq$ [Mg/Fe] $\leq$ 0.05 dex and 0.2 $\leq$ [Ca/Fe] $\leq$ 0.6: [VFH2013] PA-N147-1, Hodge III, [CS82] C39, Bol 2, Ext 8, and [GPH2009] KK 197-2. All of them have extended blue HBs with the maximum T_{eff} in the range 8000–12600 K. This can be judged from the isochrone data used in the spectrum modelling and by comparison them with the observed color-magnitude diagrams (S2024). Unfortunately, the available wavelength range did not include Na lines. As a result, we conclude that these six very metal-poor GCs contain MPs.

3 On the sources of multiple populations in metal-poor GCs

One of the studied GCs, Ext 8, exhibits the lower metallicity ([Fe/H] ~ -2.8 dex) among all known GCs (Larsen et al. 2022, S2024). This value is below the inferred

"metallicity floor", i.e. the minimum metallicity estimated in a sample of about two thousand GCs from 28 galaxies (Beasley et al. 2019). The chemical composition of Ext 8 is unique among all known objects in the Universe (Larsen et al. 2022, S2024). It is characterised, in particular, by a very low Mg abundance ([Mg/Fe] $\sim -0.4 \div -0.3$ dex). Note, that the distribution of GCs by colour and metallicity is bimodal in many massive galaxies with the metallicity peaks near [Fe/H] = -1.6 dex and [Fe/H] = -0.6 dex (e.g., Beasley et al. 2019; Acharova et al. 2022 and references therein), while GCs with [Fe/H] < -2 dex are very rare. The same metallicity distribution is demonstrated by circumgalactic clouds (CGCs) at various redshifts (Acharova et al. 2022). CGCs are structures containing gas of different densities and ionization degrees. Based on the statistical analysis of the distribution of elemental abundances in GCs and CGCs and the comparison of the calculations based on it with the models of supernovae yields, it has been concluded that GCs could form in CGCs (Acharova et al. 2022). The metallicity of ultra-faint dwarf galaxies (UFDs) (Simon 2019) is similar to that of very-low-metallicity GCs. UFDs have predominantly old stellar populations and are observed in the vicinity of our own and some nearby galaxies. Due to their low mass and low stellar density, their detection at large distances from us is difficult. GCs were not found in or near UFDs. The models of pair-instability supernovae yields were used to explain the observed elemental abundances in UFDs (Sanati et al. 2023).

Because the processes of the chemical evolution mentioned in Sec. 2 cannot occur in low-mass stars, and MPs are observed even among low-mass stars in Galactic GCs, it is suggested, that stars in GCs originated from the gas enriched by massive stars of the first generation (MM2022). These could be fast-rotating massive stars (FRMSs) with the masses from 12 to 50 $M_{\odot}$ (Carretta et al. 2010) (hereafter: C2010). Stellar wind from these objects enriched the interstellar medium of young gravitationally bound GCs. However, after a few million years, these stars exploded as SNe. The explosion of numerous SNe inevitably blew gas out of GCs together with the wind from FRMSs. In order for the products of stellar evolution to remain in GCs, the ratio of the gravitational potential to the number of massive stars in GCs should be similar to that in dwarf galaxies where the contribution of supernova enrichment is observed. The fact that variations in Fe and s-process elements are present in anomalous GCs suggests that such massive GCs existed. In general, the most massive GCS in our Galaxy are the old and low-metallicity GCs (C2010). Otherwise, GCs should be located at the centers of galaxies so that SNe outflows can return back to GCs (Shapiro et al. 2010).

Asymptotic giant branch (AGB) stars with the masses from 4 to 8 $M_{\odot}$ can be responsible for the observed MPs in GCs (C2010, MM2022). Their enriched shells

are ejected as planetary nebulae and serve as the material for next generations of stars. Let us estimate the initial mass of the primordial population, needed to provide the material for the second generation stars in GCs. We assume, following Larsen et al. (2020), who studied Ext 8, that the total mass of a metal-poor GC is $10^6 M_\odot$, that the observed Mg abundance can be reproduced with two populations having lower and higher Mg abundances than this value, and each population makes up half of the stars. Although the last point is only a hypothesis based on measurements of absorption line intensities in the spectrum, it cannot be ruled out. It should be noted that variations of Mg abundances are more significant in low-metallicity GCs (MM2022). The normalising condition of the Salpeter (1955) IMF is the following: $\int_{0.1}^{50} 0.1716 \cdot m \cdot m^{-2.35} dm = 1$ (see, e.g., Larsen et al. 2022, more on the fact that the Salpeter IMF can be successfully applied to analysing the IL spectra of GCs). Let us calculate the mass fraction returned into the interstellar medium of Ext 8 from AGB stars: $\int_4^8 0.1716 \cdot (\mathrm{m} - \mathrm{m_w}) \cdot \mathrm{m}^{-2.35} \mathrm{dm} = 0.06$, where $\mathrm{m_w} = 0.08 \cdot \mathrm{m} + 0.47$ is the mass of the stellar residue of the white dwarf for $\mathrm{m} \leq 9\mathrm{M}_\odot$ (Weidemann 2000). Calculated in the same way the mass fraction returned to Ext 8 from FRMs stars with the masses from 12 to 50 $M_\odot$ gives 8 % and does not depend on the mass of the cluster. If one supposes that only AGB stars form the mass returned into the interstellar medium and that it has moved to the stars of the second generation with time, then $0.5 \cdot 10^6 M_\odot$ is 6 % of the initial mass of the cluster. Note, that the value 6 % does not depend on the mass of the cluster. In this case, the initial mass has been equal to $\sim 10^7 M_\odot$ and this GC contains $\sim$8 % of the initial stellar mass. This result is consistent with the data on the mass loss for many GCs in our Galaxy (C2010). The mass $\sim 10^7 M_\odot$ is comparable to the mass of a dwarf galaxy.

The actual situation with determining sources of MPs is much more complicated (e.g. Winter & Clarke 2023). In order to precisely calculate the mass budget of MPs in GCs and its evolution with time, it is necessary to take into account binary stars, sub-stellar companions, and stellar-mass black holes (e.g. Gieles & Gnedin 2023). Space observations have revealed signatures of different dynamical evolution of first and second generation stars (Scalco et al. 2024). It is of interest that the fraction of second generation stars varies from cluster to cluster and correlates with the present-day stellar density and cluster mass (Lagioia et al. 2024).

4 Summary

In Sec. 2, we considered the signatures of MPs that can be detected in our analysis (S2024) of low-resolution IL spectra of extragalactic GCs: low Mg abundance, high Ca and Na abundances, and high Y value set by the isochrone of stellar evolution

used to model the IL spectrum. The temperature $T_{\rm eff} > 8000$ K of bluest HB stars argue in favour of the presence of MPs in old low-metallicity GCs.

We discussed the relationship between the initial and present-day masses of GCs with sources of MPs: AGB and FRMSs. (Sec. 3). By calculation of the mass fraction returned from massive stars into interstellar medium, we have shown that the initial mass of the cluster was approximately 8 times larger than the present-day one. This result is consistent with the data on the mass loss for many GCs in our Galaxy (e.g. C2010).

Funding

The work was partially supported by the Ministry of Science and Higher Education of the Russian Federation grant 075-15-2022-262 (13.MNPMU.21.0003).

References

Acharova I., Sharina M., and Kazakov E., 2022, Monthly Notices of the Royal Astronomical Society, 511, p. 800
Beasley M., Leaman R., Gallart C., et al., 2019, Monthly Notices of the Royal Astronomical Society, 487, p. 1986
Bertelli G., Girardi L., Marigo P., and Nasi E., 2008, Astronomy and Astrophysics, 484, p. 815
Carretta E., Bragaglia A., Gratton R., et al., 2010, Astronomy and Astrophysics, 516, p. 55
Gieles M. and Gnedin O., 2023, Monthly Notices of the Royal Astronomical Society, 522, p. 5340
Kraft R., 1994, Publications of the Astronomical Society of the Pacific, 106, p. 553
Lagioia E., Milone A., Legnardi M., et al., 2024, Astrophysical Journal, Submitted, arXiv:2406.16824
Larsen S., Eitner P., Magg E., et al., 2022, Astronomy and Astrophysics, 660, p. 88
Larsen S., Romanowsky A., Brodie J., and Wasserman A., 2020, Science, 370, p. 970
Lee H., Yoon S., and Lee Y., 2000, Astrophysical Journal, 120, p. 998
Milone A. and Marino A., 2022, Universe, 8, p. 359
Salpeter E., 1955, Astrophysical Journal, 121, p. 161
Sanati M., Jeanquartier F., Revaz Y., and Jablonka P., 2023, Astronomy and Astrophysics, 669, p. 94
Scalco M., Gerasimov R., Bedin L., et al., 2024, Astronomische Nachrichten, 345, p. 40018
Shapiro K., Genzel R., and Forster S., 2010, Monthly Notices of the Royal Astronomical Society (Letters), 403, p. 36
Sharina M., Maricheva M., Kniazev A., et al., 2024, Monthly Notices of the Royal Astronomical Society, 528, p. 7165
Sharina M., Shimansky V., and Shimanskaya N., 2020, Astrophysical Bulletin, 75, p. 247
Simon J., 2019, Annual Review of Astronomy and Astrophysics, 57, p. 375
Weidemann V., 2000, Astronomy and Astrophysics, 363, p. 647
Winter A. and Clarke C., 2023, Monthly Notices of the Royal Astronomical Society, 521, p. 1646

MODERN ASTRONOMY: FROM THE EARLY UNIVERSE TO EXOPLANETS AND BLACK HOLES

An X-ray study of the dwarf nova candidate OGLE-BLG-DN-0064 using Chandra data

A. Sibgatullin, V. Dodon, and I. Galiullin

Kazan Federal University, 18 Kremlyovskaya, Kazan, 420008 Russia

Abstract. OGLE-BLG-DN-0064 (hereafter, OGLE-64) has been identified as a possible dwarf nova candidate due to the optical outburst activity recorded by the Optical Gravitational Lensing Experiment (OGLE) survey. We study the X-ray properties of OGLE-64 using the Chandra archival data. OGLE-64 shows an X-ray luminosity of $L_X \approx 1.5 \times 10^{32}$ erg/s in the 0.5–7 keV energy band and a high ratio of X-ray flux to optical flux $F_X/F_{\rm opt} \approx 1.5$. We found no significant optical and X-ray periodicity with the timing analyses. The X-ray spectrum of OGLE-64 can be approximated by a power-law model with a photon index of $\Gamma \approx 1.9$ and an optically thin plasma model with a temperature of $kT \approx 6.4$ keV. The isobaric cooling flow model gives an accretion rate in the system of about $\dot{M}_{\rm acc} \approx 5.4 \times 10^{-11}\,M_\odot$/yr and the white dwarf mass of $M_{\rm WD} \approx 0.8\,M_\odot$. The X-ray properties and the optical outburst activity suggest that OGLE-64 is a dwarf nova.

Keywords: stars: cataclysmic variables, dwarf novae, binaries, white dwarfs; X-ray: general

DOI: 10.26119/VAK2024.089

1 Introduction

Cataclysmic variables (CVs) are close binary systems consisting of an accreting white dwarf and a donor star, filling its Roche Lobe (Warner 1995). Dwarf novae are CVs that exhibit regular outbursting activity, best described by the disk instability model (Lasota 2001). CVs typically show X-ray luminosities in the $L_X \sim 10^{30}$–10^{33} erg/s range (Mukai 2017).

We found OGLE-64 as an X-ray source (2CXO J173917.7−214735) while searching for new CV candidates in the Chandra Source Catalog v2.0 (Evans et al. 2010), cross-matched with Gaia DR3 (Galiullin et al., submitted to A&A). OGLE-64 shows a high ratio of X-ray flux to optical flux, $F_X/F_{\rm opt} \approx 1.5$, compared to other objects in the catalog. OGLE-64 matches with a Gaia DR3 object (id: 4117235609421426560) within a 2 arcsec search radius, having a distance to the object of 872 ± 126 pc (Eyer et al. 2023). OGLE-64 is a variable object, which was first noted as a possible dwarf nova candidate in 2015 due to its outbursting behavior detected by the Optical Gravitational Lensing Experiment (OGLE) survey (Mróz et al. 2015). Fig. 1 shows the Chandra false-color X-ray image (Obsid: 12945) of OGLE-64 and the optical image of the same sky region from Pan-STARRS (Chambers et al. 2016).

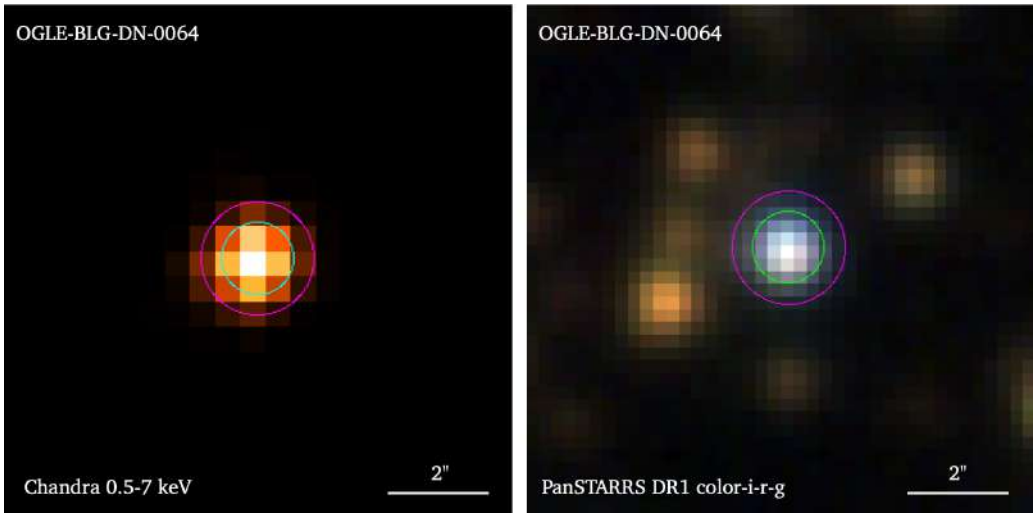

Fig. 1. Left panel: The Chandra X-ray image of OGLE-64 in the 0.5–7 keV energy band. Right panel: Color image of OGLE-64 obtained by combining Pan-STARRS gri images. The inner circle corresponds to the error region for the X-ray source detection, and the outer circle represents the region containing 90% of the counts from the X-ray source.

2 Analysis and Results

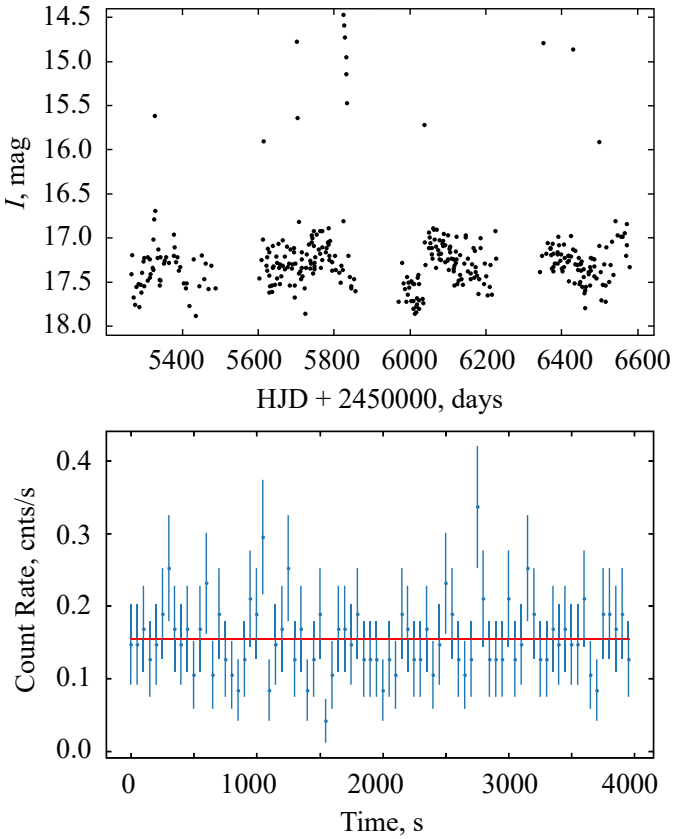

Fig. 2. Top panel: OGLE light curve of OGLE-64 on I band. Bottom panel: Chandra X-ray light curve of OGLE-64 in the 0.5–7 keV energy band. The red solid line shows the mean count rate.

We used a pre-calibrated optical light curve from the OGLE survey to search for possible periodic signals with timing analysis. We extracted the X-ray spectrum and light curve from the Chandra archival data (Obsid: 12945) using the `Chandra Interactive Analysis of Observation` (`CIAO`) (Fruscione et al. 2006) package. We analyzed the X-ray spectrum of OGLE-64 in the 0.5–7 keV energy band using the `XSPEC` package (Arnaud 1996). We grouped the X-ray spectrum of OGLE-64 to have at least three counts per spectral channel. We applied C-statistics (Cash 1979) to find the best-fit parameters and compute the errors at the 90% confidence level. We used the Tuebingen–Boulder interstellar absorption model with abundances from Wilms et al. (2000) to include a Galactic absorption component.

2.1 Timing analysis

We used the Lomb–Scargle periodogram (Lomb 1976; Scargle 1982) and Fast Fourier Transformation (using `XRONOS` sub-package in `FTOOLS`, HEASARC[1]) to search for periodic signals in the optical and X-ray light curves, respectively. We applied a sigma-clipping technique to the optical light curve to remove all data points caused by an outburst. To statistically estimate the significance of the peaks in the periodogram, we simulated 2000 nonperiodic light curves with constant fluxes. We generated the distribution of the maximum power of peaks in periodograms for nonperiodic light curves and obtained the values corresponding to the 3σ confidence level. The top panel of Fig. 2 shows the optical light curve with an outburst of about 3 mag. The bottom panel of Fig. 2 shows the X-ray light curve from the Chandra data. We found no significant periodicity neither for the optical nor the X-ray light curves.

2.2 X-ray spectrum, luminosity, and accretion rate

The top panel of Fig. 3 shows the X-ray spectrum of OGLE-64 along with the different models used in the fit. Initially, we approximated the X-ray spectrum of OGLE-64 by a power-law model. The fitted parameters are $N_{\rm H} = 3.3^{+1.1}_{-2.3} \times 10^{21}$ cm^{-2} for a hydrogen column density and $\Gamma = 1.85 \pm 0.22$ for a photon index (C-stat/dof: 118.82/124). The fit with an optically thermal plasma emission model gives a temperature of $kT = 6.44^{+3.62}_{-1.79}$ keV and $N_{\rm H} = (2.1 \pm 0.7) \times 10^{21}$ cm^{-2} (C-stat/dof: 122.81/124). We computed the absorption-corrected X-ray flux of OGLE-64 by integrating the power-law model. Using the distance to the object, we computed the X-ray luminosity of the OGLE-64 in the 0.5–7 keV (2–10 keV) energy band to be $L_X = (1.50 \pm 0.48) \times 10^{32}$–$(1.07 \pm 0.35) \times 10^{32}$ erg/s.

We used the isobaric cooling flow model to compute the accretion rate of OGLE-64. The fitted parameters are $N_{\rm H} = (2.8 \pm 1.0) \times 10^{21}$ cm^{-2}, $kT_{\rm max} = 18.93^{+28.92}_{-8.32}$ keV, and $\dot{M}_{\rm acc} = 5.37^{+3.60}_{-2.65} \times 10^{-11}\, M_\odot$/yr for the accretion rate (C-stat/dof: 119.27/122). To compute the white dwarf's mass, we used the relation between the shock temperature and mass, $kT_{\rm max} = (3/16) \times (GM_{\rm WD} \times m_{\rm H} \times \mu)/R_{\rm WD}$ (Frank et al. 2002), where $m_{\rm H}$ is the mass of hydrogen atom, μ is the mean molecular weight (here we use $\mu = 0.615$), G is the Newton's gravitational constant, $M_{\rm WD}$ and $R_{\rm WD}$ are the white dwarf's mass and radius respectively. Using the WD mass-radius relation (Nauenberg 1972), we computed the white dwarf's mass to be $M_{\rm WD} \approx 0.81^{+0.38}_{-0.23}\, M_\odot$.

3 Discussion and conclusion

The X-ray properties and the observed optical outbursts of about 3 mag suggest that OGLE-64 is a dwarf nova. OGLE-64 shows an accretion rate of $\dot{M}_{\rm acc} \approx 5 \times 10^{-11}\, M_\odot$/yr

[1] https://heasarc.gsfc.nasa.gov/

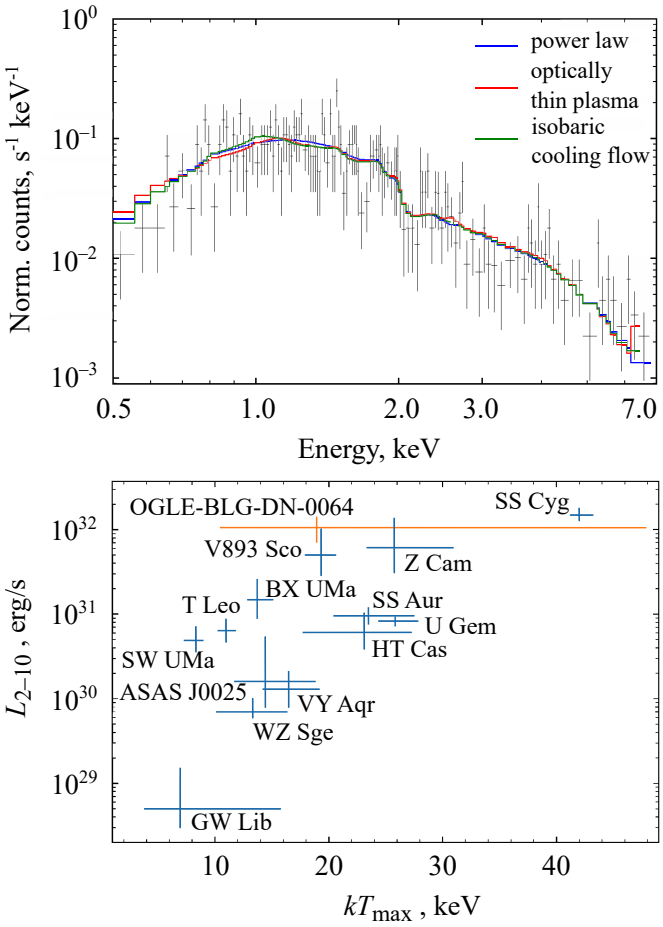

Fig. 3. Top panel: The Chandra X-ray spectrum of OGLE-64 along with the different models used in the fit. Bottom panel: The X-ray Luminosity L_X (2–10 keV)—maximum temperature $kT_{\max}$ diagram for some of the known dwarf novae (Byckling et al. 2010). OGLE-64 shows a relatively high X-ray luminosity, compared to other dwarf novae.

and a WD mass of $M_{\rm WD} \approx 0.8\,M_{\odot}$. The bottom panel of Fig. 3 shows the X-ray luminosity (2–10 keV energy band) versus the temperature $kT_{\max}$ (from the isobaric cooling flow model) diagram for some known dwarf novae (Byckling et al. 2010). OGLE-64 shows a relatively high X-ray luminosity of $L_X \approx 10^{32}$ erg/s, compared to some known dwarf novae. Such a high X-ray luminosity is mostly typical of magnetic systems. However, the photon index $\Gamma \sim 2$ and the temperature $kT \sim 6$ keV are typical for non-magnetic CVs in a quiescent state (see e.g., Galiullin & Gilfanov 2021). Our preliminary analysis shows no significant periodicity in the X-ray and

the optical light curves. The absence of X-ray variability disagrees with the possible magnetic nature of OGLE-64 but might be explained by the almost face-on inclination angle ($i \sim 0°$) of the system. The non-detection of the orbital period in the optical OGLE light curve also hints at the system's low inclination angle. OGLE-64 requires future spectroscopic follow-up observations. The presence of Balmer emission lines might confirm the object as a CV, and the presence of the high-excitation He II λ4686 emission line might imply a magnetic nature of the white dwarf.

Acknowledgements. This research has made use of data obtained from the Chandra Data Archive and the Chandra Source Catalog, and software provided by the Chandra X-ray Center (CXC) in the application packages CIAO and Sherpa. We thank the members of the OGLE team, for their contribution to the collection of the OGLE photometric data. This work has made use of data from the European Space Agency (ESA) mission Gaia (https://www.cosmos.esa.int/gaia), processed by the Gaia Data Processing and Analysis Consortium (DPAC, https://www.cosmos.esa.int/web/gaia/dpac/consortium). Funding for the DPAC has been provided by national institutions, in particular the institutions participating in the Gaia Multilateral Agreement. Authors acknowledge the support from Kazan Federal University.

References

Arnaud K.A., 1996, ASP Conf. Ser., 101, p. 17
Byckling K., Mukai K., Thorstensen J.R., et al., 2010, Monthly Notices of the Royal Astronomical Society, 408, 4, p. 2298
Cash W., 1979, Astrophysical Journal, 228, p. 939
Chambers K.C., Magnier E.A., Metcalfe N., et al., 2016, arXiv e-prints, arXiv:1612.05560
Evans I.N., Primini F.A., Glotfelty K.J., et al., 2010, Astrophysical Journal Supplement, 189, 1, p. 37
Eyer L., Audard M., Holl B., et al., 2023, Astronomy & Astrophysics, 674, id. A13
Frank J., King A., Raine D.J., 2002, Cambridge University Press, ISBN 0521620538
Fruscione A., McDowell J.C., Allen G.E., et al., 2006, Proceedings of the SPIE, 6270, id. 62701V
Galiullin I.I. and Gilfanov M.R., 2021, Astronomy Letters, 47, 9, p. 587
Lasota J.-P., 2001, New Astronomy Reviews, 45, 7, p. 449
Lomb N.R., 1976, Astrophysics and Space Science, 39, 2, p. 447
Mróz P., Udalski A., Poleski R., et al., 2015, Acta Astronomica, 65, 4, p. 313
Mukai K., 2017, Publications of the Astronomical Society of the Pacific, 129, 976, p. 062001
Nauenberg M., 1972, Astrophysical Journal, 175, p. 417
Scargle J.D., 1982, Astrophysical Journal, 263, p. 835
Warner B., 1995, Camb. Astrophys. Ser., 28
Wilms J., Allen A., McCray R., 2000, Astrophysical Journal, 542, 2, p. 914

VAK 2024 MODERN ASTRONOMY: FROM THE EARLY UNIVERSE TO EXOPLANETS AND BLACK HOLES 300 years Russian Academy of Sciences

Formation of Be stars in binary systems with conservative mass exchange

E. Staritsin

K.A. Barkhatova Kourovka Astronomical Observatory, Ural Federal University,
51 Prospect Lenina, Ekaterinburg, 620000 Russia

Abstract. In the case of conservative mass exchange in a binary system in the Hertzsprung gap, the mass of the accreting star can increase by up to two times. The accreted matter brings Keplerian angular momentum with it. The meridional circulation transfers 80–85% of the incoming angular momentum to the surface of the accretor. The increase in the mass and angular momentum of the accretor occurs due to the loss of this part of the angular momentum. After the mass exchange is completed, most of the angular momentum is concentrated in the accreted layers. The accretor has a large enough angular momentum to maintain its status as a Be star during its subsequent evolution on the main sequence.

Keywords: stars: binaries; emission-line; Be; early-type; rotation

DOI: 10.26119/VAK2024.090

1 Introduction

Recently, a number of Be stars have been discovered in binary systems with sdO subdwarf (Chojnowski et al. 2018; Wang et al. 2023). The most studied representative of systems of this type is the binary system ϕ Per (Gies et al. 1998). This system could have been formed as a result of conservative mass exchange in the Hertzsprung gap (Schootemeijer et al. 2018). The mass range of Be stars in these systems overlaps with the range of masses of accreting components in long-period Algols. The observed characteristics of long-period Algols can also be reproduced (except for rotation) within the framework of the hypothesis of conservative mass exchange in the case of the shell source burning donor (Van Rensbergen & De Greve 2020). The periods of binary systems with Be stars are longer than those of long-period Algols. The axial rotation of the Be stars is also greater than that of the accreting components in the long-period Algols. We have studied the possibility of spinning-up of Be stars in the process a of conservative mass exchange. The initial parameters of binary systems are chosen to cover the range of masses of Be stars observed in systems with O-subdwarfs. The possibility of the spinning-up of accreting component has also been studied depending on the initial distance between the stars of the pair.

2 Calculation data

We have considered conservative mass exchange in a system with the initial masses of the components $(M_d)_0$ and $(M_a)_0$ of $6\,M_\odot$ and $5\,M_\odot$ and the distance between the components A_0 of $30\,R_\odot$, as well as with the initial masses of the components $3\,M_\odot$ and $2.5\,M_\odot$ and the distances of $30\,R_\odot$ and $15\,R_\odot$. The first and second systems are similar to the progenitors of the Be star systems ϕ Per (Vanbeveren et al. 1998) and BD -01° 1603, the third system is similar to the progenitor of the long-period system of the Algol type RX Gem.

3 Calculation results

After the mass exchange has started, the mass of the accretor begins to increase. The angular velocity of the accretor surface also increases. In the accreted matter, a cell of meridional circulation is formed (Staritsin 2021, 2022, 2023a,b, 2024a). The bottom of the cell goes down into the accretor interior. The circulation transfers part of the angular momentum of the accreted layers into the interior of the accretor. The mass of the layers, into which this part of the angular momentum enters, increases with time in the process of the mass exchange. The mass fraction of these layers changes during the mass exchange in approximately the same way in accretors with

different initial masses. However, the fraction of mass that falls on the convective core is smaller, the smaller the initial mass of the accretor. Angular momentum begins to enter the convective core at the very end of the mass exchange if $(M_a)_0 = 2.5\,M_\odot$, but before the end of the mass exchange if $(M_a)_0 = 5\,M_\odot$. After the mass exchange, angular momentum continues to flow into the convective core. The angular velocity of the convective core increases (Fig. 1).

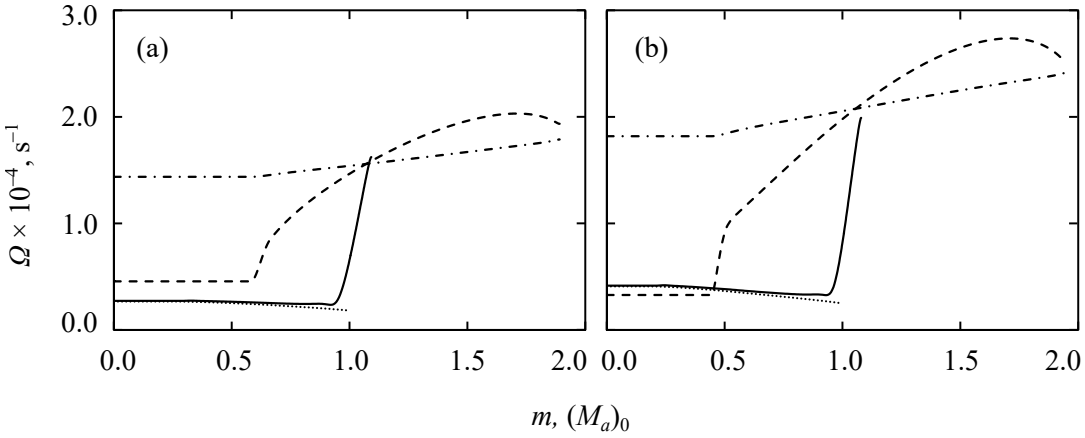

Fig. 1. Angular velocity in the interior of the accretor before the mass exchange (dotted line), when the surface receives Kepler rotation (solid line), at the end of the mass exchange (dashed line), and after relaxation towards thermal equilibrium (dot-dashed line) in the cases where the initial mass of the accretor is $(M_a)_0 = 5\,M_\odot$ (a) and $(M_a)_0 = 2.5\,M_\odot$ (b).

After the increase of the mass of the accretor by 10%, the angular velocity of the surface takes the value of the Kepler velocity (Staritsin 2022, 2023a,b, 2024a). Further, another cell of the meridional circulation is created in the accreted layers. Circulation transfers part of the angular momentum of the accreted layers to the surface of the accretor. This part of the angular momentum can be taken away from the accretor by the disk (Paczynski 1991; Bisnovatyi-Kogan 1993). As a result, the angular momentum coming with the accreted layers is reduced by 80% (Staritsin 2024b). The angular velocity of the accretor surface keeps the Kepler value. The boundary between the two circulation cells moves outward. Therefore, a small part of the angular momentum that came with the accreted layers at this stage of the mass exchange is transferred to the inner layers of the accretor.

The rate of mass exchange in the Hertzsprung gap depends on the initial distance between the components of the binary system. The response of a star to an increase

in mass depends on the accretion rate. In the case of $A_0 = 15\,R_\odot$, the accretion rate is less than in the case of $A_0 = 30\,R_\odot$. The increase in the size of the accretor is smaller. The Kepler moment at the boundary of the accretor is also smaller. Therefore, the accreted matter brings less angular momentum in the case of $A_0 = 15\,R_\odot$ than in the case of $A_0 = 30\,R_\odot$. Nevertheless, the angular momentum of the accretor after the mass exchange is the same in both cases. Only the amount of angular momentum transferred by the circulation to the surface is lost by the accretor changes (Fig. 2).

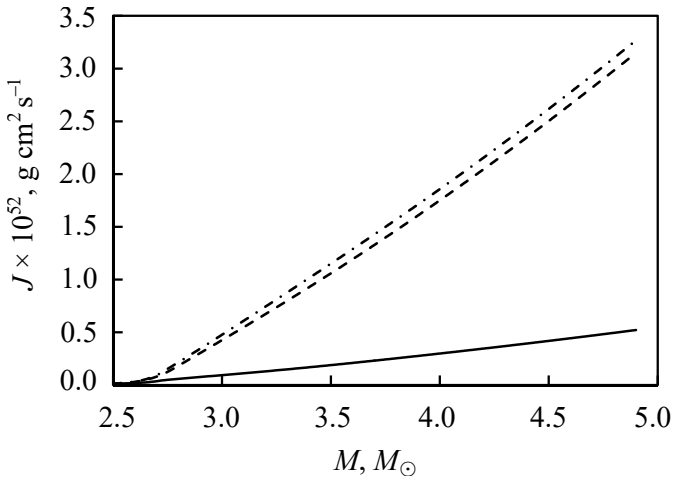

Fig. 2. Angular momentum brought by accreted matter in cases where $A_0 = 30\,R_\odot$ (dot-dashed line) and $A_0 = 15\,R_\odot$ (dashed line), and angular momentum of the accretor (solid line) as functions of its mass.

Due to mass exchange, the mass of the accretor almost doubles. Most of the angular momentum is concentrated in the accreted matter. The distribution of angular momentum in a single star is approximately the same. However, the angular momentum of the convective core and its adjacent layers in the case of an accretor is less than that of a single star of the same mass. After the mass exchange is completed, the circulation continues to transfer angular momentum from the outer layers to the inner layers. The rotation of the accretor becomes subcritical, but remains typical for Be stars of the early spectral subclass. The angular momentum of the accretor is large enough to maintain the status of a Be star during evolution on the main sequence.

4 Summary

In the case of conservative mass exchange in the Hertzsprung gap, the meridional circulation transfers 80–85% of the angular momentum that came with the accreted matter to the surface of the accretor. The loss of this part of the angular momentum allows the accretor to increase the mass and angular momentum during the mass exchange. Meridional circulation and shear turbulence transfer a small portion of the angular momentum that came with the accreted matter to the inner layers of the accretor. After the mass exchange is completed, most of the angular momentum is in the accreted layers. The angular momentum of the accretor does not depend on the initial distance between the components of the binary system. With different initial masses of the progenitors of the Be + sdO binary systems, the accretor obtains an angular momentum large enough to maintain the status of a Be star during the subsequent evolution on the main sequence.

Funding

This work was supported by the Ministry of Science and Education project No. FEUZ-2023-0019.

References

Bisnovatyi-Kogan G.S., 1993, Astronomy & Astrophysics, 274, p. 796
Chojnowski S.D., Labadie-Bartz J., Rivinius T., et al., 2018, Astrophysical Journal, 865, 1, id. 76
Gies D.R., Bagnuolo W.G., Ferrara E.C., et al., 1998, Astrophysical Journal, 493, 1, p. 440
Paczynski B., 1991, Astrophysical Journal, 370, p. 597
Van Rensbergen W. and De Greve J.P., 2020, Astronomy & Astrophysics, 642, id. A183
Schootemeijer A., Götberg Y., de Mink S.E., et al., 2018, Astronomy & Astrophysics, 615, id. A30
Staritsin E., 2021, Astronomy & Astrophysics, 646, id. A90
Staritsin E., 2022, Research in Astronomy and Astrophysics, 22, 10, id. 105015
Staritsin E.I., 2023a, Astronomy Reports, 67, 9, p. 959
Staritsin E.I., 2023b, INASAN Science Reports, 8, 2, p. 54
Staritsin E., 2024a, Research in Astronomy and Astrophysics, 24, 1, id. 015001
Staritsin E., 2024b, Research in Astronomy and Astrophysics, accepted
Vanbeveren D., De Loore C., Van Rensbergen W., 1998, Astronomy and Astrophysics Review, 9, 1-2, p. 63
Wang L., Gies D.R., Peters G.J., et al., 2023, Astronomical Journal, 165, 5, id. 203

BAK 2024 MODERN ASTRONOMY: FROM THE EARLY UNIVERSE TO EXOPLANETS AND BLACK HOLES 300 years Russian Academy of Sciences

MHD-Modeling of the molecular filament evolution with numerical FLASH code

I. Sultanov and S. Khaibrakhmanov

Chelyabinsk State University, 129 Br. Kashirinykh, Chelyabinsk, 454001 Russia

Abstract. We study numerically the gravitational fragmentation of a cylindrical molecular cloud with large-scale magnetic field. The simulations are performed with the help of the MHD code `FLASH`. We consider two cases: gravitational instability of the filament with initially deformed surface (model of Chandrasekhar and Fermi), and the instability of longitudinal compressible waves (model of Stodolkeiwicz). The simulations under typical parameters show that two types of the cores can be formed as a result of the fragmentation. Gravitational focusing leads to the formation of two massive clumps at the ends of filaments. Those cores move towards the cloud center with supersonic speeds. The instability of initial perturbations results in smaller evenly distributed cores inside the filament. The cores formed due to the instability of compressible waves have almost spherical shapes, while the cores resulted from the fragmentation of the filament with deformed surface are flattened. Typical sizes of the cores of 0.01–0.02 pc are in agreement with observations.

Keywords: ISM: clouds, evolution, magnetic fields; magnetohydrodynamics (MHD); methods: numerical

DOI: 10.26119/VAK2024.091

1 Introduction

Modern observations show that interstellar clouds have a filamentary structure, which is traced from H I super clouds to individual molecular clouds (André et al. 2014). Filaments appear as elongated structures in the emission maps of the interstellar medium. Such filaments can be either cylindrical clouds or gas-dust layers which are seen edge-on (Dudorov & Khaibrakhmanov 2017). Observations show that the typical width of molecular filaments in the regions of star formation is of 0.1 pc, and their length varies from several pc to tens of pc. The temperature in the filaments ranges from 10 K to 25 K, and the gas density ranges from 10^4 cm^{-3} up to 10^5 cm^{-3} (Dudorov & Khaibrakhmanov 2017). Polarization mapping revealed the presence of large-scale magnetic fields in filaments. The magnetic field strength increases with the column density and lies in the range from 10^{-5} G for low column density clouds with $N = 10^{19}$ cm^{-2} up to 10^{-3} G for the dense filaments with $N = 10^{23}$ cm^{-2}.

Most protostellar clouds in which star formation occurs are located within filamentary molecular clouds (Konyves et al. 2015). The core formation is associated with the process of gravitational fragmentation (Chandrasekhar & Fermi 1953; Stodólkiewicz 1963; Ostriker 1964). Different regimes of the filament fragmentation are possible depending on its initial state: gravitational collapse at the ends of filament, gravitational fragmentation of the filament with the subsequent formation of evenly distributed cores, and global collapse of the filament towards the center of the cloud (Seifried & Walch 2015). Magnetic field has a great effect on the filament evolution. Almost constant filament width of the order of 0.1 pc can be maintained by magnetic pressure gradient (Dudorov & Khaibrakhmanov 2017). The magnetic field prevents global collapse of the filament towards its axis, so that the collapse becomes possible only at the ends of filament (Sultanov & Khaibrakhmanov 2024).

In this work we perform numerical simulations to study the gravitational fragmentation of the filaments with parallel magnetic field. Based on the simulations, we analyse the properties of molecular cloud cores forming as a result of the fragmentation.

2 Model

2.1 Perturbations

We consider two models of the gravitational fragmentation. In the first model (Chandrasekhar & Fermi 1953), periodic deformations of the filament surface are introduced. The imcompressible deformations lead to the fragmentation if the wavelength of the deformation exceeds a certain critical value. In the second model (Stodólkiewicz 1963), small compressible waves traveling along the cloud axis are considered. The

waves become gravitationally unstable and lead to the cloud fragmentation, if the wavelength exceeds a critical length.

2.2 Problem statement

We simulate the gravitational collapse of a cylindrical molecular cloud (filament) with length $H_0 = 2$ pc and radius $r_0 = 0.1$ pc. The molecular weight of the gas is $\mu = 2.31$, temperature $T_0 = 10$ K, adiabatic index $\gamma = 1.001$, concentration $n_0 = 2.6 \times 10^4$ cm^{-3}. Mass of the cloud is $10\,M_\odot$. Corresponding free fall time is $t_{\rm ff} = 2 \times 10^5$ years.

We run two simulations: adopting the model of Stodólkiewicz (1963) (STD) and the model of Chandrasekhar & Fermi (1953) (CF). Magnetic field is parallel to the main axis and magnetic field strengths are 10^{-5} G and 4.8×10^{-5} G respectively for STD and CF runs. Corresponding critical wavelengths are $\lambda_{\rm STD} = 0.244$ pc and $\lambda_{\rm CF} = 1.25$ pc.

In the initial setup, we introduce the small perturbations with $\lambda = 1.19\,\lambda_{\rm STD}$ for run STD and $\lambda = 0.52\,\lambda_{\rm CF}$ for run CF.

2.3 Basic equations and solution methods

We study the evolution of the molecular filament using the system of ideal MHD equations. The equations are solved with the help of the numerical code `FLASH 4`, in which the adaptive mesh refinement (AMR) technology is implemented (Fryxell et al. 2018). The equations of ideal MHD are solved using the Godunov-type MUSCL scheme (van Leer 1979). We consider a 3D problem in Cartesian coordinates. The z-axis corresponds to the symmetry axis of the filament. The sizes of the computational domain in the x-, y-, and z-directions are $1 \times 1 \times 3$ pc^3, and 7 levels of the AMR grid are used. The sizes of the largest cell in the x-, y-, and z-directions are $0.12 \times 0.12 \times 0.12$ pc^3, the sizes of the smallest cells are $0.002 \times 0.002 \times 0.002$ pc^3, which corresponds to the effective grid resolution of $512 \times 512 \times 1536$ at the 7th AMR level. The Poisson's equation for gravity is solved using the multipole method based on the Barnes–Hut tree (Barnes & Hut 1986).

3 Results

In Fig. 1, we plot the gas density distribution and magnetic field lines in the x–z plane for run STD at $t = 0$, $1.26\,t_{\rm ff}$ and for run CF at $t = 0$, $1.5\,t_{\rm ff}$. Final moments of time in runs STD and CF correspond to moments, when gravitational collapse of the cores formed at the end of filament starts. In run CF the filament has a stronger initial magnetic field; therefore, its cores form and start to collapse later.

Figure 1 shows that growth of small perturbations leads to filament fragmentation and subsequent formation of cores in both cases. In order to analyse cores properties, we define cores as the densest parts inside the filament.

In run STD nine cores have formed, as indicated in Fig. 1b. Cores 1 and 2 (end cores, hereafter) are the result of the gravitational focusing at the filament's edges, while cores 2–8 (internal cores, hereafter) formed due to the growth of initial perturbations. Internal cores are equidistant from each other at 0.28 pc or $0.96\,\lambda$ approximately and have almost spherical shape. Cores 3–7 have diameter and density of about 0.006 pc and 7×10^6 cm^{-3}, while cores 2 and 8, located close to the ends, are larger and more massive, of around 0.002 pc and 3.2×10^9 cm^{-3}. End cores are flattened along the magnetic field direction and have sizes of 0.0038×0.002 pc. Cores 1, 9 and 2, 8 are moving towards the cloud center with supersonic velocities of approximately 3 km/s.

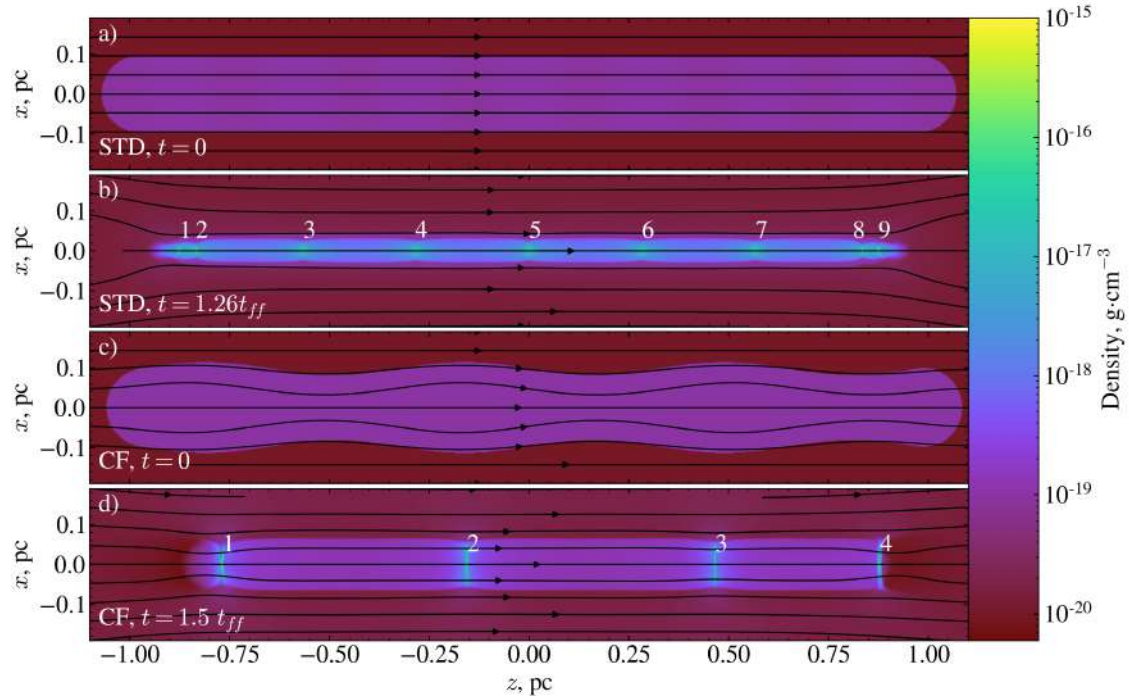

Fig. 1. The distribution of gas density (color map) and magnetic field lines (black lines with arrows) in the x–z-plane for two considered cases. Panels (a) and (b): run STD at $t = 0$ and $t = 1.25\,t_{\rm ff}$, respectively. Panels (c) and (d): run CF at $t = 0$ and $t = 1.5\,t_{\rm ff}$ respectively.

In run CF, four cores have formed. Distance between cores 1, 2 and 3 is about 0.614 pc or 0.94 λ. These cores are formed due to the gravitational instability of initial surface deformations, and have similar properties. The shape of the core 1 is closer to the spherical one, because of additional effect of gravitational focusing at the end of filament. This core has flattened envelope. Cores 2–4 are flattened along magnetic field, and have typical sizes of 0.013×0.002 pc (cores 2 and 3) and 0.004×0.002 pc (core 4). Cores density varies in the range from 10^7 cm^{-3} in the filament center up to 10^8 cm^{-3} at its ends. Cores 1 and 4 are moving towards the cloud center with supersonic velocities of 4 km/s and 2 km/s.

4 Summary

Our simulations have shown that the different kinds of the initial perturbations in the molecular filaments lead to different properties of the cores formed as a result of the fragmentation. Gravitational instability of compressible waves results in larger cores as compared to the case of the filament with deformed surface. In the former case, the cores are more spherical, while in the latter case the cores has flattened shape. Typical maximum sizes of the cores formed in the case of initially deformed filament are 0.01 pc, which is in agreement with values obtained from observations for the TMC1 region in the Taurus Molecular Cloud (Kirk et al. 2024).

Acknowledgements. The simulations were carried out using the computational cluster of the Chelyabinsk State University.

Funding

The work is financially supported by the Russian Science Foundation (No. 24-22-20041).

References

André P., Di Francesco J., Ward-Thompson D., et al., 2014, Protostars and Planets VI, ed. Beuther H., Klessen R.S., Dullemond C.P., Henning T., p. 27
Barnes J. and Hut P., 1986, Nature, 326, 6096, p. 446
Chandrasekhar S. and Fermi E., 1953, Astrophysical journal, 118, p. 116
Dudorov A.E. and Khaibrakhmanov S.A., 2017, Open Astronomy, 26, 1, p. 285
Fryxell B., Olson K., Ricker P., et al., 2000, Astrophysical Journal Supplement, 131, 1, p. 273
Kirk J.M., Ward-Thompson D., Di Francesco J., et al., 2024, Monthly Notices of the Royal Astronomical Society, 532, 4, p. 4661
Konyves V., André Ph., Men'shchikov A., et al., 2015, Astronomy & Astrophysics, 584, id. A91
van Leer B., 1979, Journal of Computational Physics, 32, 1, p. 101
Ostriker J., 1964, Astrophysical Journal, 140, p. 1056
Seifried D. and Walch S., 2015, Monthly Notices of the Royal Astronomical Society, 452, 3, p. 2410
Stodólkiewicz J.S, 1963, Acta Astronomica, 13, p. 30
Sultanov I.M. and Khaibrakhmanov S.A., 2024, Astronomy Reports, 68, 1, p. 60

MODERN ASTRONOMY: FROM THE EARLY UNIVERSE TO EXOPLANETS AND BLACK HOLES

Spectroscopy of B stars in the very young open star cluster IC 1805

A. Tarasov

Crimean Astrophysical Observatory of the Russian Academy of Sciences, Nauchny, 298409 Russia

Abstract. Based on moderate-resolution spectra in the range 4200–5200 Å, we have studied late O and early B stars in the very young open star cluster IC 1805. The temperatures of the stars under the study have been derived by the differential method, in which simple parameters were chosen for a number of spectral lines and were then compared with the analogous parameters from an extensive sample of O–B stars. Accurate $T_{\rm eff}$ estimates have been obtained for them from model atmospheres. Applying this method for the sample of objects under the study has allowed the cluster age $t = 2 \pm 0.5$ Myr and distance modulus $(v–V)_0 = 11\overset{\rm m}{.}5$ to be determined with confidence.

Keywords: stars: spectroscopic observations; open star clusters; age of cluster

DOI: 10.26119/VAK2024.092

1 Introduction

The very young open star cluster IC 1805 is a part of the OB association Cas OB6 in the Perseus arm and is located within the H II region W4. The cluster has been well-studied photometrically. It was investigated in the UBV system by Massey et al. (1995), etc. and in the medium-band Vilnius system by Straižys et al. (2013). The spectral classification for bright O–B stars has been performed repeatedly. The cluster was shown to be extended and to have a diameter of 20–25 arcmin with a low concentration of stars to the center. The distance to the cluster was estimated from spectroscopic observations to be 1.9–2.4 kpc. Since most of the cluster objects are faint, there are few spectroscopic studies of the physical parameters of stars and they are concentrated mainly on the atmospheres and their nonstationarity in O stars. Most of the authors estimated the age to be 1–6 Myr. This means that only the most massive O stars have left the zero-age main sequence. Therefore, the main goal of this paper was an accurate determination of the temperatures of late O and early B cluster stars, their positions on the main sequence, and, consequently, a refinement of the cluster age by a method different from the photometric one based on spectroscopic observations.

2 Observations and temperature determination

All spectroscopic observations of the OB stars in the cluster IC 1805 were performed with a moderate resolution spectrograph mounted at the Nasmyth focus of the 2.6-m ZTSh telescope at the Crimean Astrophysical Observatory. The spectra were taken in the wavelength range 4200–5200 Å with a resolution of about 1.5 Å and a signal-to-noise ratio, as a rule, better than 100. In total, we took the spectra for 24 cluster O and B stars. In addition, we took the spectra for more than 30 B stars from the list by Lyubimkov et al. (2000, 2002) with the same instrumental settings, for which their atmospheric parameters were determined with a high accuracy. These spectra were subsequently used to determine the effective temperature $T_{\rm eff}$ for the cluster B stars.

We used the differential method to determine the effective temperatures $T_{\rm eff}$ of the late O and B stars in the cluster. Since the cluster age is known approximately and, according to various estimates, lies within the range 1–6 Myr, it is reasonable to assume that all B stars of the spectral types B0–B6 are normal dwarfs. Hence, we took the spectra of more than 30 stars from the list by Lyubimkov et al. (2000, 2002) satisfying this criterion with the same instrumental settings of the spectrograph as those used in the observations of cluster stars.

To determine the temperature, we chose the following parameters of the spectra: the ratio of the residual line fluxes $F(\mathrm{He\,I}\,4471)/F(\mathrm{Mg\,II}\,4481)$; the equivalent widths W_λ of the Hβ and Hγ lines; the residual fluxes of metal lines, several He I and He II lines. The criteria chosen to determine $T_{\rm eff}$ have different sensitivities, depending on the stellar temperature. As an example, Fig. 1a, b present the derived dependences to determine the temperature from the parameters $F(\mathrm{He\,I}\,4471)/F(\mathrm{Mg\,II}\,4481)$ and $W_\lambda(\mathrm{H}\gamma)$. According to the set of criteria listed above, the errors in $T_{\rm eff}$ for non-emission-line OB stars did not exceed 500°.

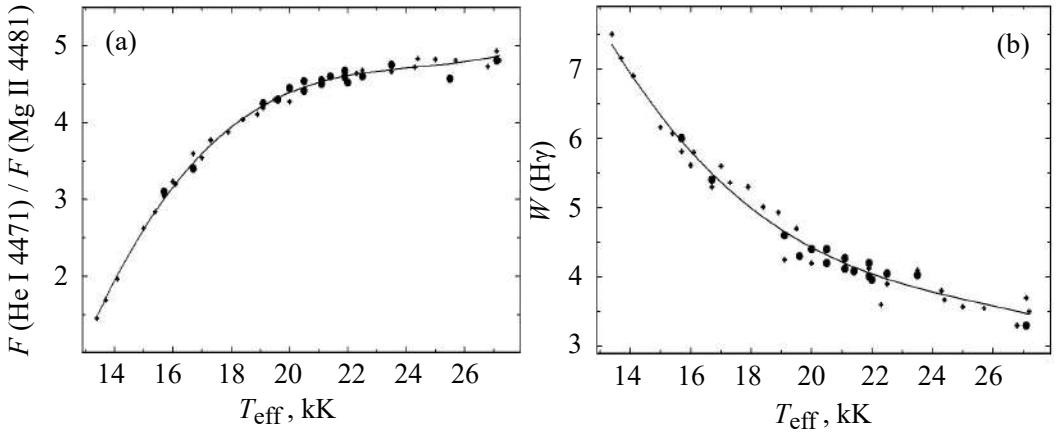

Fig. 1. Examples of the dependences used to determine $T_{\rm eff}$ from the observed line parameters, $F(\mathrm{He\,I}\,4471)/F(\mathrm{Mg\,II}\,4481)$ (a) and $W_\lambda(\mathrm{H}\gamma)$ (b). The crosses mark the parameters of the standard stars from the list by Lyubimkov et al. (2000, 2002) obtained in this paper with the same instrumental settings as those for the objects under the study; the solid curve indicates the polynomial dependence constructed from these data; the filled circles indicate the temperatures of the stars under the study estimated from the set of several criteria whose list is given in the text.

3 The cluster age

The cluster IC 1805 is fairly remote and located at the edge of the Perseus arm on the inside. There are relatively few background stars of this arm in this direction, but a noticeable number of Orion arm stars are present, as confirmed by detailed medium band photometric studies in the visible and near infrared ranges (Straižys et al. 2013). To determine the cluster age, we used the V-band observations taken from the WEBDA database and the values of $T_{\rm eff}$ determined above. The interstellar extinction A_V toward the cluster was studied in detail by Straižys et al. (2013) and is about $2\overset{\mathrm{m}}{.}5$.

4 Conclusion

The obtained results were presented in Fig. 2. As follows from the figure, we managed to estimate the cluster age with confidence using the $T_{\rm eff}$ as a parameter independent of photometric observations. The isochrone shown in the figure was constructed from the evolutionary models of Bressan et al. (2012) for solar metallicity. The best agreement of the observational data with the theoretical calculations was achieved for the cluster age $t = 2.0 \pm 0.5$ Myr and distance modulus $(v–V)_0 = 11\overset{\rm m}{.}5$.

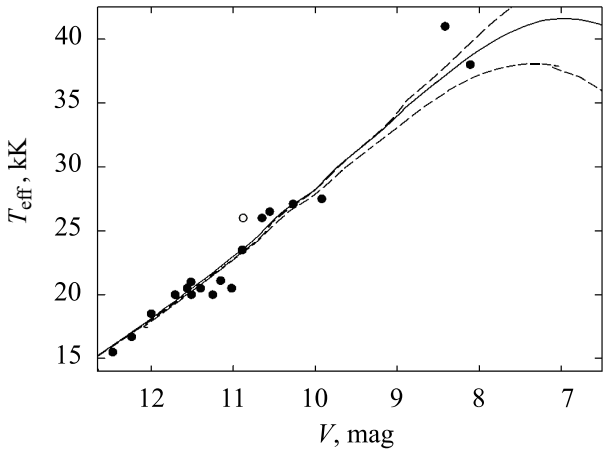

Fig. 2. The $T_{\rm eff}$–V diagram constructed from the stars in the cluster IC 1805. The filled circles indicate the OB stars; the open circle indicates the Be star MWC 50. The solid curve is the isochrone constructed for a cluster with an age t = 2 Myr, metallicity Z = 0.02, and distance modulus $(v–V)_0 = 11\overset{\rm m}{.}5$. The isochrones marked by the dashed lines correspond to the age of 1 Myr and 3 Myr respectively.

References

Bressan P., Marigo A., Girardi L., et al., 2012, Monthly Notices of the Royal Astronomical Society, 427, 1, p. 127

Lyubimkov S., Lambert D., Rachkovskaya T., et al., 2000, Monthly Notices of the Royal Astronomical Society, 316, 1, p. 19

Lyubimkov S., Rachkovskaya T., Rostopchin S., et al., 2002, Monthly Notices of the Royal Astronomical Society, 333, 1, p. 9

Massey P., Johnson K., DeGioia-Eastwood K., 1995, Astophysical Journal, 454, 1, p. 151

Straižys V., Boyle R.,Janusz R., et al., 2013, Astronomy & Astrophyscs, 554, 1, id. A3

MODERN ASTRONOMY: FROM THE EARLY UNIVERSE TO EXOPLANETS AND BLACK HOLES

Activity of symbiotic star CI Cyg between 2008 and 2012

T. Tarasova

Crimean Astrophysical Observatory of the Russian Academy of Sciences, Nauchny, 298409 Russia

Abstract. The activity of the classical symbiotic star CI Cyg from 2006 to 2012 was studied based on the photometric and spectrophotometric data. The flux of the strongest spectral lines were calculated. It has been shown that the fluxes of Hα, He I λ5876 lines with a low ionization potential were increased in the outburst. At the same time, the flux of lines with a high ionization potential of [Ne V] λ3426, [Fe VII] λ6087 lines were decreased or disappeared completely. In addition, during outbursts the molecular bands belonging to the cold component weakened and the ultraviolet excess behind the Balmer jump decreased or disappeared. At the maximum and close to it, only the emission lines H I, He I and Fe II were observed in the spectra. A comparison was made with the previous period of activity in 1971–1975. It is noted that both periods of activity have similar properties. In particular, a series of outbursts were observed, with each of the subsequent outburst being weaker than the previous one. In addition, the curve of eclipsing in the first outburst of the series was wider than the subsequent ones in both periods of activity. Besides, the brightness of the star weakened before the first flashes of the series.

Keywords: stars: symbiotic; individual: CI Cyg

DOI: 10.26119/VAK2024.093

1 Introduction

CI Cyg is a symbiotic eclipsing star consisting of a cold giant of the spectral class M5.5 II and a hot component, most likely a white dwarf. This star belongs to a small number of symbiotic stars in which the cold component fills its Roche lobe or is close to filling it. Between 1970 and 1978, the star was in an active phase consisting of a series of outburst with amplitudes up to almost 3 magnitudes (Belyakina 1983; Kenyon et al. 1991). After quiescent state, it shows a new series of the outbursts in 2008, 2010 and 2012 years. The activity of CI Cyg in 2008 were studied by Siviero et al. (2009). The second outburst of 2010 was described by Teyssier (2011). Our observations cover the period of activity from 2008 to 2012. Therefore, the aim of this work was to study the activity of CI Cyg from 2008 to 2012 year and compare it with the activity from 1971 to 1975 years.

2 Observation

The low-resolution spectra ($R = 1000$ and $R = 1300$) were obtained using a spectrograph mounted at the Nesmyth focus of the 2.6-m ZTSh telescope. The detector was a SPEC-10 CCD camera (1340×100) pixels. The spectrophotometric standart HR 7534 was used to calibrate the measured flux in the star spectrum.

3 A light curves analysis

Photometric observations were taken from the Siviero et al. (2009); Sekeráš et al. (2019) and from the AAVSO database. Fig. 1 shows the phase light curve for all three outbursts. Phase was calculated according to the ephemeris $V_{\min} = 2442690 + 853.8E$, where the epoch is the photocentre of the 1975 eclipse. The orbital period was taken from Fekel et al. (2000). It can be seen that the 2008 outburst occurred during the eclipse of the active region by the cold component. The beginning of the outburst in 2010 and 2012 occurs when the active region around the white dwarf and the cold component are visible. In fact, the shape of the eclipse curves of the 2008 outburst differ from curves of the eclipse in 2010 and 2012.

4 The spectral evolution

In the spectra, obtained during the period of the star, the molecular bands of the cold component are enhanced and the lines of high ionization potential are present, such as [Ne V], [Fe VII], He II. In the spectra of the star during the outburst the molecular bands belonging to the cold component weakened, the ultraviolet excess behind the

Balmer jump disappeared, as well as the lines of high ionization potentials [Ne V], [Fe VII], He II. In the next outbursts in 2010 years, in the spectrum obtained before the maximum brightness there are weak lines [Fe VII] and [Ne V]. In addition, some excess radiation is observed behind the Balmer jump, although less than when the star was in a quiet state. In 2012, a similar behavior of the flux in the continuum and spectral lines was observed. The variability of the flux of the lines Hα, He I λ5876, He II λ4686, [Ne V] λ3426 and [Fe VII] λ6086 are shown on Fig. 2.

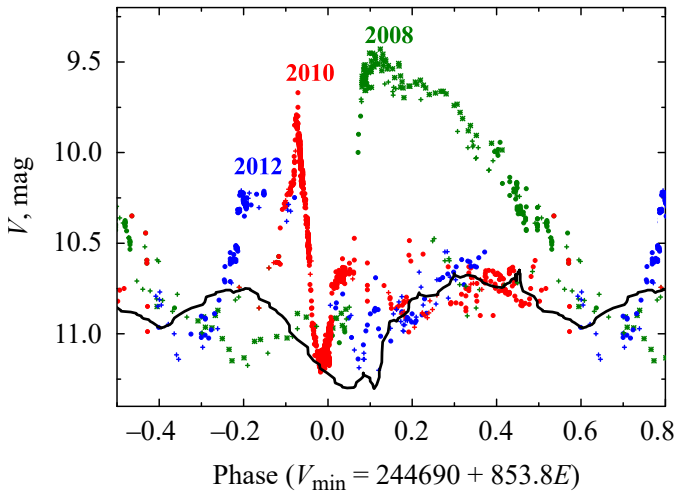

Fig. 1. Phase curves of outburst 2008, 2010, 2012. A solid black curve depicts the phase curve of a star in a quite state.

5 Conclusions

The symbiotic star CI Cyg entered a new period of activity with a series of outbursts in 2008, 2010, 2012. In the year 2008, the shape of the eclipse curve is wide, but the shape of the eclipse curves is narrow in the years 2010 and 2012. The different shape of the eclipse curves appears to be related to the variability of the eclipsed component. A similar series of outbursts was observed in the previous period of activity from 1971 to 1975. As then, the first flash had a wide minimum, and the rest had a narrow minimum. In addition, the similarity was also traced in the fact that before the outburst in 2008, as well as before the flash of 1971, the brightness of the star fell. The observed variability in the shape of the eclipse curve seems to be due to the variability of the gas envelope around the hot component. The different behavior

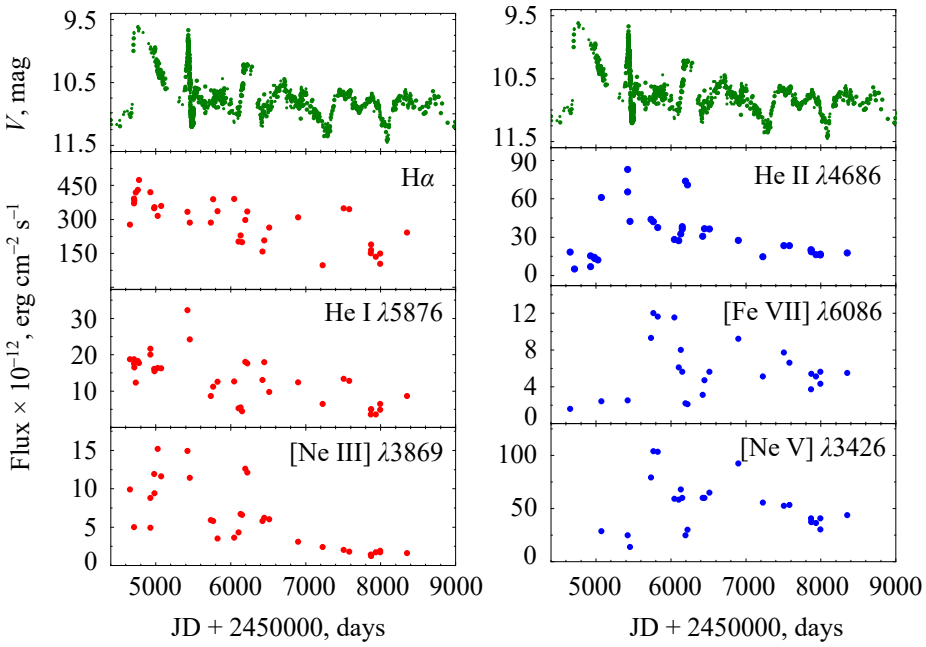

Fig. 2. Light curve in V-band and variation of line fluxes.

of the fluxes during the outbursts in 2010 and 2012 from the fluxes in 2008 is due to the fact that the hot radiation from the white dwarf during these outburst is not fully eclipsed by the envelope around the white dwarf formed during the outburst. It is possible that such a shell may be a disk-shaped object.

Acknowledgements. We acknowledge the variable-star observations from the AAVSO International Database were contributed by observers worldwide and used in this research.

References

Belyakina T.S., 1983, Izvestiya Krymskoi Astrofizicheskoi Observatorii, 68, p. 108
Fekel F.C., Joyce R.R., Hinkle K.H., et al., 2000, Astronomical Journal, 119, 3, p. 1375
Kenyon S.J., Oliversen N.A., Mikolajewska J., et al., 1991, Astronomical Journal, 101, p. 637
Sekeráš M., Skopal A., Shugarov S., et al., 2019, Contributions of the Astronomical Observatory Skalnaté Pleso, 49, 1, p. 19
Siviero A., Munari U., Dallporta S., et al., 2009, Monthly Notices of the Royal Astronomical Society, 399, 4, p. 2139
Teyssier F., 2011, Journal of the American Association of Variable Star Observers, 39, 1, p. 41

MODERN ASTRONOMY: FROM THE EARLY UNIVERSE TO EXOPLANETS AND BLACK HOLES

Study of a compact source with an enhanced NH_2D/NH_3 abundance ratio in the S187 region

E. Trofimova[1], I. Zinchenko[1], P. Zemlyanukha[1], A. Punanova[2], and C. Henkel[3,4]

[1] Federal Research Center A.V. Gaponov-Grekhov Institute of Applied Physics of the Russian Academy of Science, 46 Ul'yanov str., Nizhny Novgorod, 603950 Russia
[2] Department of Space, Earth and Environment, Chalmers University of Technology, Onsala Space Observatory, 90 Observatorievägen, Onsala, SE-439 92 Sweden
[3] Max-Planck-Institut für Radioastronomie, 69 Auf dem Hügel, Bonn, 53121 Germany
[4] Astronomy Department, King Abdulaziz University, 80203 PO Box, Jeddah, 21589 Saudi Arabia

Abstract. When analyzing data obtained with the Onsala 20-m radio telescope (Sweden) in 2018, a compact peak of NH_2D emission with an enhanced ratio of NH_2D/NH_3 column densities was discovered in the S187 region. This peak is not associated with any known astronomical object from the SIMBAD database, but previously obtained dust emission maps have a peak in this region. Additional observations of this region were carried out in 2023 with the Onsala telescope. The kinetic temperature in the center of the source was determined using the rotational diagrams of the CH_3CN and CH_3CCH molecules, and it turned out to be quite high (according to various estimates, approximately from 30 K to 50 K). Based on the spectra of the $C^{18}O$ molecule and dust emission, estimates of the column density of molecular hydrogen were obtained. Deuterated NH_2D and DCO^+ molecules were detected in this region, while no noticeable emission of the DCN molecule was detected. Estimates of the column densities at the center of the source were obtained by processing the spectra of NH_2D, DCO^+, $HC^{18}O^+$ and HC_3N molecules. Maps of the integral intensities of these molecules were also constructed. The ratio of the abundances of ortho- and para-NH_2D, as well as the ratio of NH_2D and the main isotopologue of NH_3 were found. The possible nature of the source is discussed.

Keywords: ISM: clouds, molecules; individual: S187

DOI: 10.26119/VAK2024.094

1 Introduction

Study of molecular deuteration in various interstellar environments represents an important part of astrochemical research. In 2017–2018 we performed a survey of a large sample of high-mass star-forming regions with the Onsala 20-m radio telescope in the lines of several deuterated molecules and their hydrogenated isotopologues (Trofimova et al. 2020; Trofimova et al., Astronomy Reports, accepted). During this survey we tentatively detected a compact peak of the ortho-NH_2D emission in the S187 region far away from the NH_3 peak. Later this peak was also observed with the IRAM 30-m radio telescope (Pazukhin et al. 2023). However, it was located at the very edge of the map. Here we present preliminary results of additional observations of this area with the Onsala radio telescope in 2023.

2 Observations and main results

The observations with the Onsala 20-m radio telescope were carried out in several frequency ranges: 71.8–74.2 GHz, 83.8–86.2 GHz, 97.1–99.5 GHz and 109.1–111.5 GHz. The area was mapped at the lower frequencies. At the higher frequencies only the peak was observed. Details of the observations will be presented in forthcoming publications. The emission of about 20 molecules was detected, such as ortho- and para-NH_2D, CH_3CN and CH_3CCH, DCO^+, HC_3N, H_2CO, $HC^{18}O^+$, $C^{18}O$ and other molecules. For several of them the estimates of column densities were obtained and also the maps of integral intensities were constructed. The DCO^+ emission peak coincides with the NH_2D peak. At the same time the DCN emission was not detected. We also analyze data obtained with the 100-m Effelsberg radio telescope (Pazukhin et al. 2023). A weak $NH_3(1,1)$ line emission was detected toward the NH_2D peak that was discussed here.

In Fig. 1, we present the mosaic map of the ortho-NH_2D emission and an overlay of the ortho-NH_2D emission contours on the image of this region in continuum at 1.2 mm (Zinchenko et al. 2009). The data confirm a compact source centered at RA(J2000) = $01^h23^m30\overset{s}{.}1$, Dec(J2000) = $61°48'06''$ with the size comparable to or smaller than the beam size (about $40''$). This NH_2D peak is not associated with any known astronomical object in the SIMBAD database, but map of the dust emission shows a peak at this location.

Using the rotational diagrams of CH_3CN and CH_3CCH, the gas kinetic temperature (T_k) in the source was estimated to be 32.5 ± 2.2 K and 47.1 ± 0.2 K respectively. The molecular hydrogen column density $N(H_2)$ from the $C^{18}O$ data under the usual assumptions about the $C^{18}O$ abundance, is $5.3 \pm 0.02 \times 10^{22}$ cm^{-2} for $T_k = 32.5$ K and $7.3 \pm 0.02 \times 10^{22}$ cm^{-2} for $T_k = 47.1$ K. From the dust emission $N(H_2) \sim 3 \times 10^{22}$ cm^{-2}.

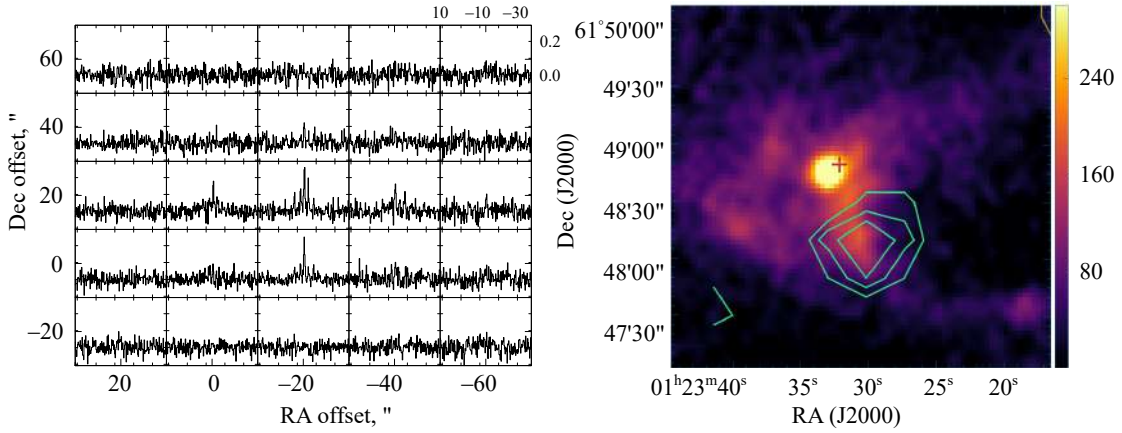

Fig. 1. Left panel: the mosaic map of the ortho-NH_2D emission toward the compact source discussed in this paper. Right panel: contours of the ortho-NH_2D emission overlaid on the image of this region in continuum at 1.2 mm (Zinchenko et al. 2009). The position of the IRAS source is marked with a cross.

In Fig. 2, we present spectra of the ortho- and para-NH_2D as well as $NH_3(1,1)$ at the ortho-NH_2D emission peak. The line width is 0.74 ± 0.08 km/s for ortho-NH_2D, 0.49 ± 0.04 km/s for para-NH_2D and 1.49 ± 0.29 km/s for $NH_3(1,1)$. The optical depth of the main component in the ortho-NH_2D line is 2.1 ± 0.6.

The ortho/para ratio for NH_2D varies approximately from 2.5 to 4.6 depending on the assumed gas density (in the range of 10^4 cm^{-3} to 10^6 cm^{-3}) and kinetic temperature. It increases with increasing both of them. Further, we assume this ratio equal to 3, according to the spin statistics (Sipilä et al. 2015).

Then, we estimate the full NH_2D column density and relative abundance. The relative abundance varies from 1.2×10^{-9} to 5.1×10^{-11} for $T_k = 32.5$ K and from 5.3×10^{-10} to 3.5×10^{-11} for $T_k = 47.1$ K.

The estimates of the column densities of the main isotopologue of NH_3 at the peak of ortho-NH_2D were obtained. The NH_2D/NH_3 abundance ratio is 6.4–3.7 for the assumed gas density of 10^4 cm^{-3}, 0.8–0.6 for the gas density of 10^5 cm^{-3}, and 0.4–0.35 for the gas density of 10^6 cm^{-3}. With increasing gas density this ratio estimate noticeably decreases. In any case it is very high.

3 Discussion and conclusions

In general, the data show a rather compact (less than 0.2 pc) and quite warm (approximately from 30 K to 50 K) source without any indication of the star formation activity. The observed very high ammonia deuteration at such a temperature is un-

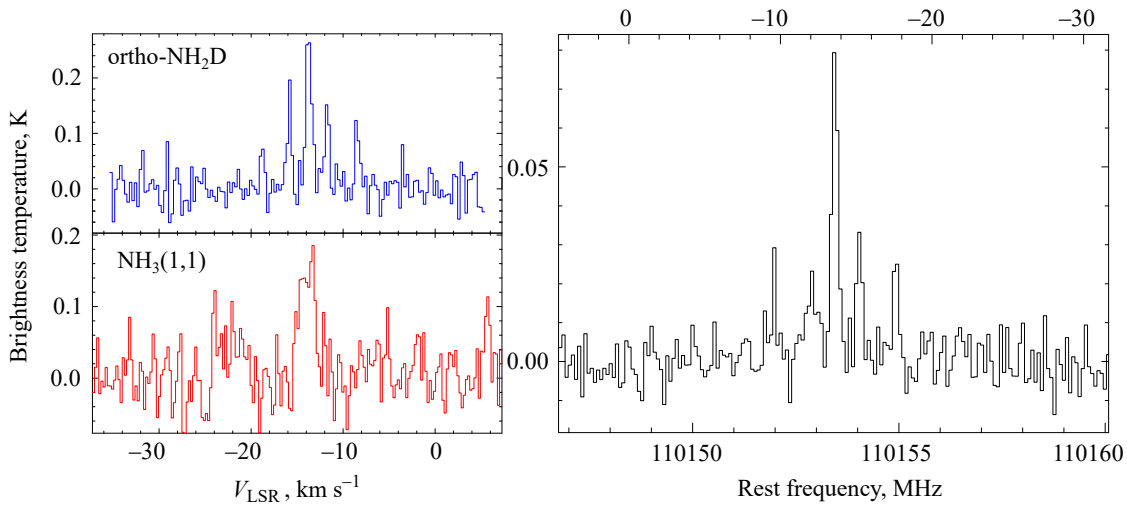

Fig. 2. Left panel: spectra of ortho-NH_2D (blue) and $NH_3(1,1)$ (red) toward the ortho-NH_2D emission peak. Right panel: spectrum of the para-NH_2D at the same position.

usual. It is worth noting that all these estimates refer to the rather large beam of the 20-m antenna. A presence of a much more compact (and probably cold) core in the interiors is not excluded. Observations with a significantly higher angular resolution would be very helpful in this respect.

Acknowledgements. We acknowledge support from Onsala Space Observatory for the provisioning of its facilities/observational support. The Onsala Space Observatory national research infrastrcuture is funded through Swedish Research Council project No. 2017-00648.

Funding

This work was supported by the Russian Science Foundation project No. 24-12-00153.

References

Pazukhin A.G., Zinchenko I.I., Trofimova E.A., et al., 2023, Monthly Notices of the Royal Astronomical Society, 526, 3, p. 3673

Sipilä O., Harju J., Caselli P., et al., 2015, Astronomy & Astrophysics, 581, id. A122

Trofimova E.A., Zinchenko I.I., Zemlyanukha P.M., et al., 2020, Astronomy Reports, 64, 3, p. 244

Zinchenko I., Caselli P., Pirogov L., 2009, Monthly Notices of the Royal Astronomical Society, 395, 431, p. 2234

MODERN ASTRONOMY: FROM THE EARLY UNIVERSE TO EXOPLANETS AND BLACK HOLES

A sphere or a disk? Accretion of gas onto isolated stellar-mass black holes

D. Zagorulia[1] and G. Beskin[2,3]

[1] Moscow Institute of Physics and Technology, 9 Institutskiy Per., Dolgoprudny, 141701 Russia
[2] Special Astrophysical Observatory of the Russian Academy of Sciences, Nizhny Arkhyz, 369167 Russia
[3] Kazan Federal University, 18 Kremlevskaya, Kazan, 420008 Russia

Abstract. The most crucial problem in constructing a coherent model of the universe is the behavior of spacetime in the vicinity of the event horizons of black holes (BH). These regions can be accessible to direct observations only at low rates of spherical accretion. Based on the analysis of the current characteristics of interstellar gas turbulence, it has been shown that the spherical mode of accretion, unlike the disk mode, occurs at sufficiently low densities of the medium (excluding clouds and "hot" zones). In this case, disks can form only around virtually stationary Kerr and Schwarzschild BHs.

Keywords: stars: black holes; accretion, accretion disks; ISM: clouds

DOI: 10.26119/VAK2024.095

1 Introduction

Despite extensive research, the quest for a quantum theory of gravity remains unresolved. This is highlighted by physical paradoxes and their proposed resolutions, often related to near black hole (BH) event horizons (EHs). BHs with their intense gravitational fields serve as critical testing grounds for new and old (e.g., General Relativity) macroscopic theories (Will 2006), and methods of quantizing gravity. A significant issue is the paradox of information loss in BHs (Hawking 2005), leading to numerous theoretical ideas, such as a firewall near the EH (high-energy quanta that destroy information of matter accreting onto the BH (Almheiri et al. 2013) and BH complementarity, where an observer can detect information either approaching the horizon or inside the BH, with these observations being mutually incompatible (Susskind et al. 1993). These theories remain untested experimentally. Direct detection of the EH and its surroundings is necessary, specifically by registering photons emitted from the immediate vicinity of the EH. High accretion rates in galactic cores and binary X-ray systems obscure the EH, but solitary stellar-mass BHs might provide accessible horizons due to low interstellar medium (IM) accretion rates and peculiar velocities but only for spherical accretion (Beskin & Karpov 2005).

This study focuses on feasibility of spherical accretion for observing EHs, considering modern understandings of the structure and dynamics of the IM.

2 Accretion onto a Schwarzschild black hole

Davies & Pringle (1980) considered accretion onto a supersonic BH, taking into account the inhomogeneity of IM. Assuming velocity and density gradients are small, it was found that accretion is still described by the Bondi–Hoyle formula and the specific angular momentum of the captured material is zero. However, this is generally not true, and angular momentum can be significant. This specific angular momentum is $l_m = \frac{1}{4}\Delta V_{r_c}$ (Illarionov & Sunyaev 1975), where ΔV is the change in velocity at the distance $2r_c$, $r_c = 2GM/(V^2 + c_s^2)$ (Bondi & Hoyle 1944), and c_s is the speed of sound. Numerical simulations have led to a realistic expression for the specific angular momentum $l \sim 0.1 l_m$ (Ruffert 1999).

For spherical accretion, the specific angular momentum of captured material must be less than it is in the last stable orbit of the BH, i.e. $l < \sqrt{3} c r_g$ for the Schwarzschild metric (Zeldovich & Novikov 1971). Then,

$$\Delta V < 40\sqrt{3}\frac{V_0^2}{c}, \text{ where } V_0 = \sqrt{V^2 + c_s^2}. \quad (1)$$

Analysis of new data in the recent studies of Lee & Lee (2019); Chepurnov & Lazarian (2010) demonstrates a good agreement of the turbulence spectrum with the

Kolmogorov spectrum on scales of tens of meters, which is crucial for estimating velocity dispersion and density fluctuations. As we will see, for practically any BH velocity, turbulent motions in the IM cannot hinder spherical accretion. Moreover, density fluctuations also cannot hinder it. From the work of Armstrong et al. (1995),

$$\frac{\Delta\rho}{\rho} \sim \left(\frac{R}{1\ \mathrm{pc}}\right)^{11/6},$$

substituting into $l_m = \dfrac{\Delta\rho}{4\rho} V_K r_c$, where $V_K = V_0/\sqrt{2}$ is the Keplerian speed at the capture radius. At the distance of $2r_c$, we obtain: $V_0 > 2.80 M_{10}^{0.393}$ [km/s][1] for specific momentum of the captured gas not exceeding that of the last stable orbit.

2.1 Location of a black hole in cold clouds

Suppose the molecular cloud has a temperature T and concentration n. For cold and dense clouds ($T \sim 100$ K, $n \sim 100$ cm^{-3}), assuming a Kolmogorov spectrum of turbulence, the following expression for ΔV was obtained by Cen (2021)

$$\Delta V = \sqrt{\frac{14}{11}} \left(\frac{68 K r_c}{11 G M^2}\right)^{1/5} \sigma_{\mathrm{pc}} \left(\frac{2r_c}{1\ \mathrm{pc}}\right)^{\gamma}. \tag{2}$$

Suppose the cloud is a sphere with a radius $2r_c$, then the total kinetic energy is $K = 16\pi n r_c^3 kT$. Let $M_{10} = M \times 10^{-1}$ M$_\odot$, after a bit of algebra[2] with eq. (1, 2). If the cloud is located in the center of the galaxy, then $\sigma_{\mathrm{pc}} \simeq 1.03$ km/s, $\gamma \simeq 0.63$ (Cen 2021), we obtain $V_0 > 4.15 M_{10}^{0.212}$, or $V > 3.97$. However, if the cloud is located in the galactic disk, then $\sigma_{\mathrm{pc}} \simeq 0.46$, $\gamma \simeq 0.57$. We get $V_0 > 3.71 M_{10}^{0.205}$, or $V > 3.52$.

2.2 Location of a black hole in warm clouds

In warm clouds ($T \sim 10^3$ K, $n \sim 0.1$ cm^{-3}), ΔV could be expressed as (Larson 1981)

$$(\Delta V)^2 = 1.1 \times \left(\frac{2r_c}{1\ \mathrm{pc}}\right)^{0.76} \ [\mathrm{km/s}]^2, \tag{3}$$

by substituting eq. (1), we get $V_0 > 16.59 M_{10}^{0.138}$, or $V > 16.16$ (Beskin & Karpov 2005).

3 Accretion onto a Kerr black hole

Similar steps can be applied to a Kerr BH, but then the last stable orbit will depend on a, the specific angular momentum parameter of the BH, and its direction of

[1] All the estimates are given in [km/s], if not written otherwise
[2] https://github.com/dimicorn/accretion_bh

rotation. If $a > 0$ ("+"), the specific angular momentum of captured material must be $l_+ < cr_g/\sqrt{3}$, otherwise $a < 0$ ("−"), $l_- < 11cr_g/\sqrt{3}$ (Zeldovich & Novikov 1971). Then,

$$\Delta V_+ < \frac{40\sqrt{3}}{3}\frac{V_0^2}{c}, \qquad \Delta V_- < \frac{440\sqrt{3}}{3}\frac{V_0^2}{c}. \tag{4}$$

Substituting it into eq. (2, 3) we obtain estimates for cold clouds in the center of the galaxy: $V_{0+} > 5.20M_{10}^{0.212}$, or $V_+ > 5.06$; $V_{0-} > 3.17M_{10}^{0.205}$, or $V_- > 2.95$. Doing the same for cold clouds in the galactic disk, we get $V_{0+} > 4.67M_{10}^{0.212}$, or $V_+ > 4.52$; $V_{0-} > 2.82M_{10}^{0.205}$, or $V_- > 2.56$. And we obtain estimates for warm clouds: $V_{0+} > 24.69M_{10}^{0.138}$, or $V_+ > 24.41$; $V_{0-} > 10.36M_{10}^{0.138}$, or $V_- > 9.67$.

4 Summary

We have shown that for isolated BHs of stellar masses at typical velocities of Galactic stars (less than 15 km/s), spherical accretion of IM is realized. The obtained result allows to identify areas in the Galaxy where isolated BHs are localized, whose EHs (ergospheres) are in principle accessible for observations. Searches in these zones for peculiar objects with observational manifestations predicted for accreting isolated stellar-mass BHs may lead to the discovery of the latter.

Acknowledgements. The work was partially carried out within the framework of the state assignment of the SAO RAS, approved by the Ministry of Science and Higher Education of the Russian Federation, and partially supported by the SAL Program of the KFU.

References

Almheiri A., Marolf D., Polchinski J., et al., 2013, Journal of High Energy Physics, 2013, p. 62
Armstrong J., Rickett B., Spangler S., 1995, Astrophysical Journal, 443, p. 209
Beskin G. and Karpov S., 2005, Astronomy & Astrophysics, 440, p. 223
Bondi H. and Hoyle F., 1944, Monthly Notices of the Royal Astronomical Society, 104, p. 273
Cen R., 2021, Astrophysical Journal Lettrers, 906, id. L4
Chepurnov A. and Lazarian A., 2010, Astrophysical Journal, 710, p. 853
Davies R. and Pringle J., 1980, Monthly Notices of the Royal Astronomical Society, 191, pp. 599
Hawking S., 2005, Physical Review D, 72, id. 084013
Illarionov A. and Sunyaev, R., 1975, Astronomy & Astrophysics, 191, p. 599
Larson R., 1981, Monthly Notices of the Royal Astronomical Society, 194, p. 809
Lee K. and Lee L., 2019, Nature Astronomy, 3, p. 154
Ruffert M., 1999, Astronomy & Astrophysics, 346, p. 861
Susskind L., Thorlacius L., Uglum J., 1993, Physical Review D, 48, id. 3743
Will C., 2006, Living Reviews in Relativity, 17, p. 4
Zeldovich J.B. and Novikov I.D., 1971, The Theory of Gravitation and Evolution of Stars, Moscow: Science

VAK 2024 MODERN ASTRONOMY: FROM THE EARLY UNIVERSE TO EXOPLANETS AND BLACK HOLES 300 years Russian Academy of Sciences

Study of the high-mass star-forming region S255IR at various scales

I. Zinchenko[1], S. Liu[2], D. Ojha[3], Y. Su[2], and P. Zemlyanukha[1]

[1] Federal Research Center A.V. Gaponov-Grekhov Institute of Applied Physics of the Russian Academy of Sciences, 46 Ul'yanov str., Nizhny Novgorod, 603950 Russia
[2] Institute of Astronomy and Astrophysics, Academia Sinica, 11F of Astronomy-Mathematics Building, AS/NTU No. 1, Sec. 4, Roosevelt Rd, Taipei, 10617 Taiwan
[3] Department of Astronomy and Astrophysics of the Tata Institute of Fundamental Research, Homi Bhabha Road, Mumbai, 400005 India

Abstract. The core of S255IR-SMA1 contains the protostar NIRS3 with a mass of about $20\,M_\odot$. A few years ago, the first b urst o f l uminosity f or m assive protostars, caused by an episodic accretion event, was recorded here. We have been studying this object for a long time with various instruments, including ALMA. The general morphology and kinematics of this area have been investigated. Disk-shaped structures, jets and outflows have been identified and studied in detail. We have recently observed this object with ALMA at a resolution an order of magnitude higher than previously achieved—about 15 milliarcseconds, corresponding to about 25 AU. This paper presents new results from the analysis of these data together with observations in other bands. The new data show an inhomogeneous disk structure, an ionized region around the protostar, and the presence of a jet observed in the submillimeter continuum consisting of individual knots whose orientation differs markedly from that on large scales. The submillimeter emission from the jet most likely represents bremsstrahlung from ionized gas. Based on observations of the lines of some molecules, the kinematics and physical properties of this region are discussed. Methanol maser emission associated with the jet is observed.

Keywords: stars: formation, massive; ISM: clouds, molecules; submillimeter: ISM; individual: S255IR

DOI: 10.26119/VAK2024.096

1 Introduction

There are still several competing scenarios for high mass star formation (e.g., Tan et al. 2014; Motte et al. 2018; Padoan et al. 2020; Rosen et al. 2020). A key question is whether this process is a scaled-up version of the low-mass star formation or is significantly different. Observations at different scales are essential to choose between different scenarios.

In recent years, much attention has been paid to the luminosity bursts of massive protostars, which are thought to be caused by episodic disk-mediated accretion events. There are theoretical models that predict such a behavior (e.g., Meyer et al. 2017, 2019). To date, several such bursts have been recorded (see the summary in Wolf et al. 2024). One of the first of them was the burst in S255IR NIRS3, observed at IR (Caratti O Garatti et al. 2017) and submillimeter (Liu et al. 2018) wavelengths and accompanied by the methanol maser flare (Moscadelli et al. 2017; Szymczak et al. 2018).

The large star-forming complex sandwiched between the evolved H II regions S255 and S257 (Ojha et al. 2011) is a well-known and actively studied area of high-mass star formation. It contains two major star-forming sites: S255IR and S255N. Here we focus on the first one.

The distance to S255IR is estimated to be $1.78^{+0.12}_{-0.11}$ kpc from the maser parallax measurements (Burns et al. 2016). It contains three major cores SMA1, SMA2 and SMA3 (Wang et al. 2011) and several smaller condensations (Zinchenko et al. 2020). The SMA1 core harbors about 20 $M_\odot$ protostar NIRS3 (Zinchenko et al. 2015). The mass is estimated from the bolometric luminosity of $3 \times 10^4\, L_\odot$ at the assumed distance. Here we summarize and discuss the main results of our investigations of this object.

2 Observational data

We have observed the S255IR area with several single-dish radio telescopes (IRAM 30-m, OSO 29-m, MPIfR 100-m radiotelescope in Effelsberg) and with radio interferometers (ALMA, GMRT, SMA, VLA). These observations include imaging in the continuum and in many molecular lines. The frequency coverage was from 600 MHz (GMRT) to 350 GHz (ALMA). The angular resolution ranged from 40 arcseconds (for single-dish observations) to 15 milliarcseconds (for ALMA observations). At the distance to S255IR, 1 arcsecond corresponds to 1800 AU. In addition, we combine our radio data with our and other available data in other bands, especially with IR observations.

3 Structure of S255IR at various scales

In Fig. 1 we present a composite image of the S255IR area (size about 1′ or 0.5 pc) in several lines and in the continuum.

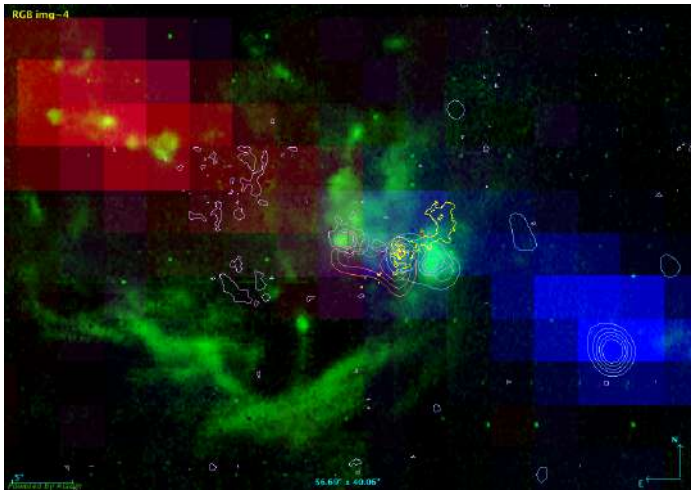

Fig. 1. S255IR area in the 2.12 μm H_2 line (green) and high-velocity CO(3–2) emission (red and blue). The yellow contours show the 0.9 mm emission (ALMA), the orange and blue contours show the high-velocity HCN(4–3) emission, the magenta contours show the 1.64 μm Fe II emission. The NIR data are from SINFONI observations (Wang et al. 2011). The radio data are from Zinchenko et al. (2012, 2015, 2020).

There are several H_2 knots aligned along the IR jet direction (PA $\approx 67°$) that were observed many years ago (Howard et al. 1997). The knots closest to S255IR-SMA1 also show strong Fe II emission and are associated with the high-velocity HCN(4–3) and HCO^+(4–3) emission (Zinchenko et al. 2015). These knots also coincide with the radio knots with non-thermal radio spectra (Obonyo et al. 2021). Apparently, these knots are associated with bow shocks and dense molecular gas. With the projected expansion velocity of about 450 km/s for the NE lobe (Fedriani et al. 2023; Cesaroni et al. 2023) and 285 km/s for the SW lobe (Cesaroni et al. 2024) their ejection happened about 60–70 years ago. Assuming the same velocity, the most distant knots were ejected several hundred years ago.

The distant H_2 NE knots coincide with the red-shifted CO(3–2) outflow lobe observed with the IRAM 30-m radio telescope (Fig. 1). The H_2 knots in the SW direction are less pronounced (although visible). The peak of the SW CO(3–2) outflow lobe coincides with the dense high-velocity clump seen in the HCN(4–3) and CS(7–6)

lines (Zinchenko et al. 2015). It is worth noting that there are two almost parallel outflows here, originating from the SMA1 and SMA2 cores (Zinchenko et al. 2020). The above connections suggest that the CO(3–2) outflow observed with the 30-m IRAM radio telescope originates from the SMA1 core.

Our ALMA observations at about 150 mas resolution show that this core represents a rotating and infalling envelope (pseudo-disk) around the NIRS3 protostar (Liu et al. 2020). In Fig. 2 we present some results from our latest (performed in September 2021) ALMA observations of this object at an order of magnitude higher resolution of about 15 mas, corresponding to 25 AU (Zinchenko et al., A&A, submitted).

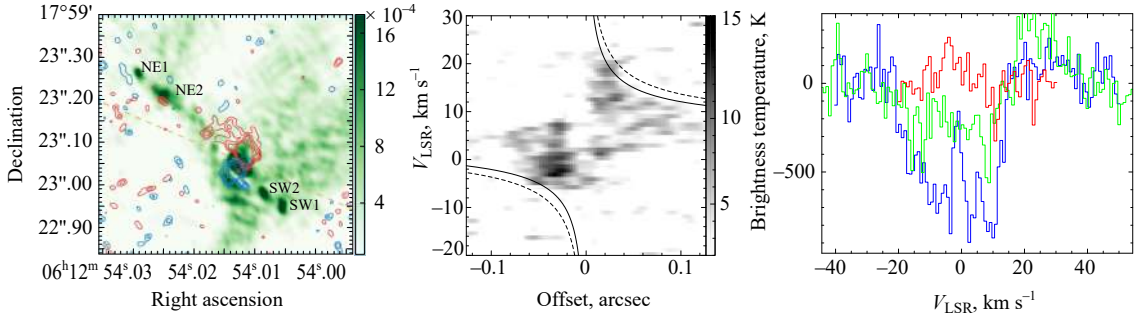

Fig. 2. Left panel: the image of the S255IR area in the continuum obtained with ALMA at 0.9 mm with about 15 mas resolution (Zinchenko et al., in preparation). The knots in the jet are marked. The red and blue contours show the emission in the $C^{34}S$(7–6) line wings. The dashed line indicates the jet orientation at larger scales (PA $\approx 67°$). Central panel: the PV diagram in the $C^{34}S$(7–6) line along the major axis of the disk. The curves correspond to the Keplerian rotation around the central mass of $M \sin^2 i = 10\,M_\odot$ (solid) and $M \sin^2 i = 15\,M_\odot$ (dashed), where i is the inclination angle. Right panel: spectra of the $C^{34}S$(7–6) (red), SiO(8–7) and CO(3–2) (blue) emission towards the central continuum peak.

The continuum image shows the central bright source (brightness temperature is about 850 K), which practically coincides with the NIRS3 position, and two pairs of bright knots (80–110 K), one pair in each outflow lobe, which is located almost on a straight line along with the central source. The position angle of this line is approximately 47°. Obviously, these knots belong to the jet emanating from the central source. Note that the central source is elongated approximately in the direction of the jet. The position angle of the jet differs by about 20° from that observed at larger scales (Fig. 2), as also found in some other observations at small scales (Hirota et al. 2021; Cesaroni et al. 2023). These results are consistent with the jet precession proposed in some previous works (Obonyo et al. 2021; Cesaroni et al. 2023). The

pairs of knots imply two ejection events with a time interval of about 1.5 yr. This is in good agreement with the 6.7 GHz methanol maser light curve (Szymczak et al. 2018).

The high brightness of the central source and its morphology imply a significant contribution of the free-free emission. Taking into account the flux measurements at lower frequencies from 3 GHz to 92 GHz (Obonyo et al. 2021; Cesaroni et al. 2023, 2024) we estimated the contributions of the ionized gas and dust emission assuming an optically thin free-free component. For the ionized gas we obtain the emission measure of $EM \sim 10^{10}\,\mathrm{pc/cm^6}$ and the electron density of $n_e \sim 10^7\,\mathrm{cm^{-3}}$. Such properties are typical of hypercompact H II regions. It is probably surrounded by a dust cocoon. An alternative model assumes a partially optically thick hypercompact H II region, which better explains the spectral index in the range 92–340 GHz. The emission from the knots in the jetappears to be dominated by the free-free component.

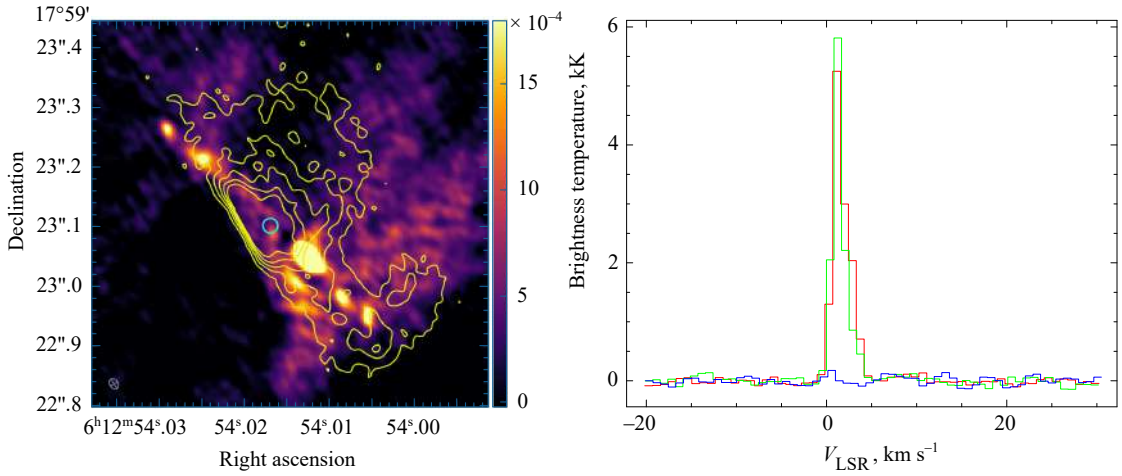

Fig. 3. Left panel: the continuum image of S255IR at 0.9 mm overlaid with contours of the CH_3OH 12_1–12_0 A^{-+} emission. Right panel: spectra of the CH_3OH 12_1–12_0 A^{-+} (red), 14_1–14_0 A^{-+} (green) and $^{13}CH_3OH$ 14_1–14_0 A^{-+} (blue) emission at the position marked by the circle.

Figure 2 shows a disk-like rotating structure around the central source. The molecular emission is very inhomogeneous, implying clumping. The PV diagrams in several lines (see an example in Fig. 2) indicate a sub-Keplerian rotation. There are also deep absorption features in the molecular spectra towards the bright central source. The deepest features are red-shifted relative to the systemic velocity of the core, suggesting an infall.

Previously we detected a new methanol maser line (14_1–14_0 A^{-+} at 349.1 GHz) toward S255IR-SMA1 (Zinchenko et al. 2017). In the new data, its intensity is consistent with the previous measurements, which show a decay since 2016 (Salii et al. 2022). Now there was another line of this series in the observed bands, 12_1–12_0 A^{-+}. It also shows the maser effect (Fig. 3). These masers are apparently associated with the jet and coincide with some other methanol masers recently discovered here (Baek et al. 2023).

4 Conclusions

In general, the observations of S255IR confirm the disk accretion scenario as the formation mechanism for about $20\,M_\odot$ stars. Further studies of its evolution after the recent accretion burst would be very important.

Funding

This work was supported by the Russian Science Foundation project No. 24-12-00153.

References

Baek G., Lee J., Evans N., et al., 2023, Astrophysical Journal Letters, 954, id. L25
Burns R., Handa T., Nagayama T., et al., 2016, MNRAS, 460, p. 283
Caratti O Garatti A., Stecklum B., Garcia Lopez R., et al., 2017, Nature Physics, 13, p. 276
Cesaroni R., Moscadelli L., Caratti o Garatti A., et al., 2023, Astron. & Astrophys., 680, p. A110
Cesaroni R., Moscadelli L., Caratti o Garatti A., et al., 2024, Astron. & Astrophys., 683, id. L15
Fedriani R., Caratti o Garatti A., Cesaroni R., et al., 2023, Astron. & Astrophys., 676, p. A107
Hirota T., Cesaroni R., Moscadelli L., et al., 2021, Astron. & Astrophys., 647, p. A23
Howard E.M., Pipher J.L., Forrest W.J. 1997, Astrophysical Journal, 481, p. 327
Liu S., Su Y., Zinchenko I., et al., 2020, Astrophysical Journal, 904, p. 181
Liu S., Su Y., Zinchenko I., et al., 2018, Astrophysical Journal, 863, id. L12
Meyer D., Vorobyov E., Elbakyan V., et al., 2019, MNRAS, 482, p. 5459
Meyer D., Vorobyov E., Kuiper R., et al., 2017, MNRAS, 464, id. L90
Moscadelli L., Sanna A., Goddi C., et al., 2017, Astron. & Astrophys., 600, id. L8
Motte F., Bontemps S., Louvet F. 2018, Annual Rev. Astron. Astrophys., 56, p. 41
Obonyo W., Lumsden S., Hoare M., et al., 2021, MNRAS, 501, p. 5197
Ojha D., Samal M., Pandey A., et al., 2011, Astrophysical Journal, 738, p. 156
Padoan P., Pan L., Juvela M., et al., 2020, Astrophysical Journal, 900, p. 82
Rosen A., Offner S., Sadavoy S., et al., 2020, Space Science Reviews, 216, p. 62
Salii S., Zinchenko I., Liu S., et al., 2022, MNRAS, 512, p. 3215
Szymczak M., Olech M., Wolak P., et al., 2018, Astron. & Astrophys., 617, p. A80
Tan J., Beltrán M., Caselli P., et al., 2014, Protostars and Planets VI, p. 149
Wang Y., Beuther H., Bik A., et al., 2011, Astron. & Astrophys., 527, p. A32
Wolf V., Stecklum B., Garatti A., et al., 2024, arXiv e-prints, arXiv:2405.10427
Zinchenko I., Liu S., Su Y., et al., 2012, Astrophysical Journal, 755, p. 177
Zinchenko I., Liu S., Su Y., et al., 2015, Astrophysical Journal, 810, p. 10
Zinchenko I., Liu S., Su Y., et al., 2017, Astron. & Astrophys., 606, id. L6
Zinchenko I., Liu S., Su Y., et al., 2020, Astrophysical Journal, 889, p. 43

MODERN ASTRONOMY: FROM THE EARLY UNIVERSE TO EXOPLANETS AND BLACK HOLES

Comparison of the dynamics of coronal holes identified by two detection methods in solar activity cycles 24-25

O. Andreeva

Crimean Astrophysical Observatory of the Russian Academy of Sciences, Nauchny, 298409 Russia

Abstract. In this study, we analyze for the first time the long-term variations of coronal holes (CHs) identified by two different automatic detection schemes: Spatial Possibilistic Clustering Algorithm (SPoCA) and Convolutional Neural Network (CNN193). The source material was the observational data acquired by the Atmospheric Imaging Assembly instrument onboard the Solar Dynamics Observatory (AIA/SDO) in the Fe XII 19.3 nm line in the period from June 16, 2010, to May 13, 2021. An initial analysis comparing the long-term variations of the CH areas extracted by the SPoCA method and used by us in earlier works to study their evolution at different stages of the 24th and at the beginning of the 25th cycles showed fairly good agreement with the trend of the CH areas identified by the CNN193 algorithm for the same period. Both schemes reveal hemispheric asymmetry in the generation of CHs both in time and in amplitude.

Keywords: methods: data analysis; techniques: image processing; Sun: corona

DOI: 10.26119/VAK2024.097

1 Introduction

Coronal holes, regions where magnetic field lines are open to outer space and appear darker in extreme ultraviolet (EUV) and soft X-ray (SXR) images, have lower solar coronal density and temperature due to the special configuration of the magnetic field. CHs are usually associated with high-velocity solar wind (SW) streams and allow us to estimate the SW parameters and the corresponding geomagnetic effects. CHs are of interest both for short-term space weather forecasting and for forecasting on longer time scales. Methods for identifying CHs are diverse and range from fully manual procedures to fully automatic ones using observations at different wavelengths. Currently, automatic detection schemes are the standard approach for detecting CHs in EUV images acquired by AIA/SDO (Lemen et al. 2012). One reason for this is the huge amount of archival data transmitted daily. However, factors such as the noisy nature of solar images, instrumental effects, and others make it difficult to identify CHs using these automated schemes. The astronomical community has put a lot of effort into finding the optimal algorithm for extracting CHs. In a recent work, Reiss et al. (2024) analyzed CHs detections in 29 SDO solar images by 14 of the best known automatic schemes. The authors showed that the choice of automatic detection scheme can have a significant impact on the size and shape of CH regions, their physical properties, and hence the interpretation of the results.

2 Data and methods for detecting coronal holes

Historically, in our previous work to investigate coronal holes from observations of the AIA/SDO instrument in the Fe XII 19.3 nm line, we used the Heliophysical Events Knowledge (HEK) base (Hurlburt et al. 2012). The tool used to extract the area information was the SPoCA-suite of procedures (Verbeeck et al. 2014). SPoCA uses fuzzy clustering and allows us to distinguish CHs, active regions and quiet Sun in a solar image. In Andreeva (2023), we obtained a series of cyclic variations of the CH areas of the entire visible surface of the solar disk, separately in the N and S hemispheres, and identified the contribution of polar and non-polar CHs to the overall dynamics of solar activity of the 24th and the ascending phase of the 25th cycles. With these results, we would like to compare how it relates to variations in the CH areas extracted by other algorithms.

For comparison, the development of CNN193 by Russian colleagues (Illarionov & Tlatov 2018) was chosen, which uses a neural network to detect CHs at the widely used wavelength of 19.3 nm. The neural network is trained on segmentation maps of CHs monitored by solar scientists and then tested on a new set of images. The detection of CHs is performed on both solar disk images and synoptic maps of the

Sun, which are a compilation of successive disk images over the Sun's rotation period. Guided by the idea that the concept of CHs should be the same in both cases, the authors investigated universal models that can learn the CH segmentation from disk images and reproduce the same segmentation from synoptic maps. The simulation showed quite good results (Illarionov et al. 2020), which interested us. The author of this model, E. Illarionov, kindly provided us with data on the magnetic fluxes and areas of CHs segmented with CNN193. Next, the behavior of long-term CH variations extracted from solar disk images using the SPoCA algorithm will be compared with CH variations segmented on synoptic maps using the CNN193 convolutional neural network model.

It should be noted here that in our works we considered two types of CHs: polar and non-polar. Polar CHs are located at the solar poles, sometimes descending to middle and low latitudes and even passing to the opposite hemisphere. Non-polar CHs are mainly confined to low, middle, sometimes high latitudes, but not associated with polar CHs. For the authors of the CNN193 model, the boundary separating polar and low-latitude zones is $\Theta = \pm 50^{\circ}$. We admit that such a separation could affect the result of the comparison.

3 Dynamics of coronal holes detected by SPoCA and CNN193 methods

Comparison of methods of CH segmentation on separate images has been performed repeatedly. However, we are not yet aware of any work on analyzing the long-term variations of CHs segmented by different automated methods. In this study, we compared the behavior of CHs identified by SPoCA and CNN193 methods from June 16, 2010 to May 13, 2021. Figure 1 shows the behavior of polar CHs in hemispheres during the period. Figure 2 shows the behavior of polar and non-polar CHs on the entire visible surface of the Sun's disk over the same period. The top and middle panels of Fig. 1 and Fig. 2 represent the variations of magnetic fluxes and CH areas extracted by the CNN193 method. The lower panel is the areas of the CHs extracted by the SPoCA method.

Figure 1 shows that the variations of magnetic fluxes of polar CHs extracted by CNN193 in hemispheres almost repeat the variations of CH areas. Similar dynamics is observed for the CHs extracted by the SPoCA method. Both methods show that during the 24th cycle and the early phase of the 25th cycle, the solar dynamo operated differently in the hemispheres in terms of CH generation. You can see the pronounced peaks in the hemispheric dominance of CH areas. During the ascending phase in 2011–2012 and in 2015, the Southern Hemisphere led in terms of maximum polar

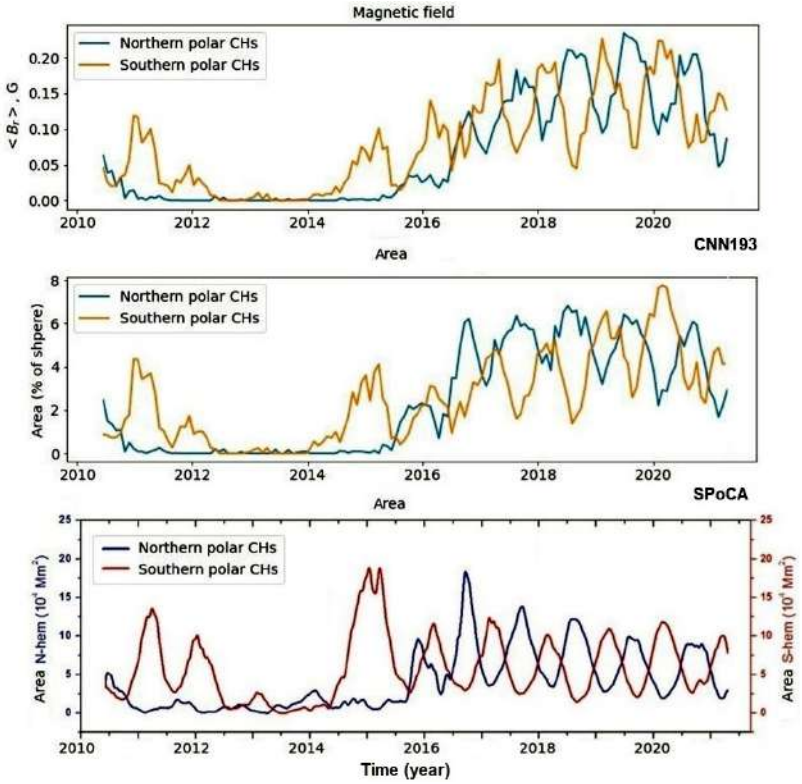

Fig. 1. Dynamics of polar CHs in the N and S hemispheres in the period from June 16, 2010, to May 13, 2021. The variations of magnetic fluxes (top panel) and CH areas (middle panel) identified by the CNN193 method. The bottom panel is the areas of the CHs identified by the SPoCA method.

CH areas. Overall, a marked increase in polar CHs extracted by CNN193 in both hemispheres during the decline phase and at the 24/25 solar minimum is seen. A similar pattern is observed for the polar CHs identified by SPoCA, but the increase is less pronounced.

All panels of Fig. 2 show two maxima of magnetic flux and regions of polar CHs observed in 2011–2012 and 2015 – the phases of solar activity ascending and descending. After the decline phase and at the minimum of 24/25 cycles, the total areas of polar CHs approach the average level of values. The maxima of non-polar areas in 2013–2014 are consistent with the second maximum of cycle 24 determined from sunspots by us earlier. The total areas of non-polar CHs (SPoCA) have low values at the beginning of the study period, and in the decline phase of the 24th cycle and in the minimum of the 24/25 cycles, these CHs practically disappear. The low-latitude CHs segmented by the CNN193 increase in the decline phase and the

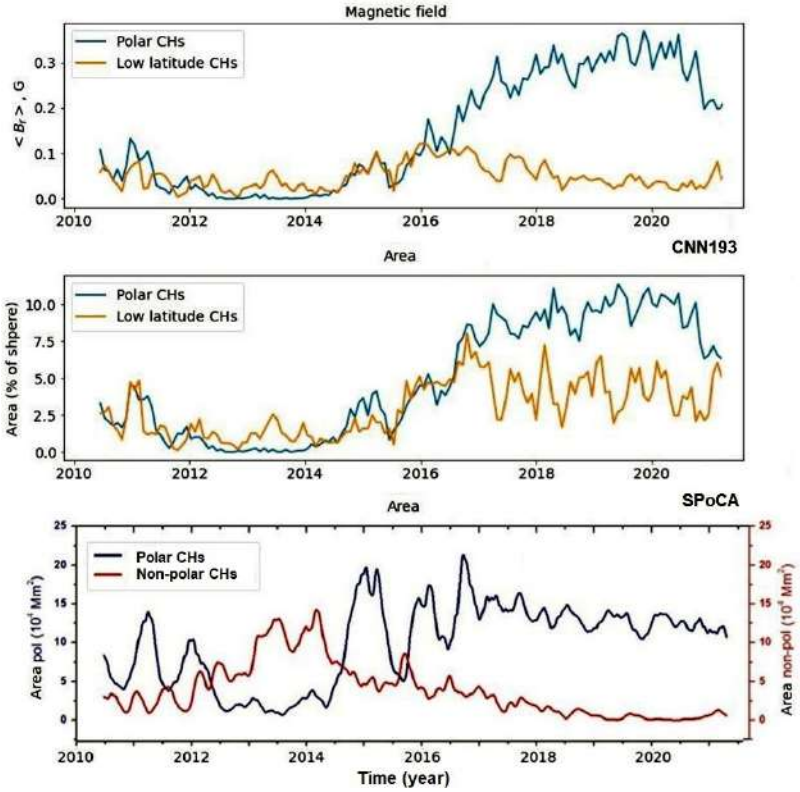

Fig. 2. Dynamics of polar and non-polar CHs on the visible solar surface in the period from June 16, 2010, to May 13, 2021. The variations of magnetic fluxes (top panel) and CH areas (middle panel) identified by the CNN193 method. The bottom panel is the areas of the CHs identified by the SPoCA method.

minimum of cycles 24/25 in the same way as the polar CHs, but with much smaller amplitude. The magnetic flux (CNN193) of low-latitude CHs drops markedly.

4 Conclusions

In this study, the dynamics of coronal holes, identified by two different automatic methods, on the scales of the solar cycle was analyzed for the first time. An initial comparison of the dynamics of the CH areas identified by the SPoCA method and used in our previous studies to investigate their evolution at different stages of the 24th and early 25th cycles showed fairly good agreement with the trend of the CH regions identified by the CNN193 over the same period. An initial analysis comparing the dynamics of the CH areas extracted by the SPoCA method and used in our

previous works to investigate their evolution at different stages of the 24th and early 25th cycles, has shown fairly good agreement with the dynamics of the CH areas defined by CNN193 over the same period. Both schemes reveal hemispheric asymmetry in the generation of CHs both in time and amplitude.

Acknowledgements. The author would like to thank NASA/SDO science group for making data publicly available. Special thanks to E. Illarionov for providing data on magnetic fluxes and areas of CHs extracted by the CNN193 method.

Funding

This work was supported by the Ministry of Science and Higher Education of the Russian Federation under the State Assignment (Topic No. 122022400224-7).

References

Andreeva O., 2023, Advances in Space Research, 71, 4, p. 1915
Hurlburt N., Cheung M., Schrijver C., et al., 2012, Solar Physics, 275, 1-2, p. 67
Illarionov E. and Tlatov A., 2018, Monthly Notices of the Royal Astronomical Society, 481, 4, p. 5014
Illarionov E., Kosovichev A., Tlatov A., 2020, Astrophysical Journal, 903, 2, id. 115
Lemen J.R., Title A.M., Akin D.J., et al., 2012, Solar Physics, 275, 1-2, p. 17
Reiss M.A., Muglach K., Mason E., et al., 2024, Astrophysical Journal Supplement Series, 271, 1, id. 6
Verbeeck C., Delouille V., Mampaey B., et al., 2014, Astronomy & Astrophysics, 561, id. A29

VAK 2024 MODERN ASTRONOMY: FROM THE EARLY UNIVERSE TO EXOPLANETS AND BLACK HOLES 300 years Russian Academy of Sciences

Radio spectroscopy of the solar corona

V. Bogod, M. Lebedev, N. Ovchinnikova, A. Ripak, and E. Kurochkin

St. Petersburg Branch of the Special Astrophysical Observatory of the Russian Academy of Sciences, St. Petersburg, 196140 Russia

Abstract. The presence of continuous cooling and heating processes is a crucial condition that determines the existence of the solar corona. The defining aspects of the corona include the magnetic field, low plasma density, and high temperature of the corona. In this regard, the study of low-contrast structures in optical ranges is limited even with the use of large specialized telescopes. The radio range provides higher sensitivity, which can be used to detect very weak structures of emerging activity. However, the radio astronomical range also faces challenges in observation, both in terms of spatial resolution and the limitations of dynamic range due to the high temperature of the Sun's corona.

Observations show that the use of instruments with a large effective area allows us to overcome the main problem associated with the influence of powerful radiation from the quiet Sun, which amplifies equipment noise. The high sensitivity of the RATAN-600 reflector radio telescope to weak signals in radiation flux was used in the decimeter range for the detection of weak microwave bursts at a level of 10^{-3} s.f.u. Research and theoretical developments have shown that microwave bursts are caused by magnetic reconnection, which leads to the generation of accelerated particles that excite plasma waves at the second harmonic of the plasma frequency.

Due to significant changes in the concept of radio spectroscopy, work has begun on creating a series of broadband spectral complexes covering several octaves. The results of the first series of observations using the complex in the range of 1-3 GHz for searching for and studying quasi-periodic pulsations in the solar corona are presented here.

A by-product of these observations was the detection of narrow-band absorption in the frequency range 1560–1665 MHz, near the well-known OH absorption line (1612–1720 MHz).

Keywords: Sun: corona, radio radiation

DOI: 10.26119/VAK2024.098

1 Introduction

Despite its proximity to the Earth, the corona of our star, the Sun, is difficult to study. This is due to its high temperature of about 1–2 MK, high transparency, and the complexity of its many structures. To study the activity of the corona by its radio emission, small radio telescopes without the spatial resolution are usually used to study the Sun as a star. On the other hand, to study the details of spatial structures, the use of solar radio interferometers (radio heliographs) has become more cost-effective than using radio telescopes with a single reflector. However, in large reflectors it is easier to achieve:

I) a large effective collecting area and consequently high sensitivity to radiation flux; II) octaval instant spectrum of intensity and polarization of radiation from individual solar objects to determine the mechanism of emission; III) high frequency and temporal resolution for studying dynamic and spectral structures (such as lines); IV) a large dynamic range to observe signals from nano-flares and powerful flares simultaneously, among others. The listed parameters are extremely important for solving problems related to the heating of the corona (model Parker 1988), searching for emission lines in the corona, constructing height magnetic maps of the corona, studying the flare process at both weak and powerful energy levels, etc.

In this work, we report a significant step in creating a tool suitable for many solar tasks using the existing RATAN-600 reflector. It is capable of covering a frequency range from 1 GHz to 18 GHz (in 2024 and up to 100 GHz in the future), with a sensitivity to radiation flux (down to 0.001 s.f.u.), a relative frequency resolution of up to 10^{-5}, a temporal resolution of about 1 ms, and a large dynamic range of at least 90 dB in regular observations (Ripak et al. 2023). The first test series of observations were carried out in the 1–3 GHz range, which demonstrates the high information potential of the combination of a reflector radio telescope and high-resolution spectroscopy.

2 Current Tasks in Solar Corona Physics

2.1 Temperature Inhomogeneity of the Corona at Radio Waves

The initial observations with the new spectral complex at RATAN-600 have detected the existence of thermal inhomogeneities with brightness oscillation amplitudes in the range of 0.001–0.002 s.f.u. in both emission and absorption. Since they are registered over a wide frequency range of 1–3 GHz, this indicates the presence of cold and hot layers larger than 150 Mm in the hot corona. The estimated brightness temperatures are from 3×10^3 to 10^5 K (Bogod et al. 2023). Multifrequency high sensitivity observations with a resolution of 4 MHz, conducted as one-dimensional scans of a quiet Sun,

showed wide temperature fluctuations across the solar disk. Fluctuations occurred at a level of ±1 s.f.u. relative to the calculated level of the quiet Sun, which was determined using the Principal Component method by Ovchinnikova et al. (2022). At $T = 1.0 \times 10^6$ K and a density of $N = 10^8$ cm^{-3}, at frequencies of 1–3 GHz, the temperature gradient was $dT/dz = 11$ K/km (i.e., 1100 K over a 100 Km interval) for both warm and cold temperature layers.

2.2 The Problem of Coronal Heating

Parker's theory of coronal heating is well known (Parker 1988). This theory remains unconfirmed, since observations are available only in X-ray and ultraviolet ranges from satellites, with energies 10^4 times higher than radio waves. However, detecting them in the radio range is also a difficult task. Our estimates indicate that RATAN-600 may register a set of nanoflares with energies up to 10^{21} erg, which may be a decisive fact for proving this theory. This will be tested during the upcoming minimum of solar activity.

2.3 Registration of Fine Frequency Structure (Lines)

Observations of the Sun at RATAN-600 using a spectropolarimetric complex in the range of 1–3 GHz revealed line radio emission from individual active regions of the Sun located in the cold filament or on the limb under the prominence, as well as during the observation of coronal rain. Absorption was found in the spectrum region of 1.5–1.65 GHz. The observed line structure corresponds to the hyperfine splitting frequencies in the ground state of $X^2\Pi_{3/2}$ hydroxyl (OH) 1612–1720 MHz. As the observed region passes through the antenna's beam pattern of the telescope, the absorption line shifts in frequency due to changes in the energy levels of the OH molecule in the magnetic field, the magnitude of which varies in the direction along the filament. A detailed description of the technique for detecting the hydroxyl absorption line in the range of 1.6–1.7 GHz is given in the work Ovchinnikova et al. (2024).

2.4 Registration of Frequency Structure of Radio Bursts

Due to the large dynamic range and high time resolution of the solar receiving equipment (about 119 spectra per second in the entire frequency range), scanning the Sun with the antenna beam directed along the declination parallel allows recording changes in the spectral density of the radio emission flux at a level of 0.1 s.f.u. (10^3 Jy) within the beam width. In the frequency range of 1–3 GHz, the beam width (BW) of the RATAN-600 antenna system (AS) South+Flat strongly depends on the wavelength, while the spatial resolution of the AS changes three times. Therefore, when

operating over a wide frequency band, observational data undergo convolution with a theoretical horizontal BW calculated using aperture integration methods. During high-resolution observations (1 MHz) and in the mode of tracking a selected Active Region (AR), the horn of the complex is accurately positioned at the focus of the radio telescope, whereas during multi-azimuth observations in the standard mode with a resolution of 4 MHz, the horn is shifted from the focus by 430 mm (Fig. 1).

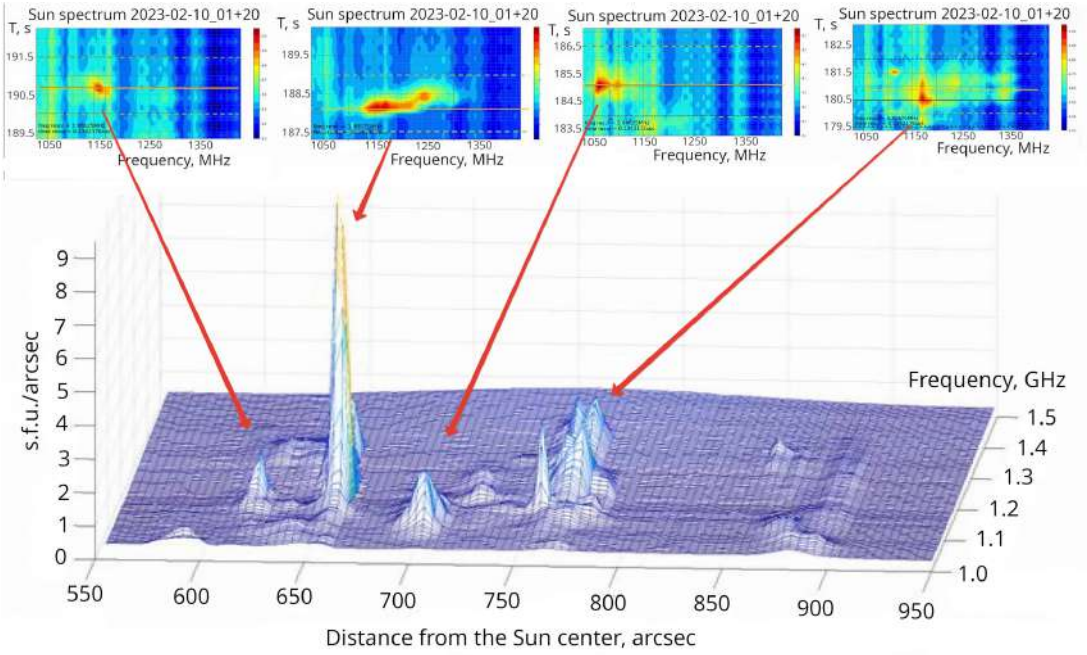

Fig. 1. A flare in the NOAA complex 13213 (13209) is presented as a multitude of individual radio sources with sizes ranging 10–15 arcseconds, with intensity levels 1–10 s.f.u., covering the frequency range 1.0–1.4 GHz, with bandwidths of individual radio sources ranging 20–50 MHz. At the top, frequency maps of the radio sources are shown with frequency and time axes. Below, the coordinate axis runs along the parallel of declination, and the other axes reflect intensity and frequency. The dotted envelope line indicates the scanning type without frequency resolution.

To estimate the sensitivity, we will calculate the conditions for registering a single flare with a brightness temperature of about 10^6 K and dimensions of $1'' \times 1''$. For a wavelength of 20 cm, the parameters chosen are: $S = 1000\,\mathrm{m}^2$, $\Delta f = 10\,\mathrm{MHz}$, $\tau = 10\,\mathrm{s}$, and $T_{\mathrm{sys}} = 150\,\mathrm{K}$. The estimated noise sensitivity of the radiometer in the absence of a solar signal gives $\delta T = (1.5 \times 10^{-2})\,\mathrm{K}$, while in the presence of the solar signal ($T_\odot = 6000\,\mathrm{K}$), it is about 0.6 K. Thus, the sensitivity for the flux density ΔF

in the antenna + radiometer system, considering $S = 1000\,\mathrm{m}^2$ and $T_\odot = 6000\,\mathrm{K}$, will be $\Delta F = 2 \times 10^{-3}\,\mathrm{s.f.u.}$.

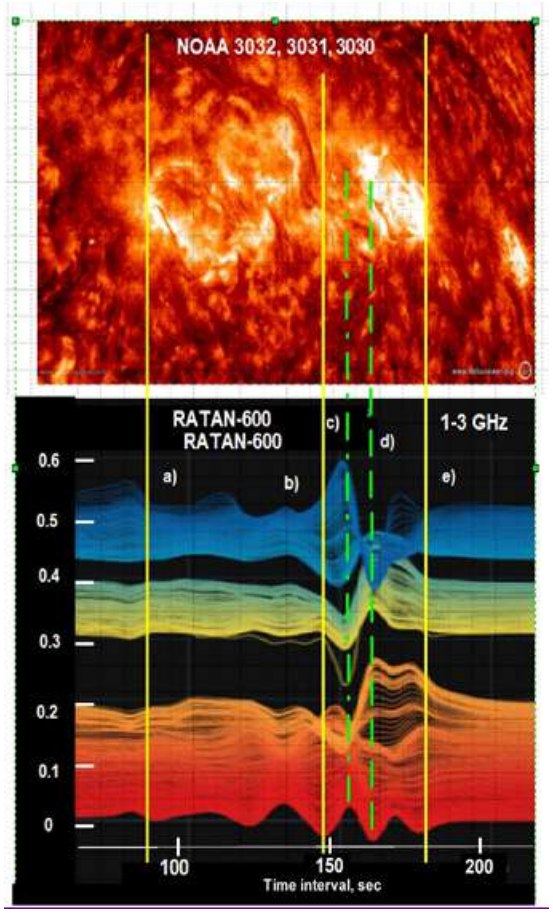

Fig. 2. Radio Registration of the Phenomenon of "Coronal Rain" on June 18, 2022. The horizontal axis represents the time scale of scanning at a speed of 15″/sec. The scale of the vertical axis is shown in s.f.u. At the top, a representation of the active region complex consisting of AR 3032, 3031, and 3030 is shown based on data from the SDO satellite. Below, spectral scans in the range of 1–3 GHz with a frequency resolution of 4 MHz are presented. Frequency gaps correspond to bands of suppressive anti-interference filters. Yellow vertical lines denote the boundaries of the active region complex along the scanning longitude. Green vertical lines mark the locations of the highest frequency activity, where regions c) with a double change in signal intensity predominately occur. This interesting phenomenon indicates thermal turbulence in the coronal plasma, which is characteristic of the "coronal rain" phenomenon. Outside the active region, the radio frequency response stabilizes, and temperature effects gradually fade. The labels a), b), c), d), and e) indicate different activity levels within the active complex, with c) and d) being the most active. This observation refers to the "coronal rain" on the solar disk, whereas this phenomenon is usually observed on the solar limb in the X-ray and extreme ultraviolet ranges.

2.5 Registration of the "Coronal Rain" Phenomenon in Radio Waves

The phenomenon of "coronal rain" has long been known from observations in the Hα and Ca II H lines as well as in the EUV range on satellites such as Hinode, SDO, and others (Antolin 2020). It is characterized by the presence of dense and cold plasma, primarily found in prominences. The large effective area of RATAN-600 (about 1000 m^2 on average across the range from 1 GHz to 40 GHz) allows achieving high parameters in the dynamic range (more than 90 dB), which distinguishes it from existing instruments on a global scale. New spectral observations have shown

for the first time the existence of such a structure in coronal altitudes in the decimeter wavelength range (Fig. 2).

3 Conclusions (Summary)

The review is devoted to the work dedicated to the creation of a new method for analyzing radio emission from the solar corona. Thanks to modern technologies, new receiving equipment with exceptional parameters has been created for analyzing the properties of the high-temperature and optically thin corona using spectral analysis on a new high-resolution spectral complex in the 1–3 GHz range on the RATAN-600 radio telescope. Its high sensitivity is confirmed by measuring weak signals on the disk at the level of 0.01–0.001 s.f.u. in a wide frequency range. A number of new phenomena have been registered, including various depressions in the AR emission spectra, uneven thermal distribution in detailed temperature spectra, and the behavior of flare plasma with high frequency resolution. Unique registrations of the coronal rain phenomenon on the disk and on the limbs of the Sun have also been obtained. Preliminary interpretations have been proposed, which require further development.

Acknowledgements. Observations with the SAO RAS telescopes are supported by the Ministry of Science and Higher Education of the Russian Federation. The renovation of telescope equipment is currently provided within the national project "Science and Universities".

Funding

Observations with the SAO RAS telescopes are supported by the Ministry of Science and Higher Education of the Russian Federation. The renovation of telescope equipment is currently provided within the national project "Science and Universities".

References

Antolin P., 2020, Plasma Physics and Controlled Fusion, 62, 1, id. 014016
Bogod V.M., Lebedev M.K., Ovchinnikova N.E., et al., 2023, Cosmic Research, 61, 1, p. 27
Ovchinnikova N.E., Bogod V.M., Lebedev M.K., 2024, Solnechno-zemnaya fizika, 10, 3, p. 21
Ovchinnikova N.E., Lebedev M.K., Bogod V.M., et al., 2022, Proceedings of Science, 425, id. 007
Parker E.N., 1988, Astrophysical Journal, 330, p. 474
Ripak A.M., Bogod V.M., Grenkov S.A., et al., 2023, Astrophysical Bulletin, 78, 4, p. 657

MODERN ASTRONOMY: FROM THE EARLY UNIVERSE TO EXOPLANETS AND BLACK HOLES

Asteroid activity: spectral features and probable physical reasons

V. Busarev[1,2]

[1] Lomonosov Moscow State University, Sternberg Astronomical Institute (SAI MSU), Universitetsky pr., 13, Moscow, 119234 Russia
[2] Institute of Astronomy (INASAN) RAS, Pyatnitskaya str., 48, Moscow, 119017 Russia

Abstract. Spectral signs of sublimation-driven dust activity of main-belt asteroids with primitive mineralogy (of C, B, F, G, and X types) are considered. The reflectance spectra of active asteroids of primitive types are compared with model ones of a conditionally active C-type asteroid surrounded by a dust exosphere consisting of submicron aggregate particles of different composition. This phenomenon in primitive asteroids may be impact-induced and become subsequently periodic near perihelion if connected with considerable water ice deposits of the asteroids. Significant additional factors influencing the primitive-type active asteroids, although secondary by random nature, are flares and eruptive events on the Sun, and electrostatic field of photoemission nature on the sunlit side of the bodies. We argue that the formation of aggregate dust particles in a dust exosphere of active asteroids may be one of the fundamental processes.

Keywords: asteroids: general; comets: general; methods: observational, radiative transfer, scattering

DOI: 10.26119/VAK2024.099

1 Introduction

To date, 60 objects of approximately one kilometer in size have been discovered moving in asteroid orbits in the Main Asteroid Belt (MAB) that have shown various signs of dust activity. To systematize the data from different sources as well as mechanisms proposed to explain activity of the bodies, considerable efforts have been undertaken (e.g., Jewitt 2021; Hsieh et al. 2023; Chandler et al. 2024, and references therein). The authors formulated basic criteria, by which a predominant mechanism of each body's activity was proposed. The most common is the sublimation-driven dust activity (SDA) of primitive asteroids.

2 Activity of primitive asteroids and possibilities of its detection by spectral methods

The frequent SDA events in the MAB can be explained by assuming that primitive-type asteroids (C, B, G, F and partly X), which have low-temperature mineralogy, initially contained water ice. Considering the very low thermal conductivity of the surface destroyed layer (regolith) of asteroids, numerical modeling (Schorghofer 2008) has proven the possibility of preserving water ice in their depths for several billion years. As for CO_2 ice (close in thermophysical parameters to water ice), its volatility is almost seven orders of magnitude higher than that of H_2O ice (e.g., Chandler et al. 2020). That makes unlikely presence of CO_2 ice in main-belt asteroids for a long time. Since the content of bound water in carbonaceous chondrites (as probable fragments of primitive asteroids) reaches 20 wt. (e.g., Jarosewich 1990; Alexander et al. 2018), the initial content of unbound H_2O in primitive-type asteroids, as their parent bodies, should not be less. So, the bodies may be considered as first candidates for active asteroids (AAs).

We proceed from the possibility of SDA and related dust exosphere (DE) formation around primitive asteroids whose subsurface matter includes water ice sublimating at high subsolar temperatures near perihelion. The first reflectance spectra of primitive AAs, 145 Adeona, 704 Interamnia, 779 Nina, and 1474 Baira, have been detected in September 2012, close to their perihelia. These spectra are shown in Fig. 1(a–d) in comparison with their canonic reflectance spectra from the SMASSII database obtained when the asteroids were inactive (Busarev et al. 2016). We assumed that the maxima discovered near $0.4-0.5\,\mu m$ and/or $0.6-0.7\,\mu m$, which are atypical for the surface matter of asteroids, are characteristic of a DE around bodies. Importantly, the reflectance spectra of 145 Adeona, 704 Interamnia, 779 Nina, and 1474 Baira in September 2012 were obtained in the period of solar activity maximum, when frequent solar flares and eruptive coronal mass ejection (CMEs) took

place. Hence, the asteroid DEs were exposed to impacts of the shock waves from the CMEs, radiation pressure and solar wind. As a result, the concentration of dust particles affecting the optical thickness of the DEs of these AAs was high.

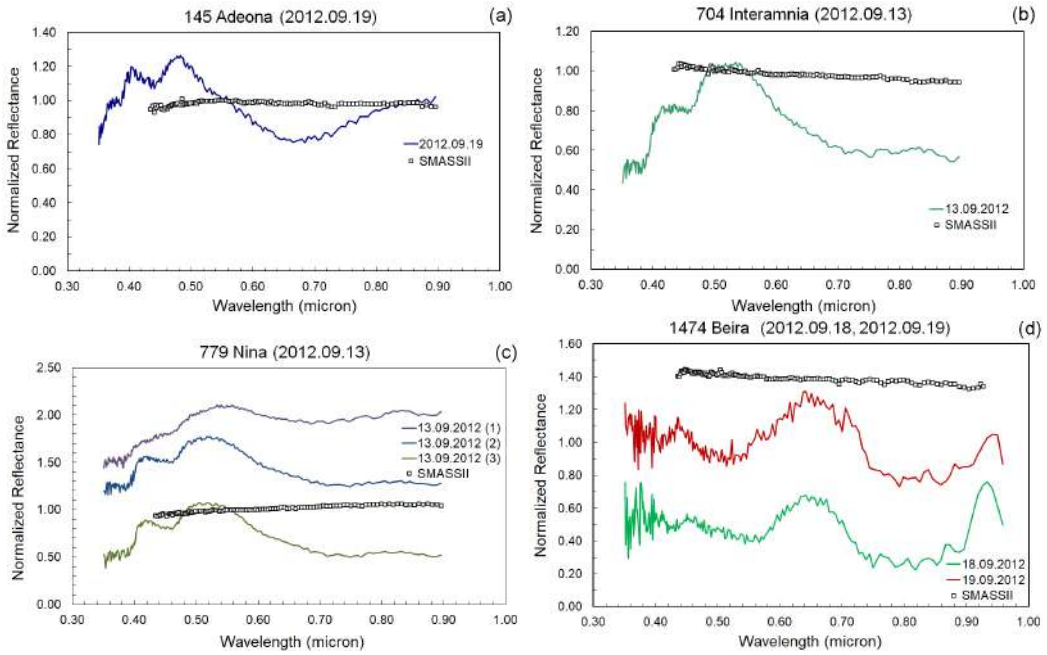

Fig. 1. Reflectance spectra of primitive AAs 145 Adeona (a), 704 Interamnia (b), 779 Nina (c), and 1474 Beira (d) obtained in September 2012 compared with their reflectance spectra from the SMASSII database registered in inactive states of the bodies (Busarev et al. 2016).

To substantiate our assumptions about the features of the observed reflectance spectra of AAs, numerical model spectra of a conditional AA of C-type were calculated (Busarev et al. 2021 and references therein). Examples of the model spectra for dust aggregate particles of different compositions (water ice, tholins, and olivine) and two structures of dust aggregates (dense and fluffy) in the DE above the asteroid surface are shown in Fig. 2(a–f). The optical thickness of the exosphere was $\tau = 0.5$, and the material of aggregates, the radii (r) of smaller constituents in the aggregates are specified in the diagrams.

Thus, a good coincidence of observational reflectance spectra of primitive AAs 145 Adeona, 704 Interamnia, 779 Nina, and 1474 Beira with numerically modeled ones of a conditional active C-type asteroid surrounded by an optically thin DE is

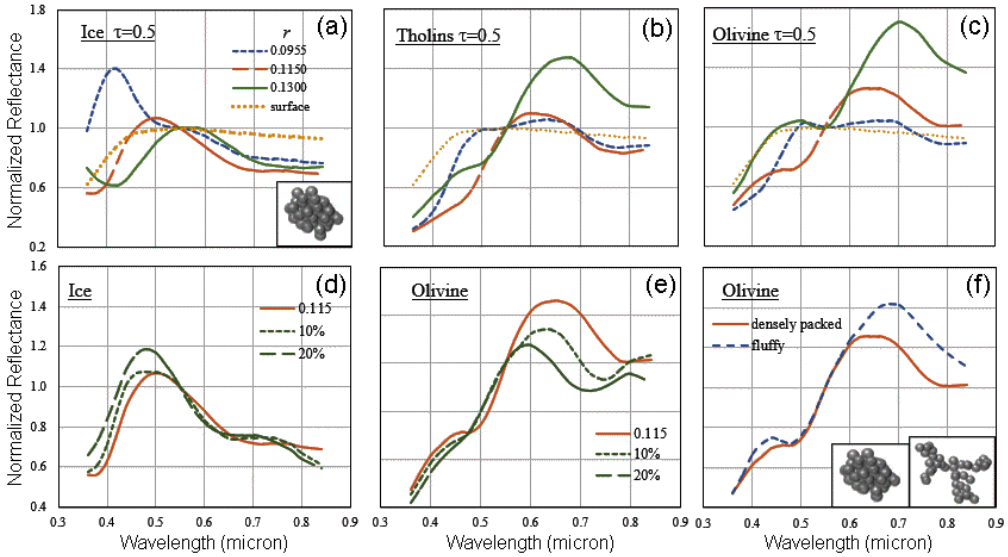

Fig. 2. Normalized model reflectance spectrum of a conditional AA of C-type (reflectance spectrum of its surface is shown by the dotted line) surrounded by a DE with optical thinness $\tau = 0.5$ from dust aggregates of various compositions (water ice, tholins and olivine). The sizes of smaller components in aggregates are given in microns in (a) and (b). The structures of dense and fluffy dust aggregates are shown in the insets (Busarev et al. 2021).

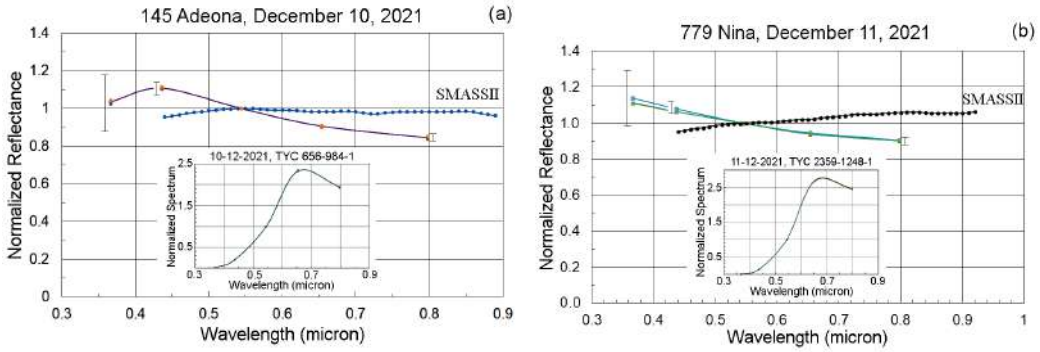

Fig. 3. Normalized reflectance spectra of AAs 145 Adeona (a) and 779 Nina (b) obtained in December 2021 and approximated by the UBVRI-data in comparison with their reflectance spectra from SMASSII database. Normalized approximated spectra of the corresponding non-variable reference stars are given in the insets (Busarev et al. 2023).

a confirmation of SDA and the presence of a related DE around these and similar asteroids.

Moreover, we confirmed activity of two from mentioned AAs, 145 Adeona and 779 Nina, by their UBVRI-photometry in December 2021 at the Caucasian Mountain Observatory (CMO) of the SAI MSU. The normalized approximated reflectance spectra of the asteroids are shown in Fig. 3(a, b) in comparison with their spectra from the SMASSII database obtained when the asteroids were inactive. To check the stability of the photometric conditions, we used non-variable reference stars observed simultaneously with the asteroids. The normalized approximated spectra of these stars are given in the insets of the figures for comparison with those of the asteroids.

As seen from Fig. 3, the later reflectance spectra of AAs 145 Adeona and 779 Nina are more smoothed than those of the asteroids in Fig. 1, obtained in September 2012. Modeled reflectance spectra of a conditional active C-type asteroid show (Busarev et al. 2023, 2024; Criswell 1972) that smoothed spectra of AAs correspond to a lower optical thinness (up to ~ 0.1) of the DE.

3 On the possibility of the formation of dust aggregates in the plasma sheath of primitive AAs

As is known from the results of the first space studies of the lunar surface (e.g., Criswell 1972; Rennilson & Criswell et al. 1974), the force of electrostatic field of photoemission nature can exceed the force of gravity and is capable to tear charged dust particles of submicron and micron sizes from the surface and to bring them into a state of levitation. Such particles, together with electrons and protons, form a plasma-dust shell (plasma sheath), with a thickness from centimeters near the subsolar point to about a kilometer near the terminator, "sliding" above the sunlit surface of a rotating airless body. Theoretical calculations and model simulations show (e.g., Nitter & Havnes et al. 1992; Lee 1996; Colwell et al. 2005; Poppe et al. 2015) that the smallest charged dust particles ($\sim 10^{-2}$ microns and less), once inside this plasma sheath, are accelerated by the increasing electrostatic gradient (up to $\sim 300\,V/m$) so that they are ejected from the gravitational field of the body. At the same time, particles of a slightly larger size, from 10^{-2} to $1\,\mu m$, in the same conditions balance between the forces of the electrostatic and gravitational fields, but can be ejected at any moment under the influence of fluctuations in the solar wind or radiation pressure.

Thus, we assume that: a temporal DE formed on a primitive AA due to SPA could partly coincide with the plasma sheath above the sunlit surface of the body and

replenish the plasma sheath with new submicron dust particles during the rotation of the asteroid; it leads to an increase in the optical thickness of the DE to ~ 0.5

We assume that the growth of submicron aggregate dust particles in the plasma sheath of AAs may be analogous to dust coagulation in protoplanetary disks (e.g., Matthews et al. 2018).

Funding

This work was supported by the Russian Scientific Foundation (grant RNF 22-12-00115).

References

Alexander C., McKeegan K., Altwegg K., 2018, Meteorites, Asteroids, and Comets. Space Science Reviews, 214, id. 36

Busarev V., Barabanov S., Puzin V.B., 2016, Solar System Research, 50, 4, p. 281

Busarev V., Petrova E., Irsmambetova T.R., et al., 2021, Icarus, 369, id. 114634

Busarev V., Petrova E., Shcherbina M.P., et al., 2023, Solar System Research, 57, 5, p. 449

Busarev V., Petrova E., Puzin V.B., et al., 2024, Solar System Research, 58, 3, p. 315

Chandler C., Kueny J., Trujillo Ch., et al., 2020, Astrophysical Journal Letters, 892, 2, id. L38

Chandler C., Trujillo Ch., Oldroyd W.J., et al., 2024, Astronomical Journal, 167, 4, id. 156

Colwell J., Gulbis A., Horányi M., et al., 2005, Icarus, 175, 1, p. 159

Criswell D., 1972, Proc. Third Lunar Science Conf., Geochim. Cosmochim. Acta, Suppl. 3, 3, p. 2671

Hsieh H., Micheli M., Kelley M.S., et al., 2023, Planetary Science Journal, 4, 3, id. 43

Jarosewich C., 1990, Meteoritics, 25, 4, p. 323

Jewitt D., 2012, Astronomical Journal, 143, 3, id. 66

Lee P., 1996, Icarus, 124, 1, p. 181

Matthews L., Shotorban B., Hyde T.W., 2018, Physical Review E, 97, id. 053207

Nitter T. and Havnes O., 1992, Earth, Moon, and Planets, 56, 1, p. 7

Poppe A., Zimmerman M., Halekas J.S., et al., 2015, Planetary and Space Science, 119, p. 111

Rennilson J. and Criswell D., 1974, Moon, 10, 2 p. 121

Schorghofer N., 2008, Astrophysical Journal, 682, 1, p. 697

MODERN ASTRONOMY: FROM THE EARLY UNIVERSE TO EXOPLANETS AND BLACK HOLES

Formation of quasi-periodic oscillations in the solar corona

S. Derteev, M. Sapraliev, N. Shividov, and B. Mikhalyaev

Kalmyk State University named after B.B. Gorodovikov, Elista, 358000 Russia

Abstract. The dispersion of acoustic waves in the rarefied high-temperature plasma of the solar corona and its role in the propagation of disturbances occurring in the corona are analyzed. We believe that the quasi-periodic oscillations (QPOs) that are recorded when observing propagating disturbances in coronal holes and loops are formed as a result of the combined effect of dispersion and damping of compressive waves. Observations and wavelet analysis show that their spectra are continuous, where the periods are distinguished by corresponding maxima. The shape of spectrum is characteristic of localized disturbances. The study is based on the simple model of non-adiabatic waves in high-temperature plasma, taking into account the properties of thermal conductivity, radiative cooling and constant heating.

Keywords: Sun: corona, helioseismology, oscillations

DOI: 10.26119/VAK2024.100

1 Introduction

The propagating disturbances (PDs) observed in the circumsolar corona, coronal loops and holes are considered. PDs are recorded in variations of radiation intensity and are also called compression waves.

An example of PD analysis is shown in Fig. 1. PDs are identified as slow waves. It is a time signal showing the change in intensity over time at a certain selected observation point. It contains a number of maxima, so the idea arises to consider it as a periodic or quasi-periodic process; its wavelet spectrum and the global wavelet spectrum, which highlights the maxima by periods throughout the entire observation time are shown.

As you can see, there are two clear maxima in the spectrum, that is, we can talk about two periods. The authors claim QPOs with two periods. We draw attention to the fact that these periods do not actually operate over the entire interval of observation time. The periods change, that is, they are irregular. What kind of two-period oscillations can we talk about here?

Further, the time signal bears little resemblance to a superposition of two harmonic oscillations. Rather, it consists of several signals that have the form of sharp maxima. We say that there are triangular maxima here.

The next remark is that disturbances are considered as waves, but their propagation speed is significantly different from the speed of sound and the speed of a slow wave.

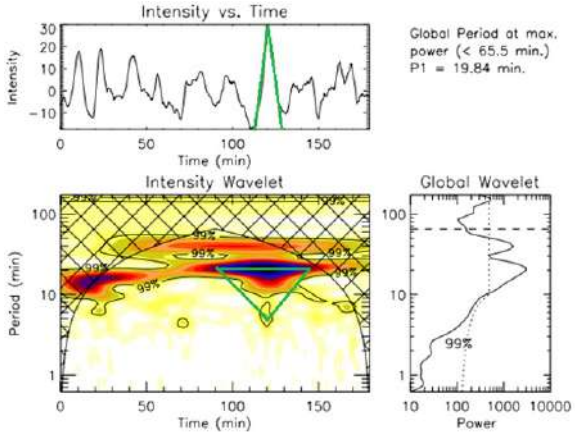

Fig. 1. The time signal (top panel), wavelet spectra and global wavelet (bottom panel) (Banerjee et al. 2011).

Similar observations are found in other papers on this issue, for example, Krishna Prasad et al. (2012); Gupta (2014). The maxima are triangular, the periods are irregular, and the speed of propagation of disturbances is significantly less than the speed of sound. These properties suggest that we are not dealing with waves.

2 Dispersion relation

To interpret PDs in the solar corona, we used a theoretical model of non-adiabatic acoustic waves in a high-temperature plasma with classical Spitzer thermal conductivity, CHIANTI[1] radiative-loss function and constant heating function. We consider equations of the gas dynamics (Derteev et al. 2023; Mikhalyaev et al. 2023; Derteev et al. 2024). We set the dimensions: $m(\rho) = 1.037 \cdot 10^{-12}\,\mathrm{kg\,m^{-3}}$, $m(\omega) = 0.1\,\mathrm{s^{-1}}$, $m(k) = 10^{-6}\,\mathrm{m^{-1}}$, $m(C_\mathrm{s}) = 10^5\,\mathrm{m\,s^{-1}}$, $m(x) = 10^6\,\mathrm{m}$, $m(t) = 10\,\mathrm{s}$.

Let us consider wave distributions in the form of functions $\exp(i\tilde{k}\tilde{x} - i\tilde{\omega}\tilde{t})$ and write the dispersion relation in the form

$$\frac{\tilde{\omega}^3}{\tilde{n}_0^3} + i\frac{\tilde{\omega}^2}{\tilde{n}_0^2}\left(B_1\frac{\tilde{k}^2}{\tilde{n}_0^2} + B_2\right) - \frac{\tilde{\omega}}{\tilde{n}_0}\tilde{C}_s^2\frac{\tilde{k}^2}{\tilde{n}_0^2} + i\frac{1}{\gamma}\left(-B_1\frac{\tilde{k}^2}{\tilde{n}_0^2} - B_2 + B_3\right)\tilde{C}_s^2\frac{\tilde{k}^2}{\tilde{n}_0^2} = 0, \quad (1)$$

where

$$B_1 = \frac{(\gamma-1)Mm(k)^2}{Rm(\rho)m(\omega)}\varkappa(T_0), B_2 = \frac{(\gamma-1)M}{Rm(\omega)}m(\rho)\Lambda'(T_0), B_3 = \frac{(\gamma-1)M}{RT_0m(\omega)}m(\rho)\Lambda(T_0). \quad (2)$$

3 QPOs in the acoustic waves

We have studied the properties of dispersion and damping of acoustic waves, which play a major role in the occurrence of QPOs. Figure 2 shows the dependence of the group velocity on the period. There are two minima. We number them from right to left. We call the right minimum the first and denote it as P_1; it is caused by heating and radiative cooling. The left minimum of P_2 is caused rather by the action of thermal conductivity; it can be called a thermal minimum. Comparison of the figures shows that radiation affects oscillations only at large periods. The thermal minimum P_2 divides periods into short and long.

Using the found dispersion, we consider the wave packet in the form of the Fourier integral

$$\rho = \varepsilon\rho_0\int_0^{k_\mathrm{max}} F(k)\mathrm{e}^{-\delta(k)t}\cos(kx - \omega(k)t)dk, \quad (3)$$

[1] https://chiantidatabase.org/

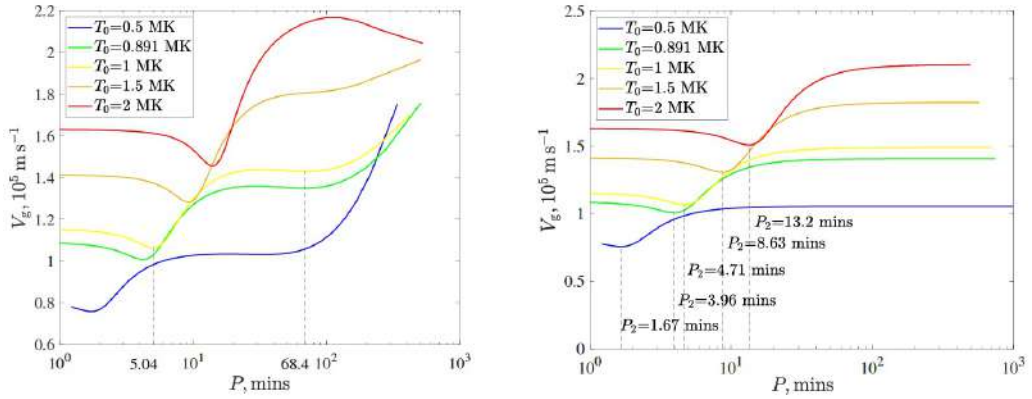

Fig. 2. Group velocity $V_g(P)$ for $n_0 = 10^{15}$ m^{-3} when taking into account the thermal conductivity and heating and cooling (left), and the thermal conductivity only (right). Shown in dashed lines for $T_0 = 1$ MK (left) (Derteev et al. 2024).

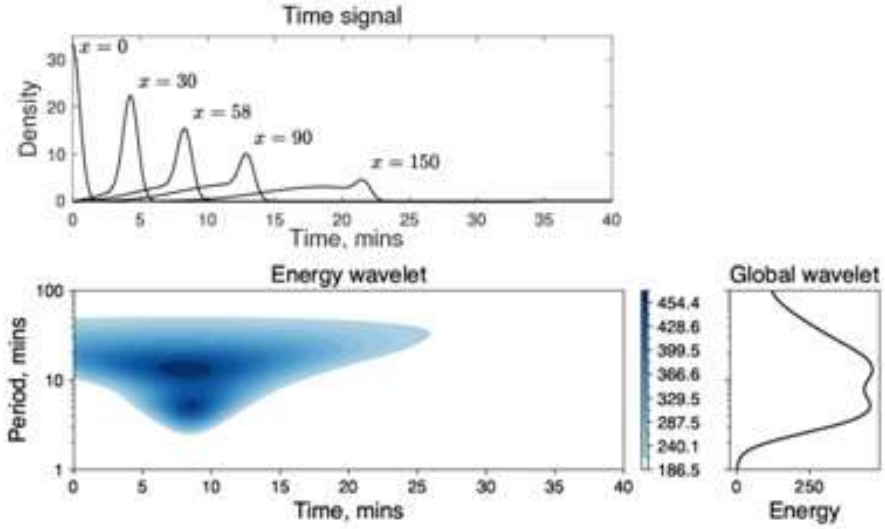

Fig. 3. Original time signals (top plot) and wavelet spectrum at the distance $x = 58$ Mm from the source of pulse generation (bottom plot). The initial pulse length $d = 5.3$ Mm. Plasma parameters: T_0= 1 MK, $n_0 = 0.45 \cdot 10^{15}$m^{-3} (Derteev et al. 2024).

with spectral density $F(k) = \mathrm{e}^{-d^2k^2/4}$ of Gaussian shape, as in the original pulse. d denotes the length of the initial pulse. We take it small, so that the initial disturbance has the form of a localized pulse. By setting a constant coordinate x, we obtain time signals at a given observation point. The source of disturbance is at the origin of coordinates. We use wavelet analysis to study time signals from Python library[2]

$$f(\tau) = \frac{1}{\sqrt{2\pi}}\mathrm{e}^{-\tau^2/2}\mathrm{e}^{i6\tau}. \tag{4}$$

Figure 3 shows the disturbance, time signals and wavelet spectrum when it has two maxima at $x = 58$ mm. According to the generally accepted point of view, we have QPOs here. Since the duration of the maximum increases with the period, the wavelet has a triangular shape, as does the time signal itself. The signal can be distinguished by a short-period part, which forms a sharp peak. It has a short duration and quickly decays. The structure of the signal shows regularities in the splitting of the spectrum into two parts, which we call short P_s and long P_l periods. The signal can be considered as a superposition of two wave packets – waves-counterparts. Thus, we show that from the initial localized pulse, under the action mainly of thermal conductivity, two separate wave packets can arise, which give two maxima in the wavelet spectrum. The QPO mechanism is described in the paper Roberts et al. (1984), and its practical application is described in the paper Derteev et al. (2024).

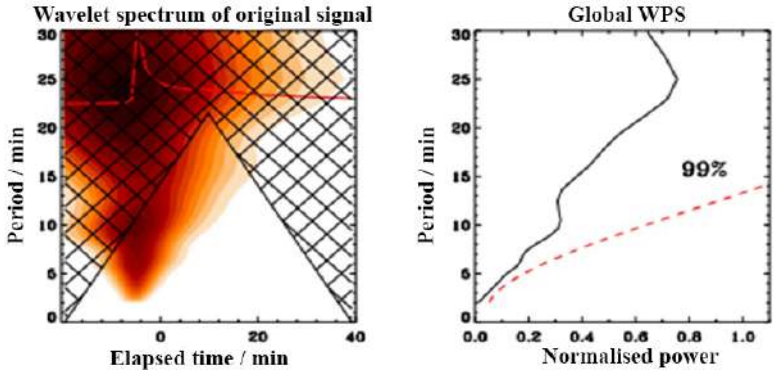

Fig. 4. Triangular signals and triangular wavelet spectra in observations of the paper Nakariakov et al. (2018).

The first separate triangular-shaped signal was noted in the paper Berghmans & Clette (1999), but did not attract much attention. We now assume that the so-

[2] https://github.com/PyWavelets/pywt/tree/main/pywt

called propagating disturbances or compressive waves are formed from such separate signals. A similar separate triangular signal is shown in Fig. 4. From the shape of the signal itself, it is clear that it consists of two wave packets with different periods. These periods are obtained in the wavelet spectrum. The wavelet spectrum also has a triangular shape.

4 Conclusions

The results of the work show that the original time signal contains individual triangular-shaped signals. In the wavelet spectrum, they correspond in time to pairs of maxima of a triangular shape (Fig. 1, the triangular signal and the corresponding triangle in the wavelet spectrum are highlighted by green lines). Propagating disturbances can be considered as a sequence of separate pulses. This explains such properties as the sharpness of maxima and irregularity of periods.

We propose to divide propagating disturbances into individual triangular-shaped perturbations instead of looking for a harmonic envelope in them. Then what can we call quasi-periodic oscillations?

In the spectrum of each individual triangular disturbance there are short and long periods, the duration of the oscillations is of the order of the period. The oscillations damp quickly, so the duration of disturbance itself is determined by a long period and in observations is 20–30 minutes. It follows that QPOs exist for only 20–30 minutes, then we observe other QPOs with a different pair of periods.

A sequence of triangular disturbances gives a sequence of QPOs, the periods of which may or may not coincide depending on the properties of the original pulses.

Funding

This work was supported by the Ministry of Science and Higher Education of the Russian Federation under the contract 075-03-2024-113.

References

Banerjee D., Gupta G.R., Teriaca L., 2011, Space Science Reviews, 158, 2-4, p. 267
Berghmans D. and Clette F., 1999, Solar Physics, 186, 1-2, id. 207
Derteev S., Shividov N., Bembitov D., et al., 2023, Physics, 5, p. 215
Derteev S.B., Sapraliev M.E., Shividov N.K., et al., 2024, Solar Physics, 299, 10, id. 141
Gupta G.R., 2014, Astronomy & Astrophysics, 568, id. A96
Krishna Prasad S., Banerjee D., Singh J., 2012, Solar Physics, 281, 1, id. 67
Mikhalyaev B.B., Derteev S.B., Shividov N.K., et al., 2023, Solar Physics, 298, 9, id. 102
Nakariakov V.M, Kolotkov D.Y., Kupriyanova E.G., et al., 2018, Plasma Physics and Controlled Fusion, 61, id. 014024
Roberts B., Edwin P.M., Benz A.O., 1984, Astrophysical Journal, 279, p. 857

Morphometric parameters of fresh lunar craters

E. Feoktistova, Zh. Rodionova, and V. Shevchenko

Sternberg State Astronomical Institute, Lomonosov Moscow State University, Moscow, 119234 Russia

Abstract. We study the morphometric parameters of 111 lunar craters with a diameter of 10 km or more, the formation of which, according to some researchers, can be attributed to the Copernican period. These craters were selected by analyzing data from the Diviner spectrometer on board the LRO probe. The purpose of this work is to study the morphometric characteristics of such craters in order to identify their characteristic features. According to the results obtained, the morphometric parameters of the fresh lunar craters are significantly similar to the morphometric parameters of lunar craters of the 1st degree of degradation (well-preserved craters) according to the classification of the SAI MSU.

Keywords: Moon; craters

DOI: 10.26119/VAK2024.101

1 Introduction

Impact craters have appeared on the lunar surface throughout its history, which is 4.6 billion years. The youngest lunar craters were formed during the Copernican period, which began 1.1 billion years ago and continues to the present time. The shape of an impact crater is determined by the parameters of the collision that formed it and the age of the crater. Quantitative characteristics of the crater shape are its morphometric parameters. The main morphometric parameters of impact craters, following Slodarzh (2021), are their diameters, the inclination angles of the external and inner slopes, the maximum and minimum depths and the height of the crater bottom. Analysis of data obtained by the Diviner infrared spectrometer on the LRO probe showed that 111 lunar craters are clearly visible in the IR range: the ejecta of these craters heated and cooled more slowly than the surrounding surface. The authors of the work Mazrouei et al. (2019) attribute this to the fact that these craters were formed over the last billion years and their ejecta have not yet been fragmented by the fall of other bodies and contain a significant number of large fragments. We compared the morphometric parameters of such craters with the morphometric parameters of well-preserved lunar craters.

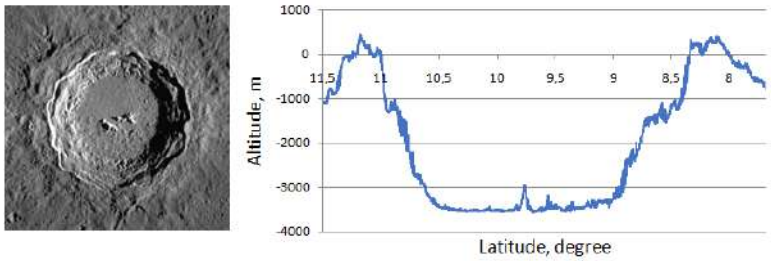

Fig. 1. Altitude profile of the Copernicus crater, (the image of the crater was obtained by the WAC camera of the LRO probe (https://www.lroc.asu.edu/about)).

2 Comparison of morphometric parameters of craters

According to the classification of craters by the degree of degradation of the SAI MSU, impact craters can be divided into 5 degradation classes: class 1 includes well-preserved craters that have a pronounced clear rim and often a system of rays, crater-ruins belong to the 5th degradation class. Degradation class 1 craters make up 19 % (2850) of the total number of lunar craters with a diameter of 10 km or more.

The degree of degradation of a crater does not always depend on its age: for example, the Sharonov crater (12.4° N, 173.3° E), which belongs to the 1st degradation class, was formed in the Eratosthenes period of lunar history (3.2–1.1 billion years ago). In this paper, we attempted to determine the morphometric features of fresh craters that would allow us to distinguish them from well-preserved craters of different ages. In the Morphological Catalog of Craters of the Moon (Rodionova et al. 1987), craters related to the 1st degradation class were selected. To determine the morphometric parameters of the craters, data from the LOLA altimeter of the LRO probe were used (https://ode.rsl.wustl.edu/moon/). Altitude profiles of 111 fresh craters (Mazrouei et al. 2019) and 150 craters of the 1st degradation class were studied (Fig.1). The distribution of craters by diameter for both crater groups is similar: the diameters of most craters in both groups (92 % of craters Mazrouei et al. (2019) and 96 % of craters of the 1st degradation class according to the classification of the SAI MSU) lie in the range of 10–30 km with a maximum in the range of 10–20 km.

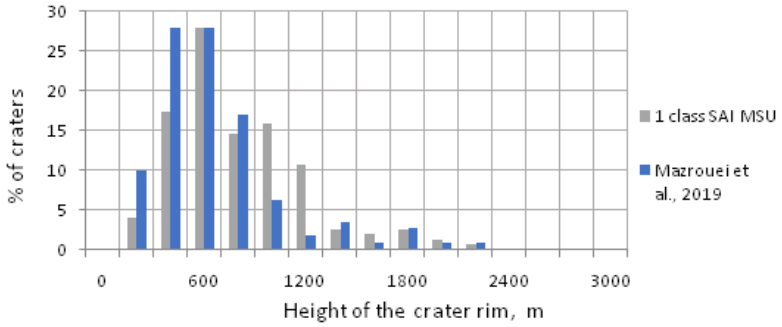

Fig. 2. Distribution of craters from Mazrouei et al. (2019) and craters of the 1st degradation class by the height of the rim.

As can be seen from Fig. 2, height of the crater rim for both groups lies in the range of 200–2000 m. About 60 % of the craters of the 1st degradation class and 81 % of fresh craters from Mazrouei et al. (2019) have a rim height of 400–800 m. The values of the inclination angles of the inner slopes of the craters for both groups of craters are approximately the same, ranging from 10 to 40 degrees. For the majority of craters of degradation class 1 according to the SAI MSU (73 %), the inclination angles of the inner walls of the crater lie within the range of 20–25 degrees. Most of the craters from Mazrouei et al. (2019) have steeper inner slopes: the inner slope angles of such craters are in the range of 25–35 degrees. Most craters of degradation class 1 according to the SAI MSU classification (86 %) have inclination angles of

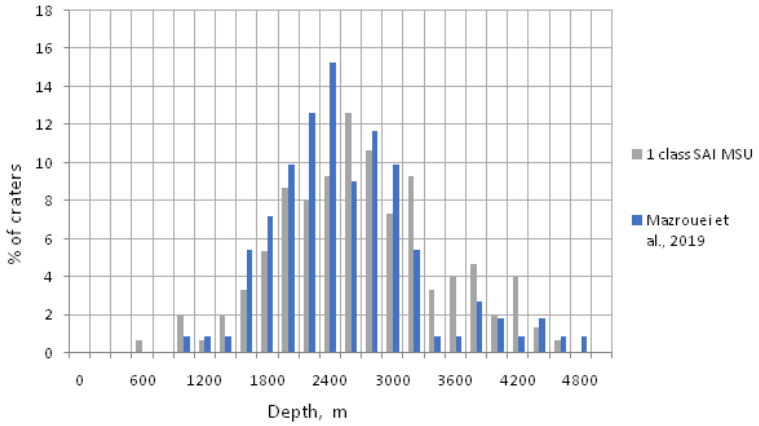

Fig. 3. Distribution by depth of fresh craters and craters of the 1st class of degradation.

external walls within the range of 2–8 degrees. The outer rims of the craters from Mazrouei et al. (2019) are on average slightly steeper: the inclination angles of the outer walls of the majority (85 %) of these craters are in the range of 4–12 degrees. The depth distribution of craters of both groups shows similarities. The depths of most of the craters of the 1st class of degradation according to the SAI MSU (71 %) lie within the range of 1800–3200 m (Fig. 3). The depths of the majority (86 %) of fresh craters from Mazrouei et al. (2019) lie approximately within the same range (1600–3200 m).

3 Conclusions

The morphometric parameters of lunar craters Mazrouei et al. (2019) are largely similar to the morphometric parameters of lunar craters of the 1st degree of degradation according to the SAI MSU. At the same time, the craters from Mazrouei et al. (2019) have slightly steeper inner and external slopes. Thus, no significant differences were found in the morphometry of craters determined by thermophysical properties as fresh from the morphometry of well-preserved lunar craters according to the SAI MSU data.

References

Slodarzh N., 2021, Vupusknaya kvalifikatsionnaya rabota bakalavra, p. 271
Mazrouei S., Ghent R., Bottke W., et al., 2019, Science, 363, 6424, p. 253
Rodionova Zh.F., Karlov A.A., Skobeleva T.P., et al., 1987, Morphological Catalogue of the Craters of the Moon, Moscow University Press

MODERN ASTRONOMY: FROM THE EARLY UNIVERSE TO EXOPLANETS AND BLACK HOLES

Longitudinal magnetic field gradients and vertical electric currents in active regions with different flare productivity levels

Yu. Fursyak

Crimean Astrophysical Observatory of the Russian Academy of Sciences, Nauchny, Crimea, 298409 Russia

Abstract. The purpose of the work performed was to search for parameters of longitudinal magnetic field gradients and vertical electric currents, and their values, which could serve as the basis for creating criteria for short-term forecasting of changes in the flare productivity of an active region (AR). In the course of the study, a threshold (critical) value of the average unsigned vertical electric current density ($< |j_z| >$) was identified, equal to 2.7 mA m^{-2}; it is shown that in all ARs with high flare activity, the value of $< |j_z| >$ is above the threshold; it is shown that a rapid increase in the parameter $< |j_z| >$ above the critical value, especially in ARs, in which additional ascent of the magnetic flux was recorded during their monitoring time, indicates an increase in AR flare activity in the time interval of 18-20 hours. A threshold value of the transverse component of the longitudinal magnetic field gradient between pairs of sunspots in the AR ($max(\nabla_\perp B_z)_{sp}$), equal to 0.118 G km^{-1}, was also found. In the AR NOAA 11283, a study of the dynamics of the value made it possible to detect a time delay of 19 hours between the beginning of its stable growth and the time of the beginning of the development of the first of a series of powerful solar flares.

Keywords: Sun: activity, flares, magnetic fields, electric currents

DOI: 10.26119/VAK2024.102

1 Introduction

Solar flares and coronal mass ejections have a significant impact on living organisms and technical systems on Earth, in its atmosphere and outer space. Considering the level of development of civilization and, at the same time, the almost complete absence of effective countermeasures, a qualitative forecast of solar activity becomes a task closely related to the everyday needs of humanity.

There are a large number of criteria that allow one to assess the probability of a solar flare (or series of solar flares) occurring in an active region (AR) with a lead time of up to several days (see Altyntsev et al. (1982); Severny et al. (1979), and many others). In recent decades, due to the emergence of new instruments for studying the Sun, which have high spatial and temporal resolution, it has become possible not only to clarify existing forecast criteria, but also to develop new ones, based, among other things, on the study of the dynamics of certain parameters in the solar atmosphere over significant (several days) time intervals. We present the results of a study on the dynamics of the gradients of longitudinal magnetic field and vertical electric currents in ARs with different levels of flare productivity based on observations obtained during the 24th solar cycle. These results may be of some interest in the context of forecasting solar flare activity with a lead time of about a day.

2 Methods and data used

The gradient (or rather the transverse component of the gradient) of the longitudinal magnetic field $\nabla_\perp B_z$ is calculated between pairs of sunspots in the AR as the absolute value of the difference in the maximum (minimum) values of the magnetic field strength in the sunspots, divided by the distance between these points (more detailed see Fursyak (2023)):

$$\nabla_\perp B_z = \frac{|B_{zimax} - B_{zjmax}|}{\sqrt{(x_i - x_j)^2 + (y_i - y_j)^2}} \tag{1}$$

To calculate the magnitude of the vertical electric current (more detailed see Fursyak (2018)) an integral approach is used. Method based on the Stoke's formula:

$$I = \frac{1}{\mu_0} \int_L B_l dl \tag{2}$$

where $\mu_0 = 4\pi \times 10^{-7}$ H m^{-1} is the magnetic constant in the SI; L is a closed rectangular contour of 5×5 pixels in size; B_l – the values of the transverse components

of the magnetic field in the direction of the contour bypass; dl – the integration element equal to the pixel size on the magnetogram.

All studies were performed using magnetographic data from the Helioseismic and Magnetic Imager (HMI/SDO, Scherrer et al. (2012)), available on the Joint Science Operation Center (JSOC) website[1], data series hmi.sharp_cea_720s.

3 Results

3.1 Vertical electric currents

Statistical analysis made it possible to detect a relationship between average unsigned density of the vertical electric current averaged over the monitoring time of the AR $< \overline{|j_z|} >$ (time averaged is indicated by the overbar) and the level of flare activity of the AR (flare index, FI, Abramenko (2005)) with Pearson's r = 0.66 (see Fig 1), and the threshold (critical) value of the $< \overline{|j_z|} >$ equal to 2.7 mA m^{-2} (vertical red dotted line with a long dash; also see Fursyak (2018)). The latest results (vertical red dotted line with a short dash) showed that flares of X-ray classes X are observed only in ARs for which the value of the parameter $< \overline{|j_z|} >$ not lower than 2.85 mA m^{-2}. It can also be seen (blue vertical dotted line with a short dash) that for all ARs with low activity the value of $< \overline{|j_z|} >$ is no higher than 3.3 mA m^{-2}.

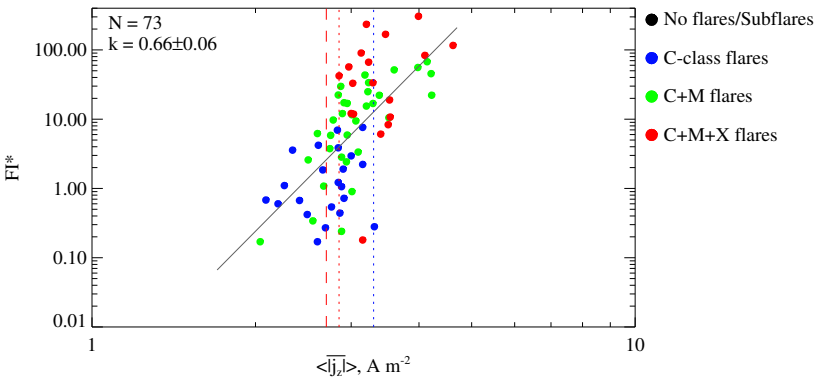

Fig. 1. Relationship between average unsigned density of the vertical electric current averaged over the monitoring time of the AR and the flare index of the AR ($< \overline{|j_z|} >$ – FI) for a sample of 73 ARs of the 24th solar activity cycle.

The most interesting was the study of the dynamics of $< |j_z| >$ in the ARs NOAA 11158 and 12673, which have high activity, in which an growth of the magnetic flux

[1] http://jsoc2.stanford.edu/ajax/lookdata2.html

was observed during their monitoring time. It is shown (Fig. 2, AR NOAA 11158 for example) that: 1) there is a rapid increase in the parameter $< |j_z| >$ above the critical value; 2) the moment of the beginning of a rapid increase in the value $< |j_z| >$ does not coincide in time with the beginning of the growth of the total unsigned magnetic flux (Φ) of the AR; 3) the total unsigned magnetic flux of the AR increases over a time interval of several days, while the time of rapid increase of the value $< |j_z| >$ does not exceed 6-7 hours; 4) a rapid increase in the value of $< |j_z| >$ is observed 18-19 hours before the start of the first powerful solar flare in the AR.

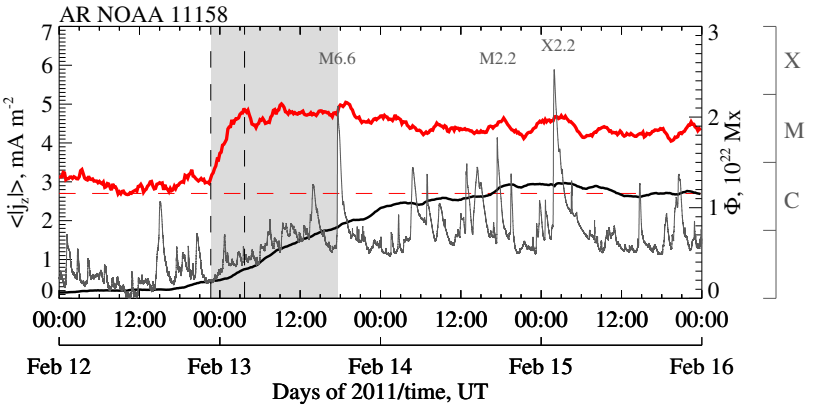

Fig. 2. Dynamics the parameters $< |j_z| >$ (red curve) and Φ (black curve) for the AR NOAA 11158. The following are shown: the critical level of $< |j_z| >$ (horizontal red dotted line); the time interval of the rapid increase of the parameter $< |j_z| >$ (vertical dotted lines); the time interval between the onset of the increase in the magnitude of $< |j_z| >$ and the first powerful X-ray solar flare (marked in gray). The most powerful solar flares recorded in the AR are indicate.

3.2 Longitudinal magnetic field gradients

Statistical analysis (Fig. 3) made it possible to detect a relationship between the maximum value of the transverse component of the longitudinal magnetic field gradient between pairs of sunspots $max(\nabla_\perp B_z)_{sp}$ and level of AR flare activity with the Pearson's r = 0.63, as well as a threshold value equal to 0.118 G km^{-1} (Fig. 3 vertical red dotted line with a long dash; also see Fursyak (2023, 2024)). It is also shown that for all ARs with low activity the value $\overline{max(\nabla_\perp B_z)_{sp}}$ (time-averaged parameter) is no higher than 0.2 G km^{-1} (Fig. 3, vertical blue dotted line with a short dash).

A study of the dynamics of the value in the AR NOAA 11283, in which intense movement of one of the developed sunspots was recorded, showed the following

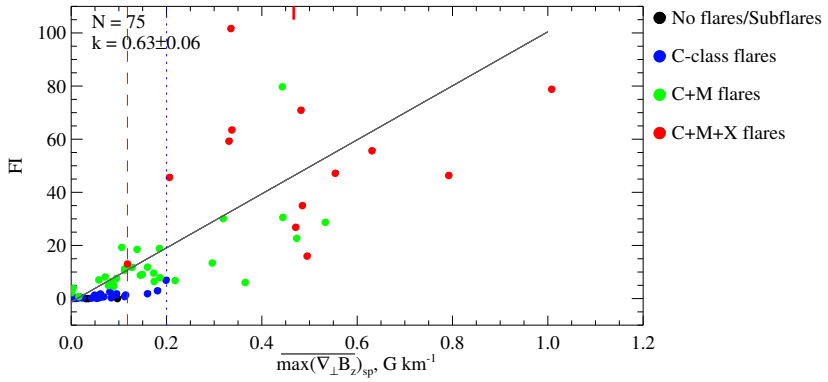

Fig. 3. Relationship between maximum value of the transverse component of the longitudinal magnetic field gradient between pairs of sunspots in the AR averaged over the its monitoring time and the flare index of the AR ($\overline{max(\nabla_\perp B_z)_{sp}}$ – FI) for a sample of 75 ARs of the 24th solar activity cycle.

(Fig. 4): 1) there is a stable smooth increase in the magnitude of $max(\nabla_\perp B_z)_{sp}$ above the threshold value with practically unchanged total unsigned magnetic flux of the AR; thus, the increase in the parameter $max(\nabla_\perp B_z)_{sp}$ is due solely to the movement of the sunspots in the AR; 2) an increase in the value $max(\nabla_\perp B_z)_{sp}$ above the threshold value is observed 19 hours before the M5.3 class X-ray flare, the first of a series of powerful flares in the AR.

4 Summary

Studies of longitudinal magnetic field gradients and vertical electric currents carried out based on observational data obtained during the 24th solar cycle allow us to draw the following conclusions:

1. There is a relationship between the value of the average unsigned vertical electric current density averaged over the AR monitoring time $< \overline{|j_z|} >$ and the level of flare activity of the AR (flare index) with Pearson's $r = 0.66$.
2. A threshold (critical) value of $< \overline{|j_z|} >$ equal to 2.7 mA m^{-2} was detected; exceeding the threshold value is typical for ARs with higher flare activity.
3. In the ARs NOAA 11158 and 12673 a sharp increase in the $< |j_z| >$ value above the threshold level was observed 18-19 hours before the first solar flare of high X-ray class.
4. There is a relationship between the magnitude of the transverse component of the gradient of the longitudinal magnetic field between pairs of sunspots in the AR ($max(\nabla_\perp B_z)_{sp}$) and the level of its flare activity with a Pearson's $r = 0.63$.

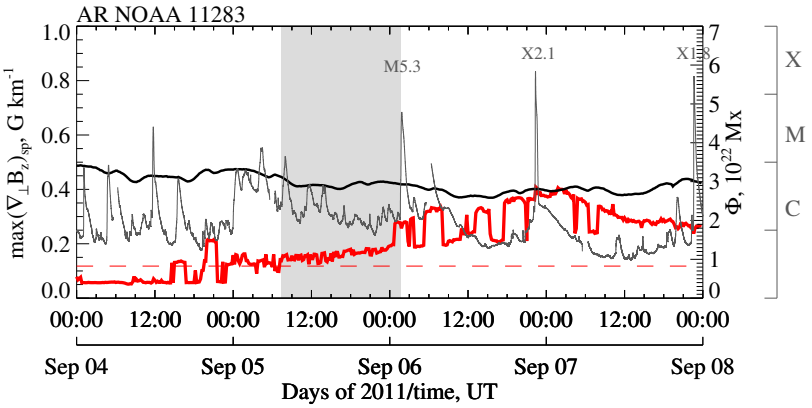

Fig. 4. Dynamics of the parameters $max(\nabla_\perp B_z)_{sp}$ (red curve) and Φ (black curve) for the AR NOAA 11283. The following are shown: the critical level of the $max(\nabla_\perp B_z)_{sp}$ (horizontal red dotted line); the time interval between the onset of the increase in the magnitude of $max(\nabla_\perp B_z)_{sp}$ and the first powerful solar flare (marked in gray). The most powerful solar flares recorded in the AR are indicate.

5. A threshold value of the parameter $\overline{max(\nabla_\perp B_z)_{sp}}$ equal to 0.118 G km^{-1} was detected.
6. In the AR NOAA 11283 a time delay of 19 hours between stable increase the parameter $max(\nabla_\perp B_z)_{sp}$ above the threshold level and the time of the beginning of the first of a series of powerful solar flares (M5.3 X-ray class) was detected.

Funding

This work was supported by the Ministry of Science and Higher Education of the Russian Federation (state assignment No. 122022400224-7).

References

Abramenko V.I., 2005, Astrophysical Journal, 629, 2, p. 1141
Altyntsev A.T., Banin V.G., Kuklin G.V., et al., 1982, Solar flares, Moscow, Science Press
Fursyak Yu.A, 2023, Astrophysics, 66, 4, p. 532
Fursyak Yu.A., 2018, Geomagnetism and Aeronomy, 58, 8, p. 1129
Fursyak Yu.A., 2024, Astrophysics, 67, 1, p. 67
Scherrer P.H., Schou J., Bush R.I., et al., 2012, Solar Physics, 275, 1-2, p. 207
Severny A.B., Stepanyan N.N., Steshenko N.V., 1979, in: NOAA Solar-Terrestial Predictions Proceedings, 1, p. 72

MODERN ASTRONOMY: FROM THE EARLY UNIVERSE TO EXOPLANETS AND BLACK HOLES

Magnetic reconnection flux in eruptive and confined solar flares

O. Gopasyuk

Crimean Astrophysical Observatory of the Russian Academy of Sciences, Nauchny, Crimea, 298409 Russia

Abstract. The magnetic properties of 59 flare events (38 eruptive and 21 confined) of GOES class M5.0 and above between February 2011 and December 2022 were analyzed. To identify the statistical properties of magnetic reconnection fluxes, we used the observational data from Solar Dynamics Observatory. The flare durations were analyzed using data from the GOES. The correlation between the GOES peak X-ray flux of a flare and magnetic reconnection flux is strong both for confined and eruptive flares. Eruptive flares show statistically larger magnetic reconnection flux and ribbon area than confined flares. The magnetic reconnection flux is strongly correlated with the flare duration. There is an approximately linear relationship between rise and decay times: the longer the rise time, the longer the decay time. We found a relation between the fraction of active regions (ARs) involved in reconnection process and the eruptive character of large flares. The probability that AR-induced flares will be associated with a coronal mass ejection (CME) increases with the fraction of ARs involved in the reconnection.

Keywords: Sun: magnetic fields, flares, coronal mass ejection

DOI: 10.26119/VAK2024.103

1 Introduction

Magnetic reconnection is responsible for the explosive release of energy on the Sun, resulting in solar flares. During magnetic reconnection the transformation of magnetic energy into the kinetic energy of accelerated particles and thermal energy occurs. Flare events associated with observed CMEs are called eruptive flares, while flares not associated with CMEs are called confined flares. A large number of statistical studies have compared magnetic properties of confined and eruptive flares, including total reconnection magnetic flux $\Phi_{\rm RB}$ and reconnection rate (e.g., Tschernitz et al. 2018; Kazachenko 2023; Gopasyuk 2024), total unsigned magnetic flux of a flare-hosting AR, $\Phi_{\rm AR}$ (Li et al. 2020), fractions of the AR magnetic flux or area swept by flare ribbons, $\Phi_{\rm RB}$ and $S_{\rm RB}$, relative to the total AR flux or area, $\Phi_{\rm RB}/\Phi_{\rm AR}$ and $S_{\rm RB}/S_{\rm AR}$, respectively (Toriumi et al. 2017; Tschernitz et al. 2018; Gopasyuk 2024).

In this paper, we present the results of a statistical study of total reconnection fluxes, flare ribbon areas, and flare duration for eruptive and confined events. We also derive quantitative connections between the fraction of the ARs involved in reconnection and the eruptive nature of large flares during the period of solar cycle 24 and the growth phase of solar cycle 25.

2 Data and Methods

We examined the magnetic properties of 59 flares (38 eruptive and 21 confined) of GOES class M5.0 and above from data presented by Gopasyuk (2024). We choose events that are sufficiently isolated in time from other events (that is, the FWHM of the GOES X-ray light curves is well-defined). Thus, the eruptive flare SOL2012-03-07T01:14 was excluded from the data. The flares occurred within 40° of the central meridian from February 2011 to December 2022. The magnetic properties of flare ribbons and ARs were calculated by Gopasyuk (2024) based on the sequences of SDO/AIA images in the 1600 Å band and the preflare normal component of the magnetic field was obtained from SDO/HMI vector magnetograms.

We also have used the parent 2-s (1-s) for flares of 2011-2017 (2021-2022) GOES data sampling to define time scales for each event: e-folding rise $\tau_{\rm rise}$ and decay $\tau_{\rm decay}$ times, and durations at half maximum (FWHM) of the 1 – 8 Å band. We defined $\tau_{\rm rise}$ and $\tau_{\rm decay}$ using the GOES X-ray flux $F_{\rm SXR}$ and its time derivative $\dot{F}_{\rm SXR}$ at the half-maximum times from the GOES data as $\tau = F_{\rm SXR}/\dot{F}_{\rm SXR}$. Measuring the e-folding decay time at the half-maximum point may systematically miss the longer time scale, if present, but it more accurately reflects the energy of the flare (impulse phase).

3 Statistical Results

Figure 1(a-f) shows plots of the GOES peak X-ray flux versus the ribbon and AR magnetic properties. The correlation between the GOES peak X-ray flux and $\Phi_{\rm RB}$ is strong (the Spearman correlation coefficient $r_s = 0.6(0.7)$ for eruptive (confined) flares, Fig. 1(a)) in agreement with earlier studies (e.g., Kazachenko 2023), implying that larger flares have more magnetic field involved in reconnection. Similarly, the GOES peak X-ray flux shows a high correlation with $S_{\rm RB}$ ($r_s = 0.5(0.6)$ for eruptive (confined) flares, Fig. 1(b)). For a fixed GOES peak X-ray flux, confined and eruptive flares have the same $\Phi_{\rm RB}$ and $S_{\rm RB}$.

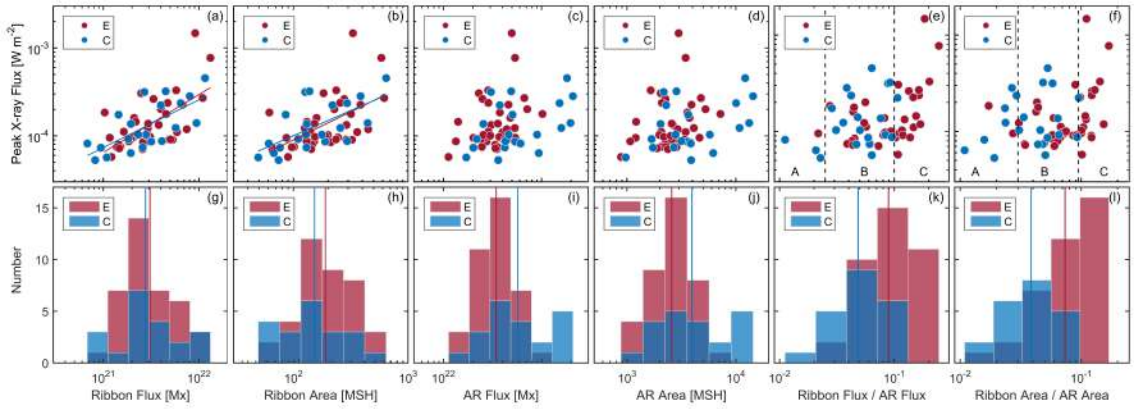

Fig. 1. Scatter plots between the GOES peak X-ray flux and different physical variables (top row), and distributions of various physical variables (bottom row) for eruptive (red) and confined (blue) events. The red and blue straight lines in panels (a–b) show the results of linear fitting for eruptive and confined events respectively. The two dashed vertical lines in panel (e) respectively refer to $\Phi_{\rm RB}/\Phi_{\rm AR}$ of 0.025 and 0.100. The two dashed vertical lines in panel (f) respectively correspond to $S_{\rm RB}/S_{\rm AR}$ of 0.030 and 0.095. Vertical lines in panels (g–l) indicate the log-mean value for each variable within eruptive and confined flare groups.

The correlation between $\Phi_{\rm AR}$ and the GOES peak X-ray flux is weak ($r_s = 0.3(0.4)$ for eruptive (confined) flares, Fig. 1(c)) – larger ARs could host both large and small flares. The AR area $S_{\rm AR}$ and the GOES peak X-ray flux (Fig. 1(d)) also show a weak correlation with a correlation coefficient r_s of 0.3 for both classes of flares. At the same time distributions of magnetic properties (Fig. 1(g–j)) show that $\Phi_{\rm RB}$ and $S_{\rm RB}$ are larger for eruptive flares, while $\Phi_{\rm AR}$ and $S_{\rm AR}$ are larger for confined flares. This leads to the fact that the proportion of ARs involved in reconnection ($\Phi_{\rm RB}/\Phi_{\rm AR}$ and $S_{\rm RB}/S_{\rm AR}$) is higher in eruptive flares (Fig. 1(k–l)).

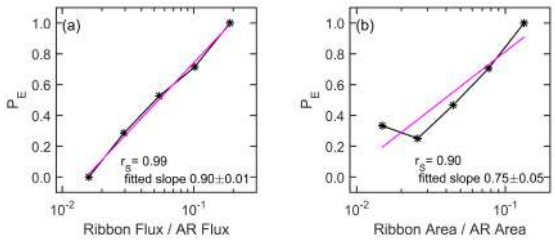

Fig. 2. Proportions of eruptive flares P_E versus Φ_{RB}/Φ_{AR} and S_{RB}/S_{AR}. The magneta lines show the results of linear fitting. Slopes and Spearman correlation coefficients r_s are shown in the lower right corner.

Figure 1(e) shows the scatter plot of the GOES peak X-ray flux versus Φ_{RB}/Φ_{AR}. Flares that are hosted by the ARs with small Φ_{RB}/Φ_{AR} do not generate CMEs (Area A). About 75% of events occurring in ARs with Φ_{RB}/Φ_{AR} less than 0.025 are confined. An overwhelming majority of flares hosted by the ARs with Φ_{RB}/Φ_{AR} higher than 0.100 generate CMEs (Area C). If an AR has a moderate Φ_{RB}/Φ_{AR} (more than 0.025 and less than 0.100, Area B), the probability of eruptive and confined events is apparently almost the same. The scatter plot of the flare peak X-ray flux versus S_{RB}/S_{AR} shows a similar trend (Fig. 1(f)). About 78% of flares in ARs with S_{RB}/S_{AR} less than 0.030 are confined (Area A) and more than 94% flares in the ARs with S_{RB}/S_{AR} more than 0.095 are eruptive (Area C). Approximately equal numbers of confined and eruptive flares occur at intermediate area ratios (0.030–0.095, Area B). Histograms (Fig. 1(k–l)) show that there are significant differences in the distribution of the fraction of ARs involved in reconnection between eruptive and confined flares. Eruptive flares have a large fraction of ARs participating in reconnection. Based on the number distributions of Φ_{RB}/Φ_{AR} and S_{RB}/S_{AR} we show in Fig. 2 the relations of the proportions of eruptive flares P_E ($P_E = N_E/(N_E + N_C)$, N_E and N_C are the numbers of eruptive and confined events respectively) with Φ_{RB}/Φ_{AR} and S_{RB}/S_{AR}. It can be seen that P_E increases with Φ_{RB}/Φ_{AR}. The P_E has a strong correlation with Φ_{RB}/Φ_{AR} with a correlation coefficient r_s of 0.99. Similarly, P_E shows a strong correlation with S_{RB}/S_{AR} ($r_s = 0.90$). This result is similar to the statistical result of Toriumi et al. (2017), who showed the parameter of the ribbon area normalized by the sunspot area determines whether a given flare is eruptive or not. They suggested that the relative structural relationship between the flaring region and the entire AR controls the CME productivity.

In Fig. 3 we analyze how the parameters related to the temporal behavior of the flare (FWHM, τ_{rise}, and τ_{decay}) scale with different physical variables. It can be seen that the dependences do not show significant differences between eruptive and

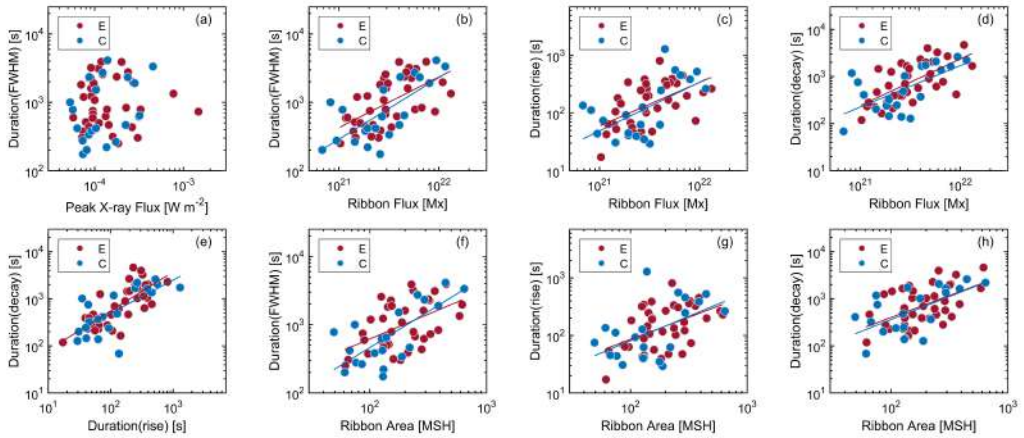

Fig. 3. Scatter plots showing the FWHM, rise and decay times as a function of different physical variables for eruptive (red) and confined (blue) events. The red and blue straight lines show the results of linear fitting respectively for eruptive and confined events.

confined flares. The flare duration FWHM is not related to the GOES peak X-ray flux (Fig. 3(a)). In contrast, the magnetic reconnection flux has a strong correlation with flare temporal parameters, including the duration FWHM ($r_s = 0.6(0.7)$ for eruptive (confined) flares, Fig. 3(b)), τ_{rise} ($r_s = 0.6(0.5)$ for eruptive (confined) flares, Fig. 3(c)) and τ_{decay} ($r_s = 0.7$ for both classes of flares, Fig. 3(d)). The relationship between flare duration and Φ_{RB} shows that the more magnetic flux is involved, the longer the reconnection processes last. The flare ribbon area has a moderate to strong correlation with flare temporal parameters, including the duration FWHM ($r_s = 0.5(0.7)$ for eruptive (confined) flares, Fig. 3(f)), τ_{rise} ($r_s = 0.4$ for both classes of flares, Fig. 3(g)) and τ_{decay} ($r_s = 0.5(0.6)$ for eruptive (confined) flares, Fig. 3(h)). The relationship between flare duration and S_{RB} may also be accepted if we assume that the strengths of the field lines are not so different among the events. In Fig. 3(e) we show the decay time versus the rise time. In this case there is an approximate linear relationship between the rise and decay times, with a longer rise time leading to a longer decay time ($r_s = 0.8(0.7)$ for eruptive (confined) flares). However, even in this case, no difference is observed in the behavior of flares with and without a CME.

4 Summary

This paper presents the results of a statistical analysis of the magnetic reconnection flux and duration of 59 (38 eruptive and 21 confined) solar flares with GOES magnitude M5.0 and above based on a dataset compiled by Gopasyuk (2024). The

dates of the events cover the period from February 2011 to December 2022, i.e. they practically cover the entire 24th solar cycle and the growth phase of the 25th solar cycle. The main results of our study are as follows.

The correlation between the flare GOES peak X-ray flux and magnetic reconnection flux is strong both for confined and eruptive flares.

We found that the fraction of the AR magnetic flux $\Phi_{\rm RB}/\Phi_{\rm AR}$ involved in the reconnection process plays a significant role in controlling the eruptive nature of flares, and the proportion of eruptive flares exhibits a strong correlation with $\Phi_{\rm RB}/\Phi_{\rm AR}$ ($r_s = 0.99$). About 75% of flares originating from ARs with a ratio magnetic flux less than 0.025 are confined, i.e., they are not associated with a CME. About 100% of events occurring in ARs with $\Phi_{\rm RB}/\Phi_{\rm AR}$ greater than 0.100 are eruptive.

Not all eruptive flares have a long duration. Some flares with CMEs showed a very impulsive rise time, and short durations, and some flares without CMEs were long-duration events. Flare duration (FWHM, $\tau_{\rm rise}$, $\tau_{\rm decay}$) has a moderate to high correlation with $S_{\rm RB}$, and $\Phi_{\rm RB}$ and all these relations showed approximately linear correlations.

Acknowledgements. We acknowledge the GOES and SDO HMI/AIA teams for the availability of the high-quality scientific data.

Funding

This work was supported in the framework of the state assignment on the topic "Research of the Universe objects by observations in radio and optical wavelength ranges" by the Ministry of Science and Higher Education of the Russian Federation under the state registration No. 122022400225-4.

References

Gopasyuk O.S., 2024, Geomagnetism and Aeronomy, 64, 8 in press
Kazachenko M.D., 2023, Astrophysical Journal, 958, 2, id. 104
Li T., Hou Y., Yang S., et al., 2020, Astrophysical Journal, 900, 2, id. 128
Toriumi S., Schrijver C.J., Harra L.K., et al., 2017, Astrophysical Journal, 834, 1, id. 56
Tschernitz J., Veronig A.M., Thalmann J.K., et al., 2018, Astrophysical Journal, 853, 1, id. 41

VAK 2024 MODERN ASTRONOMY: FROM THE EARLY UNIVERSE TO EXOPLANETS AND BLACK HOLES 300 years Russian Academy of Sciences

Susceptibility of electromagnetic fields in the Solar System to gravitational wave effects from relativistic binary star systems

L. Grunskaya[1], V. Isakevich[2], and D. Isakevich[2]

[1] Vladimir State University, Vladimir, 600000 Russia
[2] Eigenvector LLC, 50 Gorkogo St, Vladimir, 600005 Russia

Abstract. Using an eigenvector and signal component analyzer (eigenoscope), the problem of identifying the impact of gravitational waves of relativistic binary star systems (RBSS) with large and small eccentricity on the vertical component of the electric field strength (E_z) in the Earth's atmospheric surface layer in the infra-low frequency (ILF) range at high harmonics of the EDS circulation frequencies has been solved. The results were obtained using monitoring data at four spatially separated E_z observation stations. A model is proposed to explain the effect of the gravitational wave influence of relativistic binary star systems on the vertical component of the Earth's electric field strength in the surface layer of the atmosphere, previously discovered by the authors. The model considers as the mechanism the disturbance of the Earth's orbit by gravitational waves from relativistic binary star systems, leading to small displacements of the Earth relative to the free space charge in the troposphere. The estimates of the amplitude of the E_z components, spectrally localized at the frequencies of gravitational waves of relativistic binary star systems, obtained on the basis of the presented model do not contradict the experimental results.

Keywords: gravitation; gravitational waves; Earth; (stars:) binaries: general; relativistic processes; atmospheric effects; methods: statistical

DOI: 10.26119/VAK2024.104

1 Introduction

Using an eigenvector and signal component analyzer (eigenoscope), the problem of identifying the impact of gravitational waves of relativistic binary star systems (RBSS) with large and small eccentricity on the vertical component of the electric field strength (E_z) in the Earth's atmospheric surface layer in the infra-low frequency (ILF) range at high harmonics of the EDS circulation frequencies has been solved.

2 Observation

The results were obtained using monitoring data at four spatially separated E_z observation stations (three Rosgidromet stations at Voeikovo, Verkhnee Dubrovo, Dusheti and Experimental base of the Department of General and Applied Physics of Vladimir State University). All these time series have the same sampling time equal to 3600 sec; some data about the series is presented in Table 1.

Table 1. The used time series of E_z observations.

No.	Observation station	Total sample count	Duration, days	Duration, months	Duration, years
1	Voeikovo	170000	7083	236	20
2	Dusheti	120000	5000	167	14
3	Verkhnee Dubrovo	120000	5000	167	14
4	VlSU experimental base	36000	1500	50	4

When forming a sample of eigenvectors spectrally localized at the frequencies of gravitational waves according to eq. (3), six RBSSs were selected from the Johnston list (see the second column of Table 2) having a high eccentricity (0.58–0.89).

Table 2. The selected high-eccentricity relativistic binaries (e is eccentricity, n are the orders of multiples).

No.	**RB**	**T , days**	**e**	**n**	**Frequency range, μHz**
1	J0514-4002A	18.785	0.889	1–90	0.6161338 . . . 55.452045
2	J1811-1736	18.77917	0.82802	1–90	0.6163251 . . . 55.46926
3	J1823-1115	357.7620	0.79461	20–70	0.6470265 . . . 2.2645926
4	J1750-37	17.3	0.71	1–36	0.6690216 . . . 24.084778
5	J2305+4707	12.3395445	0.65837	1–25	0.9379661 . . . 23.449152
6	J1740-3052	231.02965	0.578872	10–16	0.5009779 ∗ . . . 0.8015646

Forty-three low-eccentricity RBSSs were selected from Johnston's list and their doubled orbital frequencies were calculated.

3 Analysis

3.1 Theoretical background

The classical work Zeldovich & Novikov (1975) shows that energy irradiated by the RBSS gravitational waves at the multiplied orbital frequency energy is proportional to

$$g(n,e) = \frac{n^4}{32}[g_1(n,e) + g_2(n,e) + g_3(n,e)], \tag{1}$$

where

$$g_1(n,e) = [J_{n-2}(ne) - 2eJ_{n-1}(ne) + \frac{2}{n}J_n(ne) + 2eJ_{n+1}(ne) - J_{n+2}(ne)]^2,$$

$$g_2(n,e) = (1-e^2)[J_{n-2}(ne) - 2J_n(ne) + J_{n+2}(ne)]^2,$$

$$g_3(n,e) = \frac{4}{3n^2}\left[J_n(ne)\right]^2,$$

n is the order of the multiplied frequency; e is the eccentricity; $J_n(x)$ is Bessel function.

Use of eq. (1) allows to compute the ratio

$$G_{R.2}(n,e) = \frac{g(n,e)}{g(2,e)}, \tag{2}$$

which can be used to select promising RBSSs that have GW irradiance at multiple frequencies above the second order. Johnston's list contains many RBSSs with high eccentricity. Those that have the eq. (2) ratio above 1 and multiple frequencies satisfying the condition

$$5T < (n_{k,j}F_j)^{-1} < MT\,, \qquad j = \overline{1:Q}\,, \tag{3}$$

where T is the sampling time (equals to 3600 sec in our work); $n_{k,j}$ is the allowable order of the multiplied (of order k) orbital frequency of j-th RBSS; F_j, $j = \overline{1:Q}$ are the RBSS orbital frequencies; Q is the high-eccentricity RBSS count (6 in our work); MT is the analysis span of the eigenoscope (1000 hours in the current work), has been selected.

The ratio eq. (2) obviously corresponds to the condition

$$\lim_{e\to 0, n\neq 2} \frac{g(n,e)}{g(2,e)} = 0$$

therefore the small-eccentricity RBSSs irradiate GW at the doubled orbital frequency only.

The ranges of GW irradiation frequencies for high-eccentricity RBSS indices are shown in Table 2, column 5.

3.2 Analyzer construction

A satisfactory analyzer design (called an igenoscope (Isakevich et al. 2011, 2017)) uses a representation of a time series of observations in a finite range of analysis and decomposes observations into uncorrelated components. It enables spectrally localized components identification and analysis of individual behavior of the non-correlated components. It uses simple, reasonable and widely known criteria for component identification and decision making.

Eigenoscope is an analyzer which use signal representation at the covariance matrix eigenvectors orthonormal basis; the covariance matrix is computed for an ensemble consisting of the signal pieces (duration of each piece is 1000 hours). The signal analysis takes place in the basis which is not given apriori but adapted for the specific covariance matrix. Eigenoscope decomposes signal to non-correlated components which have the same shape since the covariance matrix eigenvectors and the eigennumbers are equal to a mean component capacity in the ensemble. Therefore individual properties of the signal non-correlated components at a finite analysis span are freely exposed while we analyze the signal using eigenoscopy.

The ensemble for the current task is formed as a trajectory matrix which consists of all the signal pieces of a predefined length.

Eigenpairs has been computed for each covariance matrix. Each eigenpair consists of an eigenvector and a corresponding eigennumber. An amplitude spectrum has been computed for each of the eigenvectors; this spectrum has been normalized to its maximal value in order to estimate the eigenvector spectral localization band. The frequency band of spectral localization is estimated as a band in which the normalized amplitude spectrum exceeds $1/\sqrt{2}$. We suppose that an eigenvector is spectrally localized at some frequency if this frequency lays in the eigenvector's spectral localization band.

Indices of the eigenvectors which are spectrally localized near the RBSS irradiation frequencies are listed separately. To estimate the spectral localization of each eigenvector, the coherence coefficient was used, which is the ratio of the maximum

amplitude value to the average amplitude in the spectrum of the eigenvector amplitude.

A set of coherence ratios of eigenvectors spectrally localized near the frequencies of gravitational waves and a sample of eigenvalues (which are the mean square values of uncorrelated components) corresponding to these eigenvectors are formed. For further comparison, test sets of coherence ratios and eigennumbers are formed. A statistical decision is made concerning abnormal behavior of uncorrelated components of E_{z}, which are spectrally localized at the frequencies of RBSS gravitational waves .

Decision for the components which are localized at the GW frequencies of low-eccentricity RBSS is made using the Bernoulli test scheme. Smirnov-Kolmogorov criterion is used for the high-eccentricity GW irradiation frequencies.

4 Estimations of influence

Probability of the case that the samples belong to random variables having the same distribution law is estimated using Smirnov-Kolmogorov criterion. Probability estimation for coherence ratios for each of the time series is less than 10^{-7}; estimation for the normalized eigennumbers is less than $7 \cdot 10^{-8}$ for each time series. The difference between the sets of eigenpairs is significant and is extremely unlikely to be occasional. This means that at all observation stations the coherence ratios and eigenvalues have different distribution laws for the eigenvectors spectrally localized at gravitational waves frequencies and for the eigenvectors spectrally localized at test samples frequencies. So, until proven otherwise it must be assumed that the differences are due to factors that distinguish the compared samples, i.e to the gravitational-wave impact of RBSS on E_{z} (Grunskaya et al. 2023).

Median value have been estimated for all eigennumbers and all coherence ratios for each of the time series. The estimates are exceeded by eigenvalues and coherence ratios for eigenvectors that are spectrally localized at each of the forty-three doubled RBSS rotation frequencies. Estimations of the Bernoulli test false alarm probability are less than 10^{-9} (Grunskaya et al. 2014, 2023).

5 Summary

Using eigenoscopy (analysis of a time series in the basis of eigenvectors of their covariance matrix at a finite analysis span) made it possible to reveal the non-correlated components spectrally localized at the gravitational irradiation frequencies of the known relativistic binary star systems; these components have been revealed in the Earth electric field vertical projection at the infra-low frequency range. Coherence

ratios of these components differ from those of the components spectrally localized at the other frequencies; the difference is statistically significant. The same effect is observed for the components amplitudes. The revealed components are not observable using classic spectral analysis; they are mixed with the other components in the analysis channel and are perceived as a noise.

A model is proposed to explain the effect of the gravitational wave influence of relativistic binary star systems on the vertical component of the Earth's electric field strength in the surface layer of the atmosphere, previously discovered by the authors. The model considers as a mechanism the disturbance of the Earth's orbit by gravitational waves from relativistic binary star systems, leading to small displacements of the Earth relative to the free space charge in the troposphere. The estimates of the amplitude of the E_z components, spectrally localized at the frequencies of gravitational waves of relativistic binary star systems, obtained on the basis of the presented model do not contradict the experimental results.

Acknowledgements. The results of this work are based on the observation data of the Earth electric field donated by Y. M. Schwartz (Voeikovo, Verkhnee Dubrovo, Dusheti stations); on the data recorded at the experimental ground of Department of General and Applied Physics of Vladimir State University (lead by L.V. Grunskaya); on the RBSS list published by Johnston at his site and on the innovative processing methods (called eigenoscopy).

Funding

This work was not supported by any grants.

References

Grunskaya L., Isakevich V., Isakevich D., 2023, Gravitation and Cosmology, 29, 3, p. 283

Grunskaya L., Isakevich V., Isakevich D., et al., 2014, Space, Time and Fundamental Interactions, 2, p. 54

Grunskaya L., Isakevich V., Isakevich D., et al., 2013, Space, Time and Fundamental Interactions, 3–4, p. 117

Isakevich V., Isakevich D., Grunskaya L., 2011, The signal eigenvectors' and components' analyser, RU116242U1, 20.05.2012

Isakevich V. and Isakevich D., 2017, Signal eigenvectors' and components' spectrum analyzer, RU178399U1, 03.04.2018

Zel'dovich Y. and Novikov I., 1975, The Structure and Evolution of the Universe, Moscow, Nauka

MODERN ASTRONOMY: FROM THE EARLY UNIVERSE TO EXOPLANETS AND BLACK HOLES

Magnetic multipoles of the Sun from observations of the mean magnetic field

V. Haneychuk

Crimean Astrophysical Observatory of the Russian Academy of Sciences, Nauchny, Crimea, 298409 Russia

Abstract. The data of the mean magnetic field (MMF) of the Sun from the Wilcox Solar Observatory from 1975 to 2023 (49 years, number of daily measurements $N = 14516$) were analyzed to identify the main periodicities over short time intervals. The wavelet-spectrum of these data shows that the MMF has significant rotational harmonics from the first to the third, although sometimes there are higher orders up to the sixth harmonic inclusively. Each of these harmonics corresponds to its own multiplet of the magnetic field (dipole, quadrupole and higher components). Rotation harmonics were identified in the original data series and an approximated time series was built from them. In this case, wavelet-spectrum data and refined parameters of sinusoids obtained using the least squares method were used. The constructed approximated data series contains more than 90% of the power of the original series.
The main components of the Sun's rotation change their amplitude, frequency and phase over time. Changes in the amplitude of oscillations occur depending on solar activity–they are usually maximal in the second half of the cycle. Rotational frequencies change over time, but do not show dependence on solar activity. The maximal amplitude of rotation component most often has a frequency of the main period of about $P \approx 27$ day (55.4% in time), as well as its half value $P/2 \approx 13.5$ day (38.2%); the share of periods $P/3 \approx 9$ day is 6.1%, the rest–no more than 0.3%. This means that the Sun predominantly appears as a magnetic horizontal dipole (≈55% of the time), but the quadrupole component is also very significant and occupies 38% of the time. In general, different multipoles are almost always present on the Sun, but the predominance of one or another component of the multipole does not reveal any patterns and is practically independent on solar activity.

Keywords: Sun: magnetic fields, rotation

DOI: 10.26119/VAK2024.105

1 Introduction

The mean magnetic field (MMF) of the Sun as a star is the average value of the magnetic flux from the entire visible solar hemisphere. Its measurements began in 1968 by Severny (1969) at the Crimean Astrophysical Observatory, and then continued in other observatories.

The periodicity of MMF has been studied by different authors, see, for example, Rivin & Obridko (1992), Haneychuk (1999), Chaplin et al. (2003), Haneychuk et al. (2003), Kotov (2020), Haneychuk & Kotov (2021). As has been shown, the main changes in the MMF are associated with the rotation of the Sun. This can be seen directly in the measurement data themselves, and, of course, in the power spectra or periodograms, where peaks in the region of 26–27 days dominate. This main harmonic of the rotation of the MMF is associated with the magnetic horizontal dipole of the Sun. The second harmonic of rotation has a period of about 13.5 days and is associated with the quadrupole component of the magnetic field. Higher harmonics reflect the presence of higher multipoles.

This article analyzes changes in the MMF over 49 years of observations in order to identify the main multipoles or their horizontal components present on the surface of the Sun.

2 Observation

To analyze changes in the MMF, an observational data of the Wilcox Solar Observatory (Scherrer et al. 1977) was used, because it is homogeneous, the longest and most numerous. Observations have been carried out on the same instrument since 1975 and continues to this time. One measurement per day is made, taking into account the zero position of the magnetograph. The data is published on the Internet on the observatory website[1].

The observation period from 1975 to 2023 was taken for the study, the number of measurements was $N = 14516$, the total duration of the series T was about 49 years. The measurements cover more than four cycles of solar activity. The original values of the MMF usually do not exceed 1 Gauss in modulus, and at a minimum they are no more than 0.5 Gauss. Positive values correspond to the northern polarity of the magnetic field, negative ones–to the southern polarity.

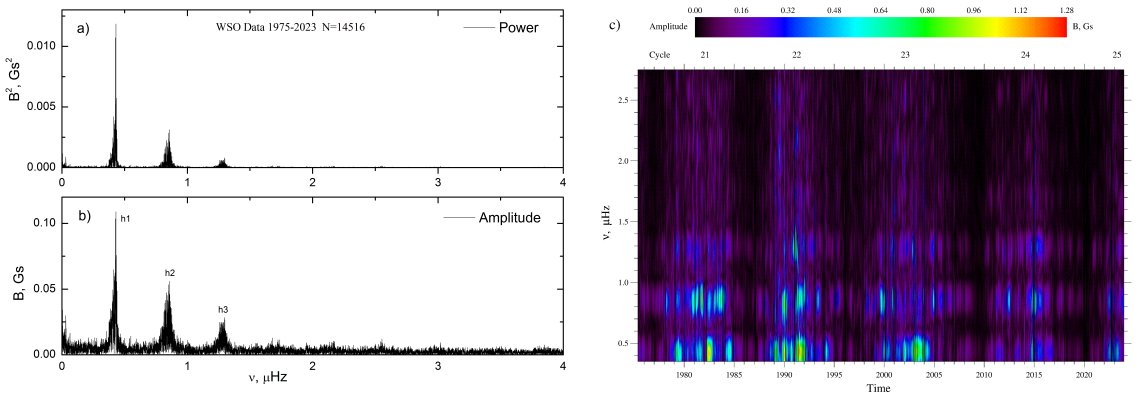

Fig. 1. a) Power spectrum of the MMF, along the x axis–frequency in μHz, along the y axis–power in Gs^2. b) Amplitude spectrum of the MMF, along the x axis–frequency, along the y axis–amplitude in Gs. c) Wavelet spectrum of the MMF, along the x axis–time in years, along the y axis–frequency in μHz, the horizontal bar at the top shows the oscillation amplitude in Gs.

3 Spectra of observational data

Figure 1(a) shows the power spectrum of the studied series of the MMF. Three groups of peaks associated with the rotation of the Sun are clearly visible on it. The highest peak corresponds to the main rotation harmonic with a period P of about 27 days. The second most powerful group of peaks corresponds to the second harmonic of rotation with periods in the region of $P/2 \approx 13.5$ day. The third, smallest in power, group of peaks in the region of $P/3 \approx 9$ day is also noticeable. No higher rotation harmonics are observed. For a more detailed search for high harmonics, the amplitude spectrum of this series of MMFs was constructed (Fig. 1(b)). The first three fundamental harmonics of rotation are marked on the graph. Higher harmonics do not show themselves here either.

Figure 1(c) shows the wavelet spectrum of the studied series, which shows the change in the amplitude of MMF oscillations with time. The window width was taken to be 60 days. The graph clearly shows that the maximum amplitudes of oscillations are observed during the maximum of solar activity, which can be seen also directly from observational data. It can also be seen that there are three horizontal bands of increased power, which correspond to the first three harmonics of rotation. Here, however, it is noticeable that there is a certain oscillation power in the region of higher frequencies, which corresponds to harmonics from the fourth to the sixth.

[1] http://wso.stanford.edu/

They are not preserved in the spectra of the entire data series (Fig. 1(a, b), since they have a random phase and small amplitudes.

From Fig. 1 it follows that the studied MMF series contains mainly the first three harmonics of rotation. This means that we can try to approximate the original data with sinusoids of these harmonics. In this way they can be separated and then examined in detail.

4 Approximation of the original data series

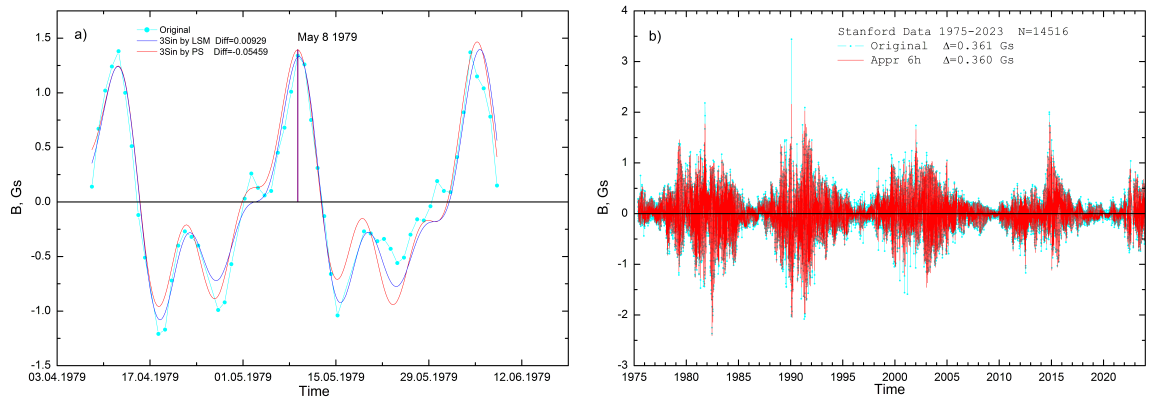

Fig. 2. a) An example of approximation of the original data series for May 8, 1979: cyan color–original data, red color–approximation by sum of three sinusoids from the power spectrum, blue–sum of three sinusoids calculated by the least squares method; the vertical line marks the point for which the approximation was carried out. b) Comparison of the original data series (cyan color) and the artificial series constructed from the main harmonics of rotation (red color).

For each point of the original time series, a region around it was selected in an interval of ±30 days (two rotation periods), in which the data were approximated by sinusoids $y(t) = A_0 + A\cos(\omega t - \varphi)$. The initial values of the sinusoid parameters A_0, A, ω, φ were determined from the spectrum of this section for the maximum oscillation power. Then the first component was subtracted from the original series and the parameters of the second component were determined from the spectrum of residuals, etc. In this way, this region of the time series was approximated. Figure 2(a) shows an example of approximation for data on May 8, 1979. The sum of three sinusoids determined from the power spectrum is shown in red. To refine the parameters of the sinusoids, the least squares method (LSM) was used. The blue curve shows the LSM sinusoids approximation. For most points in the series, three sinusoids quite

satisfactorily describe changes in the MMF. However, for some points this was not enough, and then higher components were used–up to the sixth inclusive. The final criterion for selecting the approximation curve was the minimum deviations of the constructed curve from the original point.

Figure 2(b) shows a comparison of the approximated MMF series (red) with the original (cyan). The standard deviation of the two series is almost the same: $\Delta_o = 0.361$ Gs for the original series and $\Delta_a = 0.360$ Gs–for the approximated one. The original series in peak field values is larger than the approximated one. However, there are few such points. More than 90% of the power of the original data is contained in the approximated series.

5 Basic multipoles of the Sun

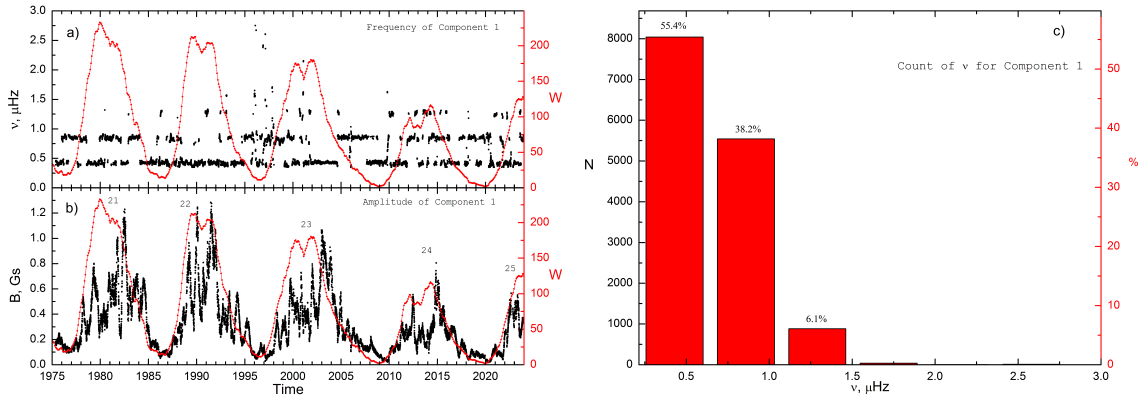

Fig. 3. a) Frequency of the first rotation component (black, left scale) as a function of time; red color–Wolf numbers curve (right scale). b) Amplitude of the first rotation component (black, left scale); red color–Wolf numbers curve (right scale). c) Frequency distribution histogram for the first rotation component: N–number of occurances, left scale; percentage–right scale.

Figure 3(b) shows the time course of the amplitude of the main (first) component of the rotation of the MMF (black color) in comparison with changes in the Wolf numbers W (red color). It can be seen that the amplitude follows the course of solar activity. It can be noted, however, that it lags somewhat behind W, especially in odd cycles 21 and 23, and has its maximum closer to the beginning of the decline phase of solar activity. Figure 3(a) shows the change over time in the frequency of the first component of rotation of the MMF (black color) and the Wolf number W (red color). Three horizontal stripes are noticeable here, which correspond to the

main harmonics of rotation or multipoles of the MMF. The lowest band is the basic harmonic (dipole), the second is the quadrupole, the third, weakest, corresponds to the period $P/3$. The change in the frequency of the main oscillation (or change in the multipole) occurs in an indefinite manner and does not depend on solar activity.

In the 21st cycle of activity on the Sun, both dipole and quadrupole components were present approximately equally in time, but at its end–in 1984–the longest interval of the dipole field began until the end of 1995. After that, at a minimum of 1996–1998 a predominance of high multipole components was observed, up to the sixth harmonic inclusive, which is very unusual for the Sun. In subsequent cycles 23–25, the Sun appeared alternately as a dipole and quadrupole with some more noticeable proportion of the octupole component. In general, different multipoles are almost always present on the Sun, but the predominance of one or another component of the multipole does not reveal any patterns and is independent on solar activity.

Figure 3(c) shows a histogram of the frequency distribution for the first rotation component. Each vertical bar shows the number N of occurrences of the main rotation components or multipoles (left red scale in percentage). The frequency of the basic rotation period $P \approx 27$ day occurs in 55.4% of cases, the second harmonic–in 38.2% of cases; the share of periods with $P/3 \approx 9$ days is 6.1%, the rest–no more than 0.3%. This means that the Sun appears predominantly as a magnetic horizontal dipole ($\approx 55\%$ of the time), but the quadrupole component is also very significant and occupies 38% of the time.

Funding

This work was supported by the Ministry of Science and Higher Education of the Russian Federation within the framework of the state assignment on the topic “General and local characteristics of the Sun”, state registration No. 122022400224-7.

References

Chaplin W.J., Dumbill A.M., Elsworth Y., et al., 2003, Monthly Notices of the Royal Astronomical Society, 343, 3, p. 813
Haneychuk V.I., 1999, Astronomy Reports, 43, 5, p. 330
Haneychuk V.I., Kotov V.A., Tsap T.T., 2003, Astronomy & Astrophysics, 403, p. 1115
Haneychuk V.I. and Kotov V.A., 2021, Open Astronomy, 30, 1, p. 176
Kotov V.A., 2020, Acta Astrophysica Taurica, 1, 2, p. 6
Rivin Y.R. and Obridko V.N., 1992, Soviet Astronomy, 36, 5, p. 557
Severny A.B., 1969, Nature, 224, 5214, p. 53
Scherrer P.H., Wilcox J.M., Svalgaard L., et al., 1977, Solar Physics, 54, 2, p. 353

MODERN ASTRONOMY: FROM THE EARLY UNIVERSE TO EXOPLANETS AND BLACK HOLES

Diversity and similarity of linear polarization among low-albedo NEAs: extremely high polarization of NEA 25330 (1999 KV4)

N. Kiselev[1,2], M. Shcherbina[2], V. Busarev[3], E. Zhuzhulina[1], N. Karpov[2], and A. Shein[2]

[1] Crimean Astrophysical Observatory of the Russian Academy of Sciences, Nauchny, Krym, 298409 Russia
[2] Institute of Astronomy of the Russian Academy of Sciences, Pyatnitskaya str., 48, Moscow, 119017 Russia
[3] Lomonosov Moscow State University, Sternberg Astronomical Institute, Universitetsky pr., 13, Moscow, 119234 Russia

Abstract. This study explores the diversity and similarity of linear polarization among low-albedo Near-Earth Asteroids (NEAs), focusing on the exceptionally high polarization of NEA 25330 (1999 KV4). Polarimetric observations are essential for understanding the physical properties of NEAs, providing insights into the nature of scattering particles and ambient physical processes that cannot be achieved using other observational methods.

Keywords: Polarimeters; polarimetric observations; asteroids: NEA 25330

DOI:10.26119/VAK2024.106

1 Introduction

Scattered radiation resulting from the interaction of unpolarized radiation with various media exhibits several properties, one of which is linear polarization. Consequently, polarimetric observations provide valuable insights into the nature of scattering particles and ambient physical processes that cannot be achieved using other observational methods.

There are several reasons for conducting polarimetric investigations of Near-Earth Objects (NEOs):

1. Obtaining the maximum phase dependence of polarization, including the polarization maximum.
2. Comparing polarization properties of comet-asteroid transition objects in the asteroid-comet continuum (ACC).
3. Identifying primitive asteroids with high volatile content that can form temporary atmospheres near the Sun.
4. Studying the physical properties of small, kilometer-sized bodies to compare surface properties of asteroids with different origins and regolith maturity.
5. Clarifying light scattering mechanisms by dust particles for various ACC objects.
6. Addressing the asteroid-comet hazard problem.

2 Observation results and analysis

Since 2019, polarization phase-angle data for 19 NEAs have been collected using the 2.6-meter telescope at the Crimean Astrophysical Observatory and the 2-meter telescope at Peak Terskol Observatory. Seventeen of these NEAs were observed for the first time, including medium-albedo S-type, high-albedo E-type (2010 XC15), and low-albedo asteroids. The polarization phase dependencies of these NEAs are illustrated in Fig.1, with a focus on low-albedo NEAs.

NEA 25330 (1999 KV4) showed a high polarization of 38.5% at a 75.7-degree phase angle. Its phase dependencies are similar to the NEAs 101955 (Bennu), 152679 (1998 KU2), and 162173 (Ryugu), allowing them to be grouped (see red curve 1 in Fig.1). Between phase angles of 30 to 50 degrees, NEA 25330's R-band polarization curve matches that of comet C/1995 O1 (Hale–Bopp) (Kiselev & Velichko 1997), though their wavelength dependencies differ.

Another group of dark asteroids with similar polarization phase dependencies (curve 3) includes 1580 (Betulia), 2100 (Ra-Shalom), and newly discovered 417264 and 37638. NEAs 159402 and 52768 (curve 4) likely resulted from the breakup of a parent body near the Sun (Kiselev et al. 2024; Emel'yanenko & Kartashova 2023).

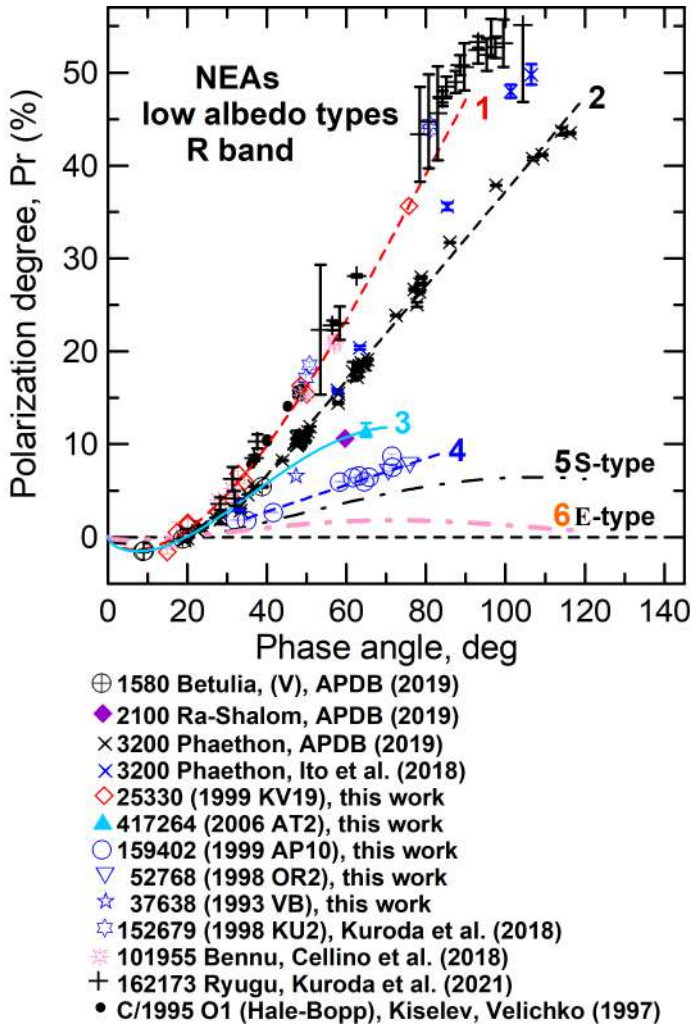

Fig. 1. Phase angle dependence of polarization (PDP) of NEAs observed with the 2.6-m telescope of the Crimean Astrophysical Observatory and the 2-m telescope of the Peak Terskol Observatory from 2019 to 2024. Data on previously observed NEAs are taken from APDB (Emel'yanenko & Kartashova (2023) and references therein). Curves 1–4 represent four groups of NEAs with differing characteristics (Kuroda et al. 2018; Cellino et al. 2018; Kuroda et al. 2021). For comparison, the average PDP of S-type NEAs (Curve 5) and PDP of E-type NEAs (Curve 6) are also shown.

Most NEA 3200 (Phaethon) data fall within the synthetic phase curve (2) margins (Lupishko 2019), but Ito et al. (2018) showed higher polarization, possibly due to Phaethon's activity. NEA 162173 (Ryugu) also shows high polarization at large phase angles, potentially indicating activity and a cometary origin with surface ice (Miura

et al. 2022). Large phase angles at small heliocentric distances can increase the photometric activity of NEAs, increasing the probability of detecting polarization changes.

3 Conclusions

New polarimetric observations of five low-albedo NEAs at large phase angles are presented, including the discovery of the asteroid 25330 (1999 KV4) with an extremely high degree of polarization. Currently, polarization data are available for only 11 NEAs. NEAs can be grouped into four clusters with close synthetic polarization curves. Additional observations are needed to study the diversity and similarity of polarization among low-albedo NEAs.

It can be assumed that the asteroid 25330 (1999 KV4), exhibiting a high degree of polarization, shows signs of sublimation activity.

Acknowledgements. The authors appreciate the Large-Scale Research Facilities (LSRF) "Zeiss-2000 Telescope" at the Core Shared Research Facilities (CSRF) "Peak Terskol Observatory" of INASAN for the opportunity to conduct the NEA observation program.

Funding

RSF grant No. 22-12-00115.

References

Cellino A., Bagnulo S., Belskaya I., et al., 2018, Monthly Notices of the Royal Astronomical Society: Letters, 481, 1, p. L49

Emel'yanenko V. and Kartashova A., 2023, INASAN Science Reports, 8, 6, p. 306

Kiselev N. and Velichko F., 1997, Earth, Moon, and Planets, 78, 1/3, p. 347

Kiselev N., Savushkin A., Petrov D., et al., 2024, Monthly Notices of the Royal Astronomical Society, 527, 2, p. 3174

Ito T., Ishiguro M., Arai T., et al., 2018, Nature Communications, 9, id. 2486

Kuroda D., Ishiguro M., Watanabe M., et al., 2018, Astronomy & Astrophysics, 611, id. A31

Kuroda D., Geem J., Akitaya H., et al., 2021, Astrophysical Journal Letters, 911, 2, id. L24

Lupishko D., 2019, NASA Planetary Data System

Miura H., Nakamura E., Kunihiro T., 2022, Astrophysical Journal Letters, 925, 2, id. L15

MODERN ASTRONOMY: FROM THE EARLY UNIVERSE TO EXOPLANETS AND BLACK HOLES

Fire-hose instability of the torsional Alfven oscillation as a mechanism of plasma layering in an experimental coronal solar loop-type magnetic arch

S. Koryagin[1,2] and M. Viktorov[1,2]

[1] A.V. Gaponov-Grekhov Institute of Applied Physics of the Russian Academy of Sciences, 46 Uljanova str., Nizhny Novgorod, 603950 Russia
[2] Lobachevsky State University, 23 Gagarin ave., Nizhny Novgorod, 603022 Russia

Abstract. The compact experimental setup "Solar Wind" (IAP RAS) is designed for modeling plasma processes in a magnetic arch of the coronal solar loop type. Arc discharges at the bases of the arch create plasma with a significantly increased ionic temperature along the magnetic force line. Optical images show that the plasma rope is stratified into two belts along the upper and lower vaults of the arch or as a near-wall cylindrical layer. The system stratifies when the longitudinal ionic pressure at the top of the loop is 2 times the magnetic pressure. The indicated pressure ratio coincides with the threshold value for the development of the fire-hose instability of the Alfven wave in a plasma with temperature anisotropy. We propose a variant of the growing torsional Alfven oscillation as a mechanism for the formation of a cylindrical layer along the plasma tube wall.

Keywords: instabilities; magnetohydrodynamics; plasmas; Sun: coronal mass ejections, filaments, prominences

DOI: 10.26119/VAK2024.107

1 Introduction

The solar corona is structured into a system of plasma arches (loops) whose characteristic length varies from the height of a homogeneous chromosphere to a value on the order of the solar radius (Zaitsev & Stepanov 2008). Magnetic loops are waveguides and resonators for the Alfven wave, magnetic and ionic sound (Stepanov et al. 2012). The small diameter of the loops compared to their length limits the plasma pressure inside them at a level well below the magnetic pressure. An increase in plasma pressure to a higher value is accompanied by flute instability (of Alfven-type surface wave) with plasma ejection at the apex of the arch.

In turn, the solar wind is characterized by a higher plasma pressure compared to the magnetic pressure, as well as by anisotropic ionic temperature relative to the direction of the local magnetic field (due to different degrees of plasma expansion along and across the magnetic force line). As a possible mechanism of isotropization of ion temperature, Yoon et al. (2019) consider the fire-hose and mirror instabilities (turbulence) of the Alfven and magnetosonic waves. The fire-hose and mirror instabilities are essentially a Weibel instability modified by the magnetic field and originates from a part of the ion (or electron) current caused by the scattering of particles on an inhomogeneous wave magnetic field (Mikhailovskii 1974, Ch. 15, 18).

2 Experimental setup "Solar Wind"

The compact laboratory setup "Solar Wind" (Viktorov et al. 2019) creates a plasma system of the coronal solar loop type in a vacuum chamber with a diameter of $D = 15$ cm. The pulse solenoid coils enclose two mutually perpendicular radial ports of the vacuum chamber and form a curved magnetic tube resembling a quarter arc of a circle. A localized vacuum arc discharge on an aluminum cathode with a diameter of 10 mm is located on the central axis of each of the solenoids and injects a plasma cloud into the base of the magnetic arc. The plasma cloud expands along the magnetic force line at a velocity $v_{i\|} = 15$ km/s, which is 3.5 times the ion-sonic velocity for a characteristic electron temperature of 3 eV and charge number of ions $Z = 1.7$. A 20 μs discharge generates a plasma blob with a length of 2 diameters of the vacuum chamber, or approximately 2.5 of the arch length $L_{\rm loop} = \pi D/4$. Encountering supersonic blobs (from each arch base) jointly form a plasma system with zero hydrodynamic velocity but increased ionic temperature along the magnetic force line.

Optical images with a long exposure time of 1 s (compared to the time of the system's existence) revealed the plasma rope layering into two belts along the upper and lower vaults of the arch or compression into a narrow cylindrical layer along the

arch wall (Viktorov et al. 2019). Photographs were taken from the facade of the arch, so it is not possible to choose one of the stratification variants. Layering was recorded at an arc discharge current $I_{\rm gen} = 8$ kA, which corresponds to an ionic density at the base of the loop (in one stream) $n_{\rm i\,foot} = 2 \cdot 10^{14}\,(I_{\rm gen}/1\ {\rm kA})\ {\rm cm}^{-3} = 1.6 \cdot 10^{15}\ {\rm cm}^{-3}$ (Viktorov et al. 2015). The tube expands $\sqrt{\alpha} = 3$ fold from a diameter of 10 mm at the foot to about 30 mm at the apex of the arch. Increasing the cross-sectional area of the rope by $\alpha = 9$ fold reduces the ion density on the way to the top to $n_{\rm i\,top} = n_{\rm i\,foot}/\alpha = 1.8 \cdot 10^{14}\ {\rm cm}^{-3}$. The longitudinal thermal pressure from the two plasma flows reaches the level $P_{\rm pl\|} = 2 n_{\rm i\,top} m_{\rm i} v_{\rm i\|}^2 = 3{,}7 \cdot 10^4\ {\rm dyn/cm}^2$, which is about 1.9 times the magnetic pressure $P_{\rm mag} = B_0^2/(8\pi) = 1.9 \cdot 10^4\ {\rm dyn/cm}^2$ for the unperturbed induction $B_0 = 700$ G at the same point (ion mass $m_{\rm i} = 27$ u).

The ratio of longitudinal plasma and magnetic pressures, $\beta_\| = P_{\rm pl\|}/P_{\rm mag}$, close to two, indicates the possible development of fire-hose instability of the Alfvén wave and magnetic sound (Mikhailovskii 1974, § 18.7–18.9); (Krall & Trivelpiece 1973, Ch. 3, § 10). The observed belts or cylindrical layer are strongly extended along the arch for a distance significantly larger than the plasma rope radius. Therefore, the local wave vectors of the waves (whose superposition forms a perturbation of the plasma density) are oriented almost perpendicular to the external magnetic field. For the indicated direction of the wave vector, the fire-hose instability of the magnetic sound is suppressed, whereas for the Alfven wave the threshold relation $\beta_\| = 2$ is the same for any wave vector.

3 Unstable torsional Alfven oscillation

Based on the energy principle of Bernstein et al. (1958), the perturbation of the magnetic field in vacuum (outside the plasma tube) has a stabilizing effect on magnetohydrodynamic instabilities, in particular, the fire-hose one. Therefore, we considered the azimuthally uniform (torsional) Alfven oscillation, which differs from the other wave modes by the zero radial component of the magnetic induction and therefore is completely localized inside the plasma rope without leaking into the vacuum (provided that the longitudinal plasma current integral over the cross section of the tube is zero).

The radial profile of the only nonzero – azimuthal – component of magnetic induction $\delta B_\phi(\rho)$ is quite arbitrary (as long as the wavelength in the radial coordinate ρ exceeds the ionic Larmor radius). This property is reflected in the dispersion equation for the square of the complex frequency $\omega = {\rm i}\gamma$ of the Alfven wave in a homogeneous plasma

$$\omega^2 = (c_{\rm A}^2 - v_{\rm i\|}^2)\, k_\|^2, \tag{1}$$

which contains only the component $k_\parallel$ of the wave vector parallel to the external magnetic field $\mathbf{B}_0$. Here, $c_\mathrm{A}^2 = B_0^2/(4\pi n_{\mathrm{i}\Sigma} m_\mathrm{i}) \equiv 2v_{\mathrm{i}\parallel}^2/\beta_\parallel$ is the square of Alfven velocity, $n_{\mathrm{i}\Sigma}$ is the total ion density over the streams, $\gamma = -\mathrm{i}\omega$ is the complex wave increment.

We have considered the paraxial Euler equation of ideal magnetic hydrodynamics for the azimuthal displacement $\xi_\phi(\eta, z)$ of a plasma element in a torsional Alfven oscillation as a model equation of the fire-hose instability in a longitudinally inhomogeneous magnetic tube (neglecting the tube curvature linking different azimuthal modes)

$$m_\mathrm{i} n_{\mathrm{i}\Sigma} \frac{\partial^2 \xi_\phi}{\partial t^2} = \frac{\partial}{\partial z}\left[m_\mathrm{i} n_{\mathrm{i}\Sigma} \left(c_\mathrm{A}^2 - v_{\mathrm{i}\parallel}^2\right) \frac{1}{\sqrt{B_0}} \frac{\partial \left(\sqrt{B_0}\, \xi_\phi\right)}{\partial z} \right]. \tag{2}$$

Here, the Alfven velocity c_A and the ion density $n_{\mathrm{i}\Sigma}$ depend on the coordinate z, measured from the apex of the arch along the central magnetic force line in the tube; the radial coordinate $\eta = \rho/r_\perp(z)$ is normalized by the tube radius $r_\perp(z) = r_\perp(0)\sqrt{B_0(0)/B_0(z)}$ and is therefore constant along the magnetic force line. The radial electric intensity δE_ρ and the magnetic induction perturbation δB_ϕ are related to the displacement ξ_ϕ by the equalities

$$\delta E_\rho = -\frac{B_0}{c}\frac{\partial \xi_\phi}{\partial t}, \qquad \delta B_\phi = \sqrt{B_0}\,\frac{\partial \left(\sqrt{B_0}\,\xi_\phi\right)}{\partial z}, \tag{3}$$

which reflect the dominant joint electric drift of ions and electrons at a velocity of $\partial\xi_\phi/\partial t = -c\,\delta E_\rho/B_0$ (for processes with frequency/increment below the ion cyclotron frequency) and the electromagnetic induction equation $\mathrm{rot}\,\delta\mathbf{E} = -c^{-1}\,\partial\,\delta\mathbf{B}/\partial t$ (taking into account the change of the distance ρ between magnetic lines of force inversely proportional to $\sqrt{B_0}$ when moving along the tube).

In the region of fire-hose instability near the apex of the arch ($c_\mathrm{A}(z) < v_{\mathrm{i}\parallel}$), only the difference $c_\mathrm{A}^2 - v_{\mathrm{i}\parallel}^2$ in eq. (2) varies significantly, changing its sign at points equidistant from the apex. Therefore, we approximate this value by a quadratic function

$$c_\mathrm{A}^2 - v_{\mathrm{i}\parallel}^2 \approx -v_{\mathrm{i}\parallel}^2\left(1 - \frac{2}{\beta_{\parallel\,\mathrm{top}}}\right) + c_{\mathrm{A\,foot}}^2\left(\frac{2z}{L_\mathrm{loop}}\right)^2,$$

where $\beta_{\parallel\,\mathrm{top}} > 2$ is the ratio of longitudinal plasma and magnetic pressures at the apex of the arch, $c_{\mathrm{A\,foot}} \gg v_{\mathrm{i}\parallel}$ iis the the Alfven velocity at the bases of the tube, which are $L_\mathrm{loop}/2$ away from the apex. The Euler eq. (2) takes the form of the Legendre equation for time-dependent perturbations following the exponential law with an increment γ, or complex frequency $\omega = \mathrm{i}\gamma$:

$$\frac{\partial}{\partial\zeta}\left(1-\zeta^2\right)\frac{\partial\xi_\phi}{\partial\zeta} + \kappa^2\xi_\phi = 0, \tag{4}$$

where the complex parameter

$$\kappa = \frac{\gamma L_{\rm loop}}{2 c_{\rm A\,foot}} ,$$

and the dimensionless coordinate

$$\zeta = \frac{2z}{L_{\rm loop}} \frac{c_{\rm A\,foot}}{v_{\rm i\parallel} \sqrt{1 - (2/\beta_{\parallel\,\rm top})}} .$$

Equation (4) must be accompanied by a boundary condition in the form of zero displacement ξ_ϕ at the tube bases, at the points $\zeta = \pm c_{\rm A\,foot}/[v_{\rm i\parallel} \sqrt{1 - (2/\beta_{\parallel\,\rm top})} \gg 1$ — zero tangential electric intensity eq. (3) on the metal cathode of the arc discharge. At the same time, the zeroing of the coefficient at the highest derivative in eq. (4) at the points $\zeta = \pm 1$ (at the boundary of the fire-hose instability region) requires an auxiliary regularization of the solution in the form of the equality of the displacement ξ_ϕ and its spatial derivative $\xi'_\phi \equiv \partial \xi_\phi / \partial \zeta$ (providing continuity of magnetic induction and electric intensity eq. (3)) at small, but non-zero distance ε from the singular points $\zeta = \pm 1$: $\xi_\phi(1-\varepsilon) = \xi_\phi(1+\varepsilon)$, $\xi'_\phi(1-\varepsilon) = \xi'_\phi(1+\varepsilon)$. Transition regions $|\zeta \mp 1| \le \varepsilon$ have an extent on the order of the distance traveled by an ion for a quarter of its cyclotron period $\omega_{Bi\,\rm top}^{-1}$: $\varepsilon \sim c_{\rm A\,foot}/[\omega_{Bi\,\rm top} L_{\rm loop} \sqrt{1 - (2/\beta_{\parallel\,\rm top})}\,]$.

In this approach, exponentially increasing solutions of the hydrodynamic eq. (2) are confined in the spatial region of the fire-hose instability and tunnel outside it to a distance of the order of $\Delta\zeta \sim \varepsilon\,|\ln\varepsilon| \ll 1$. Inside the $|\zeta| < 1 - \varepsilon$ instability region, the longitudinal azimuthal displacement profile $\xi_\phi(\zeta)$ (on the same magnetic force line $\eta = \text{const}$) is described by the sum $\xi_\phi(\eta,\zeta) = \sum_{n=0}^{\infty} a_n(\eta)\,[{\rm P}_\nu(\zeta) + (-1)^n\,{\rm P}_\nu(-\zeta)]/2$ of Ferrers functions of the first kind $\rm P_\nu$ with degree $\nu = n + \delta\nu$ close to integers $n = 0$, 1, 2…, and detuning $\delta\nu \sim 1/|\ln\varepsilon| \ll 1$, and on the outside – an analogous sum $\xi_\phi(\eta,\zeta) = \sum_{n=0}^{\infty} a_n(\eta)\,(-1)^{n\,(1-\mathrm{sign}\,\zeta)/2}\,Q_\nu(|\zeta|)/[2\,Q_\nu(1+\varepsilon)]$ of associated Legendre functions of the second kind Q_ν (Olver et al. 2010, Ch. 14).

Torsional modes of fire-hose "turbulence" increase with incremental time

$$\gamma_n = \frac{2 c_{\rm A\,foot}}{L_{\rm loop}} \sqrt{\nu\,(\nu+1)} \approx \frac{2 c_{\rm A\,foot}}{L_{\rm loop}} \sqrt{n\,(n+1)} , \qquad (5)$$

which is independent of the extent ΔL of the unstable region at the apex of the arch. Such an effect qualitatively follows from the dispersion eq. (1) for the increment $\gamma = -{\rm i}\omega$, in which the wave number is "quantized" as $k_{\parallel n} \sim \pi n/\Delta L \propto 1/\Delta L$. In turn, the extent $\Delta L = L_{\rm loop} v_{\rm i\parallel} \sqrt{1 - (2/\beta_{\parallel\,\rm top})}/c_{\rm A\ foot}$ is linearly proportional to the coupling coefficient $\sqrt{v_{\rm i\parallel}^2 - c_{\rm A\,top}^2}$ between the increment and the wave number in the relation eq. (1).

According to the expression eq. (5), the torsional modes of fire-hose "turbulence" most extended along the magnetic arch are formed in the typical time $\gamma^{-1} \sim L_{\rm loop}/(2c_{\rm A\,foot})$, during which the Alfven wave travels from the base to the top of the arch. At the same order of plasma and magnetic pressures, the indicated time is of the order or shorter than the interaction time of plasma blobs in the experimental setup (see Section 2), which allows us to observe this layer structure.

4 Summary

The plasma system of the coronal solar loop type in the compact experimental setup "Solar Wind" (IAP RAS) is characterized by an elevated ionic temperature along the magnetic force line. This feature gives rise to fire-hose instability of the Alfven wave – a collisionless mechanism of temperature isotropization. The unstable torsional Alfven oscillation is capable of redistributing the plasma from the axis to the wall of the plasma tube (at a high ramp-up rate – of the order of the ion cyclotron frequency) and thereby creating the stratification observed in the experiment in the form of a near-wall cylindrical layer.

Funding

This work was supported by grant 23-12-00317 of the Russian Science Foundation.

References

Bernstein A.B., Frieman E.A., Kruskal M.D., et al., 1958, Proceedings of the Royal Society A: Mathematical, Physical and Engineering Sciences 244, 1236, p. 17

Krall N.A. and Trivelpiece A.W., 1973, Principles of Plasma Physics, McGraw-Hill

Mikhailovskii A.B., 1974, Theory of Plasma Instabilities, v. 1: Instabilities of a Homogeneous Plasma, Springer

Olver F.W.J., Lozier D.W., Boisvert R.F., et al., 2010, NIST Handbook of Mathematical Functions, Cambridge University Press

Stepanov A.V., Zaitsev V.V., Nakariakov V.M., 2012, Coronal Seismology, Wiley-VCH

Viktorov M.E., Golubev S.V., Vodopyanov A.V., 2019, Plasma Physics and Controlled Fusion, 61, 3, p. 035001

Viktorov M.E., Vodopyanov A.V., Golubev S.V., et al., 2015, Technical Physics Letters, 41, p. 901

Yoon P.H., Seough J., Salem C.S., et al., 2019, Physical Review Letters, 123, 14, p. 145101

Zaitsev V.V. and Stepanov A.V., 2008, Physics-Uspekhi, 51, 11, p. 1123

VAK 2024 MODERN ASTRONOMY: FROM THE EARLY UNIVERSE TO EXOPLANETS AND BLACK HOLES 300 years Russian Academy of Sciences

Multi-wavelength observations of the impulsive C2.8 class flare producing photospheric impact at the penumbra region of the leading sunspot in NOAA 13256

G. Koynash[1], I. Sharykin[1], I. Zimovets[1], E. Ivanov[2], V. Kiselev[2], and B. Nizamov[3]

[1] Space Research Institute of Russian Academy of Sciences, Moscow, 117997 Russia
[2] Institute of Solar-Terrestrial Physics of Siberian Branch of Russian Academy of Sciences, Lermontov st., 126a, Irkutsk, 664033 Russia
[3] Sternberg Astronomical Institute, Universitetsky pr., 13, Moscow, 119234 Russia

Abstract. We present the results of a study of the non-eruptive C2.8 class flare in the active region (AR) NOAA 13256, which occurred on March 19,2023 from 02:12 to 02:19 UTC. This event was chosen on the basis of the test launches of the Irkutsk Solar Radio Spectropolarimeter (SOLARSPEL), Badary (ISTP RAS). Despite the low X-ray class and short duration, according to SOLARSPEL data, this impulsive flare had a complex multi-peak fine time structure, recorded at different frequencies in the microwave range. The presence of a photospheric disturbance in the vicinity of the sunspot penumbra, recorded using HMI/SDO, was of great interest for physics and motivated this study. There are few detailed multi-wavelength studies in the literature of low-power flares accompanied by a response at the photosphere level. Notably, this event was observed simultaneously by four X-ray instruments: SoLO/STIX, ASO-S/HXI, FERMI/GBM, and Konus-Wind. As a result, the unique observation conditions of this flare, from the point of view of the available instruments and various recorded physical high-energy processes, motivated us to carry out detailed research. We found that the photospheric perturbations are mostly associated with the stronger magnetic field in the penumbra rather than with the distribution of the HXR sources. The observed flare ribbons were located in the penumbral PIL region, which revealed the complexity of the larger events in terms of the spatial and temporal structure of the energy release. We also briefly discuss the observed quasi-periodic pulsations.

Keywords: Sun: solar flare, radio emission, X-ray emission, photospheric perturbations, magnetic fields

DOI: 10.26119/VAK2024.108

1 Introduction

The selected solar flare (briefly described in the abstract) is investigated due to the following peculiarities that motivated us for this research: relatively low GOES class, multi-peak impulsive energy release in the MW data, presence of photospheric impacts, and relatively simple AR morphology. Moreover, we have an abundance of observational data, making this flare unique for collecting detailed physical information. Today, there are not as many complex case studies of solar flares below the C3.0 class that are accompanied by photospheric perturbations (e.g., Song et al. 2020) in active regions with simple Hale and McIntosh classes. Furthermore, flares with white-light emission and photospheric perturbations are quite rare in the case of C-class flares (see, the statistical work of Song & Tian 2018). The main aim is to study the morphological properties of this particular solar flare: the configuration of the emission sources in the multi-wavelength data relative to each other in the AR and to the positions of the photospheric impacts and magnetic field structure.

2 Observations and Instruments

A selected C2.8 solar flare occurred near the eastern limb (S23E58) in AR NOAA 13256, on March 19, 2023. It began at 02:12 UT, reached its maximum at 02:14:54 UT, and ended at 02:19 UT. The parent AR, where the flare was located, had a Hale β class and a "simple" McIntosh class of Eho, with the magnetic field flux concentrated in a large single leading sunspot, where flare emission sources were also detected. We also registered photospheric disturbances seen in HMI 45 second data: line-of-sight (LOS) magnetograms and Dopplergrams.

This flare was simultaneously observed with the Solar Radio Spectropolarimeter (SOLARSPEL), the Nobeyama Radio Polarimeters (NoRP, Nakajima et al. 1985); Siberian Radio Heliograph (SRH, Altyntsev et al. 1985), the Atmospheric Imaging Assembly (AIA, Lemen et al. 2012), the Helioseismic and Magnetic Imager (HMI, magnetic field and mapping of photospheric impacts, Scherrer et al. 2012) onboard the Solar Dynamics Observatory (SDO); the X-Ray Sensor (XRS) onboard the Geostationary Operational Environmental Satellite (GOES), the Gamma Ray Burst Monitor (GBM, Meegan et al. 2009) onboard the FERMI, the Konus/Wind (Aptekar et al. 2009), the Spectrometer Telescope for Imaging X-rays (STIX, Krucker et al. 2020) on the Solar Orbiter and the Hard X-Ray Imager (HXI, Zhang et al. 2019) on the Advanced Space-based Solar Observatory.

SOLARSPEL is a new radio broadband spectropolarimeter located at the Badary Radioastrophysical Observatory, and its data obtained from test runs allowed us to identify the studied flare due to its impulsive multi-peak MW time series (from event

catalog of the SOLARSPEL test runs). SOLARSPEL and NoRP measure microwave (MW) emission from the entire Sun in multiple frequency channels. The MW flux is measured for a frequency grid of 48 channels in the range from 3 GHz to 24 GHz (for the studied flare, only the 3–12 GHz range is available) with circular polarization for SOLARSPEL with a time cadence of 1 s, and intensity and circular polarization at six frequencies (we detected a polarization signal only at 9.4 GHz) for NoRP with a time cadence of 0.1 s. Periodic background variations in SOLARSPEL data are due to not well-compensated instrumental effects.

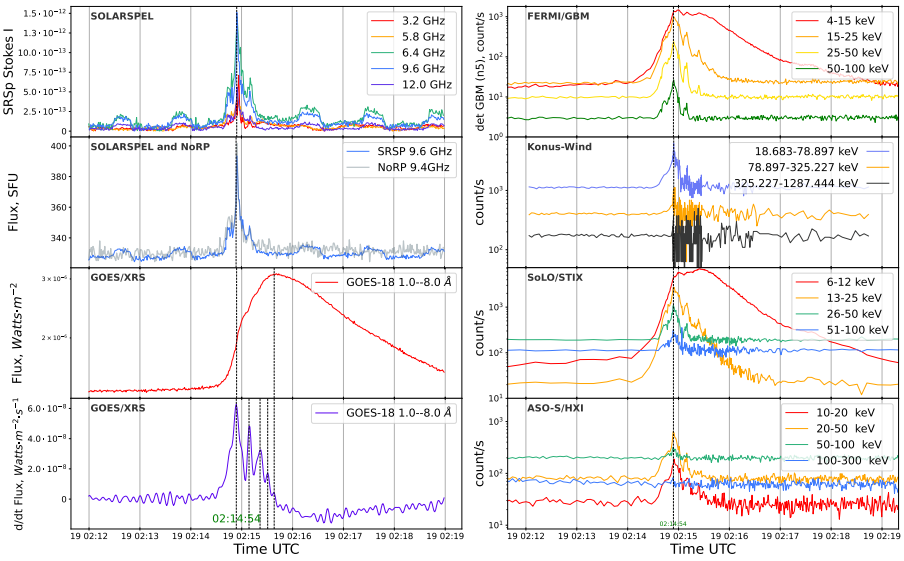

Fig. 1. Overview of the time profiles (TP) of the C2.8 GOES-class solar flare on March 19, 2023 from 02:12 to 02:19 UT. Left side: the SOLARSPEL, NoRP, GOES/XRS TSs and the time derivative of GOES/XRS. Right side: Fermi/GBM, Konus-Wind, SoLO/STIX and ASO-S/HXI.

Figure 1 shows the light curves produced by the mentioned instruments. In top left corner, we present the uncalibrated SOLARSPEL MW data at five frequencies (Stokes I). Below them are the NoRP's MW data for 9.4 GHz and the SOLARSPEL MW data at 9.6 GHz, calibrated with the NoRP's 9.4 GHz data.

3 Data Analysis and Results

We analysed SOLARSPEL and NoRP MW data, finding pronounced polarization in the radio burst. SOLARSPEL showed good sensitivity and temporal resolution with

consistent signals across a wide frequency range. Although we lacked sufficient data to fully calibrate the SOLARSPEL.

The MW and X-ray data reveal that the flare's impulsive phase consisted of a few peaks. In general, X-ray observations are consistent with the Neupert effect. Based on those data, we detected quasi-periodic pulsations (QPP) with a repeat period $P_{\rm R} \approx 12.3 \pm 2.5\,$s. QPP is a common feature of flaring energy releases in the solar atmosphere, observed in all bands, from radio and MW to hard X-rays and gamma-rays (Nakariakov & Melnikov 2009). The physical mechanisms responsible for QPP can be explained by various models (e.g., Zimovets et al. 2021). For this episode, we plan to investigate it more carefully and in detail later.

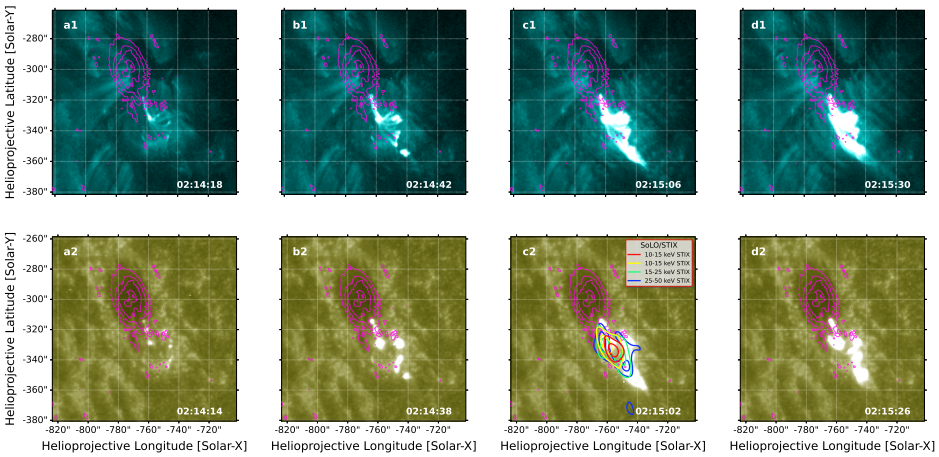

Fig. 2. The sequence of image snapshots with a field of view (FOV) of 130" × 130" of the C2.8 flare observed by SDO/AIA (EUV 131 Å – top row; UV 1600 Å – bottom row) includes SDO/HMI contours of magnetic field [1.0, 1.5, 2.0, 2.5, 3.0] kG, and contours for X-ray energy bands: 4–10 keV (red), 10–15 keV (yellow), 15–25 keV (green), 25–50 keV (blue).

However, these peaks could be connected with the multiple magnetic loops forming a magnetic arcade. To analyse the spatial structure of the flare energy release with the best available spatial resolution, we used AIA images (Fig. 2) at 131 Å (top–Fig. 2) with a time cadence of 12 s, and a low-temperature chromospheric UV band around 1600 Å(bottom–Fig. 2), with a time cadence of 24 s. In 1600 Å, we observe many localized quasi-static brightnings forming large-scale flare ribbons, with the northern one located in the sunspot penumbra. It is noteworthy that the small event shows "complexity" characteristic of large flares and cannot be considered as an "elementary" episode of flare energy release.

The STIX X-ray contour images are shown in Fig. 2(c2). We observe a typical situation with two HXR sources corresponding to the flare ribbons. A more detailed vizualization of high-energy flare processes is presented in Fig. 3. MW contour images from SRH at a few frequencies, X-ray STIX and HXI contour maps cover the AIA 1600 Å map at the flare MW peak in the corresponding figure panels (a–c). The spatial resolution of X-ray images is sufficient to resolve paired HXR sources. In the case of SRH, we observe a single flare source covering the flare UV ribbons or located between the ribbons at the highest frequencies. Possibly, we observe MW coronal sources.

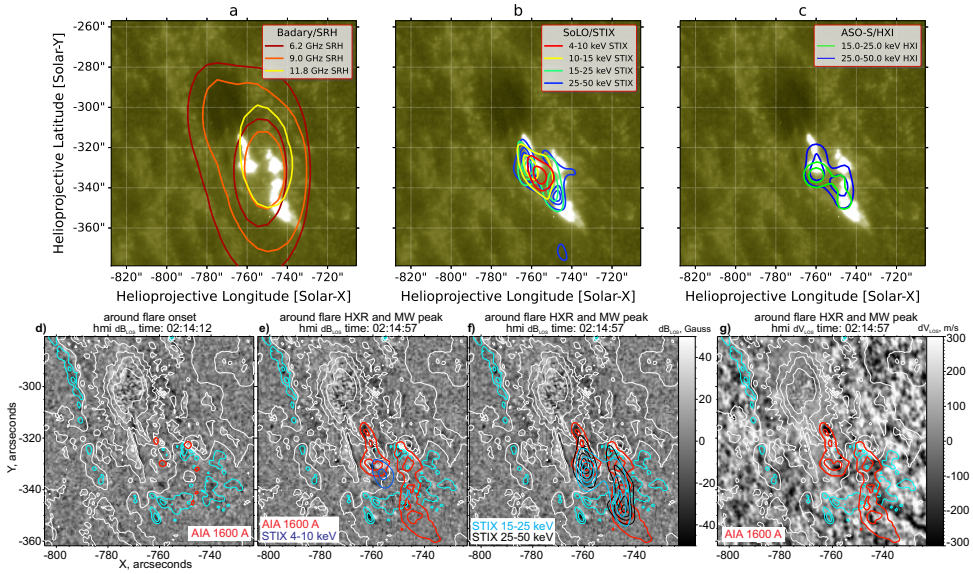

Fig. 3. Top panels show the AIA 1600 Å image with countours of SRH (a), STIX(b), HXI(c) sources. The bottom panels present photospheric perturbation observed in the HMI LOS magnetograms (d–f) and Dopplergram (g). Panel d corresponds to the flare onset, while panels (e–g) show the flare MW peak time. Red contours show the AIA 1600 Å emission sources. STIX contours are also shown in panels (e–f). Contours highlight magnetic field strengths of 1.0, 1.5, 2.0, 2.5, and 3.0 kG, with the PIL location marked by the thick white line. Different polarities are shown by white and cyan.

Weak photospheric perturbations were best observed in HMI 45-second LOS magnetograms and Dopplergrams (Fig. 3). The strongest impacts were detected in the northern ribbon (highlighted by the thick red contour in panel (e), associated with the stronger penumbral magnetic fields compared to the larger ribbon on the other side of the PIL outside the sunspot. It's worth noting that some photospheric perturbations are outside the centroids of the HXR sources (Fig. 3(f)). It seems that

the photospheric perturbation are related to the presence of the strong magnetic field. It is possible that we observe MHD motions of the magnetized plasma due to the magnetic reconnection process. However, it's also possible that some dense narrow beams of energetic particles are not seen in HXR due to the limited dynamic ranges of STIX and HXI. Additional research is needed to understand physics of the changing photospheric magnetic field and Doppler velocity in the flare ribbons.

4 Conclusions

The following conclusions for the studied flare were drawn:

1. The studied C2.8 flare reveals a complexity typical of large events despite the relatively simple morphology of the parent AR. There are two ribbons on either side of the penumbral polarity inversion line (PIL), corresponding hard X-ray sources, and a fine temporal and spatial structure of the energy release.
2. The nature of the observed MW and HXR QPPs is uncertain. The multi-peak time series may be explained by subsequent energy release in separate thin magnetic loops rooted at the flare ribbons, forming the observed fine spatial structure.
3. Photospheric perturbations are registered in the flare ribbon of the sunspot penumbra. There is no exact coincidence with the HXR emission sources. Are the flare photospheric impacts primarily connected with the magnitude and structure of the magnetic field?

Acknowledgements. We thank the numerous team members of the SRH and SOLARSPEL (Badary, ISTP RAS)[4], NoRP, SDO, GOES, STIX, HXI, GBM, and Konus-Wind for providing the data and corresponding analysis software.

References

Altyntsev A.T., Lesovoi S., Globa M., et al., 2020, Solar-Terrestrial Physics, 6, 2, p. 30
Aptekar R.L., Cline T.L., Frederiks D.D., et al., 2009, Astrophysical Journal Letters, 698, 2, p. L82
Krucker Säm, Hurford G.J., Grimm O., et al., 2020, Astronomy & Astrophysics, 642, id. A15
Lemen J.R., Title A.M., Akin D.J., et al. 2012, Solar Physics, 275, 1-2, p. 17
Meegan C., Lichti G., Bhat P.N., et al., 2009, Astrophysical Journal, 702, 1, p. 791
Nakajima H., Sekiguchi H., Sawa M., et al., 1985, Publications of Astronomical Society of Japan, 37, p. 163
Nakariakov V.M. and Melnikov V.F., Space Science Reviews, 2009, 149, 1-4, p. 119
Scherrer P.H., Schou J., Bush R.I., et al., 2012, Solar Physics, 275, 1-2, p. 207.
Song Y., Tian H., Zhu X., et al., 2020, Astrophysical Journal Letters, 893, 1, id. L13
Song Y. and Tian H., 2018, Astrophysical Journal, 867, 2, id. 159
Zhang Z., Chen D.-Y., Wu J., et al., 2019, Research in Astronomy & Astrophysics, 19, 11, id. 160
Zimovets I.V., McLaughlin J.A., Srivastava A.K., et al., 2021, Space Science Reviews, 217, p. 66

[4] https://badary.iszf.irk.ru

BAK 2024 MODERN ASTRONOMY: FROM THE EARLY UNIVERSE TO EXOPLANETS AND BLACK HOLES 300 years Russian Academy of Sciences

Morphology of average time profiles of solar flares in the microwave range

I. Motyk and L. Kashapova

Institute of Solar-Terrestrial Physics of Siberian Branch of Russian Academy of Sciences, Irkutsk, 664033 Russia

Abstract. Average flare time profiles are useful tools for determining energy evolution mechanisms both in the Sun and in stars. The study related to their construction and analysis was done in the visible and ultraviolet spectral ranges. Microwave emission, which is sensitive to various emission mechanisms, was not included in such studies. In this paper, we present the first results of reconstruction and analysis of average time profiles of solar flares using observations with the Siberian Radioheliograph. The events under consideration are flares with simple temporal behavior (without multiple bursts), but emitted in a wide frequency range. The latter feature was necessary to separate the emission of optically thick and optically thin sources. In total, we used 116 events detected during five months of observation in 2023 for the reconstruction. Each profile was normalized to its maximum value and the time scale was transformed into a universal length for all events, by deriving seconds into units equal to half the width of 50% of the maximum value for each event ($t_{\frac{1}{2}}$). The time profiles of optically thin and optically thick emission sources demonstrate similar behaviour. The pulse phase fits well to a fourth-order polynomial function. The decay phase is fitted by two exponential functions. The emission dominance, fitted by one exponent over another, changes at $t_{\frac{1}{2}}$, which is approximately equal to 1.5.

Keywords: Sun: flares; decay phase; microwave emission; average profile

DOI: 10.26119/VAK2024.109

1 Introduction

The time profile of a flare provides information about the dynamics of energy release and transfer processes. Comparison of the time profiles obtained for the same event or object in different spectral ranges usually helps to understand the altitude dynamics of evolution. By comparing the time profile of an event with that of a well-understood process or averaged time profiles, we can confirm or reject a hypothesis. As both solar and stellar flares are often complicated events, the time profiles of simple or "classic" shapes are of special interest for study. Such profiles (and hence flares) have only one peak, with a rapid increase before the peak and a gradual decline after it, without significant fluctuations in intensity. The "classical" averaged time profiles have been obtained and analysed for the UV emission from solar flares (Kashapova et al. 2021), and white light emissions from red dwarf flares (Davenport et al. 2014). The microwave (MW) emissions of flares, and especially solar flares, are assumed to be a powerful instrument for studying plasma processes. However, the averaged time profiles in this spectral range have not been obtained yet. The aim of our study is to construct and carry out a preliminary analysis of the averaged MW time profile based on observations of simple or "classical" solar flares.

2 Observational data and analysis

Usually, microwave emission from solar flares is produced by the gyrosynchrotron mechanism, and their spectra combine the emission from both optically thick and thin sources (Dulk 1985). So, the temporal behaviour of emissions from these parts can differ. For this reason, we need to construct two average time profiles for the optically thin and optically thick spectral parts. To separate MW emissions of different types, we need to analyse the spectrum over a wide range of frequencies with high spectral resolution. The Siberian Radioheliograph (SRH) is a radio telescope for observing the Sun, which allows not only to obtain images in the spectral range of 3–24 GHz, but also information about the "Sun-as-a-star" fluxes with high temporal and spectral resolution. In our study, we reconstructed time profiles using correlation plots by SRH. Time profiles of the sum of the correlation coefficients between pairs of antennas are available, and a more sensitive flux equivalent is assumed (Lesovoi & Kobets 2017). Since we normalize each event time profile, the normalized correlation graphs will from now on be thought of as normalized flux time profiles.

Automatic flare detection provided more than 600 candidates during the period from July to September 2023 and May 2024 (Rozhkova et al. 2024). Of this set, only 116 events meet the criteria for a "classical" flare. Then, on the dynamic spectrum,

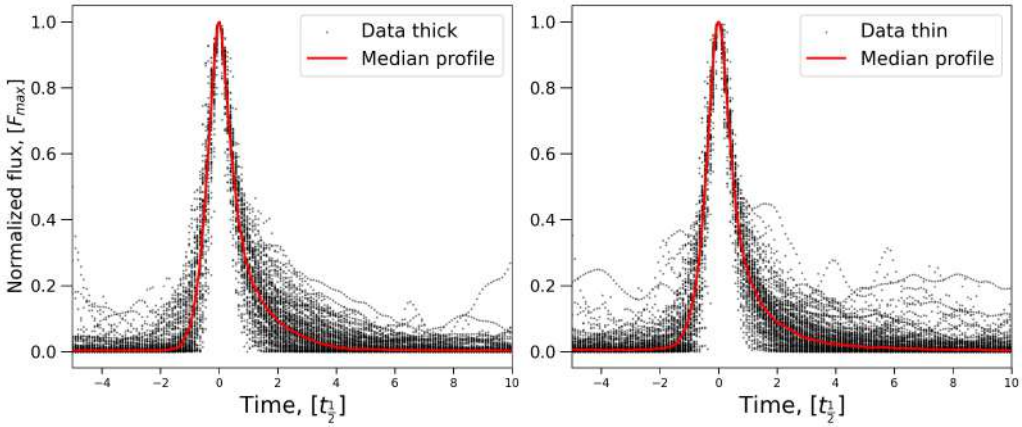

Fig. 1. Overlay of all 116 profiles of optically thick (left panel) and optically thin (right panel) parts of flare emission. Profiles scaled to relative time $t_{\frac{1}{2}}$ and maximum of flux $F_{\max}$.

we found the peak frequency for each event and separated the frequencies of emissions from optically thick and thin sources to get two time profiles. Each profile was normalized and time-scaled as done in Davenport et al. (2014). The timescale unit is the half-width of the time interval between the moments when the time profile reaches 50% of its maximum value ($t_{\frac{1}{2}}$). The temporal resolution of the time profiles was $0.001 \times t_{\frac{1}{2}}$. The average time profiles of optically thick and thin sources (shown in Fig. 1 by the red lines) are constructed by taking the median value for each time bin. The comparison of average time profiles revealed similar behaviour of optically thick and optically thin emissions (Fig. 2, left panel). As microwave gyrosynchrotron emission is the magnetic bremsstrahlung of electrons, this similarity indicates the absence of any additional factors that could distort the emission in an optically thick source, such as heated plasma or cold plasma from eruptions on the flare loop top.

3 An analytical template and summary

An important part of the analysis of the average time profile is its fitting to an analytical template that allows it to be described by a set of analytical functions. We did it for the average time profile of an optically thin source only using approaches from Davenport et al. (2014) and Kashapova et al. (2021). The rise phase is well-fitted by a fourth-order polynomial (Fig. 2, middle panel). We fitted the decay phase (right panel of Fig. 2) with two exponential functions, as was done in previous studies. The breakpoint between the domination of one exponent over another is approximately $1.5\ t_{\frac{1}{2}}$, which coincides with the times obtained by Kashapova et al. (2021) for 1600 Å

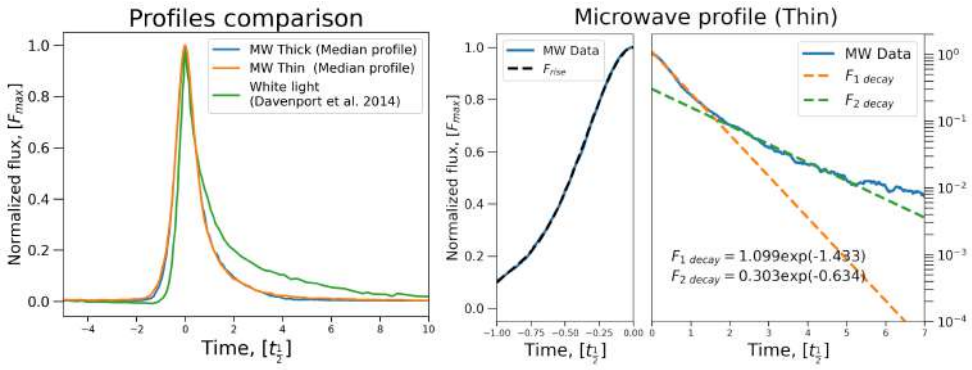

Fig. 2. Comparison of the MW time profiles of optically thick and optically thin radiation with the white light profile from Davenport et al. (2014) (left panel), the MW time profile fitted by 2 exponential functions

and 304 Å spectral bands. The 1700 Å spectral band observed by SDO/AIA is considered to be mostly related to higher levels of energy release. As the time intervals for exponential functions are the same as in Kashapova et al. (2021) ($0 < t_{\frac{1}{2}} < 1.5$ and $3 < t_{\frac{1}{2}} < 6$), then we can compare the dynamics demonstrated by analytical functions. For both exponents, it can be seen that the MW emission decays faster than the UV 1700 Å emission (-1.433 vs -0.800 in $F_{1\ \mathrm{decay}}$ function and -0.634 vs -0.336 in $F_{2\ \mathrm{decay}}$ function for MW and UV 1700 Å emissions, respectively).

This fact indicates that the "pure" gyrosynchrotron mechanism is characteristic of flares with a simple time profile. The obtained average time profiles and analytical templates derived for impulsive and decay phases can be used to analyse flare energy balance and mechanisms in more complex events.

Funding

The study was supported by a grant from the Russian Science Foundation № 24-22-00315, https://rscf.ru/project/24-22-00315/.

References

Davenport J.R.A., Hawley S.L., Hebb L., et al., 2014, Astrophysical Journal, 797, 2, id. 122
Dulk G.A., 1985, Annual Review of Astronomy and Astrophysics, 23, p. 169
Kashapova L.K., Broomhall A.M., Larionova A.I., et al., 2021, Monthly Notices of the Royal Astronomical Society, 502, 3, p. 3922
Lesovoi S.V. and Kobets V.S., 2017, Solar-Terrestrial Physics, 3, 1, p. 19
Rozhkova D.V., Kashapova L.K., Gubin A.V., 2024, Modern Astronomy: from the early Universe to Exsoplanets and Black Holes, Proc. All-Russian Astron. Conf., this Issue

MODERN ASTRONOMY: FROM THE EARLY UNIVERSE TO EXOPLANETS AND BLACK HOLES

The structure of the chromosphere along the northern limb of the Sun according to eclipse observations with RT-22 PRAO AKTs FIAN at a wavelength of 1.4 cm

V. Nagnibeda[1], N. Topchilo[1], A. Kovalenko[2], and I. Rakhimov[3]

[1] St. Petersburg State University, Universitetskaya Embankment, 7-9, St. Petersburg, 199034 Russia
[2] Pushchino Radio Astronomy Observatory, Astro Space Center, Lebedev Physical Institute, Russian Academy of Sciences, Pushchino, Moscow oblast, 142290 Russia
[3] Institute of Applied Astronomy of the Russian Academy of Sciences, Kutuzova Embankment, 10, St. Petersburg, 191187 Russia

Abstract. An acute problem in the study of the solar chromosphere is the following obvious contradiction between the results of radio astronomical measurements of the height (extension) of the chromosphere and model calculations made on the basis of classical standard atmospheric models: the height of the chromosphere according to radio data is significantly greater than the model calculations. This is largely due to the fact that the widely used models are based on UV observations and, in addition, are one-dimensional and do not take into account the strong structural inhomogeneity of the chromosphere. Numerous attempts to "improve" the models by introducing various elements of inhomogeneity and "fit" them to radio data are purely empirical and are not substantiated theoretically. In such a situation, it is important to obtain more accurate and reliable radio observation data. This is all the more important because such data can serve as a basis for testing the recently developed 3D inhomogeneous theoretical models of the solar atmosphere. The article presents new data obtained from observations of a partial solar eclipse on June 10, 2021, using the RT-22 radio telescope of the Lebedev Physical Institute at a wavelength of 1.4 cm: the estimate of the radio radius is not more than 13″. The contradictions mentioned above remain significant.

Keywords: Sun: chromosphere, radio radiation, solar eclipse

DOI: 10.26119/VAK2024.110

1 Introduction

Back in the late 1940s, I.S. Shklovsky showed that the solar corona is almost completely transparent to the short-wavelength (millimeter and short-wavelength part of the centimeter) radio wave range. This explains the accepted point of view that the observed short-wave radio emission from the quiet Sun arises in the chromosphere. It is important to note that it is generated in thermal plasma due to the bremsstrahlung under LTE conditions, and the Rayleigh-Jeans approximation for the Planck function ensures direct proportionality of the measured brightness temperature of radio emission ($T_{\rm b}$) to the plasma temperature ($T_{\rm e}$). Thus, the use of observations of short-wave radio emission from the Sun turns out to be the most convenient means of diagnosing chromospheric plasma (Loukitcheva & Nagnibeda 2000; Loukitcheva et al. 2004). Shklovsky showed that in the presence of a hot corona and a sharp transition from the cold chromosphere to the corona (transition region), characteristic and significant effects should be observed in the short-wave part of the radio range (within the framework of one-dimensional 1D concepts): brightening towards the edge of the solar disk and a bright, more than 100%, ring on the limb (narrow spike on the radial distribution of radio brightness) (Shklovsky 1957). In subsequent decades and in our time, a large number of works, both observational and theoretical, have been devoted to the study of these effects.

Important work on the study of the chromosphere was carried out in the early 1950s based on optical observations of total solar eclipses; these results were collected and summarized by Thomas and Athey in the famous book "Physics of the Solar Chromosphere" (Nagnibeda & Piotrovich 1987). It is interesting that in this book the authors examined in a separate chapter the radio emission of the chromosphere and made a very important conclusion for the topic of the article: in order for the above limb effects to be "suppressed" (and doubts about this have already been expressed), the chromosphere must be inhomogeneous and contain cold absorbent structural elements. There, the authors proposed spicules in the role of such elements, and using the example of a very simple and "primitive" model, they showed this possibility. Subsequently, many researchers proposed more plausible models, including other elements, for example, coronal loops, selecting their parameters so as to obtain good agreement with observations. However all such attempts, despite the apparent success, are made purely empirically and are not theoretically justified.

Observations of limb effects require fairly high angular resolution and have been performed for many years during solar eclipses or with large radio telescopes and interferometers. Unfortunately, the results obtained strongly depend on the actual angular resolution and the method of processing observations (reduction), so the summary of results demonstrates a significant scatter of data (see review Nagnibeda

& Piotrovich 1987). In such conditions, of great interest is the value of the solar radio radius, which characterizes the altitudinal extent of the chromosphere, and the obtaining of which depends much less on angular resolution.

The main problem remains the obvious contradiction between the results of radio radius measurements and model calculations made on the basis of classical standard models of the atmosphere (VAL – FAL), that is, the height of the chromosphere according to radio data (radio radius) is significantly greater than model calculations, despite the strong scatter of observational values. Particularly convincing were the results of measurements made from observations of the total eclipse of July 11, 1991 by different groups of observers in the millimeter range, using different instruments and in different places. The length of the chromosphere turned out to be about 5000 km, which is more than twice the model value (Belkora et al. 1992; Bastian et al. 1993; Ewell et al. 1993; White & Kundu 1994; Nagnibeda & Rozanov 1998). This is largely due to the fact that widely used models are based on UV observations, are one-dimensional, and do not take into account the strong structural inhomogeneity of the chromosphere. Such discrepancies led to a heated debate between supporters of the model of cold and extended chromosphere and the authors of the VAL – FAL models, stimulated moreover by Zirin's polemical article "The Mystery of the Chromosphere" (Zirin 1996).

An important stage in the continuation of research was the development of modern realistic inhomogeneous 3D models of the chromosphere (http://sdc.uio.no/search/simulations) and modeling of solar short-wave radio emission on their basis (Loukitcheva et al. 2015). We simulated limb effects based on the same models (Nagnibeda et al. 2021).

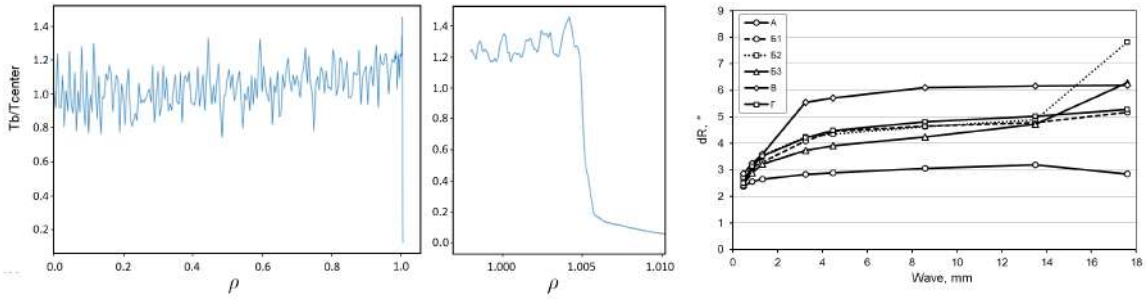

Fig. 1. Simulation results. On the left is the distribution of peak brightness temperature values along the surface of the Sun ($\rho = r/R_{\rm sun}$). In the center is the distribution of Tb at the edge of the Sun. On the right is the dependence of the change in the radio radius of the Sun on the wavelength for models with different types of chromospheric activity.

Qualitatively, the obtained results are similar to those observed ones: preservation of large fluctuations in brightness temperature along the solar surface in the mm wavelength range ("radio granulation"), absence of a sharp peak in brightness temperature on the limb, and a small change in the radio radius with wavelength (Fig. 1). However, the calculated values of the radio radius turned out to be significantly smaller than the observed ones, and the difference increases with increasing wavelength.

To obtain more accurate and reliable radio observation data, it is promising to use the modern unique ALMA instrument. Here it is important to mention observations of the Sun on a separate 12-m radio telescope ALMA, which confirmed previous radio data at short millimeter waves with better resolution (Alissandrakis et al. 2017).

2 Observations

Observations of eclipses make it possible to obtain better resolution even when using small radio telescopes. Theoretically, it can constitute small fractions of arcsec on cm waves. Of course, in real observations, such resolution cannot be obtained due to noise, the level of which is determined by the receiving equipment and control systems of the radio telescope, the state of the earth's atmosphere and the circumstances of the eclipse, etc. On the other hand, if the eclipse zone happens to include observatories with large modern radio telescopes, then their use for eclipse observations significantly improves the quality of the results due to the narrow beam.

Over the past 10 years, four solar eclipses have occurred, and large radio telescopes of Russian observatories fell within the zone of their partial phases. At the initiative of the first authors of the report, in 2021, coordinated observations were organized on large radio telescopes of observatories situated in the eclipse band: IAA RAS (RT-32 and RT-13), PRAO AKTs FIAN (RT-22) and Bauman MSTU (RT-7.5), covering a wide range of wavelengths from 2.5 mm to 13 cm (frequency 3–140 GHz).

The procedure for such observations consists of sequential pointing at a selected area of the solar disk and tracking it during the time when the area is closed or opened by the edge of the lunar disk. Within the scope of this article, we consider the observation of only the limbic regions, represented by contact regions 1 and 4.

Figure 2 shows fragments of the original signal recordings near the 1st and 4th eclipse contacts obtained on RT-22 at a wavelength of 1.4 cm, and the corresponding eclipse configurations. It is evident that the eclipse recordings are noisy, which introduces a noticeable uncertainty into the measured values.

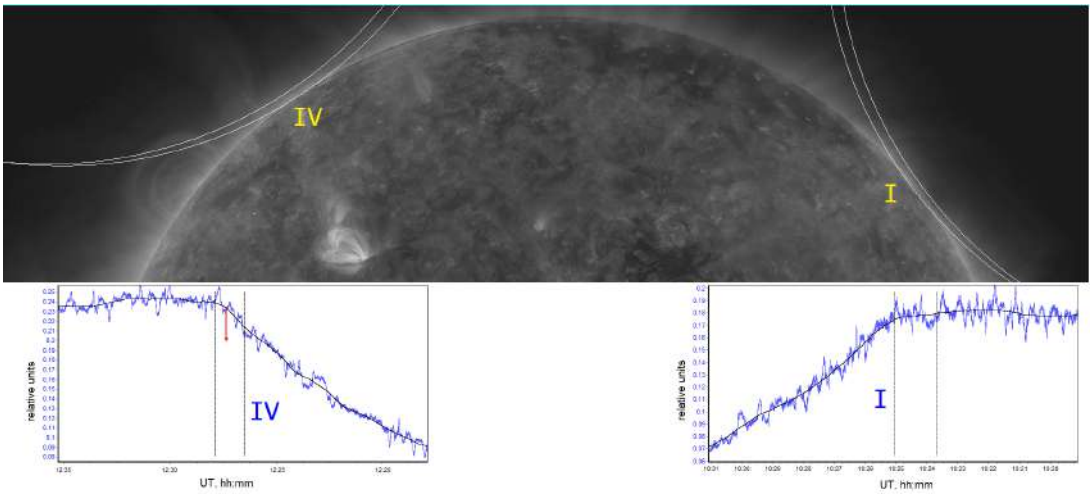

Fig. 2. Recordings near the 1st and 4th eclipse contacts. The vertical lines on the graphs correspond to the positions of the Moon's limb in the top figure. The lines located closer to the center of the disk correspond to the moments of contact. And those located further, to the moments of the Moon's edge reaching the upper boundary of the solar chromosphere.

3 Summary

The height of the edge of the solar atmosphere recorded at a wavelength of 1.4 cm is $\sim 17 - 20''$, but the estimate of the radio radius (measuring on the level 0.5 of full solar signal) based on the break in the IV contact record (red arrow) is less than $13''$. The results obtained are compared with previous measurements of the radio radius collected in Fig. 3, compiled in the paper (Ivanov et al. 2023). It is interesting that the results of our eclipse measurements on different instruments form a clearly distinguished group. Such a difference requires further analysis. One of the possible reasons may be the methodological difference in determining and measuring the radio radius. It is obvious however, that the difference in the estimates of the chromosphere extent obtained in the optical and radio ranges, which has been discussed for many years, remains significant, including the model test calculations that we performed earlier (Nagnibeda et al. 2021) for theoretical inhomogeneous models of the chromosphere and mentioned in Section 1 (Fig. 1). In Fig. 3 they are designated as ENW and CH models.

Within the error limits, the results of observations on the RT-22 PRAO and the RT-32, RT-13 IAA do not generally contradict each other.

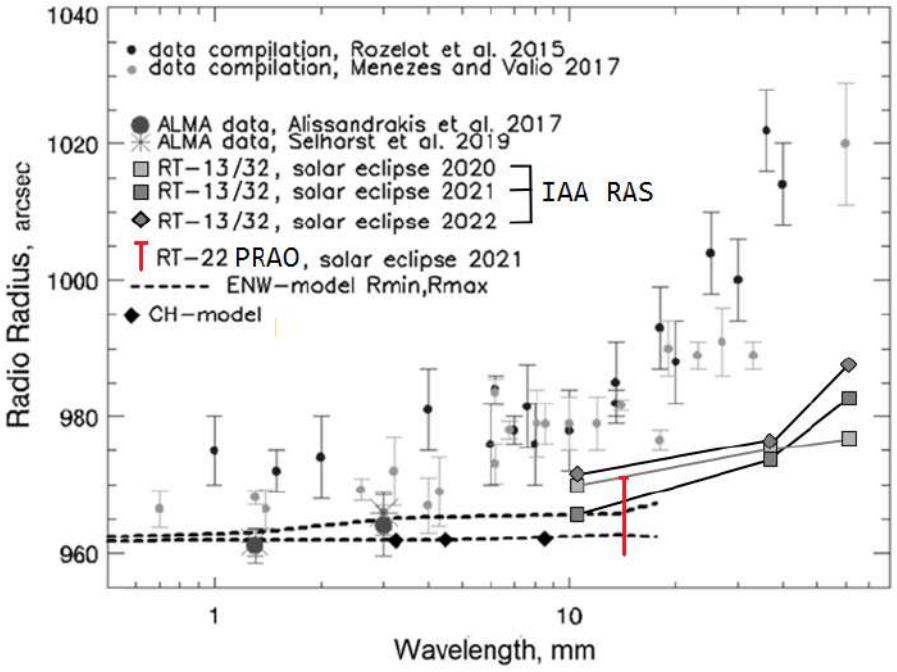

Fig. 3. Comparison of our results with previous measurements of the solar radio radius (Ivanov et al. 2023).

References

Alissandrakis C.E., Patsourakos S., Nindos A., et al., 2017, Astronomy & Astrophysics, 605, id. A78

Bastian T.S., Ewell M.W.Jr., Zirin H., 1993, Astrophysical Journal, 415, p. 364

Belkora L., Hudford G., Gary D., et al., 1992, Astrophysical Journal, 400, p. 692

Ewell M.W., Zirin H., Jensen J.B., et al., 1993, Astrophysical Journal, 403, p. 426

Ivanov D.V., Rakhimov I.A., Diakov A.A., et al., 2023, Transactions of IAA RAS, 65. p. 7

Loukitcheva M.A. and Nagnibeda V.G., 2000, Proceedings of the 1st Solar and Space Weather Euroconference, ed. A. Wilson, 463, p. 363

Loukitcheva M., Solanki S., Carlsson M., et al., 2004, Astronomy & Astrophysics, 419, p. 747

Loukitcheva M., Solanki S.K., Carlsson M., et al., 2015, Astronomy & Astrophysics, 575, id. A15

Nagnibeda V.G. and Piotrovich V.V., 1987, Trudy Astron. Obs. Leningr. Univ., 41, p. 5

Nagnibeda V.G. and Rozanov B.A., 1998, Advances in Solar Physics, 2nd Euro conf; ASPS Conf. Series, 155, p. 416

Nagnibeda V.G., Topchilo N.A., Loukitcheva M.A., et al., 2021, Geomagnetism and Aeronomy, 61, 8, p. 1150

Shklovsky I.S., 1962, Physics of the Solar Corona, State Publishing House of Physics and Mathematics Literature

White S.N. and Kundu M., 1994, Infrared Solar Physics: proceedings of the 154th Symposium of the International Astronomical Union, ed. D.M. Rabin, John T. Jefferies, and C. Lindsey, p. 167

Zirin H., 1996, Solar Physics, 169, 2, p. 313

BAK 2024 MODERN ASTRONOMY: FROM THE EARLY UNIVERSE TO EXOPLANETS AND BLACK HOLES 300 years Russian Academy of Sciences

Interpretation of polarimetric observations of hyperbolic comets

D. Petrov, E. Zhuzhulina, and N. Kiselev

Crimean Astrophysical Observatory of the Russian Academy of Sciences, Nauchny, 298409 Russia

Abstract. Polarimetric observations of comet C/2013 X1 (PANSTARRS) were compared with polarimetric data taken from the Polarimetric Comet Observations Database. To obtain a synthetic phase dependence of the degree of linear polarization of hyperbolic comets, the data were interpreted using computer simulations. In this case, computer simulation means calculating the characteristics of light scattered by particles of irregular shape and a certain chemical composition. Simulations showed that the dust ball would have to be 74 % amorphous carbon, 25 % magnesium-rich silicates, and 1 % water ice to reproduce the observed linear polarization values.

Keywords: comets: polarimetry; computer simulation

DOI: 10.26119/VAK2024.111

1 Introduction

Hyperbolic comets of the Solar System are comets with parabolic and hyperbolic orbits, i.e., the eccentricity of their orbits is greater than or equal to 1. Many of these comets may originate from the Oort cloud or from interstellar space. There are currently 468 known hyperbolic comets.

One of the newly discovered hyperbolic comets, named C/2013 X1 (PANSTARRS), was discovered on December 4, 2013 at Haleakala Observatory in Haleakala National Park on Maui, Hawaii, when the comet was at a distance of 8.9 AU. from the Sun. The eccentricity of its orbit is 1.001026±0.000002. Polarimetric observations of this comet were carried out in a broadband filter R (6400/1580 Å) on the 6-m BTA telescope of the Special Astrophysical Observatory (SAO) and on the 2.6-m Shain telescope of the Crimean Astrophysical Observatory (CrAO).

2 Comparison with other hyperbolic comets

The polarimetric observation data for comet C/2013 X1 (PANSTARRS) were compared with polarimetric data taken from the database of polarimetric observations of comets, as well as from the works (Ivanova et al. 2017; Zhuzhulina et al. 2022; Shubina et al. 2024).

It turned out that the results of polarimetric observations for comet C/2013 X1 (PANSTARRS) are in good agreement with data obtained for other hyperbolic comets in the red passband. In this regard, data interpretation was carried out using computer modeling for the synthetic phase dependence of the degree of linear polarization of hyperbolic comets. We calculated the characteristics of light scattered by model particles of irregular shape and a certain chemical composition.

3 Interpretation of observations

To interpret the observed dependence of linear polarization on phase angle, we applied the shape matrix method, and conjugate Gaussian random particles were used as model particles (see Fig. 1). A mixture of three types of particles was considered: amorphous carbon (refractive index m = 1.993 + 0.259i (Scott & Duley 1996)), high-magnesium silicates (m = 1.674 + 0.002224i (Li & Greenberg 1997)) and ice. These refractive index values are widely used to interpret cometary observations (e.g., Halder & Ganesh 2021). Particle sizes were taken from 0.49 μm (carbon), 0.83 μm (silicates), 0.39 μm (ice) to 3 μm. Averaging of particles by orientation and size was carried out according to a power law with an exponent n = 3 for all types of particles.

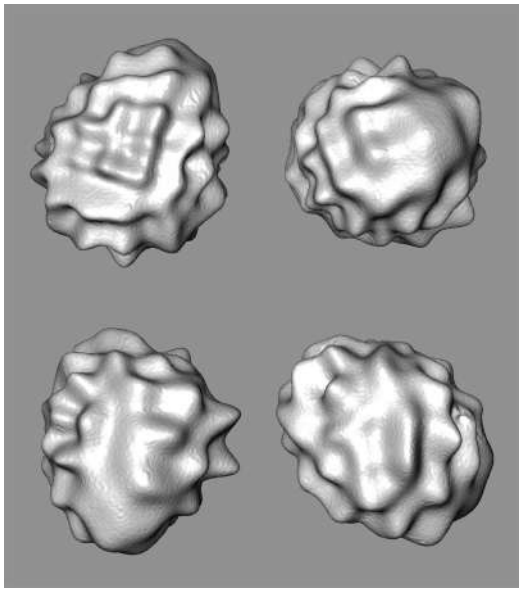

Fig. 1. Examples of conjugate Gaussian random particles.

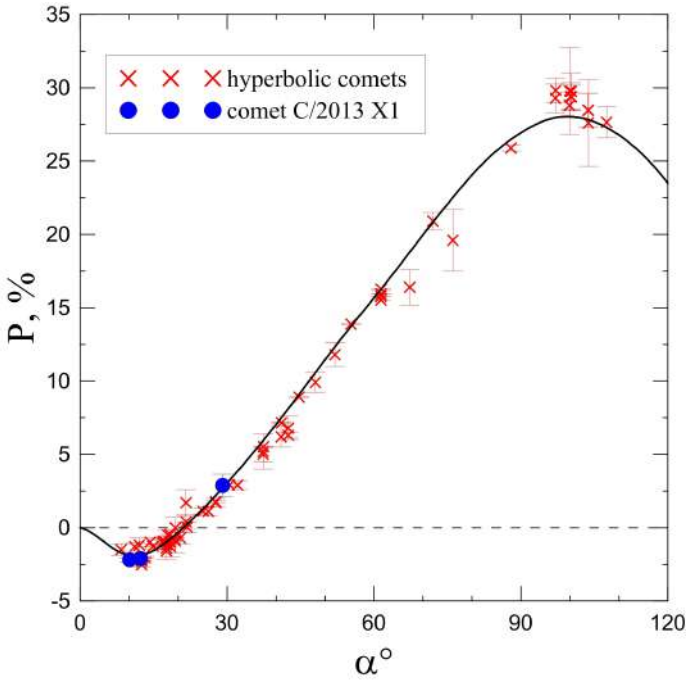

Fig. 2. Phase dependence of comet C/2013 X1 (PANSTARRS) (circles), other hyperbolic comets (crosses) and result of interpretation (line).

4 Summary

Simulations showed that the best fit between observation data and computer simulations is reached when dust coma consists of 74 % amorphous carbon, 25 % magnesium-rich silicates, and 1 % water ice (see Fig. 2). These results are in good agreement with Woodward et al. (2021) and are based on the analysis of IR spectral observations and thermal modeling.

Indeed, Woodward et al. (2021) determined that the dust composition of comet C/2013 X1 is dominated by dark dust particles (assumed as amorphous carbon) with an atomic ratio of carbon to silicon (C/Si) of 7.781±6.091, much higher than it is in carbonaceous chondrites. Thus, taking into account the best fit between the results of polarimetry and computer modeling, it can be concluded that the solid material that makes up the dust particles of comet C/2013 X1 is rich in carbon.

References

Halder P. and Ganesh S., 2021, Monthly Notices of the Royal Astronomical Society, 501, 2, p. 1766

Ivanova O., Rosenbush V., Afanasiev V., et al., 2017, Icarus, 284, p. 167

Li A. and Greenberg J.M., 1997, Astronomy & Astrophysics, 323, p. 566

Scott A. and Duley W.W., 1996, Astrophysical Journal Supplement, 105, p. 401

Shubina O., Ivanova O., Petrov D., et al., 2024, Monthly Notices of the Royal Astronomical Society, 528, 4, p. 7027

Woodward C.E., Wooden D.H., Harker D.E., et al., 2021, Planetary Science Journal, 2, 1, id. 25

Zhuzhulina E., Petrov D., Kiselev N., et al., 2022, Journal of Quantitative Spectroscopy and Radiative Transfer, 290, id. 108321

VAK 2024 MODERN ASTRONOMY: FROM THE EARLY UNIVERSE TO EXOPLANETS AND BLACK HOLES 300 years Russian Academy of Sciences

Study of the physical mechanism of a solar flare using MHD modeling over an active region: the onset of an extended surface of magnetic lines passing through a chain of current density maxima

A. Podgorny[1] and I. Podgorny[2]

[1] Lebedev Physical Institute of the Russian Academy of Sciences, Leninsky Prospect 53, Moscow, 119991 Russia

[2] Institute of Astronomy of the Russian Academy of Sciences, Pyatnitskaya Str. 48, Moscow, 119017 Russia

Abstract. The primary release of solar flare energy in the corona at altitudes of 15,000 – 70,000 km is explained by the physical mechanism of S.I. Syrovatsky, based on the rapid release of energy accumulated in the magnetic field of the current layer. The observed manifestations of the solar flare are explained by its electrodynamic model proposed by I.M. Podgorny. The model uses analogies with the electrodynamic model of a substorm, previously developed by its author. Since it is impossible to obtain the magnetic field configuration in the corona from observations, it is necessary to conduct MHD modeling. When setting the problem, no assumptions were made about the mechanism of the solar flare. For the numerical solution, an upwind absolutely implicit finite-difference scheme, conservative with respect to magnetic flux, was developed. The scheme is realized in the PERESVET computer program. A detailed study of the pre-flare state over the active region AR 10365 was conducted. The study revealed the emergence of an extended current sheet 50,000 km wide, which is a surface of magnetic lines passing through a chain of closely spaced current density maxima. The magnetic lines of the surface are in the form of arches located in the bright region of the flare emission. At the center of such a current sheet, a 3D maximum of current density does not necessarily have to be achieved. An appearance of a flare in such an arcade is explained by the fact that the main part of the surface of the magnetic arcs has properties that contribute to the development of flare instability.

Keywords: solar flare; current sheet; MHD simulation; active region

DOI: 10.26119/VAK2024.112

1 Introduction

Numerous observations show the primary release of solar flare energy in the corona at altitudes of 15,000 to 70,000 km (Lin et al. (2003) and others). This can be explained by a physical mechanism of Syrovatskii (1966) based on the accumulation of energy in the magnetic field of a current sheet formed near a singular magnetic field line. The fast release of the magnetic energy of the current sheet leads to the observed manifestations of the flare, which are explained by the electrodynamic model of the solar flare proposed by Podgorny I. et al. (2010). The model was developed based on the results of observations and MHD simulation and uses analogies with the electrodynamic model of a substorm, previously developed by its author (Podgorny I. et al. 1988).

Since it is impossible to obtain the configuration of the magnetic field in the corona from observations, to study the flare situation it is necessary to carry out MHD simulations in the solar corona. When setting the problem, no assumptions were made about the mechanism of the solar flare. All conditions were taken from observations. To study the physical mechanism of a solar flare, calculations must begin several days before the flare, when magnetic energy for the flare has not yet accumulated in the corona.

2 Problem statement and developed methods of solution

MHD simulation is performed over the active region AR 10365 during the time interval from 24.05.2003 20:48 to 27.05.2003 20:48. The computational domain in the corona has the form of a rectangular parallelepiped ($0 \leq x \leq 1$, $0 \leq y \leq 0.3$, $0 \leq z \leq 1$) ($L_0 = 4 \times 10^{10}$ cm). The lower boundary of the computational domain y=0 (XZ) contains the active region.

For the numerical solution of MHD equations, the absolutely implicit upwind finite-difference scheme, conservative relative the magnetic flux, has been developed (Podgorny A. & Podgorny I. 2004). Special methods have been developed to construct a scheme that remains stable over the longest possible time step. The magnetic field setting at the photosphere boundary was calculated from the potential magnetic field using the line-of-sight field component at the photosphere measured by SOHO MDI (http://soi.stanford.edu/magnetic/index5.html). Parallelization of calculations was carried out by computing threads on the GPU using CUDA technology.

The magnetic field configuration obtained by MHD simulation is so complex that it is often impossible to determine the positions of special lines and the current sheets appearing near them. For this purpose, a graphical search system (Podgorny A. & Podgorny I. 2013) was developed, based on the determination of the

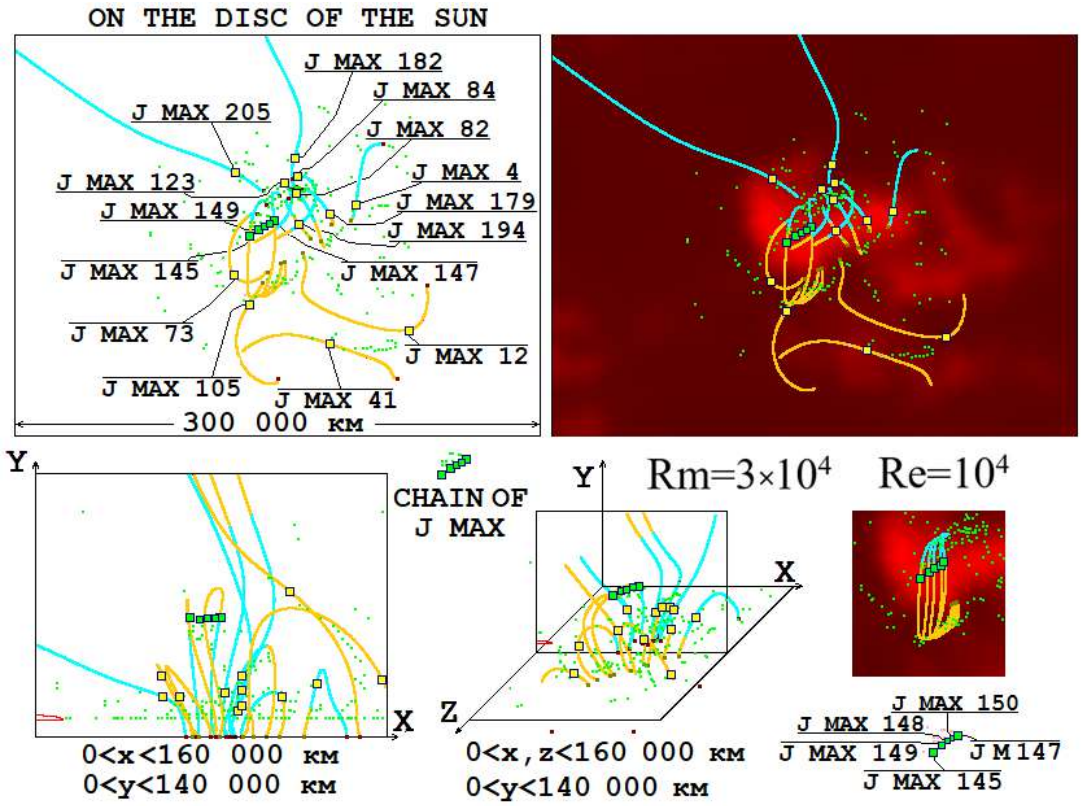

Fig. 1. The positions of the current density maxima in the calculated region of the corona in space and their projections onto the central plane of the calculated region (the plane passing through the center of the calculated region, located parallel to the solar equator and perpendicular to the solar surface) and onto the picture plane (perpendicular to the line of sight). The distribution of microwave radio emission at a frequency of 17 GHz, obtained on the solar disk using the Nobeyama radioheliograph, is superimposed on the picture plane. The magnetic field configuration is represented by magnetic lines passing through the selected current density maxima, and their projections onto the planes. The chain of maxima consists of points marked in green.

positions of the current density maxima that are achieved in the centers of current sheets.

3 Extended surface of magnetic lines passing through the chain of current density maxima

The detailed study of pre-flare state over the active region AR 10365 at 02:32:05 on May 26, 2003, three hours before the M 1.9 flare was carried out by comparing the results of numerical MHD simulation in the corona with observations of radio emission at a frequency of 17 GHz obtained at the Nobeyama Radioheliograph (NoRH). Magnetic field configuration is represented by lines passing through maxima of current density with the numbers 145, 147, 194, 179, 4, 73, 105, 41, 12, 205, 123, 82, 84, 182 (Fig. 1.). The current density maxima are numbered in descending order of current density. 3D magnetic lines in the computational domain in the corona, and projections of magnetic lines onto the central plane of the computational domain are shown. Also, the intensity distribution of microwave radiation at a frequency of 17 GHz observed on the solar disk using the Nobeyama radiheliograph (NoRH) is superimposed on the projections of magnetic lines onto the picture plane.

The magnetic field configurations at the selected points of current density maxima indicate favorable conditions for the occurrence of flares at some maxima located in the region of bright flare emission. There is no significant dominance of the diverging magnetic field in the vicinity of these maxima. At the same time, maxima with such properties also occur outside the bright region of flare emission.

The problem of coinsidence of bright flare emission regions with flare positions found from MHD simulation results can be solved by the occurrence of a surface of high current density, the current passing through a chain of current density maxima. The maxima of this chain with numbers 145, 149, 148, 150 and 147 in Fig. 1 are shown by green dots. Magnetic lines on the solar disk passing through the maxima of this chain are shown separately on an enlarged scale.

The 2nd row of Fig. 2 shows the plane and three-dimensional configurations near the chain maxima in a square and in a cube of 12,000 km. These configurations do not have properties that could significantly promote the flare release of energy. In plane configurations, the divergent magnetic field dominates over the X-type field, and in three-dimensional configurations, the field lines do not diverge much along the singular line, which means a relatively large longitudinal component of the magnetic field, stabilizing explosive instability.

The study of plane and three-dimensional configurations in a square and in a cube with a larger size of 80,000 km with the center at the 148th maximum located

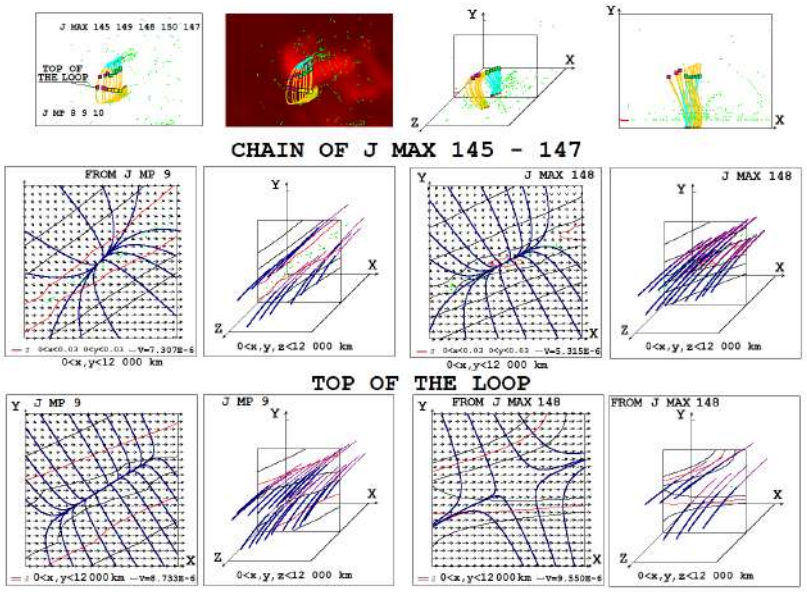

Fig. 2. Plane and spatial configurations in regions of 12,000 km in size with centers at the points of the chain of maxima and at the points at the top of the arch located on magnetic lines coming out of the points of the chain of maxima.

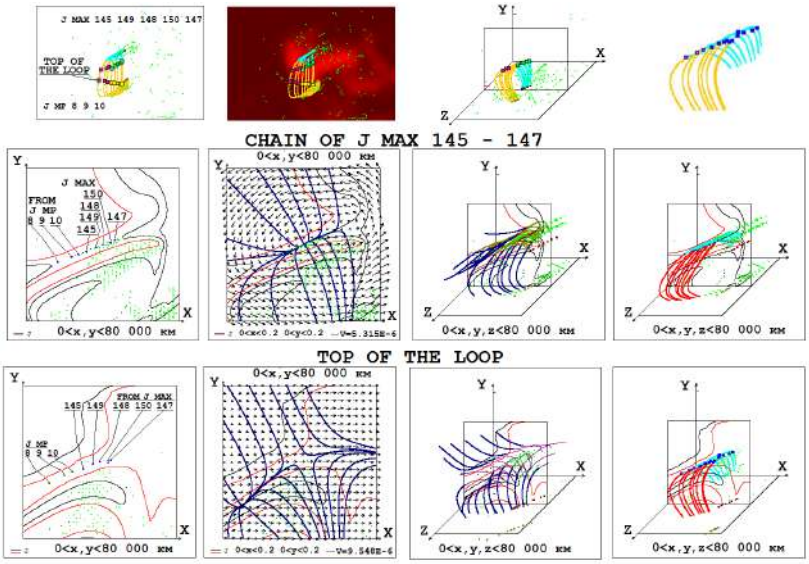

Fig. 3. Plane and spatial configurations in large regions of 80,000 km. In the central part of one of these regions there is a chain of maxima. In the central part of another region there are points at the top of an arch located on magnetic lines coming out from the points of the chain of maxima.

in the middle of the chain (Fig. 3, the second row) showed that all the chain maxima belong to the same current sheet of considerable width (50,000 km). Magnetic lines in a cube passing through the chain maxima form an arcade (Fig. 2, the last figure of the second row). In the upper rows of Fig. 2 and 3, the chain maxima points are marked in green, and the points on the tops of the loop located on magnetic lines, passing through the chain maxima points, are marked in yellow.

Magnetic field configurations (3rd row in Fig. 2) near the loop top points in the central plane of 12,000 km in size have properties that promote the development of flare instability. In most of these small regions, the X-type field dominates, while in other regions, the diverging field dominates very weakly. In the three-dimensional configuration, the field lines diverge significantly in the direction along the singular line, which means that the longitudinal component of the magnetic field is relatively weak, so that it will not be able to stabilize flare instability.

A comparison of two-dimensional and three-dimensional configurations in small regions of 12,000 km for the points of the chain of maxima and the points at the top of the arcade (Fig. 2) shows a much more favorable situation for the occurrence of flare instability at the tops of loops than at the points of the chain of maxima. The same result is obtained by comparing the magnetic field configurations in large regions (80,000 km in size) at the location of the chain of maxima and at the top of the arch (Fig. 3).

4 Conclusion

The problem of coinciding the positions of flares found as a result of MHD modeling with the observed bright region of flare radiation can be solved by the found arcade of magnetic lines passing through a chain of current density maxima. The arcade is entirely located in the bright region of pre-flare emission at a frequency of 17 GHz, obtained by the Nobeyama Radioheliograph (NoRH).

Extended version of this article is available at https://sites.lebedev.ru/ru/podgorny/file/7096.

References

Lin R.P., Krucker S., Hurford G.J., et al., 2003, Astrophysical Journal, 595, 2, p. L69

Syrovatskii S.I., 1966, Soviet physics, JETP, 23, 4, p. 754

Podgorny I.M., Balabin Y.V., Vashenyuk, et al., 2010, Astronomy Reports, 54, 7, p. 645

Podgorny I.M., Dubinin E.M., Israilevich P.L., et al., 1988, Geophysical Research Letters, 15, 13, p. 1538

Podgorny A.I. and Podgorny I.M., 2004, Computational Mathematics and Mathematical Physics, 44, 10, p. 1784

Podgorny A.I. and Podgorny I.M., 2013, Sun and Geosphere, 8, 2, p. 71

BAK 2024 MODERN ASTRONOMY: FROM THE EARLY UNIVERSE TO EXOPLANETS AND BLACK HOLES 300 years Russian Academy of Sciences

Recognition of solar flares in the microwave range of observations using machine learning

J. Shamsutdinova and L. Kashapova

Institute of Solar-Terrestrial Physics SB RAS, Irkutsk, 69167 Russia

Abstract. We present the results of testing machine learning methods for the recognition of solar flares observed in the microwave range. The catalogue of observations by the Nobeyama spectropolarimeters (NoRP) was used for both training and analysis of method effectiveness. The input data are one-dimensional temporal profiles with a frequency of 9.4 GHz, which are mostly associated with the emission of an optically thin source and the non-thermal emission from accelerated electrons. The input dataset consisted of 100 events and included temporal profiles with simple and complex structures. The aim of recognition is to distinguish between the temporal profiles of "classical" or simple-looking shapes, and "complex" ones. We compared the classification results provided by the correlation coefficient application with the results obtained using the Support Vector Machine (SVM) method with different parameters. True Positive (TP) and True Negative (TN) are values describing the number of events which the model correctly recognized, in our case, "classical" and "complex" profiles. False Postive (FP) and False Negative (FN) indicate incorrect model predictions of "classical" or "complex" profiles. The number of correctly recognized events using the correlation coefficient method was 75, compared to 90 events obtained using the SVM method. The number of false predicted events resulting from the application of the correlation coefficient was 25, versus 10 by SVM application. These results indicate the advantage of the SVM technique over the correlation coefficient approach. The SVM method allows us to process datasets using different functions as kernels - linear, polynomial and Radial Basis Function (RBF). In our study, we found that the most accurate result was provided by the RBF kernel with a gamma hyperparameter of 1.

Keywords: Sun: solar flare, radio radiation; methods: data analysis

DOI: 10.26119/VAK2024.113

1 Introduction

Nowadays, it becomes more and more important to identify events in information streams obtained from new astronomical instruments. Machine learning is a useful tool for this purpose. However, in the field of solar physics, these methods have been used to predict solar flares (Asensio Ramos et al. 2023) or identify different types of radio bursts in dynamic spectra (Xu et al. 2019). Machine learning methods have not been used for the detection and identification of solar flares in the microwave range. This paper presents the first results of testing the Support Vector Machine (SVM) for detecting solar flares using a classical temporal profile shape.

2 Dataset and the Support Vector Machine method

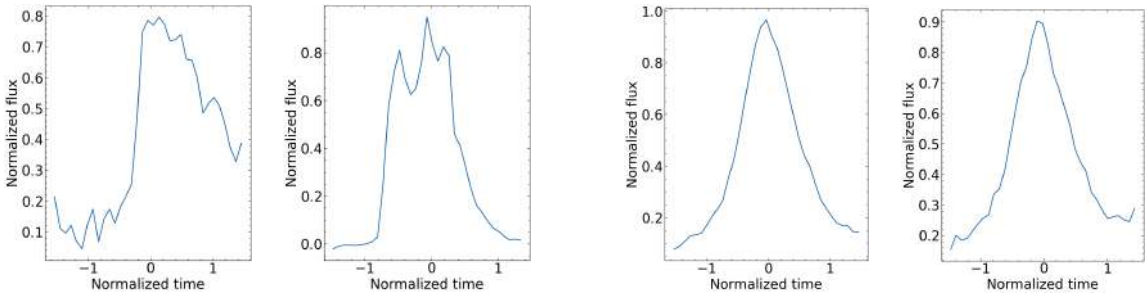

Fig. 1. Example of dataset after primary processing. Left panel: Temporal profiles with complex structure (class=0). Right panel: Temporal profiles with simple structure (class=1).

The dataset for training and testing was formed from the temporal profiles of microwave emission from the database of events observed by the Nobeyama spectropolarimeters. (NoRP) (Torii et al. 1979). The NoRP receives the intensity (I) and circular polarization (V) at frequencies of 1, 2, 4, 9.4, 17, and 35 GHz with a time resolution up to 0.1 second. We selected 100 events from the NoRP catalogue during periods of high solar activity, including 2001 and the years 2012–2014[1]. We selected intensity temporal profiles at a frequency of 9.4 GHz for recognition. The choice of frequency was determined by two reasons. The first one is the emission of the most solar flares at this frequency, which forms in the region of an optically thin source and is therefore free from additional effects. The other reason is that the Siberian Radioheliograph observes at the same frequency, and the model trained on NoRP

[1] https://solar.nro.nao.ac.jp/norp/html/event/

data can be applied to SRH data at this frequency. Before putting the data into the model, they were preprocessed. We normalized every temporal profile to its maximum intensity. The moment of the maximum was used as a zero point on the time scale. Therefore, the time during the rise phase has negative values, while the time during the decay phase has positive values. To get the same time scale for events with different durations, time was normalized using units defined by the time it took for the intensity to decrease to half of the maximum value for each time profile. The described methodology is used to reconstruct an average profile in Davenport et al. (2014). Each array contains 35 elements, which corresponds to the number of features. For training and testing, we used a dataset consisting of 100 arrays (see examples in Fig. 1). 43 profiles have a complex structure that may contain multiple peaks and/or noise that dominates the signal (class 0). The remaining 57 profiles have a classic structure (class 1).

Support Vector Machine (SVM) is a supervised machine learning algorithm used for both classification and regression. The main objective of the SVM algorithm is to find an optimal hyperplane in a high-dimensional space that can separate data points into different classes in the feature space. The hyperplane tries to maximize the margin between the closest points (support vectors) of different classes.

When the number of input features is greater than three, SVM uses kernels to transform the hyperplane into a nonlinear one. There are linear, polynomial, and Radial Basis Function (RFB) kernel functions. RFB has a gamma hyperparameter, which determines the impact of support vectors on the data. The C hyperparameter provides a correct classification of training examples against maximization of the decision function's margin. We used the GridSearch method to determine the optimal parameters for the model with different kernel functions. We optimized the model by using GridSearch to select hyperparameters based on the accuracy achieved on the test set. The optimal hyperparameters for the models are presented in the first row of Table 1. The scikit-learn library for Python was used to train the model [2]. SVM is typically used for binary classification problems and in cases where the data is not linearly separable and the cross-correlation method may not be applicable to the recognition problem.

3 Results of classification and evaluation metrics

Another way to recognize the shape of a temporal profile is to use cross-correlation between the training profiles and the analyzed one. This method is sensitive to stationary and linear relationships in the dataset. The number of correctly recognized

[2] https://scikit-learn.org

events using the correlation coefficient method for level 0.8 was 75 while compared to 90 events obtained using the SVM method. We used metrics such as precision, recall and F1 measure to evaluate the model's performance (see the example Wang et al. 2024).Precision measures how many observations predicted to be positive are actually positive. The recall measures how many positive observations we classified as positive, out of the total number of observations. F1 is the harmonic mean between precision and recall. The model is more accurate the closer F1 is to 1. The results of testing models with different kernel functions are presented in Table 1. It can be seen that the most accurate information was obtained from the RFB kernel with the gamma hyperparameter equal to 1. However, the obtained results have to be tested on a larger dataset over a wider frequency range.

Table 1. The result of testing SVM models for recognizing time profiles

	Linear (C=1, γ=1)			RBF (C=10, γ=1)			Poly (C=0.1, γ=0.1)		
	Precision	Recall	F1	Precision	Recall	F1	Precision	Recall	F1
Simple flare	0.73	0.92	0.81	0.79	0.85	0.81	0.67	0.50	0.77
Complex flare	0.88	0.62	0.73	0.82	0.75	0.78	0.85	0.92	0.63

Acknowledgements. Authors thank the team operating at the Nobeyama for the Nobeyama Radio Polarimeter database.

Funding

The research was funded by the Russian Science Foundation grant No. 24-22-00315, (https://rscf.ru/project/24-22-00315/).

References

Asensio Ramos A., Cheung M.C.M., Chifu I., et al., 2023, Living Reviews in Solar Physics, 20, 1, id. 4
Davenport J.R.A., Hawley S.L., Hebb L., et al., 2014, Astrophysical Journal, 797, 2, id. 122
Torii C., Tsukiji Y., Kobayashi S., et al., 1979, Proceedings of the Research Institute of Atmospherics, Nagoya University, 26, p. 129
Wang Y.H., Feng S.W., Du Q.F., et al., 2024, Solar Physics, 299, 4, id. 54
Xu L., Yan Y.-H., Yu X.-X., et al., 2019, Research in Astronomy and Astrophysics, 19, 9, id. 135

MODERN ASTRONOMY: FROM THE EARLY UNIVERSE TO EXOPLANETS AND BLACK HOLES

Investigation of the dynamics of the magnetic field and vertical electric current during the precursors of the M6.5 class solar flare of June 22, 2015 using vector 135-second HMI magnetograms

I. Sharykin and I. Zimovets

Space Research Institute of Russian Academy of Sciences, Profsoyuznaya Str. 84/32, Moscow, 117485 Russia

Abstract. This paper considers the M6.5 eruptive solar flare occurred on June 22, 2015, for which ultraviolet preflare emission sources in the 1 600 Å chromospheric channel have been analyzed using AIA/SDO data. Magnetic fields at the photospheric level are also analyzed using HMI/SDO vector magnetograms with a time resolution of 135 seconds. Since the selected flare has a long preflare phase (about one hour), the available time resolution of vector magnetograms is sufficient to study the flare and preflare dynamics of magnetic fields at the photospheric level. It can be noted that the literature mainly considers the change in currents during solar flares, while insufficient attention is paid to precursors. Our main goal is to provide continuous monitoring of the dynamics of electric current during the preflare period, at the beginning of the flare and during the main phases of the flare. We determined the magnetic flux (and its time derivative) in the preflare sources at the chromospheric level in comparison with the magnetic fluxes of the flare ribbons. Analysis of 135-second HMI photospheric vector magnetograms showed that there was an increase in the total vertical electric current about 1 hour before the flare. During this hour, there were variations of the mean vertical electric current density and its subsequent drop during the flare. We probably see an intermittent increase and dissipation of currents due to individual bursts in the preflare region. Also, the analysis of magnetic fluxes showed that, despite the weak preflare soft X-ray fluxes, the variations in magnetic flux during precursors are comparable in order of magnitude to what we see during the main phase of the solar flare. The difference between the time derivatives of the magnetic flux for precursor radiation sources and flare ribbons does not exceed a factor of 3.

Keywords: Sun: solar flares; precursors; magnetic field; electric current

DOI: 10.26119/VAK2024.114

1 Introduction

Precursor activity before solar flares is usually studied in the context of space weather forecasting. It is very important to understand the features of the energy accumulation processes in active regions that produce flares and coronal mass ejections. Usually precursors are considered as different transient emission brightnings or structures before the flares in the parent active region seen in different types of electromagnetic emission (e.g., Bamba et al. 2017). Despite our knowledge of the morphology of preflare processes, we do not have detailed information on the changes in the magnetic field during the preflare stage. We also have no information on the dynamics of reconnection of magnetic flux and electric currents in the time range from precursor processes to the onset of the flare, which turns into a developed impulsive phase. The main goal of the work is to capture the features of the electrodynamics of preflare processes in comparison with the subsequent impulsive phase. For this purpose, a flare (briefly described in the abstract, and also studied by the authors in the work of Artemyev et al. 2021) was selected with a well-defined grouping of precursors 1–2 hours before the flare. To study the magnetic field dynamics, we use the available high-cadence 135-second vector magnetograms (Sun et al. 2017) from HMI (Scherrer et al. 2012).

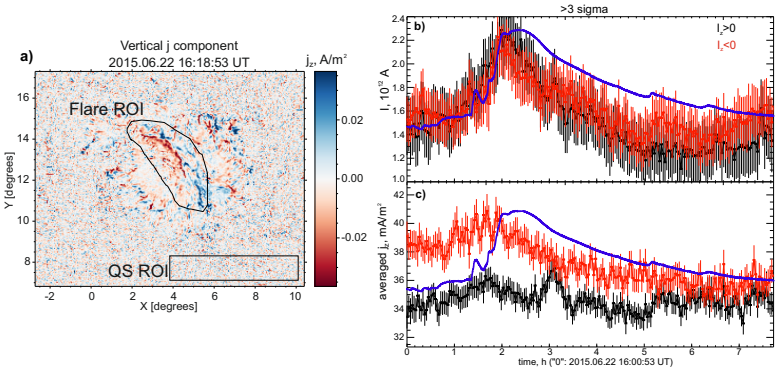

Fig. 1. Panel (a) shows the vertical electric current (j_z) map calculated from the 135-second HMI vector magnetograms. The flare ROI is marked by irregular black contour covering flare j_z "ribbons" of opposite polarities. The rectangular ROI corresponds to the place used for determination of the j_z distribution and estimation of the j_z error. Time profiles of total vertical electric current I_z and average value of j_z are shown in (b) and (c), respectively. The blue curve is the GOES X-ray lightcurve in the 1–8 Å channel.

2 Flare and preflare electrodynamics

Dynamics of the total vertical electric currents and the averaged current density in the flare region (ROI in panel a) is shown in Fig. 1 in the corresponding panels b and c. It can be noted that the gradual increase in the X-ray flux was associated with an increase in the total vertical current, amounting to only $j_z > 3\sigma$ (b). The precursory phase was accompanied by the variations of vertical current density (1–2 hours in panel (c)).

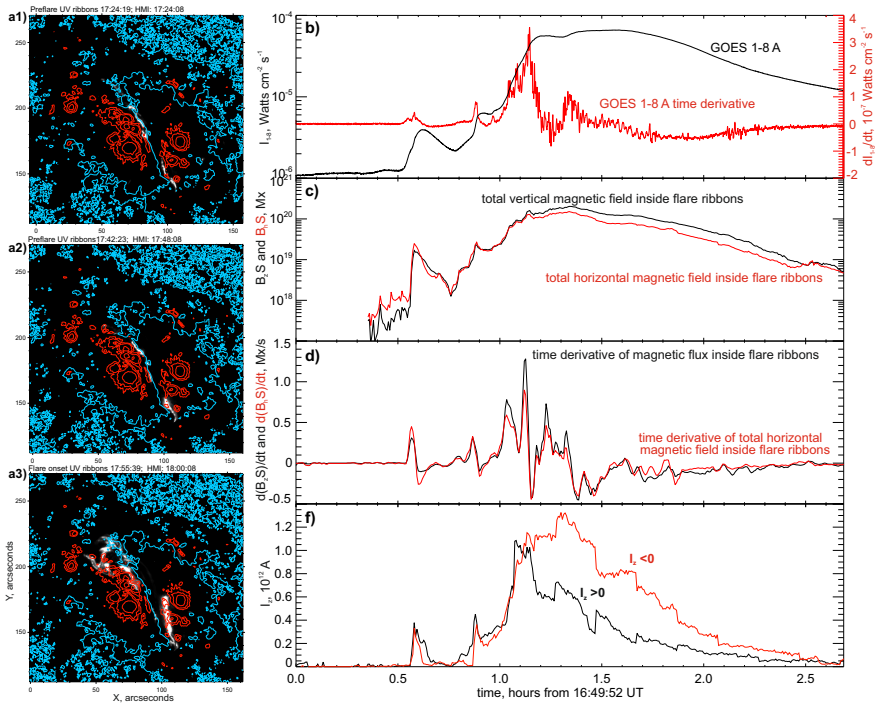

Fig. 2. Panels (a1–a3) show the preflare UV sources and the flare ribbon in the background layer compared with the superimposed B_z (red) and PIL (blue) contours. GOES X-ray 1–8 Å flux (black) and its time derivative (red) are shown in panel (b). Magnetic fluxes of vertical (black) and horizontal (red) magnetic field inside flare ribbons are shown in panel (c) and its time derivatives in panel (d). The dynamics of the total vertical electric current inside the flare ribbons is shown in (f): red and black colors correspond to negative and positive values of j_z.

We use chromospheric ultraviolet images to obtain regions of the energy release in the preflare and flare regions. The dynamics of the UV emission sources can be seen in Fig. 2(a1–a3). Initial preflare emission sources were located close to the PIL then flare ribbons began to move out of the PIL. For the regions above 300 DNs we

calculated magnetic flux (Fig. 2(c)) and its time derivative (d) usually associated with the reconnecting magnetic flux (e.g., Sharykin et al. 2020). It can be seen that the initial preflare brightnings ($t = 0.4 - 0.6$ h) were mostly in the horizontal magnetic field and the reconnecting magnetic flux was approximately two orders less then the peak during the flare. It can be noted that the largest reconnected flux during the precursor phase around $t = 0.6$ h was only one order of magnitude smaller than the peak. The values of the reconnecting magnetic flux derivative during the precursor is only 2–3 times less than the peak rate. Moreover, the characteristic duration of the precursor reconnection rate is comparable to individual peaks during the flare.

3 Concluding remarks

Analysis of the HMI 135-second vector magnetograms with the dynamics of the preflare/flare chromospheric emission sources revealed variations of the electric current density during the precursors. We probably recorded signs of dissipation of electric currents around the twisted magnetic structure along the LIP, where the precursors were localized. An analysis of the dynamics of the magnetic field around the preflare and flare emission sources showed that the precursor can be considered as an "individual" pulse-like episode of energy release, while the entire flare process is an avalanche-like process of many similar episodes of energy release (pile-up of pulses) with reconnection rates and characteristic times comparable to the preflare ones. Localized emission sources in PILs with high reconnection rates in the active region can be considered as tracers of preflare accumulation. Perhaps this fact can be used to predict solar flares once more statistical information is available.

Acknowledgements. We thank the many team members who contributed to the success of the SDO mission and, especially, the HMI instrument.

Funding

The work was supported by the Russian Science Foundation grant No. 20-72-10158.

References

Artemyev A., Zimovets I.V., Sharykin I.N., 2021, Astrophysical Journal, 923, id. 151
Bamba Y., Lee K.-S., Imada S., Kusano K., 2017, Astrophysical Journal, 840, id. 116
Sharykin I.N., Zimovets I.V., Myshyakov I.I., 2020, Astrophysical Journal, 893, id. 159
Scherrer P.H., Schou J., Bush R.I., et al., 2012, Solar Physics, 275, p. 207
Sun X., Hoeksema J.T., Liu Y., et al., 2017, Astrophysical Journal, 839, id. 67

BAK 2024 MODERN ASTRONOMY: FROM THE EARLY UNIVERSE TO EXOPLANETS AND BLACK HOLES 300 years Russian Academy of Sciences

Investigation of magnetic free energy dynamics in the M1.2-class complex solar flare of March 15, 2015 using the 135-second HMI vector magnetograms

I. Sharykin[1], I. Zimovets[1], I. Myshyakov[2], and S. Anfinogentov[2]

[1] Space Research Institute of Russian Academy of Sciences, Profsoyuznaya Str. 84/32, Moscow, 117997 Russia

[2] Institute of Solar-Terrestrial Physics, Lermontov Str. 126A, Irkutsk, 664033 Russia

Abstract. We investigate magnetic free energy (MFE) dynamics in the M1.2 solar flare occurred on March 15, 2015, 22:45 UT. We use the nonlinear force-free field (NLFFF) model of the coronal magnetic field on the basis of 135-second HMI vector magnetograms (standard magnetograms have a temporal resolution of 720 s) from the Heliosesmic and Magnetic Imager (HMI). Since we consider a rather long event (about 100 minutes) with several episodes of energy release of different temporal dynamics (pulsed or more gradual), we can find features of the MFE dynamics relative to the flare energy release stages using 135-second vector magnetograms. It is shown that the main MFE dissipation (approximately 30 % of the initial level) occurred during the two first subflare bursts seen in microwave hard X-ray ranges. These two bursts developed at low (less than 5 Mm) magnetic structures extremely elongated along the magnetic field polarity inversion line (PIL), while the other long-lasting bursts without appreciable MFE dissipation occurred in a growing flare arcade of magnetic loops. The obtained results are in favor of the fact that most of the MFE is localized in magnetic structures with a strong electric current at the PIL. It is possible that local monitoring of the preflare state around the PIL based on magnetic extrapolations with high temporal and spatial resolution will allow further improvement of methods for predicting solar flares. The dynamics of relative helicity are also studied in relation to the dynamics of the eruptions, and we found that the first impulsive subflares were accompanied by the most significant drop in helicity.

Keywords: Sun: solar flares, magnetic fields; electric currents; eruption; hard X-ray emission

DOI: 10.26119/VAK2024.115

1 Introduction

Magnetic field energy in the solar corona is believed to be the main reservoir for solar flares. The most variable part of the magnetic energy, known as "magnetic free eneregy" (MFE), can be estimated as a difference between energies of the non-linear force-free and potential magnetic fields over a parental active region. There are a lot of works showing significant changes of the MFE during the flares (e.g., Sun et al. 2012; Liu et al. 2023).

A solar flare is highly dynamic non-staionary process on time scales from subsecond time intervals to hours. The standard HMI (Scherrer et al. 2012) vector magnetograms onboard the Solar Dynamics Observatory have a 12-minute time cadence, which is insufficient to capture the features of magnetic field changes during the impulsive phases of flares. To study the dynamics of the magnetic fields and associated MFE we need special flares with long impulsive phase or with a few separated HXR bursts. A more realistic option for this study is to use the better time resolution of vector magnetograms.

Today 135-second HMI vector magnetograms are available and successfully used to study flare energy release (e.g., Sun et al. 2017; Sharykin et al. 2020). In this paper, we study the dynamics of the MFE using high-cadence HMI vector magnetograms for a specific flare consisting of several subflares with their own impulsive phases. The main aim is to determine the stage of the flare when most of the MFE disappears during the complex flare chosen for this study.

2 Analyzed dynamics of the solar flare and MFE

This work continues our previous works (Sharykin et al. 2018, 2020, we do not discuss their results here), which were devoted to the detailed quantitative multiwavelength analysis of electrodynamics, nonthermal electron dynamics and plasma heating in the system of highly sheared magnetic loops interacting at the PIL during the confined (non-eruptive) M1.2 solar flare SOL2015-03-15T22:43.

Figure 1 shows flare time profiles (a, b) presenting multistage nature (three subflares) of the entire flare event, and position of the flare emission sources (in different wave ranges) relative to the magnetic field and electric current structure in the photosphere (d–f); 135-second HMI vector magnetograms). One can see that the different flare emission sources were located very close to the PIL. They partially coincided with areas of increased vertical electric currents (e) and horizontal gradient of the vertical magnetic field (f), which is a sign of a large local amount of the MFE in the corresponding areas.

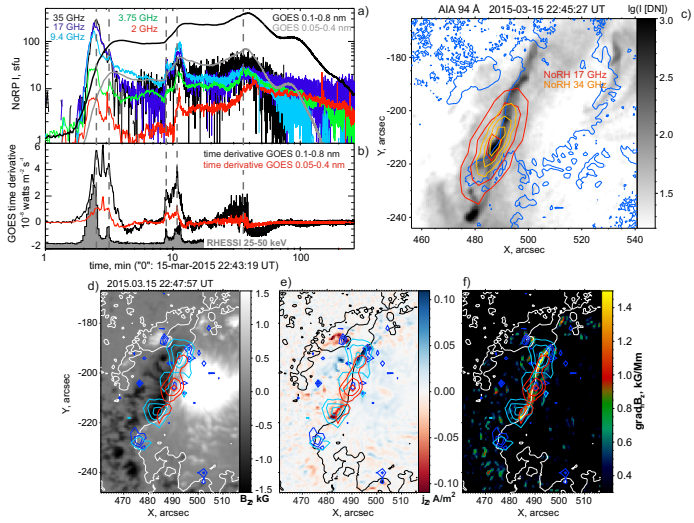

Fig. 1. Microwave time profiles (time is in log scale to show three subflares) at 5 frequencies from NoRP data are shown in panel (a) with overlayed GOES X-ray fluxes in two channels (thick grey and black curves). Panel (b) presents RHESSI 25-50 keV X-ray count rates compared with the time derivatives of GOES X-ray fluxes in 0.5–4 and 1–8 Å channels. The EUV 94 Å AIA image (background) is compared with the NoRH sources at 17 and 34 GHz (red and orange contours) in panel (c). RHESSI 6–12 and 25–50 keV X-ray sources in (d–f) are marked by red and cyan contours, respectively, and compared with: (d) B map, (e) j_z map, and (f) $\nabla_h(B_z)$ map. PIL is shown in panels (c–f) by blue, white, black and white colours, correspondingly.

Using nonlinear force-free model of the solar coronal magnetic field (NLFFF, approach of Rudenko & Myshyakov 2009) we calculated magnetic free energy with the 135-second temporal resolution and compared it with the GOES 1–8 Å lightcurve in Fig. 2(a). It is evident that the MFE experienced significant change during the first two subflares when we observe nonthermal emissions of the accelerated electrons around the PIL twisted magnetic structure. Th relative magnetic helicity (by Anfinogentov's method discussed in a review of Valori et al. 2016) also changed during an eruptive process associated with these two subflares (c–d). The dynamics of the eruption is shown by time-distance analysis performed for two observational slits crossing the bright PIL UV structure (b). Large helicity drops are usually interpreted as evacuation of helical magnetic structures due to the eruption.

3 Summary and concluding remarks

We found that the main dissipation of the MFE occurred during the first episodes of flare energy release associated with low-lying high-shear magnetic structures in

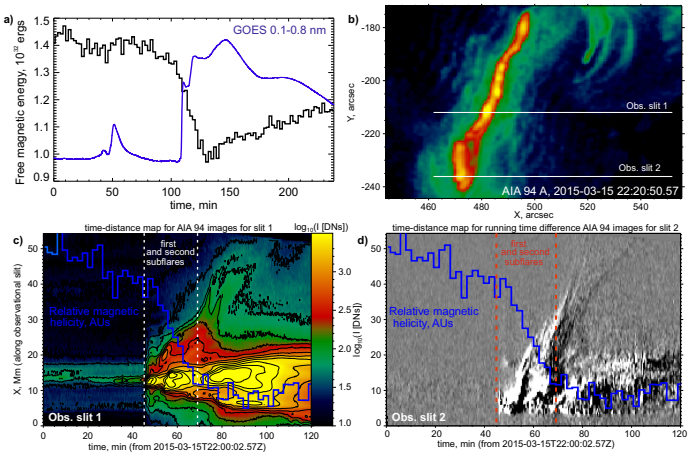

Fig. 2. The dynamics of the MFE and relative helicity in the flare region (roughly corresponding to the field of view in Fig. 1(d) and the X-ray flux of GOES 1–8 Å) is shown in panel (a). Panel (b) presents the AIA 94 Å flare image and positions of the horizontal observational slits, which were chosen to make time-distance diagram in (c) (94 Å) and (d) (running time differences of 94 Å images). The dynamics of the relative helicity is shown by the blue histogram-like curve in (c–d).

the PIL. These energy release episodes were characterized by the presence of the accelerated electrons and impulsive plasma motions (eruption). In other words, the release of MFE did not develop gradually throughout the flare event and throughout the entire volume of the AR, but was rather impulsive and concentrated in the vicinity of the PIL. Our findings suggest that processes in the PIL are critical for flaring energy releases and should be monitored to predict flares.

Acknowledgements. We thank the many members of the SDO, RHESSI and Nobeyama observatory teams for providing data and corresponding analysis software.

References

Liu Y., Welsch B.T., Valori G., et al., 2023, Astrophysical Journal, 942, id. 27
Rudenko G.V., Myshyakov I.I., 2009, Solar Physics, 257, 2, p. 287
Scherrer P.H., Schou J., Bush R.I., et al., 2012, Solar Physics, 275, p. 207
Sharykin I.N., Zimovets I.V., Myshyakov I.I., 2020, Astrophysical Journal, 893, 2, id. 159
Sharykin I.N., Zimovets I.V., Myshyakov I.I., et al., 2018, Astrophysical Journal, 864, id. 156
Sun X., Hoeksema T., Liu Y., et al., 2012, Astrophysical Journal, 748, id. 77
Sun X., Hoeksema J.T., Liu Y., et al., 2017, Astrophysical Journal, 839, id. 67
Valori G., Pariat E., Anfinogentoov S.A., et al., 2016, Space Science Reviews, 201, p. 147

MODERN ASTRONOMY: FROM THE EARLY UNIVERSE TO EXOPLANETS AND BLACK HOLES

Photospheric disturbances and acoustic sources of the helioseismic "circular" X1.5 flare of May 10, 2022

I. Sharykin and I. Zimovets

Space Research Institute of the Russian Academy of Sciences, Profsoyuznaya Str. 84/32, Moscow, 117997 Russia

Abstract. This paper is devoted to the analysis of the energy release of the X1.5-class solar flare that occurred on May 10, 2022, during which the powerful helioseismic response ("sunquake") was observed. An additional feature is the fact that this powerful sunquake was generated in the NOAA active region 13006 of Hale class $\beta\delta$, whereas earlier it was shown that the strongest helioseismic disturbances are generated in the sunspot groups with the most complex Hale class of $\beta\gamma\delta$. We analyze magnetic fields and photospheric perturbations basing on the Helioseismic and Magnetic Imager (HMI) data. Analysis of the distribution of acoustic sources and photospheric perturbations reveals a ring geometry in the form of a chain of sources roughly corresponding to the geometry of flare ribbons. The photospheric perturbations developed in two regions near the magnetic field polarity inversion line (PIL) and corresponded to two series of hard X-ray bursts seen in the KONUS/WIND data. We extrapolated the coronal magnetic field from the HMI vector magnetograms within the framework of the nonlinear force-free field (NLFFF) approximation. The geometry of the "dome with a spine" type was revealed. The regions of the photospheric perturbations approximately corresponded to the base of the dome. In this work we also briefly discuss penumbral decay and the flare dynamics of the observed δ-spot. The data obtained vividly show the local features of the magnetic fields in a relatively morphologically simple active region, where the conditions for the powerful helioseismic response during the solar flare arose. The paper also discusses the morphological properties of the active region with similar properties of the most helioseismically active regions of the 24th cycle.

Keywords: Sun: sunquakes, solar flares, active regions, magnetic fields, sunspots

DOI: 10.26119/VAK2024.116

1 Introduction

The paper is devoted to the case-study of the helioseismically active X1.5 solar flare (its helioseismicity was firstly discovered and discussed in Kosovichev et al. 2023), briefly described in the abstract. Helioseismic solar flare impacts are reffered as sunquakes and seen as concentric ripples in photospheric Dopplergrams running from compact regions connected with the sites of the flare photospheric energy release (see review of Kosovichev 2015). The catalog of helioseismically active solar flares of the 24th solar activity cycle (Sharykin & Kosovichev 2020) shows that every fifth M and X class flare or every second flare with a photospheric perturbation is characterized by the appearance of the helioseismic waves. Thus, this phenomenon is not rare and is characterised by particular interest for studying complex flare energy release.

There is still no clear understanding of the nature of sunquakes. There are a few hypothesis of the sunquake generation (e.g., see introduction in Sharykin & Kosovichev 2020): perturbations induced by nonthermal particles (electrons or ions), changing magnetic field or dissipation of electric currents. It is also possible to assume the simultaneous contribution of various mechanisms, the effectiveness of which may change as the flare develops. Today we do not know the exact cause of sunquakes and need additional research and statistical work.

One of the ways to study the physics of sunquakes is to search for unique events with special morphological properties that may indicate the necessary conditions for the occurrence of heliosesmic perturbations. This article considers such a solar flare. And the main goal of this work is to find specific features (local or global) of the active region producing solar flares accompanied by sunquakes.

2 The analysed solar flare and the used observational data

The considered sunquake was generated in the NOAA active region 13006 of Hale class $\beta\delta$ and McIntosh class Cso. Earlier in the statistical work of Sharykin & Kosovichev (2020) it was shown that the strongest helioseismic disturbances are generated in the sunspot groups with the most complex Hale class $\beta\gamma\delta$. And there were no heliosesmically active solar flares in the active regions with such "simple" (in comparison with Cso) McIntoch class during the 24th solar cycle. For example, the typical classes were: Dkc => Ekc (NOAA 12673, 5–7 September 2017); Fkc => Ekc => Fhc (NOAA 11515, 4–7 July 2012); Fkc (NOAA 12192, 20–26 October 2014); Dkc (NOAA 11429, 5–7 March 2012).

The relative global simplicity of the considered active region (compared to other ARs causing sunquake flares) with the large energy of the considered sunquake event

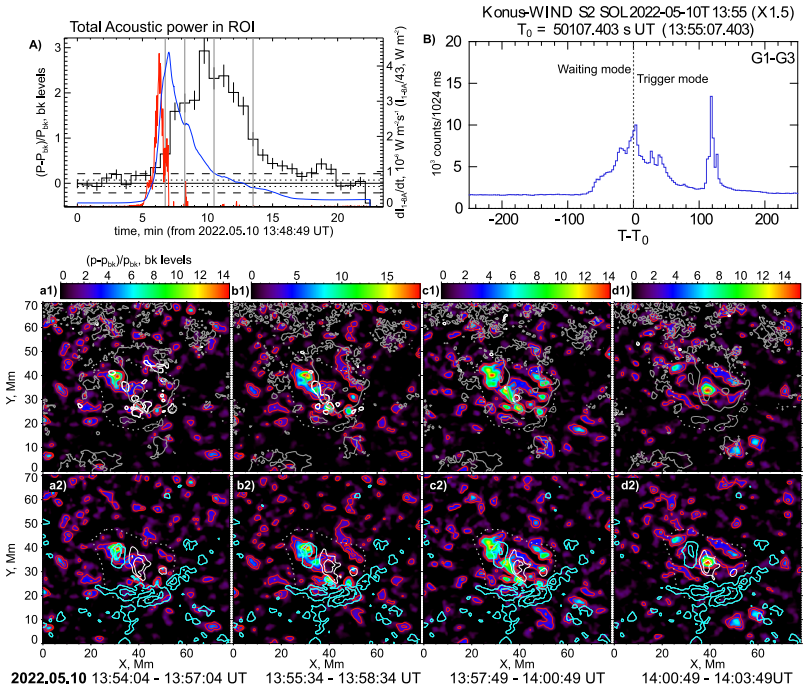

Fig. 1. Panel A: GOES 1–8 Å lightcurve (blue) and its time derivative (red); Normalized acoustic power with errors in units of background levels (black histogram). Vertical lines in A show positions of the time intervals used to generate acoustic maps in (a–d) panels. Horizontal lines show 1 and 3 sigma levels around zero acoustic power. KONUS/WIND HXR lightcurve (G1-G3 channels) is shown in panel B. Panels (a1–d1): acoustic power maps (background rainbow colored maps) with overlayed white contours (300 m/s) of LOS Doppler velocity perturbations and PIL (grey lines). Panels (a2–d2) also contain acoustic power maps, but with the overlayed contours of the magnetic field vertical component (cyan – negative, white – positive).

and X GOES flare class gives us a chance to find AR peculiarities responsible for strong sunquakes.

In this work we mostly consider line-of-sight Dopplergrams (45 seconds cadence) and vector magnetograms (Hoeksema et al. 2014) with 720 seconds cadence from the Helioseismic and Magnetic Imager (HMI, Scherrer et al. 2012) onboard the Solar Dynamics Observatory.

3 Properties of the flare phototspheric disturbances

Analysis of the sunquake event and the corresponding photospheric perturbations is shown in Fig.1. We used acoustic holography method and reconstructed the dynamics of the acoustic helioseismic power (A) in the region of interest covering the flare site

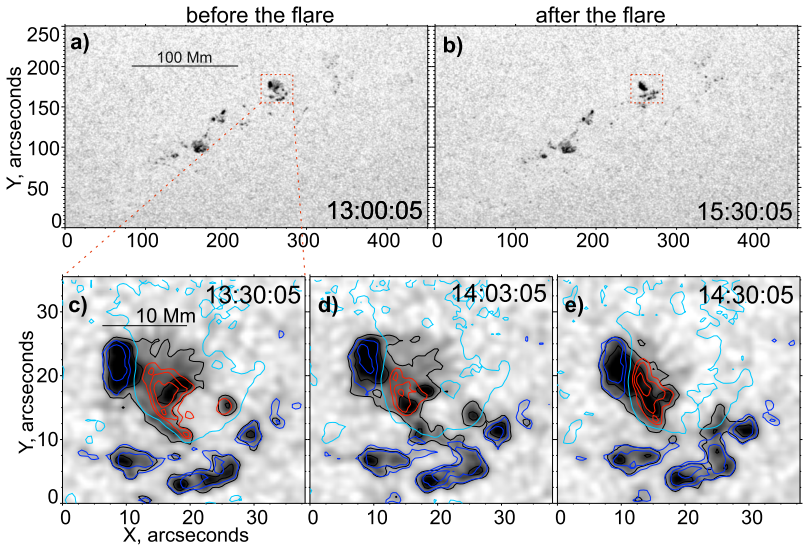

Fig. 2. HMI intensity maps of the NOAA AR 13006 for time instants before and after the flare are compared in panels (a) and (b). ROI corresponding to the main flare energy release is shown by the dashed red rectangular box in (a). Panels (c–d) present dynamics of the HMI intensity maps, LOS magnetic field for negative (blue) and positive (red) directions, and PIL (cyan) for the selected ROI.

(ROI in panels (a–d) marked by dashed contour). The time sequence of 3-minute averaged acoustic maps (a–d) shows that photospheric disturbances and acoustic sources are located along the LIP, forming a quasi-ring "chain" of impacts.

During the flare there were two HXR pulses (Fig.1–B) according to the KONUS/WIND data (18–300 keV): gradual ($\sim$ 180 s) and the impulsive ($\sim$ 30 s). These two bursts have corresponding non-spatial photospheric disturbances in the PIL (white contours of panels (a1) and (b1)). The strongest acoustic sources were located in the sunspots (a2–d2) and in the interspot PIL regions (b2–c2).

4 Dynamics of the morphology of sunspots and magnetic fields

We found significant flare-associated changes in the morphology of the leading δ-sunspot. General view of the studied active region before and after the flare is shown in Fig.2(a, b) (HMI continuum intensity maps with 45-sec cadence). The ROI around the photospheric perturbations is marked by the rectangular dashed box. Note that the asymmetric penumbra experienced decay and the leading sunspot became rather compact ($\sim$ 10 Mm) penumbra-less sunspot.

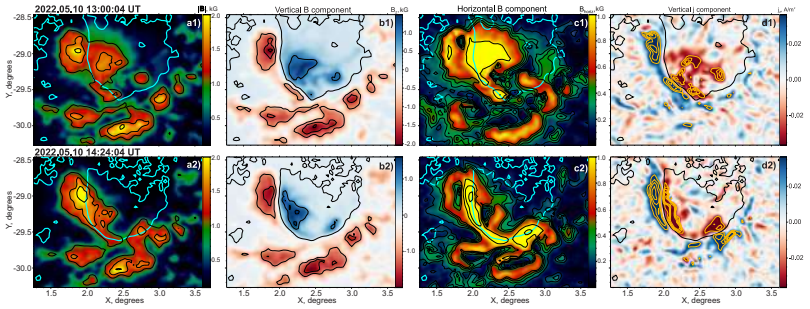

Fig. 3. The following maps deduced from HMI vector magnetograms are shown: Absolute value of magnetic field (a); Vertical magnetic component (b); Horizontal component (c); Vertical electric current density (d). PIL is shown by black (b, d) and cyan (a, c) curves. Regions of enhanced values of the magnetic field components and electric current are highlighted by contours with different levels (black in (a–c) and orange in (d)).

Penumbra decay and corresponding dynamics of the LOS magnetic field is clearly shown by three frames in Fig.3(c–e). One can note that the observed δ-spot (two umbras of opposite polarities in the common penumbra) experienced compactification and became δ-spot with a single umbra (we do not separate two initial umbras). These changes are connected with the magnetic field restructuring around the δ-spot, where the flare energy release took place. Magnetic field changes were detected in all three magnetic field components. The most dramatic changes were: 1) "compression" of the magnetic field of the δ-spot (a1–a2) and formation of a single umbra δ-spot with the PIL inside it and degradated penumbra; 2) significant changes in the distribution of the horizontal magnetic field (c1–c2) highlighting penumbral decay and growth of the horizontal component value at the PIL; 3) restructuring of the electric current system (d1–d2).

The non-linear force free modelling (NLFFF, based on the optimization method in approach of Rudenko & Myshyakov 2009) of the coronal magnetic field reveals a compact dome structure with a spine (yellow lines in Fig. 4), covering the flare δ-spot region where we observed the sunquake event. An extremely sheared current-carrying magnetic structure lying along the PIL is shown by red lines.

5 Concluding remarks

The performed analysis of the helioseismic X1.5 solar flare with the powerful sunquake in the $Cso\ \beta\delta$ active region revealed that the spatial distribution of the acoustic sources and photospheric impacts were associated with the dome-spine magnetic field topology located around the δ-spot. We found significant magnetic field changes with

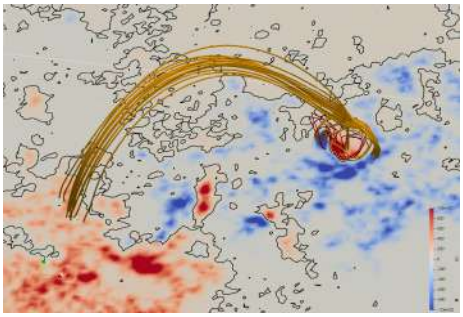

Fig. 4. Topology of the coronal magnetic field lines (based on the NLFFF reconstruction) around the flare region. The blue-red background image shows the vertical magnetic field map. The black curve is the PIL. Yellow lines mark magnetic field lines forming the dome and spine. Red lines mark the twisted magnetic structure lying along the PIL and covered by the dome.

penumbral decay during the flare with restructuring electric current system. This example of the powerful sunquake in the rather "simple" (from the point of view of McIntosh classification) active region shows that we need a dynamic δ-sunspot for efficient helioseismicity. However, this short study did not give us an answer to the question of which agent directly disturbed the photosphere. It is possible that the observed dynamics of the δ-spot magnetic field leads to effective acceleration and formation of electron (or ion) beams that effectively disturb the lower solar atmosphere. However, other mechanisms (dissipation of electric current or pulsed magnetic forces) cannot be ignored. To obtain clearer results about the nature of sounquakes, we need more case-studies, statistics and theoretical/modeling research. We believe that the conditions favorable for sunquakes in the analyzed active region discussed in this paper can provide direction for future observational and theoretical studies.

Acknowledgements. We thank the many team members who contributed to the success of the SDO mission and, especially, the HMI instrument.

Funding

The work was supported by the Russian Science Foundation grant No. 23-72-30002.

References

Hoeksema J.T., Liu Y., Hayashi K., et al., 2014, Solar Physics, 289, 9, p. 3483
Kosovichev A.G., Sadykov V.M., Stefan J.T., 2023, Astrophysical Journal, 958, 2, id. 160
Kosovichev A.G., 2015, Extraterrestrial Seismology, ed. V. Tong & R. García, p. 306
Rudenko G.V. and Myshyakov I.I., 2009, Solar Physics, 257, 2, p. 287
Sharykin I.N. and Kosovichev A.G., 2020, Astrophysical Journal, 895, 1, id. 76
Scherrer P.H., Schou J., Bush R.I., et al., 2012, Solar Physics, 275, 1-2, p. 207

MODERN ASTRONOMY: FROM THE EARLY UNIVERSE TO EXOPLANETS AND BLACK HOLES

Using *UBVRI*-photometry to detect signs of asteroid activity

M. Shcherbina[1,2] and V. Busarev[1,3]

[1] Institute of Astronomy (INASAN), 48 Pyatnitskaya St., Moscow, 119017 Russia

[2] Sternberg Astronomical Institute, Moscow State University, 13 Universitetsky pr., Moscow, 119234 Russia

3 Lomonosov Moscow State University, Moscow, 119992 Russia

Abstract. This paper focuses on the application of *UBVRI*-photometry to detect signs of sublimation-dust activity in Main Belt asteroids. Survey observations have been conducted at the Caucasian Mountain Observatory of Moscow State University since 2021, using the RC600 telescope, which has provided data for 133 asteroids. Special attention is given to primitive-type asteroids (with low-temperature mineralogy), many of which may still retain water ice in their interiors. Numerical models of light reflection by active C-type asteroids with a dust exosphere have confirmed spectral differences depending on particle composition. A qualitative criterion for the activity of a primitive asteroid was established, based on the occurrence of a negative gradient in its reflection spectrum in an active state due to ice sublimation and the formation of a dust exosphere. As a result of observations and data analysis, spectral signs of dust activity were detected in 14 primitive asteroids, confirming the effectiveness of the method used.

Keywords: methods: observational; techniques: photometric; asteroids: active asteroids

DOI: 10.26119/VAK2024.117

1 Active asteroids: relevance of research

In recent years, the distinctions between comets and asteroids have blurred, complicating their identification. Although sublimation activity is a traditional feature of comets, they can appear like asteroids as their volatile compounds are depleted or an insulating crust forms (Rickman et al. 1990). Conversely, asteroids can show comet-like activity, though the mechanism is debated. An example is 133P/Elst-Pizarro, discovered in 1996 and classified as a Main Belt comet (Elst et al. 1996). The concept of the "asteroid-comet continuum" suggests no rigid boundaries between these objects.

Active asteroids are bodies that have shown pronounced activity, such as coma or tail formation, at least once. The causes are not specified, as activity can arise from various mechanisms. The main mechanisms for Main Belt asteroids are ice sublimation (mainly water ice) and impact events. Sublimation requires ice near the surface to absorb solar energy. Primitive-type asteroids, likely formed near the early Solar System's water ice condensation boundary, are prime candidates for active asteroids.

2 Object selection criteria

For the phenomenon of sublimation activity to occur, the bodies must contain reserves of water ice. Therefore, when designing the observation program, special attention is given to low-temperature asteroids that have not undergone significant heating throughout their existence. These asteroids exhibit absorption bands in their reflection spectra characteristic of hydrosilicates (Busarev et al. 2015). Such spectral types of asteroids include C, B, F, G according to Tholen's classification, as well as B, C, and subgroups Cb, Cg, Ch, Cgh according to the SMASS II classification by Bus-Binzel. The taxonomic class X is also promising, as the asteroids within it generally exhibit characteristics similar to those mentioned above.

Ice does not necessarily need to be on the surface of a solid, airless body to sublimate; however, for remote detection, it must be present on the surface. Ice reservoirs may be located just below the surface or deeper, with the most well-preserved reservoirs likely found in larger asteroids.

Sublimation requires the presence of radiant energy, the source of which is the Sun. Many periodically active objects, particularly comets, become more active as they approach the Sun. Therefore, the observation program includes asteroids that are at minimal perihelion distances (Shcherbina et al. 2022).

3 *UBVRI*-photometric observations: observatory, methodology, and data processing

Since 2021, studies of Main Belt and near-Earth asteroids have been conducted at the Caucasian Mountain Observatory of Moscow State University (CMO MSU; elevation 2112 m) to detect signs of activity. *UBVRI*-photometric data are obtained using the semi-automatic RC600 telescope (0.6 m). The photometric system's characteristics are detailed in Petrova & Busarev (2023). Two observational programs from December 2021 to March 2022 and November 2022 to February 2023 yielded *UBVRI* data for 133 asteroids (Petrova & Busarev 2023; Busarev et al. 2024).

The method for calculating approximated reflection spectra involves dividing the integral light intensity at the effective wavelength in each photometric band (registered by the CCD from the asteroid) by the same value from a solar-analog star, considering the difference in air masses and the spectral transparency function of the atmosphere. The reflectance values are normalized to the V-band. Each asteroid was observed in three series (passes through *UBVRI* filters within a few minutes to ∼10–15 minutes, depending on brightness), compiling individual reflectance values into a single spectrum. Solar control stars (non-variable stars close to the asteroid in magnitude and coordinates on the same CCD-frame) ensured atmospheric stability. Consistent data from the three series indicated good atmospheric conditions during measurements.

4 Criteria for detecting sublimation-dust activity

After obtaining the approximated reflection spectra, an analysis identified signs of sublimation-dust activity. A clear indicator is a significant deviation from the "canonical" reflection spectrum from the SMASS II database. Figure 1 shows examples for asteroids 145 Adeona (a) and 322 Phaeo (b). Thus, a qualitative criterion was established: a significant negative gradient in the reflection spectrum of an active asteroid compared to its "classical" spectrum from the SMASSII database.

For interpreting the obtained reflection spectra of active asteroids, numerical modeling of light scattering in the exosphere of a hypothetical low-albedo (geometric albedo $A_g = 0.072$) C-type asteroid with a dust exosphere was conducted. Figure 2 shows examples of normalized reflection spectra calculated for such an asteroid, normalized to the value at $\lambda = 0.55$ μm. The optical thickness of the exosphere (τ), sizes of individual particles (R_{eff}), and monomers in aggregates (r), as well as substance designations, are indicated on the graphs and captions.

From Fig. 2b, it is evident how different the reflection spectrum of an active asteroid can be depending on the exosphere particle composition. Non-absorbing

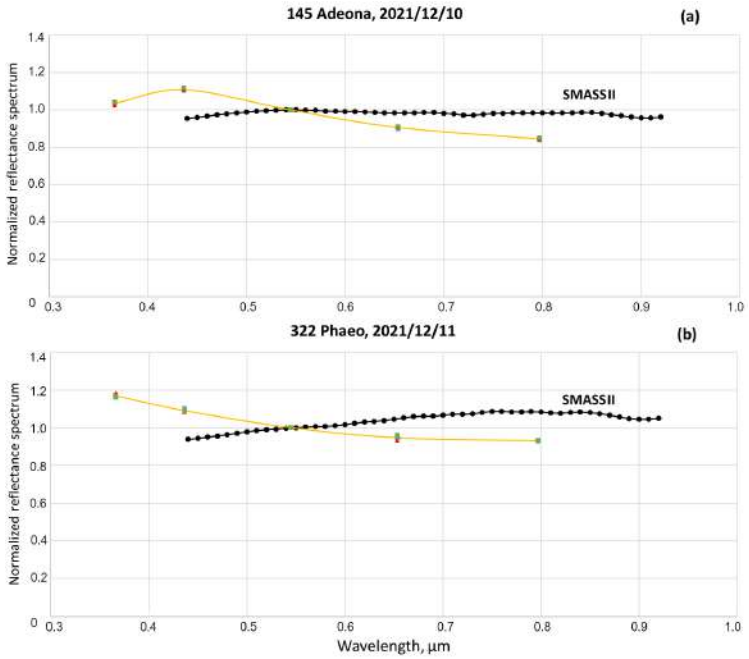

Fig. 1. Approximated normalized to 0.55 μm reflection spectra (at the effective wavelengths of $UBVRI$-photometric bands) of asteroids showing signs of activity: 145 Adeona (a); 322 Phaeo (b). Their reflection spectra from the SMASS II database are shown in black.

ice or weakly absorbing silicates significantly elevate the short-wavelength part of the spectrum, whereas submicron particles that absorb short wavelengths have the opposite effect.

To accurately determine the sublimation-dust activity of a specific asteroid, a quantitative criterion was introduced. This criterion compares the standard error of the mean intensity of light flux in the U-band from the active asteroid and a non-variable control star. According to model calculations, the U-band is the most informative for detecting asteroid activity, exhibiting the largest amplitude of short-period variations in light flux intensity caused by the solar wind (Busarev et al. 2024). The control star on the same CCD-frame, with a similar magnitude, should not show such strong variations.

5 Results

Since 2021, spectral-dust activity of varying degrees has been detected in 14 asteroids, with some objects showing repeated signs of activity. The physical parameters of these asteroids are presented in Table 1.

Table 1. Physical parameters and family affiliation (if applicable) of asteroids showing signs of activity. Note: The source of the information is indicated by superscript letters: [a] https://ssd.jpl.nasa.gov/; [b] https://www.minorplanet.info/. Classification is indicated by superscript numbers: [1] according to Tholen classification; [2] according to SMASS II classification.

Number and Name	Diameter (Effective) km	Class[a]	Geometric Albedo	Family[b]
145 Adeona	127.78[a]	C[1]	0.06[a]	Adeona
	150.95[b]	Ch[2]	0.05[b]	
164 Eva	100.25[a]	CX[1]	0.03[a]	–
	73.03[b]	X[2]	0.10[b]	
322 Phaeo	69.86[a]	X[1]	0.09[a]	Phaeo
	73.14[b]	X[2],D[2]	0.08[b]	
360 Carlova	129.13[a]	C[1]	0.04[a]	–
	115.62[b]	C[2]	0.05[b]	
521 Brixia	107.23[a]	C[1]	0.07[a]	–
	115.78[b]	Ch[2]	0.04[b]	
629 Bernardina	35.09[a]		0.14[a]	–
	29.97[b]	X[2]	0.18[b]	
750 Oskar	22.53[a]	F[1], C[1]	0.06[a]	Nysa-Polana
	20.51[b]		0.05[b]	
751 Faina	113.70[a]	C[1]	0.03[a]	Faina
	110.18[b]	Ch[2]	0.04[b]	
757 Porthlandia	32.89[a,b]	XF[1]	0.22[a]	Athor
		Xk[2]	0.16[b]	
762 Pulcova	147.34[a]	F[1], C[1]	0.04[a,b]	–
	136.88[b]	Cb[2]		
778 Theobalda	55.32[a]	F[1]	0.08[a]	Athor
	63.88[b]		0.05[b]	
779 Nina	80.57[a]		0.16[a]	–
	77.45[b]	X[2]	0.17[b]	
1121 Natascha	12.86[a]		0.29[a]	Theobalda
	12.41[b]		0.27[b]	
1687 Glarone	37.85[a]		0.14[a]	Theobalda
	33.66[b]		0.08[b]	Themis

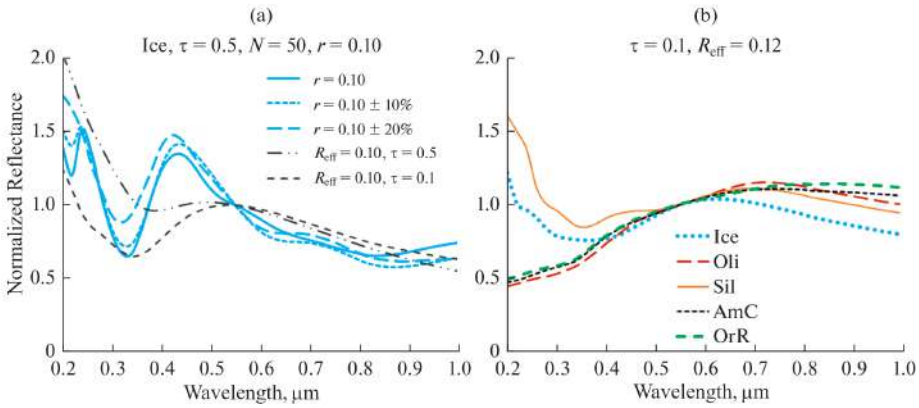

Fig. 2. Normalized reflectance spectra for a hypothetical low-albedo C-type asteroid with a dust exosphere. Numerical modeling by E.V. Petrova (Petrova & Busarev 2023). (a) The spectra for the exosphere ($\tau = 0.5$) composed of ice aggregates, with particle radii $r = 0.10$ μm or within specified limits, or homogeneous particles at specified $R_{\rm eff}$ and τ. (b) The exosphere with $\tau = 0.1$ contains homogeneous particles of different composition ($R_{\rm eff} = 0.12$ μm). "Ice" – H_2O ice, "Oli" – olivines, "Sil" – astronomical silicates, "AmC" – amorphous carbon, "OrR" – refractory organic.

Therefore, based on the presented observational and modeling results, it can be asserted that *UBVRI*-photometric survey observations are a highly sensitive and reliable method for detecting signs of sublimation-dust activity in primitive-type asteroids, likely containing water ice.

Funding

The authors express their gratitude to the Russian Science Foundation for the financial support of this work (the RSF grant No. 22-12-00115).

References

Busarev V., Barabanov S., Rusakov V., et al., 2015, Icarus, 262, p. 44
Busarev V., Petrova E., Shcherbina M., et al., 2023, Solar System Research, 57, 5, p. 449
Busarev V., Petrova E., Shcherbina M., et al., 2024, Solar System Research, 58, 6, p. 715
Elst E., Pizarro O., Pollas C., et al., 1996, International Astronomical Union Circular, 6456, id. 1
Petrova E. and Busarev V., 2023, Solar System Research, 57, 2, p. 161
Rickman H., Gustafson B., Fernandez J., 1990, Asteroids, Comets, Meteors III, Proceedings of a meeting (AMC 89), ed. C.I. Lagerkvist, H. Rickman, and B.A. Lindblad., p. 423
Shcherbina M., Busarev V., Burlak M., et al., 2022, INASAN Science Reports, 7, p. 93

Gaia Data Release 3: analysis of reflectance spectra of near-Earth asteroids and Mars-crossers

M. Shcherbina[1,2] and D. Kovaleva[1]

[1] Institute of Astronomy (INASAN), 48 Pyatnitskaya St., Moscow, 119017 Russia
[2] Sternberg Astronomical Institute, Moscow State University, 13 Universitetsky pr., Moscow, 119234 Russia

Abstract. Since July 2014, the European Space Agency (ESA) Gaia mission has been observing objects in the Solar System as part of its various scientific missions. The third data release (DR3) includes observations of more than 150,000 objects, including asteroids. Analysis of Gaia asteroid reflectance spectra has allowed for the first time to determine spectral types for many objects and to confirm or refine previously determined classes. The distribution of spectral groups coincides with the analysis of ground-based observations performed by other authors, with a sample overlap of less than 20%. The main groups include the S-group (∼60%) and the C-group (∼20–25%). Mars-crossing objects are slightly more likely to have mixed mineralogy. This distribution remains constant over different ranges of object diameters. Analysis of the distribution of spectral groups by semi-major axis and perihelion distance may serve as indirect evidence for the prevalence of sublimation-dust activity in primitive asteroids.

Keywords: astronomical databases: Gaia Data Release 3; asteroids: Near-Earth Asteroids, Mars-crossers

DOI: 10.26119/VAK2024.118

1 The Gaia Space Mission

Gaia, an ESA mission, was launched on December 19, 2013, from Kourou, French Guiana, and began operations on July 25, 2014. The mission's primary goal is to create a highly accurate three-dimensional map of the positions and velocities of stars in the Milky Way. The satellite is equipped with two telescopes and an astrometric instrument with 106 CCD detectors, enabling precise astrometric and photometric measurements. Gaia also has two spectrophotometers – the Blue Photometer (BP) and the Red Photometer (RP), operating in the wavelength ranges of 330–680 nm and 640–1050 nm, respectively. The large volume of data obtained from repeated scans of the celestial sphere by Gaia provides results for Solar System objects as well. DR3 includes information on more than 150,000 Solar System objects, making it the largest space-based survey of asteroid reflectance spectrophotometry in the visible range to date.

Reflectance spectra are calculated by dividing the flux of each spectrum by the spectrum of a solar analog and normalizing it at a wavelength of 550 nm. The calibration process removes instrumental and astrophysical effects, resulting in arrays of 60 internal flux values and their uncertainties. The spectra have been verified for internal consistency and have a signal-to-noise ratio $(S/N) > 13$. Gaia's reflectance spectra were compared with ground-based telescope data and other space missions, showing good agreement for bright objects. For each Solar System object, a reflectance spectrum is calculated at 16 points representing integral reflectance values (Gaia Collaboration 2023). An example of such a reflectance spectrum is presented in Fig.1.

2 Near-Earth Asteroids and Mars-Crossers

This study analyzes Gaia data for near-Earth asteroids (NEAs) and Mars-crossers. NEAs are divided into groups such as Atens, Apollos, and Amors based on orbital parameters, due to their proximity to Earth and potential collision threat. Mars-crossers are asteroids whose orbits intersect Mars, allowing the study of dynamic processes and migration of small bodies in the Solar System.

The investigation provides valuable data on the composition, structure, and dynamics of small bodies, crucial for developing strategies to protect Earth from possible collisions.

3 Evaluation of Asteroid Spectral Groups

This study is a continuation of the work by Shcherbina et al. (2024), which analyzed the spectral group distribution among near-Earth asteroids. Key steps in spec-

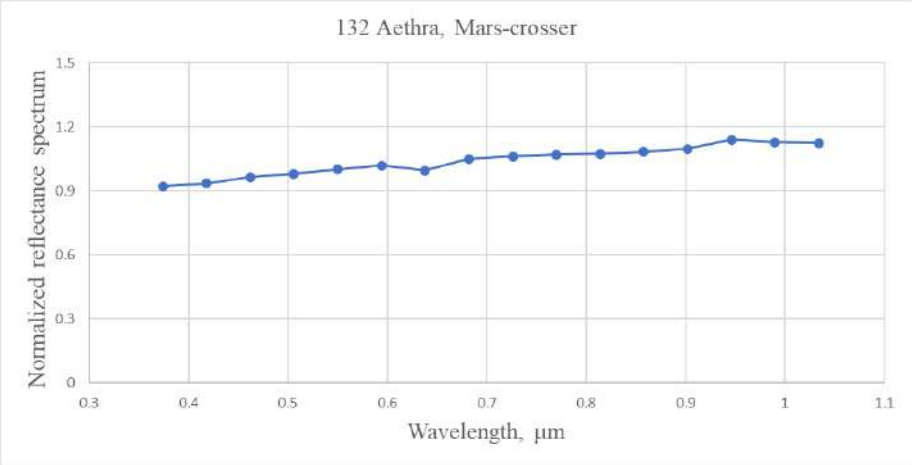

Fig. 1. Normalized reflectance spectrum of asteroid 132 Aethra (Mars-crosser) from the GDR3 catalog.

tral classification included the collection of parameters such as geometric albedo, orbital period, and diameter. The classification was performed according to the Tholen or Bus–Binzel (SMASS II) taxonomies, using data from the NASA database (https://ssd.jpl.nasa.gov/horizons/) and compared with previous studies conducted by INASAN in collaboration with SAI MSU.

The procedure, known as "spectrophotometric corridor construction", involved:

1. Extracting reflectance spectra of asteroids from the SMASS II database (Bus & Binzel 2002).
2. Determining maximum and minimum reflectance values for each wavelength, creating spectral class ranges.
3. Classifying asteroids based on albedo, spectral gradient, the presence of absorption bands, and matching with template spectra.

In cases of ambiguity, asteroids could be assigned to multiple classes. The spectral classes were divided into major groups (C, S, X) and minor groups (rare classes like Ld, T, D, V, O), considering similar mineral compositions. Some asteroids were classified as mixed due to characteristics of both high and low-temperature classes. Among the 731 reflectance spectra of Mars-crossers, 92 could not be definitively classified and were excluded from further analysis. The remaining 556 had their spectral class determined for the first time. Table1 shows the distribution of Mars-crossers and NEAs.

This study and the previous work by Shcherbina et al. (2024) were inspired by the research of Binzel et al. (2019), which presented a sample of approximately 1000

Table 1. Distribution of spectral groups of near-Earth asteroids and Mars-crossers based on GDR3 Data with supplementary spectrophotometric observations from the Terskol observatory (Bus & Binzel 2002).

Asteroids	Total Number	C-group	S-group	X-group	Minor group	Mixed
Mars-crossers	639	154	359	25	27	74
Atens	7	3	1	1	1	1
Apollos	57	12	36	1	3	5
Amors	43	8	28	0	6	1
Total number	746	177	424	27	37	81

near-Earth asteroids, including Mars-crossers. It is important to emphasize that the originality of the current sample compared to the sample used in Binzel's paper exceeds 80%. Specifically, there is an overlap of only 126 objects, while the remaining ones are new.

4 Distribution of asteroids by spectral groups

The spectral group affiliations of near-Earth asteroids and Mars-crossers were determined, and the results are presented in Fig.2. As shown, the percentage content of the main spectral groups is very similar (S-group, approximately 60%, C-group, approximately 20-25%). There is a slightly higher number of objects exhibiting signs of mixed mineralogy among the Mars-crossers, possibly due to more active impact evolution.

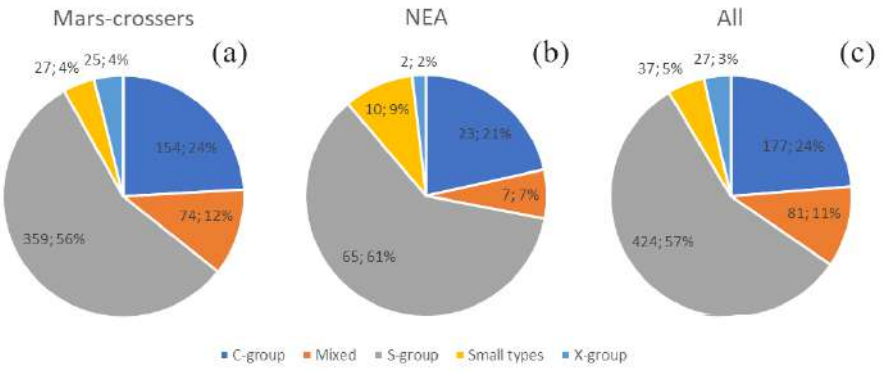

Fig. 2. Distribution by spectral groups (a) Mars-crossers; (b) near-Earth asteroids; (c) complete sample from Gaia DR3 + observations of individual near-Earth asteroids at the Terskol observatory.

The results from Binzel et al. (2019) show very similar distributions: about 60% of the population consists of S-type asteroids, 20% C-type, and 20% other classes. This distribution indicates the diversity of NEA sources, reflecting their origins from various regions of the Main Asteroid Belt.

As noted by the authors of the mentioned paper, this distribution remains constant among asteroids of different diameters (Fig. 3). Of course, the diameter values for Mars-crossers and NEAs are determined for only a small number of asteroids (311 in total, including 234 Mars-crossers and 77 NEAs). Additionally, it should be noted that diameter data may be inaccurate due to the difficulties in determining this parameter.

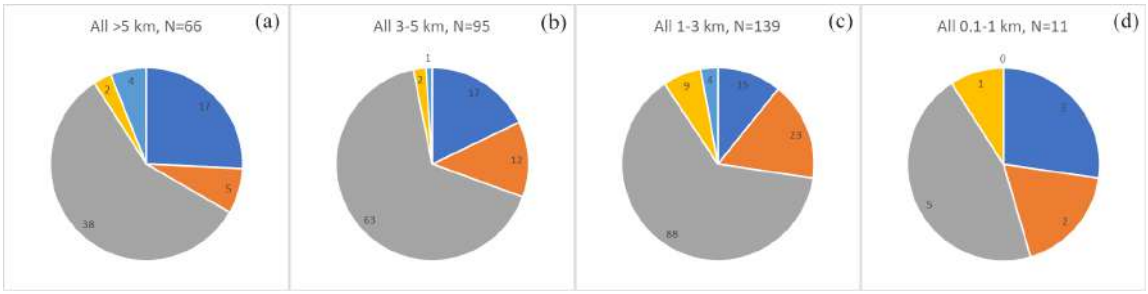

Fig. 3. Distribution of NEAs and Mars-crossers by spectral classes of asteroids of various sizes (Diameter values are taken from the NASA database). The number of asteroids included in each distribution is indicated within each sector.(a) Distribution by spectral groups for asteroids with a diameter greater than 5 km. (b) Distribution for asteroids with a diameter from 3 to 5 km. (c) Distribution for asteroids with a diameter from 1 to 3 km. (d) Distribution for asteroids with a diameter less than 1 km.

The analysis of the distribution of various spectral groups of asteroids by semi-major axis and perihelion distance of orbits shows that C-type asteroids cover almost the entire range of semi-major axis values. S-type asteroids are concentrated closer to the inner edge of the Main Belt, which is associated with their high-temperature mineralogy. Notably, despite the numerical predominance of the S-group, primitive-type asteroids (C-group) are also found at small perihelion distances. The presence of such asteroids in this zone may explain the phenomenon of sublimation activity of primitive asteroids, which is supported by the correlation of their activity with the passage of the perihelion zone, noted in several studies (e.g., Busarev et al. (2023)).

5 Conclusions

1. The analysis of reflectance spectra of asteroids from the Gaia spacecraft allowed for the first-time determination of spectral classes for many objects. For asteroids with previously determined classes recorded in the JPL NASA database, their affiliations were confirmed or refined.
2. The distribution of spectral groups in the sample matches the results of ground-based observations (Binzel et al. 2019) with a sample overlap of about 20%. The percentage content of the main spectral groups is similar: the S-group is about 60%, and the C-group is about 20–25%. Among the Mars-crossers, more objects with mixed mineralogy are observed, associated with active impact evolution.
3. This statistic is also maintained for asteroids of various diameters, as noted in the work of Binzel et al. (2019).
4. Representatives of the C-group cover a wide range of semi-major axis values and small perihelion distances, confirming the hypothesis of sublimation-dust activity of primitive-type asteroids through a comet-like mechanism.

Funding

Shcherbina M.P. expresses her gratitude to the Russian Science Foundation for the financial support of this work (RSF grant 22-12-00115).

References

Binzel R., DeMeo F., Turtelboom E., et al., 2019, Icarus, 324, p. 41
Bus S. and Binzel R., 2002, Icarus, 158, 1, p. 146
Busarev S., Petrova E., Shcherbina M., et al., 2023, Solar System Research, 57, 5, p. 449
Gaia Collaboration, 2023, Astronomy & Astrophysics, 674, id. A1
Shcherbina M., Kovaleva D., Shustov B., 2024, Solar System Research, 58, 3, p. 359

MODERN ASTRONOMY: FROM THE EARLY UNIVERSE TO EXOPLANETS AND BLACK HOLES

Peculiarities of Joule dissipation in the solar atmosphere

A. Stepanov[1,3], V. Zaitsev[2], and E. Kupriyanova[1,3]

[1] Pulkovo Observatory, Pulkovo chaussee 65, Saint Petersburg, 196140 Russia
[2] Institute of Applied Physics, Ulyanova str. 46, Nizhny Novgorod, 603950 Russia
[3] Ioffe Institute, Polytekhnicheskaya str. 26, Saint Petersburg, 194021 Russia

Abstract. The peculiarities of the electric current dissipation in the magnetic flux rope throughout the solar atmosphere from the photosphere to the corona are considered. It has been shown that the dissipation depends on both the magnitude of the electric current and the altitude. The dissipation rate reaches its maximum near an altitude of 2100 km and has a rather complex behaviour. The regions of predominance of Cowling and Spitzer resistances are determined. The consequences of these peculiarities in current problems of solar physics are discussed.

Keywords: solar atmosphere; heating; flares; Couling resistivity; Joule dissipation

DOI: 10.26119/VAK2024.119

1 Introduction

The neutral component of plasma plays an important role in Joule dissipation in the solar atmosphere. For example, a study of the output of a magnetic flux through the partially ionized solar atmosphere by Leake & Arber (2006) led to the conclusion that there is a maximum of Cowling resistivity at an altitude of $h = 1900$ km, but below 1000 km and above 2100 km up to 2300 km the resistivity was assumed to be zero. Here we used the updated model of the solar atmosphere C7 by Avrett & Loeser (2008) extending to the corona and showed that there are some peculiarities of Joule dissipation in the solar atmosphere. We also discuss the consequences of these peculiarities for problems of coronal heating, pre-flare plasma heating, white light flares (WLFs), and the formation of the transition region (TR) and sunspot light bridges (SBs).

2 The problem statement

We consider the dissipation of longitudinal electric currents in magnetic flux tubes (flux ropes) of radius r with foot-points located in the photosphere. It is assumed that the current $I = I_z$ is directed along the flux tube axis z and along the magnetic field B_z. To determine the rate of Joule dissipation, we can use the generalized Ohm's law

$$\mathbf{E} + \frac{1}{c}\mathbf{V} \times \mathbf{B} = \frac{\mathbf{j}}{\sigma} + \frac{\mathbf{j} \times \mathbf{B}}{enc} - \frac{\nabla p_e}{en} + F\frac{\mathbf{f_a} \times \mathbf{B}}{cnm_i\nu'_{ia}} - \frac{F^2\rho}{cnm_i\nu'_{ia}}\left[\frac{d\mathbf{V}}{dt} \times \mathbf{B}\right]. \qquad (1)$$

Here $\mathbf{V} = \left(\sum_k n_k m_k \mathbf{V}_k\right) / \left(\sum_k n_k m_k\right)$, $j = I/\pi r^2$, $\rho = n_a m_a + n_e m_e + n_i m_i$, $p = p_a + p_e + p_i$, $\sigma = ne^2 / \left[m_e(\nu'_{ei} + \nu'_{ea})\right]$ is the Spitzer conductivity, $\nu'_{kl} = \left[m_l/(m_k + m_l)\right]\nu_{kl}$ is the effective collision frequency, $F = \rho_a/\rho$, $n_i = n_e = n$, $\mathbf{f_a} = \nabla p_a$. According to (Zaitsev et al. 2023), the rate of Joule dissipation per unit volume of the flux tube is

$$q = \left(\mathbf{E} + \frac{1}{c}\mathbf{V} \times \mathbf{B}\right)\mathbf{j} = \frac{j_z^2}{\sigma} + \frac{F^2}{(2-F)c^2 n m_i \nu'_{ia}}(\mathbf{j} \times \mathbf{B})^2 = \frac{j_z^2}{\sigma}, \qquad (2)$$

where $B_\varphi \approx 2I/cr$. To compare the dissipation rates due to the Spitzer and Cowling resistivities we represent eq. (2) as

$$q = \frac{j_z^2}{\sigma}\left(1 + K_{cow}\right), \quad K_{cow} = \frac{F^2}{1-F}\,\omega_e\tau_e\omega_i\tau_{ia}, \qquad (3)$$

where $\omega_e = \frac{eB_\varphi}{cm_e}$, $\omega_i = \frac{eB_\varphi}{cm_i}$, $\tau_e = \frac{1}{\nu'_{ei}}$, $\tau_{ia} = \frac{1}{\nu'_{ia}}$.

3 Results

To obtain the altitude dependence of the rate of Joule dissipation $q(h)$ in a flux tube with $r = 10^8$ cm from the photosphere to corona, we used the C7 atmosphere model by Avrett & Loeser (2008). We showed that the Cowling resistivity as well as the curves of $q(h, I)$ are more complicate compared to the results obtained in Leake & Arber (2006). In particular, $q(h, I)$ exhibits a clear maximum at an altitude of $h = 2100$ km for currents $I = 3 \times 10^9$ A, 3×10^{10} A, and 3×10^{11} A corresponding to the TR (see Fig. 2 in Zaitsev et al. (2023)), such that at $h \leq 1000$ km, the Cowling resistance is smaller than that of Spitzer ($K_{cow} < 1$) for current $I < 10^{11}$ A. This is caused by the decrease in the Hall parameter $\omega_i \tau_{ia}$ in eq. (3). In other words, the Cowling resistance decreases due to the increasing role of interparticle collisions as the atmospheric density increases.

In the corona, the relative fraction of neutral atoms at a temperature of $T = 10^6$–5×10^6 K is extremely small, $F \approx 10^{-7}$ (Zaitsev et al. 2023). However, at high current values, the Joule dissipation is determined by the Cowling resistivity at a current of $I \geq 10^9$ A. This occurs because the Ampère force accelerates the ions to speeds significantly greater than the relative speed of the electrons and ions in the current. In this case, the accelerated ions give up their energy to the neutrals in one collision, while the "e-i" energy exchange occurs m_i/m_e times slower.

The threshold value of the electric current can be estimated when the Joule dissipation $q = K_{cow}\, j_z^2/\sigma \approx 2.2 \times 10^{-9} I^4/(n_e^2 r^6 T^{3/2})$ ergs cm^{-3} s^{-1} exceeds the radiation losses $q_r \approx 10^{-19} n_e^2 T^{-1/2}$ ergs cm^{-3} s^{-1}, $10^5 < T < 10^7$ K. Taking $T = 1.6 \times 10^6$ K, $n_e = 7.5 \times 10^7$ K at $h = 7 \times 10^4$ km we obtain that $q > q_r$ requires $I > 2.3 \times 10^9$ A.

4 Ring currents in the foot-points of flux tubes and white light flares

Ring or Hall currents j_φ at the foot points of magnetic flux tubes arise as a result of "gearing" of the vertical component of the magnetic field B_z and the radial component of the photospheric convection velocity V_r (Zaitsev & Stepanov 2021):

$$j_\varphi = \frac{\sigma V_r B_z}{c(1 + K'_{cow})}, \quad K'_{cow} = \frac{F^2}{2 - F}\, \omega_e \tau_e\, \omega_i \tau_{ia}. \tag{4}$$

Here instead of ω_e and ω_i in eq. (3) we use $\omega_e = \frac{eB_z}{cm_e}$, $\omega_i = \frac{eB_z}{cm_i}$, i.e., K'_{cow} does not depend on the magnitude of the ring current, but is determined by the magnitude of

the longitudinal magnetic field B_z. Hence, the rate of Joule dissipation is determined as $q = \frac{j_z}{\sigma}(1 + K'_{cow})$.

To determine the value of K'_{cow} at $h = 300$ km, where the white light flares are located, we assume that $B_z \approx 2 \times 10^3$ G, $T = 15000$ K, $n_a \approx 10^{16}$ cm^{-1} (Zaitsev & Stepanov 2021) and estimate $n_e = 2 \times 10^{15}$ cm^{-3} using the modified Saha formula we found $K'_{cow} \approx 0.07$, i.e. the Spitzer resistivity plays a decisive role in the current dissipation. The threshold for generating WLFs emission is $q(t) \geq q_r = (n_a + n_e)n_e\chi(T)$, where the radiation-loss function is $\chi(T) = (1.397 \times 10^{-8}T)^{6.15}$ for $8 \times 10^3 < T < 2 \times 10^4$ K. The inequality $q(T) \geq q_r$ means that the heating can occur at $V_r B_z \geq 10^8$ cm s^{-1} G (De Pontieu et al. 2011). Assuming that $B_z = 10^3$ G in the sunspot penumbra, the heating can occur at $V_r \geq 10^5$ cm s^{-1}, which exceeds the typical convection velocity of 3×10^4 cm s^{-1}. This may be the reason why white light flares are so rare events.

5 Consequences of peculiarities in Joule dissipation

5.1 Maximum in Joule dissipation: Coronal heating and TR formation

Dissipation rate maximum at $h \approx 2100$ km leads to very important consequences. First of all, it is dealing with the heating of solar corona, which is one of the important unsolved problems in astrophysics. Solar corona loses 10^{28} ergs s^{-1} due to radiation and thermal conductivity. Hot coronal loops are unlikely to be sources of heating due to the low electron thermal conductivity through the magnetic field. The most likely sources of heating are open magnetic flux tubes, such as type II spicules, extending into the corona (De Pontieu et al. 2011; Zaitsev et al. 2020). Heating of type II spicules in the TR, where the rate of Joule dissipation increases, may compensate for the rate of heat loss from the corona. Estimations by Zaitsev et al. (2020) have shown that this requires about 10^4 type II spicules i.e. about 1% spicules observed simultaneously on the Sun.

Type II spicules may also be responsible for TR formation. We showed in Zaitsev et al. (2023) that Joule scattering in type II spicules is very effective for the formation of the transition layer TR, and its thickness Δz depends on the magnitude of the electric current:

$$\Delta z \approx \sqrt{\frac{4k_e T_c^{7/2}}{7q_{max(I)}}}, \tag{5}$$

where $k_e \approx 0.9 \times 10^{-6}$ erg cm^{-1} K$^{-7/2}$, T_c is the coronal temperature. For example, at $I = (3 - 5) \times 10^{10}$ A, eq. 5 gives $\Delta z \approx 23$–230 km.

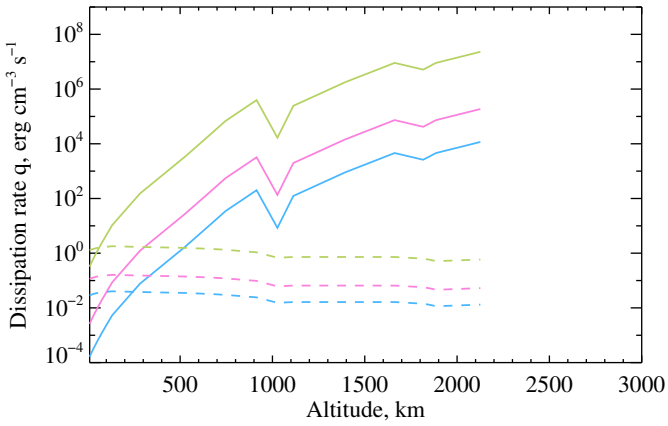

Fig. 1. Dissipation rates vs altitude for electric current magnitudes $I = 1.5 \times 10^{11}$ A (blue curves), 3×10^{11} A (magenta curves), and 10^{12} A (green curves) using the Maltby-M model with $r = 7 \times 10^{7}$ cm. The dots indicate dissipation rate under the Spitzer conductivity while the solid lines correspond to Cowling conducivity.

5.2 Formation of sunspot light bridges

Among the sunspots, a special place is occupied by light bridges (LBs), the sizes, shapes and brightness of which are very diverse. The formation of a LB begins usually at one edge of the umbra in the form of a bright thin ($\leq$ 1 arcsec) rope which gradually grows and divides the umbra into small pieces.

In our model the LB has the form of a low-lying magnetic flux rope with the foot-points rooted in the penumbra. The electric current generated at the foot-points of the LB due to convective motions in the penumbra is closed by the surface return currents. We assume also that the plasma parameters in the LB correspond to the Maltby-M umbral core model by Maltby et al. (1986). The result of calculations is presented in Fig. 1. To estimate the Joule dissipation rate for LB heating, we used the observed LB parameters by Louis et al. (2021): the length is $\approx$ 14 arcsec $\approx 10^{9}$ cm, radius is $\approx$ 1arcsec $\approx 7 \times 10^{7}$ cm, height of the top is $h \approx 10^{3}$ km, $T \approx 6800$ K, $B_z \approx 1.3$ kG, and the average electric current density $j_z \approx 0.1$ A m^{-2} corresponding to the current $I_z \approx 1.5 \times 10^{11}$ A. The result $q \approx 3$ erg cm^{-3} s^{-1} is in agreement with the observed value. The formation of LBs can be caused by a weakening of the magnetic field in the sunspot and/or a decrease in magnetic flux but not by the emergence of a new magnetic flux (Louis et al. 2021).

5.3 Heating of pre-flare plasma

Another possible evidence in favor of Joule dissipation in low solar atmosphere follows from GOES, RHESSI, SDO/AIA, and Solar Orbiter/STIX observations. The "Hot onset" interval (10–17 MK) increases at the initial soft X-ray and before any detectable hard X-ray emission Hudson et al. (2021). From the emission measurements, the electron density was estimated to be 5×10^{11} cm^{-3}, and attention was drawn to the fact that the onset of soft X-ray emission occurs in the chromospheric foot-points of low-lying loops, and not in coronal structures. From the other side, the electric currents up to $I \approx 10^{12}$ A were measured in the flare precursor (Wang et al. 2017). Thus, "hot onset" phenomena can be a consequence of the Joule heating of the low solar atmosphere.

6 Summary

1. The dependence of the Cowling resistivity on the altitude and current value is not pulse-like (Leake & Arber 2006), but is much more complex.
2. Despite the low density of neutrals in the corona, $n_a/n_e \sim 10^{-7}$, the Cowling resistivity exceeds the Spitzer resistivity at a current of $I \geq 10^9$ A.
3. In the photosphere and lower chromosphere, the Spitzer resistivity dominates over the Cowling resistivity.
4. Joule scattering features can explain a wide variety of solar phenomena, such as coronal heating, hot starts of progenitors, white light flares, and the formation of the transition region and sunspot light bridges.

Funding

This study was supported by the Russian Science Foundation grant No. 22-12-00308.

References

Avrett E.H. and Loeser R., 2008, Astrophysical Journal Supplement Series, 175, 1, p. 229
De Pontieu B., McIntosh S.W., Carlsson M., et al., 2011, Science, 331, p. 55
Hudson H.S., Simões P.J.A., Fletcher L., et al., 2021, Monthly Notices of the Royal Astronomical Society, 501, 1, p. 1273
Leake J.E. and Arber T.D., 2006, Astronomy & Astrophysics, 450, 2, p. 805
Louis R.E., Prasad A., Beck C., et al., 2021, Astronomy & Astrophysics, 652, id. L4
Maltby P., Avrett E.H., Maltby M., 1986, Astrophysical Journal, 306, p. 284
Wang H., Liu C., Ahn K., et al., 2017, Nature Astronomy, 1, id. 0085
Zaitsev V.V., Stepanov A.V., Kupriyanova E.G., 2023, Geomagnetism and Aeronomy, 63, 7, p. 947
Zaitsev V.V. and Stepanov A.V., 2021, Geomagnetism and Aeronomy, 61, 7 ,p. 917
Zaitsev V.V., Stepanov A.V., Kronshtadtov P.V., 2020, Solar Physics, 295, 12, id. 166

BAK 2024 MODERN ASTRONOMY: FROM THE EARLY UNIVERSE TO EXOPLANETS AND BLACK HOLES 300 years Russian Academy of Sciences

Differential rotation of sunspots of different magnetic polarity

K. Tlatova and A. Tlatov

Kislovodsk Mountain Astronomical Station of the Pulkovo observatory, Gagarina str. 100, Kislovodsk, 357700 Russia

Abstract. The rotation rate was analyzed depending on the latitude of individual sunspots of different m agnetic p olarity. T o i dentify s unspots, w e u sed observations of the SDO/HMI space observatory in the period 2010-2024 in the continuum and observations of magnetic fields a t t he s ame t ime. I t w as f ound t hat t he rotation rate of sunspots depends on the magnetic polarity in the 22-year Hale magnetic cycle. The dependence of the rotation rate of sunspots on latitude can be written for sunspots of leading polarity, the rotation rate can be approximated by the formula: $\omega_{\rm ld}(\theta) = 14.574 - 2.225\sin^2\theta - 0.02\sin^4\theta$ deg/day. For sunspots of trailing polarity $\omega_{\rm tr}(\theta) = 14.216 - 2.60\sin^2\theta - 0.01\sin^4\theta$ deg/day. Thus, sunspots of leading polarity rotate more than $\sim 2\%$ faster than sunspots of trailing polarity. For sunspots with magnetic flux $\Phi > 2 \cdot 10^{20}$ M x, t he r otation r ate p ractically d oes n ot c hange with increasing magnetic flux.

Keywords: Sun: sunspots; rotation

DOI: 10.26119/VAK2024.120

1 Introduction

Sunspots are often used to study long-term rotation variations. Sunspots rotate at a different rate than non-magnetic plasma. The most available data for studying long-term variations in the rotation of the Sun are data on sunspot groups. Based on the analysis of Mount Wilson observations from 1921 to 1982 Howard et al. (1984), the law of rotation of sunspot groups $\omega(\theta) = 14.52 - 2.84\sin^2\theta$ deg/day was found. According to the processing of the Greenwich Photoheliographic Results 1874-1976 (Balthasar et al. 1986), the law of rotation was found $\omega(\theta) = 14.557 - 2.85\sin^2\theta$

There are much fewer studies based on the analysis of the movement of individual sunspots. Newton & Nunn (1951), studying the movements of 139 single unipolar recurrent sunspots for 1934 – 1944, found the dependence of the sidereal velocity of rotations of the sine of latitude: $\omega(\theta) = 14.38 - 2.38\sin^2\theta$ deg/day. In Kutsenko (2021) the rotation rate was found for unipolar sunspots $\omega(\theta) = 14.28 - 2.4\sin^2\theta - 2.24\sin^4\theta$ deg/day. In Howard et al. (1984) it was found that sunspot groups rotate about 1% slower than individual sunspots.

Gilman & Howard (1984, 1985) performed the analysis of the rotation rate variation of individual sunspots according to the Mount Wilson Observatory. They processed photographic plates of observations in "white" light for the period 1917 – 1983. Gilman & Howard (1984) showed that there are rotation variations with the phase of the solar activity cycle. In Gilman & Howard (1985) sunspots with a lifetime of at least 2 days were taken for analysis. It was found that the leading sunspots rotate faster than the following sunspots, by about 0.1 deg/day, or 14 m/s.

In this study, we will consider the speed of longitudinal movement of individual sunspots depending on the magnetic properties of sunspots.

2 Data and Method

For the analysis, we used Solar Dynamics Observatory/Helioseismic and Magnetic Imager (SDO/HMI), with a cadence of 45 seconds of the hmi.Ic_45s and hdmi.M_45s series made at the same time. We took 5 images for each day. The observation data were processed automatically. To identify sunspots and pores, we used a sunspot detection procedure similar to that used at the Kislovodsk Mountain Astronomical Station (KMAS) to identify sunspots for synoptic observations (Tlatov et al. 2014).

To determine the velocity of movement, we tracked sunspots on neighboring time images. We have created tables of the characteristics of sunspots and pores, including their geographical coordinates, area, magnetic field characteristics, type of spot and others. Next, we determined the rate of movement of the geometric center of sunspots and pores $\omega = \Delta\phi/\Delta t$, where $\Delta\phi$ is the longitude shift, Δt is the time interval. The

procedure for determining the sequence in application to determining the lifetime of sunspots and pores is described in Tlatov (2023). In total, about 250 thousand pairs were allocated in neighboring images of the Sun with a time difference of 5 hours.

3 Analysis results

Sunspots can be classified according to the polarity of their magnetic field. To determine the polarity of the field, we used the superimposition of the boundaries of the spots selected in the continuum on the magnetograms of the magnetic field made on the same telescope at the same time. The Hale law was used to determine the polarity sign of the leading and trailing sunspots.

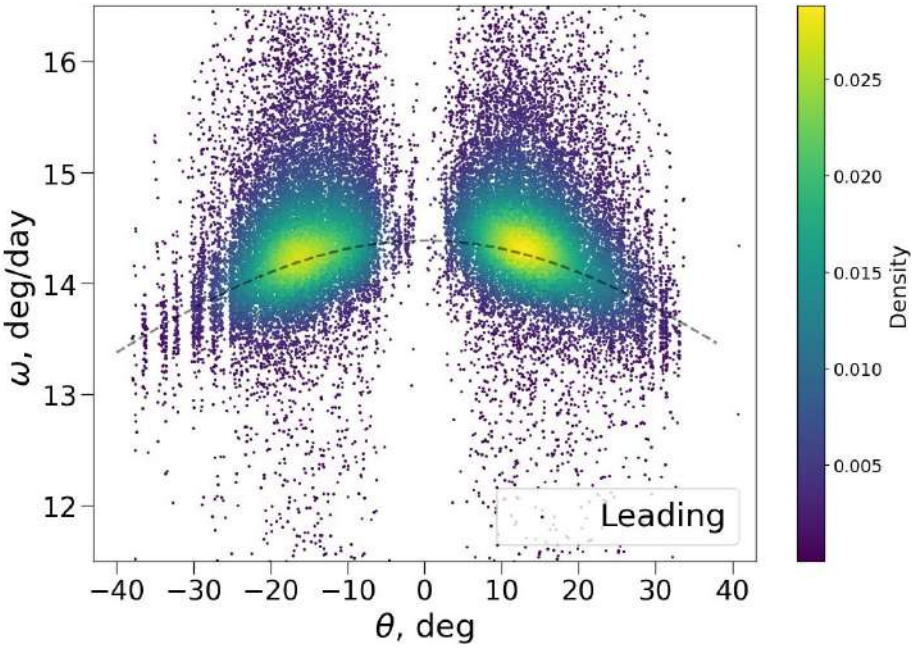

Fig. 1. Scatter plot of the rotation rate of sunspots of the leading magnetic polarity. The dotted line shows the rotation rate according to (Newton & Nunn 1951).

In total, ≈ 117 thousand sunspots of the leading polarity and ≈ 95 thousand of the trailing polarity were identified, in which the rotation rate was determined. Figure 1 shows the scatter diagram of the rotation rate of sunspots of the leading polarity, and Fig. 2 shows same diagram for sunspots of the trailing polarity. Here we consider sunspots with an area greater than $S > 20$ μhm. This limitation allowed

us to exclude solar pores from consideration. For comparison, the dotted line on the graphs shows the rotation rate of unipolar sunspots from the work (Newton & Nunn 1951). It can be noted that the center of gravity of the diagram for sunspots of the leading polarity is higher, and for spots of the trailing polarity is lower than the rotation rate of unipolar spots according to the (Newton & Nunn 1951) formula. For sunspots of leading polarity, the rotation rate can be approximated by the formula: $\omega_{\rm ld}(\theta) = 14.574 - 2.225\sin^2\theta - 0.02\sin^4\theta$. For sunspots of trailing polarity, $\omega_{\rm tr}(\theta) = 14.216 - 2.60\sin^2\theta - 0.01\sin^4\theta$ deg/day. Sunspots of leading polarity rotate $\approx 2.3\%$ faster than sunspots of trailing polarity.

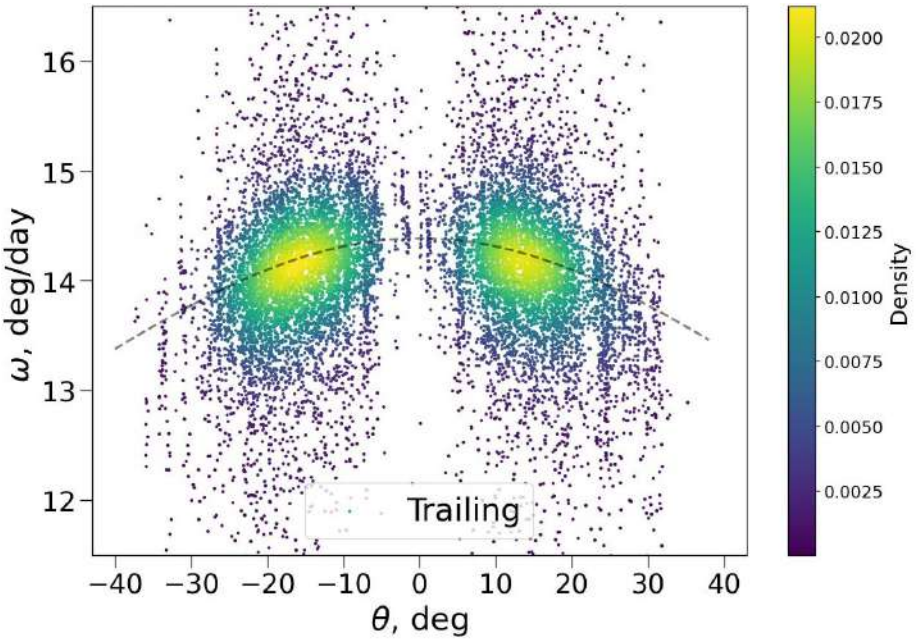

Fig. 2. Same as in Fig. 1 but for sunspots of trailing polarity.

The dependence of the differential rotation rate of sunspots of different magnetic polarity on the magnetic flux is shown in Fig. 3. Here, spots near the equator $\theta < \pm 15^o$ are considered. The following can be noted. Sunspots with low magnetic flux $\Phi < 2 \cdot 10^{20}$ Mx rotate more slowly than sunspots with large areas. For sunspots of trailing polarity with flux $\Phi > 2 \cdot 10^{20}$ Mx, the rotation rate practically does not change with increasing flux. For spots of leading polarity, with increasing flux $\Phi > 1 \cdot 10^{21}$ Mx, the rotation rate decreases.

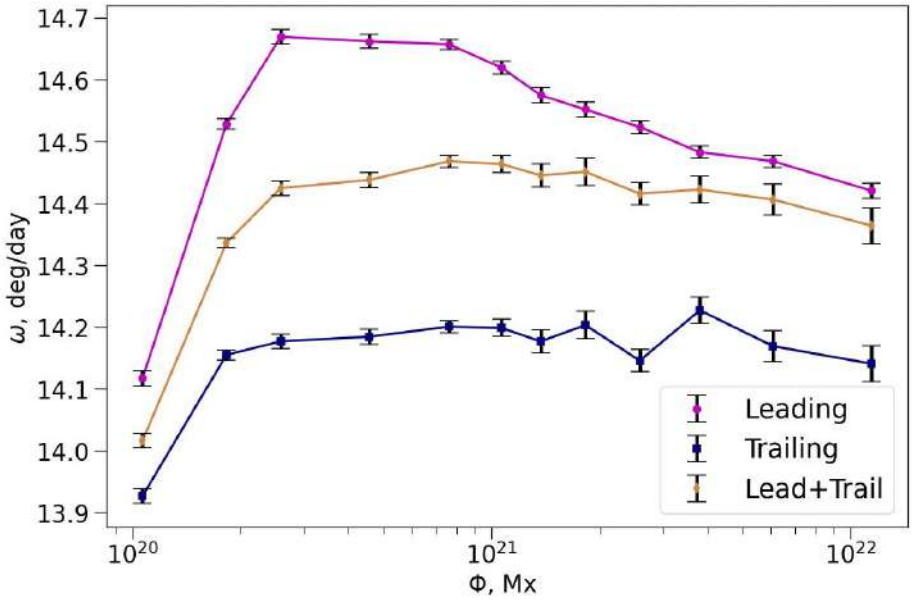

Fig. 3. Rotation rate of sunspots of different magnetic polarity depending on their magnetic flux with latitude in the range $\theta : \pm 15^o$.

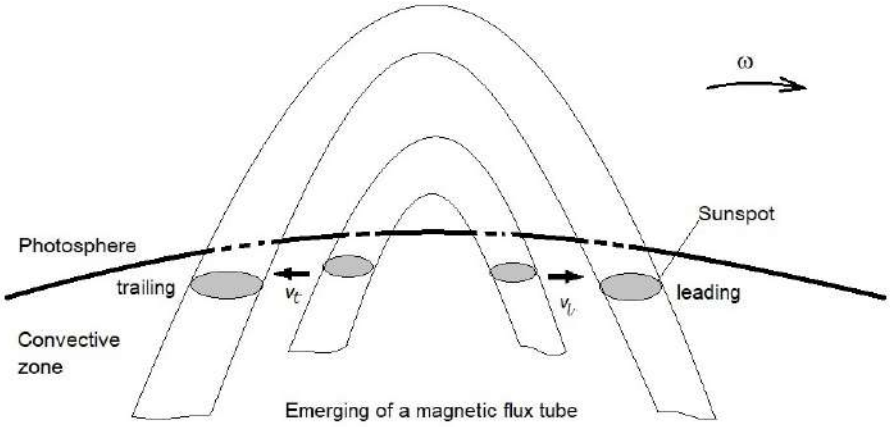

Fig. 4. Simplified diagram of the possible formation of additional speed of longitudinal displacement of sunspots during the emergence of a magnetic flux tube.

4 Discussion

Leading polarity sunspots have rotation rate $\sim$ 2.3% faster than trailing polarity sunspots, or 0.26 deg/day or 36 m/s (Fig. 1, 2). A similar result was obtained earlier (Gilman & Howard 1985). However, they did not use information about magnetic polarity and took leading and trailing spots when processing the plates in "white" light. Such a difference in speeds may be due to additional factors affecting the horizontal movement of the sunspots. Sunspots are visible as the exits of the arch of magnetic flux tubes on the photosphere. At the initial stage of ascent, the distance between the sunspots is less than in the later stages, since the distance between the legs of the arches fixed on the photosphere increases with distance from its top. This leads to the appearance of an additional observable velocity v_l for the leading sunspot directed along the rotation. For the trailing sunspots of the part, the v_t velocity is directed against rotation, which creates the effect of a slow rotation rate (Fig. 4).

Acknowledgements. Data are courtesy of NASA/SDO and the HMI science team.

Funding

This work was supported in the framework of the national project "Science" by the Ministry of Science and Higher Education of the Russian Federation under the contract No. 075-03-2024-113.

References

Balthasar H., Vazquez M., Woehl H., 1986, Astronomy & Astrophysics, 155, 1, p. 87
Gilman P.A. and Howard R., 1984, Astrophysical Journal, 283, p. 385
Gilman P.A. and Howard R., 1985, Astrophysical Journal, 295, p. 233
Howard R., Gilman P.A., Gilman P.I., 1984, Astrophysical Journal, 283, p. 373
Kutsenko A.S., 2021, Monthly Notices of the Royal Astronomical Society, 500, 4, p. 5159
Nagovitsyn Yu.A., Pevtsov A.A., Osipova A.A., 2018, Astronomy Letters, 44, 3, p. 202
Newton H.W. and Nunn M.L., 1951, Monthly Notices of the Royal Astronomical Society, 111, p. 413
Tlatov A.G., Vasil'eva V.V., Makarova V.V., et al., 2014, Solar Physics, 289, p. 1403
Tlatov A.G., 2023, Solar Physics, 298, id. 93

MODERN ASTRONOMY: FROM THE EARLY UNIVERSE TO EXOPLANETS AND BLACK HOLES

Prospects for observing the near-limb zone of the Sun using the radio telescopes RT-32 IAA RAS

N. Topchilo[1], I. Rakhimov[2], T. Andreeva[2], N. Peterova[3], and V. Nagnibeda[1]

[1] St. Petersburg State University, Universitetskaya Embankment, 7-9, St. Petersburg, 199034 Russia

[2] Institute of Applied Astronomy of the Russian Academy of Sciences, Kutuzova Embankment, 10, St. Petersburg, 191187 Russia

[3] St. Petersburg branch of Special Astrophysical Observatory of the Russian Academy of Science, Pulkovskoye Sh., 65, St. Petersburg, 196140 Russia

Abstract. The report presents the first results of test observations conducted since April 2024 on the RT-32 radio telescope of the "Svetloe" observatory at a wavelength of 3.5 cm. The observations were carried out in the quasi—circular scanning mode, a variant of scanning when the telescope sequentially tracks a number of points located on a circle.

With the beam width of this instrument being 4 arcminutes, active regions and their sunspot components are easily identified in the entire limb zone, which is problematic, for example, for the RATAN-600 radio telescope. While not having high resolution, RT-32 successfully detects faint sources above the solar limb, which are poorly visible on the SRH radioheliograph. And the joint use of all three RT-32 radio telescopes makes it possible to monitor solar activity in the summer practically throughout the entire day.

Keywords: methods: observational; Sun: coronal mass ejections (CMEs), prominences

DOI: 10.26119/VAK2024.121

1 Introduction

Observations carried out in the microwave range have shown that the chromosphere, transition region and lower corona contain a large number of non-stationary three-dimensional structures of various types and sizes. The brightness, size and relative position of individual structures are determined quite well by mapping the solar disk using modern radioheliographs (SRH, Nobeyama), interferometers (ALMA) and large variable-profile antennas (RATAN-600). But the study of the altitude structure of sources, necessary for their adequate modeling based on observations of the central regions of the solar disk, turns out to be difficult and very ambiguous. A natural solution here is to observe sources in the near-limb zone, especially in its behind-the-limb part, when the altitude structure of the source is displayed directly in the picture plane. However, observations in this region present significant difficulties due to the strong altitudinal brightness gradient of the solar atmosphere. At the same time, the raster mapping method usually employed in radio observations leads to large errors when identifying sources on the solar limb.

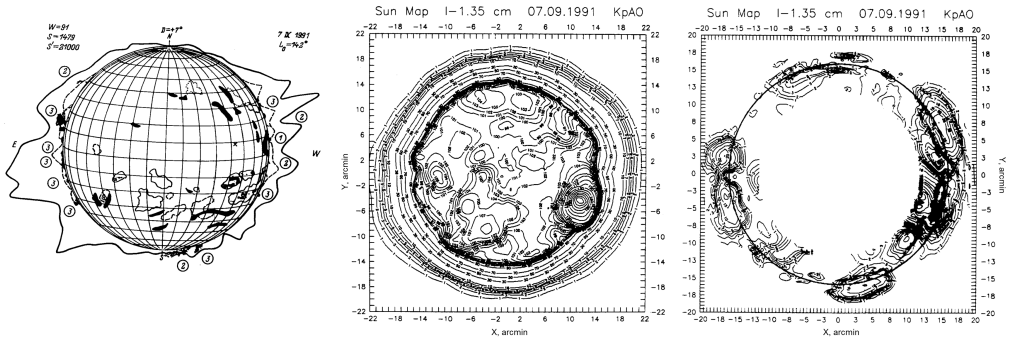

Fig. 1. An example of mapping the entire Sun at a wavelength of 1.35 cm in intensity (map in the center) and the results of identifying sources in the limb zone using circular scanning (right map). Isophotes are given as a percentage to the level of the quiet Sun. On the left are the sources visible in optics on the day of observation, according to the "Solar Data" Bulletin.

In the 80s, to improve the accuracy of near-limb observations on large full-circle antennas, a different method was proposed – circular scanning, when the telescope moves in a circle relative to the center of the solar disk. This and other developed methods were implemented on the RT-22 radio telescopes of the Lebedev Physical Institute and RT-22 of the CrAO. With their help, in the 80s–90s, observations of solar prominences behind the solar limb and filaments on the disk in the near-limb regions were carried out at waves of 8 mm and 1.35 cm. Accuracy estimates of

intensity measurements were ∼1% of the level of the quiet Sun and 0.01% in circular polarization. Their position, dimensions along the limb and height were determined, and the magnetic field was measured. Cases of observations of the rise and decay of prominences, as well as coronal mass ejections (CMEs), have been noted. The radio radius of the Sun has been measured. Similar methods have also been used for many years to map the Sun on the RT-7.5 radio telescopes of Bauman MSTU on waves 3.4 and 2.5 mm (Topchilo et al. 2023).

A typical example of solar observations made at that time is shown in Fig. 1 in the form of a complete map of the Sun obtained using raster scanning, and a map of the near-limb zone of the Sun obtained using circular scanning with the background component removed.

Based on previous results, it was proposed to implement these methods on the RT-32 radio telescopes, which are part of the Quasar-KVO complex of the IAA RAS. Technically, they are similar to previous observations, but in a longer wavelength range (3.5–12 cm).

2 Methodology and examples of limb observations of the Sun on RT-32

Initially, the Quasar-KVO radio astronomy VLBI complex of the IAA RAS was intended to solve navigation problems. However, its technical characteristics turned out to be very suitable for conducting studies of microwave radiation from the Sun. Using these radio telescopes, we carried out episodic observations of solar eclipses during two 11–year cycles of solar activity (on average every 2 years during the period 1999–2022), and in two or three observatories simultaneously (Ivanov et al. 2023). The observation technique consisted of tracking selected objects on the solar disk during the period of their coverage/opening by the lunar disk, including the places of I and IV contacts. More complex observation modes mainly associated with scanning an object, were not used yet, since they were not implemented in the version of the Mark IV "Field System" software used on the telescopes.

In this situation, to implement the circular scanning required for full-scale solar observations of the near-limb zone, it was proposed to use its discrete version – the quasi-circular scanning – a variant of scanning when the telescope sequentially tracks a number of points located on a circle. Mathematically, this corresponds to replacing a continuous function with a small set of points. For a solar radius of $\sim\ 16'$ and a half power beam width (HPBW) of $\approx\ 4'$, the minimum number of tracking points is ∼50.

Figure 2 shows two examples of quasi-circular scanning. On the left is a variant with a large step following the angle along the limb and with long tracking of points. Large signal spikes are a consequence of the antenna quickly moving from the current point to the next point. The magnitude of signal fluctuations in the tracking areas is determined by the accuracy of the telescope tracking the Sun. The signal averaged over the tracking areas (red curve) shows good tracking accuracy (the red curve is smooth, without breaks). The figure on the right shows a working version of scan records for different scanning radii. The pitch of the dots along the angle approximately corresponds to half of HPBW; along the radius, it is 1/4. The recordings clearly show the presence of radiation sources associated with solar active regions.

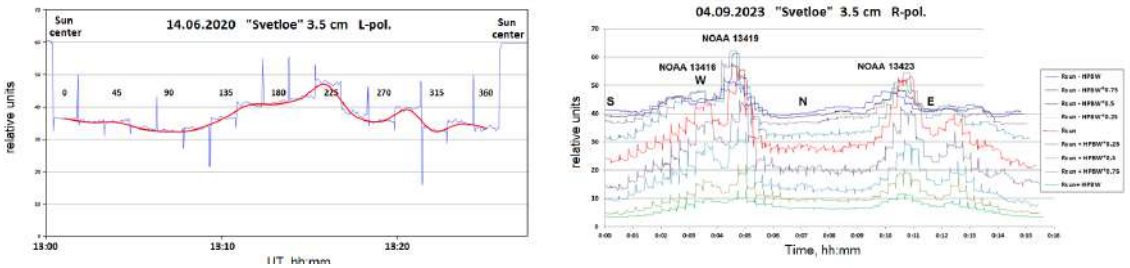

Fig. 2. Two examples of quasi-circular scanning on the RT-32 telescope of the IAA RAS at a wavelength of 3.5 cm with a step of 22.5° (left) and 7° (right). On the right, the AR numbers visible on quasi-circular scans are marked (scan radii are Rsun ± (0(red curve), 0.25, 0.5, 0.75, 1) × HPBW).

Figure 3 shows examples of quasi-circular scans obtained in March – May 2024 at the observatory "Svetloe" at a wavelength of 3.5 cm (right polarization). The scans are normalized to the level of the quiet Sun. From the above examples it is clear that noticeable activity is observed not only on the disk, but also far beyond the limb. Based on observations from April 5, 2024, a map of the Sun was constructed, similar to the central map from Fig. 1. But there the map was built using raster scans, and here, using an incomplete set of quasi-circular scans (hence the empty space in the center of the solar disk). In general, both maps are similar. Comparison with the SRH radioheliograph data (at 6 GHz) showed their agreement when corrected for different angular resolutions.

The last Fig. 4 shows maps of the near-limb zone of the Sun for May 3 and 6, 2024, obtained from a set of quasi-circular scans by subtracting the large-scale background component. The maps obtained on RT-32 at 3.5 cm are similar in nature to the map obtained on RT-22 at 1.35 cm, shown in Fig. 1 on the right, but the level

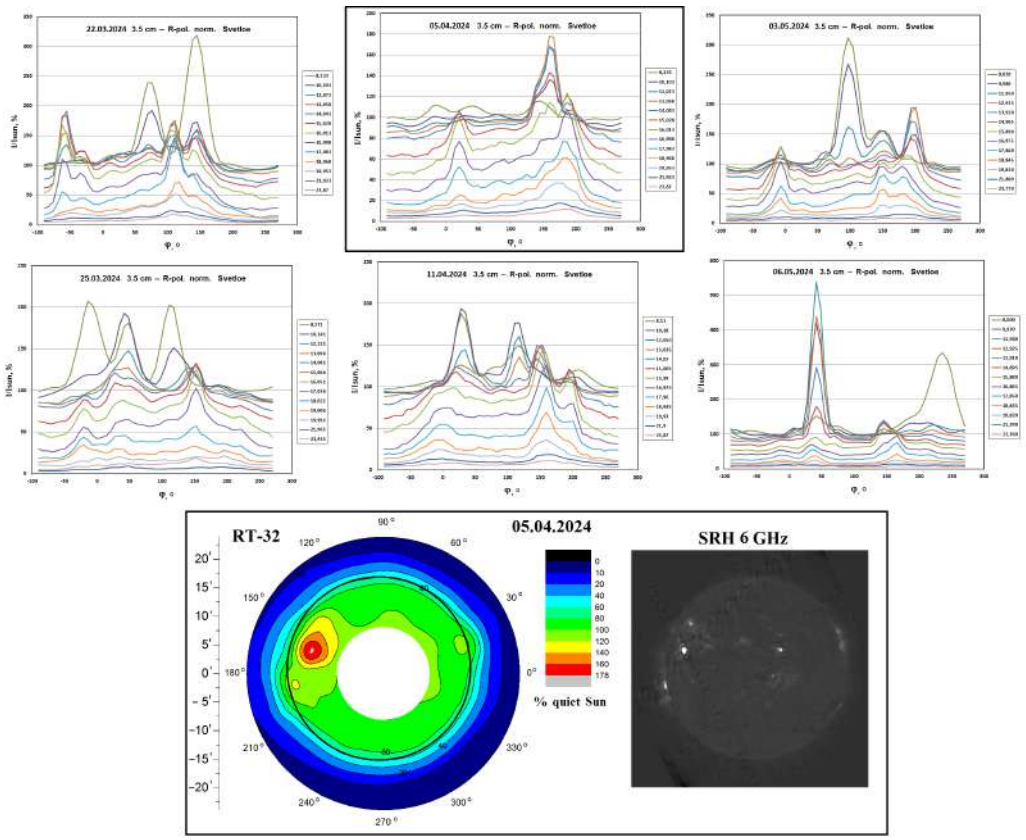

Fig. 3. Examples of circular scans in the range of radii 8–23 arcmin, obtained in April–May on RT-32 at the observatory "Svetloe", and a map for 04/05/2024 on RT-32 and the SRH radiohelograph at 6 GHz.

of solar activity on them is naturally much higher. Comparison with simultaneous observations in other frequency ranges showed the coincidence of individual structural details.

3 Summary

Observations using large single antennas such as RT-32 are certainly inferior in angular resolution to interferometric observations, but they also have their advantages, allowing:

1. direct measurement of the heights/dimensions of stationary coronal objects from observations of their position on the solar limb;

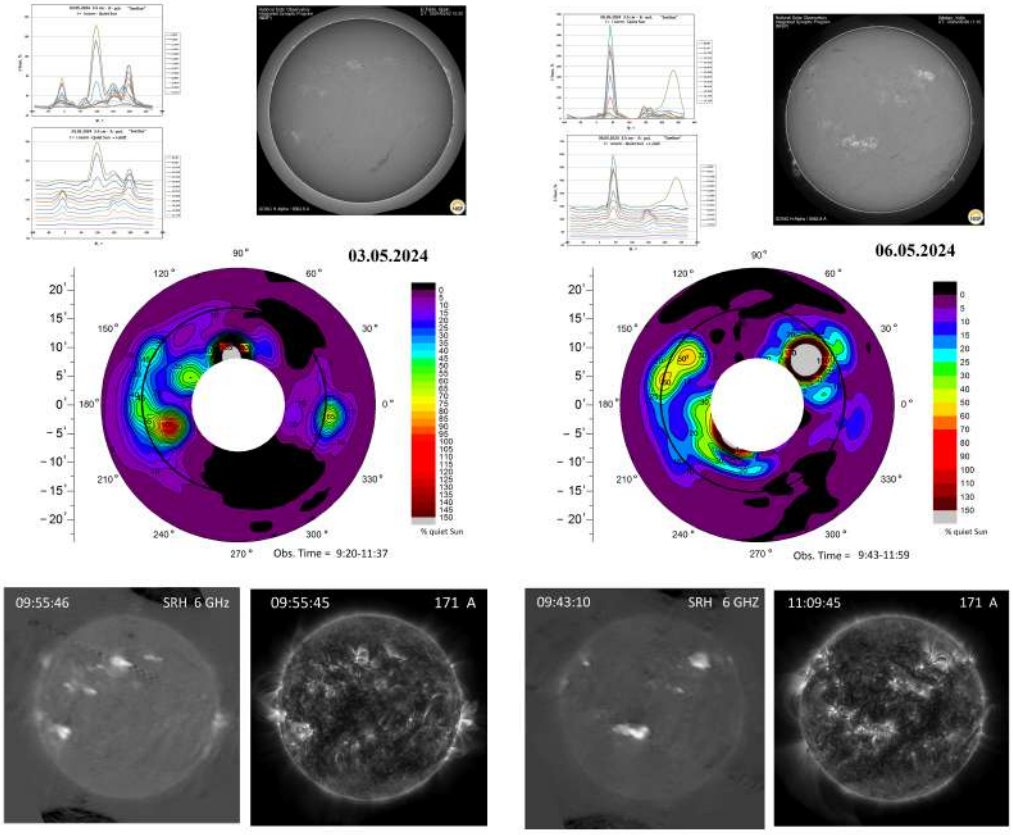

Fig. 4. Scans and maps of the near-limb zone with a removed background for 05/03/2024 and 05/06/2024 on RT-32 and comparison with observations in other wavelength ranges: on the SRH radioheliograph at 6 GHz, the space observatory SDO at 171 Å and H-alpha from NISP. The moments of observations at UT are marked in the corresponding pictures.

2. observation of prominences and measurement of their magnetic field (under development);
3. observations of the dynamics of the post-flare state of the region of the marginal or near-limb flare;
4. observation of CMEs in the lower corona, inaccessible to observations on LASCO;
5. regular measurements of the radio radius of the Sun.

References

Ivanov D.V., Rakhimov I.A., Diakov A.A., et al., 2023, Transactions of IAA RAS, 65, p. 7
Topchilo N.A., Nagnibeda V.G., Peterova N.G., 2023, Transactions of IAA RAS, 65, p. 42

VAK 2024 MODERN ASTRONOMY: FROM THE EARLY UNIVERSE TO EXOPLANETS AND BLACK HOLES 300 years Russian Academy of Sciences

Electric currents in the solar corona and the kink instability of magnetic flux rope

Yu. Tsap[1], A. Stepanov[2] and Yu. Kopylova[2]

[1] Crimean Astrophysical Observatory of the Russian Academy of Sciences, Nauchny, 298409 Russia

[2] Central Astronomical Observatory at Pulkovo of the Russian Academy of Sciences, Pulkovskoje ave. 65/1, St. Petersburg, 196140 Russia

Abstract. We found the dispersion equation for magnetohydrodynamic kink oscillations of a force-free magnetic flux rope with uncompensated longitudinal electric current under the conditions of the solar corona using the energy method and the thin magnetic flux tube approximation. It is shown that the eigenfunctions, along with the eigenvectors, impose additional restrictions on the stability conditions of the kink instability of a flux rope. This allows us to obtain not only the necessary, but also a sufficient condition for stability. The observed weak twist of coronal loops with a small (< 2–3) number of the turns of magnetic field lines around the axis indicates the dominance of unshielded magnetic flux rope in the corona of the Sun, in which the longitudinal electric currents do not exceed 10^{11}–10^{12} A.

Keywords: magnetohydrodynamics (MHD), Sun: corona, flares, coronal mass ejections (CMEs), oscillations

DOI: 10.26119/VAK2024.122

1 Introduction

It is believed that electric currents responsible for the non-potential component of the coronal magnetic field are concentrated in coronal loops, which can be modeled at least in some cases as the magnetic flux ropes. In addition to the flares, they can cause coronal mass ejections, which are the most geoeffective solar events. Despite this, there is still no clear understanding of the structure and characteristic values of coronal electric currents. In particular, it has not been possible to determine whether the currents in the corona are neutralized (shielded) or non-neutralized (unshielded), as is the case in the solar photosphere (Tsap et al. 2022).

There are two types of solar flares: confined and eruptive. The type of the flare depends on the possibility of developing either torus or kink instability (Jing et al. 2018). Torus instability arises primarily due to the restructuring of the magnetic field, while the kink instability depends on the degree of twisting of the magnetic field lines. Which mechanism is more important is not yet entirely clear. Note that Jing et al. (2018) did not reveal a dependence of the flare type on the degree of twisting of magnetic flux ropes for 38 flare events, 26 of which were accompanied by coronal mass ejections. In this regard, the question arises about the possible reason for such statistics. Previously, we considered the criteria for the magnetohydrodynamic (MHD) kink instability of both shielded and unshielded (laboratory pinch) magnetic flux rope based on the energy method (Tsap et al. 2020, 2022). Using the thin magnetic flux tube approximation with a sharp boundary, it was found that shielded flux tubes are stable with respect to kink modes (Tsap et al. 2020). However, the question of the stability of unshielded flux tubes could not be fully clarified, since the authors did not pay enough attention to studying the behavior of the eigenfunctions (displacement vectors) of the system of linearized equations of ideal MHD. As a result, the stability condition obtained by Tsap et al. (2022) is only necessary. Besides, we did not consider in detail the behavior of modes with different signs of the azimuthal wave numbers $m = \pm 1$.

The aim of this paper is to derive a dispersion relation for the kink modes of unshielded magnetic ropes (coronal loops) using the energy method and to investigate the limitations imposed by the boundary conditions at the bases of the loops in the light of recent statistical studies (Jing et al. 2018).

2 Electrical currents and coronal loop twisting

Let us consider the relationship between the electric current and the twisting of coronal loops, modeled as straight, cylindrically symmetric, unshielded magnetic flux ropes with a cross-sectional radius of a, assuming a sharp plasma–plasma boundary.

According to Ampere's law, using cylindrical coordinate system (r, φ, z) and standard notation, the longitudinal current density can be represented as

$$j_z = \frac{c}{4\pi}\frac{1}{r}\frac{\partial}{\partial r}\left(rB_\varphi\right). \tag{1}$$

Multiplying Equations (1) by area elements $2\pi r dr$, after integration we have

$$I_z = I_{zi}(r \to a) + I_{ze}(r \to a) = \frac{cB_\varphi(r)r}{2}. \tag{2}$$

Equation (2) assumes that the total electric current I_z of the shielded magnetic rope, when the azimuthal field components inside (i) and outside (e) are equal to zero, i.e. $B_\varphi(a) = B_{\varphi i}(r \to a) = B_{\varphi e}(r \to a) = 0$.

Unlike the shielded flux rope, the unshielded flux rope with the uncompensated electric current ($I_z \neq 0$), for which $B_\varphi(a) = B_{\varphi e}(r \to a) = B_{\varphi i}(r \to a)$ and $I_{ze}(r \to a) = 0$, can effectively compress the plasma because the equation of the total pressure balance takes the form (Solovev & Uralov 1979)

$$\langle p_i \rangle + \frac{\langle B_{zi}^2 \rangle}{8\pi} = p_e(a) + \frac{B_{ze}^2(a)}{8\pi} + \frac{B_\varphi^2(a)}{8\pi}. \tag{3}$$

Here p is the gas pressure, B_z and B_φ are the longitudinal and azimuthal magnetic fields, respectively (in the local cylindrical system of coordinates). The brackets denote the values averaged over the cross-section of radius a.

Let us assume that the values of coronal and photospheric electric currents are within the same order of magnitude, i.e. the longitudinal electric currents of twisted coronal loop are $I_{zi} = (1-3)\times 10^{11}$ A, which correspond to $3\times 10^{20} - 10^{21}$ statA. Therefore, according to (2) for $a = (1-3)\times 10^8$ cm we obtain

$$B_\varphi(a) = 2I_z/(ca) = 60 - 700 \text{ G}. \tag{4}$$

Using eq. (2) for the total twist angle inside a flux rope at $r = a$ we find

$$\Phi(a) = \frac{LB_{\varphi i}(a)}{aB_{zi}(a)} = \frac{2LI_z}{ca^2 B_{zi}(a)}. \tag{5}$$

For $a = (1-3)\times 10^8$ cm, $L = 3\times 10^9$ cm, $B_{zi}(a) = 300$ G, and $I_z = (1-3)\times 10^{11}$ A, from Equation (5) we get $\Phi(a) = 0.6$–66. These values of the twist angle correspond to the number of turns of the magnetic field lines around the axis of the flux rope $R \approx \Phi(a)/2\pi = 0.1$–$10$.

3 Eigenvector functions and twist instability

Let's consider an axisymmetric flux rope (cylinder) with the unperturbed tube axis, which is parallel to the z-axis with the magnetic field

$$\mathbf{B} = \begin{cases} (0, B_{\varphi i}(r), B_{zi}(r)), \ r \leqslant a; \\ (0, B_{\varphi e}(r), B_{ze}(r)), \ r > a. \end{cases} \tag{6}$$

Using standard notation, it can be easily shown that that eigenvalues $\Lambda = \Omega^2$ of the magnetic configuration with a sharp plasma–plasma boundary separating the inner and outer regions by the surface σ can be found from the following expressions (Tsap et al. 2020):

$$\Lambda = \frac{2W}{\int\limits_{V_i} \rho \mathbf{s}^2 dV + \int\limits_{V_e} \rho \mathbf{s}^2 dV} = 2\frac{W_i + W_e + W_\sigma}{\int\limits_{V_i} \rho \mathbf{s}^2 dV + \int\limits_{V_e} \rho \mathbf{s}^2 dV}\,. \tag{7}$$

Here

$$W_i = \frac{1}{2}\int\limits_{V_i} K\, dV, \quad W_e = \frac{1}{2}\int\limits_{V_e} K\, dV, \quad W_\sigma = \frac{1}{2}\oint\limits_{\sigma} \frac{d\langle P\rangle}{dn} s_n^2(\mathbf{r})\, d\sigma, \tag{8}$$

$$K = \frac{\delta B^2}{4\pi} + \frac{\mathbf{j}}{c}(\mathbf{s} \times \delta\mathbf{B}) + \gamma p(\nabla \mathbf{s})^2 + (\mathbf{s}\nabla p)\nabla \mathbf{s} + \mathbf{g}\mathbf{s}\nabla(\rho \mathbf{s}),$$

$$P = p + B^2/8\pi, \quad \langle P\rangle = P_e - P_i.$$

For the kink mode ($m = \pm 1$), neglecting gravity and using the procedure of minimization, we can find the radial displacement s_r inside a flux rope in the long-wavelength limit ($ka \ll 1$) when the plasma parameter $\beta \ll 1$ is equal to $s_0 = \text{const}$ (Tsap et al. 2020).

If the magnetic field outside a flux rope ($r > a$) is potential ($\nabla \times \mathbf{B_e} = 0$), we can take

$$B_{\varphi e} = A/r, \quad B_{ze} = \text{const}, \tag{9}$$

where $A = \text{const}$. In this case, due to minimization of W_e the radial component of eigenvector is (Tsap et al. 2022)

$$s_r(r) = s_0 \frac{kB_{ze}a^2 + mA}{kB_{ze}r^2 + mA} = s_0 \frac{a}{r}\frac{kaB_{ze} + mB_{\varphi e}(a)}{krB_{ze} + mB_{\varphi e}(r)}\,. \tag{10}$$

Equations (9) and (10) assume the following important restrictions

$$|ka|B_{ze} > B_{\varphi e}(a) \ \text{ or } \ |ka| > B_{\varphi e}(a)/B_{ze}\,. \tag{11}$$

In terms of eq. (7), (8), and (10), we can find the dispersion equation in the form

$$\Omega^2 = \frac{k^2}{4\pi}\frac{B_{zi}^2 + B_{ze}^2 + 2mB_{\varphi e}(a)B_{ze}/(ka)}{\rho_i + \rho_e + m\rho_e B_{\varphi e}/(kaB_{ze})}. \tag{12}$$

Equation (12) suggests that the kink modes ($m = -1$, $k > 0$) and ($m = 1$, $k < 0$) as well as ($m = -1$, $k < 0$) and ($m = 1$, $k > 0$) have the same eigenvalue Ω.

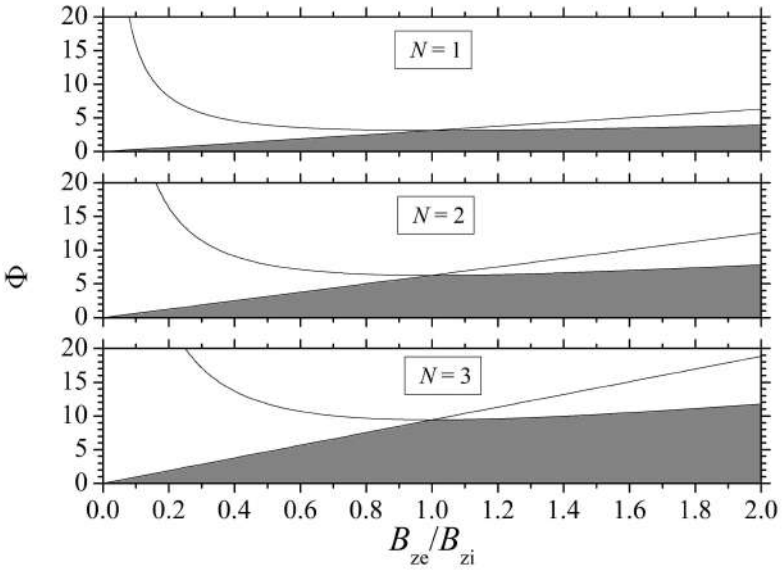

Fig. 1. The dependence of possible values of the twist angle of magnetic field lines Φ on the ratio of the longitudinal components of the magnetic field inside and outside the flux rope B_{ze}/B_{zi} for $N = 1, 2, 3$ and based on formula (16). The shaded area corresponds to the stability area.

Taking into account the condition that the footpoints of the coronal magnetic loops are frozen into photosphere and setting $|k| = \pi N/L$, where $N = 1, 2 \ldots$ are the natural numbers, from eq. (5), assuming $B_{ze} = B_{ze}(a)$, we get

$$\Phi_e(a) = LB_{\varphi e}(a)/[aB_{ze}(a)] < N\pi. \tag{13}$$

In turn, from the stability condition, according to which the numerator in the dispersion relation (12) must be positive, we have

$$\Phi(a) = \frac{LB_{\varphi i}(a)}{aB_{zi}(a)} < \frac{N\pi}{2}\frac{B_{zi}^2(a) + B_{ze}^2(a)}{B_{\varphi e}(a)B_{ze}(a)}\frac{B_{\varphi i}(a)}{B_{zi}(a)}. \tag{14}$$

The inequalities (13) and (14) are the necessary and sufficient conditions the for the magnetic flux rope stability with respect to kink modes. In case of unshielded rope, when $B_{\varphi i}(a) \approx B_{\varphi e}(a)$, inequality (14) reduces to the form

$$\Phi(a) < \frac{N\pi}{2} \frac{B_{zi}^2(a) + B_{ze}^2(a)}{B_{ze}(a) B_{zi}(a)} \,. \tag{15}$$

Note that for $B_{zi}(a) \approx B_{ze}(a)$ and $N = 2$ from (15) we get the well-known Kruskal–Shafranov stability criterion: $\Phi(a) < 2\pi$.

For the general case, according to (13) and (15), the conditions of stability are

$$\Phi(a) < N\pi \begin{cases} B_{ze}(a)/B_{zi}(a), \\ (B_{zi}^2(a) + B_{ze}^2(a))/(2B_{zi}(a)B_{ze}(a)). \end{cases} \tag{16}$$

Figure 1 shows the stability region (shaded in gray) of a magnetic flux rope at $N = 1, 2, 3$. It is seen that the total twist angle of the magnetic field lines Φ can hardly significantly exceed 12 radians, i.e. the maximum number of turns $R \approx 12/2\pi \approx 2$.

4 Summary

We have shown that coronal loops with uncompensated electric current cannot be strongly twisted ($\Phi \lesssim 10$) due to the development of kink instability. This also suggests that the electric currents cannot significantly exceed $10^{11}-10^{12}$ A in the solar corona. Thus, the twist angle of the magnetic field lines can serve as an observational criterion for identifying shielded and unshielded coronal flux ropes. At the same time, the lack of dependence of compact and eruptive solar flares on the degree of twisting of magnetic flux ropes can be explained by the coexistence of magnetic flux ropes of both types in the solar corona. However, we do not exclude that the excitation of eigenoscillations of coronal loops with footpoints, which are frozen-in to the photosphere, faces difficulties because of the dependence of eigenfrequency Ω on the signs of m and k (Terradas & Goossens 2012).

Funding

The study was funded by a grant from the RSF (No.22-12-00308).

References

Jing J., Liu C., Lee J., et al., 2018, Astrophysical Journal, 864, 2, id. 138
Solovev A.A. and Uralov A.M., 1979, Soviet Astronomy Letters, 5, p. 250
Terradas J. and Goossens M., 2012, Astronomy & Astrophysics, 548, id. A112
Tsap Yu., Stepanov A., Kopylova Yu., 2022, Astrophysical Journal, 939, 2, id. 114
Tsap Y., Fedun V., Cheremnykh O., et al., 2020, Astrophysical Journal, 901, 2, id. 99

BAK 2024 MODERN ASTRONOMY: FROM THE EARLY UNIVERSE TO EXOPLANETS AND BLACK HOLES 300 years Russian Academy of Sciences

The features of the north-south asymmetry of the magnetic flux in active regions with different magnetic morphology in solar cycles 23 and 24

A. Zhukova and V. Abramenko

Crimean Astrophysical Observatory of the Russian Academy of Sciences, Nauchny, Crimea, 298409 Russia

Abstract. We use the CrAO catalog of the magneto-morphological classes (MMC) of active regions (ARs) to study the hemispheric distribution of the number and magnetic fluxes of ARs that appeared on the disk from May 1996 to December 2021. 3047 ARs were distributed between classes of the regular (bipolar groups that obey empiric rules for sunspots) and irregular (all the rest, except for unipolar sunspots) ARs. The analysis of the results showed that all the trends are more pronounced in the flux data. For the irregular ARs, the strongest peaks in time profiles are observed in the second maximum of the cycle in the S-hemisphere. ARs of both MMC types demonstrate noticeable N-S asymmetry. The most abrupt changes are shown by the irregular ARs fluxes. For the compiled quadrupolar-like component of the flux, the evidence of oscillations with a period of about 15 years is found for all studied ARs and for the irregular groups. For the regular ARs, cross-correlation of ARs fluxes in different hemispheres in adjacent cycles showed no features. For the irregular groups, a high correspondence in flux dynamics in the N-hemisphere of cycle 23 and in the S-hemisphere of cycle 24 is found.

Keywords: Sun: activity, magnetic fields, sunspots

DOI: 10.26119/VAK2024.123

1 Introduction

Active regions (ARs) on the surface of the Sun bear imprint of the processes hidden under the photospheric level. Occurrence of ARs with atypical magnetic configuration allows us to reveal signs of complex non-linear processes in the convection zone that interfere in the global dynamo action (Abramenko et al. 2018, 2023). The hemispheric distribution of such ARs also demonstrates significant features (Zhukova et al. 2023).

According to the magneto-morphological classification (MMC) of ARs proposed earlier by CrAO (Abramenko et al. 2018; Abramenko 2021), 3047 ARs that appeared on the disc from May 1996 to December 2021, excluding unipolar spots, were distributed between the regular groups (bipolar ARs obeying empirical rules for sunspot groups) and irregular ARs (all the rest). The catalog MMC ARs CrAO[1] was used to continue the study of the North-South asymmetry of ARs with different magnetic morphology.

2 Results

Cyclic variations of ARs number and fluxes are shown in Fig. 1.

Flux time profiles are more expressive than those for the number of ARs (Fig. 1). Such a tendency was also noticed in Zhukova et al. (2024). A typical time lag between the activity in different hemispheres is found for both the regular and irregular ARs. The pattern for different MMC type ARs is not the same. For the irregular ARs, the distinct peaks observed in the second maximum may be due to the manifestation of the turbulent dynamo action (Abramenko et al. 2023).

The North-South (N-S) asymmetry is found for ARs of both MMC types. However, for the irregular ARs, it is more pronounced (especially, for ARs fluxes). The predominance of the irregular ARs in one of the hemispheres might be due to the more noticeable turbulence manifestation in the hemisphere where the magnetic field is weakened due to the interaction of the dipolar and quadrupolar components of the global field.

Synoptic maps of the magnetic field are suitable for the harmonic analysis (see, e.g., Obridko et al. (2021)). However, such data are not available for the regular and irregular ARs to date. For this reason, despite the limitations of the approach, we compiled a proxy for the dipolar and quadrupolar components of the magnetic flux using the simplest axisymmetric approximation (Hazra & Nandy 2019). Following Kitchatinov (2022), we used $F_{\rm N}$ and $F_{\rm S}$ (the part of the flux observed in the N- and S- hemispheres, respectively) to express the quadrupolar-like and dipolar-like

[1] https://sun.crao.ru/databases/catalog-mmc-ars

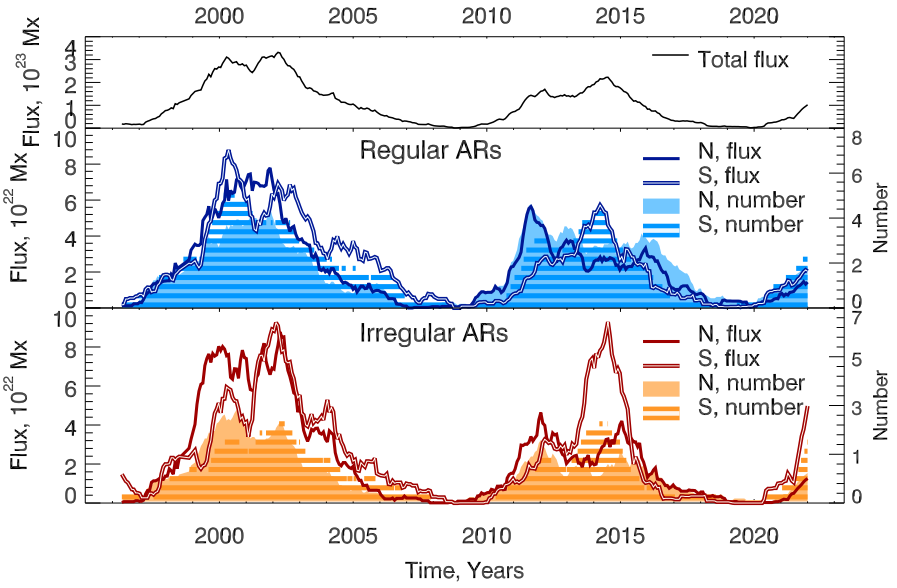

Fig. 1. Cyclic variations of ARs. Total magnetic flux (top panel); the number (fill) and fluxes (lines) of the regular (middle panel) and irregular (bottom panel) ARs in different hemispheres.

components as

$$F_{\mathbf{QL}} = \frac{(F_N + F_S)}{2} \quad \text{and} \quad F_{\mathbf{DL}} = \frac{(F_N - F_S)}{2}, \tag{1}$$

respectively.

To explore this two proxies we applied for them the auto-correlation function technique using the following equation

$$C(n\delta t) = \frac{1}{N-n} \sum_{i=1}^{N-n} F(t_i) F(t_{i+n}), \tag{2}$$

where $F(t)$ is the magnetic flux (in Maxwell), δt is the time increment, N is the total number of data points, n is the time lag.

For all types of ARs, for the dipolar-like component, the periodicity of about 12 years with anti-correlation of about minus one is observed (Fig. 2), which implies a whole cycle of about 22–24 years. For all ARs and for the irregular groups, for the quadrupolar-like component, oscillations with a period of about 15 years are found.

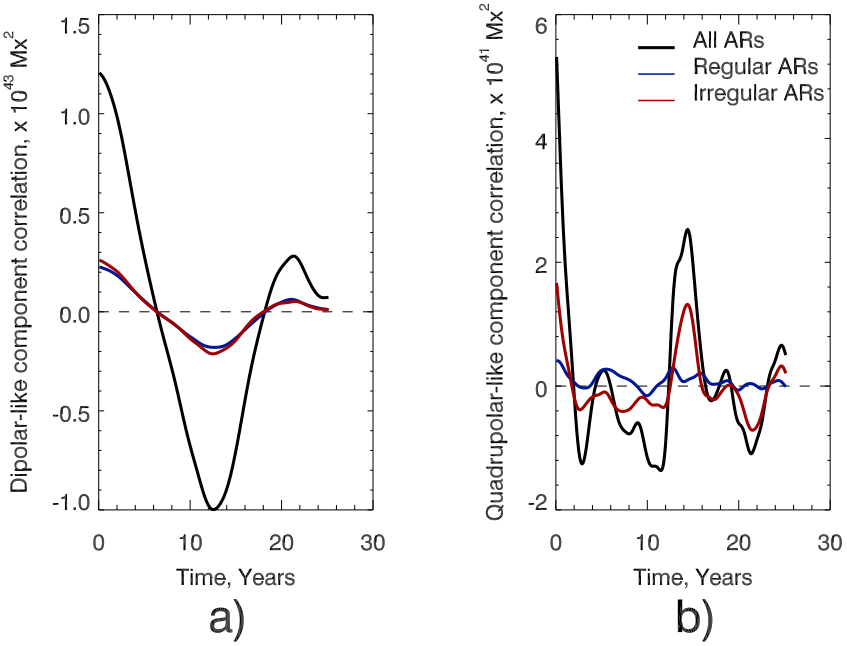

Fig. 2. Autocorrelation for the dipolar-like (a) and quadrupolar-like (b) parts of the flux.

For the regular ARs, evidence of the quadrupolar-like component oscillations are not observed.

A superposition of the dipolar and quadrupolar components implies some specific asymmetry for adjacent cycles (Sokoloff & Nesme-Ribes 1994). The activity in the N-hemisphere in the cycle n and in the S-hemisphere in the cycle $(n+1)$ is supposed to be similar. And this is also true for the S-hemisphere in the cycle n and the N-hemisphere in the cycle $(n+1)$.

To analyze the flux dynamics in different hemispheres in adjacent cycles for ARs of each MMC type, we used a cross-correlation function expressed as

$$C_{NS}(n\delta t) = \begin{cases} \frac{1}{N-|n|} \sum_{i=1}^{N-|n|} F_N(t_{i+|n|}) F_S(t_i), & n < 0 \\ \frac{1}{N-n} \sum_{i=1}^{N-n} F_N(t_i) F_S(t_{i+n}), & n \geq 0 \end{cases} . \quad (3)$$

For the regular ARs, the correlation pattern is found as typical (the main central peak and slightly lower approximately the same side peaks, Fig. 3). However, the

irregular ARs demonstrate unusual pattern with a high right-side peak and low left-side peak. It means, on the one hand, a high correspondence in the dynamics of the magnetic flux in the N-hemisphere (cycle 23) and in the S-hemisphere (cycle 24) and, on the other hand, a low correspondence in the flux dinamics in the S-hemisphere (cycle 23) and the N-hemisphere (cycle 24).

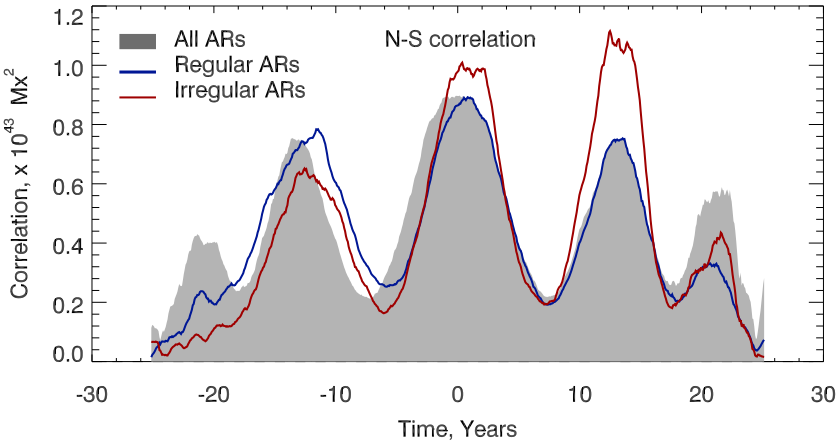

Fig. 3. Cross-correlation for ARs fluxes in different hemispheres.

3 Summary

The results of the study can be summarized as follows.

1. The peaks in the cycle maxima are more pronounced in the flux data than that in the number data. The strongest fluxes of the irregular ARs are observed in the second maximum of the cycle in the S-hemishpere.
2. The ARs of both MMC types demonstrate noticeable N-S asymmetry. The form of time profiles for the ARs of different MMC types is not the same. The most abrupt changes are shown by the irregular ARs fluxes.
3. For the compiled dipolar-like component of the magnetic flux, the periodicity of about 12 years is found for all types of ARs. For the quadrupolar-like component, the evidence of oscillations with a period of about 15 years is observed. This tendency is expressed only for all studied ARs and for the irregular groups.
4. The results of the cross-correlation analysis show a standard pattern of fluxes for the regular ARs (high central peak, weaker lateral peaks). For the irregular ARs,

an inequality of side peaks might imply a high correspondence in the dynamics of the magnetic flux in the N-hemisphere of cycle 23 and in the S-hemisphere of cycle 24 and, on contrary, a low correspondence in the flux dynamics in the S-hemisphere of cycle 23 and in the N-hemisphere of cycle 24.

5. The above findings also allow us to conclude that, despite the name, irregular ARs are not a random phenomenon, but an integral part of the cycle and may be of interest for the development of a dynamo model in modern times.

Acknowledgements. This study used the CrAO MMC ARs catalog, which is available on the CrAO website.

Funding

The study was financially supported by the Ministry of Science and Higher Education of the Russian Federation, agreement No. 122022400224-7.

References

Abramenko V., Zhukova A., Kutsenko A., 2018, Geomagnetism and Aeronomy, 58, 8, p. 1159
Abramenko V., Suleymanova R., Zhukova A., 2023, Monthly Notices of the Royal Astronomical Society, 518, 3, p. 4746
Abramenko V., 2021, Monthly Notices of the Royal Astronomical Society, 507, 3, p. 3698
Hazra S. and Nandy D., 2019, Monthly Notices of the Royal Astronomical Society, 489, 3, p. 4329
Kitchatinov L., 2022, Geomagnetism and Aeronomy, 62, 7, p. 817
Obridko V., Pipin V., Sokoloff D., et al., 2021, Monthly Notices of the Royal Astronomical Society, 504, 4, p. 4990
Sokoloff D. and Nesme-Ribes E., 1994, Astronomy & Astrophysics, 288, p. 293
Zhukova A., Sokoloff D., Abramenko V., et al., 2023, Advances in Space Research, 71, 4, p. 1984
Zhukova A., Abramenko V., Suleymanova R., 2024, Geomagnetism and Aeronomy, in print

MODERN ASTRONOMY: FROM THE EARLY UNIVERSE TO EXOPLANETS AND BLACK HOLES

Statistics of magnetic energies in solar active regions of different Hale and McIntosh classes

I. Zimovets and I. Sharykin

Space Research Institute of the Russian Academy of Sciences, 84/32, Profsoyuznaya str., Moscow, 117997 Russia

Abstract. A statistical analysis of the magnetic energies (of the nonlinear force-free and potential fields, $E_{\rm NLFFF}$, $E_{\rm POTF}$, and their difference – a proxy for the free magnetic energy, $E_{\rm FREE}$) in active regions (ARs) on the Sun of different Hale and McIntosh classes for the period from May 1, 2010 to 12 June, 2024 ($\approx$ 1.3 solar cycles) is presented. The magnetic field in ARs is calculated using the GX Simulator based on the photospheric vector magnetograms by the Helioseismic and Magnetic Imager (HMI) anboard the Solar Dynamics Observatory (SDO) and information about ARs contained in the daily Solar Region Summary (SRS) files provided by the NOAA SWPC. Distributions of different parameters have been determined in total for all ARs and separately for each Hale and McIntosh class, the mean values of the parameters and standard deviations were calculated for each class. As expected, it is found that the magnetic energies, unsigned magnetic flux, as well as the integral number of sunspots, the number of active regions, and the area of sunspots, integrated over ARs visible per day on the solar disk, exhibit an $\approx$ 11-year cyclicity. On average, magnetic energies of ARs increase with increasing Hale and McIntosh class (with sub-peaks in $E_{\rm POTF}$ and $E_{\rm NLFFF}$ for Hhx, Hkx, Cho–Cki), while the average fraction of the free magnetic energy, $E_{\rm FREE}/E_{\rm NLFFF}$ in ARs of different classes differs weakly. Correlation between $E_{\rm POTF}$ and $E_{\rm NLFFF}$ is almost identical for ARs of different Hale classes with the high values of the linear Pearson correlation coefficient, ccp, from 0.96 to 0.99. $E_{\rm FREE}$ is less correlated with $E_{\rm POTF}$ and $E_{\rm NLFFF}$ (ccp is from 0.32 to 0.71).

Keywords: Sun: activity, magnetic fields, sunspots, flares

DOI: 10.26119/VAK2024.124

1 Introduction

Active regions (ARs) are places where the brightest phenomena of solar activity occur, including such potentially geoeffective ones as flares and CMEs (e.g., Toriumi & Wang 2019). ARs are inextricably linked with sunspots. The main source of energy in ARs is the magnetic field.

The two most famous classifications of ARs are the Hale magnetic classification (5 classes: α, β, $\beta\gamma$, $\beta\delta$, $\beta\gamma\delta$) and the McIntosh morphological classification (60 classes of the Zpc type).

The purpose of this work is to collect statistics of magnetic energies in ARs for 2010–2024, in particular, to determine average values and standard deviations of magnetic energies in ARs of various Hale and McIntosh classes.

2 Data and Methods

Information about ARs is taken from the daily SRS files[1], namely: NOAA AR number, heliographic coordinates, Carrington longitude, sunspot group area ($A_{\rm SS}$), longitude size ($L_{\rm L}$), sunspot number ($N_{\rm SS}$), McIntosh and Hale classes.

Full-disk photospheric vector magnetograms of the Helioseismic and Magnetic Imager (HMI) on board the Solar Dynamics Observatory, SDO, (Scherrer et al. 2012) were used as boundary data for extrapolations. We used magnetograms around 01:00 UT for each day, which is close to the time of SRS files (00:30 UT).

Extrapolation of the magnetic field was made in approximations of potential (POTF) and nonlinear force-free fields (NLFFF) using GX Simulator (Nita et al. 2023). Cartesian coordinate system with a step of 1500 km (at $L_{\rm L} \leq 12^\circ$) or 3000 km (at $L_{\rm L} > 12^\circ$) was used. The size of the calculation area along X-axis (longitude) was $L_{\rm x} = k_{\rm x} \times L_{\rm L}$, along Y-axis (latitude) $L_{\rm y} = k_{\rm y} \times L_{\rm L}$, and along the Z-axis was equal to the larger of $L_{\rm x}$ and $L_{\rm y}$, $k_{\rm x}$ and $k_{\rm y}$ ranged from 2.4 to 12 depending on $L_{\rm L}$.

Magnetic energies $E_{\rm POTF}$ and $E_{\rm NLFFF}$ were calculated as integrals over the computational 3D boxes of each ARs as $E = \int \left(\mathbf{B}^2/8\pi\right) dV$, except 10% of voxels near the side and top boundaries. The proxy of the free magnetic energy was calculated as $E_{\rm FREE} = E_{\rm NLFFF} - E_{\rm POTF}$. Also, we calculated the total unsigned magnetic flux, $\int |B_z\,(x, y, z = 0)|\, dS$ (see Zimovets & Sharykin 2024, for details).

Calculations were made for ARs in the central part of the solar disk (within $\pm 70^\circ$) for the interval from May 1, 2010 to June 12, 2024. A total of 5144 SRS files were used. NOAA AR numbers for this interval varied from 11064 to 13711, i.e., 2647 different ARs. A total of 13414 data cubes were obtained.

[1] ftp://ftp.swpc.noaa.gov/pub/warehouse

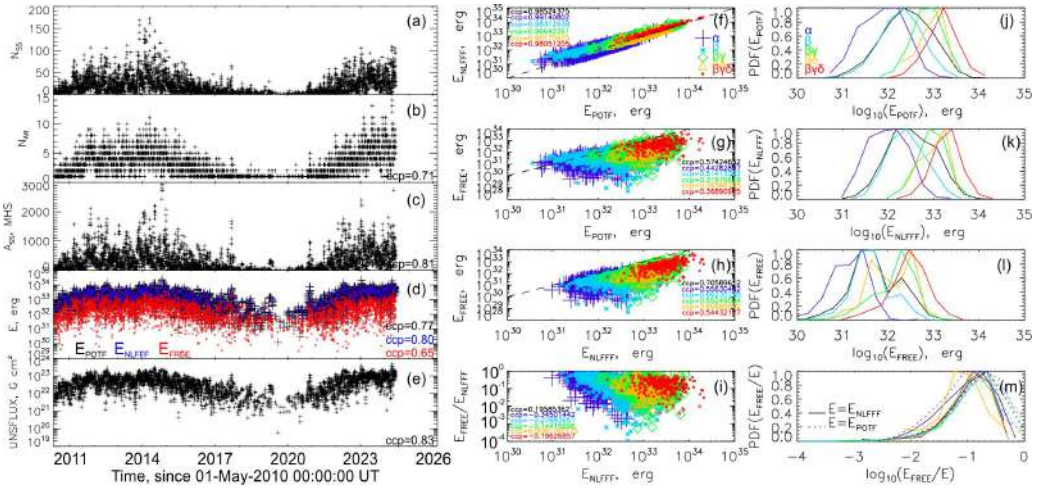

Fig. 1. (Left) Temporal behavior of parameters integrated over ARs on the solar disk with 1-day step from May 2010 to June 2024. (Middle) Paired dependences of magnetic energies in ARs of different Hale classes (f–h) and fraction of the free to total magnetic energy (j). (Right) Distributions of these parameters.

Temporal profiles of total sunspot number, number of ARs, sunspot area, magnetic energies, and unsigned magnetic flux integrated over ARs in 1-day step for the considered time interval are shown in Fig. 1(a–e). As expected, all parameters are subject to variations of the solar activity cyclicity. The parameters correlate with the sunspot number, with the linear Pearson correlation coefficient, *ccp*, ranging from 0.65 to 0.83.

For further analysis, we left only "isolated" ARs satisfying the following criteria: 1) imbalances of the magnetic flux and vertical current are less than 20%, 2) $E_{\rm FREE} > 0$. This leaves 5299 data cubes, among which 509 ARs of α class, 3525 of β, 839 of $\beta\gamma$, 97 of $\beta\delta$, and 329 of $\beta\gamma\delta$ classes. ARs of 57 McIntosh classes are present, except for three rare classes Esc, Fro, and Fri.

3 Results

3.1 ARs of Hale classes

Distributions of $E_{\rm POTF}$, $E_{\rm NLFFF}$, $E_{\rm FREE}$, and $E_{\rm FREE}/E_{\rm NLFFF}$, for Hale ARs are shown in Fig. 1(f–m). One can see: 1) on average, magnetic energies increase with increasing Hale class, 2) while the average fraction of free magnetic energy in ARs of different Hale classes differs weakly, 3) $E_{\rm FREE}$ in $\beta\delta$ ARs has two maxima, the left one is close to the maximum of the distributions for the lower classes α, β, $\beta\gamma$ and the right

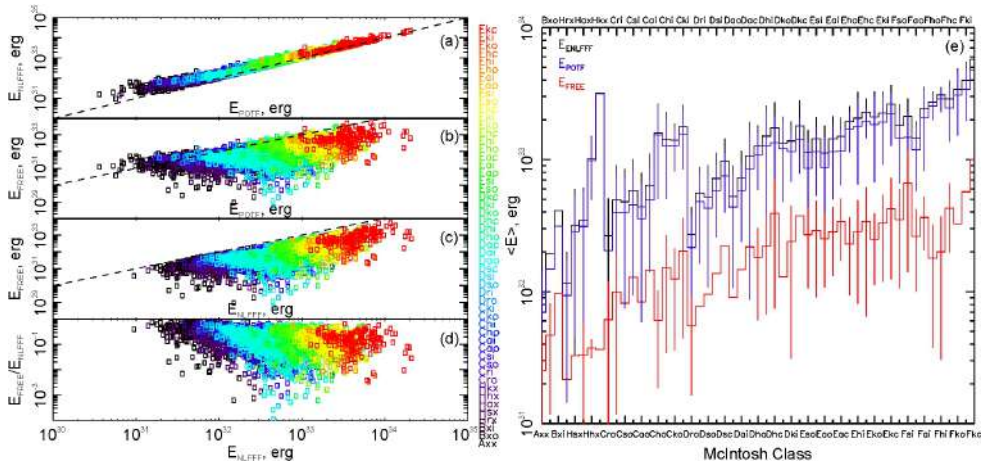

Fig. 2. Paired dependences of the magnetic energies in ARs of different McIntosh classes (a–c) and of $E_{\rm FREE}/E_{\rm NLFFF}$ (d). (e) Average magnetic energies ($E_{\rm NLFFF}$ – black, $E_{\rm POTF}$ – blue, $E_{\rm FREE}$ – red) in ARs of various McIntosh classes. Standard deviations are shown as vertical bars.

one is close to the maximum for the highest class $\beta\gamma\delta$, 4) there is high correlation between $E_{\rm NLFFF}$ and $E_{\rm POTF}$, *ccp* is almost identical for ARs of different classes (from 0.96 to 0.99), 5) $E_{\rm FREE}$ is weakly correlated with $E_{\rm POTF}$ and $E_{\rm NLFFF}$ (*ccp* from 0.32 to 0.71).

3.2 ARs of McIntosh classes

Distributions of $E_{\rm POTF}$, $E_{\rm NLFFF}$, $E_{\rm FREE}$, and $E_{\rm FREE}/E_{\rm NLFFF}$ for ARs of McIntosh classes are shown in Fig. 2(a–d), and the average values with standard deviations of $E_{\rm POTF}$, $E_{\rm NLFFF}$, and $E_{\rm FREE}$ are shown in Fig. 2(e). It can be seen: 1) on average, the magnetic energies of ARs increases with increasing McIntosh class, from small simple Axx to larger more complex *Fkc* class, 2) there are intermediate peaks of $E_{\rm POTF}$ and $E_{\rm NLFFF}$ for Hhx, Hkx, Cho–Cki classes without pronounced peaks in $E_{\rm FREE}$, 3) there is no clear dependence of $E_{\rm FREE}/E_{\rm NLFFF}$ with McIntosh class.

Acknowledgements. We are greateful for the usage of SDO/HMI and NOAA SWPC SRS data. SDO is a mission for NASAs Living With a Star (LWS) program.

References

Nita G.M., Fleishman G.D., Kuznetsov A.A., et al., 2023, Astrophysical Journal Supplement Series, 267, 1, id. 6
Scherrer P.H., Schou J., Bush R.I., et al., 2012, Solar Physics, 275, 1-2, p. 207
Toriumi S. and Wang H., 2019, Living Reviews in Solar Physics, 16, 1, id. 3
Zimovets I.V. and Sharykin I.N., 2024, Geomagnetism and Aeronomy, 64, 5, p. 603

VAK 2024 MODERN ASTRONOMY: FROM THE EARLY UNIVERSE TO EXOPLANETS AND BLACK HOLES 300 years Russian Academy of Sciences

Multipoint multiwavelength observations of a near-the-limb eruptive solar flare with quasi-periodic pulsations

I. Zimovets and I. Sharykin

Space Research Institute of the Russian Academy of Sciences, 84/32, Profsoyuznaya St, Moscow, 117997 Russia

Abstract. We present results of the analysis of multiwavelength observations of the M3.4 eruptive flare that occurred near the western limb of the Sun on September 2, 2023 (SOL2023-09-02T06:33). We use observations from the near-Earth spacecraft ASO-S/HXI, SDO/AIA, HMI, GOES/XRS, and Fermi/GBM. X-ray observations by the STIX telescope-spectrometer on board the Solar Orbiter from the opposite side of the Sun are also used. The flare was associated with a two-stage inclined ($\approx 40 - 50°$ to the radial direction) eruption, the second stage of which was accompanied by the impulsive flare phase and quasi-periodic pulsations (QPPs) of hard X-rays with a characteristic time scale $P \approx 1.56$ min. HXI observed hard X-ray sources located above the apex of a coronal Y-shaped structure, visible in the "hot" 94 and 131 Å EUV channels, behind a drop-shaped erupting plasmoid/prominence. Hard X-ray sources near the foot of the flare loops and flare ribbons were also observed, mainly after the peak of the impulsive phase. The HXI and STIX observations from different locations in the heliosphere are consistent with each other. Temporal dynamics of the spectral index of nonthermal electron flux had a "soft-hard-soft" behavior during QPPs. The observational results do not contradict the "standard" model of eruptive two-ribbon flares, where populations of electrons are accelerated episodically due to magnetic reconnection in a current sheet in the corona behind an erupting structure. However, understanding the quasi-periodicity of electron acceleration/injection requires further studies.

Keywords: Sun: flares; X-rays, gamma rays; UV radiation; coronal mass ejections (CMEs)

DOI: 10.26119/VAK2024.125

1 Introduction

Solar flares are a phenomenon of rapid transformation of magnetic energy of active regions (ARs) into other types of energy, e.g., kinetic energy of accelerated particles and their electromagnetic emission. Many flares are accompanied by quasi-periodic pulsations (QPPs). Despite large number of proposed mechanisms, there is still no complete understanding of processes leading to QPPs (e.g., Kupriyanova et al. 2020; Zimovets et al. 2021). In this regard, further detailed multi-wavelength observations with spatial resolution of QPP sources are of considerable interest. In particular, it is important to perform an analysis of observations of flares near the solar limb, for which we can determine vertical spatial structure of pulsation sources and study their relationship with eruptive processes. This may be useful for refining the "standard model" of two-ribbon flares and for incorporating the QPP mechanisms into this model.

The aim of this work is to present the results of a preliminary analysis of the M3.4-class eruptive solar flare that occurred on September 2, 2023 near the western edge of the solar disk (N06W89) in the NOAA AR 13413 of β and Dkc classes.

2 Observational data

The flare was observed by a number of space-based instruments. In the X-ray range, the flare was observed by the Hard X-ray Imager (HXI) (Zhang et al. 2019) onboard the Advanced Space-based Solar Observatory (ASO-S) (Gan et al. 2019) and by the Gamma-ray Burst Monitor (GBM; Meegan et al. 2009) onboard the Fermi in the low-Earth orbits, as well as by the X-Ray Sensor on the Geostationary Operational Environmental Satellite (GOES-16). The flare X-ray emission was also detected from the opposite side of the Sun by the Spectrometer/Telescope for Imaging X-rays (STIX; Krucker et al. 2020) onboard the Solar Orbiter (SolO). SolO was at a distance of 0.681568 AU from the Sun, the angle between the Earth, Sun's center and SolO was 155.678°, and thus the angle between the flare site, Sun's center and SolO was $\approx 66.7°$ (see Fig. 2(i)). Additionally, we used observations in the UV and EUV channels of the Atmospheric Imaging Assembly (AIA; Lemen et al. 2012) and line-of-sight magnetograms by the Helioseismic and Magnetic Imager (Scherrer et al. 2012) onboard the Solar Dynamics Observatory. Consideration of ground-based observations of the flare is beyond the scope of this article.

3 Observation analysis

Temporal behavior of X-ray emission intensities in different energy ranges is shown in Fig. 1(a–d). The flare was associated with two increases of X-ray emission. The

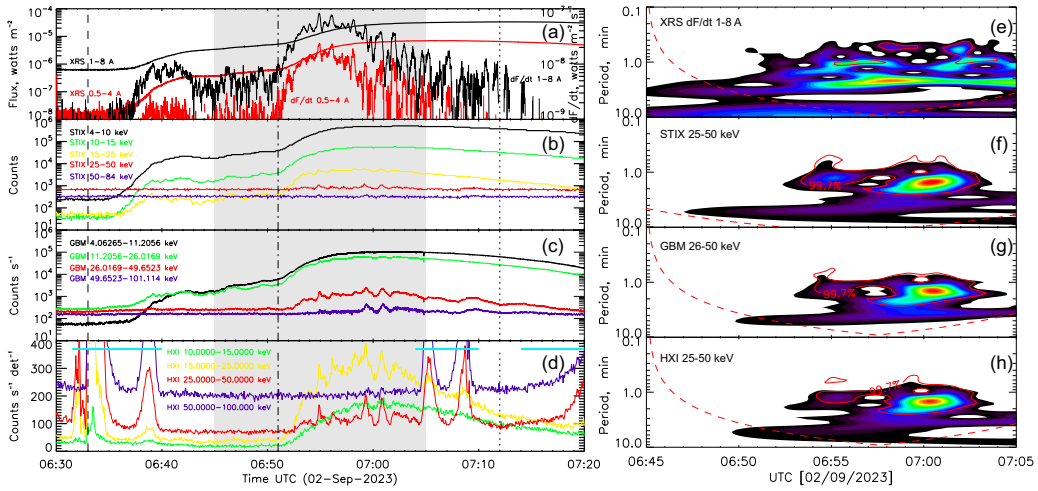

Fig. 1. (Left column) Temporal profiles of X-ray emission detected with different instruments: (a) fluxes in the GOES/XRS channels (thick, left Y-axis) and its derivative (thin, right Y-axis), (b) SolO/STIX, (c) Fermi/GBM, (d) ASO-S/HXI. The vertical dashed, dotted, and dashed-dotted lines indicate the begin, maximum of the flare X-ray flux, and the start of the impulsive phase with QPPs, respectively. The cyan horizontal lines in (d) show intervals when hard X-ray data of HXI was contaminated with radiation belts particles. (Right column) Wavelet spectra of interpolated, detrended, smoothed, and normalized profiles of X-ray emission in the time interval indicated by the gray rectangle in the left column: (e) time derivative of XRS 1–8 Å channel, (f) counts in the STIX 25–50 keV, (g) GBM $\approx 26-50$ keV, (h) HXI 25–50 keV channels.

first less intense one started at 06:33 UT and the second more powerful started at around 06:51 UT. The first increase was associate with a relatively slow rise of coronal structures observed in EUV and the second stage was associated with the fast development of an eruption. The second stage was accompanied with a sequence of hard X-ray ($\approx 15-80$ keV) QPPs (≈06:53–07:03 UT), it was the flare impulsive phase. Wavelet analysis of detrended, normalized and smoothed data of the three instruments (HXI, GBM and STIX) show that these QPPs had a characteristic time scale $P \approx 1.56$ min (Fig. 1(f–g)). These hard X-ray QPPs were not harmonic oscillations. Amplitudes and times between successive peaks were not stable.

At first, the sources of these hard X-ray QPPs were observed in the corona above the bright EUV flare loops seen in 94 and 131 Å (Fig. 2(a, d)), in the region below the departed (at an angle of $40-50^\circ$ to the radial direction) eruptive prominence. Near the middle of the QPP series, in addition to the coronal hard X-ray sources, sources from below began to be observed in the vicinity of the UV flare ribbons (Fig. 2(b, e)). There were signs of a double coronal source in the corona, the centroids at higher energies located slightly above the centroids of the lower-energy sources. After that,

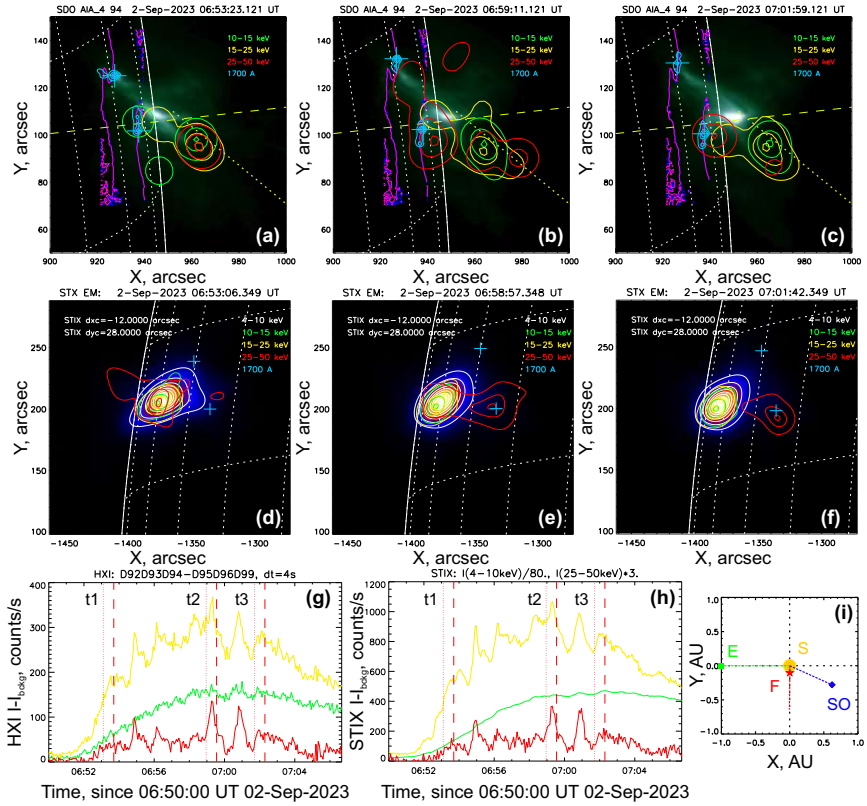

Fig. 2. (a–c) Images of the flare region from near the Earth SDO and ASO-S, and from the SolO/STIX (d–f) for three time intervals $t1 - t3$ indicated in (g, h). The background in (a–c) is the SDO/AIA 94 Å image and in (d–f) is the STIX 4–10 keV image. The cyan contours show the flare ribbons in the AIA 1700 Å, the crosses show positions of its brightest pixels. Hard X-ray sources are shown with the green (10–15 keV), yellow (15–25 keV), and red (25–50 keV) contours at 15, 55, 95% of the maxima. The yellow dashed and dotted straight lines show the radial direction through the flare site and approximate eruption direction, respectively. The blue/red curves show contours of the LOS magnetic field by SDO/HMI at ±5 Gauss. Count rates of HXI and STIX are shown in (g) and (h), respectively. The difference in light travel times from the Sun to Earth and to SolO, $dt = 163$ s, is compensated. (i) The location of the Sun (yellow), Earth (green), SolO (blue), and the flare (red) in the Ecliptic plane.

the coronal hard X-ray sources (> 25 keV) became almost invisible, and only the lower hard X-ray sources were visible (Fig. 2(c, f)) near the flare ribbons. It is worth noting that the HXI and STIX images (at different angles of view of the flare region) are in consistence with each other – they show similar morphology and dynamics of the X-ray sources.

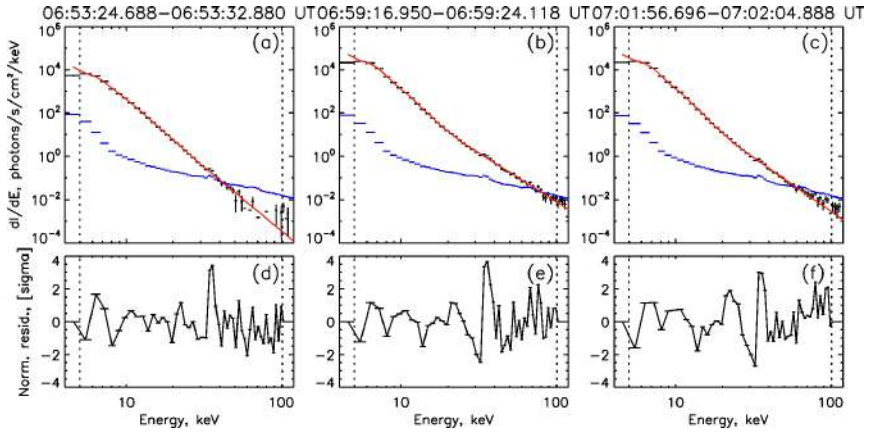

Fig. 3. (a–c) Examples of background-subtracted X-ray spectra (black), their fits with the "thermal" plus "thick2"-target models (red), and the background spectra (blue) made with Fermi/GBM data for three time intervals (see Fig. 4) within three longer intervals in Fig. 2. Errors are shown with vertical bars. (d–f) The corresponding normalized residuals.

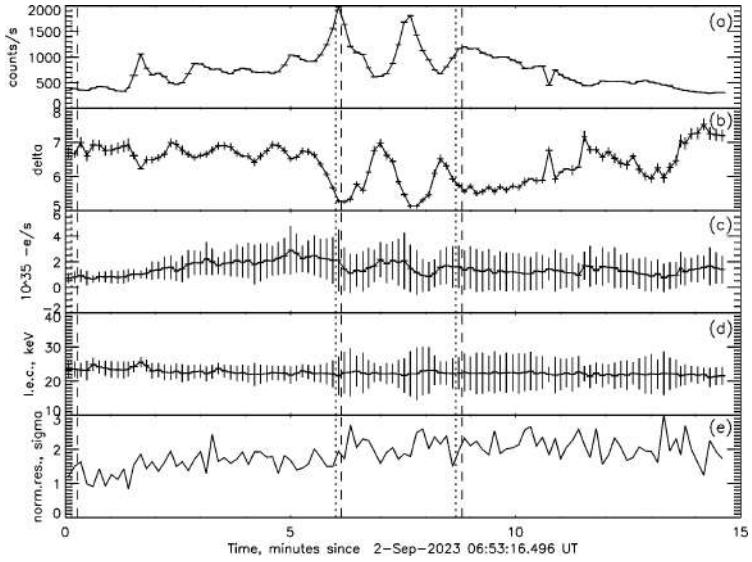

Fig. 4. Temporal profiles of parameters from fitting of X-ray spectra by Fermi/GBM data with the "thermal" plus "thick2"-target models: (a) integrated count rate in $\approx 25-100$ keV, (b) spectral index of electron flux below break, (c) total integrated electron flux, (d) low energy cutoff, (e) normalized residuals. Errors are shown with vertical bars. Pairs of vertical dotted and dashed lines indicate starts and ends of three time intervals for which the spectra are shown in Fig. 3.

We performed spectral analysis of X-ray emission (in $\approx 5-100$ keV range) detected by Fermi/GBM during the impulsive phase. Fitting of the background-

subtracted spectra was done with the use of a combination of two bremsstrahlung models: the "thermal" plasma and "thick2"-target model of nonthermal electrons (with fixed break energy, electron spectral index above the break, and high energy cutoff). Examples of the spectra with the fit model for three time intervals are shown in Fig. 3. Spectra above ≈ 15 keV are mainly the bremsstrahlung spectrum of nonthermal electrons. Dynamics of nonthermal electrons' parameters (spectral index below break, total flux, and the low energy cutoff), intensity of hard X-ray emission in $\approx 25 - 100$ keV and normalized residuals are shown in Fig. 4, from where it is seen that the electron spectral index anticorrelated with the hard X-ray intensity ($cc \approx -0.75$) and presented the "soft-hard-soft" behavior during the QPPs.

4 Conclusions

The analysis of multi-wavelength observations made with different instruments at different locations has shown that the observed QPPs are likely the result of episodic acceleration of electrons in the corona above the flare loops and below the eruptive prominence. It is consistent with the "standard" model of eruptive flares. Understanding the mechanisms underlying the quasi-periodicity requires further research.

Acknowledgements. We are grateful for the usage of ASO-S / HXI, GOES / XRS, Fermi / GBM, SolO / STIX, SDO / AIA, HMI data. SDO is a mission for NASAs Living With a Star (LWS) program. ASO-S mission is supported by the Strategic Priority Research Program on Space Science, the Chinese Academy of Sciences, Grant No. XDA15320000. We thank Prof. W.-Q. Gan for the opportunity to conduct part of this work at PMO CAS, Drs. Yang Su and Zhentong Li for help with the HXI data, and Dr. Tomek Mrozek for imaging the STIX data.

Funding

This work was supported by the Russian Science Foundation grant No. 23-72-30002.

References

Gan W.-Q., Zhu C., Deng Y.-Y., et al., 2019, Research in Astronomy & Astrophysics, 19, 11, id. 156
Kupriyanova E.G., Kolotkov D.Yu., Nakariakov V.M., et al., 2020, Solar-Terrestrial Physics, 6, 1, p. 3
Krucker S., Hurford G.J., Grimm O., et al., 2020, Astronomy & Astrophysics, 642, id. A15
Lemen J.R., Title A.M., Akin D.J., et al., 2012, Solar Physics, 275, 1-2, p. 17
Meegan C., Lichti G., Bhat P.N., et al., 2009, Astrophysical Journal, 702, p. 791
Scherrer P.H., Schou J., Bush R.I., et al., 2012, Solar Physics, 275, 1-2, p. 207
Zimovets I.V., McLaughlin J.A., Srivastava A.K., et al., 2021, Space Science Reviews, 217, 5, id. 66
Zhang Z., Chen D.-Y., Wu J., et al., 2019, Research in Astronomy and Astrophysics, 19, 11, id. 160

VAK 2024 MODERN ASTRONOMY: FROM THE EARLY UNIVERSE TO EXOPLANETS AND BLACK HOLES 300 years Russian Academy of Sciences

On the parameters of encounters of NEOs with the Earth

R. Zolotarev and B. Shustov

[1]Institute of Astronomy of the Russian Academy of Sciences, Pyatnitskaya str., 48, Moscow, 119017 Russia

Abstract. The paper presents the results of statistical modeling of the entry of near-Earth objects (NEOs) into the near-Earth space – a sphere with a radius of 0.01 AU around the Earth. The distributions of asteroids in the direction and velocity of approach to the Earth are constructed. The NEO population was modeled using the NEOMOD package and integrated for 110 years using the REBOUND package. The main results are: 1) the number of asteroids larger than 10 m in size entering to near-Earth space is approximately 1000 per year; 2) up to half of the asteroids can enter the near-Earth space from the side of the day-time-hemisphere; 3) there is anisotropy in the flux density of incoming asteroids. Typical velocity of approach to the Earth at the entrance to the near-Earth space is approximately 7.5 km/s (maximum speed can reach up to 30 km/s). These distributions can be useful in the design of a System of Observation of Day-time Asteroids (SODA).

Keywords: minor planets; asteroids: general; methods: numerical; Earth

DOI: 10.26119/VAK2024.126

1 Introduction

Currently, active development of systems for detecting and monitoring dangerous celestial bodies of natural origin is underway (see, for example, Shugarov & Shustov (2022) and NASA document)[1]. To build more efficient systems, it is necessary to know the properties of the distribution of such bodies in near-Earth space. In this work, near-Earth space (NES) is defined as the space inside a sphere with a radius of 0.01 AU (which approximately equal to the radius of the Hill sphere) around the Earth. Various objects of natural origin constantly enter the NES. By definition, a near-Earth object (NEO) is an asteroid (NEA) or comet (NEC) with a perihelion distance of less than 1.3 AU. Among NEOs, there is a class of potentially hazardous objects (PHO) – these are objects larger than 140 m, the orbit of which approaches the Earth's orbit to a distance of less than 0.05 AU. However, the modern understanding of a dangerous body includes objects up to 10 m in size (Shustov et al. 2015). Although decameter-class objects do not pose a threat of global catastrophe, their fall can lead to significant local consequences. A good example is the meteorite fall near Chelyabinsk in February 2013.

The purpose of this work is to study the distribution of NEOs with a size of 10 m or larger entering NES, according to the directions of entry and the velocity of approach to the Earth. A similar study was carried out previously in the works (Shustov et al. 2013, 2017; Vereš et al. 2009; Farnocchia et al. 2012) based on the data available at that time. Over the past time, new data has appeared and new requests have appeared, especially for the safety of space activities.

2 Methodic

To solve the problem, it is necessary to trace the dynamic evolution of the NEOs population over a sufficiently large time interval (for example, several dozen characteristic periods of the NEOs), noting all entries of asteroids into the NES sphere. When using this technique, the task can be divided into two parts: 1) building a model of the population of NEOs with object sizes of 10 m or more; 2) integration of the movement of asteroids with recording of approaches to the Earth.

To build the NEO model, the open source NEOMOD software package (Nesvorný et al. 2024) was used. The package takes into account the sources of NEOs and generates distributions of NEOs in absolute magnitude H and orbital elements of the asteroids. A population with 1 million objects with $H < 28$ was generated.

[1] https://www.whitehouse.gov/wp-content/uploads/2023/04/2023-NSTC-National-Preparedness-Strategy-and-Action-Plan-for-Near-Earth-Object-Hazards-and-Planetary-Defense.pdf (Last accessed 2024-07-25)

Taking this into account, subsequent distributions will be given in normalized form (i.e. the expected number of real objects).

At the second stage, the movement of a given population of asteroids was integrated, in which approaches to the Earth were monitored. The open code REBOUND (Rein & Liu 2012) was used. The integration technique included MERCURIUS (Rein et al. 2019) and IAS15 (Rein & Spiegel 2015) numerical integrators (which are included in the REBOUND standard library). Since the integration step cannot be arbitrarily small, the asteroid was not detected exactly on a sphere with a radius of 0.01 AU, but with some delay, i.e. at a smaller distance from the Earth (but not more than 0.0008 AU from the border).

3 Results

According to the simulation results, the number of model asteroids entering the NES over the estimated time interval (110 years) was 9950. From this, an estimate can be made for the average expected frequency of asteroids entering the NES. Since the calculation was carried out for 1 million model NEOs, which is approximately 1/11.5 of the total population of NEOMOD-generated NEO population, the expected number of occurrences in the NES is $(9950/110) \cdot 11.5 \simeq 1040$ asteroids per year. Naturally, most of these entries are made by small-sized asteroids.

Figure 1 shows the velocity of entry of asteroids into the sphere of NES with respect to the Sun-Earth-asteroid angle, normalized to a unit of solid angle and a unit of time. The figure highlights the increased concentration of objects in the direction of the Sun (0° in the figure) and in the opposite direction (180°). If we conditionally highlight the region of angles smaller than 90° (corresponds to the "everyday" definition of the daytime sky), then it is easy to see that about half of the entries into the NES occurs from the daytime hemisphere. Note that the obtained distribution is close in shape to that obtained earlier in Shustov et al. (2017), obtained using the NEOPOP model with a smaller number of asteroids.

Let us now consider the distribution of the flux of incoming asteroids in all directions. On the NES-sphere under consideration, the intersection of which is fixed, we will use a modified ecliptic coordinate system that is fixed relative to the direction of the Sun (the Sun always has coordinates (0, 0)). Figure 2 shows the flux density of incoming NEOs by directions in the described coordinate system. The average number of asteroids entering the NES in a given direction per year is shown in color. The distribution shows an increased flux density near the directions toward and against the Sun, which is also reflected in Fig. 1. The region near the ecliptic plane is also distinguished. A particularly striking feature is the decreased density in the directions

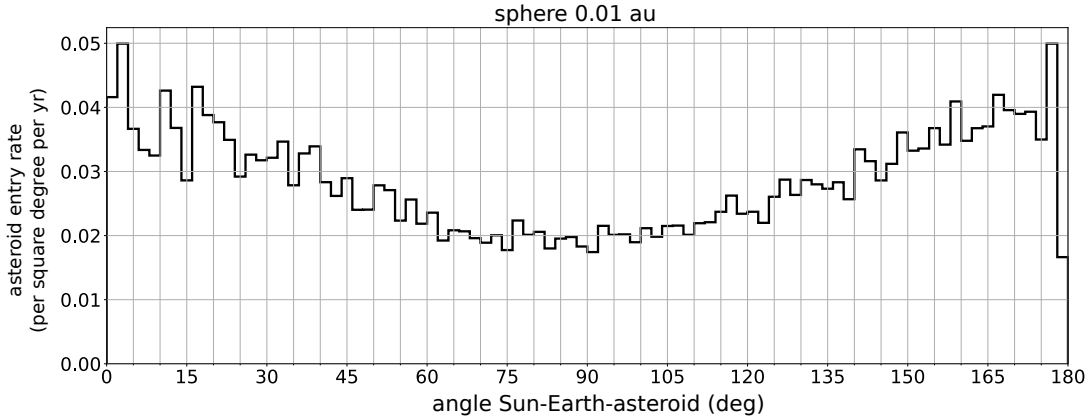

Fig. 1. Distribution of the flux density of asteroids entering the NES, by the angle between the direction to the Sun and the direction to the asteroid. 0° corresponds to the direction to the Sun.

corresponding to approximately from −120° to −60° in latitude, which corresponds to directions near the Earth's apex. Such a decrease in density is not observed in the opposite direction, near 90° in latitude. In simpler terms, there are significantly more asteroids "catching up" with the Earth than there are asteroids that the Earth "catches up" with. This is due to the structure of the NEA distribution by orbital elements.

Figure 3 shows the distribution of the velocity of approach, i.e. the rate of change of distance from an asteroid entering the NES to the Earth. The maximum of the distribution is at approximately 7.5 km/s (the value of the total spatial velocity is obviously higher). Of course, with further approach to the Earth the velocity of approach will increase. A very small proportion of asteroids entering the NES approach the Earth at a velocity of more than 30 km/s. The shape of the distribution and the position of the maximum are in qualitative agreement with the distribution constructed in Naroenkov & Shustov (2012) based on the data available at that time.

4 Summary

As a result of the calculations, an estimate was obtained for the frequency of decameter-class asteroids entering the NES, which is approximately 1000 entries per year. At the same time, there are on average about four NEOs in the NES at any given time. These are mainly relatively smaller NEAs. It should be noted that the estimate for the number of decameter and larger asteroids in the full NEO population in the NEOMOD program is approximately 11.5 million, which differs significantly from

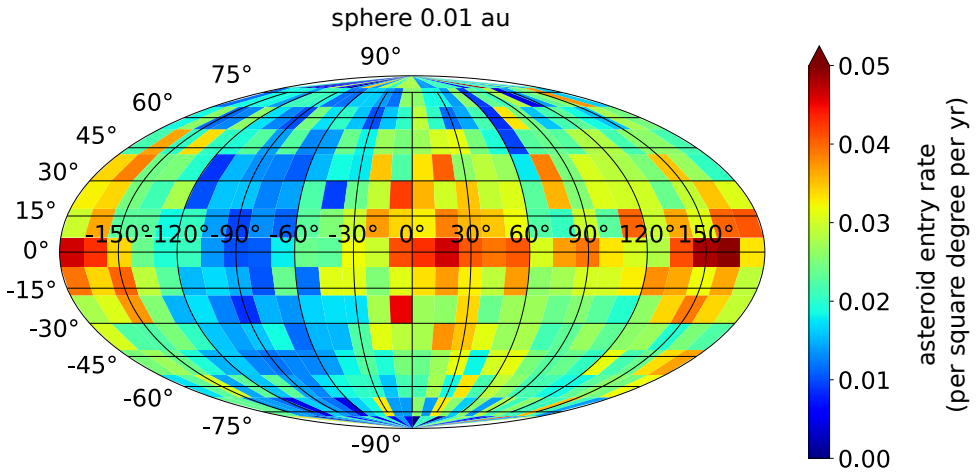

Fig. 2. Distribution of the flux density of asteroids entering the NES by directions in the modified ecliptic coordinate system.

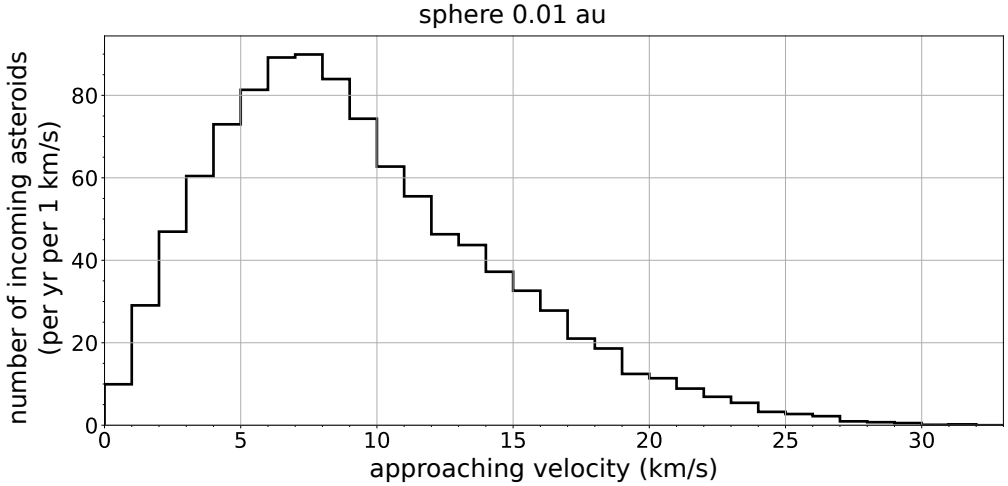

Fig. 3. Distribution of asteroids entering the NES by the velocity of approach to the Earth.

the estimate in the NEOPOP package, which predicts a population of about 65 million objects. In the above-mentioned NASA document the same estimate is about 45 million asteroids. Therefore, in order to use quantitative estimates, it is necessary to determine the expected population size and scale the expected number of approaches in accordance with the selected model.

In connection with the issues of asteroid-comet hazard, it is important to note that up to half of the asteroids enter the near-Earth space from the daytime hemisphere and cannot be detected by ground-based and near-Earth optical means.

Funding

This work was supported by the Russian Scientific Foundation (project No. 22-12-00115).

References

Farnocchia D., Bernardi F., Valsecchi G.B., 2012, Icarus, 219, 1, p. 41
Naroenkov S.A. and Shustov B.M., 2012, Cosmic Research, 50, 3, p. 221
Nesvorný D., Vokrouhlický D., Shelly F., et al., 2024, Icarus, 411, id. 115922
Rein H. and Liu S.-F., 2012, Astronomy & Astrophysics, 537, id. A128
Rein H., Hernandez D.M., Tamayo D., 2019, Monthly Notices of the Royal Astronomical Society, 485, 4, p. 5490
Rein H. and Spiegel D.S., 2015, Monthly Notices of the Royal Astronomical Society, 446, 2, p. 1424
Shugarov A.S., and Shustov B.M., 2022, INASAN Science Reports, 7, p. 85
Shustov B.M., Shugarov A.S., Naroenkov S.A., et al., 2015, Astronomy Reports, 59, 10, p. 983
Shustov B.M., Naroenkov S.A., Emel'yanenko V.V., et al., 2013, Solar System Research, 47, 4, p. 288
Shustov B.M., Naroenkov S.A., Efremova E.V., 2017, Solar System Research, 51, 1, p. 38
Vereš P., Jedicke R., Wainscoat R., et al., 2009, Icarus, 203, 2, p. 472

MODERN ASTRONOMY: FROM THE EARLY UNIVERSE TO EXOPLANETS AND BLACK HOLES

Doppler confirmation of TESS planet candidate TOI-1408.01: updated analysis and fitting

R. Baluev[1,2], G. Galazutdinov[2,3], G. Valyavin[2], V. Aitov[2], D. Gadelshin[2], A. Valeev[2,3], E. Sendzikas[2], E. Sokov[4], G. Mitiani[2], T. Burlakova[2], I. Yakunin[2], K. Antonyuk[3], V. Vlasyuk[2], I. Romanyuk[2], A. Rzaev[2], M. Yushkin[2], A. Ivanova[5], A. Tavrov[5], and O. Korablev[5]

[1] Saint Petersburg State University, 7–9 Universitetskaya Emb., Saint Petersburg, 199034 Russia
[2] Special Astrophysical Observatory of the Russian Academy of Sciences, Nizhny Arkhyz, 369167 Russia
[3] Crimean Astrophysical Observatory of RAS, Nauchny, 298409 Russia
[4] Central Astronomical Observatory at Pulkovo, Russian Academy of Sciences, 65 Pulkovskoe Shosse, Saint Petersburg, 196140 Russia
[5] Space Research Institute, Russian Academy of Sciences, 84/32 Profsoyuznaya Str., Moscow, 117997 Russia

Abstract. Based on the Doppler observations from the FFOREST spectrograph of the 6-meter telescope (BTA) and on the photometric observations from the TESS spacecraft, we provide an updated analysis for TOI-1408, an F-type main sequence star, located 140 pc away, that hosts exoplanet TOI-1408.01. We confirm t he qualitative conclusions from our initial paper: (1) a grazing transit geometry such that the planet obscures its host star by only a portion of the visible disc,(2) unreliably fitted p lanet r adius, (3) w hich n onetheless h as a l ower b ound c onstraint o f $\sim 1\ R_{\rm Jup}$, (4) unexpectedly large planet mass of $\simeq 1.7\ M_{\rm Jup}$, and (5) significant evidence in favor of a moderately eccentric orbit with $e \simeq 0.27$. This solution may suggest that the planet is likely to experience a high tidal eccentricity migration at the stage of intense orbital rounding or may indicate the possible presence of other unseen companions in the system, yet to be detected.

Keywords: techniques: radial velocities, spectroscopic; planets and satellites: detection; stars: individual: TOI-1408

DOI: 10.26119/VAK2024.127

1 Introduction

The first planet orbiting a solar type star was 51 Pegasi b, discovered in 1995 by Mayor & Queloz (1995) using the radial velocity (Doppler) technique, while the first exoplanetary transit was observed for the exoplanet HD 209458 b (Henry et al. 2000; Charbonneau et al. 2000). Since then, hundreds of hot Jupiters have been discovered. The details of their formation are still unclear (Dawson et al. 2018), but the most common view assumes that giant planets form outside the system's icy boundary and then migrate close to the star (Armitage 2007).

This paper considers Doppler observations carried out using the fiber-optic high resolution echelle spectrograph FFOREST[1] mounted on the 6-m telescope (BTA) of the Special Astrophysical Observatory of the Russian Academy of Sciences (SAO RAS). The instrument is a fiber-fed high spectral resolution echelle spectrograph with a resolving power R in the range from $\sim$30 000–35 000 to $\sim$60 000–70 000. The portable fiber-optic input module is mounted in the prime focus of the BTA. Presently, the instrument has two working fiber channels with equivalent widths of fiber cores of $0\farcs7$ and $1\farcs4$. With these cores and a binning of 2×2 pixels that we have applied, the instrument provides the resolving power of $R\sim60\,000$ and $R\sim30\,000$, respectively. An additional calibration channel provides simultaneous observation of spectra from a ThAr calibration source. Currently, the spectrograph with a CCD system constructed by the Advanced Design Laboratory of SAO RAS (Ardilanov et al. 2020) is efficient for planetary observations of stars as faint as $12^{\rm m}$. The electronics of the CCD system based an E2V CCD 4k $\times$ 4k sensor with a pixel size of 15×15 µm provides a readout noise of 2–3 electrons. For more details about FFOREST, see Valyavin et al. (2014, 2020).

Galazutdinov et al. (2023) (Paper I) reported a confirmation of the TESS candidate TOI-1408.01 based on the FFOREST Doppler observations. The planet mass was measured to be about 1.7 $M_{\rm Jup}$, apparently characterizing it as a typical hot Jupiter. But given that a large mass, the transit depth of $\sim$2 ppt provided by the TESS team appeared surprisingly small. This was explained by the "grazing transit" effect, when the planet obscures the star by only a portion of its projected disc. Additionally, the planet seemed to move along an elongated orbit with a moderate eccentricity $e\approx0.26$. This is unusual among hot Jupiters, which typically have almost circular orbits.

However, after the publication of Paper I we noticed a mistake in our script extracting photometric TESS light curves from the downloaded archive. It had been unnoticed that the TESS data archive contains results from multiple DVT pipeline

[1] Fiber-Fed Optical Russian Echelle SpecTrograph

runs, including the same observations reprocessed with a slightly different output. Therefore, there had been multiple duplicated transit light curves among the 96 ones used in our analysis (see Section 2.1 of Paper I). Here we perform a reanalysis with the correct TESS dataset, including just the latest processing available for a given light curve. This included just 57 unique transit light curves.

2 Observations and data reduction

The Doppler observations are the same 20 measurements given in Paper I. They were carried out with the BTA from 2021 to 2023 under the EXPLANATION[2] program (Valyavin et al. 2022a,b). One in-transit point was removed because it could be affected by the Rossiter–McLaughlin effect. The spectra were processed using our software DECH (Galazutdinov 2022). At the time of the observations, the FFOREST had a Doppler accuracy limit of $\sim$10–20 m/s for stellar spectra and $\sim$1 m/s for ThAr spectra.

In the Mikulski Archive for Space Telescopes[3], we identified 57 unique TESS transit light curves of TOI-1408 (this also includes some new light curves appeared after the publication of Paper I). After extracting the range of $\pm$100 min around each mid-transit point, we had 13 557 photometric data points in total.

3 Stellar parameters

We used that same star parameters as in Paper I. They were initially obtained spectroscopically using the ionization balance method optimized for solar-type stars (Takeda et al. 2002) and then refined using the MIST isochrones (Dotter 2016). For the goal of our analysis, we need the estimates of the star mass $M_\star = 1.332 \pm 0.014$ and star radius $R_\star = 1.276 \pm 0.015$, with a correlation coefficient between them of 0.87. Also, the limb-darkening coefficients were fixed at the values obtained by the trilinear interoplation of the Claret (2017) tables: $A = 0.2615$ and $B = 0.2771$ (quadratic law). Unfortunately, it is difficult to estimate their uncertainties, while our joint Doppler + transit model does not allow us to fit A and B reliably because of the degeneracies inferred by the grazing transit geometry.

4 New analysis and its results

We redid our analysis from Paper I using the same models and the same general scheme but with the correct set of TESS transit light curves. All the analysis was

[2] EXoPLANet And Transient events InvestigatiON
[3] https://archive.stsci.edu/

performed using the PLANETPACK software (Baluev 2013, 2018), which is based, in general, on optimizing the likelihood function of the task.

All the same issues appeared regarding the grazing transit geometry, which results in some model degeneracies. In particular, the planet radius r upper bound appears unconstrained and possibly limited only by *a priori* physical reasons. We can arbitrarily increase r, simultaneously increasing the transit impact parameter so that the light curve model remains nearly unchanged. This is illustrated in the left panel of Fig. 1, where we show the contour plot of the likelihood function as viewed in the $(r, R_\star)$ plane (and maximized against all the other fitted parameters). Nevertheless, based on the domains of the 2–3σ level, there is a rough *lower* limit $r \gtrsim 0.8$–$1\ R_{\rm Jup}$. It appears slightly lower than in Paper I, but still larger than that provided by the TESS team ($0.7\ R_{\rm Jup}$). As in Paper I, the TESS solution for $(r, R_\star)$ lies well outside of reasonable significance domains, while our increased planet radius estimate physically agrees with the Doppler-derived Jovian mass.

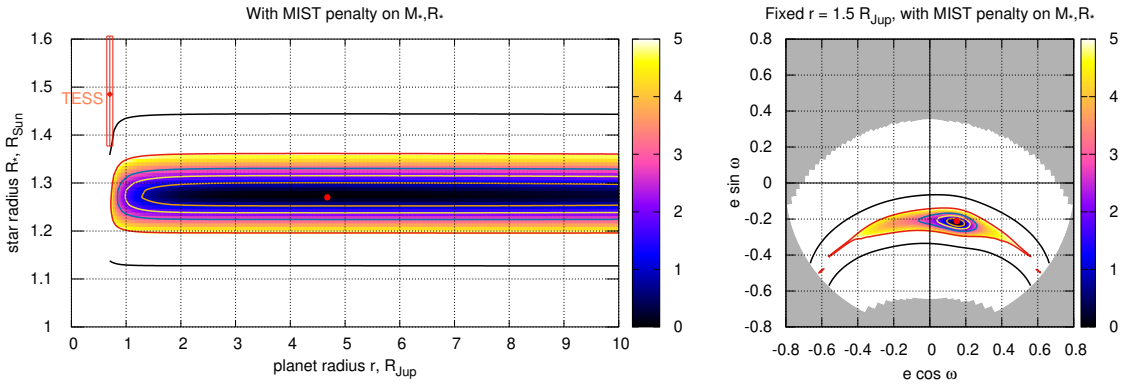

Fig. 1. Left: confidence regions for $(r, R_\star)$ constructed as level curves of the likelihood function. The five colored curves outline significance levels of 1σ, 2σ, 3σ, 5σ, and 10σ. The colormap shows the same significance (from 0 to 5σ). Right: similar confidence regions for $(e\cos\omega, e\sin\omega)$.

The updated best-fit parameters are given in Table 1, and in Fig. 2 we show the corresponding reference models together with the TESS transit light curves and our Doppler data.

In Paper I it was claimed that Doppler data reveal important hints of orbital eccentricity. In our updated analysis this conclusion looks unchanged, as can be seen from Table 1. For a more detailed presentation of the issue, we also computed 2D confidence plots for the eccentric parameters $(e\cos\omega, e\sin\omega)$, shown in the right

Table 1. Best-fit parameters for TOI-1408.

Planet				Star			
K	179 ± 22 m/s	ω	$304\overset{\circ}{.}4 \pm 5\overset{\circ}{.}4$	$M_\star$	$1.331 \pm 0.014\ M_\odot$	Radial acceleration:*	
P	$4.4247173 \pm 1.2 \cdot 10^{-6}$ d	l^*	$273\overset{\circ}{.}6 \pm 4\overset{\circ}{.}5$	$R_\star$	$1.275 \pm 0.015\ R_\odot$	c_0	-5740 ± 79 m/s
M	$1.69 \pm 0.20\ M_{\rm Jup}$	i	$84\overset{\circ}{.}819 \pm 0\overset{\circ}{.}095$	$\rho_\star$	$0.642 \pm 0.017\ \rho_\odot$	c_1	-24 ± 37 m/s/yr
a	0.05805 ± 0.00020 AU	$r/R_\star$	0.1182 ± 0.0014			RV jitter:	
e	0.265 ± 0.025	r	$1.5\ R_{\rm Jup}$ (fixed)			$\sigma_{\rm RV}$	53 ± 11 m/s

*Epoch JD2459000

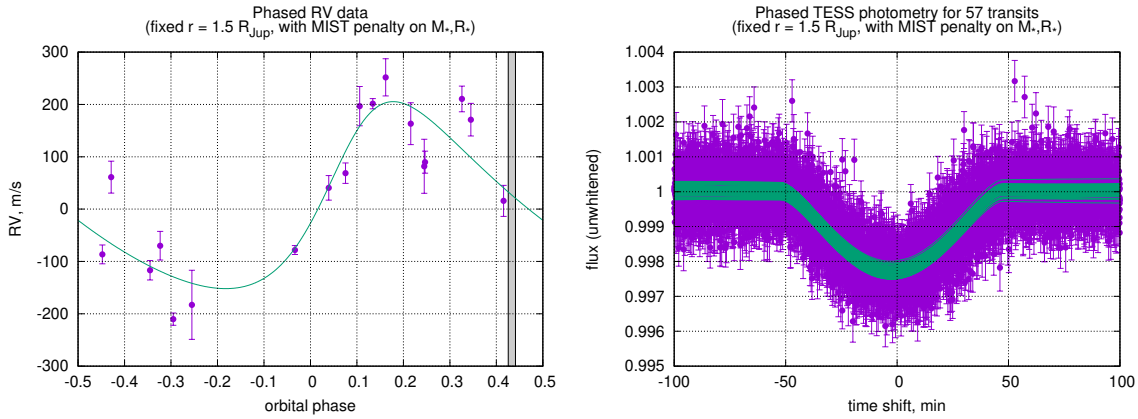

Fig. 2. Doppler and photometric data for TOI-1408 and their best-fit models. In the radial velocity panel (left), the position of the transit is marked as a vertical narrow band. In the photometry panel (right), each of 57 transits has an individual polynomial trend, so we show a bunch of close curves that differ due to these trends.

panel of Fig. 1. The zero eccentricity (the origin of coordinates) lies clearly outside of any reasonable significance level.

5 Summary

Based on the updated analysis of the TOI-1408 data with a correct set of transit light curves, we confirm all qualitative conclusions from Paper I. The light curve of the transits has a pronounced V-shape, indicating the "grazing" geometry of the planetary transit, therefore we cannot estimate the planet radius reliably. Only its lower limit can be estimated, and it appears to be $r \sim 0.8 R_{\rm Jup}$, which is higher than the TESS estimate (at least when it is considered together with the star radius estimate). The planet mass can be measured quite reliably using the FFOREST Doppler data and is about $\sim 1.7 M_{\rm Jup}$. This is unexpectedly large but physically consistent with the increased estimate for the planet radius. We also confirm the

significant evidence in favor of non-zero eccentricity. A non-zero orbital eccentricity is not typical for hot Jupiters because of the tidal orbit rounding effect. Possible explanations include the presence of an additional unseen companion that excites this eccentricity dynamically, or it is possible that we have "catched" this planet–star system before the evolutionary stage when the intense orbital rounding is finished.

Acknowledgements. We obtained the observed data at the unique scientific facility "Big Telescope Alt-Azimuthal" of SAO RAS.

Funding

The data processing was made with the financial support of grant No. 075-15-2022-262 (13.MNPMU.21.0003) of the Ministry of Science and Higher Education of the Russian Federation.

References

Ardilanov V.I., Murzin V.A., Afanasieva I.V., et al., 2020, Ground-Based Astronomy in Russia. 21st Century, Proc. All-Russian Conf., ed. I.I. Romanyuk, I.A. Yakunin, A.F. Valeev, D.O. Kudryavtsev, p. 115

Armitage P.J., 2007, arXiv:astro-ph/0701485

Baluev R.V., 2013, Astronomy and Computing, 2, p. 18

Baluev R.V., 2018, Astronomy and Computing, 25, p. 221

Charbonneau D., Brown T.M., Latham D.W., et al., 2000, Astrophysical Journal, 529, L45

Claret A., 2017, Astronomy and Astrophysics, 600, A30

Dawson R.I., Johnson J.A., 2018, Annual Review of Astronomy and Astrophysics, 56, p. 175

Dotter A., 2016, Astrophysical Journal Supplement Series, 222, p. 8

Galazutdinov G.A., 2022, Astrophysical Bulletin, 77, p. 519

Galazutdinov G.A., Baluev R.V., Valyavin G., et al., 2023, Monthly Notices of the Royal Astronomical Society, 525, L111

Henry G.W., Marcy G.W., Butler R.P., et al., 2000, Astrophysical Journal, 529, L41

Mayor M. and Queloz D., 1995, Nature, 378, p. 355

Takeda Y., Ohkubo M., Sadakane K., 2002, Publications of the Astronomical Society of Japan, 54, p. 451

Valyavin G., Beskin G., Valeev A., et al., 2022a, Astrophysical Bulletin, 77, p. 495

Valyavin G., Beskin G., Valeev A., et al., 2022b, Photonics, 9, p. 950

Valyavin G.G., Bychkov V.D., Yushkin M.V., et al., 2014, Astrophysical Bulletin, 69, p. 224

Valyavin G.G., Musaev F.A., Perkov A.V., et al., 2020, Astrophysical Bulletin, 75, p. 191

MODERN ASTRONOMY: FROM THE EARLY UNIVERSE TO EXOPLANETS AND BLACK HOLES

Cleaning the TESS observations of WASP-33 b transits from the host star photometric variability

R. Baluev[1,2] and E. Sokov[3]

[1] Saint Petersburg State University, 7–9 Universitetskaya nab., St. Petersburg, 199034 Russia
[2] Special Astrophysical Observatory of the Russian Academy of Sciences, Nizhny Arkhyz, 369167 Russia
[3] Central Astronomical Observatory at Pulkovo, Russian Academy of Sciences, 65/1 Pulkovskoje sh., St. Petersburg, 196140 Russia

Abstract. Based on the TESS observations of a δ Scuti variable WASP-33 obtained in 2019 and 2022, we thoroughly investigate the power spectrum of its photometric flux and construct a statistically exhaustive model for its variation. This model contains 30 robustly justified h armonics, t he r ed n oise, a nd q uasiperiodic n oise components. This compound model allows us to greatly improve the transit timing accuracy of the exoplanet WASP-33 b. The rms of its transit timing variation residuals is drastically reduced by a factor of 3.5, from 63 s to 18 s.

Keywords: techniques: photometric; stars: variables: delta Scuti; stars: individual: WASP-33; planets and satellites: detection

DOI: 10.26119/VAK2024.128

1 Introduction

WASP-33 (HD 15082) is a bright $8\overset{\mathrm{m}}{.}14$ fast-rotating star with $v \sin i \sim 90$ km/s, located in Andromeda. Its the only known exoplanet WASP-33 b was detected by SuperWASP (Herrero et al. 2011). Its orbital period is estimated as $1.219867 \pm 4.2 \cdot 10^{-5}$ d (von Essen et al. 2020), the mass as 2.10 ± 0.14 M_{Jup}, and the radius as 1.59 ± 0.07 R_{Jup} (Chakrabarty & Sengupta 2019). Remarkably, this exoplanet was the first ever known to orbit a δ Scuti variable.

The intrinsic variability of WASP-33 represents an obvious nuisance factor for analysing the transit light curves of its exoplanet WASP-33 b. The effect of this variability on the estimated planetary orbital parameters was previously investigated using out-of-transit observations from ground-based telescopes located in Germany and Spain (von Essen et al. 2014). Eight significant pulsation frequencies were revealed, and it was concluded that cleaning the transit light curves from stellar pulsations does not practically affect the estimated planetary parameters, though their uncertainties had decreased. Besides, it was noticed that WASP-33 pulsation phases change over time. In a later analysis of the TESS data of 2019, von Essen et al. (2020) expanded the number of pulsation harmonics to 29. They also claimed the detection of the exoplanet secondary eclipse, its phase curve variation, and the "ellipsoidal variation" appearing because of the subtle exoplanet gravitation effect on the host star shape.

Our goal here is to analyse WASP-33 pulsations based on the up-to-date TESS data (observations in 2019 and 2022) and to investigate whether (and how much) this can help us improve the transit timings accuracy for this target.

2 TESS photometry of WASP-33

TESS observed WASP-33 in sector 18 (Nov 2019) and sector 58 (Nov 2022), lasting about 1 month each. In the data validation time series downloaded from the Mikulski Archive for Space Telescopes,[4] we found 14 796 and 18 951 photometric measurements for these sectors, respectively. We also identified 17 transits in sector 18 and 21 transits in sector 58, and for each transit we extracted a ± 4 h piece of the light curve around the predicted mid-transit epoch. This subset formed our first "in-transit" dataset (ITD). The second "out-of-transit" dataset (OTD) included all the observations located at least ± 2 h away from the centers of the transits or secondary eclipses. Note that the ITD and OTD slightly overlap.

[4] https://archive.stsci.edu/

In this work we deal mainly with the OTD. Its sector 18 portion is hereafter referred to as TESS_1, and it contains 10 684 data points. The sector 58 portion (TESS_2) contains 13 625 data points. The ITD contains 8914 data points in total.

3 Statistically exhaustive model of WASP-33 variability

Our goal was to construct a statistically "exhaustive" model that represents the WASP-33 data in such a way that the residuals do not contain statistically significant periodic (or quasiperiodic) variations. In this attempt we adopted a sum of sinusoids for the deterministic part of the model:

$$\mu_n(t) = A_0 + \sum_{k=1}^{n} A_k \cos\left(2\pi f_k (t - T_0) + \varphi_k\right), \tag{1}$$

where A_k, $f_k = 1/P_k$, and φ_k are free parameters. However, the photometric variation involves significant non-deterministic part with a multiband power spectrum. It cannot be efficiently modeled by deterministic models like (1) because we would need too many terms (hundreds in our case). Such quasiperiodic variations are much better treated as a non-white noise (NWN), which offers a great reduction in the number of free parameters. Using this approach, we model the NWN correlation function:

$$k_{n'}(\Delta t_{ij}) = \left(\sigma^2_{\mathrm{TESS},i} + \sigma_0^2\right)\delta_{ij} + \sum_{k=1}^{n'} \sigma_k^2 \mathrm{e}^{-\frac{|\Delta t_{ij}|}{\tau_k}} \cos 2\pi f'_k \Delta t_{ij}, \quad \Delta t_{ij} = t_i - t_j, \tag{2}$$

where $\sigma_{\mathrm{TESS},i}$ is the TESS-provided photometric uncertainty at t_i, δ_{ij} is the Kronecker delta, and the remaining quantities (σ_k, τ_k, $f'_k = 1/P'_k$) are free parameters. This model involves the white noise (WN) portion (σ_0) and n' independent quasiperiodic (QP) components (purely NWN part). Models (1) and (2) can be fitted jointly by the maximum-likelihood method if we assume that the NWN is a random Gaussian process (GP) which implies a multivariate Gaussian distribution for the data vector.

Details of the subsequent periodogram analysis, including the statistical testing of the harmonics, are too lengthy and will be presented in another paper. We applied our algorithm separately to the TESS 2019 and 2022 observing runs, and both these datasets revealed very similar sets of harmonics. In Fig. 1 we plot all the detected harmonics in the frequency–amplitude plane (with uncertainties). Harmonics that were cross-identified by their frequencies are additionally labeled with circles. Nearly all the harmonics, namely 30 of them, can be robustly cross-identified by their frequencies. Usually, the amplitudes of the cross-identified harmonics are similar, although

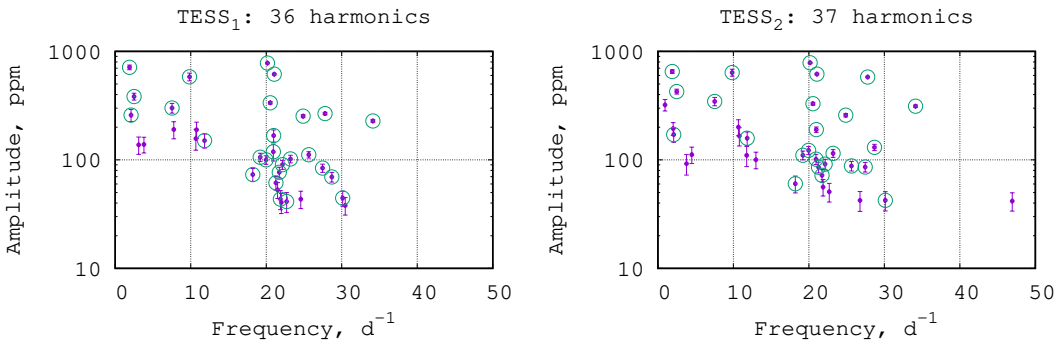

Fig. 1. All the detected harmonics in the frequency–amplitude plane.

some of them have demonstrated a large change between the 2019 and 2022 runs. One may conclude that the WASP-33 variability pattern demonstrates remarkable, though not entirely perfect, stability on the timescale of a few years at least.

Table 1 contains the best-fit NWN parameters of the GP kernel (Eq. 2). It contains the mandatory WN term, one red noise (RN) term with a period P'_1 much larger than τ_1, and one QP term with P'_2 smaller than but comparable to τ_2. The second NWN term appears nearly the same for the 2019 and 2022 datasets, although the WN and RN parts reveal significant changes.

Table 1. Estimated GP parameters.

	σ_0, ppm	σ_1, ppm	τ_1, d	P'_1, d	σ_2, ppm	τ_2, d	P'_2, d
$TESS_1$	260.4(5.3)	525(47)	0.52(13)	1.65(23)	426(23)	0.182(26)	0.1085(15)
$TESS_2$	544.6(4.9)	294(23)	0.23(98)	∞ ($\gtrsim$1.7)	470(22)	0.182(21)	0.1084(13)

4 Improving transit timing accuracy

Now let us consider how our out-of-transit photometric model of WASP-33 can be used to detrend the transit light curves. Our model contains two components: the deterministic one $\mu(t)$ (harmonics) and the GP part (NWN) expressed by the correlation function $k(\Delta t)$. Regarding the former, we can subtract the best fitting $\mu(t)$ from the ITD as if it was a predefined function: it has very small uncertainty because the number of the OTD data from which it has been derived is much larger than that of the ITD. We will call this "detrending" for shortness.

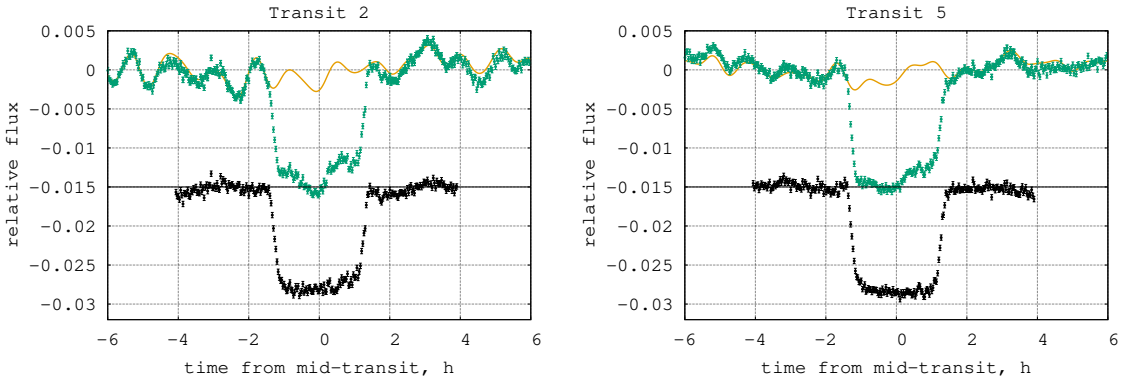

Fig. 2. Detrending examples for WASP-33 b transits 2 and 5.

Regarding the NWN part of the model, its effect can be removed by applying the whitening procedure to the ITD and the NWN model simultaneously, using the covariance matrix derived from the best-fit $k(\Delta t)$. It is unnecessarily to apply this procedure in an explicit way, and in fact it is automatically (but implicitly) applied in our NWN analysis that relies on the maximum-likelihood GP fitting. However, we will call this part of the processing as "whitening" for simplicity.

In Fig. 2 we show examples of detrending for two transits of WASP-33 b. In the figure we plot the TESS data before processing (green points), the harmonics model μ (orange curve), and the detrended ITD (black points, shifted down). One can see that detrending can remove a large portion of the host star variability; however, some nuisance variation still remains. Obviously, this variation appears because of the NWN and should be removed by whitening.

Since our whitening is implicit, we do not show any whitened data in Fig. 2. However, its effect is demonstrated in Fig. 3, where we plot the resulting transit timing residuals derived from (1) the initial (raw) ITD, (2) detrended ITD, and (3) detrended and whitened ITD. One can see that the transit timing variation (TTV) scatter remarkably reduces after each step: while the rms of the initial TTV residuals was 63 s, the detrending reduced it to 36 s, and after the whitening it dropped to 18 s. The final set of these improved transit timings will be published in another paper.

5 Conclusions

An approach based on the explicit modeling of WASP-33 variability appears extremely successful in improving its exoplanet transit timing accuracy. In total, we

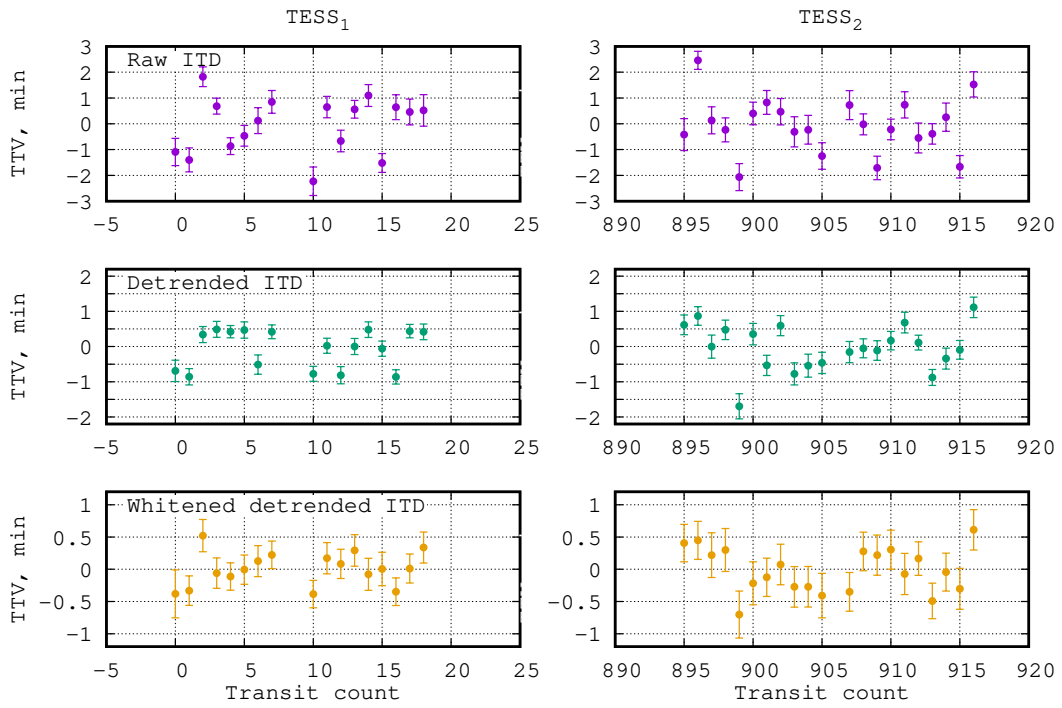

Fig. 3. WASP-33 transit timing residuals before and after ITD cleaning. Note the different ordinate ranges in the plots.

obtained a dramatic TTV rms improvement by a factor of 3.5. It is important that we take into account the deterministic as well as non-deterministic (NWN) parts of this variability. Both of them incorporate similar amounts into the total error budget.

Our results still cannot be directly applied to observations other than from TESS because the model parameters somewhat change on the timescale of a few years. Because of that, we cannot use the TESS-derived model with data obtained, e.g., years prior to TESS. However, the frequencies of the harmonics and of the QP part of the NWN look stable, so it may be possible to apply our model to older data, fixing all these frequencies but refitting harmonics amplitudes and phases as well as the variances of the NWN components. This needs additional investigation.

References

Chakrabarty A. and Sengupta S., 2019, Astronomical Journal, 158, p. 39
Herrero E., Morales J.C., Ribas I., et al., 2011, Astronomy and Astrophysics, 526, L10
von Essen C., Czesla S., Wolter U., et al., 2014, Astronomy and Astrophysics, 561, A48
von Essen C., Mallonn M., Borre C.C., et al., 2020, Astronomy and Astrophysics, 639, A34

MODERN ASTRONOMY: FROM THE EARLY UNIVERSE TO EXOPLANETS AND BLACK HOLES

Determination of the exoplanet HD 189733 b atmospheric structure based on the multicolor photometric transit observations obtained with the HST and at the Caucasian Mountain Observatory

E. Bekesov

Sternberg Astronomical Institute, Lomonosov Moscow State University,
13 Universitetskij pr-kt, Moscow, 119992 Russia

Abstract. The paper presents a study of the exoplanet HD 189733 b based on the multicolor photometric observations obtained by the Hubble Space Telescope as well as on the equipment of the Caucasian Mountain Observatory. It is shown that with all other parameters fixed, the radius of the planet obtained from the interpretation of the light curves varies, which may be a consequence of the presence of an extended Rayleigh atmosphere.

Keywords: planets and satellites: atmospheres, gaseous planets

DOI: 10.26119/VAK2024.129

1 Introduction

During the transit of an exoplanet across the disk of the parent star, the brightness of the latter decreases due to both the planet itself and its atmosphere absorbing and scattering the light. The magnitude of the brightness decrease during transit should decrease as the wavelength increases. It is based on the fact that the longer the wavelength, the less the star radiation undergoes scattering in the exoplanet atmosphere. This is expressed as a decrease in the transit depth of the light curve. When this light curve is subsequently interpreted within the framework of the black opaque circle model, this leads to differences in the determined radius of the exoplanet.

Thus, from the interpretation of the photometric data for the transits of the same exoplanet obtained in filters with different wavelength bands, it is possible to judge about the presence of an extended atmosphere on the exoplanet as well as to obtain preliminary data on its nature and structure.

2 Observed data

For the study, the author has chosen a hot super-Jupiter exoplanet HD 189733 b. This planet was chosen both because of its characteristics such as a large transit depth, small orbital eccentricity, and the brightness of the star, and because it has been extensively studied and has a significant amount of spectroscopic and photometric data. In this paper, we processed the light curves obtained in 2007 by the Hubble Space Telescope (HST) during the observations of HD 189733 b (Pont et al. 2007). The observations were carried out in ten different filters in the wavelength range from $\lambda\lambda = 5500$–6000 Å to $\lambda\lambda = 10\,000$–$10\,500$ Å. Each light curve consists of 625 points with an individual accuracy of about $\sigma \approx 10^{-4}$.

We also subsequently interpreted the observations of this exoplanetary system obtained at the Caucasian Mountain Observatory (CMO) with the RC600 telescope on July 9, 2022 and September 27, 2022. In the first case, the observations were carried out in the g' filter (central wavelength 475 nm), the light curve consisted of 803 points with an individual accuracy of $\sigma = 0.0041$. The second transit was observed in the Ic filter (central wavelength 786.5 nm), the light curve consisted of 619 points with an individual accuracy of $\sigma = 0.0099$.

3 Interpretation of the light curves

The observed data were interpreted using software, written by the author (Bekesov et al. 2021), that approximates transit light curves using the least squares method. In the interpretation, it was assumed that the brightness distribution over the star

disk has central symmetry and is described by a quadratic law. The limb darkening coefficients were taken from the theoretical calculations based on the models of stellar atmospheres (Eastman et al. 2013).

The length of the semimajor axis was fixed at $a = 0.03126$ AU, and the orbital period was $P = 2.2185752$ d (Rosenthal et al. 2021). The calculations were performed for three different eccentricities: 0, 0.01, and 0.02, with a fixed argument of pericenter $\omega = 270°$. These values were taken as corresponding to the existing estimates of the eccentricity for this planet (Bonomo et al. 2017).

The radius of the star and the orbital inclination were obtained from the interpretation of the light curve corresponding to a wavelength of 6750 Å with three free parameters. Subsequently, these values of the star radius and orbital inclination were used to interpret the remaining nine HST light curves. For the two light curves obtained at the CMO, all parameters except the radius of the planet were fixed. In this case, the same values were taken as in processing the HST observations.

The interpretation results for the space and ground-based observations are presented in Tables 1 and 2, respectively.

Table 1. Interpretation results for the HST transit light curves with fixed theoretical limb darkening coefficients and fixed $e = 0$.

λ, Å	Star radius, $R_\odot$	Linear coefficient	Quadratic coefficient	Orbital inclination, deg	Planet radius, km	Planet radius, R_J	Normalized χ^2
5750	0.756	0.60964	0.14806	85.72	82538 ± 130	1.1559 ± 0.0018	2.27896
6250	0.756	0.54384	0.18148	85.72	82542 ± 130	1.1561 ± 0.0018	1.35196
6750	0.756	0.50189	0.19045	85.72	82269 ± 130	1.1522 ± 0.0018	0.99531
7250	0.756	0.45994	0.21097	85.72	82000 ± 130	1.1484 ± 0.0018	0.96278
7750	0.756	0.42083	0.20747	85.72	81893 ± 130	1.1469 ± 0.0018	0.95105
8250	0.756	0.39202	0.21250	85.72	82003 ± 130	1.1485 ± 0.0018	1.00925
8750	0.756	0.36532	0.21735	85.72	81678 ± 130	1.1439 ± 0.0018	0.99496
9250	0.756	0.34140	0.22402	85.72	81785 ± 130	1.1454 ± 0.0018	0.91441
9750	0.756	0.32165	0.23343	85.72	81781 ± 130	1.1453 ± 0.0018	1.20305
10250	0.756	0.30189	0.24284	85.72	81678 ± 130	1.1439 ± 0.0018	1.20750

4 Modeling the atmosphere

For a preliminary assessment of the atmosphere structure, we took a simplified model in which the density distribution was described by the formula $\rho(h) = \rho_0 \exp(h/H)$, where ρ_0 is the gas density at the conditional surface, h is the height of an atmospheric layer, and H is the characteristic height.

Table 2. Interpretaion results for the transit light curves from the CMO.

Observing date	Filter	Orbital inclination, deg	Planet radius, km	Planet radius, R_J	Normalized χ^2
2022.07.09	g'	85.72	$83614\ ^{+498}_{-535}$	$1.1710\ ^{+0.0070}_{-0.0075}$	0.820982
2022.09.27	Ic	85.72	$80496\ ^{+1423}_{-1589}$	$1.1274\ ^{+0.0199}_{-0.0223}$	0.829820

The modeling was carried out using a numerical method in which the planet atmosphere was divided into thin rings, for each of which the optical thickness along the line of sight τ was calculated:

$$\tau(\xi) = 2\int_{\xi}^{R_a} \frac{\sigma(r) r\, dr}{\sqrt{r^2 - \xi^2}}, \tag{1}$$

where ξ is the target distance, $r = r_0 + h$, r_0 is the radius of the opaque circle, and R_a is the radius of the planet with the atmosphere. The volumetric opacity coefficient $\sigma(r)$ was considered proportional to the density of the atmosphere. Also, in accordance with the Rayleigh law, it was assumed that it is proportional to λ^{-4}.

To estimate the transit depth, the author introduced the concept of an effective radius, i.e., the radius of the opaque circle at which the transit depth at the midpoint would correspond to that obtained when simulating the transit with given characteristics of the atmosphere.

Using the above assumptions, the inverse problem was solved by varying three parameters: the opacity coefficient at the surface at a wavelength of 5750 Å, the radius of the opaque core, and the characteristic height of the atmosphere. The values of these quantities for which the sum of the squares of the differences between the effective radii and the radii of the planet obtained from the interpretation of the light curves turned out to be the smallest were chosen as optimal.

The opacity coefficient of the conventional surface at a wavelength of 5750 Å for all three eccentricities turned out to be equal to $1.5 \cdot 10^{-4}$ km^{-1}, which in the approximation of an atmosphere consisting of molecular hydrogen corresponds to a particle concentration of $2.1 \cdot 10^{18}$ cm^{-3} or about 3.487 mol/m^3. The characteristic height also turned out to be equal to $H \approx 1000$ km for all the three eccentricities. At the same time, the radius of the opaque core for the zero eccentricity was determined as 81 400 km, and for eccentricities of 0.01 and 0.02 it was 82 100 km and 82 800 km, respectively.

Figure 1 shows the radii obtained from the interpretation of the space and ground-based observations for a circular orbit with the model effective radii superimposed.

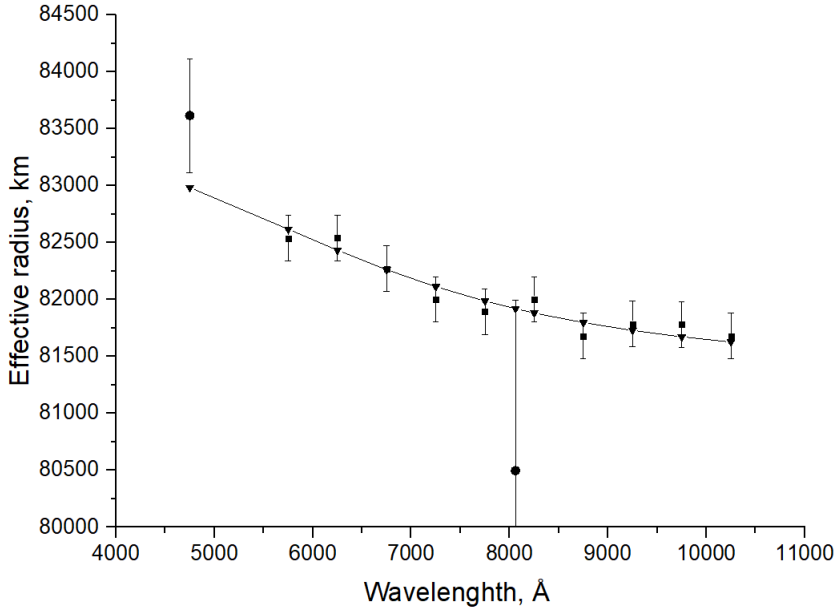

Fig. 1. Dependence of the exoplanet HD 189733 b radius on the wavelength based on the light curves obtained by the Hubble Space Telescope (squares) and our light curves in the g' and Ic filters (circles). The triangles connected by a line show the modeling results for the Rayleigh atmosphere.

Acknowledgements. The author expresses gratitude to A. M. Cherepashchuk, M. K. Abubekerov, and N. Yu. Gostev for valuable advice during the work and to K. A. Lyzenko and N. A. Maslennikova for conducting the observations and primary data processing.

References

Bekesov E.V., Belinskii A.A., Popov S.B., 2021, Astronomy Reports, 65, 12, p. 1278
Bonomo A.S., Desidera S., Benatti S., et al., Astronomy and Astrophysics, 2017, 602, p. 16
Eastman J., Gaudi B.S., Agol E., Publications of the Astronomical Society of the Pacific, 2013, 125, 923, p. 83
Pont F., Gilliland R.L., Moutou C., et al., 2007, Astronomy and Astrophysics, 476, p. 1347
Rosenthal L.J., Fulton B.J., Hirsch L.A., et al. , Astrophysical Journal Supplement Series, 255, 1, id. 8

MODERN ASTRONOMY: FROM THE EARLY UNIVERSE TO EXOPLANETS AND BLACK HOLES

Investigation of the infrared profiles of exoplanet HD 209458 b secondary eclipses

A. Fedotov[1] and R. Baluev[1,2]

[1] Saint Petersburg State University, 7–9 Universitetskaya Emb., St. Petersburg, 199034 Russia
[2] Special Astrophysical Observatory of the Russian Academy of Sciences, Nizhny Arkhyz, 369167 Russia

Abstract. In this work we process infrared light curves for 13 secondary eclipses of the exoplanet HD 209458 b, obtained with the Spitzer Space Telescope. The objective of the study was to identify any discrepancies that might be attributed to the inhomogeneity of the planet's surface brightness or a difference of the planet's shape from a sphere. Firstly, an attempt was made to ascertain whether the observed midpoint of the secondary eclipse exhibited a shift from the ephemeris moment. This could indicate the presence of a hot spot on the planet's surface that is shifted from the central meridian. The analysis allowed for the correlated noise that remained in the IRAC detector data after aperture photometry by approximating the noise with a Gaussian random process. As a result, we detected two components of red noise with different time scales: ~ 10 s and ~ 5 min. In addition, we constructed a unified model of the effect of inhomogeneous pixel sensitivity as a periodic function of the brightness centroid coordinates, which works well for all the analyzed eclipses. According to the results, the main parameters of the HD 209458 b eclipse coincided with those obtained by other authors: a depth of $0.125 \pm 0.004\%$ and a shift of the observed midpoint of -0.53 ± 0.61 min.

Keywords: planets and satellites: surfaces, general; stars: planetary systems; techniques: photometric; methods: data analysis; stars: individual: HD 209458

DOI: 10.26119/VAK2024.130

1 Introduction

The investigation of exoplanets is an important topic in modern astronomy. In the past 30 years, more than 5500 exoplanets have been discovered. It has become possible today not only to improve the methods of discovery but also to investigate planets' physical characteristics. The most significant sources of information on exoplanets are the observations of transits and secondary eclipses (events when a planet passes behind the parent star). To observe these events, it is necessary that the plane of a planet's orbit be nearly perpendicular to the picture plane. While this limits the number of planetary systems available for study, the potential for obtaining data on these systems makes them a primary target for observing efforts.

In our research, the main focus is on the study of secondary eclipses. These observations allow us to determine the orbital elements of an exoplanet and obtain information about its surface temperature. However, the main issue of our work has been the identification of a more subtle phenomenon: the uneven distribution of brightness on the planet's surface, which should affect the initial and final stages of the eclipse. Hot Jupiters are the most promising candidates for this study as they have a higher brightness relative to their parent stars and are expected to exhibit variation in the surface brightness (Rauscher & Menou 2013). The most noticeable inhomogeneities are in the infrared range, where these planets exhibit their maximum brightness.

In this study, we use the IRAC instrument data from the Spitzer Space Telescope in the 3.6 μm band. Our research focuses on the exoplanet HD 209458 b, selected due to its nearly circular orbit and large number of observations. Papers on a related topic have been published previously (Knutson et al. 2007; Majeau et al. 2012; de Wit et al. 2012). The novel aspects of this research lies in our investigation of HD 209458 b using the Gaussian random process (GP) method.

2 Data reduction

We analyzed 13 secondary eclipses. The basic calibrated data (BCD) FITS files are publicly available.[1] The observations were made between 2011 and 2015. For each eclipse we used the data within 4 hours before and after the center of the eclipse. Each eclipse consisted of 2500–3500 three-dimensional files with a size of 32×32 pixels and 64 frames in the third dimension.

We performed aperture photometry on each frame using the astropy (Astropy Collaboration et al. 2013) and photutils (Bradley et al. 2024) packages. The center

[1] https://sha.ipac.caltech.edu/applications/Spitzer/SHA/

of the aperture was determined by calculating the weighted average of the flux within a 8×8 pixel square centered on the frame. The aperture radius within which the flux was measured was 4 pixels. We subtracted the median background outside a ring with a radius of 12 pixels from the resulting flux. We removed 247 frames using the method described in Baluev et al. (2015). The outliers were detected by comparing the empirical distribution of residuals to a Gaussian. The photometric dimensions that fell into the strongly deviating tails of the distribution were removed. Finally, we binned 64 frames together. This was done to reduce the quantity of data for the next step in our work because of the limitations on available computing resources.

3 Model

We obtain a light curve that contains correlated noise. Taking this into account was the main difficulty in our work. To allow for this, we used a method that assumes that the correlated noise is a stationary Gaussian random process (the GP method). This is a development of the maximum likelihood estimation method similar to those used in Fedotov & Baluev (2022) with the use of an additional regression at the coordinates of the brightness center. The function for minimization was

$$\begin{aligned} &f(\theta,\eta) = \ln\det \mathsf{V}(\eta) + \frac{1}{\gamma}\, r^{\mathrm{T}}(\theta)\, \mathsf{V}(\eta)^{-1}\, r(\theta) \quad \overset{\theta,\eta}{\longmapsto} \quad \min, \\ &r = x - \mu(t,y,\theta), \qquad \gamma = 1 - \frac{\dim\theta}{\dim x}, \end{aligned} \tag{1}$$

where we have:

(1) input data that include the observation moments t, the primary input data x, and the auxiliary data y used in a regression model;
(2) the model μ of the curve being fitted (including possible regression against y) and the model V of the noise covariance matrix;
(3) fittable parameters θ and η.

The implementation of this method is based on the `PlanetPack` project (Baluev 2013, 2018), which is written in `C++`.

We employed two methods to analyze the data. The first approach involved correlated noise that was dependent only on time. To this end, we utilized the following

kernel function:

$$
\begin{aligned}
&k = k_{\mathrm{WN}} + k_{\mathrm{RN}} + k_{\mathrm{QPN}},\\
&k_{\mathrm{WN}}(\Delta t, \eta_{\mathrm{WN}}) = \sigma^2_{\mathrm{WN}} \times \begin{cases} 1, & \Delta t = 0, \\ 0, & \Delta t \neq 0, \end{cases} && \eta_{\mathrm{WN}} = \{\sigma_{\mathrm{WN}}\},\\
&k_{\mathrm{RN}}(\Delta t, \eta_{\mathrm{RN}}) = \sigma^2_{\mathrm{RN}} \exp\left(-\frac{\Delta t^2}{2\tau^2_{\mathrm{RN}}}\right), && \eta_{\mathrm{RN}} = \{\sigma_{\mathrm{RN}}, \tau_{\mathrm{RN}}\},\\
&k_{\mathrm{QPN}}(\Delta t, \eta_{\mathrm{QPN}}) = \sigma^2_{\mathrm{QPN}} \exp\left(-\frac{\Delta t^2}{2\tau^2_{\mathrm{QPN}}}\right) \cos\frac{2\pi\Delta t}{P_{\mathrm{QPN}}}, && \eta_{\mathrm{QPN}} = \{\sigma_{\mathrm{QPN}}, \tau_{\mathrm{QPN}}, P_{\mathrm{QPN}}\}.
\end{aligned}
\tag{2}
$$

It consists of three main components: white noise, red noise, and quasi-periodic noise. However, an analysis of the intermediate data indicates that the model does not accurately match the autocorrelation function. In order to improve the approximation, a second component of red noise was added. This resulted in the final kernel function being

$$k = k_{\mathrm{WN}} + k_{\mathrm{RN1}} + k_{\mathrm{RN2}} + k_{\mathrm{QPN}}. \tag{3}$$

In the second approach we considered the dependence of the noise component not only on time but also on the coordinates of the brightness centroid. Initially, we used a single model for the pixel sensitivity map for each eclipse, which was responsible for the received flux. The model was a two-dimensional Fourier series:

$$
\begin{aligned}
\mu(x,y) = {} & a_1\cos(2\pi x) + b_1\sin(2\pi x) + a_2\cos(2\pi y) + b_2\sin(2\pi y)\\
& + a_3\cos(2\pi(x+y)) + b_3\sin(2\pi(x+y))\\
& + a_4\cos(2\pi(x-y)) + b_4\sin(2\pi(x-y)) + c.
\end{aligned}
\tag{4}
$$

Nevertheless, the realization of the model demonstrated a tendency to degeneration. This was caused by small shifts (approximately 0.04 pixels) of the brightness centroid coordinates during observation of one eclipse. As a consequence, some components in the model became correlated. In order to overcome this issue, each eclipse was considered separately, with the basis functions decomposed in Taylor series around zero and the dependent elements eliminated. The outcome of this process was the creation of a new model, which was subsequently employed in our research:

$$
\begin{aligned}
\mu(x,y) = {} & a_1\sin(2\pi\Delta x) + a_2 2\sin^2(\pi\Delta x) + b_1\sin(2\pi\Delta y) + b_2 2\sin^2(\pi\Delta y)\\
& + d_2\sin(2\pi\Delta x)\sin(2\pi\Delta y) + c.
\end{aligned}
\tag{5}
$$

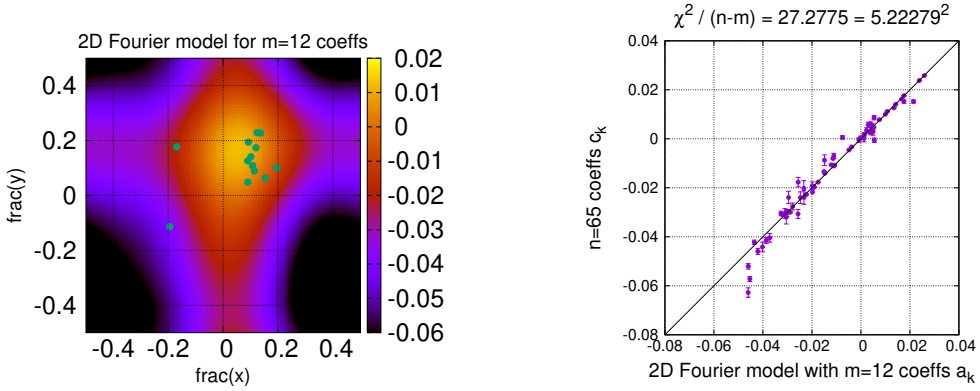

Fig. 1. Left: systematic error in fractions of the total flux as a function of the coordinates of the brightness center. Right: ratio between the 2D Fourier model and GP model coefficients.

It is also important to note that the use of approximation did not entirely remove the noise component from the data. Consequently, the model retained both red and white noise, and the kernel function became:

$$k = k_{\mathrm{WN}} + k_{\mathrm{RN}}. \tag{6}$$

Furthermore, it is necessary to consider the model of the eclipse constructed in conjunction with the noise. The planet in the model is spherical in shape and has a uniformly bright disk, which corresponds to the most basic model presented in Baluev & Shaidulin (2015). During the eclipse, the model planet moves uniformly and linearly with a certain impact parameter. In this study we did not utilize the transit data, which would have enabled us to accurately restore the characteristics of the planet. Instead, we relied on the parameters from another work (Bonomo et al. 2017) to determine the characteristics. We approximated two parameters only: the ratio of the planet's brightness to that of the star and the shift of the center of the eclipse compared to a model with zero eccentricity.

In order to account for long-period red noise, a third-order polynomial was employed. The noise parameters were considered individually for each eclipse, while the eclipse parameters were shared among all 13 eclipses.

4 Result

As a result, the next values were obtained: an eclipse center shift of 0.93 ± 3.10 min and a brightness ratio of $0.102 \pm 0.014\%$ for the first approach and -0.53 ± 0.61 min and $0.125 \pm 0.004\%$ for the second approach. These data are in agreement with the

results obtained by other authors (Evans et al. 2015). An important result is also the detection of two components of red noise in the first approach on time scales of 10 s and 5 min. In Evans et al. (2015) the red noise for different eclipses takes alternating values from one or the other of these scales. Also, the second approach allowed us to construct an overall pixel sensitivity map (Fig. 1). Although no noticeable deviations of the eclipse profile from the uniformly bright disc model could be detected (Fig. 2), the developed technique lays the foundation for more extensive work on processing the observed data from other planetary systems.

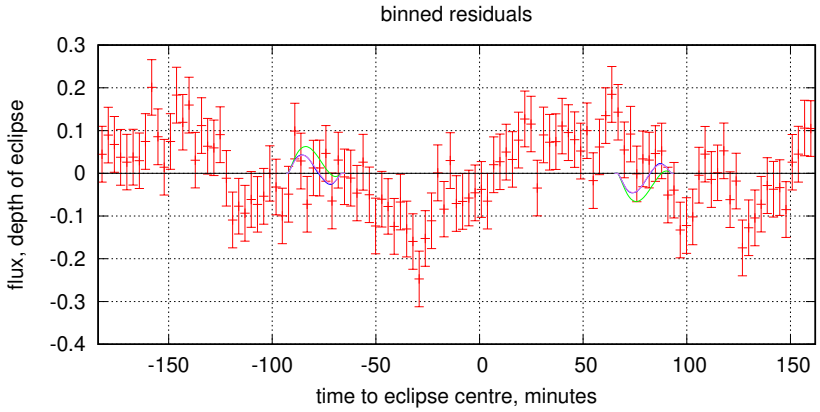

Fig. 2. Model residuals binned in 3-min intervals and the deviations due to brightness inhomogeneities from Rauscher & Menou (2013): black—uniform brightness, green—model 0 G, blue—model 3 G, violet—model 10 G.

References

Astropy Collaboration, Robitaille T.P., Tollerud E.J., et al., 2013, A&A, 558, id. A33
Baluev R.V., 2013, Astronomy and Computing, 2, p. 18
Baluev R.V., 2018, Astronomy and Computing, 25, p. 221
Baluev R.V. and Shaidulin V.S., 2015, MNRAS, 454, 4379
Baluev R.V., Sokov E.N., Shaidulin V.S., et al., 2015, MNRAS, 450, p. 3101
Bonomo A.S., Desidera S., Benatti S., et al., 2017, A&A, 602, id. A107
Bradley L., Sipőcz B., Robitaille T., et al., 2024, astropy/photutils: 1.13.0
de Wit J., Gillon M., Demory B.O., et al., 2012, A&A, 548, id. A128
Evans T.M., Aigrain S., Gibson N., et al., 2015, MNRAS, 451, p. 680
Fedotov A.A. and Baluev R.V., 2022, Astronomy at the Epoch of Multimessenger Studies, Proc. All-Russian Astron. Conf. (VAK-2021), p. 227
Knutson H.A., Charbonneau D., Allen L.E., et al., 2007, Nature, 447, p. 183
Majeau C., Agol E., Cowan N.B., 2012, ApJL, 757, id. L32
Rauscher E. and Menou K., 2013, ApJ, 764, p. 103

MODERN ASTRONOMY: FROM THE EARLY UNIVERSE TO EXOPLANETS AND BLACK HOLES

ExoClock: up-to-date ephemerides for the ARIEL mission

A. Garmash[1,2]

[1] M. A. Lavrentiev Lyceum, 10 Uchenykh St, Novosibirsk, 630068 Russia
[2] Budker Institue of Nuclear Physics, SB RAS, Novosibirsk, 630090 Russia

Abstract. Atmospheres of about 1000 exoplanets are going to be spectroscopically observed with ESA's future ARIEL mission. For the mission to be as efficient as possible, good preliminary knowledge of planet ephemerides is required before its launch, scheduled for 2029. To achieve this goal, the ExoClock project dedicated to continuous monitoring and updating the ephemerides of ARIEL candidates has been created. The project has been developed in a manner to make the best use of all available resources: observations reported in the literature, observations from space instruments, and, mainly, observations from ground-based telescopes, including both professional and amateur observatories. In this report we present our observations of exoplanet transits performed within the ExoClock project in 2022–2024.

Keywords: techniques: photometric; stars: planetary systems; astronomical databases: miscellaneous

DOI: 10.26119/VAK2024.131

1 Introduction

The next big step in exoplanet studies is going to be precise measurement of the chemical composition of their atmospheres. The first attempts made by the Hubble and Webb telescopes have demonstrated the feasibility of this goal (e.g., Madhusudhan et al. 2023; Bell et al. 2023). ESA's ARIEL (Atmospheric Remote-sensing Infrared Exoplanet Large-survey) mission (Tinetti et al. 2018, 2021) is specifically dedicated to study exoplanet atmospheres. It is scheduled to launch in 2029 and is expected to spectroscopically observe about 1000 exoplanets to study their atmospheres. To achieve this goal, thousands of transits will be observed within the lifetime of the mission. This large number underlines the necessity for precise predictions of the transit times in order to maximize the overall efficiency of the mission.

Just after the discovery, the time of the next transit for a planet is well known. However, the accuracy of predicted future transits degrades over time due to the increased number of epochs since the last observation and the stacking of the period error. In extreme cases this can mean that the transit time is practically lost, having the errors of several hours. In addition, in some cases one could expect the transit times to shift due to dynamical phenomena such as tidal orbital decay or apsidal precession due to the gravitational interactions with other yet undetected bodies in the system.

These issues can only be understood and mitigated through regular long-term observations and continuous refinement of the ephemerides. In this effort, small telescopes have been proven to be as efficient as the larger ones (Zallem et al. 2020). To provide up-to-date ephemerides for the upcoming ARIEL mission, the ExoClock project has been initiated by ESA in 2019 (Kokori et al. 2022). ExoClock is an open platform with the scope of verifying, prior to the launch of the mission, the ephemerides of the planets that are going to be observed by ARIEL. Data from all available resources, including observations from space missions and ground-based facilities both professional and amateur, are to be included in the ExoClock database. ExoClock aims at providing a continuously updated and homogeneous ephemeris service which can be valuable for general exoplanet research even beyond the ARIEL mission.

As of June 2024, 380 observers from all over the world have contributed to ExoClock by submitting over 8300 observations of transits for about 620 targets.

2 Instruments, data reduction, and photometry

Most of the transit observations reported in this paper were performed in Novosibirsk, Russia, using an 11-inch Celestron Schmidt-Cassegrain telescope with an ASI2600MM

camera. The filter type and exposure time for each target are given in Table 1. The `AstroImageJ` software (Collins et al. 2017) was used to process the images for the bias, dark current, and flat field corrections as well as to perform differential aperture photometry. In total, 23 transitions have been observed by the Novosibirsk group from October 2022 until July 2024. With the present equipment and average observing conditions, the seeing is usually at a level of 2″, as shown in Fig. 1a. The typical photometry accuracy for a single frame varies from 1.5 ppt for a star of $11^{\rm m}$ to 8 ppt for $14^{\rm m}$ with a 180 s exposure time, as shown in Fig. 1b.

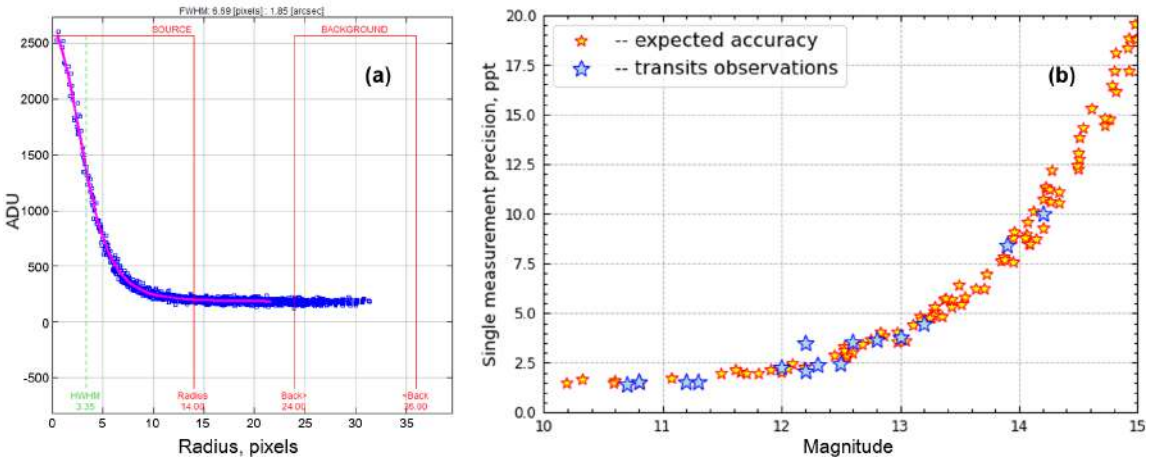

Fig. 1. (a) Typical point spread function for the present equipment and observing site. (b) The achieved standard deviation of the differential photometry measurements as a function of star magnitude with a 180 s exposer time.

3 Light curve fitting

While data reduction and photometry can be performed using tools preferred by an observer, it is of great importance to perform the final light curve modeling on the ExoClock web server to ensure maximum uniformity in the treatment of results obtained by different observers.

The final modeling of a transit is performed with the HOlomon Photometry Software package[1] (`HOPS`) specifically developed for the ExoClock project. The limb darkening coefficients (Claret et al. 2000) are calculated based on the stellar parameters (temperature, surface gravity, and metallicity) of the planet's host star as provided in

[1] https://github.com/ExoWorldsSpies/hops

Table 1. Summary of transit observations. See the ExoClock catalogue for more detail.

Target	Observing date	Filter	Exposure, s	O–C, min
HAT-P-29 b	2022-08-24	V	150	-0.62 ± 2.88
KOI-13 b	2022-08-27	V	30	-1.09 ± 2.16
HAT-P-8 b	2022-08-29	V	40	2.55 ± 1.31
WASP-3 b	2023-05-18	R	90	-1.43 ± 1.44
TrES-5 b	2023-08-01	R	200	-2.51 ± 1.58
WASP-92 b	2023-08-21	R	300	-1.87 ± 2.30
HAT-P-34 b	2023-08-29	R	60	4.52 ± 1.87
TOI-1333 b	2023-09-09	R	30	-11.66 ± 1.73
WASP-12 b	2023-10-13	R	240	-4.01 ± 1.11
WASP-52 b	2023-10-13	R	240	-1.08 ± 0.45
KELT-6 b	2024-03-18	R	120	-0.83 ± 2.16
HAT-P-12 b	2024-04-07	R	240	-0.27 ± 0.60
TOI-1842 b	2024-04-16	R	60	9.36 ± 2.74
HAT-P-27 b	2024-04-25	R	180	-1.21 ± 1.43
Qatar-10 b	2024-04-25	R	180	2.87 ± 1.31
WASP-135 b	2024-04-26	R	180	-1.79 ± 1.37
WASP-39 b	2024-04-27	R	180	0.97 ± 1.12
TOI-2154 b	2024-05-06	R	180	-3.30 ± 1.21
TOI-1431 b	2024-05-12	r'	40	0.06 ± 1.87
WASP-153 b	2024-05-13	r'	240	2.02 ± 3.46
TOI-3785 b	2024-05-15	i'	180	4.21 ± 2.02
TOI-3884 b	2024-05-16	i'	300	3.47 ± 1.30
WASP-2 b	2024-07-13	r'	180	-1.75 ± 0.65

the ExoClock catalogue[2] (ECC). During fitting, all the transit parameters except for the planet-to-star radius ratio and the transit mid-time are fixed to values from the ECC. Simultaneously with the transit model, a model for the out-of-transit effects, which are usually due to airmass variation, is applied.

An example of the fully processed data for the TOI-3884 b transit along with the model fit is shown in Fig. 2a. A similar anomaly in the photometry is apparent in the transit light curve for this target measured by TESS two years earlier, as shown in Fig. 2b. The anomaly is presumably due to a massive star spot located in a polar region of the M4 host star (Almenara et al. 2023; Libby-Roberts et al. 2023). TOI-3884 b is a super-Neptune planet that is considered as a high priority target for the study of planet atmospheres. This target is currently being monitored within the ExoClock project in an attempt to track the evolution of its transit light curve.

Besides the revision of the ephemerides, regular observation of the same target allows checking for a long-term variation of its orbital period. In some cases such

[2] ExoClock project data base: https://www.exoclock.space/database/planets

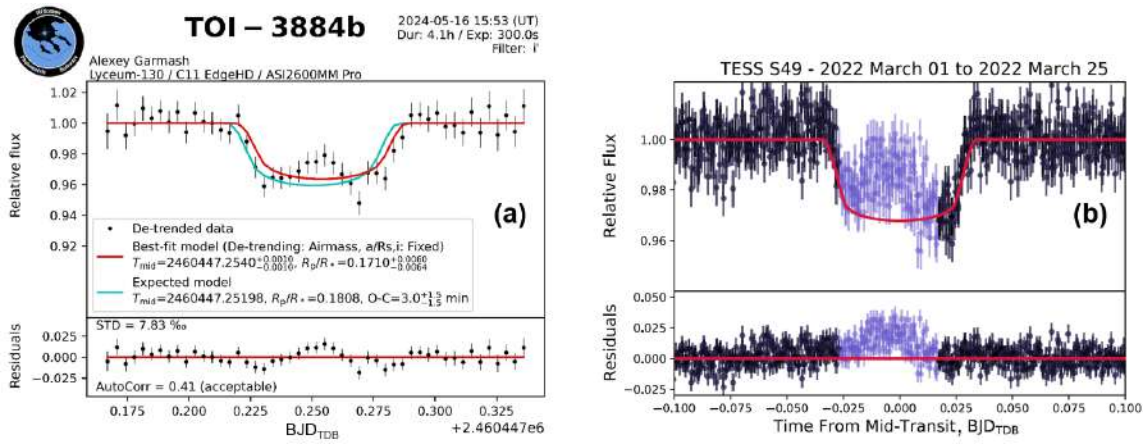

Fig. 2. (a) Example of a transit light curve measured by the Novosibirsk group for TOI-3884 b in 2024 and fitted using the `HOPS` package. (b) Transit light curve (Libby-Roberts et al. 2023) for the same target measured by TESS in 2022. A similar anomaly in the transit photometry is observed.

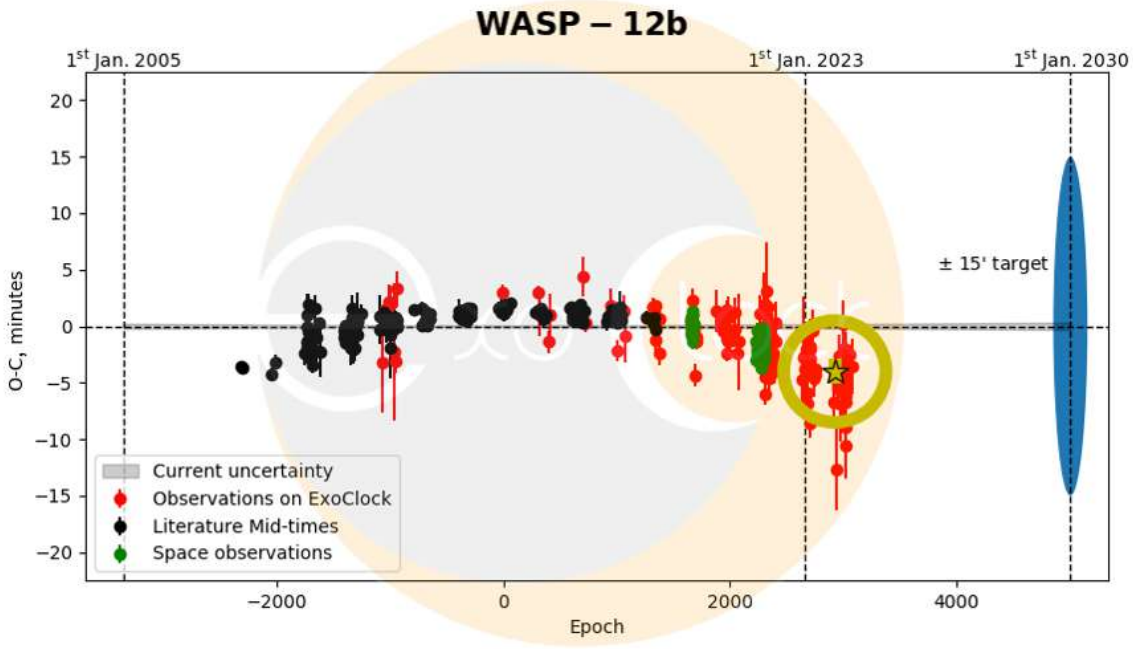

Fig. 3. O–C diagram for the exoplanet WASP-12 b from the ExoClock catalogue. The measurement from the Novosibirsk group is marked by a star symbol.

variations might indicate the presence of an additional body in the system. In the duration of the ExoClock program, 19 candidates with statistically significant transit timing variation (Kokori et al. 2023) were identified. An example of the O–C diagram (see www.exoclock.space/documents/The_OC_diagram.pdf for details) for a well known planet WASP-12 b is shown in Fig. 3. The effect was first discussed in 2019 and has been closely monitored since then by multiple ground-based telescopes as well as by the orbital TESS mission (e.g., Wong et al. 2022 and references therein). The cause of the observed variation is still under discussion with the preference given to orbit decay due to the interaction of WASP-12 b with its host star. With an orbital period of only 1.09 days and a semimajor axis of 0.023 au, there might be not only the strong tidal interaction but also mass exchange between the planet and its host star. WASP-12 b is the first and so far the only exoplanet that demonstrates the effect of orbital decay due to tidal interaction.

4 Summary

In this study we presented the transit observations of 23 exoplanets performed by the Novosibirsk group in 2022–2024 within the ExoClock project. The new measurements for transits mid-times are to be included in the upcoming ephemeris revision (Data Release D) of the ExoClock project (in preparation).

Acknowledgements. The observations were carried out at the M.A. Lavrentiev Lyceum Observatory, Novosibirsk. We are thankful for their support of the exoplanet program. AG is grateful to A. Vinokurova (BINP) for useful discussions and help in the preparation of this paper.

References

Almenara J.M., Bonfils X., Forveille T., et al., 2023, Astronomy and Astrophysics, 667, id. L11
Claret A., 2000, Astronomy and Astrophysics, 363, p. 1081
Collins K.A., Kielkopf J.F., Stassun K.G., et al., 2017, Astronomical Journal, 153, p. 77
Bell T.J., Welbanks L., Schlawin E., et al., 2023, Nature, 623, p. 709
Kokori A., Tsiaras A., Edwards B., et al., 2022, Experimental Astronomy, 53, p. 547
Kokori A., Tsiaras A., Edwards B., et al., 2023, Astrophysical Journal Supplement Series, 265, p. 4
Libby-Roberts J.E., Schutte M., Hebb L., et al., 2023, Astronomical Journal, 165, p. 249
Madhusudhan N., Sarkar S., Constantinou S., et al., 2023, Astrophysical Journal Letters, 956, id. L13
Tinetti G., Drossart P., Eccleston P., et al., 2018, Experimental Astronomy, 46, p. 135
Tinetti G., Eccleston P., Haswell C., et al., 2021, arXiv:2104.04824
Wong I., Shporer A., Vissapragada S., et al., 2022, Astronomical Journal, 163, p. 175
Zellem R.T., Pearson K.A., Blaser E., et al., 2020, Publications of the Astronomical Society of the Pacific, 132, id. 054401

BAK 2024 MODERN ASTRONOMY: FROM THE EARLY UNIVERSE TO EXOPLANETS AND BLACK HOLES 300 years Russian Academy of Sciences

Measurement of the metastable helium atomic rates important for astrophysical observations

M. Golubovsky[1,2], I. Shaikhislamov[1,3], and M. Rumenskikh[1,3]

[1] Institute of Laser Physics, SB RAS, Novosibirsk, 630090 Russia
[2] Novosibirsk State Technical University, 20 Prospekt K. Marksa, Novosibirsk, 630073 Russia
[3] Institute of Astronomy of the Russian Academy of Sciences, 48 Pyatnitskaya St., Moscow, 119017 Russia

Abstract. We present an experimental setup for measurement of the collisional rates relevant for the population of the triplet level of metastable helium. To estimate and verify the theoretical values, the absorption in helium plasma in the 1083 nm line will be measured. We are going to use plasma consisting of helium ions generated by θ-pinch, filling in a 6 m^3 volume of a vacuum chamber at concentrations of $1\,0^{12}$–10^{13} cm^{-3}. Based on the expected parameters, the optical depth $\tau = 1$ is going to be achieved with a path length $L = 1$ km. To increase the effective path length in the plasma, an optical scheme based on a concave resonator is proposed.

Keywords: atomic data; atomic processes; plasmas

DOI: 10.26119/VAK2024.132

1 Introduction

The metastable helium triplet line is widely used in astrophysics. This line has several advantages. For example, it can be detected with high quality using ground-based telescopes. The absorption in this line provides data to constrain the abundance of the second most widespread element in the Universe.

However, the constants of helium atomic processes have not been measured in experiments. They have been calculated theoretically in the framework of quantum mechanics. Thus, the experimental verification of the atomic rates remains an actual task. We propose measurement of relevant constants at the KI-1 plasma facility using θ-pinch to generate helium plasma filling in a 1.2×5 m vacuum chamber.

2 Numerical model

Before the experimental tests, the absorption should be calculated based on theoretical values. We used the kinetic model developed in a previous paper (Shaikhislamov et al. 2021). It allows for such processes as recombination, radiative decay, and transitions via collisions with electrons, hydrogen atoms, and protons. The parameters are the concentrations of ground-state helium atoms n_{He}, helium ions $n_{\mathrm{He^+}}$, hydrogen atoms n_{H} and molecules $n_{\mathrm{H_2}}$, electrons n_{e} and also the temperature. We take values close to the expected conditions in the plasma of the KI-1 facility: $n_{\mathrm{He}} = 10^{10}$ cm^{-3}, $n_{\mathrm{He^+}} = 10^{13}$ cm^{-3}, $n_{\mathrm{H}} = 10^{10}$ cm^{-3}, $n_{\mathrm{H_2}} = 10^{10}$ cm^{-3}, and $n_{\mathrm{e}} = 10^{13}$ cm^{-3}. The temperature is varied from 0.1 to 10 eV. The theoretical rates of the processes at $T = 10\,000$ K are shown in Table 1.

Table 1. Rates of different processes in the population model.

Reaction	Rate, cm^{-3} s^{-1}	Reference
$\mathrm{He}(2\,^3\mathrm{S}) + \mathrm{e} \rightarrow \mathrm{He}(2\,^1\mathrm{S})$	$1.86 \cdot 10^{-8}$	Bray et al. (2000)
$\mathrm{He}(2\,^3\mathrm{S}) + \mathrm{e} \rightarrow \mathrm{He}(2\,^1\mathrm{P})$	$4.26 \cdot 10^{-9}$	Bray et al. (2000)
$\mathrm{He}(2\,^3\mathrm{S}) + \mathrm{e} \rightarrow \mathrm{He}(3\,^3\mathrm{S})$	$7.6 \cdot 10^{-10}$	Bray et al. (2000)
$\mathrm{He}(2\,^3\mathrm{S}) + \mathrm{H} \rightarrow \mathrm{He} + \mathrm{H^+}$	$5 \cdot 10^{-10}$	Roberge & Dalgarno (1982)
$\mathrm{He}(2\,^3\mathrm{S}) + \mathrm{H_2} \rightarrow \mathrm{He} + \mathrm{H} + \mathrm{H^+}$	$5 \cdot 10^{-10}$	Roberge & Dalgarno (1982)
$\mathrm{He^+}(1\mathrm{S}) + \mathrm{e} \rightarrow \mathrm{He}(2\,^3\mathrm{S})$	$1.5 \cdot 10^{-13}$	Osterbrock & Ferland (2006)

To calculate the absorption, we use the Voigt profile taken at the maximum of the absorption cross-section $\sigma_{\max}$ and the calculated abundance $n_{\mathrm{He}(2\,^3\mathrm{S})}$ of the absorbing metastable helium state. A length of $L = 1$ km was taken as the reference length in the medium. The optical depth $\tau = n_{\mathrm{He}(2\,^3\mathrm{S})}\,\sigma_{\max}\,L$. The result of the calculations is

shown in Fig. 1. One can see that the optical depth reaches unity when temperature equals about 2.5 eV ($\approx 29\,000$ K). Thus, we have shown that a multipass scheme is required to observe the absorption experimentally.

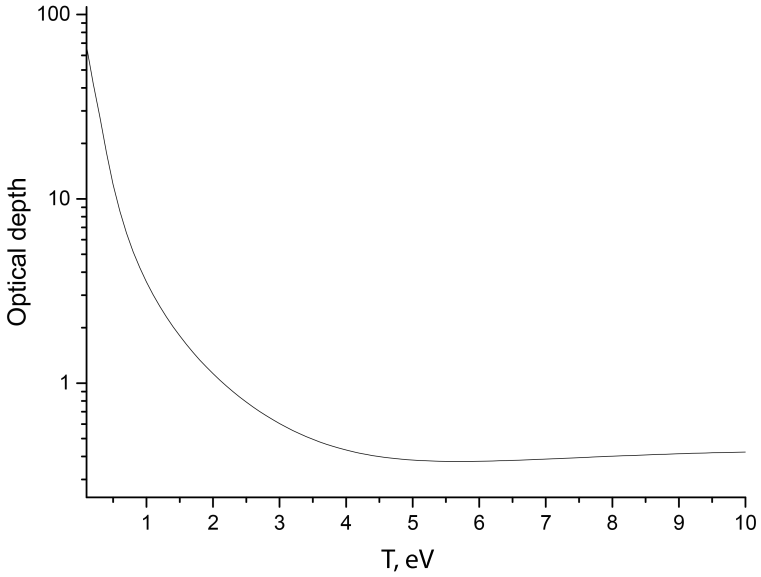

Fig. 1. The optical depth as a function of a temperature in eV units (1 eV $\approx$ 11 600 K)

3 Experimental setup

For experimental verification of theoretical rates, the plasma of the KI-1 facility θ-pinch will be used, and the measured absorption will be compared with that calculated by the model described above. We plan to add several new elements to the existing setup. First of all, it is a source of photons with wavelengths covering the range of the metastable helium line at 1083 nm. The light will be divided into two parts with a fiber-optic splitter. One part is delivered inside a concave high quality resonator with plasma which increases the effective length by more than hundred times. Another part travels outside the absorption medium in a fiber with an equivalent path length and is used for comparison and calibration. The absorption is detected after being spectrally resolved by a monochromator which resolution is less than 0.1 nm. The proposed scheme is shown in Fig. 2.

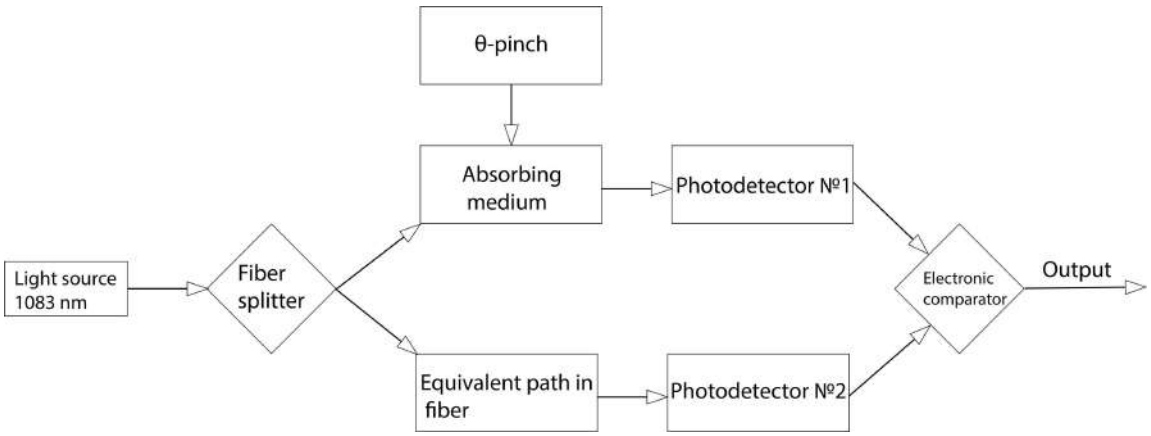

Fig. 2. Optical scheme of the experimental setup

4 Summary

We presented a proposal for experimental verification of the atomic rates related to the population and depopulation of the metastable helium triplet state which is responsible for the absorption in the 1083 nm line. For this purpose, numerical modeling was performed and the optical scheme of the experiment was developed.

Funding

This work was made in the framework of the ELAG section of the National Center for Physics and Mathematics.

References

Bray I., Burgess A., Fursa D.V., et al., 2000, Astronomy and Astrophysics Supplement Series, 146, p. 481

Osterbrock D.E. and Ferland G.J., 2006, Astrophysics Of Gas Nebulae and Active Galactic Nuclei, University Science Books

Roberge W. and Dalgarno A., 1982, Astrophysical Journal, 255, p. 489

Shaikhislamov I.F., Khodachenko M.L., Lammer H., et al., 2021, Monthly Notices of the Royal Astronomical Society, 500, p. 1404

MODERN ASTRONOMY: FROM THE EARLY UNIVERSE TO EXOPLANETS AND BLACK HOLES

Exotic red flares on stars as the observational manifestation of the asteroids in exoplanet systems

M. Ibrahimov

Institute of Astronomy of the Russian Academy of Sciences,
48 Pyatnitskaya Str., Moscow, 119017 Russia

Abstract. The published data on exotic red flares (RFs) obtained using optical/IR photometry was for the first time gathered and discussed in this paper. To date, the RFs have been observed: (a) in IR space missions (1–2 yr long IR brightening observed using WISE/NEOWISE and Spitzer in NGC 2547-ID8, HD 166191, WD 0145+234, and some others systems); (b) in five optical systems with the normal stars (UU CrB, AZ Ori, FF Ori, IX Oph, CU Cnc; three of the five systems are binaries; seven single flares were observed in 1980–2009 having a 1-hour average duration, an amplitude up to $2^{\rm m}$, and an energy up to 10^{39} erg); (c) in three optical/hi-energy systems with a compact object (V404 Cyg, MAXI J1820+070, Swift J1858.6−0814; all the systems are binaries hosting a black hole or a neutron star as a component; a "forest" of tens of flares was observed, the flares having a subsecond duration, an amplitude up to $1\overset{\rm m}{.}6$, and an energy of the order of 10^{36} erg/s); (d) in the near-IR range in the 2MASS stars (hundreds of flares were found based on the statistical study of more then 1300 2MASS M dwarfs). The RFs are suggested to be produced by a collisional impact and destruction of asteroid-like bodies in exosystems. All the above data independently supports an idea that exotic red flares are actually a real and well-distributed phenomenon. Undoubtedly, the RFs serve more deeper and wider investigation, keeping in mind their direct connection to the manifestation of asteroids in exosystems.

Keywords: stars: flare, planetary systems; minor planets, asteroids: general

DOI: 10.26119/VAK2024.133

1 Introduction

Protoplanetary and debris disks in exosystems are a natural laboratory to study terrestrial exoplanet formation processes. Such a study allows discovering a new exoworld population: exocomets and exoasteroids. The most comprehensive review on exocomets was made in Strøm et al. (2020). According to the review, four systems unambiguously demonstrate spectral and photometric features of exocomets, and 29 systems show possible exocomet evidence. For the first time, specific exocomet features were detected in the β Pic spectra (Ferlet et al. 1987). An analysis of about 1000 spectra of this system revealed about 6000 exocomet manifestations (Kiefer et al. 2014).

The Spitzer monitoring campaign to study solar-like stars with ages of 30–130 Myr and extreme debris disks revealed first exoasteroids. The aftermath of a collision of large (over 100 km in size) asteroid-like bodies observed in ID8 (2MASS J08090250−4858172) from NGC 2547 was reported in Meng et al. (2014). A detailed analysis of its IR variability allowed Su et al. (2018) to conclude about the presence of two impacts: on 2012 October 22 at a distance of 0.44 au and in early 2014 at a distance of 0.24 au (the corresponding orbital periods are 108 and 41.6 days, respectively). An analysis of 5-year (2012–2017) Spitzer observations of ID8 (together with P1121 from the M47 cluster) was made in Su et al. (2019). The long-scale Spitzer monitoring data for another two systems, V488 Per and HD 166191, were published in Rieke et al. (2021) and Su et al. (2022), respectively.

A close (less than 30 pc) white dwarf with a debris disk, WD 0145+234, was observed in 2010–2023 using three space observatories: WISE/NEOWISE, Spitzer, and JWST. Its significant and long-lasted IR brightening in 2018–2019 was detected in the WISE/NEOWISE data and interpreted as a tidal destruction of an exoasteroid in the disk of the dwarf (Wang et al. 2019). The follow-up observations of the white dwarf obtained using Spitzer and JWST support the exoasteroid breakup hypothesis (Swan et al. 2021, 2024).

To date, there are more than 5500 exoplanets, 33 systems with exocomets, and only 2–3 systems whose (space-based) IR variability is interpreted as exoasteroid manifestations. On the other side, it is expected that the small bodies in exosolar systems are much more populated and, correspondingly, more active. For example, $\sim$6000 exocomet manifestations per $\sim$1000 (ground-based) spectra were detected in β Pic (see above). If so, similar activity should be expected for the exoasteroids. A search for exoasteroid manifestations using archival ground-based observed data was undertaken and reported in this paper.

2 Red flares in the optical and near-IR bands: abundance and statistics

The main criterion to suspect exoasteroid traces in ground-based observations is a brightening or a flare in the near-IR or in the red part of the optical range. The data on such red flares (RFs) were published for five systems with the normal stars, three systems with the compact objects, and in a statistical study of flare activity for the 2MASS catalog stars.

RFs in the normal stars. Five systems hosting the normal stars have demonstrated (single) RFs. Chronologically, the RFs were observed in UU CrB (Olson 1980), AZ Ori (Mirzoyan et al. 1983; Melikian et al. 1984), FF Ori (Zakirov 1993, 1996), IX Oph (Ibrahimov 2019, 2020, 2022), and CU Cnc (Jiang & Qian 2011). Three of the five systems are binary: FF Ori and CU Cnc are eclipse binaries, and IX Oph is a spectral binary. A total of seven single flares were observed in the five systems (FF Ori and IX Oph showed two flares each, separated by about a 1 yr long interval). The first flare was observed in UU CrB in 1980, the last one in CU Cnc in 2009. All observations were obtained using 0.4–1.0 m aperture optical telescopes. The photographic pg(ubv) system was used to observe AZ Ori, the photoelectric five-color Stromgren–Crawford and Kron $uvby + I_{\rm K}$ system for UU CrB, the photoelectric Johnson $UBVR$ system for FF Ori and IX Oph, and the R-band CCD observations were made for CU Cnc (its 91-h CCD monitoring revealed four R flares, the largest one with a 73-min duration and a $0\overset{\rm m}{.}5$ amplitude was selected for the search).

The observed RFs in the normal stars have, on average, 1 h long duration (40 to 80 min), and the R-band amplitude varies from $0\overset{\rm m}{.}1$ (FF Ori) to almost $2^{\rm m}$ (IX Oph). The available multicolor observations for four systems (excluding CU Cnc) demonstrate a red maximum and an inverse amplitude distribution for the RFs (for details about the color and amplitude see the above references). The flare energy estimated for UU CrB, FF Ori, and IX Oph ranges from 10^{36} to 10^{39} erg. The available multicolor data for the RFs in UU CrB, AZ Ori, and IX Oph were transformed to the Johnson system and plotted in the $(U-B)-(B-V)$ color diagram (Fig. 1).

RFs in the systems with compact objects. Three systems hosting compact objects have demonstrated (multiple) RFs. Chronologically, the multiple RFs were observed in V404 Cyg (Gandhi et al. 2016), MAXI J1820+070 (Gandhi et al. 2018; Paice et al. 2019), and Swift J1858.6−0814 (Paice et al. 2018; Shahbaz et al. 2023). All the systems are binaries and host a black hole or a neutron star as a compact object. There are two differences between the RFs in the compact object systems (COSs) and in the normal star systems (NSSs). First, all RFs in the NSSs are single (one flare per one object per one observing season), while the COSs almost always

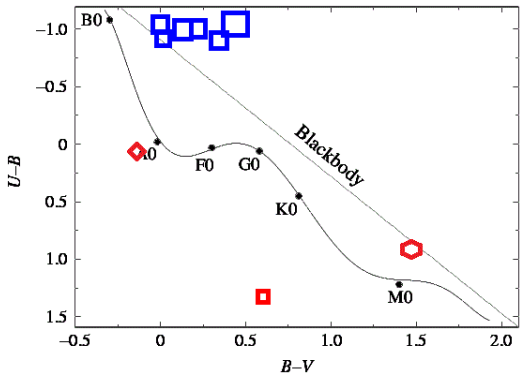

Fig. 1. Two-color diagram for three RFs observed in UU CrB (May 1980, red dimond), AZ Ori (Dec 1980, red hexagon), and IX Oph (Aug 1992, red square). The blue squares (taken from Gershberg 2015) designate flares of UV Cet-type stars.

demonstrate a "forest" of multiple RFs (tens of flares per one object per one observing run). Second, a typical duration of the RFs in the NSSs is about an hour, while the COSs have a subsecond typical duration of RFs. At the same time, the amplitude and energy for the RFs in the COSs and NSSs are comparable (an amplitude of $\sim 1\overset{\text{m}}{.}6$ for the Swift J1858.6−0814 most powerful flare and an energy of $\sim 10^{36}$ erg/s as estimated for the V404 Cyg flares).

For the first time, an important feature was observed (Fig. 2) in the optical curve morphology for the RFs in IX Oph (NSS, a flare on 1992 Aug 28) and in J1858.6−0814 (COS, a flare on 2018 Nov 09). Both RFs simultaneously exhibit a flare (brightening in the red band) and an antiflare (darkening in the blue part of the optical range). Such a phenomenon has not yet been reported for other types of flare systems. Generally, a comparison between the RFs in the NSSs and COSs looks as follows: a single hour-long powerful flare in the NSSs (the amplitude and energy up to 2^{m} and 10^{39} erg, respectively) versus a "forest" of multiple subsecond-long and equally powerful flares in the COSs (the amplitude and energy of the order of $1\overset{\text{m}}{.}6$ and 10^{36} erg/sec, respectively).

RFs in the statistical study for the 2MASS stars. A massive search for flares on low-mass stars using the SDSS and 2MASS catalogs and a multiwavelength and statistical analysis for the found flares were done in Davenport et al. (2012). So far, this study is unique due to its multiwavelength approach and representativeness among other studies on stellar flares from the UV to NIR ranges. Flare activity of $\sim$50 000 M dwarfs from the SDSS and 1321 M dwarfs from 2MASS has been studied. Hundreds of NIR flares were detected for the investigated M stars in 2MASS (details for the flare detection method and for the model used can be found in the original

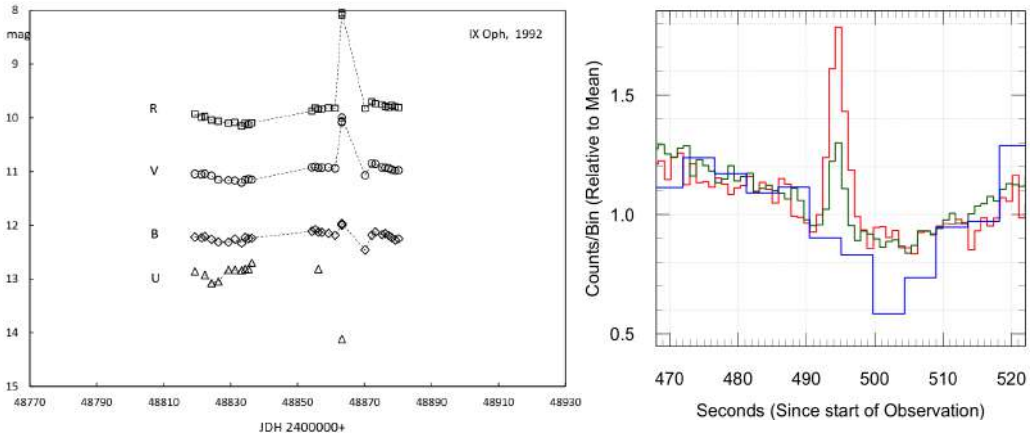

Fig. 2. Optical light curve morphology during the RFs in IX Oph (left panel, normal star system, 1992 Aug 28) and in J1858.6−0814 (right panel, compact object system, 2018 Nov 09 00:30:00 UT). Both curves demonstrate the simultaneous presence of a flare (brightening in the red band) and an antiflare (darkening in the blue part of the optical range).

paper). The averaged statistical data for all (optical and NIR) detected flares are listed in Table 2 and plotted in Fig. 6 in the paper. However, a comparison between the optical and NIR flares led to a strange result (a citation from paragraph 6, p. 67): "No simulated flares ... showed enough increase in flux to register ... a response in the JHK bands, however. The flare emission in the NIR must therefore be greatly influenced by physics not included in our ... model." It is supposed that the required physics could be found to explain the above result if one considers that a source for the 2MASS NIR flares is not the stellar but circumstellar matter (exoasteroids, etc.)

3 Summary

A search for exoasteroid manifestations using archival ground-based observed data was undertaken and reported in this paper. It was proposed that exoasteroids could be detected as exotic red flares (RFs). For the first time, the published data on the RFs obtained using optical/IR photometry was gathered and discussed. The RFs are suggested to be produced by a collision and destruction of asteroid-like bodies in exosystems. To date, the RFs have been observed:

(a) in IR space missions (1–2 yr long IR brightening observed using WISE/ NEOWISE and Spitzer in NGC 2547 ID-8, HD 166191, WD 0145+234, and some others systems);

(b) in five optical systems with the normal stars (UU CrB, AZ Ori, FF Ori, IX Oph, CU Cnc; three of the five systems are binaries; seven single flares were observed

in 1980–2009 having a 1 h average duration, an amplitude up to 2^{m}, and an energy up to 10^{39} erg);

(c) in three optical/hi-energy systems with a compact object (V404 Cyg, MAXI J1820+070, Swift J1858.6−0814; all systems are binaries hosting a black hole or a neutron star as a component; a "forest" of tens flares was observed, the flares having a subsecond duration, an amplitude up to $1\overset{m}{.}6$, and an energy of the order of 10^{36} erg/s);

(d) in the near-IR range in the 2MASS stars (hundreds of flares were found based on the statistical study of more then 1300 2MASS M dwarfs).

All the above data independently supports an idea that exotic red flares are actually a real and well-distributed phenomenon. Undoubtedly, the RFs serve more deeper and wider investigation, keeping in mind their direct connection to the manifestation of asteroids in exosystems.

References

Davenport J.R.A., Becker A.C., Kowalski A.F., et al. 2012, ApJ, 748, p. 58
Ferlet R., Hobbs L.M., Vidal-Madjar A.V., 1987, A&A, 185, p. 267
Gandhi P., Littlefair S.P., Hardy L.K., et al., 2016, MNRAS, 459, p. 554
Gandhi P., Paice J.A., Littlefair S.P., et al., 2018, Astronomer's Telegram, 11437
Gershberg R.E., 2015, Activity of solar-type main-sequence stars, Antikva, Simferopol
Ibrahimov M.A., 2019, INASAN Science Reports, 4, p. 199
Ibrahimov M.A., 2020, Ground-Based Astronomy in Russia. 21st Century, Proc. All-Russian Conf., ed. I.I. Romanyuk, I.A. Yakunin, A.F. Valeev, D.O. Kudryavtsev, p. 288
Ibrahimov M.A., 2022, Astronomy at the Epoch of Multimessenger Studies, Proc. All-Russian Astron. Conf. (VAK-2021), ed. A.M. Cherepashchuk et al., p. 233
Jiang L.Q. and Qian S.B., 2011, ASP Conference Series, 451, p. 163
Kiefer F., Lecavelier des Etangs A., Boissier J., et al., 2014, Nature, 514, 7523, p. 462
Melikian N.D., Chavushian H.S., Natsvlishvili R.Sh., et al., 1984, IBVS, 2622
Meng H.Y.A., Su K.Y.L., Rieke G.H., et al., 2014, Science, 345, p. 1032
Mirzoyan L.V., Chavushyan O.S., Melikyan N.D., et al., 1983, Astrophysics, 19, p. 411
Olson E.C., 1980, IBVS, 1825
Paice J.A., Gandhi P., Dhillon V.S., et al., 2018, Astronomer's Telegram, 12197
Paice J.A., Gandhi P., Shahbaz T., et al., 2019, MNRAS, 490, p. L62
Rieke G.H., Su K.Y.L., Melis C., et al., 2021, ApJ, 918, p. 71
Shahbaz T., Paice J.A., Rajwade K.M., et al., 2023, MNRAS, 520, p. 542
Strøm P.A., Bodewits D., Knight M.M., et al., 2020, PASP, 132, id. 101001
Su K.Y.L., Jackson A.P., Dong R., et al., 2018, LPI Contributions, 2107, id. 2025
Su K.Y.L., Jackson A.P., Gáspár A., et al., 2019, AJ, 157, p. 202
Su K.Y.L., Kennedy G.M., Schlawin E., et al., 2022, ApJ, 927, p. 135
Swan A., Farihi J., Su K.Y.L., et al., 2024, MNRAS, 529, p. L41
Swan A., Kenyon S.J., Farihi J., et al., 2021, MNRAS, 506, p. 432
Wang T.-G., Jiang N., Ge J., et al., 2019, ApJ Lett., 886, id. L5
Zakirov M.M., 1993, IBVS, 3925
Zakirov M.M., 1996, Astronomy Letters, 22, p. 593

MODERN ASTRONOMY: FROM THE EARLY UNIVERSE TO EXOPLANETS AND BLACK HOLES

Migration of planetesimals and dust particles in the Proxima Centauri exoplanetary system

S. Ipatov

Vernadsky Institute of Geochemistry and Analytical Chemistry of the Russian Academy of Sciences, Moscow, 119991 Russia

Abstract. The motion of the planetesimals and dust particles from the vicinity of the orbit of planet c in the Proxima Centauri exoplanetary system was studied. The computer simulations of planetesimal motion showed that during the growth of the mass of planet c by a factor of 2, the semimajor axis of its orbit could decrease by at least a factor of 1.5. After hundreds of millions of years, some planetesimals could still move in elliptical resonant orbits inside the feeding zone of planet c that had been mainly cleared from planetesimals. The amount of water delivered to the inner planet Proxima Centauri b probably exceeded the mass of water in Earth's oceans. It is difficult to expect the existence of such a massive analogue of the Oort cloud around Proxima Centauri as around the Sun. The probability of the collisions of the dust particles with a diameter of about 100 microns migrated from the feeding zone of planet c with planet b could exceed 0.1, and it could be much greater than for the planetesimals from the same zone. More particles with diameters of the order of 10 and 100 microns can be delivered from the feeding zone of planet c to planet b than to planet c.

Keywords: gravitation; methods: numerical; celestial mechanics; planets and satellites: formation

DOI: 10.26119/VAK2024.134

1 Introduction and initial data

The motion of the planetesimals and dust particles from the vicinity of the orbit of planet c in the Proxima Centauri exoplanetary system was studied in Ipatov (2021, 2023a,b,c,d). The Proxima Centauri planetary system consists of the star (with a mass equal to 0.122 of the solar mass) and of three exoplanets. The calculations of planetesimal motion took into account the gravitational influence of the star and two planets: b ($a_{\rm b} = 0.04857$ AU, $e_{\rm b} = 0.11$, $m_{\rm b} = 1.17\ m_{\rm E}$, where $m_{\rm E}$ is the mass of the Earth) and c ($a_{\rm c} = 1.489$ AU, $e_{\rm c} = 0.04$, $m_{\rm c} = 7\ m_{\rm E}$). Other values for the mass $m_{\rm c}$ of planet c (0.7, 3.5, and 12 $m_{\rm E}$) were also considered. The late gasless stage of planet formation was studied. Planetesimals were excluded from the integration when they collided with the star or planets or reached 1200 AU from the star (the Hill radius). In each variant of the calculations, the initial values $a_\circ$ for the semimajor axes of the orbits of $N_{\rm p} = 250$ planetesimals or dust particles varied from $a_{\rm min}$ to $a_{\rm max} = a_{\rm min} + 0.1$ AU. For planetesimals, the considered values of $a_{\rm min}$ varied from 0.9 to 2.2 AU with a step $d_a = 0.1$ AU. The initial eccentricities of planetesimal orbits were equal to $e_{\rm o} = 0.02$ or $e_{\rm o} = 0.15$, and their initial inclinations were equal to $e_{\rm o}/2$ rad. Greater eccentricities could be caused by the previous mutual gravitational influence of planetesimals (Ipatov 1993, 2000). For dust particles, a_{min} was equal to 1.4 or 1.5 AU, and $e_{\rm o} = 0.02$. Schwarzet al. (2018) studied the motion of exocomets with initial eccentricities between 0.95 and 0.9999 considering the orbit of Proxima Centauri c with a semimajor axis $a_{\rm c}$ from 0.06 up to 0.3 AU.

To integrate the equations of motion for planetesimals, the symplectic algorithm RMVS3 from the SWIFT integration package of Levison & Duncan (1994) was used. Calculations with an integration step $t_s = 0.2$, 0.5, 1, or 2 Earth days gave similar results. In most calculations, the integration time step t_s was equal to 1 day. The considered time interval usually exceeded 100 Myr. For some variants it reached 1000 Myr. In each variant, the calculations were made for fixed values of $a_{\rm min}$, e_o, and t_s. The planetesimals with planet d ($a_{\rm d} = 0.02895$ AU, $m_{\rm d} = 0.29\ m_{\rm E}$, $e_{\rm d} = i_{\rm d} = 0$) were calculated based on the arrays of orbits of migrating planetesimals and planets similar to Ipatov (2000, 2019).

2 Calculation results

2.1 The feeding zone of Proxima Centauri c

The calculations showed that after hundreds of million years, some planetesimals could still move in elliptical orbits inside the feeding zone of planet c that had been mainly cleared from planetesimals. The initial semimajor axes for the planetesimals

that still had elliptical orbits at the end of the considered evolution were presented in Ipatov (2023c). The range ($a_{\rm min,e}$, $a_{\rm max,e}$) of the initial semimajor axes $a_{\rm o}$ of the orbits for which planetesimals were mainly ejected into hyperbolic orbits or collided with planets was about $a_{\rm min,e} = a_{\rm c}(1 - e_{\rm c}) - e_{\rm o}a_{\rm min,e} - k_{\rm min}a_{\rm c}\mu^{1/3}$ and $a_{\rm max,e} = a_{\rm c}(1 + e_{\rm c}) + e_{\rm o}a_{\rm max,e} + k_{\rm max}a_{\rm c}\mu^{1/3}$, where $k_{\rm min} = 2.54$ and $k_{\rm max} = 2.40$ at $e_{\rm o} = 0.02$, $k_{\rm min} = 2.23$ and $k_{\rm max} = 4.3$ at $e_{\rm o} = 0.15$, $a_{\rm c}$ and $e_{\rm c} = 0.04$ are the semimajor axis and eccentricity of the planet c orbit, and μ is the ratio of the mass of planet c to the star mass. Often after hundreds of millions of years, the remaining planetesimals could move inside the feeding zone in some resonances with the planet, e.g., in the resonances 1:1 (as the Jupiter trojans), 5:4, and 3:4. The number of such remaining planetesimals was greater at small eccentricities. Examples of the evolution of the semimajor axis, perihelion, and aphelion of the orbit of a planetesimal moving in such resonances are presented in Ipatov (2023c). Some planetesimals had been moving for a long time in resonances even if before getting in these resonances they moved in nonresonant orbits. For some (typically resonant) subregions of $a_{\rm o}$ located outside the main feeding zone of planet c, planetesimals could be ejected into hyperbolic orbits or could collide with planets.

There can be more analogues of the asteroid and trans-Neptunian belts in the planetary system near Proxima Centauri than in the Solar System. The smaller ratio of the mass of the planet Proxima Centauri c to the mass of the star than that for Jupiter, the larger ratio of the semimajor axes of the orbits of planets c and b than that for Jupiter and Mars, and only one large planet in the Proxima Centauri system can be the reasons for such possible differences in the belts and the possible existence of a planet(s) between the orbits of planets Proxima Centauri b and c.

2.2 Probabilities of the collisions of planetesimals with the exoplanet Proxima Centauri c and of their ejection into hyperbolic orbits

At evolution times $T = 1$, 10, and 100 Myr, the fraction $p_{\rm el}$ of the initial planetesimals remaining in elliptical orbits was presented in Ipatov (2023a). At $T = 100$ Myr, the $p_{\rm el}$ value was not more than 0.06 at $1.2 \le a_{\rm o} \le 1.7$ AU and $2.0 \le a_{\rm o} \le 2.1$ AU, not more than 0.3 at $1.1 \le a_{\rm o} \le 1.2$ AU, not more than 0.2 at $1.7 \le a_{\rm o} \le 1.9$ AU, and not more than 0.1 at $2.1 \le a_{\rm o} \le 2.2$ AU for $e_{\rm o} = 0.15$. It was not more than 0.25 at $1.2 \le a_{\rm o} \le 1.8$ AU for $e_{\rm o} = 0.02$. The calculations showed that the probability $p_{\rm c}$ of a collision of a planetesimal during its dynamical lifetime with planet c was about 0.5 for $e_{\rm o} = 0.02$ and 0.25–0.3 for $e_{\rm o} = 0.15$ if the initial orbits of the planetesimals were not far from the orbit of planet c with a semimajor axis equal to 1.5 AU. The $p_{\rm c}$ value was 0.05 at $1.1 \le a_{\rm o} \le 1.2$ AU, 0.4–0.55 at $1.2 \le a_{\rm o} \le 1.7$ AU, 0.3 at $1.7 \le a_{\rm o} \le 1.8$ AU, and 0.02 at $1.8 \le a_{\rm o} \le 1.9$ AU for $e_{\rm o} = 0.02$. For $e_{\rm o} = 0.15$, this

probability $p_{\rm c}$ was about 0.15 at $1.0 \leq a_{\rm o} \leq 1.1$ AU, 0.3 at $1.1 \leq a_{\rm o} \leq 1.9$ AU, and 0.04–0.05 at $2.0 \leq a_o \leq 2.2$ AU. Most collisions of planetesimals with planet c took place during the first 10 Myr.

2.3 Estimates of the total initial mass of planetesimals in the feeding zone of Proxima Centauri c

Based on the results of calculations, Ipatov (2023a) concluded that the ratio $p_{\rm c,ej} = p_{\rm c}/p_{\rm ej}$ of the probability $p_{\rm c}$ of a collision of a planetesimal with planet c to the probability $p_{\rm ej}$ of its ejection into a hyperbolic orbit was about 0.8–1.3 and 0.4–0.6 at $e_{\rm o} = 0.02$ and $e_{\rm o} = 0.15$, respectively. This ratio was about 1.3–1.5 and 0.5–0.6 in the calculations with the mass of planet c equal to half of its present mass. The mass of planet c is 7 $m_{\rm E}$. Therefore, the total mass of the planetesimals ejected into hyperbolic orbits could be about 3.5–7 $m_{\rm E}$. The total mass of the planetesimals in the feeding zone of planet c could exceed 10 $m_{\rm E}$ and 15 $m_{\rm E}$ at $e_{\rm o} = 0.2$ and $e_{\rm o} = 0.15$, respectively. Based on the $p_{\rm ej}$ values and on the integral of energy, it is possible to conclude that the semimajor axis of the orbit of planet c could decrease by a factor not less than 1.5 during the accumulation of this planet.

2.4 Motion of planetesimals to the inner planets Proxima Centauri b and d

Only one of several hundred planetesimals which migrated from the feeding zone of Proxima Centauri c reached the orbits of Proxima Centauri b and d. Ipatov (2023a) showed that the probability of a collision of a planetesimal initially located in the feeding zone of planet c with planet b was about $2 \cdot 10^{-4}$ and 10^{-3} at $e_{\rm o}$ equal to 0.02 or 0.15, respectively. The above probability values were greater than the probability of a collision with Earth of a planetesimal migrated from the zone of the giant planets in the Solar System. The latter probability (per one planetesimal) was typically less than 10^{-5} (Marov & Ipatov 2023). Depending on the initial eccentricities of planetesimals (such variation correspond to the possible mutual gravitational influence of planetesimals), the total mass $m_{\rm c-b}$ of the material delivered from the feeding zone of planet c to planet b was estimated to be in the range from 0.002 $m_{\rm E}$ to 0.02 $m_{\rm E}$. The temperature of planet c is considered to be much below zero, and the feeding zone of planet c was located farther from the star than the snow line. At fraction $k_{\rm ice}$ of the ice in the planetesimals between 0.05 and 0.5, the values of $m_{\rm ice} = k_{\rm ice} m_{\rm c-b}$ are between 10^{-4} $m_{\rm E}$ and 0.01 $m_{\rm E}$. Probably, the amount of water delivered to Proxima Centauri b exceeded the mass of water in Earth's oceans, which is $2 \cdot 10^{-4}$ $m_{\rm E}$. Planet d was not included in the integrations, but the probability of the collisions of

planetesimals with planet d was calculated based on the arrays of orbital elements of migrated planetesimals. The amount of material delivered from the feeding zone of planet c to planet d could be about twice less than that delivered to planet b. A lot of icy material and volatiles could be delivered to planets b and d.

2.5 Motion of planetesimals in the outer part of the Hill sphere of the star Proxima Centauri

For the present mass of the planet Proxima Centauri c, about 90% of ejected planetesimals moved from 500 to 1200 AU in less than 1 Myr, and not more than 1% of planetesimals had been moving in this region for more than 10 Myr but during less than a few tens of millions of years (Ipatov 2023d). For the mass of the planet embryo equal to half of the mass of planet c, the fraction of planetesimals moved from 500 to 1200 AU in less than 1 Myr was about 70–80%. The inclinations of orbits for 80% of the planetesimals that moved between 500 and 1200 AU from the star did not exceed 10°. The strongly inclined orbits of the bodies in the outer part of the Proxima Centauri Hill sphere can be mainly due to the bodies that came into the Hill sphere from outside. The radius of the Hill sphere of the star Proxima Centauri is by an order of magnitude smaller than the radius of the outer boundary of the Hills cloud in the Solar System and is two orders of magnitude smaller than the Hill radius of the Sun. Therefore, it is difficult to expect the existence of such a massive analogue of the Oort cloud near this star as near the Sun. The consideration of the gravitational influence of the binary star system α Centauri AB would not change the above conclusions because the motion of planetesimals was considered inside (mainly deep inside) the Hill spere of Proxima Centaury and the ejected planetesimals had very small chances to return into the sphere.

2.6 Migration of dust particles in the Proxima Centauri system

The migration of dust particles in the Proxima Centauri system was studied in Ipatov (2023b) similarly to the calculations for the Solar System (Ipatov 2010). The Bulirsh–Stoer code was used for integrations. The relative error per integration step was taken to be less than 10^{-8}. The gravitational influence of the star and two planets (b and c), the Poynting–Robertson drag, radiation pressure, and star wind drag were taken into account. The particles were excluded from the integration when they collided with the star or the planets or reached 500 AU from the star. Similarly to the Solar System, the ratio of the star wind drag to the Poynting–Robertson drag was considered to be 0.35. In different variants, the ratio β of the radiation pressure force to the gravitational force varied from 0.0002 to 1. For silicate particles

in the Solar System, such β values correspond to particle diameters d from 2000 to 0.4 microns; and d is proportional to $1/\beta$. For water ice at a density equal to 1 g/cm^3, d is greater by a factor of 2.4 than for silicate particles. Although the initial orbits of dust particles were close to the orbit of planet c, and planet c is more massive than planet b, at $0.001 \leq \beta \leq 0.1$ more particles collided with the inner planet b than with the larger planet c. In the Solar System, silicate particles with $0.001 \leq \beta \leq 0.1$ correspond to diameters from 4 to 400 microns. At such β values, dust particles effectively deliver matter (including volatiles) to planet b. The probabilities of the collisions of particles with planet b for $e_o = 0.02$ were about 0.15–0.2, 0.1, 0.06–0.08, and 0.016–0.03 at $0.001 \leq \beta \leq 0.004$, $\beta = 0.01$, $\beta = 0.02$, and $0.04 \leq \beta \leq 0.1$, respectively. For $e_o = 0.15$, the probabilities were about 0.07–0.15, 0.04, and 0.01–0.03 for $0.001 \leq \beta \leq 0.01$ (diameters of the particles about 100 microns), $\beta = 0.02$, and $0.04 \leq \beta \leq 0.1$, respectively. The probabilities of the collisions of particles with planet c for $e_o = 0.02$ were about 0.016–0.05, 0.02, and 0.01–0.02 for $0.001 \leq \beta \leq 0.004$, $\beta = 0.01$, and $0.02 \leq \beta \leq 0.1$, respectively. For $e_o = 0.15$, the probabilities did not exceed 0.03 for all considered variants. At $\beta \geq 0.4$, most particles were ejected into hyperbolic orbits. For $0.004 \leq \beta \leq 0.2$, most particles collided with the star with the maximum collision probability at $\beta = 0.04$. The evolution times of the dust disks under consideration were generally shorter for larger β. They were 300 years at β=1 and several million years at $0.004 \leq \beta \leq 0.04$.

Funding

The studies were carried out under the state contract of the Vernadsky Institute of Geochemistry and Analytical Chemistry of the Russian Academy of Sciences.

References

Ipatov S.I., 1993, Solar System Research, 27, 1, p. 65
Ipatov S.I., 2000, Migration of celestial bodies in the Solar System, Editorial URSS, Moscow
Ipatov S.I., 2010, IAU Symposium, 263, p. 41
Ipatov S.I., 2019, Solar System Research, 53, 5, p. 332
Ipatov S.I., 2021, Bulletin of the American Astronomical Society, 53, 3, id. 2021n3i1126
Ipatov S.I., 2023a, Meteoritics and Planetary Science, 58, 6, p. 752
Ipatov S.I., 2023b, Meteoritics and Planetary Science, 58, S1, p. A131
Ipatov S.I., 2023c, Solar System Research, 57, 3, p. 236
Ipatov S.I., 2023d, Solar System Research, 57, 6, p. 612
Levison H.F. and Duncan M.J., 1994, Icarus, 108, p. 18
Marov M.Ya. and Ipatov S.I., 2023, Physics–Uspekhi, 66, 1, p. 2
Schwarz R., Bazso A., Georgakarakos N., et al., 2018, Monhly Notices of the Royal Astronomical Society, 480, p. 3595

MODERN ASTRONOMY: FROM THE EARLY UNIVERSE TO EXOPLANETS AND BLACK HOLES

Migration of planetesimals in the TRAPPIST-1 exoplanetary system

S. Ipatov

Vernadsky Institute of Geochemistry and Analytical Chemistry of the Russian Academy of Sciences, Moscow, 119991 Russia

Abstract. The calculations of the motion of planetesimals at the late stages of accumulation of planets in the TRAPPIST-1 system were made. In each calculation variant, initial orbits of planetesimals were near one of the planets. The number of collisions of planetesimals with the planets were calculated. The calculations has shown that the outer layers of neighboring exoplanets in the TRAPPIST-1 system can include similar material if there were a lot of planetesimals near their orbits at the late stages of the accumulation of the exoplanets.

Keywords: gravitation; methods: numerical; celestial mechanics; planets and satellites: formation

DOI: 10.26119/VAK2024.135

1 Introduction and initial data

The aim of the calculations presented below was to study the mixing of planetesimals at the late gasless stages of accumulation of planets in the TRAPPIST-1 system. The TRAPPIST-1 exoplanet system consists of a star with a mass equal to 0.09 solar masses and seven planets (from b to h depending on the distance from the star) with masses from 0.33 to 1.37 Earth masses. The semimajor axes of the orbits of these planets range from 0.012 to 0.062 AU. The orbital elements and masses of the planets are presented in Table 1. The motion of planetesimals under the gravitational influence of the star and the seven planets of TRAPPIST-1 was studied. In each variant of the calculations, the initial values of the semimajor axes of the orbits of $N_\mathrm{p} = 250$ or $N_\mathrm{p} = 1000$ planetesimals varied from a_min to a_max around the semimajor axis of the orbit of one of the planets, the initial eccentricities of their orbits were equal to $e_\mathrm{o} = 0.02$ or $e_\mathrm{o} = 0.15$, and their initial inclinations were equal to $e_\mathrm{o}/2$ rad. The values of a_min and a_max are presented in Table 1. Calculations were also carried out at $a_\mathrm{min} = 0.07$ AU. In these calculations, $a_\mathrm{max} = 0.1$ AU at $N_\mathrm{p} = 250$ and $a_\mathrm{max} = 0.09$ AU at $N_\mathrm{p} = 1000$. Greater eccentricities could be caused by the previous mutual gravitational influence of planetesimals. To integrate the equations of motion, the symplectic algorithm RMVS3 from the SWIFT package of Levison & Duncan (1994) was used. Calculations with an integration step t_s equal to 0.01, 0.02, 0.04, or 0.1 Earth days gave similar results. In each variant, the calculations were made for the same disk and for fixed values of e_o and t_s. The planetesimals that collided with planets or the star or were ejected into hyperbolic orbits (reaching 50 AU from the star) were excluded from the integration. The considered model of mixing bodies in the zone of the TRAPPIST-1 planets can also characterize the migration of the bodies ejected from some planets after collisions of these planets with some planetesimals or other bodies. Earlier, the migration of planetesimals in our Solar System was studied, e.g., by Ipatov (1993, 2019); Marov & Ipatov (2023), and the migration of planetesimals in the Proxima Centauri exoplanetary system was studied by Ipatov (2023a,b,c).

2 Results of calculations

The calculation results showed that no more than 3% of planetesimals were thrown into hyperbolic orbits. There were no collisions of planetesimals with the parent star in the considered calculation options. More than a half of the planetesimals from the disks originally located near the orbits of planets b to g collided with the planets in less than 1000 years, and from disks b to d even in 250 years. The planetesimals with dynamic lifetimes of more than 100 thousand years were usually

Table 1. Orbital elements, masses m (in Earth masses $m_{\rm E}$) of exoplanets in the TRAPPIST-1 system, and the values of $a_{\rm min}$ and $a_{\rm max}$ for the considered disks near planets b, c, d, e, f, g, and h.

Planets	$m/m_{\rm E}$	a, AU	e	$a_{\rm min}$, AU	$a_{\rm max}$, AU
b	1.37	0.0115	0.0062	0.0094	0.0137
c	1.31	0.0158	0.0065	0.0137	0.0190
d	0.39	0.0223	0.0084	0.0190	0.0258
e	0.69	0.0292	0.0051	0.0258	0.0339
f	1.04	0.0385	0.0101	0.0339	0.0427
g	1.32	0.0468	0.0021	0.0427	0.0544
h	0.33	0.0619	0.0057	0.0544	0.0694

ejected into hyperbolic orbits or collided with planet h. The times of evolution of disks for planets b–h varied from 12 thousand to more than 60 million years. In the variants with a large time of the evolution of a disk, most of the total time could be due to the last planetesimal, which often was ejected into a hyperbolic orbit.

The fraction of planetesimals that collided with a host planet (compared to collisions with all planets) generally decreased with increasing time intervals. This fraction was usually smaller for the disks located farther from the star. At $N_{\rm p} = 1000$ for disks c–h, the fraction f_1 of planetesimals that collided with the host planet was between 0.37 and 0.63 at $e_{\rm o} = 0.02$ and between 0.27 and 0.53 at $e_{\rm o} = 0.15$. The second and third values (f_2 and f_3) of the fraction of planetesimals (among all initial planetesimals) that collided with a neighboring planet were in the ranges of 0.17–0.28 and 0.11–0.17 at $e_{\rm o} = 0.02$ and 0.2–0.32 and 0.08–0.19 at $e_{\rm o} = 0.15$. For disk b and $e_{\rm o} = 0.02$, the fractions f_1, f_2, and f_3 were 0.78–0.8, 0.18–0.2, and 0.01–0.012, respectively, (the range is for calculations with a step t_s equal to 0.01 and 0.02). For disk b and $e_{\rm o}$=0.15, the fractions f_1, f_2, and f_3 were 0.74, 0.22–0.23, and 0.015–0.021. The fraction of planetesimals collided with the host planet (compared to collisions with all planets) typically decreased within the considered time interval. In each calculation variant, there was at least one planet for which the number of collided planetesimals was greater than 25% of the number of collisions of planetesimals with the host planet. The total number of collisions of all planetesimals with planets c–h was greater than that for 100 kyr (the numbers for 100 kyr were presented in Ipatov (2022)) by not more than 4%. However, last collisions of planetesimals with planets could be after a few million years. For the initial disk near the orbit of planet h (with a mass $m_{\rm h} = 0.33\ m_{\rm E}$, where $m_{\rm E}$ is the mass of Earth), the number of collisions of planetesimals with planet g (with a mass $m_{\rm g} = 1.32\ m_{\rm E}$) was approximately the same as with planet h. The planetesimals migrating from distances greater than 0.7 AU could collide with any of the planets, but the majority of their collisions ($\geq 70\%$)

were with planets g and h, and the proportion of collisions was greater for the planets farther from the star.

3 Summary

The outer layers of neighboring exoplanets in the TRAPPIST-1 system can include similar material if there were a lot of planetesimals near their orbits at the late stages of the accumulation of the exoplanets.

Funding

This work was supported by the Ministry of Science and Higher Education of the Russian Federation within the state contract of the Vernadsky Institute of Geochemistry and Analytical Chemistry, Russian Academy of Sciences.

References

Ipatov S.I., 1993, Solar System Research, 27, 1, p. 65
Ipatov S.I., 2019, Solar System Research, 53, 5, p. 332
Ipatov S.I., 2022, Thirteenth Moscow Solar System Symposium, Conference abstracts, p. 378
Ipatov S.I., 2023a, Meteoritics and Planetary Science, 58, 6, p. 752
Ipatov S.I., 2023b, Solar System Research, 57, 3, p. 236
Ipatov S.I., 2023c, Solar System Research, 57, 6, p. 612
Levison H.F. and Duncan M.J., 1994, Icarus, 108, p. 18
Marov M.Ya. and Ipatov S.I., 2023, Physics-Uspekhi, 66, 1, p. 2

VAK 2024 MODERN ASTRONOMY: FROM THE EARLY UNIVERSE TO EXOPLANETS AND BLACK HOLES 300 years Russian Academy of Sciences

Investigation of the dynamical evolution of the compact planetary system K2-72

E. Kuznetsov and A. Perminov

Ural Federal University, Ekaterinburg, 620000 Russia

Abstract. We consider the dynamic evolution of the compact four-planet system K2-72. The star K2-72 is an M-type dwarf. The system contains three Earth-like planets and one super-Earth. We searched for low-order resonances within the uncertainty of determining the periods of the planets. To determine the resonant combinations of the semimajor axes of the orbits, the ratio of the mean motions of neighboring planets was represented as a segment of a sequence of convergent fractions. We considered a few scenarios for the evolution of the K2-72 system over 100 Myr using the Posidonius software, which allows for tidal interactions. We have shown that the compact planetary system K2-72 likely evolves beyond low-order resonances. A significant change in the semimajor axes of the orbits of the planets K2-72 b and K2-72 d leads to the moving of the adjacent planets b–d and d–c out of the 7/5 and 8/5 resonance regions, respectively. The adjacent planets K2-72 d and K2-72 c are located far from the 2/1 resonance, which excludes the possibility of forming chains of mean motion resonances and, hence, 3-planet mean motion resonances. If the orbital eccentricities do not exceed 0.03, the evolution of the compact planetary system K2-72 over 100 Myr remains stable even in the presence of tidal perturbations.

Keywords: planets and satellites: dynamical evolution and stability

DOI: 10.26119/VAK2024.136

1 Introduction

At present, several dozen compact planetary systems containing more than two planets with masses of the order of the Earth's mass are known . It is shown that the stable evolution of compact planetary systems requires the presence of resonances that prevent close encounters of planets moving in neighboring orbits (see, for example, the five-planet systems Kepler-80 (MacDonald et al. 2016), K2-138 (MacDonald et al. 2022), and the seven-planet system TRAPPIST-1 (Luger et al. 2017)). In this case, resonances between pairs of planets can form chains. The longest resonance chain known to date exists in the TRAPPIST-1 system: 8/5–5/3–3/2–3/2–4/3–3/2 (Murphy & Armitage 2022). In the K2-138 system, five planets form the longest chain consisting of identical 3:2 resonances (MacDonald et al. 2022). On the other hand, simulation results show that in wide systems with massive planets, chains of high-order resonances can lead to the destruction of planetary systems (Murphy & Armitage 2022).

We consider the dynamic evolution of the compact four-planet system K2-72. The star K2-72 is an M-type dwarf. The system contains three Earth-like planets and one super-Earth. We searched for low-order resonances within the uncertainty of determining the periods of the planets. We considered a few scenarios for the evolution of the K2-72 system over 100 Myr using the Posidonius software (Blanco-Cuaresma & Bolmont 2017), which allows for tidal interactions.

2 Resonance arguments

When analyzing the resonance properties of planetary systems, it is necessary to study the behavior of the resonance arguments. For two planets i and $i+1$, which are in a mean motion resonance $k_i/(k_i–l_i)$, the resonance argument can be given as follows (Huang & Ormel 2022):

$$\varphi_{i,\ i+1,\ i+s} = (k_i - l_i)\,\lambda_i - k_i\lambda_{i+1} + l_i\varpi_{i+s}, \tag{1}$$

where l_i is the order of resonance, λ_i and λ_{i+1} are the mean longitudes of planets i and $i+1$, respectively, ϖ_{i+s} is the longitude of the pericenter of planet i ($s=0$) or $i+1$ ($s=1$). For the next pair of planets $i+1$ and $i+2$, which are in resonance $k_{i+1}/(k_{i+1}–l_{i+1})$, the resonance argument is defined as follows:

$$\varphi_{i+1,\ i+2,\ i+1+s} = (k_{i+1} - l_{i+1})\,\lambda_{i+1} - k_{i+1}\lambda_{i+2} + l_{i+1}\varpi_{i+1+s}. \tag{2}$$

Instead of two resonances between two adjacent pairs of planets, one can consider three-body resonances. In this case the three-body resonance is a chain of two two-body resonances $k_i/(k_i–l_i)$ and $k_{i+1}/(k_{i+1}–l_{i+1})$ with the resonance argument which

does not depend on the the longitude of the pericenter (Huang & Ormel 2022):

$$\Phi^{p,\ p+q,\ q}_{i,\ i+1,\ i+2} = p\lambda_i - (p+q)\,\lambda_{i+1} + q\lambda_{i+2}, \tag{3}$$

where $p = l_{i+1}(k_i – l_i)$, $q = l_i k_{i+1}$. For three-body resonances we will use the following notation: $(p, –(p+q), q)$.

3 Compact planetary system K2-72

The host star K2-72 is an M2 dwarf with a mass of $0.27^{+0.08}_{-0.09}$ $M_\odot$ and a radius of $0.33^{+0.03}_{-0.03}$ $R_\odot$. Table 1 gives the parameters of the K2-72 planetary system. The radii R of the planets are expressed in Earth radii $R_\oplus$. Planetary masses m are expressed in Earth masses $M_\oplus$ and calculated from the radii of the planets R, assuming that the density ϱ of a planet depends on its radius as (Weiss & Marcy 2014)

$$\varrho = 2.43 + 3.39\left(\frac{R}{R_\oplus}\right)\ \mathrm{g\,cm^{-3}} \tag{4}$$

for $R < 1.5\ R_\oplus$. The orbital elements P, e, i, and g are the period, eccentricity, inclination, and periapsis argument, respectively. The moment T_{conj} corresponds to the conjunction of the planet with the star.

Table 1. Parameters of the planetary system K2-72 (Dressing et al. 2017).

Parameter	K2-72 b	K2-72 c	K2-72 d	K2-72 e
R, $R_\oplus$	1.08 ± 0.11	1.16 ± 0.13	1.01 ± 0.12	$1.29^{+0.14}_{-0.13}$
m, $M_\oplus$	$1.39^{+0.58}_{-0.44}$	$1.80^{+0.85}_{-0.63}$	$1.09^{+0.55}_{-0.39}$	$2.65^{+1.18}_{-0.85}$
P, day	5.577212 ± 0.00042	15.189034 ± 0.0031	$7.760178^{+0.001496}_{-0.001496}$	$24.158868^{+0.003726}_{-0.003850}$
e	$0.11^{+0.02}_{-0.09}$	$0.11^{+0.02}_{-0.09}$	$0.11^{+0.02}_{-0.09}$	$0.11^{+0.02}_{-0.09}$
i, deg	$89.15^{+0.59}_{-0.86}$	$89.54^{+0.32}_{-0.44}$	$89.26^{+0.5}_{-0.7}$	$89.68^{+0.22}_{-0.32}$
g, deg	7.49^{+120}_{-134}	16.83^{+113}_{-138}	14.28^{+114}_{-137}	11.39^{+117}_{-136}

4 Numerical simulations

For compact systems, an important factor affecting their evolution is tidal interaction; therefore, we considered a few scenarios for the evolution of the K2-72 system over 100 Myr using the Posidonius software (Blanco-Cuaresma & Bolmont 2017),

which takes into account tidal interactions. At nominal values of the periods and eccentricities, the simulation ended with the decay of the system 3 Myr after the start of integration. This is because at eccentricities of 0.11 the distance at the apocenter of the planet K2-72 b orbit becomes greater than the distance at the pericenter of the planet K2-72 d orbit. If the initial eccentricities of orbits of all the planets are set equal to the minimum value of 0.02, the system remains stable over the entire considered interval of 100 Myr for all star masses from 0.18 to 0.35 $M_{\odot}$.

The results of the simulations including tidal interactions show that the compact four-planet system K2-72 can have a stable dynamical evolution in the absence of low-order resonances. Based on the results of numerical simulations with the Posidonius software, we obtained the limits on the maximum eccentricities of the orbits of the planets at which the system remains stable over 100 Myr (see Table 2). If the initial eccentricity values are greater than those given in Table 2, the system decays. If the orbital eccentricities do not exceed 0.03, the evolution of the compact planetary system K2-72 over 100 Myr remains stable even in the presence of tidal perturbations. In the case the initial eccentricities of the orbits of the three planets are equal to 0.04, the eccentricities of the orbits of one of the planets K2-72 d or K2-72 e should not exceed 0.03 to ensure the stability of the system.

Table 2. Initial values of orbital eccentricities e_0 at which the planetary system does not disintegrate.

Initial	K2-72 b	K2-72 c	K2-72 d	K2-72 e
e_0	0.04	0.04	0.04	0.03
e_0	0.04	0.04	0.03	0.04
e_0	≤ 0.03	≤ 0.03	≤ 0.03	≤ 0.03

5 Resonant properties of K2-72

In Dressing et al. (2017) it was noted that the orbital periods of the planets are close to commensurability, and it was suggested that mean-motion resonances (MMR) may exist in the K2-72 system. We performed a search for possible resonances in the system for the case when the numerator and denominator in the approximation $k_i/(k_i - l_i)$ of the ratio of the periods P_j/P_i of adjacent planets i and j do not exceed 10. For each resonance, we estimated the resonance offset (Charalambous et al. 2023):

$$\Delta_{ij} = \frac{P_j}{P_i} - \frac{k_i}{k_i - l_i}. \quad (5)$$

Table 3 gives the potential mean-motion resonances and resonance offsets Δ (Eq. 5) for adjacent planets of the K2-72 system. The arrangement of planets in the system in order of distance from the star: 1—K2-72 b, 2—K2-72 d, 3—K2-72 c, 4—K2-72 e.

Table 3. Mean-motion resonances and resonance offsets for the K2-72 system.

Adjacent planets		MMR	Δ
K2-72 b–K2-72 d	(1–2)	7/5	0.0086
K2-72 d–K2-72 c	(2–3)	2/1	0.0427
K2-72 c–K2-72 e	(3–4)	8/5	0.0095

We have shown that the compact planetary system K2-72 likely evolves beyond low-order resonances. A significant change in the semimajor axes of the orbits of the planets K2-72 b and K2-72 d leads to the moving of the adjacent planets b–d and d–c out of the 7/5 and 8/5 resonance regions, respectively. The adjacent planets K2-72 d and K2-72 c are located far from the 2/1 resonance, which excludes the possibility of forming chains of mean motion resonances and, hence, three-planet mean motion resonances (see Fig. 1).

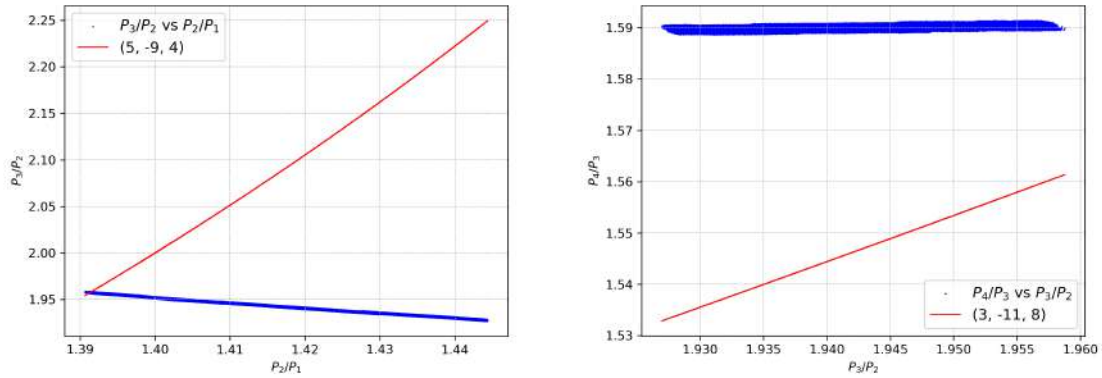

Fig. 1. Evolution of the period ratios of adjacent planets in the K2-72 system over 100 Myr: P_3/P_2 vs P_2/P_1 (left panel) and P_4/P_3 vs P_3/P_2 (right panel). The blue dots correspond to the ratio of the periods of adjacent planets, the red lines show the positions of the three-body resonances. The system evolves from left to right.

6 Conclusions

The study shows that the compact planetary system K2-72 is not resonant. Under the initial conditions corresponding to the masses and orbital elements of the planets determined from observations with their errors taken into account, the evolution of the K2-72 system is stable and regular over of 100 Myr for initial orbital eccentricities not exceeding 0.3.

Acknowledgements. This research has made use of the Catalogue of Exoplanets database (https://exoplanet.eu/catalog/all_fields/).

Funding

The study was supported by the Ministry of Science and Higher Education of the Russian Federation via state assignment project FEUZ-2020-0038.

References

Blanco-Cuaresma S. and Bolmont E., 2017, EWASS Special Session 4 (2017): Star-planet interactions (EWASS-SS4-2017)

Charalambous C., Teyssandier J., Libert A.S., 2023, Astronomy and Astrophysics, 677, A160

Dressing C.D., Vanderburg A., Schlieder J.E., et al., 2017, Astronomical Journal, 154, p. 207

Huang S. and Ormel C.W., 2022, Monthly Notices of the Royal Astronomical Society, 511, p. 3814

Luger R., Sestovic M., Kruse E., et al., 2017, Nature Astronomy, 1, id. 0129

MacDonald M.G., Feil L., Quinn T., et al., 2022, Astronomical Journal, 163, p. 162

MacDonald M.G., Ragozzine D., Fabrycky D.C., et al., 2016, Astronomical Journal, 152, p. 105

Murphy M.M. and Armitage P.J., 2022, Monthly Notices of the Royal Astronomical Society, 512, p. 2750

Weiss L.M. and Marcy G.W., 2014, Astrophysical Journal Letters, 783, L6

BAK 2024 MODERN ASTRONOMY: FROM THE EARLY UNIVERSE TO EXOPLANETS AND BLACK HOLES 300 years Russian Academy of Sciences

Interpretation of the Balmer-alpha line absorption in the exoplanet WASP-69 b

I. Miroshnichenko, S. Sharipov, M. Rumenskikh, and I. Shaikhislamov

Institute of Laser Physics, SB RAS, Novosibirsk, 630090 Russia

Abstract. In this work, the absorption in the Hα line of the exoplanet Wasp-69 b was simulated. A three-dimensional self-consistent multifluid magnetohydrodynamic (MHD) model of the atmosphere was used to calculate the characteristic distributions of density, velocity, and temperature of various components in the atmosphere of WASP-69 b. To obtain the profile of hydrogen atoms excited to the second energy level H(2ℓ), a Monte Carlo model of Lyα photon transport in the atmosphere, obtained by MHD simulation, was used. Three main sources were taken into account as the "pumping" of the atmosphere with Lyα photons in the model: the photons incident from the star, photons generated in the process of collisions of hydrogen atoms with electrons, and photons arising in the process of recombination of electrons and protons in the atmosphere of the planet. Modeling of the resonant scattering of Lyα photons on hydrogen atoms was performed in the approximation of partially coherent isotropic scattering. The calculations have shown that the population of the hydrogen excited to the second energy level due to the pumping by intra-atmospheric Lyα photons is insignificant and does not lead to absorption in the Hα line, but such absorption can appear due to the pumping by stellar photons. Nevertheless, judging by the observed data obtained and their analysis, the absorption in this line was not detected, which may indicate a low intensity of the Lyα line radiation from the parent star.

Keywords: radiative transfer; atmospheric effects; methods: numerical; planets and satellites: atmospheres

DOI: 10.26119/VAK2024.137

1 Introduction

The warm Neptune WASP-69 b, discovered 10 years ago, is still of interest to researchers. This planet is one of the few that demonstrate sufficiently high absorption in the sodium doublet and metastable helium lines. A comparison of transit absorptions with numerical modeling has shown that the atmosphere of this planet is outflowing at a rate of about 10^{11} g/s, forming a long helium tail of 7 planetary radii. The absorption in the hydrogen Hα line was also measured (Khalafinejad et al. 2021), but despite the high level of absorption in the He I($2\,^3$S) line, the relatively large calculated helium content in the upper layers of the planet's atmosphere, and the intense outflow of planetary matter, all but one of the measurements showed no absorption in the Hα line. In Guilluy et al. (2024), this anomalous observation is associated with the activity of the parent star. The goal of this paper is to model and interpret the absorption in the Hα line.

2 Methods

In order to obtain the absorption spectrum in the Hα line, it is necessary to find the distribution of hydrogen atoms excited to the second energy level H(2ℓ). For this purpose, the transport of Lyα photons in the planet's atmosphere was calculated using the Monte Carlo method. The input atmospheric parameters required for the calculation, such as the distributions of the concentration of hydrogen atoms, free electrons, protons, and temperature, were taken from the results of three-dimensional self-consistent hydrodynamic modeling (Shaikhislamov et al. 2018; Khodachenko et al. 2019). The photon transport model assumes three main ways of "pumping" the atmosphere with Lyα photons: the photons incident from the star, photons generated in the process of collisions of hydrogen atoms with electrons, and photons arising in the process of recombination of electrons and protons in the planet's atmosphere. A detailed description of the Monte Carlo model can be found in Miroshnichenko et al. (2021). Here we only briefly describe the main provisions. The radiation field is represented as a discrete set of photon packets, each packet has coordinates (x, y, z), propagation direction (n_x, n_y, n_z), frequency ν expressed in units of Doppler velocity, and "weight" w reflecting the number of real photons in one photon packet. The photons flying from the star (hereinafter the stellar photons) are generated uniformly along a spherical front incident on the atmosphere. The atmospheric photons include collisional and recombination photons: the photons generated in collisions with electrons and in recombination processes, respectively. The atmospheric photons are distributed uniformly throughout the atmosphere and have an isotropic distribution of their propagation direction. The velocity (frequency) is chosen randomly from the

Maxwell–Boltzmann distribution based on the local temperature, while the influence of suprathermal particles is not taken into account. The "weight" of atmospheric photon packets is calculated according to the rates of Lyα photon production in the corresponding reactions. Packet tracing is performed as follows: an optical path is randomly determined for each packet; after the packet has traveled it, it is absorbed by a hydrogen atom and then re-emitted with new random characteristics. Such a photon exists until it leaves the computational domain or de-excitation occurs as a result of one of the reactions: photoionization, spontaneous relaxation, or collisional de-excitation. Modeling of the resonant scattering of Lyα photons on hydrogen atoms is performed in the approximation of partially coherent isotropic scattering. A full description of the approach and the implementation of frequency sampling after scattering can be found in (Zheng & Miralda-Escudé 2002; Dijkstra et al. 2019). After all photon packets cease to exist in the computational domain, an axisymmetric profile H(2ℓ) is constructed in cylindrical coordinates, based on which the absorption profile $\alpha(v)$ is calculated.

3 Results

The calculation of the absorption in the Hα line was carried out for two sets of parameters since they showed the best agreement with the measured He I($2\,^3$S) absorption line. The results of these calculations were used as initial parameters for the Monte Carlo model.

As for most stars, the emission spectrum at short wavelengths has not been measured for WASP-69. In the Monte Carlo model, one of the main parameters is the Lyα line intensity ($I_{\mathrm{Ly}\alpha}$) at a distance of 1 AU, measured in units of erg cm^{-2} s^{-1}. The $I_{\mathrm{Ly}\alpha}$ value determines the contribution of stellar photons to the generation of H(2ℓ). It was estimated based on the method proposed in Linsky et al. (2013). The method assumes a relationship between the rotation period of a star, its effective temperature, and the flux in the Lyα line. For WASP-69, the rotation period is 23.07 days and the effective temperature is 4700 K, which gives a flux of $I_{\mathrm{Ly}\alpha} = 17.8$ erg cm^{-2} s^{-1}. Having this estimation, we choose the $I_{\mathrm{Ly}\alpha}$ range from 5 to 20 erg cm^{-2} s^{-1} to determine the best fit to the observations.

Figure 1 (left) shows the obtained absorption profiles that demonstrate the best agreement with the observed data. It is evident from the figure that the best agreement is achieved with the parameters $F_{\mathrm{XUV}} = 3$ erg cm^{-2} s^{-1} and $I_{\mathrm{Ly}\alpha} = 8.9$ erg cm^{-2} s^{-1}, which agrees with both the absorption in the He I($2\,^3$S) line and the estimate based on Linsky et al. (2013). At the same time, regardless of the radiation parameters, the main contribution to the absorption is made by the

stellar photons. For the case of $F_{\rm XUV} = 3$ erg cm^{-2} s^{-1} and $I_{{\rm Ly}\alpha} = 8.9$ erg cm^{-2} s^{-1}, the contribution of the stellar, collisional, and recombination photons was 98.58%, 0.12%, and 1.3%, respectively. Similar relationships are observed for all the obtained results.

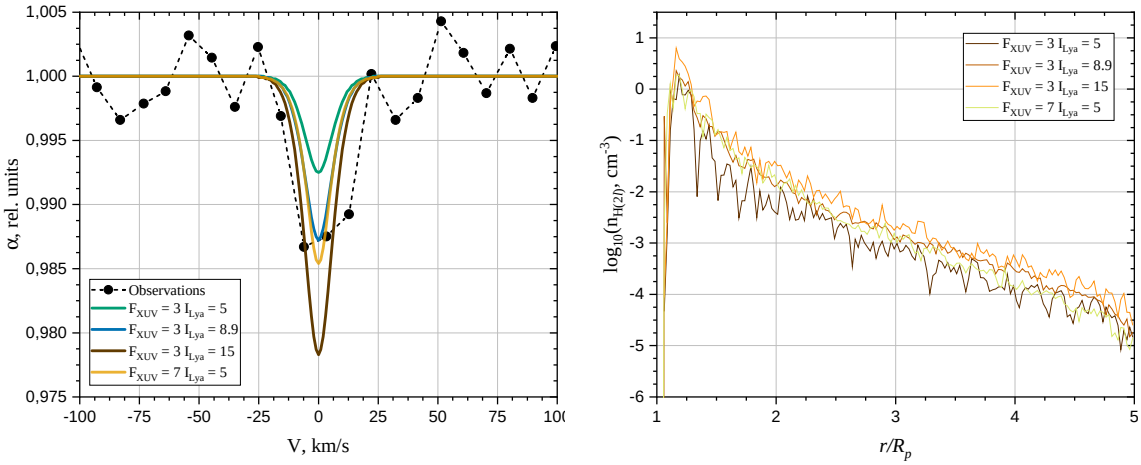

Fig. 1: Left: calculated absorption profiles in Hα for the most suitable parameters. Right: concentration profiles of excited hydrogen atoms along the planet–star axis.

The low contribution of atmospheric photons to the absorption is due to the low rates of Lyα photon production reactions in the atmosphere, which are to a large extent determined by the temperature. Figure 2 shows the rates of Lyα photon production reactions in the recombination and collision processes for $F_{\rm XUV} = 3$ and 7 erg cm^{-2} s^{-1}.

Since the reaction rates determine the weight of the photon packets in the model, which in turn reflects the number of real photons, it follows from Fig. 2 that the content of H(2ℓ) generated by atmospheric processes is low. The obtained profiles of the H(2ℓ) concentration along the line connecting the centers of the star and the planet are shown in Fig. 1 (right). In more detail, Fig. 3 presents the contributions of different types of photons to the absorption and generation of H(2ℓ). Thus, the observed absorption and distribution of H(2ℓ) are almost completely determined by the stellar radiation. As suggested by the production reaction rates, the H(2ℓ) profiles are determined by the stellar photons.

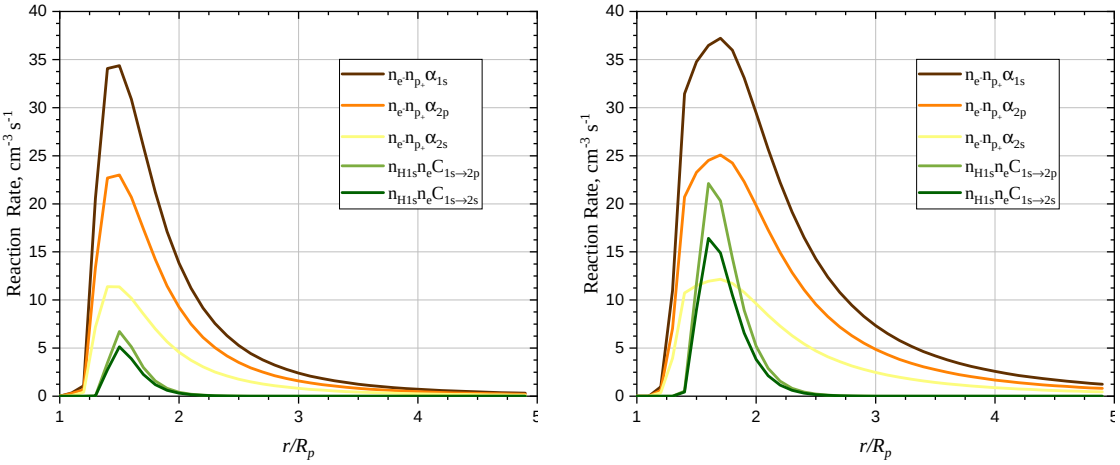

Fig. 2: Reaction rates of Lyα photon generation for $F_{\rm XUV} = 3$ erg cm^{-2} s^{-1} (left) and $F_{\rm XUV} = 7$ erg cm^{-2} s^{-1} (right).

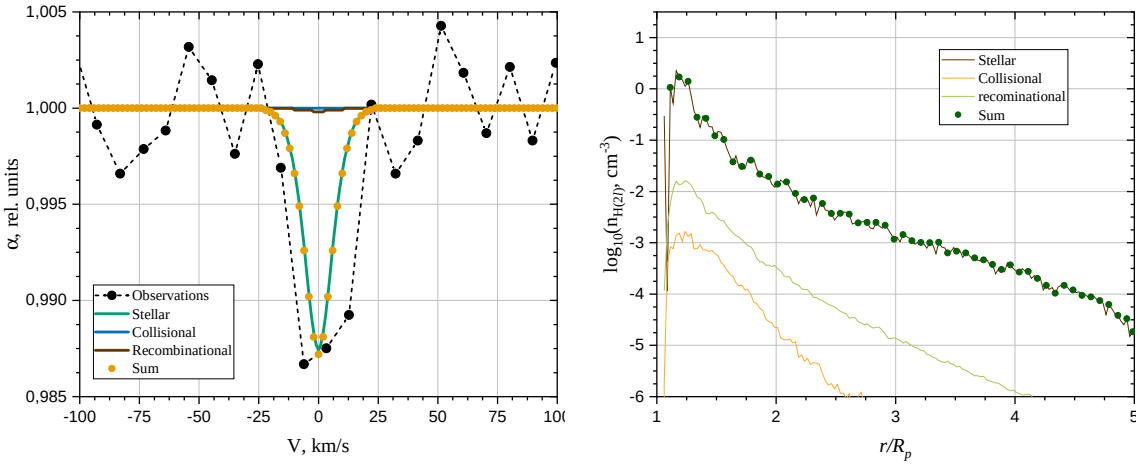

Fig. 3: Left: absorption profiles for different photon types. Right: density profile for H(2ℓ). Here $F_{\rm XUV} = 3$ erg cm^{-2} s^{-1} and $I_{{\rm Ly}\alpha} = 8.9$ erg cm^{-2} s^{-1}.

4 Summary

Using the Monte Carlo method for tracing Lyα photons in the atmosphere of the exoplanet WASP-69 b, we obtained the absorption spectrum in the Hα line. The model results are in good agreement with the observed data. It was found that the greatest contribution to the absorption is made by the stellar photons, while the photons generated in atmospheric processes have almost no effect on the absorption. In addition, the concentration profiles of the hydrogen atoms excited to the second energy level were obtained, from which it follows that the H(2ℓ) content is within 10^0–10^{-2} cm^{-3} in the atmospheric layer of about 1.5 R_p. It was also found that the main absorption occurs in the same layer. The model results also additionally confirm the estimate of the physicochemical parameters of the system: $n_\mathrm{He}/n_\mathrm{H} = 0.2$ and $F_\mathrm{XUV} = 3$ erg cm^{-2} s^{-1}, since the best agreement with the observed data in the Hα line was obtained with these values.

Funding

This work was carried out as part of RSF project No. 23-72-10060.

References

Dijkstra M., Prochaska J.X., Ouchi M., et al., 2019, Saas-Fee Advanced Course, 46
Guilluy G., D'Arpa M., Bonomo A., et al., 2024, Astronomy & Astrophysics, 686, id. A83
Khalafinejad S., Molaverdikhani K., Blecic J., et al., 2021, Astronomy & Astrophysics, 656, id. A142
Khodachenko M., Shaikhislamov I., Lammer H., et al., 2019, Astrophysical Journal, 885, p. 67
Linsky J.L., France K., Ayres T., 2013, Astrophysical Journal, 766, p. 69
Miroshnichenko I., Shaikhislamov I., Berezutskii A., et al., 2021, Astronomy Reports, 65, p. 61
Shaikhislamov I., Khodachenko M., Lammer H., et al., 2018, Monthly Notices of the Royal Astronomical Society, 481, p. 5315
Zheng Z. and Miralda-Escudé J., 2002, Astrophysical Journal, 578, p. 33

BAK 2024 MODERN ASTRONOMY: FROM THE EARLY UNIVERSE TO EXOPLANETS AND BLACK HOLES 300 years Russian Academy of Sciences

Simulation of the Hα absorption for the hot Jupiter HAT-P-32 b

S. Sharipov, I. Miroshnichenko, I. Shaikhislamov, and M. Rumenskikh

Institute of Laser Physics, SB RAS, Novosibirsk, 630090 Russia

Abstract. The paper presents the results of modeling the absorption spectrum in the Hα and He 10 830 Å lines for the hot Jupiter HAT-P-32 b. The simulation was carried out using a 3D hydrodynamic model coupled to a Monte Carlo model of Lyα photon transfer. It was determined that to explain the absorption in both lines at a ratio H/He = 99/1, high values of the XUV flux and stellar Lyα flux are required: $F_{\rm XUV} = 100$ erg cm^{-2} s^{-1} and $I_{{\rm Ly}\alpha} = 600$ erg cm^{-2} s^{-1}, which may indicate high activity of the star. New parameters were also found that describe the absorption at H/He = 97/3 while requiring less extreme $F_{\rm XUV} = 25$ erg cm^{-2} s^{-1} and $I_{{\rm Ly}\alpha} = 600$ erg cm^{-2} s^{-1}. Monte Carlo modeling showed that the absorption in the Hα line is formed by stellar photons producing H(2) concentrations at a level of 10^2–10^3 cm^{-3} in the atmospheric layer up to $2R_{\rm p}$, where the absorption occurs.

Keywords: planets and satellites: atmospheres; radiative transfer; scattering; hydrodynamics

DOI: 10.26119/VAK2024.138

1 Introduction

Over the past two decades, with the help of transit spectroscopy escaping hydrogen and helium atmospheres around many planets have been detected. Initially, the ultraviolet hydrogen line Lyα was used, in which the excess absorption is formed by H(1s) atoms. As well, observations in the optical Hα line began to be used, which are able to probe planetary hydrogen atoms in the excited state H(2). In addition to hydrogen, for some planets it is possible to measure the absorption in the infrared He 10 830 Å line of the helium triplet, which results from the transition between the $2\,^3$S and $2\,^3$P states.

Both the Hα and He 10 830 Å lines are practically not contaminated by the interstellar medium and Earth's atmosphere, which allows the use of ground-based facilities with high spectral resolution and provides high-quality information about the planetary atmosphere. Modeling the absorption in both lines helps constrain the atmosphere physical parameters. The purpose of this work is to constrain the parameters of the upper atmosphere of the hot Jupiter HAT-P-32 b using a 3D hydrodynamic model and a Monte Carlo radiative transfer model as well as to interpret the observed absorption in the Balmer Hα line.

2 Method

To simulate the planetary atmosphere, we used a 3D self-consistent hydrodynamic model (Shaikhislamov et al. 2020). It includes the H, H^+, He, He^+, and He($2\,^3$S) atoms and free electrons, and the stellar wind is also included in the consideration. The solar parameters for the stellar wind were chosen. A pressure of 1 µbar and a temperature of 1700 K were specified at the lower boundary in the calculations. The metallicity was equal to the solar metallicity: [Fe/H] = −0.04.

The Hα line absorption was calculated based on the Monte Carlo simulations of Lyα radiation transfer (Miroshnichenko et al. 2021). The model takes into account both stellar and atmospheric photons. The atmospheric photons are born as a result of recombination and collisions with electrons, and the stellar ones arrive in the form of a spherical front. The stellar photon frequency is sampled from a double Gaussian distribution centered at ±65 km/s with a width of 38 km/s. We also calculated the absorption in the He 10 830 Å line for additional validation of atmospheric parameters. The absorption in the helium line was calculated in the non-local thermodynamic equilibrium (NLTE) approximation.

3 Observations

Using the CARMENES instrument, Czesla et al. (2022) detected time-dependent absorption in the Hα and He 10 830 Å lines, for which the absorption depth at the transit center was about 5% and 6.6%, respectively. Also in a recent work using the Hobby–Eberly Telescope, Zhang et al. (2023) obtained an absorption in the He 10 830 Å line at a level of 8.2%, which may indicate a high level of activity of the star. HAT-P-32 is an F-type star with a mass $M_\star = 1.160\ M_\odot$, a radius $R_\star = 1.219\ R_\odot$, and an effective temperature of 6000 K. HAT-P-32 b is a hot Jupiter with a mass $M_\mathrm{p} = 0.75 M_J$, a radius $R_\mathrm{p} = 1.789\ R_\mathrm{J}$, and an equilibrium temperature of 1700 K.

It is well known that for most hot Jupiters, the stellar XUV radiation ($\lambda < 912$ Å) is the main energy source to drive planetary winds and atmospheric escape. Based on the spectral energy distribution (SED), we estimated the XUV flux at a reference distance of 1 AU as $F_\mathrm{XUV} = 100\ \mathrm{erg\,cm^{-2}\,s^{-1}}$. Another important parameter for calculating the absorption in the Hα line is the intensity of the star emission in the Lyα line; it was estimated based on Linsky et al. (2013) as $I_{\mathrm{Ly}\alpha} = 45\ \mathrm{erg\,cm^{-2}\,s^{-1}}$. It should be noted that these parameters are widely varied to achieve agreement with the observations. Using a 1D hydrodynamic model, Yan et al. (2024) estimated these parameters as $F_\mathrm{XUV} = 490\ \mathrm{erg\,cm^{-2}\,s^{-1}}$ and $I_{\mathrm{Ly}\alpha} = 460\ \mathrm{erg\,cm^{-2}\,s^{-1}}$, and the ratio H/He turned out to be H/He $\geq$ 99/1. Similar results were obtained in earlier works.

4 Results

In this work, we considered different helium abundances in the planetary atmosphere: H/He = 92/8, 97/3, and 99.5/0.5. For each case, the most appropriate F_XUV and $I_{\mathrm{Ly}\alpha}$ at a distance of 1 AU were determined to fit the observations. The approximation was assessed using the χ^2 criterion. For brevity, we present only the spectra in the Hα line.

4.1 H/He = 99/1

Since there are a number of studies (Czesla et al. 2022; Yan et al. 2024) convincingly showing that a helium abundance of 1% describes the observations well, we will first consider this value. Figure 1 shows the absorption spectra in the Hα line which give the best agreement with the observations; for each value of F_XUV, the intensity of the Lyα line varied from 40 to $10^4\ \mathrm{erg\,cm^{-2}\,s^{-1}}$. It can be seen that higher values of F_XUV are in better agreement with the line width but require significantly larger values of $I_{\mathrm{Ly}\alpha}$. Note that even in the case of the smallest $F_\mathrm{XUV} = 25\ \mathrm{erg\,cm^{-2}\,s^{-1}}$, an

intensity of the order of $I_{\mathrm{Ly}\alpha} = 400$ erg cm^{-2} s^{-1} is required, which is approximately 10 times higher than the typical value for F-type stars. The calculations show that for the same intensities of the Lyα line, the absorption depth decreases as F_{XUV} increases. To determine the best option, we additionally considered the absorption in the He 10 830 Å line. Table 1 shows the obtained absorption values and the calculated mass-loss rate in the planet's atmosphere. The best agreement is achieved at $F_{\mathrm{XUV}} = 200$ erg cm^{-2} s^{-1} and $I_{\mathrm{Ly}\alpha} = 1500$ erg cm^{-2} s^{-1}, but the two adjacent rows of the table also satisfy the observations. At low XUV fluxes, the absorption in the helium line is insufficient and requires a lower H/He ratio.

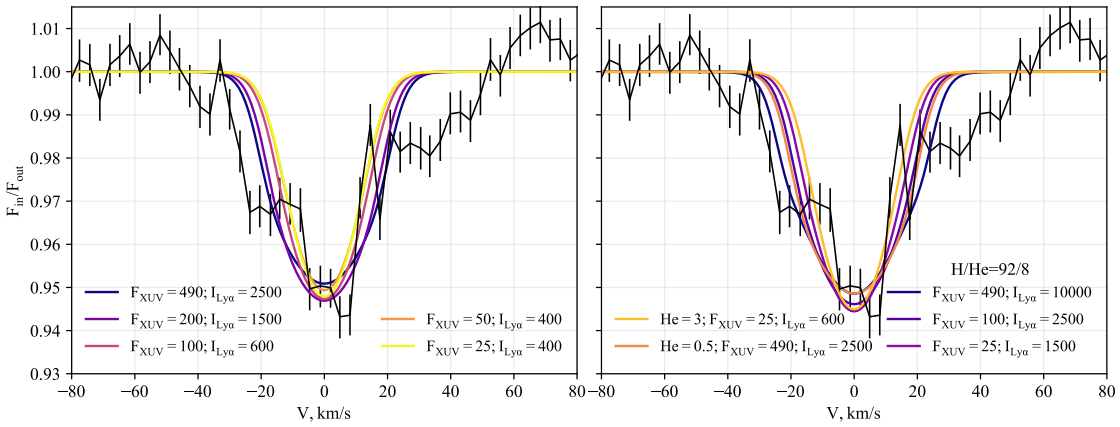

Fig. 1. Calculated best-fit spectra in the Hα line for various atmospheric and radiation parameters.

For F5–G9 stars, there is a limit on the ratio of the flux in the Lyα line to the flux in the X-ray range ($\lambda < 100$ Å). Linsky et al. (2013) found that $0.6 < F_{\mathrm{Ly}\alpha}/F_{\mathrm{X}} \lesssim 100$. Based on SED, $F_{\mathrm{X}} \approx 15$ erg cm^{-2} s^{-1}, which gives an upper limit on the Lyα line intensity of approximately 1500 erg cm^{-2} s^{-1}. Thus, at the ratio H/He = 99/1, the best parameters are $F_{\mathrm{XUV}} = 100$ erg cm^{-2} s^{-1} and $I_{\mathrm{Ly}\alpha} = 600$ erg cm^{-2} s^{-1}.

4.2 H/He = 92/8, 97/3, and 99.5/0.5

The spectra that best describe the observations are shown in Fig. 1, the results are also given in Table 1. The ratio H/He = 92/8 requires very high intensities of the Lyα line, which do not satisfy the constraints obtained above. For the case of H/He = 92/8, the values of $F_{\mathrm{XUV}} = 5$ erg cm^{-2} s^{-1} and $I_{\mathrm{Ly}\alpha} = 2000$ erg cm^{-2} s^{-1} are required, which describe the Hα absorption line width worse. Thus, it is not possible

Table 1. Calculated absorption depth in the Hα and He 10 830 Å lines and the mass-loss rates. The measured absorptions are 5% and 6.6%, respectively.

$F_{\rm XUV}$, erg cm^{-2} s^{-1}	$I_{{\rm Ly}\alpha}$, erg cm^{-2} s^{-1}	Hα, %	He($2\,^3$S), %	$\dot{M}$, 10^{12} g/s
	H/He = 99/1			
490	2500	4.91	7.02	4.13
200	1500	5.30	6.18	2.94
100	600	5.27	5.92	2.49
50	400	5.07	4.83	1.71
25	400	5.21	3.49	1.12
	H/He = 92/8			
490	10000	5.14	21.55	3.14
100	2500	5.39	15.80	1.64
25	1500	5.55	9.68	0.76
5	2000	4.99	5.23	0.29
	H/He = 99.5/0.5			
490	2500	5.14	4.29	4.23
	H/He = 97/3			
25	1500	5.51	6.96	1.03

to find parameters that approximate both lines well and satisfy the restrictions, which rejects such a scenario.

Similar results were obtained for the ratio H/He = 99.5/0.5. Such a case, firstly, requires too high values of $I_{{\rm Ly}\alpha}$ and, secondly, does not agree with the absorption depth in the He 10 830 Å line. To fit the helium line, $F_{\rm XUV} = 10^3$ erg cm^{-2} s^{-1} is required, therefore we also consider this scenario irrelevant.

Unlike the two previous scenarios, for the case of H/He = 97/3 we were able to find parameters that satisfy all the restrictions with less extreme radiation parameters. At values of $F_{\rm XUV} = 25$ erg cm^{-2} s^{-1} and $I_{{\rm Ly}\alpha} = 600$ erg cm^{-2} s^{-1}, the calculated spectra satisfy the observations. This case has an insignificantly higher χ^2 than the best result for H/He = 99/1, which indicates that a second possible solution has been found.

5 Conclusions

Summing up, we can draw a number of important conclusions. In the case of HAT-P-32 b, the degeneracy of solutions with different helium abundances is ob-

served. A decrease in the H/He ratio requires larger values of $I_{\mathrm{Ly}\alpha}$ to agree with the observed Hα absorption while at the same time a smaller F_{XUV} is required to agree with He 10 830 Å, which in turn narrows the line and increases the absorption depth in Hα and requires even greater intensities. It can also be noted that at the same radiation parameters a decrease in H/He reduces the absorption depth in Hα.

An analysis of the obtained spectra showed that regardless of the radiation parameters the absorption in the Hα line is formed due to the H(2) atomic state excited by stellar radiation. The atmospheric photons make an insignificant contribution to the H(2) generation and absorption. Figure 2 shows the resulting H(2) and temperature profiles along the planet–star line. It can be seen that the maximum H(2) concentration is located approximately at a distance of $1.5R_{\mathrm{p}}$ and amounts to 10^2–10^3 cm^{-3}, and the main concentration and absorption are located in the layer up to $2R_{\mathrm{p}}$. Also, at large F_{XUV} the concentration drops faster, narrowing the absorption region. The temperature profiles peak at 2—2.5 R_{p} at 1.1–1.2 $\times$ 10^4 K, which is consistent with other model results, but they show variation in shape as F_{XUV} falls. Also, a decrease of H/He ratio shifts the temperature peak lower and increases the overall temperature.

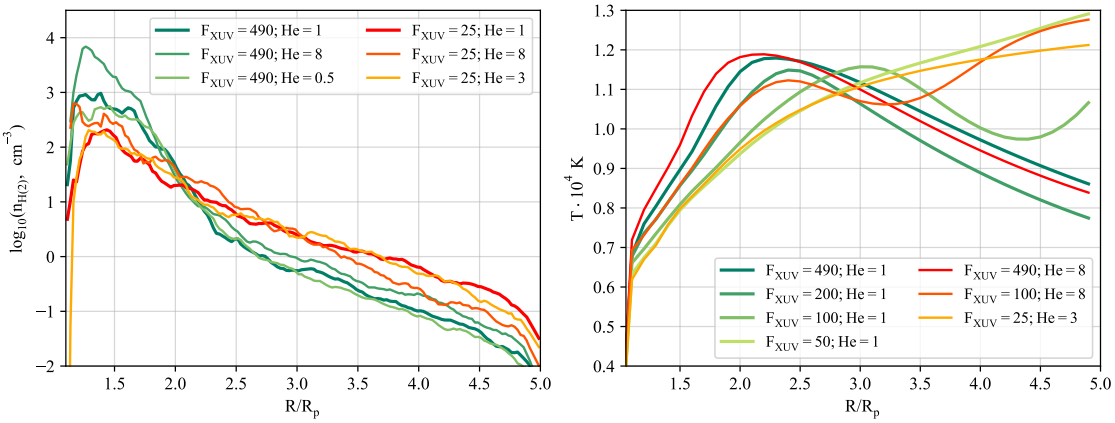

Fig. 2. Obtained H(2) concentrations and the temperature profiles along the planetary atmosphere.

In general, we reproduced the results of other models for the ratio H/He $\geq$ 99/1. Also, a new solution was found that alleviates the problem of low helium abundance and requires less extreme parameters of the star radiation.

Funding

This work was carried out as part of RSF project No. 23-72-10060.

References

Czesla S., Lampón M., Sanz-Forcada J., et al., 2022, Astronomy and Astrophysics, 657, id. A6
Linsky J.L., France K., Ayres T., 2013, Astrophysical Journal, 766, 2, id. A69
Miroshnichenko I.B., Shaikhislamov I.F., Berezutskii A.G., et al., 2021, Astronomy Reports, 65, p. 61
Shaikhislamov I.F., Khodachenko M.L., Lammer H., et al., 2020, Monthly Notices of the Royal Astronomical Society, 491, p. 3435
Yan D., Guo J., Seon K., et al., 2024, Astronomy and Astrophysics, 686, id. A208
Zhang Z., Morley C.V., Gully-Santiago M., et al., 2023, Science Advances, 9, id. eadf8736

MODERN ASTRONOMY: FROM THE EARLY UNIVERSE TO EXOPLANETS AND BLACK HOLES

Transit absorption in the oxygen lines for constraining the atmosphere temperature of hot exoplanets

A. Shepelin, M. Golubovsky, and I. Shaikhislamov

Institute of Laser Physics of the Siberian Branch of the Russian Academy of Sciences, Novosibirsk, 630090 Russia

Abstract. Atomic oxygen, due to its unique chemical properties, is widely used in astrophysics to study chemical composition, nucleosynthesis conditions, and the processes of formation and evolution. The recent detection of the O I 1304 Å and 7774 Å lines in the upper atmospheres of exoplanets using space and ground-based telescopes opens the possibility to evaluate its abundance in these objects and constrain important atmospheric parameters. However, the simple approximation of thermodynamic equilibrium is often inaccurate in describing the formation and absorption for many spectral lines in stars and hot exoplanets. The development of a kinetic model that takes into account detailed radiative and collisional processes in advanced atomic models is required to interpret the observations. In this work we for the first time analyze the advantages of transit absorption measurement of two oxygen lines simultaneously.

Keywords: planets and satellites: atmospheres; line: profiles; a tmospheric effects; methods: numerical

DOI: 10.26119/VAK2024.139

1 Introduction

Detecting oxygen in the atmospheres of other planets is an important aspect of astronomical research. The processes of planet formation and evolution are influenced by oxygen through many molecules it forms (Madhusudhan et al. 2012). Furthermore, the element plays a significant role in the chemical evolution of the Milky Way and possibly other galaxies (Tinsley 1979; McWilliam 1997).

In exoplanet research, the O I 1304 Å transit absorption was measured in the atmospheres of the hot Jupiters HD 209458 b (Vidal-Madjar et al. 2004; Ben-Jaffel & Hosseini 2010) and HD 189733 b (Ben-Jaffel & Ballester 2013) using the Hubble Space Telescope. Recently, the possibility of probing the upper atmospheres of exoplanets by transit observations in the He I 10 830 Å line was proposed (Oklopčić & Hirata 2018). It can be measured by ground-based telescopes since it weakly interacts with the interstellar medium and Earth's atmosphere. Since then, this line has been observed in atmospheres of more than 30 exoplanets, yielding a positive detection in more than half of the instances (Fossati et al. 2021). The first detection of the atomic oxygen line at 7774 Å in the atmosphere of the hot Jupiter KELT-9 b was reported in Borsa et al. (2021). This infrared line can also be observed by ground-based telescopes, greatly increasing our means to detect oxygen in exoplanet atmospheres.

The absorption in the 1304 Å line is connected to the ground state of O I, while that of the 7774 Å line to the excited level with an energy of 9.146 eV. Thus, the measurement of these two different lines opens the possibility to remove the degeneracy in the calculations of oxygen abundance and derive such an important parameter of the atmosphere as temperature. The difference in the line widths can give information on the velocities in the atmosphere. This work aims at evaluating this method in a relatively wide parametric space of planet masses and temperatures, including some particular exoplanets. To this end, we use our newly developed `Astrea`[1] library for space plasma non-local thermodynamic equilibrium (NLTE) kinetics.

2 Modeling

The modeling process can be divided into several stages. The first one is to construct the atmospheric structure. We assume hydrostatic equilibrium at a given temperature and a planet mass to obtain the density profiles of electrons and other elements. For a preliminary study we assume a static atmosphere, which is sufficient in many cases as the largest absorption in the lines of interest comes from a relatively close region around the exoplanet. The solar oxygen abundance is taken. The electron density was

[1] https://astreaproject.ru

obtained from the photoionization – radiative recombination balance (Shaikhislamov et al. 2014; Trammell et al. 2011). The second step is the calculation of the population of the oxygen excited levels taking into account the propagation and absorption of stellar radiation in the modeled atmosphere. Finally, the absorption profiles in the lines are calculated in the 3D geometry.

The computation scheme for the population of the excited levels has the following form:

$$\mathbf{n}_{\tau+1} = P\mathbf{n}_\tau = (I - Q\Delta t)^{-1}\mathbf{n}_\tau, \tag{1}$$

where $\mathbf{n}_{\tau+1}$ is the level population vector at the $\tau + 1$ iteration, $\mathbf{n}_\tau$ is the level population vector at the τ iteration, P is the evolution operator, I is the identity matrix, Q is the overall transition rate matrix, and Δt is the time step. We take the asymptotic stationary solution as a result.

The overall transition rate matrix Q can be expressed from the transition rate matrix R, where each matrix element R_{ab} corresponds to the $a \to b$ transition rate:

$$Q_{ij} = \begin{cases} -\sum_{k \neq i} R_{ik}, & i = j \\ R_{ji}, & i \neq j \end{cases}. \tag{2}$$

The transition rate R_{ab} depends on the transition type (`Astrea` includes ten different radiative and collisional bound-bound and bound-free transitions) and in the general case has the scattering integral form:

$$R_{ab} = n_y \int_{x_0}^{\infty} F(x)\sigma(x)dx, \tag{3}$$

where n_y is the number density of scattering particles, x is the scattering characteristic (frequency, energy, velocity, etc.), x_0 is the line center (x process activation), $F(x)$ is the x value distribution, and $\sigma(x)$ is the process cross section. This paper considers the modified O I–II (51 + 1 levels) model (Sitnova et al. 2013; Barklem 2006).

The spectrally resolved absorption $\alpha(v) = 1 - \kappa(v)$ is calculated as integrals along the line of sight from the stellar disk to the observer at a mid-transit of a planet, using the Tasitsiomi approximation of the Voigt integral (Tasitsiomi 2006; Khodachenko et al. 2017).

3 Results

As the reference parameters we take those of the HD 209458 system with corresponding stellar spectra from Salz et al. (2016). The base atmosphere pressure $p_0 = 0.1$ bar.

Figure 1 shows, as an example, the absorption profiles of the two O I lines for a number of temperatures in the HD 209458 b upper atmosphere. For systematic study we made calculations for three different groups of planet masses from Neptunes to Jupiters and to massive hot Jupiters and for a number of temperatures from 250 to 2.5×10^5 K.

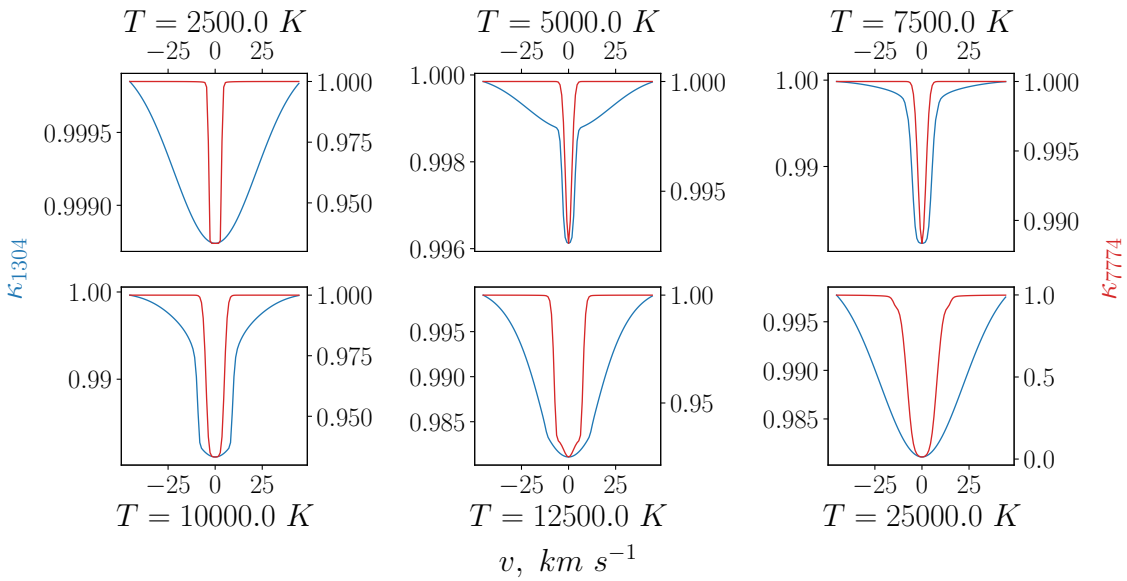

Fig. 1: Examples of the O I 1304 Å and 7774 Å absorption profiles at the mid-transit of HD 209458 b assuming different temperatures of the upper atmosphere. The horizontal axis is in the Doppler velocity units.

The absorptions in the two lines were compared by the integrals over typical line widths and by the maximum amplitudes (Fig. 2). These two methods give qualitatively the same results and prove the following concept: the relation between the two lines indeed varies with temperature in the range of interest ($\approx 10^4$ K). Moreover, the obtained results can be used to estimate the probability of oxygen line detection for different exoplanets (Fig. 3). For example, the 7774 Å line could probably be detected in the transits of KELT-16 b ($T = 3190$ K, $m = 2.75\ m_J$) and MASCARA-5 b ($T = 2700$ K, $m = 3.12\ m_J$). Interestingly, KELT-9 b is in the parameter space most favorable for observation of the 7774 Å line absorption, corresponding to its actual and so far singular detection (Fossati et al. 2021).

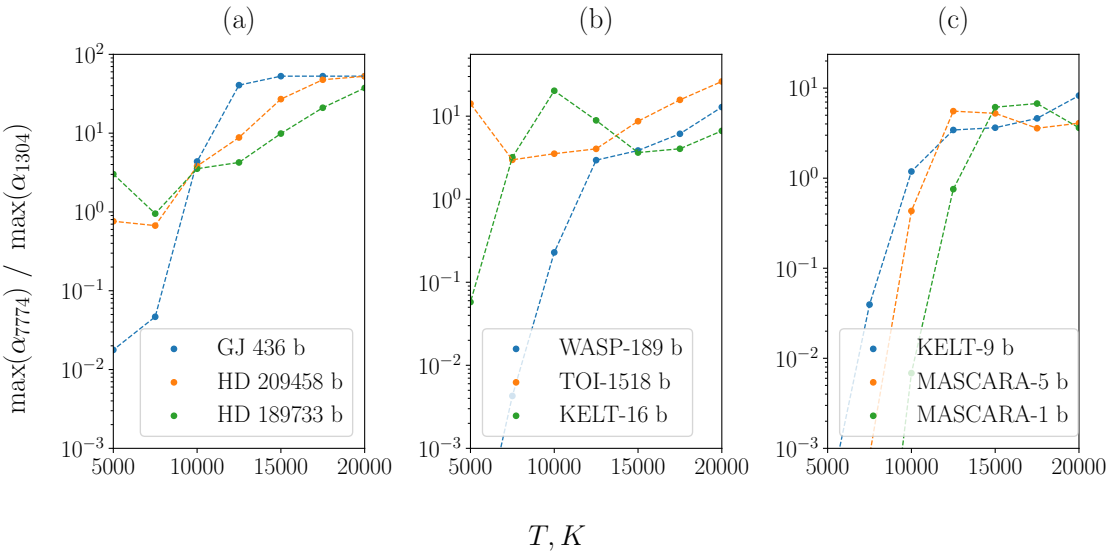

Fig. 2: The ratio between the absorptions in the O I 1304 Å and 7774 Å lines, calculated as the maximum amplitude for three groups of planets: (a), (b), and (c).

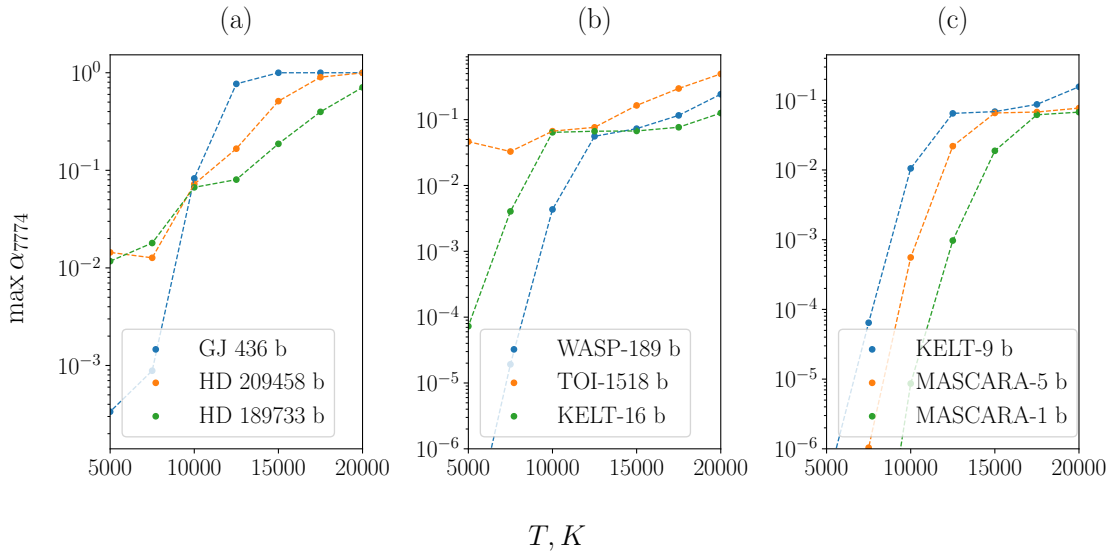

Fig. 3: Absorption at the maximum of the O I 7774 Å line for three groups of planets: (a), (b), and (c).

4 Summary

The absorption in two O I oxygen lines at 1304 Å and 7774 Å in the upper atmospheres of exoplanets was studied using a new NLTE code `Astrea`. We demonstrated that for the hot exoplanets of interest such as hot Neptunes, hot Jupiters, and ultra-hot Jupiters, the relation between these two lines can be used to constrain the temperature of the atmosphere. Also, the parametric study revealed at what kind of planets the detection of transit absorption in the 7774 Å line is possible by ground-based telescopes. Generally, it favors, as expected, hot exoplanets. The next step of the study will include 3D gas-dynamic simulations of particular exoplanets combined with kinetic modeling by the `Astrea` code.

Acknowledgements. We thank L. I. Mashonkina for the detailed oxygen model.

Funding

This work was supported by the Theoretical Physics and Mathematics Advancement Foundation "BASIS."

References

Barklem P.S., 2006, Astronomy & Astrophysics, 462, p. 781
Ben-Jaffel L. and Ballester G.E., 2013, Astronomy & Astrophysics, 553, id. A52
Ben-Jaffel L. and Hosseini S.S., 2010, Astrophysical Journal, 709, p. 1284
Borsa F., Fossati L., Koskinen T., et al., 2021, Nature Astronomy, 6, p. 226
Fossati L., Young M.E., Shulyak D., et al., 2021, Astronomy & Astrophysics, 653, id. A52
Khodachenko M.L., Shaikhislamov I.F., Lammer H., et al., 2017, Astrophysical Journal, 847, p. 126
Madhusudhan N., Lee K.K.M., Mousis O., 2012, Astrophysical Journal, 759, id. L40
McWilliam A., 1997, Annual Review of Astronomy and Astrophysics, 35, p. 503
Oklopčić A. and Hirata C.M., 2018, Astrophysical Journal, 855, id. L11
Salz M., Czesla S., Schneider P.C., et al., 2016, Astronomy & Astrophysics, 586, id. A75
Shaikhislamov I.F., Khodachenko M.L., Sasunov Y.L., et al., 2014, Astrophysical Journal, 795, p. 132
Sitnova T.M., Mashonkina L.I., Ryabchikova T.A., 2013, Astronomy Letters, 39, p. 126
Tasitsiomi A., 2006, Astrophysical Journal, 645, p. 792
Tinsley B.M., 1979, Astrophysical Journal, 229, p. 1046
Trammell G.B., Arras P., Li Z.-Y., 2011, Astrophysical Journal, 728, p. 152
Vidal-Madjar A., Désert J.-M., Lecavelier des Etangs A., et al., 2004, Astrophysical Journal, 604, p. L69

MODERN ASTRONOMY: FROM THE EARLY UNIVERSE TO EXOPLANETS AND BLACK HOLES

Orbital dynamics of the superactive comets 46P/Wirtanen and 103P/Hartley

Yu. Chernetenko and S. Pavlov

Institute of Applied Astronomy of the Russian Academy of Sciences, Kutuzova Embankment, 10, St. Petersburg, 191187 Russia

Abstract. Comets 46P/Wirtanen and 103P/Hartley are Jupiter-family short-period comets. They passed very close to the Earth in 2018 and 2010, respectively, resulting in radar observations and a large number of positional observations and, thus, they caught our attention. Radar observations have revealed the presence of ice grains in the comas surrounding comets, ejected by streams of more volatile compounds dur-ing sublimation, which allowed them to be classified as hyperactive. So far, we have not seen the results of combining positional and radar observations of comet 103P in one orbit. We managed to overcome this assuming the presence of offset between the center-of-light and the center-of-mass in positional observations of the apparition with the radar observations by the value of $S = S_0/r^2$. The components of the vector $S_0(R, T, N)$ in the orbital coordinate system associated with the comet were: $R = 264 \pm 6$ km, $T = 7 \pm 5$ km, $N = -116 \pm 5$ km. In addition, the residuals, $(O - C)$, of both comets revealed systematic deviations that could not be explained by system-atic errors of individual observatories. In addition, the light curves of these comets showed peculiarities matching with $(O - C)$ behavior. To eliminate systematic devia-tions in the positional observations, they were divided into four intervals according to the light curves. We determined a set of parameters of non-gravitational acceleration A_1, A_2, A_3 at each interval simultaneously with the determination of the orbit from all observations. This approach allowed us to get rid of deviations in $(O - C)$. The results obtained for these comets may indicate a truly complex nature of the non-gravitational acceleration acting on these comets.

Keywords: planetary systems: comets: individual (46P/Wirtanen, 103P/Hartley)

DOI: 10.26119/VAK2024.140

1 Introduction

Short-period comets 46P and 103P have a fairly long observation history. Comet 103P was studied by the Deep Impact spacecraft, mission EPOXI, which provided us with a lot of diverse information about the comet activity, its shape and rotation parameters (A'Hearn et al. 2011). Radar observations of the comets made during close approaches to the Earth have revealed the presence of ice grains in the comet's coma (Harmon et al. 2011; Kareta et al. 2023). The ice particles are delivered into the coma by streams of supervolatile substances (CO_2) whose evaporation begins at a lower temperature than the evaporation of H_2O. As a result, more H_2O is produced per unit time than it is possible during sublimation from the surface of the nucleus.

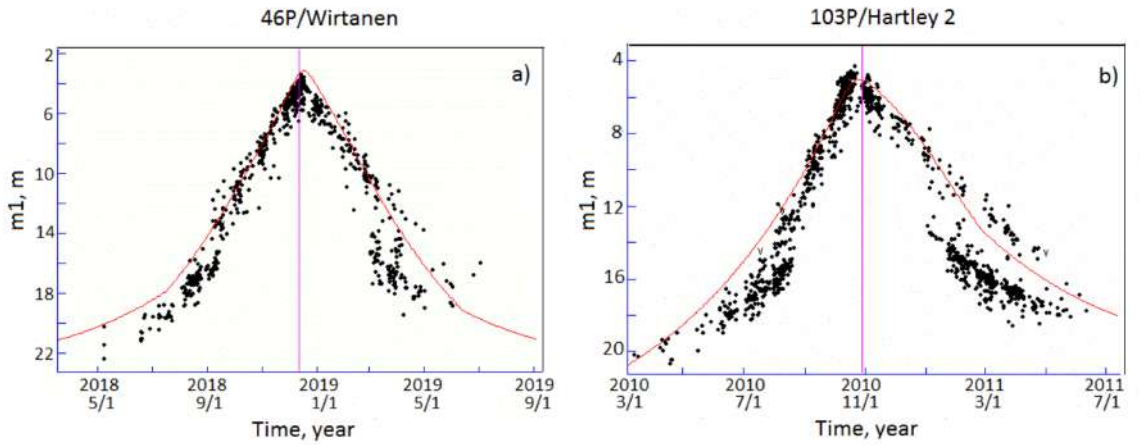

Fig. 1. Light curves of comets 46P – (a) and 103P – (b) created by Seiichi Yoshida: comet total magnitude, m1, versus time.

The light curves of these comets, Figs. 1a, b, are created by Seiichi Yoshida[1]. They demonstrate non-periodic peculiarities which is most likely due to the sublimation activity. By analyzing the comets observations, we revealed systematic deviations in $(O - C)$. Moreover, positional and radar observations of comet 103P could not be combined in one orbit. Therefore, we have set our sights on determining the orbital parameters of these comets using all available observations and identifying the reasons leading to the systematic deviations in residuals.

[1] http://www.aerith.net/

2 Results

Positional observations were taken from the website of the International Minor Planet Center[2], radar observations were taken from the website of NASA's Jet Propulsion Laboratory[3]. The solutions of the systems of normal equations were carried out using the least squares method.

The equations of motion included gravitational perturbations from all eight planets using DE 440 ephemeris (Park et al. 2021) and non-gravitational acceleration according to the Marsden model (Marsden et al. 1973).

To combine the radar and positional observations of 103P, we included an offset in the positional observations of the apparition as 103P approaches the Earth. We assumed that the center-of-light is shifted from the center-of-mass by the value of $S = S_0/r^2$ (r is heliocentric distance of the comet) and we determined the vector S_0 (R, T, N) in the orbital coordinate system along with the orbit improvement. The obtained values were $R = 264\pm6$ km, $T = 7\pm5$ km, $N = -116\pm5$ km. In this case, Root Mean Square Error (RMSE) of the positional observations was about 0.67 arcsec, of time delay observations − 0.48 μs, of Doppler observations − 0.13 Hz. It can be seen that the vector of offset is close to the orbital plane (the angle with the orbital plane is about 23.7°) and directed predominantly away from the Sun. This result does not contradict with the conclusion of the paper A'Hearn et al. (2011).

However, taking offset into account cannot help to remove systematic deviations in the residuals of positional observations, Fig. 2a, the limits of ± 3 RMSE are shown by red lines. These deviations can't be explained by the errors of the individual observatories, since the comet was observed by 168 observatories and the observations were evenly distributed. Therefore, systematic deviations are probably related with the complex rotation of the irregularly shaped nucleus which may include: 1) the seasonal effect of non-gravitational acceleration; 2) tumbling of the axis of rotation; 3) changes in the sublimation rate, approximated in this work by the function $g(r)$ (Marsden et al. 1973).

Since the features in the comet's light curve may indicate changes in the comet's sublimation activity, we used them to divide the observations into four intervals in which particular parameters of non-gravitational acceleration were determined. We used this approach to get rid of systematic deviations in $(O - C)$. We determined the parameters of non-gravitation accelerations separately in each interval together with the orbital parameters common to the entire observation period (Table 1). Since

[2] http://www.minorplanetcenter.net/
[3] https://ssd.jpl.nasa.gov/sb/radar.html

there are about 6000 observations of the comet during this apparition, such approach turned out to be possible. By analyzing the data in Table 1, we can say that the highest value of non-gravitation acceleration was during the first interval. This may be explained by the sublimation of CO_2 during the comet's approach to the Sun. The values of transversal parameter of non-gravitational acceleration, A_2, changed sign after passing perihelion, that may be caused either by tumbling of the comet nucleus or by substantially irregularly shaped nucleus of 103P. Δv in Table 1 shows the changes of the comet's velocity along the orbit due to the action of the transversal acceleration A_2.

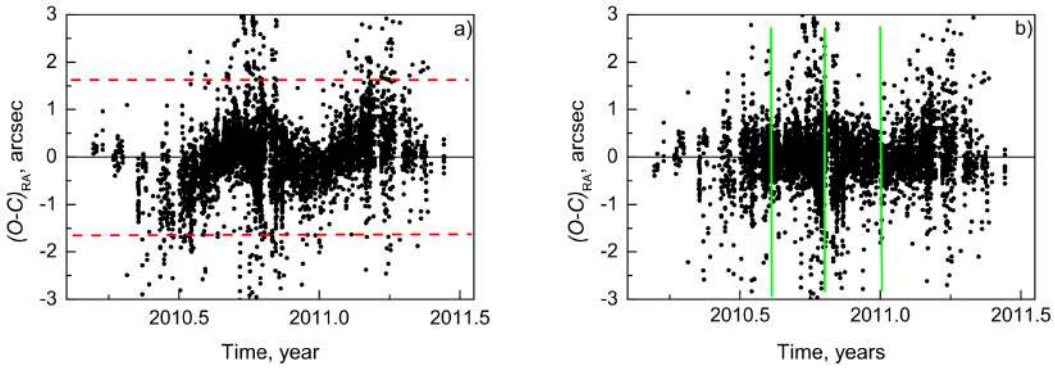

Fig. 2. Residuals in right ascension for comet 103P: (a) – for entire interval, (b) – for four intervals. Red lines on the panel (a) show ±3 RMSE limits, green lines on the panel (b) show individual intervals.

Table 1. Non-gravitational parameters of the comet 103P ($A_1, A_2, A_3 \cdot 10^{-8}$ au/day^{-2}).

Para-	Observation interval, year				Entire interval, year
meter	2010.16-2010.66	2010.66-2010.82	2010.82-2011.00	2011.00-2011.45	2010.16-2011.45
A_1	0.231±0.123	0.518±0.024	0.358±0.020	−0.490±0.060	0.092±0.003
A_2	−0.641±0.046	−0.318±0.018	0.333±0.028	0.227±0.034	0.075±0.003
A_3	−0.234±0.056	0.224±0.019	−0.022±0.021	0.021±0.020	0.004±0.002
Δv, cm/s	−1.10	−0.66	0.53	0.39	0.13
RMSE	0.484 arcsec				0.540 arcsec

It was not necessary to account offset between the center-of-light and the center-of-mass to combine radar and positional observations of comet 46P; however, we

evaluated the time delay for the maximum of $g(r)$, which was about 14 days. Figure 3a shows $(O-C)$ after orbit improvement. One can see systematic deviations in the residuals within ± 3 RMSE similar to 103P. As for comet 103P, to get rid of them, we divided the observations into four intervals according to the light curve, Fig. 1a, and determined the parameters of non-gravitational accelerations at each interval separately along with the orbit parameters. Figure 3b shows that this allowed us to significantly reduce systematic deviations; however, the RMSE values for all observations did not change much. Table 2 presents the parameters of non-gravitational accelerations obtained for four intervals and for entire interval of observations.

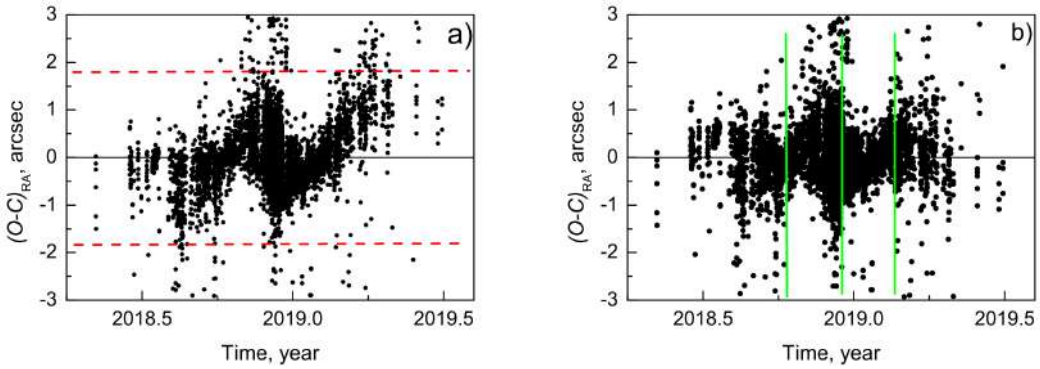

Fig. 3. Residuals in right ascension for comet 46P: (a) – for entire interval, (b) – for four intervals. Red lines on the panel (a) show ±3 RMSE limits, green lines on the panel (b) show individual intervals.

Table 2. Non-gravitational parameters of the comet 46P ($A_1, A_2, A_3 \cdot 10^{-8}$ au/day^{-2}).

Parameter	Observation interval, year				Entire interval, year
	2018.35-2018.81	2018.81-2018.96	2018.96-2019.10	2019.10-2019.50	2018.35-2019.50
A_1	0.823±0.101	0.466±0.008	0.344±0.040	1.566±0.193	0.446±0.002
A_2	−0.463±0.021	−0.231±0.014	−0.295±0.027	0.530±0.040	−0.209±0.003
A_3	0.157±0.027	0.084±0.011	−0.082±0.028	0.499±0.076	0.075±0.002
Δv, cm/s	−0.81	−0.40	−0.51	0.92	−0.31
RMSE, optic.	0.535 arcsec				0.601 arcsec
RMSE, delay	0.680 μs				0.691 μs
RMSE, Dopp.	0.003 Hz				0.004 Hz

3 Summary

In this research, we obtained the orbits of hyperactive comets 46P and 103P, and considered in more detail their apparitions during which they came close to the Earth. Combining radar and positional observations of comet 103P was possible only by taking into account the offset between the center-of-light and the center-of-mass in positional observations. The total offset was ~ 300 km at a distance of 1 au.

We also noticed systematic deviations in $(O - C)$ in the positional observations of both comets. Dividing the entire observation interval into several intervals in accordance with the light curves and determining the parameters of non-gravitational acceleration in each interval helped to get rid of them. This allowed us to reveal the irregular nature of the change in non-gravitational acceleration within one apparition, which is probably a consequence of the complex rotation of the comet nuclei.

Acknowledgements. This research has made use of data and services provided by the International Astronomical Union's Minor Planet Center and NASA's Jet Propulsion Laboratory.

References

A'Hearn M.F., Belton M.J.S., Delamere W.A., et al., 2011, Science, 332, 6036, p. 1396
Harmon J.K., Nolan M.C., Howell E.S., et al., 2011, Astrophysical Journal Letters, 734, 1, id. L1, p. 1
Kareta T., Noonan J.W., Harris W.M., et al., 2023, Planetary Science Journal, 4, 5, p. 85
Marsden B.G., Sekanina Z., and Yeomans D.K., 1973, Astronomical Journal, 78, p. 211
Park R.S., Folkner W.M., Williams J.G., et al., 2021, Astronomical Journal, 161, 3, id. 105

BAK 2024 MODERN ASTRONOMY: FROM THE EARLY UNIVERSE TO EXOPLANETS AND BLACK HOLES 300 years Russian Academy of Sciences

Length of day multifractal dynamics

S. Denisenko and S. Petrov

Saint-Petersburg State University, 7-9 Universitetskaya Emb., St. Petersburg, 199034 Russia

Abstract. In this work, the power spectral densities (PSD) of several combined and instrumental length of day (LOD) multifractal time series are computed. As a result, a stable power spectrum, practically independent of the type of time series, of multifractal structure is obtained. The power spectrum of the duration of the day can be divided into three frequency bands. For periods of less than three months, the LOD behaves like a power noise with a score close to −1.5. Over periods of three months to three years, LOD behaves almost like white noise. Finally, over periods of more than three years, the LOD also exhibits power noise behavior with a score of about −1.5. It turns out that the revealed structure practically does not depend on the type of time series (combined or instrumental), its length, and the parameters of the method for assessing PSD.

Keywords: Earth: rotation; length of day; fractals

DOI: 10.26119/VAK2024.141

1 Introduction

As a measure of the speed of the Earth's rotational motion, the duration of the day or length of day (LOD) is traditionally used, that is, the deviation of the instantaneous duration of the average solar day from 86 400 atomic seconds. It is also known, that the LOD time series exhibit a complex structure in which small, but regular, tidal and seasonal fluctuations are superimposed on powerful irregular fluctuations of unknown nature with a characteristic time scale from units to tens of years.

Regular tidal LOD variations are basically due to deformations of the solid Earth under the action of zonal tides. They are well described by simple linear theory of tidal deformation with the use of Love numbers. Typical amplitude of tidal variations are of the order of fractions of millisecond. Regular seasonal LOD fluctuations are due to atmospheric circulation, namely, the motion term of the atsmospheric angular mometum, which is due to variations of zonal atmospheric winds.

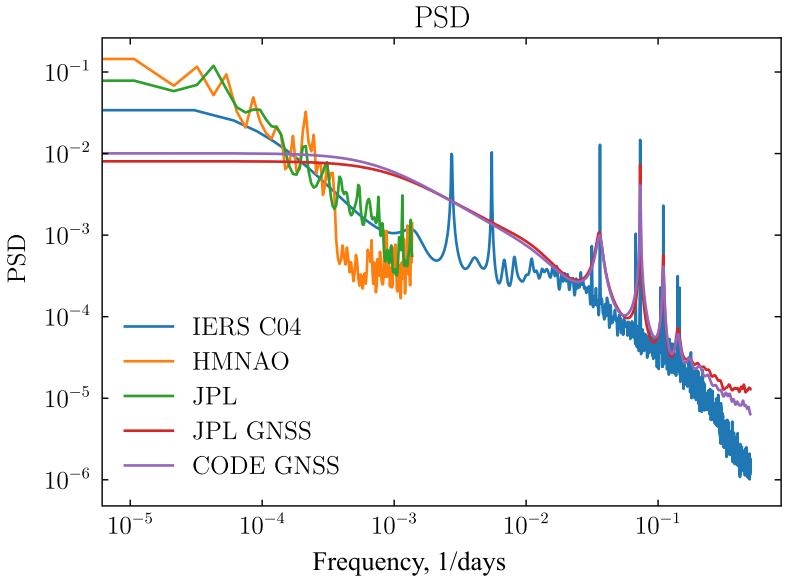

Fig. 1. Power spectrum density for different series.

On the other hand, on the regular tidal and seasonal LOD variations, huge irregular or chaotic variations of decadal timesacle are superimposed. Their nature is still unknown and is probably conditioned by currents in the Earth's liquid core, or variations of the Solar wind, or both of these effects together.

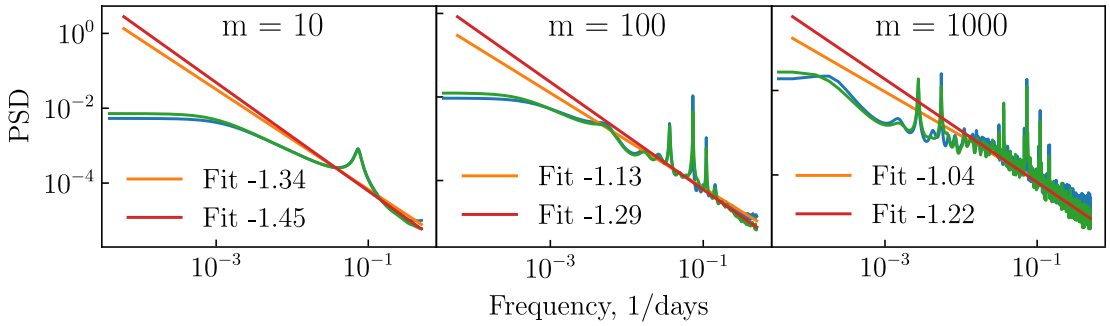

Fig. 2. Linear fit of PSD for different filter length for Burg metod, JPL (blue) and CODE (green).

Putting aside the physical nature of decadal LOD fluctuations, in this work, we concentrate on phenomenological analysis of the LOD time series. Since the appearance of the decadal LOD fluctuations is nonlinear, then it is natural to expect that this phenomenon may exhibit a fractal structure, that is already shown by e.g. Frede & Mazzega (1999a,b). These authors have shown that long term structure of the LOD time series is chaotic and fractal. In this study, we concentrate on multifractal structure of the LOD time series with the use of their spectral analysis.

2 Observational data

We selected five different LOD time series: estimates from the combined Jet Propulsion Laboratory (JPL) Earth orientation series LUNAR97[1], Her Majesty's Nautical Almanac Office (HMNAO) measurement of the Earth's rotation from 720 BC to AD 2015 (Morrison et al. 2021), International Earth Rotation and Reference Systems Service (IERS) combined Earth rotation parameter solution C04, and Center for Orbit Determination in Europe (CODE) operational series[2]. Of all these data, HMNAO and JPL that have been going on since the 17th century are the longest ones. The combined IERS C04 series that have been going on since the 19th century are shorter. Finally, JPL Global Navigation Satellite Systems (GNSS) and CODE GNSS are the instrumental series based on GNSS data alone. They are the shortest ones and started only about 25 years ago.

[1] Gross R.S., Marcus S.L., Dickey J.O., 1993, Determination of the Excess Length-of-Day Since 1630, JPL Open Repository https://hdl.handle.net/2014/35000

[2] Dach R., Schaer S., Daniel A., et al., 2024, CODE final product series for the IGS, Published by Astronomical Institute, University of Bern https://boris.unibe.ch/197025/

It is also important to note that accuracy of these series varies significantly not only from series to series but also may differ for various time periods. Also, the longest series are combined from different observations from old and imprecise Lunar occultations to modern and most precise GNSS and very-long-baseline interferometry (VLBI) data.

3 Spectral analysis of LOD series

The well known Burg or Maximum entropy spectral estimation method is used in this study. The only variation of the standard method implemented here is that we do not limit the filter length, but instead allow it to be as big as as necessary to obtain a decent spectral resolution.

In Fig. 1, the power spectral densities for different LOD time series is shown in logarithmic scale on both axes. It can be seen from the figure that different LOD time series reveal similar power spectra. Differences in spectra may be due to different observational data that was used and degree of smoothing in the series.

In Fig. 2, power spectra for GNSS series are shown for different values of filter length in Burg method. It can be seen that values of the fitted exponents converge well with the increase of filter length. However, JPL and CODE series give slightly different fitted exponents. This effect should be the subject of further analysis.

4 Summary

A stable multifractal structure, practically independent of the type of time series, was revealed in the resulting power spectrum. The power spectrum of the duration of the day can be divided into three frequency ranges. For periods of less than three months and more than three years, LOD behaves like a power noise with a score close to -1.5. For periods from three months to three years, LOD behaves almost like white noise. It turns out that the revealed structure practically does not depend on the type of time series (combined or instrumental), its length, and the parameters of the spectral power estimation method.

References

Frede V. and Mazzega P., 1999a, Geophysical Journal International, 137, 2, p. 551

Frede V. and Mazzega P., 1999b, Geophysical Journal International, 137, 2, p. 565

Morrison L.V., Stephenson F.R., Hohenkerk C.Y., 2021, Proceedings of the Royal Society A, 477, p. 20200776

VAK 2024 MODERN ASTRONOMY: FROM THE EARLY UNIVERSE TO EXOPLANETS AND BLACK HOLES 300 years Russian Academy of Sciences

On the issues of estimating the accuracy of Earth rotation parameters

I. Gayazov, S. Kurdubov, and E. Skurikhina

Institute of Applied Astronomy of the Russian Academy of Sciences, 10 Kutuzov Emb., St. Petersburg, 191187 Russia

Abstract. Earth rotation parameters (ERP) are determined at the Institute of Applied Astronomy (IAA) by processing the following types of observations: Very Long Baseline Interferometry (VLBI), Global Navigation Satellite Systems (GNSS) and Satellite Laser Ranging (SLR). The IAA also carries out special sessions of VLBI observations on radio telescopes of the Quasar network for ERP determination in various modes. The accuracy of the obtained series is estimated by comparison with the combined results of the International Earth Rotation and Reference Systems Service (IERS) usually accepted as reference. The accuracy of various ERP series has been analyzed also using a method based on the assumption that there can be no abrupt changes in ERP and after removing the intra-day variations the series should be sufficiently smooth. In this method the evaluation is performed without calculating the differences of two independent series and is related only to the internal properties of the series. The article presents an overview of the results of the analysis and concludes that the proposed technique can be used to estimate the accuracy of the ERP series.

Keywords: Earth: rotation; methods: observational, statistical

DOI: 10.26119/VAK2024.142

1 Introduction

Earth rotation parameters consisting of Earth pole coordinates (Xp, Yp), celestial pole coordinates (Xc, Yc) and Universal time (UT1) are determined at present by methods of VLBI, GNSS and SLR. These methods determine parameters with different completeness, discreteness and frequency as shown in Table 1. The accuracy of the same parameters obtained by different methods may differ significantly. It is supposed that the combination of results obtained by various analysis centers based on different types of observations gives the highest accuracy.

Table 1. Time characteristics of ERP determination techniques (all values in days).

Parameters	VLBI method		GNSS method		SLR method	
	Sample interval	Observations duration	Sample interval	Observations duration	Sample interval	Observations duration
Xp, Yp	3	1	0.25	1	1	2–4
Xc, Yc	3	1				
UT1	1, 3	0.042, 1				

Support for the functioning of global navigation satellite systems imposes the highest requirements on the accuracy of ERP. Estimation of the real accuracy of the parameters remains an open problem for both the combined series and the individual ones produced by analysis centers.

2 Motivation

Within the framework of ERP service operating at the IAA since 1995 (Gayazov et al. 2016) ERP are determined from all types of observations performed at global network stations. Since 2012 IAA ERP service also conducts processing of special sessions of VLBI observations carried out on radio telescopes of the Quasar network for ERP determination (Ivanov et al. 2022). Since 2016 1^{h} sessions on RT-13 radio telescopes have been performed up to 6 times a day for UT1 determination. The accuracy of all series is usually estimated by comparison with the combined data of the IERS[1] accepted as reference. Comparison of UT1 series obtained from 1^{h} sessions of VLBI observations on Quasar network radio telescopes with the final series of IERS is shown in Fig. 1. Depending on time interval values of root-mean-square (RMS) of differences are within 50–60 μs for UT1 series from single baseline observations on radio telescopes RT-32 (Fig. 1a) and within 20–30 μs for series obtained from observations on three new generation radio telescopes RT-13 (Fig. 1b).

The necessity of an adequate assessment of the accuracy of UT1 series from Quasar network observations was the main motivation for this analysis.

[1] https://www.iers.org/

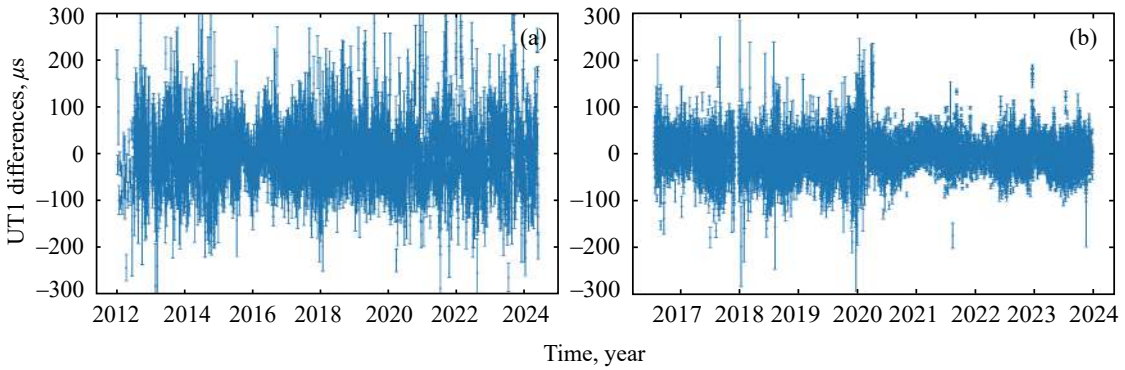

Fig. 1. UT1 series from Quasar network observations compared to IERS finals.

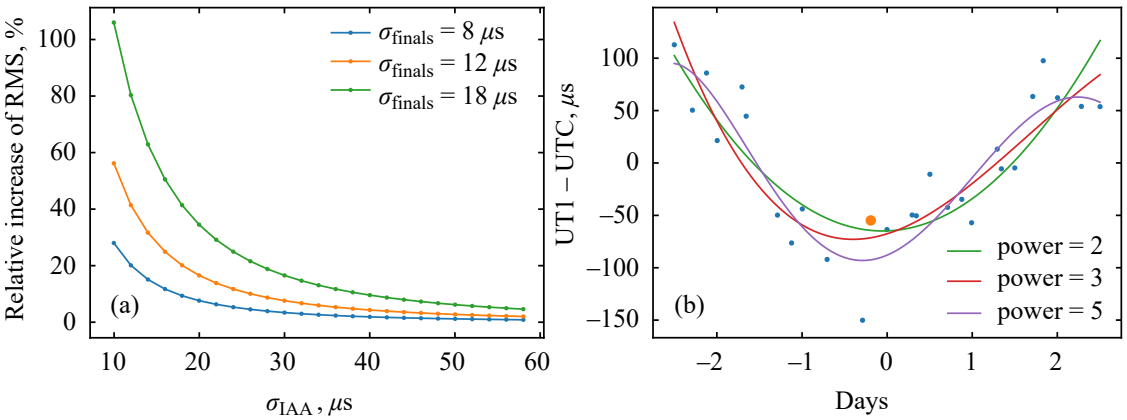

Fig. 2. RMS dependence on errors of IERS finals series (a) and errors from interpolation by various degree polynomials (b).

There are several types of ERP accuracy estimations used in practice:

1) formal estimates from the Least Square Method solution;
2) estimates obtained when combining results of analysis centers within one technique;
3) estimates obtained when combining results of analysis centers and of different techniques to form the IERS finals series;
4) estimates obtained by comparing with IERS finals.

Estimates can be obtained also from internal consistency analysis of series based on the smoothness criterion. This approach has been used in our analysis.

When we compare our series with series IERS finals the variances of both series contribute as RMS $= \sqrt{\sigma^2_{\text{IAA}} + \sigma^2_{\text{finals}}}$. This cannot be neglected in the case when the

values of the variances are close. Fig. 2a demonstrates the essential dependence of RMS on the accuracy of the finals series in the area of 20 μs.

When comparing individual series with IERS combined data additional differences occur due to interpolation errors depending on degree of used polynomials (Fig. 2b).

The standard approach to estimating the accuracy of series consists of evaluating RMS by comparing with IERS finals. But a number of questions have been raised about the quality of IERS series of UT1 during the past few years. The combining procedure for obtaining the IERS series has not been described in detail for recent years (IERS annual reports have not been published since 2019). Weights of individual series of analysis centers are unknown. Monthly RMS values for UT1 results of different analysis centers taken from official IERS bulletins B are presented in Fig. 3 for $24^{\rm h}$ sessions (a) and $1^{\rm h}$ sessions (b). One can see increasing dispersion of results of analysis centers after 2020.

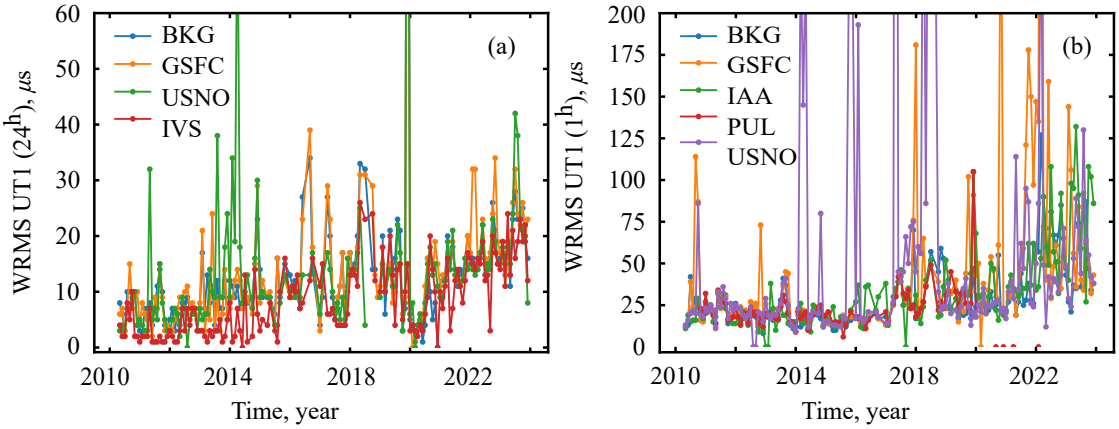

Fig. 3. Weighted RMS of monthly UT1 series of analysis centers from $24^{\rm h}$ (a) and $1^{\rm h}$ (b) VLBI sessions.

3 Analysis of smoothed series

We analyzed various ERP series using a method (Kurdubov & Skurikhina 2021) based on the assumption that changes in the Earth's rotation cannot occur too fast and after removal of intra-day variations the UT1 series should be smooth enough. A smoothed series is constructed by sliding interpolation of values by polynomials of various degree using $2N$ points of the series around the interpolated point excepting the point itself (N points forward and backward). RMS of differences of the original

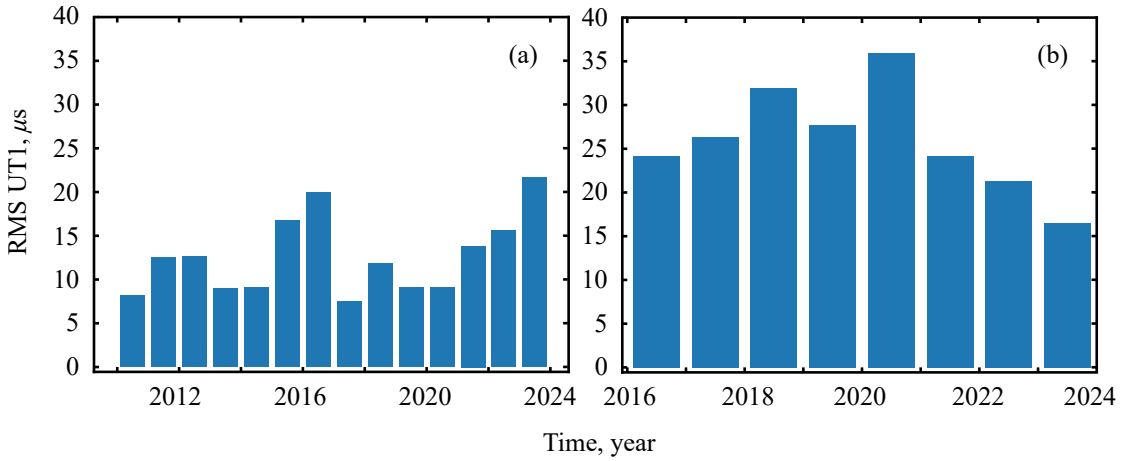

Fig. 4. Annually averaged accuracy estimations of UT1 series from IERS finals (a) and from Quasar RT-13 1^{h} sessions (b).

and interpolated series are used as an estimate of the internal accuracy of the series. From analysis of the UT1 series IERS finals in (Kurdubov & Skurikhina 2021) the optimal values for N and the polynomial degree (P) have been settled as $N = 3$ and $P = 5$.

This technique has been used for the analysis of final UT1 series of IERS. Annual averages of obtained internal estimates for UT1 from IERS finals starting from 2010 are presented in Fig. 4a. Analogous results for UT1 series obtained from observations of the Quasar RT-13 stations network are shown in Fig. 4b.

It can be seen in Fig. 4a that internal estimates for IERS finals are close to dispersion of data in Fig. 3a and have shown an analogous degradation trend in recent years as seen in Fig. 3a, b. We suppose that the following factors can be responsible for this:

1) different analysis centers present a different set of products;
2) using observations of new VGOS stations with inaccurate coordinates;
3) unevenness of data distribution (series with unequal moments, different density);
4) undeclared changes in IERS combination scheme;
5) influence of interpolation schemes;
6) errors in intra-day variations model or its degradation with time.

As a good test for the technique used we consider its implementation for pole coordinates obtained from GNSS observations. Fig. 5a, b show the data from IERS Bulletins B and Fig. 5c, d show annual average values of RMS obtained using the proposed technique. It can be seen that the common level of our estimations is very close to dispersion of results of different analysis centers.

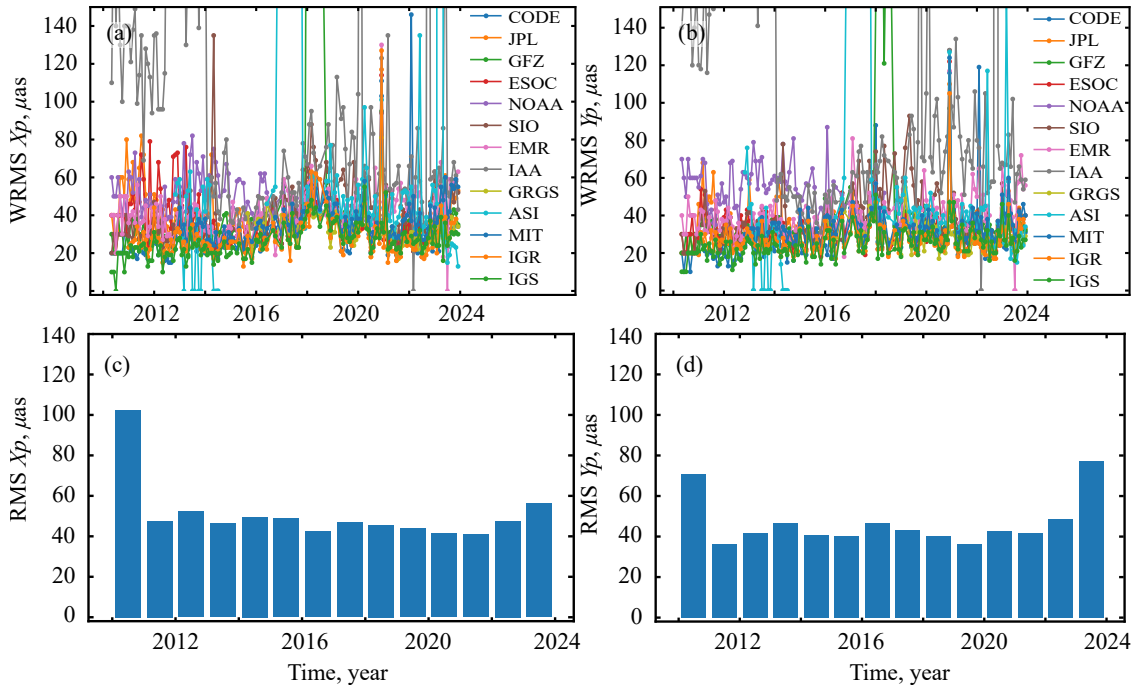

Fig. 5. Bulletine B data for pole coordinates from GNSS observations (a, b) and annual estimations obtained using proposed technique (c, d).

4 Summary

UT1 series IERS finals have shown noticeable degradation of accuracy in recent years due to a few negatively affecting factors. It is important to develop independent criteria for estimating the accuracy of our own ERP series. Adequate accuracy estimates can be obtained using the technique based on the smoothness criterion. Estimates of internal accuracy of UT1 series obtained from Quasar RT-13 network observations in recent years are at the same level as that of UT1 series from IERS finals.

References

Gayazov I.S., Gubanov V.S., Kurdubov S.L., et al., 2016, Transactions of IAA RAS, 39, p. 23

Ivanov D., Ipatov I., Marshalov D., et al., 2022, IVS 2022 General Meeting Proceedings, ed. Armstrong K.L., Behrend D., Baver K.D., NASA/CP-20220018789, p. 37

Kurdubov S.L. and Skurikhina E.A., 2021, Transactions of IAA RAS., 57, p. 23

MODERN ASTRONOMY: FROM THE EARLY UNIVERSE TO EXOPLANETS AND BLACK HOLES

Exchange of meteorites between the terrestrial planets and the Moon

S. Ipatov

Vernadsky Institute of Geochemistry and Analytical Chemistry of RAS, Moscow, 119991 Russia

Abstract. The evolution of the orbits of bodies ejected from the Earth, Moon, Mercury and Mars was studied. The probabilities of collisions of ejected bodies with planets depended on ejection velocities, ejection angles and points of ejection. At a velocity of ejection close to the parabolic velocity, most of bodies fell onto the planet from which they had been ejected. Below results are presented not for such small ejection velocities. At ejection velocities about 12-14 km/s, the fraction of bodies ejected from the Earth that fall back onto the Earth was about 0.15-0.25. The total number of bodies ejected from the Earth and delivered to the Earth and Venus probably did not differ m uch. T he p robability o f c ollisions o f b odies e jected f rom t he E arth w ith the Moon moving in its present orbit was of the order of 0.01. Probabilities of collisions of bodies ejected from the Earth with Mercury were about 0.02-0.08 at ejection velocities greater than 11.3 km/s. The probabilities of collisions of bodies ejected from the Earth with Mars did not exceed 0.025. For the ejection of bodies from the present orbit of the Moon, probabilities of collisions of ejected bodies with planets were similar to those ejected from the Earth if we consider smaller ejection velocities from the Moon than from the Earth. The probability of a collision of a body ejected from Mars with Mars usually did not exceed 0.04 at an ejection velocity greater than 5.3 km/s. The fraction of bodies ejected from Mars and collided with Mercury was typically less than 0.08. Probabilities of collisions of bodies ejected from Mars with the Earth and Venus were about 0.1-0.2 (each) at an ejection velocity between 5.05 and 10 km/s. Most of bodies ejected from Mercury fall back onto Mercury. Probabilities of collisions of bodies ejected from Mercury with the Earth typically did not exceed 0.02 and 0.1 at an ejection velocity less than 8 km/s and 15 km/s, respectively. The fraction of bodies ejected from Mercury and collided with Venus was greater than that with the Earth typically by an order of magnitude. Probabilities of collisions of bodies with Venus were about 0.1-0.3 at a velocity of ejection from Mercury between 4.3 and 10 km/s.

Keywords: planets and satellites: terrestrial planets; meteorites, meteors, meteoroids

DOI: 10.26119/VAK2024.143

1 Introduction and initial data

Gladman et al. (2005) and Reyes–Ruiz et al. (2012) studied the motion of bodies ejected from the Earth at collisions of bodies-impactors with the Earth during 30 Kyr. Considered initial velocities were perpendicular to the surface of the Earth. Wetherill (1984) considered the evolution of the orbits of bodies ejected from Mars in random directions with velocity of ejection varied from 5 to 7 km/s. Gladman et al. (1995, 1996) and Gladman (1997) simulated the evolution of the orbits of bodies ejected from the Moon (with ejection velocities of 2.3 and 3.5 km/s), Mars (with the values $v_{inf} = (v_{ej}^2 - v_{esc}^2)^{1/2}$ of a velocity at the infinity from 1 to 3.3 km/s, where v_{esc} is the escape velocity), and Mercury (with v_{inf}=1 km/s). They studied characteristic times before the collisions of these bodies with the Earth and the fraction of bodies that fell onto the Earth. Gladman & Coffey (2009) studied the planetary-influenced motion of bodies ejected from Mercury with velocities equal to 4, 9, 14, 20, and 25 km/s.

In each my calculation variant, the motion of $N_\circ$=250 bodies ejected from a celestial object was studied for fixed values of an ejection angle i_{ej}, a velocity v_{ej} of ejection, a place of ejection, and a time step t_s of integration. In different variants, the values of i_{ej} equaled to 15°, 30°, 45°, 60°, 89° or 90°. For ejection from the Earth v_{ej} equaled mainly to 11.22, 11.5, 12, 12.7, 14, 16.4, or 20 km/s. In most calculations, bodies started directly from surface of a considered celectial object. For Mars, Mercury, and Moon, v_{ej} varied from a parabolic velocity on the surface of a celestial object to 20 km/s. In each variant, bodies started from one of six considered opposite points on planet's surface (Ipatov, 2024). For the starting points F and C, the motion of the bodies started at most and least distant points of the planet's surface from the Sun (located on the line from the Sun to the planet), respectively. For the points W and B, the bodies started from the forward point on the planet's surface in the direction of the planet's motion and from the back point on the opposite side of the planet, respectively (from apex and antapex). For the points U and D, the bodies started from points on the planet's surface with the maximum and minimum values of z (with the z axis perpendicular to the plane of the planet's orbit), respectively.

The motion of bodies was studied during the dynamical lifetime T_{end} of all bodies, which equaled to a few hundred Myrs. During this time interval, all bodies collided with planets or the Sun or were ejected into hyperbolic orbits. The gravitational influence of the Sun and all eight planets was taken into account. Bodies that collided with planets or the Sun or reached 2000 AU from the Sun were excluded from integration. The symplectic code from the SWIFT integration package by Levison & Duncan (1994) was used for integration of the motion equations. The considered time integration step t_s equaled to 1, 2, 5, or 10 days. For the Earth and Mars, the results

of calculations with different t_s were compared and gave similar results. For ejection from the Earth, Moon, and Mars most of calculations were done with t_s=5 days. Motion of bodies ejected from Mercury studied with t_s=1 day. Probabilities of collisions of bodies with the Moon were calculated based on the arrays of orbital elements of bodies (Ipatov, 2019, 2024). Such ejection was often at the stage of accumulation of the terrestrial planets and at the Late Heavy Bombardment.

2 Results of calculations

2.1 Probabilities of collisions of bodies ejected from the Earth with the Earth and the Moon

At ejection velocities $v_{ej} \leq 11.25$ km/s, i.e., slightly greater than the parabolic velocity, most of the bodies ejected from the Earth fell back onto the Earth. At v_{ej} equal to 11.5 or 12 km/s, the values of the probabilities p_e of collisions of bodies with the Earth did not differ much for different starting points on the Earth's surface. At v_{ej}=11.5 km/s, the probability p_e of collisions of bodies ejected from the Earth with the Earth was about 0.2–0.3. At ejection velocities about 12–14 km/s, the value of p_e was about 0.15–0.25, mean velocities of collisions of bodies with the Earth and the Moon were about 14–20 and 10–16 km/s, respectively. The value of p_e is greater for smaller ejection velocity. The ratio of the probability of collisions of bodies with the Earth to the probabilities of collisions of bodies with other planets and the Sun usually decreased with time. For example, the ratio of probabilities of collisions of bodies with the Sun at T=T_{end} and at T=10 Myr could reach 5, although the ratio of p_e at these times could be less than 1.5. The significant difference in the results for different ejection points was for bodies ejected from the forward point W of the Earth's motion at $v_{ej} \geq 16.4$ km/s and $i_{ej} \geq 45°$. In this case, more than 80% of the bodies were thrown into hyperbolic orbits, most of other bodies collided with the Sun, and p_E could be 0.

The probability of collisions of bodies ejected from the Earth with the Moon moving in its present orbit was of the order of 0.01 (Ipatov, 2024). A large Moon embryo should be formed close to the Earth in order to accumulate material ejected from the Earth's mantle which is not rich in iron. For more efficient growth of the Moon embryo, it is desirable that after some collisions of impactor bodies with the Earth, the ejected bodies did not simply fly out of the crater, but some of the matter went into orbits around the Earth, as in the multi-impact model.

2.2 Probabilities of collisions of bodies ejected from the Earth with Venus, Mercury, Mars, and the Sun

In considered calculations, the probabilities p_v of collisions of the bodies ejected from the Earth with Venus at the end of evolution were often about 0.2–0.35 at $11.5 \leq v_{ej} \leq 16.4$ km/s. The values of p_v were about p_e at $v_{ej}=11.5$ km/s, were greater than p_e at $v_{ej} \geq 12$ km/s, and were less than p_e at $v_{ej} \leq 11.4$ km/s. The total number of ejected bodies delivered to the Earth and Venus probably did not differ much. The obtained results testify in favour of that the upper layers of the Earth and Venus can contain similar material. Probabilities of collisions of bodies ejected from the Earth with Mercury at $T=T_{end}$ were about 0.02–0.08 and 0.03–0.05 at $11.3 \leq v_{ej} \leq 11.5$ and $12 \leq v_{ej} \leq 20$ km/s, respectively. The probabilities of collisions of bodies with Mars were smaller than those with Mercury and did not exceed 0.012 and 0.025 at $T=10$ Myr and $T=T_{end}$, respectively. More material ejected from the Earth was delivered to Mercury than to Mars. The probabilities of collisions of bodies with Jupiter were of the order of 0.001. The fraction of bodies colliding with the Sun often ranged from 0.2 to 0.5 at $11.3 \leq v_{ej} \leq 14$ km/s. The fraction of bodies ejected into hyperbolic orbits was mainly greater for a greater ejection velocity. During a whole considered time interval it did not exceed 0.1 at $v_{ej} \leq 12$ km/s. At $v_{ej} \geq 16.4$ km/s and $i_{ej} \geq 60°$, all bodies were ejected from the Solar System if they started from the front (in the direction of the motion) point W of the Earth. At $i_{ej}=45°$ and $v_{ej}=16.4$ km/s, the fraction of bodies ejected from the Solar System was about 0.25–0.27 if points of ejection were not in the front or back of the Earth's motion. The fractions of collisions of bodies ejected from the Earth with planets could be similar to the fractions of collisions of planetesimals with planets for planetesimals that were left in the feeding zone of the Earth at the late stages of its formation. More detailed studies of the migration of bodies ejected from the Earth are presented in the paper which is in press in Icarus.

2.3 Probabilities of collisions of bodies ejected from the Moon with the Earth

At the ejection of bodies from point F for the present orbit of the Moon (with its distance from the Earth $r_{ME}=60r_E$, where r_E is the radius of the Earth), $T=10$ Myr, and $30° \leq i_{ej} \leq 60°$, p_e was about 0.2–0.25 at $v_{ej}=2.5$ km/s, 0.13–0.14 at $v_{ej}=5$ km/s, and 0.06–0.07 at $12 \leq v_{ej} \leq 16.4$ km/s. At $T=T_{end}$ and $15° \leq i_{ej} \leq 89°$ p_e was about 0.27–0.35 at $v_{ej}=2.5$ km/s, 0.2–0.25 at $v_{ej}=5$ km/s, and 0.1–0.14 at $12 \leq v_{ej} \leq 16.4$ km/s. That is, at velocities slightly greater than the parabolic velocity, the values of p_e could be approximately the same for the ejection of bodies from the Earth and the Moon, but for different ejection velocities, if we take into account the lower minimum velocities of bodies ejected from the Moon. For $v_{ej}=11.22$ km/s, $T=10$

Myr, $30^\circ \le i_{ej} \le 60^\circ$, and $r_{ME}=37r_E$, the value of p_E was about 0.04–0.13. Bodies ejected from the lunar embryo, which was moving close to the Earth, fell back onto the Earth and the Moon if their ejection velocity was less than the corresponding parabolic velocity. At $v_{ej}=2.5$ km/s and $r_{ME}=3r_E$ the dynamical lifetime of the ejected bodies was less than 5 days. At $r_{ME}=5r_E$ and $v_{ej}=2.5$ km/s, most of the ejected bodies quickly fell onto the Earth, but at $i_{ej} \le 30^\circ$ some of the bodies left the Hill sphere of the Earth. At $v_{ej}=5$ km/s (approximately the parabolic velocity of the Earth at $r_{ME}=5r_E$), $T=T_{end}$, and $r_{ME}=5r_E$, the value of p_e was about 0.3 (0.26–0.37) for i_{ej} from 15° to 89°.

2.4 Probabilities of collisions of bodies ejected from Mars with planets

The probability p_{ma} of a collision of a body ejected from Mars with Mars was considerable only at an ejection velocity v_{ej} close to the parabolic velocity. Below the results for $v_{ej} \ge 5.05$ km/s are presented. For such v_{ej}, the values of p_{ma} were relatively small. For ejection of bodies from points C, D, F, and U, the values of p_{ma} were mainly about 0.04–0.25, 0.01–0.04, and 0–0.02 at $5.05 \le v_{ej} \le 5.3$, $5.5 \le v_{ej} \le 10$, and $15 \le v_{ej} \le 20$ km/s, respectively. For point B, the value of p_{ma} was typically smaller than for the above points. For point W, $p_{ma}=0$ at $15 \le v_{ej} \le 20$ km/s, and p_{ma} could exceed 0.3 at $v_{ej}=5.05$ km/s. Probabilities p_e of collisions of bodies ejected from Mars with the Earth for points C, D, F, and U were mainly about 0.08–0.16 and 0–0.16 at $5.05 \le v_{ej} \le 10$ and $15 \le v_{ej} \le 20$ km/s, respectively. For point B, p_e could exceed 0.24. For point W, the values of p_e were in the range between 0 and 0.15. Often, at $v_{ej} \ge 5.2$ km/s, the probabilities of collisions of bodies with Venus were slightly greater than those with the Earth. Probabilities p_v of collisions of bodies ejected from Mars with Venus for points C, D, F, and U were mainly about 0.08–0.2 and 0.02–0.2 at $5.05 \le v_{ej} \le 10$ and $15 \le v_{ej} \le 20$ km/s, respectively. For point B, the value of p_e could exceed 0.3. For point W, p_e was in the range between 0 and 0.18. Bodies ejected from Mars could collide with the Earth after 0.1 Myr, and some of the bodies could collide with the Earth after hundreds of million years. For example, for point F at $v_{ej}=6$ km/s, $i_{ej}=45^\circ$, $t_s=5^d$, and $N_\circ=250$, there were 32 collisions with the Earth between 0.22 and 270.9 Myr. Among these collisions there were 4, 7, 6, 7, 2, 4, and 2 collisions at time $t<1$, $1<t<5$, $5<t<20$, $20<t<50$, $50<t<200$, and $t>200$ Myr, respectively. In this case about a half of bodies collided with the Earth after 20 Myr, and some martian meteorites could travel for tens of million years in space before their collisions with the Earth.

The fraction of bodies ejected from Mars and then colliding with Mercury was usually less than 0.06 and was greater than the fraction of bodies colliding with Mars for $v_{ej} \ge 6$ km/s. For ejection from points C, D, F, and U, the values of the fraction

p_{me} of bodies collided with Mercury were mainly about 0.02–0.08 at $5.05 \leq v_{ej} \leq 20$ km/s. For point B, the value of p_{me} was in a wider range (0.016–0.2) than for the above four points. For point W, $p_{me}=0$ at $15 \leq v_{ej} \leq 20$ km/s, and it could exceed 0.06 at $v_{ej}=5.1$ km/s. The values of the fraction of bodies collided with the Sun were typically between 0.2 and 0.9 for points C, D, F, U, and B. Usually, at $5.1 \leq v_{ej} \leq 8$ km/s more than a half of bodies collided with the Sun. The probability of ejection of a body into a hyperbolic orbit was less than 0.1 at $v_{ej} \leq 6$ km/s, but it could exceed 0.9 at $v_{ej}=20$ km/s. For point W and $15 \leq v_{ej} \leq 20$ km/s, almost all bodies were ejected into hyperbolic orbits. For point B less than 10% of bodies were ejected into hyperbolic orbits. For other four points, the probability of such ejection varied from 0.02 to 0.9 depending on an ejection velocity and an ejection angle.

2.5 Probabilities of collisions of bodies ejected from Mercury with planets

Most of the bodies ejected from Mercury fell back onto Mercury. The probabilities of collisions of bodies ejected from Mercury with the Earth usually did not exceed 0.02 and 0.1 at $v_{ej}<8$ km/s and $v_{ej}<15$ km/s, respectively. The probabilities of their collisions with Venus were usually about 0.2–0.3 at $6 \leq v_{ej} \leq 10$ km/s. The fraction of bodies colliding with Venus was usually greater by an order of magnitude than with Earth. The difference was larger at lower ejection velocities. The fraction of bodies ejected into hyperbolic orbits did not exceed 0.01 for most calculation variants.

Funding

The studies were carried out under government-financed research project for the Vernadsky Institute of Geochemistry and Analytical Chemistry of the Russian Academy of Sciences.

References

Gladman B.J., 1997, Icarus, 130, p. 228
Gladman B.J. and Coffey J.R., 2009, Meteoritics & Planetary Science, 44, 2, p. 285
Gladman B.J., Burns J.A., Duncan, M.J., et al., 1995, Icarus, 118, p. 302
Gladman B.J., Burns J.A., Duncan M.J., et al., 1996, Science, 271, 5254, p. 1387
Gladman B.J., Dones L., Levison H.F., et al., 2005, Astrobiology, 5, 4, p. 483
Ipatov S.I., 2019, Solar System Research, 53, 5, p. 332
Ipatov S.I., 2024, Solar System Research, 58, 1, p. 94
Levison H.F. and Duncan M.J., 1994, Icarus, 108, 1, p. 18
Reyes–Ruiz M., Chavez C.E., Aceves H., et al., 2012, Icarus, 220, 2, p. 777
Wetherill G.W., 1984, Meteoritics, 19, 1, p. 1

MODERN ASTRONOMY: FROM THE EARLY UNIVERSE TO EXOPLANETS AND BLACK HOLES

Detecting low signal-to-noise meteor images in the astronomical camera video stream

I. Izmailov[1], M. Khovrichev[1,2], A. Tolstoy[1], S. Pavlov[1], and D. Bikulova[1,2]

[1] Institute of Applied Astronomy of the Russian Academy of Sciences, 10 Kutuzova Emb., St. Petersburg, 191187 Russia

[2] Central Astronomical Observatory of the Russian Academy of Sciences at Pulkovo, 65/1 Pulkovskoye ave., St. Petersburg, 196140 Russia

Abstract. The analysis of space mission data, such as Long Duration Exposure Facility (LDEF), reveals that the majority of meteor particles fall within the microgram to milligram range. This range corresponds to meteor absolute magnitudes from 5–6 mag to 10–11 mag. Global Meteor Network (GMN) and Mini-MegaTORTORA (MMT) database analysis shows a noticeable decrease in the number of detected meteors fainter than threshold "limiting magnitude minus about 2 mag". This implies that there may be a loss of faint meteors at low signal-to-noise ratios. Therefore, it is crucial to improve the methods for detecting faint meteor events. We present a technique focused on real-time data processing. The key components of the pipeline involve rapidly identifying local peaks and then projecting the chosen points from a series of frames onto a reference frame within a sub-series of several images for analysis using the Hough transform. Initial test observations indicate an increasing trend in the number of faint meteor detections.

Keywords: techniques: image processing; meteors; meteoroids

DOI: 10.26119/VAK2024.144

1 Introduction

Significant improvements in astronomical cameras, image detectors, and modern image analysis techniques cause the intensification of meteor observations worldwide. This provides new quality data for investigations in a wide set of astronomical fields regarding the Solar system structure from cosmogonic aspects to dust particle dynamics. On the practical side, the exponential increase in the number of artificial satellites requires a forecast of the meteoroid flux within the near-Earth space.

Modern meteor observations in the optical bandpass are typically carried out using wide-angle cameras that capture full frames at a rate of 10 frames per second. The data generated by this system is too large to be completely stored, so it is better to analyze the frame stream in real-time mode.

Some existing meteor networks, such as the GMN (Vida et al. 2021) provide broad geographic coverage and effectively detect pairs of baseline meteor images. These networks rely on a large number of amateur-level cameras. Hence, they are focused on identifying relatively bright meteor events. More specialized systems, like MMT (Karpov et al. 2019) or Ground Wide Angle Camera (GWAC, Chen et al. 2023), conduct effective meteor monitoring and provide information about hundreds of thousands of events up to 10th magnitude through their databases.

Our analysis of the meteor databases indicates that the current video stream processing pipelines may not detect low signal-to-noise images associated with faint meteor events. We present our view on the solution of the problem in this paper.

2 Low signal-to-noise meteor image detection pipeline

It is not difficult to plot a histogram of the meteor event detection versus magnitude using, for example, the MMT database. This is presented in Karpov and colleagues' paper (Karpov et al. 2019). The deficit of meteors fainter than 8th magnitude indicates a problem of low-signal-to-noise detections. Source image shape measurements and extraction of elongated images are effective for relatively well-saturated images. The authors of the GWAC system use binarization and median filtration procedures that exclude faint events. Despite this, both systems are powerful facilities for meteor astronomy. They provided great results and data sets. The next-generation survey systems probably will be based on 40-cm to 100-cm lenses and an f-ratio of $f/1.2$. This requires fast image analysis in a real-time mode and detection quality improvement.

The well-known Hough transform-based technique is often found in meteor detection discussions. This is a natural approach to extracting elongated meteor images.

This method is typically used for direct pixel array analysis. This is a computationally intensive method. We attempt to apply the Hough transform to the x, y array that contains pixel coordinates of all possible local maximums in the image. It is natural, that we detect a lot of false sources at the 1-σ level. It is expected that points from a set of source detections caused by meteor events will lie along a straight line (see Fig. 1). This condition is fulfilled both for one frame and for two or more consecutive frames.

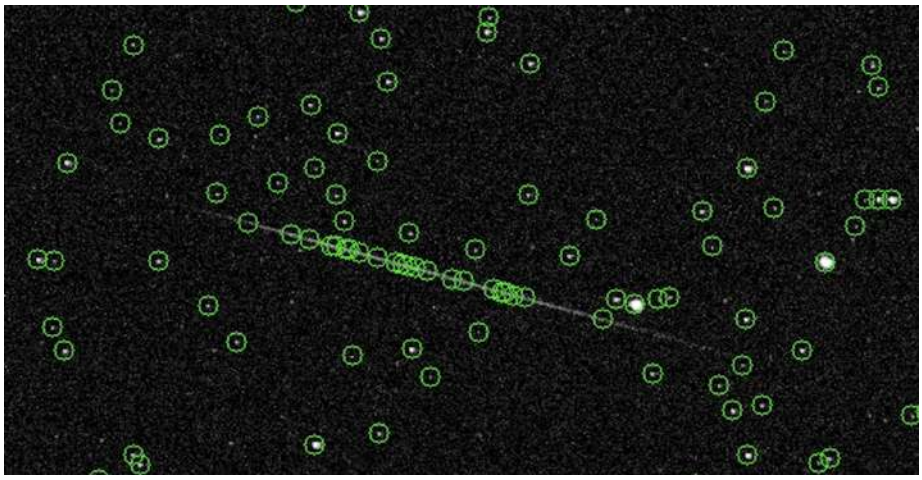

Fig. 1. A faint meteor trail was detected using the described pipeline. This is a 1962×1008 pixels fragment of the image captured using the SSA400 system developed at the Assy-Turgen Observatory (Fesenkov Astrophysical Institute, Almaty, Kazakhstan). The telescope has a D/F ratio of 400/551 mm, a field of view (FOV) of 3.7×2.5 degrees, and an angular scale of 5.6 arcseconds per pixel with 4×4 binning and QHY600 MPCIE camera (Monochrome CMOS camera, pixel size is 3.76 μm $\times$ 3.76 μm, and effective pixel area of 9576×6388).

The fundamental stages of our pipeline are outlined below:

1. Detection of all local maximums in the image.
2. Fitting the signal distributed over pixels in a very close neighborhood to each maximum by second-order surface.
3. In the "parabolic" case, we ensure that the model photocenter is near the local maximum (within 1–2 pixels). Fulfilment of these conditions allows us to interpret the local maximum as a source.
4. We apply the Hough transform to the set of all detected sources within one frame to detect a linear trail that can be a meteor image.
5. We distinguished between meteor and satellite trails by length.

6. We projected all extracted sources onto one plane from a set of consequent frames to detect meteor event images in different frames and measure their parameters.

3 Summary

We provided a brief description of our approach to the detection of faint meteor events with wide-field astronomical cameras. The described technique excludes computationally intensive calculations. Hence, this can be used for analysis of frame stream in a real-time mode.

Application of our code to data generated by the SSA400 telescope of the Assy-Turgen Observatory (Fesenkov Astrophysical Institute, Almaty, Kazakhstan) allows us to detect meteor events up to 13th magnitude during the γ Draconids radiant survey. The data flow was about 0.5 TB per hour.

Acknowledgements. The meteor observations were conducted by the 400-mm wide-angle telescope at the Assy-Turgen Observatory. The authors extend their special thanks to telescope developer, M. Krugov, for providing access to the instrument and for the insightful discussions.

Funding

The study was funded by the Russian Science Foundation project No. 24-22-20044 (https://rscf.ru/en/project/24-22-20044/).

References

Chen Y., Li G., Liu C., et al., 2023, Universe, 9, 11, id. 468

Karpov S., Orekhova N., Beskin G., et al., 2019, Revista Mexicana de Astronomía y Astrofísica (Serie de Conferencias), 51, p. 127

Vida D., Šegon D., Gural P.S., et al., 2021, Monthly Notices of the Royal Astronomical Society, 506, 4, p. 5046

BAK 2024 MODERN ASTRONOMY: FROM THE EARLY UNIVERSE TO EXOPLANETS AND BLACK HOLES 300 years Russian Academy of Sciences

Gravitational influence of the Moon on the Earth's poles movement

S. Kumakshev[1] and V. Perepelkin[2]

[1] Ishlinsky Institute for Problems in Mechanics RAS, Moscow, 119526 Russia
[2] Moscow Aviation Institute, Moscow, 125993 Russia

Abstract. For a qualitative description of the oscillations of the Earth's pole, a simplified analytical model is derived, showing the presence of the frequency of periodic gravitational external action in the coordinates of the pole. As part of the refinement of the forecast of the pole movement, long-period impacts on the pole from the Moon were found and identified. Among the main characteristics of the Moon's orbit, the rotation of the node of the lunar orbit and the rotation of the perigee were chosen from the project The JPL Horizons 2024. The study used a number of C01 observational and measurement data from the International Earth Rotation Service (IERS). The observations were processed over a 122-year interval, starting in 1900 and up to 2023. In this work, as a result of numerical processing of C01 observational data, it was possible to identify quasi-stationary harmonics with the frequency of rotation of the node of the lunar orbit (as well as with a doubled frequency) and with the frequency of rotation of the perigee. The found harmonics are phase-coordinated with the positions of the node of the lunar orbit and its perigee. This confirms the existence of a mechanism of gravitational influence of the Moon (as well as other massive bodies of the Solar System) on the fluctuations of the Earth's pole. The amplitudes of these harmonics show the scale of the gravitational influence from the Moon.

Keywords: astrometry; celestial mechanics; Moon; Earth

DOI: 10.26119/VAK2024.145

1 Introduction

Under the assumption that the Moon provides a gravitational influence on the movement of the Earth's poles, long-period variations of the Moon's trajectory, the rotation of the node of the lunar orbit and the rotation of the perigee, were chosen as a reason. It was previously shown that long-period lunar harmonics are present in variations of the amplitudes of the Chandler and annual components (Perepelkin et al. 2019, 2022).

2 Analytical model

We will show how the frequency of the external periodic gravitational influence arises in a change in the coordinates of the Earth's pole.

The analysis of pole oscillations is similar to the study of the gyroscope axis motion under the action of disturbing torques, taking into account viscoelastic deformations of the Earth. The Earth and the Moon make mutual translational and rotational motion around the barycenter, which, in turn, moves in an elliptical orbit around the Sun under the action of gravitational forces according to Kepler's law. Thus, in a first approximation, the oscillations of the pole obey the kinematic and dynamic Euler equations with a variable inertia tensor (Akulenko et al. 2005; Kumakshev 2018):

$$\begin{gathered} J\dot{\omega} + \omega \times J\omega = M, \quad \omega = (p,q,r)^T, \quad J = J^* + \delta J, \quad J^* = \text{const}, \\ J^* = diag(A^*, B^*, C^*), \quad \delta J = \delta J(t), \quad \|\delta J\| \ll \|J^*\|, \end{gathered} \tag{1}$$

Here ω is the angular velocity vector, in the system of the principal axes of the body, with respect to which the inertia tensor is diagonal. Since the Earth deforms when it moves in orbit under the influence of gravitational forces, it is assumed that these main axes of inertia J^* are average values, to which a small value δJ is added. The additional terms in the equation that arise in this case are considered small and neglected.

The vector of the perturbing torques M has a complex structure. This includes, among other things, external gravitational moments. Euler's kinematic equations with respect to the orbital coordinate system have the following form:

$$\begin{gathered} \dot{\theta} = p\cos\varphi - q\sin\varphi - \omega_0(\nu)\sin\psi, \quad \dot{\nu} = \omega_0(\nu) = \omega_*(1+e\cos\nu)^2, \\ \dot{\psi} = \frac{p\sin\varphi + q\cos\varphi}{\sin\theta} - \omega_0(\nu)ctg\theta\cos\psi, \qquad e = 0.0167, \\ \dot{\varphi} = r - (p\sin\varphi + q\cos\varphi)ctg\theta + \omega_0(\nu)\frac{\cos\psi}{\sin\theta}, \end{gathered} \tag{2}$$

Here $\nu(t)$ is the true anomaly, e is the eccentricity of the orbit, ω_* is a constant determined by gravitational and focal parameters.

The [1-2] system is quite difficult to apply in practice, but important qualitative conclusions can be drawn based on it. Let's show this by taking into account the gravitational influence from the Sun. To do this, we write out the term M_q^s responsible for this effect, which is included in the vector of the disturbing torque M:

$$\begin{gathered} M_q^s = 3\omega^2[(A^* + \delta A - (C^* + \delta C))\gamma_r\gamma_p + \delta J_{pq}\gamma_r\gamma_q + \delta J_{pr}(\gamma_r^2 - \gamma_p^2) - \delta J_{rq}\gamma_p\gamma_q], \\ \omega = \omega_*(1 + e\cos\nu)^{3/2}, \quad \gamma_p = \sin\theta\sin\varphi, \qquad \gamma_q = \sin\theta\cos\varphi, \qquad \gamma_r = \cos\theta, \end{gathered} \tag{3}$$

Here γ_p, γ_q and γ_r are the guiding cosines of the gravitational torque vector relative to the associated system. To calculate $M_{p,r}^s$ a cyclic permutation of the indices p, q, r is performed. As a first approximation, we integrate the equations [2]

$$\begin{gathered} r = r^0, \quad \varphi \approx rt + \varphi^0, \quad \nu \approx \omega_* t + \nu^0, \quad \cos\theta(\nu) = a(\theta^0, \psi^0)\cos\nu, \\ \theta(0) = \theta^0 = 66°33', \quad 0.4 \le a \le 1, \quad 0 \le \psi^0 \le 2\pi, \\ \cos\theta\sin\theta = b(\theta^0, \psi^0)\cos\nu + d\cos 3\nu + \ldots, \quad 0.4 \le b \le 4/3\pi, |d| \ll 1, \end{gathered} \tag{4}$$

Now the Euler equations [1], after averaging over the fast phase φ can be represented as

$$\begin{gathered} \dot{p} + N_p q = \kappa_q r^2 + 3b\omega_*^2\chi_p^s\cos\nu, \quad N_{p,q} \approx N \approx (0.84 - 0.85)\omega_*, \\ \dot{q} - N_q p = -\kappa_p r^2 - 3b\omega_*^2\chi_q^s\cos\nu, \quad p(0) = p^0, \quad q(0) = q^0, \end{gathered} \tag{5}$$

Here N is the frequency of Chandler oscillations in years, κ_p and κ_q are slowly changing average values of $\delta J_{pr}/B^*$ and $\delta J_{qr}/A^*$. The coefficients χ_p^s and χ_q^s arise as a result of averaging over φ multipliers at $\cos\nu$ in expressions for $M_{q,p}^s$. The presence of axial symmetry suggests $\chi_{p,q}^s = \chi$, where χ is found from the experimental data of the IERS[3].

The simplified analytical model [5] contains in the right part an explicit harmonic impact with the period of the Earth's revolution around the Sun (one year). Thus, in solving such differential equations, two harmonic series appears: one with the Chandler frequency N, and the other with the annual frequency of the external driving gravitational force from the Sun. This gives an idea of how the periodic influence of the driving force appears in changing the coordinates of the Earth's pole.

However, the movement of the Earth's pole has a complex trajectory and is not completely determined by two main processes: periodic with a period of one

[3] http://www.iers.org

year and quasi-periodic with an irregular Chandler frequency (Akulenko et al. 2005; Kumakshev 2018). The frequency analysis of the pole oscillations shows the presence of numerous oscillatory components with rather small amplitudes. As mentioned above, the cause of additional harmonics is an external gravitational influence.

3 Numerical study

Oscillations with frequencies that coincided with the main components of the evolution of the lunar orbit - the rotation of the node of the lunar orbit and the rotation of the perigee were selected from the trajectory of the oscillation of the Earth's pole. A number of C01 observations and measurements of pole coordinates from the International Earth Rotation Service were used. The study was conducted over an interval of 122 years, from 1900 to 2023.

3.1 The longitude of the ascending node

The longitude of the ascending node of the Moon Ω (according to project The JPL Horizons[4]) was taken in the form:

$$\Omega = 125.04455501^\circ - 6962890.5431''t + 7.4722''t^2 + 0.007702''t^3 - 0.00005939''t^4, \quad (6)$$

Here $t = (TT - 2451545)/36525$, and TT is the Terrestrial Time in Julian days (see the definition in IAU 2000 Resolution B1.9).

As a result of numerical processing of the C 01 series, harmonics with a frequency of rotation of the lunar orbit node $\dot{\Omega} = 0.05373$ cycles per year, as well as a doubled frequency of $2\dot{\Omega} = 0.107$ cycles per year were selected and shown on Fig. 1.

The harmonic $-\cos\Omega$ is shown above; in the middle of the figure, harmonics with frequencies $\dot{\Omega} = 0.05373$ and $2\dot{\Omega} = 0.107$ are selected from the pole coordinates; as well as oscillations in the angle of inclination of the lunar orbit plane to the Earth's equator (below), constructed using the ephemerides of the Moon from project The JPL Horizons.

The main harmonic of the quasi-regular oscillations of the angle I is $\cos\Omega$, which is clearly visible from the figure. When comparing the graphs, it can be seen that the harmonic with a frequency of $\dot{\Omega} = 0.05373$, selected from the oscillations of the pole, has an extremum when the extremum is reached at the angle I. This happens at the moment when the node of the moon's orbit passes through the points of the spring or autumn equinox. The phase-by-phase alignment of these two processes proves the connection between them. It is also seen that the doubled frequency $2\dot{\Omega} = 0.107$,

[4] https://ssd.jpl.nasa.gov/horizons/

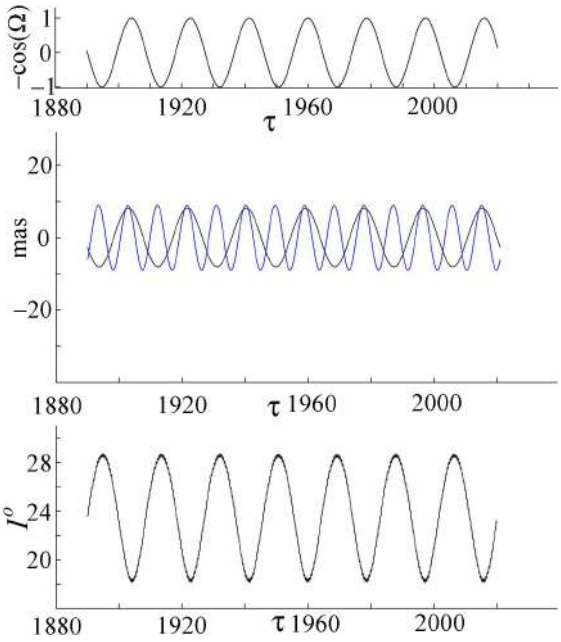

Fig. 1. The main harmonic of the longitude of the ascending node (top); harmonics selected from the coordinates of the pole (in the center); the angle of inclination of the plane of the Moon's orbit to the equator of the Earth (bottom).

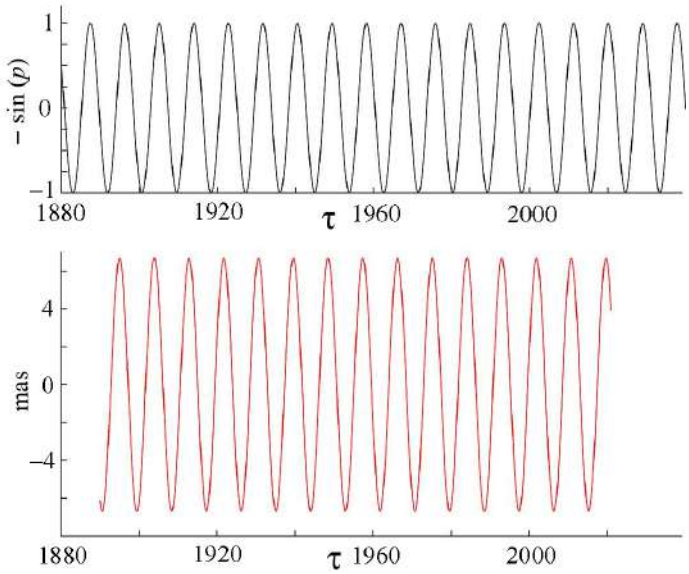

Fig. 2. The longitude of the perigee (top) and the harmonic with the same frequency, selected from the coordinates of the pole x according to the IERS data (bottom).

allocated during numerical processing of the series C 01, is phase-coordinated with the harmonic $\cos\Omega$, constructed using the ephemerides of the Moon from project The JPL Horizons.

3.2 The longitude of the perigee

According to the IERS, the longitude of the Moon's perigee p is expressed as follows:

$$p = 520.41590214^\circ + 14642259.0393''t - 38.803''t^2 - 0.044906''t^3 + 0.00020152''t^4. \quad (7)$$

In Fig. 2, this harmonic in the form of a function $-\sin p$ is depicted at the top. At the bottom of the figure there is a harmonic with the same frequency $\dot{p} = 0.11299$, but selected from the observational data of the pole oscillations for the coordinate x. It can be seen that these two oscillations are phase-coordinated. Thus, the selected harmonics from the trajectory of the Earth's pole coincide in phase with the positions of the node of the lunar orbit and its perigee. This confirms the existence of a mechanism of gravitational influence of the Moon (and other bodies of the Solar System) on the oscillations of the Earth's pole. The amplitudes of the selected harmonics from the pole coordinates show the scale of the gravitational influence of the Moon.

4 Summary

The paper examines the effect of external gravitational influence on the oscillations of the Earth's pole from the Moon. Harmonics with frequencies of long-period changes in the Moon's orbit were selected from the coordinates of the pole oscillation. A comparison of the harmonics selected from the oscillations of the Earth's pole and the evolution of the Moon's orbit showed that their phases coincide. This proves that the cause of such harmonics in the oscillations of the Earth's pole is the gravitational influence from the Moon. Taking into account such influence will increase the accuracy of forecasting the movement of the Earth's pole.

Funding

The present work was supported by the Government program FFGN-2024-0002.

References

Akulenko L.D., Kumakshev S.A., and Markov Yu.G., 2005, Doklady Physics, 50, 2, p. 106
Kumakshev S.A., 2018, Mechanics of Solids, 53, 2, p. 159
Perepelkin V.V., Rykhlova L.V., and Filippova A.S., 2019, Astronomy Reports, 63, 3, p. 238
Perepelkin V.V., Rykhlova L.V., and Wai Yan Soe, 2022, Astronomy Reports, 66, 1, p. 80

BAK 2024 MODERN ASTRONOMY: FROM THE EARLY UNIVERSE TO EXOPLANETS AND BLACK HOLES 300 years Russian Academy of Sciences

Determination of the mass of asteroid (16) Psyche and masses of other asteroids of the taxonomic class M by the dynamic method

V. Kuznetsov and Yu. Chernetenko

Institute of Applied Astronomy of the Russian Academy of Sciences, 10 Kutuzova Emb., St. Petersburg, 191187 Russia

Abstract. We use the dynamical method of estimation of the mass of perturbing asteroid by its gravitation influence on test asteroids. The positional observations of test asteroids from Minor Planet Center database and Focus Product Release of Gaia cosmic telescope are employed. The calculation of coordinates of perturbing planets is based on the ephemeris DE440. The set of test asteroids is used for estimation of perturbing mass. This set was collected by error of the mass of the perturbing asteroid for each test object. The number of test asteroids was selected particularly for each estimated mass. For the mass of asteroid (16) Psyche a value equal to $(1.1868 \pm 0.0092)\ 10^{-11}\ M_\odot$ was obtained. The masses of sixteen asteroids with numbers 55, 69, 75, 77, 83, 92, 97, 110, 129, 135, 201, 325, 441, 498, 516, and 739, that are from the taxonomic class M were estimated also. The estimated masses more than twice exceed their errors.

Keywords: planetary systems: minor planets; asteroids: general; individual: (16) Psyche

DOI: 10.26119/VAK2024.146

1 Introduction

In the coming years, the asteroid (16) Psyche will be of considerable interest to the world scientific community. In particular, the automatic mission "Psyche" was launched by National Aeronautics and Space Administration (NASA) in October 2023. Investigations are expected to begin in 2029 and until then, new information about this large asteroid with an effective diameter of about 222 km is expected from other sources. The main scientific interest is the suggestion that the asteroid is metallic and may be a naked core of protoplanet.

Over the past ten years, a range of mass values has been obtained for the asteroid (16) Psyche (Table 1). They show good agreement of the masses obtained by the dynamical method using asteroids as test particles. The values of mass and their errors in the planetary theories have a larger dispersion. We assume that with the increasing number of asteroid observations, it is relevant to clarify the mass of Psyche and the masses of other asteroids of taxonomic class M according to Tholen (1989) classification. We use the dynamic (astrometric) method of determination of the masses of asteroids. This method involves using gravitational perturbations that a more massive body put on one or more less massive bodies.

Table 1. Mass of (16) Psyche.

№	Authors	Perturbed body	Number of perturbed bodies	Mass $10^{-11}\,M_\odot$
1	Carry (2012)	–	–	1.368 ± 0.372
2	Baer & Chesley (2017)	asteroids	3	1.150 ± 0.035
3	Elkins-Tanton et al. (2020)	–	3	1.15 ± 0.35
4	Fienga et al. (2020)	planets and spacecrafts	–	1.077 ± 0.192
5	Pitjeva et al. (2021)[1]	planets and spacecrafts	–	1.567 ± 0.106
6	Park et al. (2021)	–	–	1.198
7	Vernazza et al. (2021)	asteroids	–	1.137 ± 0.146
8	Siltala & Granvik (2021)	asteroids	10	1.117 ± 0.039
9	Farnocchia et al. (2024)	asteroids	38	1.206 ± 0.013

[1] https://iaaras.ru/en/dept/ephemeris/epm/2021/

2 Calculation

Integration of the equations of motion and the variational equations is performed by the Everhart's method. The equations of motion include the perturbations from all planets, taken from ephemeris DE 440 (Park et al. 2021), dwarf planets Pluto and Ceres and 14 asteroids with numbers: 2, 3, 4, 10, 15, 31, 48, 52, 65, 87, 88,

451, 511, 704. The system of normal equations is solved by the least-squares method with respect to the orbital elements of the perturbed asteroids and the refined mass value. We employ observations from Minor Planet Center[1] and Gaia catalog. Gaia observations were taken from "Focus Product Release". This release contains observations of 156792 asteroids over 66 months from 2014 to 2020[2]. We use two schemes to assign weights: weight scheme of Ephemerides of Minor Planets[3] and the weight scheme proposed in Vereš et al. (2017). The latter is based on detailed analyses of observations from individual observatories, from which weights are assigned. For Gaia observations, a weight calculation algorithm was used as described in the FPR. The preliminary selection of test particles is based on our catalogue of asteroid approaches. Thus, the number of test particles used to estimate the mass of each perturbing asteroid is estimated in a particular way. In that way, the number of test particles that used for mass estimation of each perturbing asteroid is estimated particularly. These numbers are presented in Table 2 (the third column) for each perturbing asteroid.

3 Results

After discussing the results of using different weight systems for MPC observations, we concluded that the obtained mass values are practically independent of the adopted weight system, but the corresponding errors are smaller for Vereš system (Vereš et al. 2017). The results of solutions with this weight system will be presented later.

Table 2 shows the number of asteroid and its name, then the total number of test asteroids, N_{total} and number of asteroids with Gaia observations, N_{Gaia}. The fifth column shows the values of mass of Psyche and 16 asteroids of the taxonomic class M that we obtained. The presented mass values are at least twice as large as their errors. The Table 2 (the sixth column) shows diameters of asteroids from Jet Propulsion Laboratory (JPL)[4] and obtained densities of asteroids (the last column). The density error is estimated using the formula from Carry (2012).

The obtained value of Psyche mass and its error confirms the results of other researches that used asteroid observations. The average density of Psyche turned out to be close to 4 g/cm^3, that correspond to density of stony–iron meteorites. Only two asteroids we assessed, (441) and (739), have average density of about or more than iron density and mean densities of asteroids (55) and (83) more are far from iron density.

[1] http://www.minorplanetcenter.net/iau/mpc.html
[2] https://www.cosmos.esa.int/web/gaia/focused-product-release
[3] https://iaaras.ru/en/about/issues/emp/
[4] https://ssd.jpl.nasa.gov/tools/sbdb_lookup.html

Table 2. Masses of asteroids of the taxonomic class M.

№	Name	N_{total}	N_{Gaia}	Mass $M_\odot$	Diameter km	Density g/cm^3
16	Psyche	36	23	$(1.187 \pm 0.009)\ 10^{-11}$	222 ± 4.0	3.89 ± 0.22
55	Pandora	21	17	$(1.702 \pm 0.757)\ 10^{-13}$	84.79 ± 2.50	1.06 ± 0.48
69	Hesperia	5	4	$(2.951 \pm 0.226)\ 10^{-12}$	138.13 ± 4.70	4.25 ± 0.54
75	Eurydike	18	10	$(1.682 \pm 0.430)\ 10^{-13}$	62.38 ± 1.60	2.63 ± 0.70
77	Frigga	15	11	$(3.553 \pm 1.100)\ 10^{-13}$	61.39 ± 0.18	5.83 ± 1.81
83	Beatrix	30	20	$(4.491 \pm 0.689)\ 10^{-13}$	110.50 ± 0.83	1.26 ± 0.20
92	Undina	5	3	$(3.186 \pm 0.141)\ 10^{-12}$	126.42 ± 3.40	5.99 ± 0.55
97	Klotho	8	6	$(1.049 \pm 0.133)\ 10^{-12}$	100.72 ± 0.64	3.90 ± 0.50
110	Lydia	31	21	$(7.339 \pm 0.071)\ 10^{-13}$	86.09 ± 2.00	4.36 ± 0.31
129	Antigone	10	8	$(2.123 \pm 0.169)\ 10^{-12}$	113.00 ± 5.00	5.59 ± 0.87
135	Hertha	51	38	$(4.859 \pm 0.504)\ 10^{-13}$	79.24 ± 2.00	3.71 ± 0.48
201	Penelope	36	21	$(4.361 \pm 0.345)\ 10^{-13}$	85.88 ± 3.14	2.62 ± 0.35
325	Heidelberga	4	2	$(6.133 \pm 2.131)\ 10^{-13}$	75.72 ± 1.70	5.36 ± 1.90
441	Bathilde	17	14	$(7.386 \pm 1.087)\ 10^{-13}$	65.13 ± 1.07	10.15 ± 1.57
498	Tokio	7	4	$(5.099 \pm 1.647)\ 10^{-13}$	81.83 ± 2.30	3.53 ± 1.18
516	Amherstia	5	3	$(3.161 \pm 1.183)\ 10^{-13}$	65.14 ± 0.38	4.34 ± 1.63
739	Mandeville	3	2	$(2.402 \pm 0.201)\ 10^{-12}$	104.52 ± 1.62	7.99 ± 0.76

Acknowledgements. This work has made use of data from the European Space Agency (ESA) mission Gaia (https://www.cosmos.esa.int/gaia), processed by the Gaia Data Processing and Analysis Consortium (https://www.cosmos.esa.int/web/gaia/dpac/consortium) (DPAC). Funding for the DPAC has been provided by national institutions, in particular the institutions participating in the Gaia Multilateral Agreement.

References

Baer J. and Chesley S.R., 2017, AJ, 154, 2, id. 76
Carry B., 2012, Planetary and Space Science, 73, 1, p. 98
Elkins-Tanton L., Asphaug E., Bell J., et al., 2020, Jour. of Geoph. Res.: Planets, 125, 3, id. e06296
Farnocchia D., Fuentes-Muñoz O., Park R.S., et al., 2024, Astronomical Journal, 168, 1, id. 21
Fienga A., Avdellidou Ch., and Hanuš J., 2020, MNRAS, 492, 1, p. 589
Park R.S., Folkner W.M., Williams J.G., et al., 2021, AJ, 161, 3, id. 105
Pitjeva E., Pavlov D., Aksim D., et al., 2021, Proc. of the IAU, 364, p. 220
Siltala L. and Granvik M., 2021, ApJL, 909, 1, id. L14
Tholen D.J., 1989, Proc. of the Conf. Asteroids II, University of Arizona Press, p. 1139
Vereš P., Farnocchia D., Chesley S.R., et al., 2017, Icarus, 296, p. 139
Vernazza P., Ferrais M., Jorda L., et al., 2021, A&A, 654, id. A56

BAK 2024 MODERN ASTRONOMY: FROM THE EARLY UNIVERSE TO EXOPLANETS AND BLACK HOLES 300 years Russian Academy of Sciences

Formation scenarios of the young Emilkowalski asteroid family

E. Kuznetsov, V. Safronova, A. Perminov, and M. Vasileva

Ural Federal University, 51 Prospekt Lenina, Ekaterinburg, 620000 Russia

Abstract. The scenario of the formation of the young Emilkowalski asteroid family is based on numerical modelling of the evolution of the nominal orbits of the family members. Different variants of the orbital evolution of asteroids are considered depending on the value of the drift velocity of the large semi-major axes of the orbits caused by the influence of the diurnal Yarkovsky effect. On the basis of the analysis of the convergence of the nodes and pericentres of the orbits, estimates of the time of possible formation of all possible pairs among the family members were obtained. On the basis of these estimates, a scenario of family formation was constructed, assuming the destruction of the parent body of asteroid (14627) Emilkowalski as the main mechanism. It is shown that part of the family members could have been formed as a result of cascading disintegration of daughter bodies of the parent asteroid. The constructed scenario of the Emilkowalski family formation can be described as a stage-by-stage destruction of the parent body of asteroid (14627) Emilkowalski with elements of cascading disintegration of some fragments.

Keywords: minor planets; asteroids; individual: (14627) Emilkowalski family

DOI: 10.26119/VAK2024.147

1 Introduction

The young Emilkowalski asteroid family is located in the central Main Belt: semi-major axis $a = 2.60$ AU, eccentricity $e = 0.15$, inclination $i = 17^{\circ}.75$. Nesvorný and Vokrouhlický (2006) considered Emilkowalski family as a cluster of three asteroids in close heliocentric orbits: (14627) Emilkowalski, (126761) 2002 DW10, and (224559) 2005 WU179. The first estimate of the age of the family at 220 ± 30 kyr (Nesvorný and Vokrouhlický 2006) showed that it is a young family. Pravec et al. (2018) estimated the taxonomic type of asteroid (14627) Emilkowalski based on photometric observations as type D.

Pravec et al. (2018); Fatka et al. (2020) discovered new family members, increasing the number of asteroids in this family to nine. Age estimates of the "main asteroid (14627) Emilkowalski – secondary asteroid" pairs were obtained by Pravec et al. (2018); Fatka et al. (2020). It was shown that at least two decay events of the parent asteroid of this family occurred in the last 5 Myr. This is consistent with the scenario of cascading disintegration of the parent body. Four new members of the Emilkowalski family were discovered by Kuznetsov et al. (2025). Thus, 13 asteroids that are members of the Emilkowalski family are currently known.

In this paper, we consider the young Emilkowalski asteroid family from the point of view of studying the formation process and attempt to reconstruct the chronological sequence of the parent body breakup. For this purpose, we:

1) numerically investigate the dynamical evolution of asteroids based on known nominal orbits, considering the influence of the Yarkovsky effect;
2) estimate the ages of all possible pairs among the asteroids of the family and based on these estimates;
3) construct a basic scenario of the family formation.

2 Modelling the dynamic evolution of asteroids

Numerical simulation of the motion of asteroids of the Emilkowalski family was performed using the `Orbit9` software included in the `OrbFit`[1] software package. When modelling the dynamical evolution, perturbations from eight major planets and the dwarf planet Pluto, the Sun's oblateness, and relativistic effects were considered. The osculating elements of asteroid orbits from the AstDyS catalogue for the epoch MJD 60200 were taken as initial ones. The integration intervals were 5 Myr and 2 Myr.

Different variants of the evolution were considered: without considering the diurnal Yarkovsky effect and with this effect considered. The influence of the diurnal

[1] http://adams.dm.unipi.it/orbfit/

Yarkovsky effect was considered in the form of a constant drift rate da/dt of the semi-major axis of the asteroid's orbit a. The drift rate was estimated either from the known physical and thermophysical parameters of asteroids, or parameters characteristic of the given taxonomic class were used, if all asteroids, as well as the main asteroid of the (14627) Emilkowalski family, are of type D.

Estimation of the drift rate of the semi-major axis da/dt was performed using a modified version of the `Orbit9` software included in the `OrbFit` package (Fenucci and Novaković 2022), which provides the possibility of taking into account the influence of the Yarkovsky effect and the YORP (Yarkovsky–O'Keefe–Radzievskii–Paddack) effect on the basis of setting the dynamic (period of axial rotation and inclination of the rotation axis), physical (density) and thermophysical (heat capacity, thermal conductivity, radiation and absorption coefficients of surface layers) parameters of the asteroid.

The age of the pairs was estimated using a method based on the search for moments of convergence of the nodes and perihelion orbits (synchronous zeroing of the longitude differences of the ascending nodes $\Delta\Omega = 0$ and perihelion arguments $\Delta\omega = 0$) (see, e.g., Kuznetsov et al. 2020). Estimates of the age of pairs T were obtained as the average of $T = (T_\Omega + T_\omega)/2$ moments of zeroing the differences between the longitudes of the ascending nodes T_Ω and the perihelion arguments T_ω. In the following, we used estimates for which the relative moment difference $\delta T = (T_\Omega – T_\omega)/T < 0.1$, which provides the proximity of the zeroing moments of the differences between the longitudes of the ascending nodes and the perihelion arguments necessary for obtaining age estimates. When several evolution variants with different values of the drift rate of the semi-major axis were considered for an asteroid, the interval of possible ages of a pair was estimated.

In addition to estimates of the moments and time intervals corresponding to the convergence of the nodes and perihelion of the orbits at different drift rates of the semi-major axes of the orbits, estimates of the values of the Kholshevnikov metrics ϱ_2 and ϱ_5 (Kholshevnikov et al. 2016) were obtained when constructing the family formation scenario and their differences $\varrho_2 - \varrho_5$ were calculated. The ϱ_2 metric is defined in the five-dimensional space of Keplerian orbital elements a, e, i, Ω, ω (the position of the body in the orbit is not considered). The metric ϱ_5 is defined in the factor space of positional orbit elements a, e, i (at all possible orientations of orbital planes and apsidal lines). A small value of the difference between the metrics ϱ_2–ϱ_5 is a necessary condition for the youth of the pair (Kuznetsov et al. 2020).

3 Scenario for the formation of the Emilkowalski asteroid family

The Emilkowalski family formation scenario was constructed based on a joint analysis of the moments of convergence of the nodes and perihelion orbits and the values of the Kholshevnikov metrics. The construction of the scenario was divided into three stages. At the first stage, the moments of simultaneous convergence of nodes and perihelion orbits were analyzed for cases of asteroid orbits convergence with the orbit of the main asteroid of the (14627) Emilkowalski family. As a result, groups of asteroids corresponding to the sequence of parent body destruction events were identified. At this stage, asteroids whose orbits do not converge with the orbit of (14627) Emilkowalski were excluded from consideration. At the second stage, the proximity of the selected pairs of orbits was analyzed based on estimates of the values of the Kholshevnikov metrics ϱ_2 and ϱ_5, as well as their difference ϱ_2–ϱ_5. It was assumed that the values of metrics and their difference for the subsequent event were smaller than for the previous one. At the third stage, we analyzed the possibility of the formation of family members as a result of cascade fission of fragments of the parental body of the family. Fig. 1 shows the scheme of the constructed scenario, where for each parent body the range of fragment ages in kyr (red font) is indicated in the order of their location on the scheme. For each family member, the number or name and size in meters are given.

Note that the constructed scenario of the Emilkowalski family formation is based on the analysis of the evolution of nominal asteroid orbits. When taking into account the influence of the Yarkovsky effect, the value of the drift rate of the semi-major axis was varied for asteroids for which the direction of the rotation axis is not known. To test the proposed scenario, the probabilistic evolution of all asteroids in the family will be studied, resulting in estimates of the moments of low relative-velocity close encounters of asteroids and the attainment of minima of the Kholshevnikov metric ϱ_2. Based on these data, it is planned to refine the age estimates of the pairs and, if necessary, to correct the developed scenario.

4 Conclusions

A scenario of the formation of the Emilkowalski family was constructed based on the analysis of the evolution of the nominal orbits of asteroids. We used the method of convergence of the nodes and perihelion orbits together with the Kholshevnikov metrics to estimate the age of the pairs. The constructed model shows that the family was formed as a result of cascading destruction of the parent body. It is possible that the family is significantly younger than it was previously thought, with an age of less

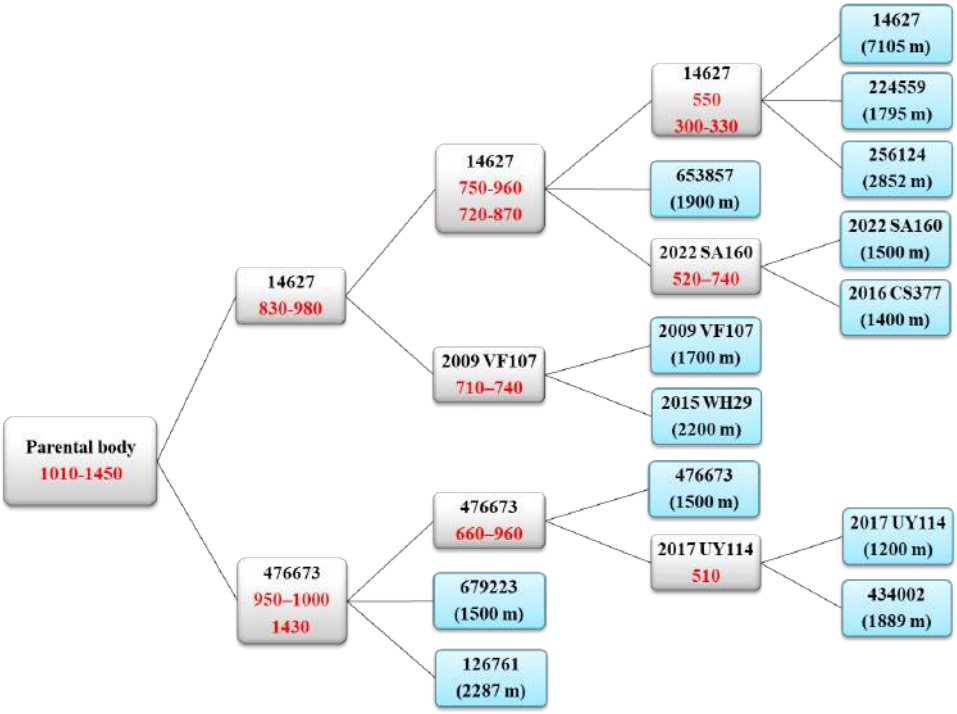

Fig. 1. Emilkowalski family formation scenario.

than 1.5 Myr. We plan to test this conclusion based on the results of a study of the probabilistic evolution.

Acknowledgements. This research used the Asteroids – Dynamic Site (AstDyS) Database (https://newton.spacedys.com/astdys/).

Funding

The study was funded by the Russian Science Foundation grant No. 24-22-00143 (https://rscf.ru/en/project/24-22-00143/).

References

Fatka P., Pravec P., Vokrouhlický D., 2020, Icarus, 338, id. 113554
Fenucci M. and Novaković B., 2022, Serbian Astronomical Journal, 204, p. 51
Kholshevnikov K.V., Kokhirova G.I., Babadzhanov P.B., et al., 2016, Monthly Notices of the Royal Astronomical Society, 462, 2, p. 2275
Kuznetsov E.D., Rosaev A.E., Plavalova E., et al., 2020, Solar System Research, 54, 3, p. 236
Kuznetsov E.D., Perminov A.S., Vasileva M.A., et al., 2025, Solar System Research, 59, in press
Nesvorný D. and Vokrouhlický D., 2006, The Astronomical Journal, 132, 5, p. 1950
Pravec P., Fatka P., Vokrouhlický D., et al., 2018, Icarus, 304, p. 110

MODERN ASTRONOMY: FROM THE EARLY UNIVERSE TO EXOPLANETS AND BLACK HOLES

The influence of uncertainty in the shape of an asteroid on the estimate of perturbation magnitudes in its rotational dynamics when approaching the Earth

K. Lobanova[1,2] and A. Melnikov[1]

[1] Central Astronomical Observatory of the Russian Academy of Sciences at Pulkovo, 65/1 Pulkovskoye ave., St. Petersburg, 196140 Russia
[2] Saint-Petersburg State University, 7-9 Universitetskaya Emb., St. Petersburg, 199034 Russia

Abstract. The shape of the vast majority of small asteroids is unknown. There are only estimates of the average diameter obtained for them on the basis of absolute magnitude and albedo under a number of assumptions. To estimate the magnitude of perturbations in the rotational dynamics of an asteroid that arise when approaching the Earth by means of numerical modeling, it is necessary to know its moments of inertia, determined, among other things, by the shape of the asteroid. By conducting massive numerical experiments to simulate a close approach of an asteroid to the Earth, the influence of the figure's parameters on the magnitude of perturbations in the rotational dynamics of the asteroid was studied. It has been established that with very fast rotation (period $P < 1$ hour), even significant errors in knowledge of the asteroid's figure do not have a significant effect on the estimate of the magnitude of the perturbations. On the contrary, with a relatively slow rotation of the asteroid ($P > 5$ hours), inaccurate specification of the parameters of the asteroid's figure can lead to a significant underestimation of the perturbation values in numerical experiments. For example, for the asteroid Apophis ($P = 30.6$ hours), the error in the estimation of the rotational period after its close approach to the Earth in 2029 can be several hours, and the uncertainty in knowledge of the orientation of the rotational axis can be tens of degrees.

Keywords: celestial mechanics; minor planets, asteroids: general; methods: numerical

DOI: 10.26119/VAK2024.148

1 Introduction

The rotational and orbital dynamics of the asteroid are closely interrelated. Planetary encounters that take place in the orbital dynamics of asteroids affect their rotational dynamics (Scheeres et al. 2000). In turn, through the Yarkovsky effect, rotation affects the orbital dynamics of the asteroid. An important task is the numerical modeling of the rotational dynamics of near-Earth asteroids. Perturbations that arise in the dynamics of an asteroid during approach can lead to a catastrophic collision in subsequent returns (Giorgini et al. 2008; Sokolov et al. 2012).

When numerically modeling the rotational dynamics of an asteroid during approach, its shape is usually approximated by a triaxial ellipsoid with semi-axes $a > b > c$ (see, for example, Pravec et al. 2014; Melnikov 2022). The moments of inertia of the asteroid ($A < B < C$), knowledge of which is necessary for modeling the gravitational interaction of the asteroid and the planet during approach, under the assumption of uniform density of the asteroid, are associated with the parameters of the figure:

$$\frac{c}{b} = \sqrt{\frac{A+B-C}{A-B+C}}, \quad \frac{b}{a} = \sqrt{\frac{A-B+C}{-A+B+C}}, \tag{1}$$

The figures of asteroids are usually known with large errors. For most asteroids, there are only estimates of diameter obtained from the absolute magnitude of the asteroid under certain simplifications. The purpose of this work was to study the influence of uncertainty in the knowledge of asteroid's figure (c/b, b/a) on the estimates of perturbations in its rotational dynamics obtained from numerical modeling of the asteroid's approach to the Earth.

2 Numerical experiments

According to the methodology described in (Lobanova & Melnikov 2024), numerical experiments were carried out to simulate asteroids approaching the Earth: (99942) Apophis (diameter $D \approx 340$ m, rotational period $P \approx 30$ hours), (367943) Duende ($D \approx 30$ m, $P \approx 8$ hours), 2012 TC4 ($D \approx 10$ m, $P \approx 12$ min) and 2023 BU ($D \sim 10$ m, $P \approx 2$ min). For all considered asteroids, $\Delta P(c/b, b/a)$ and $\Delta\gamma(c/b, b/a)$ diagrams were constructed and analyzed. The values of ΔP and $\Delta\gamma$ characterize the magnitude of perturbations in the rotational dynamics of the asteroid arising due to its approach to the Earth (for more details, see Melnikov 2022), namely: ΔP corresponds to the change in the rotational period of the asteroid, $\Delta\gamma$ corresponds

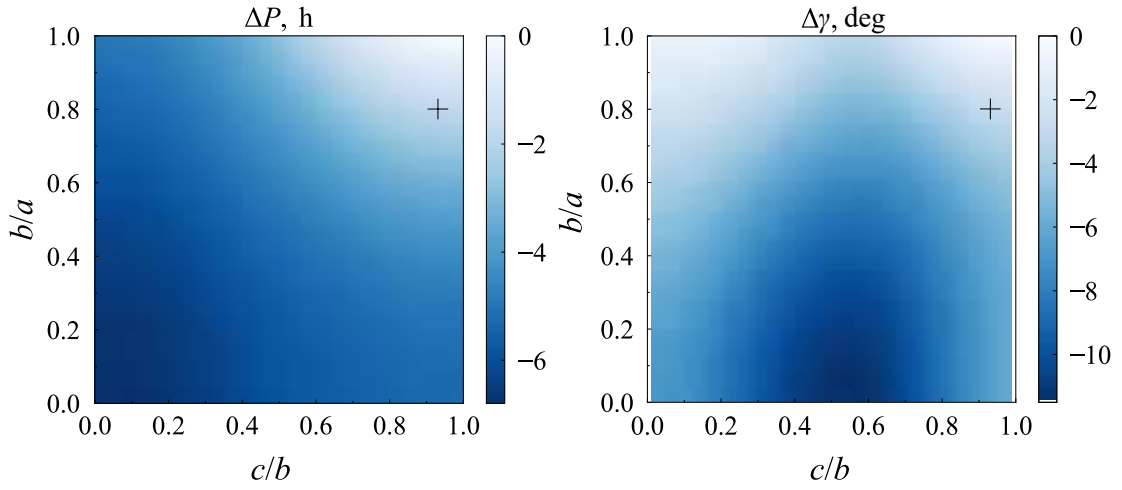

Fig. 1. Dependences of ΔP change in rotational period and $\Delta\gamma$ change in angle characterizing the deviation of the rotational axis from the normal to the orbital plane for the asteroid Apophis ($e = 4.26$, $d = 5.96\,R_E$, $P_0 = 30.6$ hours, $\gamma_0 = 140°$) due to its approach to the Earth in 2029 from the parameters c/b and b/a, characterizing the figure of the asteroid. The cross indicates the possible position of the asteroid (see Pravec et al. 2014).

to the change in the angle between the asteroid's rotational axis and the normal to the plane of its orbit.

Figures 1 and 2 show examples of diagrams for Apophis and 2012 TC4. The figures show the accepted initial (before approach) values of the period P_0 and the angle γ_0 between the axis of rotation of the asteroid and the normal to the orbital plane, and the parameters of the geocentric orbit (e, $d = a(e-1)$, where e is the eccentricity, a is the semi-major axis). It can be seen that in the case of Apophis, uncertainties in knowledge of the figure can lead to errors in the estimate of ΔP amounting to several hours; when estimating $\Delta\gamma$ the error can reach ten degrees. We made a similar conclusion from the analysis of diagrams for Duende. Fig. 2 shows that for 2012 TC4, the values of ΔP and $\Delta\gamma$ are extremely small. Therefore, uncertainties in knowledge of the 2012 TC4 figure do not affect estimates of the magnitude of perturbations that arise in the rotational dynamics due to its approach to the Earth. We obtained results similar to 2012 TC4 for the asteroid 2023 BU.

3 Summary

We studied the influence of knowledge of the parameters of the asteroid's figure on the estimates of the magnitude of perturbations that arise in the rotational dynamics

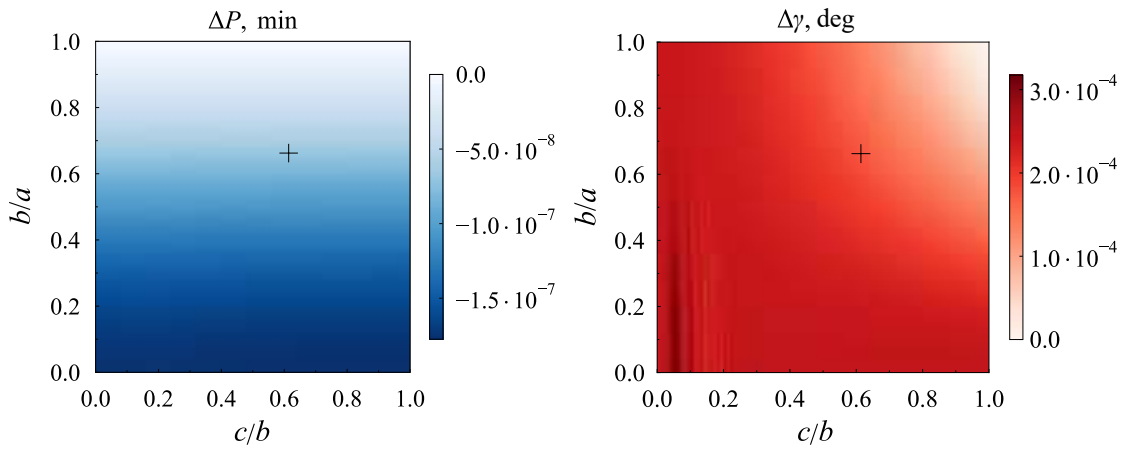

Fig. 2. The same for asteroid 2012 TC4 ($e = 6.36$, $d = 7.86\,R_E$, $P_0 = 12.25$ min, $\gamma_0 = 160°$) during its approach to the Earth in 2017. The cross indicates the possible position of the asteroid (see Lee et al. 2021).

when it approaching the Earth. It is shown, that for the asteroids Apophis and Duende with relatively slow rotation ($P > 5$ hours), errors in the determination of the parameters of the figure can lead to noticeable inaccuracies in the estimation of magnitude of perturbations: for changes in P they reach from a few to tens of hours, and for changes in γ they reach tens of degrees. For asteroids 2012 TC4 and 2023 BU with very fast rotation ($P < 1$ hour), the uncertainty in knowledge of the figure does not affect the assessment of perturbations in its rotational dynamics. Note that the amplitude of perturbations itself is small in this case.

Funding

The study was funded by a Russian Science Foundation project No. 23-22-00306, https://rscf.ru/project/23-22-00306/.

References

Giorgini J.D., Benner L.A.M., Ostro S.J., et al., 2008, Icarus, 193, 1, p. 1
Lee H.-J., Ďurech J., Vokrouhlický D., et al., 2021, Astronomical Journal, 161, 3, id. 112
Lobanova K.S. and Melnikov A.V., 2024, Solar System Research, 58, 2, p. 208
Melnikov A.V., 2022, Solar System Research, 56, 4, p. 241
Pravec P., Scheirich P., Ďurech J., et al., 2014, Icarus, 233, p. 48
Scheeres D.J., Ostro S.J., Werner R.A., et al., 2000, Icarus, 147, p. 106
Sokolov L.L., Bashakov A.A., Borisova T.P, et al., 2012, Solar System Research, 46, 4, p. 291

VAK 2024 MODERN ASTRONOMY: FROM THE EARLY UNIVERSE TO EXOPLANETS AND BLACK HOLES 300 years Russian Academy of Sciences

On mechanisms of the outbursts activity of comets 29P and 174P

Yu. Medvedev, Yu. Chernetenko, and S. Pavlov

Institute of Applied Astronomy of the Russian Academy of Sciences, St. Petersburg, 191187 Russia

Abstract. We study common features in mechanisms of the outburst activity of comet 29P/Schwassmann–Wachmann 1 and asteroid (60558) Echecles, which also has a cometary designation 174P. These celestial bodies belong to the group of centaurs, whose orbits lie between the orbits of Jupiter and Neptune. An important feature of these comets is the observed brightness outbursts, up to 6 stellar magnitudes, which do not depend on the heliocentric distance. Previously, we explained the outburst activity of comet 29P/Schwassmann–Wachmann 1 by the existence of satellites touching the surface of the comet nucleus at the pericenters of their orbits. In this work, we focused on studying the parameters of 174P outbursts. We calculated the comet's orbital elements based on the available positional observations and analyzed O–C (residuals of the orbit fit) deviations. We found correlations in $O-C$ deviations and comet's apparent magnitude and assume that an explosive emission of dust particles the total brightness of which exceeds the brightness of the nucleus takes place there and leads to deviations in O–C in the positional observations. We determined the parameters of the assumed gas-dust jet during the outbursts using the deviations in O–C. The calculations carried out allow us to conclude that in December 2005, fragments of the comet were ejected, some of which fell on the nucleus between 2006 and 2017. These collisions led to a multiple increase in the brightness of the comet.

Keywords: comets: comet 29P; comet 174P

DOI: 10.26119/VAK2024.149

1 Introduction

The purpose of this study is to search for common features in the mechanisms of outburst activity of comet 29P/Schwassmann–Wachmann 1 and asteroid (60558) Echeclus, also known as 174P. These celestial bodies belong to the group of centaurs, whose orbits lie between the orbits of Jupiter and Neptune. Members of this group have unstable, usually highly elongated orbits, crossing the orbits of the giant planets, and dynamically represent a transitional stage between main belt and Kuiper belt objects. We estimated the Lyapunov time values, which show the predicted dynamics of these comets. For comet 29P it was about 100 years, and for comet 174P it was about 40 years, which makes it difficult to study their dynamics over long time intervals.

2 Outbursts of the comet 174P

The comets under study have large nuclei, the diameters of which are estimated at approximately 60 km (https://ssd.jpl.nasa.gov). It is assumed that the surfaces of the comet nuclei are covered with a thick layer of dust. The observed brightness outbursts, up to 6 stellar magnitudes, which do not depend on the heliocentric distance, are an important feature of these comets. The velocities of matter near the surfaces of the nuclei during outbursts are low; according to observations made by the Hubble Space Telescope, the dust velocity at distances less than 1200 km from the nucleus of 29P is 17 m/s (Miles et al. 2016) and for comet 174P the dust velocity lies in the interval from 20 to 50 m/s (Rousselot et al. 2021).

To date, many hypotheses have been put forward attempting to explain the causes of the observed outbursts of comets 29P and 174P. The most widely accepted explanation is that the comet has subsurface cavities containing methane and carbon monoxide ices. The ejection of matter in this case is a consequence of the sublimation of volatile ices located on the sunlit side and causing the explosion (Rousselot et al. 2021). Other hypotheses suggest the fragmentation of the comet nucleus as a result of internal stresses (Neslusan 2014). Previously, we explained the anomalous outburst activity of comet 29P/Schwassmann–Wachmann 1 by the existence of satellites touching the surface of the comet nucleus at the pericenters of their orbits (Medvedev & Pavlov 2023). It was assumed that the satellites move in eccentric orbits and as a result of their collisions with the dust layer of the nucleus, a large amount of dust is ejected, the reflection from which causes periodic bursts of brightness. Depending on the depth of penetration of the satellites into the dust layer, the intensity of the outbursts varied.

In this work we focused on studying parameters of the outbursts of the comet 174P. Based on available positional observations, the comet orbit was calculated and the O–C (residuals of the orbit fit) were analyzed. We found systematic deviations in O–C in the positional observations of 174P that correlate with its outbursts.

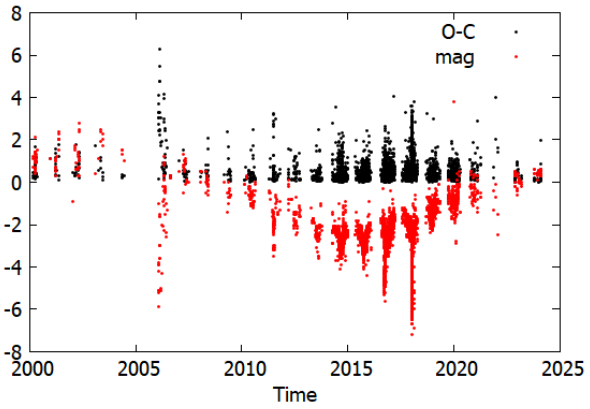

Fig. 1. The values of Δ_{O-C} and stellar magnitudes of comet 174P.

In Fig. 1, the red dots denote the magnitude values and the black dots denote $\Delta_{O-C} = \sqrt{\Delta\alpha\cos\delta^2 + \Delta\delta^2}$, where $\Delta\alpha\cos\delta$ are the O–C values for right ascension and $\Delta\delta$ for declination. For convenience of presentation of two quantities in Fig. 1 the values of stellar magnitudes are reduced by 20 units. Thus, in Fig. 1, the ordinate axis shows Δ_{O-C} in both arcseconds and the stellar magnitude.

The most statistically significant deviations in O–C were obtained for the brightness outbursts that occurred in December 2006 and 2017. We assumed that there was an explosive ejection of dust particles, the total brightness of which exceeds that of the nucleus. The outbursts lead to deviations in O–C in the positional observations, which we use to determine the parameters of the putative gas-dust jet.

2.1 Calculation

When calculating the motion of dust particles, we neglected their mutual interactions and took into account only external forces: gravitational attraction by the cometary nucleus and the Sun, acceleration by the flow of sublimating gas and light pressure. The dust particles were considered spherical. We used the simplest model of brightness distribution in coma, which implies calculating the motion of only one particle, which is considered the center-of-light.

Calculations of particle dynamics were performed in the cometocentric orbital coordinate system XYZ, where the X axis coincides with the direction to the Sun at the moment of ejection; the Y axis lies in the orbit plane perpendicular to X and the Z axis is directed from the plane and complements the coordinate system to the right–handed one. The velocity vector was determined by its absolute value, V, and two angles: λ with the X axis in the XY plane and β with the Z axis.

In the equations of motion of the particle in the comet's head, the accelerations defined by formulas (1-4) (Chernetenko & Medvedev 2020) were included:

1) gravitational attraction from the comet's nucleus

$$W_1 = -GM_n \frac{r}{|r|^3}, \tag{1}$$

where G is the gravitational constant, M_n is the mass of the nucleus, $\mathbf{r}$ is the cometocentric position vector of the particle, $|r|$ is the lenght of r;

2) gravitational attraction from the Sun

$$W_2 = -GM_S\left(\frac{r + r_c}{|r + r_c|^3} - \frac{r_c}{|r_c|^3}\right), \tag{2}$$

where M_S is the mass of the Sun, r_c is the geliocentric position vector of the comet nucleus;

3) acceleration (or deceleration) from the flow of the sublimating gas

$$W_3 = C_d\ \rho\ \frac{s}{m}\,|V_{gas} - \dot{r}|(\,V_{gas} - \dot{r}), \tag{3}$$

where C_d is the aerodynamic drag, ρ is the sublimating gas density, s is the midsection of the particle, m is the mass of the particle, V_{gas} and $\dot{r}$ are the cometocentric velocities of gas and the particle, respectively;

4) disturbing acceleration caused by solar radiation pressure

$$W_4 = -\theta_d\ \frac{s}{m}\ \frac{q_0}{c}\ \frac{r + r_c}{|r + r_c|^3}, \tag{4}$$

where θ_d is a coefficient determining the efficiency of the transmission of the solar radiation to the particle, q_0 is the solar constant, c is the speed of light.

The expansion of the Carbon monoxide (CO) gas in the comet's head was assumed to be spherically symmetric, the production rate Q(CO) to be equal to $(7.7\pm3.3)\cdot10^{26}$ mol/s and the gas velocity $|V_{gas}| = 500$ m/s.

We used the standard values for the solar mass, the speed of light, the gravitational constant, and the solar constant. The particle dynamics is related to a number

of parameters considered with comet nucleus. The following values were adopted: density of the nucleus, ρ_n =1.0 g cm^{-3} and radius of the nucleus, R_n = 60.0 km.

We determined the values of three parameters characterizing the movement of an average dust particle: initial velocity, V, and angles, λ and β. We also attempted to determine the average particle diameter, but it turned out to be insensitive to O–C deviations due to the large distance of the comet from the Earth and the Sun and the low density of the gas jet, which led to small non-gravitational accelerations in the motion of dust particles.

The parameters were calculated as follows. Some initial values were specified and the system of differential equations was numerically integrated over the outburst interval, the beginning and the end of which were determined using the change in stellar magnitude. Using these data, the O–C values in the outburst interval were considered as the observed position of the dust particle (i.e. the center-of-light) in the cometocentric coordinate system. The differences between the observed and calculated coordinates of the dust particle formed the right-hand side of the conditional equations. The differential coefficients of the three refined parameters in the conditional equations were calculated using the grid method. The initial values were then corrected using the least squares method (LSM). The values obtained as a result of this procedure were considered as final and no further refinements of the comet's orbital parameters were carried out. The procedure was used to determine the jet parameters during the 2006 and 2017 outbursts.

The obtained solutions are shown in Table 1. The table contains: the moment of the outburst, T_{jet}, the ejection velocity of the particles, V in m/s, the angles λ and β in degrees, the root–mean–square error, rms in arcseconds.

Table 1. Emission parameters and their errors.

T_{jet}	V m/s	λ °	β °	rms ″
2005.12.29	36.4±5.6	43±17	42±8	1.1
2017.12.04	17.6±0.1	42±17	15±4	0.5

The obtained results show that a powerful ejection of matter occurred at the end of 2005. We took the ejection moment of December 29. The calculated ejection velocity exceeded the comet's escape velocity. The first ejection occurred almost at the aphelion of the comet's orbit and some of the fragments entered a satellite orbit around the comet nucleus. The probable satellites moved in a plane with a large inclination to the plane of the comet's orbit, thus the ejection occurred mainly per-

pendicular to the orbital plane. As the comet nucleus moved towards perihelion, the highly inclined orbits of the satellites became unstable, they entered more elongated orbits and collided with the surface of the nucleus. In December 2017, almost at the perihelion of the comet, a collision with a fairly large satellite occurred. This resulted in the ejection of matter; the ejection speed was noticeably lower and this time did not exceed the comet's escape velocity.

3 Summary

Asteroid (60558) Echeclus was discovered active on December 30, 2005, and subsequently renamed to comet 174P/Echeclus. Observations over the next five months showed that the apparent source of activity moved away from the main body to a maximum distance of 7 arcseconds (65,000 km from the comet's nucleus) in late February 2006. The source of activity then moved back towards the main body, passing it by only 2.7 arcseconds in early May 2006 (Weissman et al. 2006). Since then, at least four outbursts have been recorded during 2006–2024.

We assume that as a result of the first ejection, some of the material fell into the orbit of the comet's satellite. Since the ejection occurred almost perpendicular to the orbital plane, their orbits were unstable, therefore, these satellites gradually fell onto the surface of the comet nucleus, causing new brightness bursts. In December 2017, a fairly large fragment probably fell onto the surface of the nucleus, which affected the positional observations of the comet. Using the $O–C$ variations, we obtained the parameters of this ejection of matter. The ejection velocity was significantly lower than during the first ejection, 17 m/s according to our calculations, which is less than the comet's escape velocity for a comet with a 60-kilometer nucleus, and the ejection direction was close to the direction obtained for the first ejection. Therefore, we believe that outburst activity of comet 174P, i.e. the fall of fragments of matter onto the surface - is similar to the one we proposed for comet 29P.

References

Chernetenko Yu. and Medvedev Yu., 2020, Monthly Notices of the Royal Astronomical Society, 493, 4, p. 5499

Medvedev Yu. and Pavlov S., 2023, Astronomy Letters, 49, 8, p. 486

Miles R., Faillace G.A., Mottola S., et al., 2016, Icarus, 272, p. 327

Neslusan L., 2014, Planetary and Space Science, 101, p. 162

Rousselot P., Kryszczyńska A., Bartczak P., et al., 2021, Monthly Notices of the Royal Astronomical Society, 507, 3, p. 3444

Weissman P., Chesley S., Choi Y., et al., 2006, Bulletin of the American Astronomical Society, 38, p. 551

MODERN ASTRONOMY: FROM THE EARLY UNIVERSE TO EXOPLANETS AND BLACK HOLES

Tidal changes in the rotational state of asteroids as evolution factor of the magnitude of the Yarkovsky effect

A. Melnikov[1], M. Khovrichev[1], I. Balyaev[1], and K. Lobanova[1,2]

[1] Pulkovo Observatory, 65/1 Pulkovskoye ave., Saint-Petersburg, 196140 Russia
[2] Saint Petersburg State University, 7/9 Universitetskaya emb., Saint-Petersburg, 199034 Russia

Abstract. We examined possible tidal-induced leaps in the rotational state parameters of the asteroids during their planet approaches. These dramatic changes in the rotational period and obliquity lead to significant changes in orbital dynamics due to the corresponding Yarkovsky acceleration A_2 leap. Our numerical simulations of asteroid rotational parameters evolution due to their planet encounters support the conclusion that significant A_2 changes can happen when planetocentric distance is less than ten planetary radii. We have found nine asteroids with anomalous A_2 values. However, there is no exact evidence that these A_2 discrepancies can be explained by tidal effects only.

Keywords: minor planets, asteroids: general

DOI: 10.26119/VAK2024.150

1 Introduction

The investigation of the Yarkovsky drift (Yarkovsky 1901) is significant for the understanding of the asteroid orbital evolution. The physical model of the Yarkovsky effect is well-developed (e.g. Vokrouhlicky et al. (2000)). It is customary to denote the nongravitational accelerations as A_1, A_2, A_3 according to Marsden et al. (1973). The A_2 value can be determined for the asteroids using the orbit improvement procedure.

The value of the considered effect depends on the rotational state of the body. Various physical phenomena can alter the rotation period (P) and axis orientation of asteroids. One such phenomenon is a tidal-induced leap in asteroid rotation during a close flyby of a planet. This paper aims to estimate the contribution of this phenomenon to the orbital dynamics of asteroids.

2 Numerical experiments

Numerical experiments were conducted to simulate the asteroid rotational dynamics during close encounters with planets (see Lobanova & Melnikov (2024)). It has been determined that under a rigid-body model, significant changes in P and γ (the angle between the axis of rotation and the normal to the orbital plane), leading to an anomalous change in A_2, can occur only during very close encounters ($d \leq 10R_{\rm E}$, where $R_{\rm E}$ is the radius of the Earth) and with a relatively slow initial rotation ($P > 5$ hours). Fig. 1 illustrates the relationship between the change in the P of the (99942) Apophis (ΔP) and the geocentric orbit parameters (d, e).

Among the numbered asteroids, there are some, like 1998 ST27, that can be described by the "rubble pile" model (Chapman 1977). For these asteroids, close encounters with planets can cause tidal deformation of their shape, resulting in a change in A_2. In Fig. 1 an example of changes in A_2 for a model asteroid similar to Apophis is shown. It is assumed that at the pericenter of the geocentric orbit, the asteroid undergoes deformation/destruction, causing changes in its inertial parameters: before approach $A/C = 0.73$, after — $A/C = 0.36$; $B/C = 0.95$ and remains unchanged. It is apparent that ΔA_2 is comparable to the current value (Pérez-Hernández et al. 2022) $A_2 = -2.9 \cdot 10^{-14}$ au/d^2 for Apophis. During tidal deformation, an asteroid's A_2 can change by a factor of 2 to 3 and even alter the direction of Yarkovsky drift.

3 Search for A_2 anomaly

Let's assume that the asteroid had the Yarkovsky parameter A_2 before its approach to the planet. Tidal effects during the approach to the planet changed the A_2 value.

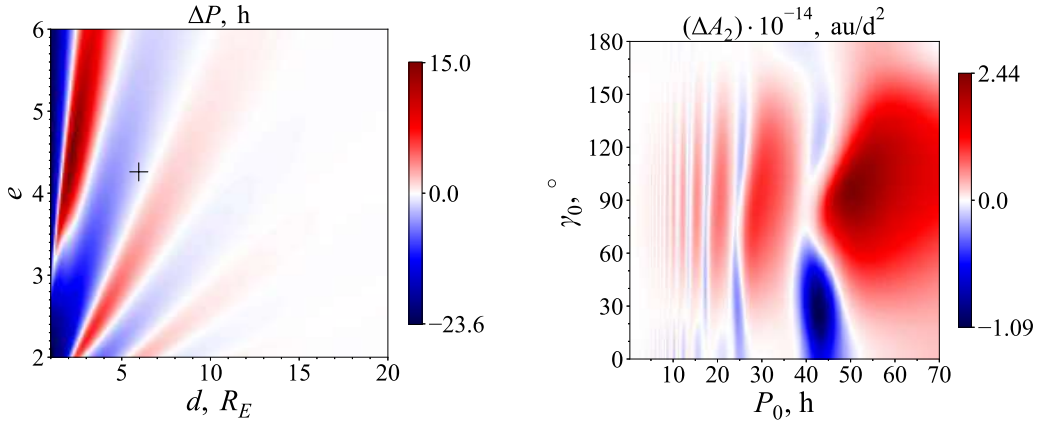

Fig. 1. The graph on the left shows how the change in the rotation period of the asteroid Apophis due to its approach to Earth in 2029 (denoted by ΔP) depends on the geocentric orbit parameters $d = a(e-1)$ and e; $A/C = 0.73$, $B/C = 0.95$, $P_0 = 30.6\,\mathrm{h}$, $\gamma = 140°$. The cross on the graph indicates the position of the asteroid (Pravec et al. 2014). The graph on the right illustrates how ΔA_2 depends on the initial values of the rotation period (P_0) and the angle (γ_0) between the axis of rotation and the normal to the orbital plane. In this case, the asteroid undergoes "deformation" at the point of approach. Before approaching, the ratio of moments of inertia is $A/C = 0.73$, but at the point of approach and beyond $A/C = 0.36$ and $B/C = 0.95$. The orbital parameters of the asteroid are the same as those of Apophis.

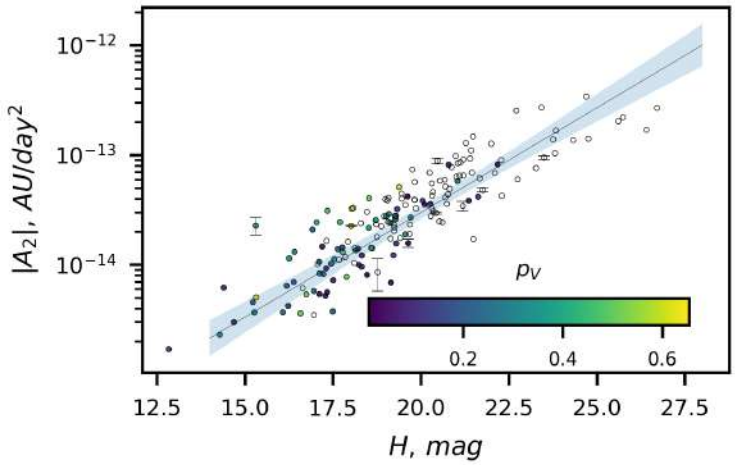

Fig. 2. A_2 as a function of H for asteroids with well-determined Yarkovsky acceleration. Error bars are shown for asteroids with the A_2 anomaly only.

Therefore, it can be expected that the A_2 estimate for the entire series of observations (usually 20–40 years), including astrometric measurements before and after the approach, will not correspond to the most probable value for asteroids with a certain absolute stellar magnitude (H) and albedo values p_v. Therefore, it was logical to try to search for asteroids with anomalous A_2 values.

Figure 2 demonstrates a well-known $A_2(H)$ relation in a logarithmic scale. We calculated the parameters of this ratio and detected 9 asteroids with A_2 value exceeding expected $A_2(H)$ in the 3σ sense. These asteroids are 2340 Hathor (1976 UA), 4179 Toutatis (1989 AC), 33342 (1998 WT24), 138175 (2000 EE104), 276033 (2002 AJ129), 363027 (1998 ST27), 437844 (1999 MN), 1995 CR and 2009 UG. The minimal geocentric distance within this list is 2.2 LD for 2002 AJ129. This significantly exceeds the effective planet-asteroid distance for the tidal-induced leap in the rotational state. Hence, there is no direct observational evidence for conducted simulation results. The A_2 anomaly for these asteroids may be explained by sublimation activity due to short perihelion distances.

4 Conclusions

Perturbations in the rotational motion of an asteroid can cause noticeable changes in the value of A_2 when the asteroid rotates relatively slowly (for periods of more than five hours) and comes close to a planet at a distance, ten times smaller than its radius. its radius. Asteroid A_2 value can change by a factor of 2 to 3 for the case of the tidal deformation. We have found nine asteroids with anomalous A_2 values. However, there is no exact evidence that these A_2 discrepancies can be explained by tidal effects only.

Funding

The study was funded by a Russian Science Foundation grant No 23-22-00306, https://rscf.ru/project/23-22-00306/.

References

Chapman C., 1977, IAU Colloquium, 39, p. 265
Lobanova K.S. and Melnikov A.V., 2024, Solar System Research, 58, 2, p. 208
Marsden B.G., Sekanina Z., and Yeomans D.K., 1973, Astronomical Journal, 78, p. 211
Pérez-Hernández J.A., Jorge A., and Benet L., 2022, Comm. Earth & Environ., 3, 1, id.10
Pravec P., Scheirich P., Ďurech J., et al., 2014, Icarus, 233, p. 48
Vokrouhlicky D., Milani A., and Chesley S.R., 2000, Icarus, 148, 1, p. 118
Yarkovsky I.O., 1901, The density of the light ether and the resistance it provides to movement, Bryansk: Yudin's typography

MODERN ASTRONOMY: FROM THE EARLY UNIVERSE TO EXOPLANETS AND BLACK HOLES

Perturbations in the rotational dynamics of small asteroids when approaching the Earth

A. Melnikov[1] and K. Lobanova[1,2]

[1] Pulkovo Observatory, 65/1 Pulkovskoye ave., Saint-Petersburg, 196140 Russia
[2] Saint Petersburg State University, 7/9 Universitetskaya emb., Saint-Petersburg, 199034 Russia

Abstract. Using numerical modeling, perturbations that occur in the rotational motion of small (10–50 m in diameter) asteroids during their close approaches to the Earth (at distances of the order of several Earth radii) are considered. For a number of asteroids (Duende, 2012 TC4 and 2023 BU), estimates of possible changes in the rotational period P and the orientation of the rotational axis due to approach to the Earth were obtained. It has been established that in the case of fast rotation of an asteroid ($P < 1$ h), perturbations in its rotational motion that arise during approach are negligible. With a relatively slow rotation of the asteroid ($P > 5$ h), perturbations can be significant: changes in P may reach several hours, and deviations of the rotation axis from the initial position may amount to tens of degrees. Such perturbations influence further orbital dynamics of a slowly rotating asteroid by changing the magnitude of the Yarkovsky effect.

Keywords: celestial mechanics; minor planets, asteroids: general; methods: numerical

DOI: 10.26119/VAK2024.151

1 Introduction

One of the important characteristics of an asteroid is its rotational state. More than 60% of currently known near-Earth asteroids are small bodies (diameter $D <$ 100 m)[3]. The period P of the asteroid's own rotation is related to the size of the asteroid (see, for example, Pravec & Harris (2000); Fenucci et al. (2024)). Among small asteroids, objects with fast ($P < 5$ h) rotation predominate. Periods $P = 5$–100 h are typical for larger asteroids ($D >$ 100–1000 m). Asteroids with $D \sim 10$ m, which are probably monolithic bodies, can have very fast rotation with $P < 1$ h. During the secular orbital evolution of a number of small asteroids, close encounters with the Earth at distances of several radii of our planet ($R_{\rm E}$) take place. Such approaches cause perturbations in the rotation of the asteroid (Scheeres et al. 2000; Boldrin et al. 2020; Melnikov 2022) and influence its further orbital dynamics (Martyusheva & Melnikov 2023; Lobanova & Melnikov 2024). Within the framework of the problem of asteroid-comet hazard, the study of the influence of close encounters with the Earth on the rotational dynamics of an asteroid is of great importance.

2 Problem statement and method

Using numerical experiments to model a close ($< 10R_{\rm E}$) approach to the Earth, the influence of the rotational speed and orientation of the asteroid's rotational axis on the magnitude of perturbations in its rotational dynamics was studied. In accordance with the methodology presented in Lobanova & Melnikov (2024), the dynamics of three small asteroids was considered: (367943) Duende ($D \approx 30$ m, $P \approx 8$ h), 2012 TC4 ($D \sim 10$ m, $P \approx 12$ min) and 2023 BU ($D \sim 10$ m, $P \approx 2$ min). On the set of initial values (before approach) of the asteroid's rotational period P_0 and the angle between the rotational axis and the normal to the orbital plane γ_0, the values $\Delta P = P_{\rm final} - P_0$ and $\Delta\gamma = \gamma_{\rm final} - \gamma_0$ were determined, where $P_{\rm final}$ and $\gamma_{\rm final}$ represent the values acquired after approach to the Earth.

3 Perturbations in asteroid rotation

Figure 1 shows diagrams of $\Delta P(P_0, \gamma_0)$ and $\Delta\gamma(P_0, \gamma_0)$, constructed for the approach of Duende to the Earth in 2013. The diagrams show the position of Duende for two models (Benson et al. 2020) of its rotation after approach ($P_0 = 8.7$ h; $\gamma_0 = 27°, 160°$). From Fig. 1 it follows that for the first model ($P_0 = 8.7$ h, $\gamma_0 = 27°$) we have: $\Delta P \approx 4$ h, $\Delta\gamma \approx 4°$, for the second model the perturbations are somewhat smaller.

[3] https://cneos.jpl.nasa.gov/stats/size.html

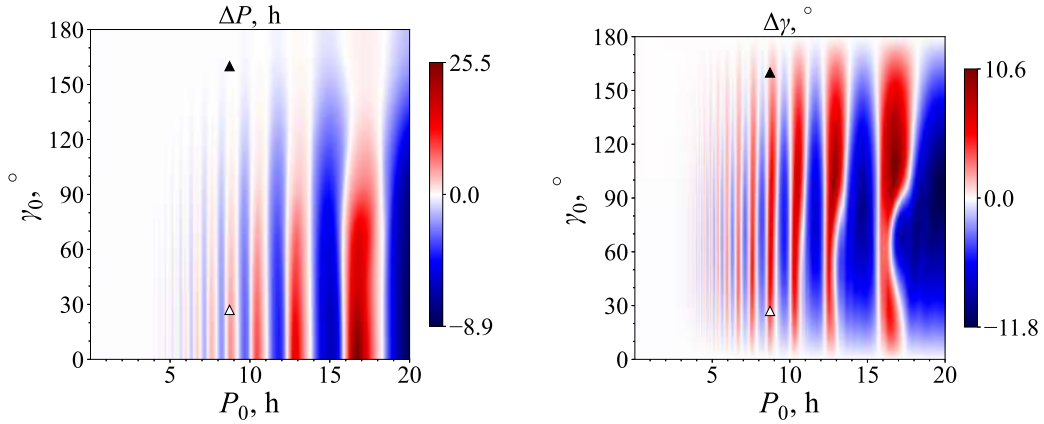

a) b)

Fig. 1. a) Dependence of the change in the rotational period ΔP of the asteroid Duende due to its approach to the Earth in 2013 on the possible initial (before the moment of approach) values of P_0 and γ_0. b) Dependence of the change $\Delta\gamma$ in angle characterizing the deviation of the rotation axis of the asteroid Duende from the normal to the orbital plane on P_0 and γ_0. Accepted orbital and inertial parameters of the asteroid Duende: $e = 4.22$, $d = 5.34R_{\rm E}$, $A/C = 0.25$, $B/C = 0.85$. Triangles indicate possible positions of the asteroid (according to Benson et al. (2020)).

Taking into account the results of our earlier (Lobanova & Melnikov 2024) modeling of the rotational dynamics of the asteroid Apophis ($D \approx 340$ m, $P \approx 30$ h) during its approach to the Earth in 2029, we can assume that asteroids with relatively slow rotation ($P > 5$ h) are characterized by significant perturbations in rotation. For example, in the cases of Apophis and Duende, when approaching the Earth, the values of $|\Delta P|$ are from a few to tens of hours, and the value of $|\Delta\gamma|$ reaches tens of degrees.

Figure 2 shows diagrams constructed for the approach of asteroid 2012 TC4 to the Earth in 2017. Analysis of the diagrams showed that perturbations for small asteroids with very fast rotation ($P < 1$ h) should be negligible: in the case of 2012 TC4 $|\Delta P| < 10^{-5}$ min, $|\Delta\gamma| < 0.01°$. For the asteroid 2023 BU, the identified magnitude of possible perturbations was even smaller.

4 Influence of perturbations on the Yarkovsky effect

In the orbital dynamics of small asteroids, a significant role is played by the Yarkovsky effect (YE) (Vokrouhlický et al. 2000), leading to a secular change in the semimajor axis of the asteroid's orbit. We studied the influence of perturbations in the rotation

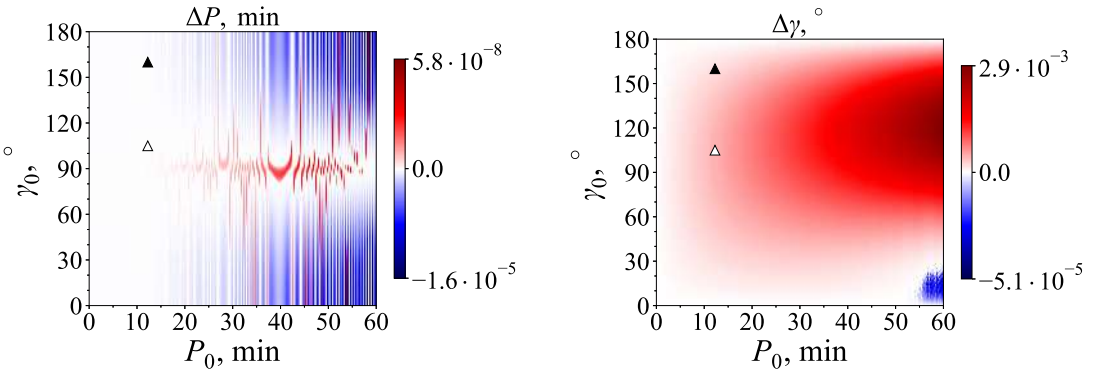

a) b)

Fig. 2. a) Dependence of the change in the rotational period ΔP of the asteroid 2012 TC4 due to its approach to the Earth in 2017 on the possible initial (before the moment of approach) values of P_0 and γ_0. b) Dependence of the change $\Delta\gamma$ in angle characterizing the deviation of the rotation axis of the asteroid 2012 TC4 from the normal to the orbital plane on P_0 and γ_0. Accepted orbital and inertial parameters of the asteroid 2012 TC4: $e = 6.36$, $d = 7.86 R_{\rm E}$, $A/C = 0.42$, $B/C = 0.81$. Triangles indicate possible positions of the asteroid (according to Lee et al. (2021)).

of asteroids due to close encounters with the Earth on the value of the parameter A_2 (Marsden et al. 1973), which characterizes the YE. Based on the obtained estimates of ΔP and $\Delta\gamma$ for all studied asteroids, the values of the YE before ($A_2^{\rm before}$) and after ($A_2^{\rm after}$) approaching the Earth were calculated.

Figure 3 for asteroids Duende and 2012 TC4 shows $\Delta A_2(P_0, \gamma_0)$ diagrams, where $\Delta A_2 = A_2^{\rm after} - A_2^{\rm before}$. It can be seen that in the case of Duende, for the adopted rotational parameters (Benson et al. 2020) there is a slight change in ΔA_2. In the case of Apophis, an almost 30% change in A_2 is possible (see Lobanova & Melnikov (2024) for more details). Close encounters with the Earth can noticeably change the magnitude of the YE in the case of small asteroids with relatively slow rotation. For asteroids with fast rotation (such as 2012 TC4 and 2023 BU), perturbations that occur in the rotational dynamics due to close encounters with the Earth have no noticeable effect on their A_2 values.

5 Summary

In this work, through numerical experiments, the perturbations arising in the rotational dynamics of small asteroids during their close approaches to the Earth were studied. It was shown that:

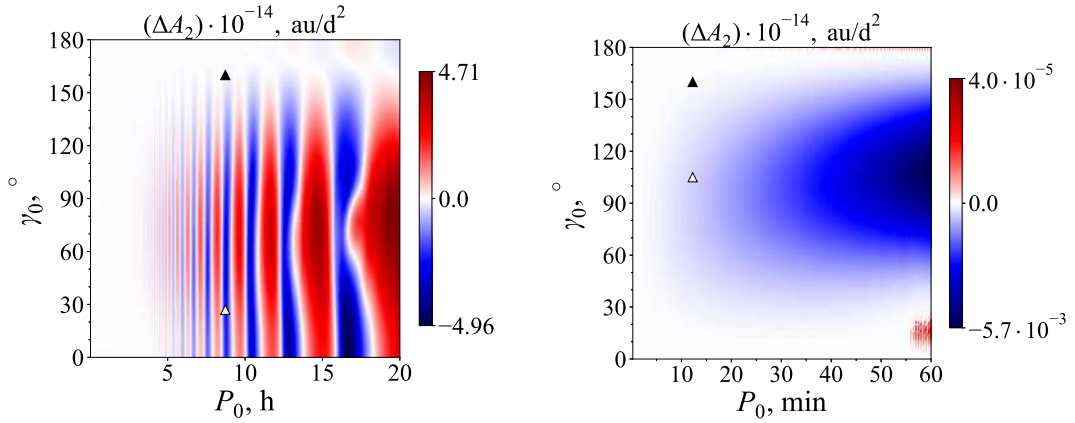

a) b)

Fig. 3. a) Dependence of the parameter ΔA_2, which characterizes the change in the magnitude of the YE, on the possible initial (before the moment of approach) values of P_0 and γ_0 for Duende during its approach to the Earth in 2013. b) The same for asteroid 2012 TC4 during its approach to the Earth in 2017. The triangles indicate possible positions of asteroids (according to Benson et al. (2020); Lee et al. (2021)).

1. For asteroids with very fast rotation ($P < 1$ h), perturbations in the rotational speed (the value of the period P) and the orientation of the rotational axis (the angle γ which characterizes the orientation of the rotational axis relative to the normal to the orbital plane) are very small. The perturbations do not affect further dynamics of the asteroid.
2. For small asteroids with relatively slow rotation ($P > 5$ h), perturbations in the rotational speed and orientation of the rotational axis can be significant: changes in P reach several to tens of hours, and changes in γ reach tens of degrees. Such perturbations must be taken into account when studying further asteroid dynamics.
3. Perturbations in rotation (in P and γ) arising due to the approach to the Earth will affect the magnitude of the Yarkovsky effect for asteroids with slow rotation and will be unnoticeable in the case of asteroids with very fast rotation.

Funding

The study was funded by a Russian Science Foundation grant № 23-22-00306, https://rscf.ru/project/23-22-00306/.

References

Benson C.J., Scheeres D.J., and Moskovitz N.A., 2020, Icarus, 340, id. 113518

Boldrin L.A.G., Araujo R.A.N., and Winter O.C., 2020, European Physical Journal – Special Topics, 229, 8, p. 1391

Fenucci M., Micheli M., Gianotto F., et al., 2024, Astronomy & Astrophysics, 682, id. A29

Lee H.-J., Ďurech J., Vokrouhlický D., et al., 2021, Astronomical Journal, 161, 3, id. 112

Lobanova K.S. and Melnikov A.V., 2024, Solar System Research, 58, 2, p. 208

Marsden B.G., Sekanina Z., and Yeomans D.K., 1973, Astronomical Journal, 78, 2, p. 211

Martyusheva A.A. and Melnikov A.V., 2023, Solar System Research, 57, 5, p. 486

Melnikov A.V., 2022, Solar System Research, 56, 4, p. 241

Pravec P. and Harris A.W., 2000, Icarus, 148, 1, p. 12

Scheeres D.J., Ostro S.J., Werner R.A., et al., 2000, Icarus, 147, 1, p. 106

Vokrouhlický D., Milani A., and Chesley S.R., 2000, Icarus, 148, 1, p. 118

VAK 2024 MODERN ASTRONOMY: FROM THE EARLY UNIVERSE TO EXOPLANETS AND BLACK HOLES 300 years Russian Academy of Sciences

The effect of encounters with interstellar objects of planetary and substellar masses on the Solar system dynamics

D. Mikryukov[1] and I. Shevchenko[1,2]

[1] Saint Petersburg State University, 7-9 Universitetskaya Emb., Saint Petersburg, 199034 Russia
[2] Institute of Applied Astronomy of the Russian Academy of Sciences, Saint Petersburg, 191187 Russia

Abstract. We explore the immediate and long-term consequences of close passages of interstellar planet-mass and substellar-mass objects for the Solar system dynamics. Two approach orbits of such objects are considered, namely, the hyperbolic orbits of two real interstellar objects, 1I/'Oumuamua and 2I/Borisov. For each orbit, a series of massive numerical experiments is performed, in which the mass of the interstellar object is varied in small steps over a broad range. It is shown that even if the interloper does not experience any close encounter with a planet of the Solar system, and has a mass typical for a free-floating planet, a disruption of the Solar system may occur on time scales of several million years.

Keywords: planets and satellites: dynamical evolution and stability; ISM: individual objects: 1I/'Oumuamua, 2I/Borisov

DOI: 10.26119/VAK2024.152

1 Introduction

A free-floating planet (FFP) is understood as a planet that is not gravitationally bound to any star. The upper mass limit for a planet is about $13M_{\rm J}$ (Jupiter masses). With a larger mass value, deuterium is ignited in the core and the object thus represents a brown dwarf (BD). The upper mass limit for BD is about $75M_{\rm J}$.

Currently, ordinary planetary systems (including circumbinary ones) are considered to be the main source of origin of FFPs. A possibility of the FFP formation in interstellar space through the gravitational collapse of interstellar gas blobs is also not excluded. Analysis of various formation mechanisms gives an estimate of the FFP concentration in the Galactic thin disc in the range from 0.24 to 200 pc^{-3} (Goulinski & Ribak 2018).

Studies of interactions of planetary systems with massive interstellar objects (MISOs), such as FFPs or BDs, are of great interest, since they directly concern the problem of stability and long-term orbital dynamics of planetary systems. In this work, we explore effects of interaction of MISOs with our Solar system. We study the immediate consequences of such encounters, as well as their impact on the long-term evolution of the Solar system.

2 Model set-up

2.1 Approach trajectories and MISO mass range

There can be many scenarios for the interaction of the Solar system with a MISO, since the choice is broad not only for the MISO mass but also for its orbit's initial conditions. Here, we consider two nominal approach trajectories: namely, the hyperbolic orbits of real interstellar objects 1I/'Oumuamua and 2I/Borisov (hereafter orbits I and II, respectively), which visited the Solar system in 2017 and 2019. These both orbits traverse the inner Solar system.

For each of these orbits, the initial state of the system (positions and velocities) is set to be the same in all our numerical experiments, only the MISO mass is varied. The number of experiments is rather large (about 2000 per orbit), since the mass is varied in small steps over a wide range, see Table 1. In this Table, the quantities ρ and τ denote the maximum interaction distance and the integration time interval, respectively (see details below).

2.2 Numerical experiments

The gravitational interaction of the Sun, MISO and eight major planets (from Mercury to Neptune) is considered. At the initial epoch T_0, the MISO is at a distance ρ

Table 1. Computation series parameters.

MISO type	Mass range	Step in mass	ρ	τ
	M_J	M_J	au	yr
FFP	0 – 13	0.01	1.2×10^4	5×10^6
BD	13 – 45	0.05	6×10^4	2×10^6

from the Sun and is approaching the Solar system. After passing the perihelion, the MISO moves further and further reaching the same distance ρ from the Sun, is excluded from the integration. The integration of the perturbed planetary configuration is, however, continued and is eventually stopped when the time elapsed since the epoch T_0 becomes equal to τ. If, during this time interval, any planet is ejected, the integration is also stopped.

In each experiment, we calculated the maximum values of the planetary eccentricities and inclinations

$$e^j_{\max} = \max e_j, \quad i^j_{\max} = \max i_j, \qquad 1 \leqslant j \leqslant 8, \tag{1}$$

as well as quantities

$$\begin{aligned} d^1_{\min} &= \min(a_3(1-e_3) - a_1(1+e_1)), \\ d^j_{\min} &= \min(a_j(1-e_j) - a_{j-1}(1+e_{j-1})), \quad 2 \leqslant j \leqslant 8, \end{aligned} \tag{2}$$

which estimate distances between two elliptical orbits (e.g. Mikryukov & Baluev 2019). To calculate all 24 quantities $e^j_{\max}, i^j_{\max}, d^j_{\min}$, $1 \leqslant j \leqslant 8$, a time step of 5 years is used, and the maxima and minima on the right-hand sides of (1) and (2) are taken over the total integration time interval (starting from T_0). At the time moment of the MISO exclusion from the system, the values of the osculating semimajor axes, eccentricities and inclinations

$$a^j_{\mathrm{imm}}, \quad e^j_{\mathrm{imm}}, \quad i^j_{\mathrm{imm}}, \quad 1 \leqslant j \leqslant 8,$$

were recorded. The accuracy of calculations in each experiment was controlled by checking the conservation of the energy integral.

2.3 Software and hardware

All calculations were performed by the IAS15 high-precision non-symplectic integrator implemented in the REBOUND package (Rein & Spiegel 2015).

The computing resources of the Joint Supercomputer Center of the Russian Academy of Sciences[3] were used. Each MPI (Message Passing Interface) process

[3] https://www.jscc.ru/

ran one instance of REBOUND with a given orbit and a given value of the MISO mass.

3 Results

Here we present the main results obtained in our numerical experiments with MISOs in orbit I. A detailed discussion of the results concerning both orbits I and II can be found in Mikryukov & Shevchenko (2024).

3.1 Planet-mass MISOs

The orbits of outermost planets, those of Uranus and Neptune, are most susceptible to immediate excitation. For other six planets, the inclinations and eccentricities are excited much less, and their parameters $e_{\rm imm}$, $i_{\rm imm}$ show much smaller variations with the increase of MISO's mass.

In the numerical experiments with planet-mass MISOs it is found that a MISO flyby is able to cause an immediate entering of a pair of planets into a mean motion resonance. This, in turn, may cause disruption of the Solar system on a secular timescale.

3.2 Substellar-mass MISOs

In the case of substellar-mass (> 13 Jovian masses) interlopers, i.e. free-floating BDs, the general conclusions about the influence of the flyby on the subsequent evolution of the planetary system are as follows.

(1) The immediate (on the timescale of $\sim$10–100 yr) consequence of the passage is a significant increase in the orbital inclinations and eccentricities of the outermost planets — Uranus and Neptune.

(2) On the intermediate timescale ($\sim 10^3$–10^5 yr), Uranus (most likely) and Neptune can be ejected from the Solar system due to close encounters with Saturn, as well as with each other.

(3) On the secular timescale ($\sim 10^6$–10^7 yr), the major perturbation wave caused by the secular interactions of the planets reaches the inner part of the Solar system.

A typical example of the long-term behaviour of eccentricities and inclinations of the outer planets, before Uranus is ejected, is presented in Fig. 1. In this example, a flyby of a MISO with a mass of $m_{\rm MISO} = 28.7 M_{\rm J}$ in orbit I causes the ejection of Uranus in about one million years after the encounter.

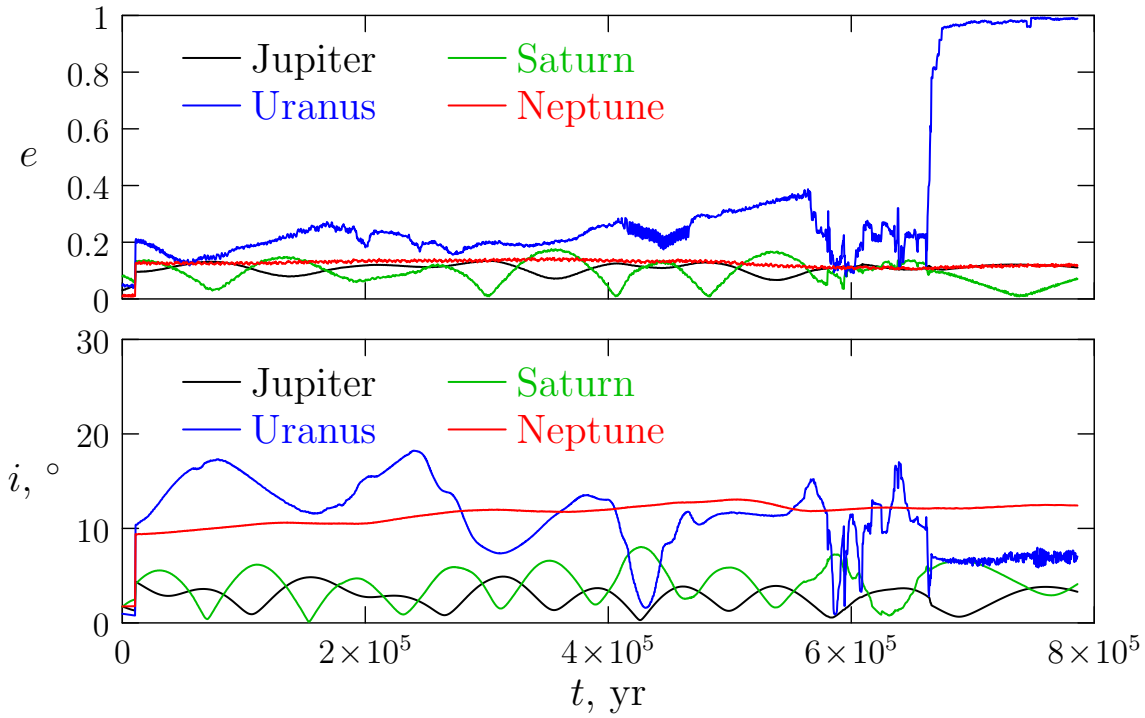

Fig. 1. The long-term behaviour of eccentricities and inclinations of the outer planets before Uranus is ejected, a typical example.

4 Summary

As follows from the performed analysis, the long-term stability of the Solar System can be disrupted even if the interstellar interloper is not very massive (a Jovian mass is enough) and does not experience any close encounter with any planet of the Solar system. The disintegration of the planetary system does not necessarily appear immediately, but may take place in several million years.

It also follows that it is unlikely that the Solar system, which has an age of more than 4 Gyr, in its past was subject to numerous encounters with objects of giant-planet and substellar masses, because such encounters induce large planetary eccentricities and inclinations and may even lead to ejections of outermost planets.

Any MISO flyby typically sets the planetary system into a more chaotic state; however, a stronger chaos, implying a smaller Lyapunov time, does not necessarily cause a more rapid disintegration, because the Lyapunov timescales and chaotic diffusion timescales can be interrelated in various, very different, fashions (Shevchenko 2020; Cincotta et al. 2022); and the system, in fact, can remain in a state of "stable

chaos", with no following disruption. Besides, the distributions of disruption times of gravitational systems of the considered type are heavy-tailed (Orlov et al. 2010; Shevchenko 2010); therefore, the disruptive effect of an encounter can occasionally be quite prolonged, with respect to values typically observed in numerical simulations.

Acknowledgements. The calculations were carried out using the computing resources of the Joint Supercomputer Center of the Russian Academy of Sciences.

Funding

This work was supported in part by the Russian Science Foundation, project 22-22-00046.

References

Cincotta P., Giordano C., and Shevchenko I., 2022, Physica D, 430, id. 133101

Goulinski N. and Ribak E., 2018, Monthly Notices of the Royal Astronomical Society, 473, 2, p. 1589

Mikryukov D.V. and Baluev R.V., 2019, Celestial Mechanics and Dynamical Astronomy, 131, 6, id. 28

Mikryukov D.V. and Shevchenko I.I., 2024, Monthly Notices of the Royal Astronomical Society, 528, 4, p. 6411

Orlov V.V., Rubinov A.V., and Shevchenko I.I., 2010, Monthly Notices of the Royal Astronomical Society, 408, 3, p. 1623

Rein H. and Spiegel D., 2015, Monthly Notices of the Royal Astronomical Society, 446, 2, p. 1424

Shevchenko I.I., 2020, Astrophysics and Space Science Library, 463, p. 1

Shevchenko I.I., 2010, Physical Review E, 81, 6, id. 066216

MODERN ASTRONOMY:
FROM THE EARLY UNIVERSE TO EXOPLANETS AND BLACK HOLES

Accuracy of orbits of small celestial bodies obtained using different software

S. Pavlov[1], Yu. Medvedev[1], T. Galushina[2], and A. Baturin[2]

[1] Institute of Applied Astronomy of the Russian Academy of Sciences, 10 Kutuzova Emb., St. Petersburg, 191187 Russia
[2] Tomsk State University, 36 Lenin Ave., Tomsk, 634050 Russia

Abstract. The threat of a collision with a potentially hazardous object (PHO) and smaller asteroids requires the ability to reliably calculate the orbits of celestial bodies. The quality of the determined orbit depends on both the accuracy and intervals of observations and on the method of their processing: the completeness of the dynamic model, the method of numerical integration, calculation errors, etc. The practical implementation of the orbit determination algorithm is associated with the peculiarities of taking into account the above factors. To assess the accuracy of motion prediction using orbits obtained with the help of different software packages, we compared the deviations in observed and calculated values of observations, i.e. $O-C$, that were not included in the orbit improvement. The $O-C$ comparison was carried out for orbits obtained using software developed in leading Russian scientific organizations with teams working on asteroid-comet dynamics: Pulkovo, Tomsk State University (TSU) and Institute of Applied Astronomy of RAS (IAA), as well as orbits presented on the Jet Propulsion Laboratory's (JPL) Horizons website. The asteroids Apophis and Phaethon were chosen as objects for which the $O-C$ comparison was performed. Observations of each asteroid were divided into two samples by time. The asteroid's orbit was improved using the earlier sample, and the later sample was used to access the accuracy of the prediction. The $O-C$ distribution profile for orbits obtained using different software turned out to be very similar, indicating the proximity of predictions. The most accurate orbits were obtained using the `Improvement` and `IDA` software developed at the IAA and TSU, respectively.

Keywords: small celestial bodies; dynamics; orbit improvement; asteroid/comet hazard

DOI: 10.26119/VAK2024.153

1 Introduction

At present, the problem of asteroid and comet hazard is given special attention. The number of potentially hazard asteroids has reached 2429 (as of July 29, 2024, IAU MPC[1]). Moreover, there is still a huge number of less bright asteroids with unknown albedo, which can also pose a danger to human safety (Reddy et al. 2024). These circumstances force us to predict the risks emanating from celestial bodies approaching the Earth, which is impossible to do without obtaining their high-quality orbits (Gehrels 1994). The accuracy of the orbit of a celestial body, i.e. predictions of its position at different moments in time, depends primarily on two components: the intervals and the accuracy of observations of the target body and the method of their processing which includes the completeness of the dynamic model, the accuracy of the transformation of coordinates between different reference systems, computational errors, rounding errors, etc. (Moyer 1971).

Today in Russia there are several software packages that allow us to determine the orbits of small celestial bodies and teams that are engaged in the development and maintenance of these programs. While developers are responsible for the quality of their software, it is necessary to have a one reference orbit in order to obtain a space threat assessment and the ability to respond in a timely manner. The aim of this work was to compare the accuracy of orbits obtained by different software available today.

For this purpose, we contacted members of research teams that study the dynamics of small celestial bodies, working in leading Russian research organizations. As a result, we could compare the orbits of the target bodies, obtained using programs developed at Tomsk State University (TSU), Central Astronomical Observatory of RAS at Pulkovo (Pulkovo), and Institute of Applied Astronomy of RAS (IAA). In total, we compared orbits obtained with four programs: `IDA` (TSU) (Galushina et al. 2021), `Baturin` (TSU), `Improvement` (IAA), `Lvov` (Pulkovo) and additionally the orbit taken from the NASA JPL Horizons website.

2 Method

To compare the accuracy of orbits obtained by different software, the asteroids Apophis (99942) and Phaethon (3200) were selected. We used positional and radar observations taken from the MPC and JPL[2] websites respectively. The observations were divided into two samples by time. The orbit of the celestial body was improved

[1] https://minorplanetcenter.net/
[2] https://ssd.jpl.nasa.gov/sb/radar.html

on the first, earlier sample, and the $O-C$ comparison (deviations between obtained and predicted values) was performed on the second, later sample.

As Kazimirchak-Polonskaya said, improving orbits is more art than science, which could be continued today—improving orbits is something akin to building neural networks, in the sense that there is a lot of uncertainty in this matter and the final result is influenced by the role of the researcher: in particular, how he weights the observations, what epoch he chooses to determine the orbit. Therefore, to reduce the role of the researcher in the process of obtaining an orbit, we fixed the epoch of improvement. The orbit was determined using the same set of observations for a given date within the sample for improvement. However, the assignment of weights to observations, the number of parameters to improve, and the force model used were left to the discretion of the researcher.

3 Results

Table 1 presents the root-mean-square (RMS) values of $O-C$ for right ascension (RA) multiplied by the cosine of declination (Decl), RMS $O-C$ values of declination (DEC) and the average values of $O-C$ deviations from zero (AV). The following notations are introduced here:

$$\mathrm{RA} = \sqrt{\frac{\sum \left[(O-C)_{\mathrm{RA}} \times \cos(\mathrm{Decl})\right]^2}{N}}; \quad \mathrm{DEC} = \sqrt{\frac{\sum (O-C)^2_{\mathrm{Decl}}}{N}};$$
$$\mathrm{AV} = \frac{\sum \sqrt{(O-C)^2_{\mathrm{Decl}} + \left[(O-C)_{\mathrm{RA}} \times \cos(\mathrm{Decl})\right]^2}}{N}, \tag{1}$$

where N denotes the number of observations.

3.1 Asteroid (99942) Apophis

The sample for improving the orbit of the asteroid Apophis consisted of 4469 positional and 46 radar observations during the 2004 and 2013 approaches. The error in presenting observations for all orbits obtained did not exceed 0.4 arcseconds. Since not all programs were capable of processing radar observations, we conducted a general comparison only on positional observations. The test sample consisted of 5061 observations during the 2021 approach. The epoch was taken at noon January 22, 2013. As an indicator of the accuracy of the predicted orbit, we calculated the deviations in $O-C$ from zero on the test sample. Fig. 1 shows the deviations in $O-C$ on the Apophis test sample for orbits obtained using different program software.

As one can see the $O-C$ distribution profile for all the orbits obtained turned out to be quite similar. The differences in the Keplerian elements between different

Table 1. Error in the representation of observations of the asteroids Apophis and Phaethon on the test sample. The first column contains the designation symbols for the software used to calculate the orbits. JPL denotes the orbit obtained from Horizons, IAA denotes the orbit obtained with the usage of `Improvement` software developed at IAA, `IDA` denotes the orbit obtained at TSU using the software package of the same name, BAT denotes the orbit obtained in TSU with A. Batrurin's software and PUL denotes the orbit obtained by V. Lvov from Pulkovo. The $O-C$ values for RA, DEC and AV are presented in arcseconds.

Designation	Apophis			Phaethon		
	RA	DEC	AV	RA	DEC	AV
JPL	0.601	0.589	0.559	0.348	0.467	0.297
IAA	0.794	0.602	0.794	0.349	0.469	0.303
IDA	1.144	0.655	1.150	0.324	0.276	0.279
BAT	1.239	0.687	1.263	0.686	0.329	0.691
PUL	2.640	1.099	2.663	0.434	0.498	0.418

orbits did not exceed: $de = 0.2 \times 10^{-6}$, $da = 0.2 \times 10^{-7}$ AU, $di = 0.2 \times 10^{-5}$ deg, $d\Omega = 0.7 \times 10^{-4}$ deg, $d\omega = 0.7 \times 10^{-4}$ deg. The minimal $O-C$ is for orbit taken from the Horizons website, since it was obtained from the entire set of observations, including observations from the test sample.

3.2 Asteroid (3200) Phaethon

The sample for improving the orbit of the asteroid Phaethon consisted of 5949 positional and 8 radar observations from 1983 to 2020. The error in presenting observations for most orbits did not exceed 0.4 arcseconds. The test sample consisted of 1524 positional observations during the 2020–2024. The epoch was taken at noon February 15, 2017. The $O-C$ distribution profile for all orbits also turned out to be quite similar. Fig. 2 shows the deviations in $O-C$ on the Phaethon test sample for orbits obtained using different software. The differences in the Keplerian elements between different orbits did not exceed: $de = 0.1 \times 10^{-5}$, $da = 0.1 \times 10^{-6}$ AU, $di = 0.5 \times 10^{-4}$ deg, $d\Omega = 0.2 \times 10^{-4}$ deg, $d\omega = 0.1 \times 10^{-3}$ deg.

4 Summary

This study was motivated by the growing interest in the problem of asteroid-comet hazard. In this work, we compared the accuracy of orbits obtained by different software developed by teams studying the dynamics of small celestial bodies. In order to ensure a unified response to a cosmic threat, it makes sense to have one or more reference orbits by which it would be possible to estimate the probability of collision with a celestial body.

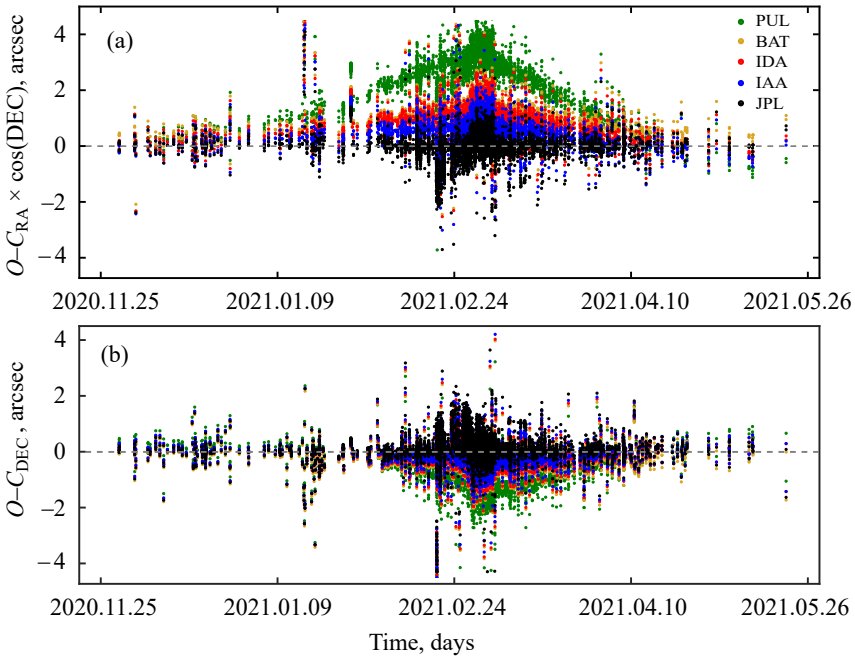

Fig. 1. Deviations in $O–C$ on the Apophis test sample for orbits obtained using different software.

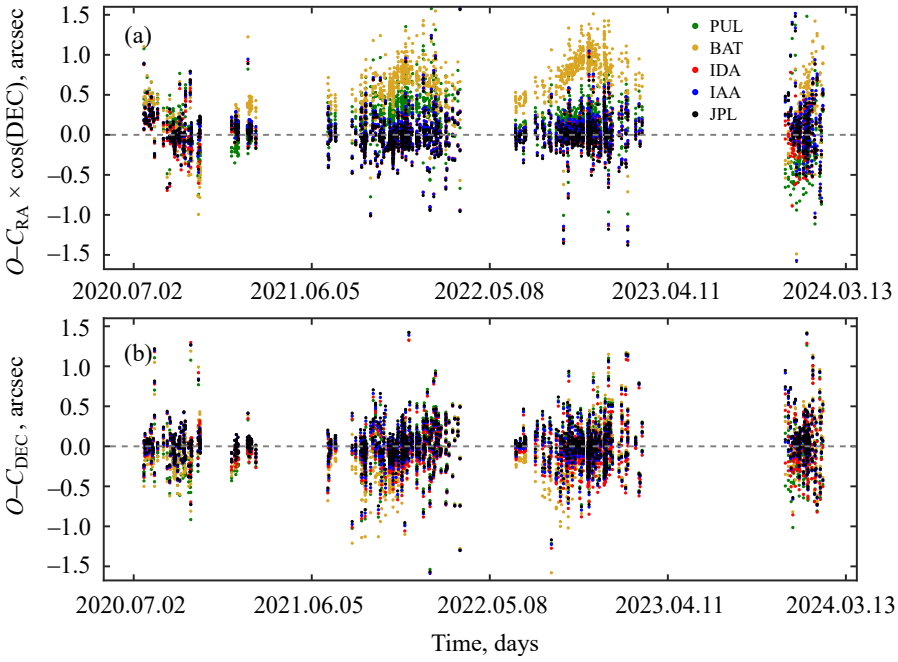

Fig. 2. Deviations in $O–C$ on the Phaethon test sample for orbits obtained using different software.

In this work, we compared orbits obtained by four programs developed at TSU, Pulkovo and IAA, as well as an orbit taken from the NASA Horizons. The accuracy of the orbits was estimated by the deviations in $O-C$ for observations not involved in the orbit improvement process. The asteroids Apophis and Phaethon were chosen as comparison objects. For the asteroid Apophis, the minimum average deviation of $O-C$ from zero was obtained for orbit calculated with the usage of `Improvement` software package developed in IAA. It amounted 0.794 arcseconds. The `IDA` software package developed at TSU was the best in predicting the orbit of asteroid Phaethon with an average $O-C$ deviation from zero of 0.279 arcseconds.

It should be noted that in order to obtain more accurate orbits, it is also necessary to process and correctly take into account radar and other types of observations in addition to positional ones, which are increasingly filling databases with observations of small bodies. It is especially important for near-Earth objects.

Acknowledgements. The authors also thank V. N. Lvov, who kindly agreed to provide the results of his calculations to conduct a more complete comparison of orbits and the corresponding software.

References

Galushina T., Letner O., 2021, Astronomical and Astrophysical Transactions, 32., 4, p. 355
Gehrels T., 1994, Tucson: University of Arizona Press
Moyer T., 1971, Technical Report 32-1527, NASA/JPL
Reddy V., Kelley M., Benner L., et al., 2024, Planetary Science Journal, 5, p. 141

MODERN ASTRONOMY: FROM THE EARLY UNIVERSE TO EXOPLANETS AND BLACK HOLES

Estimation of short-period disturbances in the motion of NEAs in the presence of an inverse-square perturbing acceleration

T. Sannikova

Crimean Astrophysical Observatory of the Russian Academy of Sciences, Nauchnyi, Crimea, 298410 Russia

Abstract. Let a point of zero mass move under the influence of attraction to the central body and a small perturbing acceleration $P' = P/r^2$, where r is the distance to the attracting center, the components of the P vector are assumed to be constant in the reference system with axes directed along the radius vector, transversal and angular momentum vector. For this problem, the equations of motion in the mean elements and formulas for the conversion from osculating elements to the mean ones in the first order of smallness were previously found. The analytical solution to the averaged equations and the Euclidean (root-mean-square over the mean anomaly) displacement norm $\varrho^2 = ||dr||^2$ were also obtained earlier, where dr represents the difference between the position vectors in the osculating and mean orbits. Using these relations, it is possible to estimate the ϱ magnitude of short-period orbital disturbances arising due to the presence of a small perturbing acceleration P', as well as the d displacement of the position of the asteroid in the mean perturbed orbit from its unperturbed position after one orbital period. For 412 near-Earth asteroids (NEAs), the ϱ displacement and the d distance were calculated. An analysis of the calculation results showed that in most cases the deviation of the osculating orbit from the mean one due to periodic perturbations is small, however, cases with the ϱ displacement of the order of several tens and hundreds of kilometers have been identified. This indicates the need to take into account short-period disturbances when short-term forecasting the movement of these objects, e.g. when planning space missions.

Keywords: celestial mechanics; minor planets, asteroids: general; methods: analytical; reference systems

DOI: 10.26119/VAK2024.154

1 Introduction

We considered the motion of the asteroid $\mathcal{A}$ under the influence of attraction to the central body $\mathcal{S}$ and perturbing acceleration P'. Let the P' vary inversely with the square of the distance from $\mathcal{S}$, that is, $P' = P/r^2$, where r is the distance to the attracting center. We introduced an orbital reference frame O with the origin in $\mathcal{S}$ and axes directed along the radius vector, the transversal (perpendicular to the radius vector in the osculating plane in the direction of motion), and the binormal (directed along the angular momentum vector). Let the P' be small compared to the main acceleration $\varkappa^2/r^2$, where $\varkappa^2$ is the product of the gravitational constant by mass $\mathcal{S}$, and the S, T, W components of the P vector are small and constant in the $\mathcal{O}$ frame.

Sannikova & Kholshevnikov (2019) applied an averaging procedure to the Euler-type equations of motion and obtained mean-elements motion equations and formulas for the conversion from osculating elements to the mean ones in the first order of smallness for this problem. Mean-elements motion equations at $S, T, W \neq 0$ and in various special cases were solved by Sannikova & Kholshevnikov (2020). Further, for this problem Sannikova (2024) obtained the Euclidean (root mean square over the mean anomaly) displacement norm $\varrho^2 = ||dr||^2$, where dr represents the difference between the position vectors on the osculating and mean orbits. Using these relations, it is possible to estimate the ϱ magnitude of short-period orbital disturbances arising due to the presence of a small perturbing acceleration P', as well as the d distance between the position of the asteroid in the mean perturbed orbit and its unperturbed position after one orbital period. Since the d displacement occurs due to secular drifts of elements under the influence of acceleration P', it characterizes the magnitude of the secular perturbation of the orbit. By comparing ϱ with d, one can decide on the possibility of neglecting periodic disturbances (more precisely, the differences between the osculating elements and the mean ones) and taking into account only the secular motion, which is given by the averaged equations.

2 Methods

Let us introduce the following notation: ϵ_n^0 are the osculating elements in the initial epoch t_0; $\bar{\epsilon}_n^0$ are the mean elements in the initial epoch t_0; $\bar{\epsilon}_n$ are the mean elements in the epoch $t = t_0 + dt$, where dt is one orbital period. The transformation of osculating elements into mean ones is carried out according to the formulas $\bar{\epsilon}_n^0 = \epsilon_n^0 - \delta\epsilon_n$, where $\delta\epsilon_n$ are the change-of-variables functions; their expressions are given in Sannikova & Kholshevnikov (2019) and Sannikova (2024). The norm of the difference between the osculating and mean elements is $\varrho^2 = a^2(V_1 S^2 + V_2 T^2 + V_3 W^2)/\varkappa^4$, where a is the

semi-major axis, expressions for the V_i functions in the form of series in powers of the eccentricity e and in powers of $\beta = e/(1+\sqrt{1-e^2})$ are given in Sannikova (2024). We obtained the $\bar{\epsilon}_n$ elements using the solutions of the averaged equations of motion given in Sannikova & Kholshevnikov (2020) and Sannikova (2021). The $\bar{\epsilon}'_n$ elements of the mean unperturbed orbit are equal to the $\bar{\epsilon}^0_n$ except for the mean anomaly, for which $\bar{M}' = \bar{M}_0 + \bar{n}_0 dt$, where $\bar{n}_0$ is mean motion at t_0. As a result, variations of the mean elements $d\bar{\epsilon}_n = \bar{\epsilon}_n - \bar{\epsilon}'_n$ over time dt were found. We used the connection of coordinates with orbital elements, to calculate the x, y, z and x', y', z' rectangular coordinates of the asteroid on the mean perturbed and unperturbed orbits at epoch t and then, we found the distance $d = ((x-x')^2 + (y-y')^2 + (z-z')^2)^{1/2}$.

3 Results

As of April 16, 2024, the Small Body Database[1] of Jet Propulsion Laboratory (JPL) included 412 near-Earth asteroids, for which the values of non-gravitational parameters A_1, A_2 or A_3 are given, and it is indicated that when modeling non-gravitational disturbances, an inverse dependence on the square of the heliocentric distance model was used. This model of forces corresponds, for example, to the presence of the Yarkovsky effect or the pressure of sunlight. Non-gravitational radial A_1, transversal A_2 and normal A_3 parameters relate to the S, T, W components as $A_1 = S/r_0^2$, $A_2 = T/r_0^2$, and $A_3 = W/r_0^2$, where $r_0 = 1$ AU.

We estimated the ϱ and d values for these 412 objects. The following constants were used in the calculations: $\varkappa^2 = 1.32712440041279419 \times 10^{20}\,\mathrm{m^3 s^{-2}}$, $1\,AU = 1.495978707 \times 10^{11}\,\mathrm{m}$, $1\,\mathrm{year} = 365.25\,\mathrm{day}$, $1\,\mathrm{day} = 86400\,\mathrm{s}$. The Table 1 shows the results of calculations. In most cases the deviation of the osculating orbit from the mean one due to periodic disturbances is small, however, cases with the ϱ displacement of the order of several tens and hundreds of kilometers have been identified, which indicates the need to take into account short-period disturbances when short-term propagating these NEAs orbits.

For 17 out of 412 NEAs ϱ exceeds 10 km, and in 4 cases ϱ is more than 100 km (see Table 1). In some cases, the magnitude of the ϱ displacement of the osculating orbit from the mean one is comparable to the d distance between the position on the mean perturbed orbit and the unperturbed position. Of the 412 NEAs, for 164 asteroids ϱ is 10% or more of d, in 6 cases more than 100%, that is, ϱ exceeds d. Thus, at times of the order of one revolution around the Sun, short-period disturbances are comparable to or exceed secular ones, so they must be taken into account when short-term forecasting the position of objects, e.g. when planning space missions.

[1] https://ssd.jpl.nasa.gov/tools/sbdb_lookup.html

Table 1. Calculation results for NEAs with the largest displacements of the osculating orbit relative to the mean one. δa and δM are the differences between osculating and mean semi-major axis and mean anomaly; $d\bar{a}$ and $d\bar{M}$ are the variations of the mean semi-major axis and mean anomaly over one orbital period; ϱ is the displacement of the osculating orbit relative to the mean orbit; d is the distance between the position of the asteroid in the mean perturbed orbit and its unperturbed position after one orbital period. Column "Note" indicates which non-gravitational parameters are given for the asteroid in the JPL database. NEAs for which ϱ exceeds d are marked with an asterisk.

Asteroid	a_0 AU	e_0	δa km	δM arcsec	$d\bar{a}$ km	$d\bar{M}$ arcsec	ϱ km	d km	Note
* 2016 NJ33	1.313	0.209	-106.885	-3.165	-4.787	0.015	651.814	40.025	$A_1A_2A_3$
* 2005 VL1	0.891	0.225	-106.944	1.490	-4.962	0.043	387.952	23.673	$A_1A_2A_3$
2006 RH120	1.033	0.025	1.987	3.950	-333.359	2.098	128.663	1639.059	$A_1A_2A_3$
* 1998 KY26	1.233	0.202	-1.624	-0.553	-1.125	0.005	104.090	6.498	$A_1A_2A_3$
2015 TC25	1.028	0.116	-13.598	0.797	-34.930	0.219	84.784	149.890	A_1A_2
2020 CD3	1.029	0.012	-0.981	-6.380	0	-1.189	70.600	876.364	A_1
* 2011 MD	1.056	0.037	-2.998	-0.262	-5.970	0.036	39.832	27.946	A_1A_2
2020 GE	1.006	0.040	2.950	-0.217	-14.442	0.093	39.247	69.241	A_1A_2
2012 LA	1.040	0.022	0.860	-1.720	12.550	-0.079	35.544	59.657	A_1A_2
2020 WY	1.020	0.029	-1.533	0.896	0	-0.545	32.094	412.848	A_1
2009 BD	1.062	0.052	-3.303	0.036	-7.756	0.047	30.256	35.581	A_1A_2
452639	2.249	0.873	-9.695	0.002	-39.013	0.113	28.799	76.567	A_2
2021 GM1	0.978	0.025	-0.066	-1.580	0	-0.505	28.505	366.538	A_1
* 2012 TC4	1.620	0.404	-12.490	0.041	-3.298	0.013	21.878	18.338	A_1A_2
* 2010 RF12	1.061	0.188	-1.974	0.128	-1.483	0.009	20.380	8.416	$A_1A_2A_3$
2016 GE1	2.065	0.520	4.806	0.002	-25.868	0.081	13.572	78.724	A_2
2013 BA74	1.754	0.445	0.374	-0.007	21.522	-0.080	10.322	73.709	A_2

Funding

This work was supported by ongoing institutional funding as part of the state assignment (topic No. 22022400207-0).

References

Sannikova T.N. and Kholshevnikov K.V., 2019, Astronomy Reports, 63, 5, p. 420
Sannikova T.N. and Kholshevnikov K.V., 2020, Astronomy Reports, 64, 9, p. 778
Sannikova T.N., 2024, Astronomy Reports, 68, 3, p. 331
Sannikova T.N., 2021, Astronomy Reports, 65, 4, p. 312

The scientific potential of the Pulkovo velocity of GNSS-stations database: geodynamics of the East European Craton

S. Smirnov[1,2], V. Gorshkov[2], N. Scherbakova[2], P. Movsesyan[1], and S. Petrov[1]

[1] St. Petersburg State University, Universitetskaya nab. 7–9–11, St. Petersburg, 199034 Russia
[2] Main (Pulkovo) Observatory of Russian Academy of Sciences, Pulkovskoe shosse 65/1, St. Petersburg, 196140 Russia

Abstract. A Velocities Data Base (VDB) for GNSS stations located on the territory of the Eastern European Platform (EEP) is being developed at Pulkovo Observatory. More than 70% of the stations belong to Russian GNSS networks. A comparison of the VDB velocities with a similar global database of the Nevada Geodetic Laboratory (NGL, USA) for common stations indicates the absence of systematic discrepancies between them, which made it possible to use the combined data from both databases for geodynamic studies in the EEP region. The kinematic parameters of the rotations of the main structural blocks of the EEP are determined and its deformation field is calculated.

Keywords: GNSS: site velocities; litospheric deformations, East European Platform

DOI: 10.26119/VAK2024.155

1 Introduction

In 2023, 50 years have passed since the beginning of the development of the global navigation satellite system (GNSS) and 30 years since the beginning of its actual operation at the first, still operating, permanent GNSS stations (hereinafter simply stations). Now, according to very rough estimates, their number has exceeded 25 thousand stations, unevenly distributed across all continents. A database of station speeds (VDB) has been created and maintained in Pulkovo on the territory approximately coinciding with the Eastern European Platform (EEP) to solve a number of scientific problems, in particular, to study the geodynamics of the EEP.

In publicly available global velocity databases, the EEP territory within Russia is represented by a couple dozen stations, which limits the reliability of geodynamic estimates. In fact, there are more than a thousand stations located on it, owned mainly by departmental and commercial geodetic organizations of Russia. This disadvantage is compensated by the VDB that we support in open access (http://www.gaoran.ru/russian/database/station/databasev_rus.html), which makes it possible to preserve inaccessible material for scientific research and, most importantly, gradually lost due to its often limited shelf life in commercial geodetic enterprises. The description of the VDB, the data processing method and a number of studies based on it are reflected in our works by Gorshkov et al. (2015, 2021). Currently, about 900 stations are supported in the datadase.

The main feature of the geodynamics of the EEP is the isostatic postglacial uplift of Fennoscandia, and seismic regional activity in the north-west of the EEP. At the same time, vertical dynamics and seismicity are almost completely absent in the Russian Plain belonging to the EEP. Fennoscandian sedimentation is mainly composed of Precambrian crystalline formations of the Baltic Shield (BS), and the sedimentation of the Russian Plain, plastic in terms of deformations, rests on the Precambrian crystalline basement of the Russian Plate (RP) and partially on the Paleozoic folded basement of the Scythian Plate. The processes of interaction of these structures in the zone of their interface cause constant deformation of the Earth's crust by several millimeters per year, both vertically and horizontally. These processes have been studied in recent years by Lidberg, et al. (2010); Gorshkov et al. (2021); Kierulf, et al. (2021); Melnik et al. (2022).

2 Comparison of VDB and NGL global database

The Geological Laboratory of the University of Nevada (NGL, USA) maintains an extensive global publicly accessible database of speeds of more than 20 thousand stations (http://geodesy.unr.edu /). The data is processed by the same package (Gipsy,

JPL) using the same precise positioning strategy as the VDB. The station speeds in NGL are calculated using the original method by Blewitt et al. (2016), the essence of which is a pairwise comparison of station positions strictly after a year, which, according to the authors, should eliminate the main problem in the analysis of GNSS positions associated with the presence of discontinuities or displacements of different nature in these series.

From both bases, stations with an observation duration of at least 2 years and with velocity errors not exceeding 0.8 mm/year for horizontal coordinates and 1.8 mm/year for vertical coordinates were selected for the EEP territory. In total, there were 1607 stations, 176 of them shared, which made it possible to conduct a comparative analysis of them. The data is taken up to and including May 2024.

From the comparison, it can be seen that the speed estimates in both databases are almost the same, so weighted average speeds were taken for common stations. This as well as the uniformity of the data processing methods used in both databases makes it possible to include the extensive material of the NGL database in the western territory of the EEP in a joint geodynamic analysis.

3 Geodynamics of the EEP

The volume and quality of the above data allow us to study the kinematic structure of the EEP region. From the point of view of geodynamics, the area of the Fennoscandia and the Russian Plate (RP) interface is most interesting as a place of interface of large geological structures. According to numerous geological and seismic data about the earth's crust in this zone, there are both weakened zones and, conversely, strength barriers, where areas of stress redistribution are formed under the influence of external factors.

3.1 Mutual rotation of Fennoscandia and Russian Plate

As mentioned in the introduction, the EEP is divided into numerous geological structures. The most significant of them is the crystalline Baltic Shield (BS), which represents most of Fennoscandia, and is mainly covered with sediments of the RP. The border of these formations runs through the Baltic Sea, the Gulf of Finland, Ladoga and Onega Lakes and the White Sea. Geologically, it is marked by the Baltic Ledge, stretching from the coast of Denmark across the Baltic Sea to the southern borders of Lake Ladoga. In addition, in the south, the Ukrainian shield is wedged into the EEP, and in the northeast, the EEP is interfaced with the Pechora platform.

The mutual motion of the blocks of the Earth's crust can be determined by calculating their instantaneous angular velocities. In accordance with Euler's theorem,

the motion of any such solid-state blocks along the spherical surface of the Earth can be represented by rotation around some axis, the nearest point of intersection of which with the Earth's surface is called the Euler pole. The joint rotation of a set of n stations belonging to one block can be represented as $v = \Omega r$, where v is the velocity matrix of stations of size $3 \times n$ for each of the three velocity coordinates, Ω is a vector column of 3×1 of the desired angular velocities of the block, r is a vector column of $1 \times 3n$ coordinates of stations. To estimate the components of the angular velocity of the block ($W_x W_y W_z$), a least squares method with a diagonal matrix of weights inverse to the dispersions of the corresponding station velocities is used.

Table 1. Angular velocity variations for BS and RP blocks

Block	N	dT	dV_i	Ω_x (mas/year)	Ω_y (mas/year)	Ω_z (mas/year)
BS	641	> 2		-0.094 ± 0.003	-0.518 ± 0.001	0.748 ± 0.007
BS	480	> 5	$3\sigma_1$	-0.091 ± 0.003	-0.517 ± 0.001	0.755 ± 0.006
RP	659	> 2	$4\sigma_1$	-0.019 ± 0.003	-0.484 ± 0.006	0.892 ± 0.007
RP	326	> 6		-0.114 ± 0.001	-0.536 ± 0.002	0.667 ± 0.003
RP	473	> 5		-0.094 ± 0.002	-0.526 ± 0.003	0.711 ± 0.004
EA	97			-0.085 ± 0.004	-0.531 ± 0.002	0.770 ± 0.005

The maximum range of Ω-solutions for both blocks is summarized in the Table 1. When analyzing numerous solutions for a combination of the above parameters, the remarkable stability of solutions for BS in contrast to solutions for RP turned out to be quite unexpected. The explanation for this fact may be that the RP is geodynamically heterogeneous due to its geological structure, and therefore, when changing the set of stations, different clusters of stations become dominant in the solution. The penultimate line of the Table 1 provides a solution that can be conditionally called the most likely solution for RP in terms of the totality of all solutions. Based on it, it can be concluded that, in general, there are no significant movements between RP and Fennoscandia. For comparison, the last line of Table 1 shows the solution for the entire Eurasian Plate (S) according to Altamimi et al. (2017), where only 97 stations located on the entire EA plate south of 55 degrees latitude were used to estimate Ω.

3.2 EEP deformation field

To determine the deformation field from the velocity field of GNSS stations, we used a well-known method by Shen, et al. (1996), in which the change in the velocity field at each point is modeled by the deformation field caused by this change and the solid-state movement of the block of the Earth's crust (displacement and rotation). The

method was refined in terms of using a more complex two-factor weight function $G = LZ$, which allows to detail the deformation field and used as an alternative to the Delaunay triangulation usually used for these purposes. Here $L_i = e^{-R_i^2/D^2}$, $Z_i = n\theta_i/4\pi$, R_i is the distance from the interpolation point to the i-th station, D is the optimal smoothing parameter, θ_i is the angle between the direction to the selected surrounding stations, the total number of which is n.

This algorithm was implemented as a publicly available StrainTool software product by the team of authors Anastasiou et al. (2019) and applied by them to study the deformation field at 298 stations in Europe, which partially intersects with the EEP territory that we are studying in its western part. All the essential features of the deformation field according to their study are naturally concentrated in the seismically active southern part of Europe (Italy, Greece). For its central and northern regions, according to their estimates, the deformation rate does not exceed 10 nanostreins/year (hereinafter ns/g). Since there are no stations on the territory of Russia in the database they used, our study expands this area up to the Urals.

As expected, the main feature of the EEP deformation field is determined by the postglacial uplift of Fennoscandia, where expansion occurs in the North–Southeast direction with a maximum velocity of about 12 ns/year in the north of the Gulf of Bothnia. On the border with the Republic of Belarus, there is a gradual zeroing of expansion in the strip passing through the Baltic Sea, the Gulf of Finland, Ladoga and Onega Lakes, practically coinciding in this part with the Baltic Ledge, and further along the western border of the White Sea and the Kola Peninsula.

Other features already located on the RP have a local, but rather stable character, which was determined by the choice of stations with a duration of observations from 2 to 5 years. In this interval, the number of stations decreases by almost a quarter, but, thanks to selection, the accuracy of their speeds increases significantly.

Stable features include the zone of expansion in the sublatitudinal direction between Lake Ladoga and Lake Onega (up to 10 ns/year), which leaves the expansion zone in Fennoscandia. This zone is centered on the Svir River, which connects these lakes. Curiously, a smaller expansion zone is present around the Neva River, connecting Ladoga and the Gulf of Finland. The zone of weaker expansion (up to 8 ns/year) then continues south of the Rybinsk reservoir, almost coinciding with the Moscow Avlakogen in strike, but orthogonal to it in the expansion vector. Another expansion zone (5-6 ns/year) coincides in extent with the Ukrainian shield and is similar to Fennoscandia in terms of the expansion vector. Two weak compression zones (5 ns/year) in the submeridional direction in the area of the Valdai upland and on the border of the Pskov region and Belarus, they practically disappear when choosing stations with an increasing duration of observations.

4 Summary

The joint use of homogeneous processing speeds of more than one and a half thousand GNSS stations from the VDB and NGL bases on the territory of the Eastern European Platform allowed us to determine a number of its geodynamic structural features.

In general, the Baltic Shield and the Russian Plate do not have mutual rotation as separate tectonic blocks of the EEP (Table 1). At the same time, the RP is not geodynamically homogeneous in full accordance with its complex geological structure. There is a significant difference in the rotation of the western and eastern parts of the RP, approximately passing through the meridian of 29 degree East. In addition, in the calculated velocity field of the deformation field, its structure is noticeable at the level from -5 to +10 ns/year for RP. It is also expected that a zone of expansion of Fennoscandia up to 12 ns/year is allocated in the deformation field, caused by its postglacial uplift.

References

Gorshkov V., Mokhnatkin A., Smirnov S., et al., 2015, Vestnik SPbU, Seires 1, 2, 3, p. 463

Gorshkov V., Mokhnatkin A., and Scherbakova N., 2021, Geodesy and cartography, 967, 1, p. 34

Melnik G., Steblov G., Galaganov O., et al. 2022, Geodesy and cartography, 980, 2, p. 26

Altamimi Z., Metivier L., Rebischung P., et al., 2017, Geophysical Journal International, 209, 3, p. 1906

Anastasiou D., Ganas A., Legrand J., et al., 2019, EGU General Assembly 2019, Geophysical Research Abstracts, 21, EGU2019-17744-1, GitHub - DSOlab/StrainTool: StrainTool: A software package to estimate strain tensor parameters

Blewitt G., Kreemer C., Hammond W., et al., 2016, Journal of Geophysical Research, 121, 3, p. 2054

Kierulf H., Steffen H., Barletta V., et al., 2021, Journal of Geodynamics, 146, p. 101845

Lidberg M., Johansson J., Scherneck H.-G., et al., 2010, Journal of Geodynamics, 50, 1, p. 8

Shen Z., Jackson D., and Ge B., 1996, Journal of Geophysical Research, 101, B12, p. 27957

MODERN ASTRONOMY: FROM THE EARLY UNIVERSE TO EXOPLANETS AND BLACK HOLES

Integer phase ambiguity resolution method for absolute GLONASS observations

K. Starikov and S. Petrov

Saint-Petersburg State University, Saint-Petersburg, 199034 Russia

Abstract. With the help of modern navigation satellite systems it is possible to determine the coordinates of points with millimeter accuracy due to the precision measurement of the carrier phase of the navigation radio signal. However, in the course of achieving this accuracy, a nontrivial problem of resolving the integer phase ambiguity arises. The most difficult part is to determine the integer number of wavelengths between the phase centers of the transmitting antenna of the navigation satellite and the receiving antenna. An exact solution to this problem using the integer least squares method, although it exists in theory, is not applicable in practice due to the prohibitively high computational complexity. In this regard, a number of authors have developed various suboptimal methods for resolving integer phase ambiguity, which allow solving a problem with varying degrees of uncertainty. In this case, the problem can be considered satisfactorily solved for relative coordinate determinations from GPS (global positioning system) and GLONASS (global navigation satellite system) observations, as well as for absolute coordinate determinations from GPS. As for the absolute determinations of coordinates from GLONASS observations, the situation is complicated by the fact that GLONASS, unlike GPS, uses frequency-division multiple access. In other words, if all GPS navigation spacecraft broadcast navigation radio signals on a single frequency, then GLONASS satellites broadcast on different frequencies. This paper generalizes one of the modern and effective methods for resolving integer ambiguity for GPS observations, MLAMBDA, to the GLONASS system. The ultimate goal of the work is an independent algorithm for absolute determination of coordinates with millimeter accuracy using the GLONASS system. In the course of the work, the MLAMBDA formalism was generalized to navigation systems with frequency division of access, and the first results of independent coordinate determinations from GLONASS observations in absolute mode were obtained.

Keywords: GNSS, GLONASS, phase ambiguity, PPP, MLAMBDA

DOI: 10.26119/VAK2024.156

1 Introduction

An absolute method for precise processing of GNSS measurements was proposed in Zumberge et al. (1997) and was called Precise Point Positioning (PPP). Initially, this method did not take into account integer phase ambiguity. In the original PPP, integer phase ambiguity was considered as part of the overall, unmodeled pseudorange error (Teunissen P.J.G. 1995). Later, new versions of PPP began to appear that attempted to isolate the integer phase ambiguity error from the overall error budget. Currently, there are two main approaches to estimating integer phase ambiguity. Firstly, FCB (fractional cycle base) methods (Chang et al. 2005), where hardware signal delays are calibrated and subtracted from the total pseudo-range error, and the remaining part is considered as a phase error. Secondly, IRC (integer recovery clock) methods (Chang et al. 2005), which are based on correction of the on-board clock of a navigation spacecraft. It was shown in Chang et al. (2005) that both methods are equivalent in principle.

2 MLAMBDA-method

This work is devoted to the development and implementation of the MLAMBDA method. This method has shown a fairly high efficiency in determining integer ambiguity. The implementation of the MLAMBDA algorithm for the GNSS absolute positioning method is considered, and it is also shown that this method is not directly applicable to the GLONASS system. The work formulates an extension of the method that allows it to be applied not only to GPS, but also to GLONASS measurements. The GLONASS and GPS systems are very close to each other, but fundamentally differ in the principle of separating signals from different satellites. The GPS system uses code division of satellite signals, so that each GPS satellite uses a unique modulation code on a common carrier frequency, while the GLONASS system implements frequency division, so that each GLONASS satellite in view uses a single modulation code on a frequency unique to each satellite. Each of the access division principles has its advantages and disadvantages, but in the case of frequency division of signals, integer phase ambiguity resolution is complicated by the presence of several carrier signals of different frequencies instead of one in the case of GPS. The authors of the article modify the MLAMBDA method so that it can also be applied to GLONASS measurements. The MLAMBDA method is a development of the LAMBDA (Least-squares AMBiguity Decorrelation Adjustment) method proposed in Teunissen P.J.G. (1995). According to Zumberge et al. (1997), the GNSS observation model can be written as

$$E(x) = Aa + Bb, D(x) = Qx, \tag{1}$$

where x is a vector of GNSS data of order m, a and b are vectors of parameters of order n and p, respectively, A and B are matrices of the observation model that relate the data vector to the model parameters. The known covariance matrix of x is Qx. The vector x is assumed to represent the differences between observations and simulated values. These may be observations with double phase differences or codes, or both. A solution is sought in such a way as to minimize the sum of squared differences between the simulated and observed data. The basic idea is to first apply an orthogonal triangular decomposition to equation (1). The first part consists of full floating-point parameters, the second part - of difference floating-point parameters and, finally, the third part - of integer parameters, that is, of phase ambiguities. The solution is then carried out in three steps. First, a floating-point solution to problem (1) is sought, assuming that all integer parameters are equal to zero. Second, the problem is solved for integer parameters using the floating point solution as an approximation to the final one. Third, the calculated parameters, both floating point and integer, are substituted into (1), and how close the quadratic norm of the solution is to the minimum is estimated through a search process.

3 Implementation of the algorithm

The LAMBDA method solves the problem using integer least squares (ILS) to obtain estimates of integer double-difference ambiguities. The LAMBDA method consists of two stages – decorrelation with reduction and search. First stage is meant to prepare problem for solving it. On the second stage, the task is to find the optimal estimate or several optimal estimates of the parameter vector in the hyperellipsoidal domain. For real-time kinematic GNSS and other high-dimensional applications, computational speed is critical. In this paper, we are working with modified LAMBDA method (MLAMBDA), which can significantly reduce the computational complexity of the LAMBDA method for high-dimensional ILS problems. Numerical results show that MLAMBDA reductions are also more computationally efficient than traditional ones. For verification purposes, in addition to the optimal estimate, a second optimal estimate, which produces the second smallest value of the objective function, is often also required. As part of this work, two stages of the LAMBDA method were implemented: reduction and search. At the current time, the authors have managed to achieve the functionality of the method for combined GPS+GLONASS measurements using third-party data on inter-frequency phase shifts. The results of the algorithm are shown below in Fig. 1. As a continuation of the work, it is planned to adapt the algorithm to the "GLONASS only" mode, as well as to estimate inter-frequency phase shifts directly from measurements.

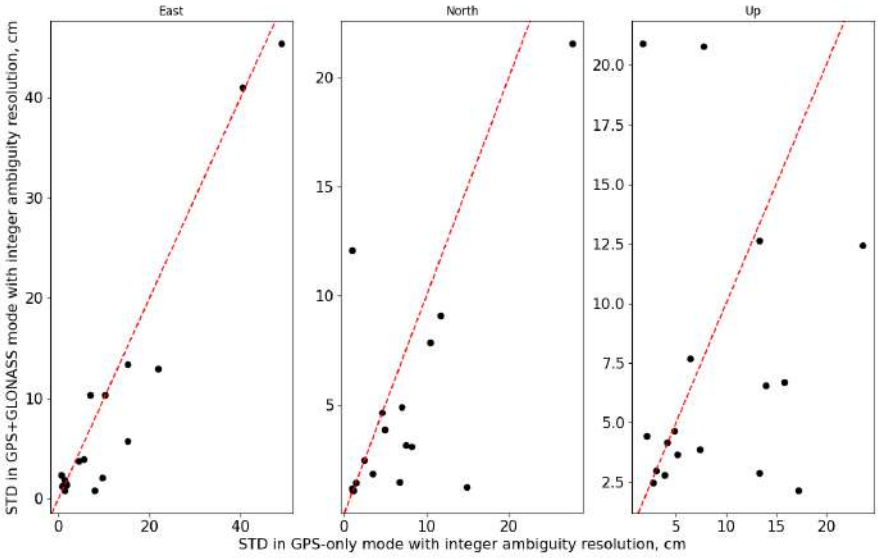

Fig. 1. Figures demonstrate RMS of 17 navigational solutions of day observations in two different modes: GPS-only and GPS+GLONASS.

4 Summary

Based on MLAMBDA, an algorithm for estimating integer phase ambiguity, applicable to satellite navigation systems with frequency division of signals, in particular to the GLONASS system, is obtained. Currently, the performance of the method has been tested in GPS+GLONASS mode, as well as using third-party data on inter-frequency phase delays. Satisfactory results of the algorithm's operation in this mode were obtained. The algorithm correctly estimates integer phase shifts both in the case of GPS and in the case of GLONASS. As a development of this work, it is planned to develop the functionality of the algorithm in the "GLONASS only" mode, and also to implement the assessment of inter-frequency phase shifts directly from observations, without resorting to third-party data sources.

References

Chang X.W., Yang X., and Zhou T., 2005, Journal of Geodesy, 79, p. 552
Teunissen P.J.G., 1995, Journal of Geodesy, 70, p. 65
Zumberge J.F., Heflin A., Jefferson D.C., et al., 1997, Journal of Geophysical Research, 102, B3, p. 5005

BAK 2024 MODERN ASTRONOMY: FROM THE EARLY UNIVERSE TO EXOPLANETS AND BLACK HOLES 300 years Russian Academy of Sciences

Identification of a new asteroid family 3854 George in the Hungaria group

T. Vinogradova

Institute of Applied Astronomy of the Russian Academy of Sciences, 10 Kutuzova Emb., St. Peterburg, 191187 Russia

Abstract. A search for asteroid families was performed in the Hungaria group. Proper elements needed for this procedure were calculated by the empirical method using distributions of osculating elements. All, more than 30 000 multi-opposition asteroids, discovered in this region to date, were used for this aim. An approach similar to the hierarchical clustering method was applied for the identification of families. As a result, two asteroid families were found: 434 Hungaria and 3854 George. 434 Hungaria family is a well known one, it includes a large fraction of asteroids in this region. A new family 3854 George was identified in the high inclination region 24°–26°. It is composed by small asteroids with diameters less than 1 km and includes about 400 members now.

Keywords: celestial mechanics; asteroids: general, minor planets; individual: 434 Hungaria, 3854 George

DOI: 10.26119/VAK2024.157

1 Introduction

The Hungaria group is a nearest to the Earth part of the asteroid belt roughly defined by semi-major axis $1.8\,\mathrm{AU} < a < 2.0\,\mathrm{AU}$, eccentricity $e < 0.2$, and inclination $15^\circ < i < 30^\circ$. There are no large asteroids in this region. Diameters of the most large asteroids seem not to exceed 15 km. One of the questions related to this group is a number of families in this region. The existence of one family is not in doubt today. The Hungaria region really contains a large family, called the Hungaria family. The family includes a large fraction of the Hungaria asteroids. Besides, there were some indications of a possible second family at higher inclinations, but up to now only small groupings have been detected here. Due to a large number of newly discovered asteroids the identification of the second family in this region became possible. More than 30 000 multi-opposition asteroids are discovered in this region to date. The source of initial osculating elements is the MPC catalogue, version Feb 2024.

2 Calculation of forced and proper elements by the empirical method

Osculating elements cannot be used for a family identification because an inclination and eccentricity oscillate periodically over a long time span under the action of perturbations. Proper elements are required for this aim. The empirical method (Vinogradova 2019) was used to calculate proper elements for all multi-opposition asteroids in this zone. Oscillations of the osculating inclination i and eccentricity e manifest themselves very clearly in the distributions of pairs: inclination–longitude of ascending node (i, Ω) in Fig. 1a, and eccentricity–longitude of perihelion (e, ϖ) in Fig. 1b. These oscillations represent classical secular perturbations. An amplitude of the oscillations and the position of the maximum correspond to forced elements i_f, Ω_f in Fig. 1a and e_f, ϖ_f in Fig. 1b.

It is possible to calculate the parameters of these curves by the least-squares method. For the population of the Hungaria group as a whole the following forced elements were calculated: $i_f = 3\overset{\circ}{.}1 \pm 0\overset{\circ}{.}02$, $\Omega_f = 115\overset{\circ}{.}6 \pm 0\overset{\circ}{.}3$, $e_f = 0.0202 \pm 0.0004$, $\varpi_f = 47\overset{\circ}{.}91 \pm 1\overset{\circ}{.}01$.

Classical secular perturbations can be excluded from osculating elements using a coordinate transformation formula if the corresponding forced elements are known (Vinogradova 2019). After eliminating the classical secular perturbations, Lidov–Kozai perturbations (Lidov 1962; Kozai 1962) may become visible in element distributions. The Lidov–Kozai perturbation is a secular one which causes long-period oscillations in the orbital inclination and eccentricity depending on the perihelion argument ω.

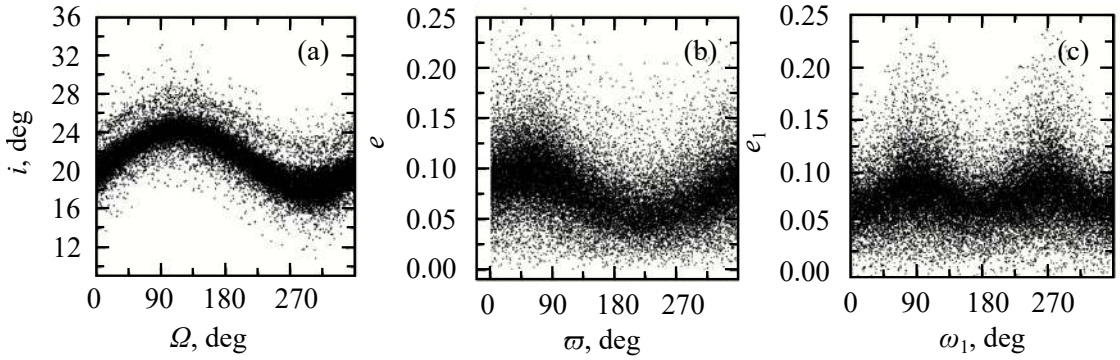

Fig. 1. Distributions of orbital elements in the Hungaria group: i, Ω (a); e, ϖ (b); e_1, Ω_1 (c) after excluding classical secular perturbations.

The plot of the eccentricity against the perihelion argument ω in Fig. 1c clearly shows how eccentricities of asteroid orbits in this region change under the action of the Lidov–Kozai perturbation. An amplitude of i oscillations is not significant here. In the high inclination region, amplitudes of the Lidov-Kozai oscillations can reach the values of 0.025 for eccentricities and $0^{\circ}.25$ for inclinations. These forced elements, related to Lidov-Kozai perturbation, were excluded in the same way as for classical secular perturbations. As a result, proper elements e_p, i_p were calculated.

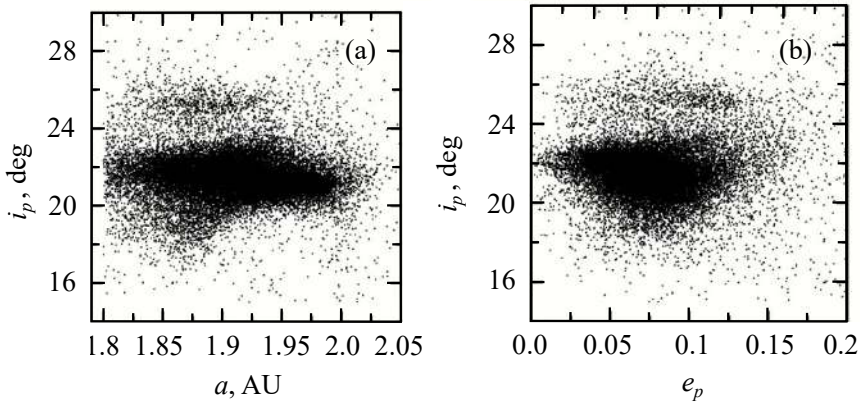

Fig. 2. Distribution of proper elements (i_p, a) and (i_p, e_p) in the Hungaria group.

Distributions of the proper elements (i_p, a) and (i_p, e_p) in the Hungaria group can be seen in Fig. 2. These distributions show well the presence of two families here. Although, it should be said that these families can be seen already in the Fig. 1a. They can be seen, but cannot be separated in osculating elements.

3 Family identification

An approach similar to the hierarchical clustering method (Zappalà et al. 1990) was used for the identification of families. This method was described in Vinogradova (2019). As a result, besides the large and well known 434 Hungaria family, a new family 3854 George was identified in the high inclination region 24°–26°. 434 Hungaria family includes about 25 000 asteroids now.

3854 George family includes about 400 members now. The family is composed by rather small asteroids with diameters less than 1 km. The distribution of absolute magnitude H of family members against a semimajor axis (H, a) is shown in Fig. 3a. The triangular shape of the distribution suggests that this population of asteroids is a real collisional family. A position of the main asteroid 3854 George is marked with a cross.

Also, a differential magnitude distribution of the 3854 George asteroids was considered in Fig. 3b. Almost all asteroids with H up to $18\overset{\mathrm{m}}{.}5$ are discovered in this region. The best fit for the family graph in the interval $17\overset{\mathrm{m}}{.}0$–$18\overset{\mathrm{m}}{.}5$ of H is a straight line with a slope of 0.48. This line is shown on the plot by a dotted line. Such slope is consistent with a young collisional family.

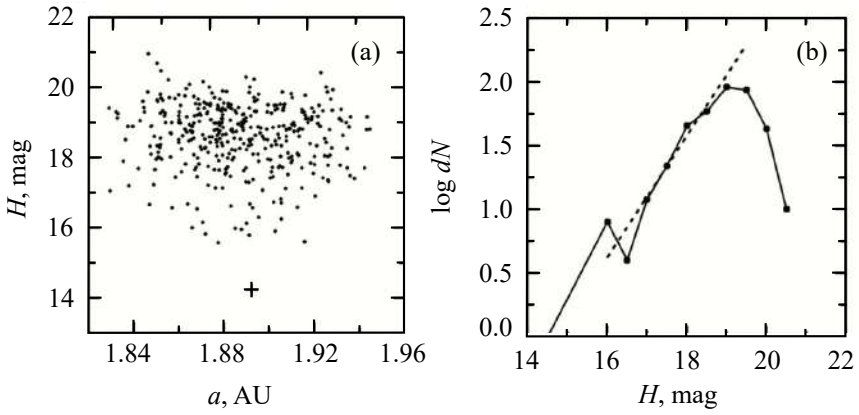

Fig. 3. Distributions for 3854 George family asteroids. Absolute magnitudes H versus semimajor axis a (a); a differential number of asteroids dN versus H (b).

References

Kozai Y., 1962, Astronomical Journal, 67, p. 591
Lidov M., 1962, Planetary and Space Science, 9, 10, p. 719
Vinogradova T., 2019, Monthly Notices of the Royal Astronomical Society, 484, p. 3755
Zappalà V., Cellino A., Farinella P., et al., 1990, Astronomical Journal, 100, p. 2030

MODERN ASTRONOMY: FROM THE EARLY UNIVERSE TO EXOPLANETS AND BLACK HOLES

Large-format photodetecting system pCam6060 with a GSENSE6060BSI CMOS detector, developed at SAO RAS and optimized for photometric methods

I. Afanasieva, V. Murzin, V. Ardilanov, N. Ivaschenko, and M. Pritychenko

Special Astrophysical Observatory of the Russian Academy of Sciences,
Nizhny Arkhyz, 369167 Russia

Abstract. The pCam6060 photodetecting system has been developed at SAO RAS based on the GSENSE6060BSI photodetector manufactured by GPixel (China) with a frame format of 6144 × 6144 active pixels and a pixel size of 10 µm. The readout speed reaches 11 fps. The back-illuminated detector has a wide spectral range of 200–1040 nm with a minimum quantum efficiency (QE) of 10% and a maximum sensitivity of 95% at 580 nm. The quantum efficiency in the near-infrared range is 58% at 850 nm. The pCam6060 system controller implements a mode of simultaneous image readout via two 12-bit video channels with different gain and their subsequent combination in the controller into a single frame with an extended 16-bit dynamic range. This method achieves simultaneously a low readout noise level (about 3 e^-) in the high-gain channel and a large dynamic range (full well capacity of about 100 000 e^-) in the low-gain channel. Back-illuminated CMOS detectors, unlike front-illuminated devices, are not susceptible to the long-term preservation of the residual charge from previous exposures, which makes them suitable for recording faint objects in photometric long-exposure observing methods. Communication between the host computer and the camera is carried out via a fiber optic line at distances of up to 50 m. Video data are recorded on the computer hard drive in real-time. The pCam6060 photodetecting system is designed for astronomical applications and has a moisture-proof design.

Keywords: instrumentation: detectors; methods: statistical

DOI: 10.26119/VAK2024.158

1 Introduction

CMOS photodetector technologies and cameras based on these technologies have long been proven in the field of astronomy (Stefanov 2022; Vlasyuk et al. 2024). Modern CMOS detectors have key parameters (noise, dark current) equal in values to CCDs, but their frame rate is ten times higher. Photometric studies in astronomy place increased demands on the characteristics of photodetecting systems such as image registration accuracy and sensitivity, low readout noise, and high coordinate and temporal accuracy. The use of large-format high-speed CMOS photodetectors with backside illumination (BSI) significantly increases camera sensitivity, both by reducing light losses in the detector itself and by expanding the spectral range in the red region of the spectrum, which enables meeting most of these requirements (Shen et al. 2022; Rogowska et al. 2019).

In this paper, we present an implementation of pCam6060: a photodetecting system based on a large-format GSENSE6060BSI scientific-class back-illuminated (BSI) photodetector manufactured by GPixel (China) with a format of 6144×6144 ten-micron pixels. The development, manufacturing, and laboratory tests of the camera prototype were carried out at the Special Astrophysical Observatory of the Russian Academy of Sciences (SAO RAS). We present the laboratory measurements of the camera photometric characteristics and describe the image correction methods used to obtain optimal characteristics in photometric observations.

2 Controller architecture and camera design

The principles of building CMOS controllers, methods for controlling high-speed CMOS photodetectors, and software design for photodetecting systems are described in detail in Ardilanov et al. (2021, 2022). The controller architecture, interaction of its nodes, structure, and characteristics of the system are described in Afanasieva et al. (2019); Ardilanov et al. (2020), where the GSENSE4040 photodetector is used.

In distinction to the described implementation, the GSENSE6060BSI photodetector video data are read via 50 digital lines. The pCam6060 controller implements simultaneous image readout via two 12-bit video channels with high (HG) and low (LG) gain outputs. The HDR (High Dynamic Range) operating readout mode allows one to combine two high and low gain frames into one 16-bit frame with a linear light–signal transfer characteristic in real time. In this mode, a low level of readout noise in the high-gain channel and a large dynamic range in the low-gain channel are simultaneously achieved, which allows us to display details of both bright and weak objects. The set of supply voltages was also changed to suit the new photodetector

(Ardilanov et al. 2021). Communication between the host computer and the photodetecting system is organized via a fiber optic line at distances of up to 50 m. The controller has an eight-channel Ethernet interface with a performance of 40 Gbit/s, providing a full-frame readout rate of 11 fps.

The GSENSE6060BSI-based camera and its internal structure are shown in Fig. 1. The camera has an optical head and a housing with electronic components. To reduce heat transfer in the optical head, the photodetector is placed in an inert gas medium. The photodetector is cooled using a set of two-stage Peltier elements, which makes it possible to reach an operating temperature of -60°C lower than the temperature of the external heat exchanger radiator. The radiator design allows air and liquid cooling. The controller's electronics are housed in two moisture-proof housings. On the back of the chamber opposite the optical input, there are connectors for the power supply, external synchronization, and interface cable.

Fig. 1. Exterior view of the pCam6060 photodetecting system (left) and the design scheme of the pCam6060 vacuum chamber internal structure (right).

The camera is attached to the optical equipment via side mounting holes. If necessary, the camera can be equipped with a lens adapter. The small dimensions of the camera ($190 \times 190 \times 170$ mm) make it possible to minimize light loss when placing the camera in the input light beam of the telescope.

The control of the GSENSE6060BSI-based camera and data acquisition are performed using a specially developed software package for Windows Server 2012 R2.

The control program allows users to set photodetector modes, control the exposure, view, analyze, and process the received images, and monitor telemetry information.

3 Results of laboratory tests

Laboratory measurements were carried out on a flat-field stand at a detector temperature of −30°C. The photometric characteristics of the pCam6060 system for the three readout modes (LG, HG, HDR) are summarized in Table 1.

Table 1. Photometric characteristics of pCam6060.

	Measured Values			**Datasheet Values**		
Parameter	LG	HG	HDR	LG	HG	HDR
Gain factor, e^-/ADU	23.8	2.39	1.43	24.2	2.42	–
Readout noise (rms), e^-	23.6	3.47	3.19	22–30	3–4	–
Full well capacity, e^-	93 200	9 300	91 500	83 000–95 000	7 000–9 500	–
Dynamic range, dB	71.9	68.6	89.1	73	70	90
Non-linearity, %	0.63	0.80	0.69	0.5–1.0	0.8–1.0	–
Photoresponse non-uniformity, %	0.5			0.7–1.5		
Gain instability, %	0.064			–		
Image lag, e^-/pixel	3–4			<2		
Dark current, e^-/s/pixel	0.2–0.3			0.04		

The GSENSE6060BSI detector does not have the long-term residual bulk image effect characteristic of FSI detectors (Janesick et al. 2014; Karpov et al. 2020). However, there was small retention: when the detector pixels had been illuminated to saturation in the previous frame, in the next frame after reset a charge of about 3 e^- remained in these pixels.

In photometry methods the stability of the video channel transfer characteristics is important. We revealed a significant dependence of the video channel gain on the detector temperature: 0.32% per degree Celsius. Therefore, to obtain the required accuracy, it is necessary to precisely stabilize the detector temperature. The controller stabilizes the photodetector temperature within ±0.1°C, and the gain instability does not exceed 0.064%.

To reduce the dark current during long exposures, the device has the following modes: lowering the pixel supply voltage and using the low-power output amplifier mode. Both of these modes were implemented in the controller. Nevertheless, the dark current we measured at long exposures remained at a fairly high level: 0.2 e^-/s/pixel at −30°C. The reasons for this are currently investigated. It is possible that this is due to the quality degree of the detector (Grade 2).

The CMOS system with a maximum QE of 95% at 580 nm is more powerful than the GSENSE4040-based system with a maximum QE of 74% at 600 nm (Ardilanov et al. 2020).

4 Methods of image correction

In the raw images obtained with the CMOS detector, there exists geometric noise caused by the interference from the operation of the multiplexer control signals and the heterogeneity of the readout channels. In addition, in the frame for the LG mode we revealed the presence of a significant number of pixels for which the bias value was significantly higher than the average value for the frame.

To reduce the geometric noise, the controller implements a real-time method for subtracting the average bias frame from each read frame (Fig. 2). This made it possible to reduce the readout noise in the corrected frames by 1.8 times in the HG mode and 12 times in the LG mode.

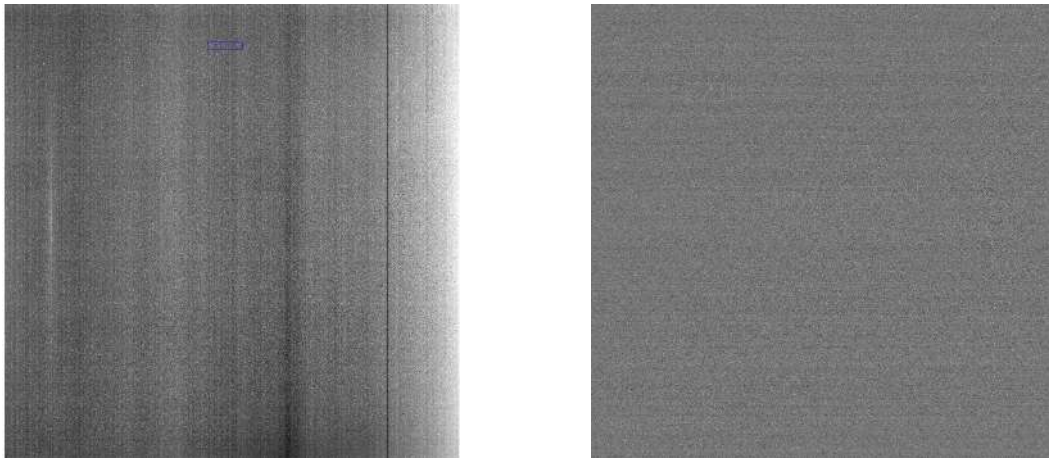

Fig. 2. The original (left) and corrected (right) bias frames in HDR mode.

To couple high and low-gain frames into an HDR frame with a linear light-signal transfer characteristic, multiplicative and additive coefficients are used, which have been previously calculated based on the measured transfer characteristics of the LG and HG channels. The resulting transfer characteristics exhibit no gain (Fig. 3, left) or dispersion shift (Fig. 3, right) in the area of the junction point.

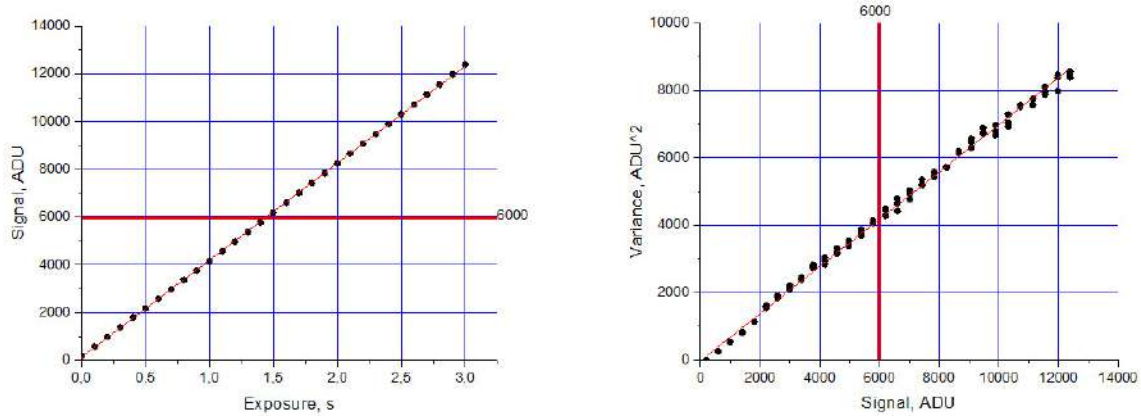

Fig. 3. Gain (left) and dispersion (right) at the junction (red line) of the LG and HG channels.

5 Summary

The developed large-format camera system with a frame rate of 11 fps and low readout noise is undoubtedly excellent for short-exposure observations. For use in long-exposure photometry, the proposed method implements dark-current reduction modes, bias frame subtraction, and video channel gain stabilization. In addition, to achieve the necessary accuracy, it will be necessary to use postprocessing of the obtained images: subtraction of the dark frame, correction of photoresponse nonuniformity in each pixel over a flat field, and correction of nonlinearity.

References

Afanasieva I.V., Murzin V.A., Ardilanov V.I., et al., 2019, Space Debris: Fundamental and Practical Aspects of the Threat, Proc. All-Russian Conf., ed. L.M. Zelenyi, B.M. Shustov, p. 52

Ardilanov V.I., Murzin V.A., Afanasieva I.V., et al., 2020, Ground-Based Astronomy in Russia. XXI century, Proc. All-Russian Conf., ed. I.I. Romanyuk, I.A. Yakunin, A.F. Valeev, D.O. Kudryavtsev, p. 115

Ardilanov V.I., Murzin V.A., Afanasieva I.V., et al., 2021, System synthesis and applied synergetics, Proc. All-Russian Conf., p. 216

Ardilanov V.I., Murzin V.A., Afanasieva I.V., et al., 2022, Astronomy at the epoch of multimessenger studies, Proc. All-Russian Astron. Conf., p. 52

Janesick J., Elliott T., Andrews J., et al., 2014, Proc. SPIE, 9211, id. 921106

Karpov S., Bajat A., Christov A., et al., 2020, Proc. SPIE, 11454, id. 114540G

Rogowska B., Konacki M., Chimicz A., et al., 2019, 20th Advanced Maui Optical and Space Surveillance Technologies Conference (AMOS 2019), p. 75

Shen C., Ma C., Gao W., 2022, Sensors, 22, p. 9991

Stefanov K.D., 2022, CMOS Image Sensors, Bristol: IOP Publishing

Vlasyuk V.V., Afanasieva I.V., Ardilanov V.I., et al., 2024, Physics-Uspekhi, 67, p. 405

VAK 2024 MODERN ASTRONOMY: FROM THE EARLY UNIVERSE TO EXOPLANETS AND BLACK HOLES 300 years Russian Academy of Sciences

Study of the astroclimate at the Baikal Astrophysical Observatory

L. Bolbasova and V. Lukin

V. E. Zuev Institute of Atmospheric Optics of the Siberian Branch of the Russian Academy of Sciences, 1, Academician Zuev square, Tomsk, 634055 Russia

Abstract. The atmospheric conditions are crucial for an astronomical observatory. Earth's atmosphere limits image quality in ground-based optical telescopes. The knowledge of the atmospheric turbulence vertical distribution above an astronomical site is significant for the design and operation of adaptive optics systems as well as for scheduling the observing time. The Baikal Astrophysical Observatory (latitude 51°50′ north, longitude 104°55′ east) is the site of the 1-meter Large Solar Vacuum Telescope (LSVT). In this study we estimate the vertical distribution of optical turbulence C_n^2, which determines all the integrated parameters for adaptive optics. A 5-year dataset (2019–2023) of temperature and wind speed at pressure levels from the National Centers for Environmental Prediction (NCEP) / National Centers for Atmospheric Research (NCAR) Reanalysis are used for the research.

Keywords: atmospheric effects; site testing; instrumentation: adaptive optics

DOI: 10.26119/VAK2024.159

1 Introduction

The Baikal Astrophysical Observatory (BAO) is part of the Institute of Solar-Terrestrial Physics of the Siberian branch of the Russian Academy of Sciences. The main tool of BAO is the 1-meter Large Solar Vacuum Telescope (LSVT). It provides observations in the visible-light and infrared spectrum. In-depth understanding of Sun's physics requires optical observations of the Sun with higher and higher angular resolution. The optical image quality is limited by atmospheric turbulence. Adaptive optics (AO) is designed to achieve near-diffraction image quality. The knowledge of the wind speed and turbulence profiles above the observing site is significant for the design of an adaptive optics system and its operation as well as for scheduling the observing time. Currently, a program on multi-conjugated adaptive optics (MCAO) is underway for the LSVT. The MCAO are the next generation systems where each deformable mirror (DM) is conjugated to a plane at a height of a strong turbulent layer in the atmosphere. The MCAO design of the LSVT should be adapted to the turbulent layers above BAO. Therefore, the knowledge of turbulent layer positions to correctly select the conjugated plane is necessary. The aim of this work is to contribute to our knowledge of the profiles of the astroclimate parameters above BAO. We have estimated the profiles of the refractive index structure constant C_n^2 above the BAO site.

2 Methods and data

A 5-year dataset (2019–2023) of temperature and wind speed at pressure levels from the NCEP/NCAR Reanalysis is used for the study. The Reanalysis datasets are created by numerical simulation along with assimilation of remote sensing data and data in situ (e.g., radiosondes, satellites, weather stations) at grid points. The large differences in elevation in mountainous regions cause errors when averaging the Reanalysis data. BAO is not a high-altitude astronomical observatory. Consequently, the accuracy of the Reanalysis data on temperature and wind is expected to be very high.

The potential temperature θ is defined as

$$\theta(h) = T(h) \left(\frac{p(h)}{1000} \right)^{-0.288} \tag{1}$$

for temperature T in kelvins and pressure p in millibars. The gradient of wind speed is calculated as follows:

$$\frac{\partial V}{\partial h} = \sqrt{\left(\frac{\partial u}{\partial h} \right)^2 + \left(\frac{\partial v}{\partial h} \right)^2}, \tag{2}$$

where v and u are the components of wind speed. We use the following equation (Tatarskii 1961) to estimate the vertical profile of the refractive index structure constant from the Reanalysis data:

$$C_n^2 = aL^{4/3}M^2, \tag{3}$$

where L is the outer scale of the atmospheric turbulent flow, $a = 2.8$ is a constant, and M is the refractive index gradient provided by the equation

$$M = \frac{\partial N}{\partial h} = \frac{-79 \cdot 10^6 \, P(h)}{\theta(h) \, T(h)} \frac{\partial \theta}{\partial h}, \tag{4}$$

where $\theta(h)$ is the profile of potential temperature, $T(h)$ is the profile of temperature in kelvins, and P is the pressure in hPa. The choice of a model for the L profile is very important. We estimate it as the largest energy scale of the atmospheric turbulent flow by the Masciadri & Jabouille (2001) model:

$$L = \sqrt{2 \, E(h) \Big/ \left(\frac{g}{\theta(h)} \frac{\partial \theta}{\partial h} \right)}, \tag{5}$$

where $g = 9.8$ m/s^2 is the acceleration of gravity, and E is the turbulent kinetic energy. We determine E as the square of wind shear (Eq. 2) (Osborn & Sarazin 2018).

3 Vertical profiles of optical turbulence

Figure 1 shows, for each month, the median vertical optical turbulence profiles calculated by Eq. (3) from the NCEP/NCAR Reanalysis data for the BAO site over a period from 2019 to 2023.

According to the Reanalysis data for the period of 5 years, the BAO site has the lowest optical turbulence from May to September. Strong optical turbulence with significant turbulence at lower heights (less than 5 km) is detected from November to January. The optical turbulence is significant in the lower layers up to a hight of 3 km from February to April and in October. A turbulent layer is located between 10 and 15 km, its turbulence varies depending on the season. An additionally layer appears below 5 km in May, July–August, and April.

4 Summary

By the NCEP/NCAR Reanalysis data about wind speed and temperature at pressure levels, we have calculated the vertical profiles of C_n^2 above the BAO site. Strong

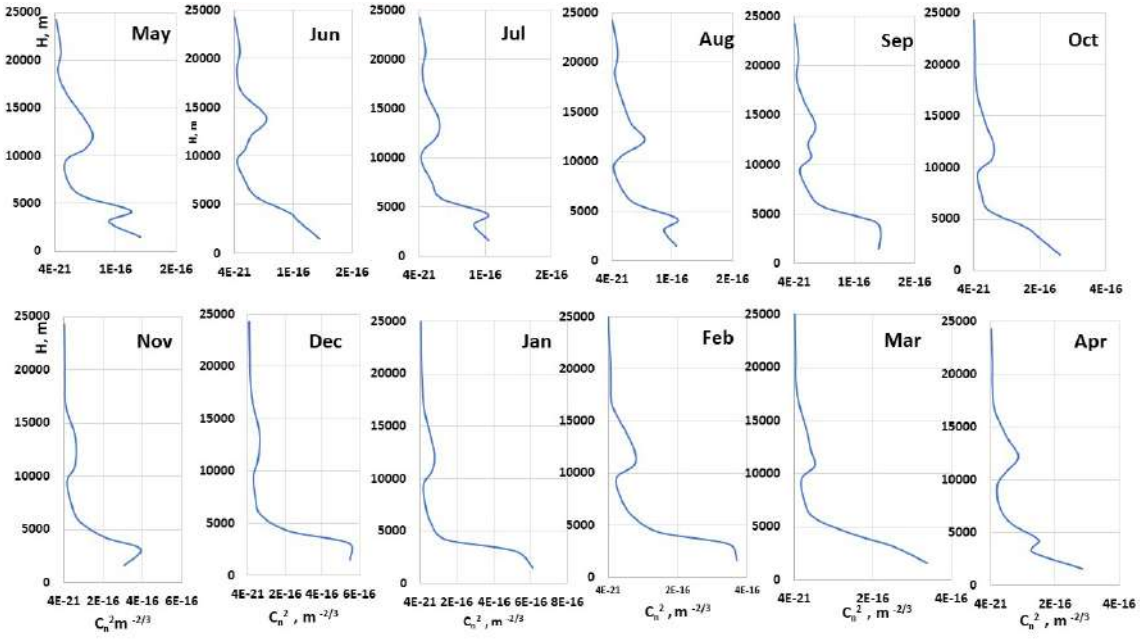

Fig. 1. Monthly median profiles of optical turbulence at the BAO site by the NCEP/NCAR Reanalysis data for the period of 2019–2023.

optical turbulence with significant turbulence at the lower heights (less than 5 km) is detected from November to January. The lowest optical turbulence is observed from May to September. Depending on the season, a layer lower 5 km and a more weaker layer between 10 and 15 km appear. The results indicate the feasibility of a ground-layer adaptive optics (GLAO) system whose DMs are conjugated with the heights less than 10 km as the most suitable for the BAO 1-m LSVT.

Funding

This study was funded by the Russian Science Foundation, grant No. 23-42-00043.

References

Masciadri E. and Jabouille P., 2001, Astronomy & Astrophysics, 376, p. 727
Osborn J. and Sarazin M., 2018, Monthly Notices of the Royal Astronomical Society, 480, p. 1278
Tatarskii V.I., 1961, Wave Propagation in a Turbulent Medium, McGraw-Hill Book Company

VAK 2024 MODERN ASTRONOMY: FROM THE EARLY UNIVERSE TO EXOPLANETS AND BLACK HOLES 300 years Russian Academy of Sciences

Precise two-stage deployment of a petal space antenna

V. Bujakas and M. Glotov

P. N. Lebedev Physical Institute of the Russian Academy of Sciences,
53 Leninsky Prospekt, Moscow, 119991 Russia

Abstract. One of the directions in modern radio astronomy is observing in the centimeter and millimeter ranges of the electromagnetic spectrum. The reflectors of radio telescopes operating in these ranges are generally parabolic mirrors. The sensitivity and angular resolution of a radio telescope depend on the mirror surface area. At the same time, due to the short wavelengths, high precision of the reflecting surface is required. This paper discusses a new design for a solid-state petal mirror. To enhance the accuracy of the reflecting surface, a two-stage deployment scheme of the petal antenna is proposed. In the first stage, a preliminary unstressed low-precision deployment of the antenna is performed. In the second stage, a high-precision fixation of the deployed reflector final state takes place. It is proposed to use self-adjusting locks to fix the final state of the deployed antenna. The results of computer and physical modeling of the new mirror design are presented. The method for controlling the deployment repeatability of the transformable reflector model is discussed.

Keywords: instrumentation: high angular resolution; telescopes; waves

DOI: 10.26119/VAK2024.160

1 Introduction

Various types of transformable structures are being developed and used for creating space antennas. Large solid-state petal antennas have found application in radio astronomy for research in the centimeter and millimeter ranges of the spectrum (Kardashev et al. 2012; Huang et al. 2018; An et al. 2020). The classical design of a petal mirror was proposed by the Dornier Corporation as part of the work on the FIRST (Far Infrared Space Telescope) project.[1] A similar design was later used in the RadioAstron project, which operated in the centimeter range of the spectrum (Alexandrov et al. 2011).

While the classical design offers compact storage and a relatively simple deployment system, it has two significant drawbacks. First, in the operational state, the long petals are cantilevered to the central mirror, resulting in low rigidity of the deployed reflector. Second, in this design, the long petal is connected to the central mirror with a cylindrical hinge. Thus, small errors in the hinge installation lead to large errors on the outer edge of the petal, which significantly reduces the antenna quality (Kovalev et al. 2014). Our task is to eliminate these drawbacks.

2 Design description

The idea behind the new design is to move to a two-stage deployment of the antenna. The design is described in detail in Bujakas & Glotov (2024). In the first stage, a preliminary low-precision unstressed deployment of the antenna occurs, and in the second stage the high-precision fixation of the final state of the deployed reflector is achieved. In the new transformable mirror design, each petal is connected to the base of the central mirror with a spherical hinge, and the actuators are moved to the outer edge of the petals. It has been previously shown (Bujakas 2022) that at each moment of preliminary deployment, the structure remains unstressed and geometrically unchanged (statically determinate).

To deploy the reflector, a deployment system consisting of identical units is used, with the number of units equal to the number of petals. These units are placed on the outer edges of the petals, connecting adjacent petals in pairs. Each unit includes an actuator, a lever used to move one petal relative to another, self-adjusting locks, and a spherical hinge. The deployment is carried out by rotating the lever counterclockwise.[2]

[1] Patent US4899167A, 1986.
[2] https://disk.yandex.ru/d/aKhLi_aC4EnXog

3 Physical model of the new petal antenna

The physical model of the petal antenna implementing the proposed two-stage deployment is shown in Fig. 1. The model consists of 23 petals and corresponds to the design presented in Section refDesignDescription. The petals and the central mirror were fabricated using 3D printing. The diameter of the mirror in the deployed state is 50 cm. During tests, we confirmed that the model deploys automatically, convincing us of the viability of the proposed two-stage antenna deployment scheme.

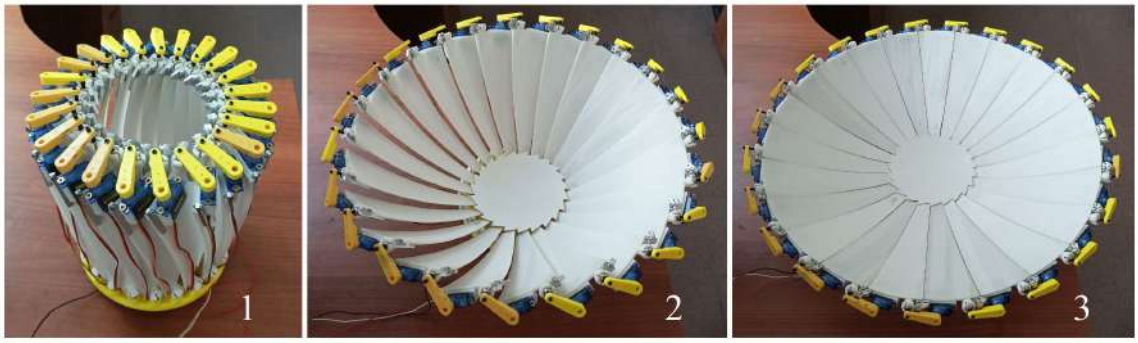

Fig. 1. The stages of deployment of the physical model: 1—mirror in the folded state, 2—partially opened mirror, 3—mirror in the opened state.

4 Deployment repeatability control using 3D scanning

The repeatability control of the model deployment was carried out using a non-contact 3D scanning method. We used a 3D scanner[3] (Fig. 2a, b) with a resolution of 1 mm, projecting a grid onto the reflective surface of the deployed mirror and determining the positions of the grid nodes to form a point cloud (Fig. 2c). The data obtained was processed using the open-source software CloudCompare[4](Fig. 2d).

Two cycles of mirror deployment and fixation were performed. At the end of each cycle, the positions of the petals were measured. The point cloud obtained from the first scan was used as a template. The point cloud from the second scan was compared to this template. Approximately fifty thousand points were automatically selected from the second cloud, and the distance from each point to the template

[3] https://support.3dsystems.com/s/article/Sense-Scanner?language=en_US
[4] https://www.cloudcompare.org/

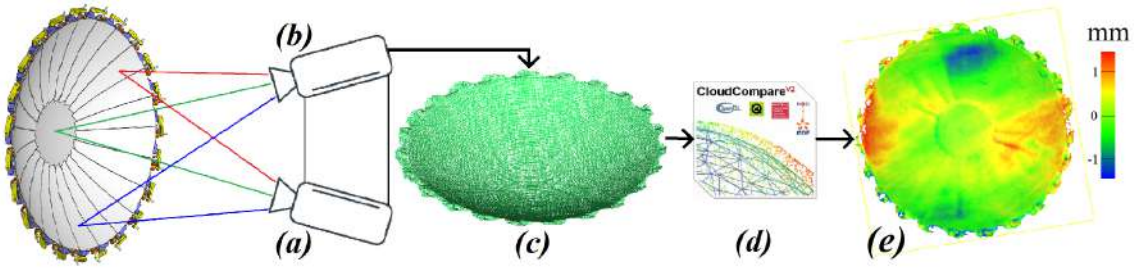

Fig. 2. The process of scanning and analyzing the mirror surface. (a, b)—3D scanner (the projection unit and registration unit, respectively); (c)—point field; (d)—CloudCompare; (e)—a result of the scanned data processing using CloudCompare.

surface was calculated. Each point and its surrounding area were assigned a color based on the distance (Fig. 2e).

The obtained data allows the determination of deformation locations and the calculation of their magnitude. Modern 3D scanners with a resolution of 0.02 mm enable high-precision control of the mirror shape and deployment repeatability.

5 Summary

This work proposes a new two-stage deployment scheme for a precise petal radio astronomy antenna. We constructed computer and physical models, which confirmed the feasibility of the new technical solution. A method for controlling the repeatability of the deployment of the transformable mirror model using 3D scanning was considered. We believe that these results could be useful in the development of new-generation space radio telescope antennas operating in the centimeter and millimeter ranges.

References

Alexandrov Yu.A., Andreyanov V.V., Babakin N.G., et al., 2011, Vestnik "NPO im. S.A. Lavochkina", 3, p. 11

An Tao, Hong Xiaoyu, Zheng Weimin, et al., 2020, Advances in Space Research, 65, 2, p. 850

Bujakas V.I., 2022, International Journal of Solids and Structures, 238, id. 111383

Bujakas V.I. and Glotov M.D., 2024, Antennas, 3, p. 58

Huang He, Guan Fu-Ling, Pan Liang-Lai, et al., 2018, Acta Astronautica, 148, p. 99

Kardashev N.S., Kovalev Y.Y., Kellermann K.I., 2012, The Radio Science Bulletin, 343, p. 22

Kovalev Yu.A., Vasilkov V.I., Popov M.V., et al., 2014, Cosmic Research, 52, 5, p. 393

MODERN ASTRONOMY: FROM THE EARLY UNIVERSE TO EXOPLANETS AND BLACK HOLES

Liquid scintillation detector based on an acrylic sphere and silicon photomultiplier matrices

I. Dzaparova, A. Yanin, E. Gorbacheva, A. Kurenya, and V. Petkov

Institute for Nuclear Reseach of the Russian Academy of Sciences,
prospekt 60-letiya Oktyabrya 7a, Moscow, 117312 Russia

Abstract. This paper presents the results of applying the matrices of silicon photomultipliers (SiPMs) as multichannel photodetectors for the scintillation detectors based on a liquid scintillator. We consider the possibility of using the SiPM matrices with an appropriate optical collector to obtain an image of the luminous tracks of charged particles passing through a scintillator. Such a method allows one to obtain an image of an event inside the scintillator volume, the analysis of which makes it possible to separate different classes of events. It is expected that the proposed particle detection technique may be useful in the creation of new large detectors for neutrino astrophysics and geophysics. The detector is an acrylic sphere with a diameter of 500 mm, filled in with a liquid scintillator. The scintillator is viewed through an optical collector based on two Fresnel lenses with two matrices of 64 SiPMs. The paper describes the data collection system and the detector design, we also demonstrate a three-dimensional image of a recorded event.

Keywords: instrumentation: detectors; techniques: image processing

DOI: 10.26119/VAK2024.161

1 Introduction

Silicon photomultipliers (SiPMs) and Fresnel lenses have already been used in the design of scintillation detectors. The Mini-EUSO telescope, launched in 2019, has Fresnel lenses and vacuum photomultiplier tubes in its design as well as the SiPMs matrices (Battisti et al. 2023). The Gamma-400 space observatory under development also explores the possibility of detecting the photons from a scintillator by focusing them through a Fresnel lens onto a SiPM (Runsto et al. 2019).

For our detector, the task is to obtain a snapshot of an event when a particle passes through the scintillator substance in order to derive an additional parameter to the measurement of the energy released for further analysis and classification of the event. It is also of interest to study the possibility of recording tracks of rare events, which may become in demand in the development of new large detectors for neutrino astrophysics and geophysics. The prospects for the application of the new technique in the Baksan Large Volume Scintillation Detector are indicated in Petkov (2016).

2 Detector design

The detector has small dimensions: the diameter of the acrylic sphere is 500 mm, which is convenient for designing the mounting structure for matrices and Fresnel lenses as well as for developing the calibration and processing techniques.

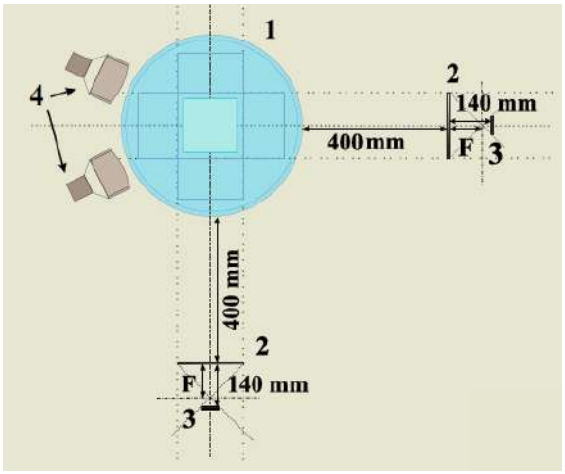

Fig. 1. Detector design (top view): 1—acrylic sphere, 2—Fresnel lens, 3—SiPM matrix, 4—vacuum photomultiplier XP4500B.

The acrylic sphere is filled with a scintillator developed at the Institute for Nuclear Research of the Russian Academy of Sciences and remaining one of the best in the world in terms of such characteristics as the scintillation output, short illumination time, and stability of the scintillator (Voevodskii et al. 1970). The SiPM matrices ARRAYJ-60035-64P-PCB of the Irish company SensL were selected as photodetectors, their maximum sensitivity (420 nm) coincides with the maximum of the photon emission spectrum of our scintillator.

The optical collector of the detector has two Fresnel lenses. Two matrices of SiPMs are arranged orthogonally. The total working volume to view is close in shape

to a cube with a face of 17 cm. The volume is highlighted in Fig. 1 in the center of the sphere. The measurements of the volume viewed by the matrix for this geometry of the optical collector were carried out using a probe with a LED mounted on it. We were recording the positions of the LED in the volume of the sphere when the image of the LED was still falling onto the edges of the matrix. The description of the measurements is given in Dzaparova et. al. (2021).

The working volume of the detector is viewed by two Photonics XP4500B vacuum photomultipliers. A trigger is generated by the coincidence of the photomultiplier anode signals with the set threshold. The next step in improving the detector design is to add a third matrix to the data acquisition system. For this purpose it was necessary to create a program for constructing three-dimensional images of recorded events. This approach to visualize the registered events is useful for the analysis even when there are only two matrices in the data acquisition system.

3 The data acquisition system and measurement results

The MDU3-GI64X2 data acquisition system from AiT Instruments consists of two 64-channel boards of 12-bit charge-to-digital converters. The data acquisition system can operate from an external trigger and can use different options for generating an internal trigger. A flat micro-coaxial cable assembly connecting the MDU3-GI64X2 input connector to a preamp board creates an interference-proof channel for transmitting analog signals. The control of the unit and data collection are implemented via the USB 3.0 interface.

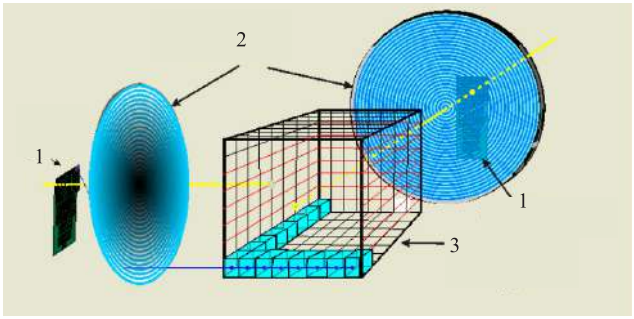

Fig. 2. The working volume of the detector divided into 512 cubes by two SiPM matrices.

The data processing program for constructing three-dimensional events based on the measurements is working in test mode: so far with data from two matrices—128 channels. Having the two projections obtained by the matrices, one can build the third projection. The viewed working volume in this case will be divided into 512 cubes (Fig. 2). Each SiPM of the first matrix detects photons from eight cubes of the corresponding SiPM row of the second matrix, then vice versa the measured values in the row of the first matrix are determined for each SiPM of the second

matrix. Thus, the program determines the coordinates and brightness of the SiPM cubes for the entire working volume of the detector.

The brightness of some cubes in event visualization is not always uniquely determined and requires the use of assumptions (before including the third matrix in the data acquisition system). Figure 3 shows a three-dimensional image of a registered event.

Fig. 3. Three-dimensional image of the registered event.

The size of the ARRAYJ-60035-64P-PCB, 8×8 SiPM matrices, is 5.04×5.04 cm^2, and the area of the working volume cube face facing the matrix is 17×17 cm^2. Thus, the cube face area is 11 times larger than the area of the matrix. It is assumed that after connection of the third matrix, the parameters of the optical system will remain the same for the time being, in order to simplify testing both the event visualization program and the optical system.

4 Summary

Necessary conditions have been created to connect three SiPMs matrices to the data acquisition system. A trigger for the measurements is generated by the coincidence of the anode signals from the vacuum photomultipliers with the set threshold. The construction for the installation of the third matrix has also been prepared. Further increase in the number of matrices included in the data acquisition system while reducing the volume viewed by a matrix requires creation of another calibration system both to obtain an image at the required scale and to verify the accuracy of the location of the matrices in the detection system.

References

Dzaparova I., Yanin A., Gorbacheva E., et al., 2021, Izvestiya Krymskoj Astrofizicheskoj Observatorii, 117, 1, p. 76

Battisti M., Bertaina M.E., Arnon E., et al., 2024, Proceedings of Science, 444, id. 353

Petkov V.B., 2016, Physics of Particles and Nuclei, 47, 6, p. 975

Runtso M.F., Arkhangelskaja I.V., Arkhangelskiy A.I., et al., 2019, Journal of Physics: Conference Series, 1390, id. 012134

Voevodskii A.V., Dadykin V.L., Ryazhskaya O.G., et al., 1970, Pribory i tekhnika eksperimenta, 1, p. 85

MODERN ASTRONOMY: FROM THE EARLY UNIVERSE TO EXOPLANETS AND BLACK HOLES

RadioAstron project: calibration of the space radio telescope during the flight in 2011–2018 in the 1.35, 6.2, 18, 92 cm bands using improved primary calibration scales

A. Ermakov[1], V. Vasilkov[1], P. Voitsik[1], Yu. A. Kovalev[1], M. Lisakov[1], and Yu. Yu. Kovalev[2]

[1] Astro Space Center of P. N. Lebedev Physical Institute, 84/32 Profsoyuznaya St., Moscow, 117997 Russia
[2] Max-Planck-Institut für Radioastronomie, Auf dem Hügel 69, Bonn, 53121 Germany

Abstract. We summarize the results of processing calibration telemetry sessions for the four known primary calibrators of spectral radio flux density—Cassiopeia A, Crab Nebula, Cygnus A, and Virgo A—in the autonomous observation mode with the space radio telescope (SRT) in flight. A new system of automated data processing was used, previously successfully tested in similar processing of the measurements with the SRT in 2015–2018 in the 6.2, 18, and 92 cm bands. The calibration of the SRT intrinsic noise and the internal artificial generators of the noise signal (NG) was performed for two versions of the primary scale of spectral radio flux density: the generally accepted original scale by Baars et al. suggested in 1977 and its improved version based on the results from newer publications. The main differences between the versions are related to the fact that the actual rate of secular variation in the fluxes of astronomical calibrators differs from the extrapolated values in the previously accepted scale. Preliminary results for the SRT calibration with the improved scale coincide within 10–15 percent with the results published earlier.

Keywords: methods: observational

DOI: 10.26119/VAK2024.162

1 Introduction

The article presents the results of processing the data from the Noise Generator (NG) and the intrinsic noise of the SRT at four wavelengths for the entire flight in 2011–2018 using four astronomical calibrators. The results were obtained with a unified automated data processing system in contrast to the earlier approaches.

2 Processing and analysis

Four known astronomical primary calibrators were used: Cassiopeia A, Crab Nebula, Cygnus A, and Virgo A. The data were processed using an automated system that had previously been successfully tested in similar processing of the 2015–2018 SRT measurements in the 6.2, 18, and 92 cm bands, but relative to only Cas A and the Crab Nebula (Ermakov & Kovalev 2020; Kovalev et al. 2020, 2022) in the primary scales by Baars et al. (1977); Perley & Butler (2017).

Each calibration session consists of recording a response to the activation of the noise signal generator, measuring the intrinsic noise of the SRT system, and scanning a calibration source. The resulting values in volts are converted into units of spectral flux density for the NG and the SRT ($F_{\rm ns}$ and $F_{\rm sys}$).

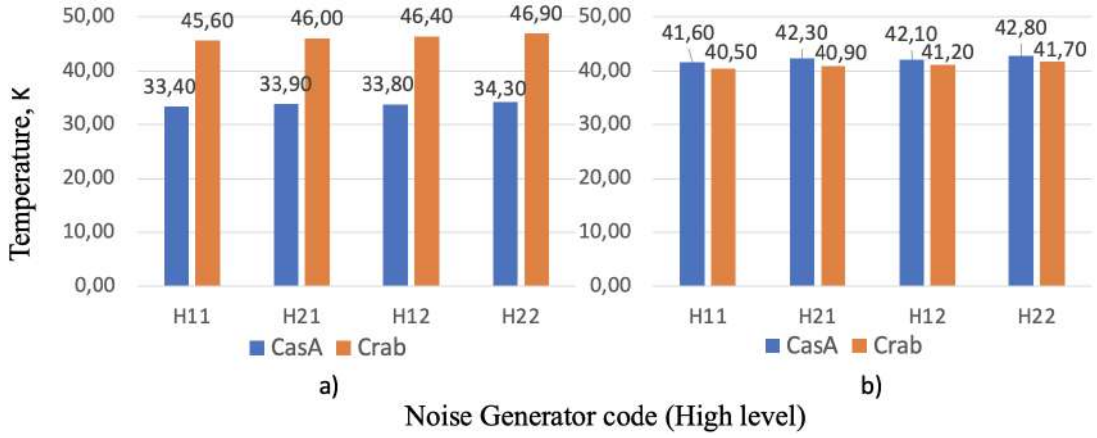

Fig. 1. Average values over 2011–2018 in the 18 cm band for four (out of eight) noise generators. The left panel shows the calibration carried out relative to the standard primary scale by Baars et al. (1977). The same NG values from 2011–2018 but calibrated according to the new scale by Perley & Butler (2017) are shown on the right.

The monitoring results for the first half of the SRT flight coincide with the second half: the calibrations of noise generators are stable relative to Crab and Cas A, the

average error over 8 years is 2–5%. However, there is still discrepancies in calibrations relative to different astronomical sources: the calibrations according to Crab differ from the calibrations according to Cas A by 25–35%. Figure 1 shows the average values for four out of eight NGs over the entire SRT flight for the 18 cm range. Figure 1a clearly shows how much the NG calibrations differ relative to different calibrators. Recalculating the calibrations to the corrected scale eliminates this difference (Fig. 1b).

In addition to the Crab and Cas A calibrations, the calibrations relative to Cygnus-A and Virgo-A for the entire duration of the SRT flight were also processed. The analysis shows that the calibrations in the new scale also agree well with each other. Figure 2 shows the ratios of the NG calibration between the four calibrators. The ratios in the new scale are close to one and are within an error of 10–15%, which characterizes the accuracy of the spectral flux density scale in which the calibration was performed. Thus, in processing the observations and analyzing the calibrations obtained for the entire SRT flight, we were convinced of the operability of the method for checking the spectral flux density scales and also convinced of the stability of the parameters during the entire operation of the SRT in three wavelength ranges.

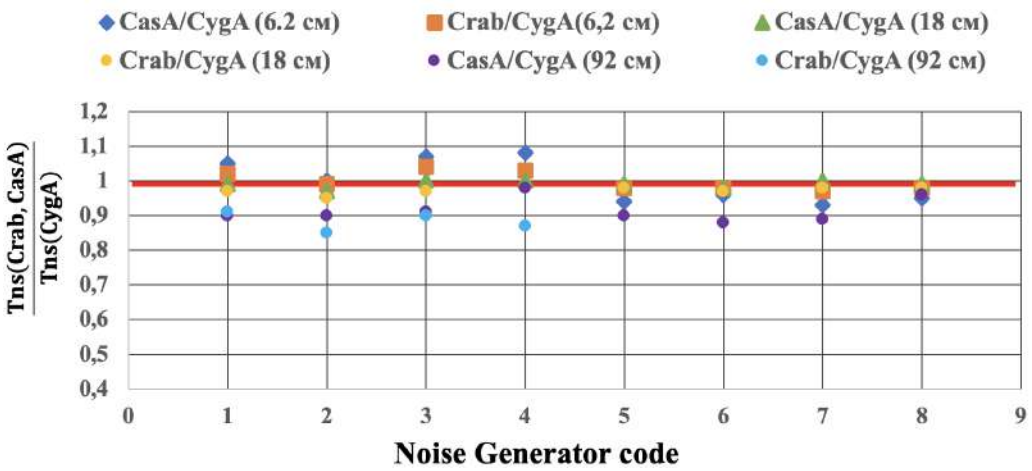

Fig. 2. The ratios between the calibrations calculated using different calibrators in the new scale. The values should lie near the red line, around one.

All the observed calibration data at the shortest wavelength of 1.35 cm were also processed using the unified automated data processing system. Figure 3 shows an example of the obtained results. The analysis of the results is in progress.

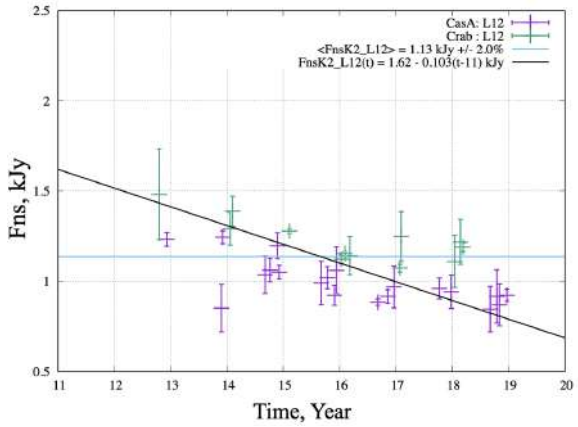

Fig. 3. An example of the calibration results for one of eight NGs for 2011–2018 in the 1.35 cm range using Cas A and Crab. The known drift of the NG power can be seen.

3 Conclusions

1. The previously tested system for mass automated processing of calibration observations was used to calibrate the observations relative to the Crab Nebula and Cas A during the first half of the SRT flight in 2011–2014 for the bands of 6.2–92 cm.
2. The automated system has processed the observations of Cyg A and Vir A for the entire SRT flight in 2011–2018 in the bands of 6.2, 18, and 92 cm.
3. With a small modification, the system has processed a new range of 1.35 cm for all the years of the SRT flight. The hypothesis about the drift of the NG power over time is confirmed. All the data have been processed, the analysis continues.
4. We have shown that the SRT parameters ($F_{\rm ns}$ and $F_{\rm sys}$—system equivalent flux density, SEFD) are stable within a small error of 2–3% relative to each of the four calibrators at 6, 18, and 92 cm.
5. The transition to the new scale of spectral flux density eliminates the difference in the SRT calibrations calculated relative to different astronomical calibrators. The method has been tested on several new calibration scales.

References

Baars J.W.M., Genzel R., Pauliny-Toth I.I.K., et al., 1977, Astronomy & Astrophysics, 61, p. 99
Ermakov A.N. and Kovalev Yu.A., 2020, Transactions of IAA RAS, 54, p. 21
Kovalev Yu.A., Vasil'kov V.I., Ermakov A.N., et al., 2020, Transactions of IAA RAS, 54, p. 32
Kovalev Yu.A., Vasilkov V.I., Ermakov A.N., et al., 2022, Astrophysical Bulletin, 77, p. 360
Perley R.A. and Butler B.J., 2017, Astrophysical Journal Supplement Series, 230, 1, id. 7

BAK 2024 MODERN ASTRONOMY: FROM THE EARLY UNIVERSE TO EXOPLANETS AND BLACK HOLES 300 years Russian Academy of Sciences

The impact of technical constraints on the possibility of resolving the pulsar magnetosphere by observing its scintillations

E. Fadeev[1], A. Andrianov[1], M. Burgin[1], M. Popov[1], A. Rudnitskiy[1], T. Smirnova[2], and V. Soglasnov[1]

[1] Lebedev Physical Institute, Astro Space Center, 84/32 Profsoyuznaya, Moscow, 117997 Russia
[2] Lebedev Physical Institute, Pushchino Radio Astronomy Observatory, Pushchino, 142290 Russia

Abstract. Variation in the pulsar dynamic spectra with pulse longitude had in the past been interpreted as a result of the spatial motion of the pulsar emission region and led to some conclusions about the altitude of the emission regions or the magnetosphere structure. Motivated by this research, we used the VLBI observations of PSR B1237+25 with the Arecibo and Green Bank radio telescopes at 324 MHz, performed as part of a RadioAstron observing program, and analyzed scintillations at separate longitudes of the pulse profile. We have found that the fringe phase characteristics of the visibility function vary quasi-sinusoidally as a function of longitude. Also, the dynamic spectra from each of the telescopes shift in frequency as a function of longitude. However, we have found that these shifts arise from the low-level digitizing of the pulsar signal. After correcting for these digital effects, the frequency shifts have largely disappeared. The residual effects may be of instrumental origin or indicate the pulse emission altitudes well below the pulsar light cylinder radius.

Keywords: scattering; pulsars: individual: B1237+25; ISM: general; techniques: high angular resolution; methods: data analysis

DOI: 10.26119/VAK2024.163

1 Introduction

Pulsars are observed through the inhomogeneous interstellar plasma, which acts as a lens or an interferometer with an extremely long baseline, potentially providing extremely high spatial resolution. The first evidence of resolving the magnetosphere of a pulsar with interstellar interferometry was reported by Wolszczan & Cordes (1987), who estimated the altitude of the emission region close to the light cylinder radius $r_{\rm LC}$. Since then, there have been a few apparently successful attempts to spatially resolve this region, but so far no a consistent picture has been obtained as to the altitude of the emission regions near the pulsar or close to $r_{\rm LC}$.

2 Observations

We carried out VLBI observations of PSR B1237+25 the with the Arecibo Telescope and the Green Bank Telescope (GBT) at 324 MHz in a bandwidth of 16 MHz in right and left circular polarizations. The observations were made as part of the RadioAstron space VLBI science program on December 22, 2017, and February 26, 2018. The data were processed at the Astro Space Center (ASC) using the ASC software correlator with gating and incoherent dedispersion applied.

3 Data processing

The pulse profiles are shown in Fig. 1a. We divided the pulse window into nine subwindows w_k with $0 \leqslant k \leqslant 8$. Then, in each window we computed a complex cross-spectrum for the Arecibo–GBT baseline and an autospectrum (dynamic spectrum) for each of the two radio telescopes.

For every single pulse and every subwindow, we computed the complex visibility function $V_k(\tau)$ as the inverse Fourier transform of the cross-spectrum. Then we computed for each subwindow in the pulse profile the phase φ_k of $V_k(\tau)$ relative to the phase in the subwindow w_4: $(\varphi_k - \varphi_4)$. We found that in a delay window of approximately ± 125 ns the curves of phase differences could be approximated by straight lines with a fitted slope. In Fig. 1b we plot for the two polarizations and two days of observations the values of the varying slopes and their standard errors derived from the fitting for each subwindow with respect to the value for the window w_4. We note that this pattern is very similar to the comparable pattern of phase versus longitude presented by Wolszczan & Cordes (1987).

We can also see the frequency shift in our dynamic spectra as a function of longitude for each of the two telescopes separately. In Fig. 1c, d, we show the dynamic spectra in the windows w_0 and w_8 respectively. The latter one is slightly but clearly

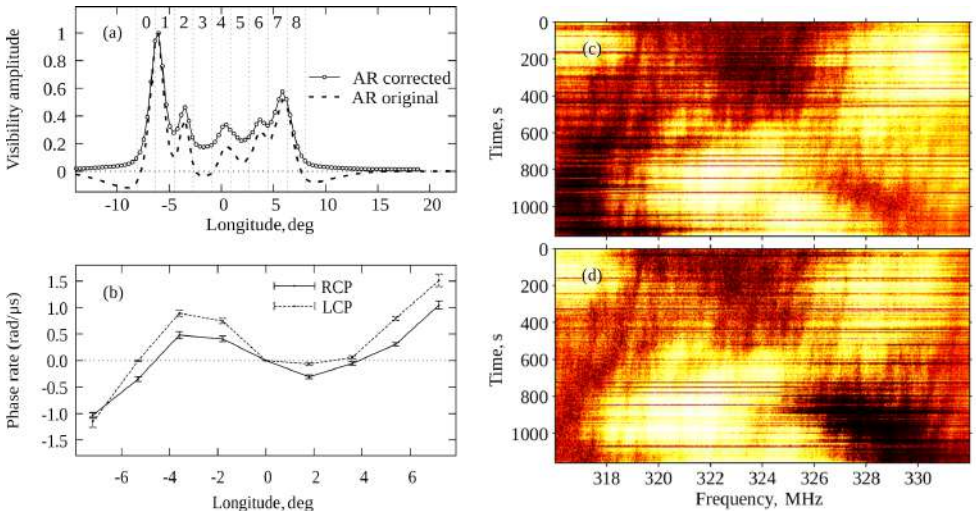

Fig. 1. (a) Average profile of PSR B1237+25 for the original data and the profile after correction. The vertical dashed lines indicate the nine on-pulse subwindows, w_0 to w_8, used as gates for the correlation and for our analysis. (b) The variation rate of the visibility phases as a function of pulsar longitude for both senses of polarization for the observing epoch December 22, 2017. (c, d) The dynamic spectra observed with the Arecibo Telescope in the longitude windows w_0 (top) and w_8 (bottom). A shift of about 1 MHz toward lower frequencies from w_0 to w_8 is clearly visible.

shifted toward lower frequencies with respect to the former. The time-averaged spectrum in the window w_0 has an excess at higher frequencies, while the spectrum in the window w_8 has the opposite distortion as it is shown in Fig. 2 (left).

The reason for the distortions can be traced back to the effects of digitizing a non-stationary stochastic signal like the pulsar signals studied in Jenet & Anderson (1998). For one-bit digitizing, the excess of spectral power density at relatively high frequencies leads to a false deficiency of spectral power density at relatively low frequencies. The same effect can be seen under saturation conditions for the two-bit (four-level) digitizing used at both the Arecibo Telescope and the GBT. We switched off the automatic gain control on both telescopes as it would have not worked correctly for pulsar observations due to its inertia. In these circumstances, the digitizer was saturated by strong pulses which were turning it into a pseudo-two-level system.

Due to interstellar dispersion, the pulsar signal arrives at the telescope earlier at higher frequencies, affecting the energy redistribution within the bandwidth. The incoherent dedispersion algorithm used by the correlator was not able to fully compensate for the dispersion delay. Since all the VLBI observations of the RadioAstron mission had been archived, we applied the corrections of two-bit sampling to the

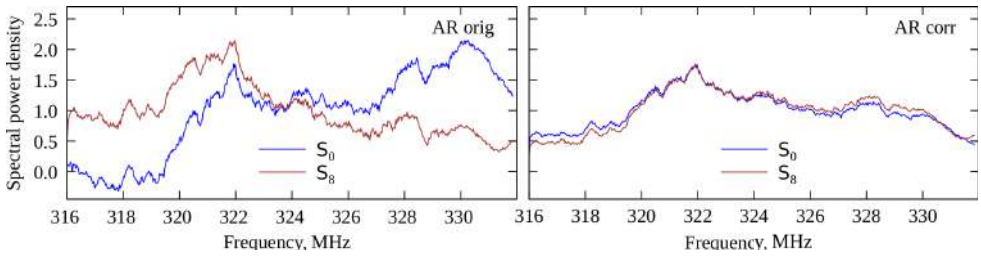

Fig. 2. Time-averaged left circular polarization spectra for the leading (S_0) and trailing (S_8) windows, each with the spectrum for the off-pulse subtracted. The left and right panels show the spectra before correction and the corrected spectra, respectively.

original VLBI data. Moreover, we also dedispersed the data coherently (Girin et al. 2023). As a result, most of the frequency effects disappeared (see Fig. 1a and Fig. 2, right panel). We did not investigate the nature of the residual effects. These effects could be instrumental or caused by the actual motion of the emission region. For further information see Popov et al. (2023).

4 Summary

- In the VLBI data as well as in the data from a particular telescope, the frequency shift demonstrates a non-monotonic pattern as a function of pulsar longitude.
- We attribute the distortions and frequency shifts of the longitude-dependent dynamic spectra mostly to the uncorrected low-level digitizing of the data.
- Upper limits of any astrophysics-related frequency shifts suggest that the altitude of the emission regions for PSR B1237+25 is well below $r_{\rm LC}$.
- In view of our analysis, we think that observations with the intent to resolve the pulsar magnetosphere need to be critically evaluated in terms of these constraints on interstellar interferometry.

Acknowledgements. The RadioAstron project is led by the Astro Space Center of the Lebedev Physical Institute of the Russian Academy of Sciences and the Lavochkin Scientific and Production Association under a contract with the Russian Federal Space Agency in collaboration with partner organizations in Russia and other countries.

References

Girin I.A., Likhachev S.F., Andrianov A.S., et al., 2023, Astronomy and Computing, 45, id. 100754
Jenet F.A. and Anderson S.B., 1998, PASP, 110, p. 1467
Popov M.V., Bartel N., Andrianov A.S., et al., 2023, ApJ, 954, p. 126
Wolszczan A. and Cordes J.M., 1987, ApJL, 320, L35

MODERN ASTRONOMY: FROM THE EARLY UNIVERSE TO EXOPLANETS AND BLACK HOLES

New panoramic camera for SAO RAS BTA

M. Fokin, V. Komarov, I. Shaldyrvan, and V. Komarova

Special Astrophysical Observatory of the Russian Academy of Sciences,
Nizhny Arkhyz, 369167 Russia

Abstract. The development of a new multifunctional panoramic sky-viewing system for the 6-m optical telescope BTA at the Upper Scientific Site (VNP) of the Special Astrophysical Observatory of the Russian Academy of Sciences (SAO RAS) is described. The new viewing system based on an IP camera with a CMOS detector is being created to replace the panoramic system of the previous generation. The multifunctional online operating mode of the new system will provide remote monitoring of the sky over the VNP both at night and in the daytime (in color mode) with a variable field of view ranging from 5° to 87° and the ability of 360° scanning in azimuth and 90° by elevation angle. It is also possible to obtain not only the images of the night sky with stars and/or the Moon but also images of the Sun in daytime with sunspots resolved.

Keywords: methods: observational; techniques: image processing

DOI: 10.26119/VAK2024.164

1 Introduction

In astronomical observations at the BTA and other optical telescopes located at the VNP of SAO RAS, remote round-the-clock video monitoring of both the entire celestial hemisphere and the panorama of the surroundings near the observing facilities is necessary. For this purpose, a digital television complex of the BTA and Zeiss-1000 telescopes was developed more than 20 years ago (Komarov et al. 2002). Its television cameras operate around the clock and are constantly modernized. Currently, there is a need to replace the outdated systems of this complex partially or even completely. One of such systems is the panoramic sky-viewing camera at the VNP.

2 Panoramic sky-viewing system in operation

The current panoramic sky-viewing system FEP50/10K, which is part of the digital television complex, has been operating and providing round-the-clock monitoring since 2008. The main characteristics of FEP-50/10K are given in Table 1.

Table 1. Characteristics of the panoramic viewing systems.

Parameter	FEP-50/10K	FEP-87/5[(a)]
Scanning angle (azimuth/elevation), deg	330/90	360+[(b)]/180
FOV, deg	10–50	5–87
Pointing accuracy, deg	±1	±0.5
Limited magnitude	9[(c)]	11
Operating mode	b/w	color+b/w
Format	4:3	16:9
Resolution, pix	768 × 576	1920 × 1080
Operation in direct sunlight	–	+[(d)]

[(a)] optional; [(b)] unlimited azimuth rotation; [(c)] $T_{\rm exp} = 2^{\rm s}.5$; [(d)] with solar filter.

The FEP50/10K system does not fit our current needs for a number of reasons, some outdated parameters being the essential ones. Therefore, either modernization of FEP50/10K or its complete replacement is necessary. The second way, in our opinion, is the most promising, so we have started developing and creating a new online panoramic camera for the VNP of the SAO RAS.

3 New online panoramic viewing system

Currently, we create a new panoramic viewing system for the VNP of the SAO RAS based on an IP camera with a CMOS detector. It is designed for remote monitoring

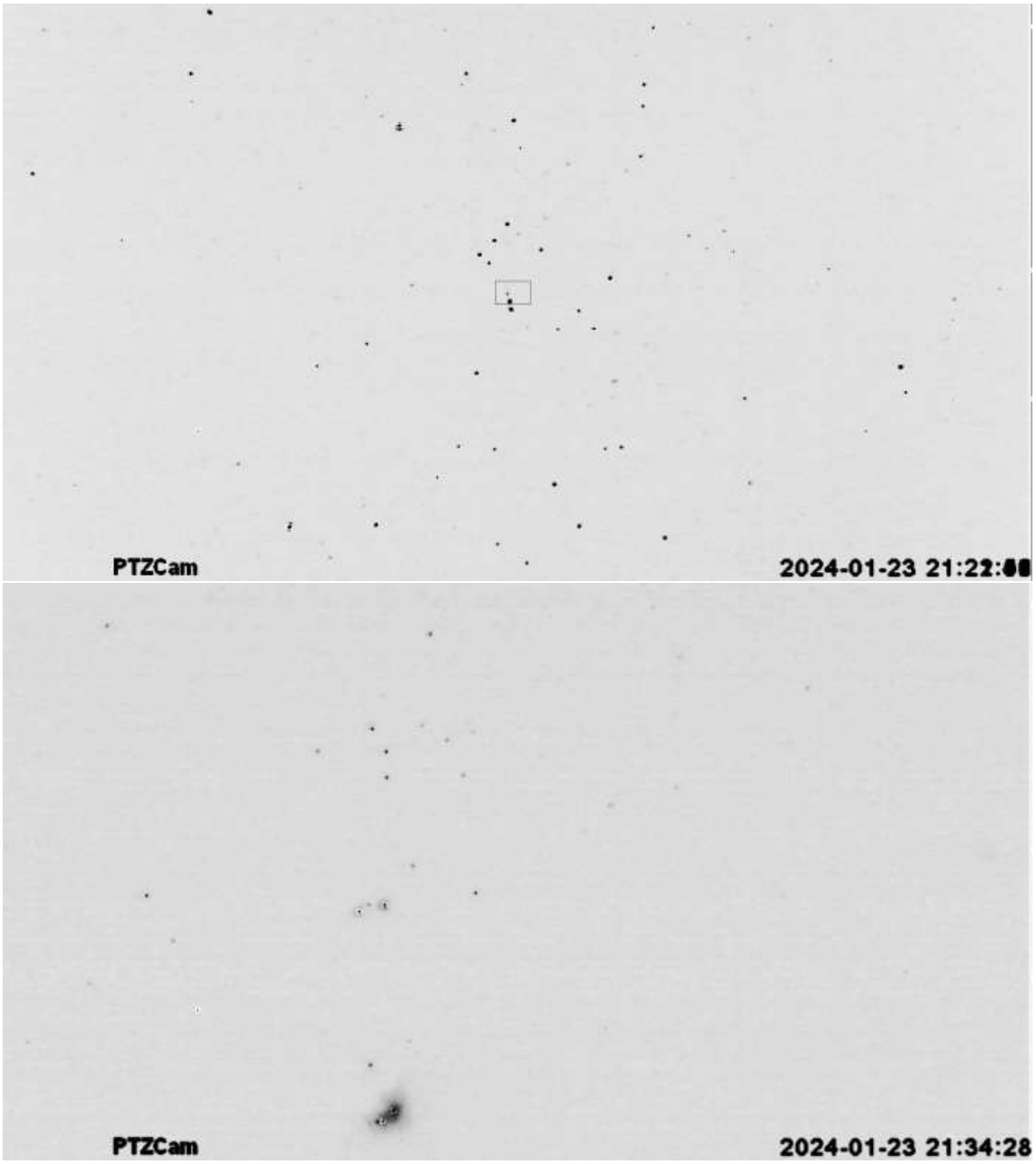

Fig. 1. Top: a series of 12 images of a sky region in the direction of the constellation Orion with a 87° FOV, the total exposure time is 12×80 ms, b/w mode. The rectangle in the center highlights the area shown in the bottom panel. Bottom: an image of the sky area taken in the same direction as the upper one but at maximum zoom (FOV = 5°), the exposure time is 80 ms, b/w mode. The images are given in inverted colors.

with a variable field of view (FOV) both at night and in the daytime (in color mode) and the ability of scanning over a wide angle range.

When choosing the receiver and components, we kept in mind the fact that the photodetector should have high sensitivity and be mass-produced. The SONY IMX291 sensor with an aspect ratio of 16:9, which is the most suitable for a viewing system, was selected to meet these requirements. The JZC-N83020 camera was chosen as a receiver. It is equipped with a 30X zoom lens and a Sony IMX291 CMOS detector with a format of 1/2.8 inches and high sensitivity. The varifocal lens provides a variable field of view from 5° to 87°. At a low price, the receiver has the necessary characteristics to operate as part of the complex of VNP viewing systems (see Table 1).

The camera is able to take images of the Sun and sunspots with good resolution. For this purpose, an EYSDON solar filter with a diameter of 46.5 mm is used. The panoramic camera was tested in the night time on 23 and 30 January, 2024. Examples of images taken at minimum and maximum zoom are presented in Fig. 1.

4 Conclusion

The development of a new panoramic system using an IP camera based on a CMOS sensor has been presented. The advantage of the new system compared to the previously developed one is the possibility of the online remote video monitoring of the sky, weather conditions, and surroundings in the vicinity of the SAO RAS optical telescopes both at night and in the daytime (in color mode) with variable FOV of a wider range: from 5° to 87°. It has the ability of azimuthal scanning without limitation, i.e., the camera can be rotated by more than 360° degrees. The scanning by elevation angle is from horizon to horizon: 180°. The azimuth and elevation coordinates are shown in the resulting images. It is also possible to take images of the solar disk with sunspots resolved. The system control is remote via a web interface.

References

Komarov V., Fomenko A., Vitkovskij V., et al., 2002, Bulletin of the Special Astrophysical Observatory, 53, p. 134

VAK 2024 MODERN ASTRONOMY: FROM THE EARLY UNIVERSE TO EXOPLANETS AND BLACK HOLES 300 years Russian Academy of Sciences

Four-channel wide-field cluster for survey tasks and synchronous multicolor photometry

M. Ibrahimov, M. Nalivkin, and A. Shugarov

Institute of Astronomy of the Russian Academy of Sciences,
48 Pyatnitskaya str., Moscow, 119017 Russia

Abstract. A new wide-field optical instrument of the Institute of Astronomy of the Russian Academy of Sciences (INASAN) is described. It has been implemented under the bilateral Russia–Uzbekistan collaboration in astronomy in 2023–2025. The instrument comprises four identical wide-field 28-cm aperture telescopes on a common mount designed for all-sky surveys and photometry. For a single exposure, the cluster takes an image of a 7 square degree field in four photometric bands simultaneously with a 1.26 ″/px scale. The technical and optoelectronic characteristics of the cluster are presented and discussed. The plan is to install the cluster at the Maidanak Astronomical Observatory, which has a large amount of clear night time (about 2500 hours per year) with a median seeing of 0.″7. The INASAN cluster will become one of the most informative positional photometric multiband observing systems in Russia. It will also be useful in a global network of multiband wide-field optical instruments including the BRICS astronomical network.

Keywords: surveys; telescopes; methods: observational; techniques: photometric; instrumentation: photometers; stars: variables: general

DOI: 10.26119/VAK2024.165

1 Introduction

Currently, the concept of building a survey telescope using several small telescopes mounted on a common mount is gaining popularity. This approach is often more economical and faster to implement, since telescopes of smaller apertures and detectors of smaller formats are often available as mass-produced commercial products.

The new INASAN four-channel cluster is created for the Russian-Uzbekistan joint project in 2023–2025 (Ibrahimov et al. 2023). The instrument is a cluster of four identical telescopes (a four-channel cluster) coaxially mounted on a common mount and designed for all-sky multicolor surveys and photometric monitoring. During one exposure, the cluster provides imaging simultaneously in four photometric bands.

According to the technical specification, the INASAN cluster is almost identical to such well-established but operating in "white light" systems as the European–Mexican cluster of the DDOTI project (Watson et al. 2016) and the US–European cluster telescopes of the second generation of the ATLAS project (Licandro et al. 2023). The fundamental scientific advantage of the INASAN cluster over the mentioned clusters is the operation in four photometric bands simultaneously. It is assumed that the INASAN cluster will become one of the most informative and demanded multicolor photometric instruments in Russia and will be included in the astronomical networks of the BRICS countries.

To maximize the scientific efficiency, the cluster is planned to be installed in Uzbekistan at the Maidanak Astronomical Observatory of the Ulugh Beg Astronomical Institute (UBAI) of the Uzbek Academy of Sciences with excellent astroclimate.

2 INASAN four-channel cluster

Since 2021 at the Zvenigorod observatory Celestron RASA 11 (Fig. 1, right panel) with the ZWO ASI6200MM Pro camera on a direct drive ASA DDM85 mount has been successfully operating as a robotic telescope. The observations are carried out in the V band, the accuracy of photometric measurements is up to RMS $= 0\overset{\mathrm{m}}{.}005$. The experience gained by INASAN during the implementation of this telescope is used in the current project to build the four-channel cluster.

The new wide-field INASAN cluster has four identical wide-field 28-cm aperture Celestron RASA 11 telescopes[1] mounted on a single mount (Fig. 1, left panel). The cluster is built primarily with commercially available components (COTS, commercial-off-the-shelf). The four 11-inch Celestron RASA 11 telescopes pointed coaxially are equivalent to one telescope with an effective aperture of 56 cm.

The new INASAN four-channel cluster will provide:

[1] https://s3.amazonaws.com/celestron-site-support-files/support_files/rasa_white_paper_web.pdf

Fig. 1. Left: layout of four Celestron RASA 11 telescopes on a fork-type equatorial mount; right: the prototype of the four-channel cluster: a robotic telescope at the INASAN Zvenigorod observatory based on the Celestron RASA 11 telescope and ZWO ASI6200MM Pro camera.

- photometric measurements of objects in a field of $3.^{\circ}3 \times 2.^{\circ}2$ simultaneously in the spectral bands $UBVR$ or $BVRI$, for objects brighter than $16^{\rm m}$ the photometric accuracy is expected to be up to $0.^{\rm m}005$;
- astrometric measurements for objects brighter than $19^{\rm m}$ with an accuracy of $0.''15$–$0.''20$;
- detection of near-Earth objects brighter than $19^{\rm m}$ with an exposure time of 30 s and SNR = 3.

The main components of the four-channel cluster are:

- equatorial mount with a direct drive and the absolute encoders Astrosib FMDD-700, which provides fast repointing at a speed of 10 deg/s and accurate tracking without the need for guidance;
- Celestron RASA 11 wide-wield telescope with an additional light baffle (4 pcs);
- ZWO ASI6200MM Pro camera (4 pcs);
- ZWO 5V-EAF focuser (4 pcs);
- set of the $UBVR$ or $BVRI$ photometric filters;

– control computer, computing server with graphics cards and data storage system;
– software package that provides the receiving, processing, and storage of the scientific data;
– dome with an automated sliding roof.

3 Summary

According to calculations, the new INASAN four-channel cluster under ideal conditions (zenith, dark night, sky background $V = 21.5$ mag/arcsec) for a 30-s exposure time and SNR = 3 is going to have a limiting sensitivity of $20\overset{\mathrm{m}}{.}13$ without a filter, and $18\overset{\mathrm{m}}{.}1$, $18\overset{\mathrm{m}}{.}6$, $19\overset{\mathrm{m}}{.}35$, $19\overset{\mathrm{m}}{.}32$, $18\overset{\mathrm{m}}{.}07$ with the U, B, V, R, I filters, respectively.

The cluster will be manufactured and tested at INASAN, thereafter it is going to be installed at the Maidanak Astronomical Observatory in Uzbekistan.

Summing up, despite the small aperture of the telescope and a small camera, the angular resolution of the cluster installed at the Maidanak Observatory is expected to be $1\overset{''}{.}5$ across the entire field of view of 7 sq. deg with a 1.26 $''$/px scale, which is enough for many scientific applications. The cluster is expected to effectively monitor objects of up to 20^{m} with a single exposure and up to 21^{m} when co-adding the frames.

Funding

This work was supported by the Ministry of Science and Higher Education of the Russian Federation, grant 075-15-2022-1221 (2022-BRICS-8847-2335).

References

Ibrahimov M.A., Nalivkin M.A., Shugarov A.S., et al., 2023, INASAN Science Reports, 8, 4, p. 195
Licandro J., Tonry J., Alarcon M.R., et al., 2023, arXiv:2302.07954
Watson A.M., Lee W.H., Troja E., et al., 2016, Proc. of SPIE, 9910, id. 99100G

MODERN ASTRONOMY: FROM THE EARLY UNIVERSE TO EXOPLANETS AND BLACK HOLES

The new 50-cm multipurpose telescope of the Russian-Cuban Observatory

M. Ibrahimov[1], M. Nalivkin[1], S. Naroenkov[1], A. Shugarov[1], O. Ponce-Rodríguez[2], and Z. Bárcenas-Fonseca[2]

[1] Institute of Astronomy of the Russian Academy of Sciences, 48 Pyatnitskaya str., Moscow, 119017 Russia
[2] Institute of Geophysics and Astronomy, Calle 212 No. 2906, Havana, 11 600 Cuba

Abstract. The international collaboration between Russia and Cuba in astronomical research first began in 2017. The first 20-cm robotic telescope of the Russian-Cuban network has been operating since 2021 in Havana. The construction of the second 50-cm telescope has been underway since 2023, and it is expected to be finished and installed in 2025 near Kislovodsk (Russia). By 2030, the plan is to build the third 1-m telescope at Valle de Picadura (Cuba). We describe the main parameters and scientific equipment of the new 50-cm telescope and discuss its role in the Russian-Cuban distributed global telescope network.

Keywords: telescopes; methods: observational; instrumentation: photometers, spectrographs; stars: variables: general

DOI: 10.26119/VAK2024.166

1 Introduction

Since 2017, the Institute of Astronomy of the Russian Academy of Sciences (INASAN), Moscow, Russia, and the Institute of Geophysics and Astronomy (IGA), Havana, Cuba, have been developing a joint international project with the aim of building a distributed multitask network of optical telescopes: the Russian-Cuban Observatory (RCO).

At the beginning of 2021, the first telescope was installed at the IGA in Havana (Bisikalo et al. 2022). In 2023, the second optical telescope of a 50-cm aperture began being built in Russia (Ibrahimov et al. 2023). According to the current plan, the third custom 1-m wide-field telescope with spectroscopic, astrometric, and photometric capabilities is going to be installed in 2030 at Villa de Picadura located 80 km east of Havana.

Global optical telescope networks are efficient tools for many observational tasks requiring long continuous observing series of the studied objects. The location of the two telescopes in Cuba and Russia is significantly important for the functionality of the Russian-Cuban network both in terms of global coverage and observing modes. The time difference of 8 hours (120°) between Cuba and Kislovodsk allows continuous observations of up to 16 hours.

As an example of continuous observation importance, we can reference the detection and tracking of newly discovered asteroids (Bisikalo et al. 2018), photometric studies of variable stars (Naroenkov et al. 2022), and the study of optical transient events, e.g., the sources of gamma-ray bursts and tidal disruption events.

At least two types of telescopes should be included in the network: the wide-field survey telescopes and the middle-aperture follow-up telescopes equipped with cameras and spectrographs.

The first telescope of the RCO network is a wide field-of-view 20-cm robotic telescope. It is a multipurpose astrometric and photometric instrument. Having more than a 3° field of view, it is capable of detecting a large number of already known and new celestial objects and providing $UBVRI$ broadband photometry. The most interesting new objects discovered by the 20-cm wide-field telescope are going to be studied in more detail with larger telescopes both in spectroscopic and photometric modes. For this purpose, a new telescope is under construction in the framework of the RCO network development. The second telescope will have an aperture of 0.5 m and two scientific instruments, a camera and a spectrograph.

The second node of the RCO network will be built at the site of the INASAN Kislovodsk Observatory. This site has relatively good astronomical seeing for the central part of Russia. The observatory already has all key infrastructure and is well accessed from the closest city of Kislovodsk.

For the RCO observing station nearby Kislovodsk, the well-proven RC500 telescope produced by Astrosib (Russia) was chosen. It has a 0.5-m aperture Ritchey–Chretien optical system with a 508-mm primary mirror housed in a carbon-fiber truss-design optical tube assembly and a two-lens field corrector. The equivalent focal ratio is $F/8$ and the focal length is 4000 mm.

The telescope is mounted on an Astrosib FMDD-700 equatorial fork mount equipped with direct-drive motors and 26-bit absolute encoders. For the telescope's dome, a well-proven Astrosib ASD-4.5 all-sky dome (4.5 m) was made and mounted on an original hyperboloid 5.4 m high pier designed at INASAN.

2 Scientific instruments of the 50-cm telescope

The 50-cm telescope has two main modes of operation: photometry and spectroscopy. Both modes are available anytime by using the telescope's folding mirror without the need to interchange the camera and spectrograph manually. The switchover time between the two instruments is less than 1 minute, which allows a very flexible observing program every night.

The main instrument for spectroscopic research is the Basic Echelle Spectrograph (BACHES). It is a compact, lightweight and inexpensive medium-resolution ($R = 20\,000$) echelle spectrograph manufactured by Baader Planetarium GmbH, well suited for remote autonomous operation at a robotic observatory. With a 0.5-m telescope, BACHES is capable of obtaining spectra of 10^{m} targets with SNR = 20 at a 30-minute exposure time. BACHES allows the acquisition of spectra of the observed object as well as calibration spectra. The spectrograph is equipped with a tip-tilt active-optics Starlight SXV-AO-USB module, which allows long spectroscopic observations with an exposure time of up to 0.5 hour and longer. BACHES has been successfully used on the 1-m telescope at the INASAN Simeiz Observatory for several years. In 2024 it will be relocated to the new 0.5-m RCO telescope.

The main imaging instrument of the new RCA 50-cm telescope is the sCMOS camera FLI Kepler 4040. It is equipped with a seven-slot filter changer FLI CFW5-7. The first five filter slots will be occupied by the standard Johnson–Cousins–Bessel $UBVRI$ system. The sixth slot of the filter wheel will be used for broadband (integral light) imaging to achieve maximum sensitivity of the telescope, for example, to search for new objects such as asteroids, comets, and space debris. The last seventh slot is kept in reserve for future scientific observing programs.

A GPS/GLONASS receiver provides high-accuracy time signals for the telescope.

The observing facility nearby Kislovodsk is controlled by a set of special software created by INASAN. It allows the control of all devices remotely and autonomously:

the weather stations, lightning detector, GPS/GLONASS receiver, all-sky camera, and surveillance cameras.

3 Summary

The first 20-cm telescope of the Russian-Cuban RCO network has already been built in Havana (Cuba) and the second 50-cm telescope is currently under construction nearby Kislovodsk (Russia). Both telescopes are designed to operate in a fully robotic mode. It will allow the Cuban and Russian astronomers to conduct research remotely, both in photometric and spectroscopic modes. Until 2030, the third 1-m telescope is expected to be built at Valle de Picadura (Cuba), which will significantly improve the Russian-Cuban network functionality both in terms of global coverage and observing modes, including more precise spectroscopy and photometry.

Some other telescopes from Russia and worldwide can be used for follow-up observations in the framework of the RCO: the INASAN 1-m and 2-m telescopes at the Simeiz and Terskol Observatories, respectively; the 0.5-m telescope of the Ussuri Department of the Institute of Applied Astronomy of the Russain Academy of Sciences; several 0.5-m – 1.5-m telescopes in Uzbekistan and Tajikistan.

Together, all the above sites allow observations along an arc of 214° (or 14.3 hours). Taking into account the length of the observing nights (6 to 12 hours), it is possible to carry out a practically round-the-clock monitoring and alert observations using the above sites. International cooperation with other countries is highly welcomed.

Funding

The Russian team acknowledges the financial support from the Ministry of Science and Higher Education of the Russian Federation (Agreement No. 075-15-2023-608 of August 30, 2023). The Cuban team acknowledges the material, technical, and financial support by the Ministry of Science, Technologies, and Environment of the Republic of Cuba.

References

Bisikalo D.V., Sachkov M.E., Ibrahimov M.A., et al., 2022, Astronomy Reports, 66, p. 38

Bisikalo D.V., Savanov I.S., Naroenkov S.A., et al., 2018, Astronomy Reports, 62, p. 367

Ibrahimov M.A., Rodríguez M.R., Bárcenas-Fonseca Z.B., et al., 2023, Revista Cubana de Física, 40, 2, p. 104

Naroenkov S.A., Savanov I.S., Sachkov M.E., et al., 2022, Astronomy Reports, 66, p. 827

VAK 2024 MODERN ASTRONOMY: FROM THE EARLY UNIVERSE TO EXOPLANETS AND BLACK HOLES 300 years Russian Academy of Sciences

Measurements of the flux densities and variability of the standard flux scale "Artificial Moon" sources on time scales of 1–8.5 years

V. Ivanov, A. Ipatov, I. Rakhimov, and T. Andreeva

Institute of Applied Astronomy of the Russian Academy of Sciences,
St. Petersburg, 191187, Russia

Abstract. We present flux density measurements for the standard radio sources of the "Artificial Moon" (AM) absolute flux scale during the time interval of 2017.5–2024.0 at wavelengths $\lambda = 3.5$ and 6.2 cm. The standard sources are weakly variable, and maintaining the accuracy of the scale requires regularly recurring calibrations. Currently, the RT-32 radio telescope at the Svetloe Observatory of the Institute of Applied Astronomy of the Russian Academy of Sciences (IAA RAS) monitors the AM flux scale standard sources to study their variability and maintain the accuracy of the scale. We determined the flux densities of the AM flux scale calibrators at two wavelengths during the time interval of 2017.5–2024.0. The measurement errors for both wavelengths did not exceed ±2%, the measurement data were averaged over time intervals of 1 year at the average epochs 2019.0, 2022.0, and 2023.0. A comparison of the standard source flux densities S for the epochs 2019.0, 2022.0, and 2023.0 with each other as well as with the flux densities S_0 at the epoch 2015.5 has shown that at time intervals of more than 1 year, there exists variation in the standard source flux densities that exceeds the standard deviations σ and the established flux scale error limits of ±3%. We conclude that it is necessary to recalibrate the standard sources at least every 2 years to maintain the accuracy of the flux scale.

Keywords: methods: data analysis, observational; telescopes

DOI: 10.26119/VAK2024.167

1 The measurements and their comparison

The flux density measurements for the standard radio sources of the "Artificial Moon" (AM) flux scale (Ivanov et al. 2018) during the time interval of 2017.5–2024.0 at wavelengths $\lambda = 3.5$ and 6.2 cm are presented.

The AM flux scale standards are strong extragalactic sources with minimum, among the others, variation of the radio emission over time. However, the observations have shown the presence of a variable component in almost all the sources, which may be a consequence of variation in the short-range components contributing to the total flux.

The standard sources are weakly variable, and maintaining the accuracy of the scale requires regular calibrations. The flux densities of the AM flux scale calibrators are recurrently measured with the RT-32 radio telescope at the Svetloe Observatory of the IAA RAS to study their variability and maintain the accuracy of the scale. In a repeating cycle, the flux densities of the AM standards 3C48, 3C123, 3C138, 3C147, 3C161, 3C196, 3C218, 3C274, 3C286, 3C348, and 3C353 are measured relative to the stable source 3C295, which serves as the primary standard. A description of the RT-32 full-circle parabolic radio telescope with a mirror diameter $D = 32$ m is given in Rakhimov et al. (2001); Finkelshtein (2001); Finkelshtein et al. (2002). The measurements are carried out according to the standard technique adopted for the radio telescopes of the Quasar system. The data processing is described in Ivanov et al. (2018). The measurement results are shown in Table 1.

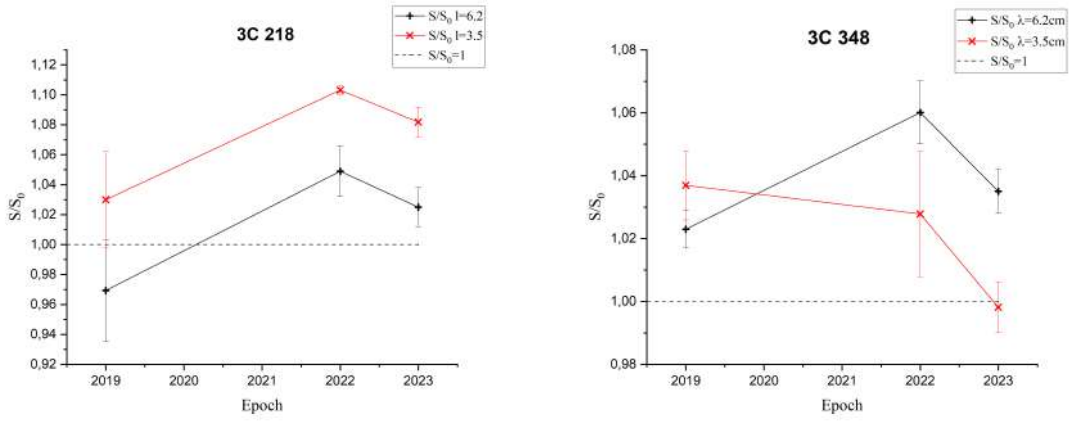

Fig. 1. Temporal dependence of the flux density ratio S/S_0 for 3C218 and 3C348 between the epochs 2015.5–2019.0, 2022.0, and 2023.0.

Table 1. Standards fluxes over time and comparison with the 2015.5 epoch. S and σ are the flux density and its standard deviation, S_0 is the flux density at the epoch 2015.5.

Source	Epoch	$\lambda = 6.2$ cm				$\lambda = 3.5$ cm			
		S, Jy	σ, Jy	S/S_0	σ/S	S, Jy	σ, Jy	S/S_0	σ/S
3C48	2015.5	5.08				3.18			
	2019.0	5.12	0.15	1.01	0.03	3.37	0.07	1.06	0.02
	2022.0	5.0	0.05	0.98	0.01	3.21	1.01	1.01	0.04
	2023.0	4.95	0.06	0.97	0.01	3.28	1.03	1.03	0.04
3C123	2015.5	14.53				9.37			
	2019.0	14.79	0.12	1.02	0.01	9.42	0.09	1.01	0.01
	2022.0	14.87	0.14	1.02	0.01	9.38	0.12	1.00	0.01
	2023.0	14.85	0.19	1.03	0.01	9.18	0.08	0.98	0.01
3C138	2015.5	3.81				2.93			
	2019.0	3.68	0.13	0.97	0.03	3.00	0.00	1.02	0.00
	2022.0	3.77	0.04	0.99	0.01	2.88	0.02	0.98	0.01
	2023.0	3.80	0.04	1.00	0.01	2.92	0.04	1.00	0.01
3C147	2015.5	7.13				4.73			
	2019.0	7.30	0.14	1.02	0.02	4.98	0.11	1.05	0.02
	2022.0	7.17	0.07	1.01	0.01	4.72	0.04	1.00	0.01
	2023.0	7.14	0.03	1.00	0.00	4.66	0.05	0.99	0.01
3C161	2015.5	6.03				3.94			
	2019.0	6.05	0.06	1.00	0.01	3.65	0.09	0.93	0.02
	2022.0	6.24	0.04	1.03	0.01	3.82	0.22	0.97	0.06
	2023.0	6.07	0.07	1.01	0.01	3.91	0.03	0.99	0.01
3C196	2015.5	3.98				2.37			
	2019.0	3.95	0.03	0.99	0.01	2.37	0.03	1.00	0.01
	2022.0	3.88	0.01	0.97	0.00	2.34	0.02	0.99	0.09
	2023.0	3.83	0.02	0.96	0.01	2.34	0.01	0.99	0.01
3C218	2015.5	11.76				7.02			
	2019.0	11.40	0.39	0.97	0.03	7.23	0.23	1.03	0.03
	2022.0	12.34	0.20	1.05	0.02	7.74	0.02	1.10	0.00
	2023.0	12.06	0.16	1.02	0.01	7.59	0.08	1.08	0.01
3C274	2015.5	64.56				44.33			
	2019.0	62.90	0.29	0.97	0.00				
	2022.0	63.06	0.75	0.98	0.01	43.17	0.66	0.97	0.01
	2023.0	63.69	0.29	0.99	0.00	44.30	0.26	1.00	0.01
3C286	2015.5	6.91				5.19			
	2019.0	6.95	0.06	1.01	0.01	5.24	0.08	1.01	0.01
	2022.0	6.41	0.11	0.93	0.02	5.03	0.10	0.97	0.02
	2023.0	6.62	0.07	0.96	0.01	4.96	0.04	0.96	0.01
3C348	2015.5	11.28				6.41			
	2019.0	11.54	0.06	1.02	0.01	6.64	0.07	1.04	0.01
	2022.0	11.96	0.12	1.06	0.01	6.59	0.13	1.03	0.02
	2023.0	11.67	0.08	1.03	0.01	6.40	0.05	1.00	0.01
3C348	2015.5	19.84				13.49			
	2019.0	20.79	0.73	1.05	0.03	13.84	0.22	1.03	0.02
	2022.0	21.19	0.11	1.07	0.00	13.80	0.52	1.02	0.04
	2023.0	20.67	0.47	1.04	0.02	13.53	0.35	1.00	0.03

A comparison of the data in Table 1 for the epochs 2015.5, 2019.0, 2022.0 and 2023.0 shows (Fig. 1) that during the time interval of 2015.5–2024.0, at both wavelengths we observe variation in the flux densities of the standard sources, which significantly exceeds the standard deviations σ. For the data between 2022.0 and 2023.0, separated by an interval $\Delta t = 1$ year, there are no differences significantly greater than σ. For $\Delta t > 1$ year, the differences in some cases are significant.

The comparison of the flux density measurements for the AM flux scale standards at different epochs leads to the conclusion that it is necessary to recalibrate the standard sources at least every 2 years to maintain the accuracy of the flux scale at a level of $\pm 3\%$.

References

Finkelshtein A., 2001, Nauka v Rossii, 5, p. 20

Finkelshtein A., Ipatov A., Smolensev S., 2002, Proc. Fourth APSGP WorkShop, ed. H. Cheng, Q. Zhihan, p. 47

Ivanov V.P., Ipatov A.V., Rakhimov I.A., et al., 2018, Astronomy Reports, 62, p. 574

Rakhimov I., Akhmedov Sh., Zborovsky A., et al., 2001, All-Russian Astronomical Conference, Conference abstracts, p. 152

BAK 2024 MODERN ASTRONOMY: FROM THE EARLY UNIVERSE TO EXOPLANETS AND BLACK HOLES 300 years Russian Academy of Sciences

Tomo-V: a new tool for Doppler tomography

P. Kaygorodov

Institute of Astronomy of the Russian Academy of Sciences, 48 Pyatnitskaya str., Moscow, 119017 Russia

Abstract. The paper presents a new tool for constructing Doppler tomograms: Tomo-V (https://tomo-v.inasan.ru), developed on the basis of the Algebraic Reconstruction Technique (ART). Previously, the ART method was not widely used in tomography since its direct implementation had high computational complexity. The author developed a fast version of this algorithm, which made it possible to implement it as a web application that runs at an acceptable speed in a browser on a personal computer. Using this method, it is possible to obtain sharp tomographic images from blurred profiles; in addition, the method has shown good results in restoring images from noisy data, from a small number of profiles, and from profiles contaminated with absorption lines and the emission of an expanding envelope. Tomo-V also includes tools for analysing the obtained tomograms, allowing one to display accretion disks and Roche lobes on the tomogram as well as the back projection of the tomographic image onto the flow elements in spatial coordinates.

Keywords: binaries: spectroscopic

DOI: 10.26119/VAK2024.168

1 Introduction

To construct Doppler tomograms, methods are used similar to those utilized to construct tomographic images in other fields: medicine, defectoscopy, etc. The input data for constructing Doppler tomograms is a set of spectral line profiles obtained from observations of binary stars. The peculiarity of these data is their heterogeneity (the state of the object can change during the observations), noise, fairly low resolution, and a relatively small number of profiles that can be obtained for one object. To obtain tomograms from such data, it is necessary to use special methods, including regularization methods that allow one to restore the lost information from inconsistent input data. The most commonly used method is the maximum entropy method (MEM, Marsh & Horne 1988), which allows one to obtain images with the least possible amount of detail, which is important for interpretation. Also, to construct tomograms, the radio astronomical approach (CLEAN method, Agafonov 1997) is used, which is well suited for identifying the boundaries of the elements. These methods use a property of tomograms called the "central theorem," which allows searching for a solution in Fourier space, filling in the areas missing in the original data following a certain algorithm. In contrast, the Algebraic Reconstruction Techinque (ART, Gordon et al. 1970) uses minimization methods to find a solution directly (for Doppler tomography) in the velocity space without using the Fourier transform. Until now, this method has not been used to obtain Doppler tomograms, probably due to its high computational complexity: it requires minimization in a space with a dimension equal to the number of pixels in the desired image. For example, for an image with a resolution of 50×50 pixels, it is necessary to minimize (for example, by gradient descent) in a space with a dimension of 2500. In Tomo-V we precalculate some data that can then be reused during all of the steps, which allows us to achieve good performance of the ART method even without using a graphics processing unit. This made it possible to create a web application open for public use.[1]

2 The ART method

With the ART method we are trying to find a two-dimensional brightness distribution in the velocity space such that the projections of this distribution taken for the phases corresponding to the phases of the observed profiles has the best conformance with the observed profiles. The standard deviation χ^2 is used as a criterion. In Tomo-V each pixel in the image contributes to the luminance as a point source convolved with a Gaussian profile having a certain full width at half maximum (FWHM). Due

[1] https://tomo-v.inasan.ru

to the overlap of the Gaussian profiles of the points, nonlinearity appears which does not allow the solution to degenerate into a set of superimposed bands.

3 Working with Tomo-V

All of the computations are performed in the user's browser without any significant CPU load on the server side. On the web page, the user will see a screen divided into two parts. In the left column (initially empty) one can see a list of saved images, an area for loading previously exported data (files with the .tmv extension, see below), and a button for creating a new image. By clicking this button, the user is offered a choice: to create a test image ("Sample data...") for mastering the program as well as for experimenting with the settings or create an image built from real data ("Real data...").

If the user selects "Sample data," a window opens on the right side of the screen with an image of a test symbol and a block of settings. Next to this block is a graph for displaying the profiles. By comparing the "real" (red) profiles with the "synthetic" (blue) ones, the user can control the quality of the tomogram reconstruction. The right part of the window shows the reconstructed image, a graph with the absorption line (blue) and an additional emission (red), and elements related to the settings and control of the solution search process. To take into account the weights (for very noisy source data), one can enable the "Low SNR mode" option. The "Noize treshhold" and "Low-SNR degree" parameters can be used to adjust the weights when the low SNR mode is enabled. The "Start reconstruction" button is used to start the image construction process. In addition, on the block header there is a button for setting general parameters—the velocity range, FWHM, and resolution of the tomogram—as well as the buttons to save/export/delete the solver state and a "close" button.

The method shows rather good results in restoring images from a low number of profiles (see Fig. 1a–1d). Even complex shapes like the symbols "@" and "*" are reconstructed well from 5 profiles. Also it works well with highly blurred profiles (Fig. 1e–1i). It can also reconstruct images with satisfactory quality from highly noisy data (up to SNR = 2), but the results cannot be included in this paper due to the page limits.

If the user selects "Real data..." when creating a new image, a window for constructing an image based on real data opens. In general, it is similar to working with the test data, but on the left side there will be a button for selecting the files, a table of the loaded files, and input fields for setting the continuum level (1 by default) and system parameters (component masses and orbital period). The loaded files must be text files and contain two columns: velocity (in km/s) and intensity.

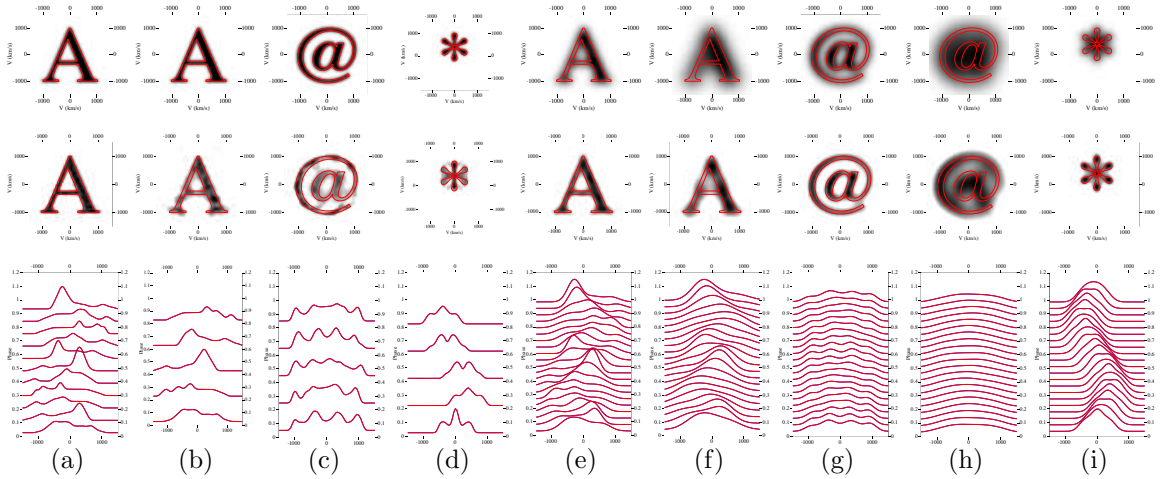

Fig. 1. The reconstruction of the symbol "A" by 11 profiles (a), the symbol "A" by 5 profiles (b), the symbol "@" by 5 profiles (c), and the symbol "*" by 5 profiles (d) with FWHM = 100; image reconstruction with FWHM = 300 km/s (e, g, i—500 iterations) and 600 km/s (f, h—1000 iterations). In the first row there are the original images (convolved with a Gaussian with the corresponding FWHM), the second row demonstrates the restored images, the third row shows the profiles by which the reconstruction was performed.

The intensities must be normalized to the continuum level, preferably so that the continuum intensity is taken as one. For each loaded file it is necessary to specify the phase (in the right part of the table, then click the "update" button), also in the right part of the table of the loaded files there is a check mark against each file, by unchecking which one can remove the corresponding profile from the calculations. The loaded profiles (the part of them that fits into the specified speed range) are immediately shown on the graph to the right of the file table. One can also load a file by specifying the phases for each profile ("Load phases from file").

Funding

Supported by joint Russian-Bulgarian grant RFBR 20-52-18015/KP-06-Russia/2-2020.

References

Agafonov M.I., 1997, ASP Conference Series, 125, p. 202
Gordon R., Bender R., Herman G.T., 1970, Journal of Theoretical Biology, 29, p. 471
Marsh T.R. and Horne K., 1988, Monthly Notices of the Royal Astronomical Society, 235, p. 269

VAK 2024 MODERN ASTRONOMY: FROM THE EARLY UNIVERSE TO EXOPLANETS AND BLACK HOLES 300 years Russian Academy of Sciences

Obtaining the Chandrayaan-3 lander coordinates on the lunar surface by the Doppler measurements of the transmitted signal with an Earth-based receiving system

E. Kazantseva, Yu. Bondarenko, D. Marshalov, and Yu. Medvedev

Institute of Applied Astronomy, Russian Academy of Sciences,
10 Nab. Kutuzova, St. Petersburg, 191187 Russia

Abstract. We determine the selenographic coordinates of the Chandrayaan-3 lander by Doppler measurements of its signal. The Chandrayaan-3 successfully landed in the south polar region of the Moon near the craters Manzinus and Simpelius on 23 August 2023 and had been transmitting scientific information and telemetry to Earth in the S and X-bands during 14 days. The accuracy of the obtained Doppler measurements do not allow unambiguous determination of the lander location on the lunar surface because the transmitter was degrading during the entire observing interval. For this reason, in our work we have evaluated the influence of the Doppler measurement characteristics on the accuracy of the transmitter location determination. It has been shown that for a signal with a relative frequency instability of the order of 10^{-13}, the achievable accuracy of coordinate determination is about 34 meters.

Keywords: ephemerides; Moon; space vehicles; techniques: radial velocities; telescopes

DOI: 10.26119/VAK2024.169

1 Introduction

To obtain the position of a spacecraft in space, the optical and radio techniques are usually used. The ground-based optical observations of spacecraft have low accuracy because they are affected by the atmosphere, and the result of the measurements is the position of the object, not its distance. In addition, such observations are limited by weather conditions and daytime. The laser and radiolocation techniques allow one to measure the distance to a spacecraft directly. Both techniques have high accuracy (of the order of centimeters), but require the presence of retroreflectors (Murphy et al. 2011) or transponders (Marshalov et al. 2020) onboard. The conventional techniques for obtaining the position of a spacecraft which is transmitting a radio signal to Earth are the Doppler and radio interferometric measurements, which allow one to obtain the velocity and direction to the spacecraft, respectively (Duev et al. 2012).

Due to the increasing number of space programs for the exploration and development of the Moon, there is a need to quickly determine the coordinates of landers with acceptable accuracy. The modern numerical ephemerides of the Moon (Vasilyev et al. 2022) allow one to obtain the location of the lander using only Doppler measurements. The goal of our work is to evaluate the accuracy of the lunar lander location by the Doppler measurements of its signal for the case of the Indian Chandrayaan-3 [1] spacecraft.

2 Doppler measurements and processing of the Chandrayaan-3 signal

The receiving of the Chandrayaan-3 signals was carried out on August 28 and from September 1 to 4, 2023, using the 13.2-meter radio telescopes at the Zelenchukskaya and Svetloe observatories, which are part of the Quasar VLBI network (Shuygina et al. 2019). The signal was recorded in the S and X-bands in the right and left circular polarizations. Carrier frequencies of 2268 and 8460 MHz were measured using the digital phase-locked loop technique (Marshalov et al. 2020).

An analysis of the Doppler measurements showed a decrease in the signal-to-noise ratio and the degradation of carrier frequency stability. The standard deviation of the signal frequency was 0.1 Hz on August 28 and increased to about 10 Hz on September 1, which was most likely due to the degradation of the transmitter clock over time. On September 4, the signal was not distinguishable from the background noise, and on the same day the Indian Space Research Organization announced the completion of the Chandrayaan-3 mission.

[1] https://www.isro.gov.in/Chandrayaan3_Details.html

In order to obtain the location of the Chandrayaan-3 transmitter on the surface of the Moon, a numerical model of the variation in the frequency of the signal received by the corresponding antenna on Earth was developed. The model took into account the positions of the planets and the Moon according to the Planetary and Lunar Ephemerides DE440 (Park et al. 2021), corrections to the Earth's rotation parameters, and the signal propagation time (Brumberg et al. 2004).

We used the variation method, which does not depend on the accuracy of the initial data. For this purpose, the lander coordinates on the Moon's surface were varied with a given step in latitude and longitude, and for each such position the frequency of the received signal at the corresponding station on Earth was calculated and compared with the real measurements using the constructed model. As a result, we determined the probable area of the lander location with a size of approximately 200×1000 km, while Chandrayaan-3 was actually located on the border of the obtained area. Thus, the accuracy of the obtained Doppler measurements of the Chandrayaan-3 signal did not allow us to unambiguously determine its location on the surface of the Moon.

3 Influence of the Doppler measurement characteristics on the determination of the transmitter location

The main influence on the accuracy of the transmitter location on the lunar surface is exerted by such characteristics of the Doppler measurements as the signal frequency deviation, the duration of the measurements, and the relative position of the transmitting and receiving stations. The signal frequency deviation is composed of the transmitter clock deviation onboard the spacecraft and the deviation of the Earth-based receiving station clock, which are 10^{-13} and 10^{-15} units of relative instability, respectively. Hence, for the transmitted frequency of 8460 MHz, the deviation of the Doppler measurements is mainly determined by the onboard clock deviation of the order of 10^{-4} Hz.

Using the constructed model, series of 20-minute duration Doppler measurements at a frequency of 8460 MHz for the Zelenchukskaya observatory were generated. The deviation of the model Doppler measurements varied within 10^{-1}–10^{-6} Hz. Based on the contemporary level of technology, the deviation of the onboard clock should be considered in the range of 10^{-5}–10^{-3} Hz. The results show that the error of the lander coordinates should be in the range from 100 m to 10 km for a 20-minute measurement interval. The influence of measurement duration and selection of receiving stations on the transmitter position error was estimated for the Doppler measurements with a standard deviation of $\sim 10^{-4}$ Hz.

The duration of the model Doppler measurements varied from 20 to 90 minutes at a frequency of 8460 MHz for the Zelenchukskaya and Svetloe observatories in all configurations. The smallest error of 34 m in the lander location is achieved for the Zelenchukskaya observatory at a 90-minute measurement interval.

4 Summary

As a result of this work, we developed a model allowing one to obtain the transmitter location on the lunar surface using the Earth-based Doppler measurements of the transmitter signal. Using this model, we determined the main dependencies of the lander position error on the signal frequency deviation, the duration of the Doppler measurements, and the configuration of the Earth-based receiving stations. For a 90-minute X-band signal with a relative frequency instability of the order of 10^{-13}, the error of the lander position on the lunar surface is about 34 meters.

Receiving the Chandrayaan-3 transmitter signals was carried out using the 13.2-meter radio telescopes at the Zelenchukskaya and Svetloe observatories in the S and X-bands. An area of about 200×1000 km for the probable lander location was determined using the Doppler measurements of the received signals. Such a result is due to the transmitter signal instability, which increased from 10^{-11} to 10^{-8} over the observing interval.

The USA and China plan to deploy a network of beacons on the lunar surface in the coming decades. The clocks in the beacons with a relative signal frequency instability of 10^{-12}–10^{-13} will allow us to build and maintain a lunar coordinate system with meter accuracy. The method we have implemented is applicable both to individual spacecraft and to radio beacon networks.

References

Brumberg V.A., Glebova N.I., Lukashova M.V., et al., 2004, Transactions of IAA RAS, 10

Duev D.A., Molera Calvés G., Pogrebenko S.V., et al., 2012, Astronomy & Astrophysics, 541, id. A43

Marshalov D., Ping J., Li W., et al., 2020, Latvian Journal of Physics and Technical Sciences, 57, p. 22

Murphy T.W. Jr., Adelberger E.G., Battat J.B.R., et al., 2011, Icarus, 211, p. 1103

Park R.S., Folkner W.M., Williams J.G., et al., 2021, The Astronomical Journal, 161, id. 105

Shuygina N., Ivanov D., Ipatov A., et al., 2019, Geodesy and Geodynamics, 10, 2, p.150

Vasilyev M.V., Yagudina E.I., Krasinsky G.A., et al., 2022, Transactions of IAA RAS, 63, p. 28

BAK 2024 MODERN ASTRONOMY: FROM THE EARLY UNIVERSE TO EXOPLANETS AND BLACK HOLES 300 years Russian Academy of Sciences

Methods for analyzing the light curves of the non-thermal radiation in active galactic nuclei

M. Khabibullina[1], V. Stolyarov[1,2], A. Mikhailov[1], D. Kudryavtsev[1], V. Vlasyuk[1], Yu. Sotnikova[1,3], T. Mufakharov[1,3], and D. Morozova[4]

[1] Special Astrophysical Observatory of the Russian Academy of Sciences, Nizhny Arkhyz, 369167 Russia
[2] Astrophysics Group, Cavendish Laboratory, University of Cambridge, Cambridge, CB3 OHE UK
[3] Kazan Federal University, 18 Kremlyovskaya St, Kazan, 420008 Russia
[4] Saint Petersburg State University, St. Petersburg, 199034 Russia

Abstract. We present different methods for analyzing the light curves of active galactic nuclei (AGNs). Based on the example of AGN multiwavelength measurements, features of the following methods are considered: (1) structure functions (SFs)—to search for variability timescales; (2) discrete correlation functions (DCFs)—to search for connections between processes; (3) the Lomb–Scargle (L–S) periodogram—to search for periodicity. We analyze advantages and disadvantages of the methods and discuss their constraints and interpretation.

Keywords: methods: data analysis, statistical, observational; radiation mechanisms: non-thermal

DOI: 10.26119/VAK2024.170

1 Introduction

The variability in AGNs across a wide range of wavelengths is a well-studied characteristic. Its timescale ranges from few minutes through days and months to decades. The parameters of flux density variations can be used to estimate the timescales of ongoing processes, constrain the size of the emission region, and describe the evolution of flaring events across the electromagnetic spectrum. These properties help study both the underlying physical process behind the variations and possible periodicities in the light curves (LCs). We demonstrate an application of several statistical methods to the analysis of long-term multiband LCs on the example of two blazars.

2 Review of the methods

Structure function analysis. The SF is a method of searching for typical timescales and periodicities in non-stationary processes (Simonettiet al. 1985). As it was mentioned by Emmanoulopoulos et al. (2010), results of SF analysis must be interpreted with some caution. Figure 1 shows the examples of SF analysis applied to the long-term (1997 Mar – 2024 Jul) LCs of Ton 599 at 8 GHz and of AO 0235+164 in the optical R band. SF breaks often occur in datasets without characteristic timescales. The position of these artificial breaks depends on the length of observations and the nature of the variation process. On the other side, intensive modeling shows that SFs derived from typical blazar observations resemble those coming from the shot-noise model. However, in the frequency domain the same model does not describe correctly the observations and thus may not be physically realistic. Also it was emphasised in the paper cited above that the data gaps affect severely the SF estimates in an unpredictable way, introducing systematic deviations, as it is clearly seen in Fig. 1 (bottom part on the right panel). Even the bootstrap method cannot yield statistically meaningful errors depicting the deviations between the gappy and continuous SFs. This effect as well as the presence of some powerful outbursts may be responsible for difficulties in SF estimation. Despite the drawbacks of the method, SFs have several advantages such as the ease of application, versatility, robustness to outliers, ability to detect timescales, and less sensitivity to trends.

Discrete correlation functions. DCFs for irregularly sampled time series are commonly used to estimate the correlation and time lags between LCs observed over approximately the same period (Edelson & Krolik 1988; Robertsonet al. 2015). The method to estimate the confidence level of a resulted DCF is outlined in Emmanoulopoulos et al. (2013), and the software is provided on GitHub.[5] The point is

[5] https://github.com/samconnolly/DELightcurveSimulation

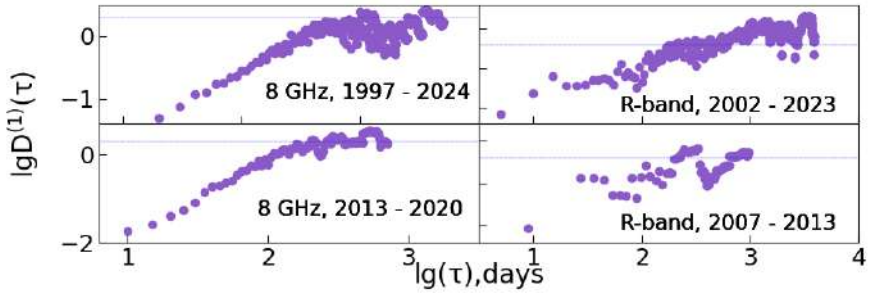

Fig. 1. The SFs for the total flux variations. Left: Ton 599. Right: AO 0235+164. There is no well-defined structure for the SF in the optical range (bottom left) due to systematic annual gaps in the measurements.

to simulate a large number of synthetic LCs having the same statistical properties (PDF, PSD) as the observed LC. They are simulated for all timestamps (e.g., days) and then are taken with the same window function as the observed LC has. To find the probability of getting a given DCF value purely by chance, one can calculate cross-correlation functions for an ensemble of paired artificial LCs and analyse the DCF values distribution for each time lag. An example of DCF calculation is shown in Fig. 2. Because of the discrete nature of the data, the DCF method may miss correlations at small times. Hufnagel & Bregman (1992) demonstrate that irregular time series can make it very difficult to determine the exact time delays between changes in different ranges. Also White & Peterson (1994) emphasize the importance of considering noise effects when interpreting DCF results because a high level of noise in the data leads to an increase in random correlations.

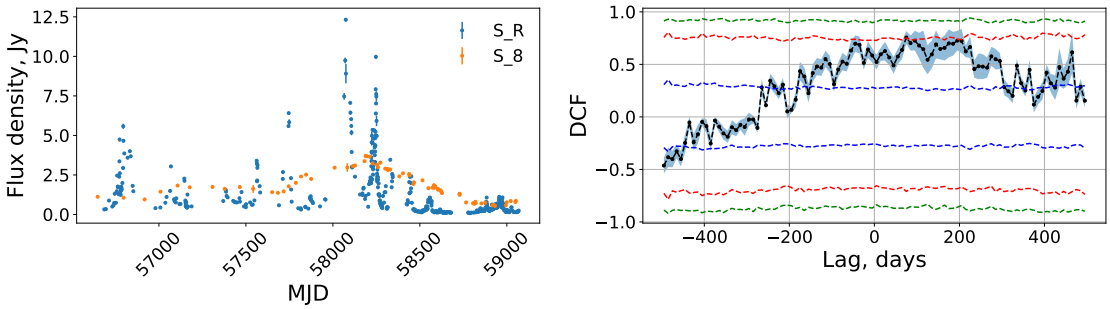

Fig. 2. Left: LCs of Ton 599 at 8 GHz and in the R band. Right: DCF with its confidence levels of 1, 2, and 3σ.

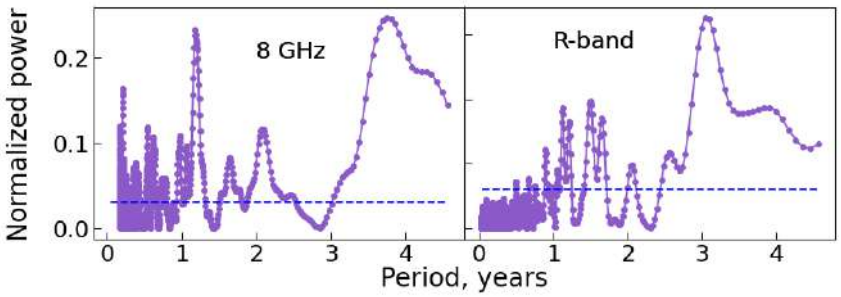

Fig. 3. The L–S periodograms of Ton 599 for the total flux variations at 8 GHz (left) and in the optical R band (right). The dashed lines show the FAP = 1 per cent level (false alarm probability).

Lomb–Scargle periodogram. The L–S periodogram (Lomb 1976; Scargle 1982) is a standard method to search for periodicity in unevenly sampled time series. The periodogram is sensitive to time series irregularity, so its results require careful interpretation. First of all, special attention should be paid to the window function. In most cases it has a shape of a "comb" with a minimum interval of one day between the successive observations and with large gaps when the source has not been observed. The convolution of the window function with the true LC spectral image in the spectral domain can lead to false peak detection. Observational errors can increase random fluctuations in the data. Strong jitter noise can mask the peaks in the spectral domain, increasing the probability of false detections. The L–S periodograms for the radio and optical long-term LCs of Ton 599 obtained in 1997 Mar – 2024 July are shown in Fig. 3.

Acknowledgements. Observations with the SAO RAS telescopes are supported by the Ministry of Science and Higher Education of the Russian Federation.

References

Edelson R.A. and Krolik J.H., 1988, ApJ, 333, p. 646
Emmanoulopoulos D., McHardy I.M., Papadakis I.E., 2013, MNRAS, 433, 2, p. 443
Emmanoulopoulos D., McHardy I.M., Uttley P., 2010, MNRAS, 404, p. 931
Hufnagel B.R. and Bregman J.N., 1992, ApJ, 386, p. 473
Lomb N.R., 1976, Ap&SS, 39, 2, p. 447
Robertson D.R.S., Gallo L.C., Zoghbi A., et al., 2015, MNRAS, 453, 4, p. 3455
Scargle J.D., 1982, ApJ, 262, p. 835
Simonetti J.H., Cordes J.M., Heeschen D.S., 1985, ApJ, 296, p. 46
White R.J., Peterson B.M., 1994, PASP, 106, p. 879.

VAK 2024 MODERN ASTRONOMY: FROM THE EARLY UNIVERSE TO EXOPLANETS AND BLACK HOLES 300 years Russian Academy of Sciences

A review of astroclimate conditions at possible locations for the Eurasian Submillimeter Telescopes (ESMT)

V. Khaikin[1], A. Shikhovtsev[2], A. Mironov[3], E. Kopylov[6], A. Khudchenko[4,5], G. Nazarov[4], P. Zemlyanukha[7], G. Makoev[1], Y.Q. Yao[8], and X. Qian[8]

[1] Special Astrophysical Observatory of the Russian Academy of Sciences, Nizhny Arkhyz, 369167 Russia
[2] Institute of Solar-Terrestrial Physics, Siberian Branch of the Russian Academy of Sciences, Irkutsk, 664033 Russia
[3] Sternberg State Astronomical Institute, Lomonosov Moscow State University, Moscow, 119992 Russia
[4] Astro Space Center of the P.N. Lebedev Physical Institute of the Russian Academy of Sciences (ASC LPI), Moscow, 117997 Russia
[5] Kotelnikov Institute of Radio Engineering and Electronics of the Russian Academy of Sciences, Moscow, 125009 Russia
[6] Institute of Astronomy of the Russian Academy of Sciences (INASAN), Moscow, 119017 Russia
[7] Institute of Applied Physics RAS, Nizhny Novgorod, 603950 Russia
[8] National Astronomical Observatories of the Chinese Academy of Sciences, Beijing, 100101 China

Abstract. The paper presents the results of studying the astroclimate at possible locations for the Eurasian Submillimeter Telescopes (ESMT), including the sites of Kurapdag in the Agul district of Dagestan, Khunzundallbak (3676 m) in the Rutul district of Dagestan, Khulugaisha peak (Eastern Sayan), Tashanta checkpoint in the intermountain basin of the Altai Republic, Boguty (3350 m) in the foothills of the Altai Mountains near the border with Mongolia, the Suffa plateau (Aktashtau, 3282 m), and the Ali region in Tibet. The expected radio brightness temperatures of the clear and cloudy atmosphere at wavelengths of 2 and 3 mm and the characteristics of the 3-mm range radiometer for measuring the optical thickness of the atmosphere are presented.

Keywords: site testing; telescopes; atmospheric effects

DOI: 10.26119/VAK2024.171

1 Introduction

Due to the high interest in the construction of large single submillimeter telescopes in Eurasia, it is relevant to study the astroclimate at possible sites for their placement (Khaikin et al. 2020, 2022; Balega et al. 2022). Several new sites are considered for the next-generation Event Horizon Telescopes (ngEHT, Raymond et al. 2021). Li et al. (2024) provide plans for the placement and equipping of a 15-m submillimeter telescope with a range of 80–690 GHz on the Quinghai-Tibet Plateau (4820 m). To study the astroclimate at possible locations for the Eurasian Submillimeter Telescopes (ESMT) (Khaikin et al. 2020) in the Russian Federation, the data from the European Center for Medium-Range Weather Forecast Reanalysis v5 (ERA5) and geodetic stations of the Global Navigation Satellite Systems (GNSS) were used.

2 Results

Figure 1 shows the measurements of precipitated water vapor (PWV) at the Ali Observatory using two methods. The analysis of astroclimate at 25 potential sites (Khaikin et al. 2020) shows that in the Russian Federation there are 3–4 places that may be suitable for placing a 20-m class submillimeter telescope: Kurapdag (3778 m) in the Agul region of Dagestan, the slope of Mt. Khunzundalilbak (3676 m) in the Rutul region of Dagestan, the Khulugaisha peak (3016 m) (Eastern Sayan), the Tashanta checkpoint (2100 m) in the intermountain basin of the Altai Republic, Boguty (3350 m) in the foothills of the Altai Mountains near the border with Mongolia. At these places, astronomical stations have been organized with various equipment installed: the automatic weather stations, GNSS stations for monitoring the PWV and geodynamics, solar photometers (pyranometers) for measuring the duration of sunny weather and the presence of clouds, ultrasonic anemometers for measuring wind pulsations and structural characteristics of the fluctuations in the refractive index of the near-surface atmosphere C_n^2. The PWV measurements obtained at one of the new astronomical stations are shown in Table 1 and Fig. 2.

Figure 3 shows the calculated radio brightness temperatures of the clear and cloudy atmosphere at the zenith at wavelengths of 3 and 2 mm in summer and winter. To measure the radio brightness temperature and the optical thickness of the clear and cloudy atmosphere at new astronomical stations using the absolute method, a radiometric complex has been developed, consisting of a broadband radiometric module of the 3-mm range, an input waveguide filter (80–100 GHz), a conical horn, and a thermostated blackbody "field" load. The measured fluctuation sensitivity of the 3-mm radiometer in the "total power" mode is 12 mK/Hz$^{1/2}$ (sustained for

Table 1. Monthly PWV statistics calculated from the GNSS measurements at the Khulugaisha astronomical station in the period from November 16, 2023 to June 24, 2024 at night and during the daytime.

Month	Min	Max	Average, mm			Median, mm			RMS, mm			δ PWV, mm		
	mm	mm	A	N	D	A	N	D	A	N	D	A	N	D
1	0.06	7.03	2.61	2.43	2.74	2.11	1.75	2.25	1.79	1.78	1.81	1.02	1.06	0.86
2	0.01	6.00	2.79	2.77	2.83	2.75	2.73	2.80	1.43	1.41	1.43	0.80	0.74	0.77
3	0.00	6.13	2.53	2.55	2.55	2.62	2.71	2.65	1.30	1.33	1.27	0.84	0.75	0.78
4	0.02	6.87	2.35	2.24	2.66	1.94	1.91	2.35	1.89	1.87	2.09	1.77	1.23	1.26
5	0.02	15.10	7.39	7.22	7.99	7.11	7.03	7.55	3.10	3.49	2.74	1.29	1.09	1.43
6	2.29	18.01	8.79	8.18	9.56	9.08	8.68	10.02	3.06	3.05	2.95	3.33	3.36	3.39

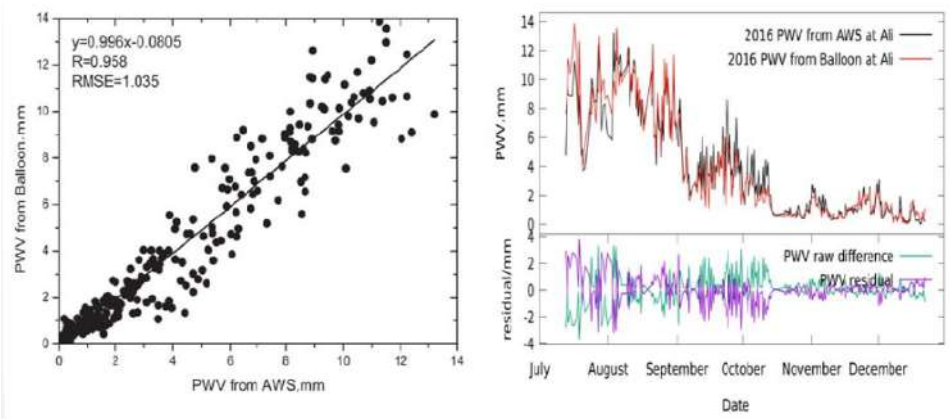

Fig. 1. PWV measurements at the Ali Observatory (5100 m) by two methods: an all-weather station (AWS) and an air balloon.

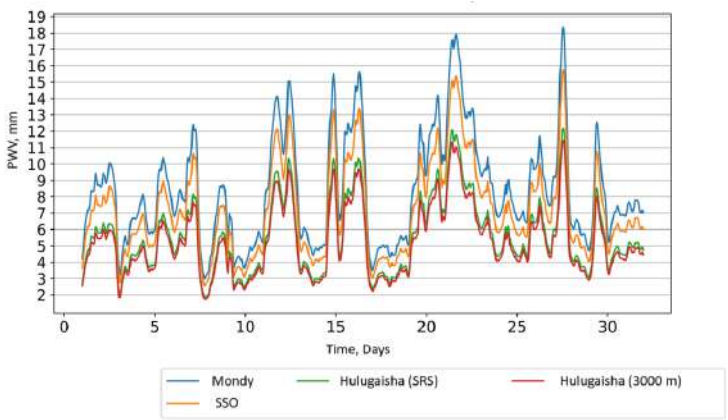

Fig. 2. Variation of hourly PWV values at different locations in May 2024, calculated from the ERA5 data.

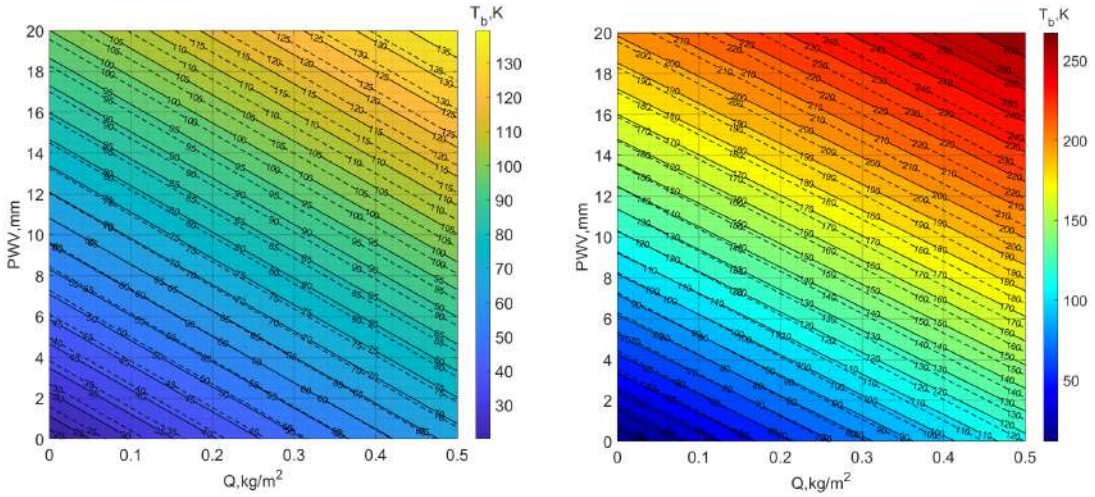

Fig. 3. The calculated radio brightness temperatures of the clear and cloudy atmosphere at the zenith at a wavelength of 3 mm (left) and 2 mm (right) for winter (−20°C, solid line) and summer (+20°C, dashed line); Q is the amount of water in the clouds.

20–30 seconds) with the noise temperature of the black body equal to 299 K at its physical temperature of 300 K.

Funding

The work was carried out within the framework of the state assignment of SAO RAS, approved by the Ministry of Science and Higher Education of the Russian Federation.

References

Balega Yu.Yu., Bataev D.K-S., Bubnov G.M., et al. 2022, Proceedings of the Russian Academy of Sciences, 502, 1, p. 5

Khaikin V., Lebedev M., Shmagin V., et al., 2020, Proceedings 2020 7th All-Russian Microwave Conference (RMC), p. 47

Khaikin V.B., Shikhovtsev A.Yu., Mironov A.P., et al., 2022, Proceedings of Science, 425, id. 072

Li J., Shi Y., Lou Zh., et al., 2025, IEEE Transactions on Terahertz Science and Technology, in print

Raymond A.W., Palumbo D., Paine S.N., et al., 2021, Astrophysical Journal Supplement Series, 253, id. 5

Universal viewing camera for SAO RAS BTA

V. Komarov, I. Shaldyrvan, V. Komarova, and M. Fokin

Special Astrophysical Observatory of the Russian Academy of Sciences,
Nizhny Arkhyz, 369167 Russia

Abstract. The development, creation, and implementation of highly sensitive observing systems both for the observing complexes and round-the-clock monitoring of sky transparency and cloudiness, are carried out at the Special Astrophysical Observatory of the Russian Academy of Sciences (SAO RAS). The latest development is the universal viewing camera presented in this work, mounted on the outside of the 6-meter telescope (BTA) prime focus cage (CPF) and monitoring a 4° field. This system looks at the sky area where an object under study in BTA observations is located, i.e., the CPF viewing camera is always directed to the same sky field a t w hich t he B TA is pointed. And the images are obtained in real time, regardless of the BTA observing program and the complexes in one of the three foci involved.

Keywords: telescopes: optical; methods: observational

DOI: 10.26119/VAK2024.172

1 Introduction

Guiding, viewing, and monitoring cameras while being auxiliary are not the least elements to support observations in visible light. The range of their application at the SAO RAS optical telescopes is broad: from the slit and field-of-view guidance tools to atmosphere control systems and security cameras, and their usage has more than twenty years of history with technical solutions corresponding to the up-to-date state of technologies.

The modern mass-production CMOS photodetectors, which we start applying in our development, are not only highly sensitive, competing with the CCD cameras in our use, but also quite small.

Our experience with CMOS cameras has allowed us to develop a new compact universal sky monitoring system for the BTA.

2 New generation BTA viewing systems

In recent years, we have been developing CCD and CMOS viewing systems for the BTA and other optical telescopes of SAO RAS along with the systems for round-the-clock sky monitoring (Komarov & Semenko 2018).

For a long time, CMOS sensors could hardly by compared with CCDs in terms of photosensitivity and image quality, and their application was limited primarily to video surveillance systems. Since 2008, the progress in the performance of CMOS matrices has stepped far forward, and at the moment the technologies used in the production of CMOS sensors allow them to compete with CCDs. The technologies applied in the production of CMOS matrices in the last decade have made possible developing rather cheap IP viewing systems for SAO RAS that have characteristics acceptable for the night-time work. Thus, it should be concluded that CMOS sensors can be effectively used in the low-light conditions. In our case it takes place in the operation of such devices as the viewing systems in the optical paths of astronomical instruments (in the situations where a small percentage of the light studied is transmitted to the viewing system) and in the all-sky cameras for monitoring the night sky as well as atmospheric conditions in order to respond to weather changes in time (Shaldyrvan et al. 2023).

3 Universal BTA Sky Monitoring System

The latest development is a universal CPF sky monitoring system with a 4° field of view. It is mounted on the outside of the BTA CPF and pointed to the same sky area where an object under study is located, i.e., the CPF viewing camera always

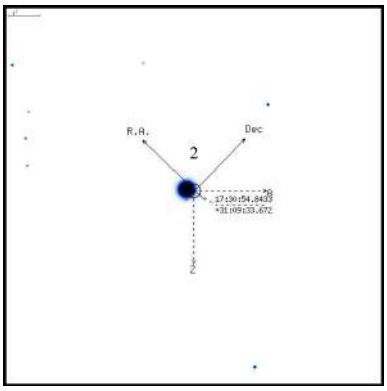

No.	Star	RA (2000)	Dec (2000)	B	V
1	HD 159118	17 31 42.534	+30 19 04.24	7.97	6.93
2	HD 158974	17 30 55.373	+31 09 29.30	6.60	5.63
3	HD 158225	17 26 45.963	+31 13 09.30	7.58	7.13
4	HD 157513	17 22 29.307	+30 31 41.52	8.47	8.42
5	HD 157329	17 21 14.712	+31 15 24.86	7.45	6.90
6	HD 156224	17 15 13.500	+30 18 04.62	8.82	7.82
7	HD 156651	17 17 26.491	+31 31 06.16	6.94	7.06
8	W Her	17 20 39.567	+32 28 03.88	6.01	5.39
9	HD 157225	17 20 45.465	+32 40 27.83	7.03	7.01

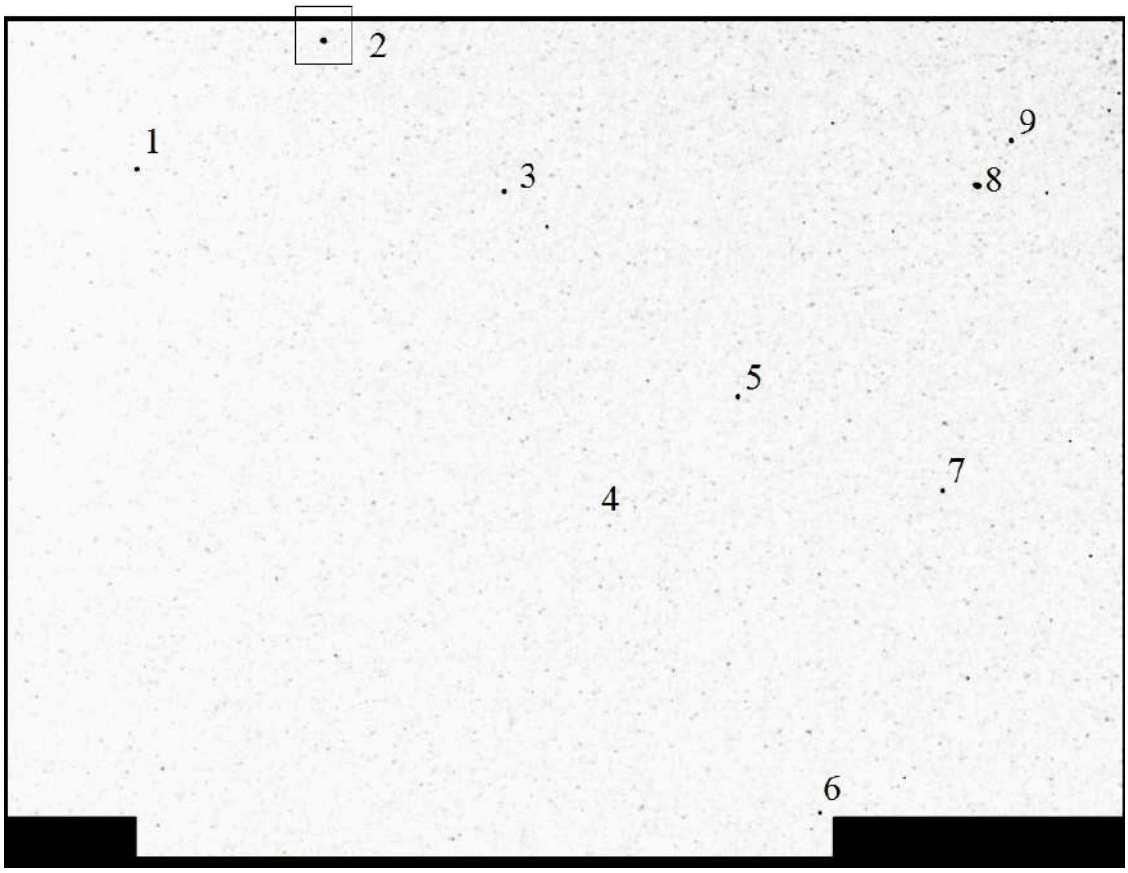

Fig. 1. Top left: a $10' \times 10'$ USNO-A2 Catalogue image simulation centered at the location RA(2000) = $17^{\rm h}30^{\rm m}54\overset{\rm s}{.}843$, Dec(2000) = $+31°09'33\overset{''}{.}67$ in the BTA observations (see the BTA TCS online page on https://www.sao.ru/tb/tcs/ → TV → BTA guide). Top right: the list of the stars marked. Bottom: a view of the sky area taken by the CPF monitoring system simultaneously with the BTA targeting at HD 158974 (No. 2 in a box of nearly $10' \times 10'$); the center (RA, Dec) is $260\overset{\circ}{.}744$, $30\overset{\circ}{.}691$; total exposure time 12×80 ms, b/w mode. The images are given in inverted colors.

follows the BTA in its pointing and tracking. The images are obtained in real time, regardless of the observing complexes in use, i.e., for any of the BTA three foci.

The main characteristics of the CPF camera are as follows: image sensor Sony IMX335; diagonal size 6.52 mm; pixel size 2.0 × 2.0 µm; maximal resolution 5 Mpixels (2592 × 1944 pixels); FOV $4\overset{\circ}{.}23 \times 3\overset{\circ}{.}18$; pixel scale $5\overset{''}{.}88$/pixel.

An example of the images obtained using the CPF sky monitoring system is shown in Fig. 1. According to preliminary estimates, reliable identification can be carried out for stars of up to 10–12 apparent magnitude, depending on the photometric conditions.

4 Conclusion

The technologies used in the production of CMOS matrices in the last decade have made it possible to create inexpensive IP cameras with characteristics acceptable for the night work. The new universal BTA viewing camera mounted on the outside of the primary focus cage is aimed at the same sky area as the BTA. The 4° field of view of the new monitoring system provides taking images of the objects that are being observed with the BTA at the moment. The images obtained in real time are outputted to remote access for further processing and identification of the objects in the field of view, they are also available as raw data in the format of a streaming video signal in the SAO RAS local network. The universal BTA monitoring system is structurally similar to the Polaris monitoring system (Shaldyrvan et al. 2024), which allows one to estimate the quality of astronomical visibility (seeing) changing due to the atmospheric conditions. Therefore, an additional feature of the universal monitoring system is providing possibility to control the seeing by the stars in the BTA field of view. And it can be done directly in the same field at which the BTA is pointed, independently of the observing equipment in one of the three BTA foci and in real-time mode.

References

Komarov V.V. and Semenko E.A., 2018, Izvestiya SFedU. Engineering Sciences, 7, p. 32

Shaldyrvan I.V., Komarov V.V., Fokin M.Yu., 2023, Izvestiya Krymskoj Astrofizicheskoj Observatorii, 119, p. 12

Shaldyrvan I., Komarov V., Komarova V., et al., 2024, Modern Astronomy: from the Early Universe to Exoplanets and Black Holes, Proc All-Russian Astron. Conf., this issue

MODERN ASTRONOMY:
FROM THE EARLY UNIVERSE TO EXOPLANETS AND BLACK HOLES

Testing the DiFX VLBI correlator in a cloud service infrastructure

A. Kononov, I. Bezrukov, and A. Melnikov

Institute of Applied Astronomy of the Russian Academy of Sciences,
Saint Petersburg, 191187 Russia

Abstract. This study explores the possibility of using cloud infrastructure to deploy the DiFX software correlator for creating a backup system in case of emergencies. The proposed approach involves running DiFX on virtual servers provided by a cloud service, allowing the reduction of financial a nd t ime r esources. T he D iFX software correlator is a primary tool for processing data obtained through Very Long Baseline Interferometry (VLBI). Running such software on cloud provider servers will enable the scaling of the data correlation system. For the experiment, the automation tools Ansible (written in Python) and Terraform were used. Ansible was utilized to deploy the necessary software on a pre-created virtual machine (VM) with Linux, while Terraform managed the provisioning of the virtual machine in the cloud environment. The study analyzes the performance and scalability of DiFX in the cloud. Additionally, the advantages and limitations of deploying DiFX in the cloud in terms of cost, flexibility, and ease of use were evaluated. This paper presents the results of testing and using cloud technologies for running DiFX and justifies t he r elevance o f d eveloping such software.

Keywords: instrumentation: interferometers; techniques: interferometric; virtual observatory tools

DOI: 10.26119/VAK2024.173

1 Introduction

This study explores the use of cloud infrastructure to deploy the DiFX[1] software correlator as a backup system. Running DiFX on cloud servers can reduce financial and time resources. DiFX is essential for processing Very Long Baseline Interferometry (VLBI) data, and cloud deployment allows scaling the data correlation system.

2 Experiment setup

The experiment was conducted in several stages.

Creating a virtual machine with the required configuration. Using Terraform,[2] a request was generated to provide a VM with specified parameters from a cloud provider. Virtual machines were created on the Yandex Cloud platform with Ubuntu 22.04 and 8, 16, and 32 computational cores. Time taken: 1 minute.

Automated software setup. To automate the software installation on the virtual machine, an Ansible[3] script was developed. Key components installed were the Intel IPP library and the DiFX VLBI correlator. Time taken: 20 minutes.

Transferring data for correlation processing. Files m5b with digitized radio signals were transferred from the Institute of Applied Astronomy (IAA RAS) to the virtual machine in Yandex Cloud using jive5ab/m5copy in four parallel streams. The peak speed was 600 Mbps, with an average of 200 Mbps. Each 2 GB file was transferred in 10 seconds.

Correlation and processing. Using the DiFX software correlator, correlation processing of the received VLBI data was performed.

Uploading results. Correlation processing results were uploaded from the virtual machine in Yandex Cloud back to the IAA RAS data storage system for further analysis.

Deleting the virtual machine. After the experiment, the virtual machine was deleted using Terraform to optimize resource usage and reduce costs.

3 Data transfer speed testing

To assess the feasibility of using cloud infrastructure for data correlation, the channel bandwidth between a Yandex Cloud virtual machine and the IAA RAS server was tested. Data were transferred in four streams using jive5ab/m5copy. The test results with the UDT protocol are shown in Fig. 1.

[1] https://www.atnf.csiro.au/people/Tasso.Tzioumis/vlbi/dokuwiki/doku.php/difx/documentation/

[2] https://terraform-provider.yandexcloud.net/

[3] https://docs.ansible.com/

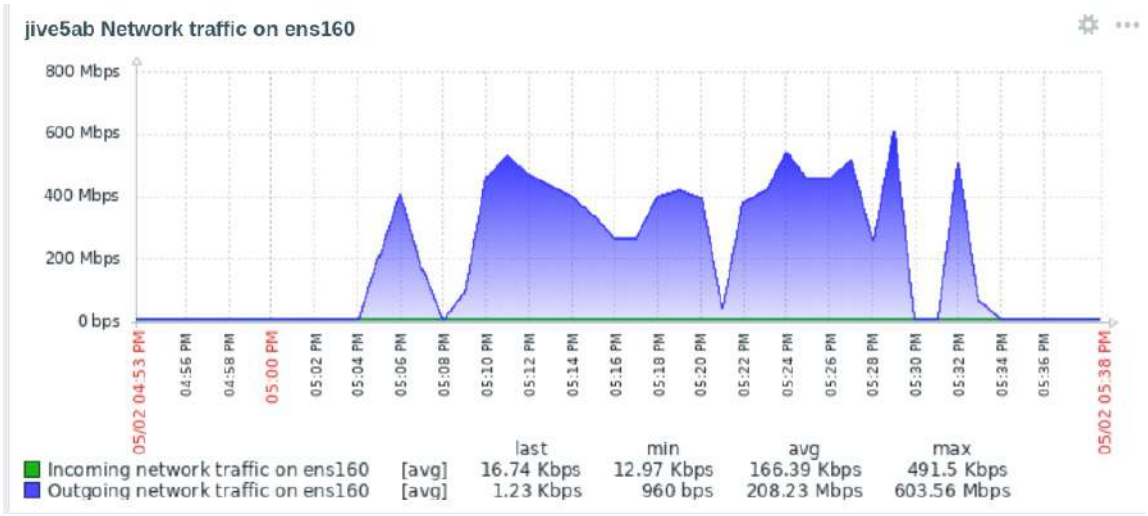

Fig. 1. Data transfer speed to a virtual machine in Yandex Cloud.

Also, iPerf3 was used to test the channel speed between the Yandex Cloud VM and the IAA RAS data storage. Each session lasted 10 seconds. From these data it has been concluded that the average transfer speed per channel is 660 Mbps, slightly higher than the peak value obtained by jive5ab.

4 Session transfer and processing

To test the DiFX correlator, the observing session ri4518 was processed. This is a 1-hour session obtained with two 32-meter VLBI telescopes ("Badary" and "Zelenchukskaya") of the IAA RAS. Data transfer was made using jive5ab/m5copy in four streams, and processing was conducted on VMs with 8, 16, and 32 cores (Table 1). An analysis has shown that data transfer time is about 35 minutes and is independent of the number of virtual machine cores. Similarly, data processing time does not depend on the number of computational node cores.

Table 1. Session transfer and processing Times

No.	Number of cores	RAM	Data transfer time	Session processing time
1	8	8 GB	34 min 48 s	38 min 48 s
2	16	16 GB	34 min 45 s	34 min 18 s
3	32	32 GB	34 min 17 s	33 min 17 s

5 Virtual machine operation

An external system monitoring tool from Yandex Cloud was used to assess the load on the virtual machine. It monitored the processor cores, disk subsystem, and network channel during three stages: software installation, data loading, and session processing. Each stage took about 1/3 of the total operating time. Monitoring results for the 32-core VM are shown in Fig. 2.

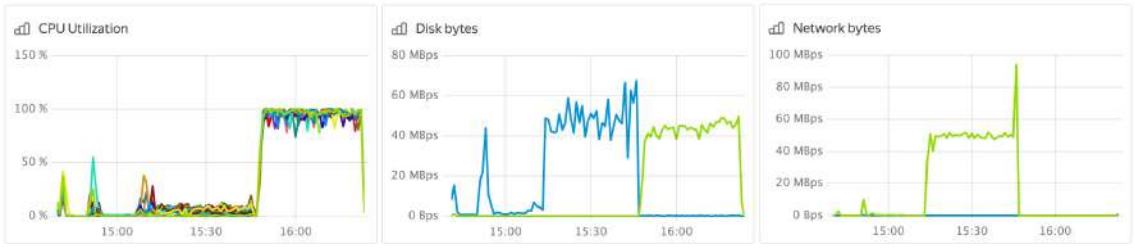

Fig. 2. Monitoring of a 32-core virtual machine.

6 Conclusions

- Software was written to automate the deployment of the DiFX software correlator environment on a virtual machine in the Yandex Cloud service.
- The file transfer speed between the virtual machine in Yandex Cloud and the data storage system of the IAA RAS was measured.
- A test transfer and correlation of a one-hour session recorded by two antennas were carried out.
- It was noted that the data transfer and processing time did not change when increasing the number of cores of the virtual machine from 8 to 16 and 32. This is a very interesting result. The reason for this can be investigated in future works.
- The solution described in the article can be used for data correlation in case of unforeseen situations.

7 Future plans

To increase session processing speed, the following options can be considered:

- using a preconfigured virtual machine image to reduce initialization time;
- shutting down rather than deinitializing the VM after processing to save time;
- parallel processing of sessions by assigning specific cores;
- processing sessions in parallel with simultaneous data transfer to the VM.

Challenges of high-resolution spectroscopy in the Nasmyth focuses of the BTA

V. Panchuk, V. Klochkova, M. Yushkin, and G. Zhuklevich

Special Astrophysical Observatory of the Russian Academy of Sciences,
Nizhny Arkhyz, 369167 Russia

Abstract. The article discusses the challenges and solutions associated with high-resolution spectroscopy on alt-azimuth mount telescopes, particularly focusing on the 6-meter BTA (Big Telescope Alt-Azimutal) and its Nasmyth focus. The main attention is given to the instability of spectra caused by the design features of the telescope and the equipment used. Special attention is paid to the issues of temperature non-uniformity and its impact on observation quality. Various stages of equipment development and testing are described along with the results of applying new technologies and methods to achieve high spectral resolution.

Keywords: instrumentation: spectrographs; telescopes

DOI: 10.26119/VAK2024.174

1 Investigation of the regular spectral equipment

The alt-azimuth design of the 6-meter telescope hinders the performance of the high spectral resolution equipment on the BTA moving part. Efforts to deel with the problem have focused on finding the observing programs that can be performed regardless of spectral instability and the methods for achieving high spectral resolution with varying equipment. Here are the main stages of the work.

During the commissioning of the BTA complex, the primary objective for the first generation of the Special Astrophysical Observatory (SAO) astronomers was to investigate the spectral equipment created by the optomechanical industry. This equipment was developed in accordance with specific technical requirements formulated by astronomers and was formally accepted following rigorous testing both in the workshop and in the observatory, but some difficulties arose because the technical specifications for the telescope and its spectral equipment were prepared at another observatory, and the acceptance was conducted by SAO astronomers.

The idea of the combination of a telescope with a fiber-fed stationary spectrograph appeared only after the BTA had been put into operation, and was optimal for the telescopes of moderate size, see the review of Panchuk et al. (2011). For 4-meter class telescopes, echelle systems placed at the coudé focus were still being developed in the 1980s (Walker & Diego 1985). For the BTA, an idea of the horizontal placement of the spectrograph in a uniform temperature layer was realized (Gusev et al. 1976; Zandin et al. 1977), where spectral resolution was limited by the dimensions of the mounted structure. An investigation of the spectral equipment mounted near the support of the BTA alt-azimuth construction revealed positional instability of high-resolution spectra. As a result, the typical spectral resolution for long photographic exposures was lower. The variety of observing programs had been limited, priority was given to the studies of relative characteristics, either measured relative to the continuum (equivalent widths) or the components of different kinds of circular polarization (measurements of the longitudinal component of the magnetic field). The search for the causes of the positional instability did not allow them to be identified either by linear scales or by characteristic times. Work was performed on the reconstruction of the optical scheme of the Main Stellar Spectrograph (MSS) long-focus camera (Gazhur et al. 1986), light and heat insulation of its volume, change of the oil supply mode at the BTA "Z"-axis drive, and methods for operating with the MSS were selected (Klochkova et al. 2008), but the main problem, the temperature non-uniformity in the volume of the vertical mount of spectrograph elements, remained.

2 Television-type photon counters

The transition to television-type photon counters in high-resolution spectroscopy was connected with matching the characteristic format of the light detector cathode with the scale of the spectrograph camera focal plane while maintaining high spectral resolution. The optimal solution was the use of a diffraction grating in high orders. As a first step, the SP161 spectrograph was reconstructed, where a medium-resolution spectrum was formed on a centimeter focal plane of the camera. The camera design made it possible to use an electron-optical converter with electromagnetic focusing, providing a record throughput (for the BTA Nasmyth-2 focus) $F_{\rm coll}/F_{\rm cam} = 3684/182 = 20$ (Gazhur et al. 1990). The positional stability of the echelle spectrum was limited by the varying orientation of the image intensifier tube focusing system due to its movement in Earth's magnetic field. The transition to solid-state small-format CCDs (charge-coupled devices) was performed on the ESPAK autocollimation echelle spectrograph developed for using both two-dimensional photon counters and CCDs (Klochkova et al. 1991).

3 CCD echelle spectrographs with small apertures

Investigation of the stability of the stellar spectra obtained with the BTA MSS were complicated by the lack of digital recording methods that would allow collecting measurement statistics remotely, without visiting the spectrograph volume. In 1989, a conference of BTA applicants was held in Odessa jointly with the BTA Program Committee (KT6T). At this conference we put forward an initiative to reconstruct the MSS for the full use of the collimated beam (by that time, a set of diffraction gratings intercepting the entire beam at any working angles had been manufactured) with spectrum recording on first CCDs. This initiative was not supported by any of the parties. Thus, we were guaranteed to lag behind the spectroscopists of the Crimean Astrophysical Observatory, where a domestic CCD camera had already been used in 1989 at the spectrograph ASP-14 in the coudé focus of the 2.6-meter telescope. At the BTA MSS, observations were continued with photographic plates with a high level of fogging. In this situation, we began work on creating an echelle spectrograph with a small-diameter collimated beam, LYNX (Panchuk et al. 1993). The format of the CCD chip used limited the size of the simultaneously recorded wavelength range, and we did not have the ability to deal with the problems of remote monitoring and control. Therefore, one of the subsequent modifications of the LYNX echelle spectrograph was built as a combination containing a set of three cross-dispersion gratings (with a density of 150, 300, and 600 gr/mm), operating in the first diffraction order, and two R2 echelles ($\tan\theta_{\rm b} = 2$). This spectrograph design

can be found in Panchuk et al. (2016), Fig. 3. The units with the dispersing elements are movable across the collimator axis ($d_{\rm coll} = 100$ mm), which provides six possible "cross-dispersion grating – echelle" combinations, optimal for operation in different wavelength ranges with required separation of the adjacent orders in the echelle spectrum. In addition to the modifications of the LYNX echelle spectrograph, other cross-dispersion designs were also constructed (Gazhur et al. 1990; Klochkova et al. 1991). The variety of the parameters of these devices made it possible to implement most of the research programs of the SAO RAS Laboratory of Astrospectroscopy (Klochkova 2012). Thus, in the late 80s – early 90s the foundations were created for designing a cross-dispersion system corresponding to the MSS investigation results and the scientific interests of the 6-meter telescope staff.

4 Increasing the aperture and spectral resolution

In 1993, we proposed a program for transition to collimated beams of large diameters (at least 250 mm). The program mainly included: (a) reconstruction of the MSS, proposed in 1989; (b) development of an echelle spectrograph installed on the Nasmyth-2 focus platform, with a horizontal arrangement of the optical scheme. The administrative decision to build the Nasmyth echelle spectrograph (NES) was made in the fall of 1996, the manufacture and assembly of the spectrograph continued throughout 1997, and first light was obtained in December 1997 (Panchuk et al. 1999). The optical scheme of the spectrograph was oriented in the plane of the Nasmyth focus platform, with all units and elements of the scheme in a uniform temperature layer; the corresponding mechanical unloading of the BTA turned out to be successful. The positional characteristics of the spectrograph were studied in Klochkova et al. (1999). It was found that the accuracy of processing individual orders allows detecting even the subtle manifestations of instability of the light detector at the beginning of cryostat freezing. After several years of NES operation, the stability of the spectrum position was checked during three days when the observations were not carried out due to weather conditions and the temperature difference between the outside air and the in-dome space was record-breaking (Panchuk et al. 2006). It was found that the shifts of the comparison spectrum lines correlated neither with the variations of meteorological parameters (temperature, atmospheric pressure, velocity) nor with the temperature variations of the NES mechanical structure. However, noticeable shifts in the positions of spectral lines were observed. An analysis of the experiments conducted at NES with other detectors revealed the effect of line shift for four different detectors, one of which (with a CCD of 2048×2048 elements) was manufactured in accordance with the European Southern Observatory standards (Sørensen 2001)

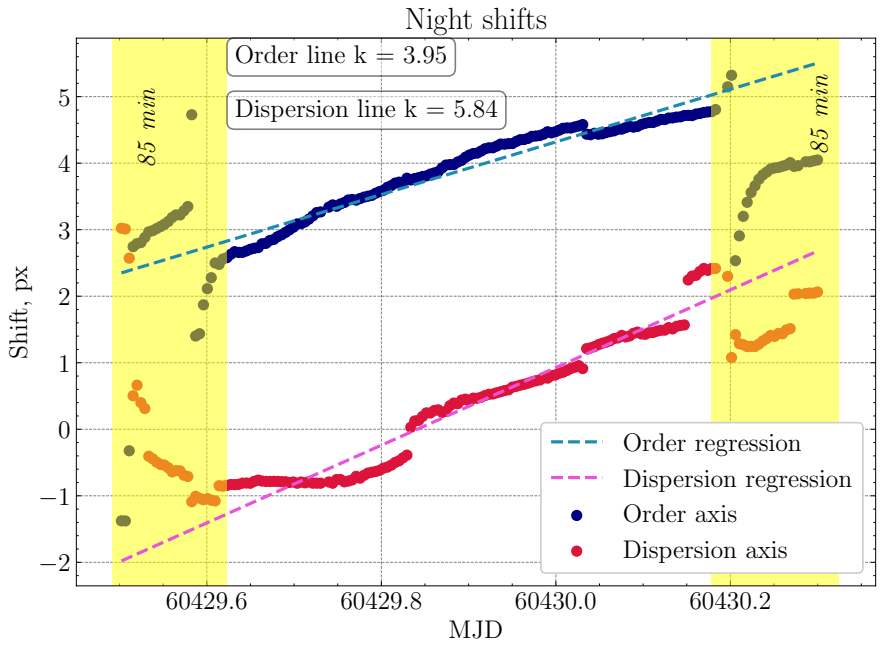

Fig. 1. Dependence of line position on time. The yellow sectors show the moments of significant instability during the filling of the cryostat with coolant. The "linear" section is approximated by a straight line, the coefficients k are shown in the figure.

and had been used on NES for 10 years. At present, NES is equipped with a system based on the 4.6k × 2k E2V CCD42-90-1-G01 chip, the system has been designed and manufactured at SAO RAS (Vlasyuk et al. 2024). The actual state of NES is described in Panchuk et al. (2017).

Subsequent investigation into the causes of image shifts on the CCD chip was conducted using the MIDAS software suite. Initially, cross-correlation algorithms were applied, which, at that time, yielded results along just one axis of the chip. For a higher precision measurement of these shifts, a specialized algorithm was required, the one that would be less universal but more focused on this specific task. Therefore, a two-dimensional optimization method has been utilized in the current study of NES stability. An analyzed image was randomly shifted relative to the reference image, then the difference image between them was calculated, a cost function was created and subsequently minimized (Powell 1964; Press et al. 1986). To prevent falling into a local minimum, the sequential Gaussian pyramid technique and a hopping algorithm (Wales & Doye 1997) were applied. This allowed the shifts along the x and y axes to be determined, the resulting combination was used to calculate image rotation. The

results are presented in Fig. 1. Sharp coordinate changes coincide with the addition of coolant into the cryostat. The nature of the coordinate variation is complex and requires further study in the laboratory conditions. For details, see technical report Zhuklevich & Panchuk (2024).

Funding

Russian Science Foundation (grant No. 22-12-00069).

References

Gazhur E.B., Klochkova V.G., Panchuk V.E., 1990, Soviet Astronomy Letters, 16, p. 202
Gazhur E.B., Naidenov I.D., Panchuk V.E., 1986, Astrofizicheskie issledovaniya, 23, p. 105
Gusev O.N., Zandin N.G., Peisakhson I.V., 1976, Optiko-mekhanicheskaya promyshlennost', 12, p. 63
Klochkova V.G., 2012, Astrophysical Bulletin, 67, p. 385
Klochkova V.G., Ermakov S.V., Panchuk V.E., et al., 1999, Preprint SAO, 135
Klochkova V.G., Panchuk V.E., Ryadchenko V.P., 1991, Soviet Astronomy Letters, 17, p. 274
Klochkova V.G., Panchuk V.E., Yushkin M.V., et al., 2008, Astrophysical Bulletin, 63, p. 386
Panchuk V.E., Klochkova V.G., Galazutdinov G.A., et al., 1993, Astronomy Letters, 19, p. 431
Panchuk V.E., Klochkova V.G., Yushkin M.V., 2017, Astronomy Reports, 61, p. 820
Panchuk V.E., Klochkova V.G., Yushkin M.V., et al., 2016, Izvestiya vysshikh uchebnykh zavedenii. Priborostroenie, 59, p. 1018
Panchuk V.E., Piskunov N.E., Klochkova V.G., et al., 1999, Preprint SAO, 135
Panchuk V.E., Yushkin M.V., Emel'yanov E.V., 2006, Preprint SAO, 212
Panchuk V.E., Yushkin M.V., Yakopov M.V., 2011, Astrophysical Bulletin, 66, p. 355
Powell M.J., 1964, The computer journal, 7, p. 155
Press W.H., Vetterling W.T., Teukolsky S.A., et al., 1986, Numerical recipes, Cambridge University Press
Sørensen, A. N. 2001, Copenhagen University Observatory
Vlasyuk V.V., Afanasieva I.V., Ardilanov V.I., et al., 2024, Physics-Uspekhi, 67, p. 405
Wales D.J. and Doye J.P., 1997, The Journal of Physical Chemistry A, 101, p. 5111
Walker D.D. and Diego F., 1985, Monthly Notices of the Royal Astronomical Society, 217, p. 355
Zandin N.G., Gusev O.N., Peisakhson I.V., 1977, Optiko-mekhanicheskaya promyshlennost', 6, p. 20
Zhuklevich G.S. and Panchuk V.E., 2024, Nauchno-tekhnicheskii otchet SAO, 361

BAK 2024 MODERN ASTRONOMY: FROM THE EARLY UNIVERSE TO EXOPLANETS AND BLACK HOLES 300 years Russian Academy of Sciences

Fast implementation of coherent dispersion compensation

S. Sergeev and Yu. Kazakevich

Lavochkin Association, JSC, Khimki, 141402 Russia

Abstract. The interstellar medium consists of gas and dust components, almost all of which are completely transparent at centimeter wavelengths. The main cause of radio wave scattering in the interstellar medium is ionized gas—plasma. The behavior of radio waves propagating through such a medium is described by the dispersion equation in a rarefied plasma. The plasma frequency is generally a function of position and time, because it depends on the electron density along the line of sight. The dispersion measure physically represents a column of free electrons between a pulsar and the Earth. Thus, the dispersion measure is a value that determines the delay of radiation pulses of cosmic objects. The delay of radio emission is due to the fact that the refractive index of the plasma depends on the wavelength. Long waves propagate more slowly than short ones, so a signal emitted simultaneously at different frequencies arrives to the observer at long waves later than at short ones. One type of astrophysical objects for which the pulse delay can be measured are pulsars. Since observations are always carried out in a certain wavelength band, the presence of a delay interferes with the study of the fine time structure of pulsar pulses. Without dispersion correction, pulsar observations in a wide frequency band become impossible. The presented work considers the implementation of the coherent dispersion compensation method on a heterogeneous computing structure. Processing in the spectral domain allows the simultaneous search for fast radio bursts (giant pulses), radio pulsars, and refinement of the dispersion measure of the found pulses. It is shown that the proposed implementation on modern computing accelerators allows real-time processing in a wide frequency band that meets modern requirements.

Keywords: pulsars: general; instrumentation: interferometers; methods: numerical

DOI: 10.26119/VAK2024.175

1 Introduction

The interstellar medium consists of gas and dust components, almost all of which are completely transparent at centimeter waves (Lorimer & Cramer 2005). The main cause of the scattering of radio waves in the interstellar medium is ionized gas, i.e., plasma.

The behavior of radio waves propagating through such a medium is described by the dispersion equation in a rarefied (collisionless) plasma:

$$w^2 = c^2k^2 + w_\mathrm{p}^2, \tag{1}$$

where k is the wave number and w_p is the plasma frequency.

The plasma frequency w_p is generally a function of position and time, because it depends on the electron density in the line of sight $n_\mathrm{e}(x,t)$ and is defined as

$$w_\mathrm{p} = \sqrt{\frac{4\pi e^2 n_\mathrm{e}}{m_\mathrm{e}}}, \tag{2}$$

where e and m_e are the electron charge and mass, respectively.

Typical values for the electron density n_e for our Galaxy are in the range of 0.01 to 1 cm^{-3}, resulting in a plasma frequency w_p from 5 to 50 kHz. This is significantly lower than pulsar observing frequencies, which are typically from 100 MHz to 10 GHz, so the approximation $w \gg w_\mathrm{p}$ is acceptable. As follows from Eq. (1), the group velocity of radio waves passing through the interstellar medium is determined as

$$v_\mathrm{g} = \frac{\partial w}{\partial k} = c\left(1 - \frac{w_\mathrm{p}^2}{w^2}\right)^{1/2} \cong c\left(1 - \frac{w_\mathrm{p}^2}{2w^2}\right), \tag{3}$$

provided that the final approximation is $w \gg w_\mathrm{p}$. The pulse signal of a pulsar (wave packet) passes at a distance d through the medium in a time T defined as

$$\begin{aligned} T &= \int_0^d \frac{1}{v_\mathrm{g}} dx \cong \frac{d}{c} + \frac{1}{2w^2 c}\int_0^d w_\mathrm{p}^2(x)\,dx \\ &= \frac{d}{c} + \frac{1}{w^2}\frac{4\pi e^2}{2cm_\mathrm{e}}\int_0^d n_\mathrm{e}(x)\,dx = \frac{d}{c} + \frac{1}{w^2}\frac{2we^2}{cm_\mathrm{e}}\mathrm{DM}. \end{aligned} \tag{4}$$

This expression is valid as long as the change in the electron density concentration n_e at a fixed wavelength can be neglected.

The dispersion measure is defined

$$\mathrm{DM} = \int n_\mathrm{e}(x)\,dx. \tag{5}$$

This parameter physically represents a column of free electrons between a pulsar and Earth. Thus, the dispersion measure is a value that determines the delay of radiation pulses of cosmic objects (Eatough et al. 2009).

The wave packet is subject to dispersion or delay in time δT:

$$\delta T = \left|\frac{\partial T}{\partial w}\right| \Delta w \cong \frac{\Delta w}{w^3}\frac{w\pi e^2}{cm_\mathrm{e}}\mathrm{DM} \cong 8.3\ \mu\mathrm{s}\ \frac{\Delta w(\mathrm{MHz})}{w^3(\mathrm{GHz})}\mathrm{DM}(\mathrm{pc\,cm^{-3}}). \tag{6}$$

Without dispersion correction, observing pulsars in a wide frequency band becomes impossible. If the delay value δT becomes comparable to the pulsar period, the pulse energy will be "smeared" over the entire period.

The best, most accurate, method is coherent dispersion correction based on the fact that dispersion is a coherent effect. This means that the phase of radio waves varies with frequency according to the dispersion measure DM. This process can be described in the frequency domain by a simple transfer function $H(w) = e^{i\,\phi(w)}$. By applying the inverse filter it is possible to completely eliminate the dispersion effect. The phase in this case is determined as

$$\phi(w; w_0) = \frac{2\pi D w^2}{w_0^2(w_0 + w)}. \tag{7}$$

Such a filter can be applied to a signal with a bandwidth Δw and a central frequency w_0. In this case, w is a frequency band offset so that $|w| < \Delta w/2 \ll w_0$. The coefficient D is related to the more commonly used dispersion measure DM as $\mathrm{DM} = 2.41 \times 10^{-4}\, D(\mathrm{s\,MHz^2})$.

The Fourier transform of $H(w)$ gives the impulse response $h(t)$ of such a dispersion compensation filter. For the filter defined by Eq. (7), this will be a chirp pulse with a width δT, centered at $t = 0$. The signal dispersion process can be represented as a convolution of the original signal with $h(t)$.

2 Realization

The fast dispersion compensation is implemented on a software correlator with a heterogeneous computing structure. Graphics processing units (GPU) or Alveo V80 can be used as computation accelerators. The software correlator can work both in FX and XF mode depending on the problem being solved. It performs the following main processing steps: bit repacking, fringe rotation and delay tracking, fractional delay correction, spectrum multiplication and integration, Van Vleck quantization correction. Additionally, the correlator can perform phase calibration signal extraction and pulsar gating and binning. For spacecraft navigation, additional tools are

used, such as detection and estimation of the Doppler shift and its variation with time and also the Kalman filter for precise frequency detection in a narrow band, which compensates for residual phase rotation. Weighted window functions are used to minimize spectral leakage. The stages of dispersion compensation are described in more detail in (Girin et al. 2023).

The fast implementation is achieved by additional manual code optimization for the low-level Parallel Thread Execution instruction set, which allows increasing the performance up to three times compared to the CUDA library. When performing a discrete Fourier transform (DFT), the data is divided into segments corresponding to the DFT length. Performing a convolution operation corresponds to a cyclic shift in the time domain, and the first n points corresponding to this time shift will be erroneously multiplied by the data at the end of the segment. To avoid such distortion, it is necessary to discard the data which leads to the loss of a signal whose duration corresponds to the time shift. As a result, it is necessary to increase the segment sizes and discard the distorted ones, which leads to an increase in the volume of the processed data. With a short DFT size, the ratio of useless and useful data may be too large. Therefore, the DFT size should be as large as possible. The high bandwidth memory of computing accelerators can be combined into a single virtual space, which allows increasing the duration of one segment to several minutes.

3 Summary

The implemented approach for dispersion compensation using a heterogeneous computing structure allows continuous processing, minimizing the introduced errors inherent to segmented processing. The implemented approach minimizes distortions and improves the quality of coherent dispersion compensation.

References

Eatough R.P., Keane E.F., Lyne A.G., 2009, Monthly Notices of the Royal Astronomical Society, 395, p. 410

Girin I.A., Likhachev S.F., Andrianov A.S., et al., 2023, Astronomy and Computing, 45, id. 100754

Lorimer D.R. and Kramer M., 2005, Handbook of pulsar astronomy, Cambridge (GB): Cambridge University Press

MODERN ASTRONOMY: FROM THE EARLY UNIVERSE TO EXOPLANETS AND BLACK HOLES

Implementation of the ALPHA UMi monitoring system at SAO RAS

I. Shaldyrvan, V. Komarov, V. Komarova, and M. Fokin

Special Astrophysical Observatory of the Russian Academy of Sciences,
Nizhny Arkhyz, 369167 Russia

Abstract. A new α UMi monitoring system based on an IP camera with a CMOS photodetector has been developed and installed at the Upper Scientific Site of the Special Astrophysical Observatory of the Russian Academy of Sciences (SAO RAS). The main aim of the development is to measure the astronomical seeing and monitor its variation. Here we briefly describe the method of differential image motion monitoring (DIMM) used as the device operational principle and give some details on the characteristics and operation of the monitoring system developed.

Keywords: methods: observational; techniques: image processing

DOI: 10.26119/VAK2024.176

1 Introduction

Monitoring systems are widely used in SAO RAS. They have been constructed for different purposes and instruments such as scientific equipment viewing cameras, telescope guidance, night-sky monitoring systems, in-dome cameras, etc. The idea of video monitoring is not limited by watching the night sky in the visible range of the spectrum. Of great importance is the examination of the star images for continuous estimates of the astronomical seeing quality and its variation caused by the atmosphere turbulence, weather conditions, etc.

To estimate the seeing, we chose the classical method of DIMM (Tokovinin 2002) with a non–classical analysis of a large number of images obtained through a single aperture (one imaging device) and applied it to the images of Polaris.

2 Method of differential image motion monitoring

As described in Tokovinin (2002), DIMM is currently a commonly accepted tool for measuring the astronomical seeing. In this method the Fried parameter is estimated by the variance of the differential image motion within two small apertures, usually cut out by a mask in one large pupil of the telescope.

This approach has a practical advantage, because it is insensitive to the shaking and tracking errors, at least of the first order. Usually, the difference in the slopes of the two DIMM subapertures is proportional to the second derivative of the wavefront, or the curvature. Thus, a DIMM module is a kind of a curvature sensor.

The success and a wide spread of DIMM has led to some confusion. It is often considered that a DIMM module is a reliable and self-calibrated tool that always gives correct measurements of the seeing. However, a number of subtle instrumental effects in the DIMM modules can distort the results. The accurate calibration and the elimination of bias in the DIMM results become a critical issue for comparing the astronomical sites and the prediction of the seeing. The equations given in Tokovinin (2002) and Sarazin & Roddier (1990) allow us to relate the variance of the image center position, the diameter of the telescope D_t, and the Fried parameter r_0:

$$\sigma_*^2 = K\lambda^2 \left(\frac{1}{r_0}\right)^{5/3} \left(\frac{1}{D_\mathrm{t}}\right)^{1/3}. \qquad (1)$$

An important conclusion from formula (1) is that to construct a device for the seeing measurements by applying this method, it is advisable to use a small-diameter lens. In this case the variance increases, and it can be measured with better accuracy. All further calculations are performed for $\lambda = 550$ nm. The parameter K depends on

the ratio of the distance between the apertures and the diameter of the apertures. For the zero distance (one aperture as in our case), $K = 0.358$.

Unlike the classical DIMM, we use a single aperture to take many images (about 100) of Polaris without guiding, these calculations require a series of images of short exposures with short intervals between them, which is not a problem for cameras with CMOS matrices.

Based on the images taken with this system, it is possible to determine the exact position of the star image center (X, Y) by the calculation of the center of mass (centroid) or by profile fitting. Since the star is shifting slightly from exposure to exposure, it is necessary to remove this trend. For short episodes of 100 frames (1-min duration approximately), it is enough to fit X and Y with a polynomial of the 2nd degree. The residuals in this case will be quite small.

After subtracting the corresponding trends from X and Y, it can be assumed that the data contain only random "wandering" of the star in the focal plane caused by wavefront tilts in the turbulent atmosphere, as shown in Fig. 1. The value characterizing the point spread is the variance σ^2.

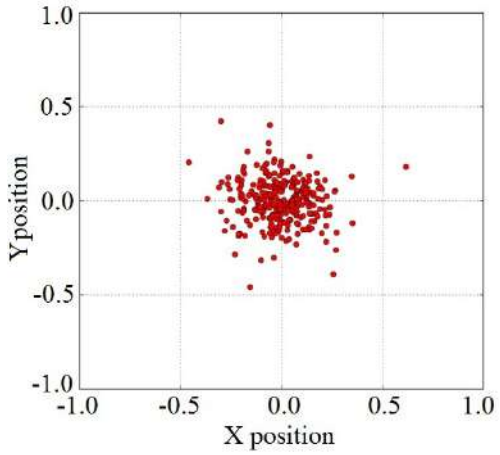

Fig. 1. Star position scattering due to atmosphere turbulence, $D_\mathrm{t} = 0.05$ m, scale $= 5''.5$/pix.

In this case, after removing the trend the average value of the coordinate will be equal to zero. The square root of the variance is the standard deviation. We are interested in the variance of the distance for the center of the star in each frame. It can be calculated as the sum of the variances for X and Y.

3 Polaris monitoring system

By converting images obtained with IP cameras into the FITS format, we get an opportunity to study various parameters of star images (Shaldyrvanet al. 2023). To measure the seeing, an IP camera with a Sony IMX335 CMOS matrix with a resolution of 2592×1944 px (aspect ratio of 4:3) and a lens with a focal length $F = 63.5$ mm and the field of view $\mathrm{H} \times \mathrm{V} = 4.^{\circ}24 \times 3.^{\circ}18$ was purchased. The resulting image scale is approximately $6''$/px. It has been verified by the astrometric calibration of the image obtained with a similar camera–lens pair mounted on the cage of the SAO RAS 6-m telescope prime focus.

We have modeled the camera enclosure and made it of weather-resistant materials. The dimensions of the enclosure allow avoiding system fluctuations due to the wind loads.

The camera has been installed on the Zeiss-1000 telescope dome roof. It is pointed at the polar region of the sky. Series of 100 images of Polaris are saved to a local network server with subsequent round-the-clock processing with a frequency of 20 minutes. For technical needs, it is also possible to access the live stream of the video signal from this viewing camera via the local network.

We use the `Python` libraries `numpy`, `scipy`, `matplotlib`, `os`, `pylab`, and `astropy` to determine the star centroid and the full width at half maximum (FWHM) and then calculate the seeing and the Fried radius r_0. The measurements are saved as a CSV-format table and stored on a server in the local network of SAO RAS as well as displayed on a web page in the form of a graph.

4 Conclusion

Thanks to the new technologies used in the production of CMOS matrices in the last decade, it became possible to create inexpensive IP cameras with characteristics acceptable for work at night time. The methods described here allows one to use images obtained by an IP camera with a CMOS matrix to calculate the astronomical seeing and the Fried radius r_0. Based on the DIMM method, we have developed the Polaris monitoring system and put it into operation at SAO RAS, where it works round-the-clock with data updating every 20 minutes.

References

Sarazin M. and Roddier F., 1990, Astronomy and Astrophysics, 227, p. 294

Shaldyrvan I.V., Komarov V.V., Fokin M.Y., 2023, Izvestiya Krymskoj Astrofizicheskoj Observatorii, 119, p. 12

Tokovinin A., 2002, Publications of the Astronomical Society of the Pacific, 114, p. 1156

MODERN ASTRONOMY:
FROM THE EARLY UNIVERSE TO EXOPLANETS AND BLACK HOLES

SODA: a system to detect daytime asteroids of the "Milky way" project

A. Shugarov and B. Shustov

Institute of Astronomy of the Russian Academy of Sciences, 48 Pyatnitskaya str., Moscow, 119017 Russia

Abstract. The "Milky Way" space safety program is under development in Russia. A part of the program implies the launch of a special spacecraft aimed to detect decameter asteroids coming from the day sky (from the sunward hemisphere) as well as to predict space weather and monitor the Sun's activity. The spacecraft will be launched to the Sun–Earth L1 point. The payload SODA (System for Observation of Daytime Asteroids) is under development at INASAN. The SODA concept is based on the results of the previous, conceptual, phase of the project. We present a general outline of SODA and give some new features in more detail. IKI RAS is responsible for the second part of the spacecraft payload related to space weather and solar activity.

Keywords: telescopes; space vehicles: instruments; asteroids: general; Sun: solar-terrestrial relations

DOI: 10.26119/VAK2024.177

1 Introduction

In recent years Roscosmos has been developing a new Russian system of ground-based telescopes and satellites called "Milky Way." It is designed to ensure the safety of space activities in the near-Earth space.[1] The "Milky Way" system is going to be important for monitoring and warning about dangerous situations in the outer space near Earth and focuses on several problems: space debris, space weather, and asteroid hazard. The implementation of this project will help strengthen scientific potential in many fields, make more accurate forecasts, and respond to potential threats in space and from space.

A part of the program implies the launch of a dedicated spacecraft to the Sun–Earth L1 point with two scientific payloads.

The first payload, SODA (System for Observation of Daytime Asteroids), is aimed at detecting decameter asteroids approaching Earth from the daytime sky directions. It is now being developed at the Institute of Astronomy of RAS (INASAN) based on the results of the conceptual phase of the project.

The second payload concerns the observations of the Sun at wavelengths from X-rays to the infrared (IR) light, magnetic field measurements, and particle detection. The payload is under development at the Space Research Institute of RAS (IKI RAS).

2 Payload for detecting daytime asteroids

The asteroid hazard poses a threat not only from the large ($\geq$ 100 m) but also from the relatively small decameter ($\geq$ 10 m) bodies. Such small bodies can be systematically detected only in the near-Earth space (several mln km). The rate of the collisions with Earth of the bodies with a size of 1 m is 1 event per month, for the 5 m bodies it is once a year, and once every 10–15 years for the 10 m asteroids. Almost half of these objects comes from the daytime sky. Neither ground-based telescopes nor telescopes at low Earth and geosynchronous orbits are capable of observing such daytime bodies.

Shustov et al. (2015) have shown that the implementation of a system for close detection of asteroids arriving from the daytime sky requires the use of a space-based system. According to the SODA concept (Shugarov et al. 2018, 2021; Shugarov & Shustov 2022), several optical telescopes are placed in the vicinity of the Sun–Earth libration point L1. SODA is going to be the first system in the world to detect most of the 10-m class daytime asteroids in real time. It will provide the Russian Federation with exclusive access (currently there are no existing analogs) to a very significant

[1] URL:https://tass.com/science/1792063?ysclid=lz5maokqlw391262954

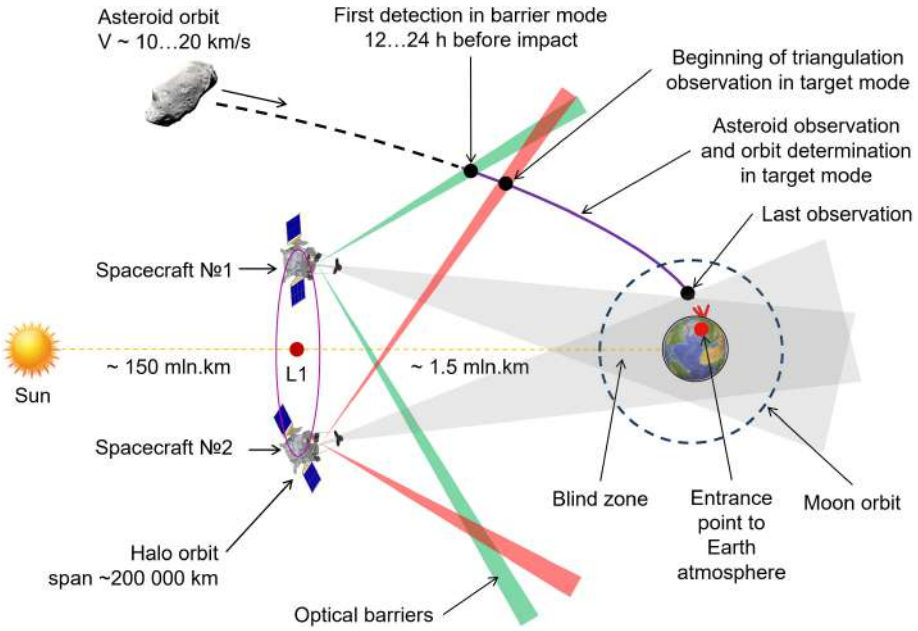

Fig. 1. SODA scheme of operation at the L1 point of the Sun-Earth system.

share (up to 50%) of information about dangerous asteroids that might collide with or fly near Earth in the coming decades.

SODA has a possible additional useful outcome. The probability that an asteroid collides with a spacecraft in the near-Earth space is extremely low; however, many small asteroids are often formed as a result of a collision of larger asteroids. Therefore, they may have a tail of small unobservable debris, since collisions always produce many small fragments. When such an asteroid with a tail crosses the near-Earth space, we may preliminary state that the probability of damage to spacecraft due to the collisions with small particles of the asteroid's tail is subject to study and it may not be negligible.

In Fig. 1 the general scheme of the SODA operation for the two spacecraft option is shown. Each spacecraft is going to be equipped with three telescopes to provide the required survey efficiency. Each telescope will observe a part (slightly above 120°) of the conical barrier around the Earth every 3 minutes. Both the target mode and the barrier detection mode can by implemented with the same telescope using a fast repointing pre-aperture mirror.

An asteroid moving from the Sun crosses the optical barrier approximately one day before its closest approach to Earth. For a typical asteroid it takes about 30 minutes to cross the barrier. This means that an asteroid is going to be observed about

8 times while crossing the barrier. The data will be transmitted to the ground center, where a preliminary orbit is to be calculated. This is sufficient to classify the object as dangerous or not. If the asteroid is classified as an object of special interest, the ground center sends a command to the SODA payload to observe the object in the target mode every 3 minutes. The last observation can be done at an angular distance between the asteroid and Earth of $\sim 5^\circ$.

The spacecraft is based on the proven Russian satellite bus Navigator, which has successfully been operating at L2 for the Spektr-RG mission. It is going to be put into orbit around L1 by a medium-class launch vehicle Soyuz-2. The total payload mass is estimated as 500 kg, and the spacecraft should not exceed 2000 kg. The lifetime of the spacecraft should be at least 5 years.

A permanent low-speed radio channel in the X-band will be used to rapidly transmit the most critical (selected) scientific data to the Ground Center. This requires placing receiving stations at the Earth eastern and western hemispheres. A high-speed X-band radio communication channel will be installed to transmit a complete set of scientific data to the Ground Center when possible.

For asteroids on collision orbits, SODA provides the issuance of a 10-hour warning (on average) before the impact as well as the asteroid entry point into the Earth atmosphere with an accuracy of 10–200 km. In the most complicated cases the system guarantees a warning no later than 4 hours before the impact. This is not enough for mitigation actions such as evacuation of the population. However, in the coming decades evacuation is not necessary and may even be harmful for most impactors of 5–20 m in size. On average, the expected number of fatalities from the 5–20 m sized asteroids is not very high. A hasty evacuation may lead to greater losses than the absence of evacuation but with civil defense actions.

The warning time of 10 hours provided by SODA is sufficient for:

- emergent call to all services (police, ambulance, etc.) to be in full readiness;
- putting infrastructure facilities to safe mode;
- early completion and cancellation of public events;
- notifying the civilians about the need to comply with certain civil defense measures, if such notification is deemed appropriate.

Due to the high completeness of the detection of daytime asteroids flying from the Sun, in coming decades SODA is going to provide almost sufficient information about sunward asteroids that pose a real threat. The coordinated work of all state departments and municipal services will ensure significant reduction of the consequences of an asteroid impact on Earth.

3 Payload for monitoring the solar wind and the Sun

The heliophysical situation, e.g., the state of solar activity and near-Earth interplanetary environment, is determined primarily by the processes occurring on the Sun. Monitoring tasks include providing regular information on both the current heliophysical situation and the heliophysical factors that allow reliable predictions of its condition. The regular remote monitoring of the Sun disk and corona in various spectral ranges (optical, UV, X-ray, IR) as well as local observations of the properties of the interplanetary medium (solar wind) directly affecting the Earth are required.

The necessary observations of the Sun include the short-wave solar radiation from the full disk, the solar magnetic field both on the entire disk and in individual active regions, images of the photosphere, chromosphere, and corona in a number of characteristic spectral lines. Based on this information, a forecast of solar activity would be made. The monitoring of the interplanetary environment at the Sun–Earth libration point L1 would allow us to determine the specific characteristics of the solar wind and interplanetary magnetic field that directly affect the Earth and quantify their effect on the ionosphere and magnetosphere, including the strength of a magnetic storm.

The space segment of the Sun and interplanetary environment monitoring is key to successful prediction of the heliogeophysical situation. Currently, the space weather forecast in Russia relies mainly (and completely in terms of the monitoring data of the interplanetary environment) on the data from foreign spacecraft; however, access to this data may be restricted at any time. In this regard, the development of Russian spacecraft with appropriate instruments for space weather and Sun monitoring is of particular importance.

The optimal location for the instrumental complex of solar wind and Sun monitoring is the vicinity of the libration point L1. For space weather monitoring this type of orbit is the only one, since it provides continuous observations of the interplanetary space at a fixed distance from the Sun, which is impossible on other types of orbits. In the case of solar monitoring this option is also preferable, since it ensures uninterrupted measurements, unlike near-Earth orbits.

Currently, IKI RAS selects scientific instruments for this project. Space weather monitoring requires a spacecraft to be close to the Sun–Earth line, a halo orbit with a span (radius) of 200 000 km has been chosen. Such an orbit is suitable for the asteroid detection payload, since a small span of the orbit allows it to minimize the amount of missing objects flying very close to the spacecraft, as in the Solar system there are practically no asteroids with highly eccentric orbits. A spacecraft with two payloads would allow us to solve steadily and in parallel both the asteroid hazard and space weather forecast problems for about 10 years.

4 Possible international cooperation

The efficiency of asteroid monitoring at L1 can be significantly increased if two spacecraft operate simultaneously. The triangulation tracking mode provides an increase in the accuracy of determining the impact region coordinates on Earth by 1–2 orders of magnitude. Also it would improve the detection completeness due to cross-compensation of the blind zones of each spacecraft and provide better redundancy.

For the Russian "Mily Way" program, the plan is to build one spacecraft. Discussions to build another similar spacecraft to operate at L1 are underway with the Chinese partners. The international coordination with ground based telescopes and radio radars would allow additional observations of the dangerous asteroids discovered by SODA.

5 Summary

The Chelyabinsk event has changed our priorities regarding the asteroid and comet hazard. We understand that it is necessary to create special space-based facilities to detect decameter-size bodies coming from the sunward hemisphere (daytime sky). A combination of the space-based (SODA) and ground-based projects is a proper way to provide a realistic real-time warning system against the decameter-size impactors.

The national "Milky Way" space safety program is under development in Russia. The spacecraft orbiting at L1 with a span of 200 000 km would allow us to solve steadily and in parallel both the asteroid hazard and space weather forecast problems for about 10 years. International collaboration is welcome for both the space and ground segments of the "Milky Way" space safety program.

Acknowledgements. The authors thank M. O. Riazantseva from the Space Research Institute of RAS for fruitful discussions and materials for this article.

References

Shugarov A., Shmagin V., Boqian X., et al., 2021, 7th IAA Planetary Defense Conference, id. 100
Shugarov A.S. and Shustov B.M., 2022, INASAN Science Reports, 7, p. 85
Shugarov A., Shustov B., Naroenkov S., 2018, Open Astronomy, 27, p. 132
Shustov B.M., Shugarov A.S., Naroenkov S.A., et al., 2015, Astronomy Reports, 59, p. 983

VAK 2024 MODERN ASTRONOMY: FROM THE EARLY UNIVERSE TO EXOPLANETS AND BLACK HOLES 300 years Russian Academy of Sciences

Continuum spectrum receiving complexes on the RATAN-600 radio telescope

P. Tsybulev, N. Nizhelskij, A. Borisov, D. Kratov, and R. Udovitskiy

Special Astrophysical Observatory of the Russian Academy of Sciences,
Nizhny Arkhyz, 369167 Russia

Abstract. The results of many years of work on the creation and modernization of the continuum spectrum receiving complexes on the RATAN-600 radio telescope are presented. These complexes are located in the cabins of four secondary mirrors of the radio telescope, three of which can simultaneously conduct observations for three independent programs using separate sectors of the radio telescope primary mirror. To date, a total of 23 radiometers (35 frequency channels) operate on the radio telescope around the clock and all year round. The receiving complexes operate according to technical and scientific programs such as observation of individual objects or round-the-clock sky surveys. The main attention is payed to increasing the sensitivity and long-term stability of the radiometers. With a large number of receivers, the operational characteristics are also important (ease of maintenance, mean time to failure, dimensions, power consumption). One of the tasks being solved is the problem of noise protection in the operating frequency ranges as well as active noise reduction in the decimeter wavelength ranges. The groundwork and prospects in this direction are presented. The immediate plans for the commissioning of new radiometers are also introduced.

Keywords: instrumentation: detectors

DOI: 10.26119/VAK2024.178

1 Introduction

The RATAN-600 radio telescope currently operates as three antenna systems: the Northern Sector, the Southern Sector (or the Southern Sector with a flat mirror) and the Western Sector. Each antenna system is equipped with its own set of receiving equipment.

RATAN-600 is a transit instrument. The observations are carried out in the mode of radio source passage at a certain azimuth. The primary horns of the radiometers are located on the focal line of the secondary mirrors, making up a "multicolor" receiving system with a range of recorded frequencies up to five octaves (1–32 GHz).

2 Complexes of continuum radiometers

The currently existing continuum radiometer complexes are presented in Table 1. They are located at four secondary mirrors ("feed cabins" 1, 2, 3, and 5) of the radio telescope.

The continuum radiometers of the centimeter waves on RATAN-600 are modular radiometers (one radiometer is one microwave module). We described this design earlier in Berlin et al. (2012); Tsybulev et al. (2018, 2022a,b). All modular uncooled radiometers are made based on modern circuit technologies using low-noise transistors, precise low-noise voltage regulators, and modern microwave components. Therefore, they show the lowest possible noise even in the absence of cooling. For example, our C band radiometer demonstrates a root mean square of noise in the low-frequency band 0–1 Hz, equal to 0.25 millikelvin. Also it demonstrates the lowest $1/f$ noise (see Tsybulev et al. 2018). While the former says about the high sensitivity of the radiometer on short timescales, the latter means preserving this sensitivity over sufficiently long time intervals and the long-term stability of the radiometer.

The modular architecture of the radiometers also means that it has a minimum number of microwave connections. It also improves the long-term stability and performance of the receivers. We also work on reducing the energy consumption of the radiometers. This is not so much to save energy as, mainly, to reduce the receiver self-heating. This approach reduces the thermal component of $1/f$ noise.

Also, the modular design means the small size of radio astronomy receivers. RATAN-600 does not have a focal point, like paraboloids, but a focal line to accommodate the input horns of the receivers. This makes it possible to place a sufficiently large number of radiometers on the focal line for quasi-simultaneous observation of radio emission in a wide frequency band. The small size of the radiometric modules helps successfully implement this task. For example, secondary mirror number 1 con-

Table 1. The RATAN-600 continuum radiometers. The last four rows correspond to one (out of four) multichannel radiometer.

Center frequency, GHz	Bandwidth, MHz	Flux density sensitivity, mJy	HPBWx, arcsec
Feed cabin No. 1			
30	5000	100	9
22.25	2500	50	11
14.4	2000	25	13
11.2	1000	15	15.5
8.2	1000	10	22
4.7	600	5	45
2.25	80	40	80
1.25	60	200	110
Feed cabin No. 2			
30	5000	200	11
22.25	2500	95	16.5
14.4	2000	50	18
11.2	1000	30	23
8.2	1000	20	30
4.7	600	10	53
Feed cabin No. 3			
30	5000	200	11
8.2	1000	20	30
4.7	600	10	53
Feed cabin No. 5			
14.4	2000	50	11
2.25	80	40	80
4.475	150	10	35
4.625	150	10	35
4.775	150	10	35
4.925	150	10	35

tains eight radiometers, which allow observations in fairly wide bands (5–15%) in the range from 1 to 32 GHz (five octaves).

We have paid great attention to the stabilization of supply voltages, stabilization of the currents in solid-state noise generators, galvanic isolation of power and control circuits, etc.

The data acquisition system for all the continuum radiometers is presented in Tsybulev (2011). Its architecture and software are unified for all the radiometers. The system is easily scalable: when new radiometers are added, new modules of the data logging system are added as well. Also, the system can operate in both low-speed ($\sim$64–512 Hz) and high-speed (up to 16 kHz) modes.

3 Decimeter-wave radiometers

Observations in the decimeter ranges—1245 MHz (bandwidth $B = 50$ MHz) and 2250 MHz ($B = 80$ MHz)—are complicated by severe interference conditions. We currently work on upgrading the decimeter radiometers to enable active rejection of the interference. Two dual-band horn antennas have been designed and manufactured for us for this task. Both antennas have two identical ranges: 1450 MHz ($B = 100$ MHz) and 2250 MHz ($B = 100$ MHz). The appearance of horn antennas is shown in Fig 1.

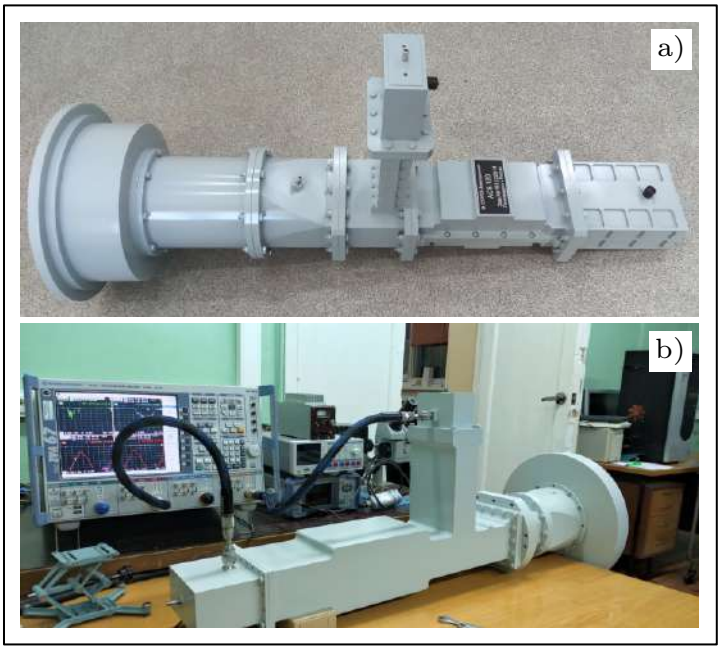

Fig. 1. Dual-band (13 and 25 cm) decimeter-wave antennas: (a) development of SKARD-Electronics, Kursk; (b) development of the Special Design Bureau of the Institute of Radioengineering and Electronics of the Russian Academy of Science.

For the possibility of active interference rejection, we develop a two-band digital receiver-spectrum analyzer designed to be used as a digital backend of the radiometer. The spectroanalyzer is designed to operate in three modes. The first is time–frequency interference suppression. This mode has a low spectral resolution of 128 channels in the 100 MHz band and low temporal resolution (100 milliseconds). In this mode, complete or partial removal of channels with interference is assumed. The remaining clear channels will be combined to receive a broadband signal. The second mode

of operation is the mode of observing fast radio bursts (FRBs). This mode will also have a high spectral resolution (32 channels in the 100 MHz band) and high temporal resolution (10 microseconds). In this case, short (<1 second) pulses will be analyzed for the presence of FRB signals. The third mode of spectroanalyzer operation is the high spectral resolution mode for observing spectral lines. The temporal resolution in this mode, as in the first one, is 100 milliseconds. The use of new antennas and spectrum analyzers at the outputs of the decimeter receivers will effectively solve all these tasks.

4 Summary

In this paper, we presented the result of many years of efforts in creation of multifrequency radiometric complexes on the RATAN-600 radio telescope. The latest results obtained with the help of our receiving systems are presented in Vlasyuk et al. (2023); Trushkin et al. (2023); Sotnikova et al. (2023); Veledina et al. (2024); Trushkin et al. (2024); Krishna Mohana et al. (2024).

Funding

This work was supported by the Ministry of Science and Higher Education of the Russian Federation.

References

Berlin A.B., Parijskij Yu.N., Nizhelskij N.A., et al., 2012, Astrophysical Bulletin, 67, 3, p. 340
Krishna Mohana A., Gupta A.C., Marscher A.P., et al., 2024, Monthly Notices of the Royal Astronomical Society, 527, p. 6970
Sotnikova Yu.V., Wu Z., Mufakharov T.V., et al., 2022, Monthly Notices of the Royal Astronomical Society, 510, p. 2495
Trushkin S.A., Bursov N.N., Shevchenko A.V., et al., 2024, The Astronomer's Telegram, 16581
Trushkin S.A., Shevchenko A.V., Bursov N.N., et al., 2023, Astrophysical Bulletin, 78, 2, p. 225
Tsybulev P.G., 2011, Astrophysical Bulletin, 66, 1, p. 109
Tsybulev P.G., Nizhelskii N.A., Dugin M.V., et al., 2018, Astrophysical Bulletin, 73, 4, p. 494
Tsybulev P.G., Nizhelskij N.A., Dugin M.V., et al., 2022a, Astrophysical Bulletin, 77, 4, p. 516
Tsybulev P.G., Nizhelskij N.A., Dugin M.V., et al., 2022b, Proceedings of Science, 425, id. 15
Veledina A., Muleri F., Poutanen J., et al., 2024, Nature Astronomy, 8, p. 1031
Vlasyuk V.V., Sotnikova Yu.V., Volvach, A.E., et al., 2023, Astrophysical Bulletin, 78, 4, p. 464

VAK 2024 MODERN ASTRONOMY: FROM THE EARLY UNIVERSE TO EXOPLANETS AND BLACK HOLES 300 years Russian Academy of Sciences

Systematic effect in the standard processing of gravitational-wave signals

V. Yershov[1], A. Raikov[2], and E. Popova[3]

[1] Saint Petersburg State University of Aerospace Instrumentation,
67 Bol'shaya Morskaya, St. Petersburg, 190000 Russia
[2] Special Astrophysical Observatory of the Russian Academy of Sciences,
Nizhny Arkhyz, 369167 Russia
[3] Central Astronomical Observatory of the Russian Academy of Sciences at Pulkovo,
65(1) Pulkovskoye shosse, St. Petersburg, 196140 Russia

Abstract. We analyze a systematic effect in the standard coordinate transformation of a gravitational-wave signal from the source to the detector reference frame. It is shown that, despite the mathematically correct application of the canonical Arnowitt–Deser–Misner transform (ADM formalism), the estimated characteristic mass of the source (a binary system of merging black holes) turns out to be affected by a systematic error if the mass estimation is based on the the time derivative of the signal frequency obtained in the detector reference frame, and not in the source reference frame. This systematic error leads to a significant overestimation of distances to gravitational wave sources, which reduces the probability that large ground-based telescopes detect possible electromagnetic afterglows associated with gravitational wave sources.

Keywords: stars: black holes; gravitational waves; methods: analytical

DOI: 10.26119/VAK2024.179

1 Introduction

Einstein's idea that a system of two massive bodies can emit gravitational waves (GWs) is based on the representation of the metric tensor as a linearized decomposition using a flat metric and a small perturbation propagating at the speed of light. This approximation of general relativity (called the quadrupole approximation) allows us to estimate the energy loss of a binary system due to the emission of GWs, which determines the orbital frequencies $f_{\rm orb}$, their derivatives in time $\dot{f}_{\rm orb} = df_{\rm orb}/d\tau$, and the characteristic (chirp) masses $\mathcal{M}$ of the system via the Einstein–Landau–Lifshitz quadrupole moment formalism (Landau & Lifshitz 1960; Peters & Mathews 1963).

It is important to note that the calculation of energy losses must be done in the source reference frame, using proper time τ. But in the vicinity of the GW detector, there is no information about the evolution of a binary black hole system in the proper coordinates of this system. With this in mind, we revisit the analysis of the first gravitational-wave signal GW150914, which has already been done by the Laser Interferometer Gravitational-Wave Observatory (LIGO) team in their paper (Abbott et al. 2016) dedicated to the discovery. That publication describes a standard scheme for processing GW signals, which is considered rigorous in terms of relativistic transformations of reference frames.

We also discuss the second publication by the same authors (Abbott et al. 2017), where they present an alternative analysis of the same signal GW150914 using the quadrupole approximation of general relativity (an approximation of flat spacetime). Both strict and approximate versions of the analysis give coinciding estimates for the parameters of the source of the GW signal.

In our view, this coincidence should be carefully examined, since the curvature of spacetime in the vicinity of the merger of binary black holes is very large. Therefore, the source and detector reference systems are different, which means that the parameters of the source estimated for the curved and flat spacetime metrics must also be different.

2 Quadrupole approximation

The case of GW150914. In the paper of Abbott et al. (2016), describing a relativistically strict method of processing the GW150914 signal, the following estimate of the characteristic (chirp) mass of this binary system is given: $\mathcal{M}^{\rm LVC16} = 30.4^{+2.1}_{-1.9}\,M_\odot$.

In their second paper, Abbott et al. (2017) used the following quadrupole approximation formula to estimate the chirp mass $\mathcal{M}$ of the system:

$$\mathcal{M}(f_{\rm gw}, \dot{f}_{\rm gw}) = \frac{c^3}{G}\left[\frac{5}{96}\pi^{-8/3} f_{\rm gw}^{-11/3}\dot{f}_{\rm gw}\right]^{3/5}, \quad (1)$$

where c is the speed of light, G is the gravitational constant, and the chirp mass is defined as $\mathcal{M} = (m_1 m_2)^{3/5}/(m_1+m_2)^{1/5}$ via the component masses m_1 and m_2. The result of this calculation, $\mathcal{M}^{\rm LVC17} \approx 37\,M_\odot$, is slightly different from the strict result, since the time intervals between the zero crossings of the signal with the abscissa used in Abbott et al. (2017) are quite noisy, and the number of points used is small. If we reduce the noise by taking the input frequencies $f_{\rm GW}$ and their derivatives $\dot{f}_{\rm GW}$ directly from a smoother frequency–time diagram (Yershov et al. 2023), then Eq. (1) gives us an average value of $\mathcal{M} = 30.1 \pm 2.4\,M_\odot$, almost identical to the original result.

Other cases from the Gravitational-Wave Transient Catalogue (GWTC). In addition, we can check whether other GW sources detected by the LIGO–Virgo–Kagra collaboration show that the source-to-detector coordinate transformation is incomplete, as is the case with the source GW150914. To this end, we compared the chirp masses published in the GWTC with the masses estimated using the quadrupole (post-Newtonian) approximation formula, Eq. (1). The result is shown in Fig. 1, the numerical values of the masses are presented in the appendix table in Yershov et al. (2023).

In this plot, the chirp masses $\mathcal{M}_{\rm GWTC}$ of the sources obtained by strict processing of GW signals are plotted along the vertical axis. These masses (in the coordinate system of the detector) are taken from Abbott et al. (2019); Venumadhav et al. (2020); Nitz et al. (2020); Abbott et al. (2020a,b,c). The chirp masses we have calculated using Eq. (1) for flat spacetime are plotted along the horizontal axis. We can see that the matched masses are grouped along the diagonal of the graph in the form of a linear dependence, and the Pearson correlation criterion for this dependence gives a correlation coefficient of $0.985^{+0.004}_{-0.008}$ and a p-value of $< 2.2 \cdot 10^{-16}$. This correlation is evidence that the gravitational time dilation correction was missing in the calculations of the chirp masses published in the GWTC, since Eq. (1) for flat spacetime that we have used does not include such a correction by definition.

3 Coordinate transformation

The metric coefficient g_{tt} near the horizons of black holes decreases greatly. Therefore, a remote observer should perceive the orbital motion of such a system as slowed

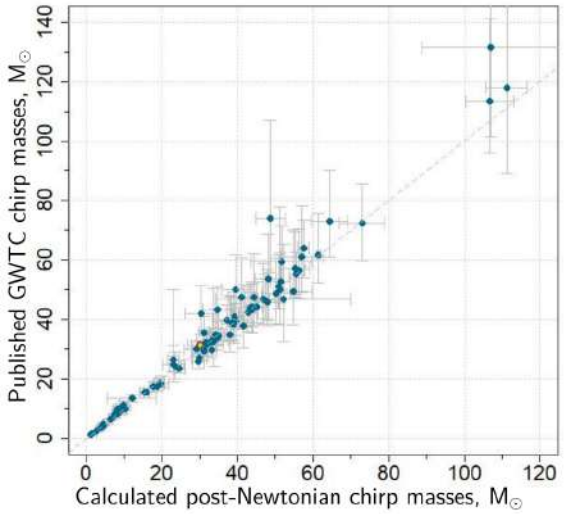

Fig. 1. Diagonal plot comparing the 97 GWTC chirp masses $\mathcal{M}_{\rm GWTC}$ (in the detector frame) and those calculated using the quadrupole post-Newtonian approximation: $\mathcal{M}_{\rm PN}$ (Eq. 1).

down. For example, for the last stable circular orbit in the Schwarzschild metric, the observed orbital frequency (and hence the frequency of GWs $f_{\rm GW} = 2f_{\rm orb}$) decreases by a factor of $\sqrt{2/3}$ (Zeldovich & Novikov 1967). Therefore, if the scheme for processing GW signals for curved spacetime gives the same result as the scheme for flat spacetime, then we can conclude that the time-dilation function $\alpha = \sqrt{g_{tt}}$ has somehow fallen out of the calculations for curved space.

A simple example given below for the case of the circular orbital motion of a test mass μ around the central mass M in the Schwarzschild metric shows how the time-dilation function α can, indeed, fall out of formalism even with an absolutely accurate relativistic calculation. For a circular orbit, the specific angular momentum $\tilde{\mathcal{L}} = p_\varphi/\mu = u_\varphi$ is

$$\tilde{\mathcal{L}} = \sqrt{\frac{rGM/c^2}{1 - 3GM/(rc^2)}}, \tag{2}$$

and the specific energy $\tilde{\mathcal{E}} = -p_t/\mu = -u_t$ is

$$\tilde{\mathcal{E}} = \frac{1 - r_g/r}{\sqrt{1 - 3GM/(rc^2)}}. \tag{3}$$

Consequently,

$$u^\varphi = \frac{d\varphi}{d\tau} = \frac{u_\varphi}{g_{\varphi\varphi}} = \frac{\tilde{\mathcal{L}}}{r^2}, \quad u^t = \frac{dt}{d\tau} = \frac{u_t}{g_{tt}} = \frac{\tilde{\mathcal{E}}}{1 - r_g/r}, \tag{4}$$

where τ is the proper (local) time in the source reference frame of the orbiter, g_{tt} and $g_{\varphi\varphi}$ are the spacetime metric coefficients for, respectively, time and the azimuthal angle in spherical coordinates, $\sqrt{g_{tt}}$ being the time-lapse function α. Then, by calculating $d\varphi/dt$ we obtain the angular frequency of the orbital motion in coordinate time t, i.e., in the reference system of a remote observer (detector):

$$\omega^{\rm det} = \frac{d\varphi/d\tau}{dt/d\tau} = \frac{u^\varphi}{u^t} = \sqrt{\frac{GM}{c^2 r^3}}, \tag{5}$$

which coincides with Kepler's non-relativistic formula for orbital motion. Thus, even though Eq. (5) is relativistically precise, the lapse and shift functions of the Schwarzschild metric fall out of the equations of motion when passing from the source reference frame (time τ) to the detector reference frame (time t) because they are canceled in the expression u^φ/u^τ.

The standard GW signal processing scheme uses a more complex coordinate transformation developed by Arnowitt et al. (1959) and abbreviated as the ADM formalism. Within this formalism, the energy-momentum tensor is integrated throughout space, after which the reduced action functional is varied, which gives equations of motion from which the lapse and shift functions are omitted, similar to Eq. (5). This mechanism of the omission of the lapse and shift functions is described in more detail in the reviews by Schäfer (1985); Schäfer & Jaranowski (2018).

4 Distance scaling

Due to the degeneracy of the relationship between the calculated chirp masses of merging binary systems and the distances to these systems, the theoretical amplitude of the GW signal is proportional to the 5/3 power of the chirp mass (Eq. 1). Therefore, if the chirp masses of GW sources are overestimated, then the estimates of distances to these sources are even more overestimated.

We can rescale these overestimated distances using the ratio between corrected and uncorrected chirp masses:

$$D_L^c = \left(\frac{\mathcal{M}^c}{\mathcal{M}}\right)^{5/3} D_L, \tag{6}$$

where D_L^c is the rescaled GW luminosity distance, D_L is the published distance, $\mathcal{M}$ and $\mathcal{M}^c$ are the original and corrected chirp masses of a coalescing binary system.

The recalculated distances D_L^c to 97 GW sources detected during the three observing runs of the LIGO–Virgo–Kagra collaboration are shown in Fig. 2 with black dots. For comparison, the original (uncorrected) chirp masses from the GWTC and their corresponding luminosity distances are shown as gray dots.

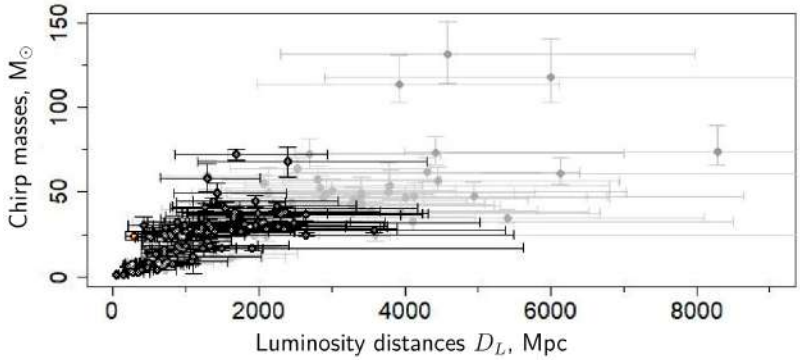

Fig. 2. Corrected chirp masses $\mathcal{M}^{\rm c}$ of 97 black hole mergers (vetical axis) from three observing runs of the LIGO–Virgo–Kagra collaboration and distances $D_L^{\rm c}$ to these systems (abscissa) corrected by Eq. (6). The gray dots mark the initial (uncorrected) chirp masses and luminosity distances of the GW systems published in the GWTC.

5 Summary

It can be concluded that in the calculated chirp masses of binary black hole systems detected by interferometric gravitational wave detectors, there is a systematic overestimation effect. This effect is accompanied by an even greater overestimation of distances to the sources of gravitational waves.

References

Abbott B.P., Abbott R., Abbott T.D., et al., 2016, Physical Review Letters, 116, id. 061102
Abbott B.P., Abbott R., Abbott T.D., et al., 2017, Annalen der Physik, 529, 1-2, id. 1600209
Abbott B.P., Abbott R., Abbott T.D., et al., 2019, Physical Review X, 9, id. 031040
Abbott B.P., Abbott R., Abbott T.D., et al., 2020a, Astrophysical Journal Letters, 892, L3
Abbott R., Abbott T.D., Abraham S., et al., 2020b, Astrophysical Journal Letters, 896, L44
Abbott R., Abbott T.D., Abraham S., et al., 2020c, Physical Review D, 102, id. 043015
Arnowitt R., Deser S., Misner C.M., 1959, Physical Review, 116, p. 1322
Landau L.D. and Lifshitz E.M., 1960, The Course of Theoretical Physics. Volume 2. The Classical Theory of Fields, Fizmatlit, Moscow
Nitz A.H., Dent T., Davies G.S., et al., 2020, Astrophysical Journal, 891, 123
Peters P.C. and Mathews J., 1963, Physical Review, 131, p. 435.
Schäfer G., 1985, Annals of Physics, 161, p. 81
Schäfer G. and Jaranowski P., 2018, Living Reviews in Relativity, 21, id. 7
Venumadhav T., Zackay B., Roulet J., et al., 2020, Physical Review D, 101, id. 083030
Yershov V.N., Raikov A.A., Popova E.A., 2023, Physica Scripta, 98, 7, id. 070519
Zeldovich Ya.B. and Novikov I.D., 1967, Relativistic Astrophysics, Nauka, Moscow, p. 82

VAK 2024 MODERN ASTRONOMY: FROM THE EARLY UNIVERSE TO EXOPLANETS AND BLACK HOLES 300 years Russian Academy of Sciences

Interactive multi-instrumental database of solar activity observations

I. Berezin[1], E. Illarionov[2], and A. Tlatov[1]

[1] Kislovodsk Mountain Astronomical Station, Kislovodsk, 357722 Russia
[2] Moscow State University, Moscow, 119991 Russia

Abstract. The project of creating a center of access to solar activity data on the basis of domestic ground-based observations is presented. The center uses a complex of automated systems for recognition of solar activity objects. The observational data are based on the continuous synoptic observations at the Kislovodsk Mountain Astronomical Station (KMAS) of the Central Astronomical Observatory of the Russian Academy of Sciences. The KMAS data we are considering are images of the solar photosphere, chromosphere, corona, and observations of the magnetic fields on the Sun. The creation of the system will allow users to find the data on individual events as well as to conduct statistical studies of a large number of events using an interactive database interface. The concept behind the operation of our computer vision system is that the data will be analyzed almost in real time as soon as they arrive to the KMAS operations center and undergo basic processing. This will allow the system to issue space weather alerts in due time as well as to create images and videos for quick viewing and to archive the solar activity data. The complex and a unique data processing pipeline consisting of hardware and control software that has been created at the KMAS is described. We build software modules that detect, track, and analyze numerous phenomena in real data streams, including flares, filaments, sunspots, active regions, coronal holes, coronal mass ejections (CMEs), coronal oscillations, and jets. Detections of CMEs and filaments are made based on the continuous data from the Solar Patrol Optical Telescopes (SPOT).

Keywords: Sun: activity, chromosphere, magnetic fields; virtual observatory tools

DOI: 10.26119/VAK2024.180

1 Introduction

The KMAS has a long history of the synoptic observations of the Sun using a wide range of instruments (Fig. 1): the white light measurements, on the basis of which the observatory has been obtaining long series of sunspot parameters since 1954; the coronograph measurements in the lines 5303 Å and 6374 Å; the chromospheric images in the cores of the Ca II K and H_α lines to determine the geometric characteristics of plages and filaments (prominences). Since 2014, daily observations of the magnetic field on the full disk of the Sun have been continuously carried out using the STOP magnetograph (Tlatov et al. 2015). In addition, the solar patrol optical telescopes (SPOT) (Berezin et al. 2023) are used to make minute-by-minute measurements of the Ca II K and H_α line profiles with a resolution of 40 000 on the full disk of the Sun, which allows detailed diagnostics of the chromospheric parameters with a spatial resolution of about $1''.5$. The observations in the radio band at wavelengths of 3.2 and 4.9 cm and the measurements of the Earth's magnetic field are also carried out in continuous mode.

Some of the most relevant data are published on the observatory website.[1] The objects (spots, filaments, etc.) are detected on the images of the Sun by computer vision methods under the control of operators, and their contours are daily plotted on the three-dimensional interactive map "Observe The Sun"[2] presented on the Internet. There is also an API[3] for querying the contours of all the objects featured on the "Observe The Sun" map.

However, for a number of technical reasons, maintaining and developing "Observe The Sun" is becoming more and more challenging each year. Therefore, there is a need to develop an alternative data presentation system. Another major challenge is to organise the open access to the huge amount of spectral and spectropolarimetric data from the SPOT and STOP instruments.

2 Description of the database

Over the entire period of the SPOT (since 2011 in the Ca II K line and since 2015 in the H_α line) and STOP (since 2014) observations, we have accumulated a large amount of low-level data: optical spectra from all over the solar disc. These are on the order of $7 \cdot 10^{11}$ complete spectral line profiles. The total volume of the dataset

[1] http://en.solarstation.ru/
[2] https://observethesun.com/
[3] https://github.com/observethesun/helio

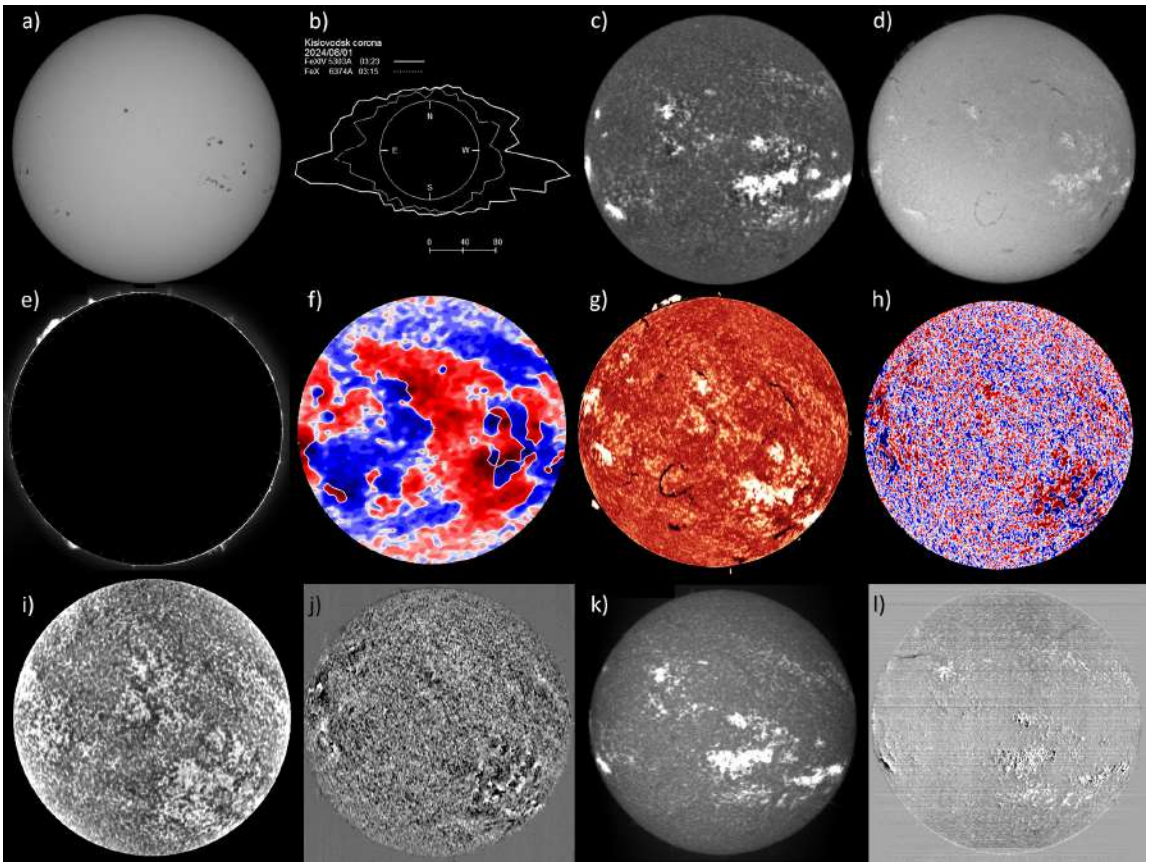

Fig. 1. The main types of the observations at the KMAS: (a) photosphere in white light; (b) coronal intensity in the lines 5303 Å and 6374 Å; (c) intensity in the core of the Ca II K line; filter measurements of the intensity in the H_α line core on the solar disc (d) and in the prominences (e); (f) line-of-sight component of the magnetic field; H_α line core image (g), H_α Doppler velocities (h), H_α line width (i), and the intensity difference in the wings of the H_α line (j) from the SPOT H_α observations; Ca II K core intensity (k) and the intensity difference in the wings of the Ca II K line (l) from the SPOT Ca II K observations.

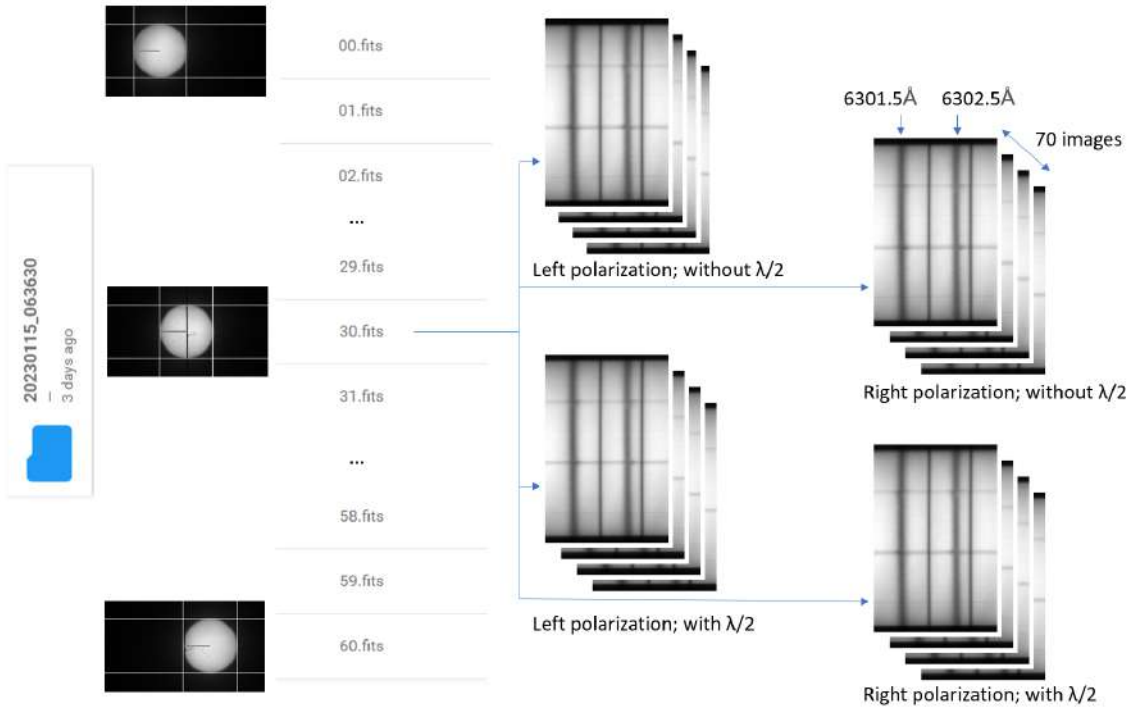

Fig. 2. Structure of the STOP magnetograph data: different polarization components of the spectra near the Fe I 6301.5 Å and 6302.5 Å magnetosensitive lines; measurements with a $\lambda/2$ plate are used to eliminate instrumental polarization.

is about 160 TB. We have organised the open access[4] to these data in cooperation with Kalmyk State University.

The data server runs on two Intel® Xeon® Silver 4214R processors and has a total disc space of 320 TB. The data are presented as level 0 and level 1 data. Level 0 are the frames of the spectra, numbered in the order in which the image of the Sun passes through the spectrograph slit. A more detailed description of the SPOT spectra can be found in Berezin et al. (2023). The STOP magnetograph data are presented in a similar way, except that at each position of the Sun's image on the spectrograph slit, spectra of four different types of light are recorded: with the left circular polarization, with the right circular polarization, and the same but with a half-wave phase plate placed in front of the instrument (Fig. 2).

Level 1 is our version of spectral data processing presented in FITS and JPG format. In the case of STOP, these are daily maps of the line-of-sight component

[4] http://solar-data.ru:8080/

of the magnetic field on the full disc of the Sun. The SPOT data are presented as multilayer images containing the intensity in the line core, Doppler shifts and spectral line width (according to the single-component chromospheric model), the intensity difference in the blue and red wings of the line, the continuum image, and 3 layers containing technical information.

3 Conclusion

The creation of a multispectral database of solar activity is a priority national task. We have presented our variant of some elements of its implementation. The open access to the lowest-level data, in our opinion, is an important element for the development of the observing and data processing methods. National databases of active regions, flares, CMEs, etc. should be created on the basis of low-level data. It is necessary to create data application models and software for users of different experience.

Funding

The study was carried out under state assignment No. 075-03-2023-121/3 of the Ministry of Science and Higher Education of the Russian Federation.

References

Berezin I.A, Tlatov A.G., Pevtsov A.A., 2023, Astrophysical Journal, 950, p. 100

Tlatov A.G., Dormidontov D.V., Kirpichev R.V., et al., 2015, Geomagnetism and Aeronomy, 55, p. 969

VAK 2024 MODERN ASTRONOMY: FROM THE EARLY UNIVERSE TO EXOPLANETS AND BLACK HOLES 300 years Russian Academy of Sciences

A method to reveal and catalog solar flares observed with the Siberian Radioheliograph: first results

D. Rozhkova, L. Kashapova, and A. Gubin

Institute of Solar-Terrestrial Physics of Siberian Branch of Russian Academy of Sciences, Irkutsk, 664033 Russia

Abstract. We present the first results of our work on creating a catalogue of solar flares observed with the Siberian Radioheliograph (SRH). A technique to find possible solar flare events has been developed. This technique is based on the analysis of the derivatives of temporal profiles and allows one to identify the start, peak, and end moments of events of various intensities. We tested this technique using time profiles of solar soft X-ray emission, which is currently the main indicator of solar flares. The results of the testing of the technique has shown good detection of flare events for one-dimensional data. As the SRH is a multi-frequency instrument, the technique has been improved by adding the ability to automatically identify events based on the simultaneous response at different frequencies.The method was tested to detect solar flares observed with the SRH in the 3–24 GHz range. In total, we revealed about 600 events of various importance classes during the summer months of 2023 and about 300 solar flares occurred in May 2024. The developed software allows one not only to reveal the onset and end of a flare but also provides dynamic spectra that can be used for further analysis of the event.

Keywords: Sun: flares; catalogs

DOI: 10.26119/VAK2024.181

1 Introduction

The volume of the observed solar data is increasing dramatically due to the development of new instruments with high temporal resolution for a wide range of the electromagnetic spectrum. This has led to the need for automated and reliable event detection in large data streams and cataloguing of the events. Nowadays, the techniques to automatically search for and identify solar flares are applied to data from several instruments. The most well-known of them is the soft X-ray emission temporal profiles obtained with the Geostationary Operational Environmental Satellite (GOES). The technique identifies solar events using observations in the 1–8 Å spectral band, which are simultaneously used to classify solar flares.[1] The GOES flare event catalogue provides valuable information for both solar physics and the studies of geoeffective events, but it should be noted that in some cases weak or slow-developing events may be missed in this catalogue. The other example of an X-ray solar flare emission catalogue is the Konus-Wind (KW) instrument database of solar flares (Lysenko et al. 2022). The catalogue presents the events that were observed by the KW instrument in trigger mode with high temporal and spectral resolution. Thus, slowly developing and weak events are still not included in the event list. The catalogues of solar flares observed with the Nobeyama Radioheliograph and Nobeyama radio polarimeters provide microwave observations.[2] However, both lists appear to be incomplete, as some weak events may have been missed.

The start of the observations with the Siberian Solar Radioheliograph (SRH, Altyntsev et al. 2020) has shown the possibility to observe events of different power and duration within the 3–24 GHz range with high spectral and temporal resolution. The aim of our study was to develop an original technique to automatically detect the events in the multi-frequency data obtained with the SRH.

2 Algorithm description and testing on the GOES data

The developed technique is based on the analysis of time profile derivatives. The time profile at any spectral band can be represented as a continuous numerical function on a uniform time scale. As the 1D evolution of a solar flare is described as a sudden increase in flux followed by a continuous decrease, we can use the derivative to determine the start, maximum, and end of the event. At the first step, we calculate the standard deviation (σ) of the time derivative profile for a time interval without events. If time derivatives are greater than 3σ, we assume that the signal is an event.

[1] https://www.swpc.noaa.gov/products/goes-x-ray-flux
[2] https://solar.nro.nao.ac.jp/norp/html/event/

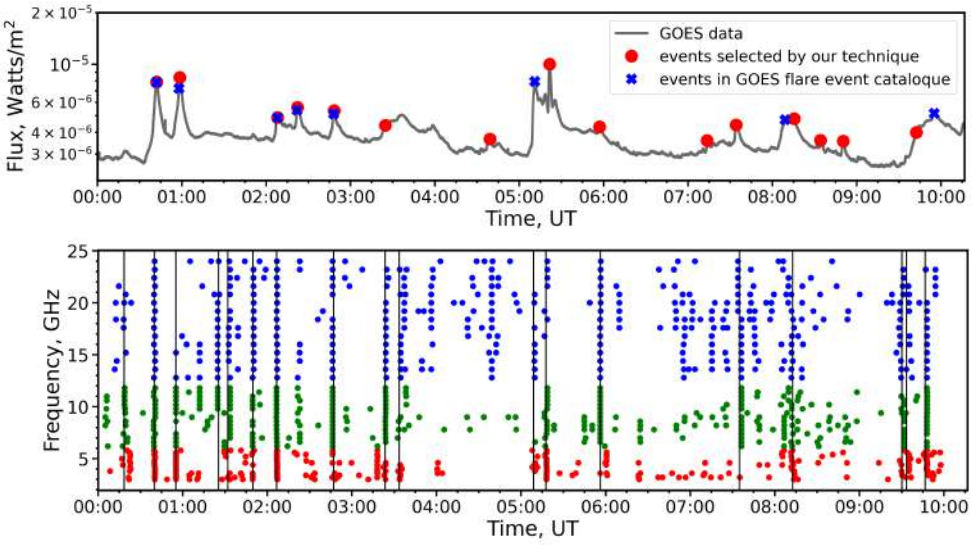

Fig. 1. Top: results of flare event detection in X-ray emission. The grey line is the 1–8 Å temporal profile on July 13, 2023. The blue marks indicate the events from the GOES flare catalogue, and the red marks show the results derived using our technique. Bottom: a chart of microwave bursts detected with the SRH within the 3–24 GHz range on July 13, 2023. The red, green, and blue colors mark the 3–6 GHz, 6–12 GHz, and 12–24 GHz arrays. The vertical lines show the selected events.

The start of the event is defined as the timestamp when the derivative has changed from the noise level to a positive value, indicating a sharp increase in the signal. The end of the event is the moment when the derivative changes from negative to the zero level, indicating the end of the decay phase. The peak of solar flares is calculated as the maximum of the time profile between the start and end moments. We tested the technique using the temporal profile of the 1–8 Å X-ray band obtained by GOES on July 13, 2023. The catalogue provided by the GOES team listed 8 events between 00:00 and 10:15 UT. Our method revealed 15 solar flares of different intensities, including some weaker events that have been not included in the GOES flare catalogue (see Fig. 1, top panel). Thus, the developed technique is effective for flare event detection and can find both powerful solar flares and the A and B class events.

3 SRH data testing and the results

The Siberian Radioheliograph is a multi-frequency interferometer consisting of three independent antenna arrays: 3–6 GHz, 6–12 GHz, and 12–24 GHz (Altyntsev et al. 2020). For solar event detection in SRH observations, we used the so-called correlation plots, which are the temporal profiles of the sum of correlation coefficients between

antenna pairs. These values are more sensitive to the occurrence of weak bursts than the usual flux (Lesovoi & Kobets 2017). As the SRH is a multi-frequency instrument, we need to improve the technique by adding the ability to automatically identify events using the results obtained from temporal profiles at each frequency. In most cases, a burst seen at a single frequency or a narrow-band burst can be a feature of non-solar signals or artifacts. Thus, we used the condition that a solar flare burst must be recognized simultaneously at at least 15 frequencies, and at least five frequencies should be in two different antenna arrays. This condition strongly limits the number of flare events. To keep the information about other possible events, we provide the information about all the revealed peaks in the chart. The peaks of the bursts related to the same event may not coincide at different frequencies. This can be due to both the features of SRH observations and the physical factors. Therefore, we assume that the bursts at different frequencies belong to the same event within an interval of 200 seconds. The example of a chart for the observation on July 13, 2023 is shown in Fig. 1 (the bottom panel). One can see that 18 events have satisfied the strict selection criteria and some of the events are weak and almost unrecognisable in X-rays.

The start and end moments of the events allow us to reconstruct the dynamic spectra of selected events using both correlation plots and fluxes in sfu (solar flux inits). These spectra provide information for further studies and allow us to obtain preliminary information about the spectral properties of a flare. In total, we have revealed about 600 events of various classes of importance during the June–September period of 2023, and about 300 solar flares occurred during May 2024.

Acknowledgements. The authors thank the GOES team for free access to the observed data.

Funding

The research was funded by the Russian Science Foundation, project No. 24-22-00315, (https://rscf.ru/project/24-22-00315/).

References

Altyntsev A., Lesovoi S., Globa M., et al., 2020, Solar-Terrestrial Physics, 6, p. 30

Lesovoi S. and Kobets V., 2017, Solar-Terrestrial Physics, 3, p. 19

Lysenko A., Ulanov M., Kuznetsov A., et al., 2022, Astrophysical Journal Supplement Series, 262, p. 32

MODERN ASTRONOMY: FROM THE EARLY UNIVERSE TO EXOPLANETS AND BLACK HOLES

Interactive service of geoeffective phenomena

M. Sapraliev, O. Mikhalyaev, L. Kharldaev, and B. Mikhalyaev

Kalmyk State University named after B. B. Gorodovikov, Elista, 358000 Russia

Abstract. This work attempts to develop an online service for the specialists and amateurs interested in the problem of space weather forecasting. It is based on the scheme of the existing "Observe the Sun" service developed by the employees of the Kislovodsk Mountain Astronomical Station (KMAS) of the Central Astronomical Observatory of the Russian Academy of Sciences for rapid demonstration of current solar activity phenomena. At the first stage, we consider one of the geoeffective factors, the solar wind, for calculation of which there exist generally accepted models. The initial data are the observations of the photospheric magnetic field, regularly carried out at the KMAS. The coronal field at the source surface and the velocity field are calculated using the well-known potential field source surface (PFSS) and Wang–Sheeley–Arge (WSA) models. At the next stage, we plan to simulate the solar wind flow at a distance of up to 1 AU and evaluate its geoeffectiveness.

Keywords: Sun: solar wind, corona, magnetic fields

DOI: 10.26119/VAK2024.182

1 Introduction

A promising direction in the development of solar and space weather services is the creation of various online resources designed to demonstrate active solar phenomena in real time. An example of such a domestic resource is the interactive three-dimensional synoptic map "Observe the Sun,"[1] created on the basis of observational data from the Kislovodsk Mountain Astronomical Station (KMAS) of the Central Astronomical Observatory of the Russian Academy of Sciences. There one can find, in particular, information about spots, flocculi, and prominences. Concerning the application of space weather forecasting, it is natural to create a similar map containing the information about geoeffective phenomena. This is a difficult task, since confident prediction of active phenomena such as flares and coronal mass ejections is an intractable problem to date. However, it is possible to obtaine some results such as the prediction of high-speed plasma flows. There is a developed Wang–Sheeley–Arge (WSA) method for calculating the solar wind velocity field based on the structure of the coronal magnetic field. We made an attempt to construct an interactive map using the KMAS photospheric magnetic field observations. They allow one to systematically evaluate the geoeffectiveness of high-speed solar plasma flows within the frameworks of the existing models. The KMAS has been recording coronal mass ejections using the Solar Telescope for Operative Prediction (STOP).They can serve as a basis for expanding the capabilities of the interactive map.

2 Magnetic field

The main input data are the distributions of the magnetic induction radial component B_r in the Sun's photosphere, represented in FITS files. We download these magnetograms from the KMAS website.[2] In addition, the magnetograms from the Global Oscillation Network Group (GONG) observatories are downloaded. An example of the images obtained from these FITS files is shown in Fig. 1.

A common method for modeling magnetic fields in the solar and stellar atmospheres is the potential field source surface (PFSS) model (Altschuler & Newkirk 1969; Mackay & Yeates 1999). The PFSS equations assume that there is zero electric current in the region of interest, which leads to the equations:

$$\nabla \cdot \mathbf{B} = 0, \quad \nabla \times \mathbf{B} = 0. \tag{1}$$

The system of equations (1) is solved in a spherical shell between the surface of the star and a tunable outer radius called the "source surface." The B_r boundary

[1] https://observethesun.com
[2] https://solarstation.ru

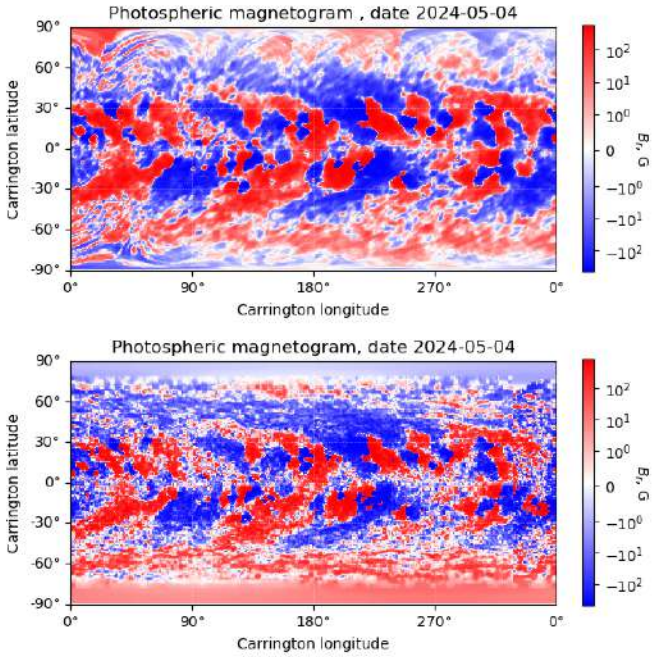

Fig. 1. The STOP (top) and GONG (bottom) distributions of B_r in the photosphere on 04.05.2024.

conditions are set at the inner boundary, and the condition of a purely radial magnetic field is superimposed at the source surface, which mimics the effect of fleeing stellar wind. The `pfsspy`[3] software is a well-documented library with tested functionality for performing the PFSS extrapolation. We computed the PFSS model and obtained the source surface layer. An example of the resulting image is shown in Fig. 2.

Wang & Sheeley (1990) introduced the parameter f_s characterizing the divergence of the force lines. The magnetic fields at the source surface ($B_{\rm S}$) and at the photospheric surface ($B_{\rm P}$) are used in the calculation of this parameter. Arge & Pizzo (2000) obtained a correlation coefficient of 0.39 between the wind speed and the divergence parameter f_s. These calculations has formed the basis of the widely used and cited WSA method (Arge & Pizzo 2000; Argeet al. 2004).

Belovet al. (2006) used the following velocity model:

$$V_{\rm SW}(t) = (393.2 \pm 7.6) + (192.9 \pm 40.0)\, W_S + (3.94 \pm 0.35)\, |B_{\rm S}| - (0.019 \pm 0.004)\, |B_{\rm P}|, \quad (2)$$

where

$$W_{\rm S} = 6.25\, (B_{\rm S}/B_{\rm P})^2. \quad (3)$$

[3] https://github.com/dstansby/pfsspy/tree/main

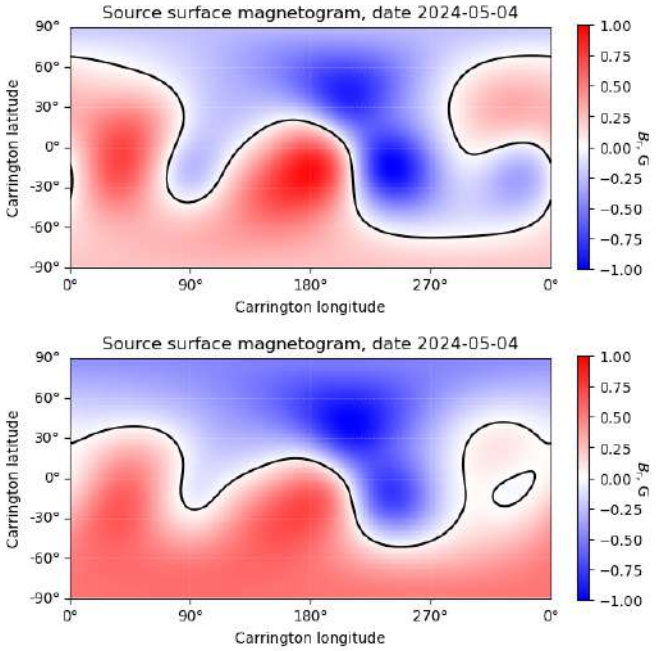

Fig. 2. The STOP (top) and GONG (bottom) distributions of B_r on the source surface on 04.05.2024.

Using this model, we obtained images of the solar wind speed distribution on the source surface. An example of the constructed image is shown in Fig. 3.

3 Interactive three-dimensional map

A three-dimensional model of the coronal magnetic field is implemented on the laboratory website. Using the `pfsspy` module, magnetic field streamlines are constructed. The seeds for line tracing are formed with a sufficiently small step, which allows us to achieve a resolution of $30'$. At the ends of the open magnetic lines lying on the photosphere, we form a set of points. This set is divided by the DBSCAN[4] algorithm into separate clusters which correspond to coronal holes. We find the parameters of the coronal holes such as area, magnetic flux, mean and maximum magnetic induction. In addition, the median is calculated from the set of cluster points to determine the center of the coronal hole. Its coordinates together with the date forms a unique identifier: the Solar Object Locator (SOL). Figure 4 demonstrates a resulting coronal hole. Similar visualization can be seen in Berezin & Tlatov (2022). The interactivity

[4] https://scikit-learn.org/stable/modules/generated/sklearn.cluster.DBSCAN.html

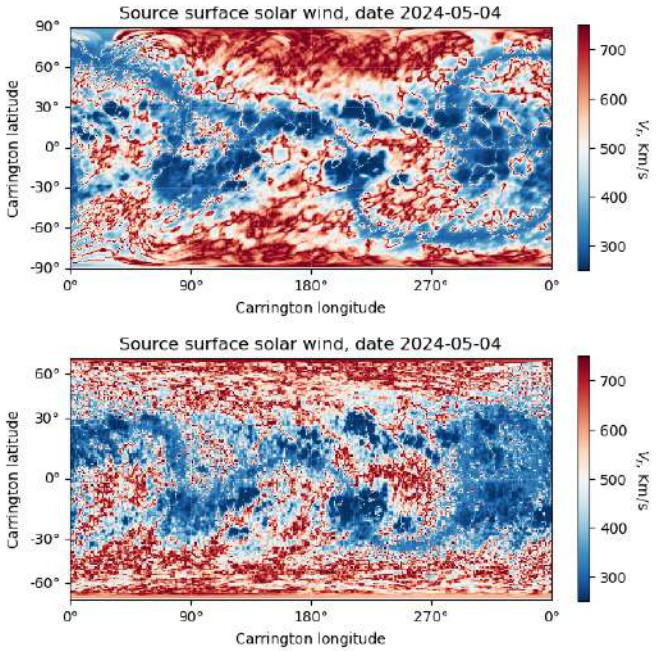

Fig. 3. The STOP (top) and GONG (bottom) distributions of V_r on the source surface on 04.05.2024.

of the model provides the possibility to change the viewing angle by mouse click and drag and the image size by scrolling the mouse wheel. A calendar is implemented on top, where one can select a desired date. The "hide details" button removes the coronal hole legend, leaving only the unique identifier.

4 Discussion

At this moment, we reconstruct the magnetic field of the solar corona in the potential approximation, assuming that the field on the photosphere is directed along the radius. Of course, a magnetic field with a horizontal component, as well as a nonpotential magnetic field, may give a more accurate picture. We can move to such an approach as soon as satisfactory theoretical models are available. The same is true for the velocity field at the source surface, for the calculation of which different approaches are possible. Considering the coronal hole parameters such as the total magnetic flux or the mean and maximum magnetic induction, we believe that they may be relevant for the development of new promising models of the velocity field.

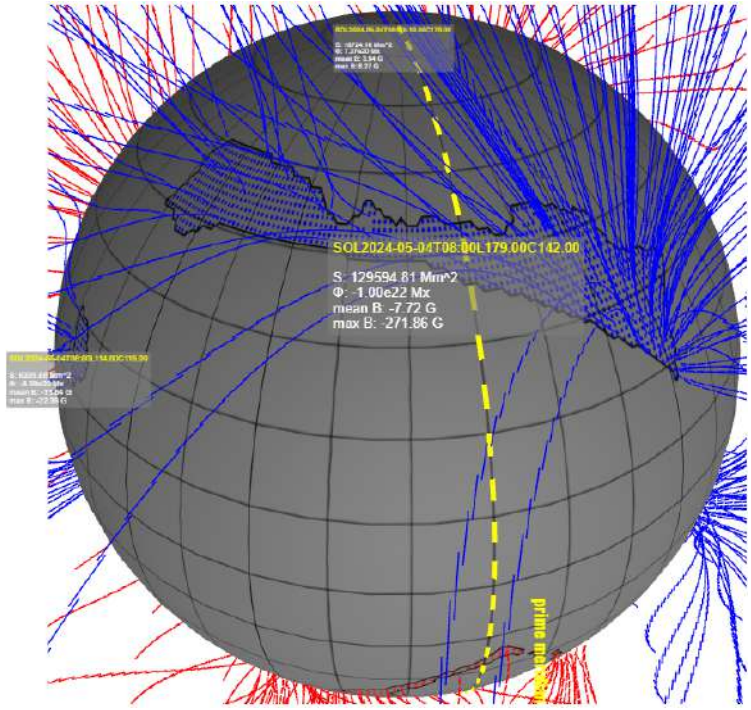

Fig. 4. A coronal hole image on 04.05.2024.

Acknowledgements. This research has made use of the observational data of the Kislovodsk Mountain Astronomical Station of the Pulkovo observatory and the observations of the Global Oscillation Network Group.

Funding

This work was supported by the Ministry of Science and Higher Education of the Russian Federation under contract No. 075-03-2024-113.

References

Altschuler M.D. and Newkirk G., 1969, Solar Physics, 9, 1, p. 131
Arge C.N., Luhmann J.G., Odstrcil D., et al., 2004, Journal of Atmospheric and Solar-Terrestrial Physics, 66, p. 1295
Arge C.N. and Pizzo V.J., 2000, Journal of Geophysical Research, 105, p. 10465
Belov A.V., Obridko V.N., Shelting B.D., 2006, Geomagnetism and Aeronomy, 46, 4, p. 456
Berezin I. and Tlatov A., 2022, Universe, 8, 12, id. 646
Mackay D.H. and Yeates A.R., 1999, Solar Physics, 9, p. 1
Wang Y.M. and Sheeley N.R. Jr., 1990, Astrophysical Journal, 355, p. 726

VAK 2024 MODERN ASTRONOMY: FROM THE EARLY UNIVERSE TO EXOPLANETS AND BLACK HOLES 300 years Russian Academy of Sciences

Improving the Quasar VLBI Network for data transfer with the National Research Computer Network of Russia

I. Bezrukov[1], A. Salnikov[1], V. Vasiliev[1], R. Plotnikov[2], A. Evseev[2], and A. Abramov[2]

[1] Institute of Applied Astronomy of the Russian Academy of Sciences, St. Petersburg, 191187 Russia

[2] National Research Centre "Kurchatov Institute," 1 Akademika Kurchatova Pl, Moscow, 123182 Russia

Abstract. This article presents the results of the phased integration of the VLBI complex "Quasar" into the National Research Computer Network of Russia (NIKS). The VLBI complex "Quasar" has implemented e-VLBI technology in Russia, enabling near real-time radio interferometric observations. This technology is critical for high-precision determination of Universal Time, which is essential for fundamental and applied space research, particularly for the GLONASS system. The complex consists of three observatories: "Badary" (Republic of Buryatia), "Zelenchukskaya" (Karachay-Cherkess Republic), and "Svetloe" (Leningrad Region), with a fourth under construction in Primorsky Krai. Each observatory can register data at speeds up to 16 Gbit/s, while the correlator in St. Petersburg can receive data at up to 96 Gbit/s. The current data transmission from "Badary" and "Zelenchukskaya" is limited to 2 Gbit/s, restricting the complex's functionality. Increasing the transfer speed to 8 Gbit/s or more would significantly improve capabilities. This article details the results of the data transfer speed tests conducted during hourly sessions to the Center for Correlation Processing of RAS in the NIKS network. Additionally, the article explores options for connecting the nearby academic organizations of the IAA RAS to the NIKS network via fiber-optic cable, enhancing the overall data transmission efficiency and reliability of the VLBI complex. The integration of these observatories into NIKS is expected to enhance the "Quasar" VLBI complex, enabling more robust and rapid data processing for various scientific applications.

Keywords: techniques: interferometric; telescopes

DOI: 10.26119/VAK2024.183

1 Introduction

The very-long-baseline interferometry (VLBI) complex "Quasar" has implemented e-VLBI technology in Russia, enabling near real-time radio interferometric observations. This technology ensures high-precision determination of Universal Time for fundamental and applied space research, particularly for the GLONASS system. The work at the Institute of Applied Astronomy of RAS (IAA RAS) provides independence in determining Earth Orientation Parameters (EOP). The complex consists of three observatories: "Badary" (Republic of Buryatia), "Zelenchukskaya" (Karachay-Cherkess Republic), and "Svetloe" (Leningrad Region), with a fourth under construction in Primorsky Territory. Each observatory can register data at speeds up to 16 Gbit/s, while the correlator in St. Petersburg can receive data at up to 96 Gbit/s. Current data transmission from "Badary" and "Zelenchukskaya" is limited to 2 Gbit/s, restricting the complex's functionality. Increasing the transfer speed to 8 Gbit/s or more would significantly improve capabilities.

A potential solution is integrating the Institute's network infrastructure into the National Research Computer Network of Russia (NIKS),[1] a successful example of such integration is given in Abramov et al. (2023).

2 NIKS bandwidth testing

To assess the NIKS network as a communication channel, bandwidth tests were conducted between the "Badary" observatory (connected via Rostelecom at 2 Gbit/s) and NIKS in St. Petersburg. For about a week, the data reception channel had been switched from the Veroline telecommunications service provider currently in use to NIKS. The test results are shown in Fig. 1. The results indicate that NIKS provides data transfer speeds comparable to Veroline, with consistent performance maintained across hourly observation sessions.

3 "Svetloe" observatory – CCP RAS channel testing

Following the positive test results, a phased transition to NIKS was planned for the VLBI complex observatories' data transmission to the Center for Correlation Processing of RAS (CCP RAS). Initially, the CCP RAS was connected to NIKS via a 40 Gbit/s channel, while the "Svetloe" observatory was connected at 4 Gbit/s. Figure 2 shows the data transmission results from the "Svetloe" observatory to the CCP RAS in July 2024. The speed tests revealed that organizing data transmission in four 1 Gbit/s streams efficiently utilized the allocated bandwidth.

[1] https://niks.su/

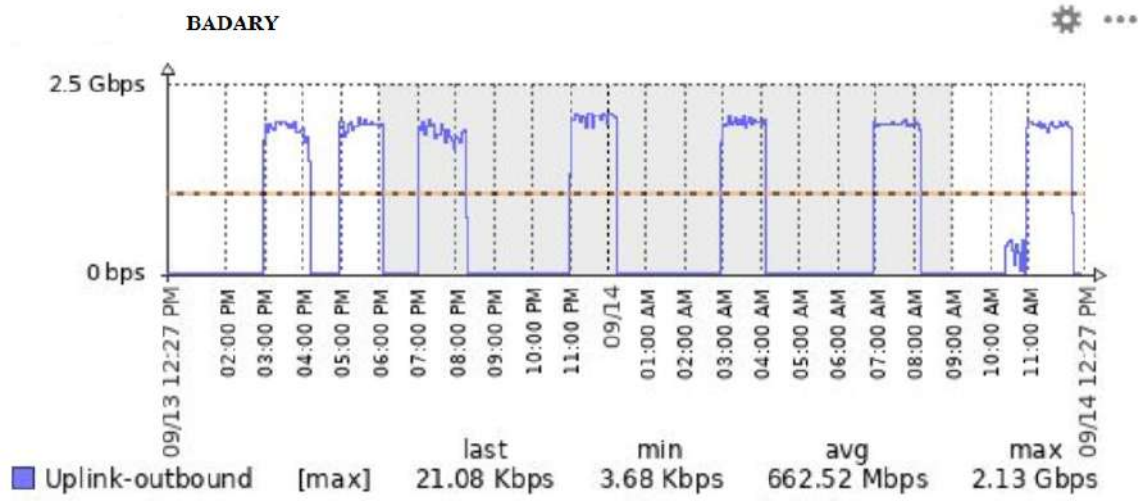

Fig. 1. Data transmission of hourly sessions from the "Badary" observatory to the CCP RAS via NIKS, St. Petersburg.

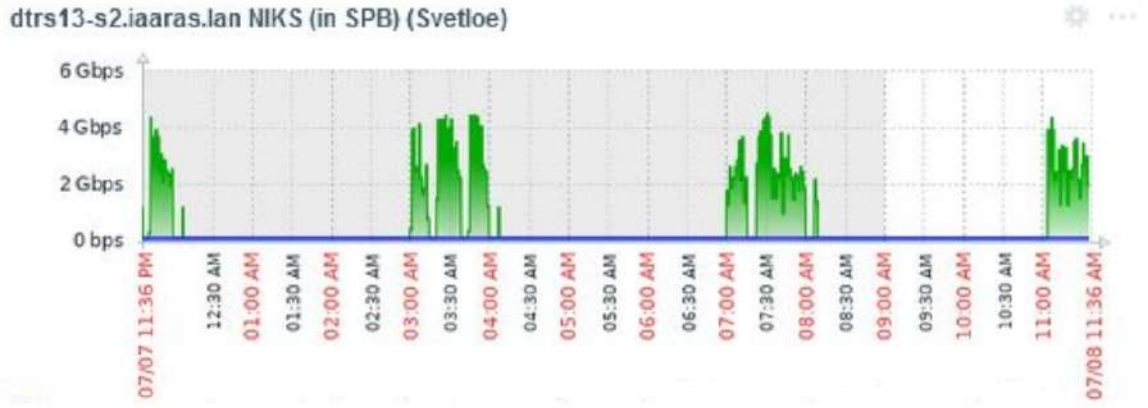

Fig. 2. Data transmission of hourly sessions from the "Svetloe" observatory to the CCP RAS through NIKS.

4 NIKS integration plans

Based on the positive interaction with NIKS, further integration of the observatories and nearby RAS institutes are planned.

First stage (2024). Connecting the "Zelenchukskaya" observatory to NIKS at 4 Gbit/s, establishing a regional access node for future expansion to other facilities like RATAN-600 of SAO RAS.

Second stage. Developing solutions to connect the "Badary" observatory and the nearby observatory of the Institute of Solar-Terrestrial Physics of the SB RAS to NIKS (currently connected to the Internet at 0.1 Gbit/s). Considering a possibility to switch the St. Petersburg units of the IAA RAS to NIKS to improve fault tolerance and data processing quality.

5 Conclusions

Successful cooperation with NIKS in 2024 enabled access to the NIKS network (traffic exchange node in St. Petersburg SPB-IX BM-18) for the CCP RAS via fiber-optic cable (FOC) with a bandwidth of 40 Gbit/s and for the "Svetloe" observatory of the IAA RAS VLBI complex in the Leningrad region via FOC with a bandwidth of 4 Gbit/s. This collaboration marked a significant milestone in enhancing the data transmission infrastructure for the "Quasar" VLBI complex.

The broadband access to the NIKS network for the CCP RAS and "Svetloe" observatory has ensured reliable data transmission from the observatory to the CCP RAS at a speed of about 4 Gbit/s. This improvement reduced the data transmission time of the hourly session to one hour, greatly increasing the efficiency of data processing and enabling more duly scientific analysis.

Additionally, a preliminary agreement was reached between NIKS and Rostelecom to connect the "Zelenchukskaya" observatory via FOC with a bandwidth of 4 Gbit/s in 2024. This forthcoming connection is expected to further enhance the data transmission capabilities of the VLBI complex, supporting higher data throughput and enabling more comprehensive and rapid data analysis.

References

Abramov A., Gonchar A., Evseev A., et al., 2023, Information Technologies, 12, p. 615

BAK 2024 MODERN ASTRONOMY: FROM THE EARLY UNIVERSE TO EXOPLANETS AND BLACK HOLES 300 years Russian Academy of Sciences

Information system and general archive of SAO RAS observations

O. Zhelenkova, T. Plyaskina, V. Shergin, G. Mal'kova, A. Velichko, and M. Kyabishev

Special Astrophysical Observatory of the Russian Academy of Sciences, Nizhny Arkhyz, 369167 Russia

Abstract. The telescopes of the Special Astrophysical Observatory of the Russian Academy of Sciences provide unique observational material. For observations, various astronomical instruments and data acquisition systems are used, which record observations with different data structures and descriptive parameters. The general archive of the observatory contains more than two dozen digital collections with observations obtained on various instruments. Maintaining an archival system requires software development, metadata management, fault tolerance, and periodic migration of files to modern storage media, which is important to ensure the long-term preservation of digital information. The archival system consists of three interconnected components that provide accumulation, long-term storage, and access to the data. The information system is implemented based on free PostgreSQL. The access to the archived files is provided through a web interface that supports queries by device, date, coordinates, object name, program applicant, and observer. The archive size is about 3 TB and its database contains more than 4 million records. The archive system uses two servers with directly connected storage systems. The main server implements data access, and the test server is used for development and testing. This configuration provides both permanent access to the files and the ability to modernize the information system.

Keywords: methods: observational, data analysis; astronomical databases: miscellaneous

DOI: 10.26119/VAK2024.184

1 Introduction

The history of the archive of SAO RAS observations began in the early 80s of the last century, when the accumulation of the data obtained on RATAN-600 and BTA had started to be carried out in digital form. This was the impetus for the development of the concept of a digital data bank (Vitkovskij et al. 1987; Kononov et al. 1990) as well as for the work on standardizing the observation file formats. The first digital archive was organized for the surveys of the Cold Experiment (Berlin et al. 1984). The self-documenting FITS format (Wells et al. 1981), which is the de facto standard for the presentation of astronomical data, came into use at the observatory in the late 1980s. This standard was first adapted to our observations and applied to the files (Vitkovskij et al. 1988) obtained with the observatory's first CCD camera (Borisenko et al. 1990). The FLEX format similar to FITS was then developed for the continuum radiometer data and used for the RATAN-600 observations.

As the data volume grew, the moment came when the information from the reel-to-reel magnetic tapes had to be rewritten onto various digital media such as streamer tapes, data cassettes, magneto-optical disks, and, finally, onto optical disks, which had begun to be used for permanent storage of the archive data since 1994. The experience of migrating the information and storing the data on streamers and magneto-optical disks was not very successful, since some part of the observations were lost.

According to the concept of an observatory databank (Vitkovskij et al. 1987), the general archive consists of local archives, with the local archive being a digital collection obtained by a single observing method provided by an astronomical instrument and its data acquisition system. The data in the general archive is stored in FITS and FLEX formats, the internal file format of the MIDAS system (Warmels 1992), as well as in binary files with text descriptions archived in tar files.

By 1999, the archive had contained more than 100 GB of data, and a search system had already been needed to access the archived files. Together with colleagues from the South Russian Regional Center for Informatization of Rostov State University and based on the local archive of the radiometer data from RATAN-600 feed cabin No. 1, a prototype of an information system with web access based on the Oracle DBMS[1] was created (Vitkovskij et al. 2000). For each observation in the database, a service block was formed from the parameters of the observation file recorded in the file header. It also included the attributes to identify the file.

In further work with the local archives, it turned out that the service information block contains an excessive number of parameters. We had to limit ourselves to

[1] https://www.oracle.com/cis/

those attributes that had been present in the files of all the local archives. And this attribute turned out to be the date of observation. Taking this into account, as well as the experience of the developing of the prototype, in 2003 we implemented an information system based on a trial version of Oracle. The information system had implemented the search by observing date in 14 local archives with the ability to copy files via a web interface (Zhelenkova et al. 2003, 2004).

To expand the number of the types of queries to observation files, a next version of the search system based on PostgreSQL[2] was implemented. It had provided data search using the standard set of queries. To describe each file in the database, the number of attributes had been increased, including the identification and location of the file in the storage space. In 2003, the IAU General Assembly passed a resolution[3] on the observations obtained by the publicly funded observatories, which noted that an observatory was obliged to place data in the public domain after the copyright of the applicants for the program expires. These provisions were taken into account in a new version of the search system (Zhelenkova et al. 2007, 2010).

Since 2013, using the software developed by Shergin (2014) we have been performing automatic coordinate calibration of direct images and/or correction of file headers. Files processed in this way are written to special local archives. To date, more than 300 thousand files from 4 local archives have been processed in this way.

In 2018, radio data was added that had to be migrated to our system from another archive system that was no longer supported. This doubled the number of files in the information system. At first, we implemented the access to files based only on observation date. Since 2023, the search for radio observations has been carried out using the standard set of requests.

The archival system is regularly updated with new data. The local archives of decommissioned instruments continue to be maintained. When new observing instruments are put into operation, a new local archive is organized and added to the system.

Basic information about the current state of the observatory's general archive of observations is presented in Zhelenkova et al. (2017, 2019, 2023).

2 The archive system

The general archive stores the data obtained with the observing methods used on the observatory's telescopes. This data includes observations, service files used in

[2] https://www.postgresql.org
[3] https://www.atnf.csiro.au/people/Ray.Norris/WGAD/Resolution.htm

processing the raw data, and observation logs. The archival system consists of three components:

(1) accumulation—cascade scheme of archiving;
(2) storage—hardware and software for permanent data storage;
(3) search and access—information system with web access.

The archive system has two databases located on two servers. Each server storage space has same structure and content. One server supports the working version of the archive, the second one supports the test version, with which we carry out and test all new developments. The support of the two databases ensures consistent data addition.

2.1 Cascade archiving scheme and storage space

The cascade archiving scheme defines the flow of data from the acquisition system to permanent archival storage. First, during observations, the data is accumulated on the acquisition system computer of this observing method. When the observing program changes, the data is moved to a dedicated space on the file server intended to the observing method. Then, from the observations obtained by one method, the image of an archive disk is formed. Its structure is formed according to the following rules:

(1) a label is generated with the disk number and the name of the local archive;
(2) observations from one night are placed in one directory, the name of which corresponds to the date of the observations;
(3) one observation is recorded in one file.

Then the image is written to an optical disc. Such a disk is part of the permanent offline storage of the archival system.

To ensure the integrity of data in case of destruction of physical media or input/output errors, we have two levels of the archive storage. The offline level is closed to user access. It includes two copies of optical disks with archival data and is used by an archive administrator when they need to restore data in the case of emergency failures.

The archive storage space on a dedicated server includes the PRIME directory, in which the copies of the optical disks are located, and the DATA directory, in which the copies of the disks are placed after verification and correction by our software tools.

Each disk is copied into the PRIME and DATA spaces into directories with names corresponding to the disk number in the offline level of the archive. The physical structure of the directories is superimposed on the logical structure, reflecting the distribution of the disks among local archives.

2.2 Information system

The information system of the general archive of observations is implemented in the PostgreSQL DBMS. Each observation file is described in the database tables by about 30 attributes. They are used for the dynamic formation of the web interface, for mapping the FITS parameters, and for file identification.

The database schema includes two dozen tables and views. The tables of the information system can be divided into three groups based on the frequency of adding new records. The first group includes the tables which are filled in when creating a database. New records can only be added in these tables when a new local archive is added into the information system. Such uploads do not occur often, so these tables can be considered as static. The second group comprises the tables that can be updated during CD/DVD disk analysis when a new item is added into the system for the first time, for example, a new observing program, an observer, etc. The third group includes the tables with the information about each archived file. Entries are added to the tables when ingesting new disks. In this process the tables of the first two groups are used for the analysis of a new disk. A special place is occupied by the table that links the attributes of the tables which store the information about observation files, with FITS header keywords and UCDs (Unified Content Descriptors) (Derriere et al. 2004).

3 Conclusion

Since astronomical observations do not lose scientific significance over time, their preservation is one of the main tasks of a digital archive.

Permanent archival storage means storing digital data collections for decades. This requires the mandatory storage, along with the collection files, of the description of its organization and metadata that allows the information to be interpreted. A permanent archive must search, access, and display the digital objects it stores, even if storage technologies change.

Since 2003, we have been taking into account these circumstances when developing and maintaining the archival system of the observatory. This experience of the management of various digital collections allowed us to develop the following approach to data preservation: data duplication, and on various types of digital media. To ensure the durability of the information system, the duplication of the database have been implemented on two dedicated servers. If one server fails, the second server can provide access to data. This also allows the archival system to be developed both in terms of software and in terms of adding new collections, because these actions are performed on the test server, and after verification they are transferred to the

working server. We also note that this organization of the archival system allows us to rewrite digital collections onto a new type of media.

Taking into account the existing equipment, the prospect of increasing data volumes, and modern technologies for supporting the persistent archives, we are considering a possibility to organize software-defined storage for our archive based on the iRODS software (http://irods.org) or similar systems (Zhelenkova et al. 2020).

References

Berlin A.B., Gassanov L.G., Gol'Nev V.Y., et al., 1984, Soobshcheniya Spetsial'noj Astrofizicheskoj Observatorii, 41

Borisenko A.N., Vitkovskij V.V., Zhelenkova O.P., et al., 1990, Bulletin of the Special Astrophysics Observatory, 32, p. 128

Derriere S., Gray N., McDowell J.C., et al., 2004, ASP Conf. Ser., 314, p. 315

Kononov V.K., Monosov M.L., Vitkovskij V.V., et al., 1990, Soobshcheniya Spetsial'noj Astrofizicheskoj Observatorii, 65, p. 32

Shergin V.S., 2014, Software for automatic calibration of coordinates of direct images, Tech. rep., SAO RAS

Vitkovskij V.V., Kononov V.K., Lipovetchkij V.A., et al., 1987, Development of the SAO AS USSR Archive, Tech. rep., SAO AS USSR

Vitkovskij V., Zhelenkova O., Kalinina N., et al., 2000, Baltic Astronomy, 9, p. 578

Vitkovskij V.V., Zhelenkova O.P., Ryadchenko V.P., et al., 1988, Soobshcheniya Spetsial'noj Astrofizicheskoj Observatorii, 59, p. 60

Warmels R.H., 1992, ASP Conf. Ser., 25, p. 115

Wells D.C., Greisen E.W., Harten R.H., 1981, Astronomy & Astrophysics Supplement, 44, p. 363

Zhelenkova O., Vitkovskij V., Chernenkov V., et. al., 2020, ASP Conf. Ser., 527, p. 69

Zhelenkova O.P., Vitkovskij V.V., Kalinina N.A., et al., 2003, Digital Libraries: Advanced Methods and Technologies, Electronic Collections, Proc. 5th All-Russian Conf., p. 359

Zhelenkova O.P., Vitkovskij V.V., Malkova G.A., et al., 2004, Digital Libraries: Advanced Methods and Technologies, Electronic Collections, Proc. 6th All-Russian Conf., p. 145

Zhelenkova O.P., Vitkovskij V.V., Plyaskina T.A., 2010, International Virtual Observatory—results of the first decade, Digital Libraries, Proc. Meeting, 13

Zhelenkova O.P., Vitkovskij V.V., Plyaskina T.A., et al., 2007, Open Internet access to the general archive of observations of the SAO RAS in the context of virtual observatory standards, Tech. rep., SAO RAS

Zhelenkova O.P., Vitkovskij V.V., Plyaskina T.A., et al., 2017, System synthesis and applied synergetics, Proc. All-Russian Conf., p. 143

Zhelenkova O.P., Vitkovskij V.V., Plyaskina T.A., et al., 2019, ASP Conf. Ser., 521, p. 128

Zhelenkova O.P., Vitkovskij V.V., Plyaskina T.A., et al., 2023, Acta Astrophysica Taurica, 4, p. 9

MODERN ASTRONOMY: FROM THE EARLY UNIVERSE TO EXOPLANETS AND BLACK HOLES

Teaching the basics of data science on astronomical data and catalogs

N. Arkhipova[1], A. Luzhnov[1], and N. Fedorov[2]

[1] National Research University "Higher School of Economics", 20 Myasnitskaya str., Moscow, 101000 Russia

[2] St.Petersburg State Maritime Technical University, 3 Lotsmanskaya str., St. Petersburg, 190121 Russia

Abstract. Today it is difficult to imagine research in the field of astronomy and astrophysics without qualitative and quantitative analysis of data obtained using modern astronomical instruments, the quantity and quality of which has grown significantly over the past quarter century. However, until now, this topic has not been studied in school astronomical education and pre-university training, which significantly hinders the inclusion of applicants and elementary students in scientific a nd r esearch work. Therefore, our report will describe the methods of teaching astronomical data analysis and working with astronomical catalogs of famous space projects. The results of testing these techniques when working with students of the HSE (Higher School of Economics) Lyceum and the Center for Pedagogical Excellence will also be discussed.

Keywords: astronomical databases: catalogs, reviews

DOI: 10.26119/VAK2024.185

1 Introduction

Due to the large number of modern ground-based and space observatories, the improvement of the quality of information receivers and the increase in the operating time of telescopes in the mode of surveys of the celestial sphere, a significant increase in observational data is observed in modern astrophysics. In this regard, today there is a serious problem of the methodology of teaching modern astronomy in the field of working with astronomical data (Korolev et al. 2021). Therefore, studying only the classical astronomy course does not give an idea of the modern work of astronomers and trends in the development of science (Drobchik & Nevzorov 2018), (Tihomirova et al. 2020). The most important, in our opinion, is the introduction into the astronomy training program of methods of working with astronomical data and numerous astronomical data catalogs that have appeared in recent decades, teaching modern schoolchildren and students methods of mathematical processing of observational data, as well as the ability to identify and find dependencies and correlations in these data. These methods will help students to connect more effectively and productively to research in astronomy at the modern level.

2 Working with astronomical observational data

2.1 Messier catalog

As a starting example when working with catalogs, it is logical to choose one of the first catalogs that appeared in astronomy, namely the Messier catalog. It is studied within the framework of basic astronomy and there are enough objects for visual demonstration.

As the first task when working with this catalog, you can display all the catalog objects in equatorial coordinates in a stereographic projection or in a Mollweide projection (Fig.1).

Also, using this catalog, we can consider the problem of finding the coordinates of the center of the Galaxy, studying the subsystem of globular clusters, finding their average position.

2.2 FITS-files

Most astronomical data files are stored in a special Flexible Image Transport System (FITS) format. This format differs from classic graphic formats in that, in addition to the main image, it stores additional metadata about that image. Therefore, the first step is to teach students how to work with this format, for example, based on the analysis of images from the Hubble telescope. Interesting and accessible tasks

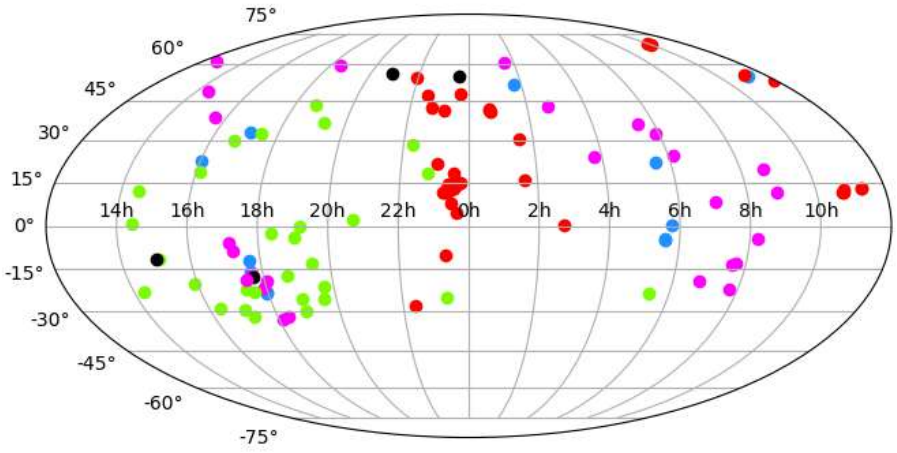

Fig. 1. Messier objects on the map in the Mollweide projection. Galaxies — red, open star clusters — pink, globular star clusters — green, nebulae — blue, others — black.

for schoolchildren here are: determining the background of the sky, counting the number of elements in a photo (stars, galaxies) and analyzing objects, for example, determining the size of the halo and the nucleus of the galaxy.

2.3 Hershel catalog

As an example of a modern catalog, we can consider the catalog of galaxies obtained by the Herschel Space Observatory, which is the predecessor of the James Webb Space Observatory, with the catalog of which it will be possible to work similarly in the future. And the first task when working with this catalog is a simple task — visualization of the catalog, i.e. displaying its objects — galaxies in a given area of the sky in equatorial coordinates.

Further analysis and search for correlations by parameters are already research work and depend on the level of further training of students. For example, one can study the correlation between the redshift of galaxies and their number in the region of the celestial sphere, limited by a certain radius.

2.4 The Hipparcos and Gaia catalog

Next, we propose to investigate the properties of variable stars according to the astronomical catalog created based on the results of the Hipparcos and Gaia space observatories.

Based on these catalogs, it is possible to study the spatial distribution of variable stars in our Galaxy in galactic coordinates and make sure that the stars gravitate

to a planar distribution, which means that our Galaxy has the appearance of a flat disk.

The next task is to independently obtain the "period-luminosity" dependence for classical cepheids according to the Hipparcos and Gaia catalog. This dependence is a very important stage in constructing the distance scale in the Universe — it allowed E.Hubble to determine the distances to other galaxies and build a Hubble diagram, which led to the discovery of the expansion of the Universe. And now schoolchildren and students can independently repeat this work using the catalogues of cepheids of modern space observatories and reproduce this dependence on their own.

3 Results and conclusions

According to the listed range of tasks, lessons were conducted for students of the Center for Pedagogical Excellence and the Lyceum of the Higher School of Economics. The teaching staff was highly appreciated and the significant usefulness of such classes was noted, since they:

1. introduce students to the latest achievements in the field of astronomical research;
2. teach scientific research skills;
3. cover several subject areas at once and establish interdisciplinary connections;
4. allow the use of interdisciplinary competencies to solve scientific problems.

In the course of this work, several final qualification papers have been completed and a textbook with a detailed analysis of each of the tasks is being prepared for publication.

References

Drobchik T. and Nevzorov B., 2018, Vocational education in Russia and abroad, 1, 29, p. 113
Korolev M.Yu., Petrova E.B., Chulkova G.M., 2023, Teacher XXI century, 1, 1, p. 71
Tihomirova E.N., Irodova I.A., 2017, Yaroslavl Pedagogical Bulletin, 2, p. 72

MODERN ASTRONOMY: FROM THE EARLY UNIVERSE TO EXOPLANETS AND BLACK HOLES

Comparison of educational results in Astronomy for high school students in St. Petersburg

V. Grigoryev[1,2]

[1] Crimean Astrophysical Observatory, p. Nauchny, Bakhchisaray, Crimea, 298409, Russia
[2] Lyceum "Physical-Technical High School", 8-3A Hlopina St, Saint Petersburg, 194021, Russia

Abstract. During five academic years from 2018 to 2024, students in grades 10 and 11 of three different High Schools in St. Petersburg studied the subject of Astronomy as part of the school curriculum under the guidance of the author of this study. 15 classes of at least 20 people were taught. During this time, several approaches of educational process were used, but the methodology of academic achievements in this subject was carried out in the most identical way. This paper describes the approaches of educational process during the designated time, describes the methodology for measuring academic achievements. Based on this methodology, measurable educational results were obtained in the subject of Astronomy among students, an analysis of these results was carried out, features were identified, and a justification for differences in academic achievements was proposed.

Keywords: general: miscellaneous — Interdisciplinary astronomy: Astronomy education — educational sciences: academic performance

DOI: 10.26119/VAK2024.186

1 Introduction

Throughout several academic years (2018-21, 2022-23) I gave regular Astronomy lessons for 11th grade students in three different educational organizations in St. Petersburg. In the 2023-2024 academic year, the course of Astronomy course was taught to the 10th grade participants as well. The teaching methodology was somewhat different, and the purpose of this study is to understand which of the methods ultimately gives what educational results, perhaps adjusted for the level of the educational organisation. By educational results, I mean the results of writing tests assigments (control works: CW-1 and CW-2) averaged by groups of students and topics.

Various sources that contain information on the comparison of homogeneous educational outcomes have been found, but it is primarily applied to university students ,(Pogrebnikov et al. 2021)or it forecasts bachelor's student performance based on the results of the Russian Unified State Exam (Zamkov, Peresetskiy 2013). It was not possible to find a comparison of the results of educational activities within the framework of one school, especially within one subject.

The three educational organizations (EOs) are: General education high school 564 (GEHS), The Lyceum 366 with advanced study of physics and mathematics (PhML) and Lyceum Physical-Technical High School (PTHS)[3]. In each of these EOs, I taught Astronomy in either two or three groups of senior students: 11A and 11B or 10A, 10B and 10C. Due to volume restrictions, not all the details will be pointed out here. It is recommended to read the entire article by following the link[4].

2 Approaches

In the 2018–21 (GEHS and PhML) academic years, the Astronomy course continued for two semesters. I was required to give each student six assessment grades per semester: five grades could be obtained for work throughout the half-year (homework, reports, participation in astronomical Olympiads, preparation for the CW and other bonuses), the sixth grade — for the CW.

The contents of the Astronomy course was naturally divided into topics. The first quarter of academic year is Astrometry (coordinates on the celestial sphere, culminations, time). The second quarter was devoted to the Solar system and celestial mechanics (characteristics and motion of planets, configurations, cosmic velocities). Before the New Year vacation, there was a CW-1 on the material covered in the semester. The third quarter was focused on Astrophysics (stellar magnitudes, physics

[3] http://school564.ru/, http://www.fml366.org/, http://www.school.ioffe.ru/
[4] https://vk.cc/cyxBgm

and evolution of stars, H-R diagram). The fourth quarter covered Galactic and Extragalactic astronomy. In the middle of May, the CW-2 on the material completed in the semester took place. In the 2022-24 (PTSH only) academic years the course was shortened to one semester, so two assessment grades per semester were given for the CW-s. The coursebook "Astronomy 10-11" by Charugin V.M. (2018) was used.

There were different approaches in different academic years:

- 2018–2019 —"Demanding approach". Self-solving tasks from the coursebook, additional series of problems, strict deadlines;
- 2019–2020 — "Mixed approach". A wide range of options for obtaining assessment grades (tasks from coursebook or an additional collection of problems book, individual homework assingments[5], different bonuses), the only requirement is the number of assessment grades;
- 2020–2021 — "Least demanding approach". The least stringent deadlines for tasks, the possibility of rewriting individual homeworks;
- 2022–2023 — as in previous approach, but the duration of the course is only one semester, no coursebooks;
- 2023–2024 — as in previous approach, but studying 10-th grades and using coursebooks for writing CW-s only, not for homeworks (due to amount of coursebooks).

3 Methodology for evaluating educational results

I consider the results of writing CW-s averaged by groups of students and by topics to be the main tool for evaluating the knowledge gained.

All academic years, the format of the CW-s was identical. The contents variants were individual, in each variant there were 14 questions (one question for one topic), in each of the questions there was one correct answer out of four options. The students had the opportunity to compose the first 10 questions on their own during the preparation for the CW (this was one more way to get the assessment, and the opportunity for me to quickly accumulate an extensive database of the questions), the questions from 11 to 14 were compiled by me and were associated with images displayed on the screen during the CW. In my opinion, the students' compilation of questions for the CW remarkably manifests the level of understanding of the material, even better than the CW itself. During the CW, the students were allowed to use their own notes, their coursebooks, their calculators (not smartphones), as well as reference data issued during the course.

However, in May of 2019-2020, an exception occurred: due to compelled distant homeschooling, the CW-2 was also carried out online with filling in a questionnaire

[5] How to create homogeneous variants, see my speech https://youtu.be/6LqgrWe7rC8 (PIEF-2021)

(as an individual homework), an astronomical hour was allotted for entering answers. In this regard, good results of the work could be expected.

The CW check was performed in automated mode in MS Excel. Thus the students knew their results the same evening when they wrote the test. Since the students took the tasks for themselves after the CW, they had an opportunity to appeal their results. There were successful appeals, because sometimes there were inaccuracies in the question, the answer was not recognized, an option number was forgotten, etc.

4 Results

The results are shown in the plots below (see Fig. 1 and Fig. 2). The charts are broken down by year and educational organization. One can say that the higher the percentage of a topic, the better the relevant group understands it. The larger the area occupied by the one colour plot, the better the whole material is understood on average. The average percentage (see Fig. 3) and deviation through all topics for each group of students was calculated additionally.

In the case of the CW-1 in the GEHS, there are no fundamental differences in the results, except that the 11A of 2019–2020 is slightly knocked out, perhaps this is the influence of the class tutor, or maybe it was just possible to assemble more "intellectual" class. One can notice a real "sagging" of the results in both classes in the PhML in 2019–2020 academic year, which may occur due precisely to a change in the approach: the requirements have become less stringent. At the same time, the results in one of the classes are even at the GEHS level. In the case of the PTSH 11th grades, one can see that the results are generally at the PhFML level, although slightly worse. I think this is adequate, especially considering that only six months of study were allocated for the astronomy course instead of a year, and even without coursebooks. With coursebooks in the 10th grades, the results became less scattered, while the control quality remained the same.

The results of the CW-2 in the case of the GEHS again do not demonstrate any significant change as a result of a change in methodology. The obvious outlier in the 2019-2020 academic year is explained by doing the CW at home at the computer (which makes it impossible to completely exclude the influence of communications) and, again, 11A performs clearly better than 11B, which probably indicates a greater number of clever students. I explain the less good results in CW-2 than in CW-1 in the PhML on average by the fact that Astrophysics is a significantly different science in its essence and content than what studied in the first semester (for example, half of celestial mechanics is included in the course of Physics). In case of the PTSH, the results look pretty even, in addition, 10th graders with coursebooks produce

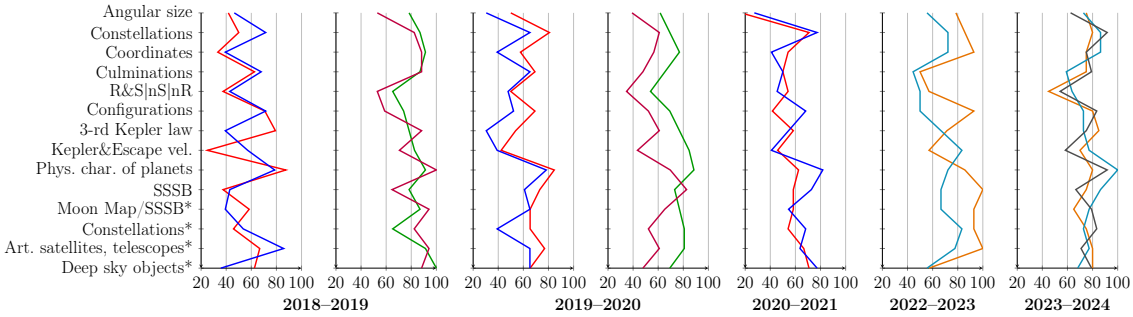

Fig. 1. The results of the CW-1: percentage of mastering a specific topic. Academic year is places under the specific plots. Groups are visualised with different colors: GEHS (11A, 11B), PhML (11A, 11B), PTHS (11A or 10A, 11B or 10B, 10C). Abbreviations used: R&S/nS/nR = star Rise and Set daily/star doesn't Set/star doesn't Rise, SSSB = Small Solar System bodies. Topics marked with * need an image.

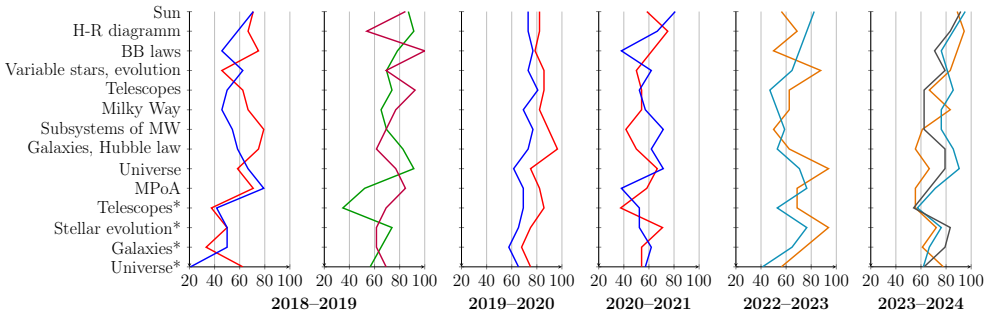

Fig. 2. The same as in Fig. 1, but for CW-2. Abbreviations used: H-R diagramm = Hertzshprung–Russel diagramm, BB = Black body, MW = Milky Way, MPoA = Modern Problems of Astronomy. Topics marked with * need an image.

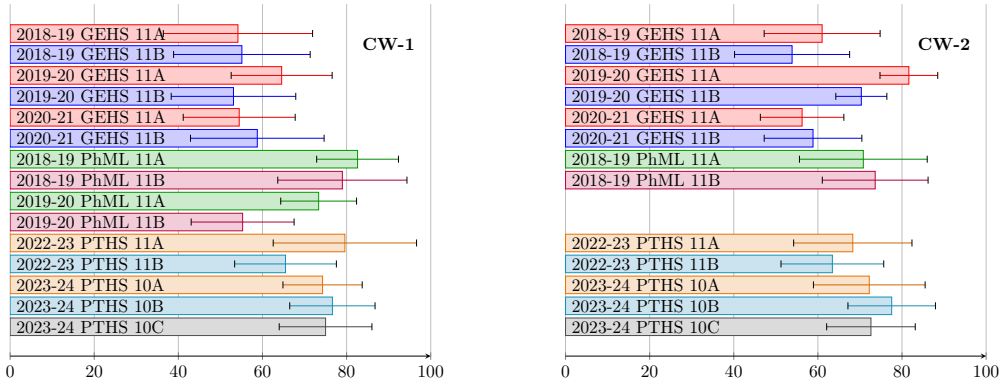

Fig. 3. Average percentage through all topics in CW-s and its deviation.

better results than 11th graders, and on average the same level of PhML. That is, in general, one can conclude that age has practically no effect on the studying of this course of Astronomy. In addition, the coursebook itself is intended for studying in grades 10-11.

5 Conclusion

As we can see, in the PhML, the results of doing the CWs are on average better than in the GEHS. This is quite natural: Astronomy is more understandable if you have a mathematical mindset, because there are many formulas, geometry is involved, etc. In case of the PTSH, the six-month course was mastered by students at the level of the annual course in the PhML.

However, what is more interesting, regardless of my approach to the pedagogical process, the results are on average the same, although in the case of PhML, it is possible that softening the requirements leads to slightly less good results, but this cannot be confidently stated, due to incomplete research in this EO. In addition, one can come to an obvious conclusion: having an opportunity to rely on the coursebook provides a better outcome than having no one.

References

1. Pogrebnikov, A. K., Shestakov, V. N., & Yakunin, Yu. Yu., 2021, Perspektivy nauki i obrazovania, Volume 54, 4 , p. 80
2. Zamkov O.O. and Peresetskiy A.A., 2013, Applied Econometrics, 30, 2 , p. 93
3. Charugin V.M., 2018 Astronomy 10–11 grades: coursebook for general educational school: base level // Prosveschenie, 2018, ISBN 978-5-09-053903-6.

Practical work on asteroid-comet hazard based on open data as a component of astronomical education

I. Kuznetsova and M. Prokhorov

Sternberg Astronomical Institute of M.V.Lomonosov Moscow State University,
13 Universitetkiy prospekt, Moscow, 119991 Russia

Abstract. Astronomical education is the basis for the worldview of modern man. However, not all universities and technical colleges in Russia teach astronomy courses. The proposed practical work based on open scientific data can be used in the system of astronomical education for both schoolchildren and students of natural sciences.

Keywords: Moon; minor planets, asteroids: general; comets: general; astronomical databases: miscellaneous

DOI: 10.26119/VAK2024.187

1 Introduction

It all started in 1699, when by decree of Tsar Peter I, the School of Mathematical and Navigational Sciences appeared in Moscow. It was the first educational institution in Russia where astronomy was taught. The Sukharev Tower was built specifically for it in 1692-1695, where an observatory was equipped. "1/2 of the school's graduates, in addition to sailors, included engineers, artillerymen, teachers at other schools, surveyors, architects, civil officials, clerks, and artisans" (Veselago 1852). From that moment on, the science of celestial bodies became a compulsory discipline in technical schools: In 1715 the School was transferred to the New Capital, where the Maritime Academy was created on its basis.

In the 19th century in the Russian Empire, astronomy ("cosmography") was taught at the highest level. The fact that astronomy has been studied in secondary schools for 100 years is a unique fact in world pedagogy. In the Russian Empire, there were observatories in the following cities: Vilnius (1752), Kharkov (1808), Dorpat, now Tartu (1810), Moscow (1831), Kazan (1838), St. Petersburg, Pulkovo (1839), Kiev (1845) , Odessa (1871), Tashkent (1874), Simeiz (1908), and astronomy was taught at the following universities: St. Petersburg, University of Imperator's Acasemy of Sciences (1724), Moscow ($\sim$1764), Derpt (1802), Vilnus (1803), Kazan (1810), St. Petersburg (1819), Kyiv (1833), Odessa (1865).

In the first years of the USSR, the teaching of astronomy deteriorated significantly. But already from 1932 astronomy became an independent subject at school (35 hours). Its main purpose is the fight against religious views. A real astronomical boom occurred in the USSR with the beginning of the Space Age.

The second "failure" of astronomy occurred in 1993, when "the school was excommunicated from astronomy". Astronomical olympiads and scientists involved in the popularization of astronomy helped to survive it. Since 2017, astronomy has returned to the School Curriculum. However, only 4 universities teach a classical course in astronomy: in Moscow, St. Petersburg, Kazan and the Urals.

2 New type of practical works

We think there is a gap in astronomy teaching that can be filled with interesting, practical works based on open-access scientific data. We have developed one such work, which estimates the frequency of asteroid impacts on Earth based on crater count on the Moon and Mercury. This work has methodological advantages over traditional ones: 1) it touches on a topic that is relevant and interesting to students; 2) forms an objective idea of the diverse connections of the studied objects in nature; 3) is multidisciplinary, containing a large set of reference data from various fields;

4) the work is visual; 5) allows you to vary the material used; 6) does not require expensive equipment; 7) allows distance learning; 8) can be used in teaching various specialties (but not professional astronomers).

Conducting laboratory work involves:

- introduction to the concept of asteroid-comet hazard;
- study of possible mechanisms for the formation of craters and calculation of their sizes on the Earth, on the Moon and on Mercury depending on the parameters;
- training in the basics of research activities;
- estimating the frequency of asteroid impacts on Earth from photographs of the Moon and Mercury.

The data for the work — photographs of the Moon, reference data on geology and physics — was taken from open sources.

The proposed laboratory work allows the student to independently conduct a small but complete scientific research on a current topic and compare his results with the results of modern scientists. In laboratory work, the student gets acquainted with and operates with data from several sciences: physics, astronomy, geology. This approach encourages the student to become more familiar with scientific activities earlier and more deeply.

Even without changing its plan and content of laboratory work, the large volume of the archive of source data makes it possible to provide a large number of students with independent source materials. At the same time, you can easily modify the work in several ways. For example, assume that the image scale is not constant within the frame. The change in scale may be due to the tilt of the spacecraft camera towards the lunar surface. In this case, the student will be required to construct a scale model within the fragment to count craters.

Another possibility is to calculate the density of craters on the more cratered continents of the Moon and on the seas less rich in craters. This difference is explained by the fact that in the first billion years of the Moon's existence, the seas were filled with lava, which hid the previously formed craters. The goal of such work might be to compare asteroid impact rates during the "late heavy asteroid bombardment" of the Solar System with impact rates in later periods (including the present). For this option, the reference book must include the ages of the lunar seas.

Another option is to determine and compare the frequencies of asteroid impacts on the Moon and Mercury (as an option: on the Moon and Mars). The end result of this option will be to compare the frequency of asteroid impacts in different parts of the Solar System (at different distances from the Sun).

The practical work consists of four parts: *review*, containing a brief overview of the problem of asteroid-comet hazard, *theoretical*, *practical* and *methodological*. The

theoretical part suggests solving assessment problems. Such problems, containing rather rough estimates, are useful as methodological point of view: they use simple and understandable physical models, to solve them it is necessary to involve various data from independent sources, and the estimates made are comparable with measurements presented in the relevant scientific sources.

In the practical part, it is proposed to measure the sizes of craters and count their number on a section of the lunar surface from its photograph, and then estimate the frequency of events associated with impact cratering. The frames were taken from the open archive of photographs[1] of the Lunar-Orbiter spacecraft. In this archive, several of the largest craters are circled on each frame, the diameters of which are known (but not indicated in the figure). This data allows us to determine the scale for measuring the remaining craters and the surface area of the Moon included in the frame. As a result of the calculations, the average frequency of objects falling on the Moon and Earth during the existence of the Solar System (4.6 billion years) is estimated.

Unlike the Moon, on Earth you can find either the youngest craters that have not yet been destroyed by erosion, or the largest. Today, about 200 craters with proven impact origin are known on Earth (AKO 2010). Of these, only 40 are suitable for statistical analysis, i.e. they have a diameter of more than 3 km and an age of less than 250 million years, and have been dated with an accuracy better than 10 million years. The average age of these craters is approximately 50 million years (Napier 2006), which is approximately 50–100 times less than on the Moon. Analysis of impact craters on Earth says that the fall of bodies creating craters with a diameter of $D > 1$ km occurs approximately once every 1000 years (Medvedev et al. 1996). This is about 8 times rarer than estimates for craters on the Moon.

The methodological part contains an approximate description of the sequence of work, methodological recommendations and the results of the time management we carried out when testing the methodology.

3 Conclusions

Astronomy is a discipline that shapes the worldview of modern man. We propose to strengthen its position both in universities and in schools by offering practical work in the form of a small research project, which contains all the necessary information and a description of the methodology for its implementation based on open scientific sources. The proposed practical work is the first such work. The advantage of this is that a student can independently do a small but comprehensive scientific research

[1] http://www.lpi.usra.edu/resources/lunarorbiter/

on a current topic and compare his results with the results of modern scientific research. It is also good that the student gets acquainted with and operates with data from several sciences: physics, astronomy, geology. This stimulates earlier and deeper familiarization with scientific activities. The work can be carried out at any university and can also be included in distance learning courses. It should also be noted that there is great potential variability in these work. Even without changing plan and content of it, the large volume of the source data archive makes it possible to provide a large number of students with independent source materials. At the same time, you can easily modify the work in several ways.

Acknowledgements. This work is dedicated to the 300th anniversary of the Russian Academy of Sciences.

References

2010, Asteroid-comet danger. Yesterday, today, tomorrow, Moscow: Fizmatlit

Medvedev Yu.D., Sveshnikov M.L., Sokol'skii A.G., et al., 1996, Asteroid-comet hazard, St. Petersburg: ITA RAS

Napier W.M., 2006, Monthly Notices of the Royal Astronomical Society, 366, p. 977

Veselago F.F., 1852, Essay on the history of the naval cadet corps, St. Petersburg

Creation and development of domestic scientific and educational space infrastructure and its use as a tool for ground-based and space astronomy

K. Starikov

Saint-Petersburg State University, Saint-Petersburg, 199034 Russia

Abstract. An overview of current advances in the use of small spacecraft for astronomical research and space education is provided. Existing projects, their goals, achievements and plans for implementation are reviewed. The current results of the authors in creating a scientific and educational digital platform for research and educational space activities are presented.

Keywords: space vehicles, site testing, instrumentation: miscellaneous

DOI: 10.26119/VAK2024.188

1 Introduction

Technologies are becoming more and more accessible. Today in Russia there are programs that allow scientific and educational organizations (universities and schools) to launch their own small spacecraft. These satellites, having a small size and standardized shape, make it possible not to spend large amounts of money on a mission, while at the same time they have great potential for conducting serious scientific experiments and research. An example of this is the scientific results obtained from dozens of small satellites launched by organizations in different countries in recent years. In addition, projects are being developed in the ground segment, which, with the right approach and connection with space technologies, can create a unique research and educational infrastructure in the world for the development of methods for various astronomical activities.

2 Small space technologies

The first spacecraft, which were launched in the 60–70s of the last century, weighed more than one ton, and were used for a seemingly simple task: photographing the earth's surface from space.

With the rapid development of microelectronics, it became possible to create lighter satellites, and the number of tasks performed by one device increased. In 1999, a satellite format called CubeSat was invented. Its goal was to reduce the cost and time of satellite development and increase the availability of launches.

One of the important requirements for this format is the monolithic structure of the spacecraft, i.e. a CubeSat cannot contain detachable parts. This condition makes it possible to reduce the formation of space debris in Earth orbits. Another important condition for the CubeSat configuration is that it is prohibited to install explosive devices or tanks with explosive substances, as well as tanks under a pressure of more than 1.2 atmospheres, on board the device. This limits the range of possible equipment (primarily propulsion systems), but it creates the possibility of launching devices from the International Space Station without a threat to the crew. This launch scheme is considered promising in light of the ease of manufacturing devices, the developing technology for creating satellite formations and the regularity of launches of transport spacecraft to the ISS.

Figure 1 made by Erik Kulu (Nanosats[1] database) shows launch statistics by type of organization responsible for the satellite. Significant increase in recent years is present. Despite the fact that the majority are commercial satellite networks, the

[1] https://www.nanosats.eu

number of scientific and educational equipment on nanosatellites does not cease to grow from year to year. This can also be evidenced by the large number of publications on the results of experiments carried out on small satellites in recent years.

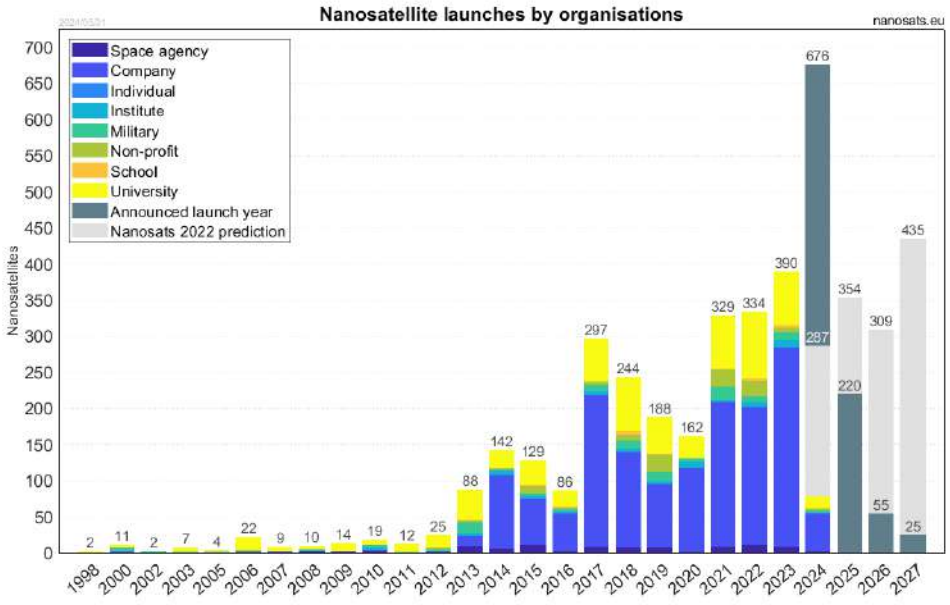

Fig. 1. Number of CubeSat launches by organizations.

For example, in Bogomolov et al. (2022) Moscow State University has shown the development of a project for a multi-satellite constellation designed to monitor cosmic radiation. A number of small satellites of CubeSat format by the institution were launched into selected orbits crossing the wide range of magnetic drift shells. The primary scope for the project is the operational monitoring of near-Earth's radiation environment, i.e. fluxes of electrons and protons of Earth's radiation belts and energetic particles of solar and galactic origin. This multi-satellite constellation made it possible to simultaneously measure particle and quantum fluxes in various regions of near-Earth space using the same type of instruments. A special compact detector of gamma quanta and energetic charged particles (electrons and protons) DeCoR has been developed for these satellites, allowing radiation monitoring using CubeSats.

According to Münz et al. (2024), gamma-ray burst detection was implemented on the GRBAlpha and VZLUSAT-2 CubeSats. These satellites carried a pair of identical

detectors. These instruments, which detect gamma rays in the range of $30-900$ keV, consist of a 56 cm^2 5 mm thin CsI(Tl) scintillator read-out by a row of multi-pixel photon counters (MPPC or SiPM). The scientific motivation is to detect gamma-ray bursts and other HE transient events and serve as a pathfinder for a larger constellation of nanosatellites that could localize these events via triangulation. In early July 2024, GRBAlpha detected 140 such transients, while VZLUSAT-2 had 83 positive detections confirmed by larger GRB missions. Almost a hundred of them are identified as gamma-ray bursts, including extremely bright GRB 221009A and GRB 230307A, detected by both satellites. Authors were able to characterize the degradation of SiPMs in polar orbit and optimize the duty cycle of the detector system also by using SatNOGS radio network for downlink.

An example of achieving results using astrometry is the Bobcat-1 CubeSat mission. Croissant et al. (2020) shows the mission design with a very detailed description of all the decisions taken during the mission preparation phase. The main objective of the mission was to evaluate the performance of GNSS inter-constellation time offset estimation from Low Earth orbit (LEO). A preliminary data analysis was performed in Croissant et al. (2021).

3 Ground technologies for small space

Recently, open technologies for the ground segment have been actively developing. A striking example, described in Croissant et al. (2022), is SatNOGS — a network of satellite ground stations around the world, optimized for modularity, built from readily available and inexpensive tools and resources. The rate of Low Earth Orbit (LEO) satellite launches increases with the participation of old and new entities. In this growing environment, SatNOGS provides many tools to track, identify, receive telemetry from sateliites, monitor them and assist operators in command/control operations. SatNOGS has built a global community dedicated to its values of free and open source code, developing ground station hardware designs (antennas, rotators, electronics), SDR-based communications software, satellite planning and mission monitoring platforms. Although SatNOGS has created a huge number of useful tools over its history, user experience shows that integrating this type of network into the educational and scientific process remains difficult. To achieve the goals of making this kind of technology more useful for schools and universities, the SONIKS project was created. It is an open source project, as it is based on SatNOGS technologies, but the main goal of the project is to create a new scientific and educational environment for the development of various types of important work related to space.

4 Space-π

Our domestic space infrastructure for educational and scientific purposes is gradually developing. At the moment there are two projects which provide opportunities to launch scientific and educational missions in space: Space-π and Universat (Roscosmos).

Universat is focused only on solving specific applied problems. Space-π is more of a scientific and educational project, in which schoolchildren, students, universities and domestic companies participate. The project allows schoolchildren to learn how small spacecraft are designed, how a payload is created and how a space experiment is implemented with its help. Young people study systems for obtaining space information and the possibilities of controlling a satellite in orbit.

When implementing their ideas, schoolchildren receive professional support from university professors, designers, programmers — all those who create satellite platforms, payloads and ground stations.

The goal of Space-π is to form a network of 100 CubeSats within several years for the mass involvement of school-age youth in space technology. As of July 2024, the Space-π project has launched 45 satellites since its start in 2021. These CubeSats have been used for various types of scientific and applied missions: remote sensing, observations of the Sun and its flares, deep space observation, testing of space components and technologies, the Internet of Things, launching a lilac sprout, etc.

5 SONIKS

In 2023, the domestic open-source educational project SONIKS[2] — Network of complexes of open ground research stations – began operating. Based on SatNOGS technology, its main objectives are scientific research and educational areas. SONIKS is focused on developing new open and easy ways to connect domestic youth — students and young scientists — with space research and modern technologies, providing free access to all data and code base developed.

One of the current achievements is the launch of a satellite radio signal reception network. Thanks to the Geoscan company, which provided 50 ground stations with antennas throughout Russia free of charge, schoolchildren from different regions of the country can now receive signals from many satellites. Currently, the SONIKS network contains information on more than 1800 satellites and 3482 transmitters. At the moment, more than 30 ground stations are connected to the network. Over the 8 months of network operation, more than 5.5 million data packets were received from

[2] https://sonik.space

satellites in space. The platform itself is open to all. Users can work with satellite data for educational or research purposes: space photos, data from satellite payloads (sensors, receivers, engines) and telemetry.

This platform is unique for Russia and opens up a lot of opportunities for the development of domestic scientific and educational infrastructure. The development of an open radio telescope and an open network of optical ground stations is planned for the future.

6 Summary

In conclusion, it should be noted that in Russia today there is a very good pace of development of the scientific and educational space, which, as my work has shown, is capable of solving serious research problems with a thorough approach. To cope with such a pace, we need both government support in the form of developing projects to launch scientific and educational satellites and obtain data from these devices,as well as local work — in universities and scientific organizations — creating scientific laboratories and design bureaus where students, graduate students, and young scientists could work together with professionals on real projects that will be launched into low-Earth orbit, and in the future, with real series of observations obtained using their own equipment. Such activities will certainly have a positive impact on the youth and the scientific environment — making it more accessible, more exciting and more interesting to implement. It can also help increase scientific data for certain experiments and ultimately reduce the cost of expensive scientific equipment that has been launched so far.

References

Bogomolov A.V., Bogomolov V.V., Iyudin A.F., et al., 2022, Universe, 8, 5, id. 282

Croissant K., Jenkins G., McKnight R., et al., 2020, Proceedings of the 33rd International Technical Meeting of the Satellite Division of The Institute of Navigation, ION GNSS+ 2020, p. 1383

Croissant K., Jenkins G., McKnight R., et al., 2021, Proceedings of the 2021 International Technical Meeting of The Institute of Navigation, January 2021, p. 625

Croissant K., White D., Adamopoulos V., et al., 2022, 36th Annual AIAA/USU, Conference on Small Satellites, id. SSC22-VI-04

Münz F., Řipa, J., Pal A., et al., 2024, Proc. of SPIE, 13093, id. 130936J